**pmd*CRC**

Project Y4 Final Report – Parts III & IV
January 2005 – July 2008

# Concepts to targets: a scale-integrated mineral systems study of the Eastern Yilgarn Craton

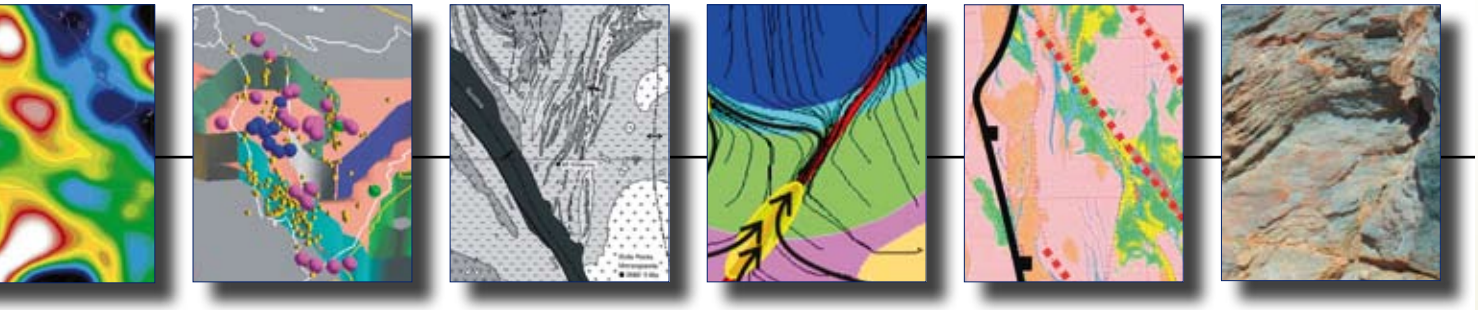

Compiled by the Y4 Project Team

pmd*CRC

*Map of district-scale Eastern Goldfields gold prospectivity generated by integrating the new process understanding of the gold mineral system with practical mappable proxies of these processes. This map represents a 'test' of the Five Answers proposed by the Y4 project team and has 'discovered' over 75% of the contained gold in ~10% of the area. See Part III for further details.*

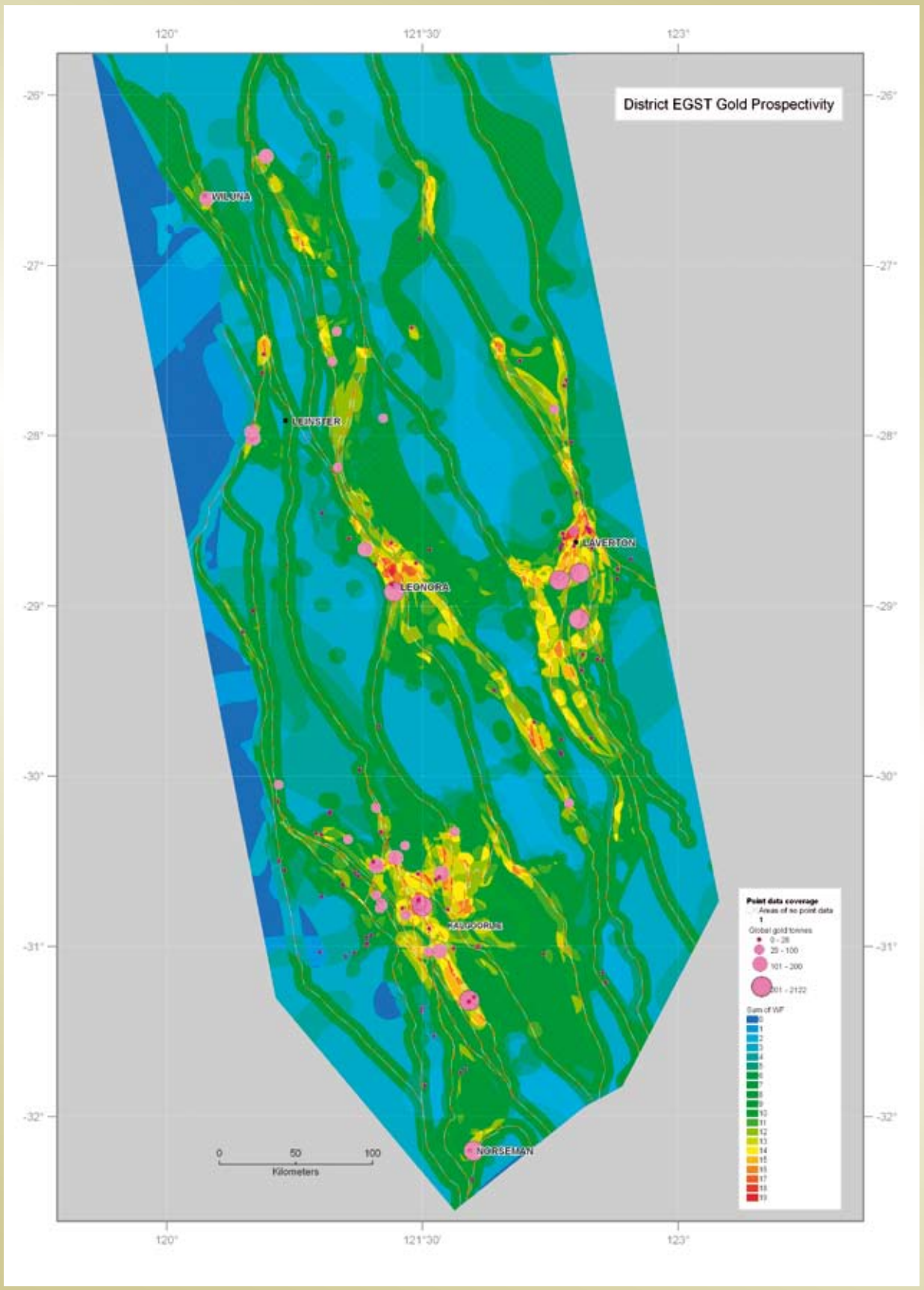

## Core Partners





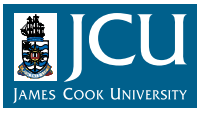




## Sponsors















## CONTENTS


Part III: The science behind the five answers 10

3.1 Question 1: Geodynamics of the Eastern Goldfields Superterrane 10

Abstract 10

3.1.0 Introduction 10

3.1.1 The Yilgarn Craton 11

3.1.2 Tectonic constrains from greenstones 13

3.1.2.1 ~2.94 Ga time slice 14

3.1.2.2 ~2.81 Ga time slice 14

3.1.2.3 Nd depleted-mantle model age ($T_{DM}$) map excursus 14

3.1.2.4 ~2.76 Ga time slice 19

3.1.2.5 ~2.715–2.65 Ga time slice 19

3.1.2.6 2.715–2.69 Ga tectono-stratigraphic associations 19

3.1.2.7 2.69–2.665 Ga tectono-stratigraphic associations 22

3.1.2.8 2.665–2.650 Ga tectono-stratigraphic associations – Late Basin deposition 24

3.1.3 Tectonic constraints from granites 26

3.1.3.1 High-Ca granites 27

3.1.3.2 Low-Ca granites 30

3.1.3.3 High-HFSE granites 30

3.1.3.4 Mafic granites 30

3.1.3.5 Syenites 30

3.1.4 Tectonic constraints from the deformation history 32

3.1.4.1 $D_1$ – ENE extension (<2.67 Ga) 32

3.1.4.2 $D_2$ – ENE contraction (east ~2.670 Ga, west ~2.665 Ga) 33

3.1.4.3 $D_3$ – mid orogenic ~ENE extension (east ~2.665 Ga, west ~2.660 Ga) 33

3.1.4.4 $D_4$ – (a) ENE and (2.655 Ga) (b) ESE contraction (east ~2.655 Ga, west ~2.650 Ga) 34

3.1.4.5 $D_5$ – NE-SW contraction (east <2.655 Ga, west <2.650 Ga) 35

3.1.4.6 Post $D_5$ deformation 35

3.1.5 Metamorphic constraints on tectonic models 35

3.1.5.1 Ma – rare, high-T, high-G (2.720–2.685 Ga) 36

3.1.5.2 M1 – discrete, medium-P, low-G metamorphism (2.720–2.685 Ga) 36

3.1.5.3 M2 – granite pervaded, moderate-G, regional metamorphism (2.685–2.665 Ga) 37

3.1.5.4 M3a – extension related, high-G metamorphism (2.665–2.650 Ga) 38

3.1.5.5 M3b – fault kinematics, high-G alteration and gold mineralisation (2.650–2.620 Ga) 39

3.1.6 EGST Geodynamics and the Au mineral system 39

3.1.6.1 Preferred Geodynamic model – para-authochtonous convergent margin model 41

3.1.7 Acknowledgements 45

3.1.8 References 45

3.2 A revised structural-event framework for the Eastern Goldfields Superterrane 53

Abstract 53

3.2.1 Introduction 53

3.2.2 Previous Structural Frameworks 55

3.2.2.1 DE: Early Extension 56

3.2.2.2 D1: N-S contraction 56

3.2.2.3 Late Basins 56

3.2.2.4 D2: E-W contraction 56

3.2.2.5 Local Extension 57

3.2.2.6 D3: ongoing E-W contraction 57

3.2.2.7 D4: late contraction 58

3.2.2.8 Late extension (collapse) 58

3.2.2.9 Granite structural studies 58

3.2.3 A new structural-event framework 58

3.2.3.1 Introduction 58

3.2.3.2 Changes to the paradigm 59

3.2.3.3 D1: long-lived extension and granite-greenstone formation 60

3.2.3.4 D2: ~ENE-WSW contraction and termination of an arc 62

3.2.3.5 The seismic insights for crustal architecture – extension or contraction? 64

3.2.3.6 D3: Granite doming, extension and Late Basin Formation 65

3.2.3.7 D4: progressive contraction and sinistral strike-slip 70

3.2.3.8 D5: dextral strike-slip 72

3.2.3.9 D6: Low-strain vertical shortening 75

3.2.3.10 D7 and other minor events 75

3.2.4 Timing constraints of deformation 75

3.2.4.1 D1 constraints 76

3.2.4.2 D2 constraints 76

3.2.4.3 D3 constraints 76

3.2.4.4 D4 constraints 76

3.2.4.5 D5 constraints 77

3.2.4.6 Post D5 and younger event age constraints 77

3.2.5 Conclusions and implications for predictive gold discovery 77

3.2.6 Acknowledgements 77

3.2.7 References 77

3.3 Question 2: Big systems-big signatures – anatomy of the Archaean Yilgarn Craton and implications for world-class gold mineral systems 83

Abstract 83

3.3.1 Introduction 83

3.3.2 West Australian lithosphere 84

3.3.3 Yilgarn lithospheric architecture 85

3.3.3.1 Tomographic features of the Yilgarn Craton 86

3.3.3.2 Geodynamic interpretations of the tomography 87

3.3.3.3 Tomography and implications for big systems 89

3.3.4 Crustal architecture 89

3.3.4.1 Crustal structure inferred from potential fields 89

3.3.4.2 Crustal structure inferred from geochemistry-stratigraphy, isotopes and inheritance patterns 89

3.3.4.3 Crustal structure inferred from Receiver Function velocity profiles 93

3.3.4.4 Crustal structure inferred from seismic reflection profiles 96

3.3.4.5 Crustal structure inferred from wide-angle seismic reflection survey 101

3.3.4.6 Crustal structure inferred from magnetotelluric (MT) profiling 102

3.3.5 Integrated 3D architecture of a world-class gold mineral system: implications for predictive mineral discovery 105

3.3.5.1 Terrane boundaries 105

3.3.5.2 Lithosphere-Asthenosphere boundary (LAB) 105

3.3.5.3 3D architecture 106

3.3.5.4 Kalgoorlie: the great coincidence 107

3.3.6 Conclusions 108

3.3.7 Acknowledgements 108

3.3.8 References 108

3.4 Question 3: Multiple fluid reservoirs in Eastern Yilgarn gold systems 113

3.4.1 Introduction 113

3.4.2 Section 1: Alteration mineralogy and fluid inclusion constraints on end-member fluids and chemical gradients 113

3.4.2.1 Deposit- to district-scale zoning patterns 113

3.4.2.2 Constraints on temporal evolution of fluids 117

3.4.2.3 Mineralogical constraints on redox and pH 117

3.4.2.4 Chemical gradients and fluid types 121

3.4.3 Section 2: Isotopic constraints (S, C, O, Ne, Ar, Pb and Sr) on fluid reservoirs and chemical gradients in Eastern Yilgarn gold systems 123
3.4.3.1 Introduction 123
3.4.3.2 Stable isotopes of sulphur, carbon and oxygen 124
3.4.3.3 $\delta^{13}C$ of carbonate: evidence of mantle $CO_2$ reservoir 125
3.4.3.4 Influence of redox state on $\delta^{13}C$ of carbonate 125
3.4.3.5 Sources of methane and equilibrium between reduced and oxidised C species 127
3.4.3.6 Mantle methane: Evidence from noble gas studies 129
3.4.3.7 Redox effects on $\delta^{34}S$ sufides and sulphates 130
3.4.3.8 S, Sr and Pb isotope contraints on $SO_2$/sulphate reservoir(s) 132
3.4.3.9 Positive $\delta^{34}S$ sulphide values and constraints on the redox states 136
3.4.3.10 Controls on variation of $\delta^{18}O$ in carbonate: T versus activity of $H_2O$ 137
3.4.3.11 Deuterium isotopes and meteoric fluids in Archaean Au deposits 139
3.4.4 Section 3: Concept and characteristics of end-member fluids: a discussion 139
3.4.4.1 Introduction 139
3.4.4.2 Are multiple fluids and mixing models necessary? 140
3.4.4.3 Fluid 1: Ambient Fluid 140
3.4.4.4 Fluid 2: Volatiles of magmatic affinity 142
3.4.4.5 Fluid 3: Redox variation with depth, the crustal continuum model and origin of the reduced fluid 142
3.4.5 Section 4: Deep Earth Fluids 145
3.4.5.1 Introduction 145
3.4.5.2 The oxidation state of the mantle 145
3.4.5.3 Composition of hydridic fluids 146
3.4.5.4 Pathways of hydridic fluids through the crust 147
3.4.5.5 Signatures of hydridic fluids in the crust 147
3.4.6 References 149
3.5 Question 5: Depositional processes in Eastern Yilgarn gold systems 154
3.5.1 Introduction 154
3.5.2 Fluids, Chemical Gradients and Fluid Mixing 154
3.5.3 Constraints on the chemical gradients 156
3.5.3.1 Introduction 156
3.5.3.2 Evidence of redox gradients 156
3.5.3.3 Evidence of gradients in $H_2O$ activity and salinity 157
3.5.3.4 Evidence of pH gradients 157
3.5.3.5 Evidence of sulphur activity gradients 158
3.5.4 Mapping Fluid Pathways and Chemical Gradients in the Victory–Defiance Complex, St Ives 159
3.5.4.1 Introduction 159
3.5.4.2 Mapping an upflow zone of oxidised fluids 159
3.5.4.3 Mapping lateral flow of oxidised fluid 163
3.5.4.4 $\delta^{13}C$ mapping of reduced fluid upflow zones and lateral flow 165
3.5.4.5 The distribution of fuchsite: Mapping reduced and acid domains 166
3.5.5 Summary of Gold Transport and Depositional Mechanisms 166
3.5.6 Conclusions 167
3.5.7 References: 167
3.6 Reactive transport models: from geochemistry to geophysics to exploration targets 169
Abstract 169
3.6.1 Introduction 169
3.6.1.1 Background to reactive transport modelling 169
3.6.1.2 Geophysical modelling of reactive transport models 169
3.6.2 Results 171
3.6.2.1 Geophysical signatures 171
3.6.2.2 Differing station spacings 171
3.6.3 The Victory-Defiance region, St Ives Gold Mine 172
3.6.4 Implications for exploration 174
3.6.5 References 175
3.7 Archaean gold mineralisation in the Eastern Yilgarn: Insights from numerical models 177
3.7.1 Introduction 177
3.7.2 Insights from numerical models 177
3.7.2.1 Geodynamics 177
3.7.2.2 Architecture 183

3.7.2.3 Fluid sources and reservoirs 184
3.7.2.4 Fluid pathways and drivers 185
3.7.2.5 Depositional mechanisms 188
3.7.3 Conclusions 189
3.7.4 References 189

3.8 Architecture and geodynamic evolution of the St Ives region, south central Kalgoorlie Terrane, Western Australia 191
Abstract 191
3.8.1 Introduction 191
3.8.2 Regional geological setting 192
3.8.3 Mineralisation 192
3.8.4 Stratigraphic architecture in the St Ives region 194
3.8.4.1 Felsic and mafic intrusions 194
3.8.5 Regional 3D architectural setting 197
3.8.6 Geodynamics and structural history of the St Ives gold camp 201
3.8.6.1 Previous work 201
3.8.6.2 A new structural framework for the St Ives region 202
3.8.7 Discussion and exploration implications 210
3.8.9 Conclusions 212
3.8.10 Acknowledgements 212
3.8.11 References 212

3.9 Structural evolution of the Victory to Kambalda region of the St Ives gold camp: the role of early formed structures on the development of a major gold system 218
3.9.1 Introduction 218
3.9.2 Methodology 219
3.9.3 Structural interpretation and field observations 223
3.9.3.1 Structural variation in D2/D4 folding along strike 223
3.9.3.2 WNW-trending faults 228
3.9.3.3 Early D3 extension syn-late basin development 236
3.9.3.4 Transpressional and transtensional zones 236
3.9.3.5 Late stage dextral faulting (D5) 243
3.9.4 Proposed structural evolution 245
3.9.4.1 Early D1 extensional architecture 245
3.9.4.2 D2 inversion (E-W compression) 248
3.9.4.3 D3 Extension and late basin development (NE-SW extension) 250
3.9.4.4 D4 Main stage gold mineralization (E-W to WNW-ESE compression) 251
3.9.4.5 D5 late stage dextral faulting and reactivation (NE-SW shortening) 252
3.9.5 Acknowledgements 252
3.9.6 References 253

3.10 Chemical architecture of the Leviathan Complex, St Ives Gold Camp 254
3.10.1 Introduction 254
3.10.2 Regional geological setting 254
3.10.3 Geological architecture of the Leviathan Complex 254
3.10.3.1 Introduction 254
3.10.3.2 Geological and structural architecture 257
3.10.3.3 Fabric development 264
3.10.4 Chemical architecture of the SIGC and the Leviathan Complex 268
3.10.4.1 Camp Scale zoning 268
3.10.4.2 Hydrothermal alteration mapping in chemical space 271
3.10.5 Hydrothermal alteration mapping in the Leviathan complex 273
3.10.5.1 Distribution of magnetite and pyrrhotite 273
3.10.5.2 Distribution of epidote, biotite, amphibole and anhydrite 277
3.10.5.3 Tracking redox switches with sulphur and carbon isotopes 281
3.10.5.4 Intersecting fabrics and gold grade 281
3.10.6 Discussion 282
3.10.7 Conclusions 288
3.10.8 References 289

3.11 Architectural and geodynamic controls during gold mineralisation around the Archaean Scotia-Kanowna Dome, Kalgoorlie Terrane, Western Australia 291
Abstract 291
3.11.1 Introduction 292
3.11.2 Regional geological setting 292
3.11.2.1 Deposit locations and production histories 294
3.11.3 3D architecture of the Scotia-Kanowna Dome 296

3.11.4 Detailed architecture and structural controls on gold mineralisation in key areas 298
3.11.4.1 Paddington 298
3.11.4.2 Kanowna Belle 300
3.11.4.3 Ballarat-Last Chance 306
3.11.4.4 Red Hill 309
3.11.4.5 Gordon-Sirdar area 311
3.11.4.6 Mulgarrie 312
3.11.4.7 Woodcutters 314
3.11.5 Regional correlation and implications for predictive mineral discovery 316
3.11.6 Conclusions 321
3.11.7 Acknowledgements 321
3.11.8 References 321
3.12 The 4D architecture of the Laverton camp, Eastern Yilgarn Craton 325
Abstract 325
3.12.1 Introduction 326
3.12.2 Regional fault orientation and granite/ gneiss domes 327
3.12.3 Stratigraphy 328
3.12.4 Deep tapping faults (fluid pathways lower crust) 329
3.12.5 Constraining the 3D architecture 330
3.12.5.1 Cross-sections 332
3.12.5.2 Gravity data modelling 333
3.12.6 Structural and lithological interpretations 334
3.12.6.1 D1 334
3.12.6.2 D2 337
3.12.6.3 D3a/D3b 337
3.12.6.4 D4a 338
3.12.6.5 D4b 338
3.12.6.6 D5 339
3.12.7 Fluid/melt focussing 339
3.12.7.1 Au deposition (Sunrise Dam and Wallaby deposits) 339
3.12.7.2 Porphyries 341
3.12.8 Generic numerical models: results for models with a range of far-field stress orientations 342
3.12.8.1 Painted faults 344
3.12.9 Conclusions 346
3.12.10 References 347
3.13 Fluid-chemical evolution of the Sunrise Dam mineral system 350
3.13.1 Introduction 350
3.13.2 Geological Setting 350
3.13.2.1 Lithology 350
3.13.3 Methods for Determining Geochemical Architecture and 4D Evolution 350
3.13.3.1 Workflow used at SRD 351
3.13.4 3D Geochemistry 351
3.13.4.1 Assay Isosurfaces 351
3.13.5 3D Stable Isotopes 352
3.13.5.1 Carbon 352
3.13.5.2 Oxygen 352
3.13.5.3 Sulphur 352
3.13.6 3D Logging Data 355
3.13.6.1 Banded Iron Formation (ACI) 355
3.13.6.2 Fuchsite Alteration 356
3.13.7 Previous Geochronology 356
3.13.7.1 Molybdenite 358
3.13.8 Geochemistry and Petrography 358
3.13.8.1 Key Alteration Indices 358
3.13.8.2 Thick Laminated Veins 359
3.13.8.3 Target 9 porphyry Gold 359
3.13.8.4 Mafic Unit 361
3.13.8.5 Porphyry Geochemistry 363
3.13.9 Assemblages and Fluids at SRD 363
3.13.9.1 Nominally Reduced assemblages 363
3.13.9.2 Nominally Oxidised assemblages 364
3.13.10 Mineral Assemblages and Textures 364
3.13.10.1 Thick Laminated Veins (SSZ) 364
3.13.11 Apatite Chemistry and Deep Fluids 372
3.13.12 Summary of the chemical evolution of SRD 374
3.13.13 References 375
Part IV: Project Deliverables (see DVD) 377
Summary of Deliverable #1 New time-space event history database, charts, and maps 377
Summary of Deliverable #2 Reports on an updated structural history/stratigraphy (unravelling the D's) 378
Summary of Deliverable #3 Maps and reports of regional metamorphism and PTt history integrated with structural and alteration history 378

Summary of Deliverable #4 Report on likely geodynamic models of the Yilgarn, with appropriate tests and possible analogues, and a workshop 380

Summary of Deliverable #5 3D maps/GIS of specific districts to be built on Y2 regional 3D map (Laverton, Kalgoorlie-Kambalda, Agnew) 381

Summary of Deliverable #6 Map and report on the early extensional architecture and history 381

Summary of Deliverable #7 Reports on the character of key faults, especially the deep-tapping 'cracks'. Acquire new data (MT and tomography). 382

Summary of Deliverable #8 Report on an improved geologically intelligent geophysical inversions, supported by a rock property database 384

Summary of Deliverable #9 Reports and chemical models on the end-member fluids (magmatic, basinal, meteoric, metamorphic, mantle?) 385

Summary of Deliverable #10 Reports, maps and databases on integrated mineral paragenesis and architecture and chemical modelling for selected camps and deposits 387

Summary of Deliverable #11 Reports on integrated numerical models of fluid flow for generic and site specific scenarios 387

Summary of Deliverable #12 Regional footprint maps of alteration and fluid flow based on geochemistry, ASTER, HYMAP 388

Summary of Deliverable #13 Regional footprint maps of alteration and fluid flow based on geochemistry, ASTER, HYMAP 389

Summary of Deliverable #14 Reports on the integrated structural controls of ore shoots with the regional framework, linked to alteration and mineralogy (e.g., Wallaby, Sunrise, St Ives, KB) 390

Summary of Deliverable #15 Report on reactive transport models tested against specific sites where paragenesis and structure understood 390

Part V: Data (see usb drive)

**PART III: THE SCIENCE BEHIND THE FIVE ANSWERS**

## 3.1 Question 1: Geodynamics of the Eastern Goldfields Superterrane

**K. Czarnota[1], D.C. Champion[1], B. Goscombe[3], R.S. Blewett[1], P.A. Henson[1], P.B., K.F. Cassidy[1,2], and Groenewald, B.[4]**

[1] ***pmd**CRC* c/o Geoscience Australia, GPO Box 378, Canberra, ACT, 2601, Australia.

[2] Rubicon Resources, PO Box 534, West Perth, WA, 6872, Australia.

[3] ***pmd**CRC* c/o Integrated Terrane Analysis, 18 Cambridge Rd, Aldgate, SA, 5154, Australia.

[4] Geological Survey of Western Australia, PO Box 1664, Kalgoorlie, WA, 6443, Australia.

### Abstract

Over the last decade there have been significant advances in our understanding of the: stratigraphy; magmatism; deformation; metamorphism; and timing of mineralisation, in the Eastern Goldfields Superterrane (EGST) of Yilgarn Craton, WA. The integration of these disciplines has enabled a holistic review of the tectonic history of the EGST, thereby providing a para-autochthonous geodynamic context for its mineralisation.

A significant advance has been the recognition of a ~2.81 Ga rifting event off the eastern margin of the Youanmi Terrane which set up the north-northwest trending architecture of the EGST, as expressed in the Nd $T_{DM}$ map.

Rifting was followed by the establishment of a convergent margin characterised by a west dipping subduction zone to the east of the EGST. Subduction resulted in the deposition of the 2.715–2.67 Ga volcanic stratigraphy and the emplacement of voluminous TTG magmatism, which resulted in magmatic thickening of the crust. Volcanism was terminated by a ~5 Ma pulse of east-northeast contraction which triggering lithospheric and lower crustal delamination associated with mid-orogenic extension.

The lack of ultra-high pressure metamorphism and the presence of high geothermal gradients preclude this event from recording a continent-continent collision.

Mid-orogenic extension initiated at 2.665 Ga resulted in the introduction of metasomatised mantle melts (Mafic-granites and Syenites), deposition of late-stage siliciclastic basins (which record anticlockwise PTt paths) and the start of significant economic gold mineralisation in the EGST. The delamination associated with this event resulted in significant heat input into the base of the crust, which eventually led to the emplacement of Low-Ca (crustal melt) granites and cratonisation of the EGST.

Major gold mineralisation postdates delamination, and was associated with renewed compression-transpression (~2.650 Ga) and the development of steep sinistral and later dextral (syn Low-Ca granites) strike-slip faults.

**Keywords:** *Archaean, Yilgarn, Eastern Goldfields Superterrane, geodynamics, tectonics, subduction, extension, delamination, gold.*

### 3.1.0 Introduction

The Eastern Goldfields Superterrane (EGST) of the Yilgarn Craton is one of the most important Late Archaean metallogenic provinces in the world. Although, it hosts numerous world class gold and nickel deposits, consensus regarding the geodynamic setting of this economically important terrane is still lacking. In part, this is due to uncertainty regarding the nature of plate tectonics in the Archaean and its role in the formation of Archaean granite-greenstone belts of which the EGST is one.

For example, Hamilton (2003) argued that terrestrial plate tectonics began to operate only about 2.0 Ga, while authors such as de Wit (1998) argued for the validity of using plate tectonic boundary processes to decipher the Archaean rock record. Another school of thought has modern-style plate-tectonic processes commencing some time in the Mesoarchaean, e.g., Smithies et al. (2003). Certainly most workers have advocated modern-style tectonics operating in the Neoarchaean and this school of thought has dominated research into geodynamics of the Yilgarn Craton. Even within this group, however, a consensus on a common geodynamic model has not been reached. Models range from autochthonous or para-autochthonous models

advocating the development of the EGST within a sialic rift (Groves and Batt, 1984; Hammond and Nisbet, 1992) and/or plume geodynamic setting (e.g., Archibald et al. 1978; Campbell and Hill, 1988; Bateman et al., 2001) through to allochthonous tectonic models advocating the accretion of different fragments of a volcanic arc to a pre-existing continental margin (e.g., Myers, 1995, Barley et al., 2006).

In this paper we aim to outline a revised geodynamic model for the EGST that best honours (with the minimum of *ad hoc* assumptions) the geological constraints, and provides a context for the mineral systems found within. To achieve this end we review the constraints on geodynamic interpretations arising from the study of: greenstone stratigraphy; magmatism; deformation and metamorphism, and integrate the salient features arising from these disciplines into one consistent geodynamic model for the EGST.

### 3.1.1 The Yilgarn Craton

The EGST is part of the large Yilgarn Craton that consists of meta-volcanic, sedimentary rocks and granites that formed principally between ~3050 and 2600 Ma with minor older components to >3.7 Ga. The Yilgarn Craton has long been subdivided into a series of terranes, starting with Gee et al. (1981), Myers (1990), Swager et al. (1990) and Barley et al. (2002) through to the most recent subdivision by Cassidy et al. (2006), which is adopted in this text. The Yilgarn Craton is currently subdivided into six terranes, three of which constitute the EGST (Figure 3.1.1). For a more detailed description of the terranes and domains of the Yilgarn Craton the reader is referred to Cassidy et al. (2006).

In the west, the Narryer Terrane and the South West Terrane are dominated by granite and granitic gneiss, whereas the central Youanmi Terrane and the EGST are

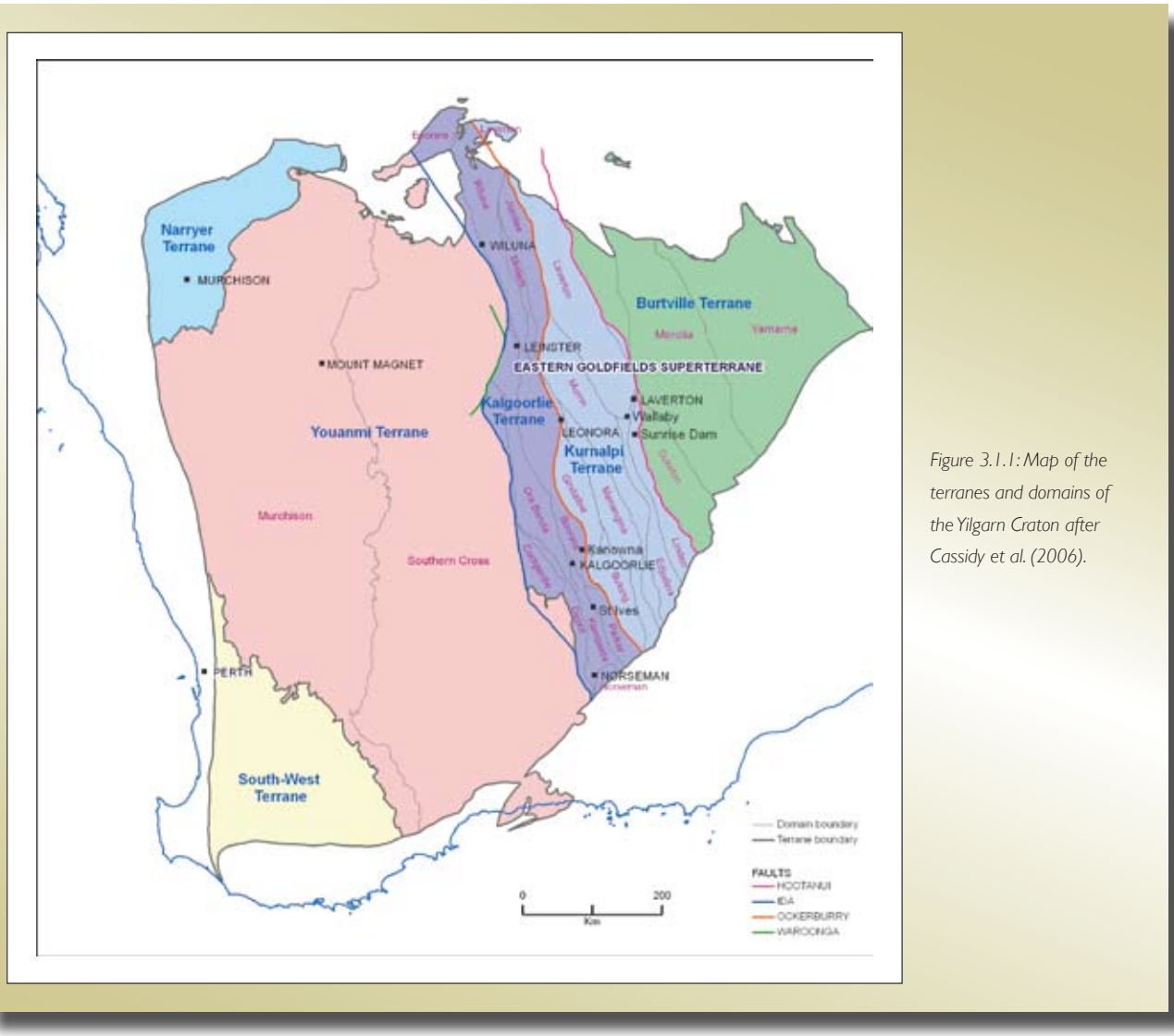


*Figure 3.1.1: Map of the terranes and domains of the Yilgarn Craton after Cassidy et al. (2006).*

*Figure 3.1.2: Integrated tectonic framework for the Eastern Goldfields Superterrane showing the interrelationship between stratigraphy, granite history, tectonic mode, deformation history, metamorphism and age of gold mineralisation.*

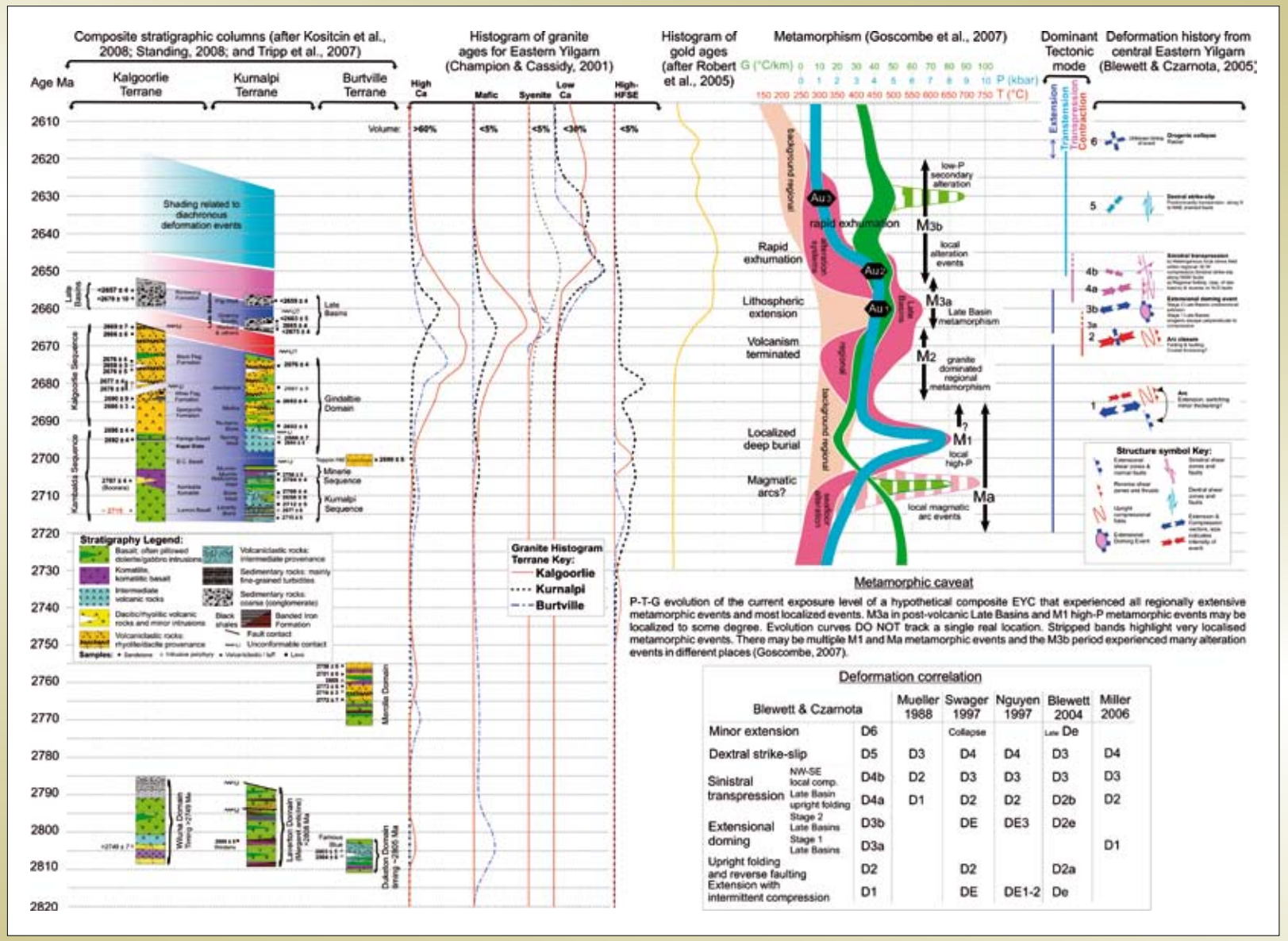


**Metamorphic caveat**

P-T-G evolution of the current exposure level of a hypothetical composite EYC that experienced all regionally extensive metamorphic events and most localized events. M3a in post-volcanic Late Basins and M1 high-P metamorphic events may be localized to some degree. Evolution curves DO NOT track a single real location. Stripped bands highlight very localised metamorphic events. There may be multiple M1 and Ma metamorphic events and the M3b period experienced many alteration events in different places (Goscombe, 2007).

**Deformation correlation**

| Blewett & Czarnota | | Mueller 1988 | Swager 1997 | Nguyen 1997 | Blewett 2004 | Miller 2006 |
|---|---|---|---|---|---|---|
| Minor extension | D6 | | Collapse | | Late De | |
| Dextral strike-slip | D5 | D3 | D4 | D4 | D3 | D4 |
| Sinistral transpression | NW-SE local comp. D4b | D2 | D3 | D3 | D3 | D3 |
| | Late Basin upright folding D4a | D1 | D2 | D2 | D2b | D2 |
| Extensional doming | Stage 2 Late Basins D3b | | DE | DE3 | D2e | |
| | Stage 1 Late Basins D3a | | | | | D1 |
| Upright folding and reverse faulting | D2 | | D2 | | D2a | |
| Extension with intermittent compression | D1 | | DE | DE1-2 | De | |

composed of north-trending greenstone belts separated by extensive granites and granitic gneiss. The Narryer Terrane in the northwest part of the craton consists of ~ 3.73–2.6 Ga high-grade gneiss, supracrustal and granitic rocks. The South West Terrane consists of >3.2–2.6 Ga high-grade gneiss, supracrustal and granitic rocks. The Youanmi Terrane consists of ~3.01–2.63 Ga greenstones and granitic rocks.

The EGST consists of three tectono-stratigraphic terranes, defined on the basis of distinct volcanic facies, geochemistry, and age of volcanism that range from ~2.94 to 2.66 Ga. From west to east, these are the Kalgoorlie, Kurnalpi and Burtville Terranes. Each terrane is further subdivided into domains, which define contiguous blocks of tectonostratigraphy. The terranes and domains of the EGST are bound by an interconnected system of faults (Swager et al., 1992, Swager, 1997; Liu et al., 2001; Champion, 2006). From west to east, the terrane-bounding fault systems are the Ida, Ockerburry and Hootanui (Figure 3.1.1). Each terrane contains a record of at least two distinct periods of volcanism including a fragmented record at ~2.81 Ga and a more consistent record starting around 2.72 Ga (Figure 3.1.2).

This subdivision of the Yilgarn Craton into tectonostratigraphic terranes is based on the assumption that the Yilgarn Craton represents the accretion of allochthonous, exotic crustal fragments (Myers 1990, 1995). While this tectonic assumption is not necessarily valid (Swager, 1997) the terminology is nevertheless a useful geographical subdivision which groups rocks with common geological features and hence is used in this text without presuming an allochthonous origin. The term superterrane is used to denote a group of related, adjacent terranes.

### 3.1.2 Tectonic constrains from greenstones

Greenstones of the EGST can be subdivided into four distinct time slices: ~2.94 Ga, ~2.81 Ga, ~2.76 Ga and 2.715–2.62 Ga. Each of these time slices is associated with granite magmatism (Figure 3.1.2) and corresponds with peaks in inherited zircons from granitoids (Figure 3.1.3, after Cassidy and Champion, 2004). This indicates each time slice represents periods of new crustal growth. It is also significant to note that the oldest peak of inherited zircons (~2.95 Ga) match the oldest known rocks, indicating there is almost a continuous record of rock formation and recycling preserved in the exposures of the EGST. Based on this inference it should be possible to reconstruct the geodynamics of the EGST from 2.95 Ga to the present.

In the following each of the four time slices are discuss in turn. The aim of this review is to integrate the past two decades of research in the EGST and elucidate the constraints each of these time slices places on potential geodynamic models.

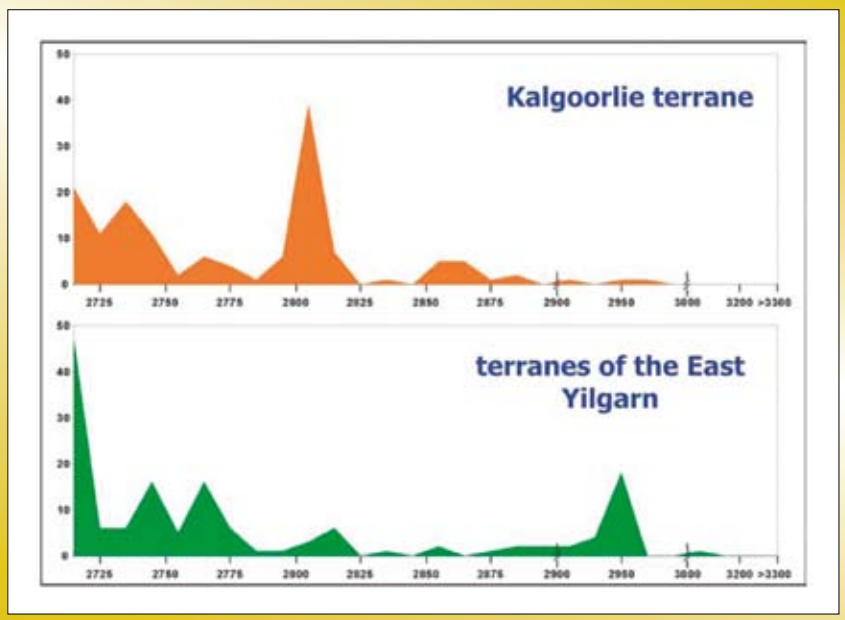


*Figure 3.1.3: Histogram of zircon inheritance ages from plutonic rocks of the EGST (from Cassidy, 2004).*

### 3.1.2.1 ~2.94 Ga time slice

The ~2.94 Ga time slice consists of the oldest and least preserved rocks of the EGST. It includes the felsic volcanics of the Penneshaw Formation in the Kalgoorlie Terrane (Nelson, 1995) and the Mt. Joanna and Dingo Range High-Ca gneissic granites of the Burtville Terrane (Dunphy et al., 2003). The U-Pb zircon crystallisation age of the Mt. Joanna gneissic granite (2939±6 Ma) is similar to its Nd depleted-mantle model age ($T_{DM}$ = 3160 Ma), indicating minimal involvement of older crust, and suggesting primitive crust formation during this time slice, possibly in a volcanic arc setting. All that can be said conclusively is that ~2.94 Ga rocks, at least locally, form basement to subsequent greenstones since younger granites contain ~2.94 Ga inherited zircons. It is noted, however, that no unequivocal non-conformal relationships with younger stratigraphic packages have been documented.

Similar age rocks are preserved in the Cue domain of the Youanmi Terrane where ulramafic/mafic and felsic volcanic rocks and some granites also exhibit $T_{DM}$ ages similar to their U-Pb zircon crystallisation ages. In addition the Youanmi Terrane also consists of ~3.0 Ga granites and greenstones.

The similarity of crystallisation ages and juvenile Nd signatures between the oldest rocks preserved in the EGST and the granites and greenstones of the Youanmi Terrane, together with the inherited zircon record from granitic rocks (Figure 3.1.3), can be used to support the hypothesis that the Youanmi Terrane forms basement to the EGST.

### 3.1.2.2 ~2.81 Ga time slice

~2.81 Ga supracrustal rocks occur across the three terranes of the EGST. They predominantly consist of tholeiitic pillow basalt, komatiites and banded iron formation. Tholeiitic basalts of the Kurnalpi Terrane which overlie the ultramafic sequence around Windarra are inferred to be ~2.81 Ga based on the ~2.81 Ga constraint on the underlying ultramafic sequence (Kositcin et al., 2008). These tholeiitic basalts display relatively low MgO, approximately chondritic ratios of moderately incompatible elements, and slight LREE depletion (Barley et al., 2006). Depleted REE trends indicate derivation of these magmas from a mantle protolith that was previously depleted, and also suggest an absence of mantle metasomatism and/or lack of crustal contamination (Barley et al., 2006) consistent with deposition of the mafic/ultramafic package in a rift tectonic setting, i.e., non arc-related.

In the Burtville Terrane a mafic/ultramafic sequence is overlain by 2.81 Ga intermediate to felsic andesitic volcanics (Famous Blue; Kositcin et al., 2008) and in the Kalgoorlie Terrane there are ~2.81 High-Ca granite intrusions (Twin Hills; Dunphy et al., 2003), which together are more indicative of a subduction-related tectonic setting rather than a rift. However, the andesitic volcanics in the Burtville Terrane could represent contaminated, non arc-related, tholeiitic magmatism and the High-Ca granites in the Kalgoorlie Terrane, which contain 2.91 Ga inherited zircon (unpublished GA data) may represent crustal melts generated within a rift tectonic setting.

### 3.1.2.3 Nd depleted-mantle model age ($T_{DM}$) map excursus

A possible answer to the above tectonic mode dilemma comes from a consideration of the Nd $T_{DM}$ map of the Yilgarn Craton presented in Figure 3.1.4 (Champion and Cassidy, 2007). This map is based on granite samples of all ages across the Yilgarn Craton and may be viewed simplistically as an estimate of the bulk ('average') age of the crust (see below). The EGST displays a clearly north-northwest trending grain with alternating intermediate (3.05–2.9 Ga) and young (2.9–2.72) model ages. On face value this pattern seems to indicate the EGST is a rifted margin from the Youanmi Terrane. The question then becomes does such a simple interpretation fit the known data? To answer this question we first need to consider when this pattern was temporally established?

Given that the Nd $T_{DM}$ map was constructed from granites of all ages across the Yilgarn (though mostly ca. 2.75–2.63 Ga), combined with the complexities of granite formation (mixing, multiple sources etc.) it is, perhaps, surprising that the resultant map displays such a remarkably consistent pattern of model age distribution. Reasons for this patterning, and interpretation of such are discussed in detail in Champion and Cassidy (in prep). However, to gain insight into the formation of this pattern in the EGST, and how we are interpreting it, we will consider a typical high-HFSE (high field strength element) granite from the Kurnalpi Terrane – the Yarri

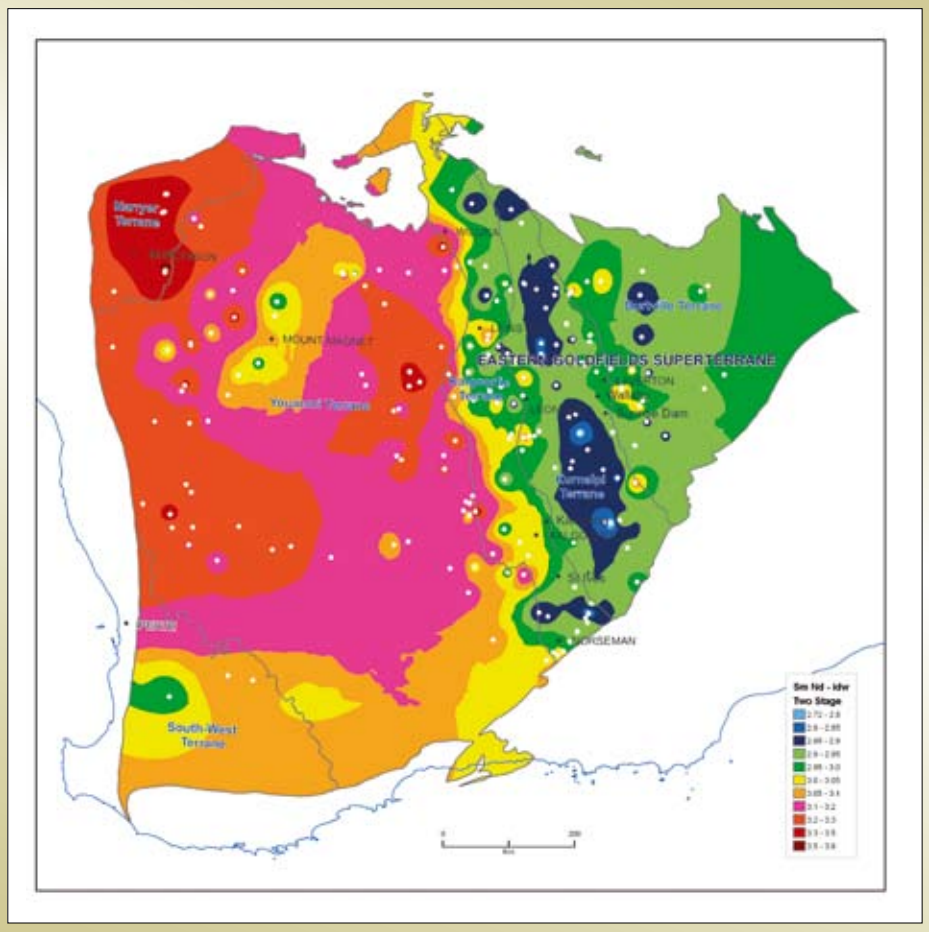


*Figure 3.1.4: Nd depleted-mantle model age map of the Yilgarn Craton. Image produced by griding Nd depleted-mantle model ages calculated from Sm-Nd point data (from Champion and Cassidy, in prep).*

Monzogranite, which has a U-Pb crystallisation age of 2.714 Ga (GA OZCHRON data base) and a Nd $T_{DM}$ age of 2.81 Ga (Champion and Cassidy, in prep). Since high-HFSE granites are dominantly crustal melts (Champion and Sheraton, 1997) these two ages provide a robust minimum and an approximate (model-dependent) maximum age, respectively, for the age of the granite protolith, i.e., the middle and lower crust. In this manner, the patterns depicted in the Nd $T_{DM}$ map can be interpreted as a proxy for crustal age and structure, and, hence, can be used to constrain the growth of the Yilgarn crust. Accordingly, we can assume that the crustal protolith for the Yarrie Monzogranite and, by extension, the young model age zone around it, was developed by crustal growth ~2.715–2.81 Ga.

The lack of crustal contamination of the ~2.8 Ga basalts from the Kurnalpi Terrane coupled with the spatial coexistence of the young Nd $T_{DM}$ model ages (~2.81 Ga) suggests that the Kurnalpi Terrane was the loci of significant crustal extension at ~2.81 Ga (assuming a autochthonous model). In such a scenario, the zones of intermediate Nd $T_{DM}$ ages are, therefore, interpreted as zones of lesser crustal thinning of the underlying ~2.95 Ga basement (Figure 3.1.5a). It follows that in these zones of less crustal thinning the elevated geothermal gradient associated with extension resulted in crustal melting and the generation of the ~2.8 Ga High-Ca granites and felsic volcanics of the Kalgoorlie and Burtville Terranes. This model implies the εNd signature of later magmatism largely reflects the 2.81 Ga architecture.

A rift tectonic model at ~2.81 Ga has also been advocated for the emplacement of the Windimurra mafic/ultramafic intrusion in the eastern Murchison Domain of the Youanmi Terrane (Champion et al., 2000). It is interesting to note that the two most gold- endowed regions of the Yilgarn Craton (i.e., EGST and Murchison Domain) both seem to be sites of ~2.81 Ga lithospheric extension. This correlation indicates this event was critical in establishing the fertility of the Yilgarn yet the exact process resulting in this increased fertility is still unknown.

*Figure 3.1.5(a): Scaled schematic cross-sections through the EGST representing critical features of the autochthonous convergent margin tectonic model for the EGST. ~2.81 Ga time slice illustrating rifting off the eastern margin of the Youanmi Terrane.*

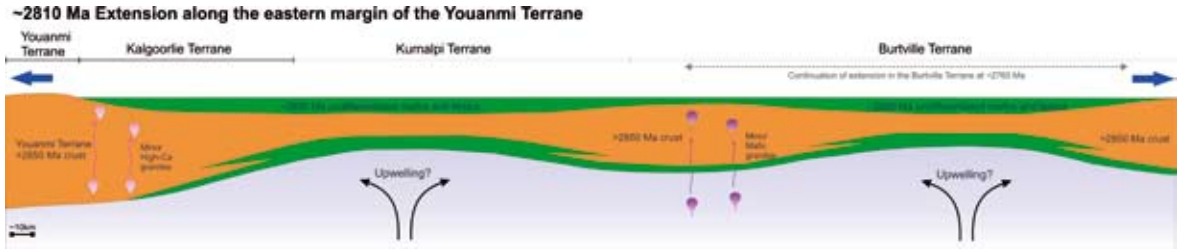


*Figure 3.1.5(b): ~2.715–2.690 Ga arc and back-arc volcanism associated with the initiation of a west dipping subduction zone. Westward younging andesitic volcanism in the east and mafic/ultramafic, possibly plume related volcanism in the back-arc setting.*

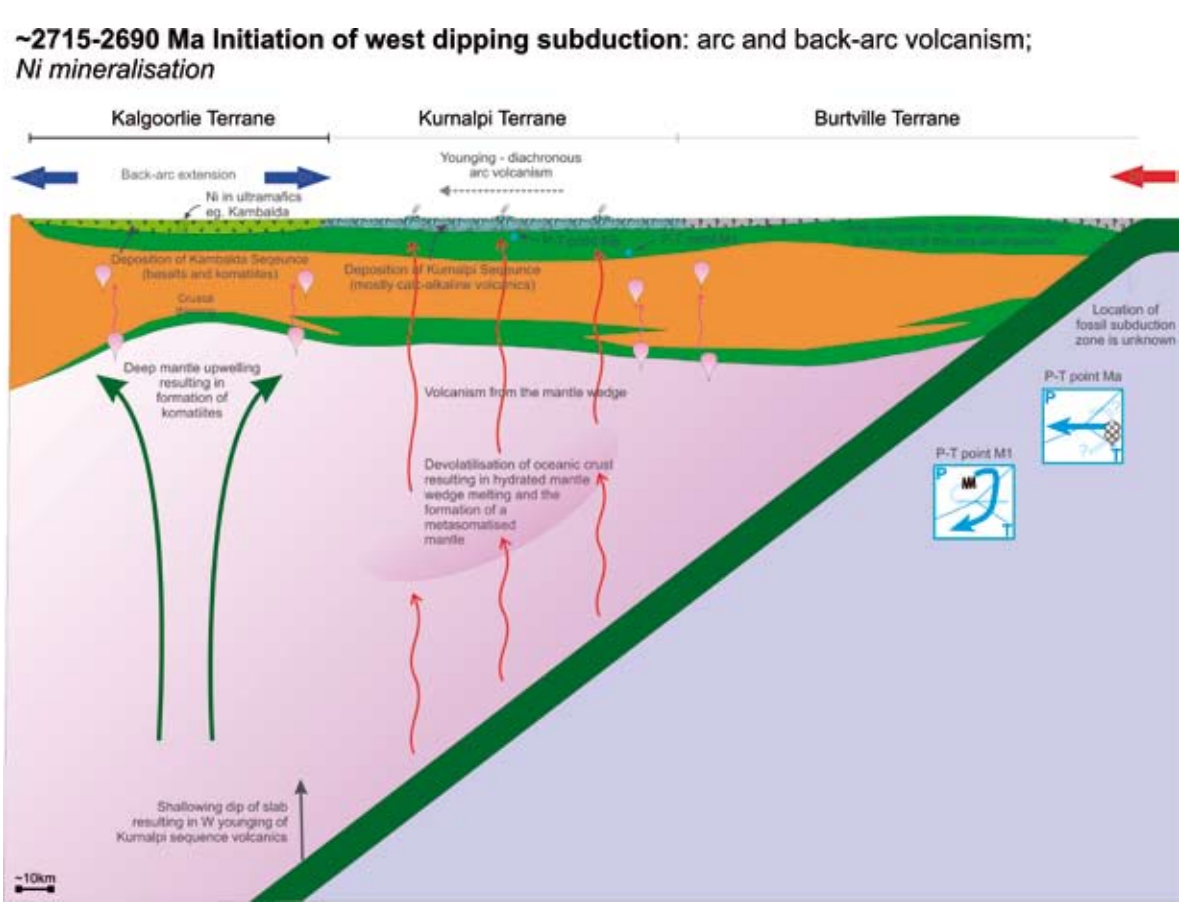

*Figure 3.1.5(c): ~2.690–2.670 Ga shallowing of subduction slab associated with voluminous High-Ca granite magmatism resulting in magmatic crustal thickening within an overall extensional regime associated with bimodal volcanism and inferred slab roll back.*

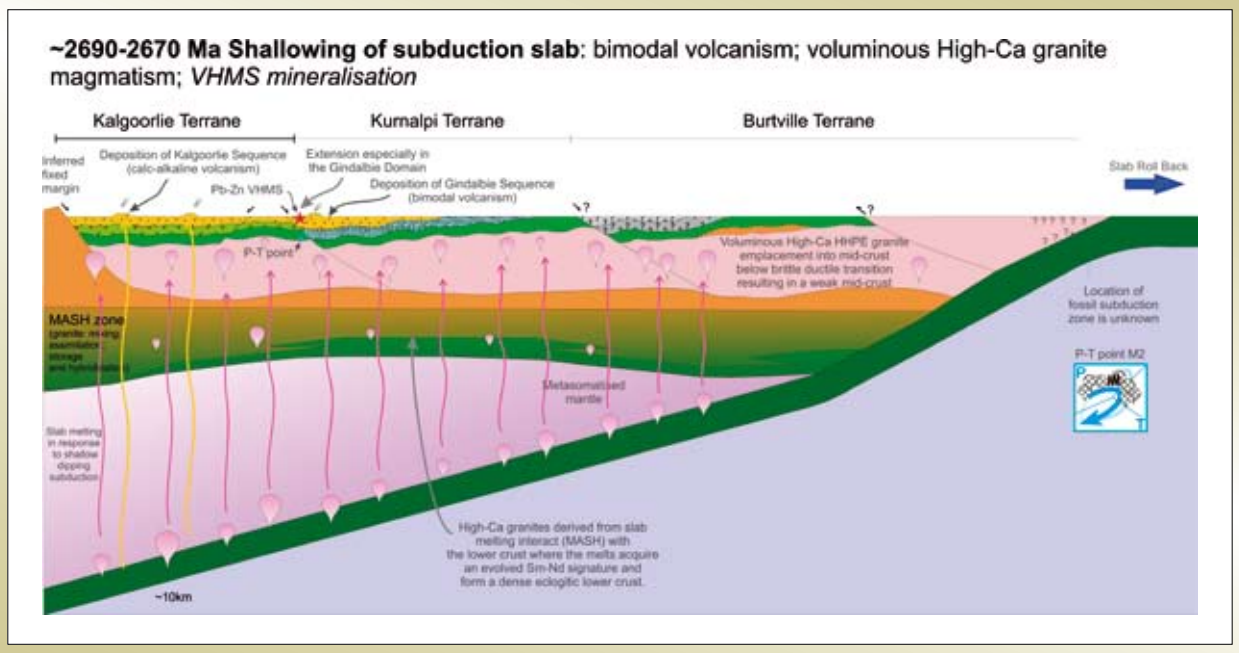


*Figure 3.1.5(d): ~2.670–2.663 Ga diachronous east–west to east-northeast–west-southwest contraction resulting in minor mechanical crustal thickening and termination of volcanism.*

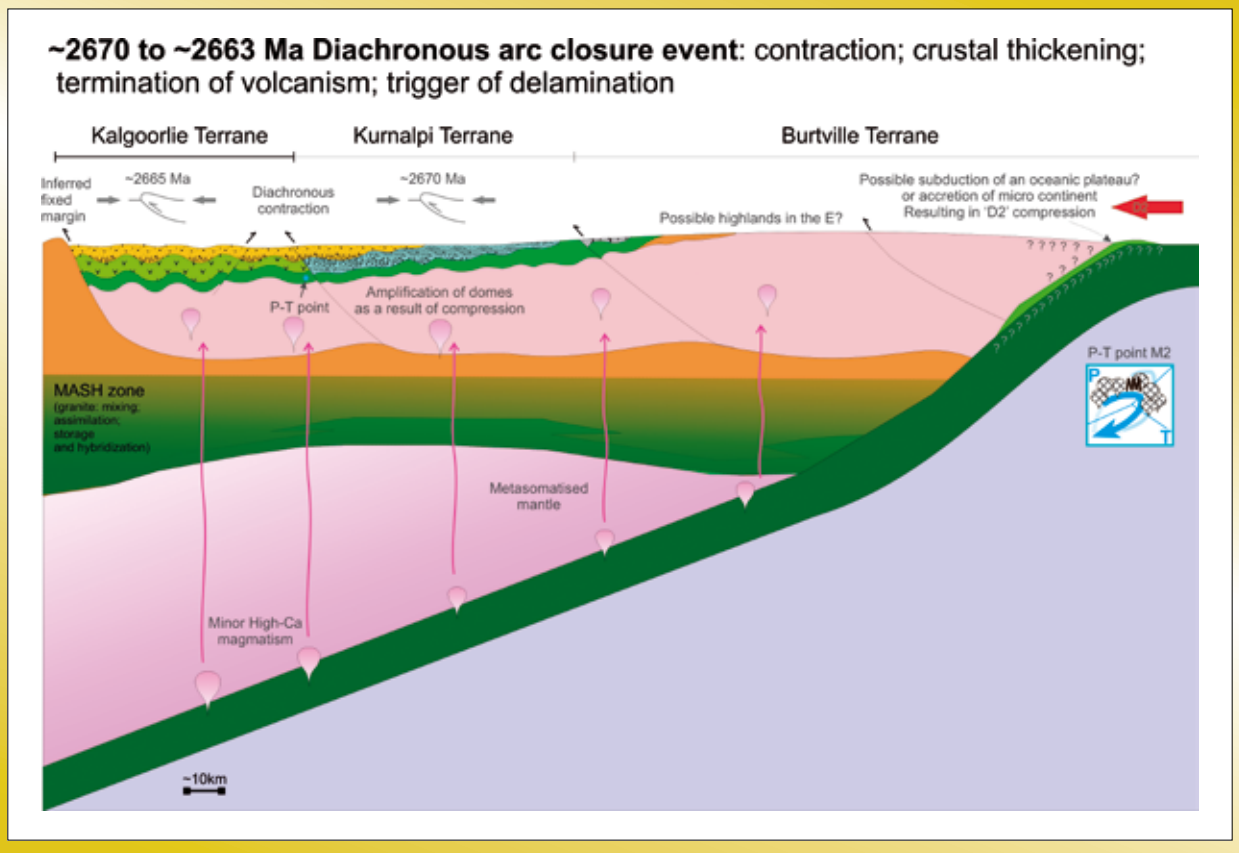

*Figure 3.1.5(e): ~2.665–2.650 Ga diachronous mid-orogenic lithospheric extensions and delamination of the lower crust resulting in: granite cored core complex formation; late basin deposition; introduction of metasomatised mantle melts; and, the start of significant economic gold mineralisation in the EGST. This period of extension is associated with downward fluid flow and storage of fluid in the crust.*

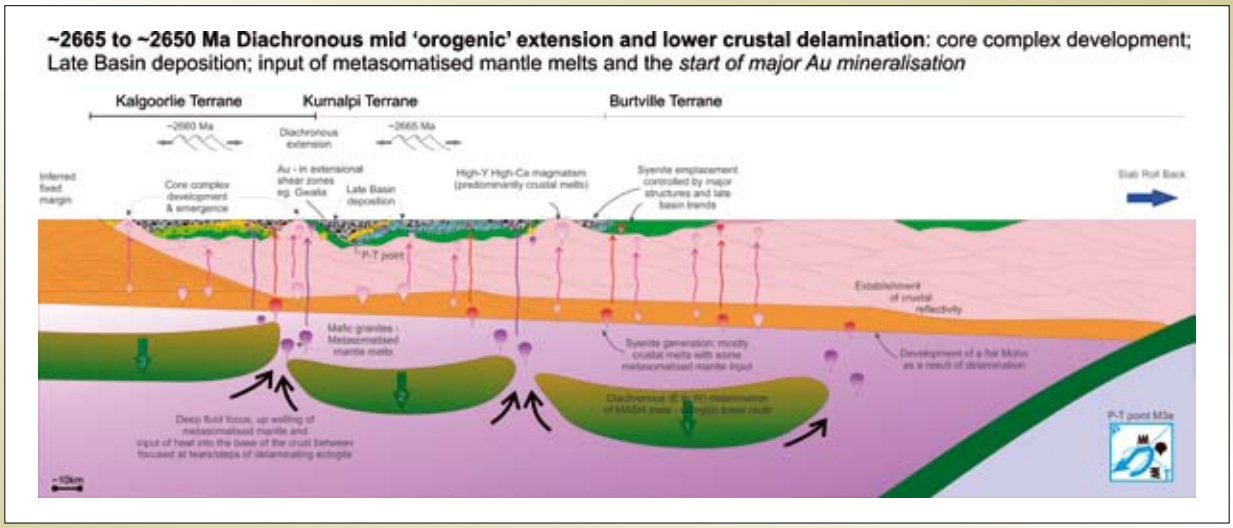


*Figure 3.1.5(f): ~2660–2645 resumed east-northeast contraction and inversion of extension followed by a switch in compression to west-northwest directed resulting in sinistral transpression along major north-northwest striking shear zones and the development of local stress heterogeneities which aid fluid flow focusing. Switch from High- to Low-Ca granite magmatism.*

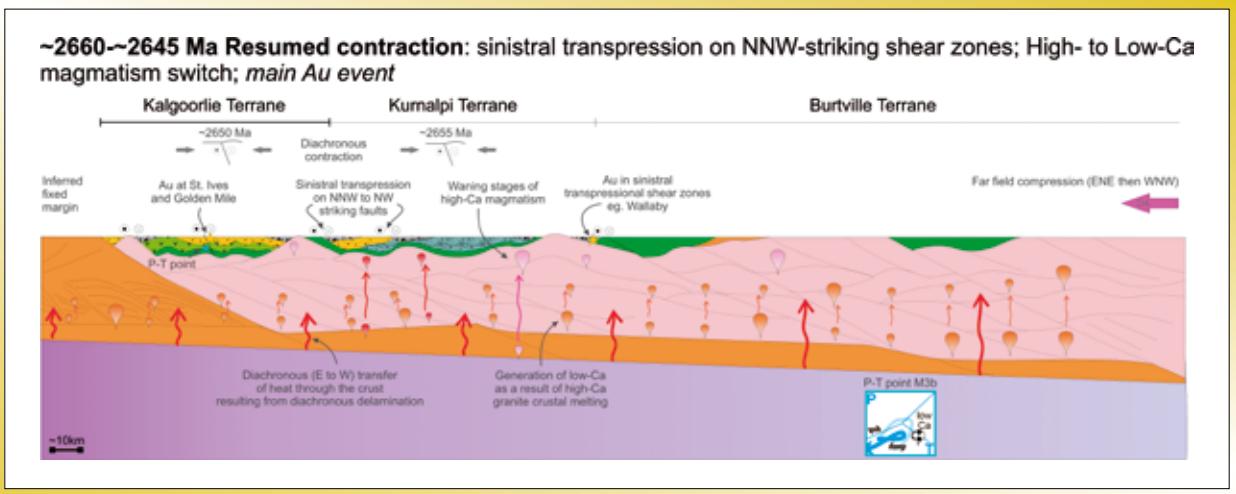

*Figure 3.1.5(g): ~2.650–2.620 Ga dextral strike-slip faulting associated with southwest directed contraction and gold mineralisation. Emplacement of Low-Ca granites resulting in the cratonisation of the EGST.*

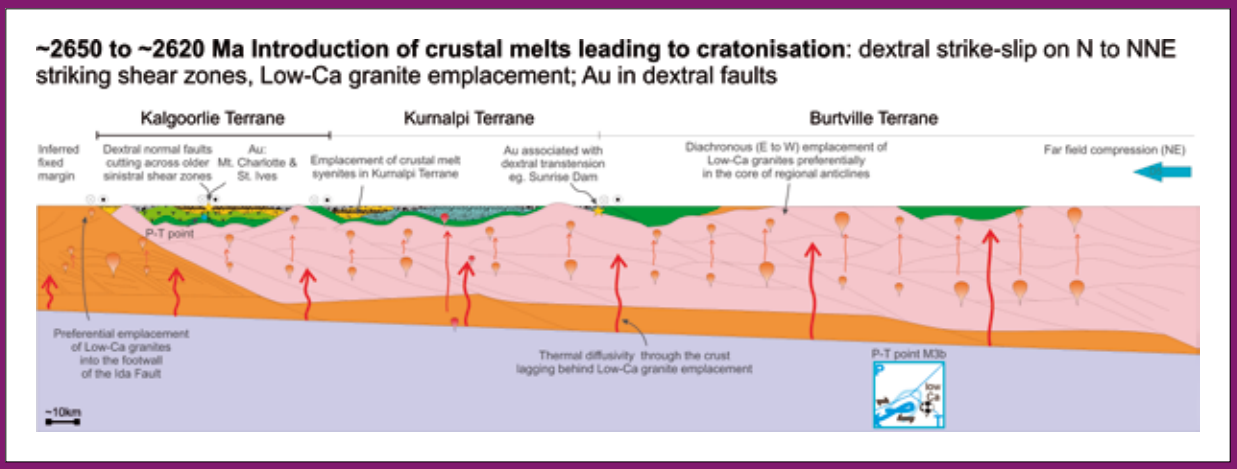


### 3.1.2.4 ~2.76 Ga time slice

The only definitively ~2.76 Ga age greenstones occur in the Merolia domain of the Burtville Terrane although the old greenstone sequence around Leonora (constrained to >2.749 Ga) could also be part of this time slice. In the Merolia domain the greenstone record consists of basaltic, komatiitic and felsic volcanism and shallow water sedimentation (Barley et al., 2006; Standing, 2008). It was temporally associated with limited High-Ca magmatism in the Burtville and Kalgoorlie Terranes (Figure 3.1.2). The stratigraphic association of this period are interpreted by Standing (2008) to represent a rift tectonic setting, consistent with a continuation of episodic extension from ~2.81 through to ~2.76 Ga.

### 3.1.2.5 ~2.715–2.65 Ga time slice

2.715–2.65 Ga greenstones of the EGST are the best preserved, most studied and economically endowed tectonic sequences in the Yilgarn Craton. They represent one prolonged tectonic cycle best preserved in the Kalgoorlie and Kurnalpi Terranes. The 2.715–2.65 Ga time slice can be further subdivided into temporal groups of tectono-stratigraphic associations: 2.715–2.690 Ga, 2.690–2.665 Ga and 2.665–2.650 Ga.

### 3.1.2.6 2.715–2.69 Ga tectono-stratigraphic associations

#### Kambalda Sequence

The 2.715–2.690 Ga Kambalda Sequence of predominantly tholeiitic and komatiitic mafic-ultramafic rocks and minor interbedded calc-alkaline volcanics (Swager et al., 1992; Kositcin et al., 2008) is perhaps the best studied stratigraphic section in the EGST and has formed the basis for a number of geodynamic models proposed for the Kalgoorlie Terrane and, hence, deserves special attention. It consists of a stratigraphic sequence from bottom to top of: lower basalt; ultramafic dominated unit, and upper basalt sequence, with minor interbedded felsic volcanics (Figure 3.1.2). The sequence has been most comprehensively described from the Kambalda Domain (Swager, 1997 and references therein), – Lunnon Basalt, komatiite (Kambalda Komatiite, Hannans Lake Serpentinite, Silver Lake Peridotite, Tripod Hill Komatiite); Devons Consol Basalt and Paringa Basalt. In this domain the basal Lunnon Basalt, has tholeiite chemistry with flat to slightly depleted light rare earth element (LREE) patterns, and εNd > 0. The komatiite sequences (locally hosting nickel mineralization) are up to several kilometres thick with individual flows ranging from 2 to >100m, that are locally separated by thin (<5m) fine-grained metasedimentary beds. The komatiite magmas are typically up to 32 wt% MgO in the Kalgoorlie Terrane and define a flow field >100,000 km$^2$. The mafic rocks overlying the komatiite unit are more Mg-rich than the

underlying lower basalts, with elevated LREE contents and more variable εNd (> 0 and < 0; Chauvel et al., 1985; Arndt and Jenner, 1986; Claoue-Long et al., 1988; Morris, 1993; Bateman et al., 2001). The chemistry of basaltic rocks overlying the komatiite unit, and parts of the komatiite unit itself (Lesher and Arndt, 1995) most likely result from assimilation of crustal material by komatiite magma combined with fractional crystallization (AFC of De Paolo, 1981), although the nature of the contaminant and the extent of contamination are still debated (Arndt and Jenner, 1986; Jochum et al., 1991; Morris, 1993; Lesher and Arndt, 1995; Bateman et al., 2001). Crustal contamination of mafic magmas from the Kambalda Sequence is independently supported by the occurrence of ~2.9 and 3.1 Ga zircon xenocrysts from Kambalda and the Norseman Domain (Compston et al., 1986; Nelson, 1997) indicating that the greenstone volcanics were erupted on pre-existing continental crust. The age of zircon xenocryst coincides with the age of granites and greenstones in the Youanmi Terrane further supporting the theory the Youanmi Terrane underlies the EGST.

Assuming dry melting of the mantle, the high MgO content of komatiites in the Kalgoorlie Terrane requires a high degree of partial melting with elevated thermal anomalies at depths greater than 200 to 250 km (*cf.* Arndt et al., 1997). This thermal requirement, together with the recognition of the basalt-komatiite-basalt-felsic volcanic stratigraphic sequence and later timing of granitic intrusion, led to a model attributing much of the development of the EGST to a mantle plume (Campbell and Hill, 1988; Campbell et al., 1989; Griffiths and Campbell, 1990; Hill et al., 1992). In the model of Campbell et al. (1989) and Hill et al. (1992), a 600–800 km diameter komatiite plume initiated at the core mantle boundary and ascended due to thermal buoyancy. As the plume head and thermal anomaly approached the lower lithosphere boundary, melting ensued to produce basaltic magma while the plume mushroomed to a diameter of 2000 km. The first melts produced the tholeiitic lower basalt unit, followed by eruption of komatiite magma comprising the plume axis. Assimilation of crustal material by the waning plume axis, coupled with fractional crystallization, produced the komatiitic basalts of the overlying mafic unit. Bateman et al. (2001) recognised HREE-depletion in the Paringa Basalt and argued that the later basaltic magmas were derived from deeper in the plume, with residual garnet in the source, where as the earlier mafic/ultramafic sequence was derived from shallower parts. Furthermore, in the plume model (Campbell et al., 1989), the younger felsic volcanism (Kalgoorlie Sequence), are interpreted to represent melting of the underlying continental crust by thermal effects related to the rising plume.

Such plume tectonics are generally controversial. De Witt (1998), in challenging the plume hypothesis, advocated komatiites could be formed by wet melting of the mantle associated with subduction zone settings. This form of melting is inferred to have occurred in response to a hotter Archaean mantle which resulted in the formation of heavily altered mid ocean ridge basalts during the Neoarchaean. One test of this model would be the presence of hydrous minerals in the komatiites (Parmen and Grove, 2005); although, due to the secondary nature of most of the mineralogy this test is inconclusive. Further, numerous komatiites (and associated basalts) have strong LILE (large ion lithophile elements) and REE (rare earth element) depleted signatures suggesting no evidence of subduction, a likely source of water.

Some authors such as Hamilton (2003), and references therein, argue against the operation of plumes at all, especially from the core-mantle boundary. Their arguments largely hinge on the premise the 660 km discontinuity is a mechanical discontinuity that cannot be penetrated by a plume. However, research on modern plume-inferred flood basalts argues that plumes are typically generated precisely at the 660 km discontinuity and last approximately 5–15 Myr (Condie, 2001). This implies the 20 Myr time scale of inferred plume-related Kambalda Sequence volcanism could be attributed to a short lived plume event.

Despite the criticism the plume model does neatly explains the major elements of the Kambalda Sequence stratigraphy. However, taking into consideration the geology of the EGST as a whole it fails to explain a lot of the salient features suggesting the deep mantle up welling or plume associated with the deposition of the Kambalda Stratigraphy needs to be placed within a boarder geodynamic context.

Taking into consideration the architecture of the Kalgoorlie Terrane alone the Kambalda Sequence is distributed in long linear NNW trending troughs indicative of a far-field extensional control on deposition (Connors et al., 2003).

This architecture is contrary to a radial distribution as would be expected under a purely plume controlled model indicating a broader understanding of the geodynamic context of the EGST is required to explain all of the features associated with the Kambalda Sequence.

Without addressing the plume debate, Barely et al., (1989), based on the presupposition that modern tectonics operated during the Neoarchaean, argued for a back-arc basin origin for the Kambalda Sequence. Their argument was based on the recognition of submarine depositional sequences, hemipelagic sedimentation and the presence of calc-alkaline volcanics. This interpretation was supported by sequence stratigraphic analysis conducted by Krapež (1997), who argued the Kambalda Sequence preserves most of the features of a back-arc basin. In this model the basaltic and komatiitic volcanism is interpreted to originate from decompression melting due to periodic thermal up welling above a steeply dipping subduction zone. The lack of High-Ca granites of this age interval (Figure 3.1.2) is used to further support a back-arc rather than an intra-arc tectonic setting. A weakness of this model is that the authors never proposed an alternative explanation for the high MgO concentration within the komatiites.

## Kurnalpi Sequence

The majority of the Kurnalpi Terrane consists of ~2.715–2.704 Ga calc-alkaline intermediate volcanics and volcaniclastic sedimentary rocks. It is dominated by andesitic complexes (Figure 3.1.6c) with associated quartz-poor volcaniclastic sedimentary rocks and mafic intrusive rocks (Barley et al., 2008). Barley et al. (1989, 2008) interpreted the volcanic rocks as proximal to medial submarine facies of submarine to locally emergent intra-oceanic arc-related volcanoes. Mafic through to felsic volcanics display consistent flat HREE and LILE-enriched trends with Nb, Ta, Ti negative anomalies in basaltic end members (Figure 3.1.6f; Barley et al., 2002). Based on these data Barley et al. (2002) argued the calc-alkaline volcanic complexes are identical in facies and geochemistry to modern intra-arc volcanic complexes, and hence hydrated mantle wedge melting is viewed as the main mechanism for magma genesis. Morris and Witt (1997) also advocated a subduction setting for the Kurnalpi Terrane calc-alkaline magmatism, but suggested a continental arc environment.

In contrast, Hallberg and Giles (1986) argued the calc-alkaline complexes were triggered by 'hot spot' activity rather than subduction because they display a widely

*Figure 3.1.6: $SiO_2$ versus $Zr/TiO_2$ plots of volcanic rocks from Kalgoorlie (a), Gindalbie (b) and Kurnalpi (c) Terranes (plots after Winchester and Floyd, 1977); Primordial mantle-normalised multi-element plots for analyses of volcanic rocks from Kalgoorlie (d), Gindalbie (e) and Kurnalpi (f) Terranes (normalisation factors after Anders and Grevesse, 1989). Figure from Barley et al. (2002).*

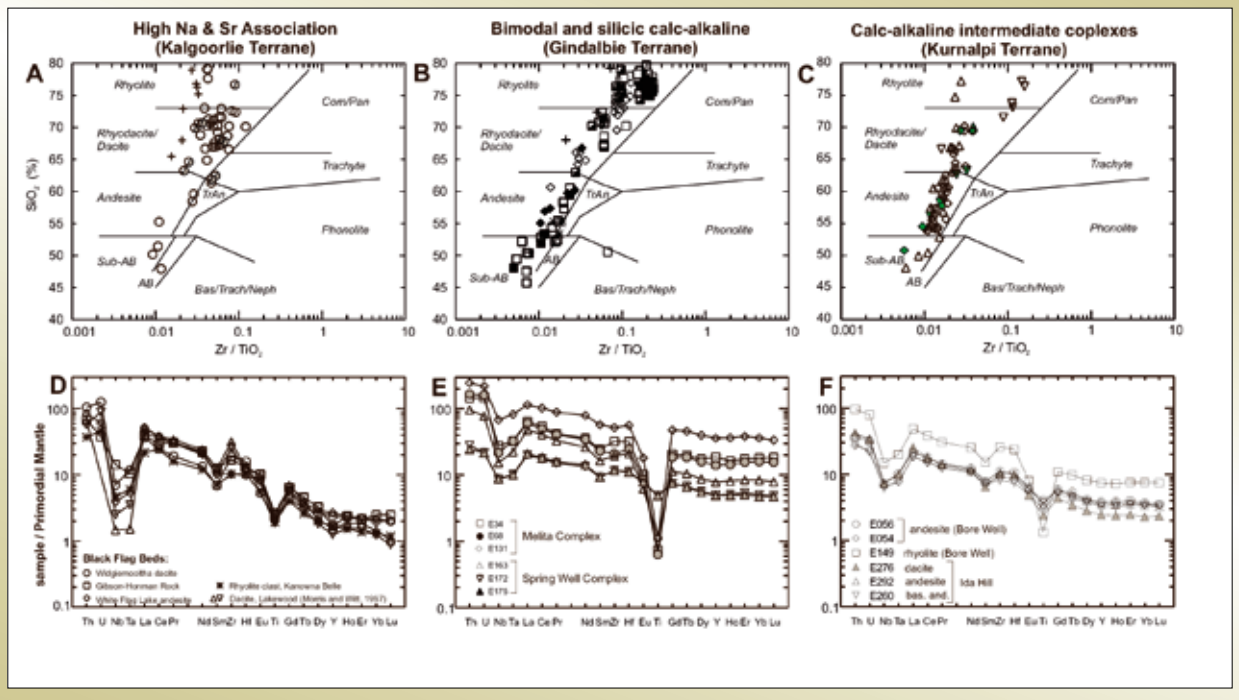

scattered spatial distribution. However, with additional geochronology, Barley et al. (2008) were able to demonstrate a temporal east-west trend from ~2.715 Ga in the east to ~2.704 Ga in the central region (around Welcome Well), and then to younger related rocks in the west (e.g. Spring Well, ~2.69 Ga; Melita ~2.68 Ga), supporting the interpretation the Kurnalpi Terrane represents a volcanic arc or rifted arc tectonic setting. East to west younging of volcanism is further expressed in the continuation of calc-alkaline volcanism associated with the Kalgoorlie Sequence of the Kalgoorlie Terrane during the 2.900–2.665 Ga time slice. The simplest interpretation of this pattern of diachronous volcanism is to attribute it to a shallowing of the subducting slab (e.g., Morris and Witt, 1997; Figure 3.1.5b). A similar pattern of arc-related volcanism younging towards the interior of an inferred continent associated with a shallowing of subduction is observed in the Andes (Haschke et al., 2002).

The east-west younging of volcanism could also be a function of younger extension ($D_3$) along the east-dipping, terrane-bounding Ockerburry Fault, which resulted in the preservation of younger stratigraphy in the western part of the Kurnalpi Terrane. Henson et al. (2008) argued based on the preservation of older andesite volcanic complexes adjacent to late basins (indicating minimal uplift and erosion pre-Late Basins) for non-deposition of the younger volcanic complexes around Laverton.

A comparison of ~2.715–2.69 tectono-stratigraphic associations across the Kurnalpi and Kalgoorlie Terranes reveals a strong east-west asymmetry. The presence of coeval arc-related rocks in the Kurnalpi Terrane and mafic/ultramafic rocks in the Kalgoorlie Terrane is hard to explain using a plume model. Morris (1993) also pointed out that the plume model cannot account for parts of the greenstone stratigraphy north of Kalgoorlie, and the occurrence of interbedded felsic volcanic rocks throughout the Kambalda Sequence. Barley et al. (1989) argued the simplest interpretation of the east-west contemporaneous tectono-stratigraphic asymmetry is that it represents the development of an ensialic volcanic arc and back-arc basin in response to a single westward-dipping subduction zone within an overall continental convergent plate-margin (Figure 3.1.5b). This tectonic model links Archaean gold deposits with younger mesothermal, epithermal, and porphyry gold deposits, which commonly form within convergent tectonic margin setting.

### 3.1.2.7 2.69–2.665 Ga tectono-stratigraphic associations

#### Kalgoorlie Sequence

The Kalgoorlie Sequence unconformably overlies the Kambalda Sequence and consists of a >3,000 metre thick succession of andesitic, dacitic (dominant) and rhyolitic volcaniclastic (Figure 3.1.6a) and epiclastic rocks with subordinate lavas (Barley et al., 2002; Kositcin et al., 2008; Krapež and Hand, 2008). Felsic volcanic rocks of the Kalgoorlie Sequence, are dominantly of tonalite-trondhemite-granodiorite (TTG) composition. They have steep REE patterns, are depleted in the HREE, typically show no Eu anomaly (Figure 3.1.6d), have elevated Sr/Y ratios and $Na_2O/K_2O > 1$ (Morris and Witt, 1997; Barley et al., 2002). This geochemical signature indicates the involvement of garnet in the melt source region and is typically interpreted to indicate the melting of basaltic protoliths at high pressures. Similar rocks are found in modern convergent margins where slab melting is thought to be occurring in response to shallow subduction of young and hot lithosphere rather than the overlying mantle wedge (Drummond and Defant, 1990).

The compositional change from Kambalda to Kalgoorlie sequence stratigraphy suggests a change in the tectonic setting related to a transition from a plume or back arc environment to a convergent margin plate tectonic setting. Yet, Bateman et al. (2001) arguing for a plume model, contended that the 2.71 to 2.67 Ga felsic volcanic rocks do not show an evolution in composition as would be expected in a transition from plume to subduction tectonics. However, this argument is only valid if the felsic volcanics are genetically related to plume magmatism (e.g., by fractionation from a basaltic melt) and not if (as in the dominant plume mode) the plume simply provides a thermal input for melting of the crust in which case no variation would be expected.

Campbell and Hill (1988) recognized an ~20 Ma time gap between initiation of Kambalda Sequence basaltic volcanism and initiation of Kalgoorlie Sequence felsic volcanism and High-Ca magmatism (Figure 3.1.2). They attributed this gap to the time needed to conduct heat from the top of a new mantle plume into a lower crustal anatectic zone. Hill et al. (1992) revised these calculations and concluded that significant felsic magmatism could occur on the order of 30 to 50 Ma (post-plume). This

equates to the time scale of greenstone formation in the Kalgoorlie terrane and, hence, they argued for a plume tectonics model to explain the entire volcanic and magmatic rock record of the Kalgoorlie Terrane.

However, as in the 2.715–2.690 time slice the plume theory falls short in explaining the entire rock record. Major limitation of the plume model include that it does not take into consideration the mass balance problem (see granite section on High-Ca granites) associated with the generation of voluminous High-Ca granites associated with Kalgoorlie Sequence volcanism. Neither does the plume model account for the generation of the Syenites and Low-Ca granites (Figure 3.1.2) which require a second thermal pulse (Smithies and Champion, 1999) or at the least a continuation of felsic magmatism for 75 Ma after the plume event. These two considerations significantly weaken the case for plume tectonics as the sole means of explaining the entire Kalgoorlie Terrane rock record.

Krapež and Hand (2008) argued the presence of coeval mafic and felsic magmatism in the Kalgoorlie Sequence indicate deposition during an extensional tectonic mode. Volcanogenic provenance, spatially linked volcanism and plutonic magmatism, and a deep-marine depositional environment support an intra-arc setting. Krapež and Hand (2008) also recognized six depositional sequences that record uplift-subsidence cycles and the presence of retrogradational longitudinal fans of a linear trough basin, consistent with basin lengthening and deepening. They argued these depositional environments are most consistent with strike-slip controls on basin deposition rather than orthogonal extension. Consequently they putting forward a pull-apart basin formation model associated with strike-slip faulting and amalgamation of arc-related terranes, similar to the modern Philippines Archipelago. However, the Philippines Archipelago is developed on a juvenile crust where as the EGST is developed on pre-existing crust, requiring Krapež and Hand (2008) to suggest the architecture of the EGST is more akin to the western North American Cordillera. While this model may explain facies stacking trends it does not identify the structures along which the inferred amalgamation occurred, nor does it fit the structural record (Blewett and Czarnota, 2007a,b; Blewett et al., 2008b) or account for the $T_{DM}$ model age signatures of the various terranes. Furthermore the constant need for qualifying statements necessary to make the strike-slip model viable reveals an inherent weakness in the model.

Recent work on the upper parts of the Kalgoorlie Sequence in the St Ives area has highlighted the presence of linear north-northwest trending early normal growth faults associated with the deposition of volcaniclastic packages (Squire et al., 2007; Blewett et al., 2008b). This indicates that the deposition of these units is not related to step overs on strike-slip faults and places doubt on the strike-slip model proposed by Krapež and Hand (2008). Based on the presence of mafic and felsic cobble conglomerate in the upper parts of the Kalgoorlie Sequence, Squire et al. (2007) suggested that the upper most part of the sequence may have been deposited in a contractional rather than extensional tectonic setting. This interpretation of the final stages of Kalgoorlie Sequence deposition is consistent with the observation by Blewett and Czarnota (2007a,b) that $D_2$ deformation shuts off volcanism in the EGST at ~2670 Ma.

### Gindalbi Domain

In the younger western part of the Kurnalpi Terrane (Gindalbie Domain), a linear belt of ~2.695–2.68 Ga bimodal rhyolite-basalt and felsic calc-alkaline complexes (Figure 3.1.6b) unconformably overlies the ~2.715–2.704 Ga calc-alkaline Kurnalpi Sequence (Swager, 1995, 1997; Brown et al., 2001; Barley et al., 2008). Barley et al., (2008) recognised that the Kurnalpi Sequence is separated from the bimodal and felsic-subalkaline association by ~ 2.698 Ga deep-marine tholeiitic basalts and komatiites, implying the onset of Gindalbie Domain volcanism records an arc rejuvenation event. Felsic rocks of the Gindalbie Domain are characterized by flat REE patterns with well-developed negative Eu anomalies (Figure 3.1.6e), low Sr and high Y (hence low Sr/Y), with $Na_2O/K_2O$ usually > 1. Witt et al. (1996) and Morris and Witt (1997) argued this chemistry is typical of magmas generated by melting of felsic crust.

An extensional tectonic mode has been advocated for the deposition of the Gindalbie Domain sequence based on the presence of bimodal volcanism and contemporaneous A-type granite intrusion (High-HFSE granites; Hallberg, 1985; Champion and Sheraton, 1997). The lithological association is interpreted to represent an inter arc-rift (Hallberg and Giles, 1986; Barley et al., 2008) controlled

by extension along the north-northwest-striking Ockerburry Fault (Figure 3.1.5c).

The ~2.695–2.68 Ga period of extension is associated with ~ 2.692 Ga Teutonic Bore and Jaguar Cu-Zn volcanic-hosted massive sulphide (VHMS) mineralisation in felsic-subalkaline volcanics along the western edge of the young $T_{DM}$ model age zone (Huston et al., 2005). Both the distribution of base metal mineralisation and the locus of extension are controlled by NNW trending structures highlighting the significance of the ~2.81 Ga inherited rift architecture.

The inferred extensional tectonic mode in the Gindalbie Domain is contrary to the tectonic mode expected based on the presence of subduction slab melts in the Kalgoorlie Sequence which infers a shallowing of the subduction slab. This apparent discrepancy remains unresolved for now.

### 3.1.2.8 2.665–2.650 Ga tectono-stratigraphic associations – Late Basin deposition

The deposition of the Late Basins marks a fundamental change in the geodynamics of the EGST from volcanic-dominated sedimentation to clastic-dominated sedimentation with extensive recycling. Late Basins are coarse siliciclastic sequences with granite detritus (Krapež, 1997) that unconformably overlie, or are in fault contact with, pre-folded older volcanic-dominated sequences (Blewett et al. 2004a). They are mostly preserved within the hanging wall of terrane- and domain-bounding faults, which may have controlled their deposition.

The timing of Late Basin deposition is diachronous across the EGST, constrained to 2.665 Ga in the Kurnalpi Terrane and <2.657 Ga in the Kalgoorlie Terrane based on SHRIMP U-Pb detrital zircon and dating of intrusive porphyries and syenites (Krapež et al., 2000; Fletcher et al., 2001; Sircombe et al., 2007; Kositcin et al., 2008). Two facies types are recorded: fluvial, and turbiditic (Krapež, 1997). Krapež et al. (2000) suggested that the fluvial facies are older than turbidite facies as the former have restricted provenance and the latter a more diverse zircon population reflecting a larger source area evolving through time.

Provenance studies using SHRIMP U-Pb dating of detrital zircons indicate multiple older sources corresponding to known ages of greenstones and granites in the EGST (Barley et al., 2002; 2003). Some old populations, however, have no recognised source in the EGST suggesting, that by Late Basin time, the EGST was connected with the Youanmi Terrane. With the exception of some zircons from the Kurrawang and Jones Creek conglomerates, the age and isotopic characteristics of these sources reflect major magmatic and crustal recycling (Krapež et al., 2000).

The geodynamic model for late basin deposition is contentious. Krapež and Barley (2008) argue Late Basins were deposited in two stages separated by an inversion event. The Kalgoorlie Terrane records a change from fluvial to deep-marine where as the Kurnalpi Terrane records a change from distal to proximal deep-marine facies tracts. In both the Kalgoorlie and Kurnalpi Terranes sparse southeast directed palaeocurrents indicate uplift to the north-controlled sediment dispersal (Krapež and Barley, 2008). Lithofacies stacking is aggradational with forward-stepping facies tracts between depositional sequence-sets, and back-stepping within depositional sequences. Compressional deformation predates, postdates and according to Krapež and Barley (2008) is syn-Late Basin deposition, although, Late Basin stratigraphy is a typical of synorogenic basins. These constraints led, Krapež and Barley (2008) to suggest they were deposited within a strike-slip regime. They argue for north- or northwest-convergence between the Burtville Terrane to the east and the ancestral Yilgarn continent to the northwest associated with the obduction of the EGST over pre-existing continental crust. This tectonic mode is inferred to have produced a south-propagating orogen, with the Kalgoorlie and Kurnalpi Terranes trapped between a tectonic escape corridor. In this model escape to the south between strike-slip faults is inferred to have produced back-stepping facies tracts that simulated basin lengthening, whereas forward-stepping of facies tracts occurred in response to south-propagating uplift.

An alternative to the strike-slip model is that the Late Basins were deposited in narrow extensional grabens, a model advocated by Hallberg (1985) and Blewett and Czarnota (2007). There are five lines of argument favouring this model over the model proposed by Krapež and Barley (2008). Firstly, by definition Late Basins record the exhumation of granite domes since they are the first record of granite detritus. The majority of large granite domes in the EGST are enveloped by extensional shear zones on their margins, a likely record of their exhumation. Late Basins lie in the hanging wall to these shear zones

(McIntyre and Martyn, 2005; Czarnota et al., 2007, Blewett et al., 2008b; see deformation history below) implying a genetic link. Furthermore, Late Basins and the extensional shear zones record metamorphic anticlockwise PTt paths with burial down to 4 kbars (~12 km), a signature indicative of lithospheric extension (Goscombe et al., 2007; see metamorphic section below). It follows then that the extensional shear zones on the edges of granites domes and the extensional history recorded by the basins are genetically linked.

The relationship between the Bundarra batholith on the southwest side of the Keith-Kilkenny Shear System and the Yilgangi Basins (Figure 3.1.7) to the northeast illustrates the relationship between extension unroofing of high-Ca granite batholiths and Late Basin deposition. The Late Basins contain immature sediments (Hallberg and Giles, 1986)) and record a maximum deposition age of 2.660 Ga (Kositcin et al., 2008). The adjacent Bandoora batholith is mostly composed of approximately 2.660 Ga high-Ca granites (Figure 3.1.2, 2.660 Ga High-Ca peak in Kurnalpi Terrane), a likely source of detritus in the Late Basins and is wrapped around by an extensional shear zone (Blewett and Czarnota, 2007). These relationships indicate the emplacement and exhumation of the granite dome as well as Late Basins deposition was rapid under an extensional regime.

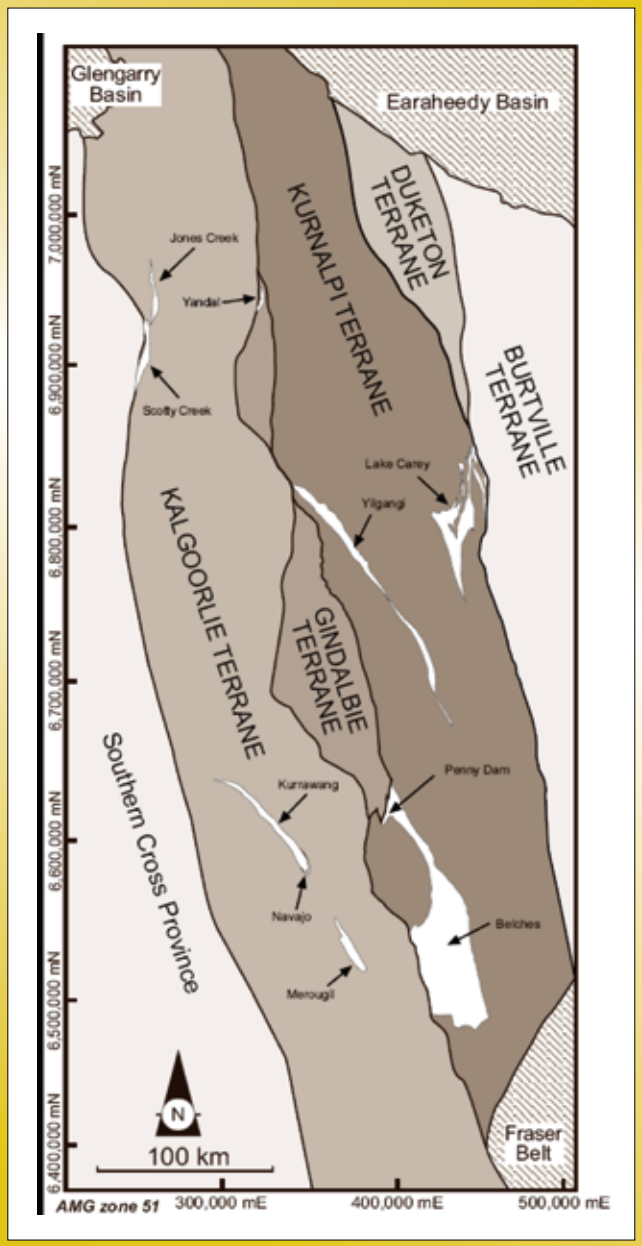


*Figure 3.1.7: Late Basin distribution with respect to the Terranes and Domains of the EGST. Notice the northwest trend of Late Basins except near terrane bounding faults (from Krapež and Barley, 2008). Following the nomenclature outlined in Cassidy et al., (2006) the Gindalbie and Duketon Terranes labelled above have been classified as Domains of the Kurnalpi and Burtville Terranes respectively.*

Secondly, Krapež and Barley (2008) link Late Basin deposition to the final stages of obduction or terrane accretion. If such an event occurred one would expect a record of continent-continent collision to be preserved in the metamorphic history as well as in the seismic profiles through the crust. However, in neither of these two data sets is there evidence of such an event (see metamorphic and deformation sections below).

Thirdly, the NW convergence vector inferred by Krapež and Barley (2008) does not tie in with the structural history as defined by Blewett and Czarnota (2007a,b). The only phase of NW-SE contraction ($D_{4b}$) overprints an earlier ENE-WSW contraction ($D_{4a}$) recorded in the Late Basins and therefore can not be linked to Late Basin deposition (see deformation section for more details). Furthermore under a tectonic escape model suggested by Krapež and Barley (2008) one would expect sinistral movement along the ~north-south striking Hootanui Fault System and dextral movement along the ~north-south striking Ida Fault System in contrast consistent structural overprinting relationships with distinct kinematics have been document across these shear zones and the EGST (Mueller et al., 1988; Blewett and Czarnota, 2007a,b; Blewett et al., 2008b).

Fourthly, there is a temporal (Figure 3.1.2) and spatial (Smithies and Champion, 1999) association of Late Basins with syenites. Syenites are generally emplaced during tectonic extension (e.g., Kadioğlu et al., 2006) thereby further supporting the hypothesis that Late Basins were deposited under the influence of a far field extensional mode.

Lastly, Czarnota et al. (2007) suggested the Late Basins can be subdivided into two groups based on their geometry. The older basins ~2.665 Ga (Stage 1, e.g., Wallaby Basin at the northern end of the Lake Carey Basin in Figure 3.1.7) wrap around the southern margins of granite domes where as the younger basins ~2.660 Ga (Stage 2, e.g., Yilgangi) are more elongate and strike predominantly northwest (Figure 3.1.7). Czarnota et al. (2007) suggested these two stages of basin evolution may reflect two periods of extension. The first related to orogen parallel extrusion (Davis and Maidens, 2003) with down toward the south-southeast extension, consistent with the development of highlands to the north-northwest as inferred by Krapež and Barley (2008) and the second to unidirectional northeast extension. However, these two trends can be simply explained by a northeast extension vector superimposed on the inherited north-northwest striking ~2.81 Ga structural grain. The interplay between the newly formed northwest striking faults and the inherited north-northwest striking grain results in local heterogeneities and hence local variations in the geometry of the basins (see Blewett et al., 2008 and analogue modelling by McClay et al., 2002). Therefore this model can account for the two main Late Basin geometries and also explains the north-south strike of the Scotty Creek basin (Figure 3.1.7).

In summary while the strike-slip model advanced by Krapež and Barley (2008) adequately explains the facies staking trends the timing and architectural relationships of the Late Basin with respect to large granite domes and extensional shear zones together with their overall fining upward trend are more consistent with an extensional geodynamic setting rather than a strike-slip mode.

### 3.1.3 Tectonic constraints from granites

Granites and granitic gneisses comprise approximately 70 percent of the solid geology surface area of the EGST. Due to their sheer volume any model for the tectonic evolution of the EGST has to account for granite genesis and emplacement. Furthermore the study of granites combining geochemistry, geochronology, Sm-Nd isotopic composition and the presence of inherited zircons provides our best constraint on the crustal evolution of the EGST.

Before the seminal work of Champion and Sheraton (1997), granites in the Yilgarn Craton were classified either based on their structural characteristics (Bettenay, 1977; Witt and Swager, 1989; Champion and Sheraton, 1993; Witt and Davy, 1993) or on their relationships with greenstone belts (Sofoulis, 1963; Perring et al., 1989; Cassidy et al., 1991). With increased geochronology (e.g., Nelson, 1997) the structural classification was shown to be inappropriate since some 'syn-' and 'post-kinematic' granites were shown to be of the same age. Since then this apparent structural discrepancy has been attributed to localised strain partitioning on the edges of competent granite intrusions (a feature of granite/greenstone belts). The later subdivisions have some merit since some geochemical distinct granites (e.g., Mafic granites) predominantly intrude greenstones (Champion and Cassidy, 2007), however the two dominant granite

groups recognised by Champion and Sheraton (1997) occur as both 'internal and external' to the greenstone belts indicating this form of classification is of limited value.

Eighty percent of EGST granites are biotite-bearing monzogranites or granodiorites, therefore, morphological classifications are generally of limited use, though detailed mineralogical differences do exist (e.g., Champion and Cassidy, 2000, 2007). With this limitation in mind Champion and Sheraton (1997) classified the granites of the EGST primarily based on their geochemistry. They recognised two major groups (High-Ca and Low-Ca), and three minor groups (High-HFSE, Mafic and Syenitic). This classification was then extended across the entire Yilgarn Craton (Cassidy et al., 2002; Champion and Cassidy, 2002; 2007), and functions as the bench mark for understanding the granite history of the Yilgarn Craton. The characteristics of the five major groups are outlined in Table 3.1.1 and their temporal distribution with respect to the three major terranes of the EGST is outlined in Figure 3.1.2.

### 3.1.3.1 High-Ca granites

The most abundant are the High-Ca granites, which account for more than 60 percent of the granites or over 40 percent of all rock types in the EGST, and probably significantly more by volume. Current exposures of High-Ca granites range from greenschist through to granulite metamorphic facies indicating High-Ca granites make up the majority of the crust to a depth of at least 15 km. Such voluminous granite magmatism necessitates a predominantly extensional tectonic mode to generate the space required during granite emplacement.

High-Ca granites are felsic (68–77wt% SiO2), sodic rocks with heterogeneous LILE enrichment characterised by Sr-undepleted and Y-depleted signatures. These characteristics indicate they were derived from a plagioclase-poor basaltic precursor at pressures large enough to stabilise significant garnet in the residue after melting with an addition of a crustal component; either within thickened mafic crust or melting of subducting oceanic crust (Champion and Cassidy, 2002; 2007).

The High-Ca granites can be subdivided into two groups marked by strong and minor Y-depletion (Figure 3.1.8; Champion and Sheraton, 1997). The subordinate Y-high subgroup is also marked by LILE enrichment indicating this group was either the product of shallower melting with greater crustal contamination or may entirely represent the product of crustal melting. There is also a temporal distribution of these two granite types with the volumetrically dominant Y-low subgroup (>70% of High-Ca granites, Figure 3.1.8) peaking at ~2.675 Ga and the subordinate Y-high and LILE enriched subgroup peaking at 2.66 Ga indicating the first significant recycling of crust commenced during this second peak (Figure 3.1.2). Champion and Cassidy (2007) speculated the onset of significant High-Ca magmatism was associated with a shallowing of the subduction slab. This speculation is consistent with the observed westward shift in the loci of volcanism associated with the deposition of the Kalgoorlie Sequence and Gindalbie Domain volcanics, and with the geochemistry of the volcanic rocks, as pointed out by Morris and Witt (1997). Champion and Cassidy (2007) pointed out too much slab shallowing, however, would have presumably resulted in compression. This conflicts with the inferred extensional tectonic model for the deposition of these volcanic sequences (see discussion above), and, hence, a period of slab roll back is inferred.

Since High-Ca granites are so volumetrically significant it is necessary to consider the source of the granitic melt. If we assume the low-Y subgroup represents at least 10 km of crustal thickness the required eclogitic residue, assuming 10–20% melt extraction from a basaltic precursor (Rapp et al., 1991; Martin, 1994), would be between 50 and 100 km thick. This implies a mafic crust of even greater thickness if the High-Ca granites were dominantly crustal in origin.

The present day crustal structure and composition, consisting of <40km thick crust with subordinate up to 30 percent mafic layers (Drummond et al., 1993; Goleby et al., 1993) is not what would be expected if the High-Ca granites were derived from a mafic source in the lower part of a thickened crust. Therefore this model is either invalid or, as Champion and Smithies (1999) argued, this layer has been delaminated. However, while the delamination model elegantly accounts for the present day crustal structure and other aspects of the EGST (see following) it is nevertheless hard to envisage a process that would have led to the generation of a 100km thick mafic crust in the first place.

Table 3.1.1: Characteristics of the five granite groups in the Yilgarn Craton (after Cassidy et al., 2002 and Champion and Cassidy, 2007)

| Group<br>Area % | Lithologies | Field Characteristics | Geochemistry | Youanmi Terrane | Eastern Goldfields Superterrane | EGST Heat Production[1] | Comments |
|---|---|---|---|---|---|---|---|
| **High-Ca**<br>>60% | **granodiorite, granite, trondhjemite.** distributed both within and external to greenstone belts | strongly deformed to gneissic to mildly deformed; typically ovoid plutons (elongate parallel to structural grain); minor dykes/sills and small bodies; some allanite or sphene | high $Na_2O$, $Na_2O/K_2O$, low Th, LREE, Zr; mostly Y-depleted, Sr undepleted; range of LILE, LREE and Th contents; younger rocks extend to more LILE enriched compositions | >3.0 Ga-2.9? Ga, ca. 2.81 Ga, ca. 2.76 to 2.68 Ga; mostly 2.73–2.68 Ga | ca. 2.8 Ga (minor remnants); 2.74–2.65 Ga; majority 2.685 to 2.655 Ga; youngest members appear to occur within Kalgoorlie Terrane | $3.06 \times 10^{-6}$ uW/m$^3$ at 2.670 Ga assuming a density of 2650 kg/m$^3$ | high pressure partial melting of basaltic protoliths |
| **Low-Ca**<br>>20% | **granodiorite, granite** mostly external to greenstone belts | mildly deformed to undeformed, locally strongly deformed; large intrusions (sheet-like) to small pods and dykes; biotite-dominant; allanite, sphene and fluorite-bearing | high $K_2O$, low $Na_2O$, high Rb, Th, LREE, Zr; moderately fractionated end-members | 2.65–2.6? Ga; mostly 2.65 to 2.63 Ga; possibly also 2.685 Ga | 2.655 to 2.63 Ga | $10.22 \times 10^{-6}$ uW/m$^3$ at 2.645 Ga assuming a density of 2650 kg/m$^3$ | partial melting of High-Ca type source rocks |
| **High-HFSE**<br>5–10% | **granite, minor granodiorite** mostly internal or marginal to greenstone belts | variably deformed, high level intrusives, commonly spatially associated with volcanic rocks and volcanic complexes; presence of amphibole in a very felsic rock is diagnostic | distinctive combination of high FeO*, MgO, $TiO_2$, Y, Zr with low Rb, Pb, Sr, $Al_2O_3$ | 3.01 to 2.92 Ga?, ca. 2.81 Ga, 2.76 Ga to 2.45 and younger?; also 2655–2620 Ma | >2.72 Ga to 2.665 Ga; 2.7 to 2.68 Ga most common; mostly geographically restricted to Kurnalpi Terrane and north-east Kalgoorlie Terrane | $3.63 \times 10^{-6}$ uW/m$^3$ at 2.700 Ga assuming a density of 2650 kg/m$^3$ | spatial association with VHMS mineral systems |
| **Mafic**<br>5–10% | **diorite, granodiorite, granite, tonalite and trondhjemite** | variably deformed, distinctive dark-looking granites; form moderate to small sized plutons and common dykes and sills; common amphibole ± biotite ± pyroxene | low $SiO_2$ (55–70+%), moderate to high Ni, Cr, MgO; range of LILE, LREE and Th; subdivided into high- and low-LILE | 3.01 to 2.92 Ga?, ca. 2.81 Ga, 2.76 Ga to 2.10 Ga | >2.72 Ga to 2.65 Ga; possibly younger? LILE-enriched members tend to be ca. 2.665 and younger | $3.70 \times 10^{-6}$ uW/m$^3$ at 2.700 Ga assuming a density of 2700 kg/m$^3$ | common spatial association with gold mineralisation, especially high-LILE members |
| **Syenitic**<br><5% | **syenite, quartz syenite** internal or marginal to greenstone belt | commonly undeformed; distinctive red granites with green pyroxene (or amphibole); K-feldspar rich, little or no quartz | high total alkalis ($Na_2O + K_2O$) 10–12%; commonly low MgO, FeO*, $TiO_2$ | none | ca. 2.65 Ga, and 2.655–2.645 Ga | $4.31 \times 10^{-6}$ uW/m$^3$ at 2.665 Ga assuming a density of 2650 kg/m$^3$ | some spatial association with gold mineralisation |

1 Heat production is calculated using the formula outlined in Turcotte and Schubert (1982)

For this reason, an origin via partial melting of the subducting slab is preferred for the generation of the low-Y subgroup. However, as argued by Champion and Sheraton, 1997), $T_{DM}$ model ages and inherited zircons indicate the High-Ca granites have a significant crustal component, as does the presence of high-Y High-Ca granites which indicate additional non-slab sources (Champion and Sheraton, 1997). The apparent discrepancy between subduction derived melting and crustal $\varepsilon_{Nd}$ signatures is problematic, but perhaps can be explained through deep-crustal hybridisation processes such as the proposed MASH (melting, assimilation, storage and homogenisation) zones of Hildreth and Moorbath (1988) at the mantle-crust boundary as depicted in Figure 3.1.5c,d. Significant amounts of crustal interaction, up to 30–50% (dependent on REE contents and isotopic signatures of components), at garnet stable conditions (depths >35 km), would have been required for slab melts to acquire a crustal signature (see Champion and Cassidy, in prep for details), indicating that MASH zones, if indeed present, would have been thick. Areas of greatest ~2.81 Ga extension and, hence, greatest ~2.81 Ga juvenile crust formation and underplating (Figure 3.1.5a) are inferred to have had a larger ~2.81 Ga crustal contribution in the MASH zone (e.g., Kurnalpi Terrane) and hence the generation of younger $T_{DM}$ model ages as opposed to zone of lesser ~2.81 Ga crustal extension (e.g., Kalgoorlie Terrane) which represent sites with greater interaction with older crust thereby resulting in older $\varepsilon_{Nd}$ model ages (Figures 3.1.5c, d).

One may argue that from a MASH model point of view it is feasible that the observed isotopic pattern is in part, a reflection of crustal thickness not crustal age. That is, less mixing occurred in thinned crust such as the Kurnalpi Terrane. However, within each isotopic zone there are granites over a range of time with similar isotopic signatures such that the $T_{DM}$ model ages simply can't be a function of crustal thickness unless the crustal thickness didn't change over time.

*Figure 3.1.8: Sr/Y versus Y plot of EGST High-Ca granites illustrating the continuum between the high-Y (red) and low-Y (grey) subgroups which make up 20 and 70% of EGST High-Ca granites, respectively.*

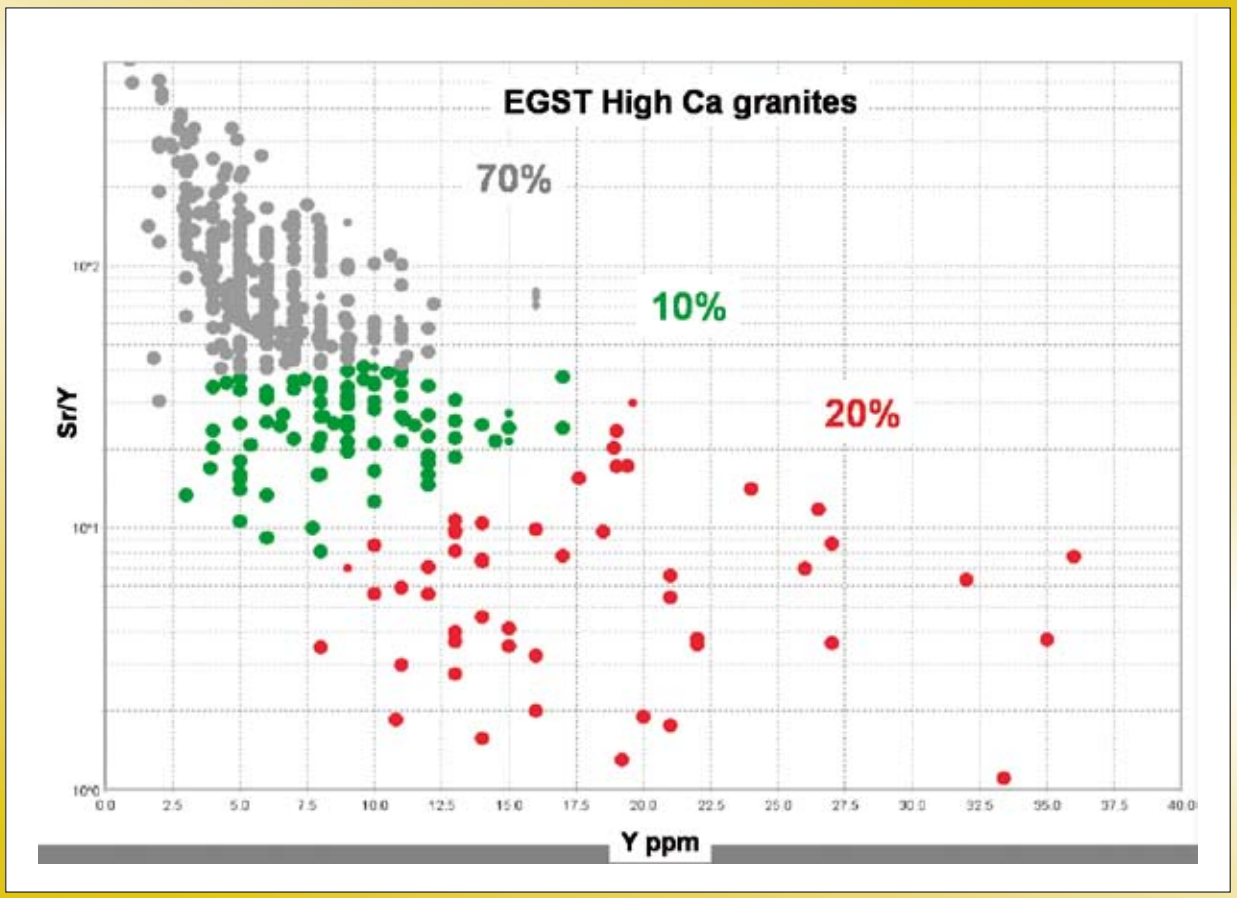

### 3.1.3.2 Low-Ca granites

The younger Low-Ca granites (Figure 3.1.2) are the second most voluminous group in the EGST, constituting approximately 20% of granite volume. They are chemically distinct from the High-Ca granites, characterised by high-LILE, strong enrichment in LREE and some HFSE, and compositions consistent with fractional crystallisation (Champion and Sheraton, 1997). They were derived by partial melting of broadly tonalitic crust; that is they represent reworking of older High-Ca granitic crust and hence mark a significant change in the thermal regime of the crust (Champion and Cassidy, 2007). The emplacement of Low-Ca granites is diachronous across the Yilgarn Craton with the first peak in the east at 2.65 Ga in the Burtville and Kurnalpi Terranes and subsequently at 2.645 Ga in the Kalgoorlie Terrane. Likewise the waning of Low-Ca granite magmatism is also diachronous with the last peaks in Low-Ca magmatism in the Burtville, Kurnalpi and Kalgoorlie Terranes at approximately 2.64 Ga, 2.63 Ga and 2.62 Ga respectively (Figure 3.1.2).

Low-Ca granites are characterised by high values of HHPE (high heat producing elements). Their heat production (Table 3.1.1) calculated at 2.645 Ga is very high at $10.22x10^{-6}$ uW/$m^3$ assuming a density of 2650 kg/$m^3$ using the formula outlined in Turcotte and Schubert (1982). The Low-Ca heat production is three times greater than of the High-Ca granites ($3.06x10^{-6}$ uW/$m^3$ at 2.670 Ga assuming a density of 2650kg/$m^3$) from which they were derived. This variation is attributed to a transfer of HHPE from the High-Ca granites in the middle crust to the upper crust in the Low-Ca granites and hence the effective cratonisation of the Yilgarn Craton (Cassidy et al., 2006).

### 3.1.3.3 High-HFSE granites

High-HFSE granites are volumetrically minor, representing less than 5% of granites in the EGST. They are subvolcanic, often associated with volcanics and include similar composition felsic volcanic rocks. They are very felsic (>74% $SiO_2$) with distinct A-type characteristics displaying a unique combination of high FeO, MgO, $TiO_2$, Y, Zr and low LILE (especially Rb, Pb), Sr and $Al_2O_3$ (Champion and Cassidy, 2002; 2007). The high-HFSE granites are crustal melts which display a localised spatial distribution best interpreted as related to extension during intracontinental rifting (Hallberg and Giles, 1986). The persistence of high-HFSE granites from ~2.72 to ~2.78 (Figure 3.1.2) further supports the interpretation this period of volcanic greenstone deposition was predominantly controlled by an extensional tectonic mode (Figure 3.1.5c).

### 3.1.3.4 Mafic granites

Mafic granites are volumetrically, minor representing less than 5% of granites in the EGST. Yet their unique geochemistry and proximity to gold mineralisation makes them tectonically and economically significant. They are mostly characterised by low and variable silica content (50 to >70% $SiO_2$), moderate to high Ni, Cr, MgO and a range of LILE, LREE and Th. They have been subdivided into high- and low-LILE subgroups with the latter typically associated with gold mineralisation (Champion and Sheraton, 1997; Champion and Cassidy, 2000, 2002, 2007). To explain the variations in LILE and LREE, Champion and Sheraton (1997) invoked the interaction of mantle and crustal components to generate these magmas. Beakhouse (2007), studying similar granites (Sanukitoids) in the Canadian Superior Province, argued they represent a metasomatised mantle source and provide the strongest evidence for the operation of subduction in the Neoarchaean. In the Beakhouse (2007) model the above chemical variation is attributed to the partial melting of a long-term depleted mantle that was metasomatically enriched in a wide range of LILE and HFSE shortly before melting with the broad compositional spectrum in part reflecting assimilation and fractional crystallisation processes. Mafic granites were emplaced after the cessation of volcanism and low-Y subgroup High-Ca magmatism. They are temporally associated with the onset of Late Basin deposition and the initiation of syenite emplacement at 2.665 Ga (Figures 3.1.2, 3.1.5e).

### 3.1.3.5 Syenites

Syenites represent less than 5% of granites in the EGST. The syenite group (55–75% $SiO_2$) is characterised by their high $Na_2O$, $K_2O$, and total alkalis (>10%) with commonly low MgO, FeO and $TiO_2$ (Libby, 1978; Johnson, 1991; Witt and Davy, 1997; Champion and Sheraton, 1997). Smithies and Champion (1999) subdivided the syenites of the EGST into four spatially and compositionally

distinct suites and argued for an anhydrous crustal origin for these magmas. The combination of features that suggest a crustal origin are as follows: lack of associated mafic magmatism; high LILE; inherited zircons with similar ages to whole rock Sm-Nd model ages; evidence for regional source heterogeneity; constant and distinct suite La/Y and Nb/Y ratios; as well as compositional similarities to Low-Ca granites. However extreme enrichment in Sr and Ba in the Mount Monger Suite of the Kalgoorlie Terrane and the Wallaby Syenite of the Kurnalpi Terrane indicates that the source of some of the Syenites may have been metasomatised before or during melting. Syenite emplacement occurred in association with two peaks at 2.665 Ma in the Kalgoorlie, Kurnalpi and Burtville Terranes and 2.650 Ga in the Kurnalpi Terrane. All of the metasomatised syenites data so far (including the Kurnalpi Terrane 2.664 Wallaby Syenite (Salier et al. 2004)) were emplaced at ~2.665 Ga in association with Mafic-granites were as the 2.650 Ga peak corresponds to the crustally-derived Low-Ca granites of the Kurnalpi Terrane (Figure 3.1.2) and ~2.63–2.64 Ga minor calc-alkaline lamprophyres (Rock et al., 1990). Smithies and Champion (1999) also recognised a spatial association of the four suites with major NNW to NW trending faults indicating the emplacement of Syenites was clearly controlled by these major crustal structures (e.g., Libby, 1978).

### Delamination model

Smithies and Champion (1999) argued syenite magmas and Low-Ca granites were the product of a Yilgarn Craton-wide delamination event. They based their hypothesis on two supporting lines of evidence. Firstly they noted the EGST-wide distribution of Syenites and the craton-wide distribution of Low-Ca granites. Secondly they recognised the formation of Syenites requires temperatures >900°C and the time lag between High-Ca granite magmatism and Syenite emplacement precludes the generation of Syenites related to any High-Ca granite related thermal regime (typically in the range of 750–850°C). This second point is in contrast to arguments forwarded by Campbell and Hill (1988) who argued for a single thermal anomaly at the base of the lithosphere was responsible for the 100 Myr (~2.7–2.6 Ga) EGST rock record. A combination of these two lines of evidence presented by Smithies and Champion (1999) necessitates a craton-wide heat pulse for the generation of Syenites and Low-Ca granites.

Based on the presupposition Low-Ca granites were crustal melts, Smithies and Champion (1999) argued that delamination occurred at ~2.650 Ga in response to the falling away of the gravitationally unstable dense, restitic-eclogitic lower crust, triggered by ~2.665–2.660 Ga '$D_2$' east-west compression. Delamination resulted in crustal extension, the generation of a flat MOHO and metasomatism of the post-delaminated lower crust where crustal scale fractures facilitated volatile exchange and hence led to the generation of metasomatised Syenites. Incorporating the ideas of Kent et al. (1996), they argued for metamorphic dehydration of the crust associated with the heat pulse and the associated input of mantle-derived volatiles and mineralising fluids into crustal penetrating fractures.

Since the work of Smithies and Champion (1999) there have been a number of advances in our understanding of the EGST that warrant a revision of the above model. Firstly Late Basin deposition and the intrusion of metasomatised mantle melts has been linked to ~2.665–2.660 Ga diachronous extension. Secondly, two peaks in High-Ca granite magmatism have been recognised. The first High-Ca granite peak is associated with TTG volcanism in the Kalgoorlie Sequence and, hence, linked to subduction zone tectonic processes. The second High-Ca granite peak is, here, attributed to crustal melting based on its chemistry and the lack of volcanism during this time period. Thirdly the timing of $D_2$ contraction has been recognised to be diachronous and short lived across the EGST initiating at around 2.670 Ga in the Kurnalpi Terrane.

Considering these new constraints it is suggested that delamination of the lower crustal MASH zone occurred in response to diachronous $D_2$ compression, which shut off volcanism and resulted in crustal extension resulting in: Late Basin deposition; rapid input of heat into the base of the crust; and emplacement of metasomatised mantle melts (Figure 3.1.5e). It is postulated, diachronous thermal diffusion through the crust resulted initially in the generation of high-Y High-Ca granite from the lower-crust and subsequently Low-Ca granites from the mid crust (Figures 3.1.5f, g).

A modern examples of delamination associated with a subduction zone setting with diachronous convergence is well documented by Stern et al., (2006) from the

Taupo Volcanic Zone in New Zealand. In this example delamination occurs through Rayleigh-Taylor instabilities in a spatially restricted zone rather than across the whole northern island. Nevertheless, this example demonstrates, that delamination events do occur associated with metasomatised mantle melts and ongoing subduction. The unresolved question of how to trigger craton wide delamination across the Yilgarn Craton, however, remains.

The delamination model can be test by considering the time scale of thermal diffusivity through the crust and comparing it to the length scale (thickness) of the crust. In the Kurnalpi Terrane mid-orogenic extension is constrained to have initiated at ~2.665 Ga and Low-Ca magmatism terminated at 2.630 Ga. These two events can be used as proxies for the initiation of delamination and the complete diffusion of the heat supplied to the base during delamination respectively.

Applying the thermal diffusivity equation given by Campbell and Hill (1988):

$t=x^2/2D$

where t is time, x is distance and D is the diffusivity of heat which we assume to be 1 x $10^{-6}$ $m^2s^{-1}$ (Campbell and Hill, 1988), the length scale corresponding to a time scale of 35 Myr is 47km. This length scale approximates the inferred crustal thickness at the end of the Low-Ca event (~ 40 km present crustal thickness plus 5–7 km of erosion). Therefore, this simple calculation indicates the rock record after the inferred period of lower crustal delamination is approximately consistent with the rate it would take to diffuse heat through the crust.

A short-coming of the delamination model, and an area for future research, is a lack of understanding related to how the Archaean lithosphere behaved during this delamination event. The lower boundary of the Archaean lithosphere underneath the Yilgarn craton is uncertain but must lie at a depth between 120 km and 200 km (Blewett et al., 2008a). Griffin and O'Reilly (2007) argued the thick and buoyant Archaean lithosphere would resist delamination. Yet the seismic data over the Yilgarn craton shows a flat MOHO commonly interpreted as a telltale sign of delamination (Nelson, 1992).

The tomography data of the EGST shows a 25 km thick fast (>4.8 km/sec) shear wave velocity layer at 120 km depth. This surface has been suggested by Blewett (2004), to represent the delaminated part of the upper crust which froze during the process of delamination. The thickness of this layer approximates the thickness of the MASH zone inferred to have formed as a result of High-Ca granite magmatism. The freezing, and hence preservation of the delaminated lower crust may be due to the buoyancy of the Archaean lithosphere which only allowed approximately 60 km of mantle material to upwell into the base of the crust. The steps or tears in this high velocity layer are inferred to linked to sites of metasomatised mantle upwelling and hence the generation of Mafic-granites and Syenites associated with deep crustal structures (Figure 3.1.5e).

### 3.1.4 Tectonic constraints from the deformation history

Gold deposits of the EGST are structurally controlled, hence the deformation history of the EGST has been extensively studied. Numerous authors have identified regionally correlated contractional deformation events across the EGST. This ability to correlate regional deformation events associated with horizontal stresses supports the argument for the operation of horizontal plate tectonics as opposed to vertical tectonics during the Neoarchaean.

A detailed review of EGST deformation events is presented in Blewett et al. (2008b) and hence this discussion is restricted to a review of the salient features and controversies.

#### 3.1.4.1 $D_1$ – ENE extension (<2.67 Ga)

The EGST displays a pronounced NNW-oriented structural grain defined by the regional fault pattern and elongate granitoid bodies (Gee, 1979). This structural trend has been commonly attributed to '$D_2$' ENE-WSW contraction (Swager, 1997), however as discussed above the NNW-striking grain as revealed in the Nd $T_{DM}$ map (Figure 3.1.4) was most likely established early in the tectonic history of EGST associated with ~2.81 Ga rifting event. Therefore, the major NNW trending faults mark the trend of major crustal structures which have been reused through out the deformation history of the EGST and are not merely the expression of '$D_2$' deformation.

A study of the structural over printing relationships across the central and northern Yilgarn by Blewett and Czarnota (2007) revealed that all the three terranes of the EGST display a common structural history post-2.67 Ga. This places constraints on any allochthonous model for the development of the EGST by indicating the terranes of the EGST were together by 2.67 Ga. Macroscopic pre-2.67 Ga structures cannot be correlated across the EGST due to overprinting effects of subsequent deformation and have been grouped together and termed $D_1$. This earliest group of structures predominantly consists of extensional shear zones with minor contractional structures interpreted to represent subduction related deformation.

### 3.1.4.2 $D_2$ – ENE contraction (east ~2.670 Ga, west ~2.665 Ga)

The first phase of mesoscopic deformation (that can be correlated between terranes) is associated with east-northeast contraction ($D_2$), and the development of north-northwest striking upright folds. Surprisingly this event is not associated with an EGST-wide penetrative foliation although locally intense regions of $D_2$ foliation are preserved (e.g., Westralia and Tarmoola). $D_2$ folds affected the youngest volcanic sequences across the EGST but are unconformably overlain by Late Basins (Blewett et al., 2004) and in places cross cut by granite domes (Blewett and Czarnota, 2007). These relationships constrain $D_2$ deformation to between the end of volcanism and Late Basin deposition.

The preserved rock record implies $D_2$ deformation was diachronous across the EGST (Figure 3.1.2). In the Kurnalpi Terrane the youngest preserved volcanics are at ~2.675 Ga and Late Basin deposition commenced at 2.665 Ga. Where as, in the Kalgoorlie Terrane volcanism shut off at ~2.665 Ga and Late Basin deposition is constrained to <2.660 Ga.

The lack of a pervasive fabric and the general open nature of $F_2$ folds indicate $D_2$ resulted in minor crustal thickening. However, $D_2$ occurred at the tail end of significant magmatic crustal thickening through High-Ca granite intrusion. Consequently even through $D_2$ was only minor it was the catalyst for crustal over thickening which triggered $D_3$ lithospheric extension and lower crustal delamination.

### 3.1.4.3 $D_3$ – mid orogenic ~ENE extension (east ~2.665 Ga, west ~2.660 Ga)

The $D_3$ event is a period of lithospheric extension in response to magmatic and tectonic crustal thickening which resulted in lower crustal delamination. The characteristic structural features of $D_3$ extension are: the development of large extensional detachment shear zones around large granite domes; the exhumation of lower plate granites and greenstones; and, the development of accommodation space in the upper plate across northwest striking normal faults necessary for the deposition of the Late Basins (Figure 3.1. 5e).

Extension along the margins of large granite domes has long been recognised in the EGST. Williams et al. (1989), and Williams and Whitaker (1993) identified extension along the north-eastern and south-eastern edges of the Raeside and Mt Margaret Batholith, respectively. Williams and Currie (1993) documented approximately 2–3 kbars of metamorphic grade excision across the sons of Gwalia extensional shear zone. However, these authors linked this extension to the deposition of the mafic/ultramafic sequence at approximately 2.70 Ga rather than Late Basin deposition (the first record of granite detritus).

Swager and Nelson (1997) constrained the timing of a similar style of extension along the western edge of the Kirgella Dome in the Burtville Terrane to approximately 2.660 Ga. Based on this age they argued this phase of extension overlapped with regional east-west contraction as defined by Swager (2007). Davis and Maidens (2003) likewise recognised extension at this time but argued for an orogen parallel extrusion model with down to the south-southeast extension thereby accounting for the prominent north-northwest striking stretching lineation in some large granites and granite gneisses (Hammond and Nisbet, 1992; Williams and Whitaker, 1993). McIntyre and Martyn (2005) linked this phase of extension to the deposition of the Wallaby Late Basin but also advocated for an orogen parallel extrusion model.

In contrast, Blewett and Czarnota (2007) argued for a whole scale switch in the deformation history from $D_2$ east-northeast contraction to $D_3$ northeast-directed extension. They documented extensional shear zones around most of the large granite domes in the central EGST and associated radial extension vectors. They attributed the radial extension to local stress field

heterogeneities associated with rising granite domes and assigned more significance to the regional map patterns in establishing the far field extension direction. They interpreted the northwest strike of the Late Basins (Figure 3.1.7) and large granite domes together with down-to-the-east asymmetry in reflection seismic profiles (see below) as evidence for a far-field northeast-directed extension vector. They also realised the characteristic rhomboid fault network pattern in the EGST was established due to the superposition of the $D_3$ northwest striking structural grain and the inherited ~2.81 Ga north-northwest striking structural grain.

Blewett and Czarnota (2007) also documented $D_3$ extensional shear zones cross cutting syenite and mafic granites thereby constraining $D_3$ extension to syn- to post 2.665 Ga (e.g., extensional foliation in: 2663±3 Ma Lawlers Tonalite (Fletcher et al., 2001) and 2664±2 Ma Hanns Camp Syenite (GA, Oz Chron)).

Blewett and Czarnota (2007) and Czarnota et al. (2007) showed it is possible to link surface $D_3$ extensional kinematics with reflectors in crustal seismic profiles at Leonora. This observation led to the recognition the seismic architecture of the EGST was mostly developed during extension rather than contraction thereby discounting previous fold and thrust belt interpretations (Drummond et al., 2000; Goleby et al., 2003) and obduction tectonic models (e.g., Archibald, 2002; Barley, 2006) in favour of extensional geometries earlier advocated by Hammond and Nisbet (1993).

The attribution of the majority of the architecture of the EGST to the $D_3$ event implies the crustal penetrating shear zones were initiated during this phase of deformation thereby establishing a connectivity with the metasomatised mantle during $D_3$ (Figure 3.1.5e). This connectivity is expressed in the magmatic record by the first arrival of syenite and mafic granites coincident with Late Basin deposition and their intrusion along northwest striking structures (Smithies and Champion, 1999). It is this link with the enriched mantle that is attributed as the cause for the initiation of significant gold mineralisation in the EGST during $D_3$ (Figure 3.1. 2).

$D_3$ deformation was also significant in storing fluid in the crust. Numerical deformation driven fluid flow modelling by Sheldon et al. (2007) indicated the switch in tectonic mode from extension ($D_3$) to contraction ($D_4$) results in a reversal in the direction of fluid flow. An extensional tectonic model results in predominately downward flow where as a switch to contraction results in focused upward flow. Therefore it can be inferred that not only did the $D_3$ extensional event develop the architecture necessary for subsequent fluid focusing but it also stored mineralising fluids associated with metasomatised mantle melts (Cleverly et al., 2007) introduced during $D_3$ extension.

### 3.1.4.4 $D_4$ – (a) ENE and (2.655 Ga) (b) ESE contraction (east ~2.655 Ga, west ~2.650 Ga)

Deposition of the Late Basins was immediately followed by resumed contraction $D_4$ (Figure 3.1.5f) resulting in tight to isoclinal folding and faulting of the Late Basins and heterogeneous strain partitioning along the flanks of newly formed granite domes (Blewett et al., 2008b). The inherited extensional architecture controlled the localisation of $D_4$ structures and facilitated fluid focusing. $D_4$ deformation was associated with two separate palaeostress fields $D_{4a}$ and $D_{4b}$.

$D_{4a}$ contraction was oriented ~east-northeast–west-southwest and resulted in reverse faulting and folding. $D_{4a}$ was more intense than $D_2$ and together these two deformations constitute the '$D_2$' event described by Swager (1997). Apart from locations within Late Basins (which act as a time marker) $D_2$ and $D_{4a}$ deformation is indistinguishable in the field (Blewett et al., 2008b).

Continued shorting was associated with a rotation or switch in the principle stress direction during $D_{4b}$ to ~east-southeast–west-northwest directed shorting. This second phase of deformation was characterised by sinistral transpressional shear zones along northwest to north-northwest striking fault zones in regions with steep stratigraphic dips, where thrusting and flattening ceased to be effective in dissipating the stress. It is speculated the northwest to north-northwest faults zones initiated as extensional growth faults during $D_1$ and $D_3$ and localised strain during $D_{4b}$ due to the significant competency contracts across them (e.g., Henson et al., 2008).

The $D_{4b}$ event marks the initiation of strike-slip deformation in the EGST and a significant change from prior phases of dip-slip east-northeast to northeast directed extension and contraction. This switch to strike-slip deformation resulted in the ironing out of down dip

heterogeneities established during prior dip-slip movement on long-lived structures. This ironing out process resulted in the localisation of damage zones and associated fluid flow. Blewett and Czarnota, (2007) documented a highly anisotropic $D_{4b}$ palaeostress field which is attributed to this process as well as the effect of ironing out of the highly anisotropic domal architecture established during $D_3$ extension.

While $D_{4b}$ was significant in localising fluid flow and the majority of gold mineralisation lies within $D_{4b}$ shear zones (e.g., Super Pit, St Ives camp, Wallaby (Bateman and Berline, 2006; Miller, 2006)) that is not to say that $D_{4b}$ shear zones are characterised by large displacements. In fact apart from the major northwest to north-northwest trending sinistral shear zones, which display a high component of pure shear, most of the other structures associated with this event are medium to low strain (Blewett and Czarnota, 2007). Furthermore, the success of stress transfer modelling in predicting the localisation of gold deposits associated with constraining and/or releasing bends along strike-slip faults (e.g., Cox and Ruming, 2004) indicates these faults do not have large displacements otherwise their heterogeneities would be ironed out. Attributing the initial of $D_{4b}$ to periods of extension provides an explanation as to why gold mineralisation is distributed along miss-oriented faults at St Ives (Crawford and Cox, 2007).

$D_{4b}$ was also associated with the development of significant stress transfer structures. S-over-N thrusts in the Kambalda and Kanowna area (Foster, Tramways Republican, and Fitzroy) described by Swager (1997) as '$D_1$' are attributed to have formed during $D_{4b}$. The reassignment of these structure to $D_{4b}$ is firstly based on the recognition that they cut $F_2$ folds and an earlier north-northwest striking foliation and are therefore younger, not older, than $D_2$ (Blewett et al., 2008b). Secondly, that they are spatialy associated with north-northwest striking sinistral shear zones (Blewett, 2004; Blewett and Czarnota, 2007; Blewett et al., 2008b).

#### 3.1.4.5 $D_5$ – NE-SW contraction (east <2.655 Ga, west <2.650 Ga)

$D_{4b}$ sinistral transpressional shear zones are overprinted by north to north-northeast striking $D_5$ dextral faults and shear zones (Blewett and Czarnota, 2007; Miller, 2006; Mueller et al., 1988; Figure 3.1.5g). Blewett et al. (2004b) constrained the timing of $D_5$ to syn-Low-Ca granite emplacement, at 2.650 and 2.645 Ga in the Kurnalpi and Kalgoorlie Terranes respectively, indicating it may be diachronous across the EGST. Czarnota et al. (2007), based on a study of the central EGST, interpreted $D_5$ as a transtensional event allowing for the introduction of the moderately voluminous Low-Ca granites and accounting for the development of mostly north-northeast striking dextral normal faults (Blewett and Czarnota, 2007; Miller, 2006). However around Kalgoorlie, Blewett et al. (2008c) and Muller et al. (1988) argued $D_5$ is transpressional.

The principal stress during $D_5$ deformation is constrained using P-T dihedra analysis to be ~northeast-southwest directed (Blewett and Czarnota, 2007). Hence the palaeostress switch from $D_{4b}$ to $D_5$ represents the largest change in the palaeostress observed in the EGST. It is this palaeostress switch which is interpreted to have triggered another period of gold mineralisation. The bulk of the mineralisation at Mt. Charlotte (Bateman and Berline, 2006), Sunrise Dam (Miller, 2006) and Wiluna (Hagemann, 1992) is hosted in $D_5$ dextral normal faults.

#### 3.1.4.6 Post $D_5$ deformation

Following $D_5$ the EGST was affected by another two phases of deformation with uncertain relative timing. One involved a phase of vertical shortening resulting in the development of horizontal crenulations in highly foliated zones and normal faults with no preferred orientation (Blewett and Czarnota, 2007; Weinberg and van der Borgh, 2008). The second deformation event was associated with the development of brittle predominantly west-southwest striking sinistral faults interpreted by Blewett and Czarnota (2007) to be related to Proterozoic dyke events.

### 3.1.5 Metamorphic constraints on tectonic models

In the last two years a significant advance has been made in the study of metamorphism in the EGST. Goscombe et al. (2007) have derived temporal and spatial metamorphic patterns which place significant constraints on previous tectonic models. Past models mostly assumed an invariant crustal depth with a single prograde metamorphic event (e.g., Binns et al., 1976) where as, Goscombe et al. (2007) identified large variations in peak metamorphic crustal

depths (12–30 km) across the EGST, and five distinct metamorphic events (Figure 3.1.2). However unlike stress field switching, thermal events involve slow rates, conductive delays and a history less punctuated than the structural evolution, necessitating broad thermal events and continuums between them, particularly from M2 to M3a and M3b (Figure 3.1.2). The work of Goscombe et al., (2007) builds on studies by Archibald (1978), Ridley (1993), Witt (1991), Witt et al. (1997) and Mikucki (1997) who examined pressure variations, P-T evolutions and the relationships to tectonics.

### 3.1.5.1 Ma – rare, high-T, high-G (2.720–2.685 Ga)

Granulite metamorphism is recognised in only two localities: a cluster in the northern part of the Southern Duketon Domain and in one location in the northern part of the Gindalbie Domain (Figure 3.1.1). These granulites are statically metamorphosed gabbros, preserving ghosted ophitic textures, recrystallised to granoblastic two-pyroxene assemblages. Peak metamorphic conditions of ~730 °C at low pressures between 2.5–5.0 kbar, indicating very high average thermal gradients (G – simply the ratio T/depth assuming a density of 2.8 gm/cm$^3$) between 45–80 °C/km. These high-temperature (T) high-geothermal gradient conditions in the upper-crust are most likely formed in a high heat flow magmatic arc environment (Ma). Such a scenario would result in small high grade domains, widely scattered and of different ages, reflecting multiple magmatic arcs (Figure 3.1.2). In contrast, formation in either an extensional or plume setting would result in widespread distribution, which is not recorded in the EGST.

### 3.1.5.2 M1 – discrete, medium-P, low-G metamorphism (2.720–2.685 Ga)

Rare, but widely distributed medium-pressure (P >6 kbar up to 8.7 kbar), high-T (>600 °C) and uniquely low average thermal gradient (G ≤20 °C/km) metamorphic parageneses are found almost exclusively associated with high-strain shear zones (e.g. Ida, Ockerburry, Celia and Hootanui Fault systems) predominantly on the edges of large granite domes (Figure 3.1.9a). Lu-Hf dating of representative metamorphic events yielded unreasonably old ages although the relative ages between events are likely significant. A single Lu-Hf garnet age from one of these high-grade parageneses is 15 Myrs older than Lu-Hf ages for garnets from regional metamorphic parageneses and 30–35 Myrs older than Lu-Hf ages for metamorphic garnet in a post-volcanic Late Basin. Consequently, these medium-P high- T parageneses are thought to be early formed, prior to pervasive regional metamorphic events. This is substantiated by overprinting of medium-P rocks within shear zones by lower grade shear assemblages characterized by high average thermal gradients (G ≥40°C/km). Peak-T was attained at peak-P and was followed by near isothermal decompression, either in the same M1 metamorphic cycle or during a later exhumation event.

The geodynamic setting for early, medium-P parageneses is unknown but can be explained by two competing end-member processes:

1. Assuming widespread regional M1 metamorphism the current restricted distribution is due to late-stage exhumation bringing only a portion into the shallow crustal (i.e. by $D_3$ and M3a extensional telescoping). This scenario is supported by exposures within shear zones but nevertheless would predict more widespread relict medium-P parageneses, such as in garnet cores, boudins and xenoliths.

2. If M1 metamorphism was spatially restricted at the time of formation, then the currently exposed distribution is significant. In this case the tectonic setting would be responsible for discrete, thin, arcuate zones of rapid down advection followed by rapid exhumation, such that thermal diffusion could not keep pace with pressure change. Such a process may possibly occur within a shallow and/or slow subduction setting, although typical modern day subduction geothermal gradients (G<18°C/km) are lower than recorded for M1 (G≤20°C/km). Alternatively it is a result of downward advection of greenstones associated with granitic diapiric overturning (e.g. Collins and Van Kranendonk, 1999). However the Lu/Hf garnet ages preclude a diapiric overturning interpretation by constraining M1 metamorphism to pre-High-Ca granite magmatism (Figure 3.1.2), an obvious driver for diapirism. Therefore a down advection setting more akin to subduction is the favoured interpretation for M1, ascribing the atypical geothermal gradients to higher heat flow during the Archaean (de Wit, 1998).

*Figure 3.1.9: Distributions of metamorphic parageneses and effects during two metamorphic periods from Goscombe et al. (2007). a) M1 and Ma parageneses highlighting the distribution of high pressure metamorphism b) M2 metamorphic pattern – a composite including M3a parageneses, which cannot be isolated. Nevertheless, the widespread distribution of M2 effects is thought generally correct, temperature remaining elevated in parts, forming a continuum with M3a.*

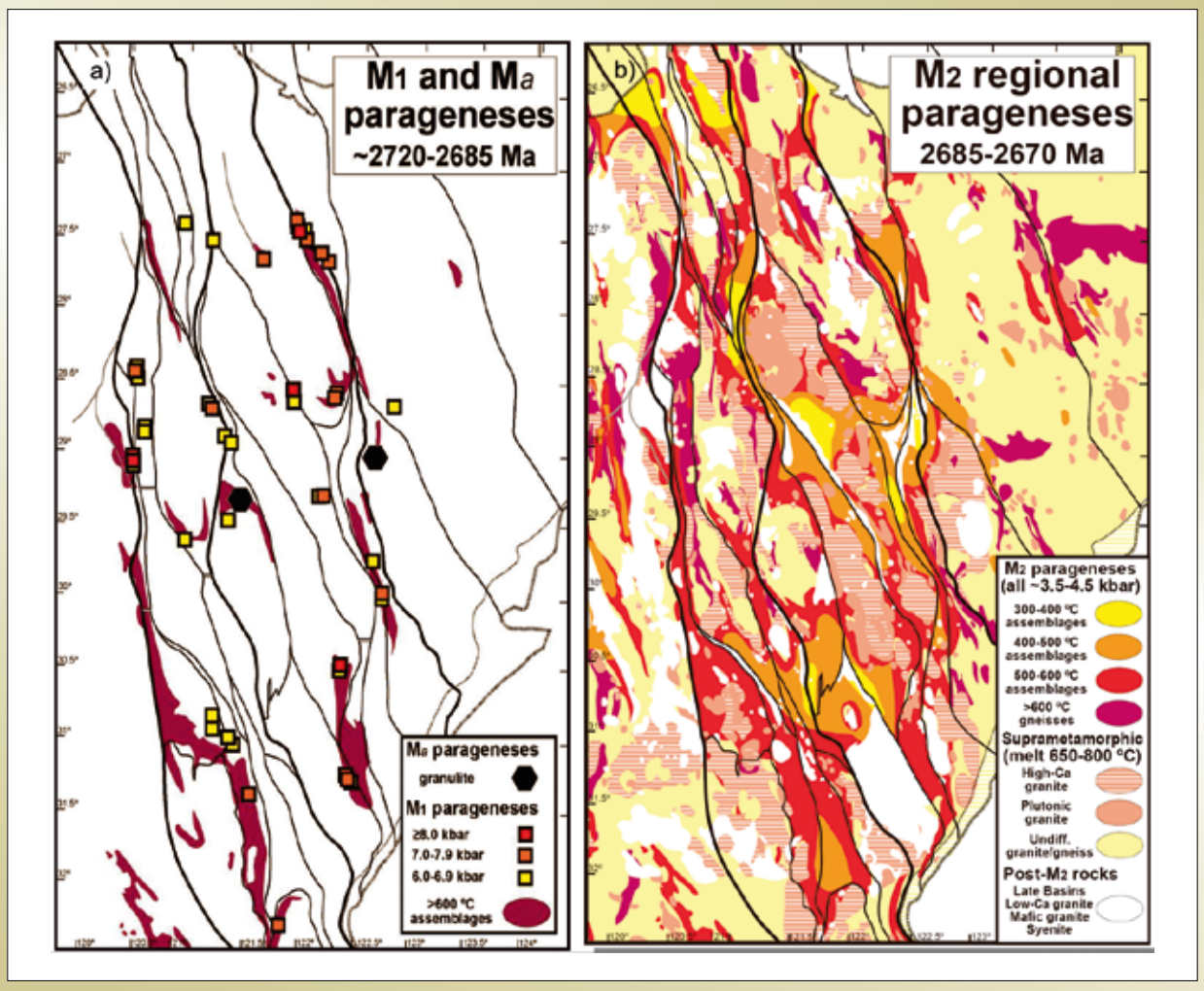


### 3.1.5.3 M2 – granite pervaded, moderate-G, regional metamorphism (2.685–2.665 Ga)

M2 is a phase of regional matrix parageneses with temperature ranging between 300–550°C across greenstone belts, with elevated average thermal gradients of 30–40°C/km throughout the EGST. Tight clockwise paths evolved through maximum prograde pressures of 6 kbar and peak metamorphic pressures of 3.5–5.0 kbar. Metamorphic temperatures increase toward granite/gneiss domes (Mikucki and Roberts, 2003) and the moderately elevated thermal gradients are consistent with a "regional-contact" type of metamorphism dominated by conduction and heat supplied by large volumes of High-Ca granites. M2 metamorphic mineral growth was variably accompanied by deformation, ranging from essentially no strain to syn-kinematic well-developed fabrics. Lu-Hf garnet ages indicate M2 metamorphism overlaps with the last phases of $D_1$ extension related to High-Ca granite emplacement and $D_2$ contraction, consistent with field and textural observations.

Ridley (1993) recognised that the universally low pressure and elevated average thermal gradient, mitigates against widespread crustal over-thickening, such as in a collisional orogen as has been previously suggested for the Yilgarn Craton (Groves and Phillips, 1987). The spatial association of M2 field gradients and distribution of High-Ca granites (Figure 3.1.9b) of broadly similar age (Figure 3.1.2), infer that metamorphism was in a thermally inversely stratified crust with elevated thermal gradients in the upper crust due to neutral buoyancy pooling of large volumes of granite.

### 3.1.5.4 M3a – extension related, high-G metamorphism (2.665–2.650 Ga)

Late Basins are a crucial time marker that "samples" the PT conditions of the thermal regime in operation between 2.665 and 2.650 Ga. Their deposition was associated with an extension related thermal pulse characterised by tight anticlockwise P-T paths to peak conditions of 500–580°C and 4.0±1 kbar, that define a moderately high average thermal gradients of 40–50°C/km (Figure 3.1.10). Peak metamorphism accompanied a static stress regime, subsequent to the formation of a bedding-parallel mica foliation. These PT conditions are diagnostic of lithospheric extensional settings. Other extensional basins such as the Kanmantoo Trough in South Australia and the Irindina Province in the Arunta, along with thermal modelling show that basin fill, burial and metamorphism can all occur in short, 2–10 Myr. time frames. Consequently, M3a metamorphism is interpreted to have accompanied ongoing Late Basin fill and hence constrains the timing of M3a to 2.665–2.650 Ga and immediately afterwards.

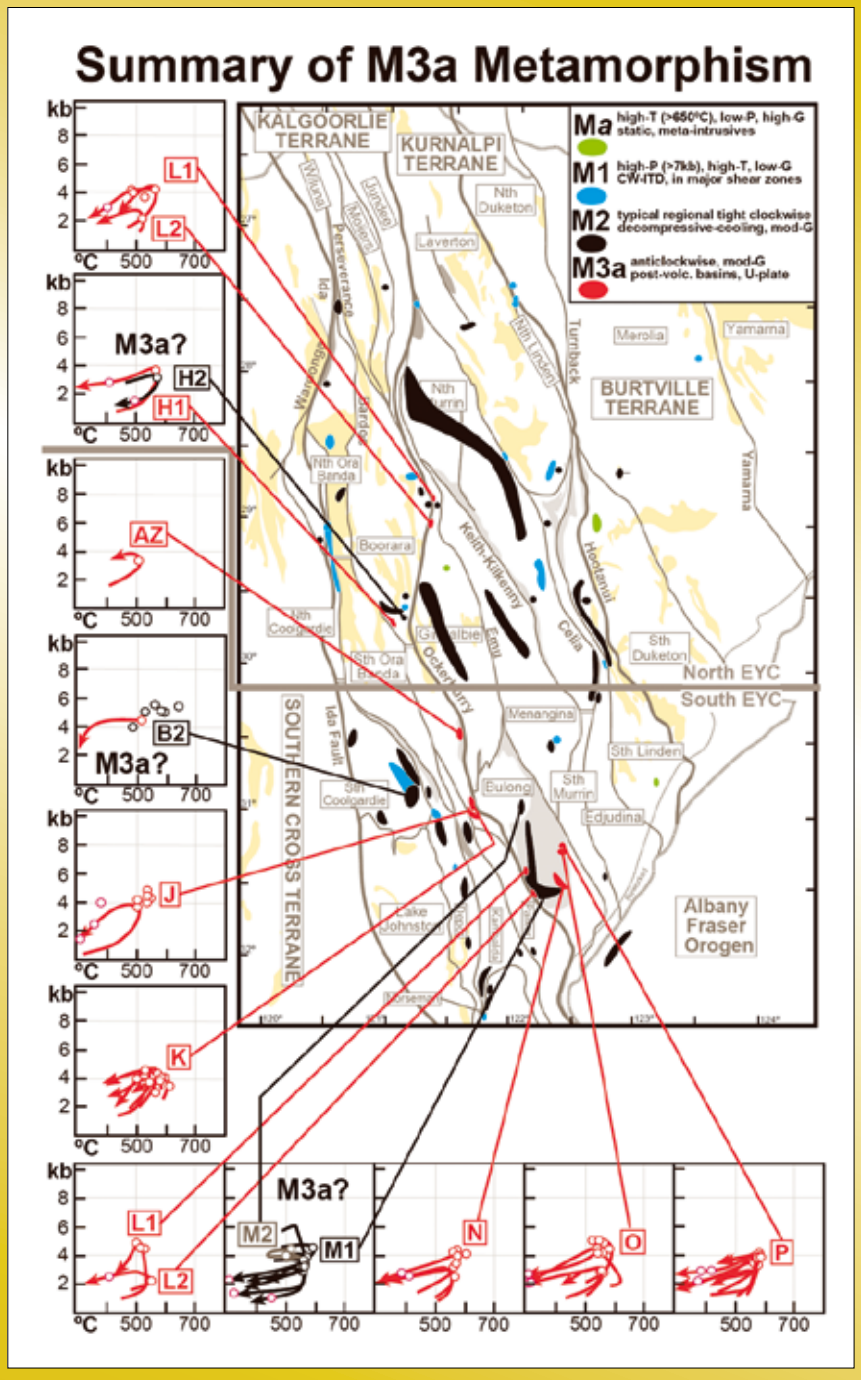


*Figure 3.1.10: Summary of M3a metamorphism, highlighting anticlockwise P-T paths defining a corridor parallel with the Ockerburry Shear System.*

The current known distribution of the M3a thermal overprint is restricted to the vicinity of the Ockerburry Fault and within Late Basins (Figure 3.1.10) and therefore supports a model of restricted M3a thermal effects along spaced elongate domains of high heat flow associated with maximum rifting, coinciding with the exposed and eroded Late Basins. The M3a thermal peak may be more wide spread but this footprint is obscured by the pre-existing M2 paragenesis. If exhumation of medium-P M1 parageneses and old (>2.72 Ga) stratigraphic units occurred as a result of M3a extensional telescoping as initially suggested by William and Currie (1993), then these rock units are diagnostic indicators of the lower-plate margins to zones of extreme M3a extension.

Metamorphic and stratigraphic patterns indicating the preservation of M1 metamorphic assemblages and old stratigraphy adjacent to large granite domes is consistent with extensional telescoping of the crust or core complex formation during M3a. During this period of extension ($D_3$) transport is inferred to be towards the northeast away from lower-plate domal cores, stepping outwards to successively younger extensional structures resulting in exhumation of panels of deeper crustal levels and juxtaposition against shallow crustal level rocks. This process would eventually lead to the exhumation of lower crustal granites and the shedding of granitic detritus to form Late Basins, with burial of these basins to a depth of 10–12 km.

The recognition of a post-2.665 Ga high-heat flow regime accompanying Late Basin infill, has implications for driving basinal brine circulation, and the release of large volumes of hydrous fluid into the upper crust by dewatering and dehydration reactions (Figure 3.1.11).

### 3.1.5.5 M3b – fault kinematics, high-G alteration and gold mineralisation (2.650–2.620 Ga)

The last metamorphic event recorded in the EGST is associated with multiple localised hydrothermal alteration events accompanying exhumation from 4 kbar to 1 kbar. This event is associated with a switch in the tectonic mode from dip-slip extension ($D_3$) to multiple strike-slip events ($D_4$-$D_5$) through a period of high but waning regional thermal gradients and multiple Au-mineralisation events.

Multiple metamorphic mineral growth events occurred within hydrothermal alteration assemblages that over-print regional metamorphic parageneses (M2–M3a). Mineral growth events define a broad continuum of elevated average thermal gradients that persisted from M3a (Figure 3.1.2). This long lived, high thermal budget is ascribed to the conductive thermal lag from $D_3$ extension and possible related delamination (see granite section) and the emplacement of significant volumes of Low-Ca granites which display a prolonged history in the Kalgoorlie Terrane (Figure 3.1.2).

Hydrothermal alteration associated with main phase Au-mineralization (~2.65–2.64 Ga) occurred across a wide range of temperatures 250–500˚C but similar crustal depths of 3.0–3.5 kbar, across most parts of the EGST, indicating moderately elevated thermal gradients of 30–50˚C/km. This represents crustal levels only 3 km shallower than peak metamorphism during M2 and M3a. Multiple fluid generations and fluid types, ranging from $H_2O$-rich to $CO_2$±$CH_4$-rich are evident in different alteration systems. Later episodes of alteration and Au-mineralization (~2.64–2.62 Ga) occurred at pressures as low as 1 kbar, while still at relatively elevated alteration temperatures (250–350 ˚C), indicating very high average thermal gradients (G >70˚C/km). This event coincides with a secondary peak of shallow crustal, Low-Ca granites, which possibly supplied the heat necessary to drive fluid circulation and gold remobilisation.

The large volumes of hydrous fluids responsible for much of the M3b alteration were most likely sourced from the dehydration of hydrous minerals in Late Basins. This inference is supported by stable isotope and fluid inclusion salinity data indicating meteroric fluid had undergone exchange in post-volcanic sedimentary basins (e.g., Mikucki, 1997). The strong causal relationships between M3a and M3b intimately links Au-mineralization with $D_3$ extension and the thermal evolution of the crust.

## 3.1.6 EGST Geodynamics and the Au mineral system

The above review of constraints on the geological evolution of the EGST highlights a number of various geodynamic models proposed for the EGST. At each point in time over the last quarter of a century there have been a number of competing models but the general development of

ideas can be traced as follows. Initial geodynamic models advocated an authochthonous development of greenstones on a pre existing sialic crust related to plume activity (e.g., Archibald and Bettenay, 1977). These models were followed by para-authochtonous convergent margin models (e.g., Barley et al. 1989) and eventually allochthonous models highlighting the importance of accretionary tectonics (e.g., Myers, 1995).

Each of these models has developed in sophistication through time and has found new proponents in the last decade. The ensialic plume model has most recently been advocated by Bateman et al. (2001), the para-authochtonous convergent margin model by Blewett and Czarnota (2007) and the allochthonous accretionary model by Archibald (2002) and Barley et al. (2006) who argued for whole scale obduction of the EGST over pre-existing crust.

In this paper we have tried to provide a way out of the geodynamic morass by integrating research into the stratigraphy, geochemistry, structural geology, geophysics and metamorphic petrology of the granites and greenstones of the EGST while providing insights into gold mineralisation along the way (Figure 3.1.2). This integration has been made possible through advances

*Figure 3.1.11: Model for 2.665–2.650 Ga lithospheric extension and the consequent outcomes of; post-volcanic Late Basin rifts, listric growth fault architecture, input of mantle components into the shallow crust such as mafic granites and $CO_2$-metalrich fluid, M3a post-kinematic thermal perturbation resulting in Low-Ca crustal melting, $H_2O$-rich fluid release and fluid driving and ultimately resulting in fluid mixing and primary gold mineralisation. A lagging cause and effect outcome is secondary gold mineralisation, by remobilisation during the M3b thermal perturbation associated with emplacement of the Low-Ca crustal melts and development of suitable mineralization sites by strike-slip reactivation of structures.*

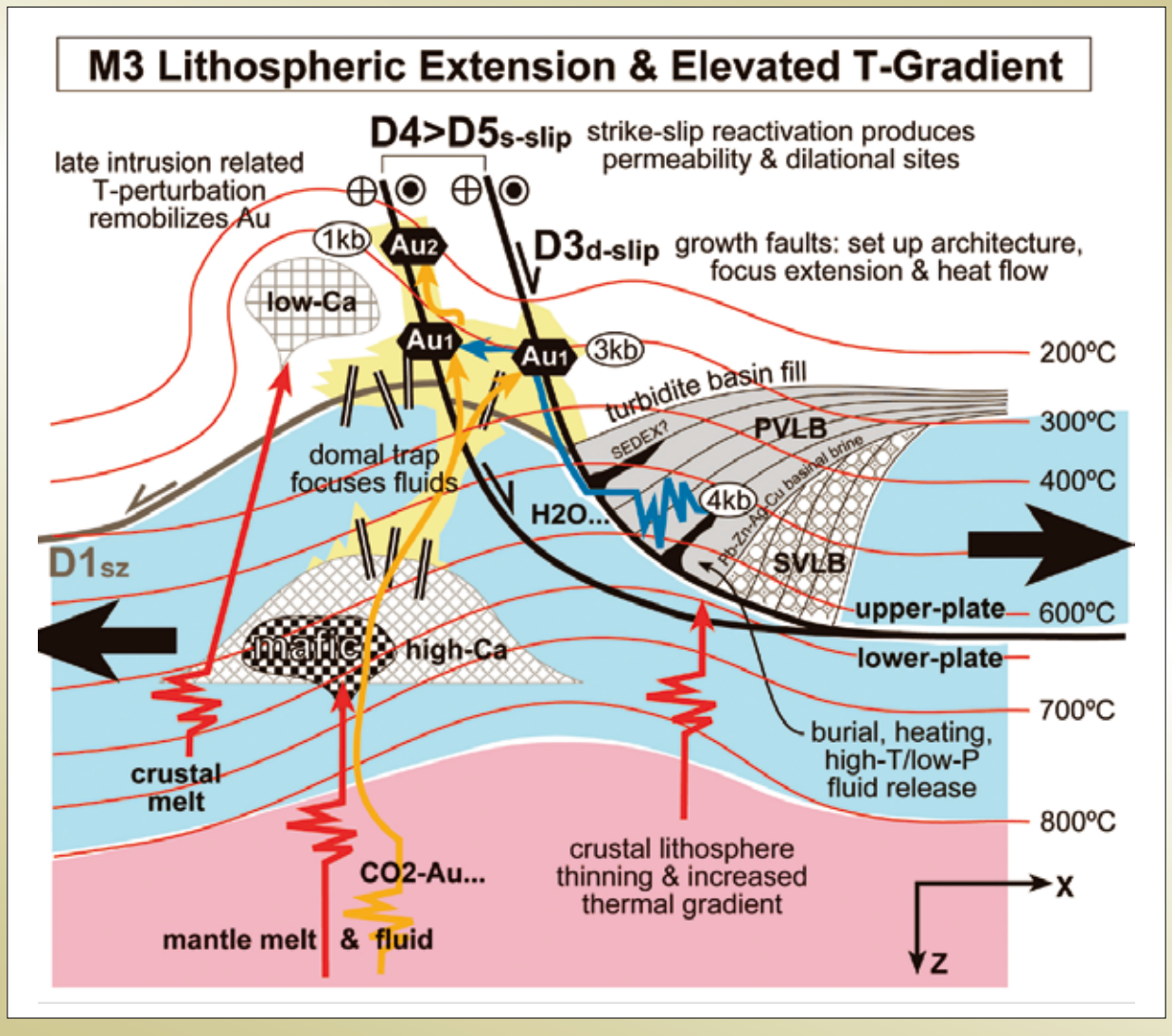

in geochronology, which have enabled links to be made between otherwise disparate fields of study. The ability to link these various disciplines has reduced the range of viable geodynamic interpretations, which honour most of the known constraints. From the above review the model that best fits the available constraints and provides the most self consistent insight into the gold mineral system of the EGST is a para-authochtonous convergent margin model.

### 3.1.6.1 Preferred Geodynamic model – para-authochtonous convergent margin model

The key elements of the para-authochtonous convergent margin model are presented in Table 3.1.2. The following summary links the preferred interpretation of the various aspects of the geodynamic history into one coherent model. The intention of this summary is to show the links between the various aspects of the geodynamic history rather than focusing on a discussion of the pros and cons of various geodynamic interpretations which have been covered in the above. A strength of this model is that it considers the granite/greenstone history pre 2.720 Ga where as most past tectonic models have only considered the post 2.720 Ga rock record. The rock record at >2.940 Ga is treated as basement most likely developed within a volcanic arc setting.

The ~2.81 Ga event has been interpreted to be a period of rifting mafic underplating across the Yilgarn Craton (Figure 3.1.5a). Rifting was localised in the Murchison Domain and on the eastern margin of the Youanmi Terrane (i.e. the EGST). The two loci of ~2810 Ma extension are the two most gold endowed regions of the Yilgarn Craton indicating this period of lithospheric extension was critical in determining the gold fertility of these two regions. However the exact process controlling this endowment process is yet unknown. Empirical observations indicate regions of partial crustal thinning are more prospective for Au mineralisation in the EGST than regions of juvenile crust. However juvenile crust in the Abitibi is well endowed in gold mineralisation (Huston et al, 2005) indicating this is a false positive correlation.

The ~2.81 Ga rift geometry was subsequently inverted associated with the initiation of 2.715 Ga subduction on the eastern margin of the EGST. Back arc extension with a possible plume input resulted in the deposition of the Kambalda Sequence with related komatiite hosted Ni mineralisation (Figure 3.1.5b). Progressive westward shallowing of the subducting slab resulted in westward younging of hydrated mantle wedge volcanism in the Kurnalpi Terrane, eventually resulting in slab melting. The crust around volcanic centres was metamorphosed at high temperatures and geothermal gradients (Ma) where as other regions were subject to localised moderate pressures with low geothermal gradients related to a shallowing of the subducting slab (M1).

Slab melting initiated at ~2.69 Ga and continued to ~2.67 Ga, resulting in Kalgoorlie Sequence felsic volcanism and voluminous High-Ca granite magmatism across the EGST (Figure 3.1.5c). Voluminous High-Ca granite slab melts interacted with the lower crust through a process of melting, assimilation, storage and homogenisation (MASH) which resulted in the granites acquiring a crustal signature and the generation of a thick, gravitationally unstable, eclogite-restite layer at the base of the crust. Neutral buoyancy pooling of voluminous High-Ca granites at the brittle ductile transition resulted in approximately 10 to 15 km of magmatic crustal thickening and the establishment of a density and thermal inversion in the upper crust, preconditioning the crust for $D_3$ extension.

The period from ~2.715 to ~2.670 Ga was controlled predominantly by an east-northeast to northeast extensional tectonic mode related to slab roll back. Deposition of tectonic sequence was mainly controlled by the inherited north-northwest tectonic grain established during ~2.81 Ga extension. Extension was particularly focused along the eastern side of the Ockerburry Fault between ~2.69 and 2.675 Ga resulting in Gindalbie Domain bimodal volcanism and VHMS mineralisation (Figure 3.1.5c).

Ongoing shallowing of the subduction slab or the subduction of a speculated oceanic plateau resulted in diachronous east-northeast compression ($D_2$) across the EGST (Figure 3.1.5d). This event resulted in the termination of volcanism at ~2.670 and 2.665 Ga in the east and west respectively. Contractional deformation resulted in minor crustal thickening and triggered lower crustal delamination of the eclogitic restite layer. Initial phases of delamination may have been associated with orogen parallel extrusion ($D_{3a}$) before whole scale northeast directed lithospheric extension ($D_{3b}$) occurred, related to inferred renewed slab roll back (Figure 3.1.5e).

Table 3.1.2: List of the main geodynamic elements of the preferred autochthonous convergent margin tectonic model for the EGST

| Timing (Ma) | Events | Notes |
|---|---|---|
| ≥2940 | Oceanic subduction zone? | • formation of an early juvenile Youanmi Terrane |
| ~2810 | Extension along the eastern margin of the Youanmi Terrane | • deposition of mafic/ultramafic sequence in a series of grabens on thinned continental crust ($D_1$) in the EGST and the Murchison Domain of the Youanmi Terrane |
| ~2715–2690 | Initiation of west dipping subduction | • westward younging of andesitic arc magmatism in the east and mafic/ultra mafic volcanism associated with back-arc extension in the west and ($D_1$; back arc plume input?)<br>• locally developed low average thermal gradient, moderate pressure metamorphism (M1) |
| ~2690–2665 | Shallowing of subduction slab | • shallowing of subduction slab resulting in TTG felsic volcanism and voluminous High-Ca granite magmatism due to slab melting.<br>• magmatic crustal thickening, in an overall extensional tectonic setting ($D_1$)<br>• development of a High-Ca granite MASH zone resulting in the formation of a thick eclogite restite layer at the base of the crust<br>• regional moderately high average thermal gradient matrix metamorphism (M2) |
| W~2670 E ~2665 | Diachronous arc closure event (compression) | • diachronous short lived (~5 Ma) ENE-WSW contraction ($D_2$) resulting in minor crustal thickening triggering delamination of eclogite restite layer at the base of the crust<br>• Similar metamorphic conditions to above with tight clockwise P-T loops (M2) |
| W ~2665 E ~2660 | Mid 'orogenic' extension and Lower crustal delamination | Delamination of thick eclogite restite coupled with lithospheric extension ($D_3$) resulted in:<br>• rapid addition of heat into the base of the crust<br>• generation of metasomatised mantle melts and their introduction into the crust along major extensional crustal shear zones, thereby establishing a connectivity with the mantle<br>• development of granite cored metamorphic core complexes aided by the intrusion of high-Y High-Ca granite crustal melts<br>• exhumation of granites and the lower crust, erosion and deposition of Late Basins in narrow extensional grabens ($D_3$)<br>• burial of Late Basins to a depth of 10–12 km resulting in the introduction of hydrous fluids into the upper crust (basinal brine and hydrous mineral dewatering of late basins)<br>• downward fluid flow along extensional structures and storage of fluids in the crust<br>• localised high average thermal gradient, anticlockwise P-T path in Late Basins and along the Ockerburry (M3a)<br>• **start of significant economic gold mineralisation (the golden age)** |

*continued*

Table 3.1.2: List of the main geodynamic elements of the preferred autochthonous convergent margin tectonic model for the EGST *continued*

| Timing (Ma) | Events | Notes |
|---|---|---|
| W ~2655<br>E ~2650 | Resumed contraction | • resumed ENE contraction ($D_{4a}$) and inversion of extension followed by a switch in contraction to WNW directed ($D_{4a}$) resulting in sinistral transpression along major NNW striking shear zones and the development of local stress heterogeneities<br>• switch from High- to Low-Ca granite magmatism<br>• multiple localised hydrothermal alteration parageneses with high average thermal gradients (M3b)<br>• **major Au event due to fluid focusing during contraction and the ironing out of the inherited extensional architecture** |
| W ~2650<br>E ~2645 | Introduction of crustal melts | • initiation of Low-Ca granite emplacement<br>• stress switch to NE-SW contraction ($D_5$) resulting in the development of N to NNE striking predominantly dextral normal strike-slip shear/fault zones<br>• similar metamorphic conditions to above (M3b)<br>• **continuation of Au mineralisation in very brittle structures** |
| W ~2630<br>E ~2620 | Cratonisation | • continuation of $D_5$ deformation<br>• termination of Low-Ca granite magmatism resulting from a transfer of HHPE into the upper crust |

Delamination of the lower crust resulted in upwelling of metasomatised mantle into the bases of the crust along tears and/or breaks in the delaminating slab. This up welling of metasomatised mantle resulted in the generated of Mafic granite and metasomatised Syenites which were emplaced along extensional shear zones in the upper crust. Crustal penetrating extensional shear zones may have controlled the sites of tears or breaks in the delaminating slab. The metasomatised mantle magmas provided an "elevator" for the introduction of mantle fluids into the crust thereby establishing connectivity with the mantle.

The introduction of rapid heat input into the base of the crust through lower crustal delamination resulted in the production of crustal melts. The first phase of melting produced high-Y High-Ca granites, with progressive thermal diffusion through the crust resulting in the generation of Low-Ca granite.

Mid-orogenic lithospheric extension was associated with lower crustal exhumation, resulting in granite core complex formation aided by the intrusion of crustal derived high-Y High-Ca granites. The exhumation of granite domes provided detritus for Late Basin deposition, which like the $D_2$ compression event, was diachronous across the EGST, occurring at 2.665 and <2.660 Ga in the east and west respectively. Late Basin deposition was controlled by northwest striking faults oblique to the north-northwest striking inherited architecture resulting in the development of a rhomboid fault network which controlled subsequent deformation. Late Basins were buried during extension to a depth of 10–12 km thereby introducing large volumes of fluids into the upper crust through dewatering of basinal brines and dehydration of hydrous minerals under elevated geothermal gradients. These fluids were stored in the crust during extension and focused upwards during later inversion.

$D_3$ mid-orogenic extension marks the onset of the first significant gold mineralisation in the EGST. Extension related gold deposits (e.g., Gwalia, Lancefield) lie in high strain ductile extensional shear zones associated with dynamic permeability creation. These deposits lie along shear zones with the greatest amount of movement where high grade or old units have been juxtaposed against lower grade or younger units, thereby providing a regional tool for exploration for this style of mineralisation.

It is not surprising that $D_3$ marks the onset of significant gold mineralisation in the EGST since it is the event during which the gross architecture, connectivity with the mantle and access to hydrous fluids are brought together in one self-consistent process. Subsequent period of contraction ($D_4$ and $D_5$) can be seen as merely a means of focusing fluids within the framework of the inherited $D_3$ architecture.

The $D_3$ domal architecture was inverted during $D_4$ brittle-ductile deformation (Figure 3.1.5f). Initially this deformation was associated with $D_{4a}$ east-northeast contraction associated with upright folding of the Late Basins and reverse dip-slip movement along $D_3$ extensional structures.

The palaeostress field rotated to east-southeast directed contraction during $D_{4b}$ deformation which resulted in sinistral transpression along northwest to north-northwest trending structures. The onset of strike-slip deformation resulted in the creation of numerous fluid focusing sites with significant structural complexity and the development of locally variable and complex stress fields as the anisotropy in the orogen was being 'ironed out'. It is this second phase of $D_4$ deformation at ~2.650 and 2.645 Ga in the east and west respectively, which is best endowed in gold mineralisation. This period of deformation was associated with multiple localised hydrothermal alteration events presumably linked to the seismogenic cycle and heterogeneous palaeostress conditions, which resulted in efficient fluid focusing and gold mineralisation.

The last phase of gold mineralisation is linked to a stress switch to northeast-southwest contraction and the emplacement of Low-Ca granites (Figure 3.1.5g). This $D_5$ stress switch resulted in the development of north to northeast-striking brittle ductile dextral normal strike-slip faults.

Low-Ca granites were preferentially emplaced into the cores of regional pre formed granite domes and into the footwall of the Ida Fault. Termination of Low-Ca granite magmatism was diachronous across the EGST at approximately 2.640, 2.630 and 2.620 Ga in the Burtville, Kurnalpi and Kalgoorlie Terranes. The diachronous termination of Low-Ca magmatism was a function of the initial diachroneity of lower crustal delamination and reflects the time taken for the heat input associated

with the delamination event to diffuse through the crust. Low-Ca granite magmatism was prolonged in the Kalgoorlie Terrane thereby driving fluid circulation and gold mineralisation for a greater period in this region of the crust.

The emplacement of Low-Ca granites resulted in the transfer of high heat producing elements from the middle to the upper crust and hence the effective cratonisation of the EGST and hence the end of significant tectonic activity in the EGST.

### 3.1.7 Acknowledgements

We thank the ***pmd*CRC*** sponsors for their ongoing commitment to the Y4 project. In particular we thank Bruce Hobbs, Jon Hronsky and Regan Patten for insightful discussions on the geodynamics of the Yilgarn. Published with the permission of the CEO's of the ***pmd*CRC*** and GA.

### 3.1.8 References

Anders, E., and Grevesse, N. 1989. Abundances of the elements: Meteoritic and solar. Geochimica et Cosmochimica Acta, 53, 197–214.

Archibald, N.J., 2002. An allochthonous model for the greenstone belt evolution in the Menzies-Norseman area, Eastern Goldfields Province: implications for gold mineralisation. http://www.agcrc.csiro.au/publications/yilgarn98/abstracts/archibald1.html p.5. accessed on 4/11/2003.

Archibald, N.J., Bettenay, L.F., Binns, R.A., Groves, D.I., and Gunthorpe, R.J., 1978. The evolution of Archaean greenstone terrains, Eastern Goldfields Province, Western Australia. Precambrian Research, 6, 103–131.

Arndt, H.T., and Jenner, G.A., 1986. Crustally contaminated komatiites and basalts from Kambalda, Western Australia. Chemical Geology, 56, 229–255.

Arndt, H.T., Kerr, A.C. and Tarney, J., 1997. Dynamic melting in plume heads: the formation of Gorgona komatiites and basalts. Earth and Planetary Science Letters, 146, 289–301.

Atherton, M.P., and Petford, N., 1993. Generation of sodium-rich magmas from newly underplated basaltic crust. Nature, 362, 144–146.

Barley, M.E., Blewett, R.S., Cassidy K.F., Champion D.C., Czarnota K., Doyle M.G., Krapež, B., Kositcin N., Pickard A.L., and Weinberg F., 2006. Tectonostratigraphic and structural architecture of the eastern Yilgarn Craton. Australian Minerals Industry Association Report, P763/***pmd*CRC*** Project Y1.

Barley, M.E., Brown, S.J.A., Cas, R.A.F., Cassidy, K.F., Champion, D.C., Gardoll, S.J., and Krapež, B., 2003. An integrated geological and metallogenic framework for the eastern Yilgarn Craton: Developing geodynamic models of highly mineralised Archaean granite-greenstone terranes. Australian Minerals Industry Association Report, P624.

Barley, M.E., Brown, S.J., Krapež B. and Cas R.A.F. 2002. Tectono-stratigraphic analysis of the Eastern Yilgarn Craton: an improved geological framework for exploration in Archaean terranes. Australian Minerals Industry Association Report, P437A.

Barley, M.E., Eisenlohr, B.N., Groves, D.I., Perring, C.S., and Vearncombe, J.R., 1989. Late Archaean convergent margin tectonics and gold mineralisation: a new look at the Norseman-Wiluna belt, Western Australia. Geology, 17, 826–829.

Barley, M.E., Stuart, J.A., Krapež, B., and Kositcin, N., 2008. Physical volcanology and geochemistry of a Late Archaean volcanic arc: Kurnalpi and Gindalbie Terranes, Eastern Goldfields Superterrane, Western Australia. Precambrian Research, 161, 53–76.

Bateman, R., and Bierlein, F.P., 2007, On Kalgoorlie (Australia), Timmins-Porcupine (Canada), and factors in intense gold mineralisation, Ore Geology Reviews, 32, 187–206.

Bateman R., Costa S., Swe T., Lambert D., 2001. Archaean mafic magmatism in the Kalgoorlie area of the Yilgarn Craton, Western Australia: a geochemical and Nd isotopic study of the petrogenetic and tectonic evolution of a greenstone belt. Precambrian Research, 108, 75–112.

Beakhouse, G.P., 2007. Gold, granite and late Archaean tectonics: a Superior Province perspective. In: Bierlein,

F.P., and Knox-Robinson, C.M., (eds), Proceedings of Geoconferences (WA) Inc. Kalgoorlie '07 Conference. Geoscience Australia Record 2007/14, 191–196.

Bettenay, L.F. 1977. Regional geology and petrogenesis of Archaean granitoids in the southeastern Yilgarn Block~ Ph.D. thesis, Univ. West. Aust. pp. 328.

Binns, R.A., Gunthorpe, R.J., and Groves, D.I., 1976. Metamorphic patterns and development of greenstone belts in eastern Yilgarn Block, Western Australia. John Wiley and Sons, New York, USA, 303–313.

Blewett, R.S., 2004. An assessment of the utility of the new 3D data versus the 2D data at a regional scale: geodynamic insights. In: Blewett R.S. and Hitchman A.P. (eds) 3D Geological models of the eastern Yilgarn Craton. ***pmd****CRC* Y2 Final Report, p139–159.

Blewett, R.S., Cassidy, K.F., Champion, D.C., Henson, P.A., Goleby, B.R., Jones, L., and Groenewald, P.B., 2004. The Wangkathaa Orogeny: an example of episodic regional '$D_2$' in the late Archaean Eastern Goldfields Province, Western Australia. Precambrian Research, 130, 139–159.

Blewett, R.S., Cassidy, K.F., Champion, D.C., and Whitaker, A.J., 2004b. The characterisation of deformation events in time across the Eastern Goldfields Province, Western Australia. Geoscience Australia Record, 2004/10 [CDROM].

Blewett, R.S., and Czarnota, K., 2007a. A new integrated tectonic framework of the Eastern Goldfields Superterrane. In: Bierlein, F.P., and Knox-Robinson, C.M., (eds), Proceedings of Geoconferences (WA) Inc. Kalgoorlie '07 Conference. Geoscience Australia Record 2007/14, 27–32.

Blewett, R.S., and Czarnota, K., 2007b. The Y1-P763 project final report November 2005. Module 3 – Terrane Structure: Tectonostratigraphic architecture and uplift history of the Eastern Yilgarn Craton, Geoscience Australia Record 2007/15.

Blewett, R.S., Cassidy, K.F., Henson, P.A., Roy, I.G., Champion, D.C., and Fomin, T., 2008a Question 2: Big systems-big signatures – anatomy of the Archaean Yilgarn Craton and implications for world-class gold mineral systems. This volume.

Blewett, R.S., Czarnota, K., Henson, P.A., 2008b. A revised structural-event framework for the Eastern Goldfields Superterrane. This volume.

Blewett, R.S., Squire R., Henson R.S., Miller, J.M., and Champion D.C., 2008c. Architecture and geodynamic evolution of the St Ives region, south central Kalgoorlie Terrane, Western Australia. This volume.

Brown, S.J.A., Krapež, B, Beresford, S.W., Cassidy, K.F., Champion, D.C., Barley, M.E., and Cas, R.A.F., 2001. Archaean volcanic and sedimentary environments of the Eastern Goldfields Province, Western Australia – a field guide. Western Australia Geological Survey Record, 2001/13, 66p.

Campbell, I.H., Griffiths, R.W., and Hill, R.I., 1989. Melting in an Archaean mantle plume: heads it's basalts, tails it's komatiites. Nature, 339, 697–699.

Campbell, I.H., and Hill, R.I., 1988. A two-stage model for the formation of the granite-greenstone terrains of the Kalgoorlie-Norseman area, Western Australia. Earth and Planetary Science Letters, 90, 11–25.

Cassidy, K.F., Barley, M.E., Groves, D.I., Perring, C.S. and Hallberg, J.A., 1991. An overview of the nature, distribution and inferred tectonic setting of granitoids of the late-Archaean Norsemen-Wiluna Belt. Precambrian Research, 51, 51–83.

Cassidy, K.F., Champion, D.C., McNaughton, N.J., Fletcher, I.R., Whitaker, A.J., Bastrakova, I.V., and Budd, A.R., 2002. Characterisation and metallogenic significance of Archaean granitoids of the Yilgarn Craton, Western Australia. Minerals and Energy Research Institute of Western Australia (MERIWA), Report No. 222, 514p.

Cassidy, K.F., 2004. Chapter 1: Geological evolution of the eastern Yilgarn Craton (EYC). In: Blewett R.S. and Hitchman A.P. (eds) 3D Geological models of the eastern Yilgarn Craton. ***pmd****CRC* Y2 Final Report, p1–19.

Cassidy, K.F., and Champion, D.C., 2004. Crustal evolution of the Yilgarn Craton from Nd isotopes and granite geochronology: implications for metallogeny. In Muhling, J., et al., (Eds), SEG 2004, Predictive Mineral Discovery Under Cover. Centre for Global Metallogeny,

The University of Western Australia, Publication 33, 317–320.

Cassidy, K.F., Champion, D.C., Krapež B., Barley M.E., Brown S.J.A., Blewett R.S., Groenewald P.B. and Tyler I.M. 2006. A revised geological framework for the Yilgarn Craton, Western Australia, Western Australia Geological Survey, Record 2006/8, pp8.

Champion, D.C. 2006. Terrane, domain and fault system nomenclature. In: R.S. Blewett and A.P. Hitchman (eds) 3D Geological Models of the Eastern Yilgarn Craton – Y2 Final Report ***pmd*CRC***. Geoscience Australia Record 2006/04, 19–38. [DVD-ROM]

Champion, D.C., and Cassidy, K.F., 2000. Chapter 2 Granites of the northern Eastern Goldfields: their distribution, age, geochemistry, petrogenesis, relationship with mineralisation, and implications for tectonic environment. In: Cassidy, K.F., Champion, D.C., McNaughton, N.J., Fletcher, I.R., Whitaker, A.J., Bastrakova, I.V. and BUDD, A.R. AMIRA P482 report – The Characterisation and Metallogenic Significance of Archaean Granitoids of the Yilgarn Craton http://www.doir.wa.gov.au/meriwa/reports/minexplor.PDF

Champion, D.C., and Cassidy, K.F., 2002. Granites in the Leonora-Laverton transect area, north eastern Yilgarn Craton: In Cassidy, K.F., (Ed), Geology, geochronology and geophysics of the north eastern Yilgarn Craton, with an emphasis on the Leonora-Laverton transect area. Geoscience Australia, Record 2002/18, 13–35.

Champion, D.C. and Cassidy, K.F. 2007. An overview of the Yilgarn Craton and its crustal evolution. In: in Bierlein, F.P., and Knox-Robinson, C.M., (eds), 2007. Proceedings of Geoconferences (WA) Inc. Kalgoorlie '07 Conference. Geoscience Australia Record 2007/14, p13–35.

Champion, D.C., Cassidy, K.F. and Budd, A., 2000. Chapter 8 Overview of the Yilgarn Craton magmatism: Implications for crustal development. In: Cassidy, K.F., Champion, D.C., McNaughton, N.J., Fletcher, I.R., Whitaker, A.J., Bastrakova, I.V. and BUDD, A.R. AMIRA P482 report – The Characterisation and Metallogenic Significance of Archaean Granitoids of the Yilgarn Craton http://www.doir.wa.gov.au/meriwa/reports/minexplor.PDF

Champion, D.C., Sheraton, J.W., 1993. Geochemistry of granitoids in the Leonora-Laverton region, Eastern Goldfields Province. In: Williams, P.R., Haldane, J.A. (Compilers), An International Conference on Crustal Evolution, Metallogeny and Exploration of the Eastern Goldfields. Australian Geological Survey Organisation Record 1993/54, pp. 39–46.

Champion, D.C., and Sheraton, J.W., 1997. Geochemistry and Nd isotope systematics of Archaean granites of the Eastern Goldfields, Yilgarn Craton, Australia; implications for crustal growth processes. Precambrian Research, 83, 109–132.

Chauvel, C., Dupre, B. and Jenner G.A., 1985. The Sm-Nd age of Kambalda volcanics is 500 Ma too old! Earth and Planetary Science Letters, 74, 315–324.

Claoué-Long, J.C., Compston, W., and Cowden, A., 1988. The age of the Kambalda greenstones resolved by ion microprobe – implications for Archaean dating methods. Earth and Planetary Science Letters, 89, 239–259.

Cleverley, J.S., Walshe, J.L., and Nugus, M., 2007. Tracing deep fluid sources in gold deposits of the Eastern Goldfields. In: in Bierlein, F.P., and Knox-Robinson, C.M., (eds), 2007. Proceedings of Geoconferences (WA) Inc. Kalgoorlie '07 Conference. Geoscience Australia Record 2007/14, p133–137.

Collins W.J. and Van Kranendonk M.J. 1999, Model for the development of kyanite during partial convective overturn of Archaean granite-greenstone terranes: the Pilbara Craton, Australia. Journal of Metamorphic Geology, 17, 145–156.

Compston, W., Williams, I.S., Campbell, I.H., and Gresham, J.J., 1986. Zircon xenocrysts from the Kambalda volcanics: age constraints and direct evidence for older continental crust below the Kambalda-Norseman greenstones. Earth and Planetary Science Letters, 76, 299–311.

Condie, K.C., 2001. Mantle plumes and their record in earth history. Cambridge University press 306p.

Connors, K., Donaldson, J., Morrison, B., Davy, C., and Neumyar, P., 2003, The Stratigraphy of the Kambalda-St Ives District: workshop notes Goldfields Pty Ltd St Ives

operation, unpublished Technical note No: TN SIG0329, 99 p.

Cox S.F., Ruming K., 2004. The St Ives mesothermal gold system, Western Australia – a case of golden aftershocks? Journal of Structural Geology, 26, 1109–1125.

Crawford, M.A., and Cox, S.F., 2007. The Mechanical and fluid pressure evolution of the Argo shear system during gold mineralisation. Proceedings of the SGTSG deformation in the desert conference. Geological Society of Australia, p57.

Czarnota, K., Blewett R., Champion D.C., Henson P.A., and Cassidy K.F., 2007. Significance of extensional tectonics in orogenic gold systems: an example from the Eastern Goldfields Superterrane, Yilgarn Craton, Australia. In: Andrew C.L., et al., (eds) Digging Deeper. Proceedings of the Ninth Biennial Meeting of the Society for Geology Applied to Mineral Deposits Dublin, Ireland 20th–23rd August 2007. p1431–1434.

Davis B.K., and Maidens E., 2003. Archaean orogen-parallel extension: evidence from the northernEastern Goldfields Province, Yilgarn Craton. Precambrian Research, 127, 229–248.

De Paolo, D.J., 1981. Trace elements and isotopic effects of combined wallrock assimilation and fractional crystallisation. Earth and Planetary Science Letters, 53, 189–202.

De Wit, M.J., 1998. On Archaean granites, greenstones, cratons and tectonics: does the evidence demand a verdict? Precambrian Research, 91, 181–226.

Drummond, M.S. and Defant, M.J., 1990. A model for tronjemite-tonalite-dacite genesis and crustal growth via slab melting – Archaean to modern comparisons. Journal of Geophysical Research, 95, 21503–21521.

Drummond, B.J., Goleby, B.R., and Swager, C.P., 2000. Crustal signature of Late Archaean tectonic episodes in the Yilgarn craton, Western Australia: evidence from deep seismic sounding. Tectonophysics, 329, 193–221.

Dunphy, J.M., Fletcher, I.R., Cassidy, K.F., and Champion, D.C., 2003. Compilation of SHRIMP U-Pb geochronological data, Yilgarn Craton, Western Australia, 2001–2002. Geoscience Australia Record 2003/15, 139p.

Fletcher, I.R., Dunphy, J.M., Cassidy, K.F., and Champion, D.C., 2001. Compilation of SHRIMP U-Pb geochronological data, Yilgarn Craton, Western Australia, 2000–2001. Geoscience Australia, Record 2001/47, 111p.

Gee, R.D., Baxter, J.L., Wilde, S.A., and Williams, I.R., 1981. Crustal development in the Archaean Yilgarn Block, Western Australia. Geological Society of Australia, Special Publication, 7, 43–56.

Goleby, B.R., Blewett, R.S., Groenewald, P.B., Cassidy, K.F., Champion, D.C., Korsch, R.J., Whitaker, A., Jones, L.E.A., Bell, B., and Carlson, G., 2003. Seismic interpretation of the northeastern Yilgarn Craton seismic data. In Goleby, B.R., Blewett, R.S., Groenewald, P.B., Cassidy, K.F., Champion, D.C., Jones, L.E.A., Korsch, R.J., Shevchenko, S., and Apak, S.N., (Eds), The 2001 Northeastern Yilgarn Deep Seismic Reflection Survey. Geoscience Australia, Record 2003/28, 143p.

Goscombe, B., Blewett, R.S, Czarnota, K., Maas, R., and Groenewald, B.A., 2007, Broad thermo-barometric evolution of the Eastern Goldfields Superterrane. In: in Bierlein, F.P., and Knox-Robinson, C.M., (eds), 2007. Proceedings of Geoconferences (WA) Inc. Kalgoorlie '07 Conference. Geoscience Australia Record 2007/14, p33–38.

Griffin, W.L., and O'Reilly, S.Y., 2007. The earliest subcontinental lithospheric mantle. In: Van Kranendonk, M.J., Smithies, R.H., and Bennett V.C. (eds), Earth's Oldest Rocks. Developments in Precambrian Geology, 15, 1013–1036.

Griffiths, R.W., and Campbell, I.H., 1990. Stirring and structure in mantle plumes. Earth and Planetary Science Letters, 99, 66–78.

Groves, D.I., and Batt, W.D., 1984. Spatial and temporal variations of Archaean metallogenic associations in terms of evolution of granitoid-greenstone terrains with particular emphasis on the Western Australian Shield. In Kroner, A., Hanson, G.N., and Goodwin, A.M., (Eds), Archaean Geochemistry: the Origin and Evolution of the Archaean Continental Crust, 73–98, Springer-Verlag.

Groves, D.I., and Phillips, G.N., 1987. The genesis and tectonic controls on Archaean gold deposits of the Western Australian Shield: a metamorphic replacement model. Ore Geology Reviews, 2, 287–322.

Hagemann S G, Groves D I, Ridley J R and Vearncombe J V, 1992. The Archaean lode-gold deposits at Wiluna, Western Australia: high-level brittle-style mineralization in a strike-slip regime. Economic Geology 87: 1022–1053.

Hamilton, W.B., 2003. An alternative Earth. GSA Today 11, 1–12.

Hallberg, J.A., 1985. Geology and mineral deposits of the Leonora–Laverton area, northeastern Yilgarn Block, Western Australia. Hesperian Press, Perth, Western Australia, 140p.

Hallberg, J.A., and Giles, C.W., 1986. Archaean felsic volcanism in the northeastern Yilgarn Block, Western Australia. Australian Journal of Earth Sciences, 33, 413–427.

Hammond, R.L., and Nisbet, B.W., 1992. Towards a structural and tectonic framework for the Norseman-Wiluna Greenstone Belt, Western Australia. In Glover, J.E., and Ho, S.E., (Eds), The Archaean – Terrains, Processes and Metallogeny. Geology Department and University Extension, The University of Western Australia, Publication 22, 39–50.

Hammond, R.L., and Nisbet, B.W., 1993. Archaean crustal processes as outlined by structural geology, Eastern Goldfields Province of Western Australia. In: Williams, P.R., Haldane, J.A. (Compilers), Kalgoorlie 93 – An international conference on crustal evolution, metallogeny, and exploration of the Eastern Goldfields. Aust. Geol. Surv. Org., Rec 1993/54, 39–46.

Haschke, M. R., Scheuber, E., Günther, A., and Reutter, K.-J., 2002. Evolutionary cycles during the Andean orogeny: repeated slab breakoff and flat subduction? Terra Nova 14, 49–55.

Henson, P.A., Miller J.M., Zhang Y., Blewett R.S. and Czarnota K., 2008. The 4D architecture of the Laverton camp, Eastern Yilgarn Craton. This volume.

Hildreth, W., and Moorbath, S., 1988. Crustal contributions to arc magmatism in the Andes of Central Chile. Contribution to mineralogy and petrology, 98, 455–489.

Hill, R.I., Chappell, B.W. and Campbell, I.H., 1992. Late Archaean granites of the southeastern Yilgarn Block, Western Australia: age, geochemistry and origin. Royal Society Edinburgh, Transactions, 83, 211–226.

Huston D.L., Champion, D.C., and Cassidy, K.F., 2005. Tectonic controls on the endowment of Archaean cratons in VHMS deposits: Evidence from Pb and Nd isotopes. In: Mao J., Bierlein F.P. (eds), Mineral Deposit Research: Meeting the Global Challenge, Berlin/Heidelberg. Springer, Chapter 1–4, p15–18.

Jochum, K.P., Arndt, N.T. and Hofmann, A.W., 1991. Nb-Th-La in komatiites and basalts: constraints on komatiite petrogenesis and mantle evolution. Earth and Planetary Science Letters, 107, 272–289.

Libby, W.G., 1978. The felsic alkaline rocks. Western Australia Geological Survey Report 9, 111–137.

Kadioğlu, Y.K., Dilek, Y., and Foland, K.A., 2006. Slab break-off and syncollisional origin of the Late Cretaceous magmatism in the Central Anatolian crystalline complex, Turkey. Special Paper 409: Postcollisional Tectonics and Magmatism in the Mediterranean Region and Asia, 409, 381–415.

Kent, A.J.R., Cassidy, K.F., and Fanning, C.M., 1996. Archaean gold mineralisation synchronous with the final stages of cratonisation, Yilgarn Craton, Western Australia. Geology, 24, 879–882.

Kositcin, N., Brown S.J.A., Barley M.E., Krapež B., Cassidy K.F., and Champion D.C., 2008. SHRIMP U-Pb zircon age constraints on the Late Archaean tectonostratigraphic architecture of the Eastern Goldfields Superterrane, Yilgarn Craton, Western Australia, Precambrian Res., 161, 5–33

Krapež B., 1997. Sequence-stratigraphic concepts applied to the identification of depositional basins and global tectonic cycles. Australian Journal of Earth Science 44, 1–36.

Krapež B., Brown. S.J.A., Hand J., Barley M.E., and Cas R.A.F., 2000. Age constraints on recycled crust and supracrustal sources of Archaean metasedimentary sequences, Eastern Goldfields Province, Western Australia: evidence from SHRIMP zircon dating. Tectonophysics 322, 89–133.

Krapež B., and Hand J.L., 2008. Late Archaean deep-marine volcaniclastic sedimentation in an arc-related basin: the Kalgoorlie Sequence of the Eastern Goldfields Superterrane, Yilgarn Craton, Western Australia, Precambrian Research, 161, 89–113.

Krapež B., and Barley, M.E., 2008. Late Archaean synorogenic basins of the Eastern Goldfields Superterrane, Yilgarn Craton, Western Australia. Part III: Signatures of tectonic escape in an arc-continent collision zone. Precambrian Research, 161, 183–199.

Lesher, C.M., and Arndt, N.T., 1995. REE and Nd isotope geochemistry, petrogenesis and volcanic evolution of contaminated komatiites at Kambalda, Western Australia. Lithos, 34, 127–157.

Libby, W.G., 1978. The felsic alkaline rocks. Western Australia Geological Survey Report 9, 111–137.

Liu, S.F., Stewart, A.J., Farrell, T., Whitaker, A.J., and Chen, S.F., 2001. Solid Geology of the north Eastern Goldfields, Western Australia. Geoscience Australia 1:500 000 scale print on demand map (Catalogue No 53233).

McClay, K.R., Dooley T., Whitehouse P., and Mills M., 2002. 4-D evolution of rift systems: Insights from scaled physical models. AAPG Bulletin, 86, 935–959.

McIntyre, J.R., and Martyn, J.E., 2005. Early extension in the Late Archaean northeastern Eastern Goldfields Province, Yilgarn Craton, Western Australia, Australian Journal of Earth Sciences, 52, 975–992.

Martin, H., 1994. The Archaean grey gneisses and the genesis of continental crust. In: Condie, K.C. (Ed.), Archaean Crustal Evolution. Elsevier, Amsterdam, pp. 205–259.

Mikucki, J.A., 1997. Contrasting fluid sources and mineralisation styles in the Great Eastern load-gold deposit, Lawlers, Western Australia. PhD thesis.

Mikucki E.J., and Roberts F.I. 2003. Metamorphic petrography of the Kalgoorlie region eastern goldfields granite-greenstone terrane METPET database. GSWA Record 2003/12.

Miller, J.M., 2006, Linking structure and mineralisation in Laverton, with specific reference to Sunrise Dam and Wallaby. In: A.C. Barnicoat, and R.J. Korsch (eds). Predictive Mineral Discovery CRC- Extended Abstracts for the April 2006 Conference. Geoscience Australia Record 2006/7, 62–67.

Morris, P.A., 1993. Archaean mafic and ultramafic volcanic rocks, Menzies to Norsman, Western Australia. Western Australian Geological Survey, Report, 55, 80p.

Morris, P.A., and Witt, W.K., 1997. Geochemistry and tectonic setting of two contrasting Archaean felsic volcanic associations in the Eastern Goldfields, Western Australia. Precambrian Research, 83, 83–107.

Mueller, A.G., Harris, L.B., and Lungan, A., 1988. Structural control on of greenstone-hosted gold mineralisation by transcurrent shearing: A new interpretation of the Kalgoorlie mining district, Western Australia. Ore Geology Reviews, 3, 359–387.

Myers, J.S., 1990. Precambrian tectonic evolution of part of Gondwana, southwestern Australia. Geology, 18, 537–540.

Myers, J.S. 1995. The generation and assembly of an Archaean supercontinent. Evidence from the Yilgarn craton, Western Australia. In: Coward, M.P., and Ries, A.C. (eds), Early Precambrian Processes, Geological Society Special Publication, 95, 143–154.

Nelson, D.R., 1995. Compilation of SHRIMP U-Pb zircon geochronology data, 1994. Western Australia Geological Survey, Record 1995/3, 244p.

Nelson, D.R., 1997. Evolution of the Archaean granite-greenstone terranes of the Eastern Goldfields, Western Australia: SHRIMP U-Pb zircon constraints. Precambrian Research, 83, 57–81.

Nelson, K.D., 1992. Are crustal thickness variations in old crustal belts like the Appalachians a consequence of lithospheric delamination? Geology, 20, 498–502.

Nguyen, T.P., 1997. Structural controls on gold mineralisation at the Revenge Mine and its tectonic settings in the Lefroy area, Kambalda, Western Australia, PhD thesis (unpublished), 205p.

Parman S.W., and Grove T.L., 2005. Komatiites in the plume debate. In: Foulger G.R., Natland J.H., Presnall D.C., and Anderson D.L. (eds) Plates, Plumes, and Paradigms. The Geological Society of America, Special Paper 388, 249–256.

Perring, C.S., Barley, M.E., Cassidy, K.F., Groves, D.I., McNaughton, N.J., Rock, N.M.S., Bettenay, L.F., Golding, S.D., and Hallberg, J.A., 1989. The association of linear orogenic belts, mantle-crustal magmatism and Archaean gold mineralisation in the Eastern Yilgarn Block of Western Australia. Economic Geology, Monograph 6, 571–586.

Rapp, P.R., Watson, E.B., and Miller, C.F., 1991. Partial melting of amphibolite/eclogite and the origin of Archaean trondhjemites and tonalites. Precambrian Research 51, 1 25.

Ridley, J.R. 1993. Implications of metamorphic patterns to tectonic models of the Eastern Goldfields. Australian Geological Survey Organisation, Record 54, 95–100.

Robert, F., Poulsen, K.H., Cassidy, K.F., Hodgson, C.J., 2005. Gold metallogeny of the Superior and Yilgarn Cratons. Economic Geology 100th Anniversary Volume 1001–1033.

Rock, N.M.S., Taylor, W.R., and Perring, C.S., 1990. Lamprophyres. In: Ho, S.E., Groves, D.I., and Bennett, J. (eds) Gold Deposits of the Archaean Yilgarn Block, Western Australia: Nature, genesis and Exploration Guides. Geology Department and University Extensions, Univeristy of Western Australia, Publication, 20, 128–135.

Salier B.P., Groves, D.I. , McNaughton, N.J., and Fletcher, I.R., 2004. The world-class Wallaby gold deposit, Laverton, Western Australia: An orogenic-style overprint on a magmatic-hydrothermal magnetite-calcite alteration pipe? Mineralium Deposita, 39, 473–494.

Sheldon, H.A., Barnicoat, A.C., Zhang, Y. and Ord, A., 2007. Metamorphism in the Eastern Goldfields: implications for fluid flow and mineralisation. In: in Bierlein, F.P., and Knox-Robinson, C.M., (eds), 2007. Proceedings of Geoconferences (WA) Inc. Kalgoorlie '07 Conference. Geoscience Australia Record 2007/14, p138–142.

Sircombe, K.N., Cassidy, K.F., Champion, D.C. and Tripp, G. 2007. Compilation of SHRIMP U-Pb geochronology data, Yilgarn Craton, western Australia, 2004–2006. Geoscience Record 2007/01.

Smithies, R.H., and Champion, D.C., 1999. Geochemistry of felsic igneous alkaline rocks in the Eastern Goldfields, Yilgarn Craton, Western Australia: a result of lower crustal delamination? – implications for Late Archaean tectonic evolution. Journal of the Geological Society of London, 156, 561–576.

Smithies, R.H., Champion, D.C., and Cassidy, K.F. 2003. Formation of Earth's early Archaean continental crust. Precambrian Research, 127, 89–101.

Sofoulis, J., 1963. Boorabin, W.A. Western Australia Geological Survey, 1:250 000 Geological Series Explanatory Note.

Squire, R.J., Cas R.A.F. and Champion D.C., 2007. The Black Flag Group: a vector to ore at St Ives. In: Bierlein F.P. and Knox-Robinson C.M. (editors), 2007, Proceedings of Geoconferences (WA) Inc. Kalgoorlie '07 Conference. Geoscience Australia Record 2007/14, p13–35.

Standing, J.G., 2008. Terrane amalgamation in the Eastern Goldfields Superterrane, Yilgarn Craton: Evidence from tectonostratigraphic studies of the Laverton Greenstone Belt. Precambrian Research, 161, 114–134.

Swager, C.P., 1995. Geology of the greenstone terranes in the Kurnalpi-Edjudina region, south-eastern Yilgarn Craton. Western Australia Geological Survey, Report 47, 31p.

Swager, C.P., 1997. Tectono-stratigraphy of late Archaean greenstone terranes in the southern Eastern Goldfields, Western Australia, Precambrian Research, 83, 11–42.

Swager, C.P., Goleby, B.R., Drummond, B.J., Rattenbury M.S., Williams P.R., 1997. Crustal structure of granite-greenstone terranes in the Eastern Goldfields, Yilgarn Craton, as revealed by seismic reflection profiling. Precambrian Research, 83, 43–56.

Swager, C.P., Griffin, T.J., Witt, W.K., Wyche, S., Ahmat, A.L., Hunter, W.M., and McGoldrick, P.J., 1990. Geology of the Archaean Kalgoorlie Terrane – an explanatory note. Western Australia Geological Survey, Report 1990/12.

Swager, C.P., and Nelson, D.R., 1997. Extensional emplacement of a high-grade granite gneiss complex into low-grade granite greenstones, Eastern Goldfields, Western Australia. Precambrian Research, 83, 203–209.

Swager, C.P., Witt, W.K., Griffin, T.J., Ahmat, A.L., Hunter, W.M., McGoldrick, P.J., and Wyche, S., 1992. Late Archaean granite-greenstones of the Kalgoorlie Terrane, Yilgarn Craton, Western Australia, In Glover, J.E., and Ho, S.E., (Eds), The Archaean – Terrains, Processes and Metallogeny. Geology Department and Extension Service, University of Western Australia Publication 22, 107–122.

Tripp, G.I., Cassidy, K.F., Rogers, J., Sircombe, K., and Wilson, M. 2007. Stratigraphy and structural geology of the Kalgoorlie greenstones: Key Criteria for gold exploration. In: Bierlien, F. and Knox-Robinson, C.M. (Eds), 2007, Proceedings of Geoconferences (WA) Inc. Kalgoorlie '07, Conference. Geoscience Australia Record 2007/14, p203–208.

Turcotte, D.L., and Schubert, G., 1982. Geodynamics, applications of continuum mechanics to geological problems. John Wiley and Sons, 464.

Weinberg, R.F., and van der Borgh, P., 2008. Extension and gold mineralization in the Archaean Kalgoorlie Terrane, Yilgarn Craton. Precambrian Research, 161, 77–88.

Williams, P.R., and Currie, K.L., 1993. Character and regional implications of the sheared Archaean granite-greenstone contact near Leonora, Western Australia. Precambrian Res. 62, 343–367.

Williams, P.R., and Whitaker, A.J., 1993. Gneiss domes and extensional deformation in the highly mineralised Archaean Eastern Goldfields Province, Western Australia, Ore Geology Reviews, 8, 141–162.

Williams, P.R., Etheridge, M.A., Witt, W., and Swager, C.P., 1989. Gold potential of early shear zones near Leonora, WA. Bureau of Mineral Resources Research Newsletter, 10, 6–7.

Winchester, J.A., and Floyd, P.A. 1977. Geochemical magma type discrimination-application to altered and metamorphosed basic igneous rocks. Earth and Planetary Science Letters 28, 459–469.

Witt, W.K. 1991. Regional metamorphic controls on alteration associated with gold mineralisation in the Eastern Goldfields province, Western Australia: Implications for the timing and origin of Archaean lode-gold deposits. Geology 19, 982–985.

Witt, W.K., and Davy, R., 1993. Pre- and post-folding, I-type granitoid suites in the southwest Eastern Goldfields Province: an Archaean syn-collisional plutonic event. In: Williams, P.R., Haldane, J.A. (Compilers), An International Conference on Crustal Evolution, Metallogeny and Exploration of the Eastern Goldfields. Aust. Geol. Surv. Org. Rec. 1993/54, pp. 39–46.

Witt, W.K., and Davy, R., 1997. Geology and geochemistry of Archaean granitoids in the southwest Eastern Goldfields Province, Western Australia: a syn-collisional tectonic setting? Precambrian Research, 83, 133–183.

Witt, W.K., Knight J.T., and Mikucki E.J., 1997. A synmetamorphic lateral fluid flow model for gold mineralization in the Archaean southern Kalgoorlie and Norseman terranes, Western Australia. Economic Geology, 92, 407–437.

Witt, W.K., and Swager, C.P., 1989. Structural setting and geochemistry of Archaean I-type granites in the Bardoc-Coolgardie area of the Norseman-Wiluna Belt, Western Australia. Precambrian Res. 41, 323–351.

Witt, W.K., Swager, C.P., and Nelson, D.R., 1996. 40Ar/39Ar and U-Pb constraints on the timing of gold mineralisation in the Kalgoorlie gold field, Western Australia – A discussion. Economic Geology, 91, 792–795.

## 3.2 A revised structural-event framework for the Eastern Goldfields Superterrane

**R.S. Blewett, K. Czarnota and P.A. Henson**

***pmd*CRC***, c/o Onshore Energy and Minerals Division, Geoscience Australia, GPO Box 378, Canberra, ACT, 2601, Australia

### Abstract

The tectonic grain of the Eastern Goldfields Superterrane (EGST) was established as a result of predominantly ENE-directed extension (D1 and D3) and E(ENE)-W(WSW) (D2, D4) to NE-SW (D5) contraction. The result has been a succession of NNW-striking co-planar, but temporally discrete, fabric elements that can be difficult to reliably interpret at any single location. Past workers generally interpreted the NNW-striking fabrics as 'D2' structures, and used them for correlating structural events across the region. However, these fabric elements cannot be used as the sole correlation marker. We present a new seven-fold (D1 to D7) deformation nomenclature based on kinematic analysis and cross cutting relationships. Extension, and transtension-transpression, characterised by extensional and strike-slip shear zones, are considered the dominant tectonic mode (not contraction and thrusting as previously thought). These tectonic modes are reflected in ground-based kinematic analysis, 3D map patterns, stratigraphic considerations, and deep seismic reflection imaging.

The EGST essentially faced ENE and inherited this grain during D1 extension ('DE' in Swager, 1997), which controlled the deposition of most of the greenstone stratigraphy on the eastern margin of the thinned Younami Terrane (basement). All subsequent events reused and modified this initial architecture. Late Basins and magmas from the metasomatised mantle wedge were developed in a complex extensional tectonic mode (D3) following the first contraction (D2), which resulted in arc accretion and termination of earlier volcanism and TTG magmatism. This D2 contraction did not develop significant foliation as major crustal thickening did not occur and the contractional events largely inverted a previously extended architecture. Granite doming and Late Basin sedimentation are linked by a common process of D3 extension. Upright folding (D4a) and sinistral strike-slip shearing (D4b) overprinted all but the Low-Ca (crustal melt) granites. The first N-S contraction (Swager 'D1') is younger than the Late Basins and is now considered regional D4b, and was developed during sinistral strike-slip transpression with regional σ1 oriented ESE-WNW. Low-Ca granites are associated with D5 dextral strike-slip tectonics, which was long-lived and was a result of an inclined σ1 that plunged SW. Gold is associated with all events, with D3 to D5 the most productive. Late extension or 'orogenic collapse' (D7) may not have occurred at the same time everywhere, and its intensity is variable.

**Key words:** *structure, deformation, Eastern Goldfields Superterrane, Archaean tectonics*

### 3.2.1 Introduction

The gold deposits of the Eastern Goldfields Superterrane (EGST) are structurally controlled, so the structural geology of the region has been extensively studied to both understand these controls and use this understanding to predict the location of new (structurally-controlled) ore bodies. Much of the initial regional (structural) understanding of EGST (Figure 3.2.1) was developed in the southwest part of the EGST (greater Kalgoorlie region) and was extrapolated outwards to the rest of the Superterrane. The paper by Swager (1997) represented a seminal synthesis of over 10 years of prior research and extensive mapping, and it was this work that became the benchmark structural-event framework to which other workers matched their studies.

Building on the work of Swager (1997, and references therein), we present a new integrated structural-event framework for the EGST that incorporates a further decade of research from various Geoscience Australia, Geological Survey of Western Australia, AMIRA and ***pmd*CRC*** projects. This new structural-event framework better integrates the improved understanding of the greenstone stratigraphy, granite evolution, structure, tectonic mode, and mineralisation into a coherent understanding in time and 3D space. Underpinning this revised structural-event framework are new (>10,000) structural observations from across the entire EGST. In addition to selected mapping and regional outcrop studies, focus was given to the excellent granite pavements (most with age dates) and to the mines, both areas are where exposures permit reconciliation of the key

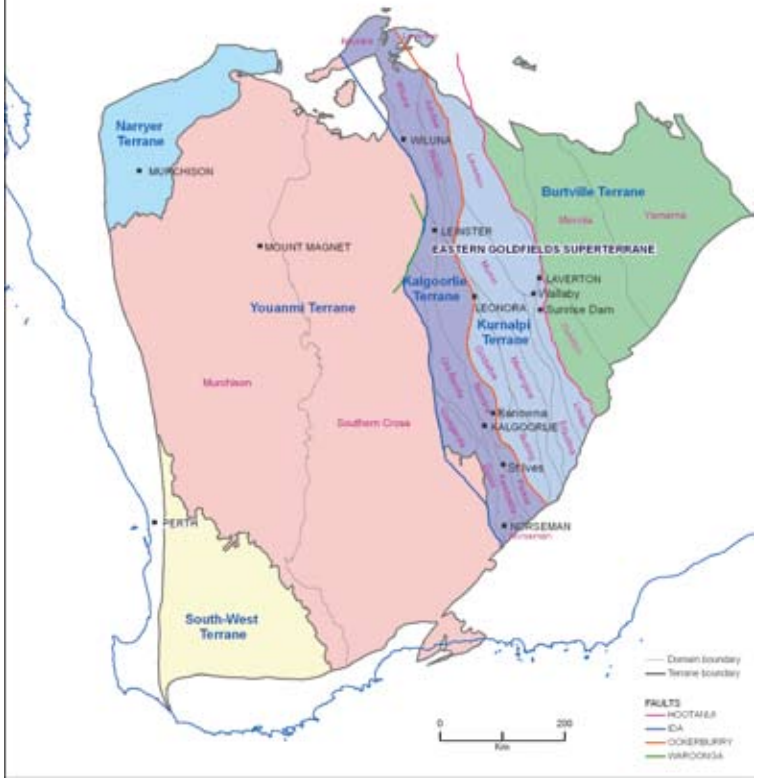


*Figure 3.2.1: Map of the terranes and domains of the EGST with superimposed major gold, nickel and VHMS mining camps after Cassidy et al. (2006).*

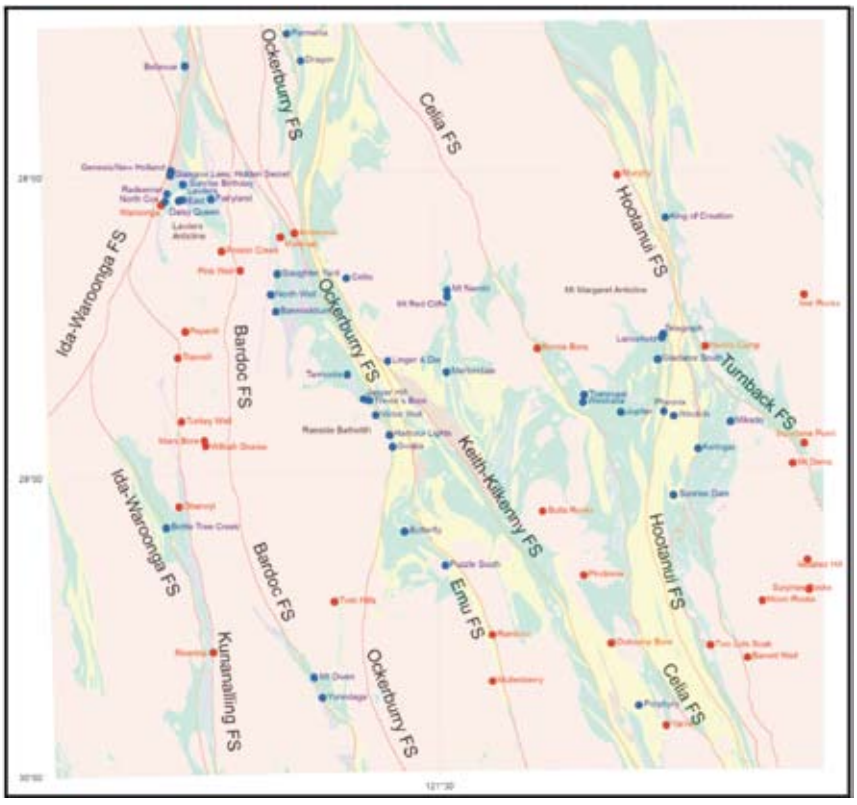


*Figure 3.2.2: Map of the central Eastern Goldfields Superterrane and sites of specific structural studies described (blue – mine sites: red – granite sites). This region was the main focus for new data acquired in this paper. Map colours are pink (granites); brown (conglomerates – Late Basins); green (mafic rocks); purple (ultramafic rocks); yellow (felsic volcanic and sedimentary rocks).*

overprinting relationships (and thus critical constraints on the framework). The geographic scope of the new study was from Wiluna in the north to Kambalda in the south, from the Ida Fault in the west to the Yamarna Domain in the east (Figures 3.2.1, 3.2.2). The new observations were made in all granite types and all the greenstone stratigraphic units. The observations were carefully chosen to across all structural positions in terms of strain and possible structural level.

To highlight new advances in understanding a review of the structural paradigm pre the Y4 ***pmd*CRC*** project is outlined before the new structural-event framework is presented and discussed. This paper accompanies the companion paper by Czarnota et al. (2008), which is a review and synthesis of the greenstone stratigraphy, granite magmatism and metamorphism with this new structure-event framework, and how these elements interrelate to the broader geodynamic system.

### 3.2.2 Previous Structural Frameworks

Modern structural geology was not systematically applied to the EGST until the studies of Platt et al. (1978), Archibald et al. (1978) and Swager (1989). These workers were the first to publish regional deformation event histories that were subsequently adopted as a framework by subsequent workers (Table 3.2.1). This summary of previous work draws on the significant (regional) studies that describe more than an individual mine or map sheet.

The pronounced NNW-oriented structural trend of the EGST (so-called 'D2' trend) is defined by the regional fault pattern and elongate granitoid bodies (Gee, 1979). The regional-scale faults form an anastomosing network of high-strain zones that bound a number of terranes or structural domains (Swager et al., 1992; Myers, 1997) that are elongate or lensoid in map pattern, and separate different greenstone successions. The characteristic map pattern of the EGST was developed by a succession of extensional and contractional deformation events that have been interpreted as regional (province-wide) in extent. Swager (1997) summarised many of the interpretations of the regional deformation history, and it is this framework that is further refined. Henson et al. (2006) produced a structural event history that honoured the 2D and 3D map patterns, and was built on the Swager (1997) and Blewett et al. (2004a) work. The map pattern analysis of Henson et al. (2006) defined the essential structural elements and their relative timing; these are further refined and integrated in this study.

Table 3.2.1: Comparative deformation chronology of various workers in the Eastern Goldfields Superterrane

Deformation correlation

| Blewett & Czarnota | | | Mueller 1988 | Swager 1997 | Nguyen 1997 | Blewett 2004 | Miller 2006 |
|---|---|---|---|---|---|---|---|
| Minor extension | | D6 | | Collapse | | Late De | |
| Dextral strike-slip | | D5 | D3 | D4 | D4 | D3 | D4 |
| Sinistral transpression | NW-SE local comp. | D4b | D2 | D3 | D3 | D3 | D3 |
| | Late Basin upright folding | D4a | D1 | D2 | D2 | D2b | D2 |
| Extensional doming | Stage 2 Late Basins | D3b | | DE | DE3 | D2e | |
| | Stage 1 Late Basins | D3a | | | | | D1 |
| Upright folding and reverse faulting | | D2 | | D2 | | D2a | |
| Extension with intermittent compression | | D1 | | DE | DE1-2 | De | |

A nomenclature of '[1]D1' to 'D4+' has been most widely used to describe the various deformation events of the EGST. Swager (1997) is the 'standard' terminology most workers have adopted (Table 3.2.1). Unfortunately most workers did not emphasise or enumerate the extensional deformation events (other than 'De' or 'DE'). Broadly, the recognised deformation (contractional history) involved early 'D1' recumbent folding and thrusting during N-S shortening, followed by E-W shortening through large-scale upright 'D2' folding and thrusting, then a period of strike-slip 'D3' faulting with associated folding, followed by continued regional 'D4' transpressive oblique and reverse faulting. Some authors have proposed early, intermediate, and late periods of extension throughout parts of this contractional history although these are not enumerated as separate events.

The following section outlines the generally used structural framework (Table 3.2.1) and is mostly based on Swager (1997, and references therein).

### 3.2.2.1 DE: Early Extension

A number of workers have suggested that early extension predated 'D1' thrusting and may represent the last stages of development of the basin in which the greenstones accumulated (e.g., Williams et al., 1989; Hammond and Nisbet 1992, 1993; Williams, 1993). These workers argued the external granites represent the substrate on which the greenstones were deposited, within an overall N-S directed core complex extensional setting. With recent advances in geochronology the majority of these 'external' granites have been shown to be younger then the surrounding greenstones (Weinberg et al., 2003), thereby negating this model. SRK (2000) suggested that the core complex model applied to the deposition of the Black Flags and younger sediments within an overall S directed extensional model. Detailed work in the Leonora area led Passchier (1994) to suggest that 'D1' recumbent folds at Leonora may have formed in an extensional setting.

### 3.2.2.2 D1: N-S contraction

Swager and Griffin (1990) suggested that the 'D1' event involved large-scale stratigraphic repetition during N-S contraction. For example, a regional-scale thrust duplex structure was interpreted to extend from Kambalda to Kalgoorlie and significantly duplicate stratigraphy. Regional 'D1' in the EGST was thought by many to have developed roughly E-W trending thrusts and folds as a result of N-S compression (e.g., Swager, 1997, and references therein).

More recent interpretations of this map pattern suggest that these so-called 'D1' thrusts are later than the first compressive event. This new interpretation is based on the observation that 'F2' folds are transected by these so-called 'D1' thrusts (Blewett, 2006). Recognition of 'D1' N-S contraction has been a long-standing problem in the northern Goldfields (see also; Wyche and Farrell, 2000, Beardsmore, 2002), and it was not observed in this study.

### 3.2.2.3 Late Basins

Swager (1997) interpreted the Late Basins (Kurrawang, Penny Dam etc.) as being developed during extension after 'D1' and before 'D2', because they transect regional 'D1' structures and they are deformed by 'D2' (in his four-fold deformation chronology). This pre-'D2' extensional phase was interpreted as oriented E-W, involving synclinal basins developed above roll-over anticlines. Other workers have described these basins as 'compressional' basins, developing synchronous with 'D2' (Liu and Chen, 1998). Krapež et al. (2000) and Weinberg et al. (2003) suggested that they were developed post-'D1' amalgamation in a strike-slip event (that is not enumerated by a separate event).

### 3.2.2.4 D2: E-W contraction

The regional 'D2' deformation was interpreted to have involved considerable E-W (ENE–WSW) crustal shortening, producing major regional-scale upright 'F2' folds (seen as granite-cored domes), together with a pervasive metamorphic foliation (Swager, 1997). The subvertical penetrative foliation developed in all rock types and across a widespread region was interpreted in most cases as a composite 'S1-S2' fabric.

The 'D2' event has been attributed with the development of the major elements of the EGST architecture, including well-preserved regionally extensive 'F2' granite-cored anticlines, commonly with doubly plunging to horizontal

1 Deformation in quotes are from other workers. The new deformation framework presented here is not placed in quotes.

fold axes. The synclines are commonly more complex fault-related structures, with Late Basins locally defining the 'F2' synclinal hinge zones (in most workers terminology). Hammond and Nisbet (1992) suggested that the regional antiforms represented hangingwall anticlines developed during W-directed thrusting, and this view was thought to be consistent with the seismic data from Kalgoorlie (Goleby et al., 1993; Drummond et al., 2000), and the seismic data and 3D model developed for the Leonora-Laverton area (Blewett et al., 2002a; 2002b; Goleby et al., 2002; Henson et al., 2004a, 2004b). These workers suggested that the seismic data represent a classical fold-and-thrust belt such as the European Alps and North American Appalachians (Rodgers, 1995).

The regional 'D2' event was considered by most workers to post-date the Late Basins. For example, the Kurrawang, Merougil, and Penny Dam basins lie in regional 'D2' synclines in the southern part of the EGST (Swager, 1997; Krapež et al., 2000; Weinberg et al., 2003). Similarly, in the Welcome Well area the Pig Well-Yilgangi basin is folded by the NW-trending Butcher Syncline (Gower, 1976) and is overprinted by a well-developed fabric interpreted as 'S2' (Williams et al., 1989; Passchier, 1994; Liu and Chen, 1998; Stewart, 1998). Swager (1997) suggested 'D2' was ca. 2665 Ma, while Krapež et al. (2000) suggested that it was ca. <2650 Ma[2]. Weinberg et al. (2003) stated that 'D2' occurred after the deposition of the Late Basins and used Krapež et al.'s (2000) young age of about 2655 Ma for his 'D2'.

### 3.2.2.5 Local Extension

Interestingly, Swager (1997) outlined a series of extensional events between many of the contractional events, although he suggested that some of these were of local extent. Swager and Nelson (1997) noted local extension (after 'D2') of the high-grade granite-gneiss domains into their final uplifted positions relative to the lower grade greenstone belts. They suggested that this extensional event was syn- to post-main granitoid emplacement at ca. 2660 Ma. Wyche and Farrell (2000) described similar relationships along the Ockerburry Fault System in the northern Eastern Goldfields.

2 Krapež et al. (2000) interpreted the detrital zircon data to give a 10 m.y. younger maximum age for the Late Basins by using the youngest grain rather than the youngest statistical population.

Most workers tended to focus on the contractional event history, and neglected the extensional part of the history. Davis and Maidens (2003), and Blewett et al. (2004a) documented important extensional events during or just after the major 'D2' contractional event. Blewett et al. (2004b) suggested that 'D2' involved two contractional ('D2a', 'D2b') events, separated by an extensional event ('D2e') together with the deposition of the 'Late Basins', and that this more complex 'D2' was diachronous (younging to the west or southwest). The timing (diachroneity) and relationship of the 'Late Basins' to a regional 'D2e' extensional event was a significant departure from the established Swager (1997) framework (Table 3.2.1).

### 3.2.2.6 D3: ongoing E-W contraction

Continued regional '$D_3$' E-W shortening resulted in the development of NNW-striking sinistral strike-slip faults and late stage foliations (Swager, 1989). En-échelon 'F3' folds with steep plunges developed as a consequence of sinistral strike-slip shearing along the already steeply tilted sequence. Hammond and Nisbet (1992) questioned the significance of the 'D3' sinistral strike-slip event. They proposed that most of the so-called late movements were rotated N-directed 'D1' thrusts that now recorded apparent sinistral kinematics.

Seismic imaging (Goleby et al., 2002), and work on the 3D geometry of the major shear zones in the Leonora-Laverton area (Figure 3.2.1) cast doubt as to the significance of steep strike-slip shearing in the EGST. The results of this work showed that most shear zones dip moderately to shallowly to the east (Blewett et al., 2002a), an apparently unlikely geometry for a significant strike-slip orogen. However, the limitation of seismic imaging is its inability to directly image steeply dipping features. Detailed analysis of reflector truncations is required to pick steep structures. With continental seismic this often proves to be challenge. However Henson et al. (2007) were able to resolve the steeply dipping strike-slip Hootanui Shear Zone (or Far Eastern) at Laverton in their more detailed 3D model of Laverton.

#### 3.2.2.7 D4: late contraction

Post 'D3' contractional structures ('D4') have been described as variably oriented kink bands and crenulation cleavages, as well as oblique-slip sinistral and dextral faults (Swager, 1997; Vearncombe, 1998; Chen et al., 2001). The NE-trending faults are mostly dextral, and the E- to ESE-trending faults are mostly sinistral, suggesting renewed E-W compression. However, Mueller et al. (1988) attributed this change in tectonism to a small anticlockwise rotation in the main shortening direction (to NE-SW). Swager (1997) considered the 'D4' structures to be ca. 2620–2600 Ma in age.

#### 3.2.2.8 Late extension (collapse)

Crustal-scale extensional faulting is recognised on the Ida Fault (Figure 3.2.1) by an abrupt eastward change in metamorphic grade, with exhumed higher-grade rocks in the footwall to the west (Swager, 1997). Seismic reflection data reveal that about 5 km of downthrow to the east occurred across the fault (Goleby et al., 1993). The orientation of the Ida Fault, parallel to the 'D2' 'compressional' structures, might infer extension or post-orogenic collapse following 'D2-D3' shortening.

Blewett et al. (2002b) and Goleby et al. (2002) noted a similar east-block down sense of extensional movement on domain-bounding faults in the Leonora-Laverton area seismic reflection data. The extensional movement on the Ida Fault is constrained as older than the stitching Clarke Well Monzogranite (2640 ±8 Ma: Nelson, 1997). This extensional movement was considered younger than peak metamorphism (Swager, 1997), and corresponded with a change in granitoid magmatism to the Low-Ca suite below the base of the greenstone sequences (Champion and Sheraton, 1997).

#### 3.2.2.9 Granite structural studies

Another feature of most structural studies in the EGST was the emphasis on the greenstone sequences. Many of the granites of the central EGST are well-exposed, with granite pavements providing unique lateral continuity to map structures. This good exposure, coupled with recent high-resolution geochronology (Cassidy et al., 2002a; Black et al. GA unpublished data), allowed Blewett et al. (2004c) to erect a new event history that was better constrained in time. The granites were also useful as they are now exposed at a range of crustal levels and a range of regions in terms of the distribution of regional strain.

### 3.2.3 A new structural-event framework

#### 3.2.3.1 Introduction

One of the first observations of the map patterns of the EGST is the extremely heterogeneous partitioning of strain (Figure 3.2.3a). For example, there are vast areas of relatively intact greenstone stratigraphy (with weak fabric development) that envelope and dip gently and young away from broad elongate gently NNW-SSE plunging granite-cored domes (Figure 3.2.3c). These areas contrast with intervening localised zones of shear-dominated high-strains (up to 5 km in width) with intense foliation, steep dips (with steeply plunging folds), and dismembered stratigraphy. These high-strain zones are commonly areas of significant reworking and were subject to intense extensional, reverse and strike-slip (both sinistral and dextral) contractional events; resulting in a pronounced NNW-trending structural grain (Figure 3.2.4). Despite being separate events, the finite strain resulted in largely co-planar fabric elements that are superficially similar but can be up to 25 Ma separated in time (Figure 3.2.5).

The direction of $\sigma 1$ throughout much of the contractional part of the sequence was oriented ENE-WSW (D2, D4a) to NE-SW (D5). The result is fabric elements maybe difficult to reliably interpret at any single location – this has been part of the problem in the past of using foliations as a correlation marker. Where the D3 extensional event separates contractional D2 from contractional D4 structures, reconciliation of these contractional structures is relatively easy. Another constraint is provided by the Late Basins or Low-Ca granites. The Late Basins, by definition, can not host a D2 structure as they overprint them. Low-Ca granites (which are <2655 Ma) can not host D1 through to D4 structures for the same reason.

However, a problem occurs where D3 is 'missing' or where the rocks are older than the Late Basin or in the case of granites, are the older High-Ca type. There are also many instances where contraction and extension are mutually exclusive and so the critical overprinting relationships are not available. The reasons for this mutual exclusivity is not well understood, but the role of the large granite batholiths

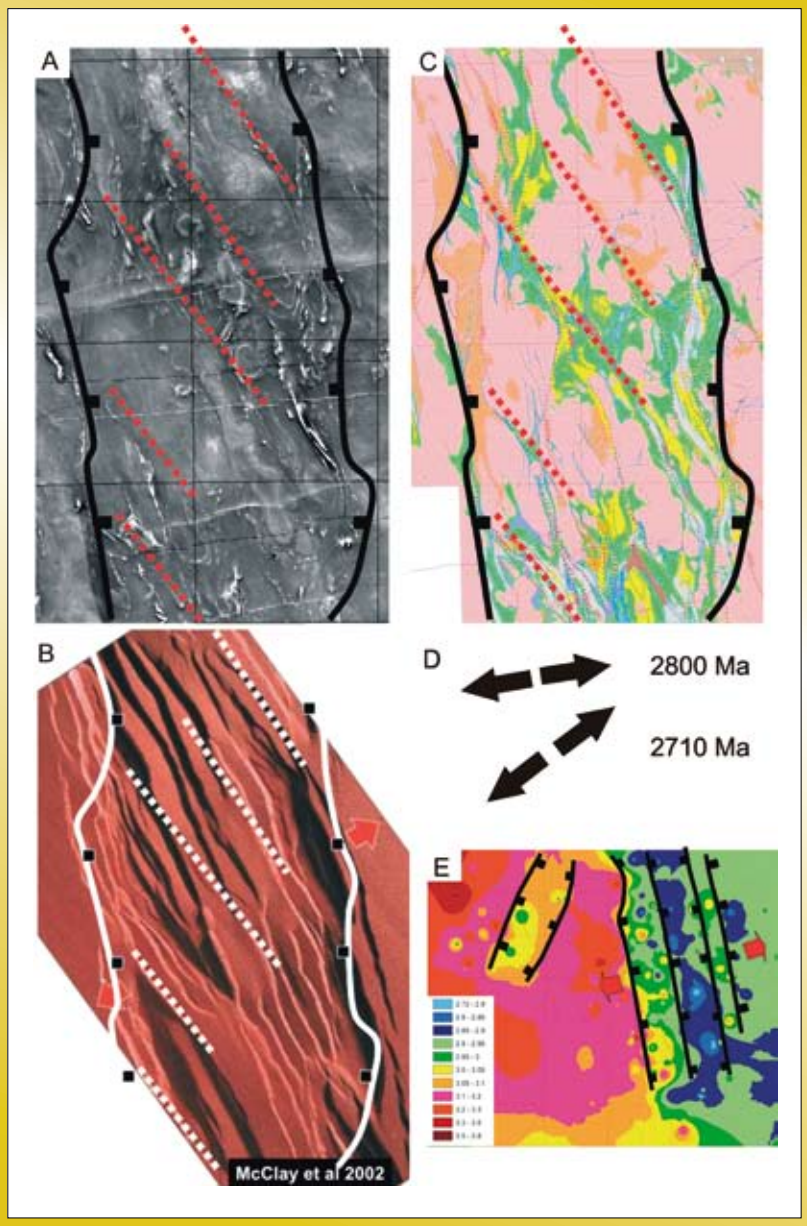


*Figure 3.2.3: a) Regional aeromagnetic image (total magnetic intensity reduced to pole) with major trends superimposed; b); Sandbox modelling of extension with a basement anisotropy showing the complex interplay of the border faults (solid lines) and the internal extension faults (pecked lines). In this model a NE-SW directed extension is superimposed upon an earlier ~E-W direction of extension. Note the similarity in the gross trends in the magnetics and geology (Figures 3a, 3c); c) Solid geology interpretation with the main magnetic trends superimposed and mirroring the geological map patterns; d) Model of two main extension directions. Earliest extension direction was just north of E-W and set up the border faults (cf. Figure 3.2.3b) and the main Sm-Nd patterns (cf. Figure 3.2.3e); e) Nd depleted-mantle model age map of the Yilgarn Craton. Image produced by griding Nd depleted-mantle model ages calculated from Sm-Nd point data from Champion and Cassidy (2007). Note the pronounced NNW trends in the distribution of crustal ages.*

in partitioning strain or in controlling a vertical component to the tectonic mode are candidates. In some localities (e.g., Riverina, Waroonga, Peperill, Mt Redcliffe, King of Creation: Figure 3.2.2) it is not possible due to lack of overprinting relationships (and without dating foliations) to determine whether a specific dominant fabric is D5, D4a, or D2!

### 3.2.3.2 Changes to the paradigm

A number of changes to the Swager (1997) and derivative paradigm is proposed here, which is based on the work of Blewett and Czarnota (2007a, b). The new structural-event framework and how it relates to significant earlier work is presented in Table 3.2.1. The main areas of change (including enumerating the extensional events) are:

1. Extension and trans-tension/pression are considered the dominant tectonic mode (not contraction), and this is reflected in 3D map patterns, stratigraphic considerations, and deep seismic reflection imaging.

2. The EGST (orogen) faced essentially E (ENE) and inherited this grain during ~2.81 Ga extension (Czarnota et al., 2008; 'DE' in Swager, 1997 terminology) and development of basins on the eastern margin of the Younami Terrane. All subsequent events re-used and modified this essential architecture. Regional contraction was oriented NE-SW to ESE-WNW.

3. Late Basins were developed in a complex extensional tectonic mode (D3[3]) following the first contraction (D2), which resulted in termination of volcanism. This D2 contraction did not develop significant foliation. Granite doming, Late Basin sedimentation and D3 extension are all linked by a common process.

4. Major crustal thickening did not occur and the contractional events largely inverted a previously extended architecture.

5. Return of σ1 to the ENE-WSW (D2) conditions occurred during D4a, which resulted in tightening of (earlier extensional developed) folds, folding, thrusting and foliation development.

6. A clockwise rotation of the stress field to ESE-WNW, coupled with the now steeply dipping stratigraphy, the orogen became unfavourable to dip slip movements and sinistral strike-slip shearing (D4b) became the dominant tectonic mode. This change resulted in the development of accommodation step-overs, where localised to district-scale N-S to NW-SE oriented contraction developed thrusts and folds across specific structures and geometries (e.g., strike-slip step-overs).

7. The timing of the first contraction N-S contraction (Swager (1997) 'D1') is younger than the Late Basins and is now considered part of the regional D4b event.

8. Low-Ca granites are associated with D5 dextral strike-slip tectonics, which was long-lived and was a result of a switch to NE-SW oriented contraction.

9. Gold is associated with all events, although the first significant economic mineralisation was associated with D3 and the most gold endowed structures are D4 and D5.

10. Late extension or vertical shortening (D6) may not have occurred at the same time everywhere, and its intensity is variable.

### 3.2.3.3 D1[4]: long-lived extension and granite-greenstone formation

One of the immediate impressions when viewing a geological or geophysical map of the EGST Craton is the prominent NNW-trending grain (Figures 3.2.3a to 3.2.3e). Many workers have interpreted this grain to be a

3 D3 is separated into D3a and D3b stages in detail, but when described collectively it is referred to as simply D3.

4 the deformation sequence (D numbers) of this New Structural Framework are not surrounded by quotes and is preferred nomenclature of Blewett & Czarnota

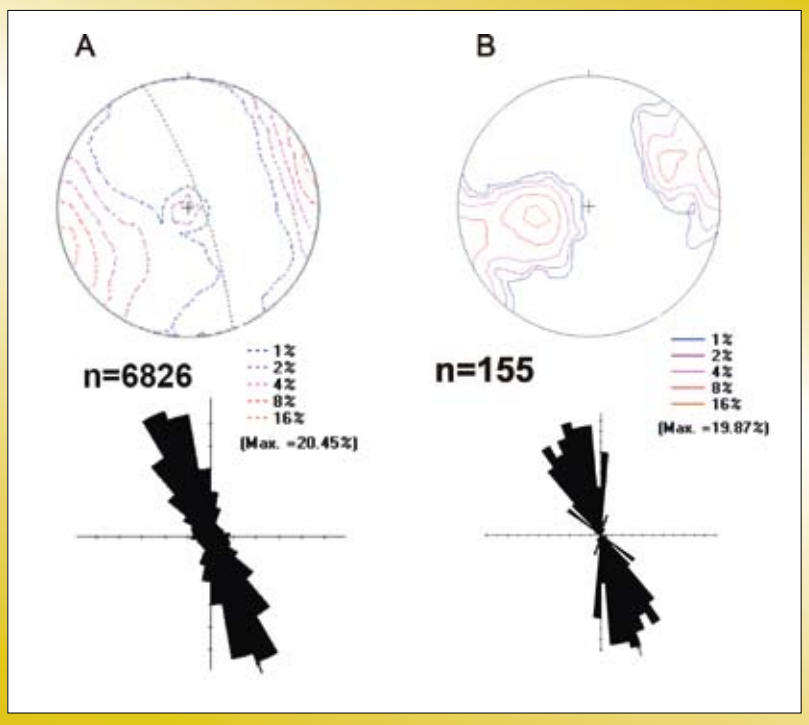


*Figure 3.2.4: a) Extract of 'S2' foliation data from Geoscience Australia's OXROX database containing regional geology data for the EGST plotted as a stereographic projection (contoured poles to planes) and rose diagram (of strikes). Note the strong NNW 'S2' trend; b) Combined stereographic projection (contoured poles to planes) and rose diagram (of strikes) of four selected sites showing the same NNW trend, but developed at different times and by different tectonic modes (cf. Figure 3.2.5).*

function of the so-called regional ENE-WSW oriented 'D2' contractional event (e.g., Gee, 1979, Swager et al., 1989, Swager, 1997, Myers, 1997).

The grain is more fundamental than simply a contractional event; it is reflected in the broad distribution of the greenstone stratigraphy (Swager et al., 1992; Swager, 1997), the granite types (Champion and Sheraton, 1997), and the Sm-Nd granite isotopes (Figure 3.2.3e). A 'corridor' of youngest εNd model ages corresponds approximately to the western Kurnalpi Terrane (Figure 3.2.1). The isotope map is interpreted in terms of an ENE-facing extensional rift at ca. 2810 Ma (Czarnota et al., 2008).

The rock record from ca. 2715 Ma to ca. 2680 Ma shows a general age progression of arc volcanism from east to west in the Kurnalpi Terrane. The geodynamic setting envisaged is one dominated by ENE-facing extension, with a W-dipping slab (located to the east) driving extension via a roll-back mechanism (Czarnota et al., 2008).
The distribution of ultramafic rocks (komatiite) in the Kambalda area change markedly across NNW-trending faults. The inference is that the faults controlling deposition

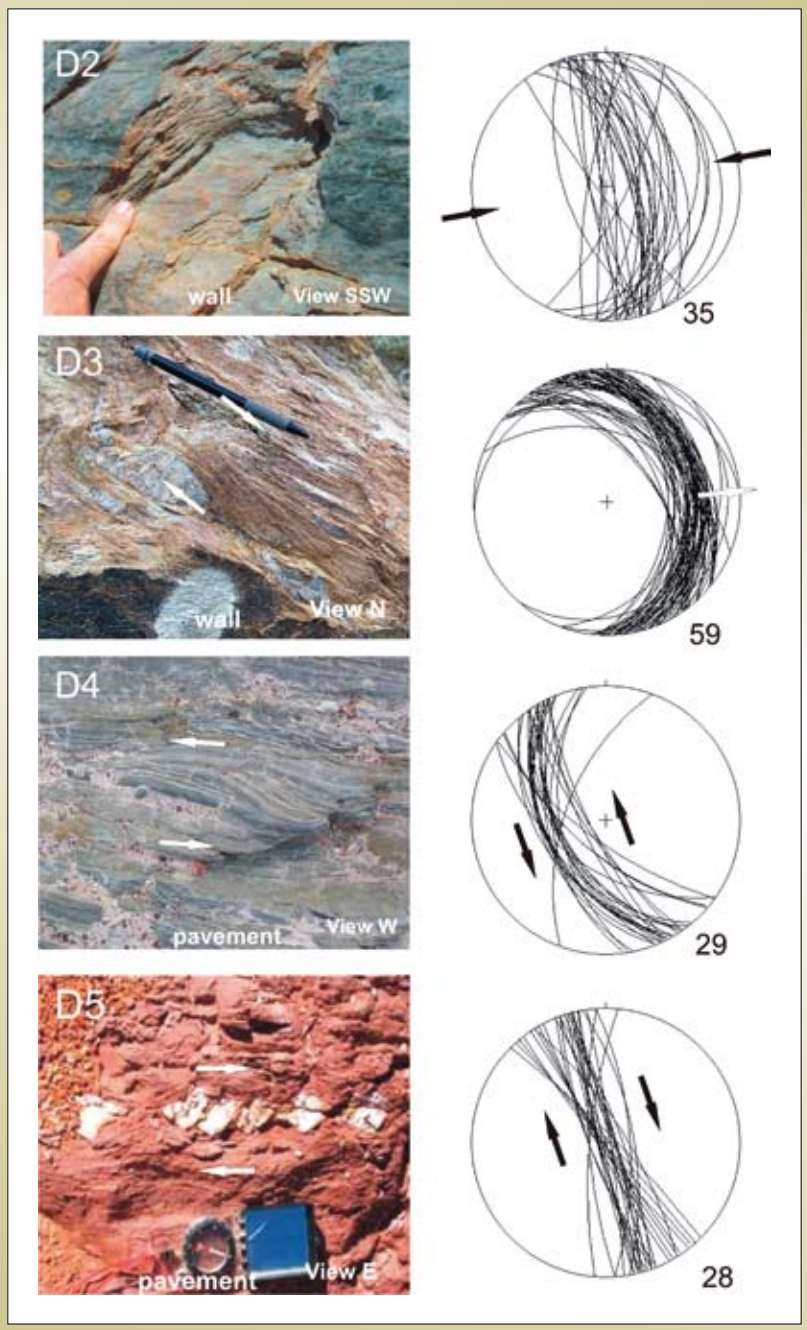


*Figure 3.2.5: Separate stereographic projections of foliations in Figure 3.2.4b: S2 (flattening ~2665 Ma), S3 (extension ~2660 Ma), S4 (flattening and sinistral strike-slip ~2650 Ma), and S5 (dextral strike-slip ~2640 Ma) all showing similar strikes and yet all are fundamentally different in their genesis and age. The superficial parallelism of penetrative fabrics of different ages has made the use of the 'S2' fabric an unreliable structural marker for correlation purposes (Czarnota and Blewett, 2007).*

were extensional, and controlled the emplacement and deposition of the lower parts of the Kambalda Sequence at around 2700 Ma within back-arc tectonic setting (Conners, et al., 2003).

Swager and Griffin (1990) noted a similar distribution of the so-called Upper Basalt above the Kambalda Komatiite. For example, across the NNW-trending Lefroy Fault System in the Boorara Domain the Upper Basalt is absent, with the Kalgoorlie Sequence (Black Flags) deposited directly upon komatiite. A similar relationship occurs with the distribution of mafic sills, with thick sills present in the Kambalda and Ora Banda Domains, and almost totally absent in the Boorara Domain. Many of these mafic sills intrude the Kalgoorlie Sequence, suggesting that extensional control was exerted with an E-W polarity through the entire greenstone sequence up to (and probably including – see later) the Late Basins (see also Miller et al., 2008).

Krapež et al. (2000) described a number of unconformities in the Kalgoorlie Sequence, with a prominent angular discordance at around 2675 Ma. Tilting during extension can account for the development of topography and therefore high points for erosion leading to the formation of angular unconformities (as opposed to contractional folding events).

Alternatively, the differences in stratigraphic thickness reflect excision by detachments, especially near the base of the Kalgoorlie Sequence or Black Flag Formation (Blewett et al., 2004b).

The external granites record a major melting and exhumation event at around 2675–2672 Ma (Cassidy et al., 2002a). The development of significant gneissic fabric elements have been dated across the entire EGST, irrespective of the terrane or the domain. The fabric elements developed at this time include melanosome-leucosome differentiated layering, which are commonly isoclinally folded and transposed. When unfolded for the effects of later upright folding, these isoclinal folds were likely recumbent and have the geometry of lower-plate folds developed during vertical flattening and extension (Blewett et al., 2004c). The widespread nature of this 2675–2672 Ma thermal event suggests that it reflects a fundamental stage in the extensional evolution of the orogen. Granites and their overlying detachments had not become emergent for the purposes of providing detritus until Late Basin times, indicating the extensional unroofing had further to develop after 2665 Ma (D3).

### Geodynamics of D1

The D1 event was extensional with a dominantly ENE-directed polarity and was likely the result of roll back of a subduction zone(s) to the ENE. The timing of the event likely includes the earliest greenstone rock record (2800 Ma) through to the onset of the first significant contraction at around 2670 Ma. Collins (2002) invoked a model of 'extensional accretionary orogens' for broad belts like the Palaeozoic Lachlan Fold Belt, and by analogy the EGST. Relicts of the older basement (maybe Youanmi Terrane) are preserved as small slivers of >2810 Ma granites and greenstones especially in the Burtville Terrane. These may represent the rifted remnants of the D1 extension.

The vast volume of High-Ca plutonism that developed during this D1 ENE-oriented extensional environment likely initiated early elongate domes – 'sowing the seeds' of the architecture seen today.

## 3.2.3.4 D2: ~ENE-WSW contraction and termination of an arc

The first significant contraction (D2) occurred diachronously at around 2670 and 2665 Ma in the Kurnalpi and Kalgoorlie Terranes respectively. It resulted in the termination of volcanism in the greenstones (Czarnota et al., 2008). The D2 structures indicate that shortening was oriented ENE-WSW, perpendicular to the grain of the D1 extensional orogen. The simplest scenario for the cause of the D2 contraction is for the accretion of an external body (an oceanic plateau) into the receding subduction zone, thus terminating volcanism and providing a wave of contraction across the orogen (Czarnota et al., 2008).

Blewett et al. (2004b) described two examples of regional macroscale F2 folds. The first in the Kalgoorlie Terrane was the N-plunging regional anticline-syncline pair at Ora Banda and its relationship with the overlying Kurrawang Basin. The second example in the western Kurnalpi Terrane was the S-plunging upright Corkscrew Anticline at Welcome Well, and its relationship to the Pig Well Basin (Figure 3.2.6a). At both these examples Late Basins unconformably overlie these folded structures, providing an

age constraint of >2660 Ma for the development of these underlying folds (Blewett et al., 2004b). These authors described the regional folds as 'D2a' (Table 3.2.1). To the east in the Kurnalpi Terrane, the map patterns of the Mt Margaret Anticline around Laverton also show that old greenstone sequences are folded more tightly than the outline of the batholith and the geometry of the 2665 ±5 Ma Wallaby Late Basin. This relationship suggests that ENE-oriented shortening had at least commenced before the Late Basins were initiated. In the southern EGST, the ENE-directed Foster Thrust at Kambalda is interpreted as a D2 structure (Blewett et al., 2008; Miller et al., 2008).

Clear examples of mesoscale D2 contraction are rare in the greenstones. Westralia which is close to the Celia Fault System has a flattening fabric (Figure 3.2.6b), while Tarmoola shows gold-bearing veins associated with D2 thrusting and dextral shear (Figure 3.2.6c). Flattening fabrics are also present in the Bannockburn mine (Figure 3.2.6e) northwest of Leonora. At a mesoscale across many of the granite sites (Blewett et al., 2004a), D2 is represented by upright asymmetrical (Z-shaped) folds, and N-S dextral shear zone transposition of D1 extensional fabric elements. There appears to be a general change from folding (Figure 3.2.6d) to dextral shearing in the 'external' granites. These fabric elements were observed across the entire EGST.

However, D2 was generally a low-strain event and developed without significant regional foliation development. We see evidence for D2 deformation in the regional map patterns, some mines (e.g., Tarmoola), and in the external granites which were deeper and hotter. We can also infer the presence of D2 by the fact that the disparate associations (as determined from their chemistry and age distribution) were brought together at a time when the late arcs shut off in the Kalgoorlie Terrane. Significant regional foliation was not developed in the greenstone sequences until the next event (D3).

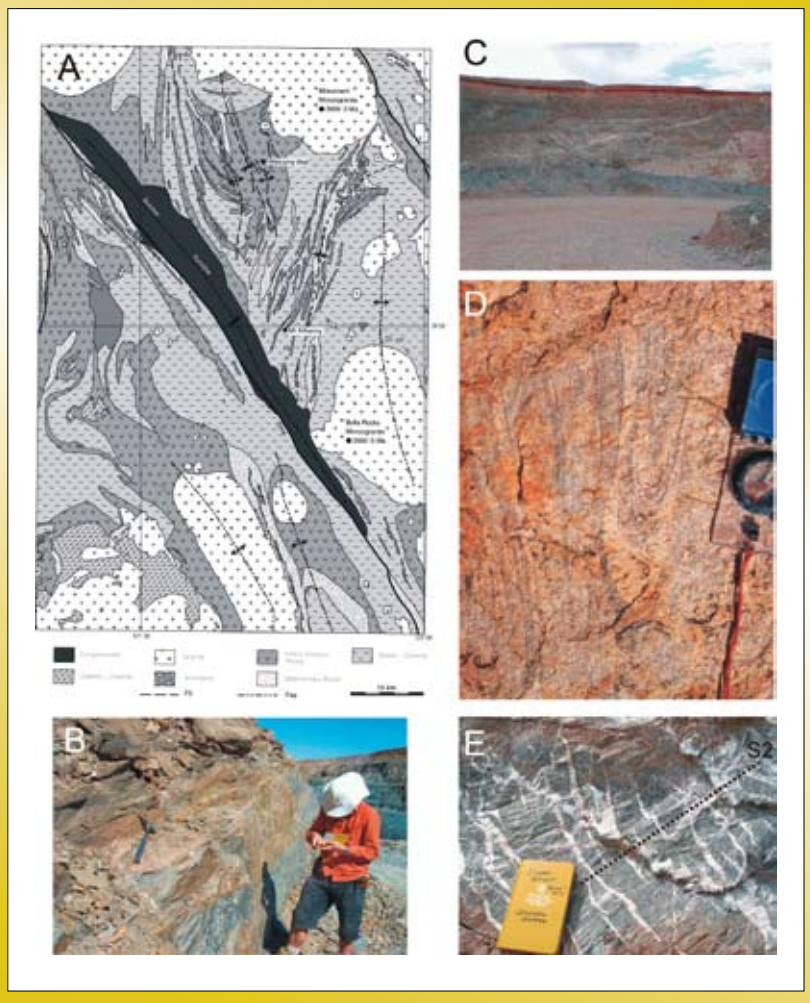


*Figure 3.2.6: a) Example of NNW trending Pig Well late basin overlying N- to NNW-trending regional F2 folds (from Blewett et al. 2004b); b) dextral strike-slip fault plane in Tarmoola gold mine near Leonora (Figure 3.2.2); c) View onto the east wall of the Tarmoola gold mine showing the dextral vein with wing crack extension veins. Dextral transpression occurred due to flattening onto a NNE trending segment of the large granite body in the pit; d) Flattening with the development of shallow plunging upright folds at Moon Rooks (Figure 3.2.2) of a D1 gneissic fabric; e) Flattening fabric and conjugate extension veins developed in the Bannockburn gold mine northwest of Leonora (Figure 3.2.2).*

### 3.2.3.5 The seismic insights for crustal architecture – extension or contraction?

Before continuing with the next phase (D3) in the secular evolution of the EGST tectonics, a digression to consider the interpretation of the deep seismic reflection data is warranted (Figure 3.2.7).

Deep seismic reflection profiling made a paradigm change in early 1990's with the first deep line (91BMREGF01) just to the north of Kalgoorlie (Goleby et al., 1993). New insights into greenstone depth, the shape of granites and granite-greenstone contacts, as well as the identification of 'detachments', has had a lasting impact on tectonic thinking in the Yilgarn. The early interpretations also favoured a contractional (fold and thrust belt) model for the development of the architecture of the EGST. Since then, higher quality vibroseis acquisition and improved processing on the Leonora to Lake Yeo line (01AGSNY1) has challenged this contractional interpretation (Blewett and Czarnota, 2007b). The following two sections provide new insights into the architecture of the EGST, and thus its likely geodynamic environment.

#### Large-scale picture of the crust

Figure 3.2.7 shows a comparison of analogue modelling crustal-scale extension (Harris et al., 2002) and the 01AGSNY1 seismic line from Leonora to Lake Yeo (Goleby et al., 2003). The analogue modelling shows the development of upright (gently plunging) folds adjacent to extensional shear zones. The models of Harris et al. (2002) are developed in plasticine, but the resultant geometries bear an uncanny resemblance to the deep crustal seismic reflection profiles (Goleby et al., 1993; 2003; Blewett et al., 2002a).

The broad antiforms in these models may be analogous to the broad antiforms such as the Mt Margaret, Raeside, and Lawlers Anticlines. In the analogue modelling, these antiforms are cored by more ductile material (the more competent layers such as the brown and black markers)

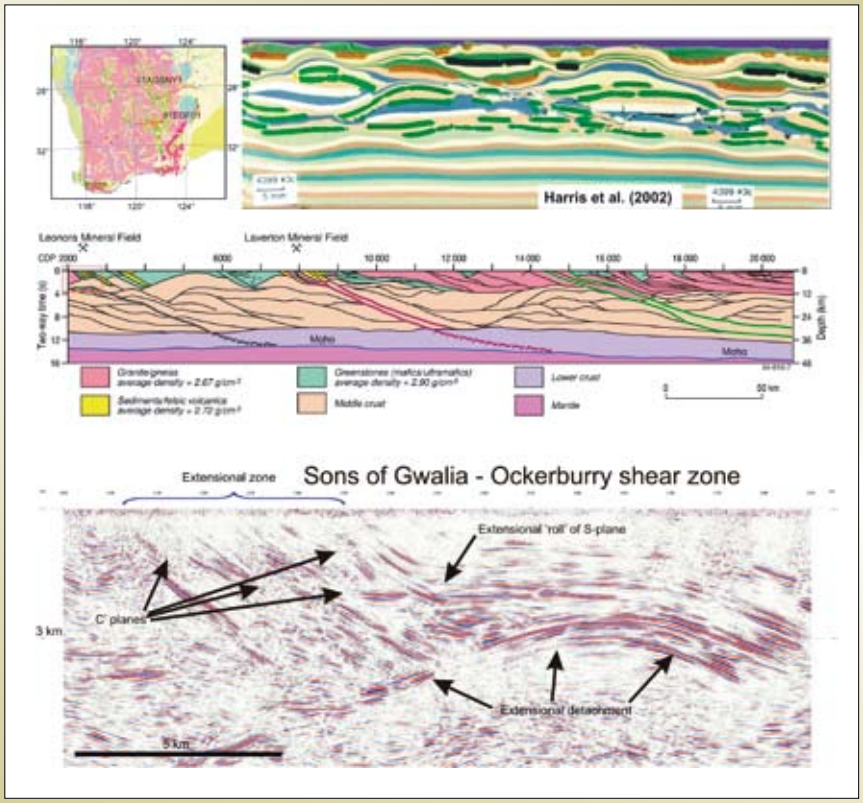


*Figure 3.2.7: Interpretation of 01AGSNY1 seismic sections from Leonora to Lake Yeo showing prominent crustal-scale features. Sections show three sub horizontal layers in the crust. Above the mantle is a thin non- to poorly-reflective layer, above this is a layer containing large-scale lozenges, and the upper crust has a complex signature recording variations in the granite-greenstone layer. The 01AGSNY1 seismic section is 384 km in length by 48 km in depth. Inset map shows location of seismic line.*

*Note the architectural similarity in style with analogue modelling of extension (after Harris et al., 2002) showing how this tectonic mode may have formed the crustal architecture imaged in the seismic (see also Blewett and Czarnota, 2007a).*

*Detailed E-W seismic seismic line through the Gwalia pit vicinity to around 6 km depth shows extensional S-C and C' planes in the events at this scale. These intense bands of reflectivity (shearing) are up to 5 km wide and roll onto a granite dome at depth. This rolling of the fabric onto a detachment is consistent with extension.*

boudinage. This inference may suggest that magmatism at the time of extension may be required to reduce the lower-plate viscosity to facilitate this doming.

Another common view has been that D2 contraction involved folding and thrusting. This view has been influenced by the observation that most of the large regional folds (many are granite cored) plunge gently to the NNW or SSE (see later about development of granite-cored folds during extension). This 'D2-thrust' view has also been influenced by the interpretation that the architecture imaged in the seismic reflection data represent a fold and thrust belt (Goleby et al., 1993, Drummond et al., 2000; Blewett et al., 2002b).

#### Seismic reflection at Leonora and Pig Well – extensional formation of a Late Basin

The project was fortunate to have access to publicly funded (GA-GSWA) seismic reflection data (01GASNY1) through the Leonora area (Figure 3.2.7). These data were interpreted as part of the ***pmd****CRC* Y2 project (Blewett et al., 2004b). The main faults, the Ockerburry and Keith-Kilkenny Shear Zones have normal (extensional) map patterns with the younger (Late Basin in brown) on older basement greenstone (green and yellow). The 01GASNY1 seismic line is a high-quality dataset that was reprocessed by Dr. Leonie Jones at Geoscience Australia. The result was the resolution of macro-scale extensional shear zones (S-C-C' relationships) that can be traced from 5–6 km depth to the surface (Figure 3.2.7).

The re-processed seismic line 01AGSNY1 across the Gwalia pit (Figure 3.2.7) shows events that are interpreted here as macroscale examples of S-C-C' relationships, consistent with mesoscale observations in the pit and surrounding locality (see later). Intense foliation (reflectivity up to 5 km wide) is imaged by the seismic line, and this soles out into a convex up detachment (analogous to core complex development).

To the east, the Keith Kilkenny Shear Zone displays a similar geometry in the seismic data, with wide zones interpreted as S-C' shear bands, consistent with an E-down sense of shear. The Pig Well Basin (Graben) appears to partly overprint (with an unconformity?) a foliation (developed during extension?), and is dragged in a normal sense by further extensional movement along this zone (Blewett et al., 2004b). Shear bands within the basin are also extensional in geometry. Examination of map patterns along strike for the Ockerburry, Emu and Keith Kilkenny Shear Zones also show younger rocks preserved on the eastern (downthrown-hangingwall) side of the faults.

What is most revealing about these seismic lines is the spacing of the intensity of reflectivity (foliation development). Intense reflectivity can be correlated at the surface with high-strain extensional shear zones. These appear to be zones up to 5 km wide both in surface mapping and in the seismic data. These can convincingly be regarded as extensional fabrics; which raises a very serious question about how NNW-trending foliations have been interpreted about the region in the past! This is the so-called 'S2' fabric (Figure 3.2.4) and it has been used as the correlation foliation by most workers for their site to site correlations, and to construct event stratigraphies. As outlined earlier, the NNW-trending foliation, commonly called 'S2' can be a strike-slip, normal/extensional dip slip, axial planar flattening, and/or a combination of these in any one locality. This variation in its genesis makes it a poor marker fabric (Czarnota and Blewett, 2007a; Figures 3.2.4, 3.2.5).

### 3.2.3.6 D3: Granite doming, extension and Late Basin Formation

Having illustrated the importance of the extensional fabrics in the architecture of the EGST, the following sections return to the secular evolution (D3 and later) of the system. D3 was a widespread event and has been subdivided into two stages (D3a and D3b). It is the first significant regional foliation developing event (in the greenstones), and has been in places incorrectly assigned 'D2' [in Swager (1997) terminology] by previous workers (see Figure 3.2.5).

#### D3: Extension and formation of Late Basins

The extensional D3 deformation event was associated with significant granite doming (especially close to the major domes), and Late Basin formation and deformation. There are two geometrical forms (and ages) of Late Basins. Stage 1 Late Basins are arcuate and located in the hanging wall of extension shear zones at the noses of some major domes, and are likely initiated during D3a extension after or in the end stages of D2 contraction. Stage 2 Late Basins are NNW-trending elongate 'rifts', and they are interpreted to have developed by D3b ENE-down asymmetrical

extension (inversion of D2 thrusts?). These basins were interpreted to have formed during the D2e extension of Blewett et al. (2004b).

The polarity of the extension of the Stage 1 basins is orthogonal to, and within the strain shadow of, the ENE-WSW directed regional D2 contraction. This D2 contraction has been estimated to have occurred at around 2665 Ma, which is within error of the formation of the Stage 1 Wallaby Basin (2665 ±5 Ma), but on geometrical arguments (above) is likely to have initiated late to post D2 contraction. The working hypothesis forwarded here is that the onset of contraction resulted in 'extrusion' of the granite domes to the NNW and SSE, orthogonal to the D2 contraction and parallel to the earlier D1 extensional grain (see also Davis and Maidens, 2003). However, the actual initiation and realisation of the Stage 1 basins did not occur until late in D2.

This phase of early D3 extension is assigned to D3a. It was associated with significant doming and multi-directional extension as granite batholiths were exhumed (and later provided detritus for the Late Basins). The Lawlers, Leonora and Laverton areas (Figure 3.2.1) are dominated by large granite batholiths in the cores of regional N-S to NNW-SSE trending anticlines.

Other workers have described important extension in the region. McIntyre and Martin (2005) suggested that the Late Basins in the Laverton area were developed as upper-plate rift basins above a detachment related to 'extrusion' of the Mt Margaret Batholith to the north. SRK (2000) described these extensional domes as core complexes, suggesting that they were developed during the formation of the main mafic-ultramafic greenstone sequences from ca. 2.7 Ga (Czarnota et al., 2008).

### D3: Extension in the Leonora area and the strong D3 overprint on D2

The Leonora area is characterised by the E-dipping margin of the Raeside Batholith, which has a sheared contact with old elements of the Kalgoorlie Terrane greenstones (basalts and ultramafic rocks). This is a favourably oriented region to record E-W shortening (D2); however evidence for D2 structures is cryptic due to the intensity of D3 extensional strain. A question remains as to whether D2 was simply strongly overprinted, or was it never, or only weakly, developed at this locality. Interestingly, there is also little evidence for significant D4 or D5 contraction at Leonora in proximity to the Raeside Batholith.

The prominent fabric element in the Leonora region is an intense L/S- and S-tectonite that was developed under E-down extension (Williams et al., 1989; Williams and Whitaker, 1993). Despite the intensity of D3 extensional strain (Figure 3.2.9b), in the lower strain domains of the mines of the region (e.g., Gwalia, Tower Hill, Harbour Lights), relicts of deformed conjugate(?) veins occur. These highly deformed veins may be the record of the D2 contraction. In support of this hypothesis is the D2-D3 relationship at Tarmoola (Figure 3.2.2). Tarmoola is located away from this intense D3 extensional shear zone on the margin of the Raeside Batholith. At this locality evidence for earlier ENE-WSW D2 contraction is well demonstrated.

Further to the west, away from the influence of the Raeside Batholith (e.g., Slaughter Yard to Mt Owen: Blewett and Czarnota, 2007a), the main D2 fabric was developed by flattening and contraction (Figure 3.2.6e). In this location, there is limited evidence for extensional fabric elements (D3 or other), indicating that the granite dome was a driving force in influence the location and intensity of D3 extensional strain.

### D3: Extension at Lawlers and the weak D2 contraction?

The Lawlers Anticline is located in the west of the Kalgoorlie Terrane (Figure 3.2.2). It is a gently N-plunging upright granite-cored dome with outward facing and younging mafic-ultramafic rocks of the Kambalda Sequence. The Lawlers Tonalite (a Mafic-type granite) in the centre of the dome has an age of 2666 ± 3 Ma (Fletcher et al., 2006). Along the western margin of the anticline lies the Scotty Creek Stage 2 Late Basin, which has a maximum depositional age of <2662±5 Ma (Dunphy et al., 2003).

In the greenstones around the Lawlers Anticline (e.g., Fairyland to North Cox: Blewett and Czarnota, 2007a), the prominent fabric element is extensional (D3). In this region (from Fairyland to North Cox: Blewett and Czarnota, 2007) it is difficult to unequivocally identify the E-W D2 contraction. The region is dominated by E-, NE-, and N-down extensional fabric elements. In Leonora it was argued above that the D2 contraction structures (although weakly developed) were largely obliterated by the intense

D3 shearing. The degree of strain (at least qualitatively) is much less at Lawlers, and large areas of intact stratigraphy are preserved (Beardsmore, 2002). The map patterns of the Lawlers Anticline (Figure 3.2.8), especially the SW limb, show that the Lawlers Tonalite intruded into an already domed sequence. This suggests either that the magmatism was concentrated into incipient antiforms developed during and after D1, and that the extension and doming was likely a long-lived process, or that D2 contraction was weak and did not leave an obvious mesoscale record but was sufficient to develop broad open folding.

Beardsmore (2002) showed in a very comprehensive mapping study of the Lawlers region that the main foliation transects the axis of the regional fold (Figure 3.2.8a). Also revealing in this study was the pattern of lineations (Figure 3.2.8b). They plunge gently to the north in the north, becoming progressively steeper NE and finally steeply E-plunging along the eastern limb of the fold. In contrast, the western limb of the fold does not have down-dip lineations like its eastern counterpart. Rather, the lineations plunge gently S and are more akin to strike-slip (Beardsmore, 2002). This pattern of foliations and

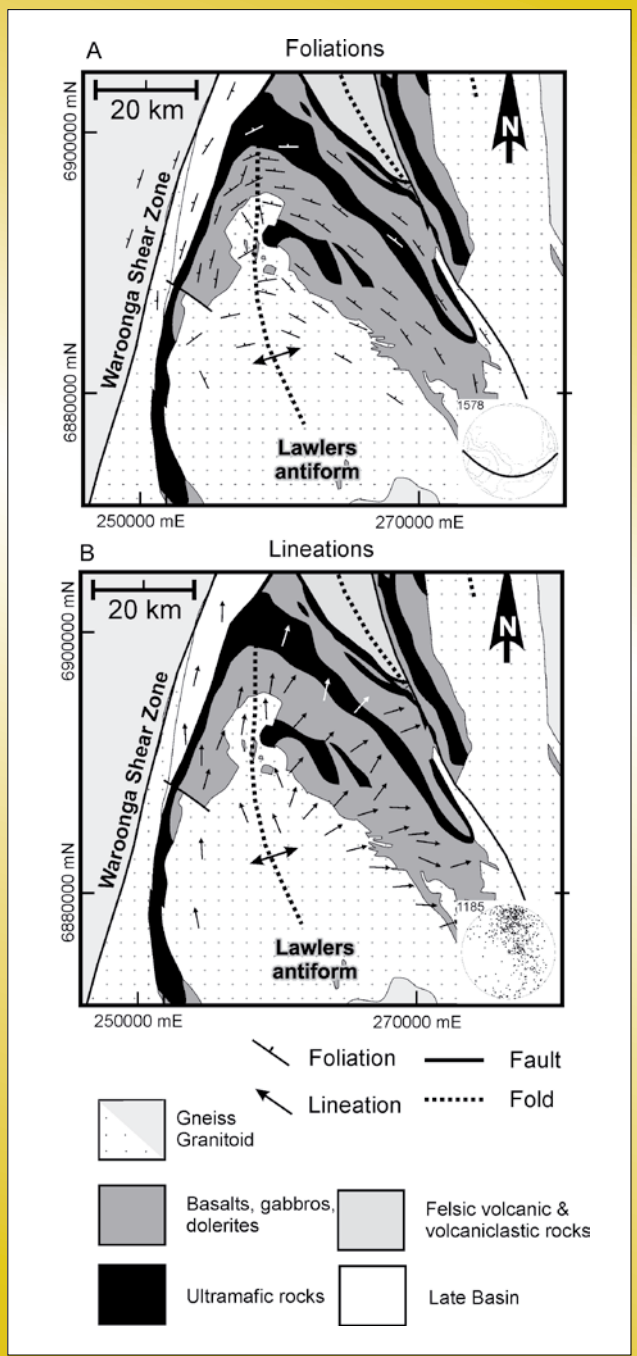


*Figure 3.2.8: Map of the main foliation and lineation in the Lawlers region after Beardsmore (2002). The red lines are major faults, and many were observed to have normal or extensional kinematics on them in this study. a) Map of the main foliation. b) Map of lineation trajectories showing the gentle (hinge parallel) plunge in the centre and north, and the steepening and rotation of the plunge to east on the SE limb of the fold. Insert: Stereonet of lineations in granites and greenstones around the Lawlers Anticline (generated from data in Beardsmore, 2002). Note that the main population plunges gently north, this is parallel to the hinge of the regional fold (and the shape of granite at depth). A second sub-population plunges steeply ENE. Note the lack of W- and SW-plunging lineations.*

lineations is not consistent with diapirism. The lineations are not radial as there are few if any down-dip lineations on the western limbs across the EGST. This is not simply a sampling problem as Beardsmore (2002) has systematically encircled the Lawlers Anticline (Figure 3.2.8).

In the Lawlers area, there is a question regarding whether there is only one foliation. Beardsmore (2002) suggested that there might be two populations, one shallow NE-dipping, and another steeper and striking NNW. Shallow fabrics in granites from the area lie on a girdle with a pole (fold axis) that plunges 23° to 359° (Figure 3.2.8). Similar relationships occur in the leucogranite in the innermost nose of the Lawlers Anticline, where two stages of deformation are recorded. Beardsmore (2002) also noted dextral shearing on the steeper NNW-trending fabric (which we would interpret as D5 dextral – see later).

The Lawlers Anticline is interpreted to record extensional uplift and exhumation, with doming and magmatism at ~2665 Ma. The overlying greenstones were domed and tilted and overprinted by extensional down to the N-, NE- and E-dipping extensional shear zones. Shear was accommodated on structures such as the Cascade Shear in the Sunrise Birthday pit (Figure 3.2.9e), and was associated with gold mineralisation. Similar extensional shear zones include the Stockyard and Caroline shears (Figure 3.2.8). These faults have apparent sinistral offset in map patterns which, when resolved kinematically, are the result of normal offsets on NE-dipping markers. This extensional mode explains the paradox for Beardsmore (2002) of the steep down-dip lineations he recorded on these shears, and negates the need for an additional deformation event to explain the geometry and relationships.

Beardsmore (2002) also described the 'rolling' of the stratigraphy on the eastern limb of the Lawlers Anticline. He noted that the lowest units dipped on average 35° to the NE, while the upper units dipped more than 75° to the NE. This change in dip was interpreted to be a function of back rotation during NE-over-SW thrusting. An alternative interpretation presented here is that this change in dips reflects the position of the stratigraphy with respect

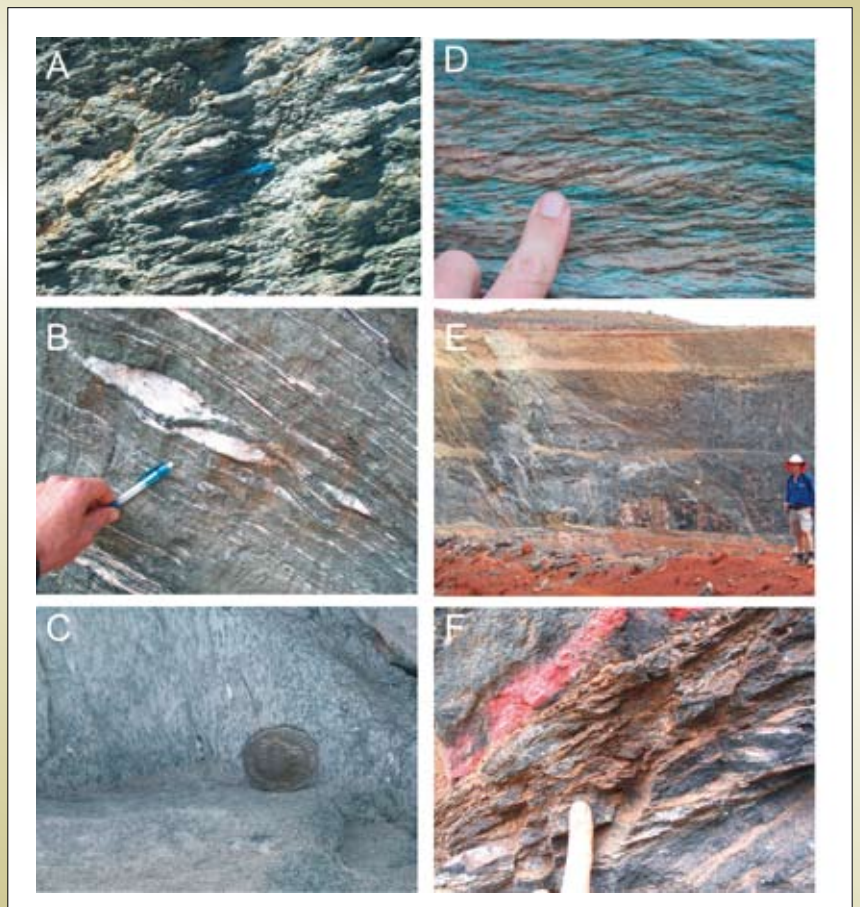


*Figure 3.2.9: a) View NE of gently-dipping S3 foliation with pronounced S-C fabric suggesting top to the left (NW) extensional shearing at Kerringal gold mine (Figure 3.2.2). This fabric is strongly overprinted by D5 dextral fabrics in this locality; b) S-C-C' extensional fabrics at Gwalia gold mine near Leonora. Compare this to the seismic image of the pit (Figure 3.2.6) with the main fabric represented by a moderate-dipping main foliation (C planes), lesser gentle to subhorizontal dipping S-planes and localised steeply dipping and limited penetrating C' planes; d) Down-dip stretching lineations in the Gwalia gold mine showing the extensional (normal) nature of these fabric elements; e) View west into the Sunrise Birthday pit showing the 'rolling' of the foliation. The majority of this host gabbro is unfoliated, with the penetrative fabric confined to high-strain (gold-rich) zones. f) Sunrise Birthday as a neo-formed S3 S-C fabric that was developed during down-to-the-north-northeast extension.*

to the C' extensional shear planes, with the associated footwall uplift and doming common to extensional systems. This uplift would be greatest closest to the main detachment; i.e., closer to the granite and therefore lowest parts of the stratigraphy. Mesoscale examples are exposed in the Genesis pit and in the distribution of the ore shells at the Fairyland deposit. The veins in the Fairyland deposit are strongly boudinaged, with a consistent NE-down pattern of steep and shallow dips (ramp and flat).

The Lawlers Anticline and the Mt Margaret Anticline are located at the western and eastern margins of the Kalgoorlie and Kurnalpi Terranes respectively. Both folds are granite-cored and are associated with significant Late Basin preservation, and gold deposits. The initiation of the antiforms may have been during D1 extension, with rising granite magma being emplaced into these incipient domes. The development of extensional shear zones and detachments within the granite and overlying greenstones tilted the country rocks so that when the Late Basins were deposited they 'found' a 'D2' prefolded sequence. The intensity of this extensional event was sufficient to finally bring the lower-plate to the surface so that granitic detritus could be sourced and deposited both locally and afar.

### Metamorphism across extensional shear zones

Low-angle extension is an effective mechanism for juxtaposing high-grade lower plate rocks against low-grade upper plate rocks. Williams et al. (1989), and later in Williams and Whitaker (1993), related the juxtaposition of high-grade greenstones (immediately adjacent to the Raeside and Mt Margaret Batholiths) against low-grade greenstones across batholith-away dipping shear zones, as a function of extension. Williams and Currie (1993) noted at least 5 km of excision from this extensional event. In these papers, Williams suggested that the extension was the 'De' event described by many workers. They may have been right, as these areas have been dominated by extension for much of their history and it is likely that this was a long-lived event.

Goscombe et al. (2007) have compiled the existing metamorphic database and also analysed all available pelitic assemblages with a probe. Their results show that the general field gradient is one of not only steadily increasing temperature towards the granites from the greenstone synforms (as Binns et al., 1976 showed), but of increasing pressure. In fact, Goscombe's results show that pressure increases dramatically close to the granites, confirming the extensional excision of deep stratigraphy inferred by Williams and Currie (1993)

In terms of the general field gradients, a question remains regarding the pressure estimates of the granites. Goscombe's work ended at the granite margins and there was uncertainty as to whether pressure dropped in the granites (i.e., do the narrow high-grade greenstones represent channel flow material from the deep crust). However, barometry on granites around the Wilbah Gneiss and Mars Bore (Figure 3.2.2) showed them to have been exhumed from around 8 kbars or 20–24 km (Morrie Duggan, unpublished GA data). If these pressure estimates represent the general case for the high-grade granite-gneiss regions, then the channel flow hypothesis is invalid and so a core-complex type model is favoured.

### Polarity of D3 deformation

The fundamental grain viewed in the seismic (Figure 3.2.7) is E-down (ENE) shearing; a 'rebirth' of the earlier D1 extension following the arc shut off and D2 contraction. However, in detail the lineations plunge to the eastern hemisphere around the domes (e.g., at Lawlers Figure 3.2.8). It has been at Lawlers (and by Williams and Whitaker, 1993 at Leonora) that the granites rose upwards in the crust while under extension and the greenstones were shed off these rising bodies. The regional far-field ENE-directed extension was enhanced locally in the domal regions by magmatism and hence resulted in the development of north-directed extension at Lawlers. The fact that greenstones slide off to the north, east, and south (and all points in between), and that the granites were locally 'extruded' to the NNW, W, and SSE, imply that the orogen was not fixed at the sides and a buoyancy component to the extension was involved. Davis and Maidens (2003) also described a late 'D2' extension in the Laverton area ('D2e'), and related this to collapse of the 'D2' orogen along its axis. In a slightly different model, SRK (2000) suggested that the polarity of extension was NNW-SSE, building on the early work of Hammond and Nisbet (1992; 1993). In these models, the NNW-trending architecture formed the transfer faults (localising Late Basins in narrow troughs in these transfers), while the main detachments were arcuate about the broad granite domes.

In both cases, SRK (2000) and Davis and Maidens (2003) mapped the local effects of a larger system.

The SRK model is appealing in many ways, but does not explain the temporal relationships of the Late Basins, nor the fact that the primary architecture in a multitude of geophysical, geochronological, geochemical and geological datasets show that the fundamental compartments strike NNW (during D1 and D3). These data all point to an ENE-directed extension direction, and may reveal something about the orientation of the orogen's margin (i.e., it was likely NNW-trending in today's reference frame).

### Geodynamic summary of $D_2/D_3$ and implications for gold

In terms of the spatial association of proximity of major gold deposits and Late Basins, it could be that the basins are a consequence of a linked process critical in the formation of Au deposits. This common process is extension and the creation of deep-connected fluid pathways onto the detachments at depth, and the formation of a domal focussing architecture. The fact that magmatism (a hot fluid) also favours the domes created by the extension may also point to a common process (or architecture) for magmatism and gold mineralisation.

Most of the gold is later than D3, yet D3 marks the onset of significant economic mineralisation in the EGST. Examples of gold found in D3 shear zones are the Lancefield deposit, the Leonora camp including the >10 Moz Gwalia deposit and the minor Sunrise Birthday deposit (Figure 3.2.2). Major gold deposits associated with subsequent deformation events are mostly located in the footwall to major shear zones. This relationship potentially indicates that major D3 mylonitic shear zones acted as a seal to fluid flow during subsequent events. The reactivation of these shear zones during periods of strike-slip shearing would allow for mixing of fluids from separate reservoirs. Furthermore it is this event which established the gross architecture of the EGST which functioned as the fluid focusing mechanism associated with the formation of the major gold deposits.

In summary, the D2 event was contractional with a dominantly ENE-WSW polarity of convergence. The timing of the event marks the first significant contraction at around 2670 Ma associated with the termination of volcanism. Non-volcanic Late Basin sedimentation commenced during the subsequent period of extension and significant exhumation of granitic substrate. The drivers of this extension may be the same as the D1 extension – roll back of the slab on the eastern margin, however, there was a fundamental change in the geodynamic setting since there is no volcanism associated with this event only clastic sedimentation.

The change from D1/D2 to D3 is marked by a spike in Mafic granite magmatism across the EGST. These magmas have sanukitoid affinity and were likely derived from a metasomatised mantle source (a good source for gold and sulphur). Earlier High-Ca magmas (peaking around ~2673 Ma) are of the low-Y subgroup, whereas after this event they change to a more transitional type (Champion and Cassidy, 2002). Furthermore, syenite magmatism began in the EGST at this time. This dramatic change in felsic magmatism suggests that a fundamental geodynamic change has occurred, rather than the system returning to the previous D1 extensional setting. Beakhouse (2007) has recently described the magmatic changes in the Archaean Superior Province of Canada. He suggested that the change from slab melting (TTG) to metasomatised mantle melting (Sanukitoid) was a function of slab detachment and/or delamination following collision. However the metamorphic history does not allow for a continent-continent collision tectonic model (Goscombe et al, 2007) there fore favouring a delamination model proposed earlier by Smithies and Champion (1999) for the generation of Syenites and Low-Ca granites.

A working model is therefore proposed where the D3 extension and its associated rock record in the EGST, were the result of lower crustal delamination with possible associated slab roll back triggered by D2 contraction (Czarnota et al., 2008). This delamination provided access to a fertile source for subsequent gold-bearing fluids and magmas by a deep pathway system linked to Late Basins.

### 3.2.3.7 D4: progressive contraction and sinistral strike-slip

D4 was a mostly low-strain contractional event across broad areas of the EGST, with localised intense high-strain corridors adjacent to steep margins of granite batholiths. Despite earlier gold during D2 and D3, the D4 event marks the onset of the most endowed period of

gold mineralisation in the EGST (at Lawlers, Laverton, Kalgoorlie and Kambalda). Two stages of progressive deformation comprise the D4 event (Table 3.2.1).

1. The first stage (D4a) involved horizontal contraction with σ1 oriented just north of E-W (similar to D2 stress field), resulting in flattening, upright folding and associated cleavage formation, and tightening of earlier domes and D2-D3 folds (Figure 3.2.10). The geometrical result was the rotation and steepening of stratigraphy (including Late Basins) along the margins of E-facing granite domes (e.g., Bardoc Tectonic Zone north of Kalgoorlie, Scotty Creek Basin at Lawlers, and the Mt Varden area north of Laverton). This event was termed 'D2' by Swager (1997) and 'D2b' by Blewett et al. (2004b) as it overprints the Late Basins (formed during D3).

2. The second stage (D4b) involved an oblique sinistral strike-slip component of shear, especially in regions with steep stratigraphic dips (where thrusting and flattening ceased to be effective in dissipating the stress). A clockwise rotation of the stress field is implied, with σ1 oriented south of E-W (see also Weinberg et al., 2003; Morey, 2007), favouring sinistral strike-slip movements (Figures 3.2.10a-f). This D4b stage equates to the 'D3' deformation of Swager (1997). The D4b deformation was characterised by a rather chaotic local stress field. In detailed PT-dihedra analysis (Blewett and Czarnota, in press), the D4b stress field was locally oriented WNW-ESE, through NW-SE, to N-S (Figure 3.2.12). However the overall regional shortening direction during D4b was oriented ESE-WSW (see also Miller, 2006; Henson et al., 2008; Miller et al., 2008).

Qualitative finite strain observations at Leonora and Laverton suggest that the most steeply dipping greenstone panels have the most intense S4 fabrics, reflecting intense D4a flattening and D4b sinistral shear (or both). In the Lawlers area, Beardsmore (2002) described a deformation event with ESE- WNW oriented σ1, post his 'D2' (E-W σ1). These structures were dominantly sinistral strike-slip faults.

The D4 contraction was recognised across all the terranes of the EGST in the granite study (Blewett et al., 2004c). The style of the deformation event is dominated by N-S to NNW-SSE trending sinistral strike-slip shear zones (Figures 3.2.10a, 3.2.10c, 3.2.10e) and both S-over-N and N-over-S thrusts (Figures 3.2.10d, 3.2.10f), which have generally been interpreted as 'D1' structures. The D4 event is expressed as the most intense deformation in the 'internal' granites (which are in general weakly deformed) of the central Kurnalpi Terrane (e.g., Outcamp

*Figure 3.2.10: Upright gently F4a plunging (to the NNW) folds of bedding in the Yunndaga gold mine near Menzies (Figure 3.2.2). These are similar in style to the F2 folds and can be easily confused. F4a folds are the first to appear in the Late Basins (e.g., the Butcher Syncline in the Pig Well basin in Figure 6a).*

Bore, Yarrie and Bernie Bore: Figure 3.2.2). Most of the associated structures are steeply dipping sinistral shear zones. At Yarrie, D4 was the gold event. NW-SE contraction is also the main gold event at Wallaby (Miller, 2006). Elsewhere in the granites, dykes of pegmatite and granite (not Low-Ca type) were intruded into the active shear zones.

The localities with particularly well-developed or intense D4a deformation reported here include Yunndaga, Puzzle, Mertondale, and Jupiter (Figure 3.2.2; Blewett and Czarnota, 2007a). Localities with intense D4b sinistral shear include Matilda, Yunndaga, Isolated Hill, Barrett Well, Two Lids Soak, Jasper Hill, Poison Creek, and Turkey Well (Figure 3.2.2; Blewett and Czarnota, 2007a).

In the Kambalda and Kanowna areas, Swager (1997) described S-over-N thrusts (Foster, Tramways Republican, and Fitzroy) as 'D1'. However, Blewett (2004) re-examined the map patterns and showed the 'D1' thrusts cut 'F2' folds and were therefore younger not older (Figure 3.2.11e). The Eastern Gobi-Alty region of Mongolia (Bayasgalan et al., 1999) is an example of how these NNW-SSE directed thrusts may have operated during D4b sinistral shear (Figure 3.2.11b). Thrusts in this example develop at the terminations of major strike-slip faults, and function as accommodation structures to rotational strain. Thrusts also develop at restraining step-overs, accommodating displacement between parallel strands of a strikes-slip fault system (Figure 3.2.11b). The elegance of this interpretation is that whole-scale rotation of the regional stress (or orogen) is not required; rather the angular change in $\sigma 1$ from D2 shortening to D4 shortening is of the order of 30°.

The magmatism of the EGST at D4 time was in the waning stages of the High-Ca type, especially in the Kalgoorlie Terrane with melts displaying a more crustal signature (low-Y subgroup of Champion and Sheraton, 1997). No volcanic products are preserved as the youngest sediments (Late Basins) which predate this event are non-volcanic. Syenite magmatism (generally absent from the Kalgoorlie Terrane) flourished at this time in the Kurnalpi Terrane. The next great change in the magmatism was the onset of Low-Ca granite crustal melts, which occurred with the next event (D5).

### 3.2.3.8 D5: dextral strike-slip

The D5 event is traditionally called 'D4' in the Swager (1997) nomenclature, and many workers have suggested that it was a progressive event from earlier 'D2' (e.g., Weinberg et al., 2003; and references therein). However, this study has shown that a significant rotation of the stress field occurred between D4b sinistral strike-slip and the D5 dextral strike-slip events. Therefore the transition was not progressive but probably marked a major plate reconfiguration. The interpretation presented here of an earlier stage of sinistral (D4b) and later dextral (D5) shearing is also supported by Mueller et al. (1988).

The main feature of the D5 deformation is the establishment of NE-SW oriented shortening. This event is remarkably consistent and predictable, with both dextral transtensional and transpressional tectonic modes. The local differences in tension/compression were the result of the influence of pre-existing fault strike and the geometry of adjacent granite batholiths and shear zones, with respect to the regional direction of $\sigma 1$ (Figures 3.2.13a-f). For example the narrow N-S striking corridor of greenstone to the north of Laverton was dominated by dextral transpression (Blewett and Czarnota, 2007a), while north-northeast striking structures underwent dextral transtension (and are more endowed in gold mineralisation) in are around Laverton and areas to the south (Miller, 2006; Blewett and Czarnota, 2007a, 2007b)

The establishment of this NE-SW shortening direction required a counter-clockwise rotation of $\sigma 1$ by around 60° between D4 and D5. Plate convergence changes of this magnitude occurred at around 38 Ma in the northern Pacific Ocean (Emperor Sea mount chain and Hawaiian Islands). This significant plate reconfiguration occurred at the same time as the world-class mineralisation in the Great Basin (Carlin etc.) of Western North America (Arehart et al., 2003). In the EGST, this switch from D4 sinistral transpression to dextral strike-slip was marked by a major change in the crust's thermal regime (emplacement of Low-Ca granite magmatism – Figure 3.2.13a).

Along the eastern margin of the Kurnalpi Terrane, dextral shear predominates, especially on the Hootanui Fault System (Blewett and Czarnota, 2007a, 2007b). Further west from the terrane boundary, D5 is partitioned into

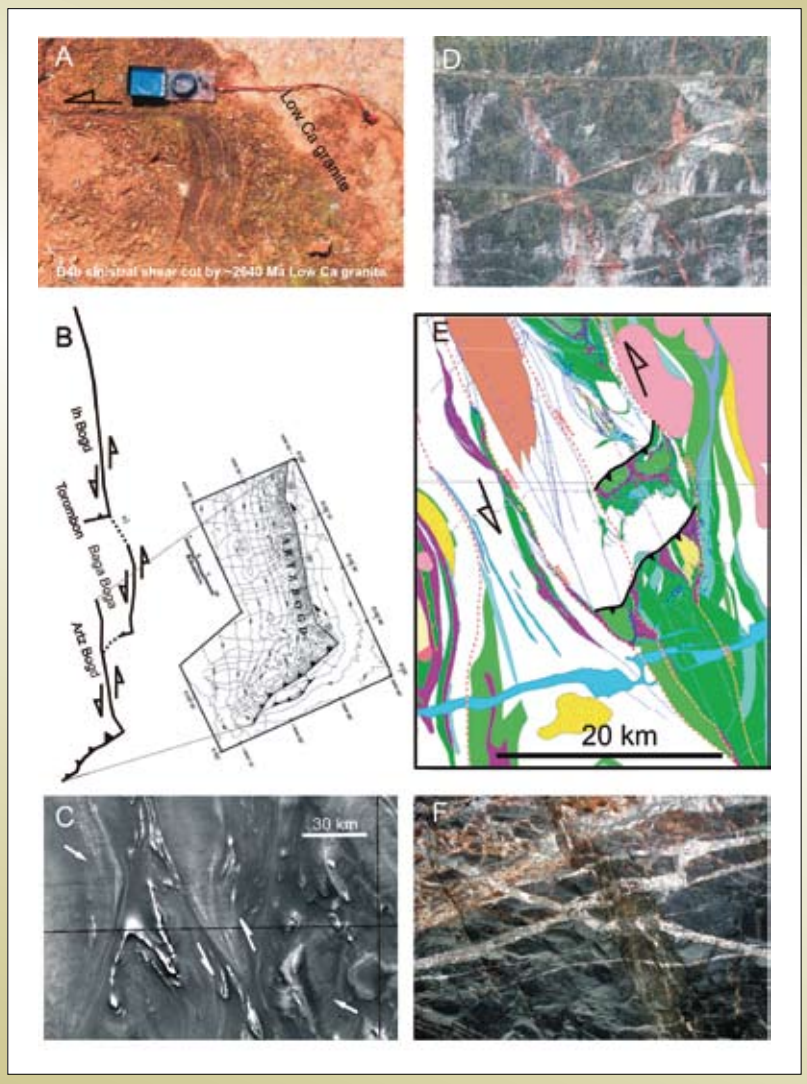


*Figure 3.2.11: a) View east onto a granite pavement with a ductile sinistral strike-slip fault being cut by a Low-Ca granite of around 2640 Ma age; b) Thrust faults developing at a high angle (and acting as transfers) to sinistral strike-slip shear zone from the Altai region of Mongolia (after Bayasgalan et al., 1999); c) Regional aeromagnetic image of the northern Leonora and southern Sir Samuel 1:250 000 sheet areas. The prominent folds and magnetic highs in the west are from Kalgoorlie Sequence ultramafic rocks enveloping the northern end of the Lawlers anticline. Note the prominent sinistral drag of the magnetic fabric (shear arrows) and the likely palaeostress being ESE-WNW oriented; d) Top to the NNW thrusting in the Jupiter gold mine west of Laverton (Figure 3.2.2). These thrusts are overprinting the syenites emplaced during the D3 extension and formation of the (now eroded at this site) Wallaby Late Basin; e) D4 NE-SW trending thrusts (Tramways and Republican) cutting NN- trending D2 folds (cf. Figure 3.2.11b). The faults were previously interpreted as 'D1' thrusts (Swager and Griffin, 1990); f) View to the northeast of mineralised contractional vein arrays developed during ESE-WNW shortening (thrusting) across the Kambalda Anticline. These contractional structures accommodate the sinistral strike-slip faulting on the edges of the anticline (see also Miller et al., 2008).*

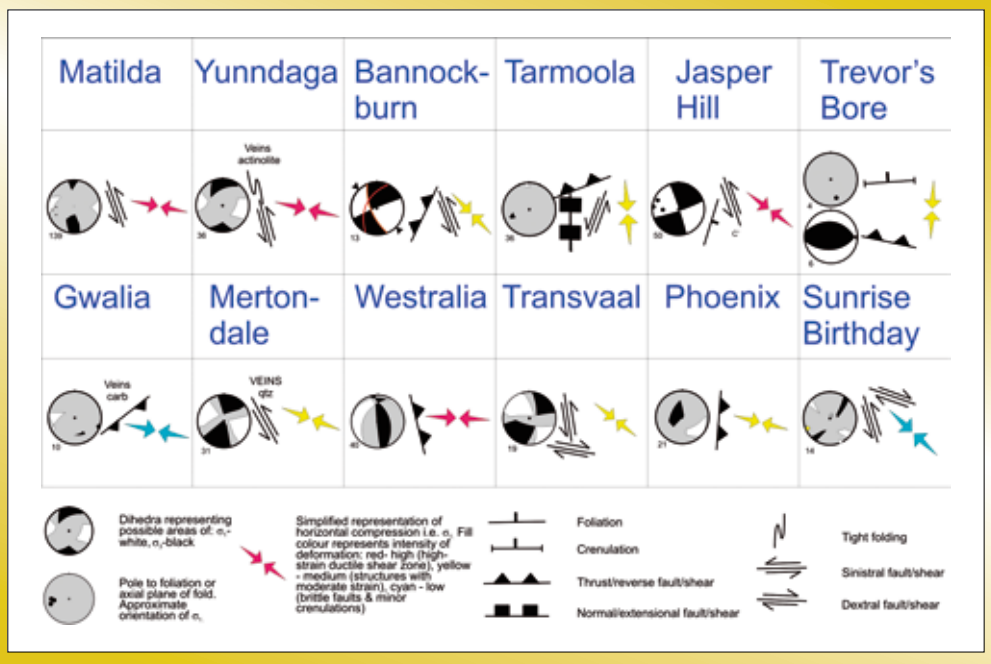


*Figure 3.2.12: P-T dihedra palaeostress constraints on D4b from the EGST (from Blewett and Czarnota, 2007a). Regions of σ1 are coloured white and σ3 are coloured black. The heterogenous palaeostress distribution is associated with the onset of north-northwest striking transpressional shear zones superimposed on a pre-existing D3 anisotropic domal architecture.*

reverse faulting, with a NE-over-SW sense of movement. This thrust reworking of the earlier D2/D3 architecture gives the impression that this late event was responsible for the formation of the architecture. The amount of thrust movement is not known, but many thrusts appear to be relatively small scale and unlikely to cause significant crustal thickening. Most of the P-T dihedra indicate that σ3 was subhorizontal, consistent with a strike-slip tectonic mode (Blewett and Czarnota, 2007a).

In some localities along the eastern margin of the Kurnalpi Terrane the entire history recorded appears to be dextral shear (e.g., King of Creation – Figure 3.2.13e). These areas are localised in north-south striking narrow corridors between large granite batholiths resulting in transpression with a high degree of flattening. In these areas it is likely the D5 event was of sufficient intensity to 'obliterate' the pre-D5 history. The fundamental grain of this D5 dextral event was oriented N-S, similar to D2.

The event is most intensely developed on the western margin of the Kalgoorlie Terrane (Ida-Waroonga Fault System) and the eastern margin of the Kurnalpi Terrane (Hootanui Fault System). The D5 event is weakest along the Ockerburry Fault Zone (except at Trevor's Bore and Victor Well), the terrane boundary between Kalgoorlie and Kurnalpi (Figures 3.2.1, 3.2.2). It is interesting to note that the boundaries with greatest lithological differences (Ida-Waroonga and Hootanui Fault Systems) recorded

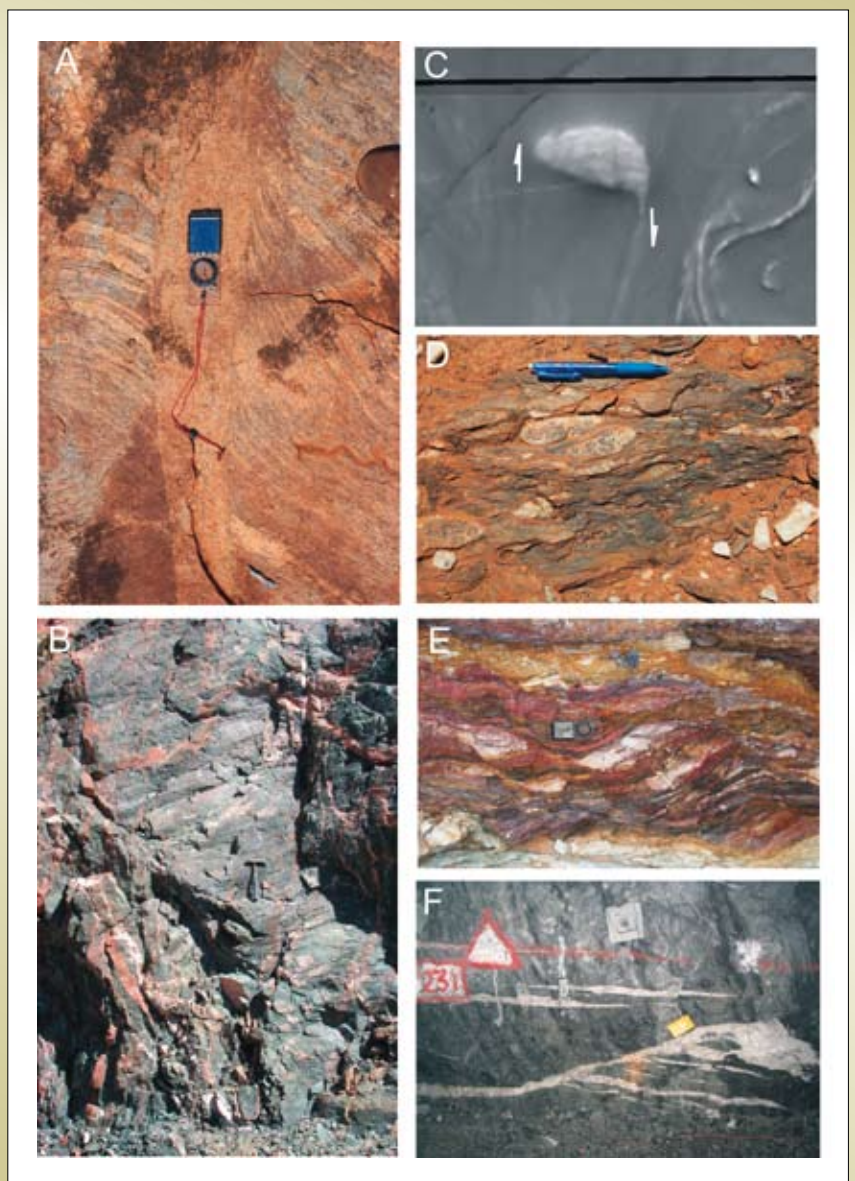


*Figure 3.2.13: Collage of photographs illustrating D5 structures (both brittle and ductile). a) Low-Ca type granite dyke intruded into an active N-S trending dextral shear zone (at Mount Surprise); b) D5 dextral slicken-lines in brittle-ductile faults that overprint D4b thrusts in the Jupiter gold mine west of Laverton; c) Magnetic granite body (not exposed) intruding the Raeside Batholith southwest of Leonora showing dextral drag on the edges of the pluton. Pluton is 3 km east to west; d) View ESE of the Scotty Creek Late Basin (along the western margin of the Kalgoorlie Terrane) with granite clasts that were exhumed and deposited during D3 extension being subjected to intense dextral strike-slip shearing and foliation development; e) View west of the dextral S-C fabrics developed in the King of Creation gold mine (Figure 3.2.2) along the eastern margin of the Kurnalpi Terrane; f) Gold-bearing D5 extension veins developed during NE-SW contraction in the Genesis-New Holland gold mine near Lawlers (Figure 3.2.2).*

the greatest degree of strain indicating this event re-used long-lived zones of crustal weakness.

A significant feature of the D5 event is that Low-Ca granites are either:

- overprinted by D5 structures (e.g., Mars Bore);
- overprint D5 structures (e.g., Ironstone Point); or,
- are emplaced into active D5 structures (e.g., Mt Denis).

These relationships are significant in that the Low-Ca granite type marks a fundamental change in the thermal régime of the crust. These are high-temperature crustal melts and were emplaced over a short period of time (<2655–2630 Ma) relative to the higher-pressure High-Ca granite type (Champion and Sheraton, 1997; Cassidy and Champion, 2004). These granite types therefore provide temporal markers and provide maximum ages for the earlier events (*cf.* Figures 3.2.11a and 3.2.13a). They make up 20% of the exposed area of granites and so are likely to be volumetrically significant. They were intruded into the domes (most are below the greenstone base), so doming and uplift likely continued throughout D5.

Gold mineralisation occurred during the D5 dextral event. Deposits include Sunrise Dam (Miller, 2006), St Ives (Miller et al., 2008), Transvaal (Blewett and Czarnota, 2007a), Wiluna camp (Hagemann et al., 1992), Golden Mile-Charlotte (Keats, 1987), St Ives camp (Nguyen, 1997 Blewett et al., 2008), and Kundana (Mueller et al., 1988). In contrast to the earlier gold-only events (D2-D4), the mineralogy associated with D5 included significant base metals and tellurides (e.g., Clout et al., 1989).

#### 3.2.3.9 D6: Low-strain vertical shortening

The last event of significance is a phase of late low-strain vertical shortening (Swager, 1997; Davis and Maidens, 2003; Weinberg et al., 2003 and Weinberg and Van Der Borg, 2008). The D6 event occurs across the EGST and is represented by the development of crenulations, with sub-horizontal axial planes at a range of amplitudes from millimetres to metres. The fold hinges plunge variably. The structural style is brittle to locally brittle-ductile normal faulting. No specific vector of extension has been defined, and the driver for this extension may have been more readjustment of localised topographic highs from earlier events rather than a regional far-field control.

The D6 event is most intensely developed (Blewett and Czarnota, 2007a) on the western margin of the Kalgoorlie Terrane (Ida-Waroonga Fault System) and the eastern margin of the Kurnalpi Terrane (Hootanui Fault System). The spatial co-incidence in intensity of D5 and subsequent collapse in D6 may be significant and reflect re-adjustment of the crust to the previously partitioned D5 event.

Swager (1997) suggested that D6 collapse was responsible for the present day juxtaposition of the high-grade Youanmi Terrane against the Kalgoorlie Terrane across the Ida-Waroonga Fault System. If the Ida-Waroonga Fault System collapse is related to the D6 event described here, then a timing constraint for D6 being older than the 2640±8 Ma Clarke Well Monzogranite (age from Nelson, 1997) is provided by the apparent stitching relationship of this pluton across the high-strain fabrics associated with the Ida Fault. However, the degree of strain associated with D6 collapse is generally low, and the metamorphic juxtaposition of this magnitude is equated with D3 extension elsewhere in the EGST.

#### 3.2.3.10 D7 and other minor events

At the largest scale, there are numerous E-W oriented low-displacement (1–2 km) sinistral faults that offset the main NNW-oriented structures (D5 and older). These are particularly common in aeromagnetic images, especially in the granite batholiths (Figure 3.2.3a). These are all likely Proterozoic in age and may reflect events at the craton margin (e.g., Albany Fraser and Capricorn), however they are both normal and reverse magnetised and so represent different times of ~N-S extension (Keats, 1987).

In the Victory-Defiance area gypsum-bearing NE-directed thrusts (reverse faults) cut an otherwise undeformed Proterozoic dolerite dyke. Numerous small displacement faults can be mapped in the granite pavements of the external granites (Blewett et al., 2004a). These structures have centimetre displacements are variably oriented. Swager (2007) also described similar structures. These are likely Proterozoic in age, with the Majestic Dyke being dated at around 2400 Ma (Turek, 1966).

### 3.2.4 Timing constraints of deformation

The best dataset available for constraining the ages of the deformation framework is available from the granite

study by Blewett et al. (2004c). This work was based on the geochronological framework established by many workers, but in particular Nelson (1996, 1997), Fletcher et al., (2001), Cassidy et al. (2002), Dunphy et al. (2003), and Lance Black et al. (GA unpublished data).

#### 3.2.4.1 D1 constraints

The D1 period is interpreted as long-lived extension, with the space creation and formation of the rock record itself as best record. A question remains as to whether the extension was episodic or continuous. The Kambalda Komatiite is dated around 2705 Ma (Nelson, 1997), and the Upper Basalt is younger than the Kapai Slate which is dated around 2692±4 Ma (Claoue-Long, et al., 1988). The Kalgoorlie Sequence (Black Flag Formation) has age ranges from 2690 to ca. 2665 Ma (Krapež et al., 2000). The Kalgoorlie Sequence has a number of unconformities, with one at around 2675 Ma. At the same time in the 'external' granites, a major melting and exhumation event occurred. The age of the gneissic fabrics are in the range of: 2672±2 (Two Lids Soak); 2675±2 (Barrett Well); 2670±10 (Ivor Rocks); 2681±4 Ma (Isolated Hill), and 2674±3 Ma (Wilbah) (ages reported in Cassidy, 2006). Such consistent data, across regionally separate sites (similar ages are reported from Duketon: Dave Champion pers comm. 2005), indicate a maximum age for metamorphism and D1 extension of around 2672 Ma.

#### 3.2.4.2 D2 constraints

The first contractional event D2 has a maximum age range constrained by the dates of deformed granites and a minimum age range from cross-cutting granites. In this study the available ages are found in the Burtville and Kurnalpi Terranes. In the Burtville Terrane D2 occurred in the range <2668±4 Ma (Ironstone Point) and inferred to be >2664±2 (Hanns Camp Syenite) based on a relative timing correlation. In the Kurnalpi Terrane D2 occurred at <2667±4 Ma (Pindinnis), >2665±4 Ma (Granny Smith Granodiorite), >2667±5 Ma (Porphyry), >2657±8 Ma (Porphyry), and is inferred to be >2660±5 Ma (Bulla Rocks) based on a relative timing correlation (ages reported in Cassidy, 2006).

#### 3.2.4.3 D3 constraints

D3 is a major lithospheric extensional event associated with the development of Late Basins and the commencement of the emplacement of the Mafic and Syenitic granites (like Granny Smith and Porphyry – see D2 constraints above). The Syenite and Mafic granite types are generally regarded as reflecting regional extension from a metasomatised mantle source region (Champion and Sheraton, 1997). A maximum age for D3 can be inferred from the overprinting extensional fabric on granites such as the 2664±2 Ma Hanns Camp Syenite and 2660±5 Ma Bulla Rocks Monzogranite. If the mineralisation at Sunrise Dam is related to the D3 extension then the overlap in Au mineralisation ages at Sunrise Dam can be used to constrain the timing of D3 to 2658±4 (ages reported by Miller, 2006). The maximum depositional ages of the Late Basins provide constraints on the age of D3 basin formation their initial burial and deformation. Late Basin ages include 2662±5 Ma (Scotty Creek: Dunphy et al., 2003); 2665±5 Ma (Jones Creek: Krapež et al., 2000); 2657±4 Ma (Kurrawang: Fletcher et al., 2001); 2664±6 Ma (Merougil: Krapež et al., 2000); 2666±5 Ma (Mt Belches: Krapež et al., 2000); 2664±4 Ma (Pig Well-Yilgangi: Barley et al., 2002); 2663±5 Ma (Granny Smith: Barley et al., 2002) These ages around 2665–2660 Ma (reported in Cassidy, 2006) are consistent with regional extension post-dating the D2 contraction and final closure of the arc(s).

#### 3.2.4.4 D4 constraints

The age of D4 can only be inferred from cross cutting relationships. It is obviously younger than the 2665–2660 Ma D3 extension. The D4a event is previously known as 'D2' (Swager, 1997) related to the inversion of the Late Basins. A maximum age for D4a is obtained from the youngest phases of the D4a deformed Scotia-Kanowna Batholith and associated porphyries in the Kanowna Belle gold mine. These felsic rocks have U-Pb SHRIMP ages of 2555±6 Ma Ross et al. (2004). The D4b ESE-WNW sinistral transpressional stage occurred prior to any Low-Ca granite type magmatism which is present across all terranes (and the Yilgarn Craton as a whole). The Low-Ca granite type granites were emplaced following a switch in palaeostress to a NE-SW directed $\sigma 1$ (D5).

#### 3.2.4.5 D5 constraints

The Low-Ca granites provide a maximum age for D5 as <2652±5 Ma (Pink Well), <2650±8 Ma (Mount Denis), and <2645±6 Ma (Surprise Rocks). At Mars Bore a dyke of Low-Ca type granite with an age of 2647±3 Ma overprints D5 dextral shear zones and is overprinted by further developed D5 dextral shear zones (demonstrating the syn-tectonic nature of these magmas). A minimum age for D5 (ages reported in Cassidy, 2006) is obtained from Low-Ca granite type dykes that overprint D5 fabric elements of 2638±2 Ma (Ironstone Point). The D5 event likely developed after around 2650 Ma and 2645 Ma in the Kurnalpi and Kalgoorlie Terranes respectively.

#### 3.2.4.6 Post D5 and younger event age constraints

The ages of post-D5 events is poorly constrained. The D6 event is a late phase of vertical shortening and may not have occurred at the same time regionally. 'Young' ages from various isotopic systems of around 2600 Ma may reflect these late events in the final cratonisation of the Yilgarn. Significant ENE-trending Proterozoic mafic dykes transect the Yilgarn Craton, and these are interpreted to be associated with the D7 contraction. Blewett et al. (2004a) described a number of poorly constrained very minor deformation events in the granites. These were interpreted by these authors as Proterozoic and related to distant reworking events on the margins of the craton (e.g., Capricon orogen in NW and Albany Fraser orogen in the SE).

### 3.2.5 Conclusions and implications for predictive gold discovery

Gold is associated with all of the events throughout the geodynamic history of the EGST, however significant gold mineralisation did not occur until the D3 extension event (Czarnota et al., 2008). The genetic link between D3 extension and Late Basin formation provides insight into the empirical observation that large gold deposits occur in proximity to Late Basins (Hall, 2007). This is because Late Basin distribution is associated with crustal penetrating shear zones developed during D3 extension. These shear zones are necessary to tap deep fluids and metals (from the mantle). The emplacement of mantle-derived Mafic and Syenitic granites into the upper crust during D3 extension reflects this deep connection to a metasomatised mantle source region. Furthermore, extension is an efficient mechanism to draw fluids down shear zones to facilitate fluid mixing (Sheldon et al., 2007). Significant gold mineralisation is hosted in high-strain extensional ductile shear zones at Gwalia, Lancefield, and the Lawlers camp. Extensional shear zones occur in other areas of the Yilgarn, so there is significant potential for finding Sons of Gwalia-like ore deposits. The D3 extension is also responsible for setting up the domal architecture of the EGST which is critical for fluid focusing during subsequent events.

The D4 sinistral transpression event was imposed on the highly anisotropic architecture developed largely during D3. This resulted in the creation of numerous depositional sites with significant structural complexity and the development of locally variable and complex stress fields as the anisotropy in the orogen was being 'ironed out'. Gold is associated with brittle-ductile sinistral strike-slip shear zones at deposits such as the Golden Mile, Wallaby and Sunrise Dam, St Ives camp, Kalgoorlie, Kanowna Belle, and Lawlers.

The final gold event was associated with D5 dextral shearing (mostly associated with brittle transtension), with deposits including Sunrise Dam, Transvaal, Wiluna camp, Mt. Charlotte, St Ives camp, and Kundana, being examples. In contrast to the earlier events (D3–4), the mineralogy associated with D5 includes base metals and tellurides and may reflect the influence of basinal fluids (Cleverley et al., 2007).

### 3.2.6 Acknowledgements

The sponsors of the Y1-P763 and ***pmd*CRC*** (Y2 and Y4 projects) are acknowledged for their financial support for these projects. The GSWA are gratefully acknowledged for providing extensive field support for field work over many field seasons.

### 3.2.7 References

Archibald, N.J., Bettenay, L.F., Binns, R.A., Groves, D.I., and Gunthorpe, R.J., 1978, The evolution of Archaean greenstone terrains, Eastern Goldfields Province, Western Australia. Precambrian Research, 6, 103–131.

Arehart, G.B., Chakurian, A.M., Tretbar, D.R., Christensen, J.N., McInnes, B.A. and Donelick, R.A., 2003, Evaluation of Radioisotope Dating of Carlin-Type Deposits in the Great Basin, Western North America, and Implications for Deposit Genesis. Economic Geology, 98, 2003, 235–248.

Barley, M.E., Brown, S.J.A., Krapež, B., and Cas, R.A.F., 2002, Tectonostratigraphic Analysis of the Eastern Yilgarn Craton: an improved geological framework for exploration in Archaean Terranes. AMIRA Project P437A, Final Report.

Bayasgalan, A., Jackson, J., Ritz, J.F., and Carretier, S., 1999, Field examples of strike-slip fault terminations in Mongolia and their tectonic significance, Tectonics, 18, 394–411.

Beakhouse, G.P., 2007, Structurally Controlled, Magmatic Hydrothermal Model for Archaean Lode Gold Deposits: A Working Hypothesis. Ontario Geological Survey Open File Report 6193, 133 p.

Beardsmore, T.J. 2002, The geology, tectonic evolution and gold mineralisation of the Lawlers region: a synopsis of present knowledge. Barrick Gold of Australia, Technical Report 1026, 279 p.

Binns, R.A., Gunthorpe, R.J., and Groves, D.I., 1976, Metamorphic patterns and development of greenstone belts in eastern Yilgarn Block, Western Australia. John Wiley & Sons, New York, USA, 303–313.

Blewett, R.S., 2006, An assessment of the utility of the new 3D data versus the 2D data at a regional scale: geodynamic insights. In R.S. Blewett and A.P. Hitchman (eds) 3D Geological Models of the Eastern Yilgarn Craton – Y2 Final Report ***pmd*CRC***. Geoscience Australia Record 2006/04, 139–159 [DVD-ROM].

Blewett, R.S., Champion, D.C., Whitaker, A.J., Bell, B., Nicoll, M., Goleby, B.R., Cassidy, K.F., and Groenewald, P.B., 2002a, A new 3D model of the Leonora-Laverton transect: implications for the tectonic evolution of the eastern Yilgarn Craton. Australian Institute of Geoscientists Bulletin, 36, 18–21.

Blewett, R.S., Champion, D.C., Whitaker, A.J., Bell, B., Nicoll, M., Goleby, B.R., Cassidy, K.F., and Groenewald, P.B., 2002b, Three dimensional (3D) model of the Leonora-Laverton transect area: implications for Eastern Goldfields tectonics and mineralisation. In Cassidy, K.F., (Ed), Geology, geochronology and geophysics of the north eastern Yilgarn Craton, with an emphasis on the Leonora-Laverton transect area. Geoscience Australia Record, 2002/18, 83–100.

Blewett, R.S., Cassidy, K.F., Champion, D.C., Henson, P.A., Goleby B.R., and Kalinowski, A.A., 2004a, An orogenic surge model for the eastern Yilgarn Craton: implications for gold mineralising systems. In Muhling, J., et al., (Eds), SEG 2004, Predictive Mineral Discovery Under Cover. Centre for Global Metallogeny, The University of Western Australia, Publication 33, 321–324.

Blewett, R.S., Cassidy, K.F., Champion, D.C., Henson, P.A., Goleby, B.R., Jones, L., and Groenewald, P.B., 2004b, The Wangkathaa Orogeny: an example of episodic regional 'D2' in the late Archaean Eastern Goldfields Province, Western Australia. Precambrian Research, 130, 139–159.

Blewett, R.S., Cassidy, K.F., Champion, D.C., and Whitaker, A.J. 2004c, The characterisation of granite deformation events in time across the Eastern Goldfields Province, Western Australia. Geoscience Australia Record 2004/10 [CDROM].

Blewett, R.S. and Czarnota, K., 2007a. The Y1-P763 project final report November 2005. Module 3 – Terrane Structure: Tectonostratigraphic architecture and uplift history of the Eastern Yilgarn Craton, Geoscience Australia Record 2007/15.

Blewett, R.S. and Czarnota, K., 2007b, A new integrated tectonic framework of the Eastern Goldfields Superterrane. In: Bierlein, F.P., and Knox-Robinson, C.M., (eds), Proceedings of Geoconferences (WA) Inc. Kalgoorlie '07 Conference. Geoscience Australia Record 2007/14, 27–32.

Cassidy, K.F., 2006, Geological Evolution of the Eastern Yilgarn Craton (EYC), and terrane, domain and fault nomenclature. In: R.S. Blewett and A.P. Hitchman (eds) 3D Geological Models of the Eastern Yilgarn Craton – Y2 Final Report ***pmd*CRC***. Geoscience Australia Record 2006/04, 1–19. [DVD-ROM]

Cassidy, K.F., and Champion D.C., 2004, Crustal evolution of the Yilgarn Craton from Nd isotopes and granite geochronology: implications for metallogeny. In Muhling, J., et al., (Eds), SEG 2004, Predictive Mineral Discovery Under Cover. Centre for Global Metallogeny, The University of Western Australia, Publication 33, 317–320.

Cassidy, K. F., Champion, D. C., Fletcher, I. R., Dunphy, J. M., Black, L. P., and Claoue-Long, J. C., 2002, Geochronological constraints on the Leonora-Laverton transect area, north-eastern Yilgarn Craton. Geoscience Australia Record 2002/18, 37–58 pp.

Cassidy, K. F., Champion, D. C., Krapež, B., Barley, M. E., Brown, S. J. A., Blewett, R. S., Groenewald, P. B., and Tyler, I. M., 2006, A revised geological framework for the Yilgarn Craton, Western Australia: Western Australia Geological Survey, Record 2006/8, 8p.

Champion, D.C., and Cassidy, K.F., 2002, Granites in the Leonora-Laverton transect area, north eastern Yilgarn Craton: In Cassidy, K.F., (Ed), Geology, geochronology and geophysics of the north eastern Yilgarn Craton, with an emphasis on the Leonora-Laverton transect area. Geoscience Australia, Record 2002/18, 13–35.

Champion, D.C., and Sheraton, J.W., 1997, Geochemistry and Nd isotope systematics of Archaean granites of the Eastern Goldfields, Yilgarn Craton, Australia; implications for crustal growth processes. Precambrian Research, 83, 109–132.

Chen, S. F., Witt, W., and Liu, S. F., 2001, Transpressional and restraining jogs in the northeastern Yilgarn Craton, Western Australia. Precambrian Research 106, 309–328.

Claoué-Long, J.C., Compston, W., and Cowden, A., 1988, The age of the Kambalda greenstones resolved by ion microprobe – implications for Archaean dating methods. Earth and Planetary Science Letters, 89, 239–259.

Cleverley, J.S., Walshe, J.L., and Nugus, M., 2007, Tracing deep fluid sources in gold deposits of the Eastern Goldfields. In: in Bierlein, F.P., and Knox-Robinson, C.M., (eds), 2007. Proceedings of Geoconferences (WA) Inc. Kalgoorlie '07 Conference. Geoscience Australia Record 2007/14, p133–137.

Clout, J. M. F., 1989, Structural and isotopic studies of the Golden Mile gold-telluride deposit, Kalgoorlie, Western Australia: Unpub. Ph.D. thesis, Monash University, 352 p.

Collins, W.J., 2002, Nature of extensional accretionary orogens. Tectonics, 21, 1024.

Connors, K., Donaldson, J., Morrison, B., Davy, C., and Neumayr, P., 2003, The Stratigraphy of the Kambalda-St Ives District: workshop notes Goldfields Pty Ltd St Ives operation, unpublished Technical note No: TN SIG0329, 99 p.

Czarnota, K. and Blewett, R.S., 2007, Don't hang it on a foliation to unravel a structural event sequence: an example from the Eastern Goldfields Superterrane. Specialist Group: Tectonics and Structural Geology, Geological Society of Australia Abstracts, Deformation I the Desert, Alice Springs, 9–13 July 2007, 75.

Davis, B.K., and Maidens, E., 2003. Archaean orogen-parallel extension; evidence from the northern Eastern Goldfields Province, Yilgarn Craton, Precambrian Research, 127, 229–248.

Drummond, B.J., Goleby, B. R., and Swager, C.P., 2000, Crustal signature of Late Archaean tectonic episodes in the Yilgarn craton, Western Australia: evidence from deep seismic sounding. Tectonophysics, 329, 193–221.

Dunphy, J.M., Fletcher, I.R., Cassidy, K.F., and Champion, D.C., 2003, Compilation of SHRIMP U-Pb geochronological data, Yilgarn Craton, Western Australia, 2001–2002. Geoscience Australia Record 2003/15, 139p.

Fletcher, I.R., Dunphy, J.M., Cassidy, K.F., and Champion, D.C., 2001, Compilation of SHRIMP U-Pb geochronological data, Yilgarn Craton, Western Australia, 2000–2001. Geoscience Australia, Record 2001/47, 111p.

Gee, R.D., 1979, Structure and tectonic style of the Western Australian Shield, Tectonophysics 58, 327–369.

Goleby, B.R., Rattenbury, M.S., Swager, C.P., Drummond, B.J., Williams, P.R., Sheraton, J.E., and Heinrich, C.A., 1993, Archaean crustal structure from seismic reflection profiling, Eastern Goldfields, Western Australia, AGSO Record, 1993/15, 54 pp.

Goleby, B., Blewett, R.S., Champion, D.C., Korsch, R.J., Bell, B., Groenewald, P.B., Jones, L.E.A., Whitaker, A.J., Cassidy, K.F., and Carlsen, G.M., 2002, Deep seismic profiling in the NE Yilgarn: insights into its crustal architecture: Australian Institute of Geoscientists Bulletin 36, 63–66.

Goleby, B.R., Blewett, R.S., Groenewald, P.B., Cassidy, K.F., Champion, D.C., Korsch, R.J., Whitaker, A., Jones, L.E.A., Bell, B., and Carlson, G., 2003, Seismic interpretation of the northeastern Yilgarn Craton seismic data. In Goleby, B.R., Blewett, R.S., Groenewald, P.B., Cassidy, K.F., Champion, D.C., Jones, L.E.A., Korsch, R.J., Shevchenko, S., and Apak, S.N., (Eds), The 2001 Northeastern Yilgarn Deep Seismic Reflection Survey. Geoscience Australia, Record 2003/28, 143p.

Goscombe, B., Blewett, R.S, Czarnota, K., Maas, R., and Groenewald, B.A., 2007, Broad thermo-barometric evolution of the Eastern Goldfields Superterrane. In: in Bierlein, F.P., and Knox-Robinson, C.M., (eds), 2007. Proceedings of Geoconferences (WA) Inc. Kalgoorlie '07 Conference. Geoscience Australia Record 2007/14, p33–38.

Gower, C.F., 1976, Laverton, Western Australia, 1:250 000 Geological series – Explanatory Notes. Australian Government Publishing Service, Canberra, 30p.

Hall, G., 2007, Exploration success in the Yilgarn Craton insights from the Placer Dome experience the need for integrated research, In Bierlien, F. et al., (eds) Kalgoorlie 2007, Geoscience Australia Record 2007. in press.

Hagemann, S.G., Groves, D.I., Ridley, J.R. and Verncombe, J.R., 1992, The Archean lode-gold deposits at Wiluna, Western Australia: High level brittle-style mineralisation in a strike-slip regime. Economic Geology, 87, 1022–1053.

Hammond, R.L., and Nisbet, B.W., 1992, Towards a structural and tectonic framework for the Norseman-Wiluna Greenstone Belt, Western Australia. In Glover, J.E., and Ho, S.E., (Eds), The Archaean – Terrains, Processes and Metallogeny. Geology Department and University Extension, The University of Western Australia, Publication 22, 39–50.

Hammond, R.L., and Nisbet, B.W., 1993, Archaean crustal processes as indicated by the structural geology, Eastern Goldfields Province of Western Australia. In, P.R. Williams and J.A. Haldane (Eds.), Kalgoorlie 93 – an international conference on crustal evolution, metallogeny, and exploration of the Eastern Goldfields. Australian Geological Survey Organisation Record 1993/54, pp. 105–114.

Harris, L.B., Koyi, H.A., and Fossen, H., 2002, Mechanisms for folding of high-grade rocks in extensional tectonic settings. Earth-Science Reviews, 59, 163–210.

Henson, P.A., Blewett, R.S., Champion, D.C., Goleby, B.R. and Cassidy, K.F., 2004a, Using 3D 'map patterns' to elucidate the tectonic history of the Eastern Yilgarn. In Barnicoat, A.C., and Korsch, R.J., (Eds), Predictive Mineral Discovery Cooperative Research Centre: Extended Abstracts from the June 2004 Conference. Geoscience Australia, Record 2004/9, 87–90.

Henson, P.A., Blewett, R.S., Champion, D.C., Goleby, B.R., and Cassidy, K.F., 2004b, A dynamic view of orogenesis and the development of the Eastern Yilgarn. In: Barnicoat, A.J., and Korsch, R.J., (Eds) Predictive Mineral Discovery Cooperative Research Centre Extended Abstracts from April 2004 conference, Geoscience Australia Record 2004/9, 91–94.

Henson, P.A. and Blewett, R.S. 2006, 3D interpretation of the Eastern Yilgarn: new architectural insights from construction of the 3D map. In R.S. Blewett and A.P. Hitchman (eds) 3D Geological Models of the Eastern Yilgarn Craton – Y2 Final Report ***pmd*CRC***. Geoscience Australia Record 2006/04, 207–216. [DVD-ROM]

Henson, P.A., Blewett, R.S., Champion, D.C., Goleby, B.R., and Czarnota, K., 2007, How does the 3D architecture of the Yilgarn Control Hydrothermal Fluid Focussing? In: Bierlein, F.P., and Knox-Robinson, C.M., (eds), Proceedings of Geoconferences (WA) Inc. Kalgoorlie '07 Conference. Geoscience Australia Record 2007/14, 56–61.

Henson, P.A., Blewett, R.S., Miller, J. McL., Roy, I.G., Czarnota, K., Zhang, Y. and Schaubs, P.M., 2008, The 4D architecture of the Laverton camp, Eastern Yilgarn Craton. This volume.

Keats, W., 1987, Regional geology of the Kalgoorlie-Boulder gold-mining district. eastern Australia Geological Survey, Record 1987/21, 44p.

Krapež, B., Brown, S.J.A., Hand, J., Barley, M.E., and Cas, R.A.F., 2000, Age constraints on recycled crustal and supracrustal sources of Archaean metasedimentary sequences, Eastern Goldfields Province, Western Australia: Evidence from SHRIMP zircon dating. Tectonophysics, 322, 89–133.

Liu, S., and Chen, S., 1998, Structural framework of the northeastern Yilgarn Craton and implications for hydrothermal gold mineralisation. Australian Geological Survey Organisation Research Newsletter, 29, 21–23.

McIntyre, J.R., and Martyn, J.E., 2005, Early extension in the Late Archaean northeastern Eastern Goldfields Province, Yilgarn Craton, Western Australia, Australian Journal of Earth Sciences, 52, 975–992.

Miller, J.M., 2006, Linking structure and mineralisation in Laverton, with specific reference to Sunrise Dam and Wallaby. In: A.C. Barnicoat, and R.J. Korsch (eds). Predictive Mineral Discovery CRC- Extended Abstracts for the April 2006 Conference. Geoscience Australia Record 2006/7, 62–67.

Miller, J.M., Tunjic, J., Donaldson, J., and Blewett, R.S., 2008, Structural evolution of the Victory to Kambalda region of the St Ives gold camp: the role of early formed structures on the development of a major gold system. Part III, this volume.

Morey, A., 2007, Controls on gold endowment within the Bardoc Tectonic Zone, Eastern Goldfields Province, Western Australia, PhD thesis Monash University (unpub).

Mueller, A.G., Harris, L.B., and Lungan, A., 1988, Structural control on of greenstone-hosted gold mineralisation by transcurrent shearing: A new interpretation of the Kalgoorlie mining district, Western Australia. Ore Geology Reviews, 3, 359–387.

Myers, J.S., 1997, Preface; Archaean geology of the Eastern Goldfields of Western Australia; regional overview. Precambrian Research, 83, 1–10.

Nelson, D.R., 1996, Compilation of SHRIMP U-Pb zircon geochronology data, 1995. Western Australia Geological Survey, Record 1996/5, 168p.

Nelson, D.R., 1997, Compilation of SHRIMP U-Pb zircon geochronology data, 1996. Geological Survey of Western Australia Record 1997/2, 189 pp.

Nguyen, T.P., 1997, Structural controls on gold mineralisation at the Revenge Mine and its tectonic setting in the Lake Lefroy area, Kambalda, Western Australia, PhD thesis (unpublished), 205p.

Passchier, C.W., 1994, Structural geology across a proposed Archaean terrane boundary in the eastern Yilgarn craton, Western Australia. Precambrian Research 68, 43–64.

Platt, J.P., Allchurch, P.D., and Rutland, R.W.R., 1978, Archaean tectonics in the Agnew supracrustal belt, Western Australia. Precambrian Research 7; 3–30. 1978.

Rodgers, J., 1995, Lines of basement uplifts with external parts of orogenic belts, American Journal of Science 295, 455–487.

Ross, A.A., Barley, M.E., Brown, S.J.A., McNaughton, N.J., Ridley, J.R., and Fletcher, I.R., 2004, Young porphyries, old zircons; new constraints on the timing of deformation and gold mineralisation in the Eastern Goldfields from SHRIMP U-Pb zircon dating at the Kanowna Belle gold mine, Western Australia. Precambrian Research. 128, 105–142.

Sheldon, H.A., Barnicoat, A.C., Zhang Y., and Ord, A., 2007, Metamorphism in the Eastern Yilgarn Craton: implications for fluid flow and mineralisation. In: Bierlein, F.P., and Knox-Robinson, C.M., (eds), Proceedings of Geoconferences (WA) Inc. Kalgoorlie '07 Conference. Geoscience Australia Record 2007/14, 138–142.

SRK Consulting, 2000, Global Archaean Synthesis – Yilgarn module. Unpublished consultants report, 88 p.

Smithies, R.H., and Champion, D.C., 1999, Geochemistry of felsic igneous alkaline rocks in the Eastern Goldfields, Yilgarn Craton, Western Australia: a result of lower crustal delamination? – implications for Late Archaean tectonic evolution. Journal of the Geological Society of London, 156, 561–576.

Stewart, A.J., 1998, Recognition, structural significance, and prospectivity of early F1 folds in the Minerie 1:100,000 sheet area, Eastern Goldfields, Western Australia: Australian Geological Survey Organisation Research Newsletter 29, 4–6.

Swager, C.P. 1989, Structure of the Kalgoorlie greenstones regional deformation history and implications for the structural setting of gold deposits within the Golden Mile. Western Australia Geological Survey Report 25, 59–84.

Swager C.P., 1997, Tectono-stratigraphy of late Archaean greenstone terranes in the southern Eastern Goldfields, Western Australia, Precambrian Research, 83, 11–42.

Swager, C.P., and Griffin, T.J., 1990, An early thrust duplex in the Kalgoorlie-Kambalda greenstone belt, Eastern Goldfields Province, Western Australia. Precambrian Research, 48, 63–73.

Swager, C.P., and Nelson, D.R., 1997, Extensional emplacement of a high-grade granite gneiss complex into low-grade granite greenstones, Eastern Goldfields, Western Australia. Precambrian Research, 83, 203–209.

Swager, C.P., Witt, W.K., Griffin, T.J., Ahmat, A.L., Hunter, W.M., McGoldrick, P.J., and Wyche, S., 1992, Late Archaean granite-greenstones of the Kalgoorlie Terrane, Yilgarn Craton, Western Australia, In Glover, J.E., and Ho, S.E., (Eds), The Archaean – Terrains, Processes and Metallogeny. Geology Department and Extension Service, University of Western Australia Publication 22, 107–122.

Turek, A, 1966, Rubidium-strontium isotopic studies in the Kalgoorlie – Norseman area, Western Australia, Unpublished PhD thesis, Australian National University, Canberra, A.C.T., 202p.

Vearncombe, J.R., 1998, Shear zones, fault networks, and Archaean gold. Geology 26, 855–858.

Weinberg, R.F., Moresi, L., and van der Borgh, P., 2003, Timing of deformation in the Norseman-Wiluna Belt, Yilgarn Craton, Western Australia. Precambrian Research, 120, 219–239.

Weinberg, R.F., and van der Borgh, P., 2008, Extension and gold mineralization in the Archean Kalgoorlie Terrane, Yilgarn Craton. Precambrian Research, 161, 77–88.

Williams, P.R., 1993, A new hypothesis for the evolution of the Eastern Goldfields Province. In Williams, P.R., and Haldane, J.A., (Eds), Kalgoorlie '93 – An International Conference on Crustal Evolution, Metallogeny, and Exploration of the Eastern Goldfields. Australian Geological Survey Organisation, Record 1993/54, 73–83.

Williams, P.R.; Currie, K.L., 1993, Character and regional implications of the sheared Archaean granite–greenstone contact near Leonora, Western Australia, Precambrian Research, 62, 343–365.

Williams P.R., Nisbet B.W. and Etheridge M.A. 1989, Shear zones, gold mineralization and structural history in the Leonora district, Eastern Goldfields Province, Western Australia. Australian Journal of Earth Sciences 36, 383–403.

Williams, P.R., and Whitaker, A.J., 1993. Gneiss domes and extensional deformation in the highly mineralised Archaean Eastern Goldfields Province, Western Australia, Ore Geology Reviews, 8, 141–162.

Wyche, S., and Farrell, T. 2000. Regional geological setting of the Yandal greenstone belt, northeast Yilgarn Craton. In: Yandal Greenstone Belt, N. Phillips, and R. Anand (eds.). Australian Institute of Geoscientists Bulletin, 32, 41–54.

## 3.3 Question 2: Big systems-big signatures – anatomy of the Archaean Yilgarn Craton and implications for world-class gold mineral systems

**R.S. Blewett[1], K.F. Cassidy[1,2], P.A. Henson[1], I. G. Roy[1], D.C. Champion[1], and T. Fomin[1]**

[1] ***pmd*CRC***, Geoscience Australia, GPO Box 378, Canberra, ACT, 2601, Australia

[2] Rubicon Resources, West Perth, WA, 6005, Australia

### Abstract

Knowledge of the crustal architecture of the Yilgarn Craton has increased greatly over the last decade through the collection of a wide range of geophysical and geochemical/isotopic data sets. This range in data varies greatly in scale from:

- lithospheric-scale studies that provide information on the entire craton down to depths in excess of 350 km, through;
- regional-scale studies that provide information at the province scale and down to depths of 30–40 km, to;
- mine- and camp-scale studies providing information on the local-scale down to the top few kilometres of the crust.

Lithospheric-scale datasets including receiver function and broadband teleseismic data map significant variations in crustal and upper mantle velocities across the Yilgarn Craton. The results provide information on potential velocity differences between the mineralised Kalgoorlie Terrane and the less mineralized Youanmi Terrane. An anomalous high velocity body (>4.8 km/s shear wave) occurs at around 100–120 km depth, and has steps and edges that correspond with mantle-derived magmas and the main gold camps. The fast velocity layer may represent mantle alteration, delaminated eclogite layer, or fossil oceanic slab.

Maps of crustal age across the craton have been derived from ~250 analyses of felsic rocks of all ages. The Nd depleted-mantle model age maps show that the source regions for the felsic rocks were initially separated from the mantle at a range of ages from 3.6–2.7 Ga. Most model ages are significantly older than the corresponding crystallisation age (200–300 My) of individual samples indicating that the crust was extensively recycled. The major changes in crustal age map the different terranes of the Yilgarn Craton and are leading to first order prospectivity for gold, nickel and base metals.

Deep crustal seismic reflection studies in the eastern part of the craton provide information on the two-dimensional crustal architecture, These seismic studies have imaged numerous shear zones and are critical in defining the gross three-dimensional architecture of the crust, which in turn, provides information on the region's mineral systems.

Magnetotelluric (MT) studies map the main boundaries of the Kalgoorlie Terrane. The data reveal that the prospective Kalgoorlie Terrane is unique in MT character, being characterised by a highly conductive (graphite-bearing?) upper crust (along strike from the Super Pit) and a dome or 'upwelling' of conductive mantle beneath.

Together these data provide first-order insights into the physical and chemical properties of the Yilgarn Craton. These insights provide geodynamic clues and constraints as to why the Yilgarn is so well endowed in metals such as gold and nickel. A convergence of many favourable architectural features occurs in the Kalgoorlie region, possibly explaining why this area is so well-endowed in comparison to others.

**Key words:** *Archaean, tomography, seismic, isotopic ages, magnetotelluric, receiver function, 3D model, mineral system, Yilgarn Craton*

### 3.3.1 Introduction

Our knowledge of the lithospheric (crustal and upper mantle) architecture of the Archaean Yilgarn Craton has increased greatly over the last few years through the collection of a wide range of geophysical and geochemical/isotopic datasets. The Yilgarn Craton is one of the world's most metal endowed geological entities, is currently a major producer for gold, nickel and aluminium, and is also host to significant resources of tin-tantalum-lithium, vanadium, uranium, rare-earth elements, zinc-copper, and iron ore.

Mineral deposits, such as the world-class gold mines at Kalgoorlie and nickel deposits at Kambalda, are the consequence of large geological systems that operate at a range of scales (from global and deep mantle to microscopic). One way to consider a mineral deposit is

to work towards understanding the entire system. The system should be viewed in terms of (1) geodynamics, (2) architecture, (3) fluid sources & reservoirs, (4) fluid pathways & drivers, and (5) depositional mechanisms (Barnicoat et al., 2007). Knowledge of the components of the system will provide constraints on, and enhance predictive models for discovery of additional mineral deposits within the region.

This paper describes the large-scale architecture of the Eastern Goldfields Superterrane (EGST; Cassidy et al., 2006) in the context of the Yilgarn Craton. Some attempt to interpret the geological significance of the various (geophysical and geochemical-isotopic) data is made in this contribution, with implications for geodynamic models and evolution of the Craton argued in a companion paper by Czarnota and others (2008 this volume).

The high-quality datasets available for analysis and described here include: broadband seismographic studies (mantle tomography and crustal receiver functions), long-wavelength potential fields and their derivatives, deep-crustal and shallow high-resolution seismic reflection profiling, wide-angle reflection, magnetotelluric data (MT), and geochemistry and isotopic dating. Not all areas of the Yilgarn Craton are equally metal endowed, and there are strong provincial and sub-provincial differences in prospectivity. The wide array of datasets described above permit better understanding these differences and provide tools to explore for the most endowed parts in the Yilgarn Craton (and elsewhere).

Taken alone, these datasets are commonly ambiguous and non-unique, and difficult to interpret in terms of the geological implications of a particular signal or signature. However, when integrated together the various uncertainties inherent in the individual datasets and techniques are diminished. The integration of these datasets has also provided new insights into the architecture of this remarkable piece of lithosphere, and reveals how these tools work best in identifying favourable tracts for predictive mineral discovery.

### 3.3.2 West Australian lithosphere

Archaean cratons are thought to be underlain by a thick, cold and stable sub-continental mantle root that has remained coupled to the crust (Jordan, 1978; Griffin et al., 1998). Jordan (1978, 1988) suggested that the density increase due to the cooling of the root was balanced by a corresponding chemical depletion in mafic components with respect to the average mantle.

Seismic tomography uses energy received from distant earthquake sources at a range of azimuths to build a velocity image of the volume of the earth through which the seismic waves have travelled. An earthquake releases different forms of seismic energy which travel through the earth. These forms of energy include P-waves (compression), S-waves (shear) and surface waves, with the latter occurring in several forms. These waves may travel directly to the receiver or may follow a path that has included reflection from one or more sub-surface structural features. The seismic tomographic technique uses P-wave, S-wave and surface waves from distant earthquakes recorded across the Yilgarn Craton with a series of long-period broad-band receivers, to provide a unique view of the lithosphere.

National studies such as SKIPPY (van der Hilst et al., 1994) reveal that the Yilgarn Craton, together with the Pilbara Craton to the north, make up a fundamentally different 'old' lithosphere compared to central Australia (Simmons et al., 2002; Fishwick et al., 2005). In western Australia, the lithosphere is characterised by a fast seismic velocity, depleted refractory mantle that is likely cold, dry and strong and is therefore less dense and buoyant. This character is in contrast to younger (Palaeozoic) eastern Australia, which has slow seismic velocities, has a relatively undepleted and fertile mantle that is, warm, wet and weak, and is therefore relatively dense and less buoyant.

Van Gerven et al. (2004) used the original 'Skippy' tomography data to characterise and compare the likely compositional variations in the upper mantle over the Archaean (western Australia), Proterozoic (northern Australia), and Phanerozoic (eastern Australia). They computed the ratio of relative changes in density and shear-wave velocity ($\zeta$) for each main block. The results for western Australia were equivocal (due to poor tomographic resolution and seismic smearing) and the $\zeta$ ratio was negative to over 200 km depth (Figure 3.3.1). Extrapolating the better results from central Australia, they suggested that a chemical depletion zone occurred between 90 and 140 km depth, supporting a tectosphere model for the Australian continental roots (van Gerven et al., 2004).

An overall negative value for ζ indicates that density is less than a corresponding shear-wave velocity; the result will be a buoyant and strong lithosphere. Buoyancy is a feature of the Yilgarn Craton and one of the reasons for its preservation despite many reworking events at the margins.

Simmons et al. (2002) estimated the lithosphere to be around 200 km thick in southwest Western Australia. Below this depth the relationship between the surface patterns and seismic anisotropy (SKS splits) is lost, suggesting a boundary with a different mantle layer below this (the asthenosphere). However, the data quality for the region was not as high as central and eastern Australia.

### 3.3.3 Yilgarn lithospheric architecture

An infill study on the initial SKIPPY work has significantly added to the imaging and resolution of the deep lithospheric features (to 350 km) from the southwest part of Australia (Fishwick et al., 2005; Goleby et al., 2006; Reading et al., 2003, 2007). Details of the operational-acquisition parameters may be found in Goleby et al. (2006).

These workers noted that despite the various approaches to processing surface wave tomography, all tend to yield similar results on a large scale; however the small-scale features of the models differ (Fishwick et al., 2005). The new data from the WACRATON study significantly improved the resolving power and permits an investigation of the relationship between mantle structure and surface geology (Fishwick et al., 2005).

The initial stage of the tomographic inversion of the surface wave data is to extract a 1D model characterising a specific great circle path from source to receiver. This is achieved with a multiple starting model approach (variations from the PREM: Preliminary Reference Earth Model) resulting in multiple inversions that provide a reliability estimate of the wave-speed profile with depth, this information is used in weighting the information from each path within the tomographic inversion (Fishwick et al., 2005).

In creating the tomographic inversion, the best 1D model representing a path-average for each source–receiver pair is used to derive a 3D velocity model. Because there are large velocity variations beneath the cratonic regions, a preliminary broad-scale model is used to obtain the large-scale structure in the region. The resulting model is then used as the reference model for the final detailed (two second) inversion.

Fishwick et al. (2005) conducted sensitivity tests on the resolution of the model to synthetic anomalies (checkerboard study). These tests illustrated that at increasing depths only large-scale anomalies are likely to be reliable. The technique as applied to the Yilgarn Craton is generally more reliable in a horizontal plane (map) than a

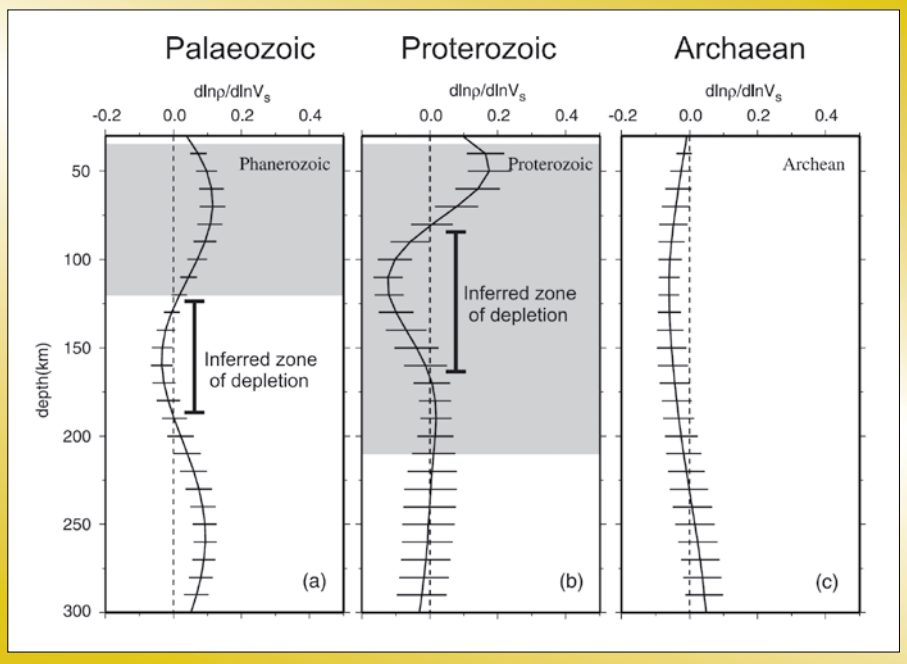


*Figure 3.3.1: Model of density-velocity ratio (ζ) for the three age-regions of Australia (a) Phanerozoic; (b) Proterozoic; and (c) Archaean. The solid curves represent the average value of ζ at a given depth, and the error bars depict one standard deviation around this average. The shaded areas denote the LAB inferred from surface wave tomography. Note the overall negative value of ζ for the Archaean. Negative values in the other two age-regions correspond to depletion zones (i.e., buoyancy).*

vertical plane (depth). This means that considering anomaly boundaries and its relationship to features vertically above or below is relatively reliable, but the depth position of such features is poorly constrained.

### 3.3.3.1 Tomographic features of the Yilgarn Craton

Initial indications support the earlier observations (e.g., Reading et al., 2003) that the Yilgarn Craton has a low velocity crust that is underlain by mantle with a shear wave velocity faster than the world average. The teleseismic S-wave speed volume has been generated to a depth of 350 km for the entire craton (Figure 3.3.2). One of the striking features of this volume is the presence of a high-velocity (>4.8 km/s) body that dips gently to the southeast, from a depth of around 70 km beneath the Murchison Province, increasing to approximately 100 km beneath the Ida Fault, then to approximately 120 km further east (Figure 3.3.2). The precise thickness of the high-velocity layer is difficult to ascertain, but it is interpreted to be around 20-25 km thick. Details of the velocity layering through the lithosphere are presented as a sequential series of depth slices in the appendix of Goleby et al. (2006).

*Figure 3.3.2: Broadband tomographic images of the Yilgarn Craton.*
*A) Oblique view from above and to the northwest of the shear-wave velocity tomographic volume. Cross sections are east-west and north-south to 350 km depth and the horizontal slice is at around 130 km.*
*B) Detailed view to the north of the >4.8 km/s shear-wave layer (pink isosurface) in the upper mantle lithosphere. The bright purple colours shown in the horizontal slice (in A) is a section through the data that this pink isosurface was constructed from. This isosurface marks a high-velocity layer around 20 km thick may be the eclogitic remains (restite) of lower crustal melts (model after Smithies and Champion, 1999), or the high-velocity layer may be a fossil subduction zone or slab.*
*C) Oblique view from above of the 4.8 km/s high-velocity isosurface with steps and edges projected vertically to the surface (yellow dots = large gold deposits, blue dots = kimberlites, purple dots = lamprophyres, green dots = carbonatites). Note the spatial relationship between large gold deposits, mantle magmas and steep edges in mantle velocity anomalies.*

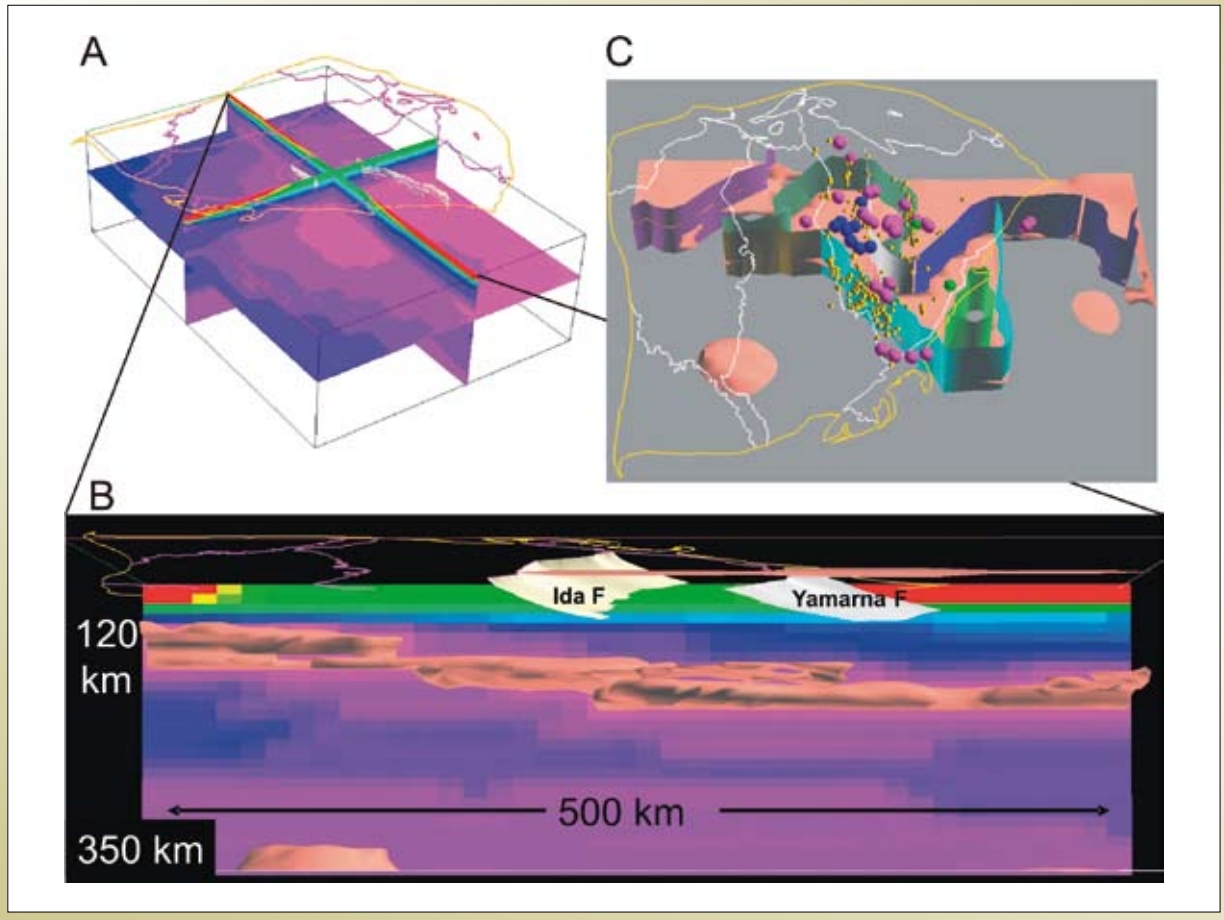

The high-velocity body is sandwiched between two layers of relatively lower shear-wave velocity lithosphere (Figure 3.3.2). The velocity increases at depths of around 300 km (Figure 3.3.2); however the depth sensitivity of the velocity gradients is not certain. One of the interesting features of the high-velocity body is the presence of steps and 'tears' in the structure. The strike of these features is at a high-angle to the main tectonic north-northwest to north-south grain of the orogen. The intersection of these 'boundaries' with the tectonic grain approximately coincides with the location of the major mineral fields of the present day (e.g., Kalgoorlie and Laverton).

Kimberlite xenocryst data (Graham et al., 2004) indicate that the lithosphere beneath the EGST was either melt metasomatised prior to emplacement of the kimberlites or the lithosphere is relatively less refractory (i.e., melt depleted). Graham et al. (2004) further suggests that the lithosphere beneath the EGST played a significant role in determining the petrophysical characteristics of the magmas that were emplaced into the EGST crust. This suggests that the lithospheric structure seen today is probably similar to that of the Archaean, as there has been very little deformation (except at the margins) since the last magmas were emplaced. The presence of Proterozoic mantle magmas (e.g., carbonatites, meloites and kimberlites), co-incident with Archaean mantle magmas, suggest that there has been limited lateral decoupling between the crust and mantle lithosphere.

### 3.3.3.2 Geodynamic interpretations of the tomography

Shear-wave (S) velocity variations can be generated by changes in temperature, bulk composition (density), structure, and fluids. The combined results of mineral physics studies with the effects of temperature and composition on seismic velocities indicate that temperature has the most dramatic effect on velocity (Goes et al., 2000). The effects of composition are much smaller than the effect of temperature, and shear wave-speed variations alone are unlikely to be able to resolve chemical variations within the mantle.

The mantle beneath the Yilgarn largely consists of harzburgite (i.e., peridotite or clinopyroxene-poor lherzolite), with the high-velocity body indicating either a compositional change from harzburgite to garnet lherzolite, or the change from garnet lherzolite to eclogite.

Although the spacing of the sample points, and hence the griding of the teleseismic S-wave volume is coarse, there is an indication that this body is not just a single southeast-dipping body but rather it is broken into a series of segments. There is a first-order spatial correlation of these breaks with the location of the largest mineral fields (gold) in the Yilgarn. A pronounced low-velocity zone (LVZ) beneath the Yilgarn Craton is not observed, and this may be a function of the relatively poor resolution of this survey in contrast to other studies.

There are currently two published suggestions as to what the high-velocity body beneath the Yilgarn Craton represents geologically (Goleby et al., 2006); *viz:* 1) a fossil southeast-dipping subduction zone, or 2) a delaminated lower crustal restite (eclogite) layer (Blewett et al., 2006).

Based on largely geochemical evidence, subduction has been proposed at various times, places and with various polarities across the Yilgarn Craton. For example, at 2760-2730 Ma, collision of the Narryer Terrane with the Youanmi Terrane was interpreted as the result of SE-directed subduction (Cassidy and Champion, 2004). Also, west-directed subduction has been proposed under the Kalgoorlie Terrane at ~2700 Ma (Morris and Witt, 1997). Subduction zone slabs in modern systems are characterised by fast S-wave velocities. For example, tomographic images of Modern subduction shows the oceanic plate or slab as relatively fast (0.5% higher than average P-wave velocity) for the entire mantle volume below Japan and eastern China (Fukao et al., 2001).

In contrast to the modern Japanese example, the high-velocity layer is at relatively shallow mantle levels under the Yilgarn, and is geometrically relatively simple. However, this simplicity may be a function of the coarse sampling resolution of the broad-band data. The high-velocity layer cannot be both the signature of a slab from opposing southeast- and west-directed subduction events.

Delamination is the removal of the lower part of the lithosphere, commonly resulting in melting under continents. By removing the lower lithosphere, the mantle can rise to higher levels, depressurise, and partially melt. There are two conditions that must be met before delamination can occur:

1. The lower parts of the lithosphere have to be gravitationally unstable by being more dense than the underlying material. The lower lithosphere can be more dense because of an intrinsic compositional difference, such as having buoyant mantle residuum beneath it, or it can become more dense through cooling, or by consisting of denser minerals.

2. The viscosity must be lowered. For lithosphere to detach and begin to flow downward under the influence of gravity, its viscosity must be low enough to allow flow (Rayleigh-Taylor instability). The flowing material is still completely solid, but it behaves according to the rules of fluid dynamics on a geological time scale.

Champion and Sheraton (1997) defined the principal granite types across the northeastern EGST, and these granite types extend throughout the entire craton (Cassidy et al., 2002). The High-Ca and Low-Ca granite types dominate by area (60% and 20% respectively). High-Ca granite types have a long-lived crystallization age range from older than 3000 Ma to ca. 2660 Ma, with a predominant emplacement age from 2700 to 2660 Ma, and have been interpreted as lower-crustal to upper-mantle melts developed during subduction (Champion and Sheraton, 1997). Low-Ca granite types are high-temperature (A type), and were emplaced after ca. 2655 Ma (most ~2640 Ma) across the entire Yilgarn (Cassidy et al., 2002). They have been interpreted as mid-crustal melts caused by a significant thermal addition near the base of the crust some 5–40 My after the peak of High-Ca magmatism. Champion and Sheraton (1997) and Smithies and Champion (1999) suggested that the delamination or convective thinning of a dense, garnet-rich, lower crust (restite from extraction of earlier voluminous High-Ca granite magma) advected heat into the base of the crust. This heat then allowed widespread crustal anatexis, and emplacement during late-orogenic extensional collapse. The presence of the relatively flat Yilgarn Moho (Drummond et al., 2000; Goleby et al., 2004) indicates some form of lower crustal thermal erosion or modification by delamination.

What evidence exists for a dense delaminated layer from early High-Ca lower-crustal melting? The velocity structure of the Yilgarn crust today shows it is essentially felsic (Drummond et al., 1993; Fomin et al., 2003; Reading et al., 2007) with no evidence of dense garnet-rich restite (eclogite or garnet amphibolite) down to 40–45 km depth. Rudnick (1995) has suggested that delaminated lower crustal layers return to the mantle (below the depth visible in the seismic reflection data). Evidence supporting the Smithies and Champion (1999) delamination model for the ultimate generation of the Low-Ca granites includes:

1. a flat Moho with a gentle east dip;

2. a crust that is thin (~40 km) relative to the depths inferred from geochemistry and petrophysics;

3. a fast S-wave velocity layer at 100–120 km that dips gently to the southeast, and;

4. a relatively simple layering of the lithosphere (suggesting the features are relatively late).

Adding the 20-25 km thickness of the high-velocity layer to the base of the crust, and taking account of up to 10 km of post Archaean erosion, a 2.65 Ga crustal thickness of around 70-75 km can be inferred. This restored estimate of crustal thickness and rheology is consistent with the inference based on geochemical models (Smithies and Champion, 1999).

The concept of crustal delamination and upper-mantle metasomatism is reflected in the alkali chemistry of diamond pathfinder indicators (M. Mitchell, De Beers, *pers. comm.*, 2004). The degree of metasomatism increases to the east, consistent with the greater distance between the present crustal base in the east than the west (Figure 3.3.2). For example, the garnets present in kimberlites (2.5-2.3 Ga) are less Ca-saturated from east to west, suggesting a more refractory mantle in the east (Graham et al., 2004). The syenite magmatism is limited to the terranes east of Kalgoorlie (Champion and Sheraton, 1997). Based on Sr-Nd isotope variations, these syenites were derived from a re-fertilised subcontinental lithospheric mantle (Graham et al., 2004). The high-velocity layer is deepest to the east (Figure 3.3.2), consistent with a greater amount of delamination and therefore enrichment or re-fertilisation of the upper mantle.

Some workers have suggested that the ~2.7 Ga mafic-ultramafic sequences and felsic magmatism in the eastern Yilgarn were the product of a large-scale mantle plume melting event (e.g., Campbell & Hill, 1988). Others

have suggested that all of the felsic magmatism across the entire Yilgarn was the result of plume tectonics (e.g., Hill, et al., 1992; van Kranendonk, 2007). Mantle plumes are thermal pulses generated in the deep Earth. Assuming the lithospheric stratification is old, the passage of a plume through the mantle would have a visible impact on any stratification. Modern mantle plumes are characterised by low velocities in both P- and S-waves.

The stratification of the mantle lithosphere in the Yilgarn shows no evidence of the passage of a mantle plume (low-velocity holes). This suggests that the mantle plume (if it existed) rose to an elevation below the base of the lithosphere (below 350 km), or that its passage to higher elevations has been obliterated by younger processes. The latter interpretation is preferred, and is consistent with the high-velocity layer being a relatively young feature (<2.7 Ga) and related to younger magmatism and delamination as discussed above.

#### 3.3.3.3 Tomography and implications for big systems

One of the most exciting aspects of this work for mineral exploration is the use of broad scale mantle features being indicators of favourable terranes. The precise role of the mantle is unclear in the gold mineral system, however the presence of mantle-derived rocks in many of the world-class deposits (or their camps) suggest a common linkage. The passage of mantle rocks into the upper crust is thought to follow steep pathways (Figure 3.3.2c). The edges and steps in the mantle tomography may therefore reflect pathways and architecture focussing or controlling deep-sourced fluids and or metals. Early examination of global tomography datasets may indicate similar areas of opportunity elsewhere on the earth.

### 3.3.4 Crustal architecture

The next scale of this system to consider is the architecture of crust. A number of datasets record information on the geometry of faults and structures (seismic and magnetic data), the distribution of mass (gravity data), the electrical properties (magnetotelluric data), the distribution of velocity (receiver functions), and the age distribution of the various crustal blocks (isotopes). The following section will consider the architecture of the crust by separately considering these datasets.

#### 3.3.4.1 Crustal structure inferred from potential fields

The regional-scale gravity data for the Eastern Yilgarn Craton has been modelled over an area extending 450 km (east-west) and 890 km (north-south). An initial gravity image with a grid interval of 800 m was prepared. The gravity image (Figure 3.3.3) reveals several NW-SE trending structures oriented in parallel or typically in an en echelon pattern. The multi-level (from 11 km to 88 km upward continued level) skeletonisation of the gravity images (Figure 3.3.4) with relatively strong horizontal gradients (worms) associated with larger levels indicates deep seated structures. One such important linear structure is still visible in the upward continued gravity data to a level of 55 km (Figure 3.3.5). Such persistent features imply relatively deep-seated structures.

Regional magnetic data show that the Yilgarn Craton is crossed by swarms of dolerite dykes that are Proterozoic and younger in age (Wingate, 2007). Of particular note is the ca. 2.4 Ga Widgemooltha suite of dykes that strike at a high-angle to the regional grain (also visible in the gravity data). These east-northeast-trending dykes are aligned parallel to the main (interpreted) extension direction (Blewett and Czarnota, 2007a) during the D1 formation of the greenstone basins (<2.80 Ga) and the major granite doming D3 event (2.66 Ga). The main gold camps have swarms of these dykes (e.g., through Kalgoorlie-Kambalda, Leonora-Laverton and Wiluna). Although these dykes are typically 200–250 My younger than the mineralisation, they may be recording deep-seated early weaknesses that acted as later steep pathways for mineralisation and subsequently even later dykes.

#### 3.3.4.2 Crustal structure inferred from geochemistry-stratigraphy, isotopes and inheritance patterns

Granites are crustal probes and provide unique information about their source area (in the mantle or crust) and the crust they pass through to the site of emplacement. An extensive geochronological database exists for the granites of the Yilgarn. The U-Pb SHRIMP analyses of zircons not only provide an emplacement-crystallisation age but record information about source areas and crustal contamination in their inheritance signatures. The Sm-Nd isotopic system provides a measure of mantle separation age and provides an indication for the age of the formation of the crust.

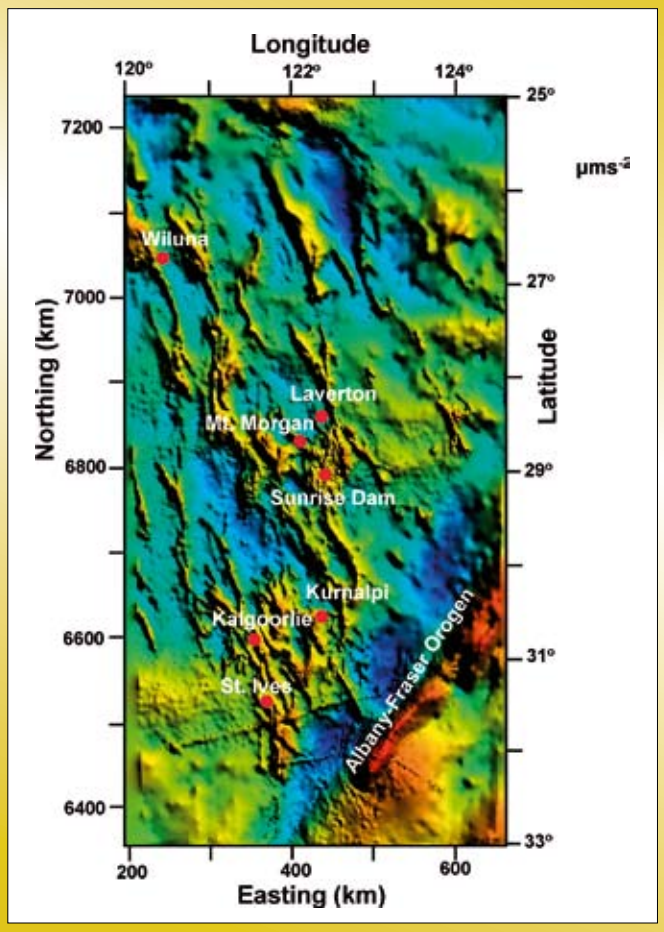


*Figure 3.3.3: Sun-angle Bouguer gravity image (800 m cell size) of Eastern Yilgarn Craton (EYC). The Bouguer gravity data is expressed in gravity unit (g.u or $\mu ms^{-2}$). 10 g.u. = 1mGal, where red is high density and blue is low density. Note the large granite batholiths that strike north-northwest and northwest (as blue colours). The yellow to red colours are mapping the distribution of greenstones. The large Widgiemooltha dykes that strike east-northeast are even imaged in the south. The Albany-Fraser Orogen strike northeast and dominates the gravity data.*

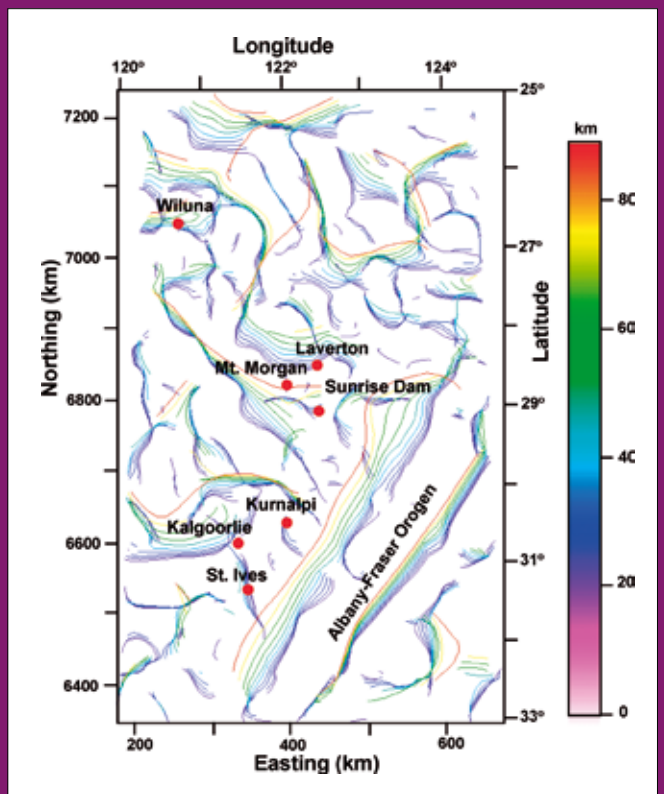


*Figure 3.3.4: Multi-level skeletonisation or worms of the gravity data is presented. The figure contains skeletonized Bouguer data continued from 11 km to 88 km. The colour bar represents the amplitude of the horizontal gradients. These worms represent changes in the very largest mass distributions in the deep crust and represent deep fundamental boundaries-structure. Note that many of the large deposits lie on multi-level worms. The strong northeast trends in the gravity in the southeast part of the map are recording the major influence of the Albany-Fraser orogen.*

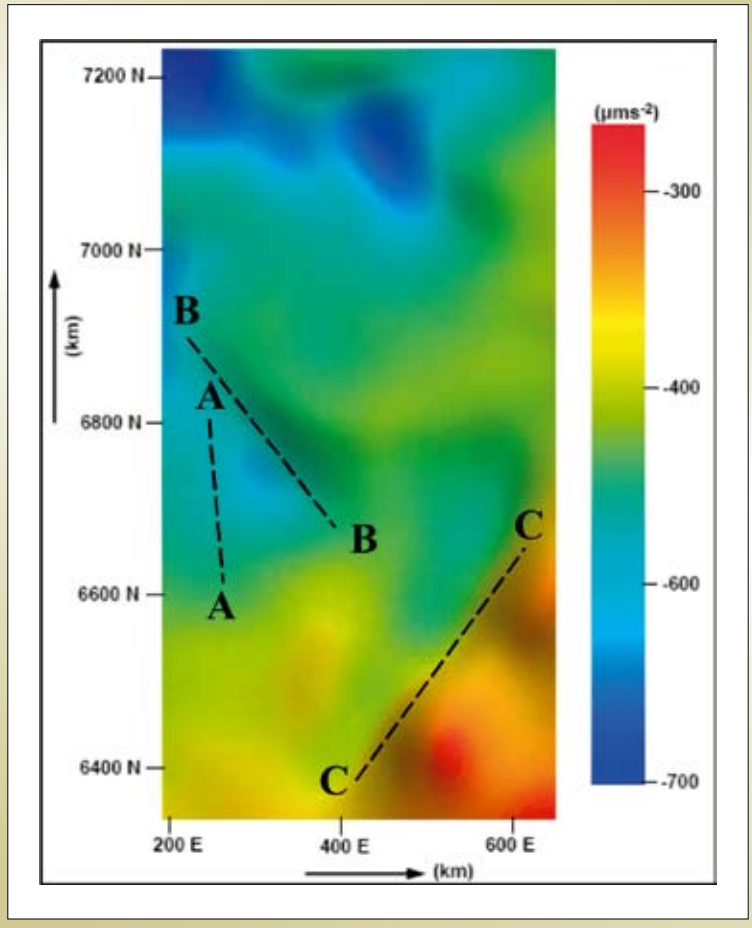


*Figure 3.3.5: Image of Bouguer gravity data upward continued to a level of 55 km. Note the main trends are imaged at these high (deep crustal) levels.*
*A) D1 extension and distribution of the greenstone belts and tectonostratigraphic terranes (e.g., the Ida Fault);*
*B) D3 extension and distribution of main granite batholiths;*
*C) Albany-Fraser collision and reworking orthogonal to the earlier events.*

These data provide constraints on the geodynamics of the Yilgarn (Cassidy and Champion, 2004; Griffin et al., 2004).

A Nd isotope map (Figure 3.3.6), constructed using depleted-mantle model ages ($Nd_{TDM}$) for felsic magmatic rocks (~250 analyses) from across the Yilgarn Craton, illustrates that in virtually all cases the Nd depleted mantle model age is significantly older than the crystallisation age of the host granite and/or felsic volcanic rock. Generally the difference is 200–300 My and sometimes over 500 My older, indicating interaction with pre-existing crust in the genesis of the felsic magmatic rocks.

There are a number of obvious divisions in the Nd map (Figure 3.3.6), with the central/western Yilgarn comprising a relatively consistent protocraton(?) of 3.3–3.1 Ga old crust, except for a belt of younger 3.0–2.95 Ga model ages in the north-west part of the terrane (Murchison Domain). The Nd map also clearly highlights the distinct isotopic character of the northwestern Yilgarn with model ages generally older than 3.3 Ga; this approximates the Narryer Terrane (Cassidy and Champion, 2004; Griffin et al., 2004).

A distinct 'break', coincident with the Ida Fault at the surface, marks the likely eastern margin of the Youanmi Terrane. East of this is an isotopically complex region (the EGST) that can be divided into several poorly defined zones. Virtually all felsic magmatic rocks east of the Ida Fault have Nd depleted-mantle model ages <3.1 Ga, and generally <2.95 Ga. The boundaries to these isotopic domains trend parallel to the tectonic and stratigraphic grain of the region, suggesting that major crustal differences are east to west. These major crustal differences and their boundaries have implications for the polarity and nature of the basin forming D1 extension (Blewett and Czarnota, 2007a, b) and the subdivision of the EGST into a number of separate terranes (Cassidy et al., 2006; Reading et al., 2007).

The zircon inheritance patterns in the Youanmi and Kalgoorlie Terranes are similar, while the Kurnalpi and

Burtville Terranes to the east of the EGST are consistently different to those further west (Cassidy, 2006). Of note, is a dominant 2.81 Ga population in the Youanmi and Kalgoorlie Terranes, with 2.81 Ga inheritance only found within 'old' domains in the Kurnalpi and Burtville Terranes. The other important populations are the 2.74–2.73 Ga zircons in granites and felsic volcanic rocks in the Kalgoorlie Terrane, a characteristic feature not present in the other eastern Yilgarn terranes (Cassidy and Champion, 2004).

The zircon inheritance data in combination with changes in the chemistry of felsic volcanism, and a subtle change in the age of High-Ca, Mafic and Low-Ca granites (Champion and Sheraton, 1997), are all consistent with the Kalgoorlie-Kurnalpi Terrane boundary marking a fundamental crustal 'break'. TTG-type dacite to rhyolite submarine volcanic and sedimentary rocks of the Kalgoorlie Sequence (incorporating the Black Flag Group) (Brown et al., 2001; Barley et al., 2002) represent a series of mainly submarine (back-) arc or intra-arc basins. In contrast, in terranes of the eastern Yilgarn, the main felsic volcanic associations are arc-rift-related bimodal basalt-rhyolite sequences and calc-alkaline arc-type sequences. The volcanism and deposition of the Kalgoorlie Sequence overlaps with emplacement of the High-Ca and Mafic granites in the Kalgoorlie Terrane, whereas in the terranes of the eastern Yilgarn, a major influx of High-Ca and Mafic granites postdate greenstone deposition.

It is also interesting to note that the type of Proterozoic alkaline ultrabasic rock changes from dominantly kimberlites in the Kalgoorlie Terrane to lamprophyres and carbonatites in the Kurnalpi and Burtville Terranes (Graham et al., 2004). This change is consistent with a fundamental 'break' on the eastern side of the Kalgoorlie Terrane, which is mapped as the Ockerburry Fault.

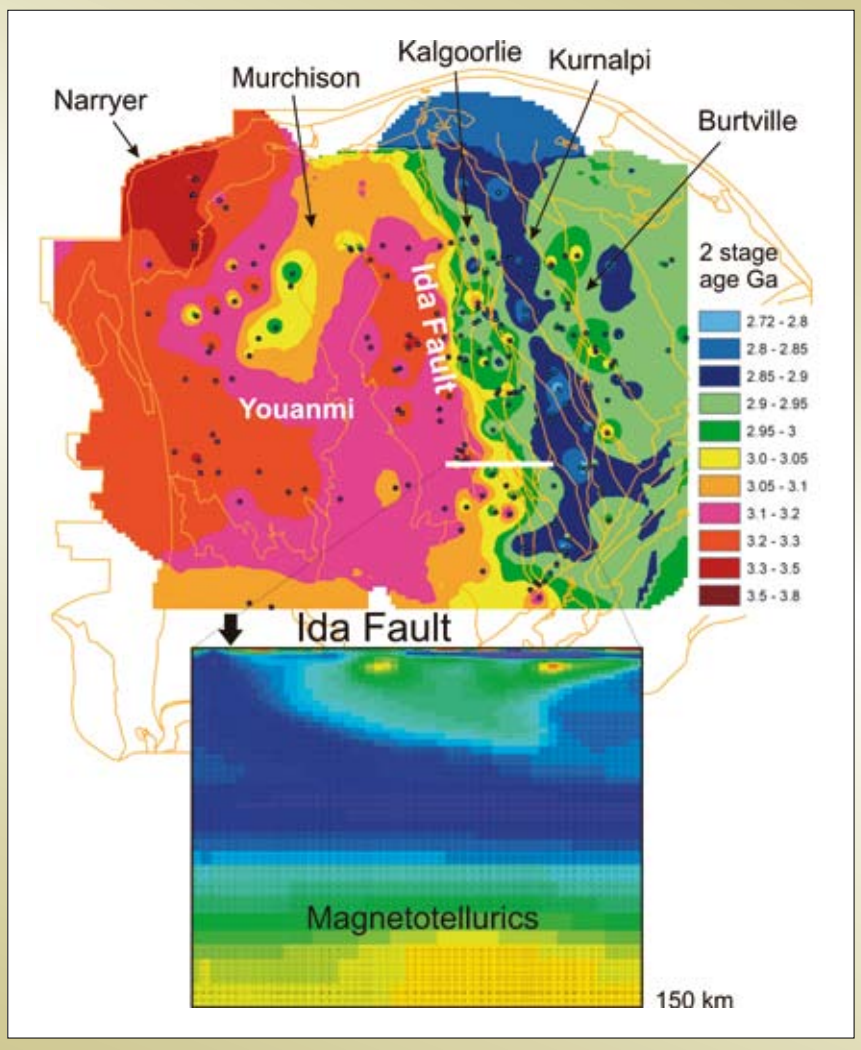


*Figure 3.3.6: The Nd isotope map (coloured by age in Ga) shows model ages for granites from across the Yilgarn Craton. In virtually all cases the Nd model age is significantly older than crystallization age of the host granite and/or felsic volcanic rock, generally 200–300 Myr and sometimes over 500 Myr older (after Cassidy and Champion, 2004). The map images the main subdivisions terranes and domains of the Yilgarn Craton (Younami, Narryer, Youanmi, Kalgoorlie, Kurnalpi, and Burtville). The Ida Fault is a major isotopic break. A section of the magnetotelluric 2D inversion is shown to 150 km and indicates that resistive (old) crust dips east beneath the Kalgoorlie Terrane, consistent with seismic reflection data.*

### Geochemistry-stratigraphy and isotope geochronology: implications for big systems

The data indicate a complex history of crustal recycling throughout the Meso- and Neoarchaean. Autochthonous development for much of the granite-greenstone terranes in a continental environment is implicated. Voluminous granite intrusion, between 2.76 and 2.63 Ga, was coincident with Neoarchaean orogeny that resulted in the amalgamation and assembly of several cratonic elements to form the present Yilgarn Craton.

In the EGST, and perhaps for the whole craton, the preferred tectonic environment is a subduction setting, possibly a long-lived accretionary margin (Czarnota et al., 2008). The importance of interaction with pre-existing continental crust for the majority of the felsic magmatic rocks in the Yilgarn Craton cannot be over emphasised. In fact, quartzofeldspathic gneisses contain rare xenocrystic zircons up to ~3.8 Ga, though typically younger than 3.1 Ga, consistent with involvement of old crust. The isotopic and geochemical (stratigraphic) patterns are arranged in elongate belts – this is consistent with rift and accretion-amalgamation rather than plume-type geodynamic models.

Interestingly, most of the large gold deposits are located in the intermediate aged crust (not most juvenile). This relationship is in contrast to the Superior Craton of Canada, where most gold (and VHMS) endowment is in the most juvenile crustal domains (e.g., Abitibi Subprovince: Percival et al, 2006)

## 3.3.4.3 Crustal structure inferred from Receiver Function velocity profiles

Receiver functions are one dimensional velocity profiles calculated for a crustal column at a specific site at the surface. These data are effective at picking the base of the crust and are consistent with Moho depths determined from other seismic techniques.

An array of receiver function velocity profiles have been calculated for the Yilgarn Craton (Reading et al., 2003), and these are distributed around the craton (Figure 3.3.7) in a series of east-west and north-south transects (with a site spacing of 20–50 km). One of the aims of the study was to determine whether there are differences in velocity structure between mineralised and un-mineralised crustal areas (Table 3.3.1).

Each deployment of the broadband recorders lasted approximately three months. Prior to the instruments being redeployed, the world earthquake catalogue was consulted to confirm that sufficient large-magnitude earthquakes, at suitable distances and range of azimuths, had occurred in the preceding three months to provide enough data to determine a velocity at that site. Instruments were then moved to the next defined site to build up a 3D velocity coverage (Goleby et al., 2006).

The receiver functions were calculated from a three component signal recorded at the receiving station by deconvolving the vertical component with the horizontal component in the radial (source-to-receiver) direction (Ammon, 1990). The calculated receiver functions are stacked for each station, to improve the signal/noise ratio. The data are modelled assuming that the structure beneath the station approximates a one dimensional layered structure where the energy from all azimuths produces the same receiver waveform. Small departures from this assumption in the form of gently dipping layers do not strongly affect the analysis.

The signal frequency corresponds to a velocity zone (region or structure) with a wavelength several kilometres across (at the depth of the Moho). This smoothing effect means that small heterogeneities do not influence the result, and this result is dominated by the large variations in the crust.

Table 3.3.1 summarises the key results of the crustal velocity character of the main blocks of the Yilgarn Craton (Reading et al., 2007). The Murchison and Southern Cross Domains have a similar character, consistent with them being part of a large body – the Youanmi Terrane (Cassidy et al., 2006). In contrast, the Eastern Goldfields Superterrane (EGST) is complex with a high degree of variability, particularly in the lower crust, in receiver function stations.

The absolute value of the shear-wave velocity is indicative of composition and metamorphic grade. The shear-wave velocities for the Yilgarn Craton is low <4.2 km/s, which are generally associated with a high proportion of felsic rock compositions (Rudnick and Fountain, 1995).

*Figure 3.3.7:*
*A) Map of receiver function stations and seismic lines acquired for the Yilgarn Craton. Note the red line which is the location of the Leonora to Laveton wide-angle reflection study (C).*
*B) Example velocity profiles for Youanmi (WT08), Kalgoorlie (WT09), and Kurnalpi (WT10) Terranes. The blue line is the average profile for the Australian crust, the red line is the calculated profile for the terrane at the recording station (after Reading et al., 2003). Note the velocity drop (dotted ellipse) at around 10 km in the Kalgoorlie Terrane. One interpretation is that this region has a high percentage of Low-Ca granites, therefore lowering the relatively high crustal velocity for the Kalgoorlie Terrane.*
*C) Final velocity model of the upper crust in the Leonora-Laverton transect (A) from refractions and wide-angle reflections recorded by 65 stations. Ranges of velocity variation in each layer correspond to velocity values at the top and bottom of each layer.*

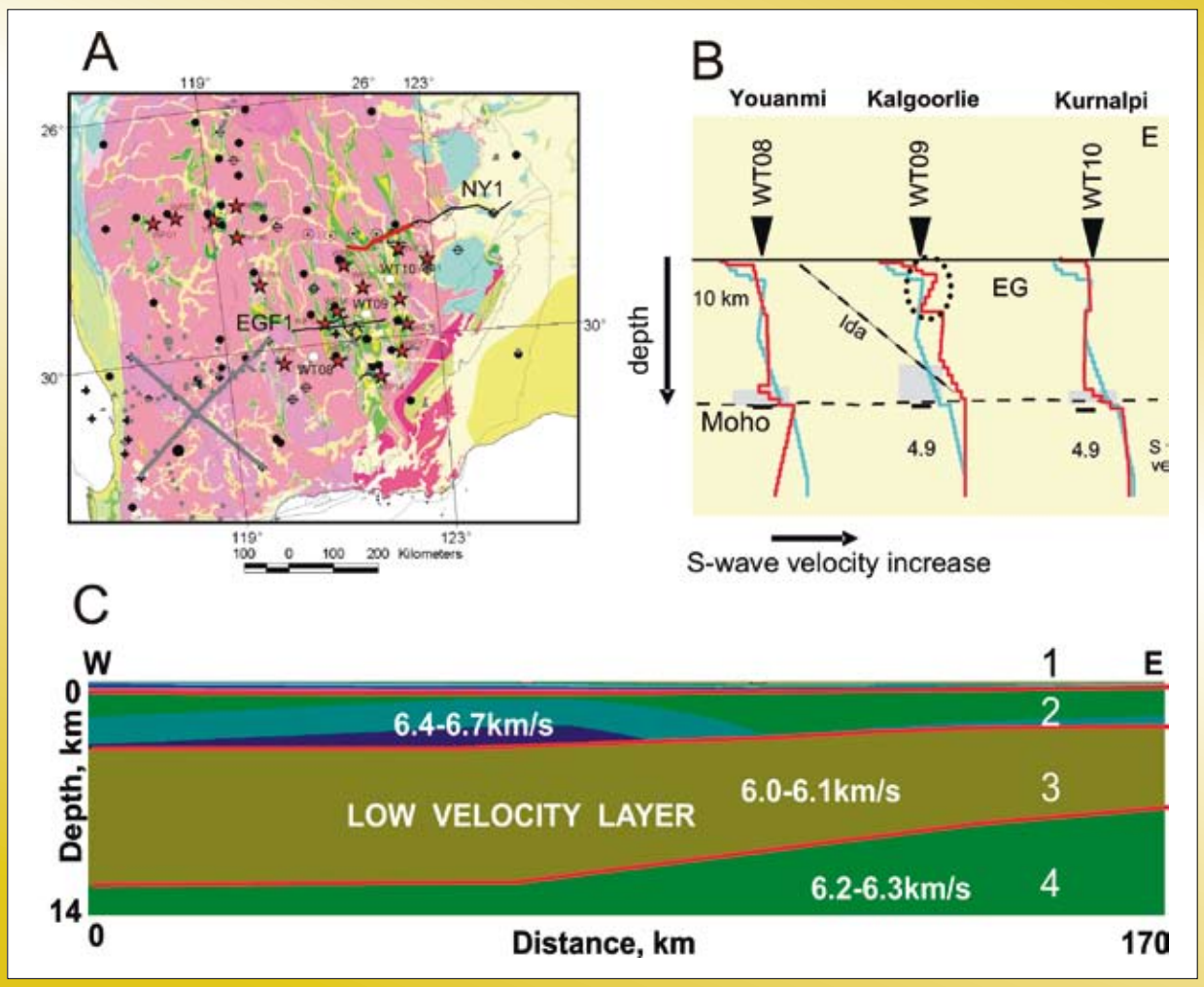


## Receiver functions and implications for big systems

Reading et al. (2007) noted a characteristic Moho depth and seismic velocity for each terrane (Table 3.3.1). The variability in the crustal profiles in the EGST is consistent with this complex entity being an amalgam of different terranes (Cassidy et al., 2006). The study of Reading et al. (2007) did not consider the different terranes (of the EGST) separately to determine if there is a systematic spatial difference in these properties. The tectonic implication from this work is that some degree of spatial-temporal separation-evolution between the EGST and the Younami Terrane was likely, and that these terranes were later brought together or amalgamated (e.g., Barley et al., 2002; Krapež and Barley, 2007; Czarnota et al., 2008). However, the zircon inheritance in <2.7 Ga granites suggests that at least part of Kalgoorlie Terrane (western EGST) is underlain by Youanmi Terrane crust, consistent with the magnetotelluric data.

The Kalgoorlie Terrane crustal profile is significantly different to the adjacent terranes' profiles (Figure 3.3.7b).

Table 3.3.1: Summary of velocity profiles determined from receiver functions for the main crustal blocks of the Yilgarn Craton, summarised after Reading et al. (2007)

| | Murchison | Southwest Gneiss | Southern Cross | Eastern Goldfields |
|---|---|---|---|---|
| Moho Depth | 34 km (eg WR05) | 36 km (eg WT04) | 38 km (eg WT08) | 42 km (eg WV05) |
| Boundary type | Sharp | Sharp away from terrane edges | Very sharp | Sharp |
| Crustal structure | Simple upper crust | Discontinuity in upper crust, | Simple upper crust | Discontinuity in upper crust, |
| Velocity profile | velocity gradient in lower crust | high velocity gradient zone above Moho | constant velocity lower crust | Lower crust velocity gradients variable |
| Lower crust S-wave velocity | 3.8 km/s | 4.2 km/s | 3.6–4.0 km/s | 4.2 km/s |
| Structural Variability | structure consistent across terrane | HVGZ thickens towards the west | structure consistent across terrane | Structure generally very variable Moho shallower towards the south |
| Average Velocity profiles for each Terrane (after Reading et al., 2007) | 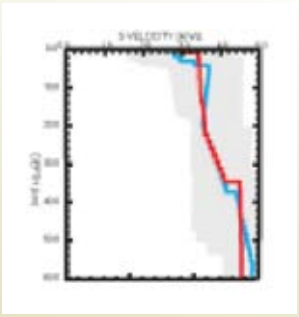 | 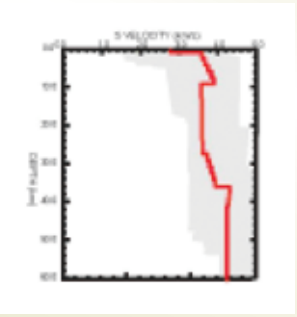 | 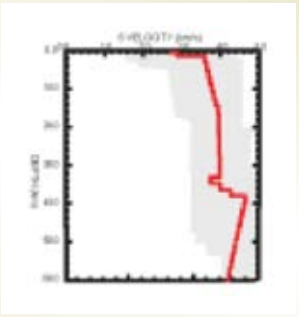 | 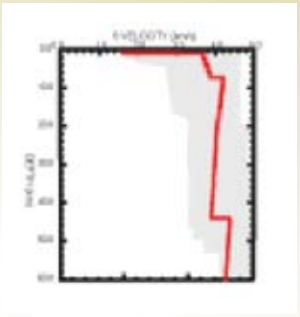 |

Despite an overall increase in velocity with depth to the base of the crust (Moho), there is a marked velocity drop from around the base of the greenstones (~5 km) to ~15 km depth. This velocity drop brings the velocity profile close to the Australian crustal average (blue line), in contrast to the overall higher velocity (than Australian average) at depth.

As velocity is a largely a function of density, the interpretation is that a significant amount of light (therefore slow) granites occur at these levels, relative to the overall faster velocities at depth for this terrane. These granites may be the Low-Ca granite types which are inferred to lie beneath many of the greenstones. This inference is based on the observation that Low-Ca granites are largely only exposed external to (that is beneath) now eroded greenstones. The corresponding relative velocity high (deeper in the crust of the Kalgoorlie Terrane velocity profile) is interpreted to reflect a more dense (hence fast) restite from Low-Ca granite anatexis.

The significance of these observations is that there are architectural differences in terms of the velocity structure (i.e., lithology) between the various terranes of the Yilgarn Craton. The Kalgoorlie Terrane is on average faster than the Australian average (the other terranes are similar to it). The Kalgoorlie Terrane is also the most endowed part of the Yilgarn for gold.

Does the velocity structure have a bearing on the endowment, and therefore prospectivity, of a terrane? Interestingly, the linkage between the velocity anomaly under the Kalgoorlie Terrane can be interpreted as a function of greater volumes of Low-Ca granites. The important relationship between domes, granites and gold is discussed elsewhere in this chapter. The receiver function data are consistent with the observations and interpretations of other data such as seismic reflection, gravity, geochemistry, and geological understanding.

### 3.3.4.4 Crustal structure inferred from seismic reflection profiles

Two regional deep seismic reflection traverses have been acquired within the EGST (Figure 3.3.8), and both lines have had a profound impact on the understanding of the region's crustal structure and geodynamics (Goleby et al., 1993; 2000; 2003; Swager et al., 1997; Drummond et al., 2000). The first was a dynamite survey (91EGF01) which was 213 km in an east-west traverse sited north of Kalgoorlie and crossing the eastern Youanmi Terrane, the Kalgoorlie Terrane into the Kurnalpi Terrane (Figure 3.3.8). The second line was 01AGSNY1, which was a vibroseis survey running east-west from Leonora, through Laverton, eastwards to the margins of the Yilgarn Craton (Figure 3.3.8). For details of the acquisition and processing parameters of these surveys see Goleby et al. (1993; 2000; 2003).

A series of shorter (typically <50 km) additional vibroseis seismic lines have been acquired (by Geoscience Australia, AGCRC and the ***pmd*CRC***) in the Kalgoorlie region and the Laverton region, and a number of exploration companies have funded detailed high-resolution lines at Kambalda (Figure 3.3.9), Leonora, and Laverton. These additional lines are important as they are focussed over the most endowed parts of the EGST and have provided an unparalleled view of the architecture of these mineral systems. Many of these lines cross one another or link with the regional lines. By joint interpretation of the vast array of detailed high-resolution lines with the back-bone regional lines and integrating these interpretations with potential field geophysics, a series of well-constrained 3D maps of the region have been constructed (Henson, 2006).

#### Seismic features of the crust

These deep seismic reflection lines have effectively imaged a number of prominent crustal-scale features (Figure 3.3.8), including: a change in the crustal thickness, a subdivision of the crust into three broad layers, an east dip to the majority of the reflections, and the presence of a series of crustal-penetrating (generally east-dipping) shear zones. The Moho is imaged as a prominent thin sub-horizontal band of reflections at about 35 km at the western edge of the province, deepening to about 46 km at its eastern edge. This eastward thickening of the crust is imaged on both the lines (Goleby et al., 2003). This eastward 'dip' of the Moho is achieved by a series of ramps and flats, in which the Moho is generally sub-horizontal for long sections before it ramps downwards over short distances (Figure 3.3.8). These depths are consistent with earlier refraction data from the southwest of the Yilgarn Craton (Dentith et al., 2000).

*Figure 3.3.8: Interpretations of a combined 01AGSNY1 and 91EGF01 seismic sections showing prominent crustal-scale features. Both sections show three sub horizontal layers in the crust. Above the mantle is a thin non- to poorly-reflective layer, above this is a layer containing large scale lozenges, and the upper crust has a complex signature recording variations in the granite-greenstone layer. The 01AGSNY1 seismic section is 384 km in length by 48 km in depth. The 91EGF01 section is 213 km in length by 45 km in depth. Inset map shows location of seismic lines. Analogue modelling after Harris et al. (2002) shows how extension may form the crustal architecture (see also Blewett and Czarnota, 2007).*

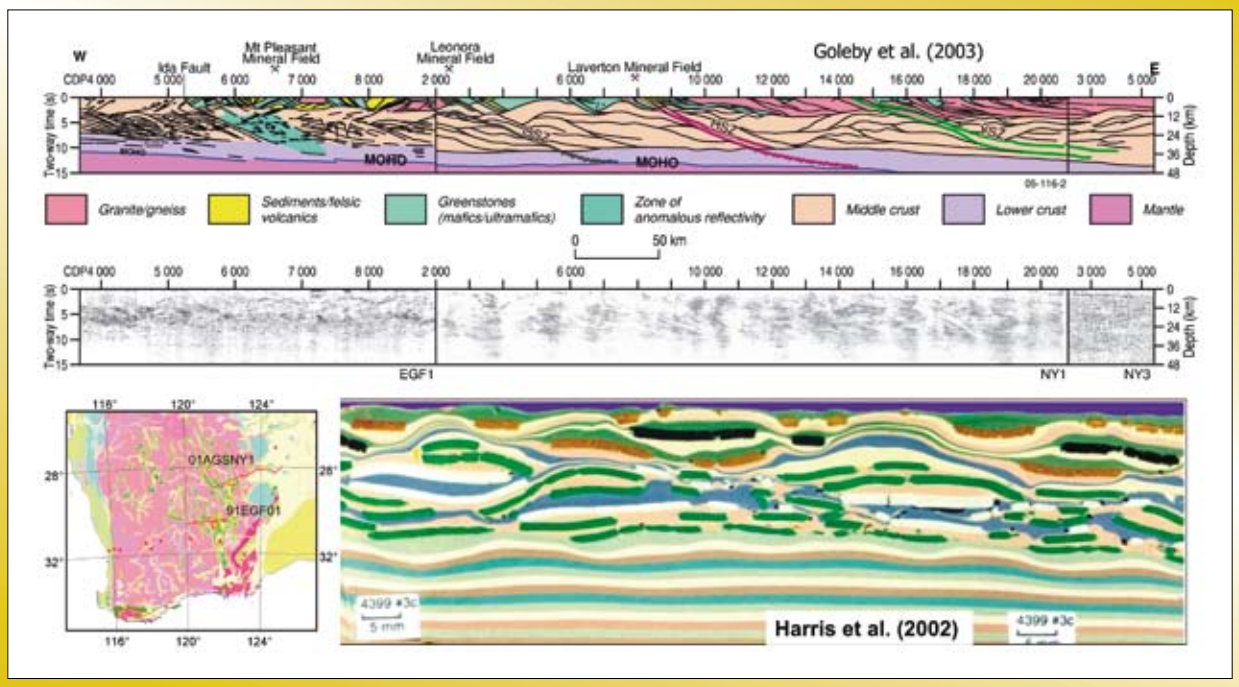


A three layered (sub-horizontal) crust comprises the EGST (Figure 3.3.8), each with different seismic characteristics. The lower layer is essentially devoid of reflections, with the exception of a few instances where dipping reflections are imaged. These have been interpreted to represent the presence of deep-penetrating shear zones (Goleby et al., 2003). The upper surface of this lower crustal ductile layer is defined by a sudden change in reflection character to a zone where overlying large packages of dipping reflections are typical. Seismic reflectivity in the middle level is characterised by numerous prominent east-dipping reflections that can be subdivided into large-scale, lozenge-like, mid-crustal bodies. Drummond et al. (2000) described duplex-like structures in the mid crust of the 91EGF01 seismic line, and interpreted these features to 'D2' thrusting and imbrication. Similar features are evident in segments of the 01AGSNY1 line, along with open upright folds and domes. There is one exception to this within the middle crust of the Kalgoorlie region, where an anomalous region of low reflectivity has been interpreted to represent either extensive deformation or large scale alteration within the area (Drummond et al., 2000). The boundary between this middle layer and the upper layer is diffuse and irregular. The upper layer is complex and variable in its seismic character, and likely imaging complexities within the granite-greenstone succession.

On the seismic reflection sections, there is also a very pronounced 30° easterly dip to the majority of the events (Figure 3.3.8). West-dipping features are imaged in a few locations. One in particular is the Bardoc Shear Zone, a highly mineralised zone containing numerous operating mines. Within the prominent east-dipping fabric, a series of distinctive east-dipping zones of reflectivity cut deep into the crust. These shear zones are the Ida Fault, the Mount George Shear Zone, the Laverton Shear Zone and the Yamarna Shear Zone. They divide the eastern Yilgarn Craton into a series of distinct domains and can be traced from the surface to the lower crust, and in three cases to the Moho. The Ida Fault, the Laverton Shear Zone and the Yamarna Shear Zone are clearly defined, whereas about 9 km of the Mount George Shear Zone, from 3 km to 12 km depth, appears to have been intruded by later granite emplacement and/or affected by subsequent deformation. All four shear zones have complex geometry, suggesting that these zones have been deformed several times.

However, detailed examination of the reflectors show that it is difficult to interpret a single plane cutting through the crust. This is especially true of the Ockerburry Fault which is imaged on both the 01AGSNY1 line and 91EGF01 line. The Ockerburry Fault is a terrane boundary and yet it appears thin skinned. Faults such as the Celia and Laverton may cut deep in the crust, yet they are relatively minor faults within terranes. The inference from these observations is that terrane accretion may have been thin-skinned thrusting and the subsequent deformation (especially late extension) occurred along different boundaries within the terranes (Blewett, 2006b).

## Tectonic mode and seismic architecture

The concept of a regional detachment was formulated from work on the regional 91EGF01 seismic line (Goleby et al., 1993). More detailed work on newer (higher quality) lines including 01AGSNY1 has shown that there is unlikely to be a single 'detachment' plane. Coupled with the thinking on a regional detachment was that this surface represented a sole thrust controlling duplexes above. The paradigm was that the EGST was preserving the contractional-accretionary history of the geodynamics.

Analogue modelling using a centrifuge to simulate crustal extension was undertaken to test the tectonic mode necessary to form the architecture of the 01AGSNY1 seismic line (Harris et al., 2002). These workers managed to replicate the broad-scale geometry of the seismic data, with deep penetrating shear zones, upright folds and domes, regional 'detachments' and recumbent folds adjacent to the high-strain shear zones. The work demonstrated that contraction was not a necessary tectonic mode to generate the seismic architecture observed.

Reprocessing of the western end of the 01AGSNY1 seismic line near the Leonora mine of Sons of Gwalia (Leonie Jones, Geoscience Australia) successfully imaged the reflection events up to the weathering zone. A beautiful match between the mesoscale to macroscale fabric of the Sons of Gwalia open pit and the seismic data was obtained (Czarnota et al., 2007). The pit is located on a high-strain extensional shear zone (Williams and Currie, 1993; Blewett and Czarnota, 2007b; 2007c) and the S-C geometry at the mesoscale is replicated in the upper two seconds (6 km depth) of the reprocessed data (Czarnota et al., 2007). The intense reflectivity imaged in the seismic continues to depth and rolls across a granite dome (core complex). This geometry continues further east and at depth, the implications being that much of what is imaged is extension not contraction (e.g., Harris et al., 2002).

The Ida Fault is the boundary between the Youanmi and Kalgoorlie Terranes and was well imaged in the 91EGF01 seismic line. Swager et al. (1997) noted the extensional

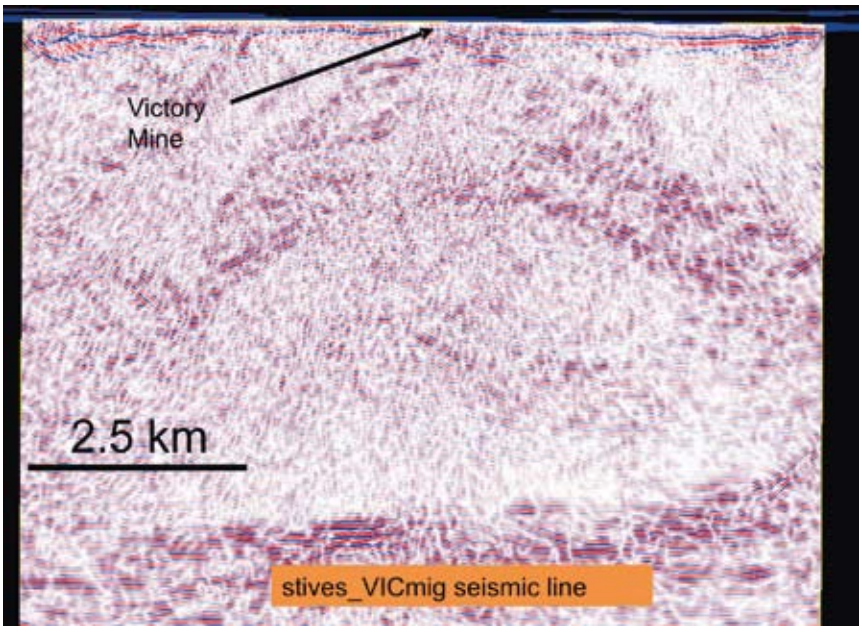


*Figure 3.3.9: View north of granite-cored dome beneath the Victory Defiance deposit at Kambalda (after St Ives Goldfields).*

geometry of this structure, but suggested it was late orogenic collapse. Blewett and Czarnota (2007b) suggested that this extensional geometry and fabric was the same as that found at Leonora, and equivalent to the doming and extension at the eastern margin of the greenstone belts, and dated at ~2660 Ma (Swager and Nelson, 1997).

### Domes and the 'Golden Corridor'

One of the major features imaged in the seismic data are domes and antiforms at three layers within the crust, including within middle crust 'imbricates', felsic gneiss below the base of the greenstones, and within the upper crustal greenstone units (Henson and Blewett, 2006). These geometries are important as many of the major gold deposits of the region have a spatial relationship with domes (Henson et al., 2005; 2007; Henson and Blewett, 2006).

The Boorara and Kambalda Domains of the Kalgoorlie Terrane are the most-richly endowed regions of the Yilgarn Craton, and they contain world-class gold deposits such as Golden Mile, Kanowna Belle and Kambalda. A 'Golden Corridor' that strikes north-northwest from Kambalda to Wiluna (and possibly as far north as Plutonic), marks the axis of the Kalgoorlie Terrane. The corridor is bounded to the west by the west-dipping Bardoc Fault System, and to the east by the east-dipping Ockerburry Fault System (Henson et al., 2006). Overall the region is an antiform with major faults dipping in opposing directions away from its apex (Figure 3.3.10), locating the major gold deposits in the footwall of these master faults and in two locations in sub-parallel subsidiary faults to the master faults (Golden Mile and Kambalda). The anticlinorium strikes north-northwest, but in detail the fold axis has a periclinal plunge giving rise to domes and basins along the axis. The wavelength of these plunge changes in the mid-crust is of the order of 30 km, which is a characteristic spacing of the region's major gold deposits (Henson et al., 2006).

The wavelength of domes varies with depth, domes from the long-wavelength deeper domes in the mid crust up to short-wavelength domes in the very upper crust (top 1–2 seconds of data). All these domes stack upon each other and form ever more focussed "funnels" for delivering

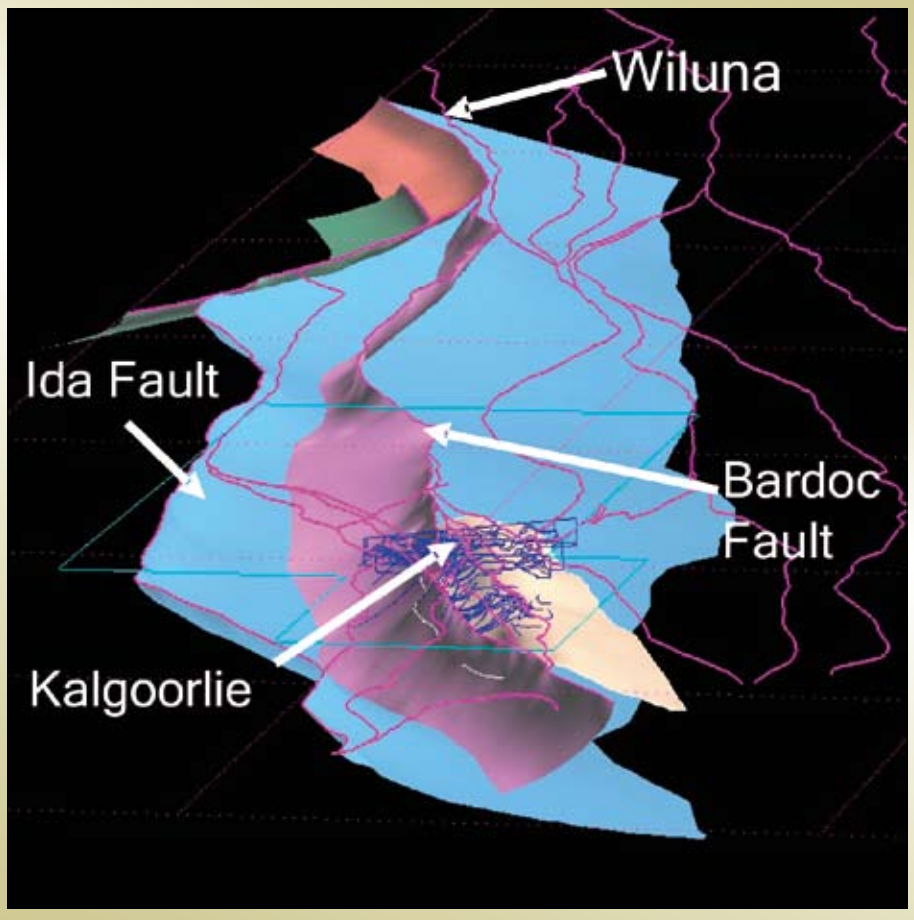


*Figure 3.3.10: The Golden Corridor is a regional anticlinorium between opposing east- and west-dipping major shear zones. This corridor, from Kambalda to Wiluna, hosts many of the region's major gold deposits.*

fluids to the deposition site (Figure 3.3.11). Structures within the mid-crust resembling large crustal 'imbricates' or domes are visible on the 91EGF01 seismic line in the Kalgoorlie region (Drummond et al., 1993) and the 01AGSNY1 seismic line in the Leonora-Laverton region (Goleby et al., 2003). A series of reflectors occur below the base of greenstone sequences and in at least one location at Kanowna Belle have been interpreted to represent a domical structure. The structure was identified using seismic lines that cross each other in the vicinity of the Scotia Kanowna Granite (Figure 3.3.8). This domical structure occurs above the original detachment surface although is well below the base of greenstone, determined using potential field modelling within the region.

In detail in the very upper crust, the domes beneath many of the major mines have a 'basal' sub-horizontal reflector that diverges from the overlying anticlinal reflector (Figure 3.3.9). Interestingly, where the maximum divergence between these reflectors occurs, large gold deposits are found. The seismic and gravity data suggest that the dome cores are granitic in composition. The question arises as to what these diverging reflectors represent and what processes operated during their formation, and when this occurred. Domes can form by contraction with antiformal thrust stacks, or granite laccoliths intruding into thrusts (Ramsay, 1987; Price and Cosgrove, 1990). Alternatively, domes can form during emplacement of granites as a sill or laccolith, or as a core complex during extension (see also Harris et al., 2002). The seismic reflection data show that the dome core is a zone of random reflectors, more characteristic of a granite intrusion (Henson and Blewett, 2006).

## Seismic reflections and implications for big systems

Deep crustal seismic reflection studies have provided excellent 2D crustal architectural information in the eastern part of the craton, which in turn, have provided information on the region's mineral systems. These seismic reflection data have been very effective in imaging the numerous shear zones within the crust as well as details within the greenstone succession and indicate that the region's major orogenic gold deposits are spatially associated with these major shear zones (Groves et al., 1989).

Interpretations of the fault architecture below the greenstone base or in the granite areas are restricted to seismic reflection data. This is because of the inability of alternative potential-field methods to map structure effectively at depth (via rock-property contrasts) or in felsic crust (as discussed above). Early interpretations of the seismic reflection data around Kalgoorlie (e.g., Goleby et al., 1993; Swager et al., 1997) noted a number of structures that penetrated the upper crustal detachment and, in some cases, intersected the Moho. Similar interpretations were made of the northeastern Yilgarn

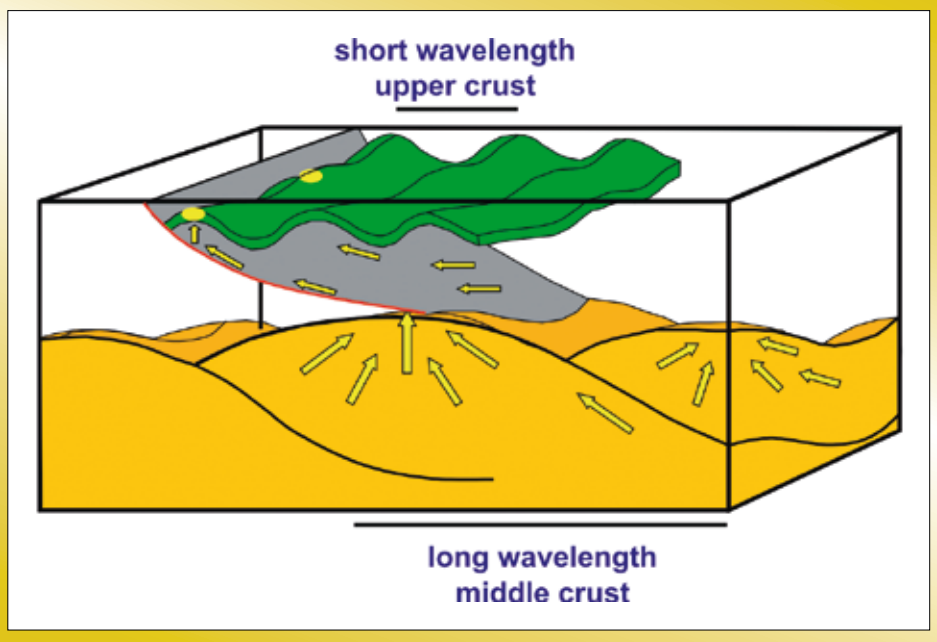


*Figure 3.3.11: Cartoon to illustrate the domes of decreasing wavelength to shallow depths permits increasing focusing of fluid (after Henson et al., 2005).*

seismic line (01AGSNY1), with three crustal-penetrating shear zones interpreted (Goleby et al., 2003).

Breaking the entire crust with a single fault plane under contraction is mechanically difficult to achieve, but is easier under extension. The seismic data shows an essentially extensional architecture. Empirically, the fact that the Yilgarn crust developed deep-penetrating structural pathways is considered to be important for a region's prospectivity, irrespective of how the structures formed or the fluid pathways operated (Goleby et al., 2003; 2004).

Blewett and Czarnota (2007b) suggested that the amount of D3 extension (2665–2655 Ma) was greater than any of the subsequent (D4 and D5) contractional inversion events and that is why the EGST is preserved. Furthermore, the thickest greenstone accumulations (basins) are preserved in these areas of greatest D3 extension (e.g., Kalgoorlie Terrane and around Laverton).

A number of important deposits (e.g., Kanowna Belle, Golden Mile, St Ives, Wallaby) are located in the region above or adjacent to domes, suggesting a relationship between domes and gold mineralisation (Henson et al., 2005). Late-stage breaches of the domes may allow concentration of gold-rich fluids (formed at the brittle-ductile transition?) within the domical structures to migrate higher in the crust. The somewhat loose analogy is with the petroleum system, where oil and gas migrate up gradients using permeable pathways into antiformal or domical trap areas. Mapping domes could therefore be a critical step in area selection, with the combination of large-scale (crustal-penetrating) faults intersecting domical traps providing a focussed fluid pathway during gold mineralisation (Henson and Blewett, 2006).

There are other features of domes that make them favourable to mineralisation. The buckle folding of a competent body (granite-cored dome) results in differing stress across the fold. Typically the outer arc of a buckle fold undergoes extension while the inner arc undergoes contraction. Between the extensional and contractional domain lies the neutral surface. Folds typically occur in pairs (i.e., antiforms and complementary synforms), which results in a switch in the location of maximum extension about the fold profile (van der Pluijm and Marshack, 1997). This change in local stress state about the fold profile gives rise to areas of dilation which would be favourable for developing permeability. At these sites (outer arc of the fold), vertical dykes and extension veins are likely to occur despite regional $\sigma_1$ being horizontal. In contrast, the areas of contraction (inner arc of the fold) have both local and regional $\sigma_1$ as subhorizontal. At these sites, the dominant extension vein sets and intrusions will be sub-horizontal (sills). Deep drilling at St Ives has defined both sills and dykes of porphyry (Mafic-type granites), consistent with their position with respect to the neutral surface of the regional antiform.

To the north of Wiluna, the Waroonga Fault System extends under relatively thin Proterozoic cover as far as Plutonic, and appears to maintain a similar geometrical relationship with the greenstone belts to its immediate east. The Plutonic gold deposit lies just to the east of the same general trend as the Bardoc Fault System and thus is likely the northernmost extension of the Golden Corridor. This northern extension of the Golden Corridor under cover may have significant area selection potential, as the region is dominated by significant gravity highs, indicative of a reasonable thickness of greenstone (Henson and Blewett, 2006).

### 3.3.4.5 Crustal structure inferred from wide-angle seismic reflection survey

A wide-angle vibroseis experiment was conducted simultaneously with the 01AGSNY1 deep seismic reflection transect using the same vibroseis sources (Fomin et al., 2003). The wide-angle survey was designed to supplement the deep seismic reflection studies with velocity information. The wide-angle technique using explosive or air-gun sources records seismic signals at very large offsets up to ~500 km depending on the input source energy and the geological environment. The seismic energy in wide-angle vibroseis experiments is designed specifically for the reflection technique. This energy is not sufficient to collect seismic signals at more then 70–80 km offsets. In our experiment, data were collected with an offset of 60–70 km to provide detailed velocity information within the top 14 km of the granite-greenstone succession between Leonora and Laverton (Fomin et al., 2006).

The velocity model derived from wide-angle data consists of four layers and shows substantial velocity variations in the upper crust of the Leonora-Laverton region (Figure 3.3.7c). In the top layer, the velocity increases from 5.0 km/sec to 5.9 km/sec in the upper 500 m. A 2 km thick

high-velocity body (6.4–6.7 km/sec) occurs in the western part of the wide-angle line. The top of the body is modelled at ~3 km depth and it is interpreted to represent mafic rocks within the greenstone succession. This high velocity body is underlain by lower velocity rocks (6.0–6.1 km/s), most likely granite-gneissic in composition. Thickness of this relatively low velocity layer varies from 4 to 8 km and it reaches ~12 km depth in the western part of the line, and it shallows to ~ 7 km in the east.

The velocity model of the middle and lower crust is based on wide-angle reflections only. Five boundaries were modelled and several versions tested for constant velocity values of 6.2, 6.5, and 7.0 km/sec. Assuming the velocity in the middle/lower crust increases from 6.4 to 6.5 km/s, the Moho depth is estimated as 33–34 km along the line. However, by changing the velocity in the middle/lower crust and shifting reflectors respectively up or down from the original positions, we can achieve similar matches for other velocity models. For the deepest reflections, the corresponding depths are estimated as 36–37 km at 7.0 km/s lower crustal velocity. Therefore, the total crustal thickness in the region can be speculatively estimated in the range 32–37 km, which is in general agreement with the seismic reflection estimate (Goleby et al., 2003) and the receiver function estimate (Reading et al., 2003). This lower crustal model is less constrained than the upper crustal model presented in Figure 3.3.7c. Lower crustal refractions and super-critical reflections from the Moho are required to better constrain it. The signal from the vibroseis source was too weak to record such refractions at larger offsets.

Comparison of the velocity model derived from wide-angle studies and interpretation of reflection section shows that there is no obvious correlation between interpreted seismic reflection horizons and velocity boundaries. The high-velocity body appears to be relatively transparent in the reflection seismic image, as there are far fewer reflective horizons interpreted in this area compared with the eastern and western flanks of the line. Such a correlation is suggestive of a relatively smooth, long wavelength velocity change around and within this body.

### Summary

This is the first Australian wide-angle experiment with high-density observations using a vibrator source supplemented by deep seismic reflection studies. Seismic velocities in the area are generally low, and are in agreement with largely felsic crust in this region. Joint interpretation of reflection and wide-angle data also shows that structural boundaries do not always follow lithological boundaries in our study area. For example, the upper crustal high-velocity body, likely to correspond to more mafic lithology than surrounding rock, appears to be void of structural boundaries mapped by reflection data.

The velocity model of the middle/lower crust, based on the wide-angle reflections only, is less constrained due to a low-level of energy from the vibroseis source for collecting data for large offsets. However, the estimates of crustal thickness of 32–37 km are consistent with other seismic techniques. The combination of wide-angle reflection and near-vertical reflection data has provided a more complete geological interpretation of the area.

## 3.3.4.6 Crustal structure inferred from magnetotelluric (MT) profiling

Magnetotellurics (MT) is a natural-source, electromagnetic (EM) geophysical method of imaging structures beneath the earth's surface. Natural variations in the earth's magnetic field induce electrical currents under the earth's surface so that joint measurements of the orthogonal components of the magnetic and electrical fields allow for the calculation of a frequency-dependent impedance tensor. This tensor provides inferences into the conductivity structure of the deep earth, which is influenced by structure as well as materials.

The technique operates through a wide range of frequencies (1/10,000 to 10,000 Hz) and is suitable for sounding a wide depth range of the earth (from upper crust to deep mantle). The source is from natural disturbances to the electromagnetic field, such as the solar wind, lightening strikes, and the diurnal variation of the earth's magnetic field (Cagniard, 1953).

The technique records time-series data of varying EM field. Recording long-period time series data requires longer recording times, which typically means that the longer the recording period (many days to months) the deeper the technique can image the earth. The long-wavelength data by their nature are smoothed. High resolution images are therefore not a feature of MT data in general.

The time series data are recorded as three components (x, y, z) of magnetic data (using a flux-gate magnetometer) and a two component (x, y) electrical field (Simpson and Bahr, 2005). However, for modelling and interpretation purposes, the commonly used data are: apparent resistivity and phase.

In 2006 the ***pmd*CRC*** conducted, in conjunction with Adelaide and Flinders Universities, the first regional deep-sounding MT survey for the Yilgarn Craton. A 130 km long MT line was acquired co-incident with the 91EGF01 seismic line (Figure 3.3.12). The survey was designed to transect the highly prospective Kalgoorlie Terrane and to determine whether the electrical properties of this lithosphere were different to adjacent less prospective areas.

A total of 26 stations were deployed at a spacing of 5–10 km apart, and were deployed for up to 2 days each. Despite some instrument failures, the final recovered data quality (18 stations) was generally of a high quality. The planned north-south cross line was not acquired, and the result was a 2D section that imaged to around 150 km depth (Figure 3.3.12). The time series MT data are processed to determine apparent resistivity and phase tensors and other associated processing parameters such as tipper, skewness and ellipticity, Lilly angle etc. It is inferred from the associated processing parameters such as tipper,

*Figure 3.3.12: True to scale comparison of the MT data (to 150 km depth) with an east-west slice of the tomographic 3D volume (to 350 km depth) along the strike of the seismic line. Note the conductive upper mantle coincides with an increase in shear-wave velocity in the tomography (purple colours) and the slower layer above (bluish colours) corresponds to a more resistive uppermost mantle (beneath the Moho). The warm red colours (in the MT) show the most conductive crust and mantle. The cool blue colours (in the MT) show the most resistive crust and mantle. The upper crust just below Kalgoorlie is highly conductive, in contrast to the largely resistive crust to the east and west. A zone of domed conductivity has been mapped in the upper mantle beneath Kalgoorlie. Both the mantle and upper crust conductivity anomalies point to the Kalgoorlie region being special in terms of electrical properties. The Moho is marked by the velocity change (green to blue) in the tomographic image. The reasons for a coincident increased conductivity and increased shear-wave velocity are uncertain.*

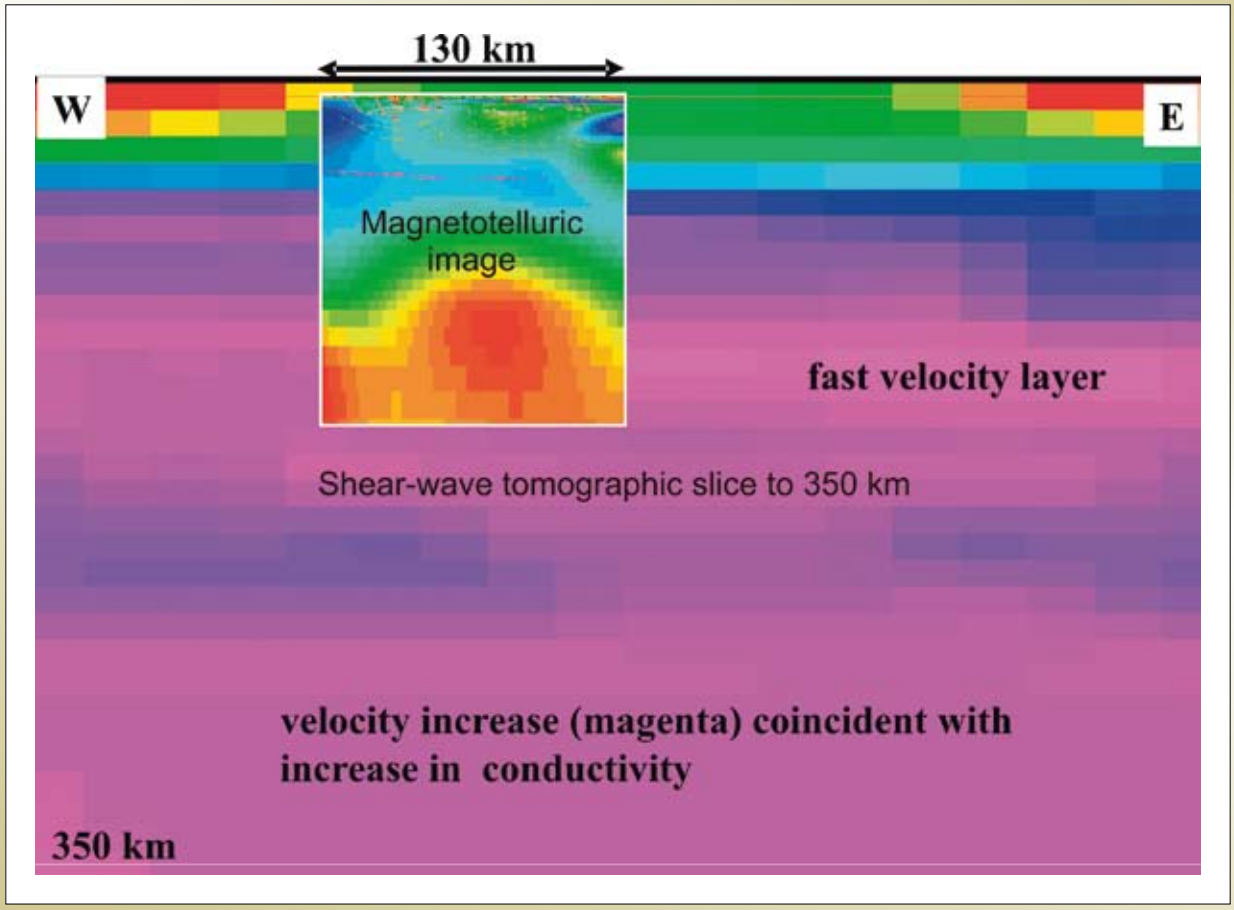

ellipticity that the MT data may be best described by 2D inverse modelling.

The conjugate gradient-based unconstrained 2D MT inversion algorithm (Mackie and Madden, 1993) is used to invert the MT data from the Kalgoorlie transect. The algorithm is packaged with the commercial software WinGLink™. Because a 2D inversion depends strongly on an *a priori* initial model, a parsimonious approach was taken while inverting and interpreting the MT data; in that a series of inversion runs (14 in total) was made with different initial models having externally imposed user defined constraints. The constraints are not 'hard', meaning that if a feature conflicts with the data then it is ignored by the modelling. A total of fourteen scenarios with various user defined constraints were obtained. We present here six such scenarios (Figure 3.3.13) (1) unconstrained, (4) moho added, (6) Ida Fault added, (8) lithosphere fixed at 130 km, (12), minor changes in modelling the deep dome (14) the final result. These six models all consistently map the same broad-scale features of the data that were observed in the original unconstrained inversion.

The unconstrained 2D inversion of the MT data provides a smoothed view of the electrical properties of the upper 150 km of the Kalgoorlie region (Figure 3.3.12). Features of the inversion include an anomalously conductive upper crust in the Kalgoorlie region, especially compared to the eastern (Kurnalpi Terrane) and western (Youanmi Terrane) ends of the section. The lower crust is typically resistive and there is a sense that the resistive Younami Terrane dips eastward beneath Kalgoorlie (consistent with the seismic reflection data). In the lower section of the model there is a highly conductive dome that arches upwards towards Kalgoorlie. The data are showing provincial differences in the electrical properties of the lithosphere and that the region beneath Kalgoorlie is anomalously conductive.

## Magnetotelluric data and implications for big systems

Highly resistive crust is mapped to the west of the Ida Fault, extending eastwards (honouring the seismically inferred dip) beneath Kalgoorlie. The Moho is approximated by a change in conductivity. The Kurnalpi Terrane (west) is also resistive and appears to dip back to the west. The highly prospective Kalgoorlie Terrane is

*Figure 3.3.13: Fourteen models were run and six of the main variations (following the successive addition of constraints) are shown. (1) unconstrained starting 2D inversion, (4) moho constraint added, (6) Listric Ida Fault constraint added, (8) lithosphere constraint added at 130 km, (12), minor changes in modelling the deep dome (14) the final result. These six models all consistently map the same broad-scale features of the data that were observed in the original unconstrained inversion. The Kalgoorlie region remains a particularly conductive section lithosphere. The MT technique may be an effective broad-pass exploration tool for mapping the passage of fluid (alteration) at the lithospheric scale.*

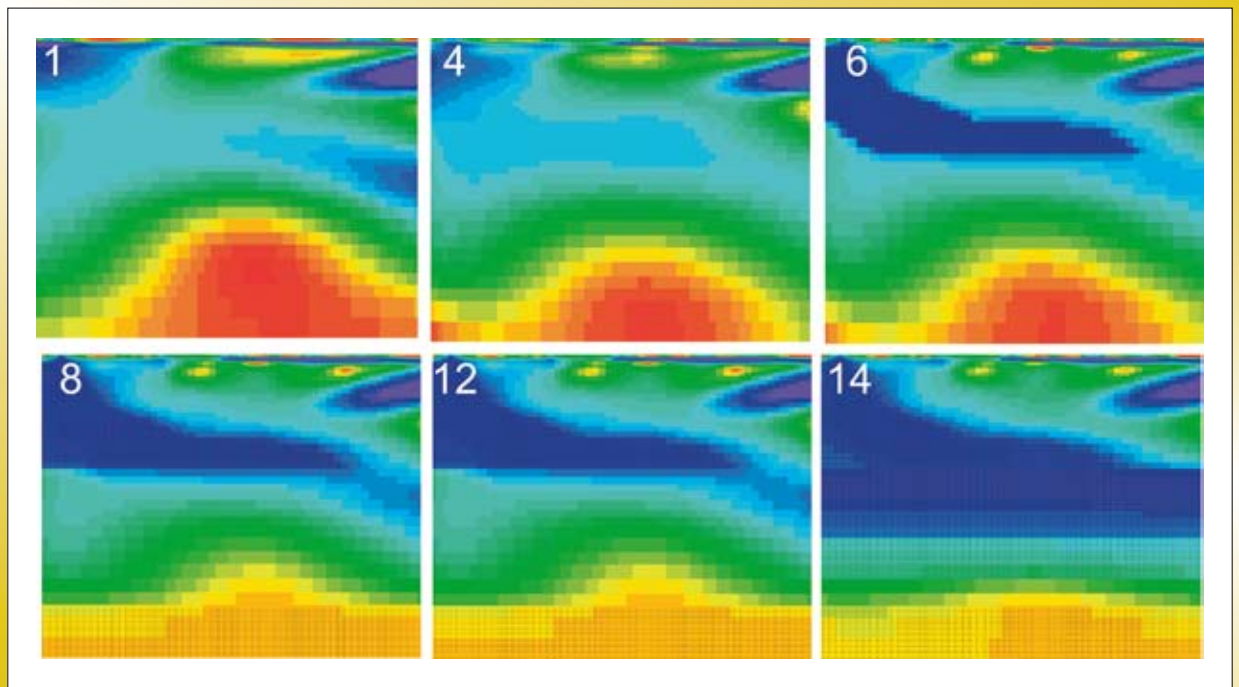

characterised by a conductive upper crust (including the Golden Corridor) and a dome or 'upwelling' of conductive mantle beneath (Figure 3.3.12). Modelling and sensitivity analysis maintains an anomaly beneath Kalgoorlie through the entire lithosphere, despite the modelling trying to smooth out the dome (Figure 3.3.13).

Causes of lithospheric conductivity is thought to be from a number of sources, including the presence of saline fluids (and magma), free hydrogen ions, graphite, sulphides and/or elevated temperatures (Haak and Hutton, 1986). At depth there is an overall increase in conductivity with temperature. The change in conductivity at around 130 km might correspond with a change in temperature (>1300°C) and mark the lithosphere-asthenosphere boundary. It is interesting to compare the MT data with the tomography at an equivalent depth (Figure 3.3.13). Around 120–130 km is the change to faster shear-wave velocity (>4.8 km/s). Despite the constrained modelling trying to flatten out the deep dome (of conductivity) in the MT data, it nevertheless remains as an anomaly and so is likely a real feature.

At shallower levels, the MT data reveal a highly conductive (up to 1000 times the resistive average crust) under Kalgoorlie. The source of the elevated conductivity is not known for certain. One source could be inter-grain graphite (Haak and Hutton, 1986) that could have been deposited at a redox boundary between an oxidised upper crust and deep reduced $CO_2$ bearing fluids (from the mantle?). The sources of conductivity in terms of other physical properties or mineralogy are debateable; however, the MT data indicate that it is an effective tool in pointing towards anomalous lithosphere. Similar relationships exist beneath the world-class Olympic Dam deposit in South Australia (Heinson et al., 2006), and so these data might be useful as first-order prospectivity tool to discriminate fertile from non-fertile terranes.

## 3.3.5 Integrated 3D architecture of a world-class gold mineral system: implications for predictive mineral discovery

One of the features of all these geophysical and geochemical techniques described above is their inherent uncertainty (non-uniqueness) in terms of what each tool is telling us about the architecture of the earth. One way of overcoming this inherent uncertainty and non-uniqueness is to integrate the methods and techniques. The advent of 3D mapping and visualisation tools has facilitated this integration and allowed powerful insights to be made from previous uncertain data.

The following discussion section will deal with four main topics of integration, viz: 1) nature of terrane boundaries, 2) lithosphere-asthenosphere boundary, 3) 3D architecture, and 4) what is special about Kalgoorlie.

### 3.3.5.1 Terrane boundaries

A number of datasets point to the fact that the Yilgarn Craton is made up of a collection of differing panels of rocks. One of the major boundaries in the craton is the Ida Fault, which is the boundary between the Youanmi and Kalgoorlie Terranes. The seismic reflection data (Figure 3.3.8) shows that there is a reflector that dips moderately to the east from an assumed surface projection (of the Ida Fault) to the mantle. The actual resolution of the data and tracing it to the surface is difficult and a west dip could interpreted from this surface point.

Independent data suggest that the boundary does dip east. The magnetotelluric data define a very resistive crust for the Youanmi Terrane, and this zone of resistive crust dips to the east beneath the conductive upper parts of the Kalgoorlie Terrane (Figure 3.3.12). The Sm-Nd data show that a major isotopic boundary coincides with the surface Ida Fault. However the isotopic boundary is a gradient of ages from 3.1 Ga to 2.9 Ga (Figure 3.3.6). A mixed age between the youngest terrane (Kurnalpi) to the east and the old Youanmi Terrane to the west may explain the intermediate ages for the Kalgoorlie Terrane. This mixing may have happened as both old (thinned wedge of Youanmi) and new crust was sampled by the ascending granites from which this map was derived (Czarnota et al., 2008). A similar conclusion may be reached by considering the zircon inheritance patterns in granites of the Kalgoorlie Terrane.

### 3.3.5.2 Lithosphere-Asthenosphere boundary (LAB)

On the basis of seismic studies, the thickness of the lithosphere of the Yilgarn Craton is estimated to be around 200 km (Simmons et al., 2002). Examination of the tomographic model of the Yilgarn does not show any

remarkable feature at this level (Figures 3.3.2, 3.3.14). It could be that the quality of the signal (due to poor radial coverage of source earthquakes) precludes the effective imaging of the lithosphere base. The magnetotelluric data provide an independent image of the LAB. The boundary has mechanical (rigid *vs.* ductile), chemical and thermal definitions (>1200°C). The MT data are effective in imaging thermal anomalies and there is a pronounced boundary at around 130 km depth (Figure 3.3.12). This conductivity interface also corresponds to an increase in shear-wave velocity in the tomography. The actual mineralogical composition of this fast layer is not certain, but it likely marks a change in chemistry. It might be the transition to the asthenosphere and therefore suggests that the Yilgarn has unusually thin lithosphere for an Archaean craton. If this is the case then it may explain the lack of success in diamond exploration – which requires a thick root below the graphite-diamond stability field.

### 3.3.5.3 3D architecture

Henson and Blewett (2006) constructed a 3D map of the EGST down to the base of the crust. The deep seismic reflection lines provided many of the architectural constraints. These constraints were tested (by forward modelling) the potential fields (Hitchman, 2006). The process of building the 3D map required construction of serial cross sections that 'stepped out' from the seismic constraints. These sections were also tested against the potential fields. A regional gravity inversion volume was constructed, with constraints from the numerous forward-modelled cross sections. The constrained inversion and was then integrated with the cross sectional skeleton to produce a series of surfaces and volumes of the 3D geology (Henson and Blewett, 2006).

One of the weaknesses of this 3D map was the reliance on the deep seismic reflection profiles, which are limited across the full 600 km length of the 3D map. The wide spread of receiver functions provide 1D velocity profiles through a column of crust and these provide independent assessment of the reliability of the regional 3D map. These data were not used in the original 3D map construction (and perhaps they should have been). The receiver functions mark velocity change with depth, and these changes are largely caused by mineralogical changes (different lithologies). Many of the changes are sharp (see Reading et al., 2003) and likely reflect significant lithological change across these velocity boundaries.

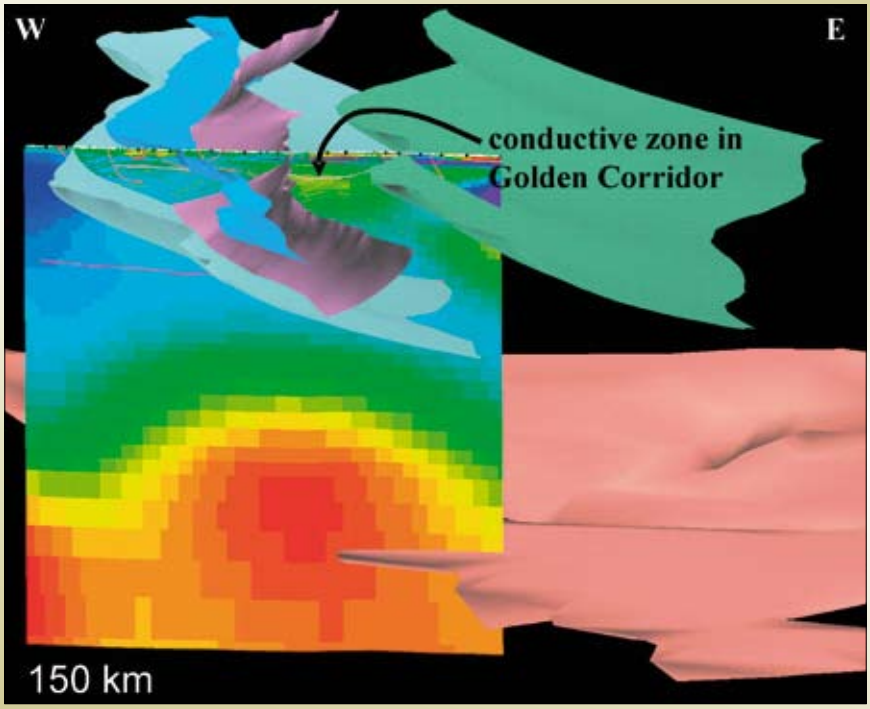


*Figure 3.3.14: View north of the integration of the regional 3D map (upper crustal fault architecture – Henson and Blewett, 2006), the unconstrained MT image (multi coloured cross section), and the >4.8 km/s shear-wave velocity isosurface from the broadband tomography (light brown shell in lower left). The conductivity dome coincides with the main edge in the velocity anomaly isosurface and points upwards towards a complex upper crustal architecture towards the Kalgoorlie region. The Golden Corridor hosts an anomalously conductive crust between the outward dipping master faults (green surface-Ockerburry Fault; purple surface-Bardoc Fault; light blue surface-Kunanalling Fault; aqua surface-Ida Fault). The fluid flow pathways from the mantle are uncertain but the Kalgoorlie region has a coincidence of many of these favourable indicators of a giant system.*

By converting the 1D velocity profiles to a 3D object (lath in 3D space) and visualising them with the 3D map a remarkable coincidence occurs. Many of the major faults mapped in the seismic reflection profiles and projected in 3D coincide with changes in velocity above and below (Figure 3.3.14). This coincidence suggests that the velocity changes (seen in teleseismic broadband data) are not artefacts and that the seismic reflection events are images of velocity changes (rock-type changes). This coincidence holds true for most of the major structures mapped in the 3D map. Minor differences between a receiver function profile and an interpreted fault occur at the greatest distance from a constraining seismic line. This suggests that the receiver functions are a valuable constraint and should be used in regional 3D map construction. It also demonstrates that the uncertainties in both techniques are probably less than the geophysicists fear, and that both disciplines have done an excellent job in imaging realistic earth structure.

#### 3.3.5.4 Kalgoorlie: the great coincidence

One of the goals of the project has been to understand why the giant mineral deposits (e.g., Kalgoorlie) are where they are (and not somewhere else). The question is answered by considering the whole system, and a critical part of the system is the role of architecture.

The Kalgoorlie region has a number of favourable architecture features at a range of scales, that all coincide to make this a special area. Many of these architectural features are poorly understood in terms of their process of formation. However, an empirical analysis is still warranted as these empirical relationships can be found elsewhere (favourable tracts) and may help in answering the question posed above.

At the largest of scales, the Kalgoorlie region lies above an edge or boundary in the fast shear-wave velocity anomaly in the mantle. The interpretation of this anomaly is controversial, however most of the world-class deposits in the Yilgarn are located vertically above these edges (Figure 3.3.2c). There are a number of edges in these data, particularly in the poorly exposed far east of the craton (opportunities?). For example, the recently discovered Tropicana deposit lies on one of these.

At the crustal scale, the long-wavelength (deep) horizontal derivatives (worms) in the gravity data show the large-scale mass distribution in the crust. The boundaries between these masses may be ancestral faults or deep weaknesses in the crust. These weaknesses are considered important in generating fluid pathways, for example the Great Basin (Carlin deposits) of the Western USA is a Mesozoic system sited above an ancient Archaean-Proterozoic boundary (Wooden et al., 1998). The presence of deep worms at a high angle to the regional trends suggests that there is an inherent deep complexity in the architecture of the Kalgoorlie Terrane. This was also a feature noted by Reading et al. (2007) in the receiver functions. The high-density of east-northeast trending Proterozoic dykes (at a high angle to the tectonic grain) may also mark a crustal weakness that was inherited during the original extension of the greenstone sequences (Blewett and Czarnota, 2007b). The Proterozoic extension (dyke emplacement) may simply be utilising ancient pathways that operated from ~2800 Ma onwards. These same pathways may have operated in the 2660–2630 Ma period of gold mineralisation (Blewett and Czarnota, 2007c).

Most of the large gold deposits lie in particular corridors of intermediate (3.0–2.9 Ga) mantle separation age crust (TDM), and this includes the linear belt of the Kalgoorlie Terrane that hosts the Kalgoorlie region. Other favourable areas (of this age) exist in the Murchison, Laverton and east of Yamarna (Figure 3.3.6). The reason for this age being favourable is not known, but it might suggest that some degree of crustal contamination is required.

Large faults, that transect the crust, are thought to be an important ingredient (pathway) for deep-sourced fluids/metals (Goleby et al., 2003). The seismic reflection technique has imaged the Ida and Ockerburry Fault Systems as major structures (terrane boundary) that transect the crust. These large faults also bound the favourable aged crust (TDM) that comprises the Kalgoorlie Terrane. The Kalgoorlie region is located between these structures in a gross regional antiform – the Golden Corridor (Henson et al., 2006). Domes and antiforms are empirically favoured structures (Bierlien et al., 2007), and their control on the architectures in the Kalgoorlie region can not be underestimated.

The passage of fluids and alteration is a good indication of the fertility of a mineral system. The magnetotelluric

(MT) data show that the lithosphere beneath Kalgoorlie is anomalously conductive. The source of this conductivity is not known, but deposition of graphite at redox boundaries is suitably conductive to account for the features. This, together with the development of an up-warped dome of mantle conductivity at the edge of a tomographic velocity anomaly, probably records the passage of fluid requires a favourable architecture and it is likely that the MT data records this.

### 3.3.6 Conclusions

The big mineral systems of the Archaean Yilgarn Craton, especially the gold system, have a footprint that can be observed in a range of datasets and observations, including geophysics, isotopes, tectono-stratigraphy and geochemistry. A convergence of favourable structures (architecture) at a range of scales from the upper mantle to the upper crust are permissive for the necessary large-scale mass and energy fluxes required to create a giant gold deposit. Of particular importance is the role of deep penetrating shear zones or faults that link the mantle with domes in the upper crust. Deep pathways beneath in the upper mantle and lower crust can be inferred from broad-band tomography and analysis of long wavelength gravity data. Geophysical data (e.g., MT and seismic) also provide evidence for the signatures of the flow of fluids through this architecture (the pathways) and they illustrate the scale of the systems is many orders of magnitude larger than the immediate deposit itself. Therefore, the mapping of these large systems provides insights into which terranes are likely to have hosted these big mineral systems. These tools and techniques can thus be analysed and applied to first-order terrane or area selection.

### 3.3.7 Acknowledgements

This paper has benefited from discussions with many people including Graham Heinson, Bruce Goleby, Jon Hronsky, Ian Tyler, Martin van Kranendonk, David Snyder, Stewart Fishwick, Graham Begg, Leonie Jones, and John Walshe. Inspiration for the MT survey came from Jon Hronsky. Terry Brennan and Malcolm Nicoll pulled together the database and built the 3D maps that were key to the results of this paper. This paper is a contribution to the Y4 ***pmd*CRC*** project and the sponsors are gratefully acknowledged for their support. Published with permission of the CEO's of the ***pmd*CRC*** and Geoscience Australia.

### 3.3.8 References

Ammon, C.J., 1990, On the non-uniqueness of receiver function inversions. Journal of Geophysical Research 95, 15303–15318.

Barley, M.E., Brown, S.J.A., Krapež, B. and Cas, R.A.F., 2002, Tectonostratigraphic Analysis of the Eastern Yilgarn Craton: an improved geological framework for exploration in Archaean Terranes. AMIRA Project P437A, Final Report.

Barnicoat, A.C., and the ***pmd*CRC*** Y4 team, 2007, Putting it all together: anatomy of a giant mineral system. *In* Kalgoorlie 2007 *edited by* F Bierlien and C Knox-Johnson: Geoscience Australia, Record 2007/14, 47–51.

Bierlein, F.P., Groves, D.I., Brown, W.M., Murphy, F.C., Fraser, S.J., and Lees, T., 2007, Scale-integrated prospectivity analysis: a pragmatic approach to exploration targeting in the Archaean Yilgarn Craton, Western Australia. In: Bierlein F.P., and Knox-Robinson, C.M., (editors), 2007. Proceedings of Geoconferences (WA) Inc. Kalgoorlie '07 Conference, 25–27 September 2007, Kalgoorlie, Western Australia. Geoscience Australia Record 2007/14, 221–225.

Blewett, R.S., 2006a, Chapter 8: a 5Q's synthesis and predictive mineral discovery. In: Blewett, R.S. and Hitchman, A.P. (eds) Final report, 3D geological models of the eastern Yilgarn Craton, Project Y2, September 2001 – December 2004. Geoscience Australia Record 2006/5, 165–170.

Blewett, R.S., 2006b, Crustal penetrating faults, do they or don't they. In: Blewett, R.S. and Hitchman, A.P. (eds) Final report, 3D geological models of the eastern Yilgarn Craton, Project Y2, September 2001 – December 2004. Geoscience Australia Record 2006/5, 216–218.

Blewett, R.S., Henson, P.R., Goleby, B.R., Champion, D.C. and Czarnota, K. 2006. Big mineral systems big signatures: insights into large scale tectonic processes in the Yilgarn Craton. Australian Earth Sciences Convention, GSA Conference Series (18th AGC), 94–95.

Blewett, R.S., and Czarnota, K., 2007a, The Y1-P763 project final report November 2005. Module 3 – Terrane Structure: Tectonostratigraphic architecture and uplift history of the Eastern Yilgarn Craton, Geoscience Australia Record 2007/15 112p. [DVD].

Blewett, R.S., and Czarnota, K., 2007b, Diversity of structurally controlled gold through time and space of the central Goldfields Superterrane – a field guide. Geological Survey of Western Australia Record 2007/19, 65p.

Blewett, RS, and Czarnota, K, 2007c, A new integrated tectonic framework of the Eastern Goldfields Superterrane, *in* Kalgoorlie 2007 *edited by* F Bierlien and C Knox-Johnson: Geoscience Australia, Record 2007/14, 27–32.

Brown, S.J.A., Krapež, B, Beresford, S.W., Cassidy, K.F., Champion, D.C., Barley, M.E., and Cas, R.A.F., 2001, Archaean volcanic and sedimentary environments of the Eastern Goldfields Province, Western Australia – a field guide. Western Australia Geological Survey Record, 2001/13, 66p.

Cagniard, L., 1953, Basic theory of the magneto-telluric method of geophysical prospecting, Geophysics, 18, 605–635.

Campbell, I.H., and Hill, R.I., 1988, A two-stage model for the formation of the granite-greenstone terrains of the Kalgoorlie-Norseman area, Western Australia: Earth and Planetary Science Letters, 90, 11–25.

Cassidy, K.F., Champion, D.C., McNaughton, N.J., Fletcher, I.R., Whitaker, A.J., Bastrakova, I.V., and Budd, A.R., 2002, Characterisation and metallogenic significance of Archaean granitoids of the Yilgarn Craton, Western Australia. Minerals and Energy Research Institute of Western Australia (MERIWA), Report No. 222, 514p.

Cassidy K.F., and Champion D.C., 2004, Crustal evolution of the Yilgarn Craton from Nd isotopes and granite geochronology: implications for metallogeny. In Muhling, J., et al., (Eds), SEG 2004, Predictive Mineral Discovery under Cover. Centre for Global Metallogeny, The University of Western Australia, Publication 33, 317–320.

Cassidy, K.F., 2006, Nd isotopic data and zircon inheritance patterns. In: Blewett, R.S. and Hitchman, A.P. (eds) Final report, 3D geological models of the eastern Yilgarn Craton, Project Y2, September 2001 – December 2004. Geoscience Australia Record 2006/5, 5–7.

Cassidy, K.F., Champion, D.C., Krapež, B., Barley, M.E., Brown, S.J.A., Blewett, R.S., Groenewald, P.B., and Tyler, I.M., 2006, A revised geological framework for the Yilgarn craton, Western Australia: Western Australia Geological Survey Record 2006/8p. 8 p.

Champion, D.C., and Sheraton, J.W., 1997, Geochemistry and Nd isotope systematics of Archaean granites of the Eastern Goldfields, Yilgarn Craton, Australia; implications for crustal growth processes. Precambrian Research, 83, 109–132.

Czarnota, K., Blewett R., Champion D.C., Henson P.A., and Cassidy K.F., 2007. Significance of extensional tectonics in orogenic gold systems: an example from the Eastern Goldfields Superterrane, Yilgarn Craton, Australia. In: Andrew C.L., et al., (eds) Digging Deeper. Proceedings of the Ninth Biennial Meeting of the Society for Geology Applied to Mineral Deposits Dublin, Ireland 20th-23rd August 2007. 1431–1434.

Czarnota, K., Champion, D.C., Cassidy, K.F., Goscombe, B., Blewett, R.S., Henson, P.A. and Groenewald, P.B., 2008, Geodynamics of the Eastern Goldfields Superterrane, *Part III this volume*.

Davis, B.K., Blewett, R.S., Squire, R. and Champion, D.C., 2008. Architectural and geodynamic controls during Au mineralisation at the Archaean Scotia-Kanowna Dome, Kalgoorlie Terrane, Western Australia, *Part III this volume*.

Dentith, M.C., Dent V.F. and Drummond, B.J., 2000, Deep crustal structure in the southwestern Yilgarn Craton, Western Australia: Tectonophysics, 325, 227–255.

Drummond, B.J., Goleby, B.R., Swager, C.P., Williams, P.R., 1993, Constraints on Archaean crustal composition and structure provided by deep seismic sounding in the Yilgarn Block. Ore Geology Reviews, 8, 117–124.

Drummond, B.J., Goleby, B.R., and Swager, C.P., 2000, Crustal signature of Late Archaean tectonic episodes in the Yilgarn craton, Western Australia: evidence from deep seismic sounding. Tectonophysics, 329, 193–221.

Fishwick, S., Kennett, B.L.N., and Reading, A.M., 2005, Contrasts in lithospheric structure with the Australian Craton- Insights from surface wave tomography. Earth and Planetary Science Letters, 2312, 163–176.

Fomin, T., Crawford, A. and Johnstone, D., 2003, A wide-angle reflection experiment with Vibroseis sources as part of a multidisciplinary seismic study of the Leonora-Laverton Tectonic Zone, Northeastern Yilgarn Craton. Exploration Geophysics, 34, 147–150.

Fomin, T. and Goleby, B.R., 2006, Lessons from joint interpretation of Vibroseis wide-angle and near-vertical reflection data in the Northeastern Yilgarn, Western Australia, Tectonophysics, 420, 301–316.

Fukao, Y., Widiyantoro, S., and Obasyashi, M., 2001, Stagnant slabs in the upper and lower mantle transition region. Reviews of Geophysics, 39, 291–323.

Goes, S., Govers, R, and Vacher, P., 2000, Shallow mantle temperatures under Europe from P and S wave tomography, Journal of Geophysical Research, 105, 11153–11169.

Goleby, B.R., Rattenbury, M.S., Swager, C.P., Drummond, B.J., Williams, P.R., Sheraton, J.E., and Heinrich, C.A., 1993, Archaean crustal structure from seismic reflection profiling, Eastern Goldfields, Western Australia. In: Williams, P.R., and Haldane, J.A., (Eds), Kalgoorlie'93 – An international conference on crustal evolution, metallogeny, and exploration of the Eastern Goldfields. Australian Geological Survey Organisation, Record 1993/54.

Goleby, B.R., Bell, B., Korsch, R.J., Sorjonen-Ward, P., Groenewald, P.B., Wyche, S., Bateman, R., Fomin, T., Witt, W., Walshe, J., Drummond, B.J., and Owen, A.J., 2000, Crustal structure and fluid flow in the Eastern Goldfields, Western Australia. Australian Geological Survey Organisation, Record, 2000/34: 109p.

Goleby, B.R., Blewett, R.S., Groenewald, P.B., Cassidy, K.F., Champion, D.C., Korsch, R.J., Whitaker, A., Jones, L.E.A., Bell, B., and Carlson, G., 2003, Seismic interpretation of the northeastern Yilgarn Craton seismic data. In: Goleby, B.R., Blewett, R.S., Groenewald, P.B., Cassidy, K.F., Champion, D.C., Jones, L.E.A., Korsch, R.J., Shevchenko, S., and Apak, S.N., (Eds), The 2001 Northeastern Yilgarn Deep Seismic Reflection Survey. Geoscience Australia, Record 2003/28, 143p.

Goleby, B.R., Blewett, R.S., Kennett, B.L.N., Jones, L.E.A., Korsch, R.J., Drummond, B.J., Fomin, T., Reading, A.M., Cassidy, K.F., Champion, D.C., Henson, P., Groenewald, P.B., Nicoll, M., and Brennan, T., 2004. Seismic: a key tool in understanding crustal architecture and mineral systems. In: Muhling, J., et al., (Eds), SEG 2004, Predictive Mineral Discovery Under Cover. Centre for Global Metallogeny, The University of Western Australia, Publication 33, 313–316.

Goleby, B.R., Blewett R.S., and Reading, A.M., 2006, Chapter 4: Tomographic studies of the Yilgarn lithosphere. In: Blewett, R.S. and Hitchman, A.P. (eds) Final report, 3D geological models of the eastern Yilgarn Craton, Project Y2, September 2001 – December 2004. Geoscience Australia Record 2006/5, 108–127. [DVD]

Graham, S., Lambert, D., and Shee, S., 2004, The petrogenesis of carbonatite, melnoite and kimberlite from the Eastern Goldfields Province, Yilgarn Craton. Lithos, 76, 519–533.

Griffin, W.L., O'Reilly, S.Y., Gaul, O., and Ionov, D.A., 1998, Secular variation in the composition of sub-continental lithospheric mantle: Geophysical and geodynamic implications, in Structure and Evolution of the Australian Continent, Geodyn. Ser., vol. 26, edited by J. Braun et al., pp. 1–26, AGU, Washington, D. C.

Griffin, W.L., Belousova, E.A., Shee, S.R., Pearson N.J. and O'Reilly, S.Y., 2004, Archaean crustal evolution in the northern Yilgarn Craton: U-Pb and Hf-isotope evidence from detrital zircons, Precambrian Research, 131, 231–282.

Groves, D.I., Barley, M.E. and Ho, S.E., 1989, Nature, genesis, and tectonic setting of mesothermal gold mineralization in the Yilgarn Block, Western Australia. In: Keays, R.R., Ramsay, W.R.H. and Groves, D.I., (eds), The geology of gold deposits: The perspective in 1988. Economic Geology Monograph 6, 71–85.

Haak, V. and Hutton, R., 1986, Electrical resistivity in continental lower crust. In: The nature of the lower continental crust. Geological Society Special Publications, 24, 35–49

Harris, L.B., Koyi, H.A., and Fossen, H., 2002, Mechanisms for folding of high-grade rocks in extensional tectonic settings. Earth-Science Reviews, 59, 163–210.

Heinson, G.H., Direen, N.G. and Gill R.M., 2006, Magnetotelluric evidence for a deep-crustal mineralizing system beneath the Olympic Dam iron oxide. Geology, 34, 573–576.

Henson, P.A., 2006, Chapter 2: An integrated geological and geophysical 3D map for the EYC. Chapter 4: Tomographic studies of the Yilgarn lithosphere. *In:* Blewett, R.S. and Hitchman, A.P. (eds) Final report, 3D geological models of the eastern Yilgarn Craton, Project Y2, September 2001 – December 2004. Geoscience Australia Record 2006/5, 39–52.

Henson, PA, Blewett, RS, Champion, DC, Goleby, BR, Cassidy, KF, Drummond, BJ, Korsch, RJ, Brennan, T, and Nicoll, M, 2005, Domes: the characteristic 3D architecture of the world-class lode-Au deposits of the Eastern Yilgarn: Economic Geology, Research Unit Contribution 64, p. 60.

Henson, P.A., and Blewett, R.S., 2006, Question 5 – metal transport and depositional processes. *In:* Blewett, R.S. and Hitchman, A.P. (eds) Final report, 3D geological models of the eastern Yilgarn Craton, Project Y2, September 2001 – December 2004. Geoscience Australia Record 2006/5, 242–252.

Henson, P.R., Champion, D.C., Blewett, R.S., and Goleby, B.R. 2006, The Golden Corridor: defining the architecture of the Yilgarn Craton's best "gold real estate". Australian Earth Sciences Convention, GSA Conference Series (18th AGC), 95 p.

Henson, PA, Blewett, RS, Champion, DC, Goleby, BR, and Czarnota, K, 2007, How does the 3D architecture of the Yilgarn control hydrothermal fluid focussing, *in* Kalgoorlie 2007 *edited by* F Bierlien and C Knox-Johnson: Geoscience Australia, Record 2007/14, 57–61.

Hill, R.I., Chappell, B.W., and Campbell, I.H., 1992, Late Archaean granites of the southeastern Yilgarn Block, Western Australia; age, geochemistry, and origin. Special Paper – Geological Society of America,.272, 211–226.

Hitchman, A.P., 2006, Potential-field data sets for building 3D maps. *In:* Blewett, R.S. and Hitchman, A.P. (eds) Final report, 3D geological models of the eastern Yilgarn Craton, Project Y2, September 2001 – December 2004. Geoscience Australia Record 2006/5, 53–73

Jordan, T.H., 1978, Composition and development of the continental tectosphere, Nature, 274, 544–548.

Jordan, T.H., 1988, Structure and formation of the continental tectosphere, Journal of Petrology Special Lithosphere Issue, 11–37.

Krapež B., and Barley, M.E., 2007, Late Archaean synorogenic basins of the Eastern Goldfields Superterrane, Yilgarn Craton, Western Australia Part III. Signatures of tectonic escape in an arc-continent collision zone. Precambrian Research, in press.

Mackie, R. L. and Madden, T. R., 1993, Three dimensional magnetotelluric inversion using conjugate gradients: Geophysical Journal International, 115, 215–229.

Morris, P.A. and Witt, W.K., 1997, Geochemistry and tectonic setting of two contrasting Archaean felsic volcanic associations in the Eastern Goldfields, Western Australia. Precambrian Research, 83, 83–107.

O'Reilly, S.Y., Griffin, W.L., Poudjom Djomani, Y.H., and Morgan, P., 2001, Are lithospheres forever? Tracking changes in subcontinental lithospheric mantle through time: GSA Today, 11, 4–10.

Percival, J.A., Sanborn, B.M., Skulski, T., Stott, G.M., Helmstaedt, H. and White, D.J., 2006, Tectonic evolution of the western Superior Province from NATMAP and Lithoprobe studies. Canadian Journal of Earth Sciences 43, 1085–1117.

Price, N.J., and Cosgrove, J.W., 1990, Analysis of geological structures. Cambridge University Press, Great Britain, 80p.

Ramsay, J.G., 1987, The Techniques of Modern Structural Geology, Volume 2: Folds and Fractures. Academic Press Inc, London.

Reading, A.M., Kennett, B.L.N., and Dentith, M.C., 2003, Seismic structure of the Yilgarn Craton, Western Australia. Australian Journal of Earth Sciences, 50, 427–438.

Reading, A.M., Kennett, B.L.N., and Goleby B.R., 2007, New constraints on the seismic structure of West Australia:

Evidence for terrane stabilization prior to the assembly of an ancient continent? Geology 35, 379–382.

Rudnick, R.L., 1995, Making continental crust. Nature, 378, 571–578.

Rudnick, R.L., and Fountain, D.M., 1995, Nature and composition of the continental crust: A lower crustal perspective. Reviews in Geophysics, 33,267–309.

Simons, F.J., van der Hilst, R.D., Montagner, J-P., and Zielhuis, A., 2002, Multimode Rayleigh wave inversion for heterogeneity and azimuthal anisotropy of the Australian upper mantle. Geophysical Journal International, 151, 738–754.

Simpson, F. and Bahr, K., 2005, Practical Magnetotellurics, Cambridge University Press, 252p.

Smithies, R.H., and Champion, D.C., 1999, Geochemistry of felsic igneous alkaline rocks in the Eastern Goldfields, Yilgarn Craton, Western Australia: a result of lower crustal delamination? – implications for Late Archaean tectonic evolution. Journal of the Geological Society of London, 156, 561–576.

Swager, C.P., and Nelson, D.R., 1997, Extensional emplacement of a high-grade granite gneiss complex into low-grade greenstones, Eastern Goldfields, Yilgarn Craton, Western Australia. Precambrian Research, 83, 203–219.

Swager, C.P., Goleby, B.R., Drummond, B.J., Rattenbury, M.S., and Williams, P.R., 1997, Crustal structure of granite-greenstone terranes in the Eastern Goldfields, Yilgarn Craton, as revealed by seismic reflection profiling. Precambrian Research, 83, 43–56.

Van der Hilst, R.D., Kennett, B.L.N., Christie, D., and Grant, J., 1994, SKIPPY: Mobile broad-arrays to study the seismic structure of the lithosphere and mantle beneath Australia, *Eos Trans. AGU*, *75*, 177 and 180, 181.

Van der Pluijm, B.A., and Marshak, S., 1997. Earth Structure: An Introduction to Structural Geology and Tectonics. WCB/McGraw-Hill, USA.

Van Gerven, L., Deschamps, F., and van der Hilst, R.D., 2004, Geophysical evidence for chemical variations in the Australian Continental Mantle, Geophysical Research Letters, 31, L17607.

Van Kranendonk, M.V.K., 2007, Litho-structural development of the Northern Murchison Domain within the context of Yilgarn craton evolution. In: Bierlein F.P. and Knox-Robinson C.M., (editors), Proceedings of Geoconferences (WA) Inc. Kalgoorlie '07 Conference, 25–27 September 2007, Kalgoorlie, Western Australia. Geoscience Australia Record 2007/14, 23–26.

Williams, P.R., Currie, K.L., 1993, Character and regional implications of the sheared Archaean granite-greenstone contact near Leonora, Western Australia. Precambrian Research 62, 343–367.

Wingate, M.T.D., 2007, Proterozoic mafic dykes in the Yilgarn Craton. In: Bierlein F.P. and Knox-Robinson C.M., (editors), Proceedings of Geoconferences (WA) Inc. Kalgoorlie '07 Conference, 25–27 September 2007, Kalgoorlie, Western Australia. Geoscience Australia Record 2007/14, 80–84.

Wooden, J.L., Kistler, R.W. and Tosdal, R.M., 1998, Pb isotopic mapping of crustal structure in the Northern Great Basin and relationships to Au Deposits. Contributions to the Gold Metallogeny of Northern Nevada, Open-File Report 98–338. 14 p.

## 3.4 Question 3: Multiple fluid reservoirs in Eastern Yilgarn gold systems

**J.L., Walshe, P., Neumayr, J., Cleverley, K., Petersen, A., Andrew, D., Whitford, G.R., Carr, M., Kendrick, C. Young, and S. Halley**

### 3.4.1 Introduction

Traditionally, models of formation of Archaean lode Au deposits have assumed one dominant aqueous carbonic fluid ($H_2O - CO_2 - NaCl \pm H_2S \pm CH_4 \pm N_2$) in the system with the $CO_2$ concentration in the fluid taken as >5 mole percent (Groves et al., 2003; Hagemann and Cassidy, 2000). In these single-fluid models Au is considered to have been transported by a reduced sulphur complex in a near neutral fluid with Au deposition occurring through fluid-rock reaction or fluid boiling. It is now recognised that asymmetric, kilometre-scale alteration footprints can be identified in the Au systems of the Yilgarn Craton of Western Australia and Au mineralisation occurs preferentially within or subjacent to boundary zones between contrasting alteration domains (Halley, 2007; Neumayr et al., 2003; Neumayr et al., 2005; Neumayr et al., 2008; Walshe et al., 2003). It is difficult to reconcile these large-scale, mineralogical and geochemical dispersion patterns with single fluid mineralisation models. Here it is argued that multiple-fluid models are required to explain the diversity of mineral alteration assemblages and patterns of mineral zoning at deposit to district scale. It is argued that it was the interplay between chemically contrasting fluids and host rocks that sustained physico-chemical gradients in the system. These gradients include redox, pH, as well as in the activity of S, C, Cl and water. Ultimately it was these physico-chemical gradients that provided the chemical drive for gold transport and deposition in the system.

The chapter is subdivided into four major sections. Section 1 begins with a summary of the spatial and temporal associations of mineral alteration assemblages at deposit to district scales, noting in particular the association of oxidised assemblages with intrusive complexes in the gold camps of the Eastern Goldfields Superterrane. Consideration of mineral stability in terms of redox/pH conditions of formation, coupled with fluid inclusion data, leads to a discussion of the evidence for physico-chemical gradients in the gold systems. It is argued that three distinct fluid types or end-members fluids are required to explain the fluid inclusion, mineralogical and isotopic constraints, the asymmetry in deposit to district-scale alteration and provide the chemical potential to sustain the physico-chemical gradients in the gold systems.

Fluid 1 is modelled as a background or ambient aqueous fluid with low concentrations of salt and $CO_2$.

Fluid 2 is modelled as an anhydrous carbonic fluid of magmatic affinity with significant levels of $SO_2$ and $CO_2$ sourced from the mantle.

Fluid 3 is modelled as a hydridic deep-Earth fluid that transported volatile species such as $CH_4$, $N_2$ as well as $H_2$, $H_2S$, HCl ±HF, precious metals and hydrides of alkali and alkali-earth elements e.g. Na and Mg.

Section 2 summarises the stable and radiogenic isotopic constraints on the nature of the end-member fluids and chemical gradients. The stable isotopes are used to identify salient chemical reactions between volatile species ($SO_2$, $CH_4$, $CO_2$, $H_2$, $H_2O$). These concepts are largely developed using a significant legacy data, particularly for the stable isotopes, but are linked to a developing understanding of zoning of both stable isotopic compositions and minerals/mineral assemblages. Section 3 is a discussion of the concept and characteristics of end-member fluids, consistent with the mineralogical, isotope and fluid inclusion constraints as well as the geological and geophysical constraints. Finally section 4 considers the possible nature of deep-Earth hydridic fluids and the likely chemical and mineralogical imprint of such fluids on the Earth's crust.

### 3.4.2 Section 1: Alteration mineralogy and fluid inclusion constraints on end-member fluids and chemical gradients

#### 3.4.2.1 Deposit- to district-scale zoning patterns

At the lode-scale alteration patterns are commonly symmetric as documented by previous studies (Eilu and Mikucki, 1996). Asymmetry in mineral zoning is most obvious at the camp or district scale. Integrating the deposit to camp-scale information makes it apparent that Au deposits occur where significant mineralogical zoning occurs. In the camps and deposits in which

magnetite, pyrite and pyrrhotite occur as alteration products, the camp-scale zoning is manifest in terms of the distribution of pyrrhotite and hydrothermal magnetite. Two main domains with respect to redox conditions of the hydrothermal fluids are distinguished: 1) Oxidised (pyrite-magnetite, pyrite-haematite assemblages) domains are centred on inferred intrusive complexes, and 2) reduced (pyrrhotite-pyrite assemblages) domains broadly flank the oxidised domains (Neumayr et al., 2008).

This reduced–oxidised classification is supported by the sulphur and carbon isotope data as well as the fluid inclusion data that provides evidence of highly oxidised and highly reduced fluids (Figure 3.4.1) Deposits can be

*Figure 3.4.1: Camp-scale redox zoning for the St Ives camp (after Neumayr et al., 2007).*
*A) Geological map of the St Ives gold camp showing the location of the major gold deposits.*
*B) Geological map of the Central Corridor in the St Ives gold camp showing the distribution of magnetite-pyrite (oxidised) and pyrrhotite-pyrite (reduced) alteration assemblages in mafic host rocks. Note that high-grade (>100 g/t) gold intersections are located at the boundary between reduced and oxidised domains. Open pit names: 1) Mars, 2) Agamemnon, 3) North Revenge Kapai, 4) Revenge, 5) West Revenge, 6) Delta/South Delta, 7) South Revenge, 8) Thunderer, 9) North Orchin, 10) Orchin, 11) Victory/Defiance, 12) Britannia/Sirius, 13) Africa.*
*C) Geological map of the Victory-Defiance area in the St Ives gold camp showing the distribution of magnetite (oxidised) and pyrrhotite (reduced) bearing alteration assemblages and sulphur isotope data. Sulphur isotopes have been analysed in pyrite from ore zones in the Victory deposit (S isotope compilation: Hodkiewicz 2003), except for one pyrrhotite sample from a reduced pathway SE of the Conqueror mineralization (this study). The latter contains the main mineralization at Conqueror. Note that the S isotopes indicate spatially a redox change from oxidised (negative $\delta^{34}S$) to reduced (positive $\delta^{34}S$) in the ore fluid exactly where sulphide-oxide mineral mapping indicates a redox change in the broad scale fluid flow. High-grade (>100 g/t Au) gold intersections are located proximal to the domain boundary of reduced and oxidised fluids as indicated in both the S isotope and sulphide-redox mineral mapping data sets.*
*D) Cross section of the Victory-Defiance deposit showing reflection seismic data and the distribution of magnetite (oxidised) and pyrrhotite (reduced) bearing alteration assemblages. Secondary magnetite occurs above the Victory – Defiance intrusive Complex mapped by the "washed-out" domains in the seismic reflection data. Position of section shown on Figure 3.4.1C. Abbreviations: BFL: Black Flag Beds, DCB: Devin Consols Basalt, DFD: Defiance Dolerite, KAM: Kambalda Komatiite, KSL: Kapai Slate, PBS: Paringa Basalt.*

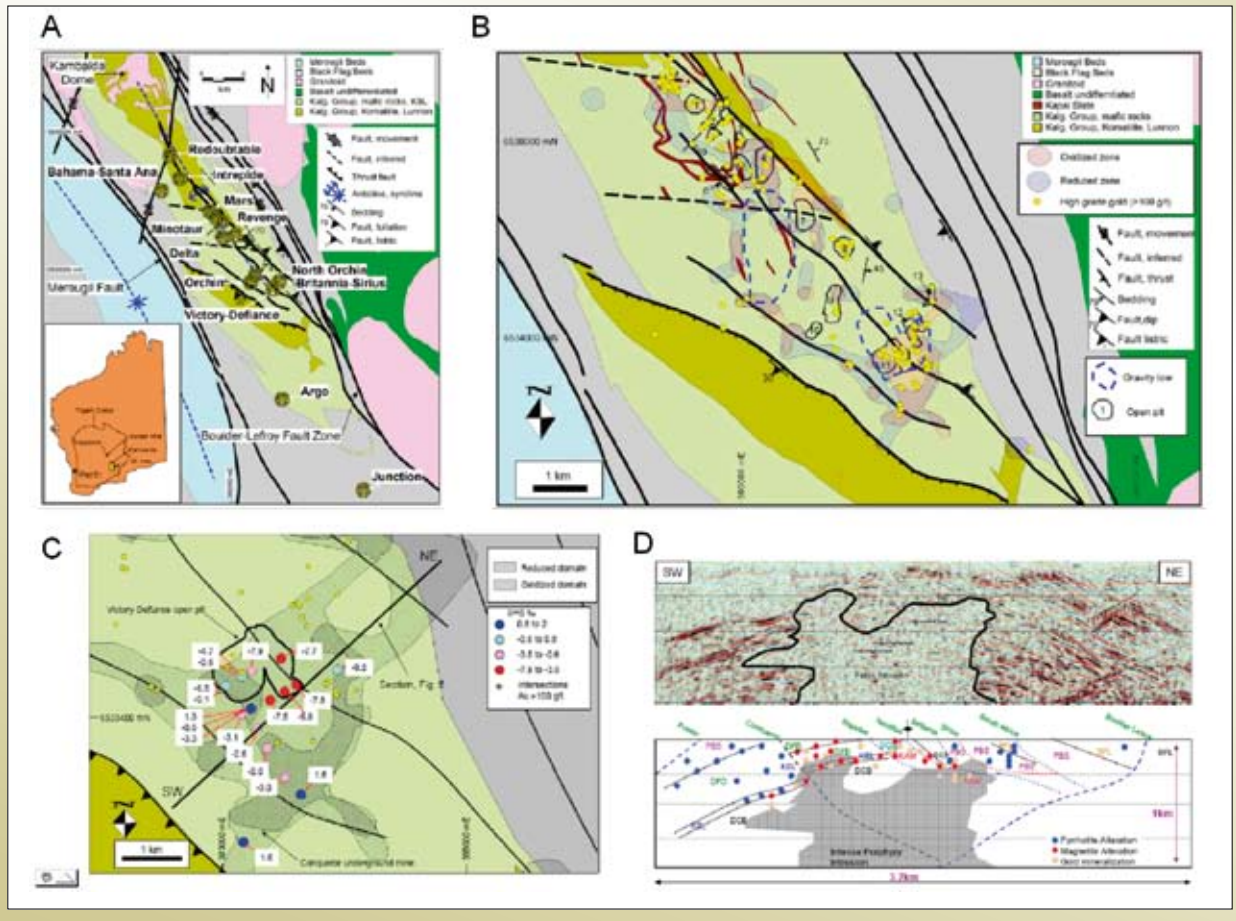

informally classified as oxidised or reduced depending on the dominant redox assemblage. Commonly both reduced and oxidised assemblages are found within or proximal to both styles of deposits. In the central corridor of the St Ives camp deposits are oxidised (e.g., Victory-Defiance; Revenge). Reduced deposits (Argo, Junction and Cave Rocks) occur to the west and southwest of the central corridor. There is a spatial association of magnetite ± haematite-bearing alteration assemblages of the central corridor with intrusive complexes, defined by gravity lows, by zones of poor reflectivity in seismic profiles and diamond drilling. Alteration assemblages in the Victory-Defiance area of the central corridor are also zoned vertically with anhydrite veining becoming common at depth. Similar changes in mineralogy have been observed at the lode scale in the Victory-Defiance complex, Conqueror deposit and Bellephoron prospects in the St Ives camp implying a link between processes that formed the district-scale alteration and processes operating at the lode-scale.

District-scale asymmetry in mineral zoning in the vicinity of the Kanowna Belle deposit is observed in the white mica chemistry (Figure 3.4.2). To the north of Kanowna Belle, in the footwall to the Fitzroy shear zone is a large (~2 km diameter) cell of high AlOH wavelength white mica and high mica crystallinity. The Kanowna Belle deposit coincides with a zoning in white-mica chemistry from phengite in the footwall (defined by high λ AlOH wavelengths, > 2208 ηm) to muscovite-paragonite in

*Figure 3.4.2: Zoning in white mica chemistry, Kanowna Belle deposit and district.*
*A) Simplified geology of the Kanowna Belle district.*
*B) Map of white mica AlOH wavelengths for the Kanowna Belle district. Warm colours: long wavelength (phengite). Cool colours: short wavelength (muscovite – paragonite). Note the strong gradient in wavelengths across the Kanowna Belle deposit from footwall (long wavelength) to hangingwall (short wavelength). The Lowes Shoot occurs within the long wavelength domain. Map locality shown on Figure 3.4.2A.*
*C) 3D model of white mica AlOH wavelengths for the Kanowna Belle deposit. Lowes Shoot shown in white. Red/brown: phengite Blue: muscovite – paragonite*

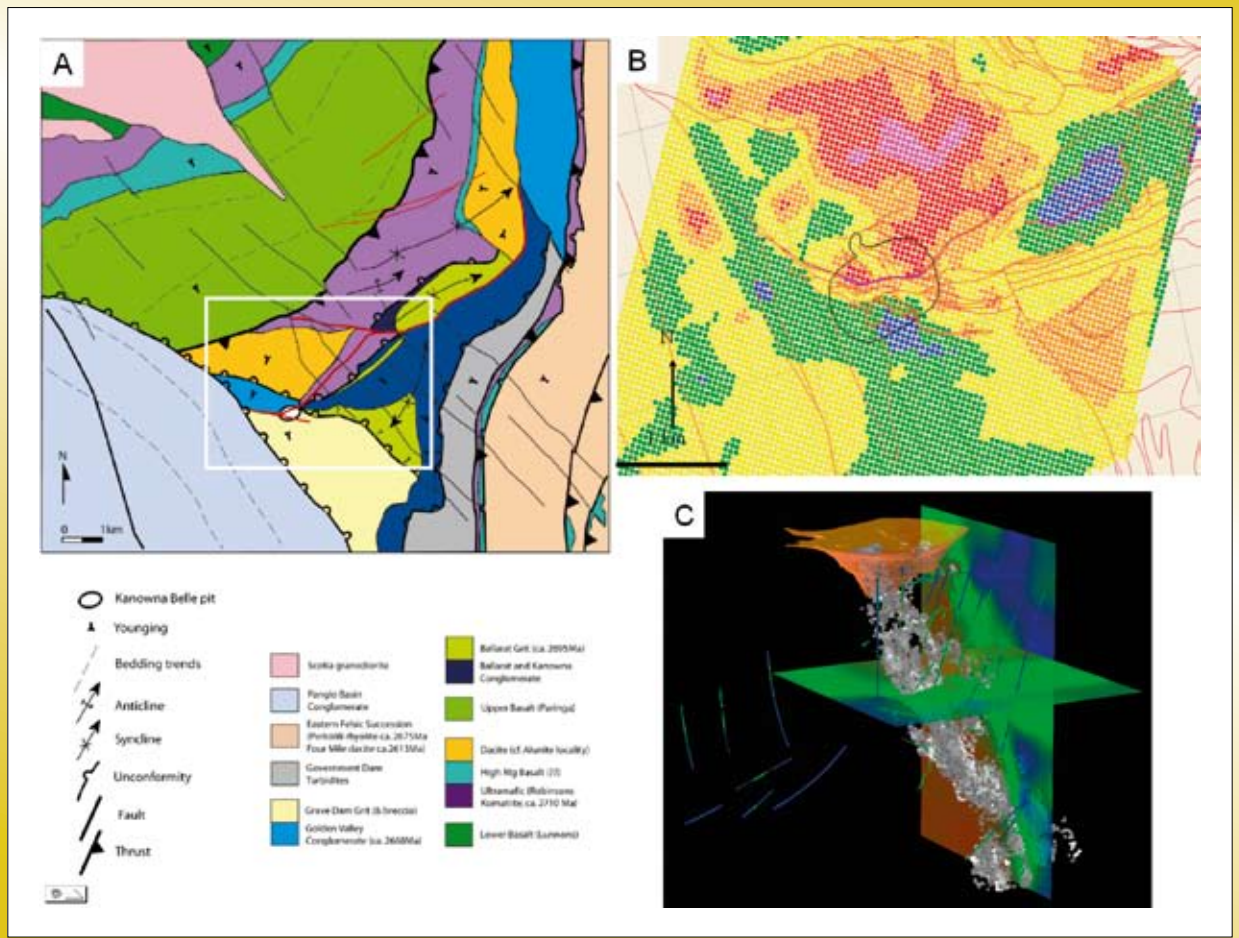

the hangingwall of the Fitzroy Fault (low λ AlOH wavelengths, 2190–2200ηm). District-scale PIMA data sets reveal that muscovite ± paragonite assemblages are focussed on major structures.

In the Laverton district, zoning in white mica chemistry and reduced oxidised assemblages are correlated. Magnetite occurs with phengite and muscovite-paragonite occurs with pyrrhotitic assemblages or chlorite ± chloritoid assemblages without magnetite. The Wallaby deposit is centred on a pipe of magnetite alteration (Figure 3.4.1) as well as occurring on the margins of ~2 km x 2 km cell of phengitic white mica, south and west of the deposit. Domains of muscovite-paragonite ± chlorite ± chloritoid occur within the district over an area ~ 20 km x 10 km, with much of the alteration focused along major structures. These domains of magnetite loss are considered domains of relatively acidic fluid conditions compared with zones of albite/phengite/magnetite stability and at least at the district-scale there appears to be an inverse correlation between acidic and oxidised fluid conditions (Figure 3.4.3).

More generally, the associations of reduced-oxidised assemblages, intrusive complexes and phengite-muscovite/paragonite assemblages may be inferred from the geophysical data sets, at least in sequences of mafic/ultramafic rocks. Gravity lows define the intrusive complexes (see the St Ives paper) and spatially associated

*Figure 3.4.3: Zoning in white mica chemistry and magnetite/pyrrhotite in the Wallaby district.*
*A) Geology environment of the Wallaby deposit, north to the Mt Margaret Dome.*
*B) Map of white mica AlOH wavelengths for the Wallaby district. Warm colours: long wavelength (phengite) focused south and west of the deposit. Cool colours: short wavelength (muscovite – paragonite) well – developed in a broad E-W band and focused on N-S trending structure.*
*C) Magnetic image of the Wallaby district showing the magnetic response of the hydrothermal magnetite in the Wallaby pipe. More subtle magnetic zones around the pipe reflect domains of pyrrhotite alteration and zones that have lost magnetic signature are interpreted as alteration zones of muscovite-paragonite ±chlorite ± chloritoid, depleted in magnetite and pyrrhotite.*

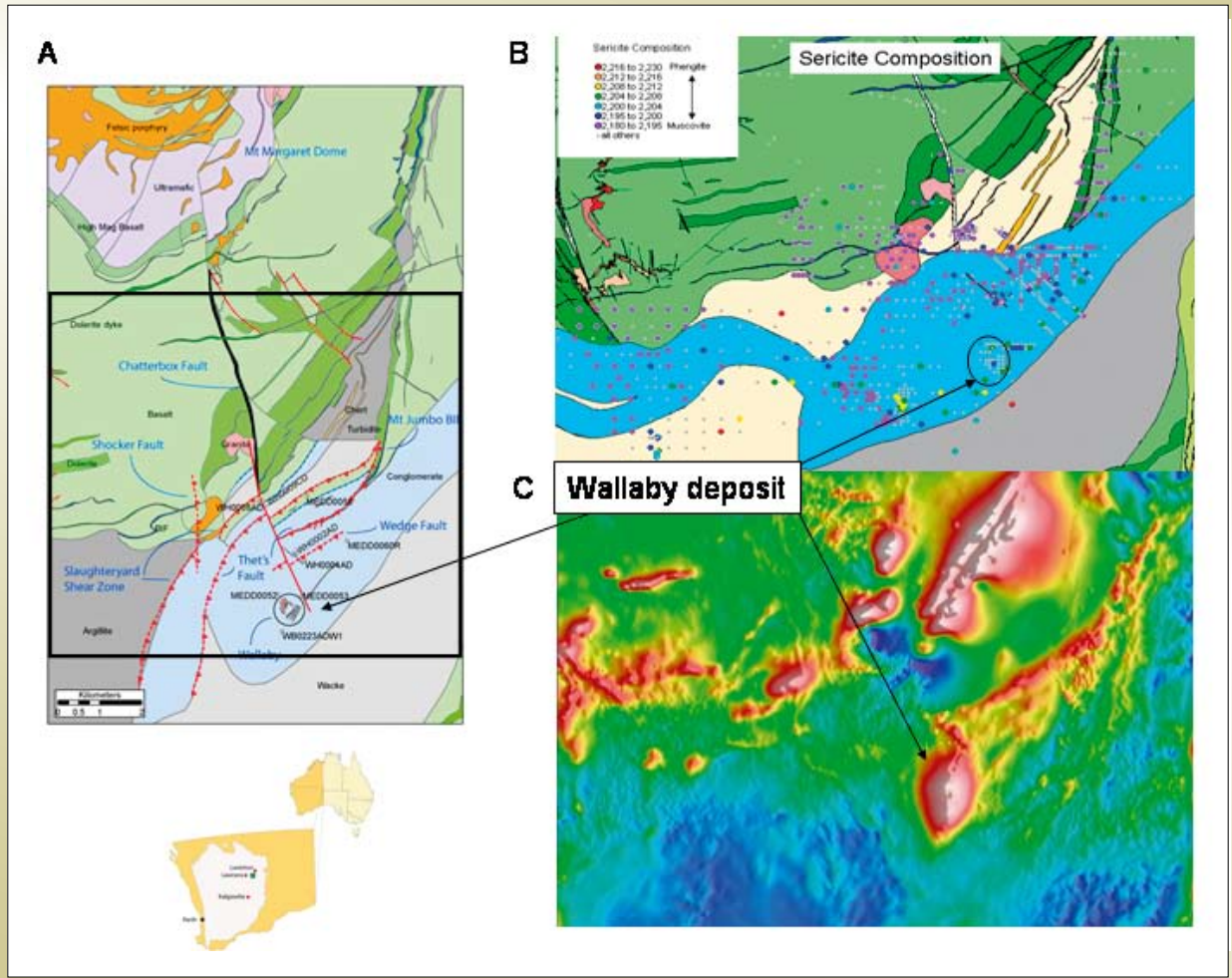

magnetic highs define hydrothermal magnetite. More subtle magnetic zones defining domains of pyrrhotite alteration and zones that have lost magnetic signature may be interpreted as alteration zones of muscovite-paragonite ±chlorite ± chloritoid, depleted in magnetite and pyrrhotite.

### 3.4.2.2 Constraints on temporal evolution of fluids

Combined studies of mineral paragenesis and nature of fluid inclusions in quartz, carbonate and albite in the St Ives Camp have provided a picture of the temporal evolution of fluids in the Au systems (Petersen et al., 2007; Petersen et al., 2005) and importantly linked fluid evolution to mineralogy. The paragenesis is subdivided into three main stages with each stage recording distinct fluid compositions.

**Stage 1:** represents an early epidote - calcite - magnetite - pyrite - chalcopyrite - quartz alteration closely associated with porphyry contacts. Epidote alteration is particularly well developed in the Devon Consols Basalt, immediately below the Kapai Slate. Fluid inclusions contain predominantly aqueous fluids with low salinity.

**Stage 2:** is the main Au deposition stage and is subdivided into reduced and oxidised assemblages on the basis of alteration mineralogy:

**stage 2A:** pyrrhotite - carbonate - amphibole - biotite ± Au ± quartz ± arsenopyrite ± pyrite alteration that reflects a relatively reduced fluid

**stage 2B:** albite - carbonate – pyrite ± Au ± magnetite ± haematite alteration that reflects a relatively oxidised fluid

**Stage 3:** is dominated by hydrothermal quartz that occurs at veins and breccias and texturally postdates both albite and carbonate. Fluid inclusions in the late stage are aqueous with large variations in the $H_2O/CO_2$ ratios and salinities (0 to up to 37 wt% equiv. NaCl). Daughter crystals of halite and/or carbonate occur.

Cross-cutting macro textures reveal that where both stage 2A and 2B occur spatially together, they are synchronous but of later timing than the epidote dominant alteration assemblage. Primary fluid inclusions in stage 2A are reduced, containing $CH_4 \pm N_2 \pm CO_2$ whereas primary fluid inclusions in stage 2B are high temperature, low salinity carbonic fluids ($CO_2 >> H_2O$) without $CH_4$.

This evolution of fluids in the St Ives Camp is used as a template for discussion of the nature of fluids in the Au systems of the Eastern Goldfields province, although it is acknowledged that it may not represent the complete picture. In particular questions of temporal versus spatial evolution of alteration assemblages and inclusion types are still being resolved.

The bulk of the gold precipitation at St Ives appears to predate quartz deposition although locally gold occurs within quartz veins. Elsewhere in the Eastern Goldfields Superterrane (e.g., Kundana and Sunrise Dam deposits) gold occurs within laminated and brecciated quartz veins. In these settings gold is commonly associated with base metal sulphides and tellurides. If quartz veins represent time markers through the Eastern Goldfields Superterrane (perhaps equating to particular geodynamic events) then possibly gold ± base metals hosted within quartz veins represents a later event (s). The deformation history of the province allows for at least 3 distinct gold events (Czarnota et al., 2008).

### 3.4.2.3 Mineralogical constraints on redox and pH

The silicate, oxide, carbonate, sulphide and sulphate minerals that formed within the gold systems, in either proximal (within metres to 100's metres of gold lodes) or distal (100s of metres to kilometres from gold lodes) include:

- Quartz, andalusite, albite, K-feldspar,
- Biotite, chlorite, chloritoid, amphibole, talc, muscovite-phengite, paragonite, tourmaline, epidote
- Haematite, magnetite
- Pyrite, pyrrhotite, arsenopyrite, loellingite
- Calcite, dolomite
- Anhydrite, celestine

The thermo-chemical stabilities of these minerals is controlled by a large number of parameters including temperature and pressure, bulk composition of the host rocks and fluid parameters (redox, pH, activities of Na, K, Mg, Ca, Cl, $H_2O$, S and C). Previous studies have established that C - S - Na - K - O-H metasomatism

is necessary to account for observed abundances in carbonate, sulphides, albite and biotite implying that the occurrences of most minerals is in some way influenced by the composition of the fluids. Fe mobility has been shown to be limited and where it occurred is accounted for from Fe was derived from local sources such as Fe-rich dolerites and iron stones.

The district scale Fe- sulphide – oxide zoning coupled with fluid inclusion data summarised above imply that significant gradients in fluid redox and pH occurred at the time of gold mineralization. Hence a key question is influence of redox and pH on the relative stability of the silicate, oxide, carbonate, sulphide and sulphate minerals and mineral assemblages that formed within the gold systems. Redox/pH effects on the stability of silicate/oxide/sulphide assemblages can be determined by assuming fluids remain saturated with respect to Fe mineral (haematite, magnetite, pyrite, pyrrhotite, ferro-tremolite) and expressing reactions between Fe-silicates and non-Fe-silicates in terms of these variables:

e.g., the reaction of Fe-biotite (annite) to albite buffered by magnetite

$2KFe_3Si_3AlO_{10}(OH)_2 + O_{2(g)} + 2NaCl_{aq} = 2NaAlSi3O_8 + 2Fe_3O_4 + 2H_2O_{(l)} + 2KCl_{(aq)}$

or the reaction of epidote to albite in the presence of pyrite

$3Ca_2FeAl_2Si_3O_{12}(OH) + 9SiO_2 + 6HCl_{(aq)} + 6NaCl_{(aq)} + 6H_2S_{(aq)} + 0.75O_{2(g)} = 3FeS_2 + 10.5H_2O_{(aq)} + 6NaAlSi_3O_8 + 6CaCl_{2(aq)}$

Following this approach the relative stabilities of the common silicate, oxide, carbonate, sulphide and sulphate minerals and mineral assemblages as a function of redox and pH are shown in Figure 3.4.4. The procedure requires constraining in some way the concentrations of a number of other solution variables: sum S ($aH_2S + aHS^- + aHSO_4^-$), aNaCl/aHCl, aKCl/aHCl, $aCaCl_2/(aHCl)^2$ and one cation activity, taken as $aNa^+$, as well as temperature and pressure.

The figure is drawn such that pH, log KCl/NaCl and log sumS are correlated. The values of aNaCl/aHCl and aKCl/aHCl were constrained by the line G-G' on the log aKCl/aHCl vs log aNaCl/aHCl plot (Figure 3.4.5A). Defining G-G' positively correlates pH and log aKCl/aNaCl for a given activity of $Na^+$. The chosen slope of G-G' has the effect of stabilizing albite with respect to K-feldspar at high pH and muscovite/andalusite relative to paragonite at low pH. At a temperature 400 °C and low to moderate pressures (up to 2 Kb) neutral pH is 5 to 6.

Log sumS and pH are correlated by the line G-G' on a plot of log sumS vs. pH (Figure 3.4.5B). The positive slope of G-G' on the log sumS vs pH plot has the effect of stabilizing pyrite ± pyrrhotite with quartz and albite, typical proximal assemblages to gold lodes. Magnetite is stable with chlorite ± biotite and these minerals commonly occur in distal settings up to kilometres from gold lodes. The value of $aCaCl_2/(aHCl)^2$ is constrained to increase with aKCl/aHCl and aNaCl/aHCl to ensure epidote and amphibole stability in proximal to distal settings with respect to biotite, chlorite and feldspar. The activity of $B(OH)_3$ was set at a level sufficient to stabilise tourmaline on the diagram. The stability fields for biotite, chlorite, epidote, albite and tourmalime assume coexisting quartz (except at pH > 10).

Some of the salient features of Figure 3.4.4 are:

1. Quartz - (Fe-Mg) - chlorite - magnetite assemblages occur at relatively acid conditions. At more oxidised but acidic conditions (above the haematite/magnetite buffer) tourmaline and andalusite are stable. Muscovite rather than tourmaline would be stable at lower activities of $B(OH)_3$ and paragonite rather andalusite at higher activities of NaCl/HCl. Chloritoid, not shown on Figure 3.4.4 occurs at acidic conditions between the chlorite and andalusite fields.

2. At neutral to mildly alkaline conditions, epidote ± anhydrite occurs at oxidised conditions compared with biotite and actinolite (Ca - Fe- Mg - amphibole) that forms at most reduced conditions in this pH interval. Epidote ± anhydrite may co-exist with either $SO_4^{2-}$ or $H_2S$ - rich fluids. The actinolite occurs in the most reduced conditions and may be stable with $CH_4$-rich fluids. Depending on precise conditions these minerals may co-exist with albite, haematite, magnetite, pyrite or pyrrhotite.

3. Albite plus quartz is stable over the whole redox range considered at neutral to alkaline conditions (pH ~ 6 to 9) with either haematite, pyrite, or pyrrhotite.

4. At ultra- alkaline conditions (pH > ~ 9) amphibole is stable rather than Fe-sulphides or oxides with albite.

If the pH is sufficiently high quartz becomes unstable and Ca – feldspar may replace albite.

5. Talc saturates at moderately alkaline conditions.

Very broadly the change in mineral assemblages from acid to alkaline conditions mirrors the deposit to district scale alteration patterns noted above. Most, if not all, of the major Au camps in the Eastern Goldfields Superterrane contain proximal mineral assemblages formed at reduced (pyrite, pyrrhotite stable) as well as oxidised conditions (haematite, magnetite, pyrite stable). Quartz, albite ± phengite are common silicates in proximal settings (condition 2; Figure 3.4.6) implying broadly mildly acidic to mildly alkaline conditions in this environment. For this pH range, epidote may be taken as an indication of more oxidised conditions and biotite/actinolite as an

*Figure 3.4.4: Log $fO_2$ - aKCl(aq)/aNaCl(aq) diagram illustrating the range of physicochemical conditions of formation of common mineral assemblages found in the gold systems of the eastern Yilgarn, both in proximal (within metres of a gold lode) and distal environments (from metres to kilometres from gold lodes). The stability fields of Fe - Al - Na - K - B- silicate minerals (coloured domains on the diagram) were constructed assuming coexistence with either haematite, magnetite, pyrite, pyrrhotite and Fe-actinolite (solid black lines on the diagram) and as a function of physicochemical parameters; redox (log $fO_2$), log KCl/NaCl, pH and log sumS for constant temperature and pressure of 400° C and 500 bars. Dashed lines on the diagram show aqueous sulphur species boundaries and saturation conditions for anhydrite and talc.*

*The phase diagram was constructed using thermodynamic data from FreeGs: web-enabled thermodynamic database for modelling of geochemical processes (Bastrakov et al., 2004; www.agso.gov.au/rural/projects/geofluids.jsp). Thermodynamic data for schorl (Fe-tourmaline) from Garofalo et al. (2000) and annite (Fe-biotite) from SUPCRT92 (Johnson et al., 1992). Activities of schorl, annite, Fe-chlorite and Fe – amphibole (actinolite) set to 0.1. Activity of epidote set to 0.5. Log aKCl(aq)/aHCl(aq) and log aNaCl(aq)/aHCl(aq) values were constrained by section G-G' on a log aKCl(aq)/aHCl(aq) vs log aNaCl(aq)/aHCl(aq) plot and sumS - pH relations constrained by section G-G' on a plot of log sumS vs pH (see following figure). Log $aNa^+$ and log aB(OH)3 taken as -1 and -0.2 respectively. Quartz and water assumed in excess except in the high pH environment where quartz is assumed to be under-saturated. Log $aCaCl2(aq)/(aHCl(aq))^2$ assumed to increase with increasing log aKCl(aq)/aHCl(aq) and log aNaCl(aq)/aHCl(aq) according to the following empirical relationship: Log $aCaCl2(aq)/(aHCl(aq))^2$ = 0.66*log aKCl(aq)/aHCl(aq) + 0.33log aNaCl(aq)/aHCl(aq)+2.95. Log $aMgCl2(aq)/(aHCl(aq))^2$ constrained by assuming dolomite undersaturated with respect to calcite by two orders of magnitude.*

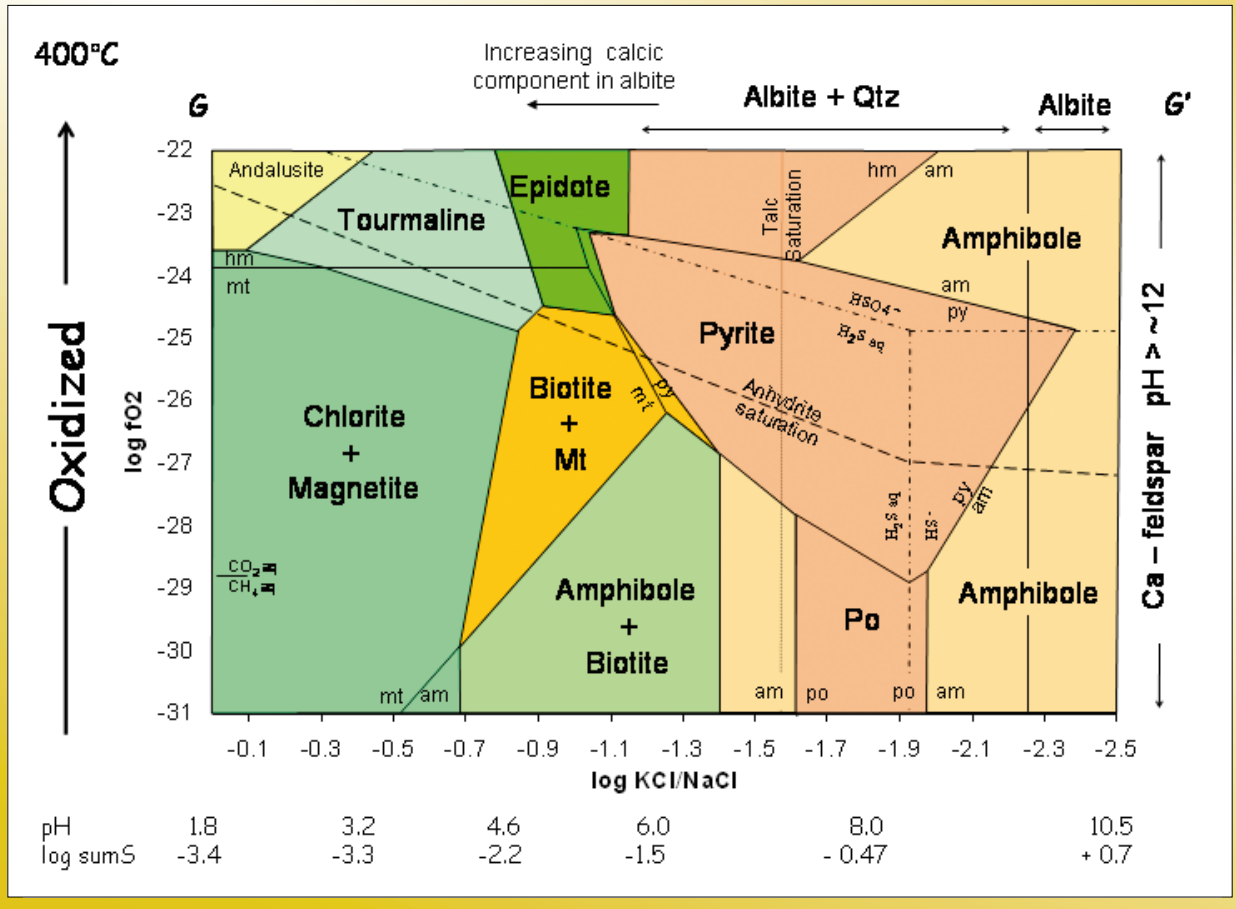

indication of more reduced conditions. Albite ± phengite may also occur distally e.g., the footwall of the Kanowna Belle deposit or the footwall of the Lancefield deposit, Laverton district.

The most acidic conditions (condition 1; Figure 3.4.6) appear to be confined to distal settings as indicated by andalusite or equivalent minerals: chloritoid, observed distally to the Golden Mile, Wallaby and Lancefield deposits and pyrophyllite observed in the Kanowna Belle district (Tom Cudahy, pers. comm., 2005). Fluids in these distal environments apparently contained lower S contents compared with fluids in proximal environments, given the paucity of sulphides in distal environments. At St Ives an assemblage of muscovite ± paragonite ± Fe-chlorite in discrete shears reflects relatively acidic conditions relatively late in the alteration/deformation history.

The assemblage of albite ± Ca-feldspar ± amphibole ± talc ± carbonate in the absence of sulphides and quartz represent ultra-alkaline conditions (condition 3; Figure 3.4.6). Detailed studies at St Ives (Klaus Petersen, pers. comm., 2006) have established that carbonate and albite were closest to gold in the mineral paragenesis. Pyrite and quartz were stable before and after gold precipitation, with most quartz growth following the bulk of the gold. This paragenesis can be accounted for by a shift, albeit transiently, to ultra-alkaline conditions. Ca-feldspar,

*Figure 3.4.5:*
*A) Log aKCl(aq)/aHCl(aq) vs. log aNaCl(aq)/aHCl(aq) diagram at 400 °C and 500 bars illustrating the conditions used (section G-G') in construction of the log $fO_2$- aKCl(aq)/aNaCl(aq) diagram. The section was selected to show the conditions of co- existence of andalusite, muscovite and albite with Fe-Al-silicates, Fe-sulphides and Fe-oxides. Details of construction and sources of thermodynamic data are as given in caption to the log $fO_2$- aKCl(aq)/aNaCl(aq) diagram. See text for discussion of the compositions of the end-member fluids shown on the figure.*
*B) Log sumS vs. pH diagram at 400 °C and 500 bars illustrating the conditions used (section G - G') in construction of the log $fO_2$- aKCl(aq)/aNaCl(aq) diagram. Section G - G' drawn such that pyrite is stable with respect to haematite and/or magnetite at neutral to alkaline conditions rather than neutral to acidic conditions. Details of construction and sources of thermodynamic data are as given in caption to the log $fO_2$- aKCl(aq)/aNaCl(aq) diagram.*

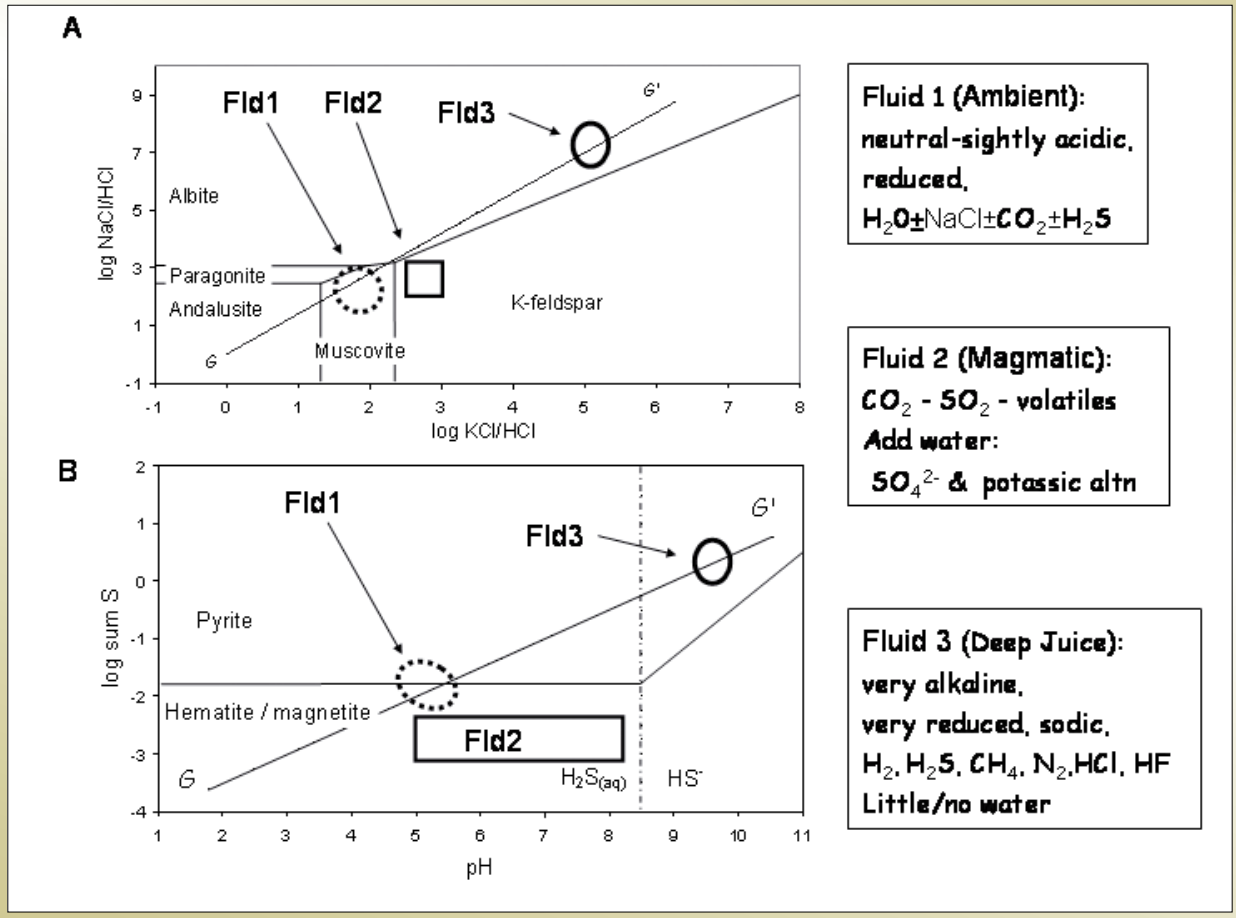

recently documented at St Ives using thermal infrared spectrometry (Tom Cudahy, pers. comm., 2007) may be an indicator of such conditions.

It is noted that Figure 3.4.4 and Figure 3.4.6 are constructed assuming magnetite is a stable hydrothermal phase. Not all deposits/camps contain secondary magnetite. The shift from magnetite/pyrrhotite/pyrite-dominated environments (Golden Mile, St Ives, Wallaby camps and districts) to pyrite-dominated environments, such as at Kanowna Belle, could reflect the influence of temperature or mafic host-rocks on the fluid system.

### 3.4.2.4 Chemical gradients and fluid types

On the basis of the mineralogical zoning and fluid inclusion data summarised above, it can be argued that all camps show evidence of physicochemical gradients in redox, pH, salinity, water activity, activities of sulphur and carbon species. These gradients may be identified within the Au systems as both a temporal evolution of the physicochemical conditions and a spatial evolution at deposit to district scales. The magnitude of variation in the physicochemical gradients implies that multiple fluids of strongly contrasting chemistry were present in the system (Neumayr et al., 2003; Neumayr et al., 2005; Walshe et al., 2003). The concept of end-member fluids or 'idealised' fluid sources or reservoirs is introduced to permit description of the observed variation in alteration mineralogy and geochemistry and model the fluid interaction processes (fluid-rock reaction, fluid mixing, fluid un-mixing) within the mineral system: in the fluid reservoirs, along fluid flow paths and at sites of deposit formation.

The magnitude of thermo-chemical gradients reflects the histories of fluids and fluid-rock interaction in the

*Figure 3.4.6: Redox/pH conditions of proximal and distal assemblages. Condition 1: Acidic conditions defined by chlorite ± magnetite ± andalusite or equivalent minerals: chloritoid, pyrophyllite, paragonite, muscovite, tourmaline. Condition 2: Mildly acidic to mildly alkaline conditions defined by albite ± phengite ± pyrite ± epidote ± biotite ± actinolite. Epidote may be taken as an indication of more oxidised conditions and biotite/actinolite as an indication of more reduced conditions. Condition 3: Ultra-alkaline conditions defined by albite ± Ca-feldspar ± amphibole ± talc ± carbonate in the absence of sulphides and quartz. Details as for Figure 3.4.4.*

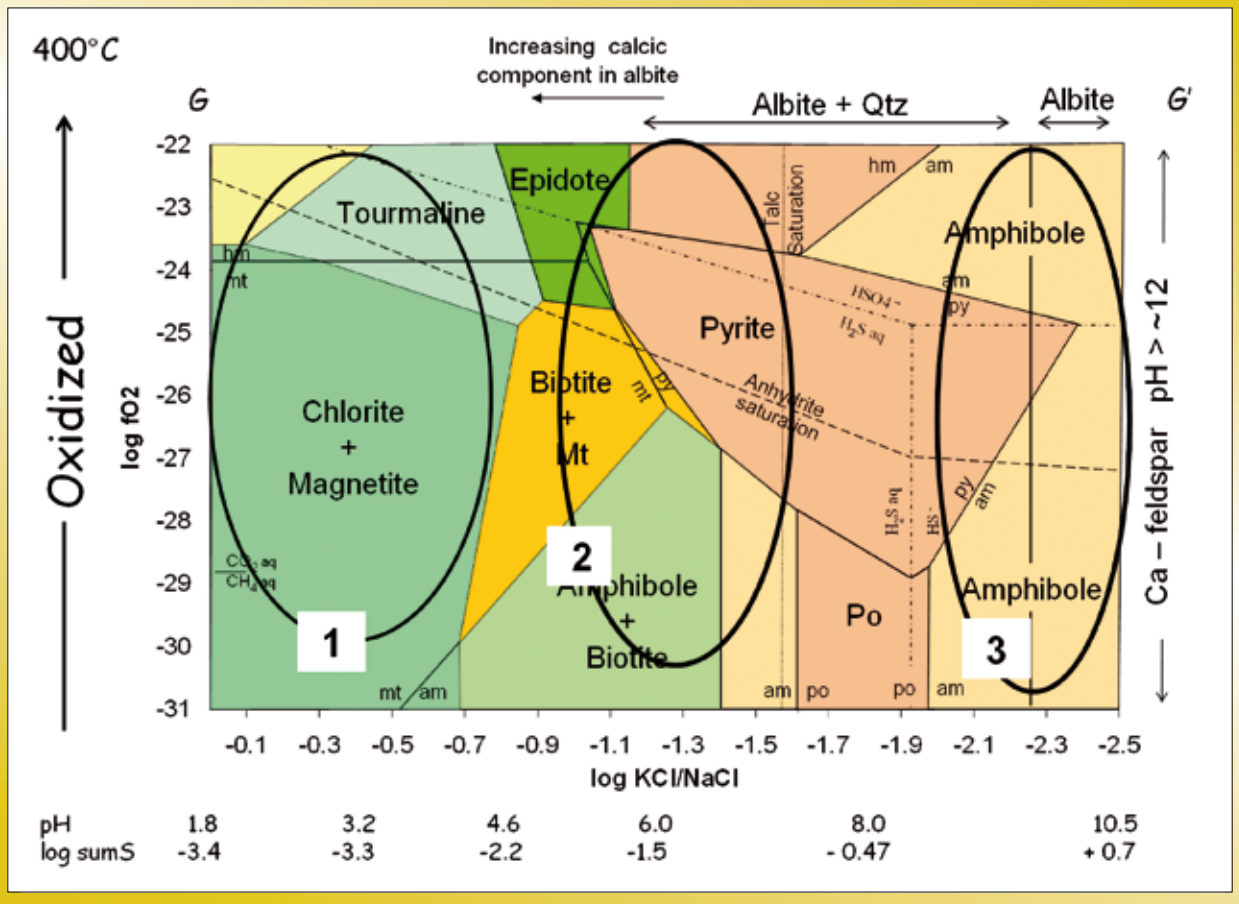

mineralizing system. Inevitably, much of the observed mineralogy and geochemistry will reflect degenerative processes along fluid pathways leading to reduction or loss of the chemical potential/activities in end-member fluids. More rarely there will be times in the system when the composition of end-member fluids remains virtually unchanged from reservoir to depositional-site, i.e., the system is strongly fluid buffered. Such times are of particular interest because of increased opportunity for mixing fluids of strongly contrasting chemistry. This process is one of the most efficient ways to sustain thermo-chemical gradients at depositional sites and create large- tonnage, high-grade deposits (Walshe et al., 2005a).

The fluid inclusion data from the St Ives camp indicate an overall temporal evolution from low salinity aqueous fluids early in the history of the St Ives gold system to anhydrous fluids; either $CO_2$ rich or $CH_4 \pm N_2$ rich at about gold stage with pyrite, albite and carbonate the stable phases. Late in the history of the system the fluids are again aqueous but also distinctly saline, with quartz the stable phase. The existence of a spatial evolution or zoning from hydrous to anhydrous fluids is the subject of on-going research (Walshe et al., 2008).

It is suggested that at least three distinct fluid types or end-members fluids are required to explain the fluid inclusion constraints, as well as the observed mineral assemblages (Figure 3.4.7), the stable isotope data and the regional footprints.

Fluid 1 is taken as a background or ambient aqueous fluid with low concentrations of salt and $CO_2$. It is likely that the major reservoirs of water during gold mineralization, late in the metamorphic history were in the late basins, although this remains largely conjectural.

The mineralogical assemblages of main gold stage at St Ives are consistent with extremes in redox state occurring at about the time of Au deposition. While much of the secondary magnetite spatially associated with the Au predates the Au – sulphide – albite - carbonate assemblages (Neumayr et al., 2003; Neumayr et al., 2008) some magnetite as well as haematite is stable with Au as inclusions in the pyrite indicating highly oxidised conditions at the time of Au deposition. The temporal association is clearly apparent in the largest deposit in the Eastern Goldfields Province, the Golden Mile (Clout, 1989) where haematite and anhydrite occur within the Au lodes with roscoelite and tellurides. The sulphides have negative sulphur isotope signatures consistent with highly oxidised environments. The mineralogical evidence for highly oxidised fluids at the time of Au mineralisation implies that the carbonic fluid of stage 2B (Fluid 2)

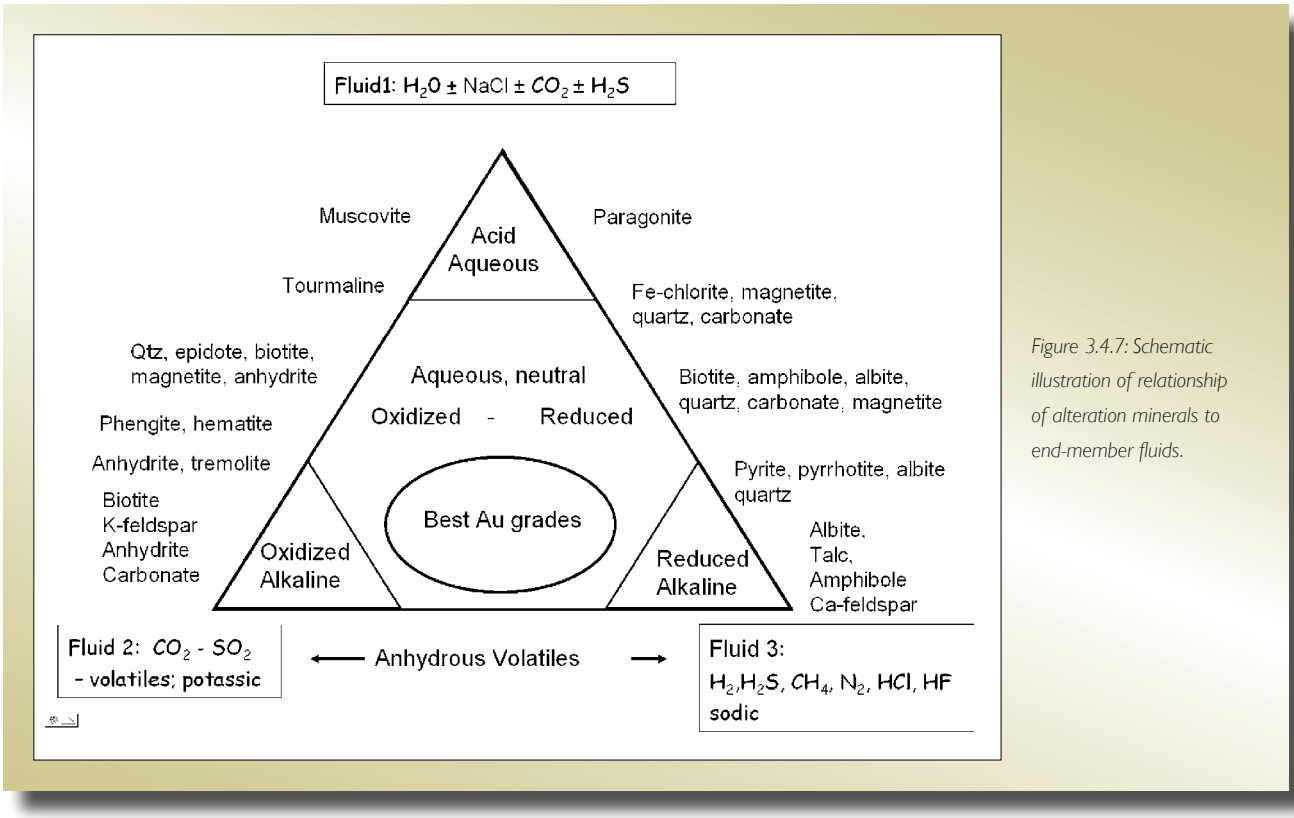


*Figure 3.4.7: Schematic illustration of relationship of alteration minerals to end-member fluids.*

contained $SO_2$ and possibly other volatile species of V, Te, W and Mo, the evidence for these last components coming particularly from mineralogical associations in the Golden Mile and Kanowna Belle deposits. This chemistry, together with the spatial association of secondary magnetite with intrusive complexes, is consistent with stage 2B fluids being oxidised magmatic volatiles. (Cooke and McPhail, 2001) argue that the telluride content of Au deposits is a magmatic contribution. Two fluids are required to form Au tellurides because of their very low solubility. Tellurium was most likely transported by oxidised magmatic volatiles and the telluride rich ores of the Golden Mile deposit formed by condensation of these magmatic vapours into Au-rich fluids within the Golden Mile Dolerite. The tellurideroscoelite-sulphate mineralogical association of the Golden Mile is a characteristic shared with deposits of the circum-Pacific (Porgera, Cripple Creek, Emperor) that are genetically linked with magmatic hydrothermal processes.

Fluid 3 is assumed to contain $CH_4$, $N_2$ as well as $H_2$, $H_2S$, HCl ±HF inferred from the alteration assemblages and the stable isotope constraints. The reduced fluid is assumed to contain sufficient $H_2$ to permit reduction of $CO_2$ to $CH_4$ and the acid species (HCl ±HF) are added to the reduced fluid to account for the inverse correlation of oxidised alteration assemblages with acidic alteration assemblages.

The origin of the reduced fluid is enigmatic and there is ongoing discussion as to whether Fluid 3 could evolve from the ambient fluid (Halley, 2007) or whether it could also be of magmatic origin (Beakhouse, 2007) or be sourced directly from the lower crust or mantle (Walshe et al., 2003).

The question of whether changes of redox pH, activity of NaCl, S, C and $H_2O$ etc, were controlled by local processes (fluid-rock reaction or *in-situ* phase separation) in contrast to being imposed by externally derived fluids, as argued here, is the subject of on-going discussion in the literature. The discussion is significant because it is these parameters along with temperature and pressure that ultimately control the metal transporting capacity of the fluids in the system. However, as the magnitude of changes in these parameters and the scale of the mineral zoning is better understood, it is becoming more difficult to rely on deposit-scale, *in-situ* processes to explain the observations. The chemical contrasts appear to be defined at the district to terrane scale. Arguably, the important end-member fluids that provided the chemical contrasts, particularly redox contrasts, were fluids related to mid to upper crustal magma chambers and the reduced fluids that are potentially sourced from deep crustal/mantle reservoirs.

### 3.4.3 Section 2: Isotopic constraints (S, C, O, Ne, Ar, Pb and Sr) on fluid reservoirs and chemical gradients in Eastern Yilgarn gold systems

#### 3.4.3.1 Introduction

In this section, the stable isotopes of sulp7hur in sulphide and sulphate, in combination stable isotopes of carbon and oxygen in carbonates, are used to identify the nature and likely sources/reservoirs of the salient volatile species: $CO_2$, $SO_2$, $H_2$, $CH_4$. Limited radiogenic isotope data (Ne, Ar isotopes of fluid inclusion, Pb isotopes of sulphide and Pb and Sr isotopes of sulphate) are used to help resolve questions of process versus source that arise with interpretations of stable isotope data. The interpretations presented in this section are largely developed using significant legacy data for the stable isotopes, but are linked to a developing understanding on the spatial zoning of stable isotopic compositions commonly at scales larger than the deposit. These data, particularly for the Victory - Defiance Complex, St Ives, are discussed in Walshe et al. (2008).

The conclusions from this review of the available isotopic data are that:

- The major reservoir of $CO_2$ was in the mantle ($\delta^{13}C$ ~ -4 to -6 ‰).
- The isotopic signal of $CO_2$ was modified both by oxidation of $CH_4$ to $CO_2$ and reduction of $CO_2$ to $CH_4$.
- Sources of $CH_4$ include sedimentary organic matter in the greenstones, from deeper in the crust or mantle and from *in-situ* reduction of $CO_2$ by $H_2$.
- Noble gas isotope studies provide evidence of a methane contribution from the mantle, consistent with argument for hydridic fluids of mantle origin.
- The major oxidant in the system was $SO_2$ of mantle origin ($\delta^{34}S$ ~ 0 ‰), although a radiogenic Pb component to the oxidised $CO_2$-$SO_2$ - rich fluids suggests reservoirs of these fluids were developed in the crust.

- Enrichments in $\delta^{18}O$ carbonate up to ~ 25 ‰ suggest breakdown of $CO_2$ -$SO_2$ - rich fluids reservoirs at least locally with $SO_2$ oxidising $CH_4$ to produce $H_2O$/hydrous alteration products. Such reactions provide a way to map the pathways of oxidised, anhydrous fluids.
- Reduced (hydridic) fluids transported radiogenic Sr.

The section begins with an overview of the stable isotope data, proceeds to a discussion of the source/redox implication of the carbon isotope data, the import of the noble gas isotopes for $CH_4$ sources, redox effects on sulphur isotopes, the radiogenic isotope constraints on the origins of $SO_2$/sulphate and the evidence for reduction of these species in anhydrous as well as aqueous domains. The final section comments on a possible meteoric water contribution to Archaean gold systems as evidenced by deuterium isotopes.

### 3.4.3.2 Stable isotopes of sulphur, carbon and oxygen

In general terms the variation in stable isotope ratios may provide constraints on:

1. Source/reservoirs(s) of isotopes,

2. Temperature of the isotope partitioning between fluids and mineral species, and

3. Redox state of the fluids.

Sulphur isotope ratios are a sensitive indicator of the oxidation state of fluids close to the $H_2S$ - $SO_4^{2-}$ buffer ($SO_4^{2-}$ ~ $H_2S$) or $H_2S$ – $SO_2$ buffers, as fractionation of $^{34}S$ and $^{32}S$ occurs between reduced and oxidised sulphur species (Ohmoto and Goldhaber, 1997). Similarly carbon isotope ratios are a sensitive indicator of the oxidation state of fluids close to the $H_2CO_{3(aq)}$ - $CH_{4(aq)}$ buffer ($H_2CO_{3(aq)}$ ~$CH_{4(aq)}$) or $CH_4$ – $CO_2$ buffers, as fractionation of $^{13}C$ and $^{12}C$ also occurs between reduced and oxidised carbon species. This means that it is possible to use the patterns of sulphur and carbon isotope fractionation to track redox variations from highly oxidised environments ($SO_4^{2-}$ or $SO_2$ the dominant species in the fluid) through intermediate oxidation states ($H_2S$, $H_2CO_{3(aq)}$ or $CO_2$ the dominant species in the fluid) to highly reduced conditions ($H_2S$ and $CH_4$ the dominant species in the fluid).

The fractionations of the carbon and sulphur isotopes are also temperature dependant but the major effect is fractionation between reduced and oxidised species. It appears that the influence of temperature on the variation of S and C isotopic compositions can largely be ignored. The fractionation of $^{18}O$ and $^{16}O$ between mineral and aqueous species is significantly dependent on temperature and this effect needs to be considered in some settings. The fractionation of $^{18}O$ and $^{16}O$ between $CO_2$ and $H_2O$ is also significant and needs to be considered in settings where the dominant fluids species is $CO_2$ rather than $H_2O$ or in transitional environments from $CO_2$-rich fluids to $H_2O$-rich fluids.

There is significant legacy of stable isotope data from studies in the Eastern Goldfields over the last 30 years that provides a basis for discussion of constraints on fluid sources and chemical processes. From the work of (Donnelly et al., 1977; Golding, 1982, 1984; Golding et al., 1985; Golding et al., 1987; Golding et al., 1989) and subsequent studies (Cassidy, 1992; Gebre-Mariam et al., 1993; Hronsky, 1993; Knight et al., 2000; Mueller, 1990; Nguyen, 1997; Ojala, 1995; Polito, 1999; Salier et al., 2005; Sang, 1991; Xu, 1999) there is a very extensive data set on the carbon and oxygen isotopic compositions of carbonates within the Yilgarn Au systems. There is more limited C isotope data on carbonaceous material (Donnelly et al., 1977; Golding, 2005) and carbon species in fluid inclusions (Polito, 1999).

Numerous sulphur isotope studies undertaken over the last 30 years (Clout, 1989; Donnelly, 1977; Harbi, 1997; Hodkiewicz, 2003; Lambert, 1984; Palin, 2000; Phillips, 1986; Ren, 1994; Salier, 2005)as well as an unpublished reports by Western Mining Report, 1987; an unpublished reconnaissance laser ablation study of deposits of the Eastern Goldfields; Kitto and Halley, pers. comm., 2000 and unpublished laser ablation study of the Golden Mile deposit; Hagemann and Bateman, pers. comm., 2001) provide a significant body of sulphur isotope data on gold deposits, mostly from the Eastern Yilgarn. The majority of these analyses are conventional sulphur isotope analyses of pyrite with a more limited set of laser-ablation analyses, again mostly of pyrite. The number of analyses of pyrrhotite is quite limited considering it is a relatively common sulphide in many deposits. There is also a very limited number of analyses of "background" sulphides that arguably

are unrelated to the Au systems. Clout (1989) obtained analyses of anhydrite in the Golden Mile deposit.

Golding and co-workers largely interpreted the variation in the carbon isotope data in terms of host rock influences and/or fluid sources defining three major reservoirs of $CO_2$. Studies of sulphur isotopes have considered the role of process as well as source on isotopic compositions with some workers linking isotopic composition to source (Cameron, 1987; Clout, 1989; Hall, 2001; Hattori, 1987; Walshe, 2003) and others to *in-situ* fluid-rock reaction processes (Evans, 2006; Palin, 2000; Phillips, 1996) that controlled local changes in redox state of the fluids.

The competing views of the importance of sources versus processes as the salient control on the stable isotopic compositions and the nature of the processes have yet to be fully resolved. What were the significant source(s) or reservoirs and what were the significant processes? To resolve these issues the current study has focused on obtaining a clearer picture of the C, S and O isotope zoning patterns at deposit to district scale and integration with the geological and mineralogical constraints (see Walshe et al., 2008). This work has been supplemented by numerical modelling to evaluate the interplay of sources and processes on the isotope zoning patterns and some limited radiogenic isotope studies of anhydrite aimed at resolving the source(s) of sulphate in the system.

#### 3.4.3.3 $\delta^{13}C$ of carbonate: evidence of mantle $CO_2$ reservoir

A summary of the variation is $\delta^{13}C$ values of carbonate, organic material and fluid inclusions from the Junction deposit is given in Figure 3.4.8. Around 95% of available $\delta^{13}C$ values of carbonate lie between 0 and -10 ‰, although values as positive as +12.7 ‰ and as negative as -21.2 ‰ are reported. Some 37 % of the values are between -4 and -6 ‰ and within the range commonly assumed for $CO_2$ from the mantle, or at least one of the major reservoir of mantle $CO_2$ (Deines, 1980; Ohmoto, 1979). The $\delta^{13}C$ values of carbonate within this range have been directly linked to igneous rocks of mantle origin. (Salier, 2003) measured isotope values from the magmatic carbonatites of -5 to -6 ‰ and $\delta^{13}C$ values of -6 and -6.3 were obtained from calcite in calcite-magnetite-biotite veins associated with the syenitic intrusions in the Wallaby pipe (this study). Hence it can be argued that a major reservoir of $CO_2$ was in the mantle. Was this the only major reservoir of $CO_2$ in the system? The following discussion makes this assumption and considers the variation in $\delta^{13}C$ values of carbonate between +12.7 and -21.2 ‰ can be explained by redox-related processes driving fractionation between reduced and oxidised carbon species.

#### 3.4.3.4 Influence of redox state on $\delta^{13}C$ of carbonate

The value of $\delta^{13}C$ in carbonate varies as a function of the redox state of the fluid in the vicinity of the $CO_2$ - $CH_4$ buffer. There is significant enrichment of $^{13}C$ in the oxidised carbon species (dolomite, calcite, ankerite, $H_2CO_3$ and $CO_2$) with respect to $CH_4$. This enrichment in $^{13}C$ is of the order of +10 to +20 ‰ $\delta^{13}C$ over the temperature range 300 to 500°C (Ohmoto, 1997). This partitioning gives rise to two important redox effects:

1. Partial reduction of oxidised carbon species ($H_2CO_3$, $CO_2$, carbonate) to $CH_4$ may lead to residual $CO_2$ and/or carbonate being enriched in $^{13}C$ (i.e., greater $\delta^{13}C$).

2. Oxidation of $CH_4$ to $CO_2$ /carbonate will lead to a decrease in $\delta^{13}C$ of the oxidised carbon species.

Reduction of oxidised carbon species to $CH_4$ requires a strong reducing agent in the fluids such as $H_2$

e.g., $CO_2 + 4H_2 = CH_4 + 2H_2O$

Conversely oxidation of $CH_4$ requires a strong oxidizing agent in the fluids most likely $SO_2$ or sulphate

e.g., $3CH_4 + 4SO_2 = 3CO_2 + 2H_2O + 4H_2S$

The effect of partial reduction on $\delta^{13}C$ of the oxidised species is shown in Figure 3.4.9. Trend A shows the increase in $\delta^{13}C$ of calcite as a function of the increasing mole fraction of $CH_4$ at 400°C for a $H_2O$ - $CH_4$- $CO_2$ fluid of assumed bulk composition. The mole fraction of $CH_4$ is a proxy for degree of partial reduction of oxidised species to methane. Trend B shows the corresponding effect on the composition of methane. At low percentage partial reduction (less than 20%) $\delta^{13}C$ $CH_4$ has values less than -20 ‰ increasing to values approaching the bulk $\delta^{13}C$ of the system (-4‰) at high degrees of partial reduction.

*Figure 3.4.8: Compilation of $\delta^{13}C$ data from the EGST for carbonate, carbonaceous matter, $CO_2$, $CH_4$ and total C ($CO_2$ + $CH_4$) in fluid inclusions. Short arrow is $\Delta^{13}C$ calcite – graphite at 400°C; long arrow is $\Delta^{13}C$ calcite – $CH_4$ at 400°C. Angled boxes across A, B and C link values of $\delta^{13}C$ carbonate, carbonaceous matter and probable $CH_4$ that potentially reflect equilibrium between reduced and oxidised carbon species at temperatures around 400°C. Sources of data: $\delta^{13}C$ data for carbonates from Golding (1982), Golding(1984), Golding et al. (1987), Mueller (1990), Sang (1991), Cassidy (1992); Hronsky (1993), Gebre-Mariam et al. (1993), Ojala (1995), Nguyen (1997), Xu (1999), Polito (1999), Knight et al. (2000) and this study. Carbonaceous matter from Kalgoorlie and Kambalda (Donnelly et al., 1977); Granny Smith deposit (Ojala, 1995; Golding 2005; Glikson, 2005). Fluid inclusion data from the Junction deposit, St Ives, Polito (1999; Tables 11.1, 12.1 and 13.1). The six $\delta^{13}C$ $CH_4$ values less than -40 in A, lie between -40 and -50 ‰. Fractionation factors from Ohmoto and Goldhaber (1997).*

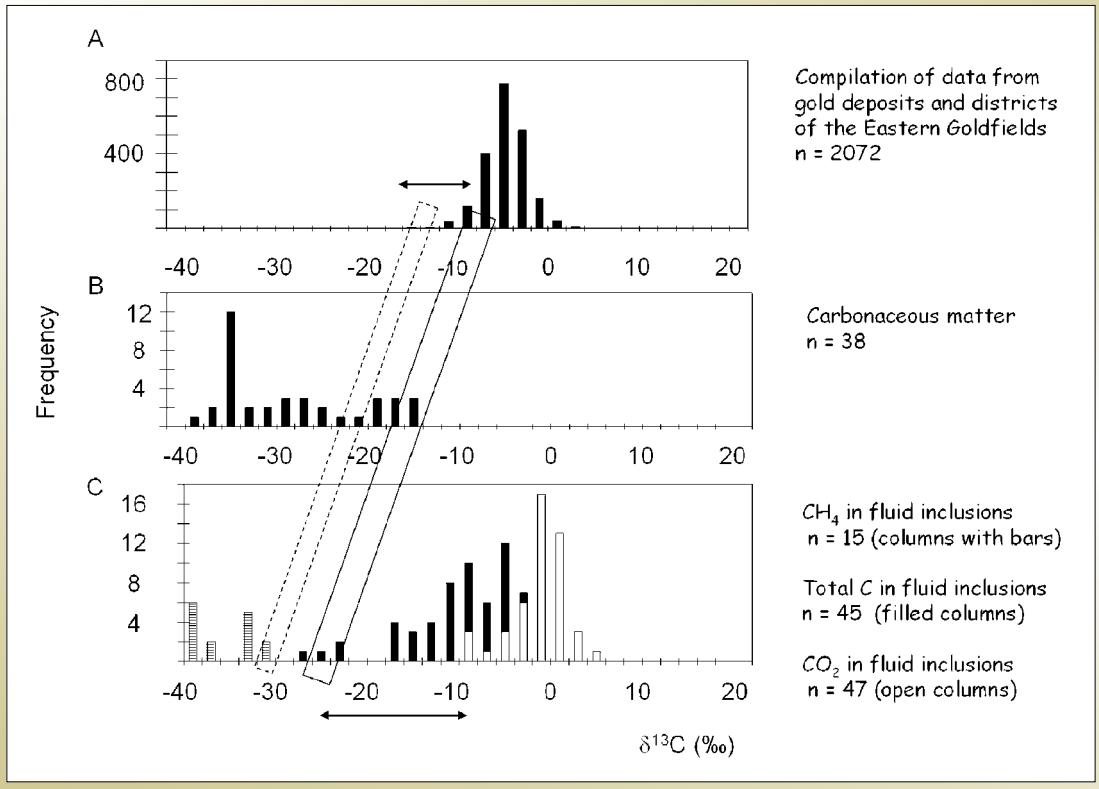


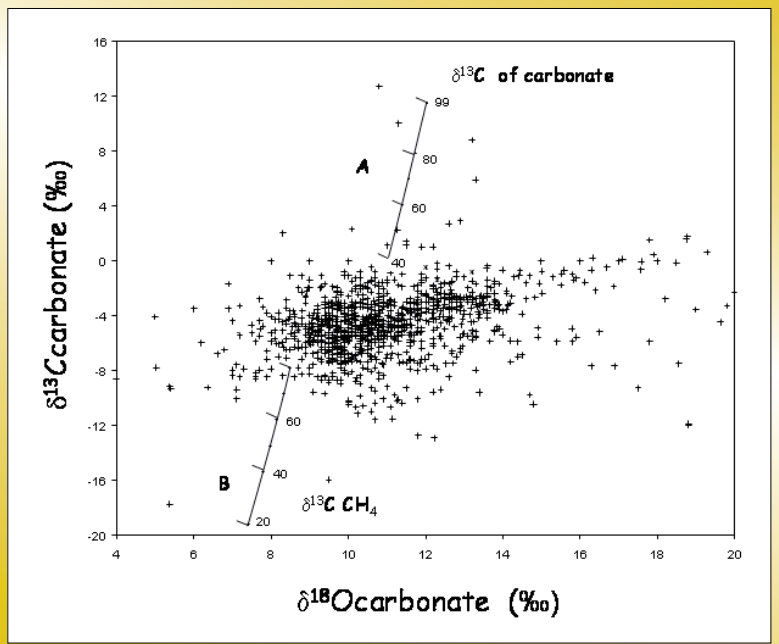


*Figure 3.4.9: Redox effects on $\delta^{13}C$ vs $\delta^{18}O$ partitioning. The isotopic composition of calcite (trend A) and $CH_4$ (trend B) is shown as a function of mole fraction of $CH_4$ ($100mCH_4 / (mCH_4 + mCO_2)$) at 400°C for $H_2O$ - $CH_4$- $CO_2$ fluid of assumed bulk composition of 8.8 $\delta^{18}O$ and -4 ‰ $\delta^{13}C$. $^{18}O$ fraction factor for calcite-$H_2O$ from O'Neil et al. (1969) and $^{13}C$ fraction factor for calcite-$CO_2$ from Chacko et al. (1991). $^{13}C$ fraction factor for $CH_4$-$CO_2$ from Bottinga (1969) and $^{18}O$ fraction factor for $CO_2$-$H_2O$ taken as 9 (Truesdell, 1974). $\delta^{13}C$ and $\delta^{18}O$ data for carbonates from Golding (1982), Golding (1984), Golding et al. (1987), Mueller (1990), Sang (1991), Cassidy (1992); Hronsky (1993), Gebre-Mariam et al. (1993), Ojala (1995), Nguyen (1997), Xu (1999), Polito (1999), Knight et al. (2000).*

Partial reduction of $CO_2$ or carbonate to $CH_4$ could account for $\delta^{13}C$ carbonate values greater than the modal values of -4 to -6 ‰; although additional sources of $CO_2$ enriched in $^{13}C$ such as seawater cannot be ruled out. Certainly partial reduction is the most obvious explanation for the very high $\delta^{13}C$ values (up to 12.7‰) observed in some carbonates (data from the St Ives Goldfields and in the Mount Charlotte and Reward deposits (Golding, 1982, 1984, 1985). In the Mount Charlotte deposit these high $\delta^{13}C$ are associated with pyrrhotite in the alteration selvages to the quartz veins.

Oxidation of $CH_4$ to $CO_2$ can account for $\delta^{13}C$ carbonate values less than the modal values of -4 to -6‰. Such a process does not necessarily require the $CH_4$ and $CO_2$ to equilibrate but that there is a sufficient oxidant available to promote the relatively fast half-reaction: the oxidation of $CH_4$ to $CO_2$. Methane-rich fluid inclusions are widely reported in studies of Archaean Au deposits: (Hagemann, 1993; Harbi, 1997; Ho, 1990; Mernagh, 1996; Mernagh, 1994; Polito, 1999; Ridley, 1999) and this study. In the Junction deposit, they are paragenetically linked to Au deposition and preferentially occur at the margins of quartz veins (Polito, 1999). In the Mount Charlotte deposit they occur in the pyrrhotite-rich Type 3 assemblage that formed at the highest temperatures (Harbi, 1997; Mernagh, 1996) in Charlotte Deeps orebody (Mikucki, 1993). As with the Junction deposit $CH_4$-rich inclusion are trapped at vein margins. In the Sand King and Missouri deposits in the Siberia district $CH_4$-rich fluids were trapped in the earliest phases of mineralisation at temperatures of 500 to 600°C and pressures of 3 to 4 kilobars. $CH_4 \pm N_2$ fluid inclusions observed in the Conqueror deposit and the Foster Thrust, during this study of the St Ives camp, are paragenetically linked to reduced sulphide and silicate assemblages (pyrrhotite-actinolite-biotite and to Au deposition.

Oxidation of $CH_4$ to $CO_2$ appears related in some way to gold deposition. Studies on the Lawlers deposit (Cassidy, 1998), the Revenge deposit (Nguyen, 1997) and on the Junction deposit (Polito, 1999) have shown the lower $\delta^{13}C$ values in carbonate commonly occur proximal to the Au deposit. In the Lawlers deposit this effect is detectable up to hundreds of metres from mineralised structures. Similar trends are observed in the data sets for the Mount Charlotte and Reward deposits and environs. In the Junction deposit carbonate in the inner biotite alteration zone is depleted in $\delta^{13}C$ with respect to carbonate in the proximal chlorite zone. Carbonates with the lowest $\delta^{13}C$ and $\delta^{18}O$ values occur in south dipping veins. (Nguyen, 1997) showed that carbonates in the Au zone of the Revenge deposit had depleted $\delta^{13}C$ and $\delta^{18}O$ values compared with carbonates from regional structures such as the Playa Fault and the Foster Thrust. Polito (1999) also demonstrated a temporal relationship of $\delta^{13}C$ $CO_2$ from fluid inclusions in quartz veins with Au mineralisation. Syn- to post-Au veins had lower $\delta^{13}C$ $CO_2$ values than early Mo-rich veins. Trends to both lower $\delta^{13}C$ and $\delta^{18}O$ values for hydrothermal carbonate are consistent with a $CH_4$ contribution associated with a high temperature fluid and support the mineralogical and fluid inclusion evidence of high temperature, reduced fluids in the Au systems at about the time of Au deposition.

### 3.4.3.5 Sources of methane and equilibrium between reduced and oxidised C species

Golding (1989) considered that the most negative $\delta^{13}C$ values in carbonate (i.e., < -10 ‰) required a $\delta^{13}C$ -depleted component from the oxidation and/or hydrolysis of organic matter (OM). Relatively pristine OM in Late Archaean sedimentary rocks has $\delta^{13}C$ -depleted isotope compositions mainly between -35 and -50 ‰ (Golding, 2005 and references therein). $\delta^{13}C$ OM associated with the gold systems in the Eastern Yilgarn (Bavinton, 1979; Donnelly, 1977; Glikson, 2005; Golding, 2005; Ojala, 1995) range from -46.3 to -15.1 ‰ (Figure 3.4.8B and Table 3.4.1) The most negative values (< -35 ‰) are considered the least modified by exchange processes that enrich the residual kerogen in $\delta^{13}C$ such as thermal decomposition of OM and high temperature exchange between organic and inorganic carbon in $CO_2$-rich metamorphic and/or hydrothermal fluids (Golding, 2005). Most $\delta^{13}C$ OM values obtained by (Donnelly, 1977) were relatively enriched on $^{13}C$, ranging between -27.8 and -15.1 ‰. These authors noted that $\delta^{13}C$ (carbonate – OM) values fall in a narrow range around +10 ‰, suggesting isotopic exchange between oxidised and reduced carbon species at moderately high temperatures.

A recent study by (Glikson, 2005) of the Granny Smith deposit (GSD241B) found two forms of carbonaceous matter could be identified from limited material; 1) the residue of the source rock organic matter (OM) after thermal stress ('spent' OM), and 2) a bitumen of medium

reflectance (Ro) values. The $\delta^{13}C$ values for carbonaceous matter varied between -39 and -24.5 ‰ with the majority of values around -35 ‰ Figure 3.4.10. Bitumen showed the most enriched carbon isotope composition of -24.6 ‰. At 400° C the value of carbonate in equilibrium with this value of bitumen would be -16.5 ‰ i.e. close to the most negative values of $\delta^{13}C$ observed in carbonate from the Eastern Goldfields Superterrane. Within the vicinity of the least negative $\delta^{13}C$ values for organic material there is a negative shift in whole rock carbonate $\delta^{13}C$ values down to -15.3 ‰ (Eilu, 1996) consistent with carbonaceous matter and carbonate approaching C isotopic equilibrium. Figure 3.4.8 provides an overview of the partitioning of $^{13}C$ partitioning between carbonates, organic material and carbon species in fluid inclusions from the Junction deposit. (Polito, 1999) measured $\delta^{13}C$ values for $CO_2$, $CH_4$ and total C ($CO_2$ + $CH_4$) extracted from fluid inclusions from the Junction deposit. The $\delta^{13}C$ values range from less than -40 ‰ to +6 ‰ (Figure 3.4.8C). The "angled boxes" across Figure 3.4.8 link values of $\delta^{13}C$ carbonate, carbonaceous matter and probable $CH_4$ that possibly reflect the following equilibria between reduced and oxidised carbon species at temperatures around 400° C:

- $\delta^{13}C$ organic matter of -15 to -18 ‰ with $\delta^{13}C$ carbonate of -7 to -10 ‰ i.e. at the lower end of the range of $\delta^{13}C$ carbonate.
- $\delta^{13}C$ sum C ($CH_4$ + $CO_2$) of -24 to -28 ‰ are close to the expected methane value for equilibrium between carbonate of $\delta^{13}C$ of -7 to - 10 ‰, OM and methane.
- OM with $\delta^{13}C$ as negative as -24 ‰ potentially equilibrated with carbonate with $\delta^{13}C$ values as negative as -16 ‰. Corresponding equilibrium values of $\delta^{13}C$ $CH_4$ should be in the range -30 to -32 ‰ (Figure 3.4.8C).

Equilibration between reduced and oxidised carbon species is difficult at temperatures below about 500 °C. Nevertheless the overall partitioning of $\delta^{13}C$ between carbonate, organic matter and methane is consistent with carbonate with $\delta^{13}C$ values at the lower end of the carbonate range (less than ~ -8 ‰) equilibrating with methane and carbonaceous matter. The possible range of $\delta^{13}C$ values for $CH_4$ and carbonaceous matter in equilibrium with carbonate is -23 to -35 ‰ and -15 to -24 ‰, respectively. Why equilibrium between reduced and oxidised species was apparently attained in some parts of the Au systems and not others is unclear?

$\delta^{13}C$ values for methane and carbonaceous matter of less than ~ -35 ‰ and ~ -25 ‰ respectively are difficult to explain by reduction of $CO_2$ from a single reservoir with $\delta^{13}C$ ~ 5 to -6 per mil. A contribution from a $CH_4$-rich reservoir with $\delta^{13}C$ ~ -35 ‰ seems likely. The $CH_4$ could be derived from sedimentary organic matter in the greenstones, from deeper in the crust or mantle. Noble gas isotope studies provide evidence of a methane contribution from the mantle (Kendrick et al., in prep; see later discussion).

The $\delta^{13}C$ studies of OM allow a contribution of methane from sedimentary sources within the greenstones. Significantly, the data provide evidence that OM was not simply a reactant within the Au mineralizing system but tended to re-equilibrate with carbonate. It is possible also

Table 3.4.1: $\delta^{13}C$ for carbonates and organic matter from interflow sedimentary rocks from the Kambalda ultramafic sequence (Bavinton, 1979)

| Sample | Location | Kerogen | Carbonate | delta C (ker-carb) |
|---|---|---|---|---|
| 9102/121.2 | HWB sediment | -21.0 | N.D. | |
| 9102/117.4 | " | -22.3 | N.D. | |
| 6034/343 | Internal sediment | -36.4 | -25.3 | 11.1 |
| 9205/1701 | " | -27.8 | -16.6 | 11.2 |
| 401 stope A | McMahon sediment | -15.5 | N.D. | |
| 401 stope B | " | -16.3 | | |
| 9185/260 | Internal sediment | -16.0 | N.D. | |
| 435/113 | " | -18.9 | -7.8 | 11.1 |
| 9171/585 | Contact sediment | -15.7 | -7.8 | 7.9 |
| 8317/792 | FWB sediment | -15.1 | -7.8 | 7.3 |
| 171/613 | talc-carbonate rock | | -6.8 | |

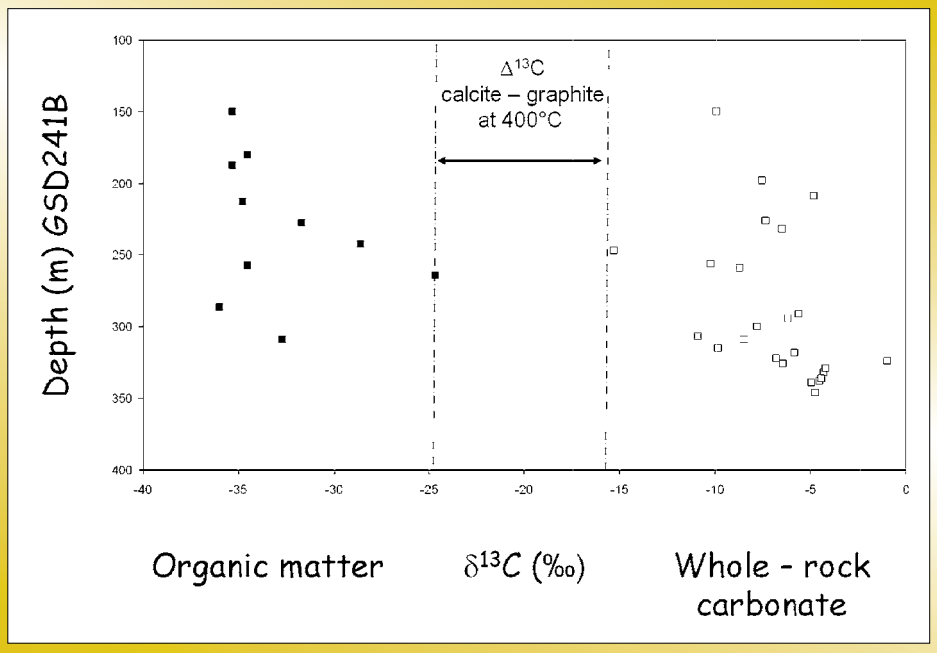


*Figure 3.4.10: $\delta^{13}C$ data for carbonaceous matter and whole-rock carbonate for Granny Smith drill hole GSD241B. Sources of data: carbonaceous matter (Golding, 2005); whole-rock carbonate data (Eilu and Mikucki, 1996). Fractionation factor for calcite-graphite is from Ohmoto and Goldhaber (1997).*

that some carbonaceous material proximal to the gold and nickel deposits was directly precipitated by reaction of $CO_2$ and $CH_4$ rather than being re-equilibrated OM. Inorganic precipitation of carbon can occur either through oxidation of methane or reduction of $CO_2$, hence the precipitation reactions may be driven by the same species driving reduction /oxidation of $CO_2$ / $CH_4$ i.e., $H_2$ and $SO_2$/sulphate.

e.g.,

$CO_2 + 2H_2 = C + 2H_2O$

$3CH_4 + 2SO_2 = 3C + 2H_2S + 4H_2O$

### 3.4.3.6 Mantle methane: Evidence from noble gas studies

Evidence for a component of $CH_4$ from the mantle has come from recent noble gas studies of fluid inclusions at St Ives (Figure 3.4.11 and Kendrick et al., 2008). Sampling for noble gas studies targeted drill holes in different parts of the alteration system. The selected samples contain mixed assemblages of $CH_4$-$CO_2$-$H_2O$-NaCl fluid inclusions that exhibit some variability but are broadly related to the oxidation state of vein mineralogy. The oxidising part of the system is dominated by $CO_2$-$H_2O$-NaCl fluid inclusions. Micro-thermometric measurements indicate $CO_2$ has a high purity with ice melting points in the range -56.6 to -57.8 °C, close to the $CO_2$ triple point. Liquid and vapour $CO_2$ in these inclusions homogenises between +12 and +31 °C into either the liquid or gaseous state. The majority of aqueous fluid inclusions have salinities of 5 to <26 wt % salt (Tm = -5 to -21.9 °C) and some have a Ca-rich composition indicated from eutectic points as low as -52 °C. Mixed aqueous-carbonic fluid inclusions have clathrate melting temperatures of +3.8 to +8.2 °C equivalent to ~ 4–11 wt % NaCl eq., and variable fractions of $CO_2$ -fill, between 0.3 and 0.9, indicate trapping in the two phase field. Samples from the 'reduced' part of the system are dominated by non-polar fluid inclusions that exhibit no phase change during cooling to -180 °C. Laser Raman indicates as many as ~80–90 % of these fluid inclusions contain pure $CH_4$ but some contain up to 20 mol % $N_2$ or 50 mol % $CO_2$ (Petersen, 2007).

Mineral separates (30–100 mg) of six fluid inclusion samples were irradiated and the fluid inclusions were analysed simultaneously for Cl, Br, I and the isotopes of Ar. The noble gas isotopes were extracted from fluid inclusions by sequential stepped heating or *in vacuo* crushing experiments which provide far more information than is available from 'bulk' analysis: each sample exhibits considerable variation in $^{40}Ar/^{36}Ar$ indicating that different populations of fluid inclusion have been decrepitated at different stages of the experiment. The results indicate a correlation between isotopic composition of Ar and fluid inclusion type supporting arguments for three fluid end-members.

$H_2O$-NaCl-dominated fluid inclusions with minor $CO_2$ have the lowest $^{40}Ar/^{36}Ar$ values of ~700–2300 and are interpreted to represent 'ambient' fluids of the mid-crust. They could be products of metamorphic volatilisation (Powell, 1991) or mixtures of metamorphic and surface-derived fluids.

$CO_2$-$H_2O$-NaCl fluid inclusions in oxidised veins spatially associated with intrusions imaged by seismic, or felsic porphyries exposed in the mine area (Neumayr, 2007; Walshe, 2006) have $^{40}Ar/^{36}Ar$ values of ≥17,000. The presence of anhydrite suggests $SO_2$-rich magmatic volatiles.

$CH_4$ fluid inclusions in reduced veins have the highest $^{40}Ar/^{36}Ar$ values of up to ~ 48,000 and are inferred to contain parts-per-trillion $^{36}Ar$. The high $^{40}Ar/^{36}Ar$ values are similar to the modern day convecting mantle (Burnard, 1997; Marty, 1997; Ballentine, 2005). Such values could not be acquired if $CH_4$ was produced by reduction of crustal $CO_2$ with lower $^{40}Ar/^{36}Ar$. An origin from natural gases in a sedimentary basin is not favoured, because $CH_4$ in these environments is typified by a parts-per-million $^{36}Ar$ concentration and $^{40}Ar/^{36}Ar$ values of <2000 (O'Nions, 1993). One mechanism for production of high purity $CH_4$ with a $^{40}Ar/^{36}Ar$ value of ~48,000, in lower-crustal basement rocks, is by serpentinisation of underlying ultramafic rocks (Malkovets, 2007; Sachan, 2007; Schmidt, 2007; Thomassot, 2007) by fluids from the Earth's surface. Alternatively methane production in the mantle could be driven by episodic release of $H_2$ from the Earth's core (Walshe, 2007). The core is possibly the largest reservoir of $H_2$ on the Earth (Williams and Henley, 2001) with potential to sustain mantle methane production through Earth history. Production of mantle $CH_4$ by episodic release of $H_2$ from the Earth's core may better explain the periodicity of major gold mineralisation epochs that occur on a time -scale of 0.5 - 1 billion years through Earth history.

Preliminary Ne-isotope analysis, confirms a mantle origin, and ongoing work will further constrain the noble gas isotope composition of the mantle end-member currently indicated to have a $^{40}Ar/^{36}Ar$ value of ≥48,000. The unexpectedly high $Cl/^{36}Ar$ values determined for samples dominated by $CH_4$ fluid inclusions suggests the presence of Cl as HCl gas.

### 3.4.3.7 Redox effects on $\delta^{34}S$ sufides and sulphates

The value of $\delta^{34}S$ in sulphides and sulphates vary as a function of the redox state of the fluid in the vicinity of the $HSO_4$-$H_2S$ buffer ($SO_2$–$H_2S$ buffer above ~ 400 °C). There is significant enrichment of $^{34}S$ in the oxidised sulphur species (anhydrite, $HSO_4$ and $SO_2$) with respect to reduced species (pyrite, pyrrhotite, $H_2S$). This enrichment in $^{34}S$ is of the order of +10 to +20 ‰ $\delta^{34}S$ over the temperature

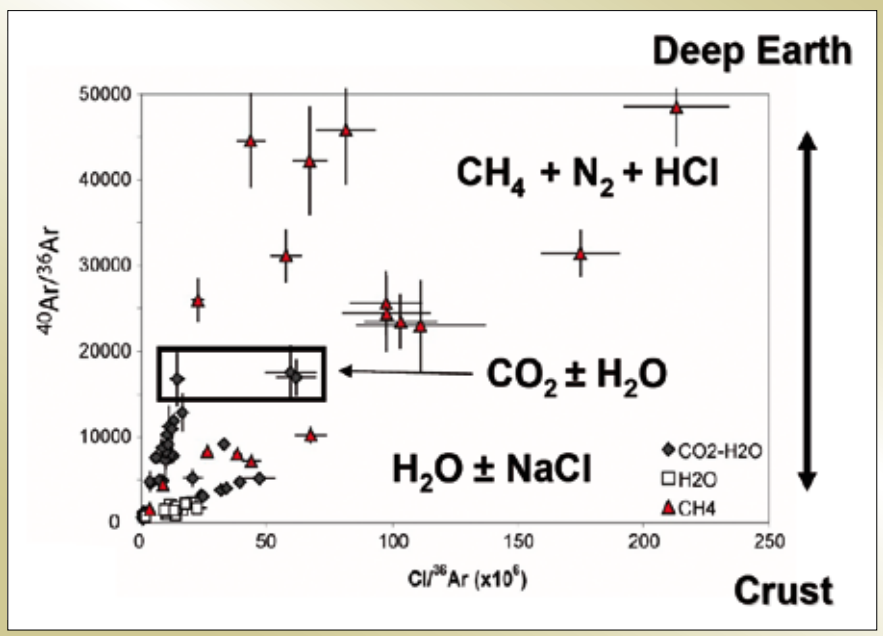


*Figure 3.4.11: Fluid inclusion $^{40}Ar/^{36}Ar$ versus $Cl/^{36}Ar$ for Au-related samples. The maximum $Cl/^{36}Ar$ values determined in samples dominated by Cl-poor $CH_4$ fluid inclusions are unlikely to be explained by Cl in low salinity $H_2O$ fluid inclusions which are very rare (< 2%) in the sample. These data are interpreted to indicate HCl is present in mantle-derived $CH_4$. The $^{36}Ar$ concentration of mantle-methane is unlikely to exceed the parts-per-trillion range because saline aqueous fluid inclusions with similar $Cl/^{36}Ar$ values contain ppb $^{36}Ar$. The spread in $^{40}Ar/^{36}Ar$ and $Cl/^{36}Ar$ can be explained by the addition of crustal $^{36}Ar$ during fluid migration. Data are from Kendrick et al. (2008).*

range 500 to 300°C (Ohmoto, 1997). This partitioning gives rise to a number of important redox effects:

1. At highly oxidised conditions with sulphate dominant in the fluid, the $\delta^{34}S$ values will be negative assuming the bulk S isotopic composition of the fluid is not greater than ~ 10 to 20 ‰, depending on the temperature.

2. Reduction of sulphate may give rise to positive $\delta^{34}S$ values of sulphides

3. Partial reduction of sulphate may lead to may lead to residual sulphate being enriched in $^{34}S$ (i.e. greater $\delta^{34}S$). Conversely oxidation of reduced sulphur species could lead to sulphate being depleted in $^{34}S$ (i.e., smaller values of $\delta^{34}S$).

The variation in sulphur isotopic composition of sulphides in the Au systems is significant. The $\delta^{34}S$ values range from -14 ‰ to +15 ‰ with about 95 % of the data occurring within the -10 ‰ and +8 ‰ interval (Figure 3.4.12A). Most deposits and camps tend to show the entire range of $\delta^{34}S$ values (*cf.* the St Ives camp with the Golden Mile and Wallaby deposits (Figure 3.4.13), but the mix of isotopic compositions is variable between deposits/camps. The Porphyry deposit, a small deposit in the Yarrie district with a total pre-mining resource of 11 tonnes of Au (Cassidy, 1992), shows a range of $\delta^{34}S$ values from –10.2 to +10.0 ‰, illustrating that wide ranges of values occur in small as well in large deposits (Hodkiewicz, 2003).

Notably the range of $\delta^{34}S$ values associated with high grade Au (greater than 10 ppm) is variable from deposit to deposit. The data of Clout (1989) show that high-grade Au tends to occur with the most negative sulphur isotope signals in pyrite ($\delta^{34}S$ of 0 to -10 ‰; Figure 3.4.14). As with the Golden Mile, the highest Au grades tend to occur with the lightest sulphur isotope values in these deposits, although the inverse does not hold. In contrast with the Golden Mile, pyrite from high-grade zones in deposits such as Wallaby and Junction, St Ives, have positive $\delta^{34}S$ values (0 to +5 ‰), although there is a limited data set for the Junction deposit (6 pyrrhotite analyses). Significant amounts of anhydrite are documented for the Golden Mile (Clout, 1989) and beneath the Victory - Defiance deposits of the St Ives camp (this study) and there are reports of minor occurrences of anhydrite from the Wallaby deposit. Sulphur isotopic composition of primary anhydrite ranges from +6 to +19 ‰ with some 35% of the data occurring between +8 and +10 ‰.

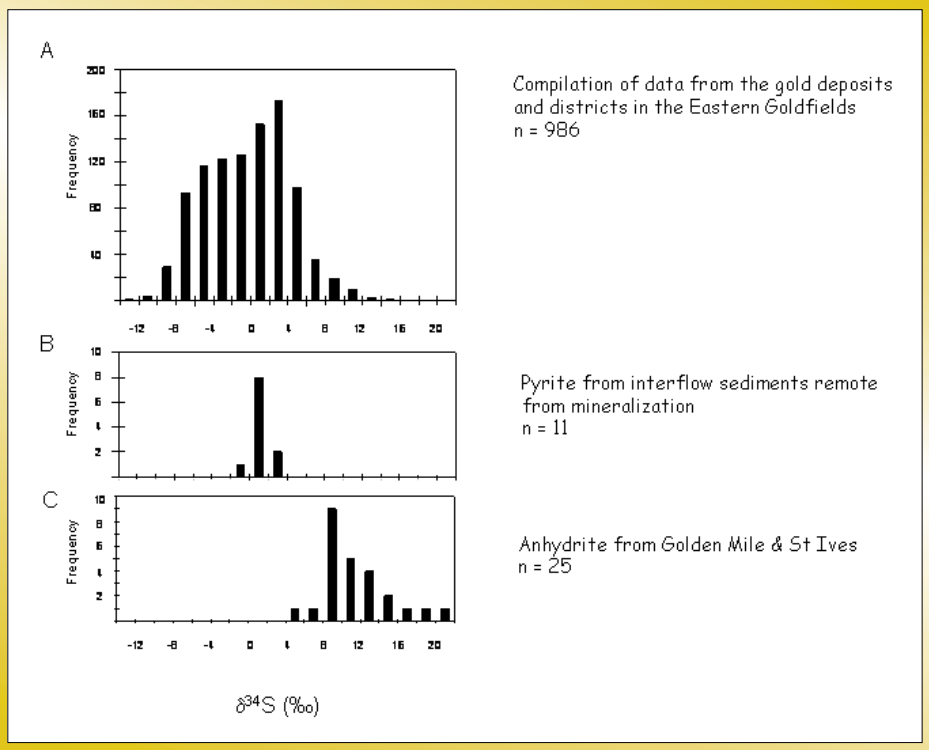


*Figure 3.4.12: Compilation of sulphur isotope data.*
*A) Compilation of sulphide data from the gold deposits and districts in the Eastern Goldfields from the following sources Hodkiewicz (2003); Palin & Xu (2000); Harbi (1997); Ren and Heithersay (1998); Clout (1989); this study; Hagemann & others unpublished data; Kitto and Halley, unpublished data; unpublished Western Mining Report (1987); n = 986.*
*B) Sulphur isotopic compositions of sulphides from sediments distal to known deposits/camps or early/ diagenetic sulphides: this study & unpublished Western Mining report (1987).*
*C) Sulphur isotopic composition of primary anhydrite from the Golden Mile; Clout (1989) and St Ives (this study).*

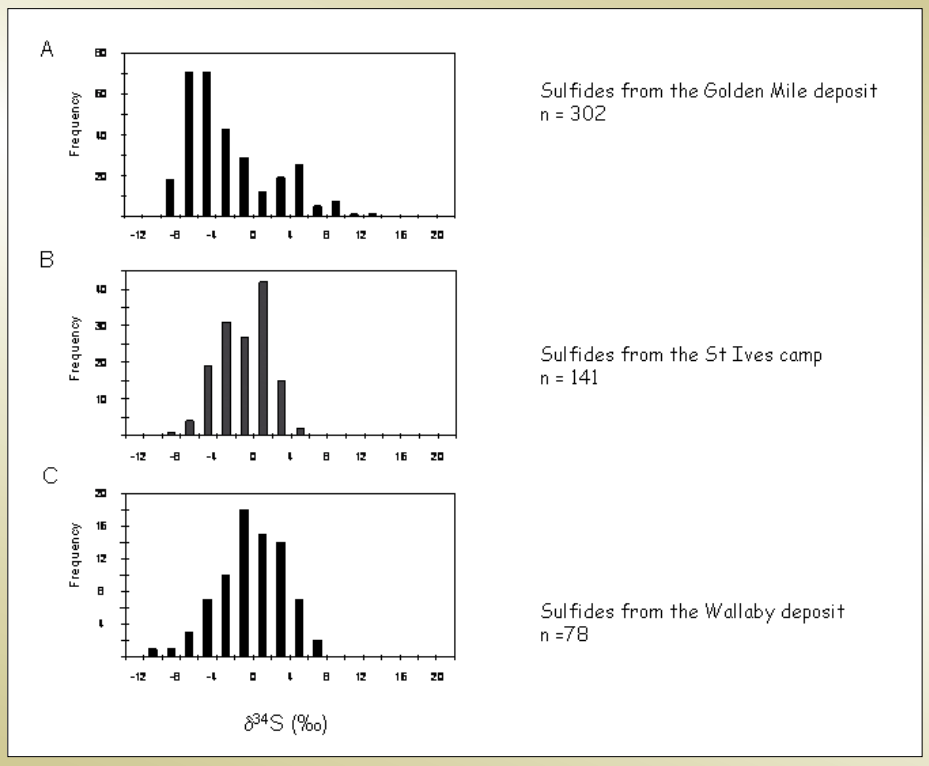


*Figure 3.4.13: Compilation of sulphur isotope data by camp: A Golden Mile deposit; data from Clout (1989) and Hagemann and Bateman unpub data; B St Ives camp; data from Hodkiewicz (2003); Palin & Xu (2000); MERIWA 358; C Wallaby deposit; MERIWA 358.*

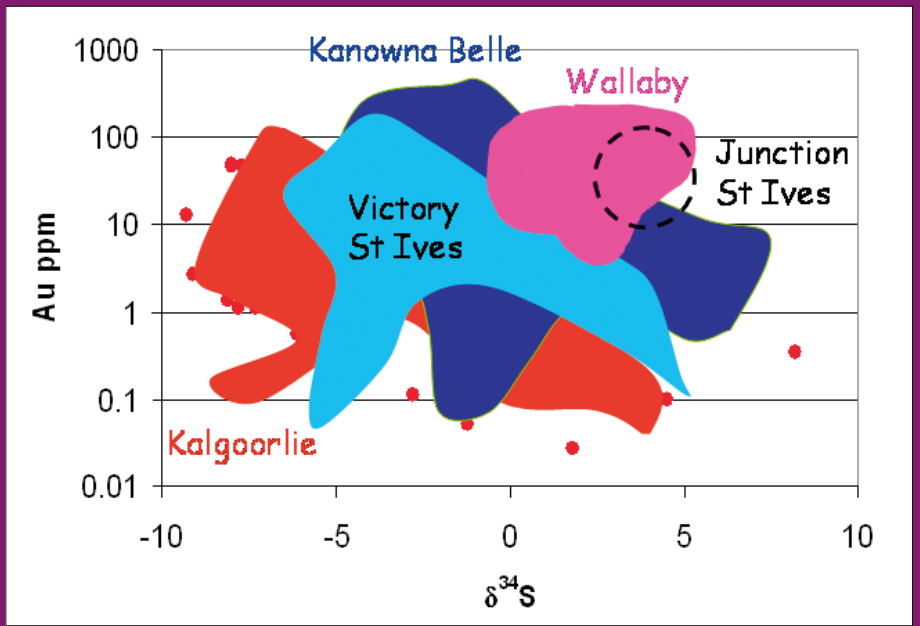


*Figure 3.4.14: Correlation of sulphur isotopes values with Au grade. The Kanowna Belle and Victory-Defiance deposits show a strong correlation between gold grade and $\delta^{34}S$ values; comparable with the Golden Mile but without the strong negative signal in the high grade gold zones. By contrast high grade zones in the Wallaby deposit and Junction, St Ives, show more limited and positive $\delta^{34}S$ values.*

### 3.4.3.8 S, Sr and Pb isotope contraints on $SO_2$/sulphate reservoir(s)

Numerous studies have used the negative isotope ratios of Au-related pyrites ($\delta^{34}S$ of 0 to -10 ‰) in some giant orogenic Au deposits (e.g., Golden Mile, Timmins and Kirkland Lake), in combination with alteration mineral assemblages that include haematite ± anhydrite ± vanadium-micas, to infer the presence of an inherently oxidised fluid in the system, most likely of magmatic origin, at the time of Au deposition (Cameron, 1987; Hall, 2001; Hattori, 1987; Walshe, 2003). The spatial association of oxidised alteration assemblages with intrusive complexes is a strong hint that the source(s) of oxidation were magmatic.

What constraints can be placed on the sulphur isotopic composition of the magmatic fluids? There is no direct information on the sulphur isotopic composition of either magmatic sulphide or sulphate *sensu strictu*, i.e., sulphide or sulphate species that equilibrated with a silicate melt. However, $\delta^{34}S$ values of sulphate in the gold systems provide a proxy for magmatic sulphur dioxide or aqueous sulphate derived from sub-solidus disproportionation of sulphur dioxide to sulphate and $H_2S$ via the reaction:

$$4H_2O + 4SO_2 = 3HSO_4^- + 3H^+ + H_2S$$

$\delta^{34}S$ values for primary anhydrite (Figure 3.4.12C) are similar to $\delta^{34}S$ values for anhydrite in porphyry Cu-Au deposits (Frikken, 2005; Heithersay, 1995). The $\delta^{34}S$ values of anhydrite will reflect the bulk $\delta^{34}S$ value for the mix of fluids in the system as well as the redox state and the temperature. Given the likely redox and temperature effects, a reasonable estimate for $\delta^{34}S$ value of sulphate in an oxidised fluid "end-member" would be of the order of +5 to +10‰ with $SO_2$ having a sulphur isotopic composition close to zero.

$^{87}Sr/^{86}Sr$ and Pb isotope ratios of anhydrite and celestine as well as Pb isotope ratios of pyrite (Figure 3.4.15 and Table 3.4.2) provide some additional constraints on magmatic versus non-magmatic fluids and possible isotopic composition of the $SO_2$ /sulphate reservoir, following the work of Clout (1989) on sulphates from the Golden Mile and (Hodkiewicz, 2003) on $\delta^{34}S$ vs. Pb isotope composition of pyrite from the Victory-Defiance complex making use of the Pb isotope data of Ho et al. (1994).

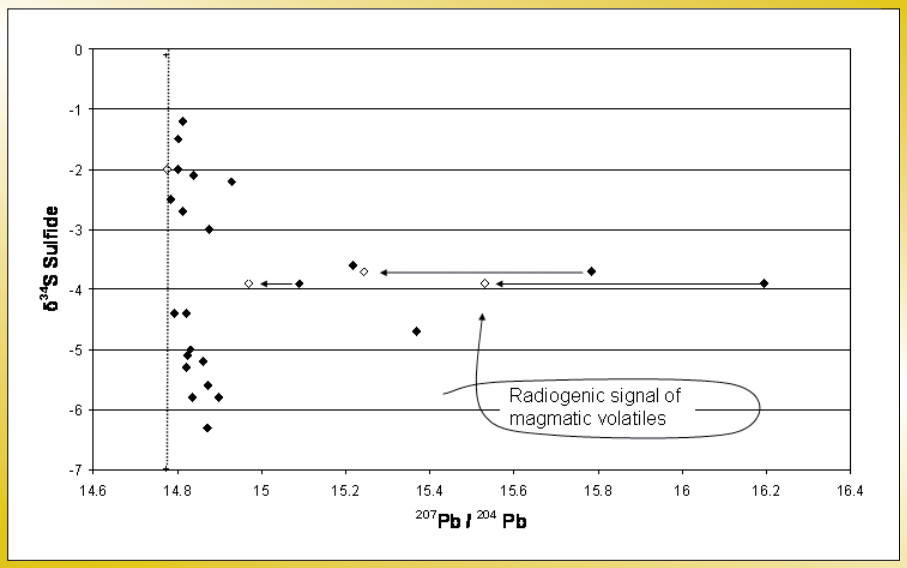


*Figure 3.4.15: $\delta^{34}S$pyrite vs. $^{207}Pb/^{204}Pb$ pyrite for pyrite from the 32 Shear Zone, Victory-Defiance complex, St Ives. Open diamonds: age corrected data; vertical dashed line is average $^{207}Pb/^{204}Pb$ galena from quartz vein within Devon Consols Basalt. The radiogenic lead signal that corresponds with $^{34}Spy$ ~ -3 to -5 ‰ is interpreted as the isotopic Pb signal condensation of volatiles of magmatic affinty (see following figure). Data sources: $^{207}Pb/^{204}Pb$ sulphides from Ho et al. (1994) and $\delta^{34}S$ pyrite from Hodkiewicz (2003).*

Table 3.4.2: $\delta^{34}S$, $^{87}Sr/^{86}Sr$, $^{206}Pb/^{204}Pb$, $^{207}Pb/^{204}Pb$ and $^{208}Pb/^{204}Pb$ for sulphate from the Victory-Defiance complex, St Ives. Analyses by Anita Andrew (Environmental Isotopes), Graham Carr and David Whitford, CSIRO, Riverside park, North Ryde, Sydney

| DDH | Depth (m) | Species | $\delta^{34}S$ sulfate | $^{206}Pb/^{204}Pb$ | $^{207}Pb/^{204}Pb$ | $^{208}Pb/^{204}Pb$ | Pb (conc) ppm | $^{87}Sr/^{86}Sr$ measured | $^{87}Sr/^{86}Sr$ normalized to 0.710240 |
|---|---|---|---|---|---|---|---|---|---|
| CD 1703A | 360.8 | anhydrite | 11.00 | 15.785 | 16.163 | 37.096 | 0.12 | 0.702101 | 0.702036 |
| CD 1703A | 509.5 | anhydrite | 9.75 | 14.036 | 14.881 | 33.797 | 0.32 | 0.712561 | 0.712495 |
| CD 1703A | 596.8 | anhydrite | 7.40 | 14.999 | 15.113 | 34.735 | 0.23 | 0.701583 | 0.701518 |
| CD 1703A | 662.5 | anhydrite | 5.96 | 15.998 | 15.463 | 35.339 | 3.62 | 0.702956 | 0.702891 |
| CD 1703A | 733.8 | celestine | 8.64 | 13.863 | 14.594 | 33.253 | 0.19 | 0.703568 | 0.703503 |
| CD 6800 | 361.8 | anhydrite | 13.58 | 14.307 | 14.97 | 34.226 | 0.82 | 0.702063 | 0.701998 |
| CD 7069 | 536.35 | anhydrite | 13.07 | 14.339 | 14.983 | 33.917 | 0.84 | 0.701516 | 0.701451 |
| CD7068 | 105 | anhydrite | 19.15 | 14.419 | 14.948 | 34.122 | 0.28 | 0.709509 | 0.709443 |
| CD7068 | 298 | anhydrite | 19.46 | 14.142 | 14.902 | 33.831 | 1.64 | 0.710793 | 0.710727 |
| CD7068 | 388.5 | anhydrite | 17.19 | 14.965 | 15.167 | 34.659 | 0.73 | 0.706509 | 0.706443 |

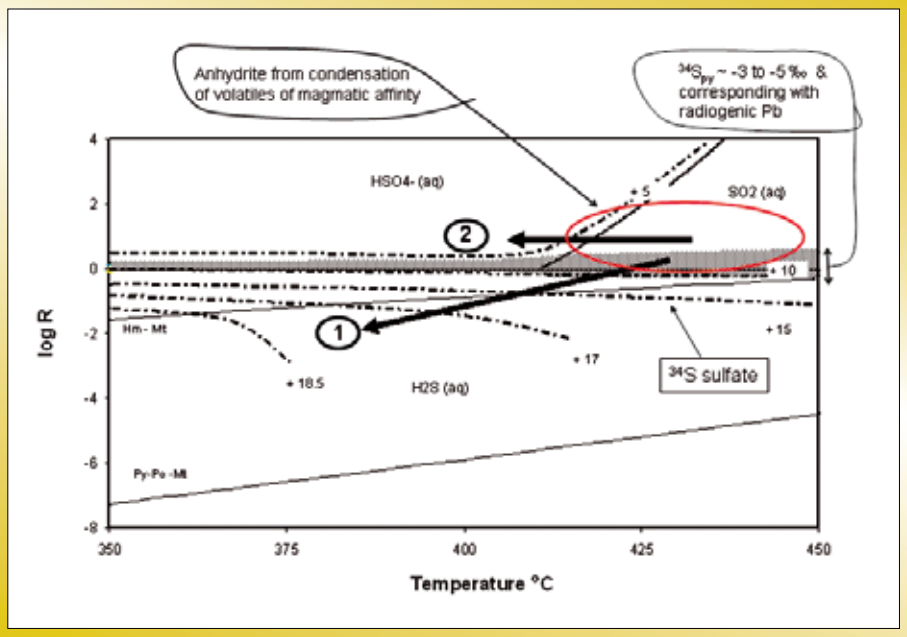


*Figure 3.4.16: Plot of log R (sum oxidised sulphur species/$H_2S$) vs Temperature showing the variation in sulphur isotopic composition of sulphate and sulphide as a function of temperature. Bulk sulphur isotopic composition of fluid is assumed to be zero. Anhydrite of ~ + 5 to +10 ‰ interpreted to reflect condensation of volatiles of magmatic affinty that contained $SO_2$ as well as radiogenic lead. Shaded area shows region of $^{34}Spy$ ~ -3 to -5 ‰ that corresponds with the radiogenic Pb isotope values. Cooling trends 1 and 2 show possible range of $^{34}S$ sulphate values derived from cooling of a high temperature fluid dominated by $SO_2$ with and without reduction respectively.*

*Figure 3.4.17: Plot of $\delta^{34}S$ sulphate versus $^{87}Sr/^{86}Sr$ for anhydrite and celestine from the Golden Mile (Clout, 1989) and Victory-Defiance complex, St Ives (this study). About 40% of the $^{87}Sr/^{86}Sr$ values are less than 0.702 and consistent with equilibration with ambient fluid/host rocks. For most $\delta^{34}S$ sulphate values above about +15‰ there is a positive correlation of $^{87}Sr/^{86}Sr$ with $\delta^{34}S$ sulphate values. These values also correlate inversely with $^{206}Pb/^{204}Pb$ in sulphate (see following figure). $\delta^{34}S$ sulphate values less than ~ +12 ‰ show a less well defined inverse correlation with $^{87}Sr/^{86}Sr$ values (although the later correlation is strongly dependent on one sample at +10 ‰) and also $^{206}Pb/^{204}Pb$ in sulphate. The preliminary interpretation is that anhydrite of ~ + 5 to +10 ‰ represents condensation of volatiles of magmatic affinity that contained $SO_2$ as well as radiogenic lead but limited (?) non-radiogenic Sr (Fluid 2). The anhydrous reduced fluid (Fluid 3) or aqueous derivatives contained radiogenic strontium. The mixing of oxidised volatiles with aqueous reduced fluids lead to the well-defined linear correlation of $^{87}Sr/^{86}Sr$ with $\delta^{34}S$ sulphate for $\delta^{34}S$ sulphate above about +15‰. The less well defined inverse correlation $\delta^{34}S$ sulphate with $^{87}Sr/^{86}Sr$ for $\delta^{34}S$ sulphate values less than ~ +12 ‰ is interpreted to reflect mixing of oxidised volatiles (Fluid 2) with anhydrous reduced fluids (Fluid 3). Re-equilibration of magmatic volatiles with ambient fluids (Fluid 1) and host rocks led to an increase in $\delta^{34}S$ sulphate only.*

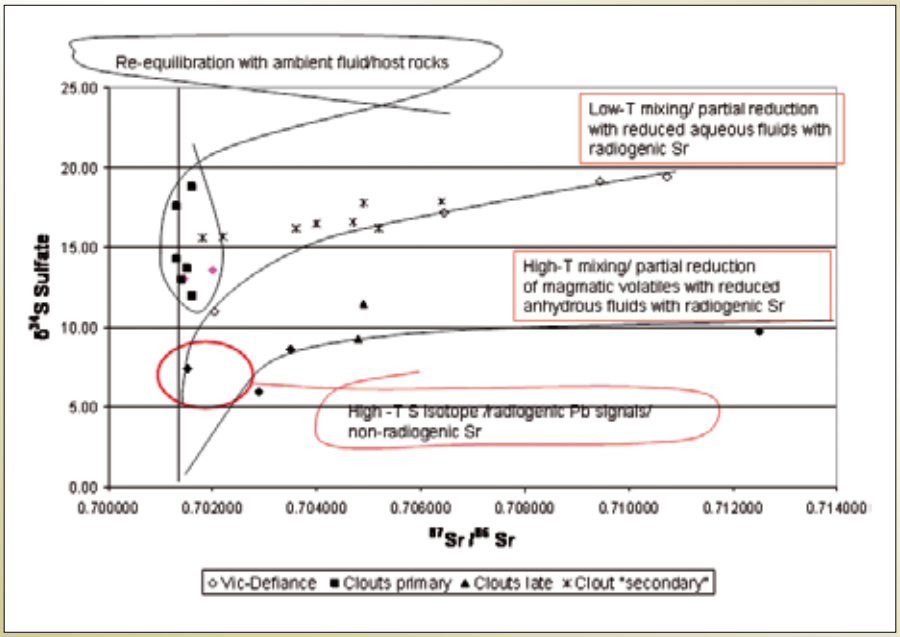

Figures 3.4.15 through to Figure 3.4.18 show that the radiogenic Pb signal documented by (Ho et al., 1994) in pyrite from the Victory - Defiance complex is limited to pyrite with $\delta^{34}S$ values in the narrow range of ~ -3.5 to -5 ‰. From Figure 3.4.16, pyrite with this range of sulphur isotopic values could have formed in equilibrium or close to equilibrium with anhydrite formed from $SO_2$ at temperatures ≥ ~ 425 °C, with $\delta^{34}S$ sulphate of the order of +5 to +10‰. Hence the radiogenic lead signal that corresponds with $^{34}Spy$ ~ -3 to -5 ‰ is interpreted as the isotopic Pb signal of condensed volatiles of magmatic affinity (Fluid 2).

A comparison of the $^{87}Sr/^{86}Sr$, $\delta^{34}S$ and $^{206}Pb/^{204}Pb$ isotope ratios of anhydrite and celestine from the Victory - Defiance Complex, St Ives (Figures 3.4.17, 3.4.18) shows that:

- For most $\delta^{34}S$ sulphate values above ~ +15‰, there is a linear positive correlation of $^{87}Sr/^{86}Sr$ with $\delta^{34}S$ sulphate values
- For most $\delta^{34}S$ sulphate values ≥ ~ +10‰ there is a well defined linear inverse correlation of $^{87}Sr/^{86}Sr$ with $^{206}Pb/^{204}Pb$ in sulphate
- For $\delta^{34}S$ sulphate values ≤ ~ +10‰ less well defined correlation exist between these isotopic ratios

If the inverse correlations between $^{87}Sr/^{86}Sr$ with $^{206}Pb/^{204}Pb$ in sulphate are primary (a question still under investigation) then the implication is that any Sr transported by oxidised volatile-rich fluids was non-radiogenic and that anhydrous reduced fluid (Fluid 3) or aqueous derivatives contained radiogenic strontium, in part sufficient to saturate celestine. Mixing of oxidised volatiles with aqueous reduced fluids could lead to the well defined linear correlations of $^{87}Sr/^{86}Sr$ with $\delta^{34}S$ sulphate and $^{206}Pb/^{204}Pb$ sulphate. The less well defined correlations of $^{87}Sr/^{86}Sr$ with $\delta^{34}S$ sulphate and $^{206}Pb/^{204}Pb$ sulphate for $\delta^{34}S$ sulphate values less than ~ +12 ‰ could reflect mixing of oxidised volatiles (Fluid 2) with anhydrous reduced fluids (Fluid 3).

The preliminary interpretation from these data is that:

- Anhydrite and celestine with $\delta^{34}S$ of ~ +5 to +10 ‰ was deposited from oxidised volatiles of magmatic affinity (Fluid 2)
- $\delta^{34}S$ of $SO_{2(g)}$ was ~ 0 ‰ assuming fluid temperatures of ~ 400 – 500 °C
- Radiogenic Pb was transported in the oxidised volatiles
- At ~ 400 – 500 °C, $\delta^{34}S$ of coexisting $H_2S_{(g)}$ was ~ -4 to -5 ‰.

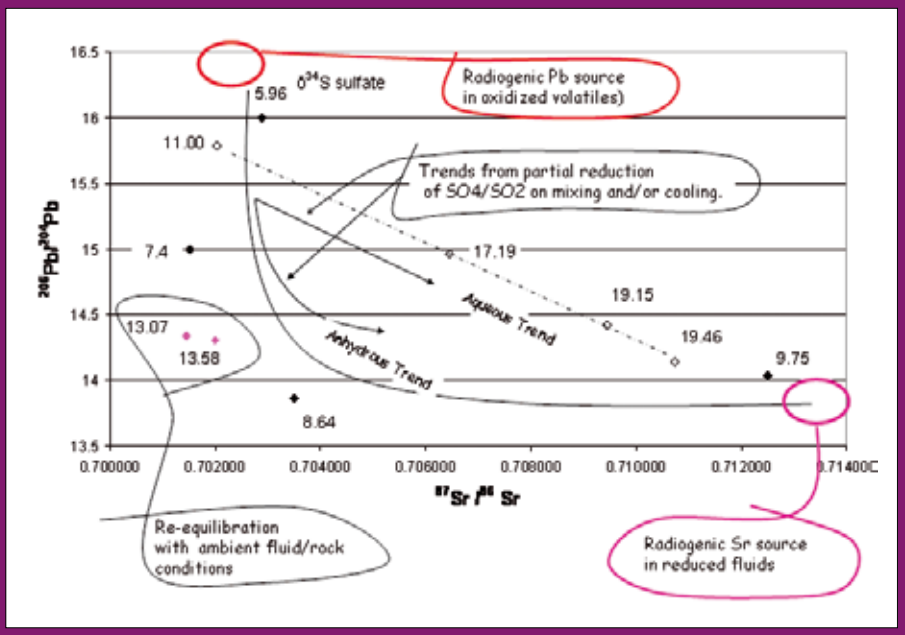


*Figure 3.4.18: Plot of $^{206}Pb/^{204}Pb$ versus $^{87}Sr/^{86}Sr$ for anhydrite and celestine from the Victory-Defiance complex, St Ives (this study). Corresponding $\delta^{34}S$ values for samples are shown on the figure. For most $\delta^{34}S$ sulphate values ≥ +10‰ there is a well defined linear inverse correlation of $^{206}Pb/^{204}Pb$ and $^{87}Sr/^{86}Sr$ that is interpreted as mixing of oxidised volatiles with aqueous reduced fluids. A less well defined non-linear mixing line for $\delta^{34}S$ sulphate values less than ~ +10 ‰ is interpreted to reflect mixing of oxidised volatiles (Fluid 2) with anhydrous reduced fluids (Fluid 3); consistent with previous figure. Samples defined as reflecting re-equilibration with ambient fluids (Fluid 1) and host rocks consistent with previous figure.*

- Radiogenic pyrite of ~ -3 to -5 ‰ $\delta^{34}S$ reflects high T sulphide deposition from fluids dominated by an oxidised sulphur component
- The anhydrous reduced fluid (Fluid 3) transported radiogenic Sr.
- Mixing and cooling of oxidised volatiles with aqueous reduced fluids (derived from mixing of Fluids 1 and 3 and fluid-rock reaction) lead to the well defined linear correlation of $^{87}Sr/^{86}Sr$ with $\delta^{34}S$ sulphate for $\delta^{34}S$ sulphate above about +15‰.
- The less well defined inverse correlation $\delta^{34}S$ sulphate with $^{87}Sr/^{86}Sr$ for $\delta^{34}S$ sulphate values less than ~ +12 ‰ is interpreted to reflect mixing of oxidised volatiles (Fluid 2) with anhydrous reduced fluids (Fluid 3).

The correlations between $^{87}Sr/^{86}Sr$, $\delta^{34}S$ and Pb isotopes ratios in sulphate are the subject of ongoing studies. It is noted that the correlation of high $^{87}Sr/^{86}Sr$ values with $\delta^{34}S$ sulphate at about +10 ‰ is dependent on one sample.

### 3.4.3.9 Positive $\delta^{34}S$ sulphide values and constraints on the redox states

A feature of the sulphur isotopic compositions of sulphides in the Au deposits of the Eastern Goldfields Superterrane (as summarised in Figures 3.4.12 and 3.4.13) is the range in $\delta^{34}S$ values both positive and negative. As the only known reservoir of positive $\delta^{34}S$ values is sulphate, the easiest explanation of the positive $\delta^{34}S$ values for sulphides is that they are derived from the reduction of that sulphate.

Reduction of sulphate requires a strong reductant such as $CH_4$ or $H_2$:

e.g.,

$CH_4 + HSO_4^- + H^+ = H_2CO_3 + H_2S + H_2O$

$4H_2 + HSO_4^- + H^+ = H_2S + 4H_2O$

Mikucki (2006) modelled the range in sulphur isotope values of minerals and aqueous species that result from mixing of sulphate - rich, highly oxidised fluid and a reduced, $CH_4$-rich fluids. The results of the numerical experiments utilizing the *HCh* geochemical modelling package (Sharov and Bastrakov, 1999) have been used to calibrate $\delta^{34}S$ pyrite with respect to redox state for pyrites of the Eastern Goldfields Superterrane (Figure 3.4.19). The calibration assumes initial $\delta^{34}S$ fluid values of 0 and +10 ‰ for the reduced and oxidised fluids, respectively.

The major findings from these experiments are:

- The $\delta^{34}S$ values of pyrite varied between ~ -10 and +6 ‰ in oxidation/reduction fluid mixing.

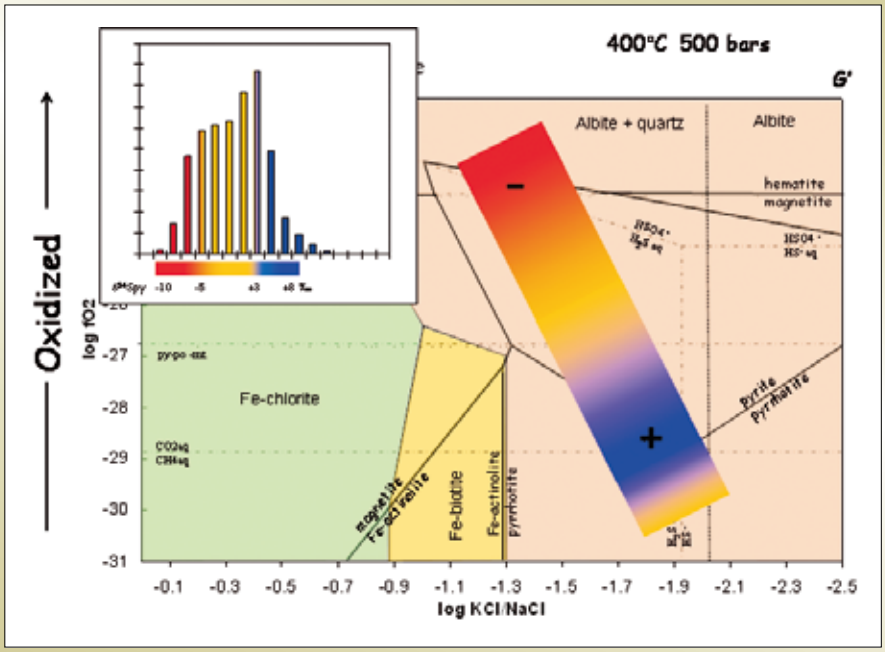


*Figure 3.4.19: Log $fO_2$- aKCl(aq)/ aNaCl(aq) illustrating the variation of $\delta^{34}S$ pyrite with redox state of the fluids, assuming mixing of a reduced $CH_4$- rich fluid and acid-oxidised, $SO_4$-rich fluid. The scheme is based on the numerical experiments of Mikucki (2004) as summarised in Figures 3.4.23 and 3.4.24. Initial $\delta^{34}S$ fluid values of 0 and +10‰ are assumed for reduced and oxidised fluids, respectively, for this figure. The strongly negative values $\delta^{34}S$ of pyrite (-5 to -10 ‰) occur at ($SO_4^{2-} \sim H_2S$) or above ($SO_4^{2-} >> H_2S$) the sulphate/sulphide buffer. The strongly positive values (+3 to +8 ‰) occur at $CO_2/CH_4$ ratios below ~ 100. The calibration of $\delta^{34}S$ of pyrite with redox state depends on the estimates of $\delta^{34}S$ for the oxidised and reduced end-member fluids as well as their respective redox states.*

- The $\delta^{34}S$ values of anhydrite and aqueous sulphate varied between ~ +13 and +15 ‰ and ~ +10 and +25 ‰, respectively, given the same initial conditions.
- At the most oxidised conditions, $\delta^{34}S$ values of pyrite were ~ -10 ‰ with $SO_4^{2-} \sim H_2S$.
- At progressively more reduced conditions, $\delta^{34}S$ values of pyrite increased with increasing reduction of aqueous sulphate. The maximum of ~ + 6 ‰, attained between the pyrite/pyrrhotite/magnetite buffer and $CH_{4(aq)}$ / $H_2CO_{3(aq)}$ buffer, reflected the complete reduction of sulphate.
- With still greater proportions of reduced fluid, $\delta^{34}S$ values of pyrite decreased toward 0 ‰; that is towards the assumed isotopic composition of the reduced end-member fluid.

The strongly positive values between the pyrite / pyrrhotite / magnetite and $CH_{4(aq)}$ / $H_2CO_{3(aq}$ redox buffers implies that high grade Au zones with $\delta^{34}S$ sulphide values 0 to +5 ‰ (e.g., Wallaby deposit, Laverton; Junction deposit, St Ives; Figure 3.4.14) formed at reduced conditions compared with high grade Au zones of the Golden Mile ($\delta^{34}S$ of 0 to -10‰). The pyrite/pyrrhotite assemblages of the Junction deposit are consistent with this interpretation as are the methane fluid inclusions documented (Polito, 1999, 2001). While the Wallaby pipe is dominated by pyrite and magnetite, pyrrhotite is a common phase in the immediate environs and minor pyrrhotite is documented in the deposit associated with biotite shears. The heavier sulphur isotope values of pyrite from the Au stage in the deposit imply redox/sulphur activity conditions close to the stability conditions of pyrrhotite. Arguably high-grade Au zones in the Kanowna Belle and Victory deposits ($\delta^{34}S$ -5 to +5 ‰; Figure 3.4.14) formed in transitional redox environments.

### 3.4.3.10 Controls on variation of $\delta^{18}O$ in carbonate: T versus activity of $H_2O$

Changes in temperature have a greater impact on oxygen than on carbon and isotope partitioning between the fluid and carbonate. For a given isotopic composition of the fluid, there is a pronounced shift to higher $\delta^{18}O$ values in the carbonate with a less pronounced shift to higher $\delta^{13}C$ values. The theoretical cooling trends shown in Figure 3.4.20 through to Figure 3.4.22 depicts the composition of calcite in equilibrium with a fluid of $\delta^{13}C$ = 0 ‰ and $\delta^{18}O$ = 6 ‰ over a temperature range of 600° to 150° C.

Some patterns on $\delta^{13}C$ vs. $\delta^{18}O$ plots suggest simple cooling trends e.g. most data from the Kanowna Belle deposit and environs lie sub-parallel the cooling trend (Figure 3.4.22). Data sets of $\delta^{13}C$ and $\delta^{18}O$ in carbonate for individual deposits such as Nevoria and Westonia (Edna May) of the Southern Cross Goldfields, Great Eastern, Lawlers and the Golden Mile show patterns consistent with temperature effects (Walshe et al., 2006).

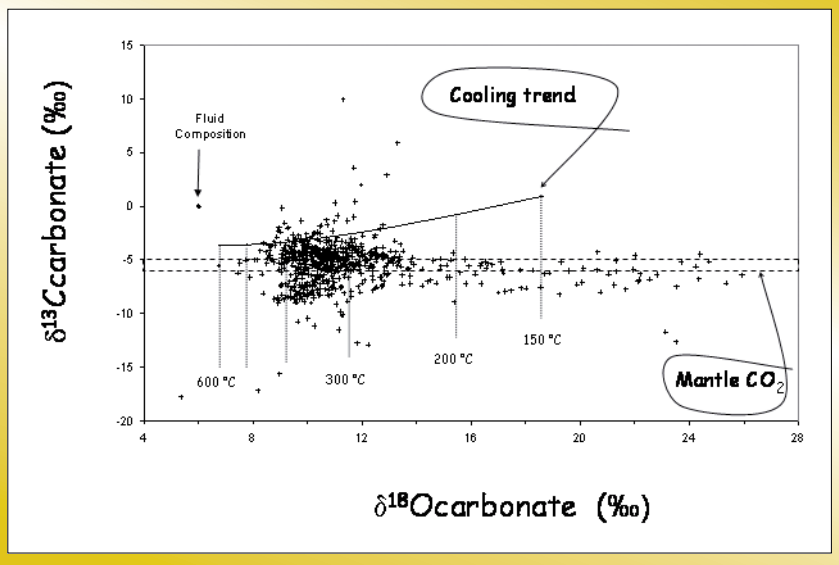


*Figure 3.4.20: $\delta^{13}C$ vs $\delta^{18}O$ plot for carbonates from the St Ives camp. The cooling trend depicts the composition of calcite in equilibrium with a fluid of composition $\delta^{13}C$ = 0 ‰ & $\delta^{18}O$ = 6 ‰ over a temperature range of 600 to 150 °C. Most data distribute around the $\delta^{13}C$ for the mantle $CO_2$ reservoir and there is no cooling trend in the data. Significant enrichments in $\delta^{18}O$ occur for $\delta^{13}C$ between -5 and -8. Calcite-$H_2O$ fraction factor for $^{18}O$ is from O'Neil et al. (1969) and calcite-$CO_2$ fraction factor for $^{13}C$ is from Chacko et al. (1991).*

However, not all deposits and districts show evidence of cooling trends in $\delta^{13}C$ versus $\delta^{18}O$ plots. For example, in the St Ives camp there is no cooling trend in the data, rather significant enrichments in $\delta^{18}O$ occur for a relative narrow range of $\delta^{13}C$ between -5 and -8 ‰ (Figure 3.4.20) that require another explanation. In other examples in the Laverton district (including the Wallaby and Lancefield deposits) there is a broad correlation of $^{18}O$ enrichment with $^{13}C$ (Figure 3.4.21) suggesting an effect of temperature coupled with other processes or variations in reservoir composition.

Another potentially significant process that needs to be considered in settings where the dominant fluids species is $CO_2$ rather than $H_2O$, or in transitional environments from $CO_2$-rich fluids to $H_2O$-rich fluids, is the fractionation of $^{18}O$ and $^{16}O$ between $CO_2$ and $H_2O$. $CO_2$ gas is enriched over liquid $H_2O$ by 8 to 12 ‰ $\delta^{18}O$ in the temperature range from 300 to 500 °C. This fractionation factor is not sufficient to account for variations in excess of 15 ‰ $\delta^{18}O$ observed in the St Ives. However the enrichment in $^{18}O$ could be accounted for by a fractionation process that progressive removes $H_2O$ from a limited volume/mass

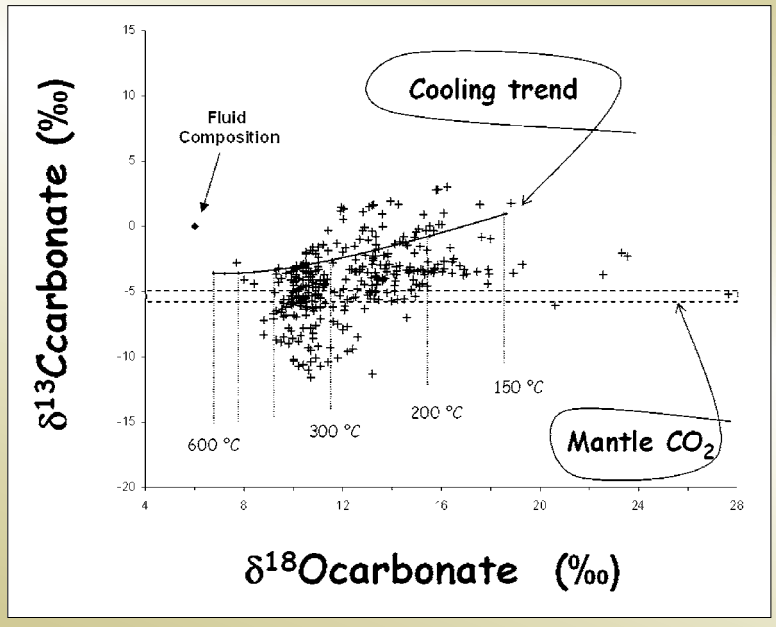


*Figure 3.4.21: $\delta^{13}C$ vs. $\delta^{18}O$ plot for carbonates from Laverton district, including the Wallaby and Lancefield deposits. The cooling trend depicts the composition of calcite in equilibrium with a fluid of composition $\delta^{13}C$ = 0 ‰ & $\delta^{18}O$ = 6 ‰ over a temperature range of 600 to 150 °C. Most data distribute above the $\delta^{13}C$ for the mantle $CO_2$ reservoir with broadly correlated enrichments $^{18}O$ with $^{13}C$. A component of the data, most notably from the Lancefield deposit, is depleted in $^{13}C$ with respect to the mantle reservoir.*

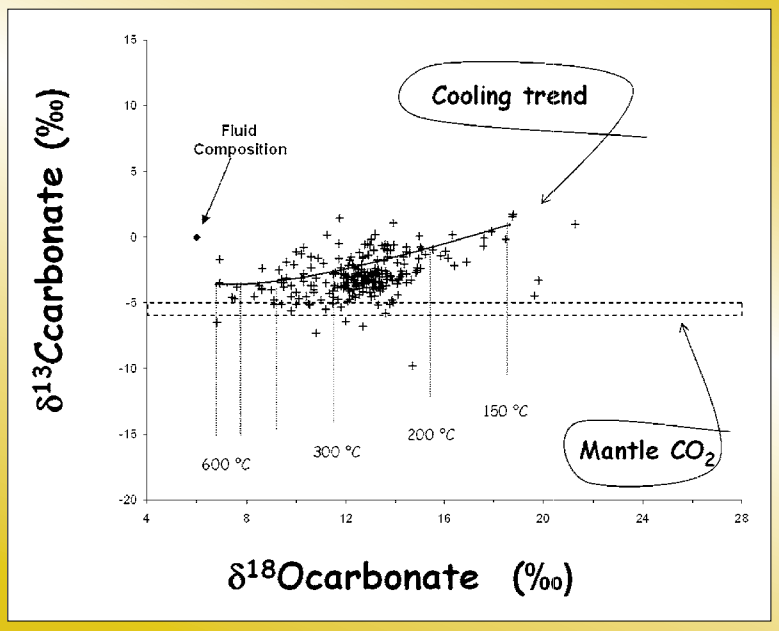


*Figure 3.4.22: $\delta^{13}C$ vs. $\delta^{18}O$ plot for carbonates from Kanowna Belle deposit and environs. The cooling trend depicts the composition of calcite in equilibrium with a fluid of composition $\delta^{13}C$ = 0 ‰ & $\delta^{18}O$ = 6 ‰ over a temperature range of 600 to 150 °C. Most data lie sub-parallel the cooling trend with $\delta^{13}C$ greater than $\delta^{13}C$ for the mantle $CO_2$ reservoir. Calcite-$H_2O$ fraction factor for $^{18}O$ is from O'Neil et al. (1969) and calcite- $CO_2$ fraction factor for $^{13}C$ is from Chacko et al. (1991).*

of oxidised C species (dolomite, calcite, ankerite, $H_2CO_3$ and $CO_2$) ± coexisting $SO_2$/sulphate, leaving a residual of $^{18}O$-enriched oxidised carbon species. A sink for $H_2O$ is required, the most obvious being the intense biotite alteration commonly association with carbonates enriched in $^{18}O$.

Possible reactions that could facilitate removal of $^{18}O$ depleted $H_2O$ as a silicate alteration product include $CO_2$ reduction reactions:

$$CO_2 + 4H_2 = CH_4 + 2H_2O(silicate)$$

and $CH_4$ oxidation reactions:

$$3CH_4 + 4SO_2 = 3CO_2 + 2H_2O(silicate) + 4H_2S$$

At St Ives, carbonates with $\delta^{18}O$ values in excess of 14 ‰ have $\delta^{13}C$ values less than the mantle $CO_2$ value (Figure 3.4.20). This suggests that oxidation of $CH_4$ by $SO_2$ rather than $H_2$ reduction of $CO_2$ was the dominant reaction.

The process of generating the $^{18}O$ enriched carbonates could have involved fluxing of a reduced $CH_4$-rich fluid through a limited volume/reservoir of $CO_2$- $SO_2$-rich fluid and progressive preferential precipitation of $^{16}O$ as biotite such that residual $SO_2$ and $CO_2$ was progressively enriched in $^{18}O$. Mass balance considerations imply concentrations of $SO_2 \geq CO_2$ in the oxidised fluid in order to sustain the methane oxidation as the $^{18}O$ enrichment mechanism.

A corollary of this interpretation is that it may be possible to use $\delta^{18}O$ of carbonate to map out the anhydrous domains of the system, in the process linking fluid inclusion data demonstrating water-poor conditions at the micro-scale to deposit to district scale alteration patterns.

#### 3.4.3.11 Deuterium isotopes and meteoric fluids in Archaean Au deposits

Epizonal Archaean lode Au deposits in Western Australia (Wiluna, Racetrack), Canada (Ross) and Zimbabwe (Commoner) are interpreted to represent shallow level equivalents to the mesozonal deposits in the same terrane. The presence of low-temperature (150° to 325°C), low salinity aqueous fluid inclusions, low inferred depth of orebody emplacement of <5km, and high $\delta D$ fluid (-6 ‰ ± 9 ‰ relative to SMOW) and low $\delta^{18}O$ fluid (4.4 ‰ ± 2.3 ‰ relative to Standard Mean Ocean Water - SMOW) values of Au related hydrothermal alteration minerals such as quartz, chlorite, and sericite have been interpreted by (Hagemann et al., 1994) as evidence for surface water influx into epizonal Achaean lode-gold deposits. The geochemical evidence for local influx of surface fluids into the hydrothermal system is further corroborated by: predominantly brittle shear zones that host orebodies, breccia hosted lodes, low temperature gangue and ore minerals such as silver sulphosalts, stibnite, precursor chalcedony, and vertical metal zonation of these orebodies. The exact chemistry of the surface fluids, and mechanism of interaction of this fluid with the ascending deep-sourced fluids, including possible disturbances in both radiogenic and C/O/S isotope signals that may reflect the input of Proterozoic or younger fluids into the systems, is the subject of on-going research.

### 3.4.4 Section 3: Concept and characteristics of end-member fluids: a discussion

#### 3.4.4.1 Introduction

It is argued that three end-member fluids are necessary to account for the geochemical characteristics of the deposits and environs in the Eastern Yilgarn Au systems, the inferred physicochemical conditions within the system, the spatial associations of Au deposits and camps with significant architectural elements of the system (transcrustal structures, intrusive complexes, district-scale structural culminations) and temporal correlations with the geodynamic and magmatic history of the terrane. Potentially, a fourth, near-surface derived fluid (meteoric fluids of (Hagemann et al., 1994)) may have been important in some parts of the Au systems.

This section begins with a discussion, from the numerical modelling perspective, of why multiple fluid models are necessary. It proceeds to summarise the inferred properties of the ambient fluids, oxidised volatiles of magmatic affinity and the sources of reduced fluid, focusing on evidence of deep-seated reduced fluids as expressed by the crustal continuum view of Archaean lode gold deposits. This discussion sets up the final section of the paper that explores the implications of mantle, or at least the lower crustal fluid reservoirs, driving the salient physicochemical gradients (redox, pH, activities of S, C, Cl) of the Eastern Yilgarn gold systems.

These anhydrous fluids have significant potential are mineralizing fluids. Aqueous fluids may dominate processes in the crust but metal transport phenomena in the mantle, in fluids other than silicate melts, are much more likely to be controlled by anhydrous fluids (Figure 3.4.2) and at depths greater than 300 to 400 km these fluids will be dominated by $H_2$ and $CH_4$ rather than $CO_2$ and $SO_2$. The "deep-earth" fluids are postulated to contain H, N, C S and halogen (Cl, F) complexes with hydridic complexes such as NaH, $MgH_2$, $AlH_3$ and $SiH_4$ potentially playing a significant role in mobilizing the common rock forming elements.

### 3.4.4.2 Are multiple fluids and mixing models necessary?

Is it possible to evolve a single "orogenic-Au" fluid through fluid-rock reactions to account for the isotopic data and other geochemical and geological constraints; either at the trap site or in some other part of the mineral system? Is it possible to oxidise a reduced "orogenic Au" fluid to generate the observed alteration assemblages and S isotope ratios?

Quantitative reaction-path modelling by (Mikucki, 2000, 2001) of reaction of reduced lode-gold fluids with a variety of greenstone-sequence host rocks showed that *in-situ* fluid-rock interaction models for oxidation of lode-gold ore fluids as suggested by (Evans, 2006; Palin, 2000; Phillips, 1996) among others are untenable. Such models cannot explain the correlation between high Au grades, negative $\delta^{34}$Spyrite values, and proximal, chlorite-absent, pyritic bleached zones found in most 'oxidised' deposits. This conclusion holds true regardless of reasonable changes in host rock, ore-fluid $CO_2$ contents ($XCO_2$ = 0.05–0.22), ore fluid temperatures (250–350˚C) or in assumptions regarding the kinetics of $CO_2$-$CH_4$ equilibrium in these hydrothermal systems. The modelling indicated that *in-situ* fluid-rock interaction is a poor mechanism for oxidising ore fluids because the high concentrations of $CO_2$ and $CH_4$ in typical lode-gold fluids result in substantial buffering capacity. As a consequence, ore fluids become oxidised only at very low f/r ratio (≤0.1) where they are in equilibrium with chlorite-ankerite-calcite - rich alteration assemblages and are Au-poor. Furthermore, the highest Au grades were observed in pyritic bleached zones that formed at high f/r ratio from ore fluids that were still reducing in character. Thus oxidation of the ore fluid had essentially no effect on Au grade in the host rocks (Palin and Xu, 2000). Mikucki (2001) attached an interesting rider to his conclusions by considering the effect of the rate of $CO_2$-$CH_4$ equilibration on the modelling. In cases where $CO_2$-$CH_4$ exchange is kinetically inhibited, infiltrating hydrothermal fluids in equilibrium with chlorite-carbonate ±pyrite ± epidote - assemblages become, first moderately oxidised ($SO_4$tot ≈ $H_2$Stot), and then highly ($SO_4$tot ≈ $H_2$Stot), oxidised with increasing rock interaction. In contrast, when $CO_2$-$CH_4$ equilibrium is allowed, infiltrating hydrothermal ore fluids only become oxidised at very low f/r ratios (<10-1). The possibility that oxidised fluids could have existed in the distal carbonate alteration zones that surround and underlie lode-gold deposits, or in the 'regional' fault-related carbonate alteration that is prevalent in ore-hosting structures, indicates that such fluids may themselves have been involved with the formation of oxidised lode-gold ore fluids.

However, if $CO_2$-$CH_4$ equilibrium did prevail, or at least for the fast step of oxidizing $CH_4$ to $CO_2$, we could expect fluids to remain buffered to moderately low oxidation states until very low f/r ratios. $\delta^{13}$C values of less than -6 ‰ with $\delta^{18}$O at ~ 8 – 12 ‰ values for hydrothermal carbonate (e.g., Figures 3.4.20, 3.4.21) are consistent with oxidation of $CH_4$ to $CO_2$ in the Au systems. Under such circumstances fluid-rock interaction, even at depth or in distal parts of the mineralising system, will not produce fluids capable of forming oxidised Archaean lode-gold deposits. The numerical modelling supports geochemical and geological argument of intrinsically oxidised and reduced fluids in Archaean Au systems.

### 3.4.4.3 Fluid 1: Ambient Fluid

Ambient fluids are taken as background aqueous fluids with low concentrations of salt and $CO_2$. Aqueous fluids with low salinity where documented in the early stages of the paragenesis at St Ives and are interpreted as the ambient fluid in the system. This $H_2O$ - $CO_2$ ± NaCl fluid is the most commonly observed fluid type in fluid inclusion studies of Archaean Au deposits (Ho et al., 1990). The fluid is inferred to have been moderately oxidizing with $CO_2$ and $H_2S$ the dominant C and S species, respectively (Mikucki, 1998). It equates to fluids of potentially diverse origins, basinal brines, metamorphic fluids or even magmatic fluids that equilibrated with the greenstones. In comparison with the fluids of the Au stage, its single diagnostic characteristic is that it is a hydrous fluid. Late in the evolution of the system, this hydrous fluid is commonly

much more saline. It is likely that the major reservoirs of water during gold mineralization, late in the metamorphic history were in the late basins, although this remains largely conjectural.

The C and O isotope characteristics of carbonate within and around deposits provide some significant clues to its history. In a number of major deposits and camps (e.g., Kalgoorlie, Kanowna Belle) and also prospects (e.g., Gidji, north of Kalgoorlie) $\delta^{13}C$ and $\delta^{18}O$ isotope data yield a broad band of values consistent with a theoretical cooling trend for a rock-buffered "ambient" fluid with $\delta^{13}C$ ~ 0 to -2 ‰ (e.g., Figure 3.4.22). A variation of temperature of formation of the carbonate of several hundreds of degrees (450–150°C) is inferred. The temperatures of carbonate formation are broadly compatible with other constraints on temperature. The calculated starting $\delta^{18}O$ composition of the $H_2O$ - $CO_2$ fluid is 6 ‰ consistent with the fluid being rock-equilibrated.

The inferred dominant $\delta^{13}C$ values for the aqueous $CO_2$ reservoir of ~ 0 and -2 is similar to that dominant $\delta^{13}C$ values measured directly in the Junction fluid inclusions by Polito (1999); see Figure 3.4.8. There are two possible explanations for this:

1. The ultimate source of $CO_2$ is sea water. Golding and co-workers suggested sea water $CO_2$ was incorporated into the greenstones during seafloor metamorphism and was subsequently recycled. Alternatively this could be seawater incorporated into the subduction and arc-magmatism cycle.

2. Mantle $CO_2$ with $\delta^{13}C$ value of -5 to -6 precipitates from alkaline fluids with $HCO_3^-$ the dominant aqueous species. Under these conditions there is little fraction of $^{13}C$ between $CO_2$, $HCO_3^-$ and carbonate, so that the $\delta^{13}C$ values of the bulk of the carbonate reflects the value of the $CO_2$ reservoir. Subsequent reworking of the carbonate by more acidic fluids led to $\delta^{13}C$ $H_2CO_3$ values in the fluids of ~ 0 to -2 ‰ which is close to the $\delta^{13}C$ value for seawater.

The available data suggest that the sulphur isotopic composition of the ambient fluid was close to zero. Sampling of background sulphides is difficult because of the size of the hydrothermal systems and the lack of outcropping sulphides. However, historical data sets of sulphides from igneous rock, nickel deposits and sedimentary rocks well outside of Au systems point to a sulphur isotope range from 0 ‰ to +3 ‰. Data obtained in this study from the St Ives and Laverton Camps for interflow sediments (Kapai Slate), Black Flag Beds, Merougil Beds and Wallaby Conglomerate yielded values between 0 and 2.8 ‰ giving an average of 1.3 ‰ for 11 samples (Figure 3.4.12 and Table 3.4.3).

Table 3.4.3: Sulphur isotopic compositions of sulphides from sediments distal to known deposits/camps or early/diagenetic sulphides.

Samples in sediments distal from known deposits/camps or early/diagentic sulfides

St Ives camp

| Area | Sample # | DDH | Metres | Description | del 34S(per mil) | Source of info |
|---|---|---|---|---|---|---|
| Victory - Defiance area | LD65020600 | LD 6502 | 60.0 | carbonaceous K.S. with abundant py | 1.80 | this study |
| Victory - Defiance area | LD65020616 | LD 6502 | 61.60 | carbonaceous K.S. with abundant py | 0.70 | this study |
| Victory - Defiance area | | | | Kapai slate, North Orchin (sub grade) | 1.70 | Western mining report 1987 |
| Foster South Area | | | | Kapai Slate | 2.40 | Western mining report 1987 |
| 5km south of Foster Soth Area | | | | Blag Flag Beds Pyritc VSW? | 0.30 | Western mining report 1987 |
| East Tramsways | | | | Kapai Seds | 0.70 | Western mining report 1987 |
| Merougil Beds | | | | Merougil pyrtic sanstone | 0.50 | Western mining report 1987 |
| Wallaby and Granny Smith | | | | | | |
| | GSD3593510 | GSD 359 | 351.0 | From seds north of Granny Smith | 1.40 | this study |
| | GSD3593675 | GSD 359 | 367.50 | From seds north of Granny Smith | 1.80 | this study |
| | LCAD0021625 | LCAD 002 | 162.50 | Distal sulfides | 2.80 | this study |
| Harmony: Chip samples | | | | | | |
| | 02CTRC016B | 02 CTRC 016 | 79-80 | py-bearing shales | 0.0 | this study |
| | | | | Average Value | 1.28 | |

### 3.4.4.4 Fluid 2: Volatiles of magmatic affinity

Volatiles of magmatic affinity are modelled as anhydrous fluids dominated by $CO_2$ and $SO_2$ but with elements such as Te, V, Mo, Bi and W. There is no direct evidence of $SO_2$ or the trace elements from the fluid inclusion studies. The presence of $SO_2$ is inferred from the occurrence of anhydrite and the variation of $\delta^{34}S$ pyrite and $\delta^{34}S$ anhydrite. Numerous studies have used the negative isotope ratios of Au-related pyrites ($\delta^{34}S$ of 0 to -10 ‰) in some giant orogenic Au deposits (e.g., Golden Mile, Timmins and Kirkland Lake), in combination with alteration mineral assemblages that include haematite ± anhydrite ± vanadium-micas, to infer the presence of an inherently oxidised fluid in the system, most likely of magmatic origin, at the time of Au deposition (Cameron, 1987; Clout, 1989; Hattori, 1987; Walshe, 2003). The spatial association of oxidised alteration assemblages with 2665–2640 Ma mafic, syenitic and lamprophyric intrusions described by (Smithies and Champion, 1999) provide compelling arguments that the oxidised fluids were magmatic or closely related fluids. The temporal association is clearly apparent in the largest deposit in the Eastern Goldfields Superterrane, the Golden Mile (Clout, 1989) where haematite and anhydrite occur within the Au lodes with roscoelite and tellurides.

The mineralogical/trace element evidence that Fluid 2 transported other volatile species such as V, Te, W and Mo is particularly apparent in the Golden Mile but the Kanowna Belle, Wallaby and Victory –Defiance deposits all show evidence of enrichment in at least some of the elements of this suite. The telluride - roscoelite- sulphate mineralogical association of the Golden Mile is a characteristic shared with deposits of the circum-Pacific (Porgera, Cripple Creek, Emperor) that are genetically linked with magmatic hydrothermal processes and (Cooke and McPhail, 2001) argue that the telluride content of Au deposits is a magmatic contribution.

The $\delta^{34}S$ of magmatic $SO_2$ is estimated at ~ 0 ‰ with high-T (400 to 500° C) anhydrite having $\delta^{34}S$ anhydrite of ~ +10 ‰ with corresponding $\delta^{34}S$ pyrite of ~ -4 to -5 ‰. The magmatic fluids are interpreted to be a source of radiogenic Pb ($^{207}Pb/^{204}Pb$ > 15.5) in comparison with the primitive ratio ($^{207}Pb/^{204}Pb$ ~ 14.8) of the host rocks, ambient fluids and deep-Earth fluids.

There may have been a sulphate value reservoir of ~ +20 ‰ that is either magmatic in origin or possibly of secondary sources as the value is equivalent to the $\delta^{34}S$ of modern seawater. The possibility that some of the radiogenic strontium signal as well as the $\delta^{34}S$ sulphate of ~ +20 ‰ is an overprint of Proterozoic/Palaeozoic surface waters has not been eliminated.

Ho et al. (1994) noted the association of radiogenic Pb in pyrite from the Victory-Defiance deposits with porphyry host rocks and attributed the radiogenic source to the host porphyry. The observations of Henson and Blewett (2004) of a series of domed surfaces cored by felsic intrusive complexes with apices in the vicinity of major gold camps hints that the domes in the mid to upper crust were reservoirs of oxidised fluids or at least focused the flow of oxidised fluids from deeper in the system. The radiogenic Pb may have been acquired by fluid/melt stored within reservoir in these mid- to - upper crustal domes. Ultimately, the oxidised magmatic fluids possibly originated from remelting of metsomatised mantle (Beakhouse, 2007; Champion and Cassidy, 2002).

The domes may also have been one of the sites for enriching a $CO_2/SO_2$ reservoir in $^{18}O$. As noted above, the process of generating the $^{18}O$-enriched carbonates could have involved fluxing of a reduced $CH_4$-rich fluid through a limited volume/reservoir of $CO_2$-$SO_2$-rich fluid and preferential precipitation of $^{16}O$ as biotite such that residual $SO_2$ and $CO_2$ was progressively enriched in $^{18}O$. Mass balance considerations imply concentrations of $SO_2 \geq CO_2$. The limited volume/reservoir of $CO_2$-$SO_2$-rich fluid could have been stored locally e.g., within structures active at the time of mineralization. Alternative the reservoir of $CO_2$-$SO_2$-rich fluid could have been deeper in the section; e.g., within mid- to upper-crustal domes.

### 3.4.4.5 Fluid 3: Redox variation with depth, the crustal continuum model and origin of the reduced fluid

The origin of the reduced fluid (Fluid 3) is enigmatic and could have evolved from the ambient fluid (Halley, 2007) or also be of magmatic origin (Beakhouse, 2007) or be sourced directly from the lower crust or mantle (Walshe et al., 2003). The concept that the reduced fluid reservoir must be from the lower crust or mantle in part rests on a series of observations encapsulated in the concept of the

crustal continuum model. Researchers from the mid 1980's (Colvine, 1989; Foster, 1989; Groves, 1993; Mikucki, 1998; Mikucki and Ridley, 1993; Witt et al., 1997; Witt and Vanderhor, 1998) have emphasised the range of metamorphic conditions and crustal depths over which Archaean lode Au deposits formed and the correlation of structural style with metamorphic grade. Prominent changes in metasomatic mineralogy with metamorphic grade are:

- Increase of pyrrhotite: pyrite ratio with depth
- Decrease in ankeritic carbonate with depth
- Increase of arsenopyrite with temperature and the occurrence of loellingite rather than arsenopyrite at the highest metamorphic grades
- Rutile giving way to ilmenite and titanite within amphibolite-facies deposits
- Occurrence of high temperature methane-rich fluid inclusions in amphibolite- and granulite-facies deposits (see Colvine, 1989 Hagemann, 1993; Mernagh, 1994; Mikucki, 1993, and references therein).

These observations led to a concept of a continuum of fluid conditions through the crust. (Colvine, 1989; Foster, 1989; Groves, 1993) envisaged a vertically extensive mineralisation system in excess of 10 km. As noted by (Witt and Vanderhor, 1998), no single deposit contains the complete range of structural styles and it is not possible to demonstrate a continuum of fluid conditions via a contiguous section through the crust. Nevertheless, systematic changes in alteration mineralogy with metamorphic grade do support the concept of an evolution in the nature of the fluid reservoirs with depth in the crust, if not a continuum of fluid with depth in the crust and contiguous deposition. Hence, geochemical characteristics (mineralogy, fluid inclusion and isotopic characteristics) of deposits in the high-grade metamorphic terranes provide a window into the nature of fluid reservoirs in the middle and lower crust, if not the mantle.

In deposits formed at 500–700° C, the $CO_2/CH_4$ ratio ranges from less than 0.01 to 100 (Ridley and Hagemann, 1999) consistent with the range in $CO_2/CH_4$ inferred from mineral assemblages, providing the maximum stability field for loellingite is assumed (Figure 3.4.24); see (Walshe, 2002) for discussion. From the phase calculations, the most reduced fluids at 500–700° C are inferred to have been anhydrous and composed dominantly of $H_2$ - $CH_4$ - $H_2S$. The crustal dimension of the redox gradient requires a reductant at depth in the Au mineralizing system. Both the fluid inclusion data and the mineral assemblages reveal that in the higher temperature and deeper deposits, redox conditions were more reduced than in the cooler/shallower deposits. This implies a reductant at depth, somewhere in the lower crust or the mantle.

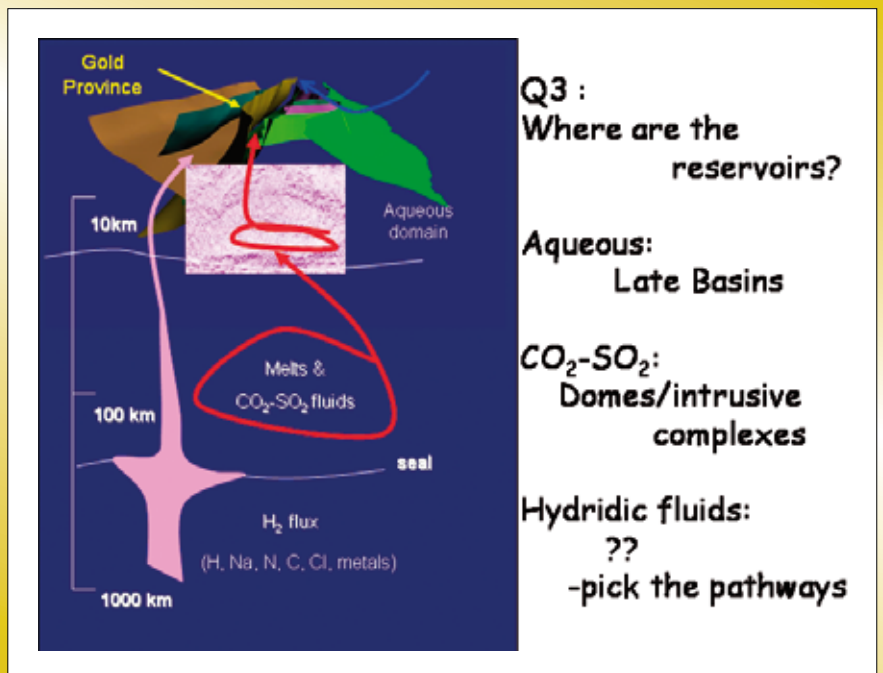


*Figure 2.4.23: Reservoirs in the Eastern Yilgarn Au system.*

One explanation for these observations may be provided by the ideas of (Mernagh et al., 2005) who report a similar pattern of redox conditions with depth from Au deposits in the Tanami region. They infer that phase separation (facilitated by elevated NaCl, $CO_2$ and/or $CH_4$ levels) is responsible for the extreme composition of inclusions. Methane in the Tanami region could be sourced from the relatively abundant carbonaceous sediments in the rock pile hosting ore deposits. It is somewhat less clear in the Yilgarn where methane could have been sourced from, especially in the higher metamorphic grade areas that contain little supracrustal material.

Alternatively the $CH_4 \pm N_2$ inclusions are interpreted as components of a hydrogen rich, or hydridic fluid (in the sense of (Larin, 1975; Walshe et al., 2005b), ultimately sourced in the mantle and introduced into the mid- and upper-crust via the trans-crustal architecture. The results of Ar and Ne isotopes studies of the dominant fluid inclusion type from the St Ives Camp (Kendrick et al., 2008) support

*Figure 3.4.24: Fluid inclusion and mineralogical constraints on deep crustal / mantle fluids from gold deposits in amphibolite-granulite facies rocks.*
*A: Redox state of Archaean lode-gold deposits relative to that of the $CO_2(g)$-$CH_4(g)$ buffer as a function of temperature at 2 kb (modified from Mikucki, 1998). Del log $fO_2$ measures the displacement from the $CO_2(g)$-$CH_4(g)$ buffer. The lower redox limit which is based on maximum stability of the assemblage pyrrhotite, ilmenite and loellingite, extends into the anhydrous fluid domain of the diagram with $H_2$ and $CH_4$ the dominant species in the fluid. Thermodynamic data for reactions involving loellingite (lo), FeAs, pyrrhotite, rutile or ilmenite from Barton and Skinner (1979). Deposit References given in Mikucki (1968) A: Racetrack, B: Golden Mile, C: Lady Bountiful, D: Wiluna; E: Mount Charlotte, F: Hunt, G-I: Norseman, north and central deposits, G-II: Norseman, southern deposits, H: Main Hill, I: Zakanaker, J: Nevoria, K: Westonia, L: Marvel Loch, M: Griffin's Find.*
*B: Composition of fluid inclusions with respect to $H_2O$-$CO_2$-$CH_4$ from the Three Mile Hill deposit, Coolgardie Goldfield and the Marvel Loch and Griffins Find deposits, Southern Cross Goldfield (from Ridley and Hagemann, 1999). Water contents determined by phase ratios and $CO_2/CH_4$ by micro-thermometry or laser-Raman spectroscopy.*
*C: Redox state of lode-gold deposits formed at amphibolite to granulite facies metamorphic conditions relative to that of the $CO_2(g)$-$CH_4(g)$ buffer (modified after Mikucki, 1998) comparing estimates from mineralogical redox buffers (boxes) with $CO_2/CH_4$ estimates from mixed aqueous–carbonic fluids (Ridley and Hagemann, 1999; Hagemann and Cassidy, 2000).*

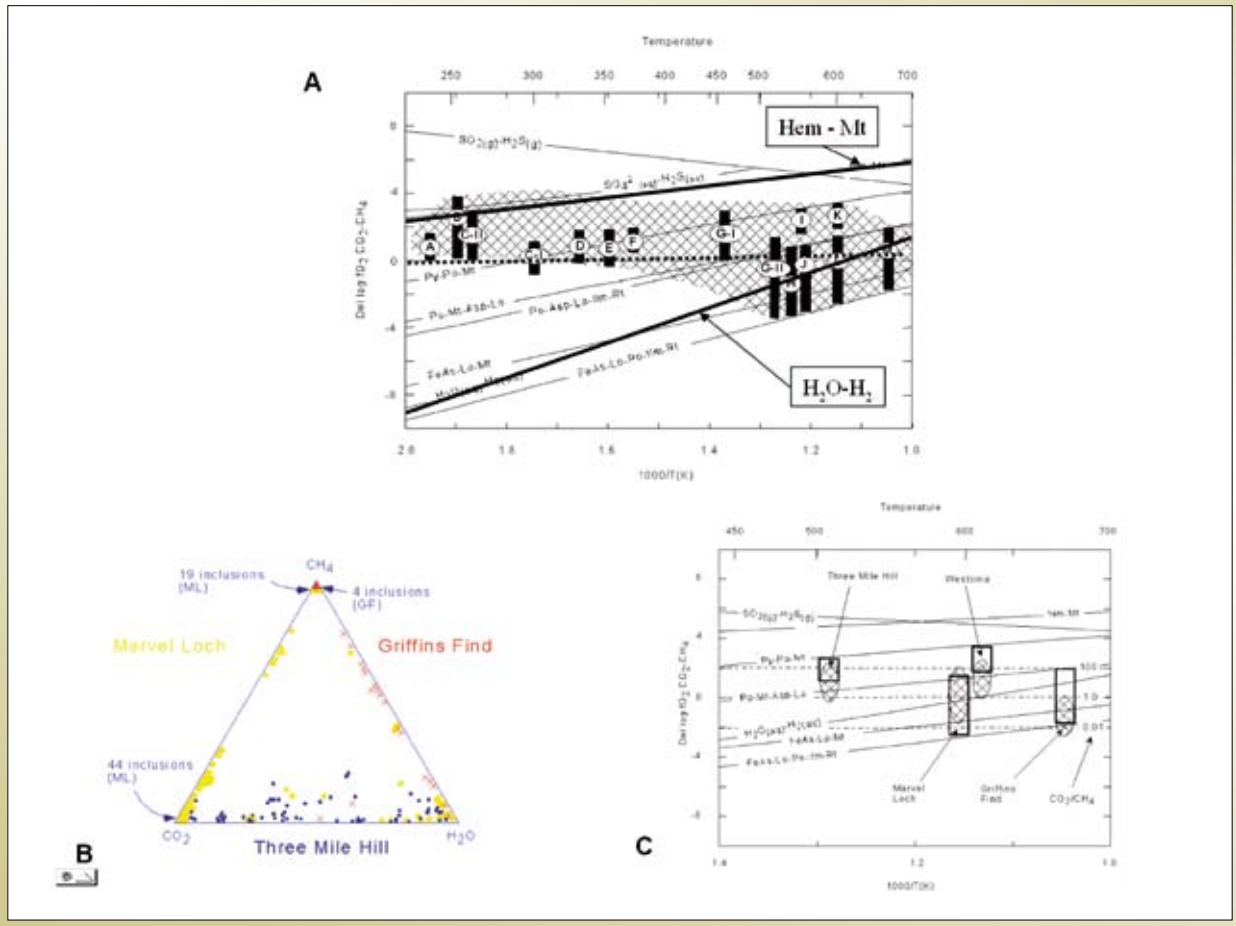

arguments that the highly reduced fluid is of mantle origin. $CH_4$ fluid inclusions in reduced veins have the highest $^{40}Ar/^{36}Ar$ values of up to ~ 48,000 and similar to the modern day convecting mantle.

### 3.4.5 Section 4: Deep Earth Fluids

#### 3.4.5.1 Introduction

A fascinating outcome of the above discussion is that the fluid reservoirs that ultimately controlled the salient physicochemical gradients in the system (redox, pH, activities of S, C, Cl) were in the mantle or at least the lower crust. Mantle tomography studies have identified structure to depths of > 100 km suggesting possible fluid pathways to at least depths of that order. The oxidised fluids possibly originated from within a metsomatised mantle wedge. The reduced fluids may also have been derived from the mantle wedge or from much greater depths. What components of the reduced fluid were sourced from the mantle remains an open question, but given the mantle signatures for the Ar and Ne, a significant component of mantle $H_2$ as well components soluble in hydridic fluids seems reasonable. In this section evidence in support of reservoirs of $H_2$-rich or hydridic fluids in the deep-Earth is reviewed, the likely chemical and mineralogical imprint of such fluids on the Earth's crust is discussed as well as possible mechanism that could allow such fluids to migrate to high levels in the crust while maintaining their chemical integrity. The times and places of deep-Earth fluid migration into the mid- and -upper crust are potentially highly significant for resource formation.

#### 3.4.5.2 The oxidation state of the mantle

The common oxidation state of the upper few hundred kilometres of the mantle is relatively high ($logfO_2$: QFM-3 to QFM+2) with $CO_2$ and $H_2O$ stable as volatile species (O'Neill and Wall, 1987). However, there is evidence that some parts of the mantle, particularly the lower mantle may be more reduced (Green et al., 1990). The occurrence of moissanite (SiC) in diamondiferous kimberlites, lamproites and volcanic rocks with inclusions of metallic Si and Fe, $Fe_3C$ (cohenite), $Fe_3Si_7$ (ferrosilicide), $CaSi_2$ (calcium disilicide), $Si_2N_2O$ (sinoite) and Fe-Ti-silicides provide mineralogical evidence of anoxic domains in the mantle. The picture emerging of the oxidation state of the mantle (McCammon, 2005) is one of an upper mantle that is relatively oxidised compared with a relatively reduced lower mantle. The inferred redox range of the upper mantle is from QFM- 4 to QFM + 2 (i.e., from 4 log units of oxygen fugacity below the quartz/fayalite/magnetite buffer to 2 units above). Under these redox conditions $CO_2$ and $H_2O$ would be the dominant species in any fluid phase (Woodland and Koch, 2003); references therein). (Jacob et al., 2004) in a study of cohenite ($Fe_3C$), native iron and troilite inclusions in garnets from polycrystalline diamond aggregates inferred redox conditions near and below the iron/wustite (IW) buffer (i.e., ~ QFM - 4.5 to -5) and fluid speciation of $CH_4$>$H_2O$>$H_2$. The maximum stability of the moissanite (SiC), present both in diamonds and also as inclusions in kimberlites is typically 5 to 6 log units below the iron/wustite buffer (Mathez et al., 1995; references therein). At such conditions $CH_4$ and $H_2$ will be greatly in excess of $CO_2$ and $H_2O$ in any fluid phase. The recent studies of nodules and inclusions in diamonds have shown that, contrary to widely held beliefs, the mantle is not monolithic in terms of redox values and that in the deeper parts of the upper mantle conditions are in general significantly reduced compared with 'normal' upper mantle.

The question of whether these highly reduced conditions are intrinsic to the inner Earth (Deines, 2002) or represent local extremes, perhaps caused by subduction of reduced carbonaceous sediments (Mathez et al., 1995), is still a matter of debate. There are several possible mechanisms to produce reduced fluids in the mantle and the depth of the reservoir will depend on the mechanism. Equilibrating a C - saturated COH fluid with a garnet-olivine-pyroxene-spinel assemblage, assuming typical mantle olivine and pyroxene compositions, leads to $CH_4$-$H_2$-rich fluid at depths greater than ~ 300 to 400 km (Figure 3.4.25). At shallower levels $CH_4$-$H_2$-rich fluid could result from serpentinisation of ultramafic rocks of the mantle wedge (Malkovets, 2007; Sachan, 2007; Schmidt, 2007; Thomassot, 2007) by fluids from the Earth's surface. Alternatively, methane production in the mantle could be driven by episodic release of $H_2$ from the Earth's core (Walshe, 2007). The core is possibly the largest reservoir of $H_2$ on the Earth (Williams and Hemley, 2001) with potential to sustain mantle methane production through Earth history. Production of mantle $CH_4$ by episodic release of $H_2$ from the Earth's core may explain the periodicity of major gold mineralisation epochs that occur on a time-scale of 0.5–1 billion years through Earth history.

*Figure 3.4.25: Redox-depth evolution of C-saturated fluids at upper mantle conditions. COH fluids will be dominated by $CH_4$ and $H_2$ at depths greater than ~ 300 km (Right panel). Maximum stability limits for graphite/diamond and for SiC (Moissanite) with respect FMQ (Fayalite, Magnetite, Qtz) are shown in left panel. Also shown are evolution paths for the mineral redox buffers IW (Iron/Wustite) and "Q"IF ("Quartz"/Iron/Fayalite; XFa = 0.1). Calculations assume $SiO_2$ activity, "Q" is buffered by mantle olivine-pyroxene assemblage except over a narrow depth interval where stishovite becomes saturated. Dotted contours indicate redox conditions set by the skaigite (ferrous/ferric component in garnet)-olivine-pyroxene buffer (Gudmundsson and Wood, 1995) for different log askiagite values assuming typical mantle olivine and pyroxene compositions. PT gradient is that of the two-layer mantle convection model (Ricter and McKenzie, 1981). Hatched box represents redox-depth conditions determined for peridotite xenoliths from localities on the southern flank of the Kaapvaal craton in South Africa (Woodland and Koch, 2003). Arrows indicate the evolution of redox conditions for this sample assuming a constant skiagite component in garnet. Sources of thermodynamic data: (Gudmundsson and Wood, 1995; NIST, 2005; Fabrichnaya, 1999; Saxena, 1996; Saxena et al., 1993). Figure constructed by Ed Mikucki in 2006 as part of MERIWA358 project.*

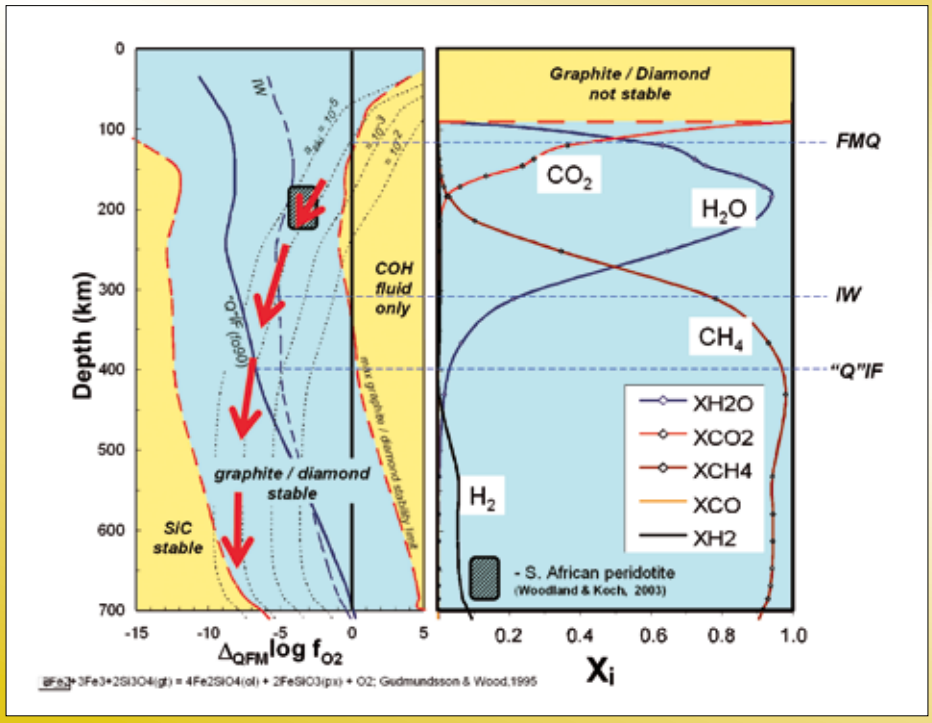


### 3.4.5.3 Composition of hydridic fluids

Hydrogen has potential to complex with most elements of the Periodic Table at high temperature and pressure to form hydrides. As hydrides are unstable in the presence of water their distribution within the Earth will reflect the distribution and state of water. The alkali and most alkali earth elements form ionic hydrides. Group 3 through 7 elements (e.g., Al, Si, N, S, Cl) form covalent hydrides. The formation of hydrides by most transition elements, lanthanides (REEs) and actinides allows the possibility of transport of a wide range of elements of metallogenic interest (e.g., Ti, V, Cr, Co, Mo, W, U, Th, Au, PGEs) within the mantle and under appropriate circumstances within the crust by fluids other than silicate melts.

Aqueous fluids may dominate processes in the crust but metal transport phenomena in the mantle, in fluids other than silicate melts, are much more likely to be controlled by anhydrous fluids and at depths greater than 300 to 400 km these fluids will be dominated by $H_2$ and $CH_4$ rather than $CO_2$. The "deep-earth" fluids are postulated to contain H, N, C S and halogen (Cl, F) complexes with hydridic complexes such as NaH, $MgH_2$, $AlH_3$ and $SiH_4$ potentially playing a significant role in mobilizing the common rock forming elements. There is potential for alkali-rich hydridic fluids, including a significant component of alkali halide, to promote alkali metasomatism on mixing with silicate melts, aqueous or carbonic fluids in the crust/upper mantle, generating reduced, alkali-rich, aqueous fluids. The decreasing stability of hydrides with increasing atomic number within any Group of the Periodic Table (Mackay and Mackay, 1968) implies Na ± Li - metasomatism will be favoured over K - metasomatism.

### 3.4.5.4 Pathways of hydridic fluids through the crust

A reduced or hydridic fluid, possibly sourced from depths > 300 to 400 km within the Earth will be highly unstable in the crustal environment. If hydridic fluids are armoured from hydrous fluids or minerals, at least transiently, there is potential for significant migration into or through the crust.

Potentially transport of hydridic fluids from the mantle into the mid to upper crust could be assisted/promoted by:

- Armouring of flow paths by anhydrous mineral precipitates,
- Armouring of flow paths by anhydrous $CO_2$-rich volatiles that limited access of aqueous crustal fluids, and
- Rapid transit.

One effective armouring mineral would be graphite. A zone of high conductivity beneath the Kalgoorlie district, defined by a magneto-telluric survey, is interpreted as a graphite-rich domain down to mid-crustal levels (Blewett et al., 2008). Carbonaceous material subjacent to gold deposits in shears or bedding commonly has C isotope signatures suggesting re-equilibration with hydrothermal fluids (Donnelly, 1977) or direct precipitation from the hydrothermal system, consistent with the geophysical evidence. A similar zone of high conductivity beneath the Olympic Dam deposit is also interpreted as a graphite-rich domain. These high conductivity zones may be defining the "armoured" pathways that permitted unstable mantle fluids to progress to high levels in the crust.

The evolution of the fluids for St Ives gold camp, from hydrous fluids to anhydrous fluids at the time of gold mineralisation, to hydrous fluids in the latter stages of the system strongly implies the system operated in the two phase region for a critical period of its history. Traditional boiling models of gold deposition have invoked phase separation in response to local changes in pressure/temperature or bulk composition. Potentially phase separation occurred over a much larger volume of the system and the dynamics of phase immiscibility may have been the driver to segregate the hydrous and anhydrous parts of the fluid system. The size of the two phase region with respect to pressure and temperature is poorly constrained for the bulk composition of interest. However, on available data the two-phase region could have extended through the crust into the mantle, aiding the flow of anhydrous fluids over vertical distances of 10s to 100s of kilometres through environments in which such fluids would normally be highly unstable.

The most likely mechanisms for rapid advection through the crust of hydridic fluids are transient, deep-lithospheric blasts of gas, or Verneshots (Morgan et al., 2004). The characteristics of Verneshots will be similar to characteristics of bolide impacts raising the possibility that some impact structures at least result from 'bottom-up' failure of the lithosphere, rather than bolide impact. The occurrence of impact structures in many major mineral provinces such as the Vredefort structure in the Witwatersrand Basin, the Carswell structure in the U-rich Athabasaca basin and the sublayer of the Sudbury igneous complex hints at some relationship between such events and supply of volatiles ± metals in mineral systems.

### 3.4.5.5 Signatures of hydridic fluids in the crust

Commonly hydridic fluids from inner Earth are likely to degrade through reaction with fluids and rocks of Earth's outer hydrous shell. Potentially such reactions could drive metasomatic, metamorphic and magmatic reactions, sustain chemical gradients (redox, pH, activity of sulphur, water and acid volatiles) in the crust and mantle and mobilise a diverse range of elements as well as well as hydrocarbons.

At the very least this metasomatic history allows the possibility of identifying flow paths of deep-Earth fluids in the crust, at district- to terrane- scales, making use of high quality geophysical, geochemical and mineralogical data sets becoming available for many mineral district. Arguably, interaction of hydridic fluids with hydrous fluids or minerals will lead to three common responses.

1. Reaction with aqueous fluids or hydrous minerals to produce highly acidic, reduced fluids.
2. Consumption of hydrogen through reaction with oxidised species or rocks (sulphate and carbonate or $CO_2$) produce neutral to alkaline, highly saline and sodic brines.
3. Reduction of carbonaceous material to produce methane or petroleum products.

A significant factor influencing the chemical evolution of deep-Earth fluids, as they react with crustal fluids and rocks and degrade to aqueous fluids of varying acidity, redox state and salinity, will be the ratio of alkali and alkali-earth halides to acid species (HCl, HF) in the deep - Earth fluid. Relatively high halogen to alkali ratios should lead to acid production through dissociation of HCl and HF in aqueous crustal fluids; assuming limited degassing of hydrogen. Loss of hydrogen through degassing, or consumption of hydrogen through reaction with oxidised species or rocks (sulphate and carbonate or $CO_2$) could lead to neutral to alkaline, highly saline, sodic and potentially magnesium, and calcic brines depending on the history of fluid rock reaction. These brines may be sufficiently alkaline to dissolve quartz. These "degraded" hydridic fluids can explain the widespread occurrence of acidic alteration (defined by the PIMA and Hylogger data sets in the Kalgoorlie and Laverton district), as well as regional scale sodic-calcic alteration and Mg-metasomatism (Figure 3.4.26). Hyper-spectral mapping of the muscovite distribution in the Kanowna Belle-Kalgoorlie district (Tom Cudahy, personal communication) has linked domains of muscovite-paragonite alteration at the mine-scale to domains of biotite - absent, muscovitic metamorphic assemblages. It is possible that these low-T metamorphic domains through the Eastern Goldfields Superterrane (Mikucki and Roberts, 2003) may actually be defining large-scale domains of acidic alteration and providing evidence of the terrane-scale "footprints" of the deep-Earth fluids in the crust.

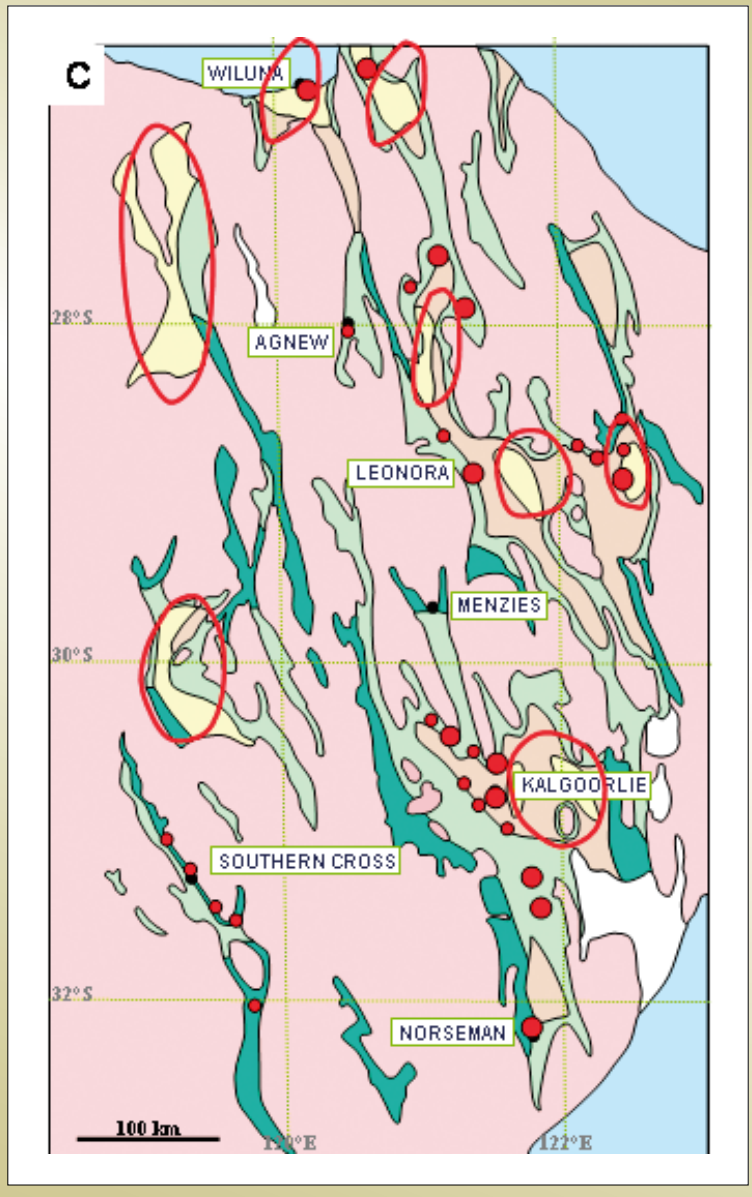


*Figure 3.4.26: Acid alteration at 3 different scales: footprints of degraded hydridic fluid? Metamorphic map of the Eastern Yilgarn showing domains of muscovitic metamorphic assemblages with biotite absent; highlighted by the red circles. Also shown are the major gold deposits.*

### 3.4.6 References

Beakhouse, G. P., 2007, Gold, granite and late Archaean tectonics: a Superior Province perspective *in* Bierlein, F. P., and Knox-Robinson, C. M., eds., Proceedings of Geoconferences (WA) Inc Kalgoorlie '07 Conference: Kalgoorlie, Geoscience Australia Record 2007/14, p. 191–196.

Blewett, R.S., Cassidy, K.F., Henson, P.A., Roy, I.G., Champion, D.C. and Fomin, T., 2008, Question 2: Big systems-big signatures – anatomy of the Archaean Yilgarn Craton and implications for world-class gold mineral systems. Part III, this volume.

Cassidy, K. F., 1992, Archaean granitoid-hosted gold deposits in greenschist to amphibolite facies terranes: a high P-T to low P-T depositional continuum equivalent to greenstone-hosted deposits, Unpublished PhD thesis, University of Western Australia, 296 p.

Champion, D. C., and Cassidy, K. F., 2002, Granites in the Leonora-Laverton transect area, north eastern Yilgarn Craton, *in* Cassidy, K. F., ed., Geology, geochronology and geophysics of the north eastern Yilgarn Craton, with an emphasis on the Leonora-Laverton transect area, Geoscience Australia, Record 2002/18, p. 13–35.

Clout, J. M. F., 1989, Structural and isotopic studies of the Golden Mile gold-telluride deposit, Kalgoorlie, Western Australia: Unpub. Ph.D. thesis, Monash University, 352 p.

Colvine, A. C., 1989, An empirical model for the formation of Archaean gold deposits: products of final cratonization of the Superior Province, Canada, *in* Keayes, R. R., Ramsay, W. R. H., and Groves, D. I., eds., The geology of gold deposits: The perspective in 1988, Economic Geology Monograph 6, p. 37–53.

Cooke, D. R., and McPhail, D. C., 2001, Epithermal Au-Ag-Te mineralization, Acupan, Baguio District, Philippines: Numerical simulations of mineral deposition: Economic Geology, v. 96, p. 109 -131.

Deines, P., 2002, The carbon isotope geochemistry of mantle xenoliths: Earth-Science Reviews, v. 58, p. 247–278.

Donnelly, T. H., Lambert, I. B., Oehler, D. Z., Hallberg, J. A., Hudson, D. R., Smith, J. W., Bavinton, O. A., and Golding, L., 1977, A reconnaissance study of stable isotope ratios in Archaean rocks from the Yilgarn Block, Western Australia. : Journal of the Geological Society of Australia, v. 24, p. 409–420.

Eilu, P., and Mikucki, E. J., 1996, Primary geochemical and isotopic dispersion haloes in Archaean lode-gold systems: assessment of alteration indices for use in district and mine-scale exploration: Perth, Minerals and Energy Research Institute of Western Australia, p. 65.

Foster, R. P., 1989, Archaean gold mineralisation in Zimbabwe: Implications for metallogenesis and exploration, *in* Keayes, R. R., Ramsay, W. R. H., and Groves, D. I., eds., The geology of gold deposits: The perspective in 1988, Economic Geology Monograph 6, p. 54 -70.

Gebre-Mariam, M., Groves, D. I., McNaughton, N. J., Mikucki, E. J., and Vearncombe, J. R., 1993, Archaean Au-Ag mineralisation at Racetrack, near Kalgoorlie, Western Australia: a high crustal-level expression of the Archaean composite lode-gold system: Mineralium Deposita, v. 28, p. 375 - 387.

Golding, S. D., 1982, An isotopic and geochemical study of gold mineralisation in the Kalgoorlie-Norseman region, Western Australia, University of Queensland, 353 p.

Golding, S. D., 1984, Stable isotope and geochemical studies of the porphyry-related gold mineralisation, Kambalda: Perth, Western Mining Coperation, p. 153.

Golding, S. D., 2005, Carbon isotope analysis report - Granny Deeps, Unpublished Report to Placer Dome Asia Pacific, p. 4.

Golding, S. D., Clark, M. E., Keele, R. A., Wilson, A. F., and Keays, R. R., 1985, Geochemistry of Archaean epigenetic gold deposits in the Eastern Goldfields Province, Western Australia, *in* Herbert, H. K., and Ho, S. E., eds., Stable isotopes and fluid processes in mineralisation 23, Geology Department and University Extension, University of Western Australia Publication p. 142–176.

Golding, S. D., Groves, D. I., McNaughton, N. J., Barley, M. E., and Rock, N. M. S., 1987, Carbon isotope composition of carbonates from contrasting alteration styles in supracrustal rocks of the Norseman-Wiluna belt, Yilgarn Block, Western Australia: Their significance to

the source of Archaean auriferous fluids, Geology Dept and University Extension, University of Western Australia Publication University of Western Australia Publication 215 - 238 p.

Golding, S. D., McNaughton, N. J., Barley, M. E., Groves, D. I., Ho, S. E., Rock, N. M. S., and Turner, J. V., 1989, Archaean carbon and oxygen reservoirs: their significance for fluid sources and circulation paths for Archaean mesothermal gold deposits of the Norseman-Wiluna Belt, Western Australia, *in* Keays, R. R., Ramsay, W. R. H., and Groves, D. I., eds., The geology of gold deposits: the perspective in 1988, Economic Geology Monograph 6, p. 376–388.

Green, D. H., Taylor, W. R., and Foley, S., 1990, The Earth's upper mantle as a source of volatiles, Geology Department and University Extension, University of Western Australia, 17–34 p.

Groves, D. I., 1993, The crustal continuum model for late Archaean lode-gold deposits of the Yilgarn Block, Western Australia: Mineralium Deposita, v. 28, p. 36–374.

Groves, D. I., Goldfarb, R. J., Robert, F., and Hart, C. J. R., 2003, Gold deposits in metamorphic belts: Overview of current understanding, outstanding problems, future research, and exploration significance: Economic Geology, v. 98, p. 1–29.

Hagemann, S. G., and Cassidy, K. F., 2000, Archaean orogenic gold deposits: Reviews in Economic Geology, v. 13, p. 9–68.

Hagemann, S. G., Gebre-Mariam, M., and Groves, D. I., 1994, Surface water influx in shallow-level Archaean lode-gold deposits in Western Australia: Geology, v. 22, p. 1067–1070.

Halley, S., 2007, Mineral mapping - how it can help us explore in the Yilgarn Craton, *in* Bierlein, F. P., and Knox-Robinson, C. M., eds., Proceedings of Geoconferences (WA) Inc Kalgoorlie '07 Conference, Geoscience Australia Record 2007/14, p. 143–144.

Henson, P. A., and Blewett, R. S., 2004, 3D interpretation of the eastern Yilgarn: New architectural insights from construction of the 3D map, *in* Blewett, R. S., and Hitchman, A. P., eds., 3D geological models of the Eastern Yilgarn Craton, ***pmd*CRC*** project Y2, final report, chapter 8.

Ho, S. E., McNaughton, N. J., and Groves, D. I., 1994, Criteria for determining initial lead isotopic compositions of pyrite in Archaean lode-gold deposits: a case study at Victory, Kambalda, Western Australia: Chemical Geology, v. 111, p. 57–84.

Hronsky, J. M. A., 1993, The role of physical and chemical processes in the formation of gold ore-shoots at the Lancefield gold deposit, Western Australia, Unpublished PhD thesis, University of Western Australia, 205 p.

Jacob, D. E., Kronz, A., and Viljoen, K. S., 2004, Cohenite, native iron and troilite inclusions in garnets from polycrystalline diamond aggregates: Contributions Mineralogy & Petrology, v. 146, p. 566–576.

Kendrick, M. A., Walshe, J. L., and Petersen, K. J., 2008, Global links between gold and mantle degassing of $^{40}$Ar plus methane: A 2.7 Ga case study: unpublished manuscript.

Knight, J. T., Ridley, J. R., and Groves, D. I., 2000, The Archaean amphibolite facies Coolgardie Goldfield, Yilgarn Craton, Western Australia: Nature, controls, and gold field-scale patterns of hydrothermal wall-rock alteration: Economic Geology, v. 95, p. 49–84.

Larin, V. M., 1975, The hypothesis of a primordial hydride Earth: Moscow, Nedra, 101 p.

Mackay, K. M., and Mackay, R. A., 1968, Introduction to Modern Inorganic Geochemistry: London, International Textbook Company Limited, 258 p.

Mathez, E. A., Fogel, R. A., Hutcheon, I. D., and Marshintsev, V. K., 1995, Carbon isotopic composition and origin of SiC from kimberlites of Yakutia, Russia: Geochimica et Cosmochimica Acta, v. 59, p. 781–791.

McCammon, C. A., 2005, Mantle oxidation state and oxygen fugacity: Constraints on mantle chemistry, structure and dynamics: Washington, DC, American Geophysical Union, 219 - 240 p.

Mernagh, T. P., Bastrakov, E. N., and Wyborn, L. A. I., 2005, A comparison of some chemical processes of ore precipitation in orogenic and intrusion-related gold

mineral systems: STOMP- Structure, Tectonics and Ore Mineralisation Processes Abstract Volume, 2005, p. 89.

Mikucki, E. J., 1998, Hydrothermal transport and depositional processes in Archaean lode-gold systems: a review: Ore Geology Reviews, v. 13, p. 307–321.

Mikucki, E. J., 2000, Thermochemical models for ore-genesis and ore-fluid formation and evolution in the Golden Mile system: Part I. Role of fluid-rock reaction and pre-lode carbonation, Report for AMIRA Project P511, 34 p.

Mikucki, E. J., 2001, Thermochemical models for ore-genesis and ore-fluid evolution in Archaean lode-gold systems: Follow-up on host-rock buffering of ore fluid oxidation states, Report for Centre for Global Metallogeny, UWA, AMIRA Project P511, 45 p.

Mikucki, E. J., 2006, Further preliminary findings on pH changes during oxidation of reduced ore fluids, *in* Walshe, J. L., Neumayr, P., Petersen, K. J., Young, C., and Roache, A., eds., Scale-integrated, architectural and geodynamic controls on alteration and geochemistry of gold systems in the Eastern Goldfields Province, Yilgarn Craton, MERIWA Project 358 Final Report, Appendix 3, p. 261–268.

Mikucki, E. J., and Ridley, J. R., 1993, The hydrothermal fluid of Archaean lode-gold deposits at different metamorphic grades: compositional constraints from ore and wallrock alteration assemblages: Mineralium Deposita, v. 28, p. 469 - 481.

Mikucki, E. J., and Roberts, F. I., 2003, Metamorphic petrography of the Kalgoorlie region, Eastern Goldfields Granite-Greenstone Terrane: METPET database, Western Australia Geological Survey Record, 2003/12.

Morgan, J. P., Reston, T. J., and Ranero, C. R., 2004, Contemporaneous mass extinctions, continental flood basalts and 'impact signals': are mantle plume-induced lithospheric gas explosions the causal link?: Earth and Planetary Science Letters, v. 217, p. 263 -284.

Mueller, A. G., 1990, The nature and genesis of high- and medium temperature Archaean gold deposits in the Yilgarn Block, including a specific study of scheelite-bearing gold skarn deposits, Unpublished PhD thesis, University of Western Australia, 144 p.

Neumayr, P., Hagemann, S. G., Walshe, J., and Morrison, R. S., 2003, Camp- to deposit-scale zonation of hydrothermal alteration in the St Ives gold camp, Yilgarn Craton, Western Australia: evidence for two fluid systems?: Mineral Exploration and Sustainable Development, Seventh Biennial SGA Meeting, Athens, 2003, p. 799–802.

Neumayr, P., Petersen, K. J., Gauthier, L., Hodge, J.L., Hagemann, S. G., Walshe, J. L., Prendergast, K., Connors, K., Horn, L., Frikken, P., Roache, A., and Blewett, R. S., 2005, Mapping of hydrothermal alteration and geochemical gradients as a tool for conceptual targeting: St Ives Gold Camp, Western Australia: Mineral Deposit Research: Meeting the Global Challenge, 8th Biennial SGA meeting, Beijing, 2005, p. 1479–1482.

Neumayr, P., Walshe, J. L., Hagemann, S. G., Petersen, K., Roache, R., Frikken, F., Horn, L., and Halley, S., 2008, Oxidised and reduced mineral assemblages in greenstone belt rocks of the St Ives gold camp, Western Australia: vectors to high- grade ore bodies in Archaean gold deposits?: Mineralium Deposita.

Nguyen, P. T., 1997, Structural controls on gold mineralisation at the Revenge Mine and its tectonic setting in the Lake Lefroy area, Kambalda, Western Australia, Unpublished PhD Thesis, University of Western Australia, 195 p.

O'Neill, H. S. C., and Wall, V. J., 1987, The olivine - orthopyroxene - spinel oxygene barometer, the nickel precipitation curve, and the oxygen fugacity of the Earth's upper mantle: Journal Petrology, v. 28, p. 1169 - 1191.

Ohmoto, H., and Goldhaber, M. B., 1997, Sulphur and Carbon isotopes, *in* Barnes, H. L., ed., Geochemistry of hydrothermal ore deposits, John Wiley and Sons, Inc., p. 517–611.

Ojala, V. J., 1995, Structural and depositional controls on gold mineralisation at the Granny Smith Mine, Laverton, Western Australia, Unpublished PhD Thesis, University of Western Australia.

Palin, J. M., and Xu, Y., 2000, Gilt by association? Origins of pyritic gold ores in the Victory mesothermal gold

deposit, Western Australia: Economic Geology, v. 95, p. 1627–1634.

Petersen, K. J., Hagemann, S. G., Neumayr, P., and Walshe, J. L., 2007, Multiple hydrothermal fluid pulses through time at the Kambalda gold deposits, Yilgarn Craton, Western Australia: 9th Biennial SGA Meeting, Mineral Exploration and Research: Digging Deeper, 20–27th August, Dublin., 2007, p. 675–678.

Petersen, K. J., Neumayr, P., Hagemann, S. G., and Walshe, J. L., 2005, Palaeohydrologic evolution of the Kambalda gold camp, *in* Bierlein, F. P., and Mao, J., eds., Mineral Deposit Research: Meeting the Global Challenge, 2: Berlin, Heidelberg, New York, Springer, p. 573–576.

Polito, P. A., 1999, Exploration implications predicted by the distribution of carbon - oxygen - hydrogen gases above and within the Junction gold deposit, Kambalda, Western Australia: Unpub. Ph.D. thesis, University of Adelaide, 260 p.

Ridley, J., and Hagemann, S. G., 1999, Interpretation of post-entrapment fluid-inclusion re-equilibration at the Three Mile Hill, Marvel Loch and Griffins Find high-temperature lode-gold deposits, Yilgarn Craton, Western Australia: Chemical Geology, v. 154, p. 257–278.

Salier, B. P., Groves, D. I., McNaughton, N. J., and Fletcher, I. R., 2005, Geochronological and stable isotope evidence for widespread orogenic gold mineralization from a deep-seated fluid source at ca 2.65 Ga in the Laverton Gold Province, Western Australia: Economic Geology, v. 100, p. 1363 -1388.

Sang, J. H., 1991, The Evolution of a Giant Hydrothermal System: a study of main and flat lode at North Kalgurlie, Kalgoorlie, Western Australia, Unpublished MSc thesis, University of Western Australia.

Sharov, Y. V., and Bastrakov, E. N., 1999, HCh: a software package for geochemical equilibrium modelling. User's guide: Geoscience Australia Records 1999/25.

Smithies, R. H., and Champion, D. C., 1999, Late Archaean felsic alkaline igneous rocks in the Eastern Goldfields, Yilgarn Craton, Western Australia; a result of lower crustal delamination?: Journal of the Geological Society of London, v. 156, p. 561–576.

Walshe, J. L., 2002, Interplay of architecture and fluids of contrasting chemistry in the Kambalda - Kalgoorlie region, Yilgarn Atlas volume II, AMIRA Project P511 Hydrothermal Systems, Giant Ore Deposits and A New Paradigm for Predictive Mineral Exploration, p. 80.

Walshe, J. L., Cooke, D. R., and Neumayr, P., 2005a, Five questions for fun and profit: A mineral systems perspective on metallogenic epochs, provinces and magmatic hydrothermal Cu and Au deposits, *in* Mao, J., and Bierlein, F. P., eds., Mineral Deposit Research: Meeting the Global Challenge, 1: Heidelberg, Springer, p. 477–480.

Walshe, J. L., Halley, S. W., Hall, G. A., and Kitto, P., 2003, Contrasting fluid systems, chemical gradients and controls on large-tonnage, high-grade Au deposits, Eastern Goldfields Province, Yilgarn Craton, Western Australia, *in* Eliopoulos, D. G., ed., Mineral Exploration and Sustainable Development, 7th Biennial SGA meeting: Athens, SGA, p. 827–830.

Walshe, J. L., Hobbs, B. E., Ord, A., Regenauer-Lieb, K., and Barnicoat, A. C., 2005b, Mineral Systems, Hydridic Fluids, the Earth's Core, Mass Extinction Events and Related Phenomena, *in* Mao, J., and Bierlein, F., eds., Mineral Deposit Research: Meeting the Global Challenge, 1: Berlin, Springer, p. 477–480.

Walshe, J. L., Neumayr, P., Petersen, K. J., Young, C., and Roache, A., 2006, Scale-integrated, architectural and geodynamic controls on alteration and geochemistry of gold systems in the Eastern Goldfields Province, Yilgarn Craton, MERIWA Project 358 Final Report, p. 287.

Williams, Q., and Hemley, R. J., 2001, Hydrogen in the deep Earth. : Annual Reviews Earth Planetary Science, v. 29, p. 365–418.

Williams, Q., and Henley, R., 2001, Hydrogen in the Deep Earth: Annual Reviews of Earth and Planetary Science Letters, v. 29, p. 365–418.

Witt, W. K., Knight, J. T., and Mikucki, E. J., 1997, A Synmetamorphic Lateral Fluid Flow Model for Gold Mineralisation in the Archaean Southern Kalgoorlie and Norseman Terranes, Western Australia: Economic Geology, v. 92, p. 407 - 437.

Witt, W. K., and Vanderhor, F., 1998, Diversity within a unified model for Archaean gold mineralization in the Yilgarn Craton of Western Australia: An overview of the late-orogenic, structurally-controlled gold deposits: Ore Geology Reviews, v. 13, p. 29–64.

Woodland, A. B., and Koch, M., 2003, Variation in oxygen fugacity with depth in the upper mantle beneath the Kaapvaal craton, southern Africa: Earth and Planetary Science Letters, v. 214, p. 295–310.

Xu, Y., 1999, The stable isotope and trace element geochemistry of the Victory gold deposit, Western Australia, Unpublished PhD thesis, Australian National University, 163 p.

## 3.5 Question 5: Depositional processes in Eastern Yilgarn gold systems

**John Walshe**

CSIRO, ***pmd****CRC*, Kensington, Perth, Western Australia.

### 3.5.1 Introduction

This review of depositional processes in Eastern Yilgarn gold systems summarises progress in understanding the nature of chemical gradients established in the system and architectural constraints on fluid mixing processes that sustained the gradients. It concludes with a summary of possible mechanisms of gold transport and deposition.

A brief review of the single-fluid models traditionally used to account for the formation of Archaean lode gold deposits leads to a discussion of evidence leads for a least three major fluid types or classes in the gold systems and the constraints on the chemical gradients that developed as a result of fluid mixing and fluid-rock reaction processes.

The key gradients considered in the discussion are redox, water activity and salinity, pH and sulphur activity. The absolute size of the redox gradient is yet to be determined but the data are sufficient to argue for reaction between oxidised fluid species (sulphate and $SO_2$) and reduced fluid species ($CH_4$, $H_2$) and the straightforward explanation is that at least two fluids have mixed to yield the gradients. The pH variation was possibly upwards of 5 to 6 units from ~ 3–4 (pyrophyllite/chloritoid/paragonite) to ~ 8–9 (albite/pyrrhotite). Gold is preferentially deposited in near neutral to alkaline environments. Potential sulphur activity varied 3–4 orders of magnitude from ~$10^{-3}$ to $10^{-4}$ m$\Sigma$S in distal settings to ~1 m$\Sigma$S in proximal settings with albite/pyrrhotite stable.

The Victory – Defiance Complex in the St Ives Gold Camp is used to illustrate progress in mapping pathways of contrasting fluid types, sites of enhanced fluid flow and sites of strong geochemical gradients related to mineralisation. Combining mapping of alteration mineralogy and isotopic variation has identified:

- an upflow zone of oxidised fluids,
- lateral flow of oxidised fluid and,
- upflow and lateral flow zones of reduced fluid.

These architectural features can be related to the East Repulse and Conqueror deposits.

The discussion of possible mechanisms of gold transport and deposition considers the implications of reacting "deep-earth" fluid ($H_2$ - NaH - HCl - $CH_4$ - $N_2$) with aqueous crustal fluids (ambient fluids) and oxidised volatiles ($CO_2$ - $SO_2$) of magmatic affinity. Domains of mixing of a "deep-earth" fluid ($H_2$ - NaH - HCl - $CH_4$ - $N_2$) with magmatic volatiles are considered to be most favourable for the formation of high grade gold deposits. Domains of mixing of a "deep-earth" fluid ($H_2$ - NaH - HCl - $CH_4$ - $N_2$) with aqueous crustal fluids led to acid alteration and gold dispersion.

### 3.5.2 Fluids, Chemical Gradients and Fluid Mixing

Traditional models of formation of Archaean lode Au deposits assume one dominant aqueous-carbonic fluid in the system (see reviews of Goldfarb et al., 2001; Groves et al., 1998; Groves et al., 2003; Hagemann and Cassidy, 2000; Ridley and Diamond, 2000, and references therein). This uniform fluid is considered a defining character of orogenic lode gold systems together with the overall timing of formation of deposits within the main phase of crustal shortening. The fluid is considered a "regional fluid" (i.e., it is not related to any specific source/reservoir) with the dominant component being a mid to lower-crustal metamorphic fluid, with possible components of deeply sourced magmatic fluids, deeply circulating meteoric water and mantle fluids. Generally the gold has been assumed to be transported as a gold sulphide complex with gold deposition driven by de-sulphidisation reactions with the wall rocks, phase separation at the deposit scale or by back-mixing of the aqueous-carbonic fluid with locally derived variants (Hagemann and Cassidy, 2000; Mikucki, 1998; Mikucki and Ridley, 1993). Commonly gold deposits occur in second and third order structures (Eisenlohr et al., 1989; Neumayr and Hagemann, 2002; Neumayr et al., 2000). Recently, (Cox and Ruming, 2004) and (Micklethwaite and Cox, 2004) have argued that the low displacement structures that host the deposits are aftershock structures whose development was driven by large slip events on the major structures being arrested at contractional or dilational jogs. Transient permeability localised fluid flow during repeated aftershock ruptures on the low displacement structures.

However, the studies that led to the development of the single-fluid did not appreciate the zoned character of the gold systems that has become apparent with district scale geophysical and geochemical studies. Nor is the diversity of fluid types as recorded in the fluid inclusions or implied by the geochemistry, particularly the isotope data, accounted for in the single-fluid models. The extremes in physicochemical conditions implied by these data are beyond the spectrum of conditions that may be generated by reaction of a single fluid of uniform composition with a range of rock types for the fluid/rock ratios expected of fluid-dominated systems. Multi - fluid models more easily account for these extremes. The multi-fluid model developed in (Walshe et al., 2008) invokes the mixing of a "deep-earth" fluid with aqueous crustal fluids and magmatic volatiles to account for the inferred thermochemical gradients. The aqueous crustal fluid (Fluid 1) is modelled as a background or ambient aqueous fluid with low concentrations of salt and $CO_2$. Volatiles of magmatic affinity (Fluid 2) are modelled as an anhydrous carbonic fluid with significant levels of $SO_2$ and $CO_2$ sourced from the mantle. The deep-Earth fluid (Fluid 3) is modelled as a hydridic fluid with volatile species such as $CH_4$, $N_2$ as well as $H_2S$, HCl ±HF, precious metals and hydrides of alkali and alkali-earth elements e.g. Na and Mg.

The aqueous-carbonic ambient fluid is equivalent to the orogenic or metamorphic fluid of earlier workers and is considered the major reservoir of water in the system. The compelling arguments for an oxidised fluid of magmatic affinity contributing to the depositional process are the spatial association of oxidised alteration assemblages in the Eastern Goldfields Superterrane with 2665–2650 Ma mafic and syenitic intrusions, together with the geochemical signals (summarised in (Walshe et al., 2008)). The source and nature of the reduced fluid is more controversial. The redox gradients are of crustal dimensions with the most reduced fluids occurring at depth and at temperatures of 500–700 °C. This redox–temperature distribution through the crust is not easily reconciled with models that utilise a reductant such as methane from sedimentary sources in the upper parts of the crustal architecture such as the Black Flag Beds or the Late Basins. Apparently, there was a source of reductant at depth and the argon isotope data (Kendrick et al., 2008; Walshe et al., 2008) suggest $H_2/CH_4$ contribution from the mantle.

From a conceptual perspective, diversity in fluid properties between different domains should be the norm in mineralising systems, whatever their ultimate origin. The rate of mineralisation is dependent on the size of the physico-chemical gradients between different domains. (Phillips, 1990) defines the rate of mineralisation (R) for steady state conditions as:

R = Fluid velocity x Σ {Change of solubility with P, T, conc * Gradient of P, T, conc }

For mineral systems in which the elements of interest are in solution, the steady state mathematical description says the rate of mineralisation at any site is dependent of 3 factors

1. The velocity of fluids transporting elements to the precipitation site

2. The change in element solubility in the fluids as a function of physicochemical parameters (P,T, redox, pH, salinity) that control solubility

3. The gradients (change with respect to length) of these physicochemical parameters

Pathways in the system will be characterised by high fluid flow but low gradients. Sites of formation of high-grade deposits will be related to persistent steep gradients in parameters critical to solubility in areas of greatest fluid flow rate. An effective mechanism to sustain thermo-chemical gradients is mixing of chemically contrasting fluids (Walshe et al., 2003). If fluid mixing was the process that sustained thermo-chemical gradients the pathways of the different fluids must be apparent in the geology as well as links to potential sites of fluids mixing. There should be quite specific relationships between types of structures in the architecture, types of alteration and geodynamic history. If this were not the case then the chemical potential of fluids would be degraded along the flow paths and the capacity of the system to create chemical contrasts at specific sites would be lost. It should be possible to map the pathways at scales larger than the deposit and utilise the knowledge of these pathways in exploration. Conversely, if there is degradation of chemical potential of the end-member fluids by fluid-fluid and fluid-rock interactions, then it ought to be possible to recognise and map the alteration products of these events. Arguably, if the processes of ore formation are inherently inefficient

processes then the "degraded" alteration patterns will be the common "footprints" in the system that need to be "navigated" to locate the "productive" pathways and sites of fluid mixing. The example of black smokers on the modern seafloor suffices to illustrate how inefficient nature can be at fixing metals on some physicochemical gradient.

## 3.5.3 Constraints on the chemical gradients

### 3.5.3.1 Introduction

The current study has significantly enhanced our understandings of gradients in physicochemical parameters such as redox, pH and activities of water, chlorine, carbon and sulphur at the time of gold mineralisation. The section summarises the evidence for key physico-chemical gradients in the Eastern Yilgarn gold systems, drawing on the report of the fluid reservoirs in gold systems (Walshe et al., 2008). A summary of properties of the proposed end-member fluids is given in Table 3.5.1.

The key gradients considered are:

- redox
- water activity and salinity
- pH
- sulphur activity

### 3.5.3.2 Evidence of redox gradients

The evidence for changing redox state and its origin in fluid mixing is best documented in the St Ives gold camp from correlation of mineral assemblages with stable isotope and fluid inclusion data.

The St Ives Gold Camp (SIGC) is zoned with respect to reduced (pyrite, pyrrhotite, arsenopyrite) and oxidised (haematite, magnetite, anhydrite) sulphide-oxide mineral assemblages and detailed paragenetic studies show that these assemblages overlapped at about the time of gold mineralisation.

The spatial variations in the S and C isotope data indicate coupled reaction of reduced and oxidised species e.g., $CH_{4(aq)} + SO_4^{--} + 2H^+ = H_2CO_{3(aq)} + H_2S_{(aq)} + H_2O$

Paragenetically constrained sulphur isotope studies in the SIGC show that the maximum variation in sulphur isotopes occurred within the gold stage; i.e., the time of maximum redox gradient was at this stage. The variation in sulphur in the SIGC is spatially related to the transition from oxidised to reduced mineral assemblages, consistent with both assemblages forming at the same time.

The absolute size of the redox gradient is yet to be determined but the data are sufficient to argue for reaction between oxidised fluid species (sulphate and $SO_2$) and

Table 3.5.1: Summary of properties of the proposed end-member fluids for Archaean gold systems

| End-member Fluid | Ambient Fluid (1) | Oxidized fluid of magmatic affinity (2) | Hydridic Fluid (3) |
|---|---|---|---|
| Major species | $H_2O$ - $CO_2$ ± NaCl | $CO_2$ | $H_2$ - NaH - NaCl -$CH_4$ - $N_2$ |
| pH (with hydration) | Neutral to slightly acid | Acidic | Highly alkaline |
| Sulphur species | $H_2S$ | $SO_2$ | $H_2S$ |
| Sulphur activity (mΣS) | ~$10^{-3}$ to $10^{-4}$ | ~$10^0$ ?? | ~$10^0$ ?? |
| Carbon activity (mΣC) | ~ $10^{-2}$ | ~ $10^0$ | ?? |
| Silicate assemblages (with hydration) | qtz- mus - alb -chl | muscovite phengite ±Kspar | biotite - albite - amphibole± qtz |
| Fe minerals (with hydration) | mt/py | hm/mt/py | po |
| C minerals | ankerite | dolomite | graphite? |

reduced fluid species ($CH_4$, $H_2$) i.e., the redox extrema were at or above the oxidised/reduced buffer for aqueous sulphur species and at or below the reduced/oxidised buffer for aqueous carbon species.

Reduced and oxidised mineral assemblages are found in most, if not all, of the major gold camps in the Eastern Goldfields Superterrane and similar ranges in C and S isotope data occur. By inference, redox gradients were common to the formation of most deposits of the Eastern Goldfields Superterrane.

### 3.5.3.3 Evidence of gradients in $H_2O$ activity and salinity

Data on the fluid evolution at the Conqueror and Revenge mines in the St Ives gold camp indicate hydrothermal fluids in the camp evolve over time (Petersen et al., 2006; Petersen et al., 2007):

From:
low salinity aqueous-carbonic fluid in stage 1 (epidote - calcite - magnetite 1- pyrite 1 - chalcopyrite - quartz)

To:
reduced $CH_4 \pm N_2 \pm CO_2$ fluids in stage 2a (Pyrrhotite - carbonate - amphibole - biotite ± quartz ± arsenopyrite ± pyrite) and;
low salinity carbonic fluids ($CO_2$ >> $H_2O$) without $CH_4$ in stage 2b (plagioclase - carbonate - pyrite 1 ± Au ± magnetite 2 ± haematite)

To:
aqueous, carbonic and aqueous-carbonic fluids with variable $H_2O/CO_2$ ratios and salinity ranges from 0 to 37 wt% equiv. NaCl in stage 3 (quartz vein system - pyrite 2 - chlorite).

These data clearly indicate some significant variations in activities of $H_2O$, salinity, $CO_2$ and $CH_4$ as the system evolved temporally. Broadly the $CO_2$ and salinity contents of the fluids increased and temperature of the fluids decreased with time. Importantly, during gold mineralisation, water activity decreased and both $CH_4 \pm N_2$ (stage 2b) and $CO_2$ (stage 2a) contents increased. The fluids at this stage were apparently anhydrous. The late aqueous fluids were highly saline compared with the early aqueous fluids. The large range in sulphur isotope ratios for stage 2 (-8 ‰ to about +4 ‰) is consistent with maximum redox gradient occurring at this stage. The correspondence of fluid evolution with mineralogical changes is a strong hint that there was a spatial as well as temporal evolution of fluid compositions in the St Ives system.

### 3.5.3.4 Evidence of pH gradients

The current assessment of pH and sulphur activity gradients is based on an understanding of the pH control on the stability of Fe - K - Na - Al - silicate minerals in the presence of Fe-S-O minerals, excess quartz and fluid. Minerals such as paragonite (Na mica), muscovite, chloritoid (Fe-kaolinite), and pyrophyllite form in a relatively acidic environment compared with minerals such as albite, phengite, and K-feldspar. The pH control on the stability of muscovite versus phengite as illustrated by the following exchange reaction:

$$2K^+ + 3(Fe,Mg)^{2+} + 9SiO_2 + 6H_2O + KAl_3Si_3O_{10}(OH)_2 = 3K(Fe,Mg)AlSi_4O_{10}(OH)_2 + 8H^+$$

At very alkaline conditions, pH ~ 8 to 9 or higher, the controlling reaction on quartz solubility is:

$$SiO_2 + 2H_2O = H_3SiO_4^- + H^+$$

Quartz dissolves with increasing pH, so assemblages with albite and no quartz may represent extremely alkaline conditions. The proximal assemblage of albite and pyrrhotite is stable in alkaline, S-rich fluids.

Deposit and district-scale PIMA data sets from Kanowna Belle and Wallaby deposits and environs reveal systematic variations in distribution of muscovite/paragonite versus phengite/albite consistent with district-scale acid alteration zones outboard of the gold deposits. The implication of these data is that gold is preferentially deposited in near-neutral to alkaline environments rather than acidic environments. The occurrence of gold with albite and without quartz implies that gold may be deposited at highly alkaline conditions (pH ~ 8 to 9 or higher).

The overall extent of the pH is yet to be defined but it seems possible that the pH variation was upwards of 5 to 6 units from ~3–4 (pyrophyllite/chloritoid/paragonite) to ~8–9 (albite/pyrrhotite). In the 3-fluid model the evolution of fluid pH is considered to reflect the history of interaction of deep-Earth fluids with crustal fluids and

rocks and degrade to aqueous fluids of varying acidity, redox state and salinity. Relatively high halogen (HCl, HF) to alkali (NaH, $MgH_2$, $CaH_2$, $SrH_2$) ratios in the deep-Earth fluids should lead to acid production through dissociation of HCl and HF in aqueous crustal fluids; assuming limited degassing of hydrogen. Loss of hydrogen through degassing, or consumption of hydrogen through reaction with oxidised species or rocks (sulphate and carbonate or $CO_2$) could lead to neutral to alkaline, highly saline, sodic and potentially magnesium, and calcic brines depending on the history of fluid rock reaction. These brines may be sufficiently alkaline to dissolve quartz but stabilise feldspars at highly alkaline conditions (pH ~8 to 9 or higher).

### 3.5.3.5 Evidence of sulphur activity gradients

Estimates of the variation in activity of sulphur in Archaean gold systems (Mikucki, 1998) ranged from $10^{-4}$ to $10^{-1}$ molal $H_2S$ at 250 to 500°C (Figure 3.5.1). More recently, the determination of the composition of fluids in equilibrium with the proximal alteration assemblage of the Junction deposit (St Ives Camp) has identified biotite–chlorite–albite–quartz–calcite–pyrrhotite. This suggests that previous estimates for both pH and S-contents of fluids coexisting with biotite-calcite – albite - pyrrhotite assemblages may be too low.

For specified T, P, composition of chlorite (aFe-chl) and salinity ($aNa^+$ ~ fixed), nature of the Fe-sulphide co-existing with chl-ab-qtz is a function of pH and $aH_2S$ as shown by:

$$Fe_5Al_2Si_4O_{10}(OH)_8+2SiO_2+2FeS_2+3H_2S + 2Na+ = 7FeS+2NaAlSi_3O_8 + 2H^+ + 6H_2O$$

From the calculations illustrated in Figure 3.5.2 (see also (Walshe et al., 2006)) albite and pyrrhotite are stable at:

- strongly alkaline (pH>7.2) and very S-rich (3–7mΣS) fluids for moderately oxidised conditions ($CO_2/CH_4$ > 1)
- weakly to moderately alkaline (pH~6.5) and moderately S-rich (~2–3mΣS) fluids for highly reducing conditions ($CO_2/CH_4$ < 1)
- Neutrality at these PT conditions is at pH ~ 5.0

Regardless of the assumptions, all conditions suggest previous estimates for pH and S-contents of fluids in equilibrium with biotite - calcite - pyrrhotite assemblages may be too low. Potential sulphur activity varied 3–4 orders of magnitude from ~ $10^{-3}$ to $10^{-4}$ mΣS in distal settings to ~ $10^0$ mΣS in proximal settings with albite/pyrrhotite stable. The oxidised (Fluid 2) and reduced (Fluid 3) anhydrous fluids are considered to have contained significant amounts of sulphur but the relative proportions of sulphur in the two fluids is unknown.

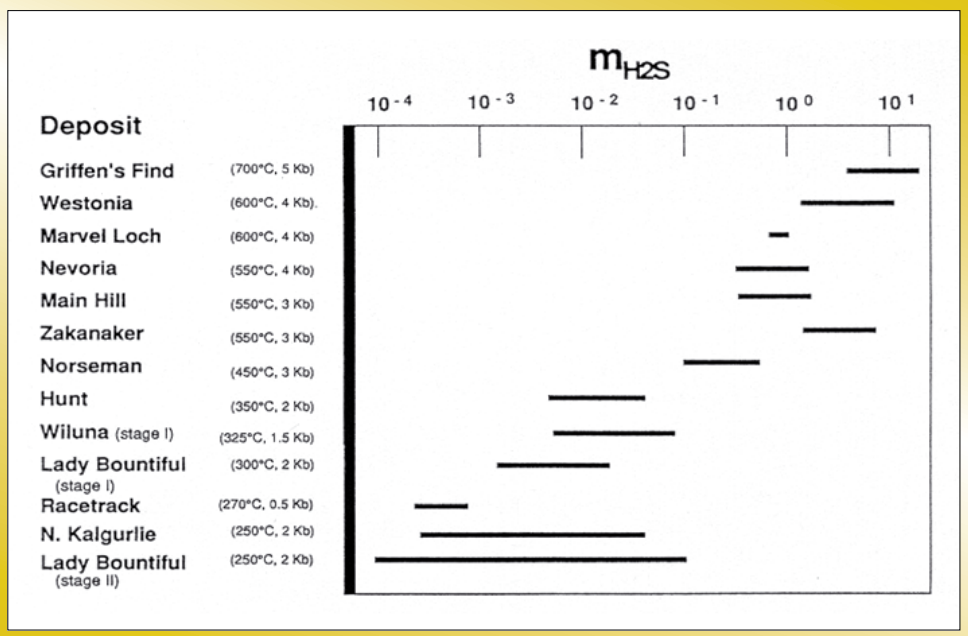


*Figure 3.5.1: Calculated ranges in $mH_2S$ for a number of Archaean lode-gold deposits from Western Australia (from Mikucki, 1998).*

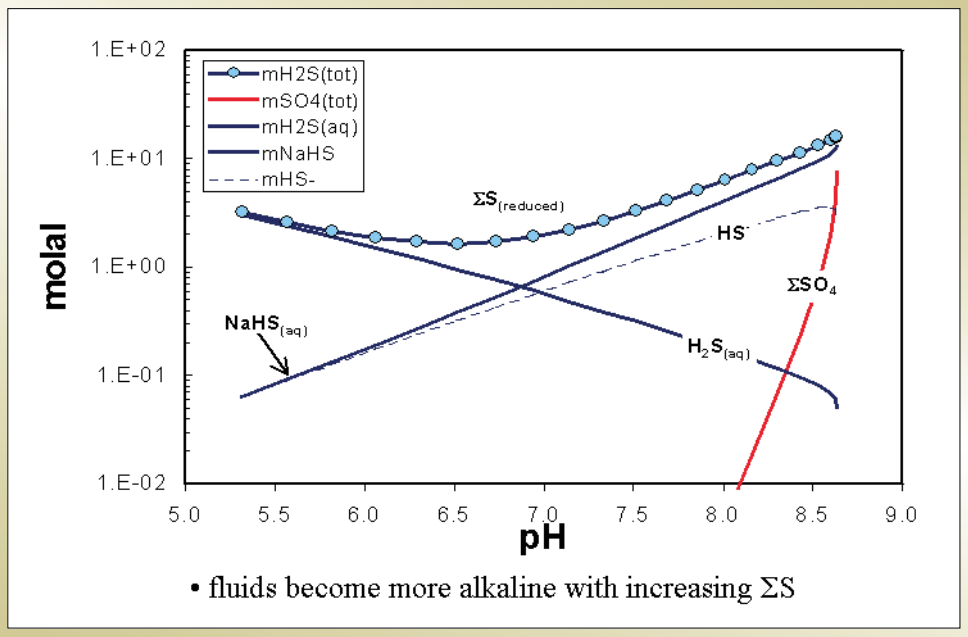


*Figure 3.5.2: Sulphur speciation in fluids equilibrated with chl(aFe-chl = 0.33)-py-po-ab-qtz at 400°C and 2Kb. HCh Run ChlPyPo0$_2$ with initial NaCl content of 9wt% (note that mECl of fluids after equilibration increase with pH).*

## 3.5.4 Mapping Fluid Pathways and Chemical Gradients in the Victory–Defiance Complex, St Ives

### 3.5.4.1 Introduction

Of the three factors controlling the rate of mineralisation, it is the gradients in physicochemical parameters, such as redox, pH, sulphur activity that can be mapped using alteration mineralogy ± isotopic information. Gradient maps should help define fluid pathways, potential sites of mineralisation and aid the understanding of depositional processes as well as the exploration effort. Considerable progress has been made on developing district-scale 2D and mine-scale 3D models of the architecture and alteration patterns to aid identification of pathways (both structural and lithological) of contrasting fluid types, aquitards (structural and lithological), sites of enhanced fluid flow and coincident sites of strong geochemical gradients; particularly for the Victory-Defiance Complex in the St Ives Gold Camp (Neumayr et al., 2008). In the Victory-Defiance Complex pathways of oxidised fluids and reduced fluids as well as domains of mixing and interaction between reduced and oxidised fluids have been mapped across the Victory-Defiance complex (Figure 3.5.3 and Figure 3.5.4), using a combination of mineralogical, isotopic and 3D architectural constraints. A summary of the isotopic interpretation for 5 drill holes (CD5653, CD6801, CD7068, CD7069 and CD7070 in the central part of the Victory-Defiance Complex is given in Figure 3.5.5 through Figure 3.5.9. Figure 3.5.10 through Figure 3.5.13 provide an overview of the interpretation across the complete Integrated Section.

The key pathways discussed are:

- an upflow zone of oxidised fluids
- lateral flow of oxidised fluid
- upflow and lateral flow zones of reduced fluid
- distribution of fuchsite: Mapping reduced and acid domains

Details of the architecture of the Victory-Defiance complex are given in Neumayr et al. (2008), and the structural evolution in Miller et al., (2008).

### 3.5.4.2 Mapping an upflow zone of oxidised fluids

The oxidised end-member fluid is modelled as anhydrous, dominated by $CO_2$ and $SO_2$ with the following isotopic properties ((Walshe et al., 2008)).

- $\delta^{34}S$ of $SO_{2(g)}$ is ~ 0 ‰
- At ~ 400 – 500 °C, $\delta^{34}S$ of coexisting $H_2S_{(g)}$ was ~ - 3.5 to -5 ‰
- Magmatic $CO_2$ was mantle derived with a $\delta^{13}C$ value of ~ -5 to -6 ‰
- Radiogenic Pb isotope signature ($^{207}Pb/^{204}Pb$ > ~ 15.5)

The inferred carbonate precipitates from the oxidised end-member fluid are:

- Carbonate with $\delta^{13}C$ of ~ -5 to -6 ‰
- Carbonate with $\delta^{18}O$ of > ~ 13 ‰ assumed to have precipitation from oxidised fluids dominated by $CO_2$ rather than $H_2O$, i.e. $CO_2 \geq H_2O$ with $\delta^{18}O$ increasing with increasing ratio of $CO_2$ / $H_2O$.

A zone of $\delta^{18}O$ values of carbonate > ~ 13 ‰ occurs in the central part of Integrated Section across the Victory Defiance Complex (Figure 3.5.5 and Figure 3.5.6; CD6801, CD7068 and CD7069). The zone is largely co-incident with the thickest section of Tripod Hill Komatiite section and is characterised by the development of intense secondary biotite within both flat and steep fabrics and along contacts with porphyries (Figure 3.5.7). Zones of epidote ± magnetite that occur in the adjacent Paringa Basalt and Devon Consols Basalt, are consistent with the interpretation of an oxidised alteration environment. These data, together with the occurrence of

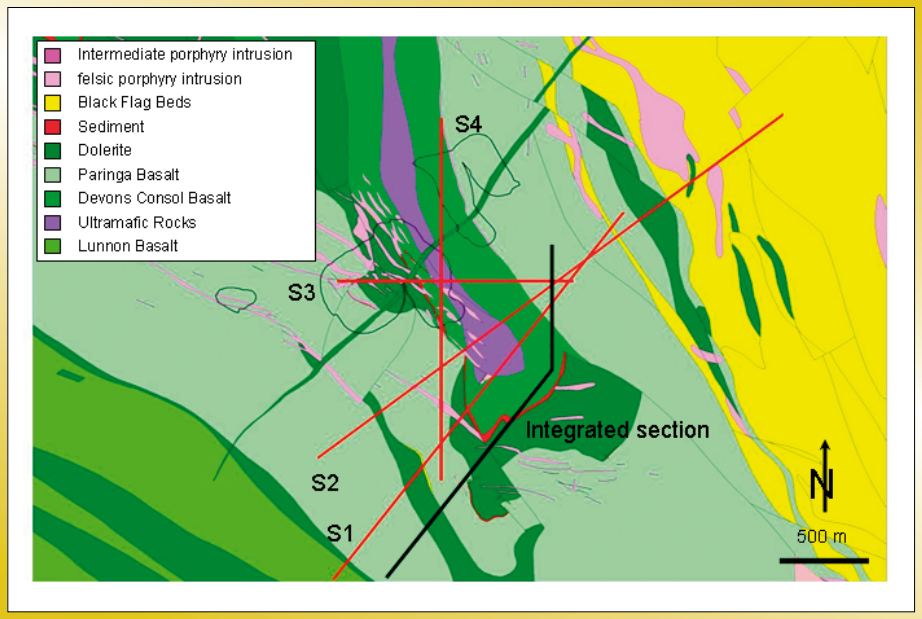


*Figure 3.5.3: Geological map of the Victory-Defiance complex showing main lithologies, open pits and the location of the Integrated Section referred to in the text. Other sections discussed in Neumayr et al. (2008).*

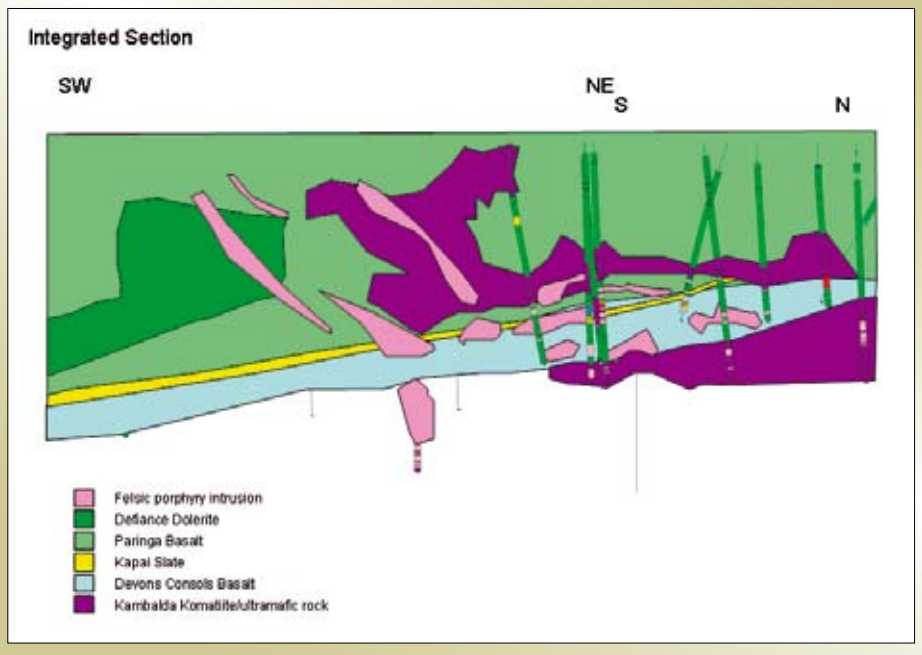


*Figure 3.5.4: Interpreted geology for the integrated section. Details of interpretation in Neumayr et al. (2008).*

anhydrite veining in the section (Figure 3.5.11) are taken to suggest the zone of intense biotite alteration centred on CD6810, CD7068 and CD7069 in section 1 was major pathway of $CO_2$-$SO_2$ - volatiles through the system.

In and around the zone of $\delta^{18}O$ > ~13 ‰ $\delta^{13}C$ carbonate values are commonly between ~ -5 and -6 ‰; the inferred range for unmodified magmatic $CO_2$, and less than -8 ‰. These values are in contrast to much of the remainder of the Integrated Section (see Figure 3.5.10). Values of $\delta^{13}C$ < - 8 ‰ are interpreted as domains of significant oxidation $CH_4$ to $CO_2$ by $SO_2$ subjacent to an upflow zone of $CO_2$-$SO_2$ -volatiles.

e.g., $3CH_4 + 4SO_2 = 3CO_2 + 2H_2O + 4H_2S$

Carbonate with $\delta^{13}C$ < -8 is characteristically associated with greater abundance of amphibole *c.f.* biotite ± chlorite alteration, consistent with a transition to more reduced fluid conditions.

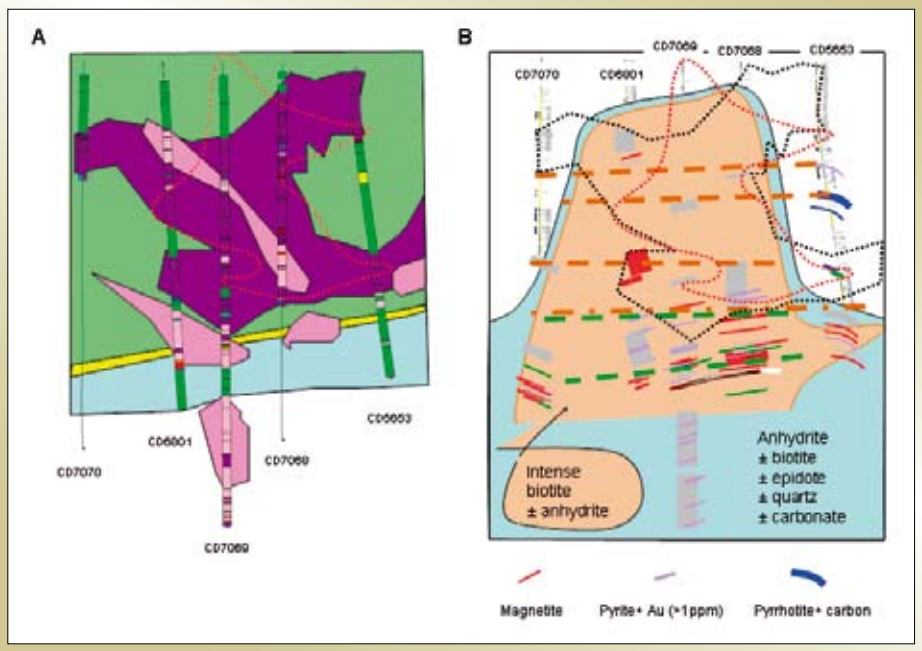


*Figure 3.5.5: Interpreted geology (A) and alteration (B) of the central part of the Integrated Section (Drill Holes CD7070, CD6801, CD7069, CD7068 and CD5653). Dashed red shows domain of $\delta^{18}O$ carbonate > ~ 13 ‰. Geology legend as for previous figure. Dashed lines show positions of domains of intense flat fabric correlated between drill holes. Brown: well developed biotite alteration; Green: Amphibole ± biotite ± chlorite.*

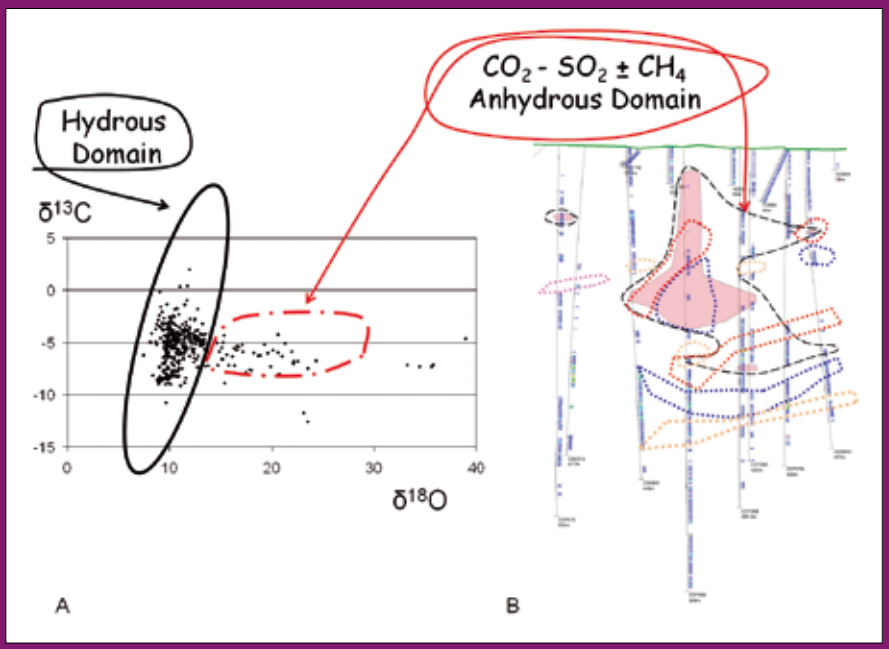


*Figure 3.5.6: Anhydrous fluid domain as mapped by $\delta^{18}O$ carbonate. A: $\delta^{13}C$ vs $\delta^{18}O$ plot showing range in $\delta^{13}C$ values for inferred anhydrous fluids ($\delta^{18}O$ > ~ 13 ‰) and hydrous fluids ($\delta^{18}O$ < ~ 13 ‰). B: Dashed black line shows $\delta^{18}O$ > ~ 13 ‰; pink shaded area $\delta^{18}O$ > ~ 20 ‰. Other contours defined on following figures. Au grades shown on profile in green, yellow and red. Red is > 10ppm.*

The inferred sulphate/sulphide precipitates of high temperature oxidised magmatic fluids (~400–500 °C), taking into account isotopic fraction factors, are:

- Anhydrite with $\delta^{34}S$ of ~ + 5 to +10 ‰
- Pyrite with $\delta^{34}S$ of ~ - 3.5 to -5 ‰.

The $\delta^{34}S$ anhydrite values for holes CD7070, CD6801 and CD7069 (Figure 3.5.5) range from ~ +8 to +10 ‰ consistent with precipitation from high temperature oxidised magmatic fluids. The $\delta^{34}S$ anhydrite values for holes CD7068 and CD5653, further east on the section, are significantly more enriched in $^{34}S$, ranging from of ~ +12 to +20 ‰.

There is also a focus of $\delta^{34}S$ pyrite values between ~ -3.5 and -5 ‰, the inferred range of high temperature sulphide in the central part of the section between CD7070 and CD7068, again consistent with an upflow zone of relatively unmodified $CO_2$-$SO_2$ – volatiles (Figure 3.5.10).


*Figure 3.5.7: Oxidised alteration assemblages.*
*A: Intense along contact between ultramafic and porphyry; CD7068/120.8m*
*B: Epidote-magnetite-pyrite alteration in DCB; CD7068/369m*
*C: Anhydrite vein CD7069/536.7m.*

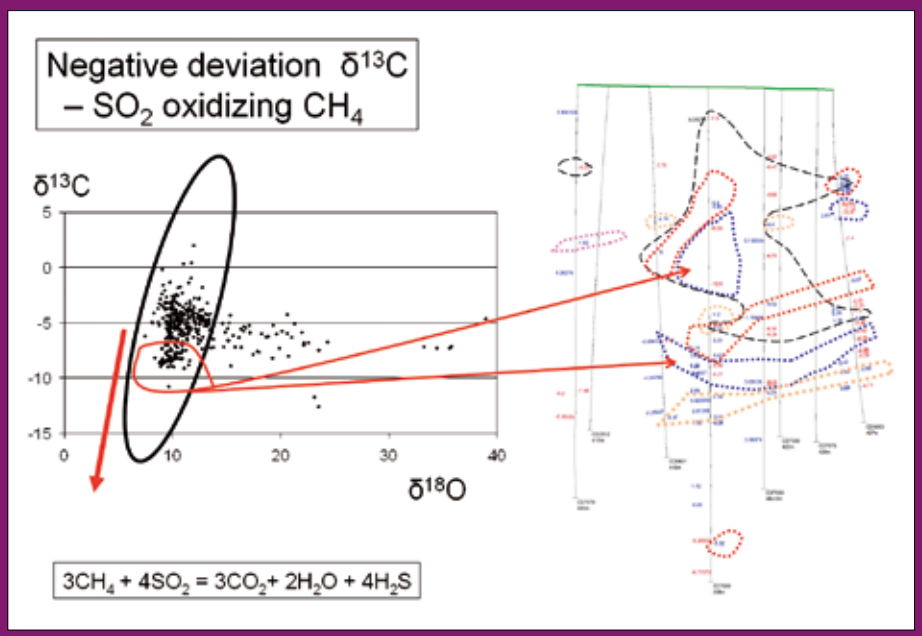


*Figure 3.5.8: Domains of oxidation of $CH_4$ to $CO_2$ by $SO_2$ as defined by $\delta^{13}C$ < - 6 ‰. Red dotted contours show domains of $\delta^{13}C$ between ~ -5 and -6 ‰ taken to be domains of unmodified magmatic $CO_2$. Dark blue dotted contours show domains of most depleted $^{13}C$ i.e. $\delta^{13}C$ < - 8 ‰. The lower domain of $\delta^{13}C$ < - 8 ‰ is coincident with greater abundance of amphibole ± biotite ± chlorite alteration in the drill core associated with flat fabrics.*

### 3.5.4.3 Mapping lateral flow of oxidised fluid

There is a laterally extensive zone of negative $\delta^{34}S$ pyrite in the Integrated Section (Figure 3.5.11) that broadly follows mapped structure and the Kapai slate (Neumayr et al., 2008) and overlaps with an zone of anhydrite veining that extends to depth. This zone is interpreted as a major zone of lateral flow of oxidised fluid.

Epidote ± magnetite is the common alteration assemblage in this zone as shown by the results of alteration logging of two drill holes through this zone using Hylogger (CD623 and CD7042) are summarised in the MERIWA358 report (p121 and p124). The Hylogger study also reported gypsum associated with epidote ± magnetite.

A comparison of the dispersion $CO_2$ and $SO_2$ based on the isotopic studies is made in Figure 3.5.12 and Figure 3.5.13.

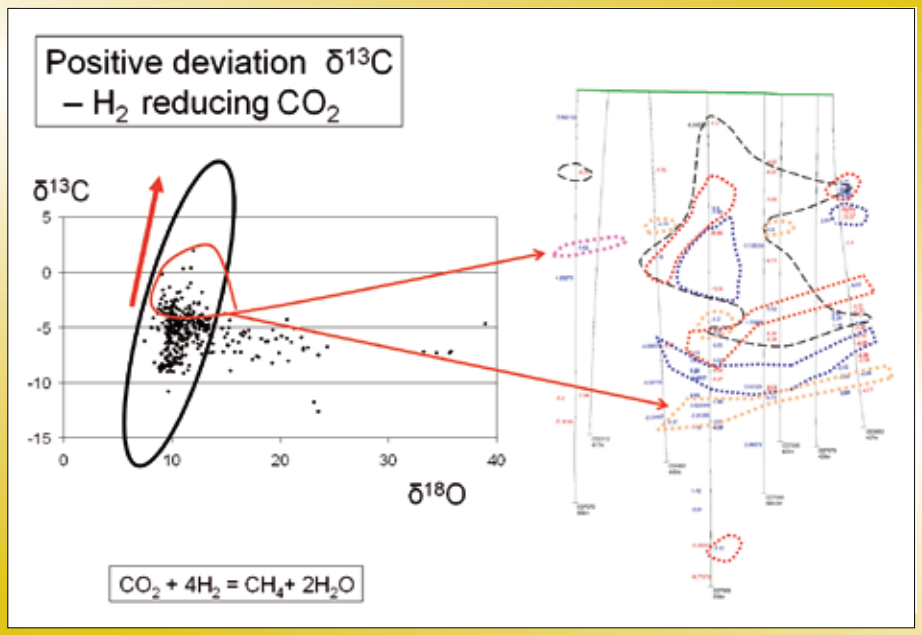


*Figure 3.5.9: Domains of reduction of $CO_2$ to $CH_4$ by $H_2$ as defined by $\delta^{13}C > -5$ ‰. Light brown dotted contours: $\delta^{13}C > -5$ but $< -4$ ‰. Pink dotted contours: $\delta^{13}C > -2$ but $< 0$ ‰. Red and blue dotted contours as for previous diagrams.*

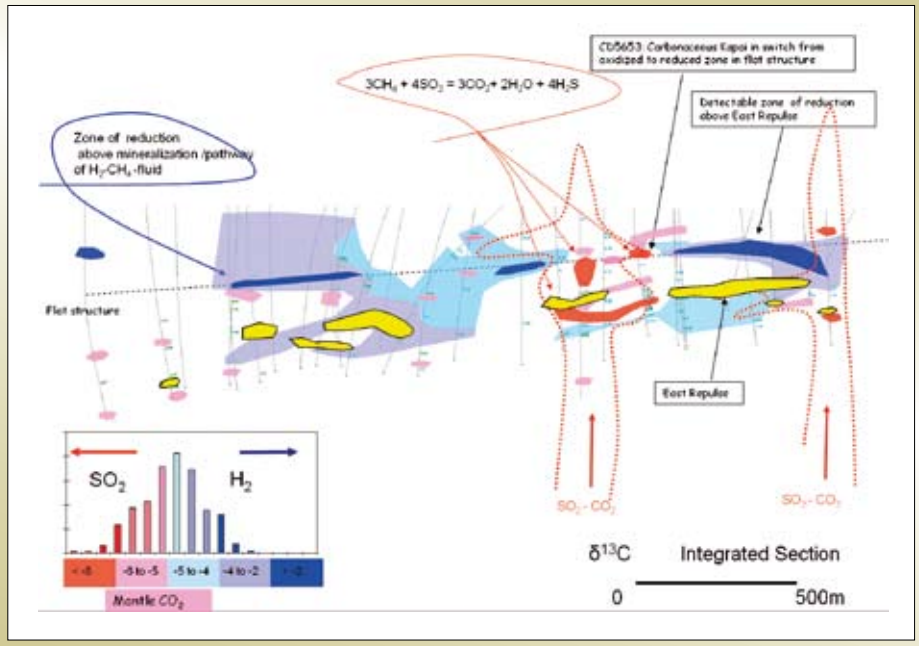


*Figure 3.5.10: Interpretation of $\delta^{13}C$ carbonate across the Integrated Section, Victory - Defiance Complex. Flat structure defined from the C isotopes (see text) and logging of drill holes shown in Figure 3B. $\delta^{13}C$ between ~ -5 and -6 ‰ taken to be domains of unmodified mantle $CO_2$. Red indicates most depleted $^{13}C$ i.e., $\delta^{13}C < -8$ ‰. These are inferred as domains of oxidation by $SO_2$ of $CH_4$ to $CO_2$. Cool colours indicate reduction of $CO_2$ to $CH_4$ by $H_2$ defined by $\delta^{13}C > -5$. Dark blue indicates foci of reduction ($\delta^{13}C > -2$). Yellow: gold mineralisation.*

The distribution of $CO_2$-$SO_2$ fluids in inferred to be relatively limited based on:

- $\delta^{13}C$ between ~ -5 and -6 ‰ taken to be domains of unmodified magmatic $CO_2$
- $\delta^{13}C$ < -8 ‰ taken as domains of oxidation of $CH_4$ by $SO_2$
- $\delta^{18}O$ > ~ 13 ‰
- $\delta^{34}S$ pyrite between ~ -3.5 and -5 ‰; the inferred range of high temperature sulphides
- $\delta^{34}S$ anhydrite between ~ +5 and +10 ‰

The main zones occur in the central part of the section (CD6801, CD7068; CS7069) and beneath the East Repulse mineralisation. By comparison, unmodified magmatic $CO_2$ ($\delta^{13}C$ between ~ -5 and -6 ‰) is more

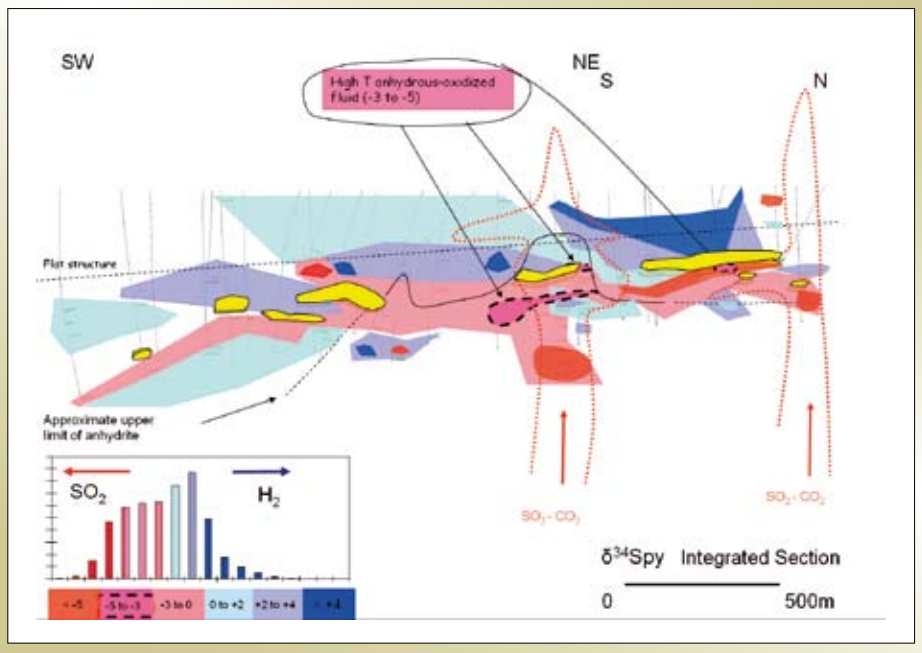


*Figure 3.5.11: Interpretation of $\delta^{34}S$ pyrite across the Integrated Section, Victory - Defiance Complex. Negative $\delta^{34}S$ pyrite values (warm colours) denote a laterally extensive zone of oxidised aqueous fluid flow that broadly follows mapped structure and the Kapai slate. Dashed black lines denote $\delta^{34}S$ pyrite between ~ - 3.5 and -5 ‰; the inferred range of high temperature sulphides. $\delta^{34}S$ pyrite values > 0 ‰ (warm colours) taken to represent domains of significant reduction of oxidised sulphur species by $CH_4 \pm H_2$ -rich fluids. Dark blue indicates foci of reduction ($\delta^{34}S$ > 4). Up flow zones of $CO_2$-$SO_2$ -fluid and flat structure as for previous figure.*

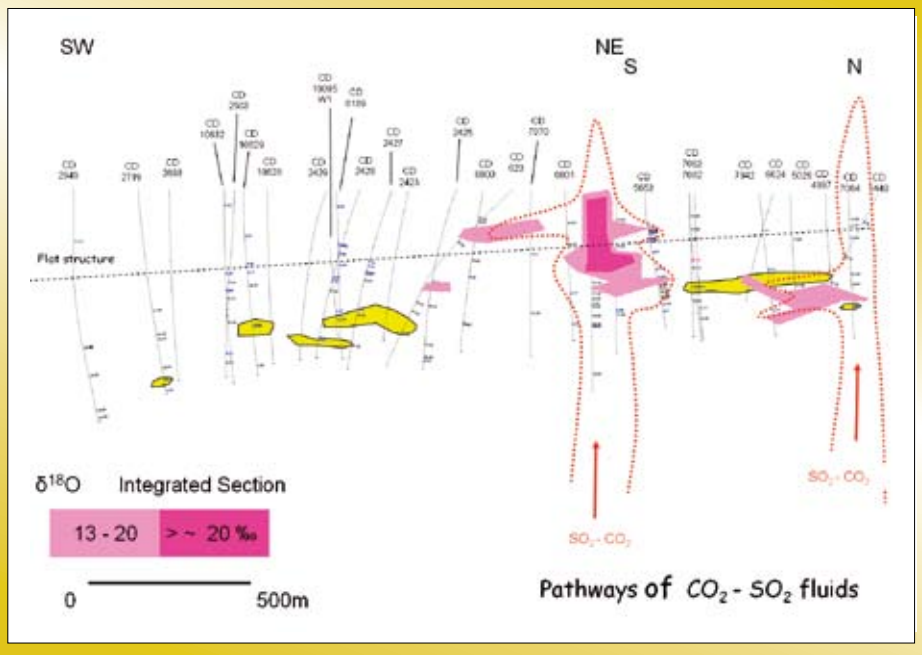


*Figure 3.5.12: Distribution of $CO_2$ - $SO_2$ fluids across the Integrated Section, Victory - Defiance Complex. Values of $\delta^{18}O$ > ~ 13 ‰ (warm colours) are inferred to map domains of anhydrous $CO_2$-$SO_2$ fluids in the central part of the section and beneath the East Repulse mineralization.*

widely dispersed, particularly along flat structures within the architecture. The more limited dispersion of $SO_2$ is consistent with the reactive nature of the species.

Domains of positive $\delta^{34}S$ pyrite (0 to >4 ‰) occur above and below the laterally extensive zone of negative $\delta^{34}S$ pyrite in Figure 3.5.11. Domains of significant positive $\delta^{34}S$ pyrite (>2‰) are taken to represent domains of reduction of oxidised sulphur species via reactions such as:

$$3CH_4 + 4SO_2 = 3CO_2 + 2H_2O + 4H_2S$$

$$3H_2 + SO_2 = 2H_2O + H_2S$$

$$CH_4 + HSO_4^- + H^+ = H_2CO_3 + H_2S + H_2O$$

$$4H_2 + HSO_4^- + H^+ = H_2S + 4H_2O$$

In these reactions, either $H_2$ or $CH_4$ may be the reducing agent (Walshe et al., 2008).

Commonly domains of $\delta^{34}S$ pyrite >2 ‰ overlap with or are spatially co-incident zones of increases in $^{13}C$ carbonate ($\delta^{13}C$ > -4 ‰); compare particularly above the Repulse mineralisation in Figure 3.5.10 and Figure 3.5.11.

The increase in $\delta^{13}C$ tracks the reduction of oxidised carbon species to $CH_4$; a reaction that requires a strong reducing agent in the fluids, most probably $H_2$ i.e.,

e.g., $CO_2 + 4H_2 = CH_4 + 2H_2O$

The implication of spatially co-incident domains of positive $\delta^{13}C$ and $\delta^{34}S$ is that $H_2$ rather than $CH_4$ is the dominant reductant species. Notably gold mineralisation occurs in the vicinity of the switches from negative to positive $\delta^{34}S$ pyrite values, consistent with argument that gold deposition is related to chemical gradients in redox or related gradients.

### 3.5.4.4 $\delta^{13}C$ mapping of reduced fluid upflow zones and lateral flow

The $\delta^{13}C$ carbonate values of > -5 ‰ show systematic zoning on the Integrated Section. These values are interpreted to reflect extent of partial reduction of $CO_2$ i.e., zoning in $\delta^{13}C$ carbonate for $\delta^{13}C$ > -5 ‰ effectively tracks the $H_2$ flux in the system.

There a reduced zoned ($\delta^{13}C$ > -4 ‰) above the major mineralised centres at East Repulse and Conqueror with a maximum value of +1.99 ‰ above the East Repulse deposit (Figure 3.5.10). The focus of reduction above East Repulse suggests there is a vertical flow path of reduced, $CH_4$ - $N_2$ - $H_2$ fluids in the area. The zones of intense reduction ($\delta^{13}C$ > -2‰) highlight a major flat structure indicating the reduced fluids dispersed preferentially along at least some of the flat structures. A carbonaceous zone in CD5653 sits within the high lighted flat structure at the cross over from reducing to oxidizing conditions along the structure. Such zones are traditionally interpreted as Kapai Slate but in this structural setting carbonaceous material is

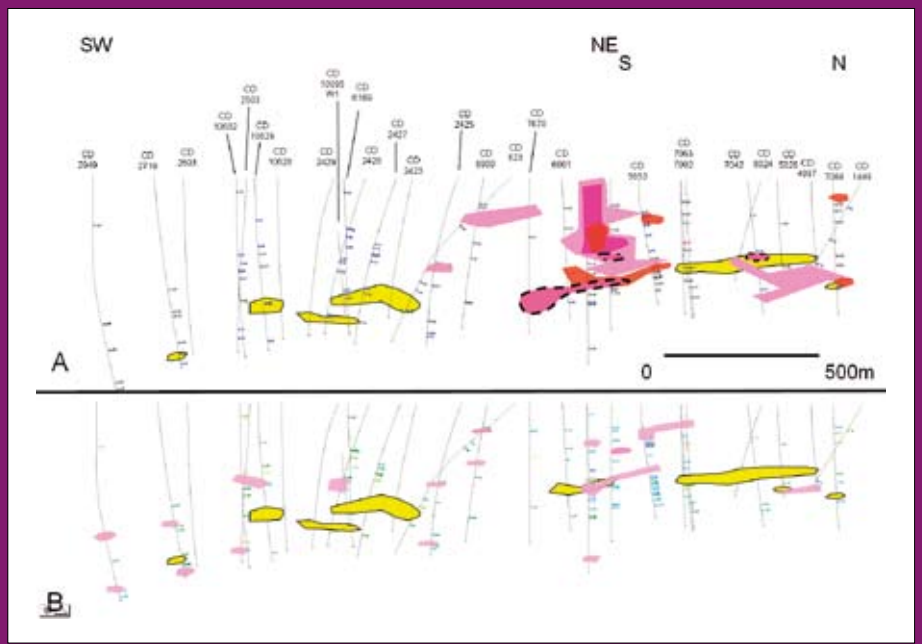


*Figure 3.5.13: Comparison of dispersion of $CO_2$ and $SO_2$. A) There is broad spatial correspondence between enriched $^{18}O$ in carbonate; $\delta^{13}C$ < -8 ‰ (domains of oxidation of $CH_4$ to $CO_2$ by $SO_2$) and $\delta^{34}S$ pyrite between ~ - 3.5 and -5 ‰ (S isotope range of high temperature sulphides) illustrated on the preceding diagrams. Collectively, these data provide a picture of the dispersion of $SO_2$. B) By contrast, $\delta^{13}C$ values between ~ -5 and -6 ‰ (inferred domains of unmodified mantle $CO_2$) are more widely dispersed.*

most likely an alteration product from the reaction of $CH_4$ and $SO_2$ i.e.,:

$$3CH_4 + 2SO_2 = 3C + 2H_2S + 4H_2O$$

The pattern of $^{13}C$ enrichment above major mineralised centres implies it will be possible to use the '$H_2$-halo' as a targeting tool. The distal but detectable zone of reduction above Conqueror mineralisation suggests up-flow zones of reduced fluids can be tracked 100s of metres above the zone of mineralisation.

#### 3.5.4.5 The distribution of fuchsite: Mapping reduced and acid domains

The maximum $\delta^{13}C$ value of ~ +2 ‰ on the Integrated Section occurs in CD5026 just below a 'fuchsitic' shear on the contact of porphyry with Paringa Basalt. In this position the fuchsite (Cr-rich mica) is some 100 m from the nearest ultramafic and implies Cr is being mobilised by reduced and probably anhydrous fluids. The mica, coupled with the positive $\delta^{13}C$ value, implies precipitation of Cr in a relatively acid and aqueous environment. This suggests the distribution of fuchsite may map areas of condensation of reduced, anhydrous fluids into aqueous fluids. Figure 3.5.14 shows the location of the 'fuchsitic' shear east of East Repulse. It is steeply dipping, N-S trending and may well be a segment of the Britannia Shear. This style of 'fuchsitic' alteration occurs above gold mineralisation within in the Sunrise Shear at the Sunrise Dam gold deposit (Cleverley and Nugus, 2008). In the Victory-Defiance complex there is potential for a repeat of the East Repulse mineralisation where the steeply dipping fuchsite shear intersects the Repulse Fault below the ultramafic.

### 3.5.5 Summary of Gold Transport and Depositional Mechanisms

Traditionally it has been assumed that gold is transported as an aqueous gold sulphide complex with gold deposition driven by de-sulphidisation reactions with the wall rocks, phase separation at the deposit scale or by back-mixing of the aqueous-carbonic fluid with locally derived variants (Hagemann and Cassidy, 2000; Mikucki, 1998; Mikucki and Ridley, 1993). However, the fluid inclusion and isotopic data summarised above indicates fluids were apparently anhydrous or close to anhydrous at the time of gold deposition. The implication is that gold was transported by complexes stable in either oxidised $CO_2$-$SO_2$-rich fluids or hydridic fluids; with Au complexing with S ± H ± N ± C ± Cl as well as possibly alkali/alkali-earth elements.

The following observations help constrain the discussion as to the nature of the species and processes involved in gold deposition:

- There is no unique association of high grade gold occurrences with any particular mineral or mineral combination.

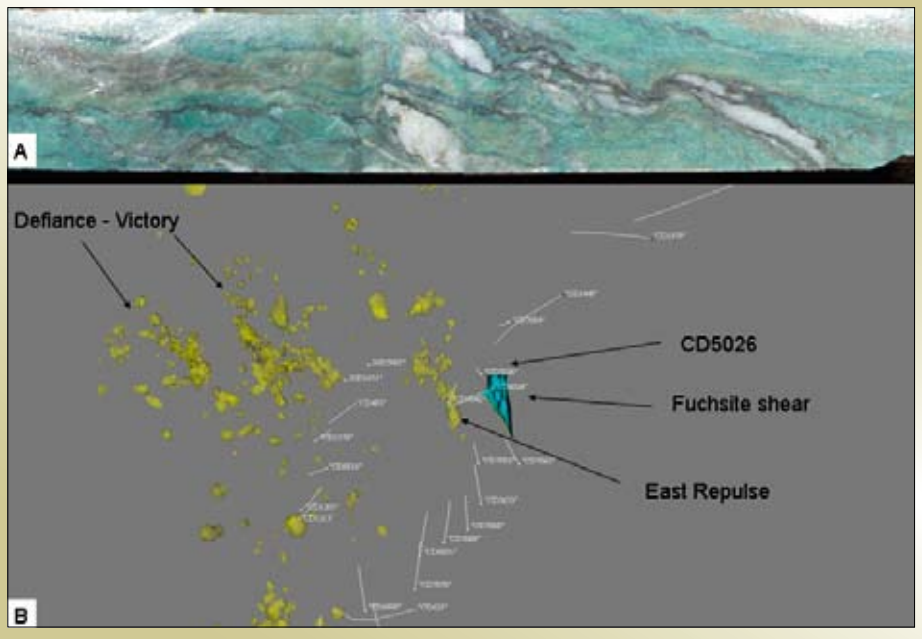


*Figure 3.5.14: Fuchsite in the East Repulse environment. A) Fuchsitic sample from CD6330 1~100. B) Location of the fuchsitic shear, east of East Repulse.*

- High grade gold zones may occur with quartz ± sulphide ± magnetite ± haematite ± carbonate ± feldspar ± mica ± amphibole ± biotite.
- Commonly high grade gold zones (≥30 g/t Au) show limited evidence of reaction with host mineral or mineral assemblages.
- Paradoxically, at the district-scale gold deposits are associated with large-scale alteration footprints while at the lode/hand-specimen scale there is commonly limited evidence of reaction with host minerals.
- Gold deposits occur on redox gradients but not all mappable gradients are related to gold deposits.
- Similarly gold deposits occur on pH gradients but not all mappable gradients are related to gold deposits.
- There is no correlation between gold grade, tonnage of the deposit and the absolute oxidation state of the system, as defined by the sulphur isotopic composition of sulphides. The redox gradient is significant not the absolute redox state.
- Gold deposits tend to occur with near-neutral to alkaline assemblages (phengite/albite rather than muscovite/paragonite) assemblages although the Bellephoron prospect in the St Ives Gold Camp (SIGC) occurs with muscovite. As with redox, the pH gradient is significant not the pH.

### 3.5.6 Conclusions

These observations can be rationalised with the 3-fluid model if gold transport and deposition is assumed to occur in the anhydrous domain involving Fluids 2 and 3 and is decoupled from transport and deposition of most other elements. Gold depositional reactions leading to the formation of high-grade Au deposits is taken to be highly specific and involve little water – hence the lack of alteration in the immediate vicinity of high grade gold zones and overall lack of correlation with any specific mineral or mineral assemblage. Gold deposition in the anhydrous domain possibly occurred because of changes in redox, sulphur activity or changes in activity of some other component such as $H_2O$, $H_2$ or HCl. It is difficult to constrain the processes on the available information obtained from minerals that grew in the hydrous domain. Gold transferred to the aqueous domain by addition of ambient fluid (Fluid 1) was largely flushed from the system or fixed in low grade deposits following fluid-rock reaction. As the volatiles of the anhydrous fluids are all soluble in water, physicochemical gradients (redox, pH) were generated in the hydrous domain. In particular the production of acidic fluids by mixing of ambient and hydridic fluids (Fluids 1 and 3) mobilised many rock-forming elements, including iron and generated wide-spread alteration. Sulphate-rich fluids generated by mixing Fluids 2 and 3 have some capacity to buffer pH via redox reactions e.g.,

$$SO_4^{2-} + 2H^+ + CH_4 = H_2S + CO_2 + 2H_2O$$

Such reactions possibly resulted in neutral/alkaline fluids, rather than acidic fluids around intrusive complexes. Commonly, gradients in the hydrous domain will be decoupled from gold deposition and the acidic fluids probably flushed much gold through the system.

### 3.5.7 References:

Cleverley, J., and Nugus, M. J., 2008, Fluid-chemical evolution of the Sunrise Dam mineral system. This volume.

Cox, S. F., and Ruming, K., 2004, The St Ives mesothermal gold system, Western Australia - a case of golden aftershocks?: Journal of Structural Geology, v. 26, p. 1109–1125.

Eisenlohr, B. N., Groves, D. I., and Partington, G. A., 1989, Crustal-scale shear zones and their significance to Archaean gold mineralisation in Western Australia: Mineralium Deposita, v. 24, p. 1–8.

Goldfarb, R. J., Groves, D. I., and Gardoll, S., 2001, Orogenic gold and geologic time: A global synthesis: Ore Geology Reviews, v. 18, p. 1–75.

Groves, D. I., Goldfarb, R. J., Gebre-Mariam, M., Hagemann, S. G., and Robert, F., 1998, Orogenic gold deposits: A proposed classification in the context of their crustal distribution and relationship to other gold deposit types: Ore Geology Reviews, v. 13, p. 7 - 27.

Groves, D. I., Goldfarb, R. J., Robert, F., and Hart, C. J. R., 2003, Gold deposits in metamorphic belts: Overview of current understanding, outstanding problems, future

research, and exploration significance: Economic Geology, v. 98, p. 1–29.

Hagemann, S. G., and Cassidy, K. F., 2000, Archaean orogenic gold deposits: Reviews in Economic Geology, v. 13, p. 9–68.

Kendrick, M. A., Walshe, J. L., and Petersen, K. J., 2008, Global links between gold and mantle degassing of $^{40}Ar$ plus methane: A 2.7 Ga case study: unpublished manuscript.

Micklethwaite, S., and Cox, S. F., 2004 Fault-segment rupture, aftershock-zone fluid flow, and mineralisation: Geology, v. 32, p. 813 - 816.

Mikucki, E. J., 1998, Hydrothermal transport and depositional processes in Archaean lode-gold systems: a review: Ore Geology Reviews, v. 13, p. 307–321.

Mikucki, E. J., and Ridley, J. R., 1993, The hydrothermal fluid of Archaean lode-gold deposits at different metamorphic grades: compositional constraints from ore and wallrock alteration assemblages: Mineralium Deposita, v. 28, p. 469 - 481.

Miller, J.M., Tunjic, J., Donaldson, J., and Blewett, R.S., 2008, Structural evolution of the Victory to Kambalda region of the St Ives gold camp: the role of early formed structures on the development of a major gold system. Part III, this volume.

Neumayr, P., and Hagemann, S. G., 2002, Hydrothermal fluid evolution within the Cadillac Tectonic Zone, Abitibi greenstone belt, Canada: Relationship to auriferous fluids in adjacent second- and third-order shear zones: Economic Geology, v. 97, p. 1203–1225.

Neumayr, P., Hagemann, S. G., and Couture, J. F., 2000, Structural setting, textures and timing of hydrothermal vein systems in the Val-d'Or Camp, Abitibi, Canada: Implications for the evolution of transcrustal, second- and higher-order fault zones and gold mineralisation: Canadian Journal of Earth Sciences, v. 37, p. 95–115.

Neumayr, P., Walshe, J. l., and Petersen, K., 2008, Alteration architecture of St Ives. this volume.

Petersen, K., Neumayr, P., Walshe, J. L., and Hagemann, S. G., 2006, Types of fluid compositions and evolution at the St Ives Gold camp. : 6th Annual V.M. Goldschmidt Conference, S2-02, 27th - 1st September, Melbourne, 2006.

Petersen, K. J., Hagemann, S. G., Neumayr, P., and Walshe, J. L., 2007, Multiple hydrothermal fluid pulses through time at the Kambalda gold deposits, Yilgarn Craton, Western Australia: 9th Biennial SGA Meeting, Mineral Exploration and Research: Digging Deeper, 20–27th August, Dublin., 2007, p. 675–678.

Phillips, O. M., 1990, Flow controlled reactions in rock fabrics: Journal of Fluid Mechanics, v. 212, p. 263–278.

Ridley, J. R., and Diamond, L. W., 2000, Fluid chemistry of orogenic lode-gold deposits and implications for genetic models: Reviews in Economic Geology, v. 13, p. 141 -162

Walshe, J. L., Halley, S. W., Hall, G. A., and Kitto, P., 2003, Contrasting fluid systems, chemical gradients and controls on large-tonnage, high-grade Au deposits, Eastern Goldfields Province, Yilgarn Craton, Western Australia, in Eliopoulos, D. G., ed., Mineral Exploration and Sustainable Development, 7th Biennial SGA meeting: Athens, SGA, p. 827–830.

Walshe, J. L., Neumayr, P., Cleverley, J., Petersen, K., Andrew, A., Whitford, D., Carr, G. R., Kendrick, M. A., Young, C., and Halley, S., 2008, Multiple fluid reservoirs in Eastern Yilgarn gold systems. this volume.

Walshe, J. L., Neumayr, P., Petersen, K. J., Young, C., and Roache, A., 2006, Scale-integrated, architectural and geodynamic controls on alteration and geochemistry of gold systems in the Eastern Goldfields Province, Yilgarn Craton, MERIWA Project 358 Final Report, p. 287.

## 3.6 Reactive transport models: from geochemistry to geophysics to exploration targets

**R. Chopping[1], J.S. Cleverley[2], P.A. Henson[1], I.G. Roy[1]**

[1] ***pmd*CRC*** c/o Geoscience Australia GPO Box 378, Canberra ACT 2601 Australia, correspondence richard.chopping@ga.gov.au

[2] CSIRO Exploration and Mining, Australian Resources Research Centre (ARRC), 26 Dick Perry Ave, Kensington WA 6151

### Abstract

The development of coupled fluid-flow and chemical reaction (reactive transport) models allows for the simulation of key ore-forming processes. These simulations produce a model of mineralogy at various time steps and show how alteration varies both spatially and temporally. As mineralogy influences the physical properties of rocks, such as density and magnetic susceptibility, we can use the reactive transport simulations to calculate the physical property changes due to chemical alteration. These changes can be forward-modelled for their various geophysical responses, allowing targets to be generated directly from numerical simulation of chemical alteration. A comparison between a simple gold-forming model and known mineralisation and architecture at the Victory-Defiance complex at the St Ives Gold Mine indicates that these targets are robust.

### 3.6.1 Introduction

#### 3.6.1.1 Background to reactive transport modelling

Within the ***pmd*CRC***, reactive transport modelling capabilities have been developed. These methods have been previously described in detail (such as Cleverley et al., 2006) but a summary is included below.

A reactive transport model is a numerical simulation where both fluid-flow and chemical reactions are simulated. An initial model is created, which specifies the mineralogy in different regions of the model, as well as a temperature and pressure regime. Porosity and permeability across the model are also specified. The first step of the reactive transport modelling process is to chemically equilibrate the initial mineralogy according to thermodynamic principles. Once this initial equilibration has taken place, fluid within the model can be transported. A series of transport steps are undertaken, where fluid is moved around the model according to the inbuilt fluid modelling code. After completing the transport stage, another chemical equilibration step is undertaken, completing the first timestep of the model. The reactive transport model then continues to perform additional timesteps, first transporting fluid and then calculating chemical reactions between the transported fluid, its contained species and and solids within the model. The reactive transport model is halted after a set period of geological time has been simulated, generally in the order of 1 to 10 My.

A simple reactive transport model has been created to simulate gold forming along a fault, with fluids driven from a cooling granite (Figures 3.6.1 and 3.6.2, after Cleverley et al., 2006). We will use this model to illustrate how reactive transport models can be used for targeting.

#### 3.6.1.2 Geophysical modelling of reactive transport models

The mineralogy of any crystalline rock predominantly controls the physical properties, such as density, magnetic susceptibility and seismic velocity, of the rock (Guéguen and Palciauskas, 1994). For example, rocks containing denser constituent minerals will, overall, be denser than another rock which contains less dense minerals; equally well, a rock composed of seismically slow minerals will be slower than one containing seismically fast minerals. A number of authors in the literature have examined methods to calculate physical properties from mineralogy (e.g., Mooney and Bleifuss, 1953; Carmichael, 1989; Wang, 2001; Ji et al., 2002; Mavko et al., 2003; King, 2005), but these methods are all some form of weighted averaging of the properties of the end-member components. The simplest methods are those relating to simple linear weighted averaging, with the weights determined by the volume or mass proportions of constituent minerals. As an example, seismic velocity can be calculated as either a weighted average of velocity, a weighted average of slowness (1/velocity), or some averaging of the minerals' elastic moduli.

For the purposes of this study, we use volumetric proportion weighted linear averaging to calculate physical

property models for a reactive transport model. By using this method, it is simple and easy to calculate the physical properties for every node of every timestep of a reactive transport model and produce a physical property model based on the reactive transport model. For some of the alteration minerals calculated using a reactive transport model, we only know properties such as seismic velocity rather than elastic moduli, and hence the use of linear averaging is the most applicable method to calculating the physical properties. We also do not consider porosity or permeability in the calculations of the physical properties, as the spatial distribution of these has changed significantly since the cessation of mineralisation in the Archaean and thus the final reactive transport model's porosity and permeability distribution does not represent the modern-day distribution.

Although these physical property models could be used to forward-model the geophysical response of a reactive transport model, they do not account for changes that have occurred post-mineralisation. For the Yilgarn Craton, the majority of the changes have been the erosion of Archaean rocks and the deposition of regolith. To simulate erosion, we can remove the top of a model; to simulate the deposition of regolith we can add a blanket of low-density, low to moderate magnetic susceptibility and slow seismic velocity material. After simulating these processes of erosion and regolith deposition, the gravity signature

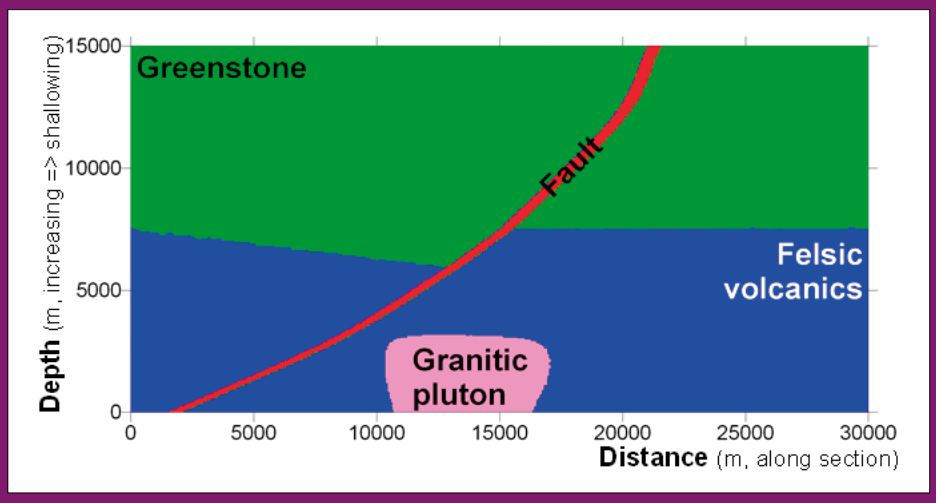


*Figure 3.6.1: Simplified geology of the listric fault model or LFM (Cleverley et al., 2006, detailed mineralogy Appendix 3 of Chopping, 2007). Through a reactive transport modelling process, a gold deposit is simulated to form along the fault, at the interface between the greenstone and felsic volcanic packages (Figure 3.6.2).*

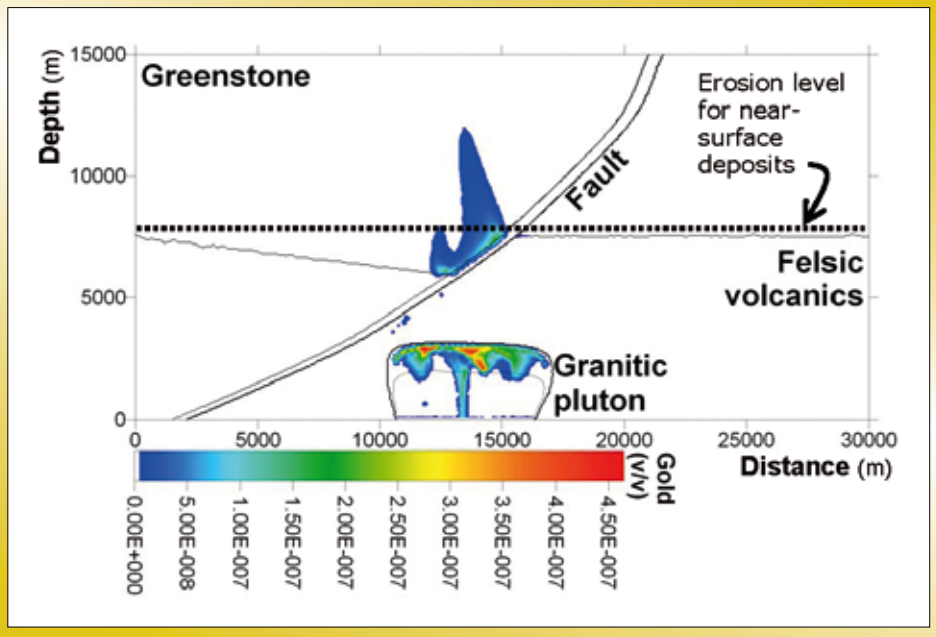


*Figure 3.6.2: Gold distribution (as volumetric proportion) within the LFM after ~1.2Ma of reactive fluid flow. For the top of the zone of high gold concentration (> 0.1ppm, by volume) to be close to (or at) the surface, the model would need to be eroded to the dashed line, removing approximately 7.5km of material from the top of the model, similar to modern-day estimates of the erosion level in the Yilgarn craton.*

of both an unaltered (initial) and altered (final) reactive transport model timestep can be computed (Figure 3.6.3).

The method of forward-modelling the gravity models produced from the reactive transport models is beyond the scope of this document, although it is discussed in Chopping (2007). For reference, the models are converted to 2D sections with regular cells 50 x 50 m in size, interpolated from the finite-element mesh of the reactive transport models using the natural neighbour interpolation method (Watson, 1999). These cells are then converted to voxels of 50 x 50 x 300000 m, creating an infinite strike 2.5D model. The forward-modelling is performed using the University of British Columbia's Geophysical Inversion Facility Grav3D and Mag3D codes (Li and Oldenburg, 1996, 1998). The magnetic parameters utilised for modelling (intensity, inclination and declination of the field) were derived from the Australian Geomagnetic Field, calculated at Kalgoorlie, 1 July 2007. Full results are discussed in Chopping (2007), but for reference below are the key results important for understanding the detectability of an ore system as well as those results required for a comparison with geophysics over a known deposit.

## 3.6.2 Results

### 3.6.2.1 Geophysical signatures

The gravity signature of alteration is simple: there is a decrease in density directly associated with the ore deposit, due to low-density inflow and outflow material (Figure 3.6.3). Outflow from the gold deposit has altered the greenstones to lower-density material such as quartz and carbonates, reducing the gravity response. Either side of the deposit there are gravity response increases, with a more substantial increase on the side of the model which has the thicker package of greenstones. Alteration increases the density of laterally distal greenstone rocks more substantially than it increases the density of laterally distal felsic volcanic rocks.

### 3.6.2.2 Differing station spacings

Gravity station spacing has an effect on the signature of alteration as we can only resolve features in the subsurface which are roughly the same width or wider than the station spacings. For 4 km gravity (regional gravity stations), we can see that we can derive the gross response of the

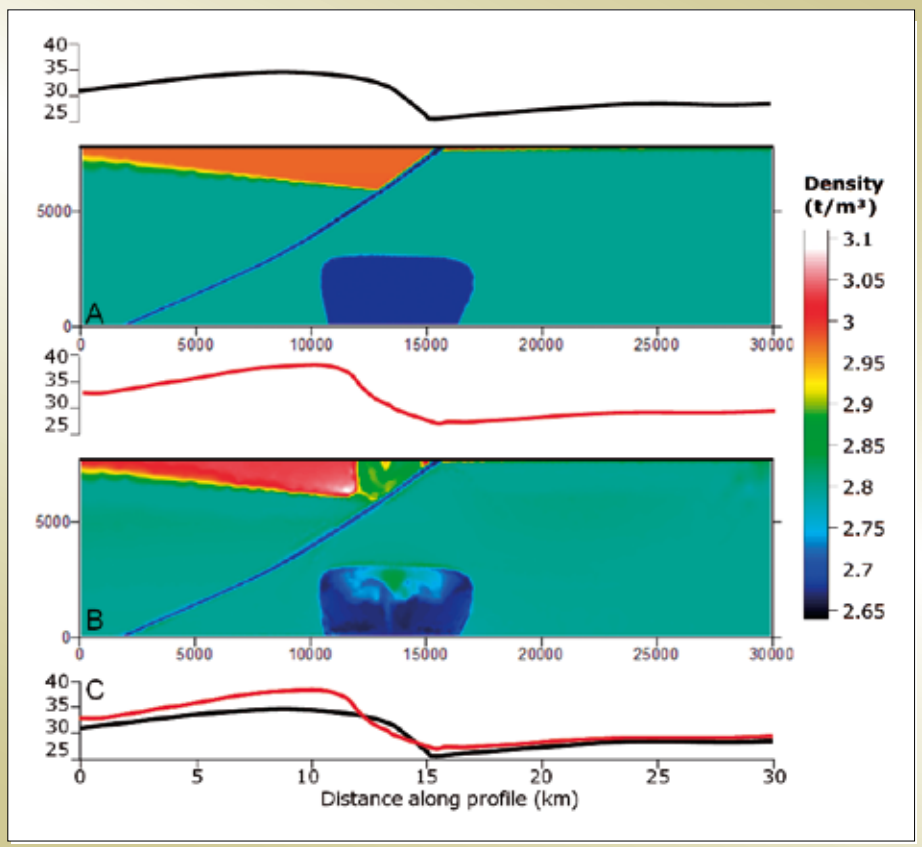


*Figure 3.6.3: Gravity signature of (A) unaltered and (B) altered listric fault model, with 7.5 km of material eroded from the model and 100 m of regolith (density = 2.0 $tm^{-3}$) deposited on the top of the model. Model densities range from 2.64 $tm^{-3}$ (dark blue) through to 3.12 $tm^{-3}$ (white). (C) Superimposed two gravity profiles, with the black profile the profile over the LFM prior to chemical alteration, and red the profile over the LFM after chemical alteration. Models are eroded as shown in Figure 3.6.2.*

architecture, but the subtle decrease above the deposit that is due to alteration is unresolved. For 1 km gravity, this decrease is substantially resolved. Furthermore, this decrease is in the order of 7% of the unaltered gravity response, indicating that reasonable precision is required in the gravity measurements. Gravity stations closer than 1 km (not shown) will provide more resolution on very subtle features, such as a reduction in gravity response due to the low-density material within the fault.

### 3.6.3 The Victory-Defiance region, St Ives Gold Mine

The Victory-Defiance region of the St Ives Gold Mine is an area of substantial gold endowment – in the order of 2.3 MOz gold (Prendergast, 2007). The region is underlain by a granite dome (Henson et al., 2005), which is clearly imaged in the mine-scale Victory seismic line (Stolz et al., 2004; also Figure 3.6.5). The solid geology of the St Ives camp is also well known; combining the Victory seismic line with the solid geology allows for a robust interpretation of the geology which underlies the Victory-Defiance Region (Figures 3.6.6 and 3.6.7).

Validation of the geological architecture was conducted using the regional gravity data as a constraint and modelling was performed in MODELVISION, using the densities of unaltered Yilgarn rocks as reported by House et al. (1999). When this was performed, there was a misfit between the seismic interpretation, forward modelling using these unaltered Yilgarn rock densities, and the observed gravity data, which must be due to one or more subsurface physical properties which are different from the properties used for modelling. This could be due to some or all of the following: a misidentification of lithology in the seismic architecture, the physical properties for each lithology were incorrect, and/or that chemical alteration has changed the physical properties.

One possible solution is to revise the architecture to provide a better fit to the available gravity data

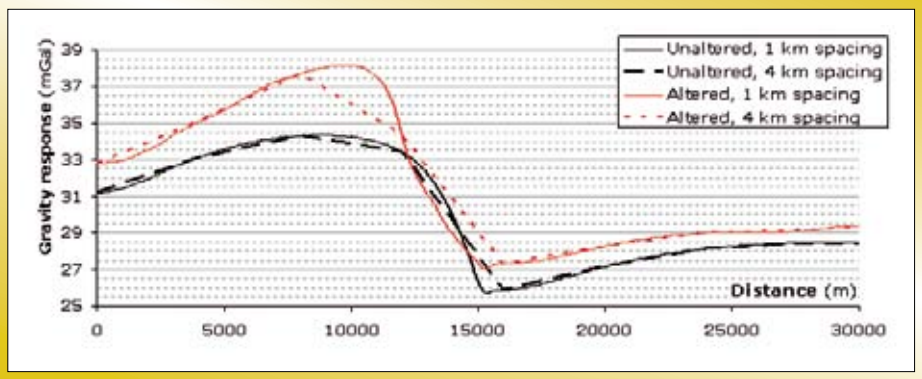


*Figure 3.6.4: Gravity profile over the listric fault model (both before and after chemical alteration has occurred) as per Figure 3.6.3 with the effects of different station spacings shown. Black indicates the unaltered gravity profiles and red indicates the altered gravity profiles. Solid lines are 1 km station spacings, dashed lines are 4 km station spacings.*

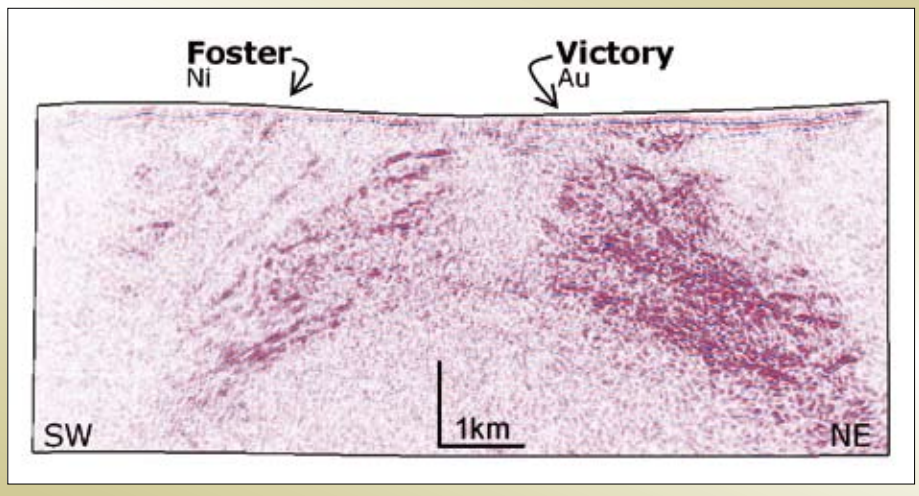


*Figure 3.6.5: The Victory mine-scale seismic line. The granite dome beneath Victory is well imaged as the zone of bland reflectivity. The position of the Victory mine is denoted by Au, and the position of the Foster nickel mine is denoted by Ni.*

(Figure 3.6.8). Note that this represents only one possible interpretation of the subsurface architecture and property distribution, as potential field data are inherently non-unique (Telford et al., 1990), with an infinite number of models able to reproduce any observed data.

If we examine the changes to the architecture that allow a better fit of the calculated to the observed gravity data (Figure 3.6.8), they have the following form (Figure 3.6.9):

- A decrease in density beneath the Victory gold mine
- An increase in density either side of the Victory gold mine
- A decrease in density beneath the Foster nickel mine
- An increase in density to the side of the Foster nickel mine

As stated above, the misfit for the seismic architecture may be due to misidentification of lithologies. Alternatively, the properties used may have been invalid, although,

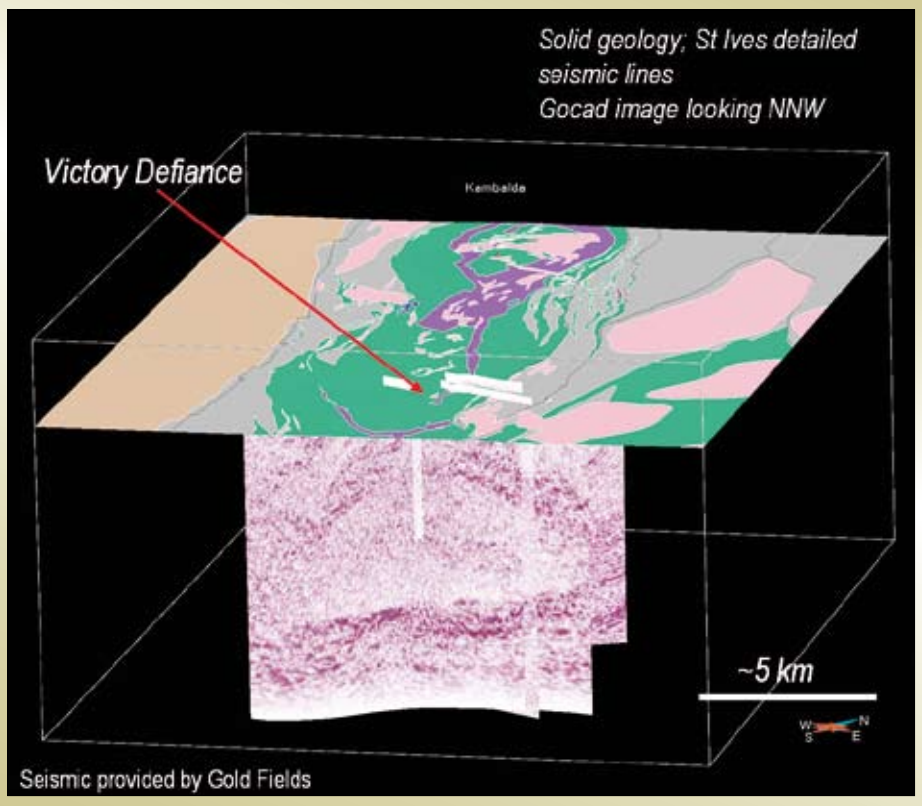


*Figure 3.6.6: 3D image showing the relationship between the surface solid geology, 3D architecture which was interpreted predominantly from the Victory seismic line. Note the very bland zone of reflectivity which is interpreted to represent the granite body which lies at depth in the centre of the Kambalda dome.*

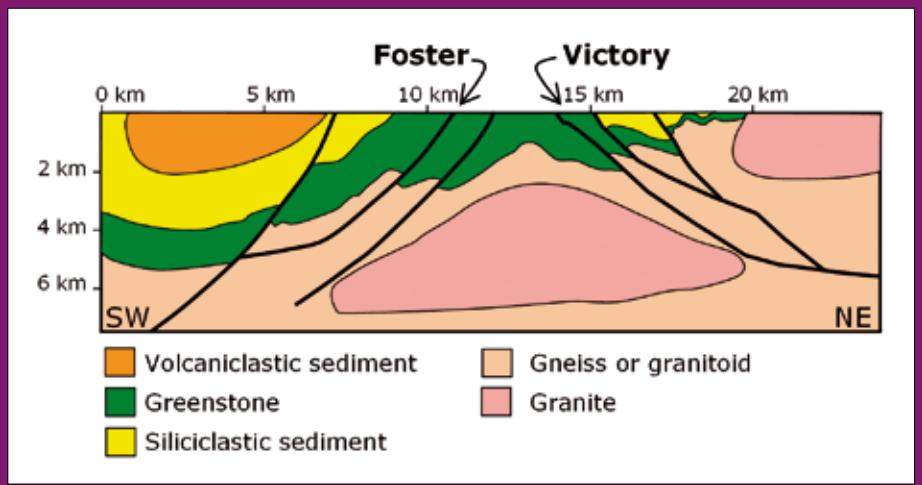


*Figure 3.6.7: Interpreted geology for the Victory seismic line and surrounding region, derived from the Victory seismic line, regional solid geology and mine-scale drilling. Dome shaped body is the bland zone shown in Figures 3.6.5 and 3.6.6.*

if this were the case then all of the units would have required their properties to be changed, which was clearly not required. An alternative hypothesis is that the misfit represents the alteration that culminates in the deposition of the 2.3 MOz Victory-Defiance orebodies. The changes in subsurface physical properties around the Victory mine are very similar to those indicated by the geophysical modelling of the listric fault model (see above). Thus, the observed gravity response for Victory-Defiance may well be the result of alteration; the misfit can be entirely attributed to this alteration rather than an incorrect interpretation of the seismic data. There is also a density decrease underneath the Foster nickel mine, which would not have formed by the exact processes simulated by the listric fault model. Generally, serpentinisation is associated with nickel deposits, and serpentinisation of a rock will decrease the density of the rock (Toft et al., 1990).

As we have independent controls on the architecture, in the form of an excellent mine-scale seismic line, modifying the architecture to match the forward-modelled gravity data simply serves to hide the signature of alteration. An implication for exploration is that the effects of alteration are significant enough to be detectable in even semi-regional (1–2 km station spacing) gravity surveys, and the use of multiple datasets (such as seismic and gravity here) are the best ways to detect alteration footprints using geophysical techniques (Figure 3.6.9). Indeed, the seismic data and gravity are sufficient to contain the signatures required to target a 2.3 MOz orebody, and this target may be evident even if it was buried by several hundred metres of cover. Note that this study has not been performed using the highest-resolution gravity data that has been acquired at St Ives; using higher resolution gravity data may allow for the development of further targets at depth using this methodology.

### 3.6.4 Implications for exploration

- Reactive transport modelling has been developed within the ***pmd*CRC*** and is capable of simulating key ore forming processes such as chemical reactions and fluid flow. These models can be used to simulate geophysical responses, allowing direct targeting from chemical models.
- Geophysical targets for a simple gold deposit have been developed. These targets indicate that directly above a buried gold deposit, there is a decrease in gravity response below that which is expected for an unaltered portion of the crust. Alteration also serves to increase the gravity response either side of a buried gold deposit. These targets correlate with observed gravity response in the Victory-Defiance region at the St Ives Gold Mine.
- Gravity station spacings can have a huge influence on the ability to interpret alteration – for mine scale alteration to be interpreted in gravity data, gravity needs to be acquired at 1 km station spacings or better.

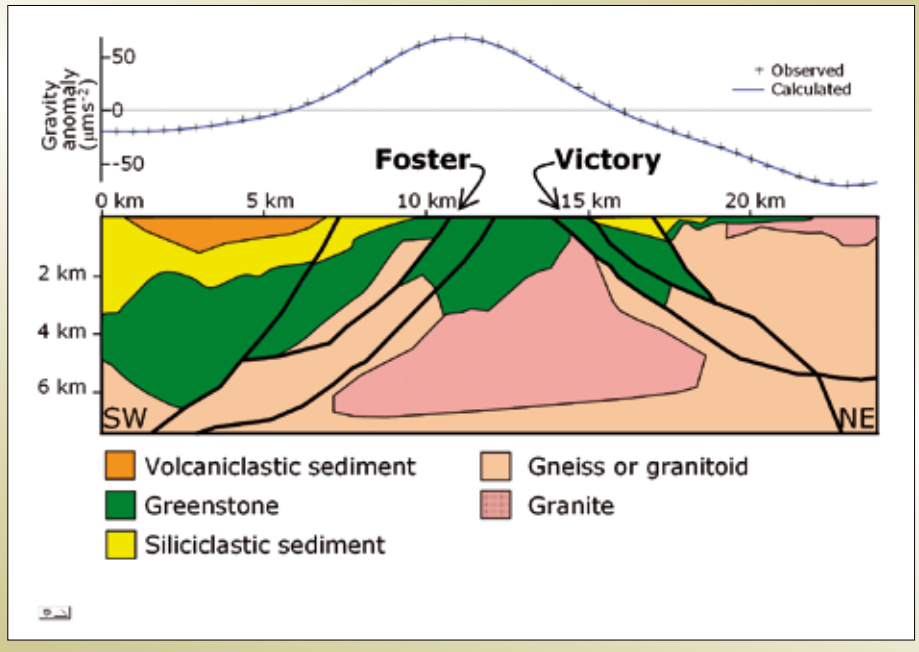


*Figure 3.6.8: MODELVISION forward-model of the interpretation of the seismic data and solid geology, with the architecture modified from the original seismic interpretation to better fit the available gravity data.*

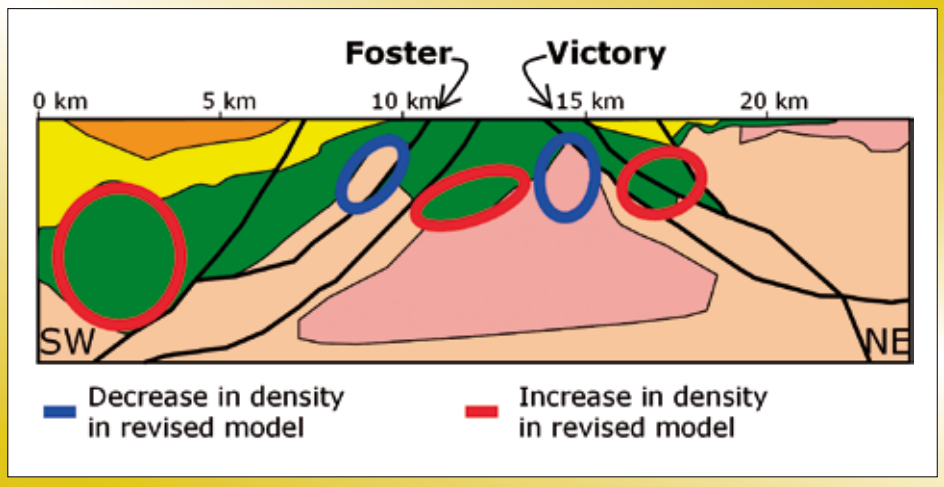


*Figure 3.6.9: The differences in density between the original seismic interpretation and the model adjusted for reduced misfit between the predicted and observed gravity response. A blue oval indicates a region that has a decrease in density in the revised architecture, and a red oval indicates a region that has an increase in density in the revised architecture. Background architecture is the model after revision by gravity modelling.*

- In regions with excellent control on architecture (from studies such as mine-scale seismic-data), mismatches between the calculated response of an architecture derived from seismic data and observed gravity data may indicate alteration rather than errors in the interpretation of the seismic data.
- Areas such as St Ives, Sunrise Dam and possible the nickel deposits of Leinster have data density suitable for exploration using these techniques.

## 3.6.5 References

Carmichael, R. S. (1989). *Practical Handbook of Physical Properties of Rocks and Minerals*. CRC Press, 741 p.

Cleverley, J. S., Hornby, P. & Poulet, T. (2006). ***pmd****RT: Combined fluid, heat and chemical modelling and its application to Yilgarn geology. In Barnicoat, A. C. & Korsch, R. J. (Eds.) *Predictive Mineral Discovery Cooperative Research Centre – Extended Abstracts from the April 2006 Conference*. Geoscience Australia, Record 2006/07.

Chopping, R. (2007). Predictive Geophysics: turning geochemical models into geophysical targets. ***pmd****CRC* Project Report: Project A3, ***pmd****CRC* Melbourne, 63p.

Guéguen, Y. & Palciauskas, V. (1994). *Introduction to the Physics of Rocks*. Princeton University Press, 294 p.

Henson, P. A., Blewett, R. S., Champion, D. C., Goleby, B.R., Cassidy, K. F., Drummond, B. J., Korsch, R. J., Brennan, T. and Nicoll, M. (2005). Domes: the characteristic 3D architecture of the world-class lode-Au deposits of the Eastern Yilgarn. In Hancock, H. (ed) *STOMP 2005: Structure, tectonics and ore mineralisation processes, Abstract Volume*. Economic Geology Research Unit, James Cook University.

House, M., Dentith, M. C., Trench, A., Groves, D. I. & Miller, D. (1999). Structure of the highly mineralised late-Archean granitoid-greenstone terrain and the underlying crust in the Kambalda-Widgiemooltha area, Western Australia, from the integration of geophysical datasets. *Exploration Geophysics*, 30, pp. 50–67.

Ji, S., Wang, Q. & Xia, B. (2002). *Handbook of Seismic Properties of Minerals, Rocks and Ores*. École Polytechnique de Montréal, 630 p.

King, M. S. (2005). Rock-physics developments in seismic exploration: A personal 50-year perspective. *Geophysics*, 70(6), pp. 3ND-8ND.

Li, Y. & Oldenburg, D. W. (1996). 3D inversion of magnetic data. *Geophysics*, 61(2), pp. 394–408.

Li, Y. & Oldenburg, D. W. (1998). 3D inversion of gravity data. *Geophysics*, 63(1), pp. 109–119.

Mavko, G., Mukerji, T. & Dvorkin, J. (2003). *The Rock Physics Handbook: Tools for Seismic Analysis in Porous Media*. Cambridge University Press, 339 p.

Mooney, H. M. & Bleifuss, R. (1953). Magnetic susceptibility measurements in Minnesota part II: Analysis of field results. *Geophysics*, 18(2), pp. 383–393.

Prendergast, K. (2007). Application of lithogeochemistry to exploration in the St Ives goldfield, Western Australia. *Geochemistry: Exploration, Environment, Analysis*, 7(2), pp. 99–108.

Stolz, N., Urosevic, M. & Connors, K. (2004). Reflection seismic surveys at St Ives Gold Mine, WA. *17th Geophysical Conference and Exhibition*. Sydney, Australia, Australian Society of Exploration Geophysicists.

Telford, W.M., Geldart, L.P. & Sheriff, R.E. (1990). *Applied Geophysics (Second Edition)*. Cambridge University Press, Cambridge. 790 p.

Toft, P. B., Arkani-Hamed, J. & Haggerty, S. E. (1990). The effects of serpentinization on density and magnetic susceptibility: a petrophysical model. *Physics of the Earth and Planetary Interiors*, 65(1–2), pp. 137–157.

Wang, Z. (2001). Fundamentals of seismic rock physics. *Geophysics*, 66(2), pp. 398–412.

Watson, D. (1999). The natural neighbour series manual and source codes. *Computers & Geosciences*, 25(4), pp. 463–466.

## 3.7 Archaean gold mineralisation in the Eastern Yilgarn: Insights from numerical models

**H. A. Sheldon, Y. Zhang and A. Ord**
CSIRO Exploration & Mining, Australian Resources Research Centre (ARRC), 26 Dick Perry Drive, Kensington, WA, 6151, Australia

### 3.7.1 Introduction

Computer simulations of geological processes provide insight into the factors that control the formation of ore deposits. Simulations can be used to test hypotheses derived from field observations; to explore the effects of changing rock properties (such as permeability or mechanical strength) and/or boundary conditions (e.g., orientation of the far-field principal stresses); and to understand interactions between geological processes (e.g., metamorphic fluid production and deformation). A suite of simulations was carried out to explore various aspects of the processes involved in Archaean gold mineralisation in the Eastern Yilgarn. Full details can be found in Section IV, deliverable 11. This paper provides an overview of the key outcomes structured around the "5 Questions".

### 3.7.2 Insights from numerical models

#### 3.7.2.1 Geodynamics

It has long been recognised that the Eastern Goldfields has been subject to a long, multistage deformation history, involving switches between contractional, extensional and strike-slip tectonics (e.g., Swager, 1989, 1997). Recent work based on structural analysis at numerous mine sites (Blewett and Czarnota, 2007a, b; Miller, 2005, 2006) and granite outcrops (Blewett et al., 2004) has led to the construction of a revised geodynamic history for the EGST, which emphasises the role of extensional events in shaping the crustal architecture (Blewett and Czarnota, 2007a). Studies of metamorphic mineral parageneses and inferred P-T-t paths (Goscombe et al., 2007) and the distribution of granite types in time and space (Champion et al., 2002) complement the structural analysis, providing further insight into the large-scale geodynamic events that were responsible for generating the observed crustal architecture and mineralisation.

An understanding of geodynamics is important for a number of reasons. Firstly, changes in the orientation and magnitude of the far-field principal stresses result in formation and reactivation of different structures at different times, depending on their orientation relative to the stress field. This in turn has implications for fluid flow in the crust, and hence for mineralisation. Secondly, geodynamics determines the timing of magmatic and metamorphic events relative to deformation. These events are important because they result in release of volatiles (which we describe as magmatic or metamorphic fluids). Magmatic and metamorphic fluids have the potential to transport gold, hence it is important to understand the timing of their release relative to mineralisation.

##### 3.7.2.1.1 Fault reactivation in varying regional stress regimes

Simulations of deformation and fluid flow in a model representing major faults in the Kalgoorlie region (Figure 3.7.1) showed that the Bardoc fault would be more active and accommodate greater fluid flow during E-W extension, while the Ida fault was more active during E-W shortening (Figure 3.7.2).

Another model was used to explore the effect of varying the shortening direction (corresponding to the maximum principal stress direction) on structures in the Laverton region. The model architecture (Figure 3.7.3) is a simplified representation of the geological architecture around Laverton, which has been interpreted as a "flower structure" in a bend of a large-scale fault system (Henson et al., 2006). This architecture was subject to horizontal shortening, with the shortening direction varying from WNW-ESE to ENE-WSW. The results (Figure 3.7.4) showed that shortening directions between NW-SE and NNW-SSE were favourable for reactivation of structures at locations corresponding to Wallaby and Sunrise Dam; orientations from NNE-SSW to ENE-WSW were unfavourable for reactivation at either location; and ENE-WSW shortening was favourable for reactivation at Sunrise Dam but not at Wallaby. These findings support an hypothesis derived from field observations, which suggests that the Wallaby fault system was more favourably oriented for mineralisation under a sinistral regime, whereas the Sunrise fault system was more favourably oriented during dextral shearing (Miller, 2006).

### 3.7.2.1.2 Local stress regimes around intrusions

Correlation of tectonic events across the Eastern Goldfields is made difficult by local stress variations associated with the complex 3D architecture, especially in the vicinity of intrusions. The radiating pattern of veins and dykes around intrusions at Wallaby (Miller, 2005) and Jupiter (Blewett and Czarnota, 2007b; Duuring et al., 2000) indicates that $\sigma_1$ was sub vertical at the time of intrusion, yet these dykes overprint and are overprinted by structures indicating a shortening (thrusting) regime characterised by sub-horizontal $\sigma_1$. This suggests that the stress regime switched from horizontal shortening ($\sigma_{h1} > \sigma_{h2} > \sigma_v$) to radial extension ($\sigma_{h1} = \sigma_{h2} < \sigma_v$) at the time of intrusion[5].

5 We assume that the far-field principal stresses are approximately horizontal (denoted by $\sigma_{h1}$ and $\sigma_{h2}$) and vertical (denoted by $\sigma_v$), with compressive stress positive.

However, it is not clear whether this switch was caused by emplacement of the intrusions (from which the veins and dykes emanate), or whether it reflects a larger-scale change in the tectonic regime at the time of emplacement. It is important to understand the effect of intrusions on principal stress orientations, because the principal stress axes determine the orientation of structures that may act as fluid pathways around the intrusion. For example, magmatic volatiles may be transported away from intrusions in tension (mode I) cracks, the orientation of which corresponds to the $\sigma_1$-$\sigma_2$ plane.

Intrusions affect the local stress regime in a number of ways. Firstly, intrusion of magma into the crust causes rotation of the principal stress axes around the intrusion as the surrounding rocks are deformed and displaced to

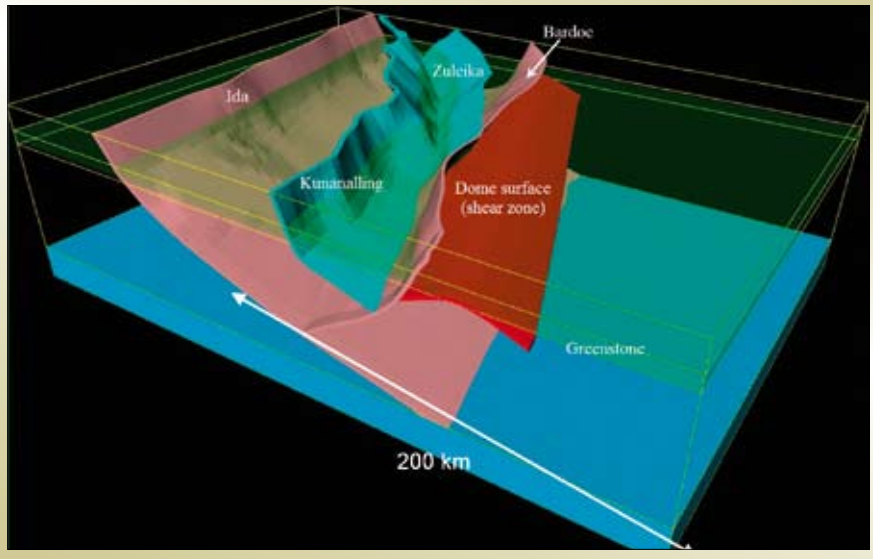


*Figure 3.7.1: Architecture of a numerical model representing major faults and a domed surface (shear zone) in the Kalgoorlie region. The model dimensions are 200km (E-W), 141km (N-S) and 55km (depth).*

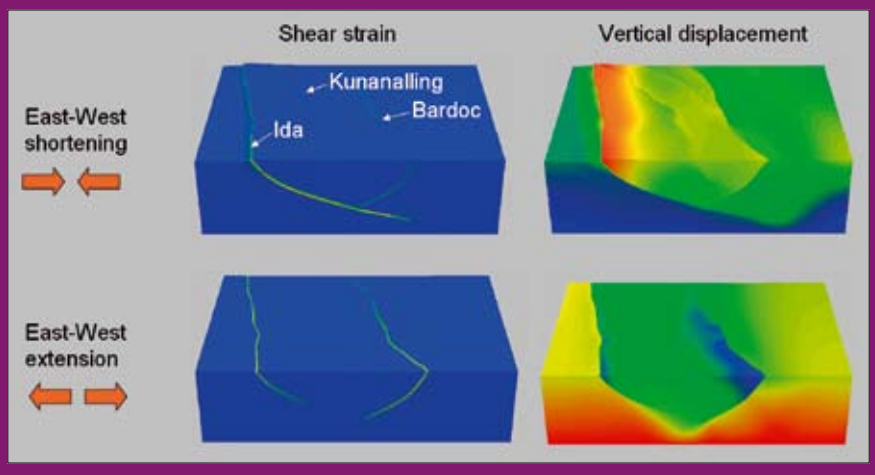


*Figure 3.7.2: Distribution of shear strain (left) and vertical displacement (right) due to E-W shortening (top) and E-W extension (bottom). The Bardoc fault is less active in the shortening regime.*

make space for the magma. Secondly, heat from the magma leads to thermal expansion in the surrounding rock and metamorphic fluid production, leading to an increase in fluid pressure which in turn results in deformation and changes in stress magnitudes and orientations. Thirdly, release of volatiles from the cooling magma (magmatic fluid production) increases fluid pressure in and around the intrusion.

Numerical models (Figures 3.7.5, 3.7.6 and 3.7.7) show that these processes can result in local rotation of the principal stresses around intrusions, however it appears that the resulting pattern of veins or dykes would not be radial unless the far-field (regional) deformation regime was already one of radial extension ($\sigma_{h1} = \sigma_{h2} < \sigma_v$; Figure 3.7.6a). A region of radial extension is developed immediate above an intrusion emplaced in a radial contraction regime ($\sigma_{h1} = \sigma_{h2} > \sigma_v$), but the resulting pattern of veins/dykes is predicted to be concentric rather than radial (Figure 3.7.6b). Furthermore, it was found that the stresses generated by magma emplacement

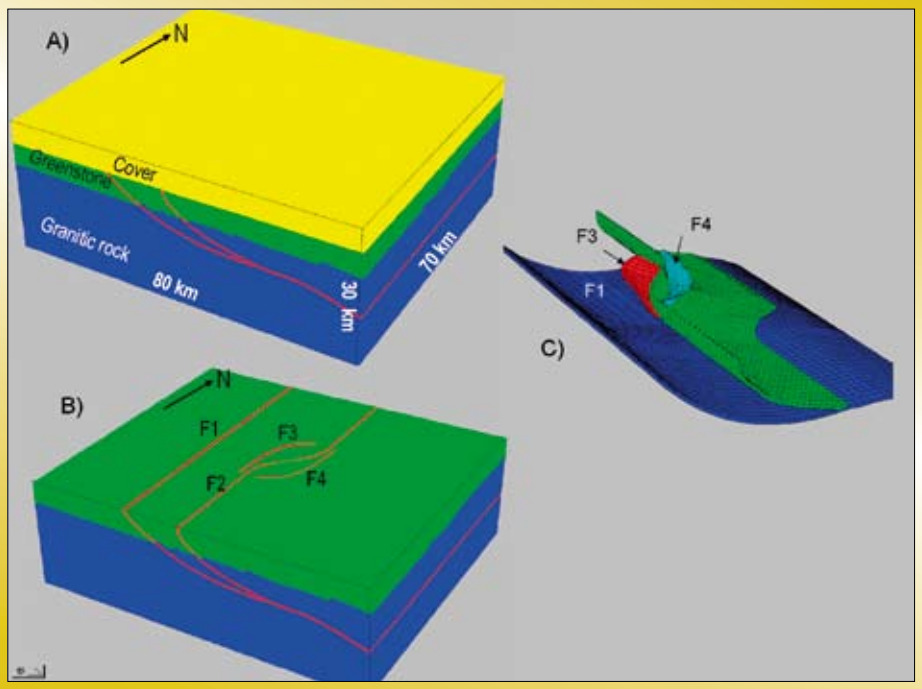


*Figure 3.7.3: Model architecture for the Laverton region.*
*A) Complete geometry showing faults (red) and lithological units.*
*B) Geometry without the cover unit.*
*C) Geometry of faults within the model. F1 represents the Celia fault, F2 the Childe-Harold fault, F3 the Wallaby fault and F4 the Sunrise shear zone.*

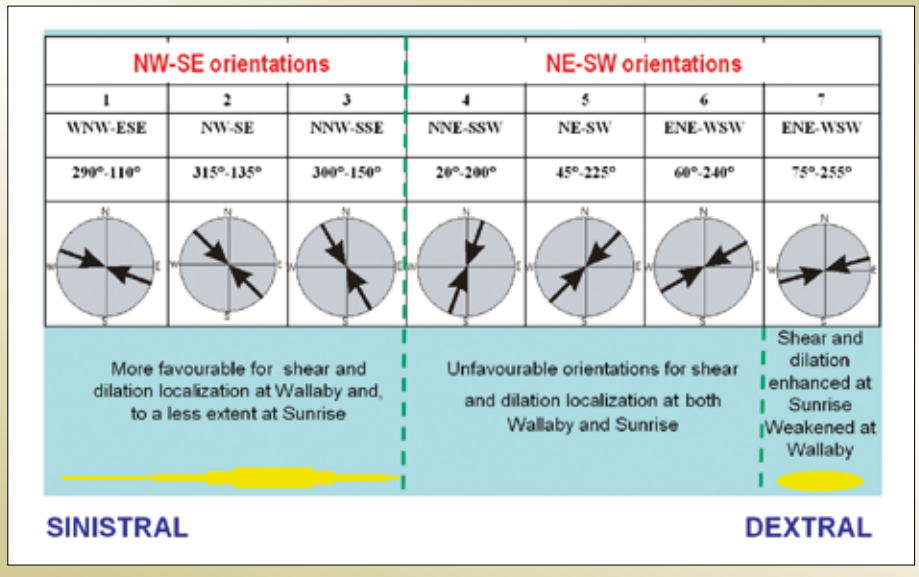


*Figure 3.7.4: Correlation between shortening directions and the potential for gold mineralisation (indicated by yellow bar thickness) based on shear strain and dilation anomalies on relevant faults.*

and associated processes were insufficient to overcome differential stresses associated with horizontal shortening ($\sigma_{h1} > \sigma_{h2} > \sigma_v$) or extension ($\sigma_{h1} < \sigma_{h2} < \sigma_v$). In such cases the orientation of veins/dykes reflects the regional stress regime, with only very minor and localised perturbations around the intrusion (Figures 3.7.6c and Figure 3.7.7).

These results suggest that the radial patterns of veins and dykes at Wallaby and Jupiter reflect a hiatus in regional shortening, with a switch from shortening to radial extension at the time of magma emplacement. It appears that the intrusion itself could not have caused this switch, although it may have been a consequence of it. The switch

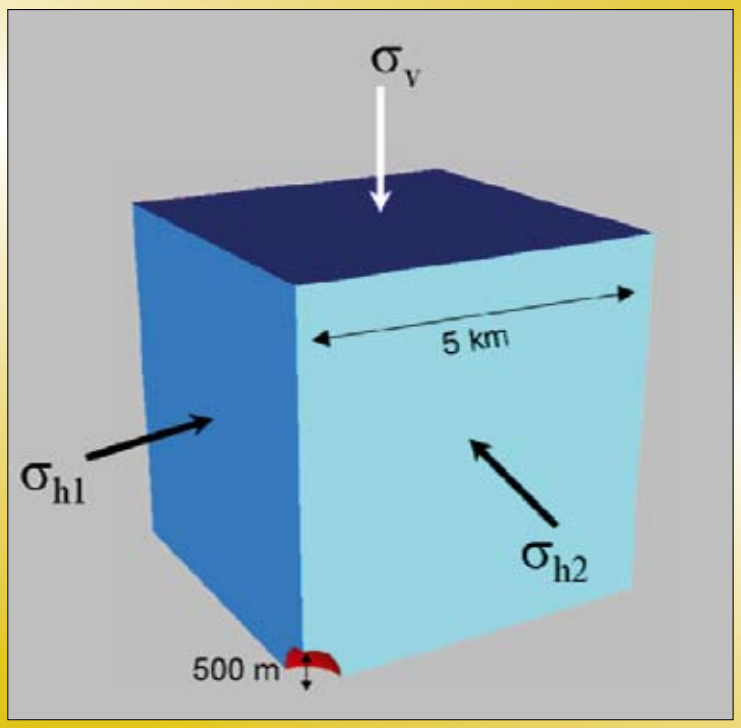


*Figure 3.7.5: Geometry of model representing a spherical intrusion. Intrusion is represented by one quarter of a sphere (red shaded area; radius 500 m) at the bottom left corner of a 5 x 5 x 5 km box. Boundaries of the box are subject to far-field stresses $\sigma_{h1}$, $\sigma_{h2}$ and $\sigma_v$. This model represents the physical effect of magma emplacement on the surrounding rocks.*

*Figure 3.7.6: Orientation of mode I cracks on a horizontal plane above a spherical intrusion subject to three deformation regimes: (A) radial extension ($\sigma_{h1} = \sigma_{h2} < \sigma_v$); (B) radial contraction ($\sigma_{h1} = \sigma_{h2} > \sigma_v$); (B) horizontal shortening ($\sigma_{h1} > \sigma_{h2} > \sigma_v$). The centre of the intrusion is located beneath the bottom left corner of these images (see Figure 3.7.5). Top row shows dip (red = 90°, blue = 0°) and strike (lines) of the $\sigma_1$-$\sigma_2$ plane. Arrows indicate relative magnitudes of the horizontal stresses acting on the model boundaries. Bottom row illustrates the expected pattern of veins/dykes corresponding to each stress regime (plan view).*

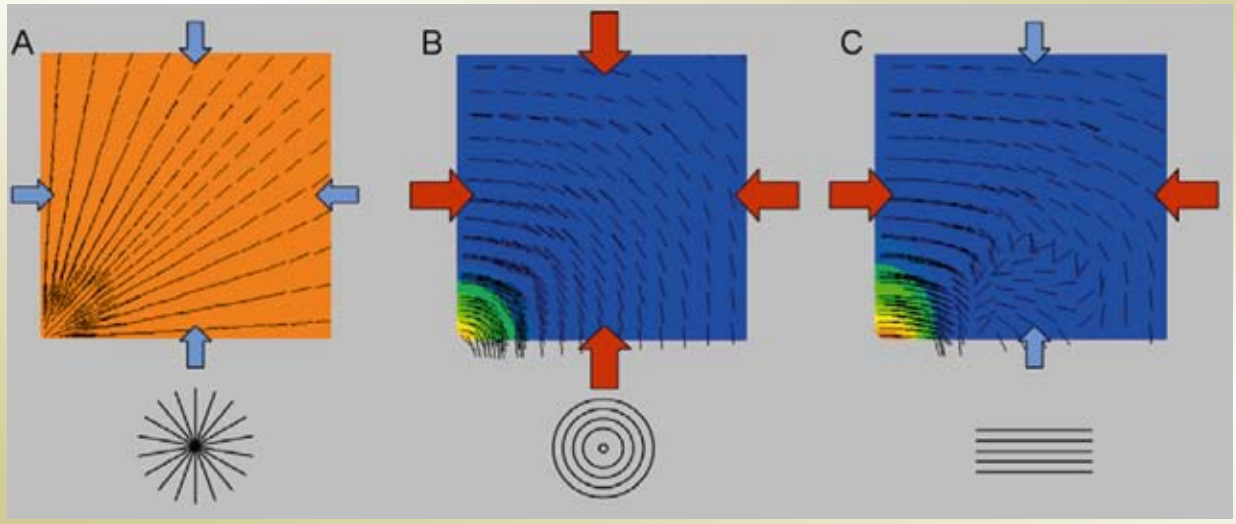

to radial extension must have occurred on a larger scale, possibly caused by formation of a magma chamber at greater depth in the crust, which acted as the source for the overlying intrusions and dykes. An interesting avenue for future research would be to use a more realistic representation of crustal rheology (c.f. the simple elastic-plastic rheology used in the models for this project) to explore the potential for generating local extensional regimes within a larger-scale horizontal shortening regime.

#### 3.7.2.1.3 Downward flow during extension

Blewett and Czarnota (2007a) emphasised the significance of extensional deformation in generating the crustal architecture of the Yilgarn, but extension also has important implications for fluid flow. In particular, extension tends to result in downward flow of shallow-sourced fluids, such as basinal brine, meteoric water and sea water. These fluids may meet with metamorphic or magmatic fluids moving up through the crust, hence extension creates opportunities for fluid mixing. This is illustrated in Figure 3.7.8a, which shows fluids from deep and shallow sources converging towards a shear zone that has developed during extensional deformation. Upward flow from the base of the model is driven by metamorphic fluid production due to a regional thermal event. A switch from horizontal extension to horizontal shortening remobilises the fluids upwards (Figure 3.7.8b).

#### 3.7.2.1.4 Timing and duration of magmatic and metamorphic events

Geodynamics determines the timing of magmatic and metamorphic events, and hence the timing of magmatic and metamorphic fluid production (Goscombe et al., 2007; Sheldon et al., 2007). Metamorphic fluid is viewed by some workers as the primary transporter of gold (e.g. Groves and Phillips, 1987; Jia and Kerrich, 1999; Witt et al., 1997), while others emphasise the role of magmatic and mantle-derived fluids in generating giant gold deposits (e.g. Walshe et al., 2008). Clearly it is important to understand the source and volume of these fluids, the timing of their release relative to the timing of mineralisation, and their migration pathways, in order to understand their role in mineralisation.

Figure 3.7.9 illustrates the timescale of metamorphic fluid production in a 15 km column of basalt (representing

*Figure 3.7.7: Principal stress orientation around intrusions. Model simulates the effects of magmatic fluid production and thermal expansion on stresses around intrusions. (A) Model geometry. Areas marked 1 and 2 represent intrusions within the granitic basement. Model size = 30 x 15 km. (B), (C) and (D) show orientation of the $\sigma_1$-$\sigma_2$ plane in scenarios representing a static regime (ends of model are fixed), an extensional regime (ends of model moving outwards) and a shortening regime (ends of model moving inwards). The $\sigma_1$-$\sigma_2$ plane is predominantly vertical in (C) and horizontal in (D), reflecting the regional stress field resulting from extension or contraction.*

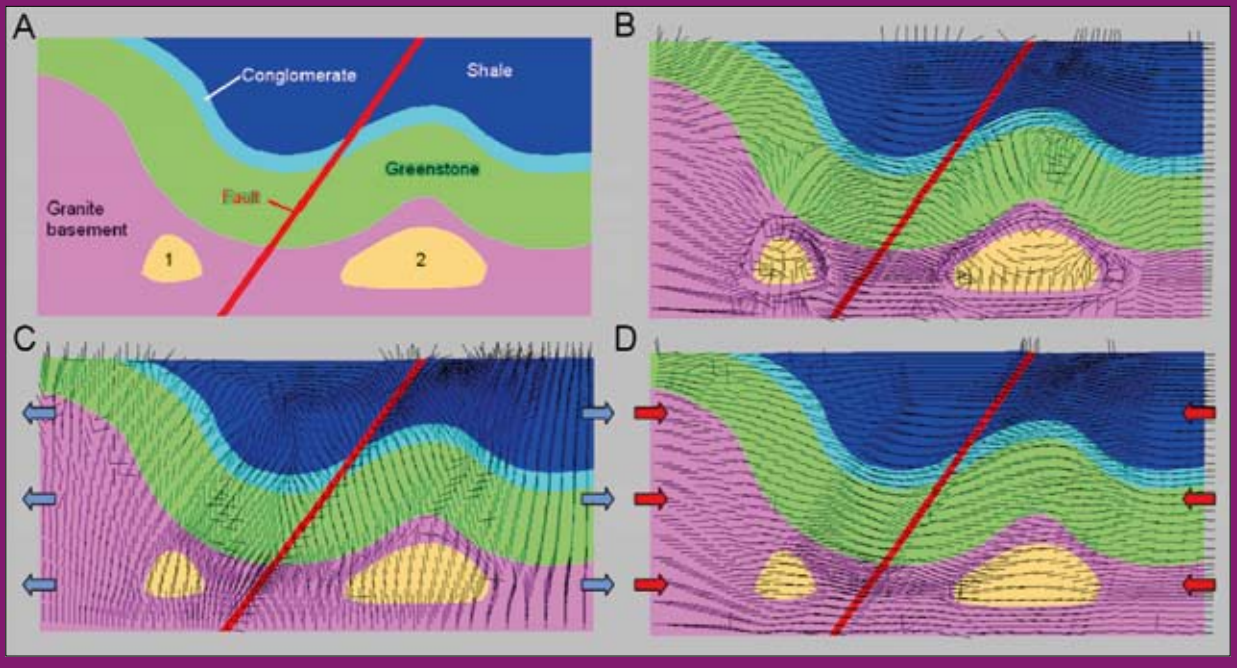

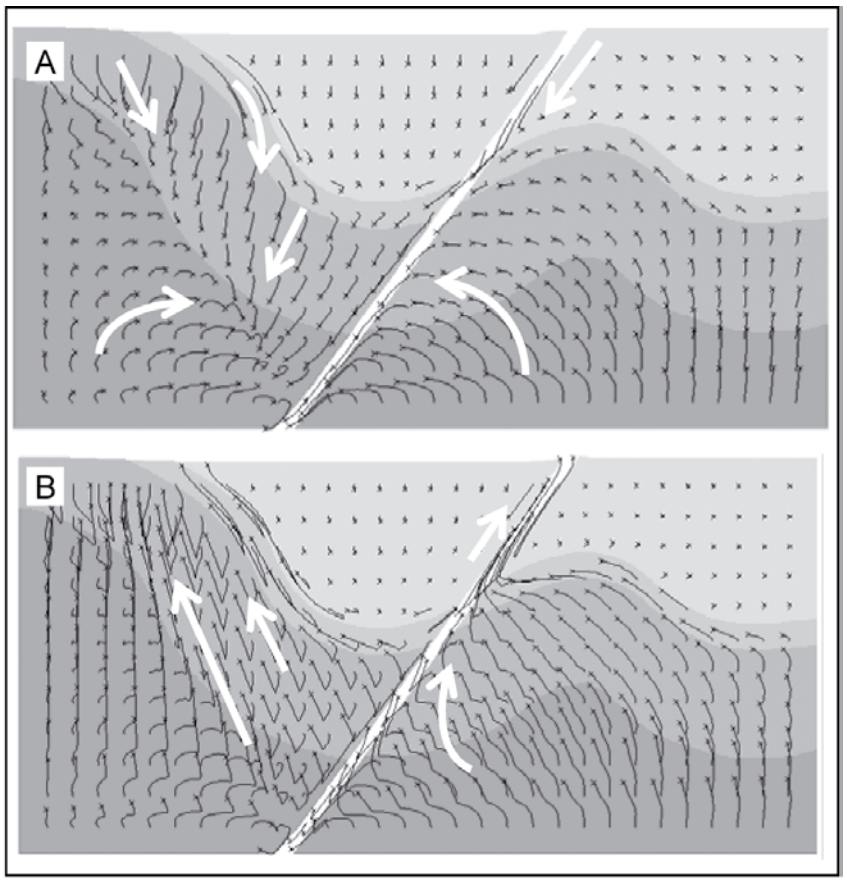


*Figure 3.7.8: Fluid particle tracks in a model with deformation and regional metamorphic fluid production driven by heating along the base of the model. Geometry (indicated by grey shading) as in Figure 3.7.7a, without the intrusions. White arrows emphasise fluid flow direction. (A) Extensional deformation draws fluids down from the top of the model. This fluid merges with metamorphic fluid moving up from the base. (B) Fluids are remobilised upwards when the deformation regime is switched from extension to shortening.*

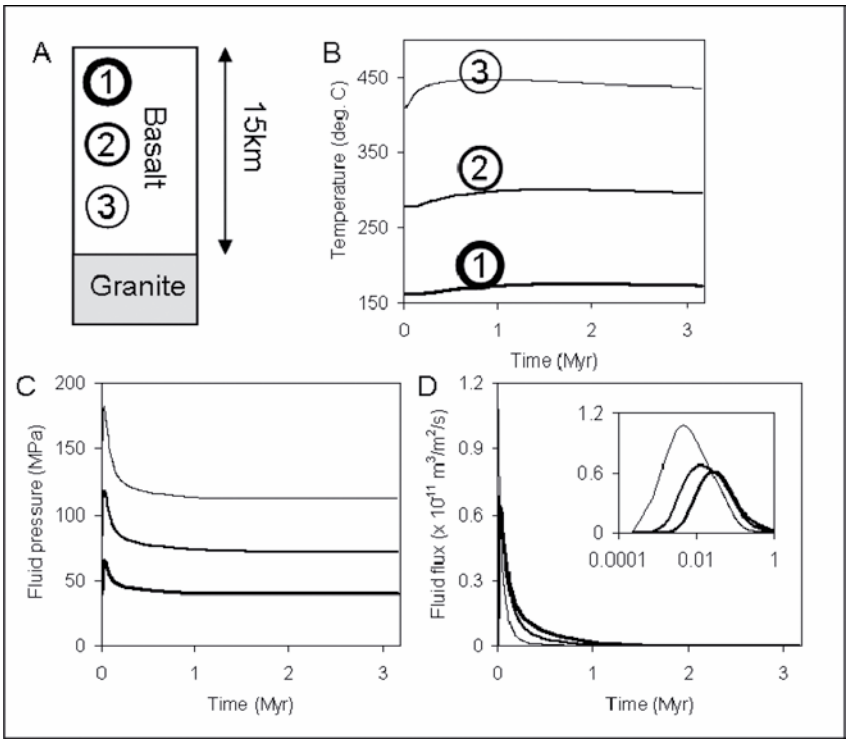


*Figure 3.7.9: Evolution of temperature, fluid pressure and fluid flux due to metamorphic fluid production in a column of basalt being heated by a layer of granitic magma. (A) Model geometry. Circles indicate history locations. (B) Histories of temperature, (C) fluid pressure and (D) fluid flux at 3 points indicated by circles in A. Inset in D shows fluid flux plotted against time on a logarithmic scale.*

greenstone) underlain by 5 km of hot granitic magma. This model could represent the effect of widespread emplacement of high-Ca granitic magma, which occurred across the Yilgarn between ~2605–2665 Ma. The evolution of fluid pressure (Figure 3.7.9c) and fluid flux (Figure 3.7.9d) indicates that fluid is produced and escapes from the crust within ~1 million years following emplacement of the granite. This places a tight constraint on the timing of mineralisation relative to metamorphism, if the metamorphic fluid is envisaged as the gold-bearing fluid. Thus, metamorphic fluids associated with high-Ca granite emplacement could have been involved in some of the older deposits (e.g. Golden Mile Fimiston lodes, Kanowna Belle, Jundee), but not the younger deposits such as Victory-Defiance, Chalice, and Mt Charlotte (see geodynamic history chart in Blewett and Czarnota (2007a) for deposit ages relative to granites). Metamorphic fluids may, however, be retained in the crust over a longer time period if they are produced during extensional deformation (see previous section and Figure 3.7.8a).

Magmatic fluid production occurs over similar timescales as metamorphic fluid production (assuming the latter is driven by heat from cooling magma), and is affected in the same way by extensional deformation. This is illustrated in Figure 3.7.10, which shows the pathways of fluid particles in the same models as were shown in Figure 3.7.7. Figure 3.7.10a shows what happens in the absence of regional extension. In this case, all of the fluid particle tracks have reached the top of the model within ~30000 years after emplacement of the intrusions, implying that all of the magmatic fluid that was produced up to this time has escaped from the system. The pattern is quite different in Figure 3.7.10b, which shows fluid pathways in an extensional regime. Most of the fluid is retained in the crust in this case, with a complex convective circulation pattern developing above one of the intrusions.

Thus, the timing of magmatic and metamorphic events relative to deformation is critical in determining the role that these fluids can play in mineralisation. Magmatic and metamorphic fluids escape from the crust within a few million years, but extensional deformation creates space which may allow these fluids to be retained in the crust.

### 3.7.2.2 Architecture

Domes have been identified as a key element of the crustal architecture in the Yilgarn (Blewett, 2004; Henson, 2004). The wavelength of these features decreases with decreasing depth in the crust, hence it has been suggested that domes may facilitate focusing of fluids into ever narrower sites as

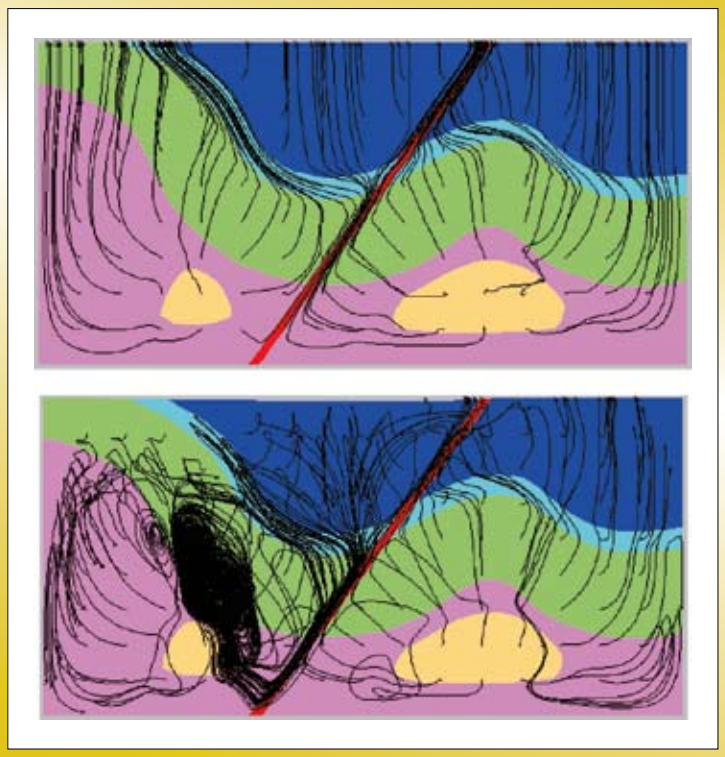

*Figure 3.7.10: (A) Pathways of initially uniformly spaced fluid particles in model without extensional deformation (corresponds to Figure 3.7.7b). (B) Pathways of initially uniformly spaced fluid particles in model with extensional deformation (corresponds to Figure 3.7.7c). Extension causes fluid to be retained in the system.*

they ascend through the crust. The nature of these domes and the mechanism of their formation is not entirely clear; one possibility is that the domes are analogous to metamorphic core complexes formed during crustal extension, with the margin of the dome representing a highly sheared detachment zone (Blewett and Czarnota, 2007a; SRK Consulting, 2000). Figure 3.7.11a shows how these extensional shear zones may act as locations of fluid focusing and mixing during extensional deformation. The geometry is analogous to the crustal architecture to the East of Leonora (Figure 3.7.11b), with the shear zone in the model corresponding to the zone of intense deformation on the margin of the Raeside Batholith. While the extensional event that created this shear zone was not necessarily the mineralising event, it was nonetheless important for setting up the architecture which provided a pathway for focused fluid flow during subsequent deformation events.

Smaller domes may simply represent granitic intrusions, in which case they would have acted as sources of magmatic fluid into the surrounding rocks. This is illustrated in Figure 3.7.1, which highlights a region of tensile failure above an elongate dome that is interpreted to exist to the East of Kalgoorlie (see Figure 3.7.1 for model geometry). Failure was driven by fluid production within the dome. The effects of magmatic fluid production are illustrated also in Figures 3.7.10 and 3.7.7.

Fluids may be focused towards the crest of a dome if the dome itself is defined by a layer of relatively high permeability, such as a shear zone. Figure 3.7.12 shows fluid pathways converging towards the crest of a dome which is capped by a low permeability shale unit, representing turbiditic sediments in a late basin.

### 3.7.2.3 Fluid sources and reservoirs

The source and nature of fluids involved in Archaean gold mineralisation has been widely debated in the literature. Some authors have argued for metamorphic fluids being the primary transporter of gold, pointing out that an economic concentration of gold could be achieved by focusing such fluids through permeable faults or shear zones (e.g. Groves and Phillips, 1987; Jia and Kerrich, 1999; Witt et al., 1997). The need for fluid focusing is reiterated by our numerical models, which show that the time-integrated fluid flux at 10 km depth due to a

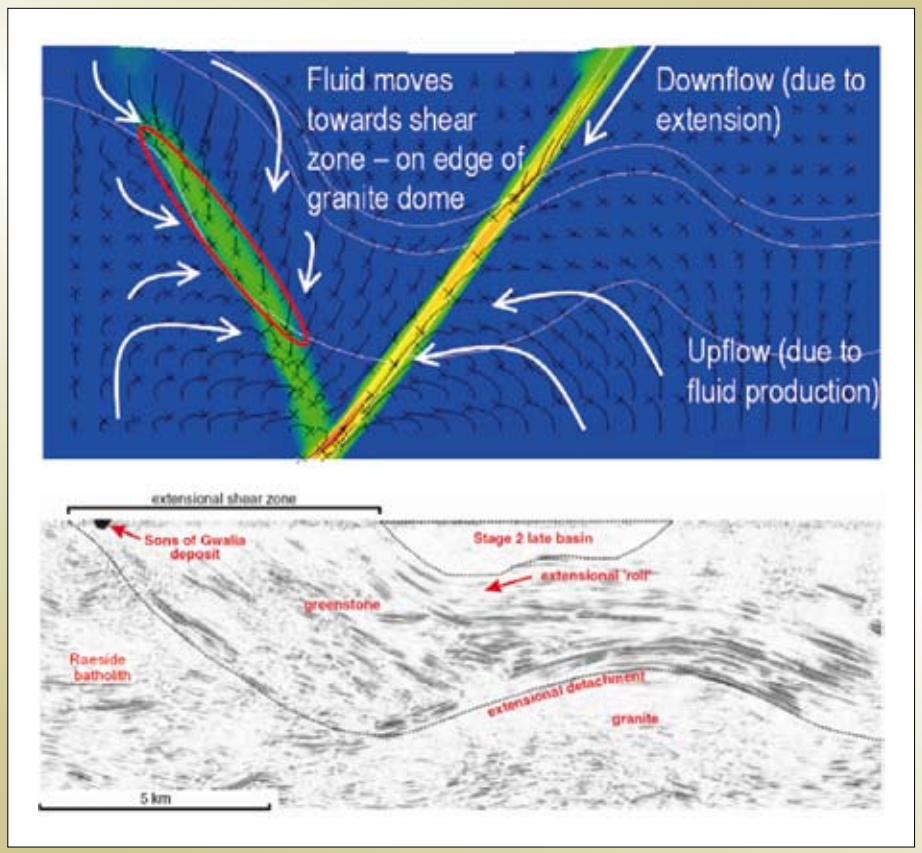


*Figure 3.7.11: (A) Extensional deformation generates a shear zone on the margin of a granite dome (Geometry as in Figure 3.7.7, without the intrusions). Fluid is focused into this shear zone from above and below. Image shows contours of shear strain and fluid particle tracks. Crosses indicate location of fluid particles. (B) Interpreted seismic section showing crustal architecture to the East of Leonora (after Blewett and Czarnota, 2007a). The geometry of the numerical model in (A) is similar to this architecture.*

regional metamorphic event is ~160 to 250 $m^3/m^2$; this is approximately 3 orders of magnitude less than the flux that is required to generate an economic gold deposit (at least 2 x 105 $m^3/m^2$; Cox, 1999). A model of metamorphic fluid production and focusing into a permeable fault zone indicates that sufficient enhancement of the flux could be achieved by focusing the fluid into a 50 m wide fault (Figure 3.7.13).

Magmatic volatiles are another type of fluid that may play an important role in gold mineralisation (e.g., Walshe et al, 2008). It is interesting to compare fluid volumes associated with magmatic and metamorphic fluid production. For example, consider the case of a 15 km column of basalt overlying a 5 km layer of mafic granitic magma containing 7 wt% water. Water released from the magma contributes ~1000 $m^3/m^2$ to the total fluid flux, while metamorphic fluids produced in the overlying basalt contribute only ~220 $m^3/m^2$ at 10 km depth (Figure 3.7.14). On the basis of volume alone this suggests that magmatic volatiles are more significant for mineralisation, without even considering their potential for carrying gold.

Shallow-source fluids such as basinal brines, meteoric water and sea water may play a role in mineralisation if they can penetrate to an appropriate depth in the crust. Figures 3.7.8 and 3.7.12 illustrate how this might be achieved during extensional deformation. The resulting fluid "reservoir" can be tapped during subsequent deformation events (e.g., Figure 3.7.8b).

### 3.7.2.4 Fluid pathways and drivers

Fluid flow is driven by gradients in hydraulic potential, which in turn are influenced by deformation, fluid production (magmatic/metamorphic), fluid density (which depends primarily on temperature) and topography. The direction of fluid flow, or the fluid pathway, is determined by the direction of the fluid pressure gradient (fluid tends to move towards lower pressure), but also by variations

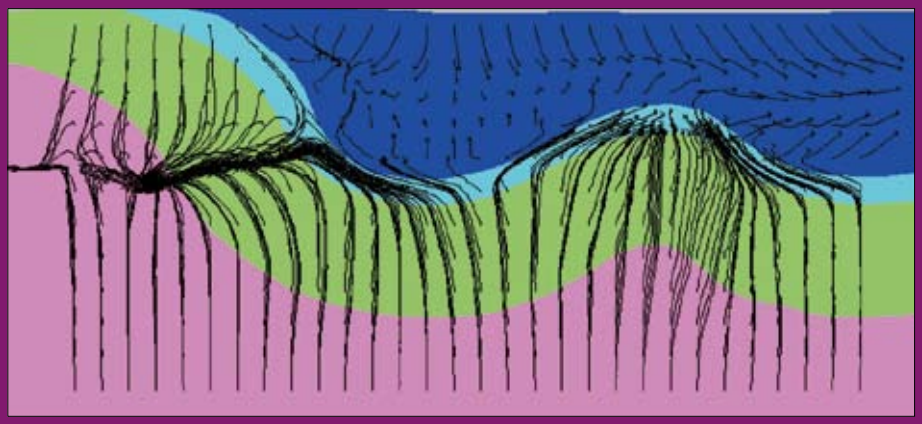

*Figure 3.7.12: Fluid particle tracks showing focusing of upward flow into a dome on the right-hand side of the model. Geometry as in Figure 3.7.7a, without the intrusions or fault. The dome is defined by a permeable conglomerate layer beneath a relatively impermeable shale layer. This model also provides a further illustration of downward flow driven by extension, particularly on the left side of the model.*

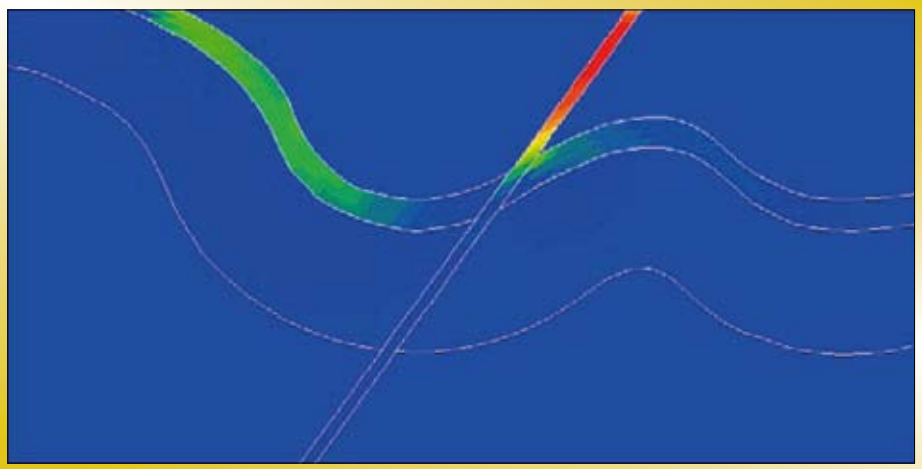

*Figure 3.7.13: Time-integrated fluid flux due to focusing of fluid produced during a regional metamorphic event. Geometry as in Figure 3.7.7a, without the intrusions. The maximum value ($1.7 \times 10^4$ $m^3/m^2$) is an order of magnitude too small to generate an economic deposit, but reducing the fault width from 500 m (as in the model) to 50 m would enhance the flux sufficiently to create a deposit in the fault.*

in permeability (fluid flow is focused through high permeability pathways, such as faults). Permeability varies with rock type, but also changes with deformation and can be enhanced by fluid production. Complex feedbacks between the factors that control fluid flow result in behaviour that cannot be predicted by considering these factors in isolation.

Convection[6] is often assumed to be the primary mode of fluid flow around intrusions. However, our numerical simulations and those of Hanson (1995) indicate that convection is overridden by thermal expansion and magmatic/metamorphic fluid production, at least in the early stages of cooling. These processes drive fluid away from intrusions. Fluid particle tracks from numerical models of cooling intrusions indicate that all of the initial pore fluid is displaced out of the system as a consequence of fluid production and thermal expansion (Figure 3.7.10a). This effect can be counteracted by extensional deformation (Figure 3.7.10b), which creates space that allows the additional fluid to be retained within the crust.

6 i.e., fluid flow driven by buoyancy, due to the variation in fluid density with temperature

Convection may occur at a later stage of cooling, once magmatic and metamorphic fluid production have waned. Convection is not necessarily restricted to the location immediately around the intrusion; a model representing intrusions located several km from a permeable fault shows that heat from the intrusions could stimulate convection cells within the plane of the fault (Figure 3.7.15; Blockeel, 2005). It has previously been suggested that such large-scale convection cells along major faults could explain the periodicity of ore deposits along such faults (Ord, *pers. comm.*). However, the size of these cells is likely to be influenced by permeability variations along the fault, and by variations in fluid properties. It seems more likely that the spacing of deposits is a function of permeability variations related to bends or jogs in these faults (Weinberg et al., 2004).

Another interesting aspect of metamorphic fluid production in the context of fluid pathways is the possibility of creating high permeability pathways emanating from intrusions (Figure 3.7.16). These pathways arise from a positive feedback between heating, fluid production, and permeability enhancement. Simple models indicate that these pathways emanate from the flanks of

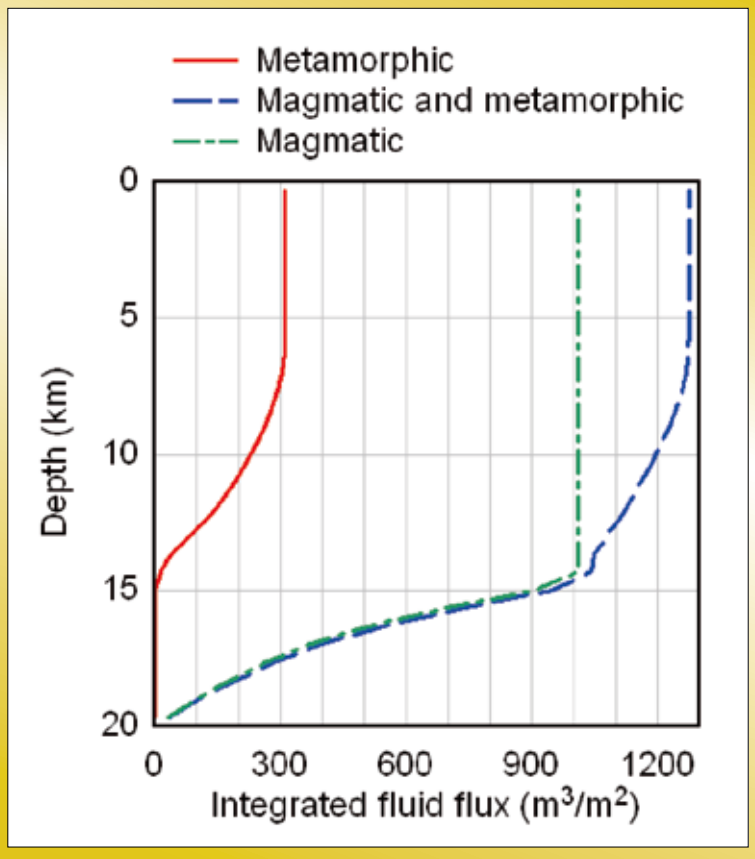


*Figure 3.7.14: Time-integrated fluid flux due to magmatic and metamorphic fluid production in a 1D column comprising 5 km of mafic granite magma overlain by 15 km of basalt (see Figure 3.7.9a). The magma releases 7 wt% water as it cools, and the basalt releases fluid as it is heated by the cooling magma. The volume of magmatic fluid is approximately 4 times greater than the volume of metamorphic fluid.*

intrusions rather than from the top; however this may depend on the size, shape and depth of the intrusion, and the prevailing stress regime. Further investigation is required to fully understand this phenomenon.

Major faults are commonly assumed to act as important fluid pathways, but the potential of a given fault to act as a fluid pathway will vary depending on its orientation relative to the far-field stress regime. This was illustrated by models representing faults in the Kalgoorlie and Laverton regions (see the section on Geodynamics; Figures 3.7.1, 3.7.3 and 3.7.4). The Laverton model illustrates how different parts of a fault system are reactivated (making them favourable for fluid flow) under varying far-field stress regimes. At a more detailed level, numerical models can be used to identify areas around jogs or bends that would be expected to have enhanced permeability following specified slip events on the fault (e.g., Micklethwaite and Cox, 2004, 2006; Sheldon and Micklethwaite, 2007). Such models emphasise the importance of minor structures as hosts for mineralisation. This may explain why structural "complexity" is an effective targeting criterion, as complexity reflects the occurrence of minor structures as well as major faults.

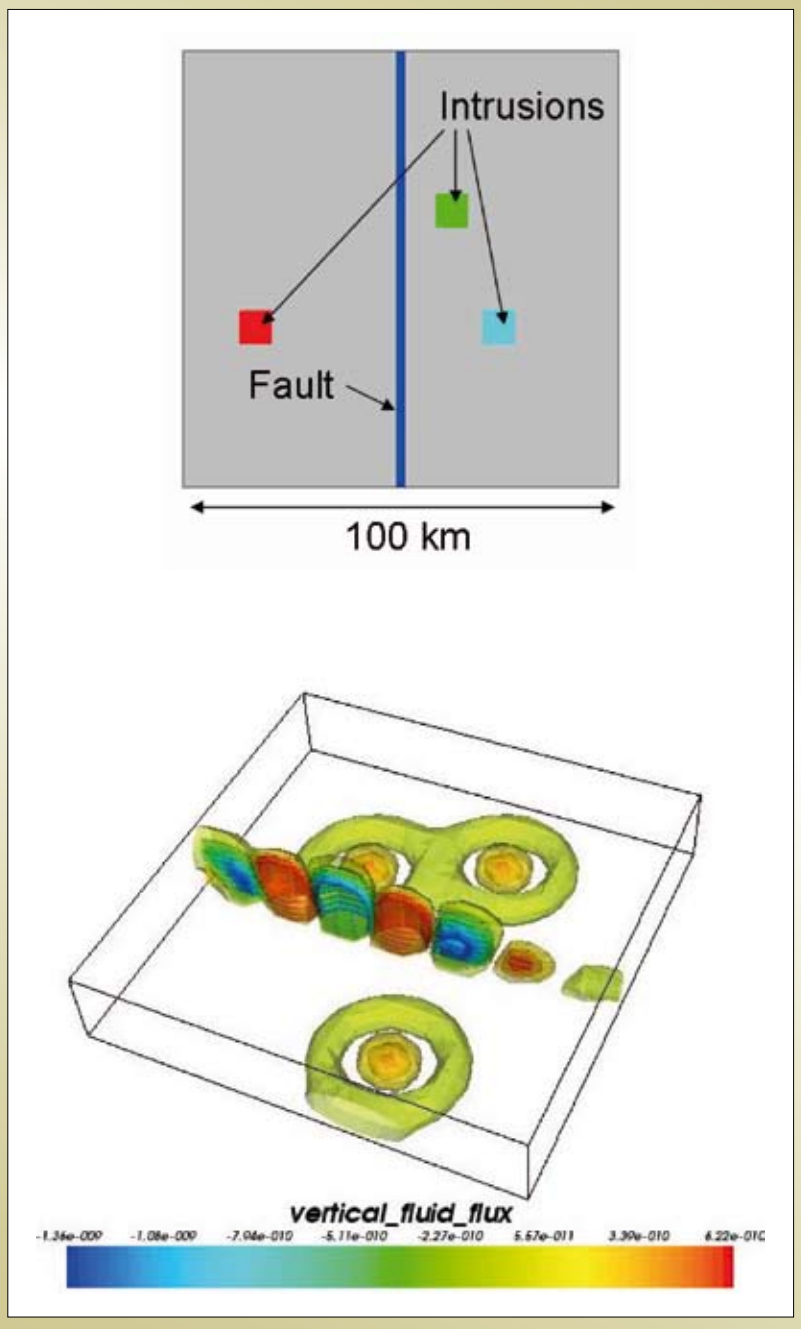


*Figure 3.7.15: Convection driven by 3 intrusions. (A) Model geometry (plan view). Fault is more permeable than the surrounding rocks. (B) Isosurfaces of vertical fluid flux (blue = downward flow, red = upward flow). Heat from intrusions drives convection in the fault, as well as around the intrusions.*

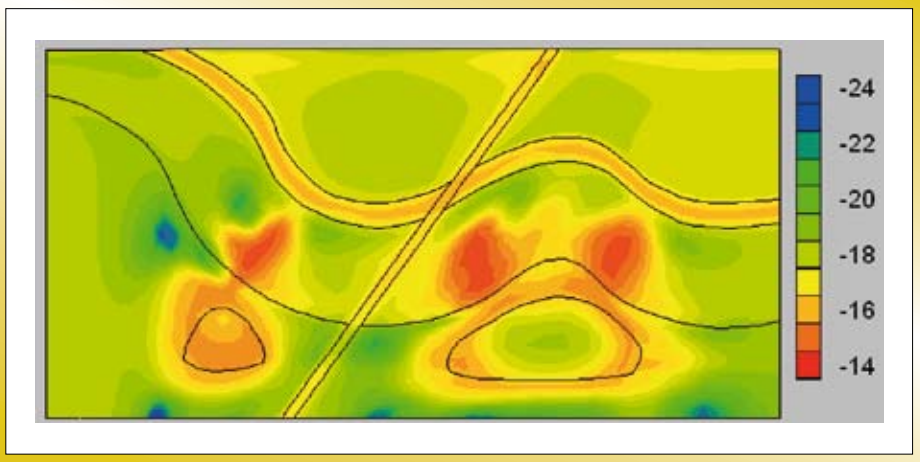


*Figure 3.7.16: Positive feedback between heat transport, metamorphic fluid production, permeability enhancement and fluid flow creates channels of high permeability (red areas) emanating from the flanks of intrusions. Model represents magmatic and metamorphic fluid production driven by two intrusions (geometry as in Figure 3.7.7a). Contour values indicate log permeability ($m^2$).*

### 3.7.2.5 Depositional mechanisms

Walshe et al. (2008) concluded that large, high grade deposits are likely to have formed by mixing of an oxidized magmatic fluid with a reduced fluid sourced from the mantle (or possibly from late basins). While it is not clear exactly how fluids become mixed on the scale of an individual vein, numerical models suggest some mechanisms for fluid mixing on the larger scale.

Firstly, extensional deformation provides favourable conditions for mixing deep and shallow-sourced fluids (see Figures 3.7.8 and 3.7.12). Mixing is likely to occur in dilatant shear zones on the margins of granite domes. The problem with this mechanism is that it is a "dead end" system; fluid accumulates but does not pass through. Thus it seems unlikely that this mechanism alone could create a large gold deposit. However, it may be an important mechanism for creating a reservoir of fluid that may subsequently be involved in mineralisation if it is focused through a narrow pathway.

The second mechanism for fluid mixing is focusing of fluid into a permeable structure. This is illustrated in Figure 3.7.17, which shows magmatic fluid from intrusions converging with fluid that is already present in a fault. In this model the fluid in the fault is also magmatic fluid, but it could equally well be a fluid from a different source, such as a mantle-derived fluid being transported from greater depth.

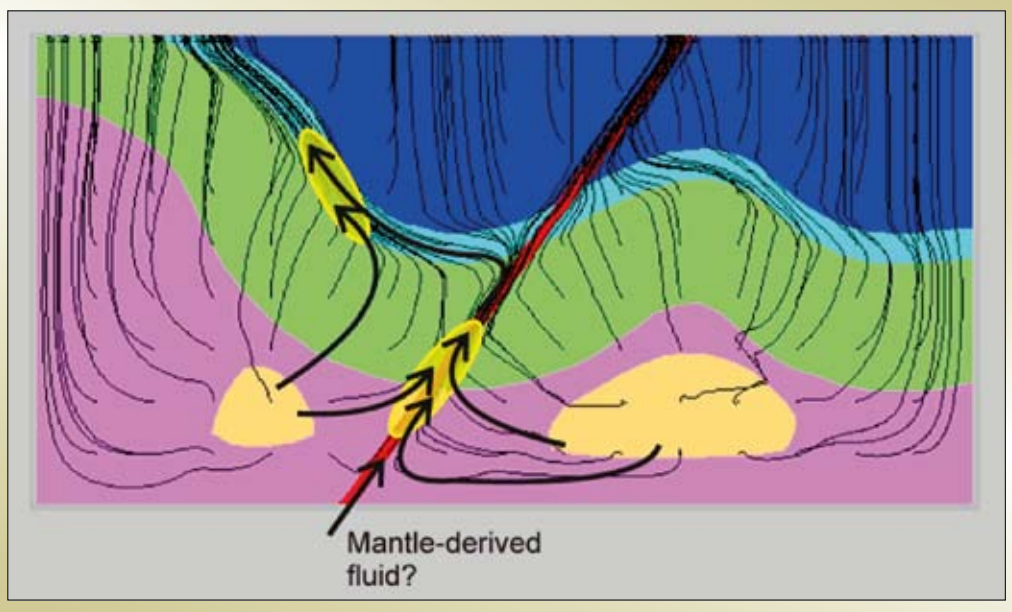


*Figure 3.7.17: Fluid mixing due to focusing into permeable pathways. Flow is driven by magmatic fluid production in this model (geometry as in Figure 3.7.7a). Mixing locations indicated by yellow shaded areas.*

### 3.7.3 Conclusions

Numerical modelling undertaken during the ***pmd*CRC*** Y4 project has provided insight into many aspects of Archaean gold mineralisation in the Yilgarn. The key outcomes are summarised below.

- Identification of favourable shortening directions for fault reactivation at Wallaby and Sunrise Dam, confirming an hypothesis based on field-based structural analysis.
- Extension drives downward flow. This provides a mechanism for drawing shallow-sourced fluids into the crust, and for retaining magmatic/metamorphic fluids that would otherwise be expelled from the system within a few million years.
- Fluid focusing into dilatant shear zones that form on the margin of granite domes during extensional deformation.
- Intrusions cause local rotation of the principal stress axes, however it seems that the stresses associated with intrusions are insufficient to override differential stresses due to regional shortening or extension. Hence, radial veins/dykes emanating from intrusions imply a larger-scale change in the stress regime at the time of magma emplacement.
- Metamorphic fluid production can create fluid pathways due to a feedback between heat transport, fluid production and permeability enhancement.
- Metamorphic fluid is sufficient to generate an economic deposit, provided it can be focused into sufficiently narrow (e.g., 50 m) permeable faults.
- Relative volumes of magmatic and metamorphic fluids (magmatic fluid approximately 4 times greater volume than metamorphic fluid)
- Convection is overridden by magmatic fluid production and thermal expansion during the early stages of cooling and crystallisation of intrusions.
- Heat from intrusions may drive convection in faults located several kilometres away.
- Opportunities for fluid mixing due to extension (mixing shallow and deep-sourced fluids) and fluid focusing (fluids from different sources converge in narrow, permeable pathways).

### 3.7.4 References

Blewett, R. S., 2004, Chapter 8: A 5Q's synthesis and predictive mineral discovery, *in* R. S. Blewett, and A. P. Hitchman, eds., Final report: 3D geological models of the Eastern Yilgarn Craton (***pmd*CRC*** Project Y2), Predictive Mineral Discovery Cooperative Research Centre (unpublished), p. 165–255.

Blewett, R. S., K. F. Cassidy, D. C. Champion, and A. J. Whitaker, 2004, The characterisation of granite deformation events in time across the Eastern Goldfields Province, Western Australia, Geoscience Australia Record 2004/10 [CD-ROM].

Blewett, R. S., and K. Czarnota, 2007a, Diversity of structurally controlled gold through time and space of the central Eastern Goldfields Superterrane - a field guide, Record, Perth, Geological Survey of Western Australia Record 2007/19, 65p.

Blewett, R. S., and K. Czarnota, 2007b, Tectonostratigraphic architecture and uplift history of the Eastern Yilgarn Craton: Module 3 - Terrane Structure, Project Y1-P763, Geoscience Australia Record 2007/15, Canberra, Geoscience Australia.

Blockeel, J., 2005, Coupled thermal and fluid flow modelling of the Kalgoorlie region, Western Australia, and implications for mineralisation, University of Exeter, Exeter, UK, 79pp. p.

Champion, D. C., K. F. Cassidy, and A. R. Budd, 2002, Chapter 8: Overview of the Yilgarn magmatism: Implications for crustal development, *in* K. F. Cassidy, D. C. Champion, I. McNaughton, I. R. Fletcher, A. J. Whitaker, I. V. Bastrakova, and A. R. Budd, eds., Characterisation and metallogenic significance of Archaean granitoids of the Yilgarn Craton, Western Australia: MERIWA Report, v. 222: Perth, MERIWA.

Cox, S. F., 1999, Deformational controls on the dynamics of fluid flow in mesothermal gold systems, *in* K. J. W. McCaffrey, L. Lonergan, and J. J. Wilkinson, eds., Fractures, fluid flow and mineralization: Geological Society of London Special Publications, v. 155: London, UK, Geological Society of London, p. 123–140.

Duuring, P., S. G. Hagemann, and D. I. Groves, 2000, Structural Setting, Hydrothermal Alteration, and Gold Mineralisation at the Archaean Syenite-Hosted Jupiter Deposit, Yilgarn Craton, Western Australia: Mineralium Deposita, v. 35, p. 402–421.

Goscombe, B., R. S. Blewett, K. Czarnota, R. Maas, and B. A. Groenewald, 2007, Broad thermo-barometric evolution of the Eastern Goldfields Superterrane: Proceedings of Geoconferences (WA) Inc. Kalgoorlie '07 Conference, p. 33–38.

Groves, D. I., and G. N. Phillips, 1987, The genesis and tectonic control on Archaean gold deposits of the Western Australian Shield: a metamorphic-replacement model: Ore Geology Reviews, v. 2, p. 287–322.

Hanson, R. B., 1995, The Hydrodynamics of Contact-Metamorphism: Geological Society of America Bulletin, v. 107, p. 595–611.

Henson, P. A., 2004, Chapter 2: An integrated geological and geophysical 3D map for the EYC, *in* R. S. Blewett, and A. P. Hitchman, eds., Final report: 3D geological models of the Eastern Yigarn Craton (***pmd****CRC* Project Y2), Predictive Mineral Discovery Cooperative Research Centre (unpublished), p. 39–73.

Henson, P. A., R. S. Blewett, D. C. Champion, B. R. Goleby, and K. Czarnota, 2006, Towards a unified architecture of the Laverton region, WA: Predictive Mineral Discovery Cooperative Research Centre - Extended abstracts from the April 2006 conference, p. 47–51.

Jia, Y. F., and R. Kerrich, 1999, Nitrogen isotope systematics of mesothermal lode gold deposits: metamorphic, granitic, meteoric water, or mantle origin?: Geology, v. 27, p. 1051–1054.

Micklethwaite, S., and S. F. Cox, 2004, Fault-segment rupture, aftershock-zone fluid flow, and mineralization: Geology, v. 32, p. 813–816.

Micklethwaite, S., and S. F. Cox, 2006, Progressive fault triggering and fluid flow in aftershock domains: Examples from mineralized Archaean fault systems: Earth and Planetary Science Letters, v. 250, p. 318–330.

Miller, J. M., 2005, The structural evolution of the Wallaby gold deposit, Laverton, WA, Predictive Mineral Discovery Cooperative Research Centre Report.

Miller, J. M., 2006, Linking structure and mineralisation in Laverton, with specific reference to Sunrise Dam and Wallaby: Predictive Mineral Discovery Cooperative Research Centre - Extended abstracts from the April 2006 conference, p. 62–67.

Sheldon, H. A., A. C. Barnicoat, Y. Zhang, and A. Ord, 2007, Metamorphism in the Eastern Goldfields: Implications for fluid flow and mineralisation: Proceedings of Geoconferences (WA) Inc. Kalgoorlie '07 Conference, p. 138–142.

Sheldon, H. A., and S. Micklethwaite, 2007, Damage and permeability around faults: Implications for mineralization: Geology, v. 35, p. 903–906.

SRK Consulting, 2000, Global Archaean synthesis - Yilgarn module: Consultant's report, p. 88.

Swager, C. P., 1989, Structure of the Kalgoorlie greenstones - regional deformation history and implications for the structural setting of gold deposists within the Golden Mile, Geological Survey of Western Australia Professional Papers, Report, Perth, p. 59–84.

Swager, C. P., 1997, Tectono-stratigraphy of late Archaean greenstone terranes in the southern Eastern Goldfields, Western Australia: Precambrian Research, v. 83, p. 11–42.

Walshe, J. L., Neumayr, P., Cleverley, J., Petersen, K., Andrew, A., Whitford, D., Carr, G. R., Kendrick, M. A., Young, C., and Halley, S., 2008, Multiple fluid reservoirs in Eastern Yilgarn gold systems. this volume.

Weinberg, R. F., P. F. Hodkiewicz, and D. I. Groves, 2004, What controls gold distribution in Archean terranes?: Geology, v. 32, p. 545–548.

Witt, W. K., J. T. Knight, and E. J. Mikucki, 1997, A synmetamorphic lateral fluid flow model for gold mineralization in the Archean Southern Kalgoorlie and Norseman Terranes, Western Australia: Economic Geology, v. 92, p. 407–437.

## 3.8 Architecture and geodynamic evolution of the St Ives region, south central Kalgoorlie Terrane, Western Australia

**R.S. Blewett[1], R. Squire[3], J.M. Miller[2], P.A. Henson[1], and D.C. Champion[1]**

[1] ***pmd*CRC*** c/o Geoscience Australia, GPO Box 378, Canberra, ACT, 2601, Australia

[2] Centre for Exploration Targeting, University of Western Australia, Crawley, Perth, Australia

[3] School of Geosciences, Monash University, Clayton, Victoria, 3800, Australia

### Abstract

A revised structural evolution comprising both extensional and contractional events has been developed for the St Ives region in the south central Kalgoorlie Terrane, and these events shaped the development of the fault architecture which controlled the location of regional anticlines, centres of magmatic emplacement and deposition of the entire Archaean greenstone succession. The centre of the St Ives region is dominated by a regional anticline and this was likely established early during the D1 extensional history. The regional anticline is an important architectural element because 1) subsequent magmatism and ultimately mineralising fluids were focussed into this up-domed region, and 2) deformation was partitioned across the limbs and crest of this structure, resulting in a complex interplay of pathways for different fluids to mix.

At least three gold mineralising events (D3, D4b, and D5) are recorded in the St Ives region. The D3 event at St Ives (and regionally) involved regional uplift and extension, resulting in the formation of late basins (Merougil Basin locally) and the emplacement of melts from a metasomatised mantle wedge source (Mafic-type porphyries). The convergence in space and time of fluids from a deforming and metamorphosing late basin and an enriched mantle is the primary reason for the fertility of the region. The most significant gold event occurred during D4b sinistral strike-slip shearing along north-northwest trending faults that were coupled across accommodation structures represented by generally east to east-northeast trending reverse faults (thrusts) and normal faults (depending on relative displacements of the adjacent sinistral strike-slip faults). Reactivation of D1 transfer structures may have influenced the siting of this later accommodation structures. The late stage mineralisation during D5 (dextral strike-slip) was associated brittle tectonics at high structural levels. The extent to which new was introduced gold in the younger events, or whether it was remobilised, is not known.

**Key words:** *Archaean, structural geology, gold mineral systems, seismic, Eastern Goldfields, Yilgarn Craton, St Ives, Kambalda.*

### 3.8.1 Introduction

The St Ives region, located near Kambalda in Western Australia, contains several world-class gold deposits and related satellite ore bodies that are concentrated near the hinge of a regional antiformal structure named the Kambalda Anticline (Figures 3.8.1a, b, c). The region is temporally and spatially linked to the same architectural and fluid system that generated Kalgoorlie's giant Golden Mile deposit, located about 60 km farther north (Weinberg et al., 2005). However, St Ives is clearly distinguished from the Golden Mile and other major gold camps in the Eastern Goldfields Superterrane (EGST) by the presence of several widely-spaced deposits rather than a single large resource (Figure 3.8.1d). This difference probably reflects variations in efficiency of the depositional mechanisms associated with the individual ore bodies, and the inability of the camp-scale architectural system at St Ives to efficiently focus the enormous volumes of mineralising fluid required to create a single giant deposit (Hronsky, 2004).

This paper investigates the early stratigraphic and structural architecture of the St Ives camp, to assess its role in controlling the location and geometries of later syn-gold structures and their deposits. St Ives contains an array of linked strike-slip and reverse faults that reactivated an earlier extensional (basin-forming) system and produced the complex variations in the location and characteristics of its numerous ore bodies (e.g., Connors et al., 2003; Miller et al., 2008). Here, we show that architectural inheritance played a crucial role in controlling the location and geometries of the syn-gold structures and their associated deposits. The influence of the pre-existing architecture during mineralisation is a common feature in the EGST (Blewett and Czarnota, 2007a, b, c), such as the Golden Mile Fault (i.e., one of the structures hosting the giant

Golden Mile deposit) that initially developed as a growth fault (Gautier et al., 2007).

Recognising differences in the spatial and temporal association of the different stratigraphic units is the most-effective method for identifying these important early structures. Reactivation of earlier structures will produce stratigraphic units with different sedimentary provenance, magmatic affinities and/or volcano-sedimentary characteristics. These broad units may be mapped out in areas with limited exposure, such as is available from drillcore or in geophysics (such as gravity and magnetics); whereas information from kinematic indicators generally requires good exposure of the structures and may only record the latest movements.

We present a refined map of the St Ives region showing subdivision of the previously undivided Black Flag Group, which identifies many of the early structures (Figure 3.8.1c). By taking both a regional and systems view of the development of the 3D architecture, we have been able to rationalise the large amount of previous (and sometimes conflicting) structural work into a new coherent structural framework that enables an understanding of the detailed fluid and depositional-site studies to be placed in context (Walshe et al., 2006; Neumayr et al., 2008). This paper also provides a stratigraphic and broader regional structural (temporal) and 3D architectural (spatial) framework for a detailed paper on the structural controls of mineralisation at St Ives (see Miller et al., 2008). By integrating this new view with the fluid studies, we have developed an improved understanding of why the St Ives camp is where is it is, but more importantly for explorers, can better-predict the location of new hidden ore bodies.

### 3.8.2 Regional geological setting

The St Ives region (gold camp) is located in the southern part of the 'Golden Corridor' (Henson, 1996), which extends over 500 km northwards through the Kalgoorlie Terrane (Kambalda to Wiluna), and hosts many of the Yilgarn Craton's largest gold (and nickel) deposits. The palaeotectonic setting of the Kalgoorlie Terrane is generally considered to have been in a back-arc (largely under extension) that developed after plume magmatism (Cassidy et al., 2006; Barley et al., 2002; Czarnota et al., 2008). The stratigraphy is dominated by early (<2.71 Ga) mafic-ultramafic successions of the Kambalda Group developed on an unknown (but likely felsic evolved basement), passing into intermediate to felsic volcanic rocks and associated volcaniclastic sedimentary rocks of the Kalgoorlie Group, and finally into clastic sedimentary rocks (<2.66 Ga) of the so-called late basins (Krapež et al., 2000). Intrusive rocks include mafic sills and dykes (including lamprophyre), and these units provide a host for many of the early discoveries in the Kambalda-St Ives region. Equally important for hosting mineralisation are the felsic intrusive rocks (porphyries); including a range in chemical types (Champion and Sheraton, 1997), with the high-P enriched Mafic-type porphyries being particularly indicative of fertility (Halley, 2007).

Many, if not all, of the major structures (domain and terrane bounding) were initiated during extension and basin formation (and magma emplacement) early in the geological history (Blewett and Czarnota, 2007c). The structures of the St Ives region are part of a larger linked architectural system (that includes Kalgoorlie and New Celebration) which developed along with the local stratigraphy.

### 3.8.3 Mineralisation

The backbone structure that links Kalgoorlie and St Ives is the Boulder-Lefroy Shear Zone (BLSZ), which hosts the giant Golden Mile and the world-class Mt. Charlotte orebodies (>1500 t Au combined); the New Celebration deposits (~100 t Au); and the world-class St Ives Gold Camp (>100 t Au; Nguyen et al., 1998; Weinberg et al., 2005). In the St Ives camp, deposits are hosted in predominantly mafic-ultramafic lavas and dolerite intrusions. In the Central Corridor, of the camp, deposits are hosted by units stratigraphically below the Blag Flag Beds (Kambalda Komatiite, Kapai Slate, Paringa Basalt, Defiance Dolerite) and along porphyry-ultramafic rock contacts. Deposits on the southwestern side of the camp (Argo and Junction) are hosted by the Junction and Condenser Dolerites that intruded the Black Flag Beds. These dolerites are correlates of the Golden Mile Dolerite and the overall lithostratigraphic setting is similar to that of the Golden Mile.

The St Ives gold camp is currently the fourth-largest gold producer in Australia and has an annual output of about 500,000 ounces of the precious metal. Gold was first discovered at Kambalda and Victory in 1897, and by 1907

*Figure 3.8.1: Location maps of the Yilgarn Craton and St Ives region.*

*A) Regional terrane map of Cassidy et al. (2006) places the Kambalda to Kalgoorlie corridor in context.*

*B) Simplified regional geological map of the southern Kambalda Domain. The red lines show the main segments of the Boulder Fault in the north with the Lefroy Fault in the south. They connect via a series of soft linkages or accommodation zones. Main mineral deposits along this corridor occur adjacent to the maximum throw or offsets on these faults, and with a spacing of around 30 km (K-Kalgoorlie, J-Jubilee, SI-St Ives).*

*C) Simplified geological map of the distribution of sedimentary sequences (dated at > 2665 Ma) occurs across major faults that host mineralisation (dated at <2650 Ma). The controlling structures of the sedimentary lithofacies and their depocentres occurs across structures are subsequently reactivated during mineralisation more than 15 My later. Mapping the differences in sediments is therefore a good predictor of major structures that might be favourable for such a reactivation (see Squire et al., 2007).*

*D) Location map of mines and pits comprising the St Ives camp south of Kambalda (after Rumming, 2006) described in the paper.*

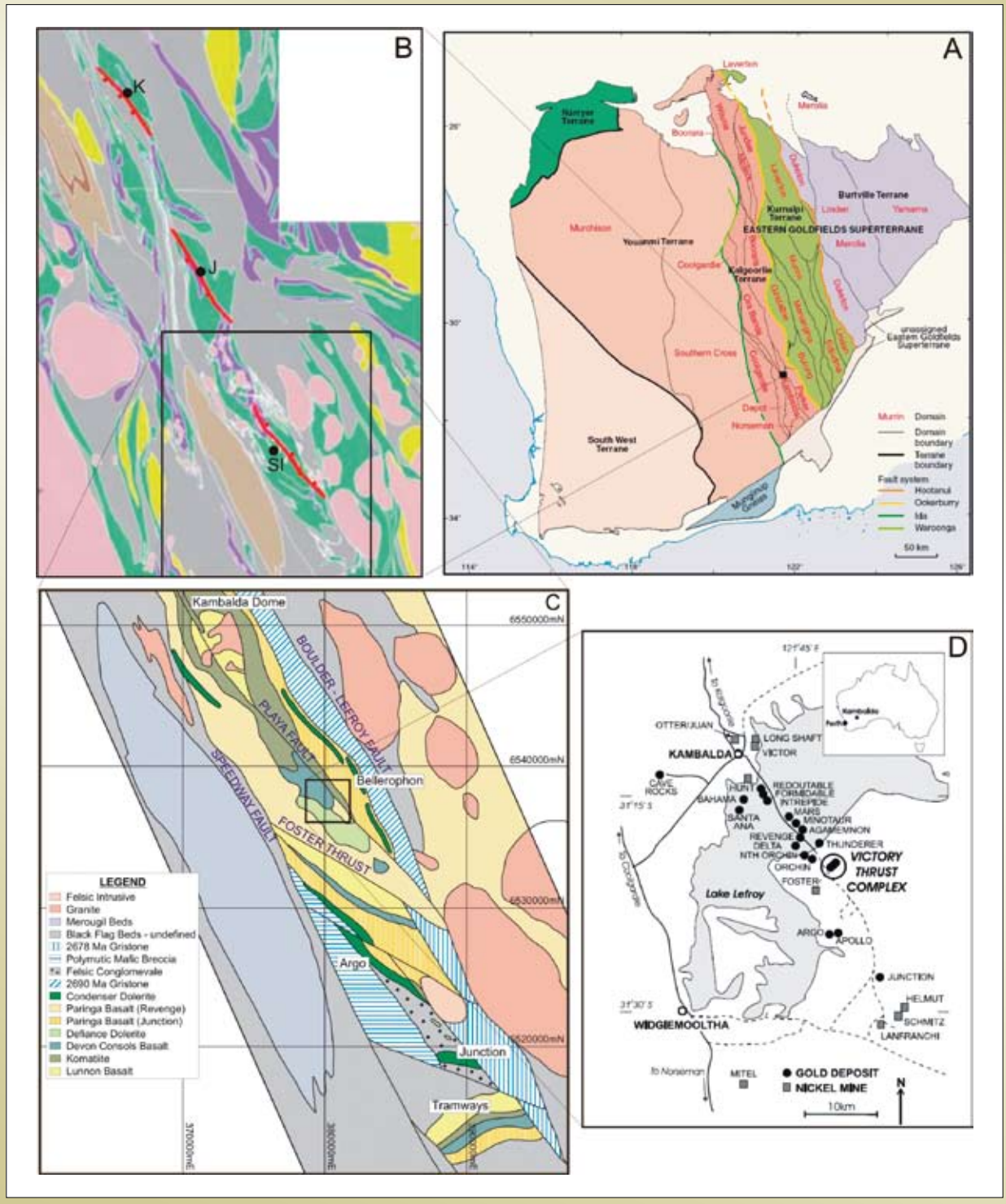

the region had produced about 31,000 ounces. Despite a hiatus in production between 1907 and 1988, the region has produced more than 9 million ounces of gold (Justin Osborne written communication, 2007). The St Ives camp also contains several world-class komatiite-hosted nickel deposits that are not the focus of this paper and thus are not discussed in detail. The main mines of the camp are Victory-Defiance (Leviathan Complex), Revenge, Argo, Junction, Mars, and Delta. Many of the deposits are located on (beneath) Lake Lefroy (Figure 3.8.1d).

The Victory-Defiance gold mine is located 20 km south of Kambalda, and received modern exploration discovered around the old workings at Victory in 1980. Underground development in 1983 confirmed a large system of shallow-dipping quartz-rich (Defiance) lodes. Further near mine exploration discovered extensive mineralisation on the Repulse shear zone and felsic intrusions (Flames) on the hangingwall of the Repulse. Further discoveries, at Orion/Britannia, Sirius and the down plunge continuation of the Defiance system at Conqueror, extended the known gold mineralisation and defined a large network of interconnected shear zones which host a variety of styles of gold-bearing lodes over an area of 2 km x 2 km (Figure 3.8.1d). Nearby discoveries to the north of Victory/Defiance, principally those at Orchin/Thunderer and at Revenge are considered part of a linked architectural system of Defiance-style shear-hosted lodes and thus part of a single gold "camp" of which Victory-Defiance is the principal deposit.

## 3.8.4 Stratigraphic architecture in the St Ives region

The stratigraphy of the Archaean rocks in the St Ives region is broadly divided in to the 2.71–2.69 Ga, predominantly mafic to ultramafic units of the Kambalda Sequence, the 2.69–2.66 Ga intermediate to felsic volcaniclastic sequences of the Kalgoorlie Sequence, and the 2.6 Ga siliciclastic packages of the Merougil Sandstone (Figure 3.8.2). Contiguous exposures of all the stratigraphic units is exposed nowhere, thus the total thickness of the Archaean successions in the St Ives region is difficult to estimate, but is likely to be at least 4 km. For simplicity, we provide a table summarising the principal characteristics of the numerous formations (Table 3.8.1) and intrusions (Table 3.8.2). Proterozoic dykes also intrude the sequence, but are not discussed here.

### 3.8.4.1 Felsic and mafic intrusions

The Kambalda and Kalgoorlie Sequences are intruded by intermediate to felsic granitoid stocks, dykes, and sills ranging from diorite to trondhjemite to rhyolite in composition (Roberts and Elias, 1990). Gravity modelling and seismic profiles show that the greenstone sequences lie upon a felsic substrate (basement) that is largely granitic in composition and was probably the source for the intrusions up into the supracrustal rocks (Henson, 2006).

The porphyries can be broadly subdivided, on the basis of petrography into mafic/lamprophyre and felsic groups (Table 3.8.2). Within each of these a number of subgroups are readily identifiable on the basis of geochemistry (Table 3.8.2), though chemical differences between subgroups are largely subtle, with the exception of the alkaline rocks (syenites) from the Little Sandy region, east of the Lefroy Fault, which have extreme Zr and Nb and high alkali contents. It is noted that textural and other petrographic characteristics are generally ambiguous in identifying porphyry-types, especially at the camp-scale, although some are distinctive, e.g., the 'Flame group', with large quartz and feldspar phenocrysts (Figure 3.8.4).

In detail, it is not entirely clear whether the mafic-felsic subdivision is universally warranted. What is evident, however, is that nearly all porphyries at St Ives can be subdivided into 2 broad end-members, i.e., enriched and unenriched. Enriched porphyries (lamprophyres, mafic and felsic members) are characterised by elevated LILE, LREE, $P_2O_5$, Zr, Th etc relative to the unenriched end-members. Geochemically plots such as $P_2O_5$, Ce or Th versus $SiO_2$ can be used to distinguish the two end-members. It has been noted elsewhere (e.g., Champion, 1997; Beakhouse, 2007) that intrusive rocks with these enriched compositions often show a strong spatial and/or temporal relationship to gold mineralisation (Scott Halley personal communication, 2007).

Geochronological controls on the porphyries is not well constrained. SHRIMP analyses of magmatic zircons from a quartz-albite felsic porphyry at Victory yielded an age date of 2673 ± 10 Ma (ANU/Claoue-Long: unpublished data; Clout, 1991), whereas a xenolithic diorite and felsic phase from the Revenge mine yielded SHRIMP ages of 2661±2 Ma and 2658±4 Ma, respectively (Nguyen 1997). The felsic porphyry dykes have equivocal field relationships

Table 3.8.1: Summary of the characteristics of Archaean formations comprising the Kambalda and Kalgoorlie Sequences and Merougil Sandstone in the St Ives region

| | |
|---|---|
| **Merougil Sandstone** | |
| **Merougil Sandstone** (<2665 Ma) | >2,500 m thick; sub-aerial quartz-rich succession subdivided into a lower conglomerate-rich package & upper sandstone-rich unit (Bader, 1994; Krapež et al., 2000); disconformity separates it from mudstone-rich units of Black Flag Group (Hand, 1998) |
| **Kalgoorlie Sequence** | |
| **Black Flag Group** (<2686 Ma) | Locally >2,000 m thick; subdivided (not in stratigraphic order) into 5 different lithofacies that are summarised below (Squire et al., 2007):<br>• Plagioclase-rich granule breccia (gritstone): massive to graded beds <5 m thick rich in feldspar crystal fragments minor felsic volcanic lithic fragments & rare quartz<br>• Volcanic sandstone & siltstone: moderately well-sorted beds >5 m thick of massive & graded volcanic sandstone & siltstone; gradational lower contact with gritstone<br>• Mudstone: Black beds generally as tops to siltstone units; much thicker near Santa Ana<br>• Mafic cobble breccia: Internally massive, thick (>15 m) units dominated by subangular clasts of aphyric basalt with lesser well-rounded rhyolitic clasts up to 150 mm across<br>• Felsic cobble conglomerate: massive & graded beds up to 10 m thick with subrounded clasts < 250 mm across of moderately plagioclase±quartz-phyric dacite |
| **Kambalda Sequence** | |
| **Paringa Basalt** (2690±5 Ma) | 500 m to 1500 m thick; massive & variolitic pillow lavas, lesser doleritic units and rare monomictic basalt breccia (hyaloclastite); contacts from pillow basalt to massive basalt to dolerite commonly gradational; 2690±5 Ma (Clout, 1991); has lower Ti/Zr compared to Devon Consols Basalt; interpreted to indicate up to 25% crustal contamination in its melt (Lesher and Arndt, 1995) |
| **Kapai Slate** (2692±4 Ma) | <10 m thick; black sulphidic mudstone with minor felsic volcaniclastic rock fragments (2692±4 Ma detrital zircons; Claoue-Long et al., 1988); interpreted to represent a combination of tuffaceous debris from distal felsic volcanic eruptions and minor chemical deposition from silica-rich exhalations that separate the Paringa and Devon Consols Basalts; however, similar-looking interflow sediments are present in both units, making identification of the boundary between the two basalts difficult |
| **Devon Consols Basalt** (2693±30 Ma) | Up to 150 m thick; pillowed and massive high-MgO basalt with abundant varioles (Figure 3a); common gradational contacts from pillow to massive basalt to dolerite; sharp (and gradational?) contact with Tripod Hill Komatiite; divided into high-Si low-Mg & low-Si high-Mg basalts (Redman and Keays, 1985); generated by crustally contaminated komatiitic melt (Compston et al., 1986; Claoue-Long et al., 1988; Lesher and Arndt, 1995); |
| **Kambalda Komatiite** (2709±4 Ma) | 100 to >1200 m thick; internally zoned ultramafic lavas <100 m thick separated by sulphidic sedimentary units (~2709±4 Ma; Claoue-Long et al., 1988); includes high-Mg flows of Silver Lake Member (contain Ni sulphide deposits) & lower-MgO flows of Tripod Hill Member (Gresham and Loftus-Hills, 1981); conformably overlies Lunnon Basalt; upper komatiite lavas are more differentiated & contain less-abundant interflow units |
| **Lunnon Basalt** (2720–2710 Ma) | >1750 m thick; abundant massive & pillow basalt, lesser monomictic basalt breccia & rare interflow sedimentary units form subaqueous tholeitiic lavas & rare sub-volcanic intrusions of ponded (rift?) lava succession (Gresham and Loftus-Hills, 1981; Squire et al., 1998); has 'lower' MgO-rich & 'upper' less–MgO-rich members separated by an interflow sediment (Redman and Keays, 1985); basalt has uniform mantle source (Morris, 1993) |

Table 3.8.2: Summary of the characteristics of the major Archaean intrusions at St Ives. Note, this table does not include minor intrusions associated with volcanic units described in Table 1

| | |
|---|---|
| **Mafic intrusions** | |
| **Dolerite** (2680±8 Ma) | <500 m thick; internally zoned dolerite and gabbro with minor aphyric basalt at margins; the Condenser & Junction Dolerites display zonation (bottom to top) of (1) pyroxenite base to (2) plagioclase-pyroxene-bearing gabbro to (3) granophyric zone (most evolved) to (4) Fe-rich plagioclase-pyroxene gabbro; Condenser & Junction Dolerites (& Golden Mile) are similar (& host big Au deposits), whereas Defiance Dolerite is high-Mg basalt; 2680±8 Ma SHRIMP U/Pb age from pegmatite zone in Condenser Dolerite. |
| **Lamprophyre** (2627±10 Ma) | Generally <3 m thick; clinopyroxene±olivine±amphibole±phyric (quartz & feldspar only found in groundmass) mafic to intermediate intrusions; subdivided into biotite-phlogopite-phyric kersantites and hornblende-augite-phyric spessartites (Rock et al., 1989). Spessartite lamprophyres in the St Ives region can be split into two end-members on the basis of geochemistry, namely, the presence (enriched) or absence (normal) of elevated $P_2O_5$, LILE, LREE and Th contents. Both types often occur together in the one region. Relative timing is not known. Kersantites, where present, are typically even more enriched than the enriched spessartites. It is clear from relationships observed in drill core that the lamprophyres are not all synchronous; their age range, however, is poorly constrained. |
| **Felsic to intermediate intrusions**<br>Five groups of felsic (to intermediate) porphyries have been recognised in the St Ives region. The great majority of porphyries exhibit broadly similar lithologically properties making distinction in the field difficult, with a strong reliance on lithogeochemistry. Even chemical differences are mostly subtle for the majority of the porphyries, consistent with their mostly common origin. The most distinctive porphyries are the Little Sandy Syenite and related rocks. | |
| **Kambalda Dome** | Although members of this group occur throughout the St Ives region they are best exemplified by the porphyries in the Kambalda dome area. These porphyries range from white, variably (biotite-) quartz-feldspar-phyric, felsic porphyries to white, fine- to medium-grained biotite granite. Chemically they are characterised by elevated $SiO_2$ (>68%; amongst the most silica-rich of the St Ives porphyries), and elevated LILE, LREE, HFSE and Th. Th contents, in particular, are distinctive. Comprises the most enriched end-member of the felsic porphyries (not including Little Sandy Syenite). |
| **Delta** | Widely distributed porphyries that include those found at Delta and Cutty Sark. Comprise grey to pink variably phyric (sparsely to strongly) biotite/amphibole-plagioclase- to quartz-feldspar-phyric porphyries. Characterised by lower $SiO_2$ contents (60–70%) and less enriched-compositions than other porphyries, i.e., lower LILE, LREE, $P_2O_5$, Zr, Th contents. Forms the 'depleted' end-member of the porphyries (with Kambalda dome group the enriched end-member). |
| **Flame** | Grey to pink-grey strongly feldspar-quartz-biotite phyric fine-grained felsic porphyries. Texturally distinctive porphyries characterised by megacrysts and large phenocrysts of subhedral to euhedral feldspar crystals and large well-shaped quartz crystals. One of the latest porphyry phases in the region. Chemically falls between Delta and Kambalda Dome groups, with most similarities, chemically, to Santa Ana group. |
| **Santa Ana** | Group of porphyries that includes those found at Santa Ana, Intrepid, Bahamas, and Little Sandy (not the Syenite). Petrographically, comprise variably phyric (strongly to sparsely), plagioclase-, to plagioclase-amphibole/biotite-, to (minor) quartz-feldspar-phyric porphyries, and medium-grained amphibole (+/- biotite) trondhjemites and granodiorites. Chemically falls between Delta and Kambalda Dome groups, with most similarities, chemically, to the Flame group. |
| **Little Sandy Syenite** | Pink to brick-red, quartz-feldspar-phyric, microsyenite. Phenocrysts Although can be identified by brick-red (haematitic) colours, the most diagnostic test for this porphyry type is lithochemistry. Little Sandy Syenite is distinguished by extreme Zr, Nb, Th, and high alkalis. Locally has fringing haematitic and/or magnetite-biotite-epidote alteration. |

with the Kambalda granodiorite. SHRIMP analyses of magmatic zircons from the Kambalda Granodiorite indicated an age of 2662±6 Ma (Compston et al., 1986). Younger ages have been reported, at least for some of the lamprophyres - 2627±10 Ma (Clark, 1987). Drill core observations indicate that the lamprophyres both cut and cross-cut felsic porphyries implicating a range in ages for the latter (or, perhaps, younger ages for some of the felsic porphyries).

### 3.8.5 Regional 3D architectural setting

Understanding the region's 3D architecture can be determined from firstly examining of the map and stratigraphic patterns and linking these to field observations (dips and strikes), and secondly from geophysics (seismic, gravity and magnetic data). Together these data are integrated to make a 3D map of the region (Henson and Blewett, 2006) which permits an assessment on the major controls on gold mineralisation in the region, and provides a framework for more detailed deposit-scaled 3D maps (e.g., Neumayr et al., 2008; Miller et al., 2008).

Map patterns show that the region between Kalgoorlie and St Ives is dominated by a regional northwest to north-northwest structural grain (Figures 1b, c) defined by major faults, gently-plunging upright regional folds and foliation development. This corridor hosts the major gold deposits of Kalgoorlie, Jubilee/New Celebration and St Ives/ Kambalda. The map pattern of the lower mafic-ultramafic

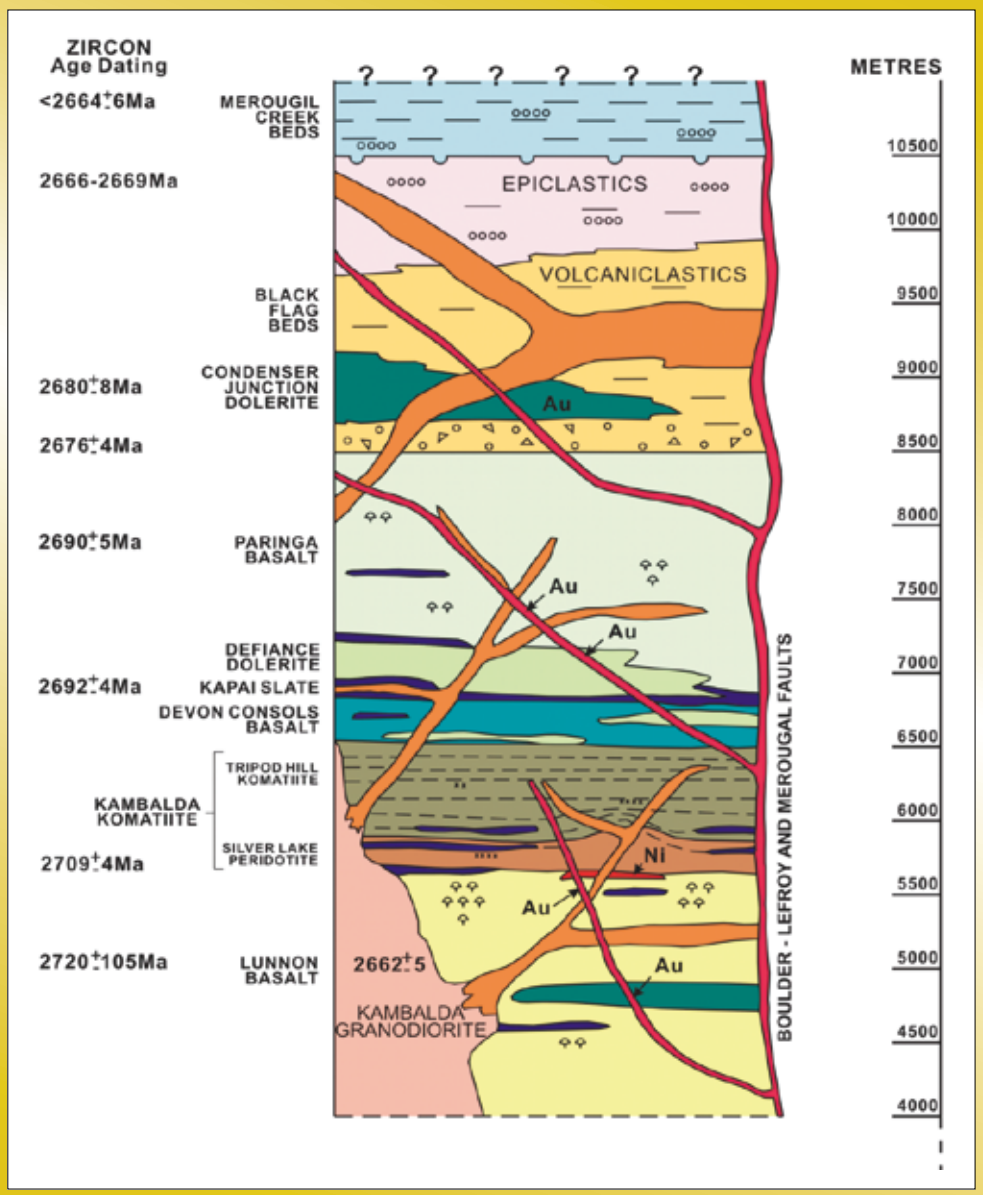


*Figure 3.8.2: Composite stratigraphic column for the St Ives camp (after Conners et al., 2003).*

units defines a series of en échelon centres (antiforms) with major bounding faults developed variably on the east and west (Figure 3.8.1b). Collectively these faults have been termed the Boulder-Lefroy Fault Zone (BLFZ).

The BLFZ from Kalgoorlie to St Ives follows an open sigmoidal trajectory, with the steeply west-dipping Kalgoorlie and New Celebration segments of the fault trending ~340. A continuous shear zone that trends ~355° provides a linkage for these segments (Figure 3.8.1b).
At Kalgoorlie, the west-dipping Boulder Fault (constrained using seismic reflection and gravity modelling) has the lower mafic sequence in its footwall (to the east) and the younger Black Flag Group in its hangingwall (to the west). This geometry is consistent with an overall normal displacement across the fault, which is contrary to a thrust interpretation of Weinberg et al. (2005). Considering the geometry of the Kalgoorlie to New Celebration Faults (Boulder Fault) as a system, the individual strands or segments initiated separately (red strands in Figure 3.8.1b) and with ongoing faulting they coalesced at their fault tips and linked into one continuous fault system.

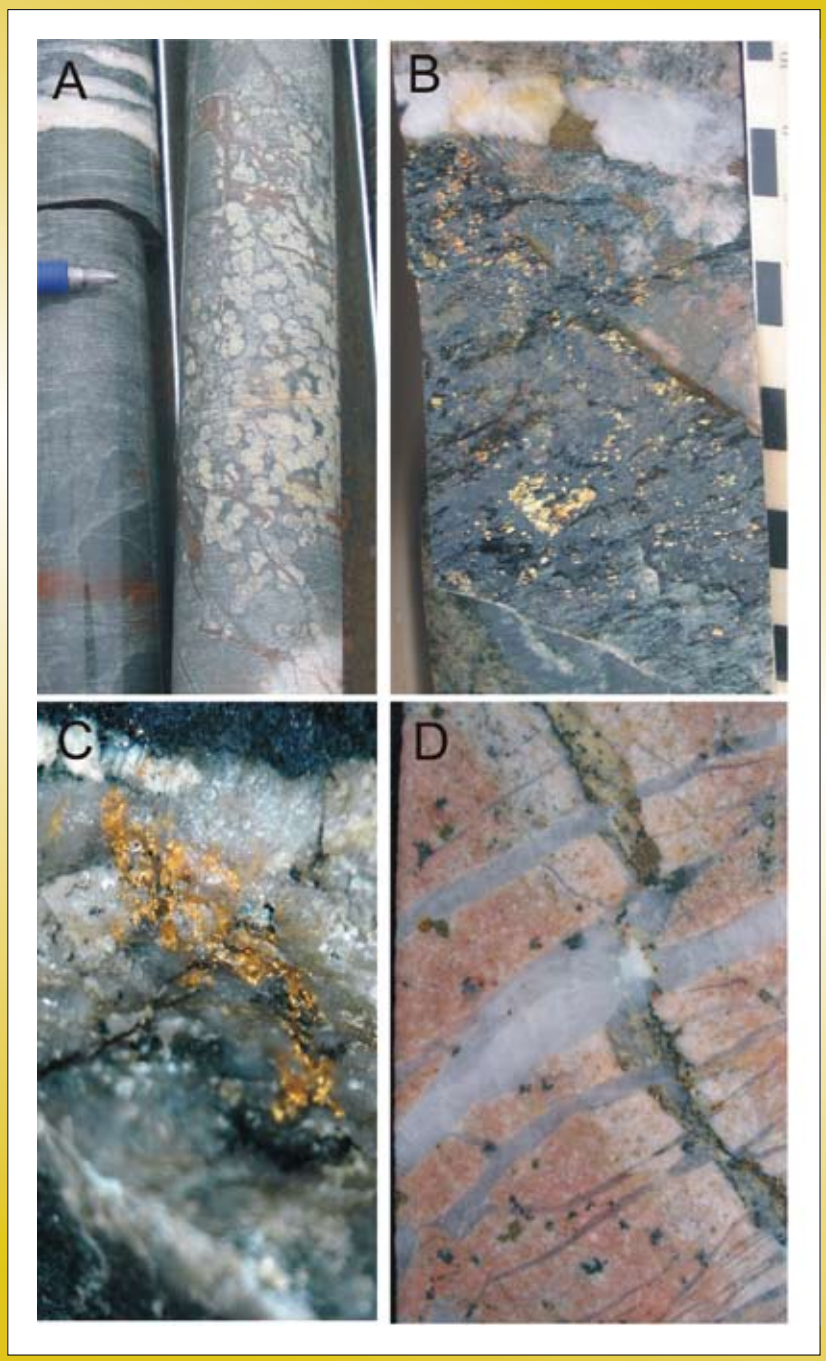


*Figure 3.8.3: A) Classic variolitic texture of the Devons Consol Basalt. This sample is altered from near the ore zone in the Victory-Defiance mine. B) Sulphides associated with sinistral oblique slip slickensides (D4b) on a shear plane from Victory-Defiance mine. C) Underside of a top to the northwest D4b thrust with visible gold in quartz vein Victory-Defiance mine. D) Mutually overprinting veins in highly altered porphyry.*


*Figure 3.8.4: Montage of the range of porphyries that occur throughout the St Ives camp. A) Mafic type porphyry (lamprophyre) from the Lighthouse area, B) Mafic type porphyry from Santa Anna area, C) Pink feldspar porphyry of the Little Sandy area east of the Playa Fault (Syenite type), D) quartz-feldspar phyric 'Flames' porphyry (High-Ca type).*

South of the Kambalda Dome, the steeply east-dipping Playa Fault is offset from the trend of the BLFZ with an en-échelon geometry similar to that observed in the Kalgoorlie and New Celebration segments to the north. Overall the stratigraphy is outward younging and reflects an extensional (normal) geometry. This is because the Lefroy Fault juxtaposes the younger Black Flag Group against the older Kambalda Sequence (Figure 3.8.1b). Other workers have described thrusting on this structure (e.g., Weinberg et al., 2005), nevertheless in terms of geometry and major architecture extension was the dominant tectonic mode. Faults to the east of the Playa Fault (Figure 3.8.5) likely originated as synthetic and antithetic normal faults to the main controlling structure and the region to the west of the Playa Fault is now an uplifted footwall block.

The architectural controls on the stratigraphy can be inferred from the thickness and provenance-source changes across domains that are bound by structures. These inferenced controls include the presence of a particular structure at the time of stratigraphic development, its likely tectonic mode (extension/contraction/strike-slip), and possibly its dip. Swager and Griffin (1990) first noted regional thickness differences across the Kalgoorlie Terrane in the upper basalt (Paringa and Devons Consols Basalts locally at St Ives) and attributed these differences to the development of extensional growth faults at the time of volcanism and greenstone basin formation. More locally, Conners et al. (2002) showed that the komatiite thickness changed dramatically about the St Ives camp. They suggested these thickness changes were controlled by east-northeast directed extension on structures the Playa, Belle Isle and Lefroy Faults (see also Miller et al., 2008).

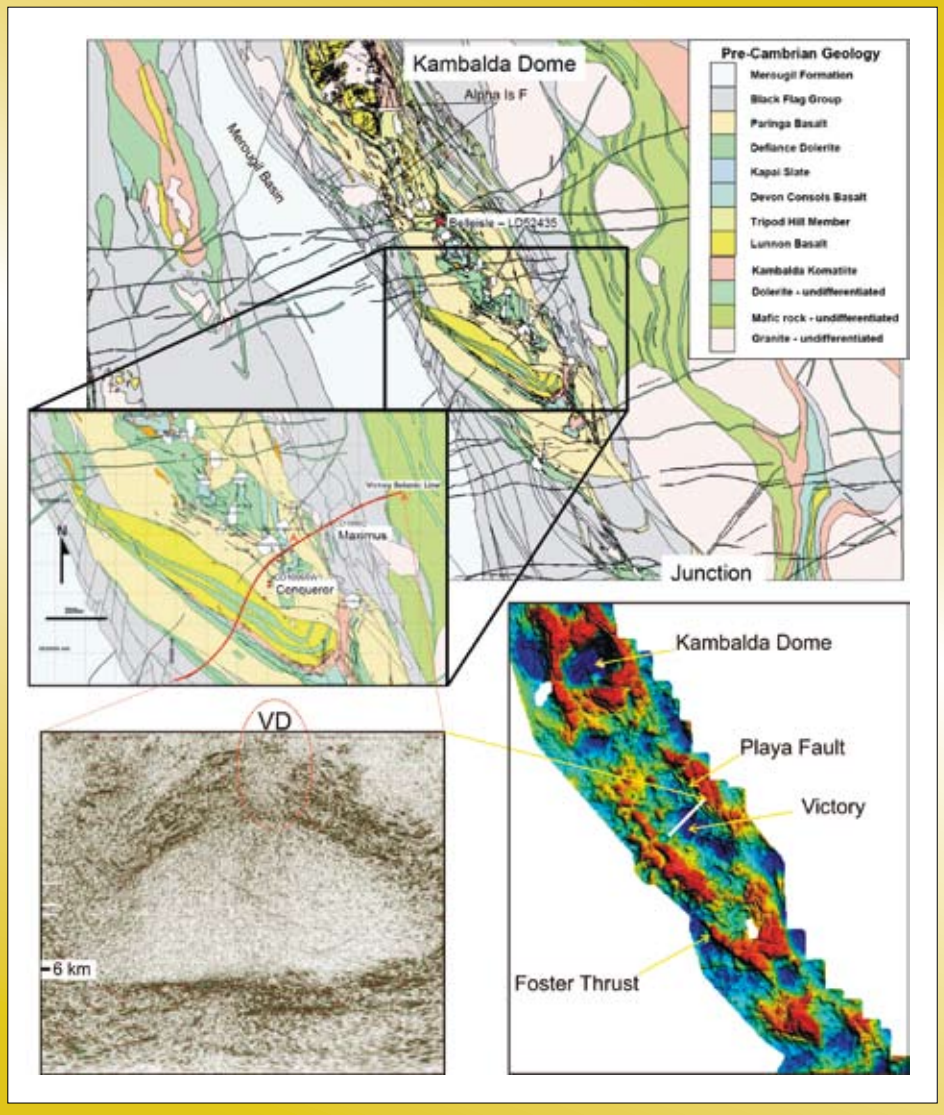


*Figure 3.8.5: Detailed geological map around the Victory-Defiance area with high-resolution seismic line showing the granite cored dome around 2.5 km beneath the mine (VD). Screens of porphyry dykes are inferred to emanate from this dome (highlighted by the seismic washout zone inside the red ellipse), many of these intersect the mine sequence and have played a crucial role in chemical, fluid and rheological contrasts for the formation of this deposit. The high-resolution gravity image clearly shows the dense (red colours) mafic-ultramafic sequence folded about the Kambalda Anticline and a number of linear structures (Fitzroy and Playa Faults). The deep blue colours represent less density from buried granites (that are imaged in the seismic profiles). Many other granite cored domes may be found in the region. Maps, seismic profile and gravity image provided courtesy of St Ives Gold Fields.*

More recent work by Squire et al. (2007) has showed that the Black Flag Group was similarly controlled by ancestral faults of what are now mineralised structures (> 30 My later). Figure 3.8.1c shows that there are four types of Black Flags Group and that these were developed in separate depocentres controlled by the fault architecture. In summary, these stratigraphic relationships indicate that extension occurred for much (if not all) the preserved Archaean stratigraphic history and the controlling faults (now mineralised) had a long history of activity and reactivity.

In terms of a deeper view of the 3D architecture, examination of the gravity map (Figure 3.8.5) provides significant insights. The gravity map clearly shows the low-density granite body in the core of the Kambalda Dome. The Victory dome is an area of gravity low and is therefore likely to be cored by buried granites. Furthermore, similar ovoid patterns of gravity lows up to 5 km across can be observed throughout the camp and these are also inferred to be granite domes. Many of these domes are lying within an overall antiformal structure and reflect a complex 3D shape with apophyses and domes protruding upwards. A granite core for this seismic feature as been confirmed by Chopping et al. (2008), who explored a series of forward models of the high-resolution gravity data in order to understand the role of a buried granite and its relationship to alteration.

Further conformation of the shape and composition of the domes at depth is provided by the seismic reflection data (Stolz et al., 2004), especially the line across the Victory-Defiance mine (Figure 3.8.5). This section beautifully images a body in the footwall to the Playa Fault with reflectivity consistent with a granitic unit (Henson, 2006; Henson and Blewett, 2006). A corresponding north-south line confirms the equant shape of this intrusion, consistent with its ovoid shape visible in the gravity map (Figure 3.8.5). The inferred granite body is hemispherical in shape with a flat base at around 6 km depth defined by a series of parallel reflectors and an arched top around 2.5 km below current exposure (Henson et al., 2005). The overlying (country rock) is arched/domed and the stratigraphy dips away from the apex. Other evidence of the buried granite is also provided by the swarms of porphyries inferred to be emanating from the apex of this dome and intruding the mine sequences (e.g., Flames Porphyry). These are the bland zone above the dome apex and marked with a red ellipse and the letters VD (Figure 3.8.5). Although this deep body is undated, porphyries in the region and intruding the Victory-Defiance complex have ages around 2660 Ma (see above). These are similar to the Kambalda Granodiorite suggesting a significant doming and development of regional antiforms synchronous with magmatism (see Czarnota et al., 2008). These rocks were intruded during D1 extension (Blewett et al., 2008; Czarnota et al., 2008) and their location in the tops of domes may have influenced or been influenced by the geometry of the region's faults. The granites and domes are located in the footwall of the east and west dipping faults (i.e., the anticline), suggesting that these rocks were emplaced into a horst position between grabens to the east and west. The change in volcaniclastic sedimentation (see above) and localised sources for the Black Flag Group suggests that the central corridor of the Kambalda Anticline was likely relatively elevated (into which magma was emplaced) and its flanks relatively depressed (into which volcanic detritus was deposited).

## 3.8.6 Geodynamics and structural history of the St Ives gold camp

### 3.8.6.1 Previous work

Previous interpretations of the deformation history for the St Ives camp vary from 2 to 4 contractional events, and depending on the study, with or without extensional events (Table 3.8.3). Significant differences exist in the various previous workers studies. These differences are partly due to improvements in exposure with development of new mines and workings, as well as the significant increase in drilling data. Most detailed structural work was conducted in the Victory-Defiance (Leviathan) Complex (Clark, 1987; Woodfull, 1993; Baltis, 1993; Bennett, 1995; Ruming, 2006), and Revenge mine (Nguyen, 1997), with additional studies in adjacent North Orchin mine (Nicholson, 2000; Marks and Strate, 2002), Argo mine (Gressier and Kolkert, 2002). These structural insights have been important in understanding the deformation evolution of the camp, but a coherent and internally consistent deformation framework has been lacking.

Prior to these detailed studies above, Gresham and Loftus-Hills (1981) focussed mainly on regional folding, while Archibald (1985) produced the first extensive synthesis of the structural, stratigraphic and metamorphic

history of the St Ives camp. Vearncombe et al. (1989) described the entire history in terms of shearing along the north-northwest-trending sinistral strike-slip faults that were linked to northwest-directed thrusts that were inverted in a subsequent extensional event. Both the thrusts and sinistral strike-slip faults were described as mineralised.

Further work in the 1990's refined the earlier structural models, although many of the studies focused on individual mines or relatively small areas. Nguyen (1997) worked mostly in the Revenge area (Figure 3.8.1d), and interpreted a comprehensive deformation history that partially correlated with the regional deformation history deduced by Swager (1997). Ruming (2006) described a comprehensive vein paragenesis for the Victory-Defiance (Leviathan) Complex (Figure 3.8.1d), and linked this with a deformation history comprising two major events and one minor event: (1) SW- to W-directed thrusting and the formation of the Victory Anticline, ('D2'); (2) broadly W- to northwest-directed thrusting ('D3'), and; (3) a northwest-southeast directed extension ('D4').

One of the major differences between this contribution and previous studies is the 'temporal position' of the north- to northwest directed thrusting. These are traditionally described as 'D1', but will be argued here, and in Blewett et al. (2008), that they are late (D4b).

### 3.8.6.2 A new structural framework for the St Ives region

The following section is an integration of previous interpretations integrated with the revised regional tectono-stratigraphic framework of Blewett et al. (2008). See Table 3.8.3 for a 'translation' of this framework from the traditional Swager (1997) nomenclature. This revised framework is a seven-fold history, and includes equal treatment of contraction and extension, this results in a larger number of D's than has been traditionally used (*cf.* Blewett and Czarnota, 2007c and Swager, 1997). This new contribution is based upon regional 3D map analysis (Henson and Blewett, 2006), potential field analysis (Chopping et al., 2008) together with targeted structural (Miller et al., 2008) and stratigraphic mapping (Squire et al., 2007).

#### D1 (ENE-WSW) extension 2720–2665 Ma

Regionally across the EGST, the D1 event has been defined as a prolonged period (2720–2665 Ma) of extensional deformation with a dominantly east-northeast-directed polarity during east-northeast-directed roll-back of a subduction zone (Blewett and Czarnota, 2007c; Czarnota et al., 2008).

Within the St Ives camp itself, the D1 extensional event has been recognised by previous workers (Nguyen, 1997; Barley et al., 2002; Conners et al., 2002). They interpreted the formation of the Kambalda sequence mafic-ultramafic stratigraphy as the volcanic product of an east-northeast-directed extensional event (enumerated as 'De1') that occurred between 2710–2690 Ma (see also Beresford et al., 2007). Conners et al. (2002) described major faults (such as the Lefroy) to have major changes in thickness (up to 5 km) of mafic-ultramafic stratigraphy across them (Figure 3.8.6). Lesser structures, such as the highly mineralised north-northwest-trending Playa Fault, also record a stratigraphic difference of around 1 km between the east and west across this structure (Conners et al., 2002). Changes in stratigraphic thickness were also described across east-west trending faults, such as the Gamma West and Mont Blanc Faults (Figure 3.8.6). Conners et al. (2002) interpreted a component of north-south extension to account for this. These ~east-west cross structures may simply reflect complex basement control and segmentation of an essentially east-northeast directed extensional system rather than a separate extensional event or vector (Figure 3.8.6).

Between 2690 and 2665 Ma the volcaniclastic Kalgoorlie Sequence (Black Flag Group) was deposited in a back-arc setting (Krapež et al., 2000; Barley et al., 2002). A number of unconformities and disconformities exist throughout the sequence, with a quiescent period between 2680 and 2670 Ma. These unconformities and disconformities were interpreted to reflect and local uplift and tilting of older sequences during ongoing extension (Blewett et al., 2004). More recent geochronological fingerprinting and provenance characterisation has recorded dramatic differences across the major north-northwest faults of the St Ives camp and across the Kambalda anticline (Squire et al., 2007) Many of these faults are strongly reactivated and the preservation of their early kinematic history can only be inferred from the stratigraphic record

Table 3.8.3: New Deformation Framework for the St Ives Region, with comparisons with previous published studies

| Blewett et al. 2008 | age | Structures and features at St Ives | Mueller 1988 | Swager 1997 | Nguyen 1997 and Conners et al. 2002 |
|---|---|---|---|---|---|
| D7 | <2400 Ma | Minor ENE contraction - intrusion of Proterozoic dykes | | | |
| D6 | ~2600 Ma? | not recognised at St Ives | | collapse | |
| D5 | 2625–2650 Ma | **Regional Dextral Transpression** (NNE faults): high level textures developed in this long lived event of NE-SW contraction manifest as folding and thrusting as well as dextral strike-slip faulting (e.g., Alpha Island Fault). Minor gold, but regionally very significant (e.g., Mt Charlotte and Sunrise Dam) - may be what was dated by Clark (1988) and Nguyen (1997) | D3 | D4 | D4 |
| D4b | 2650 Ma | **Regional Sinistral Transpression** (NNW faults): Main gold event in complex architectures with sinistral faults being accommodated across releasing and restraining bends. Releasing bends with extension E-W and ENE-WSW normal fault complexes, restraining bends with top to the NNW and SSE thrusts. Major transfer structures across Tramways and Republican Thrusts (they are not 'D1') and transect earlier F2 and F4 folds. Major foliation and vein development. | D2 | D3 | D3 |
| D4a | 2655–2650 Ma | **Regional Contraction** from ENE: inversion of Merougil Basin and upright folding and intense NNW foliation amplification of Kambalda Anticline, extensive thrusting to WSW or ENE. Gold deposition. | D1 | D2 | D2 |
| D3 | 2660–2655 Ma | **Regional Extension** to the NE: deposition of the clastic Merougil Basin, normal faults (e.g., at Santa Anna), NW dykes of porphyry (Flames), enriched porphyries, gentle diping penetrative foliation above expanding granite domes (e.g., Victory). Initial gold mineralisation. | | | DE3 |
| D2 | 2665–2660 Ma | **Regional Contraction** from ENE: Termination of volcanic stratigraphy, intrusion of Kambalda Granodiorite. Amplification of Kambalda Anticline, inversion of earlier growth faults (e.g., Playa, Foster) as thrusts. Some limited foliation development. | | | |
| D1 | >2665 Ma | **Regional Extension** to ENE: formation of Kambalda and Kalgoorlie Sequences. Development of growth faults and initial dome structure (footwall uplift) of the Kambalda Anticline. Pulsed event with internal hiatuses and unconformities | | | DE1-2 |

(Figure 3.8.1c). Significant granite production occurred during this period, with the large High-Ca granite batholiths or domes (Champion and Sheraton, 1997) being emplaced. Locally, the Kambalda Granodiorite was emplaced (~2662 Ma) into a step over or accommodation zone between opposite dipping segments of the Boulder-Lefroy Fault System in this D1 extensional environment. This suggests that the dome-anticline at Kambalda was established early and was simply tightened by later contractional events.

The D1 extension did not produced a penetrative S1 foliation in the St Ives camp, other than localised layer-parallel foliation and associated isoclinal folds in sedimentary units such as the Kapai Slate Formation (e.g., Nguyen, 1997). At the crustal level exposed in the St Ives camp, the main record of D1 extension is the in the facies and stratigraphic architecture. However, the early architecture was a key feature that controlled later fluid pathways at the time of mineralisation (see Miller et al., 2008; Neumayr et al., 2008).

### D2 (ENE-WSW) contraction 2665–2660 Ma

Across the EGST, the first significant east-northeast oriented contraction (D2) occurred around 2665–2660 Ma, terminating volcanism in the greenstones. A diachroneity (older in east and younger in the west) of around 5 My has been suggested for the onset of the D2 contractional event (Blewett et al., 2004; Czarnota et al., 2008).

Domains with disparate chemical and age associations were juxtaposed, signalling the shut off of the late-stage arcs in the Kalgoorlie Terrane (Barley et al., 2003; Cassidy et al., 2006).

In general, the D2 contraction developed without significant regional foliation development. D2 macroscopic structures indicate that shortening was oriented east-northeast–west-southwest, perpendicular to the grain of the D1 extensional orogen, and developed folds and faults.

In the Kalgoorlie Terrane, a series of upright north-northwest-trending granite-cored domes and antiforms are centred about an outward dipping and younging stratigraphy of greenstones. As suggested above these domes and anticlines likely initiated during D1 extension and were later tightened (as stratigraphy is commonly steeply dipping on the sides). To the north of the St Ives camp, is the south-plunging regional anticline-syncline pair at Ora Banda where pre-folded (north-northwest-trending) greenstone sequence is unconformably overlain by a Stage 2 late basin (Kurrawang). This relationship (together with equivalent ones at Welcome Well and Windara in the Kurnalpi Terrane to the northeast) provide an age constraint of >2660 Ma for the development of these basement folds (Blewett et al., 2004b), and infers that east-northeast-oriented shortening had at least commenced before the late basins were initiated. These workers described this folding event as D2a, but it is here simply called D2.

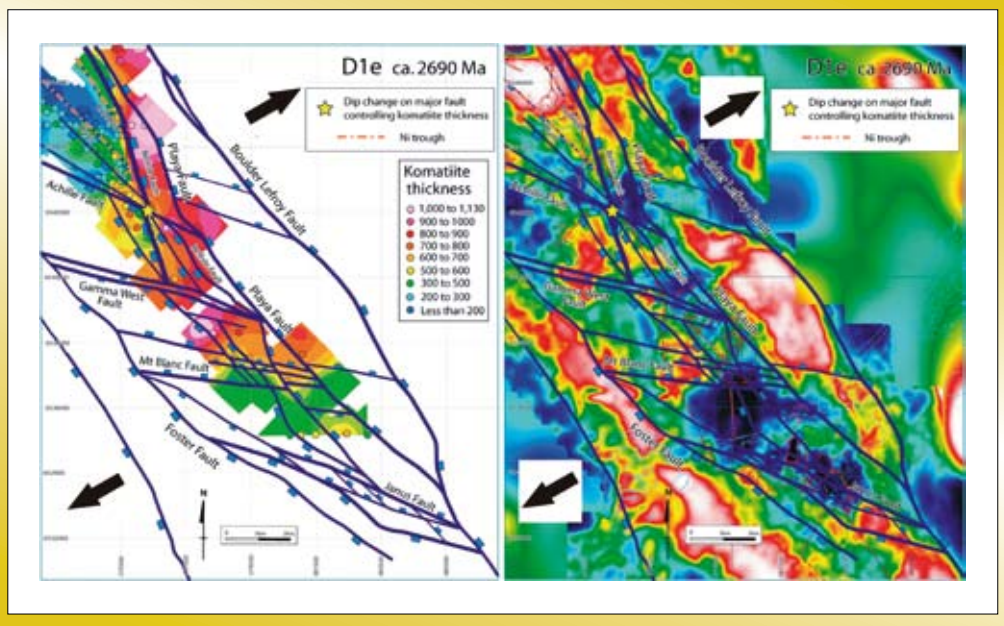


*Figure 3.8.6: Early extensional architecture with mapped onto isopachs of komatiite thickness (from Connors et al., 2005). Note the change in dip of the early faults across the Achille Fault with an associated change in komatiite thickness. The Mt Blanc Fault appears to be a key control on komatiite and also dolerite distribution. Same structural map overlain on a high pass filtered gravity image.*

In the centre of the St Ives camp lies the Kambalda Anticline. Like many of the regional antiforms, the Kambalda Dome has a weakly developed (or no) axial planar foliation (see Blewett and Czarnota, 2007a, b). Conners et al. (2002) also described large areas of greenschist facies mafic rocks throughout the camp that were intact and lacking foliation. Locally, however (e.g., in the Revenge area Figure 3.8.1d), intense steeply east-northeast-dipping flattening zones, marked by an intense S2 foliation defined by chlorite-carbonate (±amphibole), are common. These D2 flattening zones were also associated with east-trending barren carbonate-quartz veins, and together they suggest that D2 involved east-northeast to east-directed contraction. This S2 fabric is axial planar to meso- and macro-scale F2 folds (Nguyen, 1997).

Many of the D1 extensional faults were favourably oriented to reactivation during D2 contraction. Major reverse faults, such as the Foster, Repulse, Playa and Lefroy Faults, were active at this time (Miller et al., 2008). For example, the Foster Thrust has a throw of around 3 km across a 50 m wide zone of intense foliation that records reverse kinematic indicators (S-C-C') indicative of top to the north-northeast movement (Nguyen, 1997). The southeast extension of the Foster Thrust is not well constrained, and it appears to fold about the Kambalda Anticline and be truncated against the Playa Fault (Figures 3.8.1b). The Foster Thrust has a distinctive carbonate-silica alteration, and is different to the other (mineralised) shear zones in the camp. The Repulse Shear (which becomes a critical contractional jog during main stage D4b gold), and other related shears, developed as neoformed D2 linking thrusts between two reactivated (inverted) D1 extensional faults (Miller et al., 2008). Ongoing deformation during D2 and later events resulted in the neoformed faults eventually overprinting the earlier formed faults in some areas (e.g., the Janus Fault).

### D3 extension (ENE-WSW) 2660–2655 Ma

Regionally across the EGST, D2 contraction was followed by a dramatic change in tectonic mode (extensional high-strain shear zones and significant granite doming), greenstone type (late basin clastic sedimentation), and granite type (onset of Mafic- and Syenite-type granites) at D3 time (2665–2655 Ma). Two stages of D3 extension are described: D3a is multi-vector extension around exhuming granite domes (e.g., Wallaby and Kanowna Belle basins); D3b is uni-modal east-northeast-down extension (e.g., Merougil Basin to the west of the St Ives camp) along reactivated D2 thrusts and earlier D1 extensional faults (Blewett and Czarnota, 2007b, c; Blewett et al., 2008; Czarnota et al., 2008).

The D3 extensional event(s) also marked a change in the magmatic source region for felsic and intermediate magmas. The period from 2665–2655 Ma saw the introduction of Mafic-type (sanukitoid) granite magmatism across the EGST (Champion et al., 2001). These magmas are highly enriched and were derived from a metasomatised mantle source (a good source for gold and sulphur). Regionally, syenite magmatism (mantle sourced) commenced in the Kurnalpi and Burtville Terranes at this time, although these are minor magmas in the Kalgoorlie Terrane (Champion, 2006; Cassidy et al., 2006). This dramatic change in felsic magmatism suggests that a fundamental geodynamic adjustment occurred, rather than the system returning to the previous D1 extensional setting.

In the St Ives camp highly-enriched (in LILE and REE) porphyries intrude the D1 and D2 structural elements and so are D3 or younger in age. Nguyen (1997) dated a suite of quartz-albite porphyries (striking west-northwest to northwest at Revenge) at 2658 ±4 Ma, and suggested that these were related to extension and rifting during sedimentation of the Merougil Basin, consistent with the regional D3b extensional event (Blewett and Czarnota, 2007c). Ruming (2006) also described the main porphyry dyke swarm at Victory-Defiance to be a product of post D2 extension to the NE or SW, and Miller et al (2008) mapped reactivated D1 normal faults and intrusion of dyke swarms indicative of east-northeast extension.

Within the St Ives camp, mesoscale structural elements related to extension are equivocal (*cf.*, Ruming, 2006). However, Richards (1983) and Baltis (1993) both describe gently dipping crenulation cleavages and subvertical shortening (i.e., extension) that are younger than the porphyries and older than the main gold mineralisation (Figure 3.8.7). Interpreting the gently dipping crenulations as all being D3 in age is locally problematic (see below). Evidence for D3 extension is also preserved in the cross sections (and seismic reflection profiles) through the Santa Anna area (Miller et al., 2008), where normal faults throw the sequence down to the west and also cut earlier reverse

faults. In this area no inversion is observed on these (now) subvertical west-southwest dipping faults, rather the entire stratigraphy is tilted to the west along with these faults. This tilting is interpreted to be related to later D4a shortening and tightening of the Kambalda Anticline, and inversion (folding and foliation development) in the Merougil Basin further west (Figure 3.8.1).

Well-developed mesoscale examples of D3 structures are preserved in the Victory-Defiance mine. Here, the D3 structures are manifest as steeply-dipping north-northwest trending quartz veins (Figures 3.8.7, 3.8.8a, b, c). These D3 veins are commonly overprinted by reverse-sense (main gold) shear veins from later D4 events (see below).

## D4 contraction and sinistral transpression 2655–2650 Ma

Inverting the D3 extensional event after ~2655 Ma was the onset of east-northeast-oriented D4 contraction across the terranes of the EGST (Blewett et al., 2008). The D4 event has been subdivided into two distinct stages.

*Figure 3.8.7: Montage of photographs from underground outcrops and drill holes in the Victory-Defiance pit showing pronounced vertical flattening (extension). The event associated with this flattening is uncertain and it may be associated with magma pressure from below (D3) or related to transtensional zones across step overs in strike-slip faults (D4b). The overprint and crenulation of steep earlier foliation suggests that this vertical flattening is late (D4b), because there is only limited S2 foliation development. In this interpretation the foliation being crenulated is S4a, which is a pervasive north-northwest trending steeply dipping fabric. A) Down to the north normal-sense shear on faults and foliation associated with vertical flattening. B) Pervasive gently dipping S3? (flattening?) foliation cut by veins with adjacent carbonate alteration haloes. This foliation is not axial planar to a reclined thrust-ramp anticline. Note also sharp faults with top to the north apparent normal offsets. The veins form conjugate pairs that indicate σ1 was vertical, σ2 plunged E-W, σ3 plunged N-S. Section view to east onto a face around 4 m across. C) and D) Drill core (steep plunge) showing subhorizontal crenulations.*

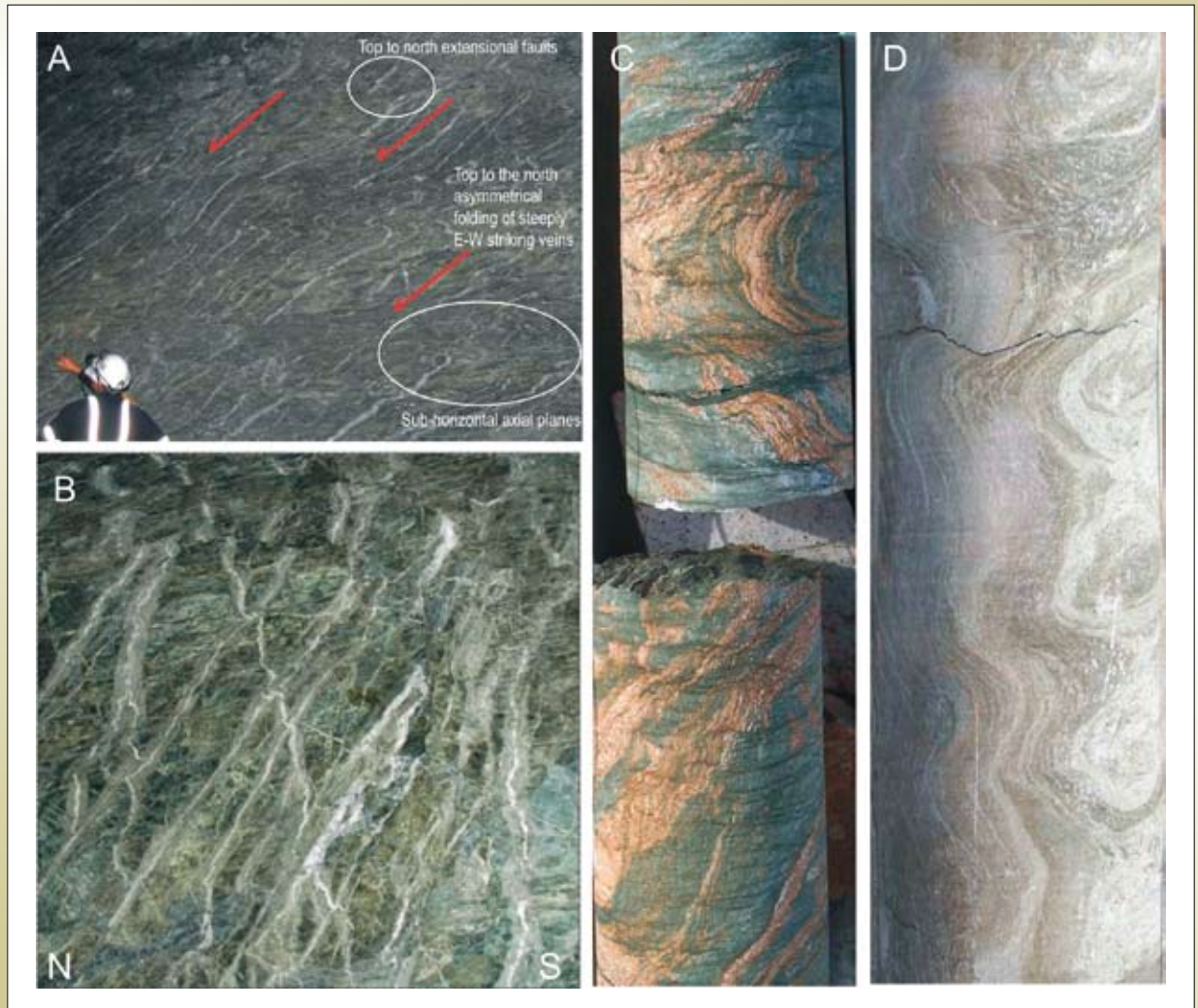

1. The first stage (D4a) involved horizontal compression with σ1 just north of east-west and a vertical σ3 (co-planar to the D2 stress field). D4a is characterised by pure shear (significant flattening), late basin inversion, north-northwest-striking upright folding and associated cleavage formation, reverse faulting and thrusting, and tightening of earlier domes and D2-D3 folds. The geometrical result was the rotation and steepening of stratigraphy (including late basins) along the margins of east-facing granite domes (e.g., Bardoc Tectonic Zone north of Kalgoorlie, Scotty Creek Basin at Lawlers, and the Mt Varden area north of Laverton). This event was termed 'D1' by Mueller et al. (1988), regional 'D2' by Swager (1997) and 'D2b' by Blewett et al. (2004b) as it overprints the late basins, and in the absence of D3 extensional elements or late basins, is easily mistaken for D2 (as defined herein).

2. The second stage (D4b) involved the development of north-northwest-striking, steeply-dipping ductile sinistral shear zones, associated with a slight clockwise rotation of σ1 to east-southeast west-northwest and a horizontal σ3. Sinistral strike-slip shear zones developed in regions with steep-dipping stratigraphy, at the limbs of regional folds and meridional dome margins, and these are commonly reactivated earlier

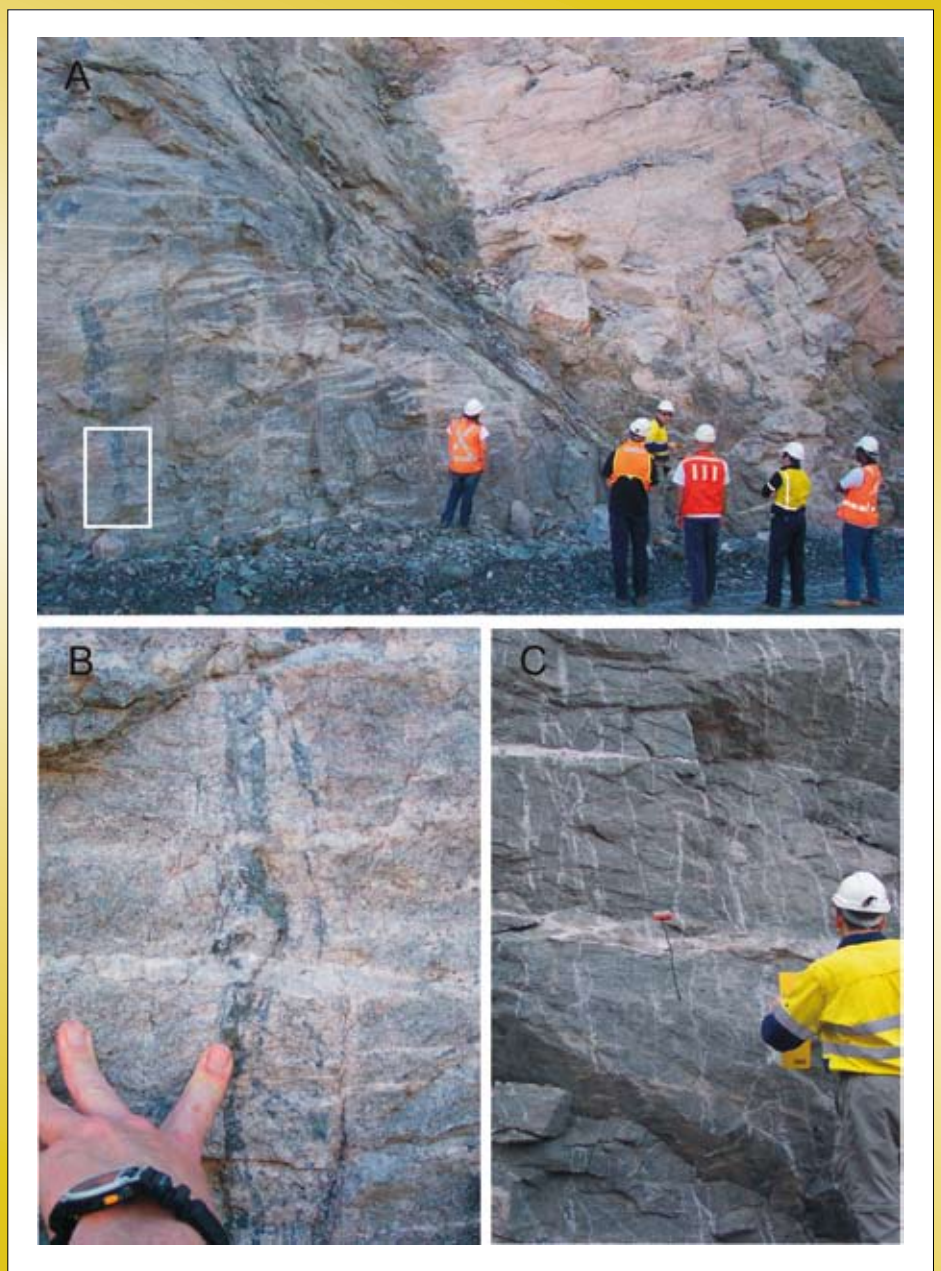


*Figure 3.8.8: A) View northeast onto the Repulse Shear Zone (top left to bottom right of photograph) with well-developed shear foliation (S4b) indicative of top to the northwest transport. White rectangle is approximate position of photograph B. B) Detail of overprinting S4b (gently dipping veins) of steeply-dipping smoky quartz veins in the footwall of the Repulse Shear Zone (see white rectangle). C) Steeply dipping conjugate S3 veins that strike northwest and indicate extension to the northeast with σ1 near vertical. These S3 vein arrays are also transected by gently dipping shear veins of likely D4b origin.*

normal (D1 and D3) and reverse (D2 and D4a) faults. Linked to these strike-slip faults across the nose of granite domes (Kanowna Belle, Laverton), or regional anticline hinges (Kambalda-Kalgoorlie) are synchronous thrusts and folds. The D4b event equates (Table 3.8.3) to the 'D2' event of Mueller et al. (1988) or the 'D3' deformation of Swager (1997), Nguyen (1997) and Weinberg et al. (2005). Most of the region's gold is associated with this event.

**D4a (ENE-WSW) contraction - thrusting <2655 Ma**

Ruming (2006) interpreted the main penetrative (primary) fabric elements in the Victory-Defiance area (Figure 3.8.1c), which are steeply dipping north-northwest-trending ductile foliations, to be associated with east-northeast- to east-directed contraction, and resultant thrusting. These fabrics (he enumerated them SWP and SEP) overprint lamprophyres (undated) and porphyries (which also intrude the lamprophyres) which are geochemically similar to the 2658 ±4 Ma porphyries at Revenge (described above). This maximum age for the foliations could be just younger than 2662 Ma and therefore these structures could be interpreted as D2 in age. However the likely age is at the younger end of the error bars of this age range (~2655 Ma), and the preferred interpretation for these structures is D4a. This interpretation is based on the inference that these lamprophyres and Mafic-type porphyries that are transected by the foliations in question were likely sourced from a metasomatised mantle wedge (Cassidy et al., 2002; Halley et al., 2007; Beakhouse, 2007). These magmas on regional grounds were not emplaced until syn to late D3 extension (Czarnota et al., 2008), and so any foliation cutting them must be younger.

Woodful (1993) and Clark (1987) described the Stage 2 veins at Victory-Defiance to have developed during east-northeast west-southwest contraction and flattening. These veins are most commonly developed in the porphyries and are translucent quartz-rich steeply dipping extension veins. Miller et al. (2008) mapped the active D4a and D4b faults in the St Ives camp, and noted that depending on the orientation of the fault, they operated as sinistral strike-slip (both transtensional and transpression) as well as reverse and normal faults. The D4a event tightened the Kambalda Anticline and tilted stratigraphy by as much as 30° (e.g., at Santa Anna). The development of the syncline and associated axial planar foliation in the Merougil Basin in the west of the area occurred during the D4a event.

**D4b (ESE-WNW) sinistral transpression ~2650 Ma**

Across the EGST the generally low-strain structures associated with the D4b event resolve a locally highly variable stress field with $\sigma 1$ ranging from east-southeast-west-northwest to north-south in orientation. This large variation in the local stress field is inferred to be a direct consequence of the development of sinistral strike-slip shear zones on a pre-existing highly anisotropic architecture, primarily composed of doubly-plunging granite domes overlain by folded greenstones (Blewett et al., 2004a; Blewett et al., 2008). The D4b event accompanied major gold mineralisation in Laverton (Miller, 2006), and occurred around 2650 Ma (Brown et al., 2002; Salier et al., 2004; Miller, 2006). Mueller et al. (1988) described this D4b event in the Kambalda Domain as the first of the significant strike-slip faulting (sinistral) events to deform the EGST (Table 3.8.3).

In the St Ives camp, the sinistral strike-slip transfer structures are represented by the main faults of the area (Playa, Lefroy and Speedway Faults), and the associated major thrusts are the Republican and Tramways Faults. Locally across the camp, $\sigma 1$ was northwest- to north-oriented across restraining bends where localised thrusts developed despite the regional stress field being oriented east-southeast–west-southwest (e.g., Tramways and Republican Thrusts). The D4b event resulted in numerous mineralised minor thrusts, sinistral-reverse shear zones and vein arrays (Baltis, 1993; Woodful, 1993; Bennent, 1995; Nguyen, 1997; Ruming, 2006) under an east-northeast west-southwest stress field (Miller et al., 2008). In the Revenge area (Figure 3.8.1d), the assemblages associated with D4b shears include chlorite-biotite-carbonate or albite-carbonate-pyrite (Nguyen, 1997).

Baltis (1993) described a complex evolution of the D4b event with co-axial stress axes oriented northwest, northeast and vertical, but varying in magnitude (i.e., $\sigma 3$ ranging from vertical during thrusting to northeast-horizontal during sinistral strike slip shearing). The sequence of events included:

1. sinistral strike-slip deformation followed by,

2. major northwest-directed thrusting that was,

3. inverted by extensional flattening crenulation and shearing (see Figure 3.8.7) which was,

4. overprinted by a final (low-strain) northwest-directed thrust event.

The last low-strain thrust event and the earlier extensional event hosted the main mineralisation event and they utilised the previously developed architecture.

Recent mapping by Miller et al. (2008) has confirmed the linkage between the northwest-directed thrusts and the strike-slip transfer faults, consistent with the regional interpretation for the corridor (Blewett and Czarnota, 2007c) and the similar relationship at Kanowna Belle (Davis et al., 2008). Previously, Vearncombe (1987) undertook a limited mapping study in the Victory-Defiance mine and adjacent Kambalda area and concluded that gold mineralisation was associated with southeast-down extension. It is likely that he described elements of this D4b extensional step-over system. Favourable geometrical relationships between sinistral strike-slip faults develop releasing bends and localised extension-dilation (normal faults) in some areas (Miller et al., 2008). For example, despite all being essentially developed during the same Db event:

- the Mars pit has sinistral-reverse and west-northwest normal (extensional) faulting;
- the Minator pit has west-over-east thrusting; and,
- the Agamemnon pit has south-south directed normal (extensional) faulting (Miller et al., 2008).

Neumayr et al. (2005; 2008) noted west-northwest trending porphyry swarms, alteration minerals and gold which is at a high angle the strike of the camp. Miller et al. (2008) interpreted these structures as transfer and accommodation structures during the D4a transpressional event. This suggests that these structures may have had an earlier inception and have been re-used during D4.

Common features seen underground and in core from the Victory-Defiance pit are gentle dipping fabrics and horizontal crenulations, and these are associated with north- and south-dipping normal faults (Figure 3.8.7). These fabric elements are cut by and cut the main gold veins and shears and are therefore interpreted to be part of the D3 extensional event (as mentioned above). The crenulations also overprint a pervasive foliation that is likely to be the S4a fabric (because S2 is weakly developed and S3 would be subhorizontal). Significant veining and alteration is associated with this event. In this location, above a major dome apex, the role of magma emplacement (developing a vertical $\sigma 1$ from below) can not be discounted in the formation of these 'extensional' structures.

This D4b sinistral transpressional event has been inferred regionally to be ~2650 Ma in age (Blewett et al., 2008). This is the main gold event (by correlation) in the St Ives camp and yet an age of 2627±7 Ma rutile age for retrograde alteration (Clark, 1989) and ~2631 Ma monazite age (Nguyen, 1997) has been commonly quoted. Three interpretations are likely: a) this is the same event as Laverton, but deformation was highly diachronous (~20 My younger in the west) between Laverton and Kambalda; b) unrealised younger mineralisation (e.g., D5) was dated, or c) the ages are reset.

### D5 (NE-SW) dextral transtension (2647–2630 Ma)

The last gold-bearing event across the EGST was developed during D5 dextral transtension (and local transpression), accompanying the emplacement of Low-Ca granites and characterised by brittle/ductile north- to north-northeast striking dextral strike/oblique-slip faults (Blewett et al., 2004a; Blewett et al., 2008). Regionally the D5 event equates to the 'D4' event of Swager (1997). Swager (1997), and later Weinberg et al. (2003), suggested that the last NE-SW contractional event was a progressive lower-strain stage from earlier 'D2' and 'D3'. However, a significant rotation of the palaeostress field (~60°) occurred between the earlier D4b sinistral ($\sigma 1$ east-southeast west-northwest) and the D5 dextral ($\sigma 1$ northeast-southwest) events, so the transition was not progressive but probably marked a major plate reconfiguration. This palaeostress rotation was noted by Nguyen (1997) and Mueller et al. (1988); both described this as a separate dextral strike-slip event, distinct from the earlier sinistral event that it overprints (Table 3.8.3). The D5 event is remarkably consistent across the EGST and therefore forms a good marker for structural correlation across the region. It also appears to be relatively long-lived and is inferred to be synchronous with the emplacement of the Low-Ca granites.

In the St Ives camp, the D5 event is manifest as brittle subvertical strike-slip north- to north-northeast trending dextral faults and east-trending sinistral faults, with the Alpha Island Fault being the best example (Figure 3.8.5). Nguyen (1997) described these structures as 'D4' and clearly overprinting the earlier sinistral strike-slip and northwest-directed thrust structural elements. Mineralisation is recorded with these D5 structures, and in the Revenge area is associated with albite-carbonate-chlorite.

More work is needed in the St Ives area to examine the further potential for gold in these structures. Elsewhere in the EGST, tellurides and base-metals are common with the gold during the D5 event (e.g., at Kanowna Belle, Mulgarrie, Sunrise Dam, Charlotte, Kundana etc). The Victory-Defiance area displays significant late-stage extension; with east-northeast west-southwest subvertical Stage 4 veins, horizontal crenulation cleavages, boudinage of Stage 3 veins, and ductile and brittle normal faults (Ruming, 2006). Based on the southeast-plunging stretching lineations and orthogonal (SW-plunging) boudin necks (of Stage 3 veins), extension in the Victory area was directed to the southeast (Vearncombe, 1987; Ruming, 2006). As these structures are mineralised they unlikely to be related to the later D6 (unmineralised) late collapse (see below). The reason extension occurred in the Victory area was due to the reversal of the shear sense of a north-northwest-trending architecture from the D4b sinistral transpression to dextral transtension across the same structures (Miller et al., 2008).

### D6 late extension

The last event inferred to be part of the EGST tectonic cycle (cratonisation of the Yilgarn) is systemic collapse (Blewett et al., 2008). This event is characterised by mostly low-strain crenulations, with sub-horizontal axial planes at a range of amplitudes from millimetres to metres. The fold hinges plunge variably. The structural style is brittle to locally brittle-ductile normal faulting. No specific vector of extension has been defined; and the driver for this extension may have been a readjustment of localised topographic highs from earlier events rather than a regional or far-field control. Structures ascribed to this event across the region have been noted previously by Swager (1997), Davis and Maidens (2003) and Weinberg et al. (2003). No definitive late extension has been identified in the St Ives camp.

### D7 (ENE-WSW) contraction (<2500 Ma)

The D7 event occurred across the EGST and was associated with minor east-northeast-oriented contraction and the emplacement of dolerite dyke swarms and minor east-west sinistral strike-slip faults. Numerous small displacement faults occur in the granite pavements of the external granites (Blewett et al., 2004a). Swager (1997) also described similar structures. These are all likely Proterozoic in age and may reflect events at the craton margin (e.g., Albany Fraser and Capricorn). In the Victory-Defiance area gypsum-bearing northeast-directed thrusts (reverse faults) cut the otherwise undeformed Proterozoic dolerite dyke.

## 3.8.7 Discussion and exploration implications

Domes-antiforms play a crucial role in the architectural development of many (all?) of the major gold deposits of the EGST (Henson et al., 2005). Many of the domes were also initiated early in the geological evolution (D1), in conjunction with the stratigraphy that was controlled by faults (e.g., Conners et al., 2002; Blewett and Czarnota 2007c; Squire et al., 2007; Blewett et al., 2008; Miller et al., 2008). The Kambalda Anticline is one such example, and this is part of a linked system that extends from St Ives to Kalgoorlie. The exploration implications of this is that the domes and, more importantly, the basin controlling faults become pathways for later mineralising fluids during reworking events. 'Looking through' the late overprints (which is commonly in contractional settings) in order to unravel the early extensional architecture, is a key task for predictive mineral discovery.

The three fault segments (Kalgoorlie, New Celebration and Playa Faults) are regularly spaced at ~30 km and all three segments trend ~340° (Figure 3.8.1b). The northern two segments dip west and the southern segment dips east. The accommodation zone between these opposing dips is occupied by the granite-cored Kambalda Dome. The age of the dome is 2662 ±6 Ma (Compston et al., 1986), suggesting that these fault segments and associated accommodation zone were active up to and during this time. Accommodation zones at fault tips are well known for their 'leakiness'. For example, many of the volcanic centres in the East African Rift are sited on the accommodation zones between opposing and linking fault segments. However, the location of the main mine camps

between St Ives and Kalgoorlie lies in the approximate centre of the original segments of the Boulder Fault (in north) and Lefroy Fault (in the south) (Figure 3.8.1). The centre of the fault segments are where maximum extensional fault displacement occurred. It is likely that in these central maximum displacement regions that the greatest synthetic-antithetic faults developed along with the bounding structures. The result was the creation of an efficient permeable architecture for later fluid flow on reactivation. The reason the Kalgoorlie is so well focussed in comparison to St Ives may be a function of the nature of this permeability creation early in the history of the belt. Numerical simulations could be used to explore the nature of these relationships and better understand the fluid flow differences around Kalgoorlie and St Ives respectively.

Another feature of the domes was their influence on the fault kinematics on reactivation. All of the large region granite-cored domes have marginal strike-slip faults linked to dome closure thrusts (e.g., Scotia-Kanowana Dome: Davis et al., 2008; the Mt Margaret Anticline: Miller, 2006; Blewett et al., 2008; the Lawlers Anticline: Blewett and Czarnota, 2007a, b). A similar relationship occurs around the Kambalda Dome with linked thrusts and sinistral strike slip faults developing during the D4b event (Blewett et al., 2008). The D4b event (~2650 Ma) involved significant rotation of the far-field stress vector from a long history of north of east to one of south of east. The rotation of the stress field was important because when this new contractional vector was applied to pre-existing structures a difficult architecture was encountered. The result was maximum damage as the system tried to 'iron-out' the bends, kink and jogs, especially basin-dome margin structures. Micklethwaite and Cox (2006) have demonstrated why contractional jogs are regions of significant damage and earthquake aftershock – and therefore sites favourable to fluid flow and hence mineralisation.

In a significant change from the Swager (1997) framework, the south-over-north thrusts from the Kambalda and Kanowna areas (*viz*, Tramways Republican, and Fitzroy) are now interpreted as relatively late – D4b (Henson et al., 2005; Blewett et al., 2008). In the past, this event was called regional 'D1' and was thought by many to have developed roughly east-west trending thrusts and folds (e.g., Archibald, 1985; Swager and Griffin, 1990; Swager, 1997; Nguyen, 1997; Conners et al., 2002; Weinberg et al., 2005). A number of problems with the Swager (1997) and others' interpretation are listed below, and they include:

- It was assumed that there was only one significant extrusive layer of komatiites, so observations of stacked komatiites pre-supposed thrust repetition. Detailed volcanology has demonstrated intrusive komatiites across the region (Trofimovs et al., 2004; Beresford et al., 2007), as well as a number of layers of flows. Intrusive komatiites are also noted in the St Ives camp. Therefore the presence of stacked komatiites does not necessarily imply thrusting.
- The 'D1' thrusting was interpreted to be the event that amalgamated the terranes. However, accreting north-northwest-trending slices with a north-south shortening vector would not be effective unless there was a major strike-slip margin and the terranes were slid in from the side (Barley et al., 2002; Krapež et al., 2007).
- The 'D1' thrusts have been only described from the dome apices and antiform closures, but if they were of regional extent they should be expected in the equivalent synformal areas.
- The inferred age of 'D1' was thought to be ~2675 Ma (Swager, 1997), which is older than the upper half of the Kalgoorlie sequence (which is as young as 2665 Ma: Krapež et al., 2000; Sircombe et al., 2007), and which was deformed by these same thrusts (see also Conners et al., 2002).
- Most importantly, the map patterns of these thrusts show that they overprint F2 folds and not the other way around (Henson et al., 2005). In the vicinity of the Tramways and Republican Thrusts in the southern part of the camp, Nguyen (1997: Fig 3.1) showed F2 folds refolded by her 'F3' folds (Table 3.8.3) that are parallel to the east-northeast-trending thrusts (which she called 'D1').

An analogy of how north-directed thrusts developed at a high angle to north-northwest-trending D4b sinistral strike-slip faults exists in the eastern Gobi-Alty region of Mongolia (Bayasgalan et al., 1999). Thrusts in this example develop at the terminations of major strike-slip faults, acting as accommodation structures to rotational strain, and at restraining step-overs, accommodating displacement between parallel strands of a strike-slip fault system. One can imagine that a granite-cored dome would be difficult

to dissect and the weaker steeper dipping greenstone belt margins accommodate D4b strain by strike-slip faulting. The strain still needs to be accommodated, and thrusting was the most effective method.

Gold was deposited three to four times 2665 to 2630 Ma in the EGST, including the St Ives region. One important unanswered question concerns the source of this gold. Did the gold come in early (during D3), synchronous with (or derived from) the Mafic-type porphyries and lamprophyres (Rock et al., 1987; Mueller et al., 2007; Halley, 2007), and then get remobilised into later structures at later times (to record the multiple events). The geologically similar Abitibi subprovince in Canada has a close temporal and spatial relationship with these rocks and gold (Beakhouse, 2007). One thing is certain, the best deposits all have the enriched magmas (Halley, 2007); so these rocks should form a first-order search criterion. However, the succession of gold events and the singular Mafic-type intrusive event in the EGST (and the St Ives region) suggests that additional processes operated here. These additional gold events maybe remobilisation of this gold into newly active structures and was driven by the EGST's strong (thermal) overprint which is seen as the large Low-Ca granite bloom (Czarnota et al., 2008). Alternatively, there was more than one gold source and structure-architecture is the key to predicting the location of gold deposits. No Low-Ca granites are exposed in the region. These are almost without exception intruded 2–3 km below the base of the greenstones and into the cores of regional domes (Blewett et al., 2007). Such a position in the St Ives area is in the top of the dome beneath the Victory-Defiance Complex, and so this may explain why the region records multiple gold events.

## 3.8.9 Conclusions

Gold was deposited in the St Ives region relatively late in its history (after 2660 Ma). Despite this, the region's endowment is determined as much by these later events as by the early history that established the fault and fold architecture as well as the broad distribution of rock packages themselves. Unravelling the early structural and architectural history, which was dominated by extension, is a critical step in predicting the distribution of later gold depositional sites. The role of early-formed anticlines (developed during footwall uplift and doming) influenced the siting of growth faults throughout greenstone deposition, and was also important in controlling the location of intrusions (both mafic and felsic). The inversion of this complex architecture permitted differential movements and therefore dilation to occur in some places in favour to others. Similarly, this complex architecture created a suitable network-pathway for a range of fluid types to meet (and mix?) and form high-grade gold deposits several times in the same place. The architectural framework in the St Ives region was likely too distributed to form a single giant deposit (*cf.* Golden Mile and St Ives), and was dominated by a number of dilation zones rather than a single highly efficient one.

## 3.8.10 Acknowledgements

We would like to express our gratitude to the geologists and management of Gold Fields St Ives for their support and encouragement throughout the ***pmd*CRC*** and in permitting us access to their ground. Published with permission of the CEO of the ***pmd*CRC*** and the CEO of Geoscience Australia (RB, PH, DC).

## 3.8.11 References

Archibald, N.J., 1985, The stratigraphy and tectono-metamorphic history of the Kambalda-Tramways area. WMC Internal Report K2889.

Bader, K., 1994, Geology of the Merougil Formation, Kambalda, Western Australia. Unpublished Honours thesis, Monash University, Victoria.

Barley, M.E., Brown, S.J.A., Krapež, B. and Cas, R.A.F., 2002, Tectonostratigraphic Analysis of the Eastern Yilgarn Craton: an improved geological framework for exploration in Archaean Terranes. AMIRA Project P437A, Final Report.

Barley M.E., Brown, S.J.A., Cas, R.A.F., Cassidy, K.F., Champion, D.C., Gardoll, S.J., and Krapež, B., 2003. An integrated geological and metallogenic framework for the eastern Yilgarn Craton: Developing geodynamic models of highly mineralised Archaean granite-greenstone terranes. AMIRA Project P624, Final Report.

Bayasgalan, A., Jackson, J., Ritz, J.F., and Carretier, S., 1999, Field examples of strike-slip fault terminations in

Mongolia and their tectonic significance, Tectonics, 18, 394–411.

Beakhouse, G.P., 2007, Structurally Controlled, Magmatic Hydrothermal Model for Archaean Lode Gold Deposits: A Working Hypothesis. Ontario Geological Survey Open File Report 6193, 133 p.

Beresford, S.W., Fiorentini, M., Hronsky, J.M.A., Rosengren, N., Bertuch, D.I., Saleem, A., Cas, R.A.F., Stone, W.E., Duuring, P., Bekker A. and Barley, M., 2007, Komatiite-hosted NI-CU-(PGE) deposits: understanding deposit and camp footprints. in Kalgoorlie 2007 edited by F Bierlien and C Knox-Johnson: Geoscience Australia, Record 2007/14, 159–163.

Bennett M.A., 1995, The structure and timing of gold mineralisation in the Victory area and its relationship to regional deformation and mineralisation in the Eastern Goldfields. Unpublished Technical Report T/005, Western Mining Corporation Pty. Ltd.

Blewett, R.S., Cassidy, K.F., Champion, D.C., and Whitaker, A.J., 2004a, The characterisation of deformation events in time across the Eastern Goldfields Province, Western Australia. Geoscience Australia Record, 2004/10 [CDROM].

Blewett, R.S., Cassidy, K.F., Champion, D.C., Henson, P.A., Goleby, B.R., Jones, L., and Groenewald, P.B., 2004b, The Wangkathaa Orogeny: an example of episodic regional 'D2' in the late Archaean Eastern Goldfields Province, Western Australia. Precambrian Research, 130, 139–159.

Blewett, R.S., and Czarnota, K., 2007a, The Y1-P763 project final report November 2005. Module 3 - Terrane Structure: Tectonostratigraphic architecture and uplift history of the Eastern Yilgarn Craton, Geoscience Australia Record 2007/15 112p. [DVD].

Blewett, R.S., and Czarnota, K., 2007b, Diversity of structurally controlled gold through time and space of the central Goldfields Superterrane – a field guide. Geological Survey of Western Australia Record 2007/19, 65p.

Blewett, RS, and Czarnota, K, 2007c, A new integrated tectonic framework of the Eastern Goldfields Superterrane, *in* Kalgoorlie 2007 *edited by* F Bierlien and C Knox-Johnson: Geoscience Australia, Record 2007/14, 27–32.

Blewett, R.S., Czarnota, K., Henson P.A. and Champion, D.C., 2008, A revised tectono-stratigraphic framework for the Eastern Yilgarn Superterrane. Part III, this volume.

Brown, S.M., Fletcher, I.R., Stein, H.J., Snee, L.W., and Groves, D.I., 2002, Geochronological constraints on pre-, syn-, and post-mineralisation events at the world-class Cleo gold deposit, Eastern Goldfields Province, Western Australia. Economic Geology, 97, 541–559.

Cassidy, K.F., Champion, D.C., Krapež, B., Barley, M.E., Brown, S.J.A., Blewett, R.S., Groenewald, P.B., and Tyler, I.M., 2006, A revised geological framework for the Yilgarn craton, Western Australia: Western Australia Geological Survey Record 2006/8, 8 p.

Champion, DC, 2006, Terrane, domain and fault system nomenclature, in 3D Geological Models of the Eastern Yilgarn Craton – Y2 Final Report ***pmd*CRC*** edited by RS Blewett and AP Hitchman: Geoscience Australia, Record 2006/4, p. 19–38 [DVD-ROM].

Champion, D.C., and Sheraton, J.W., 1997, Geochemistry and Nd isotope systematics of Archaean granites of the Eastern Goldfields, Yilgarn Craton, Australia; implications for crustal growth processes. Precambrian Research, 83, 109–132.

Chopping, R., Cleverley, J.S., Henson, P.A. and Roy, I.G., 2008, Reactive transport models: from geochemistry to geophysics to exploration targets. Part III, this volume

Clark, M.E., 1987, The geology of the Victory gold mine, Kambalda, Western Australia. Unpublished PhD thesis Queens University Ontario.

Clark, M.E., Carmichael, D.M., Hodgson, C.J., and Fu, M., 1989, Wall-rock alteration, Victory gold mine, Kambalda, Western Australia; processes and P-T-X (sub CO2) conditions of metasomatism. In: R.R. Keays, W.R.H. Ramsay, and D.I. Groves, (Eds), The geology of gold deposits; the perspective in 1988. Economic Geology Monograph 6, 445–459.

Clout, J.M.F., 1991, Geochronology of the Kambalda-Kalgoorlie area: a review. Unpublished WMC technical report No 187.

Claoué-Long, J.C., Compston, W., and Cowden, A., 1988. The age of the Kambalda greenstones resolved by ion microprobe - implications for Archaean dating methods. Earth and Planetary Science Letters, 89, 239–259.

Compston, W., Williams, I.S., Campbell, I.H., and Gresham, J.J., 1986. Zircon xenocrysts from the Kambalda volcanics: age constraints and direct evidence for older continental crust below the Kambalda-Norseman greenstones. Earth and Planetary Science Letters, 76, 299–311.

Connors, K., Donaldson, J., Morrison, B., Davy, C., and Neumyar, P., 2003, The Stratigraphy of the Kambalda-St Ives District:workshop notes Goldfields Pty Ltd St Ives operation, unpublished Technical note No: TN SIG0329, 99 p.

Czarnota, K., Champion, D.C., Cassidy, K.F., Goscombe, B., Blewett, R.S., Henson, P.A. and Groenewald, P.B., 2008, Geodynamics of the Eastern Goldfields Superterrane, *Part III this volume*.

Davis, B.K., and Maidens, E., 2003, Archaean orogen-parallel extension; evidence from the northern Eastern Goldfields Province, Yilgarn Craton, Precambrian Research, 127, 229–248.

Davis, B.K., Blewett, R.S., Squire, R., Champion, D.C. and Henson, P.A., 2008. Architectural and geodynamic controls during Au mineralisation at the Archaean Scotia-Kanowna Dome, Kalgoorlie Terrane, Western Australia, *Part III this volume*.

Gauthier, L., Hagemann S., and Robert, F., 2007, The geological setting of the Golden Mile gold deposit, Kalgoorlie, WA. *In:* Kalgoorlie 2007 *edited by* F Bierlien and C Knox-Johnson: Geoscience Australia, Record 2007/14, 181–185.

Goleby B.R., Korsch R.J., Fomin T., Bell B., Nicoll M.G., Drummond B.J., and Owen A.J., 2002, Preliminary 3-D geological model of the Kalgoorlie region, Yilgarn Craton, Western Australia, based on deep seismic-reflection and potential field data. Australian Journal of Earth Sciences 49, 917.

Goscombe, B., Blewett, R.S, Czarnota, K., Maas, R., and Groenewald, B.A., 2007, Broad thermo-barometric evolution of the Eastern Goldfields Superterrane. *In:* Bierlein, F.P., and Knox-Robinson, C.M., (Eds), 2007. Proceedings of Geoconferences (WA) Inc. Kalgoorlie '07 Conference. Geoscience Australia Record 2007/14, 33–38.

Gresham, J.J. and Loftus-Hills, 1981, The geology of the Kambalda nickel field, Western Australia. Economic Geology 76, 1373–1416.

Gressier, J.M., and Kolkert, R., 2002, Structural controls on gold mineralisation of the Argo Deposit, Western Australia. *In:* Vearncombe S. (Ed) Applied Structural Geology for Mineral Exploration and Mining, Australian Institute of Geoscientists Bulletin 36, 72–74.

Halley, S. 2007, Mineral mapping – how it can help us explore in the Yilgarn Craton. *in* Kalgoorlie 2007 *edited by* F Bierlien and C Knox-Johnson: Geoscience Australia, Record 2007/14, 143–144.

Hand, J.L., 1998, The sedimentological and stratigraphic evolution of the Black Flag Beds, Kalgoorlie, Western Australia: implications of regional stratigraphy and basin setting of the Kalgoorlie Terrane. Unpublished PhD thesis Monash University, Melbourne.

Henson, P.A., Blewett, R.S., Champion, D.C., Goleby, B.R. and Cassidy, K.F., 2004. Using 3D 'map patterns' to elucidate the tectonic history of the Eastern Yilgarn. In Barnicoat, A.C., and Korsch, R.J., (Eds), Predictive Mineral Discovery Cooperative Research Centre: Extended Abstracts from the June 2004 Conference. Geoscience Australia, Record 2004/9, 87–90.

Henson, PA, 2006, Chapter 2: An integrated geological and geophysical 3D map for the EYC, in 3D Geological Models of the Eastern Yilgarn Craton – Y2 Final Report ***pmd*CRC*** edited by RS Blewett and AP Hitchman: Geoscience Australia, Record 2006/04, p. 32–85 [DVD-ROM].

Henson, PA, and Blewett, RS, 2006, 3D interpretation of the Eastern Yilgarn: new architectural insights from construction of the 3D map, in 3D Geological Models of the Eastern Yilgarn Craton – Y2 Final Report ***pmd*CRC*** edited by RS Blewett and AP Hitchman: Geoscience Australia, Record 2006/04, p. 207–216 [DVD-ROM].

Henson, P.A., Blewett, R.S., Champion, D.C., Goleby, B.R., and Czarnota, K., 2007, How does the 3D architecture of the Yilgarn control hydrothermal fluid focussing. *In* Kalgoorlie 2007 *edited by* F Bierlien and C Knox-Johnson: Geoscience Australia, Record 2007/14, 57–61.

Krapež, B., Brown, S.J.A., Hand, J., Barley, M.E., and Cas, R.A.F., 2000, Age constraints on recycled crustal and supracrustal sources of Archaean metasedimentary sequences, Eastern Goldfields Province, Western Australia, Evidence from SHRIMP zircon dating. Tectonophysics, 322, 89–133.

Lesher C.M. and Arndt N.T., 1995, REE and Nd isotope geochemistry, petrogenesis and volcanic evolution of contaminated komatiites at Kambalda, Western Australia. Lithos 34, 127–157.

Marks, B., and Strate, T., 2002, Pinch and swell development art North Orchin mine and grade distribution. In: Vearncombe S. (Ed) Applied Structural Geology for Mineral Exploration and Mining, Australian Institute of Geoscientists Bulletin 36, 125–126.

Micklethwaite, S. and Cox, S. F., 2006, Progressive fault triggering and fluid flow in aftershock domains: Examples from mineralized Archaean fault systems: Earth and Planetary Science Letters, v. 250, p. 318–330.

Miller, J.M., 2006, Linking structure and mineralisation in Laverton, with specific reference to Sunrise Dam and Wallaby. In: A.C. Barnicoat, and R.J. Korsch (eds). Predictive Mineral Discovery CRC- Extended Abstracts for the April 2006 Conference. Geoscience Australia Record 2006/7, 62–67.

Miller, J.M., Tunjic, J., Donaldson, J., and Blewett, R.S., 2008, Structural evolution of the Victory to Kambalda region of the St Ives gold camp: the role of early formed structures on the development of a major gold system. Part III, this volume.

Morris, P.A., 1993, Physical volcanology and geochemistry of Archaean mafic and ultramafic volcanic rocks between Menzies and Norseman, Eastern Yilgarn Craton, Western Australia. Geological Survey of Western Australia Report 36.

Mueller, A.G., Harris, L.B., and Lungan, A., 1988, Structural control of greenstone-hosted gold mineralisation by transcurrent shearing; a new interpretation of the Kalgoorlie mining district, Western Australia. In Ho, S.E., and Groves, D.I., (Eds), Advances in understanding Precambrian gold deposits – Volume II. Geology Department and Extension Service, University of Western Australia, Publication 12, 355p.

Mueller, A., 2007, Copper-gold endoskarns and high-Mg monzodiorite–tonalite intrusions at Mt. Shea, Kalgoorlie, Australia: implications for the origin of gold–pyrite–tennantite mineralization in the Golden Mile. Mineralium Deposita, 42, 737–769.

Neumayr P., Hagemann S., Horn L., Walshe J.L. and Morrison R., 2004, Camp- to deposit-scale spatial zonation and temporal succession of redox indicator sulfide-oxide minerals; vectors to Archaean orogenic gold deposits; an example from the St Ives gold camp, Yilgarn Craton, Western Australia, in McPhie J. & McGoldrick P. (eds.), Dynamic Earth; past present and future, Geological Society of Australia, Hobart, 105.

Neumayr, P., Petersen, K.J., Gauthier, L., Hodge, J.L., Hagemann, S.G., Walshe, J.L., Prendergast, K., Connors, K., Horn, L., Frikken, P., Roache, A., and Blewett, R.S. 2005, Mapping of hydrothermal alteration and geochemical gradients as a tool for conceptual targeting: St Ives Gold Camp, Western Australia *In* Meeting the Global Challenge, 8th Biennial SGA meeting. *Edited by* J. Mao, and F. P. Bierlein. Springer, 1479–1482.

Neumayr, P., Walshe, J. L., Roache, A. and Petersen, K., 2008, Alteration architecture of St Ives. Part III, this report.

Nguyen P.T., 1997, Structural controls on gold mineralisation at the Revenge mine and its tectonic setting in the Lake Lefroy area, Kambalda, Western Australia. Unpublished PhD Thesis, University of Western Australia.

Nguyen, T.P., Cox, S.F., Harris, L.B., and Powell, C.M., 1998, Fault-valve behaviour in optimally oriented shear zones: an example at the Revenge gold mine, Kambalda, Western Australia. Journal of Structural Geology, 20, 1625–1640.

Nicholson, C.J., 2000, Fluid wallrock interaction and structural processes in the North Orchin gold lode, St Ives Gold Operations, Kambalda, WA. BSc Honours thesis, Australian National University, unpub.

Redman, B.A. and Keays, R.R., 1985. Archaean basic volcanism in the Eastern Goldfields Province, Yilgarn Block, Western Australia. Precambrian Research 30, 1113–1152.

Richards T.H., 1983, Provisional classification of vein types and the structural setting at the Victory Mine, Kambalda. Unpublished Internal Report No. T/101, Western Mining Corporation Pty Ltd.

Roberts, D.E. and Elias, M, 1990, Gold deposits of the Kambalda-St Ives region. In: Hughes, F.E. (ed) Geology of the Mineral Deposits of Australia and Papua New Guinea. Australian Institute of Mining and Metallurgy, Melbourne, 479–491.

Rock, N.M.S., Golding, S.D., McNaughton, N.J., Barley, M.E., Groves, D.I. and Ho, S.E., 1987, Carbon isotope composition of carbonates from contrasting alteration styles in supracrustal rocks of the Norseman-Wiluna belt, Yilgarn Block, Western Australia: Their significance to the source of Archaean auriferous fluids. Geology Dept and University Extension, University of Western Australia Publication University of Western Australia Publication 11, 215–238.

Ruming, K.J., 2006, Controls on Lode Gold Mineralisation in the Victory Thrust Complex, St Ives Goldfield, Western Australia. Unpublished PhD thesis, The University of Newcastle.

Salier, B.P., Groves, D.I., McNaughton, N.J. and Fletcher, I.R., 2004, The world-class Wallaby gold deposit, Laverton, Western Australia: An orogenic style overprint on a magmatic-hydrothermal magnetite-calcite alteration pipe? Mineralium Deposita, 39, 473–494.

Sheldon, H.A., Barnicoat, A.C., Zhang Y., and Ord, A., 2007, Metamorphism in the Eastern Yilgarn Craton: implications for fluid flow and mineralisation. *in* Kalgoorlie 2007 *edited by* F Bierlien and C Knox-Johnson: Geoscience Australia, Record 2007/14, 138–142.

Sircombe, K.N., Cassidy, K.F., Champion, D.C. & Tripp, G., 2007, Compilation of SHRIMP U-Pb geochronological data, Yilgarn Craton, western Australia, 2004–2006. Geoscience Australia Record 2007/01.

Stolz E., Urosevic M. and Connors K., 2004, Reflection seismic surveys at St Ives Gold Mine, WA 17th ASEG-PESA geophysical conference and exhibition; Integrated exploration in a changing world. Australian Society of Exploration Geophysicists and Petroleum Exploration Society of Australia, Perth, ASEG Preview, 111, 79.

Squire, R.J., Cas, R.A.F., Clout, J.M.F. and Behets, R., 1998, Volcanology of the Archaean Lunnon Basalt and its relevance to nickel sulfide-bearing trough structures at Kambalda, Western Australia. Australian Journal of Earth Sciences 45, 695–715.

Squire, R.J., Cas, R.A.F. and Champion, D.C., 2007, The Black Flag Group: a vector to ore at St Ives. *in* Kalgoorlie 2007 *edited by* F Bierlien and C Knox-Johnson: Geoscience Australia, Record 2007/14, 39–43.

SRK Consulting, 2000, Global Archaean Synthesis – Yilgarn module. Unpublished consultants report, 88 p.

Swager C.P., 1997, Tectono-stratigraphy of late Archaean greenstone terranes in the southern Eastern Goldfields, Western Australia, Precambrian Research, 83, 11–42.

Trofimovs, J., Davis, B.K., and Cas, R.A.F., 2004, Contemporaneous ultramafic and felsic intrusive and extrusive magmatism in the Archaean Boorara Domain, Eastern Goldfields Superterrane, Western Australia, and its implications. Precambrian Research, 131, 283–304.

Vearncombe, J.R., 1987, Structure of the Kambalda-Tramways corridor, Eastern Goldfields. Unpublished Internal Report. Western Mining Corporation Pty Ltd.

Vearncombe, J.R., Barley, M.E., Eisenlohr, B.N., Groves, D.I., Houstoun, S.M., Skwarnecki, M.S., Grigson, M.W., and Partington, G.A., 1989, Structural controls on mesothermal gold mineralization; examples from the Archean terranes of Southern Africa and Western Australia. Economic Geology, Monograph 6, 124–134.

Walshe, J., Neumayr, P., Petersen, K. J., Young, C., and Roache, A., 2006, Scale-integrated, architectural and geodynamic controls on alteration and geochemistry of gold systems in the Eastern Goldfields Province, Yilgarn Craton. MERIWA, M358 Project Final Report, 287 p.

Weinberg, R.F., Moresi, L., and van der Borgh, P., 2003, Timing of deformation in the Norseman-Wiluna Belt, Yilgarn Craton, Western Australia. Precambrian Research, 120, 219–239.

Weinberg, R.F., Van der Borgh, P., Bateman, R. J. and D. I. Groves, D.I., 2005, Kinematic History of the Boulder-0Lefroy Shear Zone System and Controls on Associated Gold Mineralization, Yilgarn Craton, Western Australia Economic Geology, 100, 1407–1426.

Williams, P.R., and Whitaker, A.J., 1993. Gneiss domes and extensional deformation in the highly mineralised Archaean Eastern Goldfields Province, Western Australia, Ore Geology Reviews, 8, 141–162.

Williams, P.R. and Currie, K.L., 1993, Character and regional implications of the sheared Archaean granite–greenstone contact near Leonora, Western Australia. Precambrian Research, 62, 343–365.

Woodful, C., 1993, Structural controls on gold mineralisation at the Victory Gold Mine., Kambalda, Western Australia. Unpublished MSc thesis, Melbourne University, Victoria.

## 3.9 Structural evolution of the Victory to Kambalda region of the St Ives gold camp: the role of early formed structures on the development of a major gold system

**John Miller[1], Janet Tunjic[2], Richard Blewett[3], Matt Briggs[2], John Donaldson[2]**

[1] Centre for Exploration Targeting, School of Earth and Geographical Sciences, University of Western Australia, 35 Stirling Hwy, Crawley, Western Australia, 6009

[2] St Ives Gold Mining Co, Gold Fields Australia, Kambalda Post Office, WA 6444

[3] Onshore Energy and Minerals Division, Geoscience Australia, GPO Box 378, Canberra, ACT, 2601

### 3.9.1 Introduction

All rifts in modern day, and ancient analogues, have markedly variable geometry along strike. Steps in the rift geometry are associated with arrays of both hard-linked and soft-linked transfers or accommodation zones. The geometry of a rift system where pre-existing architecture has a control on fault propagation is even more complex, with relay faults being a common feature of such systems (e.g., Keep and McClay, 1997). Any structural interpretation of a thrust or strike-slip belt should consider what the earlier rift architecture may have been as it will exert a fundamental control on the evolution of the system. The role of early rift architecture on the subsequent development of thrust belts, and the controls on mineralization, has been recognized for some time. However, one key problem is identifying these early features in old terranes, such as the Archaean Yilgarn Craton.

The world class St Ives goldfield occurs to the west of the regional Boulder-Lefroy fault zone, within the Kalgoorlie Terrane of the Eastern Goldfields Superterrane (EGST) (Cassidy et al., 2006). Previous workers have highlighted the controls dilational and contractional jogs have on the development of major gold systems along the Boulder-Lefroy Fault (e.g., Nguyen, 1997; Nguyen et al., 1998; Weinberg et al., 2004). At a regional scale, left-stepping segments, that would have been dilatant during sinistral slip, have been linked to major gold camps such as the Golden Mile, New Celebration and St Ives (Nguyen, 1997; Weinberg et al., 2004). However, at the camp-scale in the St Ives region, the major deposits are actually located on major contractional jogs (e.g., Revenge and Repulse Faults; Nguyen et al., 1998; Cox and Ruming, 2004; Ruming, 2006). Whilst the relative importance of dilatant versus contractional sites has been debated, variation in fault topography (strike and/or dip changes) is a common element to models for the development of major gold lodes (Weinberg et al., 2005).

Within the world class St Ives goldfield in the Kalgoorlie Terrane a series of WNW-trending structures, substantially oblique to the main NW to NNW-trending structural grain, have previously been identified using potential field data sets (in particular gravity; Figure 3.9.1) and isopach modelling that has mapped major thickness variations within a key komatiite lithological across the WNW-trending structures (Figure 3.9.2) (Connors et al., 2005). Neumayer et al. (2007) also inferred these WNW-trending structures existed by the analysis of the 3-D wireframes of porphyries in the Greater Revenge Area, and by specific minerals (e.g., magnetite) at a range of geological scales. The WNW-trending structures also exert an apparent control on the distribution of the Defiance Dolerite e.g., along and to the south of the Mt Blanc Fault (Figure 3.9.2). The granophyric zone within this dolerite are the best host rock type for the development of major gold deposits and delineating the three dimensional distribution of the dolerite is important for targeting. Because of the observations summarized above these NW to NNW-trending features have been related to early formed rift architecture, with a subsequent control on the development of later stage fault topography, with a potential direct feed into gold lode development (e.g., Connors et al., 2005). Although, the potential that structural thickening may account for some of the ultramafic thickening has not been eliminated.

This paper considers the structural evolution of the Victory to Kambalda region St Ives with a specific focus on;

1. Unravelling the field relationships associated with possible WNW-trending structures,

2. Linking the early rift architecture into the subsequent inversion and gold mineralization,

3. Domaining the area into transpressional and transtensional zones (during the main phase of gold),

4. Unravelling the style of deformation within transtensional fault segments along the mineralized corridor,

5. Producing a model for the development of the key fault topography associated with contractional jogs, and

6. Producing a revised structural evolution of the area (this is presented with extensive use of figures to convey the structural message).

This report uses the new EGST deformation scheme and ages compiled by Blewett and Czarnota (2007) and Blewett et al., 2008a). In this framework a major gold event for the St Ives field is inferred to have occurred at ca. 2650 Ma and has been termed D4. Nguyen (1997), Connors et al., (2005) and (Ruming 2006) termed this same event D3. The reason for the difference is that in the other deformation frameworks only contractional or strike-slip phases have assigned D numbers (D1, D2…), and extensional events are commonly defined with a De nomenclature (De1, De2). In the Blewett and Czarnota (2007) framework the extension linked to the formation of the late basins (e.g., the Merougil Creek beds Figures 3.9.1, 3.9.2) has been defined as D3 (Blewett et al., 2008a).

Nguyen (1997) presented U-Pb SHRIMP ages from hydrothermal monazite from the Revenge deposit to suggest this event occurred approximately 20 million years earlier at ca. 2630 Ma. However, recent detailed U-Pb dating of hydrothermal xenotime from the Mt Charlotte gold deposit, just to the north of the St Ives gold field, produced a 2642 ± 10 Ma age (n = 20; MSWD = 0.93) (Amira P480 project; written personal communication from Neil McNaughton, 2007). This deposit is hosted within a dextral fault system defined as D5 in the scheme of Blewett et al. (2008a), and D4 in the event history of Swager (1997), Nguyen (1997), Connors et al., (2005) and Ruming (2006). Irrespective of the deformation scheme used, this regional dextral faulting event post-dates the main stage gold at St Ives. This report uses this ca. 2640 Ma age constraint for the timing of the dextral faulting event (D5 of Blewett et al., 2008a), and therefore the main gold event at St Ives must predate this. Two companion papers accompany this work; with Blewett et al. (2008b) outlining the broader camp-scale deformation history and architecture, and Neumayr et al. (2008) describing the fluid-alteration history together with its architecture.

One additional outcome of this work has been the definition of six new exploration targets and these were highlighted in a targeting memo (see Part II). The structural domaining presented in this report was one of the key aspects used in this targeting, and was combined with known structural analogues (i.e., identifying areas with similar structural intersections). These targets, and the analogues to the targets that can be applied elsewhere in the field, have significant economic potential.

### 3.9.2 Methodology

The structural interpretation was undertaken at two scales and, because previous structural interpretations have been a key input, the new structural interpretation should be viewed as a compilation of previous work with additional interpretation. As with all structural models it is an interpretation and some areas of the model are more inferred than others. The period of time that was available to undertake the study precluded attributing each structure with the associated uncertainty, and the reason for its inclusion as an interpreted structure i.e., was it observed in pit mapping, drill data or is it an interpretation of a trend in the potential field data?

An initial 2-D interpretation was done at 1:25000 scale, with the final interpretation (Figure 3.9.3) being done at 1:15000 scale. The structural interpretation was done on an AO sheet of Milar which was used with printouts of the relevant Gold Fields Pty Ltd data sets. The final interpretation was digitized, and it is now an ARCGIS layer. Existing 3-D and 2-D data sets were also compiled into FracSIS, which were visualized during the interpretation to make sure the third dimension was incorporated into the interpretation. Modelling of drill hole data was also done using Leapfrog and was used to model the porphyries and gold within the Greater Victory Area (GVA).

The following Gold Fields Pty Ltd data sets where used during the interpretation;

- Regional Interpretative Geology Map (Gold Fields Pty Ltd, St Ives, unpublished)

- Geophysical data sets - airborne magnetics, ground magnetics, ground gravity (50 metre line spacing), sub-audio magnetics (SAM), seismic lines

- Regional gold flitches (grade contours) printed out an RL that excluded supergene and placer gold
- 2-D structural interpretation and isopachs of komatiite thickness (Connors et al., 2003)
- A camp-scale 3-D model (Gold Fields Pty Ltd, unpublished)
- The 3-D model of the Greater Revenge Area (Gold Fields Pty Ltd unpublished)
- 3-D model of the Victory area (Gold Fields Pty Ltd unpublished)
- Pit gold flitches
- Underground and open pit geological mapping (in particular from the Mars deposit and Revenge deposits)
- New sectional interpretations

The interpretation focused on producing a new map (Figure 3.9.3) that utilized the known kinematics synchronous with the main gold event (associated with E-W to NE-SW shortening e.g., Nguyen et al., 1998). The interpretation was not intended to be a new set of lines

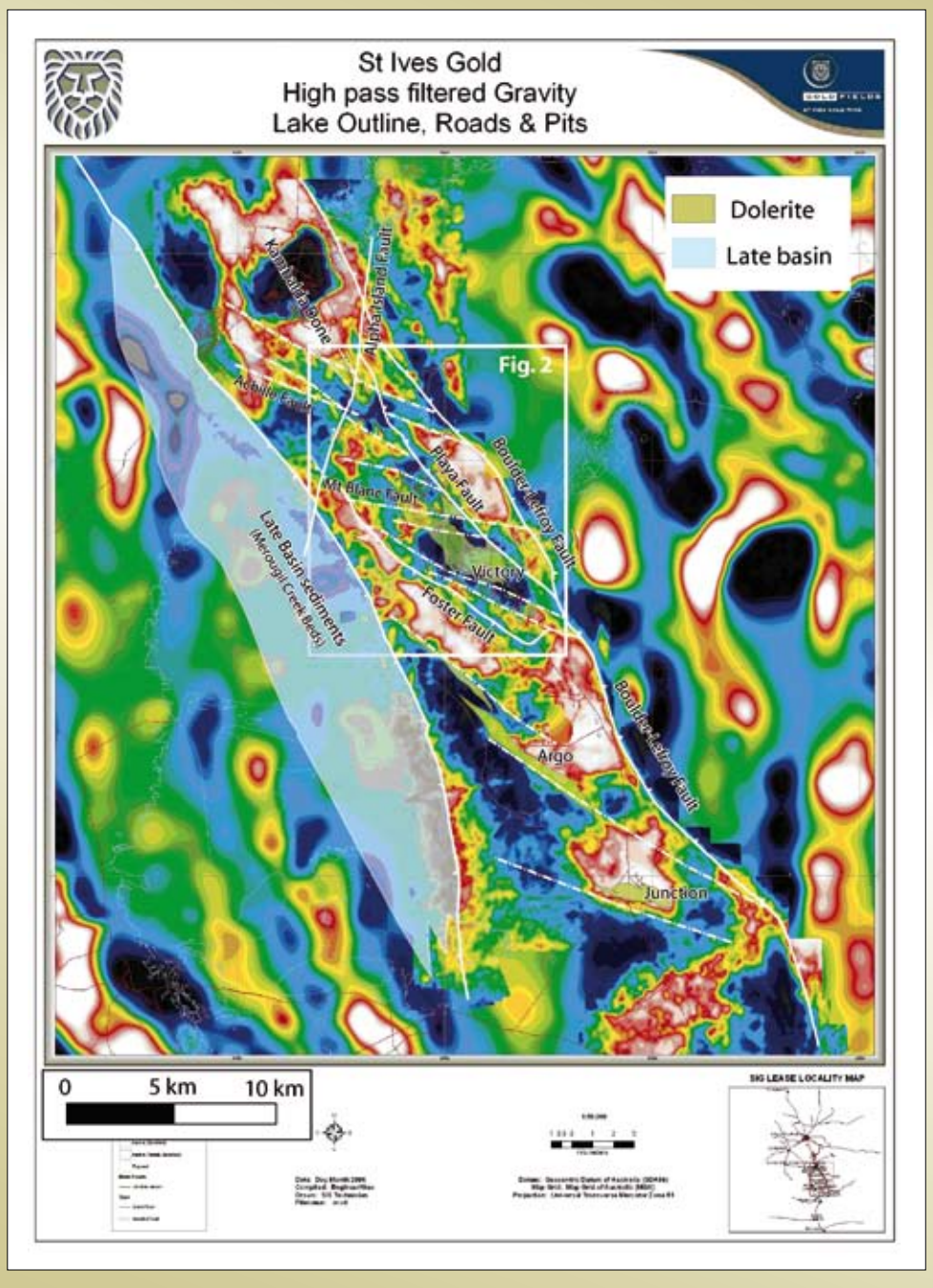


*Figure 3.9.1: High-pass filtered gravity with key gravity trends annotated. See text for explanation. Image from Gold Fields Pty Ltd.*

drawn just using potential field data, but instead to be a coherent structural map consistent with existing kinematics and field observations that highlighted potential targets as part of the analysis. A separate targeting memorandum has already been delivered to Gold Fields Pty Ltd as part of the project and this also makes an attempt at integrating the geochemistry with the structural interpretation (see Part II). Note that not all the structures interpreted in Figure 3.9.3 are inferred to have been active during gold mineralization, and only segments of these structures may have been episodically active at any one time (e.g., Cox and Ruming, 2004).

Compared to some previous studies, minimal new field data were acquired, but some focused field mapping was undertaken in critical areas of the study area and some of this work has been included. The key areas that had additional mapping where;

- Delta and Delta North deposit (Delta Shear and a newly identified transfer fault)
- Temeraire deposit (transpressional deposit parallel to the Playa and Bellisle Shears)
- Thunderer deposit (transpressional deposit)
- A lode (transtensional deposit within the Beta-Hunt mine)
- The Repulse Shear at the Victory-Defiance open pit

Critical existing kinematic data that was used as part of the study was the earlier work on the Revenge deposit (Nguyen, 1997; Nguyen et al., 1998) and also on the Victory deposit (Ruming, 2006).

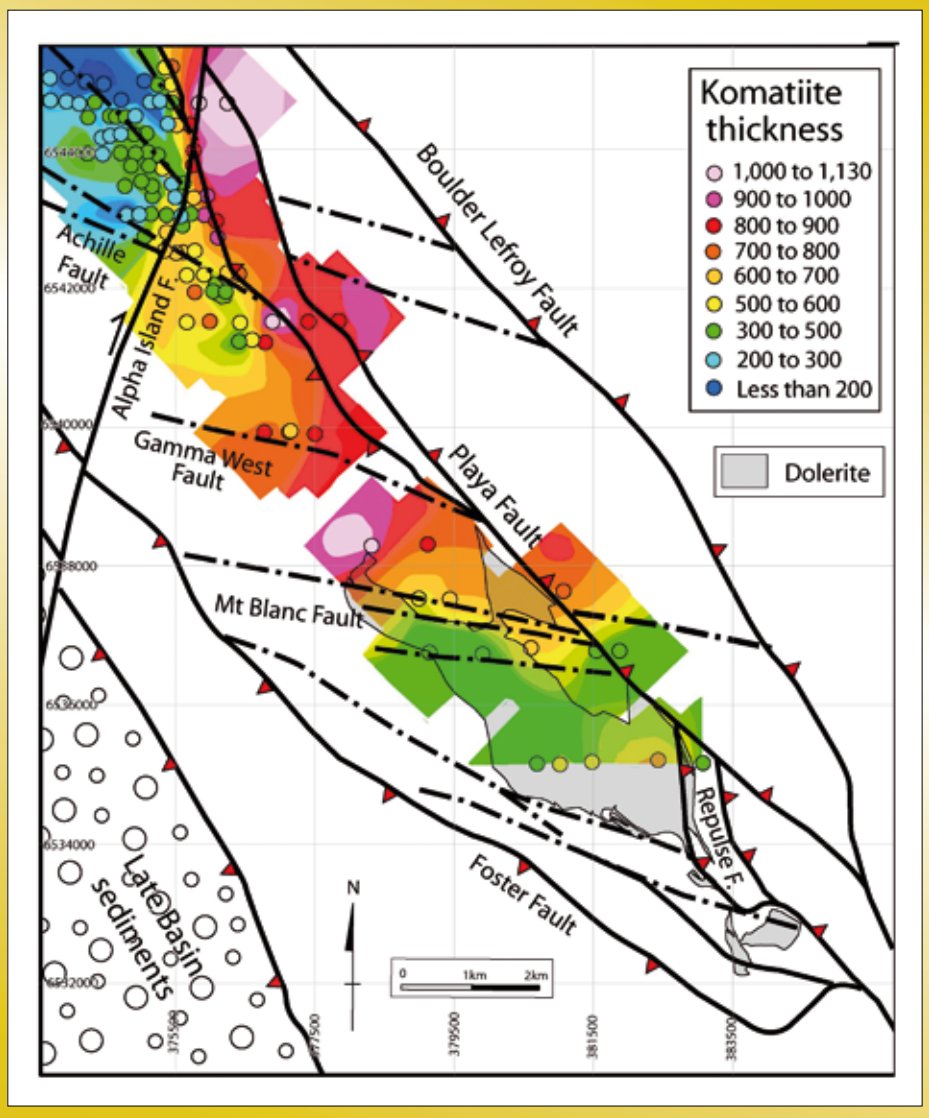


*Figure 3.9.2: Isopachs of komatiite thickness (from Connors et al., 2005) and distribution of Defiance Dolerite at the top of basement. These have been overlain with the key structural trends marked on the gravity image in Figure 3.9.1. Key WNW-trending structures have been labelled (Achille, Gamma West and Mt Blanc Faults – Connors et al., 2005). See text for discussion.*

*Figure 3.9.3: New structural interpretation for the St Ives camp. Pits are in red. The Greater Revenge Area (GRA) is defined by the Mars-Agamemnon West-South Delta-Revenge pits. The Thunderer-Orchin-Leviathan-Defiance pits define the Greater Victory Area (GVA). Kambalda Dome is at top left.*

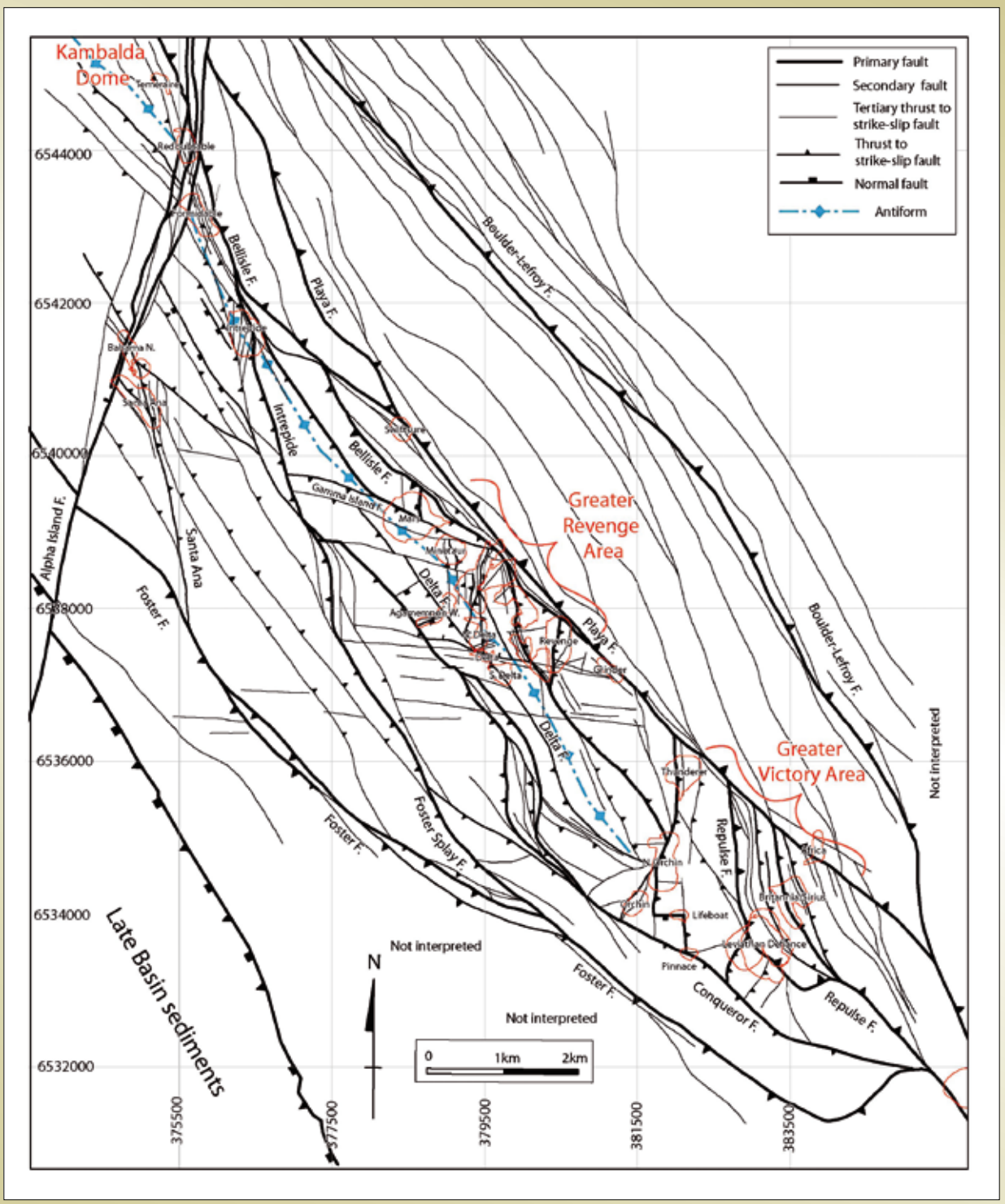

### 3.9.3 Structural interpretation and field observations

The new structural interpretation (Figure 3.9.3) does not require have any major reinterpretation of the existing unpublished Gold Fields Pty Ltd solid geology map (Figure 3.9.4). The geometry of the majority of the key faults is identical (the variations will be discussed), and the key antiformal feature in the footwall of the Playa Fault still runs down the centre of the field (the axis of this is marked on Figure 3.9.3 with it clearly highlighted in the sections in Figure 3.9.4). As part of the study some new sectional interpretations where also drafted (these are sections 1, 2 and 4 in Figure 3.9.5), which have been combined with existing interpretations (these are sections 3 and 5 in Figure 3.9.5).

Overlaying the new structural interpretation upon both the ground magnetics (Figure 3.9.6), and the high-pass filtered gravity (Figure 3.9.7), highlights that aspects of the interpretation were obtained with the different potential field data sets. The magnetic data were used to identify the altered ultramafic rocks, the late-stage cross cutting D5 dextral faults and also the boundaries of the major faults (such as the Boulder-Lefroy and Foster Faults). The major faults are commonly defined by either the consistent truncation of markers along strike and/or by major boundaries of magnetic response. Whilst the gravity data have been used to define the boundaries of the major faults, it also identified WNW-trending features that are interpreted as transfers or relay faults, and are particularly prominent in the structural interpretation for the Greater Revenge Area (see Figure 3.9.3). These WNW-trending features are also observed with the sub-audio magnetic data but are not obvious in the detailed ground magnetic data (Figure 3.9.6). In many cases these cross-cutting WNW-trending features appear to be defined by lower density plutons that have intruded along these features.

#### 3.9.3.1 Structural variation in D2/D4 folding along strike

The Kambalda Dome (Figure 3.9.8) is part of a major NNW-trending anticline that has a fold axis extending down the centre of the structural interpretation (Figures 3.9.3, 3.9.5). The Kambalda Dome is cross cut by granitoids (Figure 3.9.8), and U-Pb dating of the Kambalda granodiorite (Compston et al., 1986), and also felsic-intermediate porphyry dykes at the Revenge deposit by Nguyen (1997), indicate they are coeval and were emplaced at ca. 2660 Ma (Nguyen, 1997). However, there is a complex igneous paragenesis that has not been fully resolved and the batholiths appear to be composite. The field relationships indicate that some of the intrusive rocks were either contemporaneous with, or post-date, the regional NNW-trending folds that have been linked to what has been termed the D2 deformation event (Nguyen, 1997 and also by Blewett and Czarnota, 2007; Blewett et al., 2008a, 2008b). Later shortening further tightened the existing antiformal structure (hence the term D2/D4 folding in the section heading).

One key feature highlighted by the compilations of different sectional interpretations in Figure 3.9.5, and also Figure 3.9.8, is the variation in the apparent amount of shortening observed along strike from the Kambalda Dome. As depicted in Figure 3.9.8 the Kambalda Dome has the appearance of a tight antiform cored by Lunnon Basalt, and the overlying ultramafic and mafic volcanic sequences. The section line through the Victory Complex (section line 5-5' in Figures 3.9.4 and 3.9.5) also shows a marked amount of shortening, with what appears to be a tight to isoclinal hangingwall anticline above the Repulse Fault. The Repulse Fault has approximately 400 metres of displacement in this sectional view (as marked by the ultramafic Tripod Hills Komatiite contact with the Devon Consols Basalt), ascertaining the exact amount is complicated by the intrusive units. These two sections are in marked contrast to the Greater Revenge Area (Figures 3.9.3, 3.9.4), where extensive drilling has defined a broad open anticline (section line 4, Figure 3.9.5). If no volume loss is assumed, the open fold in the footwall of the Playa Fault reflects approximately 10% shortening via folding and faulting from the Playa Fault to the western-most defined edge of the fold (at easting 378000; Figure 3.9.5) – this estimate excludes the offset on the Playa Fault. Significantly, the Greater Revenge Area that is located in this lower strain zone, also has a substantial number of interpreted WNW-trending faults (Figure 3.9.3), this will be discussed in a later section.

The reason for the apparent major variation in shortening along strike could reflect; 1) a component of the Kambalda Dome, as shown in Figure 3.9.8, represents primary volcanic architecture not present to the same extent along strike (see Neumayr et al., 2008) or, 2) there were major

*Figure 3.9.4: Solid geology map with structural interpretation overlain. Section lines for Figure 3.9.5 are shown.*

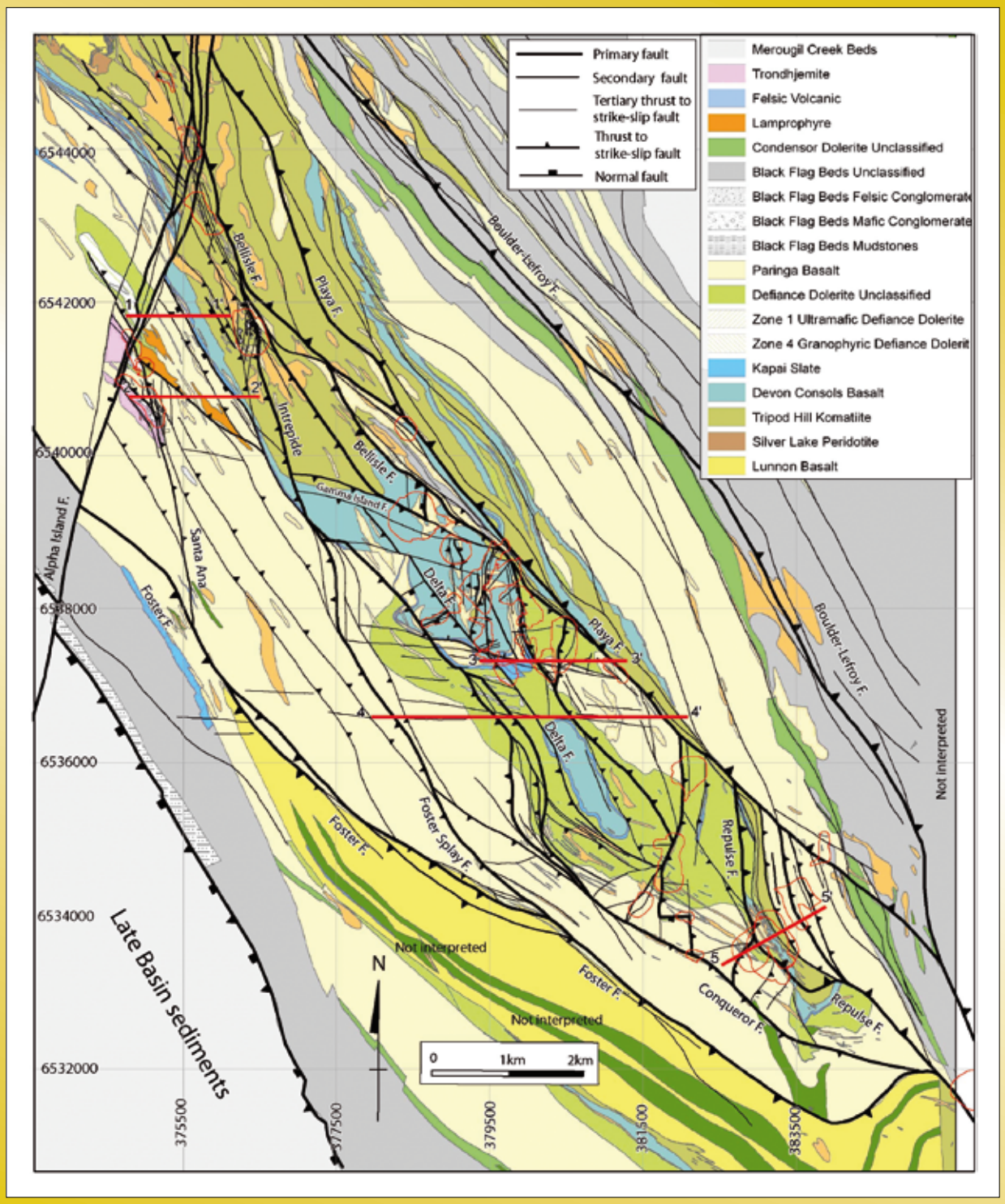

*Figure 3.9.5: Selected section lines from the St Ives goldfield. These sections are marked on Figure 3.9.4.*

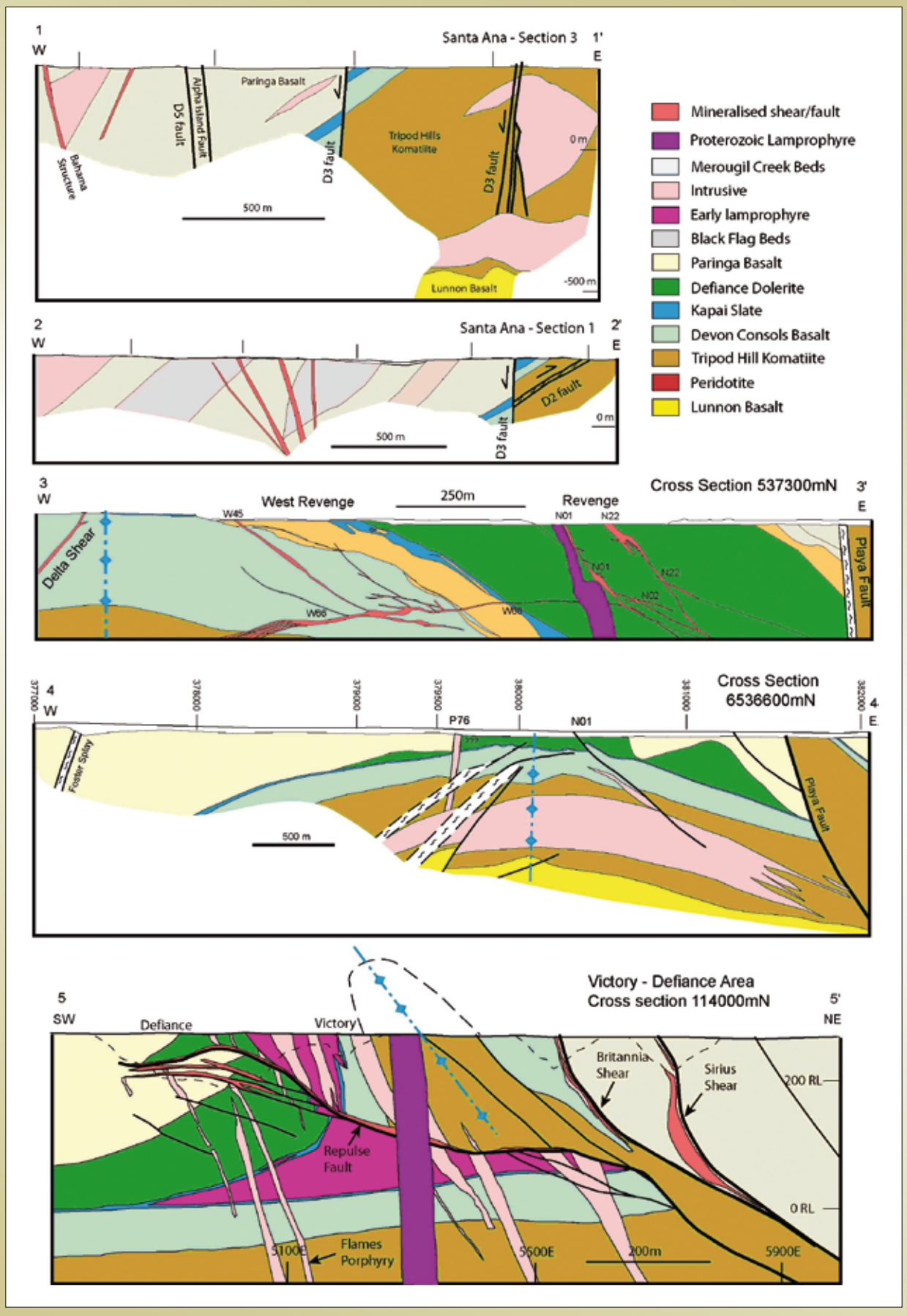

*Figure 3.9.6: Ground magnetic data overlain by structural interpretation.*

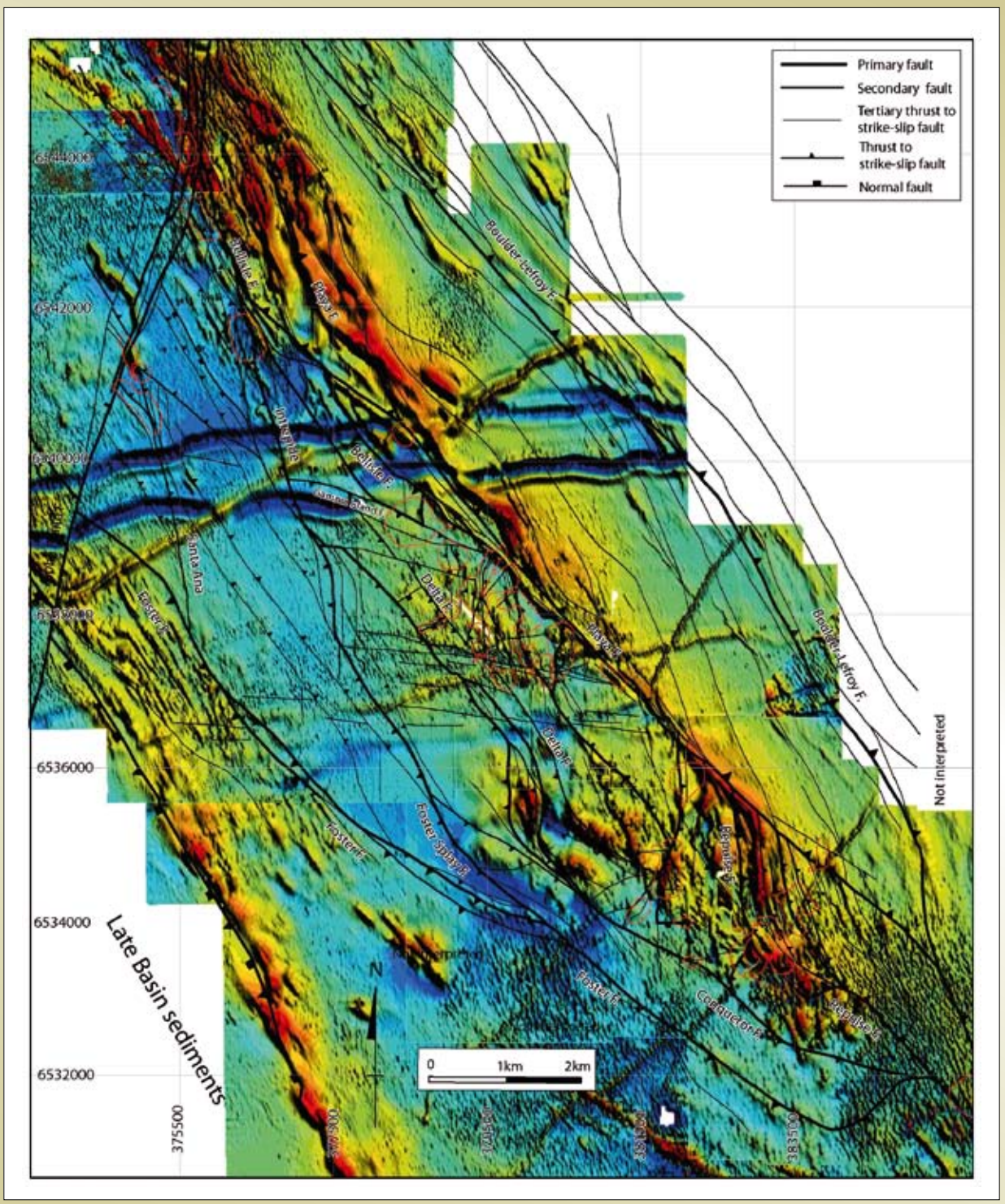

*Figure 3.9.7: Gravity (with high-pass filter) overlain by structural interpretation.*

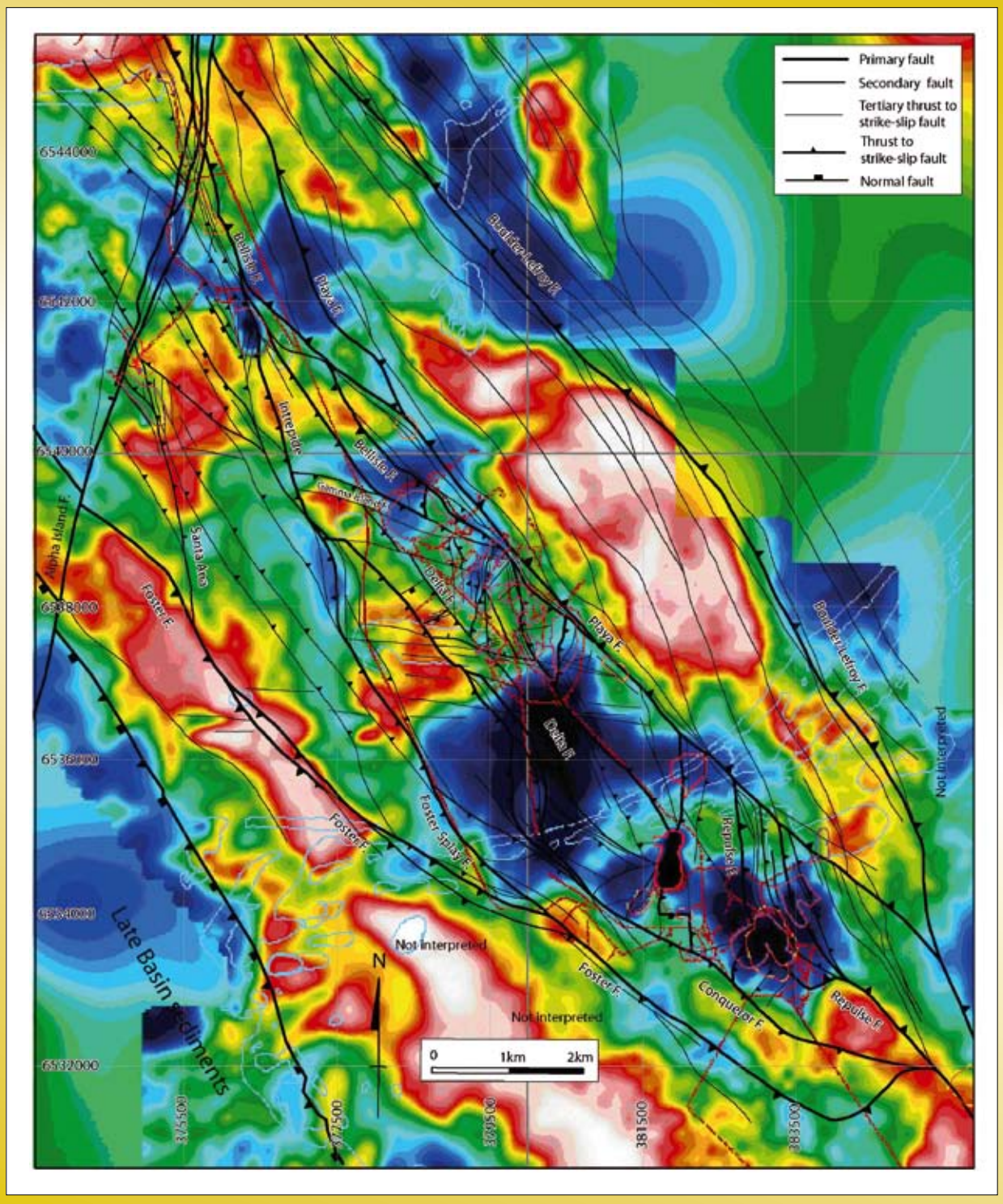

variations in strain along strike. The extent of shortening observed in the Greater Victory Area (section line 5, Figure 3.9.5) could be explained by its location within a transpressional jog, while the lack of tight folding in the Greater Revenge Area (Section line 4, Figure 3.9.5) may reflect strain partitioning, with the shortening accommodated by greater slip on the Playa and other shears, instead of by folding.

### 3.9.3.2 WNW-trending faults

There are a substantial number of interpreted WNW-trending faults in the Greater Revenge Area, that we have interpreted to be early formed rift-related faults. In the Greater Revenge Area the major antiformal structure, which is the extension south of the Kambalda Dome, is an open fold (Section line 4, Figure 3.9.5). The overall geometry suggests that only about 10% shortening occurred in the footwall of the Playa Fault. Compared to the intense strain observed in the Victory Complex (Section line 5, Figure 3.9.5), the amount of shortening in the Greater Revenge Area would not have been sufficient to destroy earlier fault architecture. For any analysis of the Greater Revenge Area the real question is "Given the relative lack of later shortening in the Greater Revenge Area, the early architecture should be there, so where is it?" This makes the Greater Revenge Area a critical field laboratory for understanding the geometry and controls of the early formed architecture on later deformation – most of the key observations discussed in this section come from this area.

Many of the WNW-trending features in the structural interpretation of this study are located in areas where similar features have been previously inferred as potential early faults (e.g., Figure 3.9.2). These features have been integrated into this new interpretation (Figure 3.9.3), and also digitized, as many of these features have now been physically mapped in both surface and open pit outcrops, and were in places active during gold mineralisation. The exact nature and field context of these WNW-trending features is one of the major outcomes of the study, and will be discussed in this section in detail.

The WNW-trending structures have been subdivided into four main types that are:

1. Steep-dipping structures that have acted as transfer faults active syn-gold – these reflect early formed features that in areas control the komatiite and dolerite distribution, fault movement during later inversion, and have also been intruded by intermediate porphyry dykes dated at ca. 2660 by Nguyen (1997).

2. Early formed steep-dipping structures that were not reactivated syn-gold, but in other respects are identical to the transfer faults active syn-gold. These are intruded by intermediate porphyry dykes intrusives, in some areas control the dolerite distribution, and from the isopach

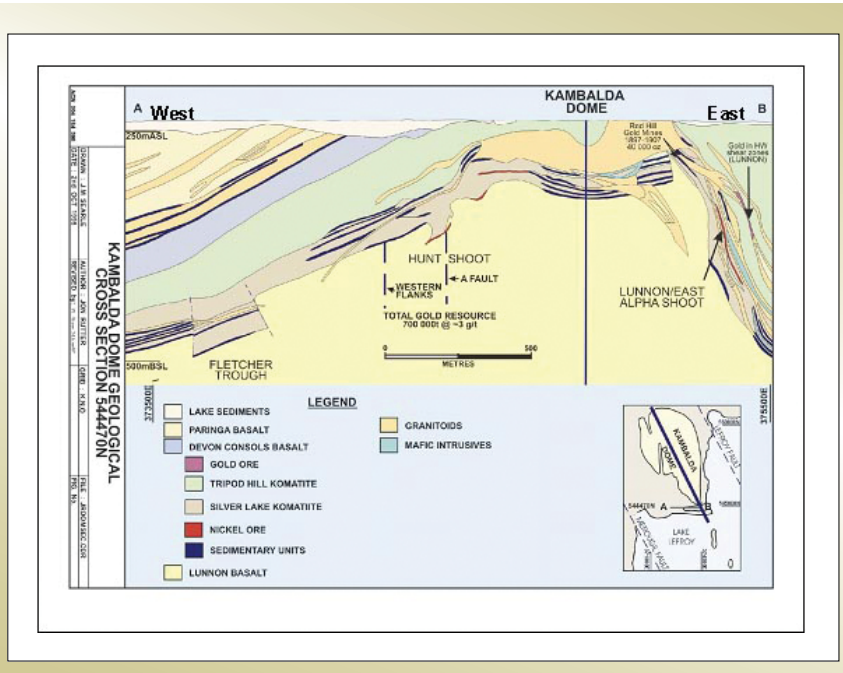


*Figure 3.9.8: Historical geological section through the Kambalda Dome compiled by Western Mining Corporation Pty Ltd geologists (dome location is marked on Figure 3.9.3). Section is viewed looking to the north.*

work (Conners et al., 2005) also some of the komatiite thickness variations.

3. Lower angle dipping WNW-trending structures that in areas have acted as bounding faults associated with transtensional step-overs. These have a control on the grade distribution, but their timing relationship to with respect to dolerite emplacement is problematic, but they are inferred to be early. In most respects these faults are interpreted to be very similar in nature to the Playa and Repulse Faults, but have a more NW- to WNW trending strike, instead of the regional NW- to NNW-trend (Blewett et al., 2008b).

4. Late stage post-gold faults and dykes that trend WNW and W. These range from late S-dipping thrusts to Proterozoic dykes (Ruming, 2006).

An additional complication for interpreting the fault system in the Greater Revenge Area is the presence of a major low angle shear beneath the currently outcropping faults exposed at either surface level or in the open cuts. This is defined as the W62 structure in section 3 (Figure 3.9.5). This W66 fault has the appearance of a low angle décollement or detachment – if this is correct some of these WNW-trending faults may not have major depth extent (although for some features this is ruled out by the isopachs and observed gravity response). To an extent the Greater Revenge Area has some similarity to the upper plate of a core complex that has been inverted.

#### 3.9.3.2.1 Steep-dipping transfer faults

The best example of steep-dipping WNW-trending transfer structures are a series of faults that have acted as a major transfer zone at the southern end of the North Delta pit (Figures 3.9.9, 3.9.10). This feature is located in close proximity to an inferred structure previously termed the Mt Blanc Fault (Connors et al., 2005), which we define as the Mount Blanc Transfer Zone. The E-dipping W45 structure terminates against this transfer zone, and there is also a step in the Delta Shear (Figures 3.9.9, 3.9.11). The steep dipping veins in the transfer zone are mineralized (Figures 3.9.11, 3.9.12). The syn-gold fault kinematics along the Mount Blanc Transfer Zone are complicated, because this steep-dipping WNW-trending structure transferred strain from a complex combination of block on block movement associated with thrusting and strike-slip movement (lower inset Figure 3.9.10). The mineralized section of the transfer appears to be a dilatant zone that is inferred to have had limited strike continuity (Figure 3.9.10).

The WNW-trending exposure of the Mount Blanc Transfer Zone in the North Delta pit can be traced across to the way across to the Revenge pit (Figure 3.9.10). In some areas between the Revenge and North Delta pits this transfer zone is exposed in surface outcrops as arrays of WNW-trending veins with niche samples grading up to 2.5 g/t (Figure 3.9.11), and there appears to be a camp-scale trend of grade that correlates with this transfer fault (Figure 3.9.9). A major porphyry dyke has also intruded parallel to this structure (Figure 3.9.10). The Mount Blanc Transfer Zone also corresponds to a linear boundary between the Paringa Basalt and the Defiance Dolerite (note red arrows on geological map in Figure 3.9.10), which is interpreted to indicate that the structure was either active synchronous with the emplacement of the Defiance Dolerite and coeval Paringa Basalt, or it was a passive feature adjacent to which the dolerite pooled. An assessment of the underground mapping at the Revenge deposit did not identify any mineralised structures trending WNW, and this is interpreted to indicate that in the Revenge deposit area, the Mount Blanc Transfer Zone existed at the point D4 gold mineralization occurred, but it was not reactivated. However, WNW-trending mineralized structures (e.g., P76) have been previously modelled in the Greater Revenge Area.

The lack of intense shortening via D2 folding in the Greater Revenge Area is the inferred reason that the WNW-trending transfer faults are readily identified in this area. The Mount Blanc Transfer Zone marks a major thickness variation in the komatiite, with greater thickness to the north of this steeply N-dipping feature (see Figure 3.9.2). One possible interpretation is that the thickness variation in the komatiite reflects post emplacement structural thickening possibly via N-S thrusting. There is no field evidence for any deformation that could have caused this thickening, and given early WNW-trending faults that control the dolerite distribution are still preserved (Figure 3.9.10), the best interpretation is that the thickness variation reflects syn-volcanism growth faulting. Alternatively, these WNW-trending structures may have also been key magma conduits and bounding features if there was an intrusive component to the emplacement of the ultramafic units.

A major porphyry dyke is parallel to the Mount Blanc Transfer Zone (Figure 3.9.10). WNW-trending porphyry dykes also exist in other areas of the structural interpretation (see also Neumayr et al., 2008), and these potentially could be a guide to the existence of other transfer structures. In the Greater Victory Area no major WNW-trending faults were interpreted during the study (Figure 3.9.3). However, Leapfrog modelling of the porphyry dykes, and also the gold distribution in this mine area (Figure 3.9.13a), identified a distinct set of WNW-trending dykes in one region (there is also a dominant set of NW-trending dykes). Significantly, when the Leapfrog models of gold grade were draped onto the Repulse Fault (the Repulse Fault is marked on Figure 3.9.3 and is also depicted in Section line 5 of Figure 3.9.5), there is a correlation between gold grade and the trend of the dykes in the footwall (Figure 3.9.13). An assessment of the vein arrays associated with mineralization adjacent to the Repulse Fault highlights that the style of deformation synchronous with the gold is a series of low angle extension veins that have predominantly developed in the porphyry dykes (Figure 3.9.13), which is consistent with their emplacement in a contraction jog. The faults in this area (such as the Repulse Fault) have shallower dips when they propagate through porphyry dykes (Figure 3.9.13b). The interpretation (Figure 3.9.13c) is that the shallower dips on the faults were produced by the faults propagating through dykes containing extensive flat-dipping veins.

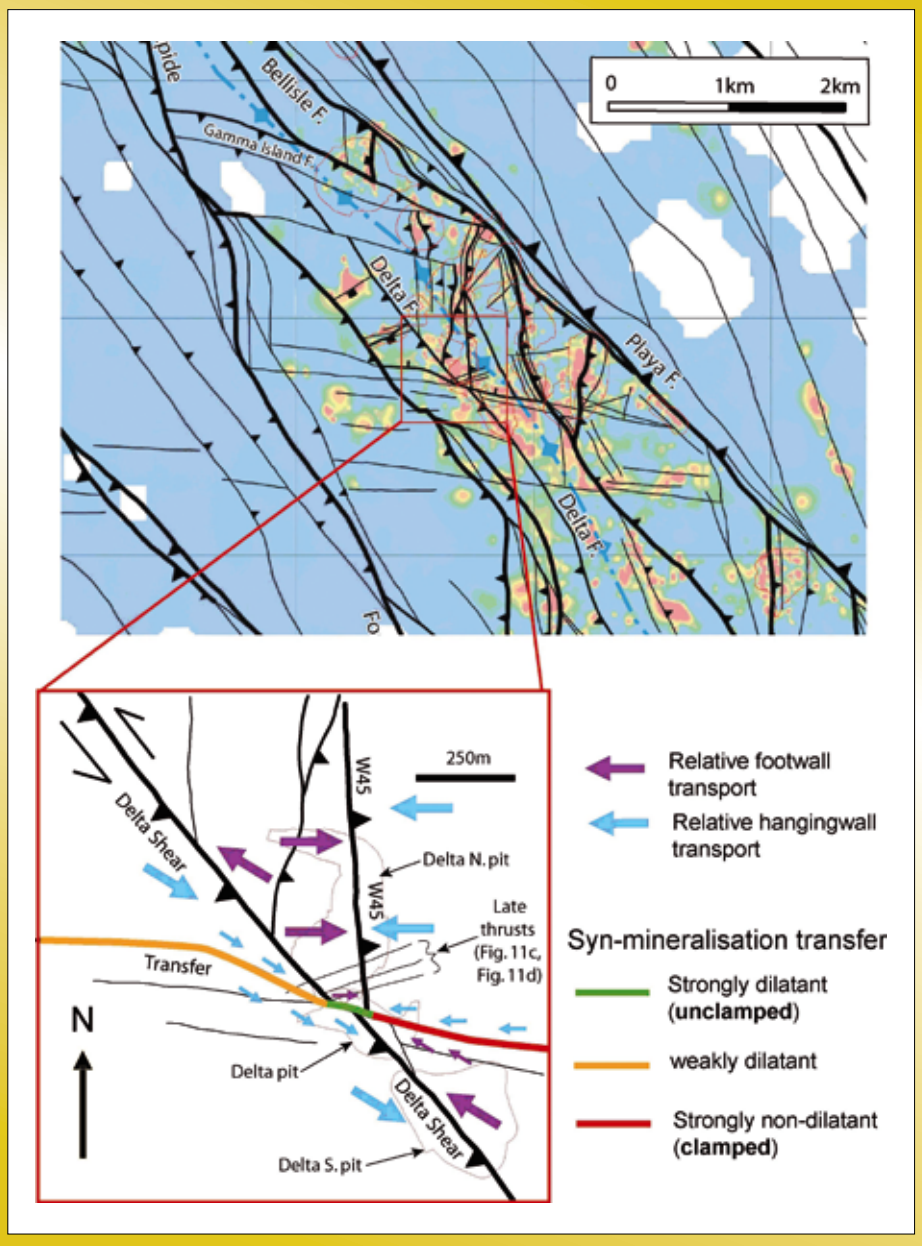


*Figure 3.9.9: The Mount Blanc Transfer Fault Zone. Gold flitch (isotropic) overlain by structural interpretation. Note large number of WNW-trending faults and WNW-trending gold grade. Lower diagram is structural/kinematic model for these structures. See text for discussion. Warm colours indicate elevated gold grades, cool colours either lack data, or have an absence of gold.*

This resulted in the formation of dilational jogs and the development of an ore shoot. The gold grade follows the dilational jog, which in turn is controlled by an underlying WNW-trending dyke.

The interpretation of the relationships observed in the Greater Victory Area is that the dykes may have intruded along an older transfer structure, but that this was strongly over printed by the D2 and D4 deformation.

The WNW-trending dykes are inferred to define an old transfer fault that was not an active structure syn-gold. The rheology of the dykes have a control on the failure mode, and they may have acted as vertical barriers to horizontal fluid flow i.e. fluids may have been channelled along the margins of the dykes (see Neumayr et al., 2007; 2008). Therefore, the WNW-trend to the gold grade in the Greater Victory Area (Figure 3.9.13) is not analogous to the WNW-trending mineralisation linked to the

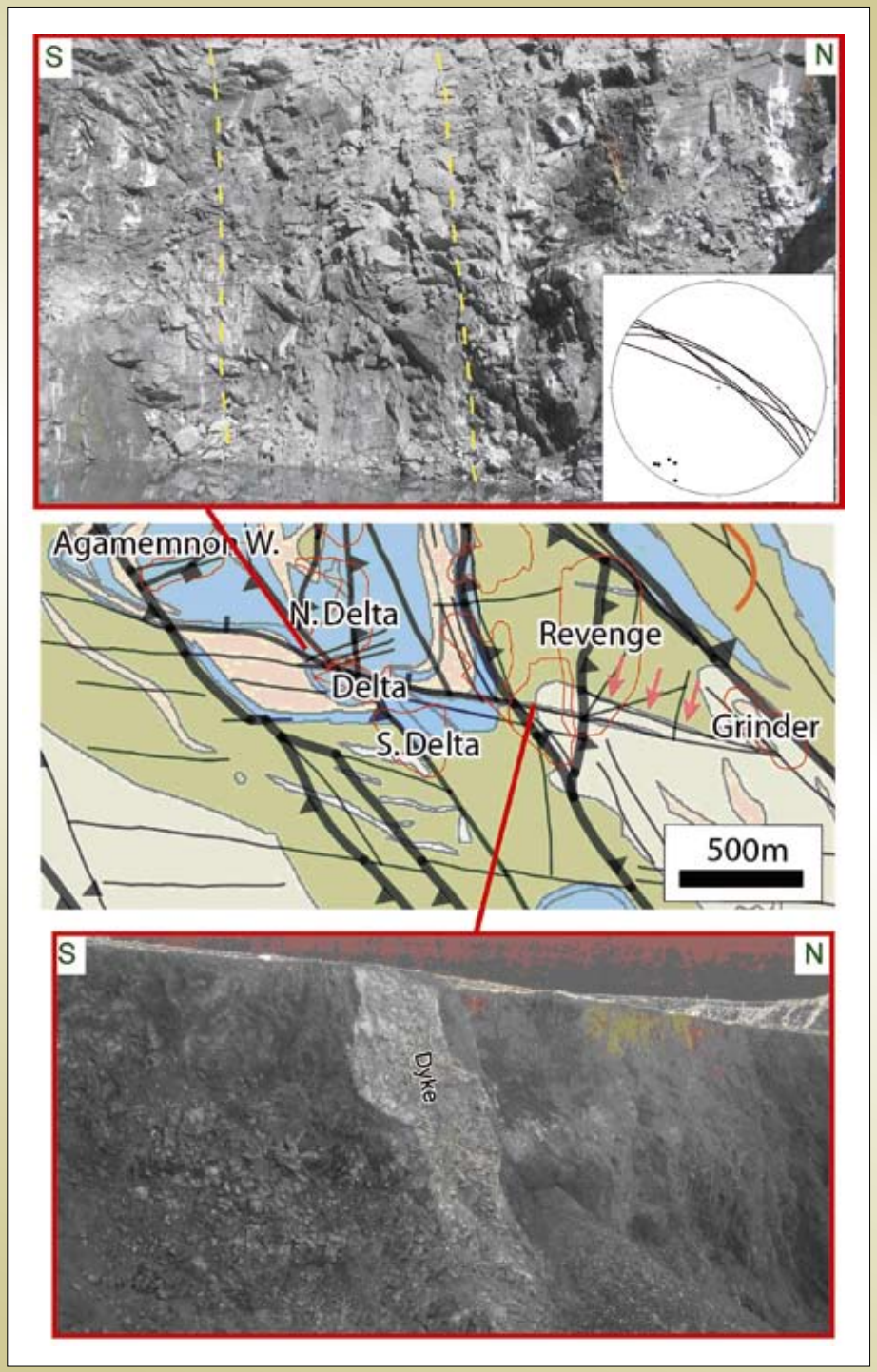


*Figure 3.9.10: Photographs of major transfer fault in Figure 3.9.9 that is part of the Mount Blanc Transfer Zone. The centre of the figure is a screen capture of the solid geology map highlighting this transfer (see key in Figure 3.9.4 for units) with structural interpretation overlain. Note the Paringa Basalt trend highlighted by the orange arrows that is parallel to the WNW-trending faults (faults have been made slightly transparent). Top photo shows mineralised transfer from southern end of the North Delta pit (this is within Devon Consols Basalt). Lower photo shows "flames-style" porphyry dyke intruding parallel to the transfer fault. Stereonet plot is of mineralized veins within the transfer zone (highlighted by dashed lines in top photograph).*

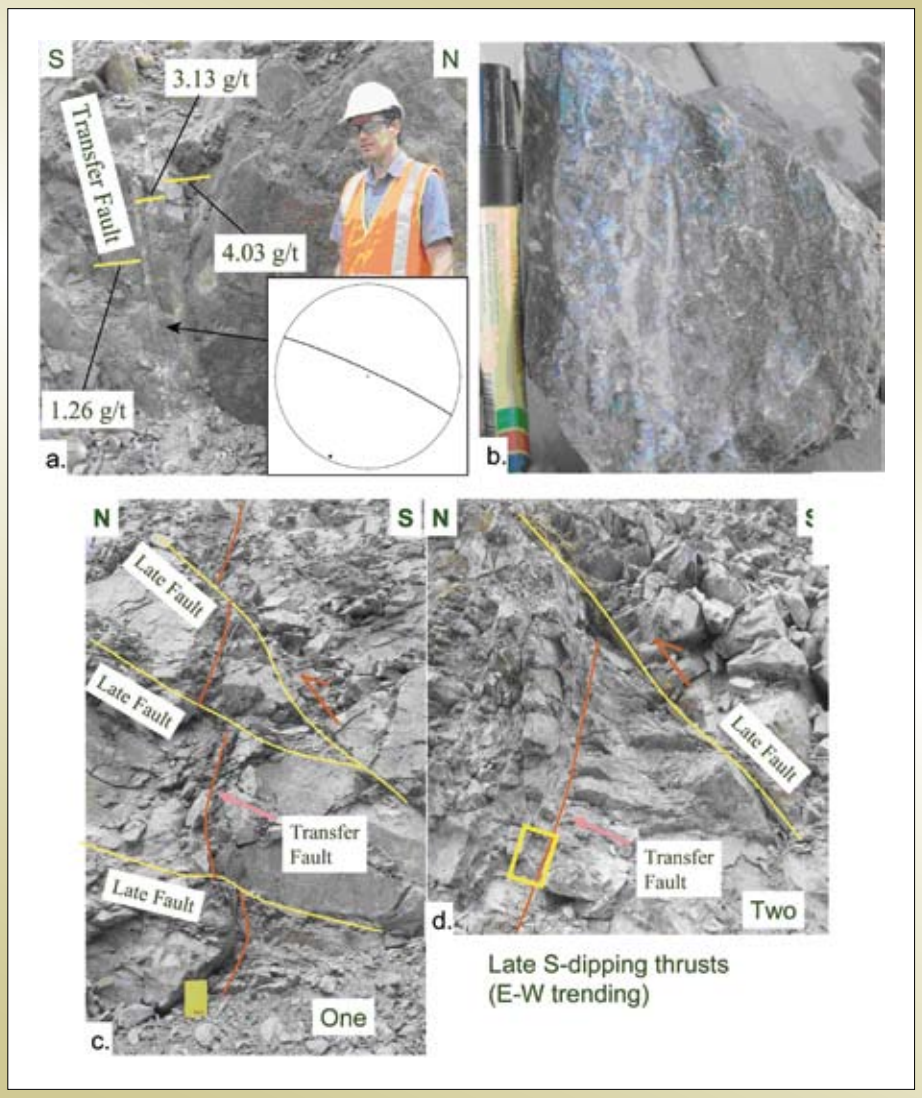


*Figure 3.9.11: Detailed photos of transfer structure at southern end of North Delta pit (transfer is shown in at top of previous figure). a) Steep-dipping mineralised vein within transfer (vein trends WNW – see stereonet). b) Detail of mineralized vein in (a). c) Late faults over printing transfer fault – these late faults trend E-W to ENE-WSW and are highlighted as late thrusts in Figure 3.9.9. d) Late faults over printing transfer fault– these faults trend E-W to ENE-WSW and are highlighted as late thrusts in Figure 3.9.9.*

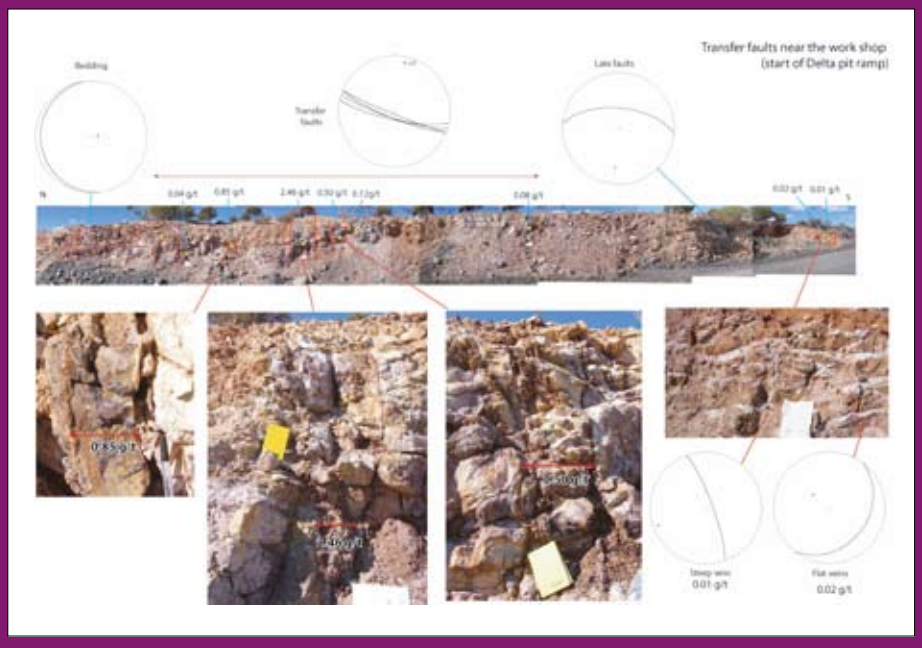


*Figure 3.9.12:Transfer faults between Delta Pit and North Delta pit that define the Mount Blanc Transfer Zone.Transfer is located at start of ramp into Delta pit.*

D4 transfer faults described from the Greater Revenge Area (Figures 3.9.9, 3.9.10, 3.9.11, 3.9.12).

### 3.9.3.2.2 WNW-trending shallower dipping faults

These types of transfer faults have much shallower dips compared to the transfer faults discussed in the previous section. The best example of this type of WNW-trending structures is the Gamma Island Shear exposed within the Mars open cut (Figure 3.9.14, 3.9.15). This structure is along the trend termed the Gamma West Fault by Connors et al., (2005), which is a major gravity trend but there is no systematic variation in komatiite isopach thickness across it (Figure 3.9.2). The Gamma Island Shear (Figure 3.9.14c) trends WNW, dips 30 to 40 to the SSW, and it defines the southern extent of the Mars Shear which terminates against it (Figure 3.9.14). The mineralization within the pit is associated with quartz vein arrays that trend N-S and are parallel to the N-striking and W-dipping Mars Shear. The gold distribution indicates that the Gamma Island Shear has a control on the mineralization (note the WNW-trending grade in Figure 15 parallel to the Gamma Island Shear which acts as a bounding fault). The quartz vein arrays associated with the mineralization dip steeply to the E (Figure 3.9.14a) which, when combined

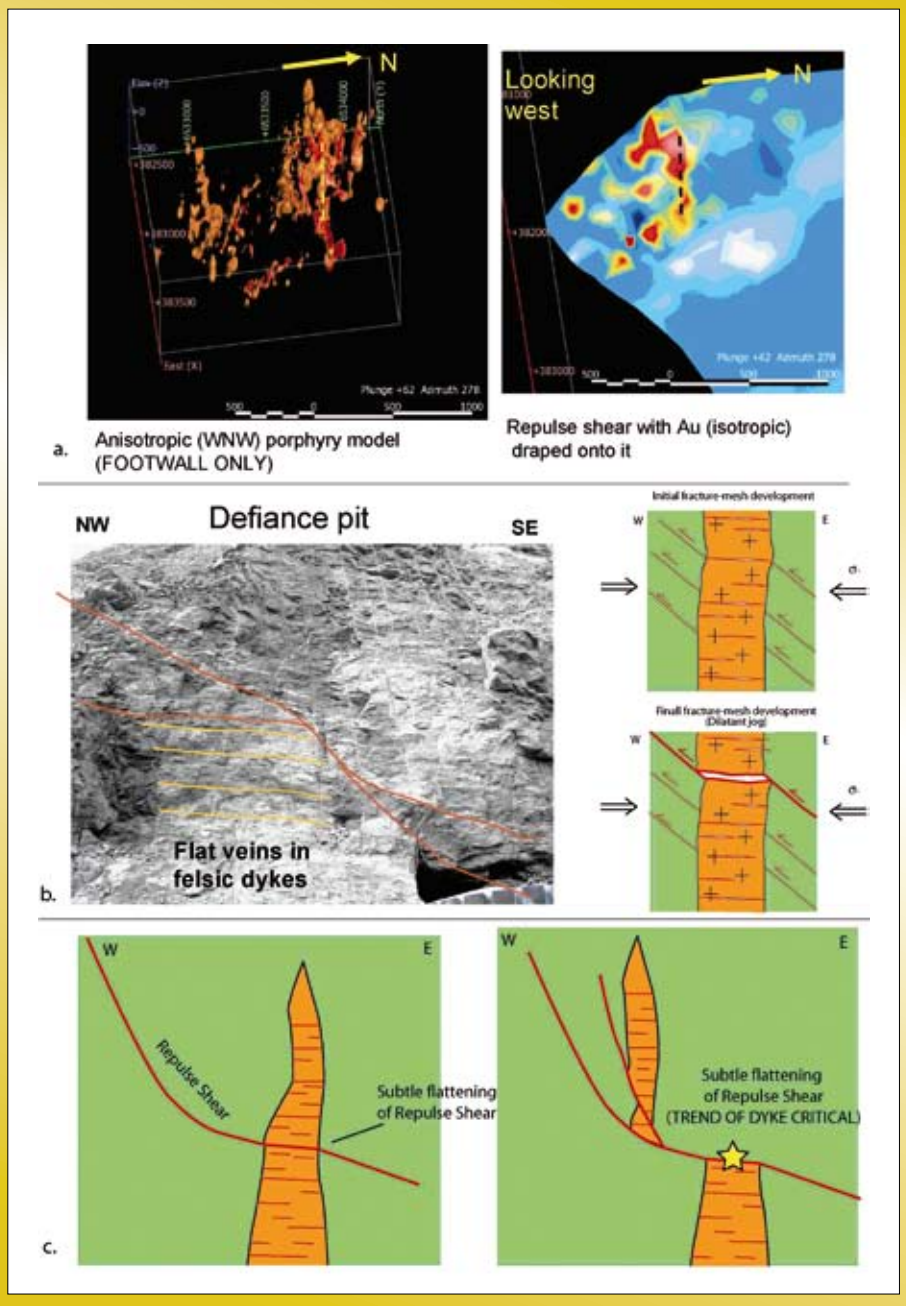


*Figure 3.9.13: Gold linked to footwall porphyry trends beneath the Repulse Shear. The dykes trend WNW- but also NW in other areas. a) Left hand figure is a view looking down to the west onto Leapfrog model of porphyry dykes in the footwall of the Repulse Shear. Right hand figure is the gold grade (isotropic model) draped onto the Repulse Shear. Note the grade trend parallel to the footwall porphyry dykes marked by the dashed lines. b) Flat mineralized veins with a porphyry and model showing how dilatant space is generated. c) High grade along the Repulse Shear is interpreted to be due to flatter zone of Repulse Shear controlled by footwall dykes. NOTE: these footwall dykes trend WNW in (a) producing a WNW-trend to the mineralization.*

with the trend of the Mars Shear, indicates the quartz veins developed in association with normal or extensional movement on the Mars Shear. Some of the mineralized veins are also extensional shear veins with geometries indicative of normal movement (Figure 3.9.14c). The kinematic interpretation is that the Mars Shear is an extensional step-over that transfers strain from the Bellisle Fault to the Gamma Island Fault (Figure 3.9.16). Unlike the Victory-Defiance or Revenge deposits, the Mars deposit sits along a transtensional segment of the fault system where the major faults trend between WNW and NW instead of between NW and N, this aspect of the system will be addressed in a later section.

In summary, the field relationships from the Gamma Island Shear indicate shallow dipping WNW-trending structures exist. These WNW-trending faults have a control on the grade distribution, their timing relationship to with respect to dolerite emplacement is problematic, but they are inferred to have formed at a similar time to the Playa-Bellisle aults. In most respects these shallow dipping WNW-trending faults are interpreted to be very similar in nature to the Playa and Repulse Faults, but have a more NW- to WNW trending strike, anticlockwise of the regional NW- to NNW-trend (Blewett et al., 2008b).

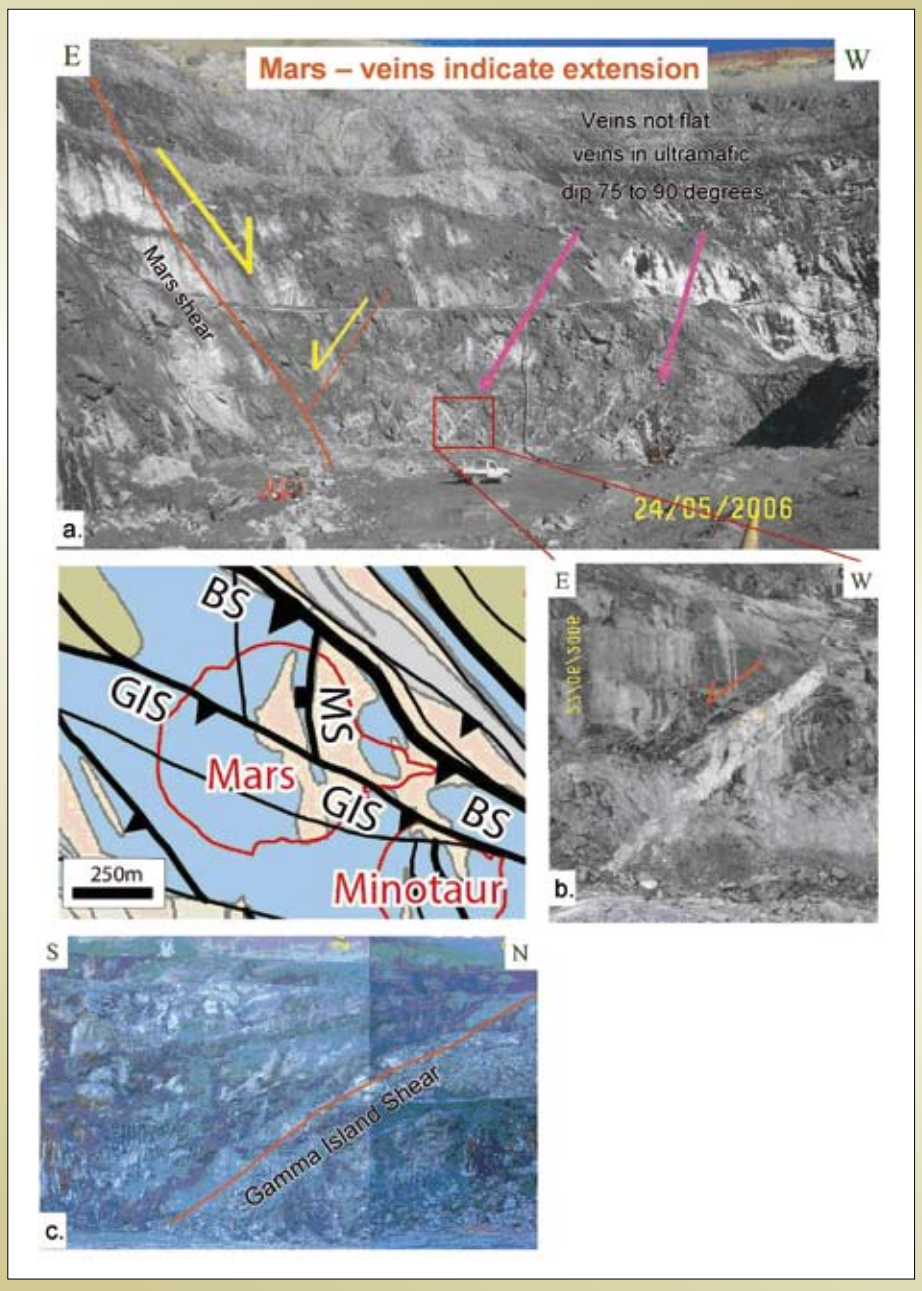


*Figure 3.9.14: Mars deposit with the Mars Shear (MS) and Gamma Island Shear (GIS). For the geological map north is aligned straight up the page. a) Main Mars Shear with steep-dipping mineralized veins. Some of these are extensional shear veins with a conjugate geometry. (b) Detail of extensional shear vein with normal movement sense. c) Gamma Island Shear (GIS).*

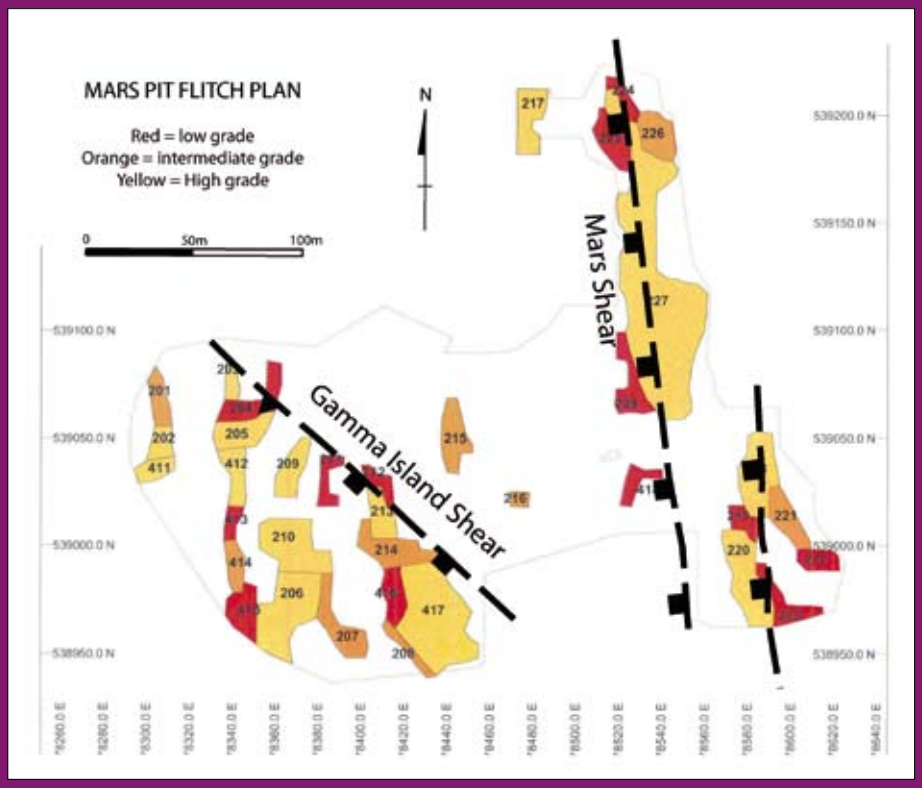


*Figure 3.9.15: Gold grade (flitch) plan highlighting Gamma Island Shear and Mars Shear have on grade distribution. The mineralized zones are N-S trending but are also controlled by the Gamma Island Shear (Note WNW-trend to grade), indicating this structure was also a controlling feature syn-gold.*

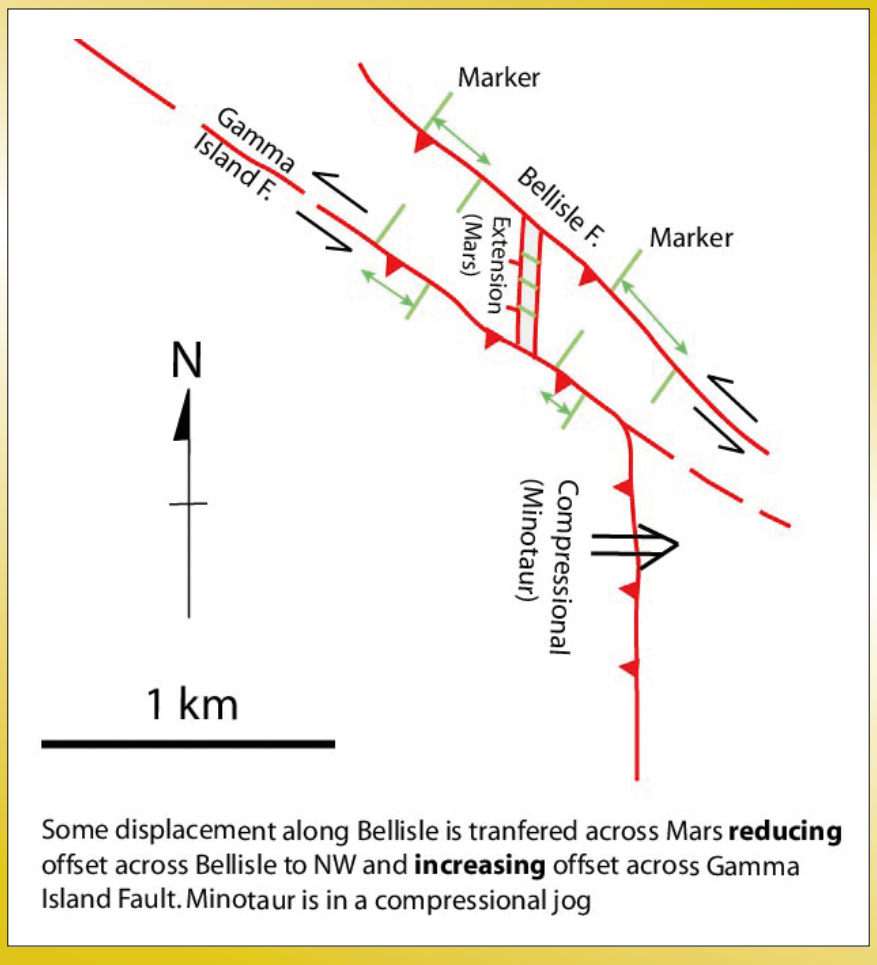


*Figure 3.9.16: Interpretation for Mars deposit. This deposit sits within a transtensional region (Figure 3.9.14) and is inferred to be an extensional step over that transfers strain from the Bellisle Fault to the Gamma Island Fault.*

#### 3.9.3.2.3 Late-stage post-gold W- and WNW-trending faults and dykes.

One feature noted during the interpretation was a number of late stage WNW- and W-trending features. The most prominent of these are the Proterozoic dykes that in many areas trend E-W. There is also a late-stage set of S-dipping thrusts that clearly over overprint the steep-dipping WNW-trending transfers. These faults are prominent in the Delta North pit (Figures 3.9.11c, 3.9.11d), but have also been identified at the Revenge deposit. These thrusts are associated with horizontal quartz veins that could potentially be confused with earlier low angle veins associated with earlier high grade gold.

### 3.9.3.3 Early D3 extension syn-late basin development

One key feature highlighted in the compiled sections is the presence of a series of normal faults identified in between the Santa Ana and Intrepide deposits (sections 1 and 2, Figure 3.9.5). These normal faults (marked on Figures 3.9.3, 3.9.4) appear to have a control on the geometry of high phosphorous intrusions (Mafic-type granites of Champion and Sheraton, 1997). These intrusions are associated with an extensive volume of low-grade gold that may be genetically linked to the intrusions (section line 1, Figure 3.9.5). The associated normal faults are adjacent to a major late basin (late basin sediments are labelled on Figure 3.9.3) and the normal faults are inferred to postdate D2 thrusts (section line 2, Figure 3.9.5), and are also cross cut by later sills and thus are not part of a late-stage post-gold phase of extension (section line 2, Figure 3.9.5). These relationships are consistent with the normal faults having formed at about the time of late basin development (at ca. 2665 Ma; e.g., Connors et al., 2005), this was linked to extension, and defined as the regional D3 event in the chronology of Blewett and Czarnota (2007). These normal faults were rotated by later shorting associated with the inversion of the late basins during the D4 event, which was also associated with major gold lode development (Blewett et al., 2008a, 2008b. The intermediate dykes that occur throughout the field area over print the D2 folds, but they are in turn over printed by all later deformation events. In summary, the normal faults and intermediate dykes (and associated plutons) appear to be broadly coeval.

The orientation of the normal faults, and the dominant trends of the intermediate dykes, suggests the extension was directed ENE-WSW to NE-SW (see also Blewett et al., 2008b). In some areas the dykes have variable trends (e.g., in the North Orchin deposit), or intrude along WNW-trending transfers (Figure 3.9.10) which may suggest in some areas there orientations represent a local intrusion relation stress field that has over whelmed the far field stress (for example the variable striking dykes at North Orchin are above a major dome imaged in the seismic lines). Field relations on the Repulse Fault in the Victory-Defiance complex (Figure 3.9.17), indicate there was a phase of NE-directed extension (interpreted to be part of the D3 event in Figure 3.9.17) prior to major thrusting on this fault associated with the development of the extensive low-angle vein arrays associated with major gold mineralization (interpreted to be part of the D4 event in Figure 17). Ruming (2006) also documented the steep vein arrays (shown in Figure 3.9.17c) and similarly interpreted that their formation during NE-SW (D3) extension predating the main stage (D4) gold veins.

### 3.9.3.4 Transpressional and transtensional zones

Previous workers have highlighted the controls dilational and contractional jogs have on the development of major gold systems along the NNW-trending Boulder-Lefroy Fault, which had a component of sinistral-slip during major gold mineralisation. At a regional scale left-stepping strike changes have been defined as transtensional jogs, while right stepping strike changes have been defined as compressional jogs e.g., Weinberg et al., (2004). During main stage gold at St Ives, defined as D4 by Blewett and Czarnota (2007), the far field major principal stress is inferred to have been WNW-ESE. A change from W-directed to NW-directed thrusting along the Repulse Fault occurred during mineralisation (Ruming, 2006), and there may have been more than one applied stress tensor (this possibility is highlighted by the two different shortening directions shown in Figure 3.9.18). The D4 stress field was applied to a pre-existing architecture, resulting in the development of transtensional and transpressional segments. Previous studies have highlighted the role of contractional fault segments within the St Ives gold field during the D4 event e.g., Nguyen et al., (1998). This D4 stress field is distinct from the earlier D2 stress field associated with the development of the main Kambalda Dome, and associated faulting, which was inferred to have been oriented NE-SW (e.g., Foster Thrust, Blewett et al., 2008b).

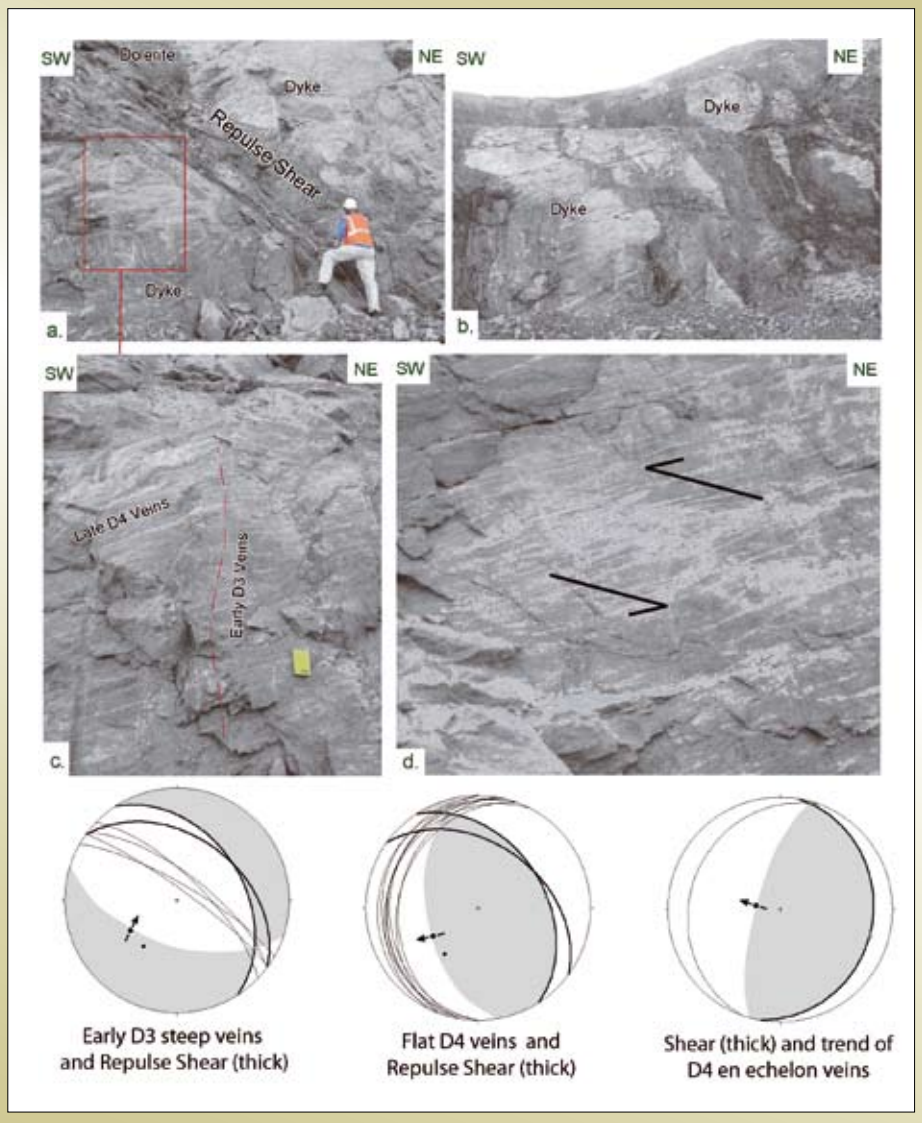


*Figure 3.9.17: Relationships along the Repulse Fault (Victory-Defiance) – see section line 5-5' in Figure 3.9.5. The early transport marked by D3 veins is extensional (by top-the-NE normal movement) followed by D4 top-the-W thrusting (see stereonets). a) Repulse shear with location of Figure 3.9.15c shown. b) Boudinaged dykes with low angle extension veins. c) Early (D3) steep veins over printed by flat extension veins (D4). Veins indicate NE-SW extension on the Repulse Shear – see stereonets. d) En Echelon Shear veins – geometry indicates top-to-the-west transport.*

As part of the study zones of transpressional and transtensional have been inferred by assessing the strike changes of key fault segments in the interpretation (Figure 3.9.18 – note inset at bottom left of this figure). This interpretation was then linked to the observed kinematics on these different segments to produce a new structural domain map. At a smaller scale the individual interactions of variably oriented faults introduces an additional layer of complexity to the fault kinematics, which has also been integrated into the interpretation. One of the aims of this approach was to be more predictive as to the style of mineralization that may occur in target areas.

Consistent with previous studies, field observations made at the NW- to N-trending fault segments identified have both sinistral reverse and reverse kinematics e.g., the Repulse Fault (Figure 3.9.17), the Thunderer Fault (Figure 3.9.19), the Delta Shear (Figure 3.9.20) and the ductile shears hosting the Temeraire deposit (Figure 3.9.21).

The major new contribution of this study has been in assessing the structural style within regions of the fault network that are transtensional. The A-lode is an example of a gold deposit located on a transtensional fault segment (Figure 3.9.18). This lode has extensional vein arrays indicative of sinistral-normal movement (Figure 3.9.22).

An assessment of the large-scale fault geometries highlights that the Bellisle Fault and the Gamma Island Shear have a left-stepping geometries splaying from the Playa Fault - the region through which these structures project should be transtensional for the syn-gold stress field i.e. the structures are a mirror image to the geometry of the

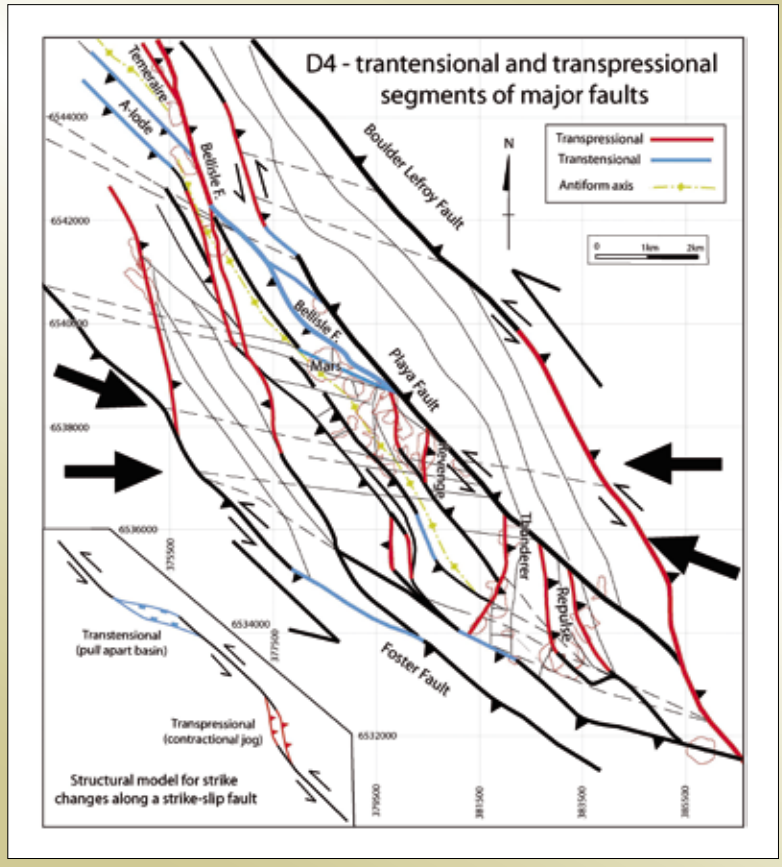


*Figure 3.9.18: Map highlighting inferred transpressional and transtensional fault segments based on strike (during main stage Au – the inferred far field stress directions are shown as large black arrows).*

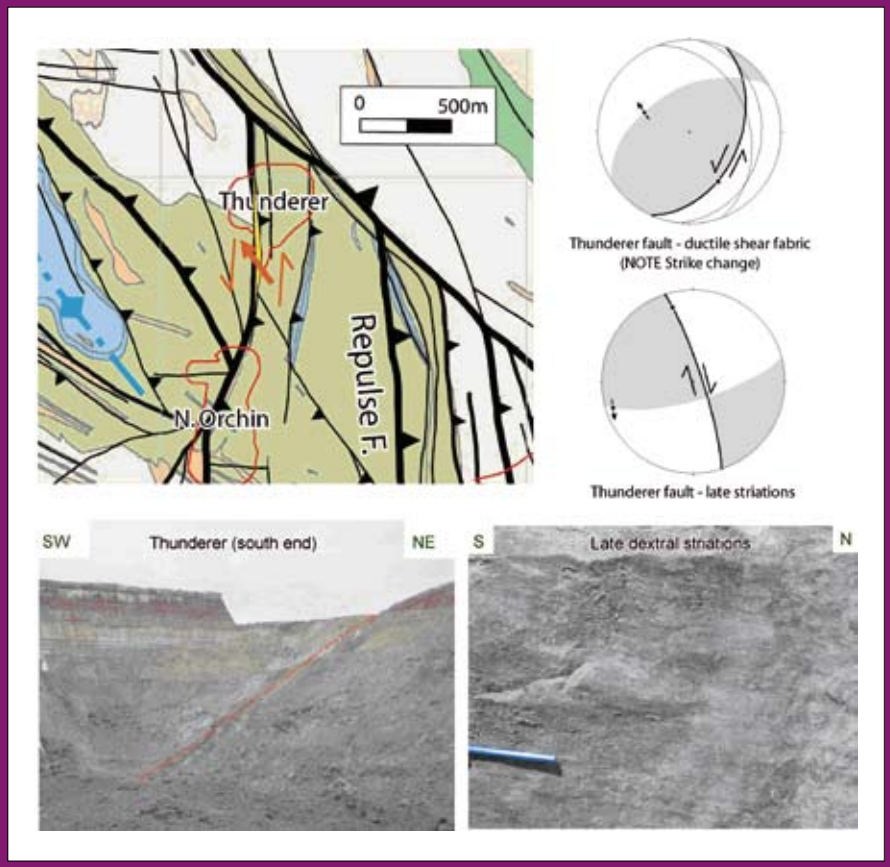


*Figure 3.9.19: Kinematics within the Thunderer deposit and map of deposit location. Ore stage lineations along the main shear (see photo of south end of pit) indicate the Thunderer Shear is a thrust with a small component of sinistral movement. The deposit appears to sit at a dilatant site at a left-stepping strike-change within this regime – see map and top right stereonet). Late stage lineations associated with hydrothermal alteration indicate a dextral over print (bottom right photo).*

Repulse and Thunderer Fault shown on Figure 3.9.18 that are both compressional structures with varying amount of sinistral movement (Figures 3.9.17, 3.9.19). The Bellisle Fault and the Gamma Island Shear are both coloured blue in Figure 3.9.18 to highlight the inferred transtensional nature of these structures (the Gamma Island Shear bisects the Mars deposit). The field relationships within this area indicate that this transtensional zone is not a simple extensional "pull-apart" structure that would normally develop along a transtensional segment of a fault i.e. as shown in the inset at the base of Figure 3.9.18. Instead the field relationships indicate that extensional step-overs developed in these transtensional regions, with strain transferred from one strike-slip structure to another (e.g. from the Bellisle Fault to the Gamma Island Shear; Figure 3.9.16) via extension on pre-existing structures, such as the Mars Shear (Figure 3.9.16). The consequence of this is that in the Greater Revenge Area some N-trending structures are extensional (e.g., Mars shear), while other N-trending structures that lie on contraction segments are pure thrusts (e.g., Revenge; Nguyen et al., 1998).

Extensional step-overs have also developed in other areas that are not readily identified via the classification of contractional and transtensional fault segments shown in Figure 3.9.18. With the exception of the intense strain observed within the hangingwall of some major contractional jogs, at a larger-scale the study area predominantly has major faults that acted as bounding structures to relatively coherent fault blocks. These fault blocks have been displaced relative to each other, and extensional step-overs have developed in some areas where major irregularities exist along the margin of a given fault block to allow "block-on-block" movement. Whether a transtensional step-over developed is a function of the relative movement of each block and the geometry of

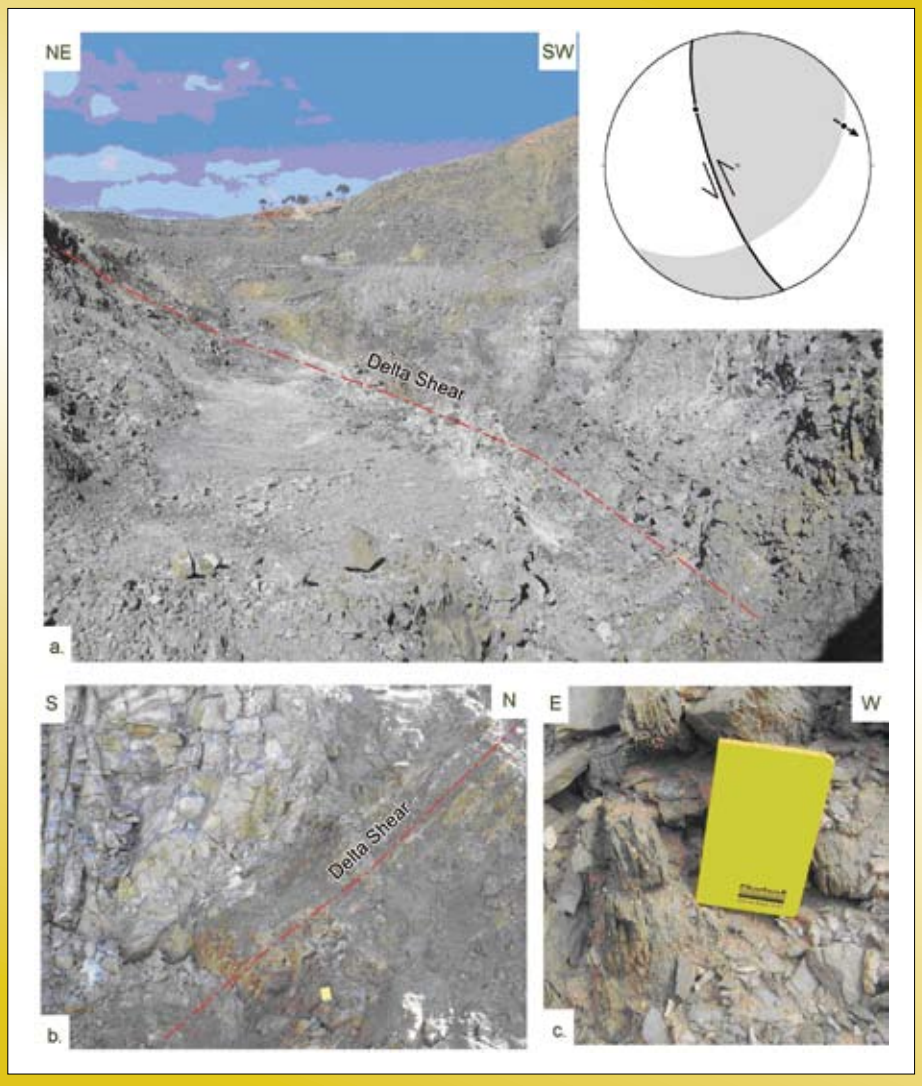


*Figure 3.9.20: Delta Pit Shear. a) view looking down the Delta Shear. Delta Pit. Stereonet of ore stage lineations indicate it is a sinistral-reverse fault b) Close up photo of Delta Shear. c) Ductile fabric associated with Delta Shear.*

the boundary between the two blocks. The best example of one of these transtensional step-overs is the Life Boat deposit (Figure 3.9.23). The West Agamemnon deposit in the Great Revenge Area is also inferred to be one of these extensional step-overs (Figures 3.9.24, 3.9.25).

The extensional step-overs are marked by extensional movement on the mineralized structure, and there is potential for additional deposits of this type in the belt as they have not been a drill target previously. The extensional step-overs can introduce marked kinematic variability into a given area because they are controlled by the topography of the edge of a given fault block, which means they can have variable orientations. The western side of the Greater Revenge Area has more than one extensional step-over (Mars and West Agamemnon), with marked complexity developing as a result (Figure 3.9.26).

Figure 3.9.27 is the final structural domain model for the structural interpretation covering the Kambalda Dome to Greater Victory Area. This domains the study area into regions dominated by 1) strike-slip faulting, 2) sinistral-reverse to reverse faulting and, 3) sinistral normal to normal faulting. The domaining integrates transtensional and transpressional zones based on the camp-scale fault trends i.e. NW-trends are most commonly transtensional, and NE-trends are most commonly transpressional. However, the smaller scale localized extensional step-overs that are hard to predict. The observed kinematics have been integrated into the figure with the black and white arrows

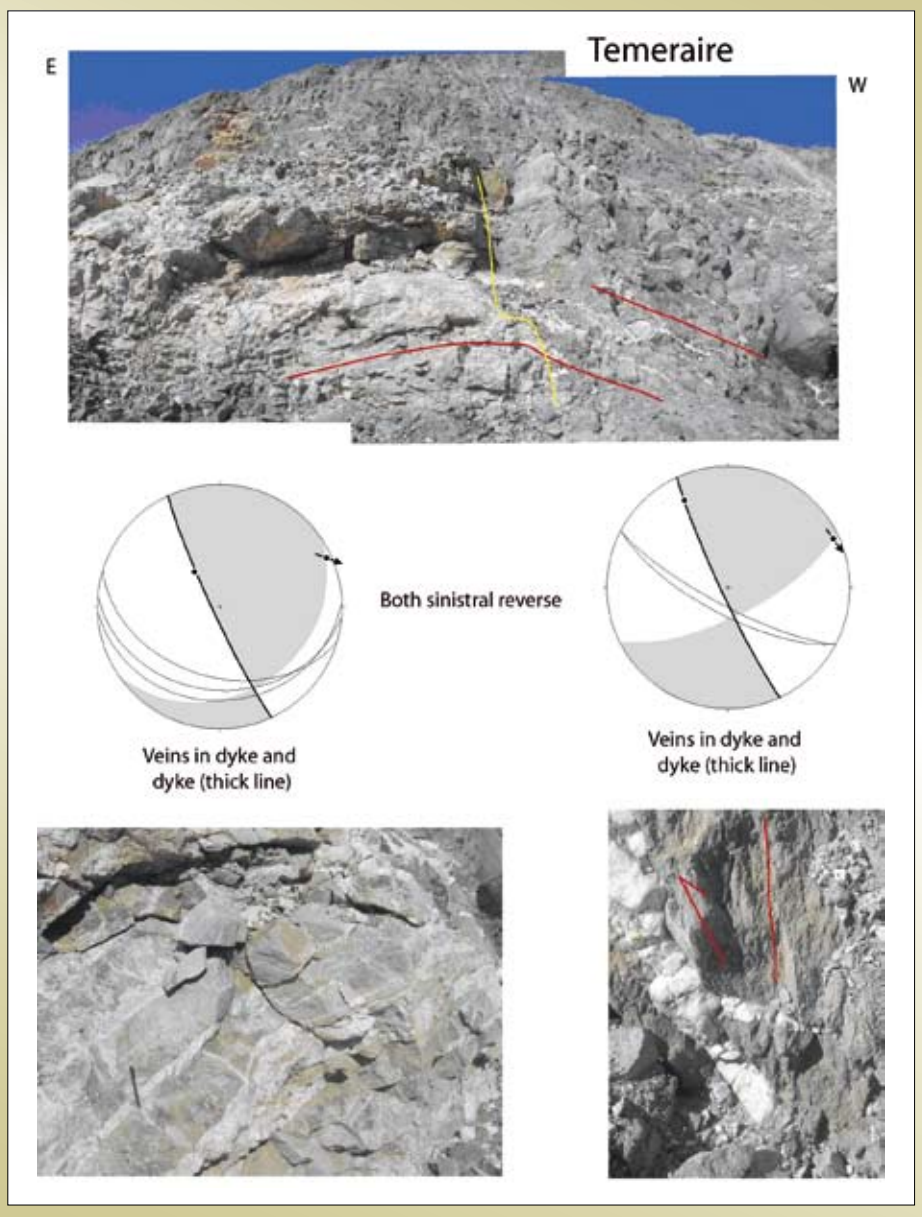


*Figure 3.9.21: Temeraire deposit (location marked on Figure 3.9.3). Mineralized veins have developed in association with a rheology contrast between ultramafic rocks and porphyry dykes. The vein relationships indicate reverse and also sinistral-reverse kinematics. Compare this to A-Lode (Figure 3.9.22).*

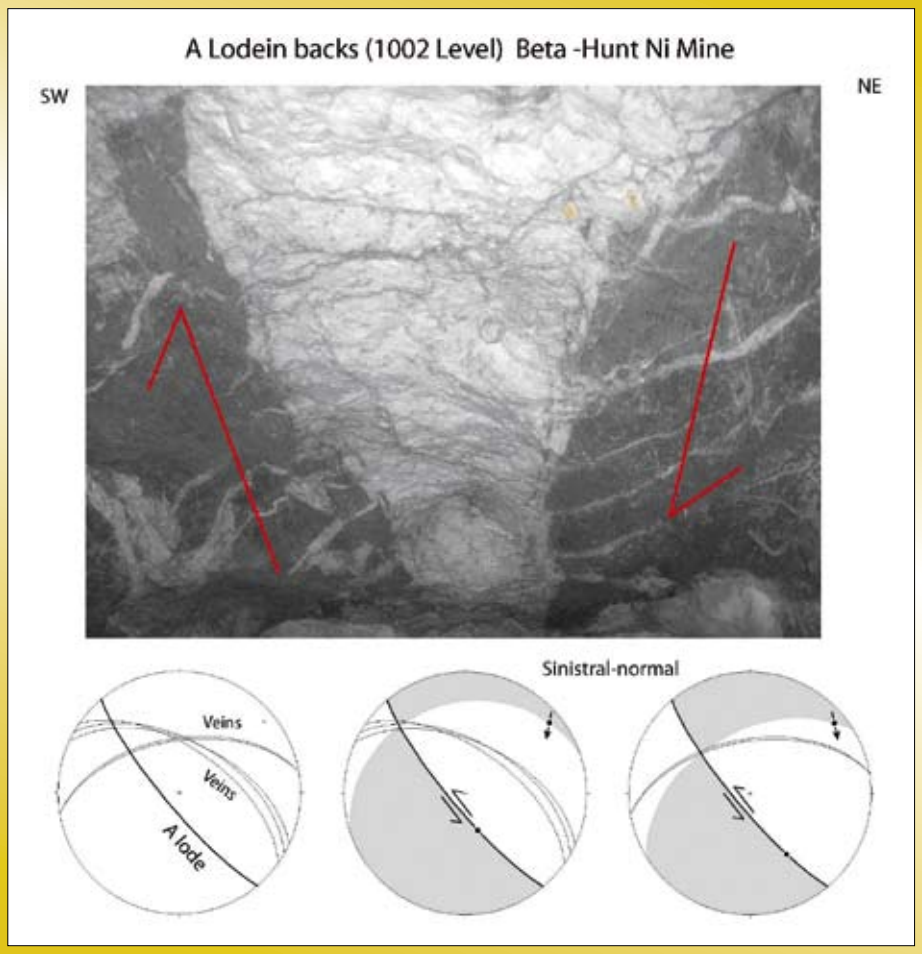


*Figure 3.9.22: A-lode – Beta Hunt mine, 1002 level. The mineralized shear is sinistral-normal. The location of A-lode on the Kambalda Done is shown in Figure 3.9.8 and also approximately in Figure 3.9.18.*

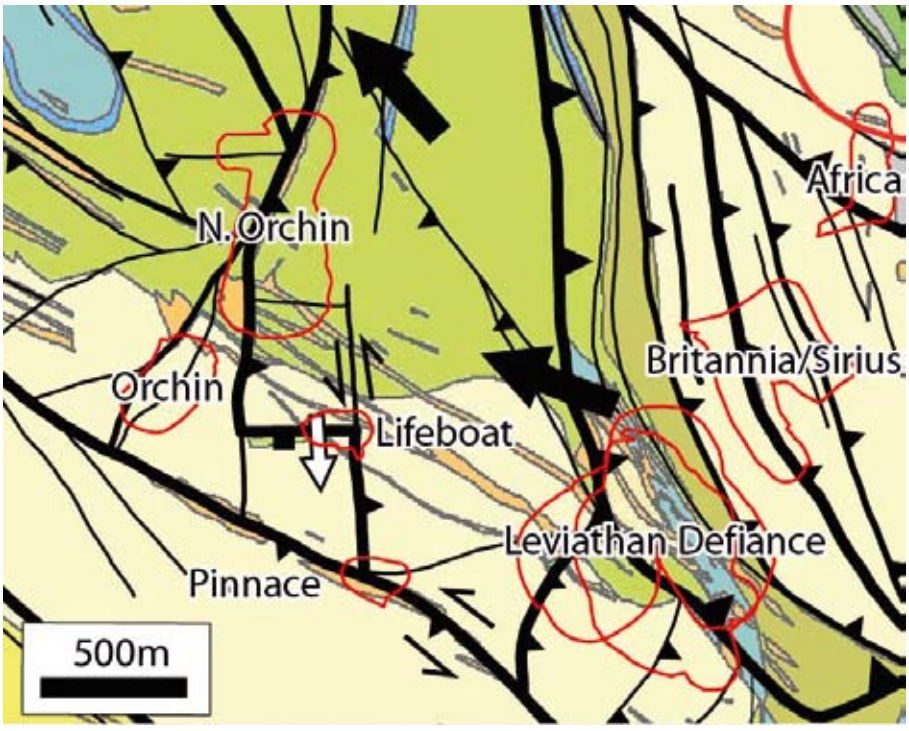


*Figure 3.9.23: Lifeboat – this deposit is an example of an extensional deposit (fragments of dolerite are exhumed within the fault system in the hangingwall of the main fault) and mapping within the pit identified normal movement. The deposit is inferred to be an extensional step over, the white arrow denotes the extensional hangingwall transport for the Lifeboat deposit, the black arrows summarize the sinistral-reverse hangingwall transport for the Repulse and Thunderer Faults*

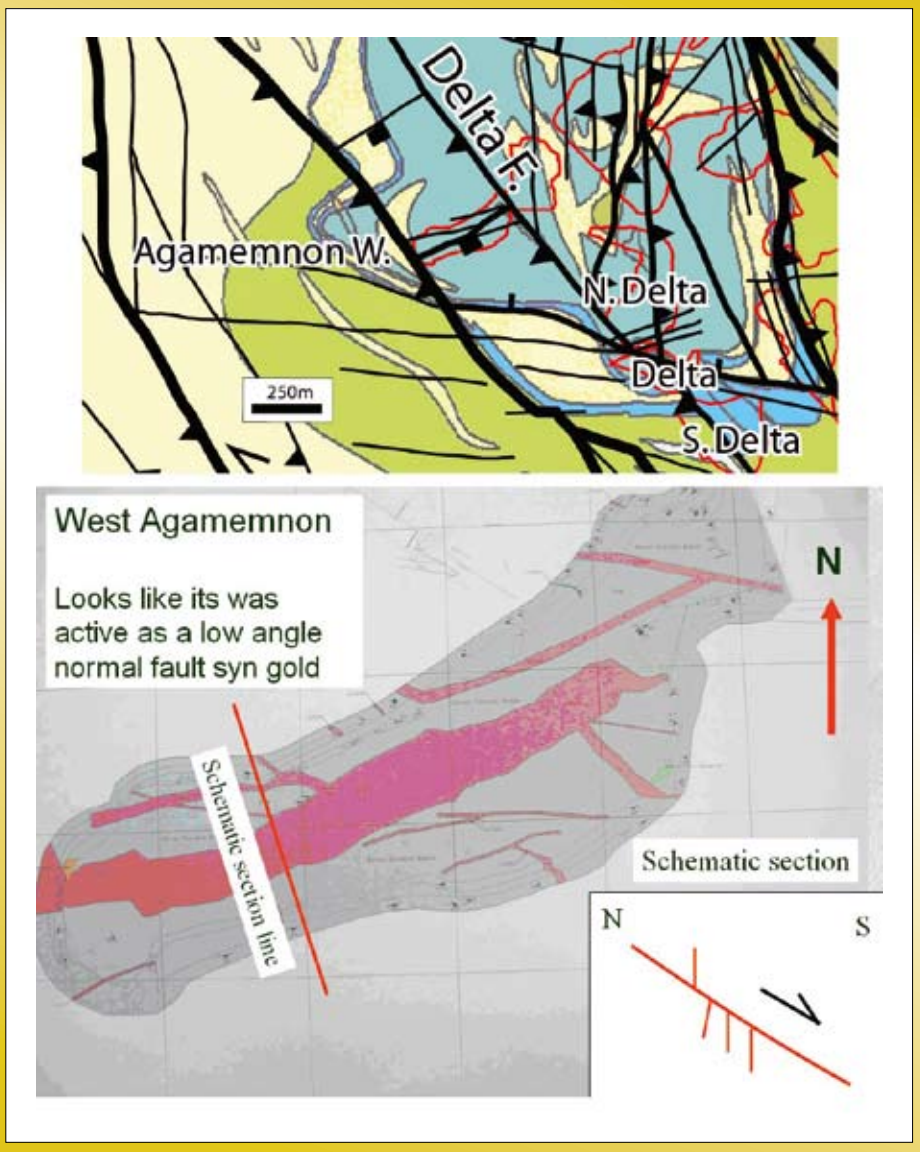


*Figure 3.9.24: Agamemnon West. This deposit has a major low angle shear dipping 25 to 30° to the SSE that is associated with steep dipping veins/shears. The geometry is indicative of normal movement on a shallow dipping fault.*

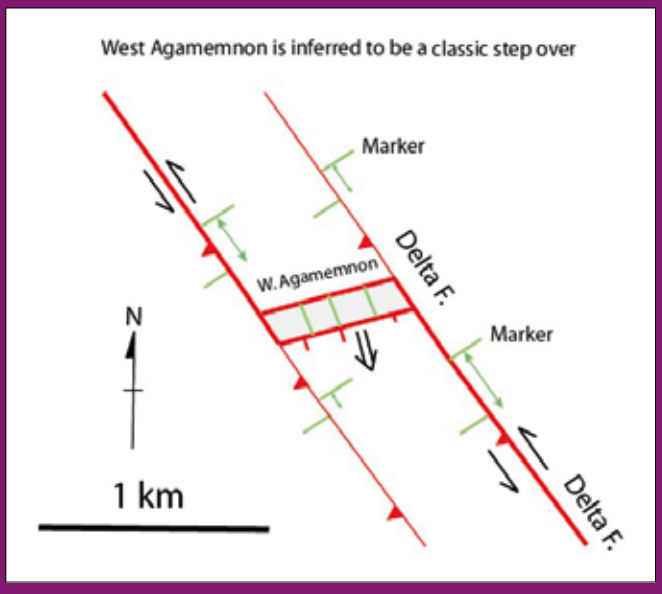


*Figure 3.9.25: Model for Agamemnon West. This is inferred to be an extensional step-over between two strike-slip faults.*

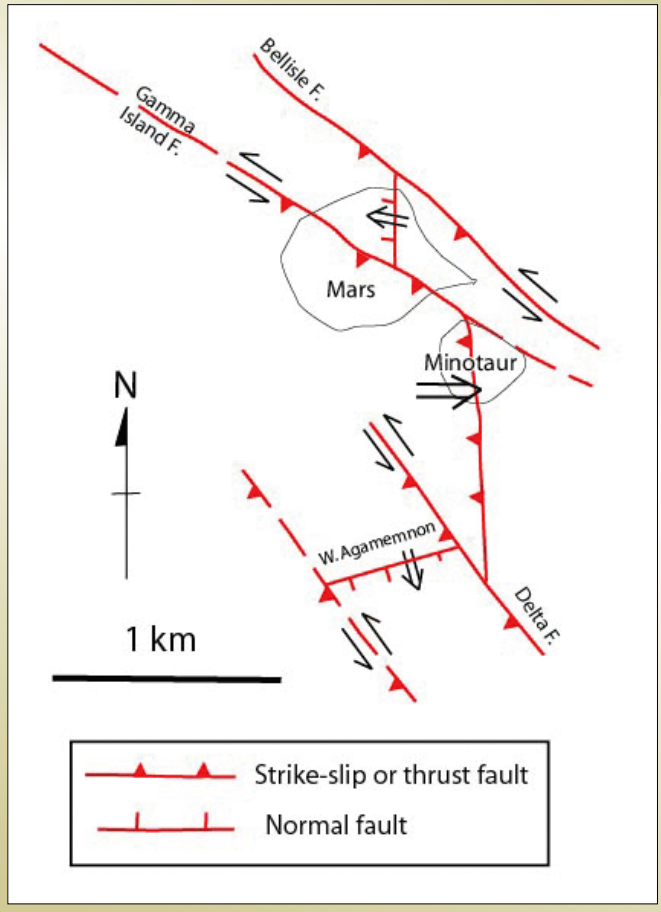


*Figure 3.9.26: Model highlighting kinematic complexity between deposits (Greater Revenge Area).*

indicating the hangingwall transport of the rocks. The white arrows represent faults with a normal or extensional movement sense, and the black arrows represent faults with a reverse movement sense

The structural domain model (Figure 3.9.27) breaks the area along the axis of the Kambalda domain into fault-bounded blocks that are inferred to be relatively internally coherent and have been displaced relative to each other. Many of the faults appear to have propagated on the flanks of the Kambalda Dome, and the interpretation includes a central domain (coded green) that overlies the underlying Kambalda Dome. The dominant reverse offset on the blocks surrounding the Central domain, combined with the fault dips, means that this domain is a footwall unit and is the structurally lowest fault bounded unit in the corridor between the Playa and Foster Faults. It is also important to recognize that not all of the faults would have been through going and active during the gold event.

The structural domain model takes into account the asymmetry introduced into the system by the strike and dip changes of the Playa Fault. As a result the transpressional domains are broken into higher and lower strain domains and, whilst some of the units on the western flank of the Kambalda Dome are symmetrically identical, they are not in the direct footwall of the Playa Fault. As a result these areas are lower strain (marked by a less intense red) and they have been interpreted to contain a more diffuse distribution of faulting that did not develop into major coherent faults that accommodated significant strain. The significance of this for the style of mineralization has not been fully assessed, but may mean the area will contain a more "smoky" distribution of gold grade instead of more localized occurrences. Furthermore, if the Playa Fault was a key gold-bearing fluid conduit, then these areas may also be less prospective.

### 3.9.3.5 Late stage dextral faulting (D5)

Late stage N- to NE-trending dextral D5 faults occur throughout the study area – note that these have been defined as D4 faults in the terminology of Swager

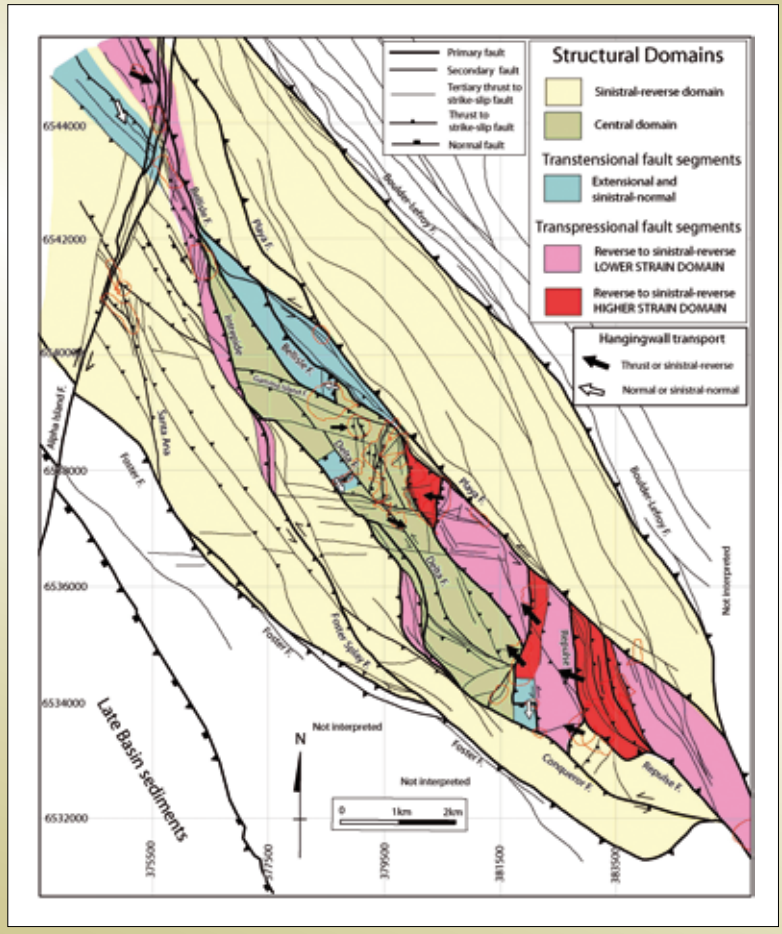


*Figure 3.9.27: Map of structural domains syn-the main gold event. Hangingwall transports for different key segments are shown.*

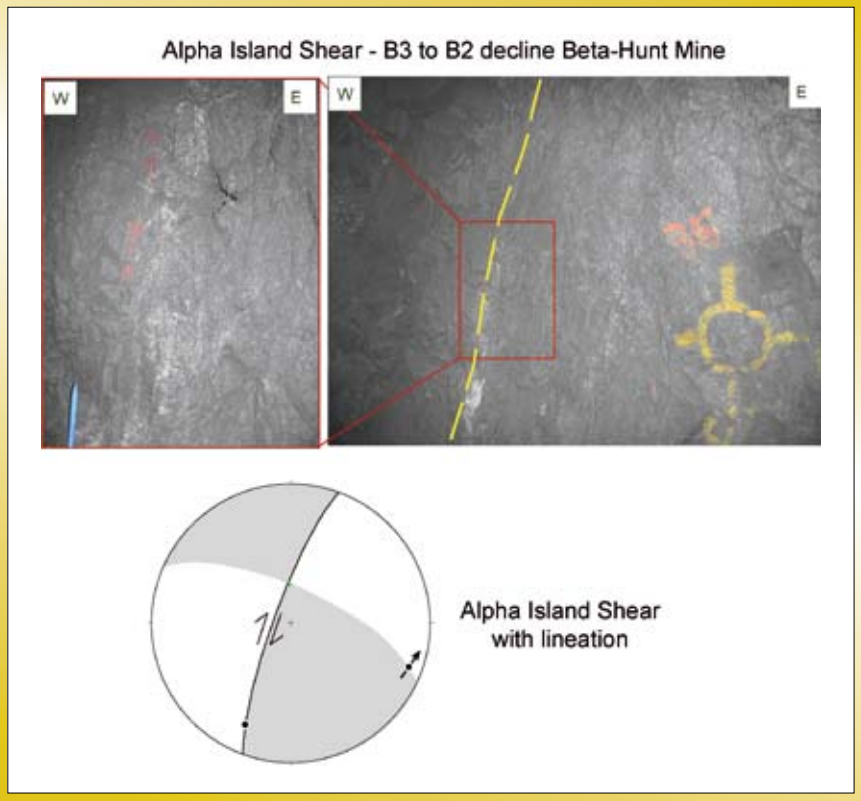


*Figure 3.9.28: Quartz-carbonate veins parallel to the Alpha Island Shear (edge of Alpha Island Shear is marked by yellow dashed line, the fault was a zone of gouge and vein at least 5 metres wide at this locality (the eastern limit of the fault was obscured). B3 to B2 decline, Beta-Hunt Mine.*

(1997) and Connors et al., (2005). The 5 million ounce Mt Charlotte deposit in Kalgoorlie is commonly linked to this regional event (Blewett et al., 2008a). In the study area, the largest of these faults is the Alpha Island Fault, which has clear dextral offsets in map vein and late-stage slickenlines indicating almost pure strike-slip movement (Figures 3.9.3, 3.9.28).

Late-stage dextral reactivation has also been observed throughout the study area e.g., late-stage dextral fibres on the Thunderer Fault are associated with strong hydrothermal alteration (Figure 3.9.19). The extent of gold mineralization associated with the D5 event has not been constrained, although any N-trending structure (such as the Thunderer Fault) may have been reactivated. A set of NE-trending veins with low grade gold within the Victory Complex (Ruming, 2006) are inferred to be linked to this event. High-grade gold in other Yilgarn deposits associated with D5 dextral faults commonly has base metal associations (e.g., at Sunrise Dam, Agnew, King of Creation and Woodcutters), and is inferred to be around 2640 Ma (Blewett et al., 2008a; Davis et al., 2008).

In other areas D5 gold is associated with top to the SW thrusting and high-grade gold develops in NE-trending accommodation zones between NW-SE trending thrusts (Davis et al., 2008)

## 3.9.4 Proposed structural evolution

### 3.9.4.1 Early D1 extensional architecture

The early fault architecture (Figures 3.9.29, 3.9.30, 3.9.31) has been inferred by integrating a large number of observations and is a highly interpretative model. In the Greater Revenge Area the Mount Blanc Transfer Zone is an early structural feature that controlled the dolerite and komatiite thickness, is a clear trend in the gravity data, and has been mapped in the field. In many areas the early WNW-trending transfer faults are transposed by later high strain zones – in most cases all of the mapping focus has on the structural complexity of the relatively thin package of rocks in the hangingwall of the major shears (e.g., the Victory Complex), and not on the deeper level underlying architecture. With the exception of the Gamma West

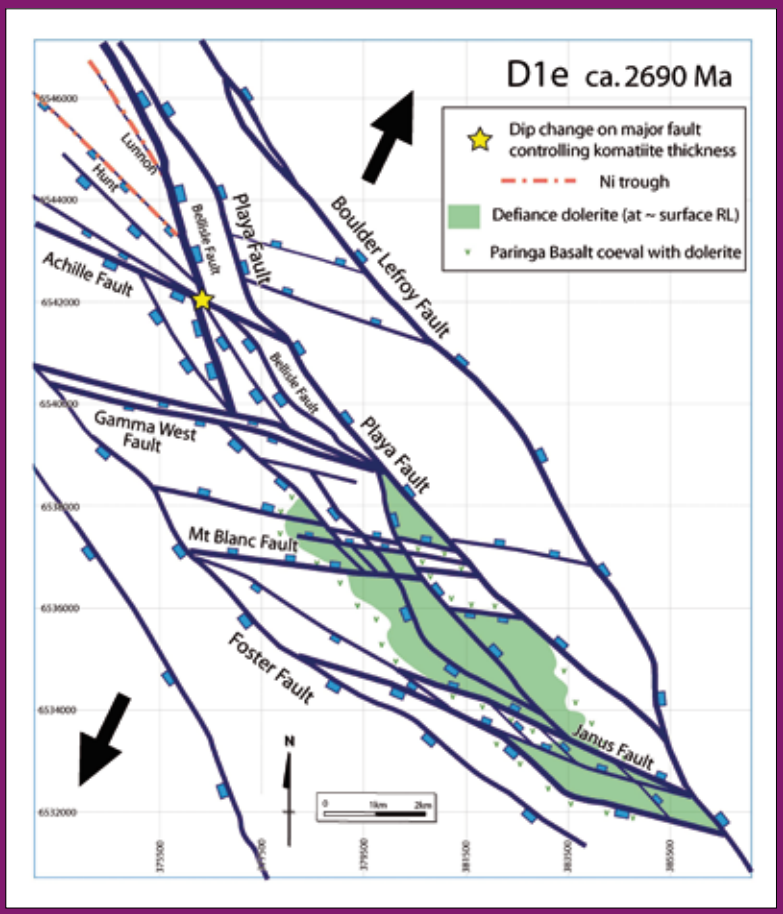


*Figure 3.9.29: Inferred geometry of the early extensional fault system, this controls the dolerite distribution. These faults have dips that match the present day dip of faults in the structural interpretation (Figure 3.9.3). Some of the dolerite contacts are inferred to be controlled by these faults. This system is inferred to have extended an earlier architecture (2.9 Ga) fault architecture (Czarnota et al., 2008), with the system representing oblique extension. The Janus Fault is an additional transfer to those named by Connors et al., (2005), and is overprinted and obscured by later faulting events. The Ni shoots (orange dashed lines) sit in a transtensional footwall zone to a left stepping fault (Bellisle Fault).*

Fault (Figure 3.9.29), which has a correlation with the Gamma Island Shear, other early structures (e.g., Achille Fault) have had to be inferred from komatiite thickness variations (Figure 3.9.30), trends in the SAM or gravity data (Figure 3.9.31), dolerite trends (Figures 3.9.2, 3.9.29), and also porphyry dyke swarms oblique to the dominant structural grain (Neumayr et al., 2007, 2008).

In the interpretation the dip of the early structures has been inferred by assuming that many of the currently mappable faults are reactivated early normal faults (the dip of the Mount Blanc Fault and Gamma West Fault in Figure 3.9.29 is based on the present day structures). For the Greater Revenge Area such an assumption is justified because the amount of shortening has been too low to destroy the early architecture. One example of an output from this style of interpretation is the dip change on a key N-S trending feature highlighted by the yellow star in Figures 3.9.29 to 3.9.31 on either side of the Achille Fault – the E-dipping segment is the Bellisle Shear, while the W-dipping segments are the mineralised structures within the Intrepide deposit. This interpretation is independently supported by the komatiite isopach data, and is discussed later in the section.

An additional WNW-trending structure has been integrated in the early fault architecture, and has been termed the Janus Fault (Figure 3.9.29), which has been over printed by later intense deformation associated with the contractional jog that defines the Victory-Defiance Complex. This structure marks the southern extent of the Defiance Dolerite, a major gravity trend, and a set of porphyry dykes that are inferred to have intruded along this structure.

The early architecture bears a strong resemblance to a rift system where a pre-existing boundary was extended obliquely to the trend of this boundary, which potentially may have been an earlier rift (see also Blewett et al., 2008b). In this interpretation the Boulder-Lefroy Fault marks the axis of the earlier boundary and the inferred extension direction was NE-SW (Figure 3.9.29). Recently published Nd model age maps clearly define an older major basement boundary (aged 3.1 to 3.0 Ga) trending NNW

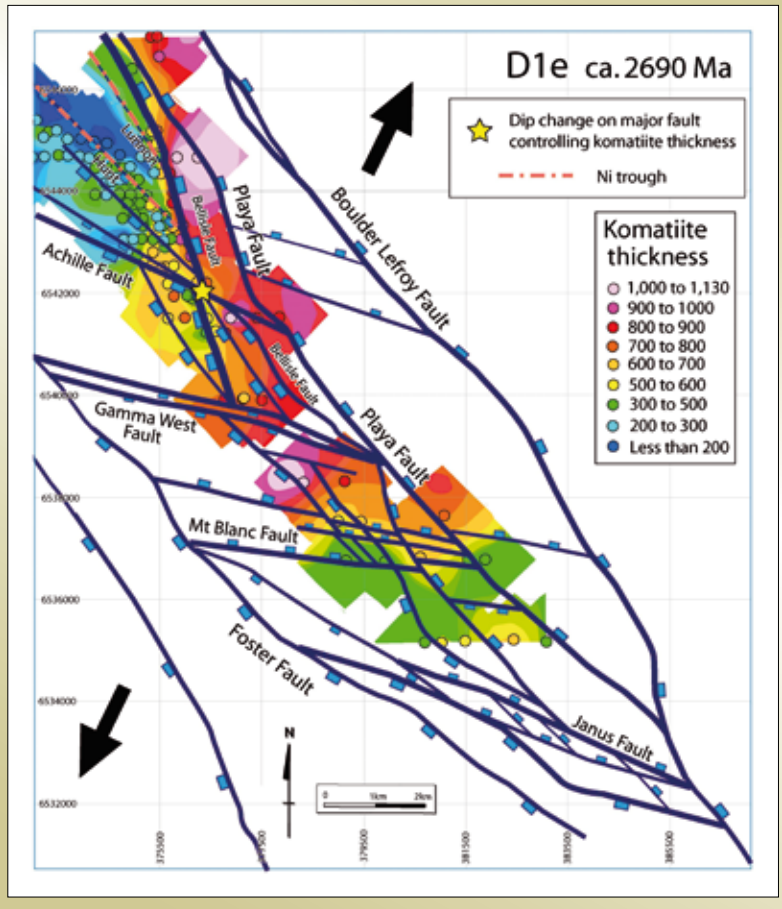


*Figure 3.9.30: Early extensional architecture with isopachs of komatiite thickness from Connors et al., (2005). Note the change in dip of the early faults across the Achille Fault with an associated change in komatiite thickness. The Mt Blanc Fault appears to be a key control on Komatiite and also dolerite distribution (see Figure 3.9.29).*

(Champion and Cassidy, 2007). Analogue modelling of this type of extensional system (Keep and McClay 1997), produced relay faults with a marked geometrical similarity to the architecture shown in Figure 3.9.29. Such relays are not strictly transfer faults that separate steps in the rift or faults of opposite polarity, as they can define small grabens with the accommodation space infilled by syn-rift sediments or volcanics – this would have occurred synchronously with rift infill in the hangingwall of the NNW-trending faults. We infer that many of the WNW-trending faults are relays that have accommodated oblique extension, in other cases these have acted as transfer faults.

The best example of an early transfer is the Achille Fault, because it separates faults with different dips – this region is marked by the yellow star in Figure 3.9.29. Significantly, this change from E- to W-dipping faults across the Achille Fault correlates with a thickness variation in the komatiite – note the sudden increase in thickness in the hangingwall of the W-dipping fault to the south of the Achille Fault. The interpretation of the early rift architecture around the Achille Fault is critical, because of the nearby komatiite-associated Ni shoots. The current interpretation suggests the Lunnon and Hunt Ni shoots may be located in the footwall of an early growth fault (the Bellisle Fault) just north of a left step in the growth fault, and the Ni shoots may be located in an area footwall collapse.

In marked contrast to the Achille Fault, the Mount Blanc Fault is inferred to have been a relay fault during D1 extension. This fault is associated with a substantial thickness increase in the komatiite units along its strike, which reflects rift units infilling the accommodation space generated in its hangingwall. Note that during later stage syn-gold D4 deformation the Mount Blanc Fault was reactivated as a transfer fault (Figure 3.9.9).

The early rift architecture is also inferred to have controlled the dolerite distribution. However, some dolerites are controlled by the distribution of the early faults; in other cases these contacts are inferred to not be fault controlled (these areas are schematically shown by the irregular dolerite contacts in Figure 3.9.29). The interaction between

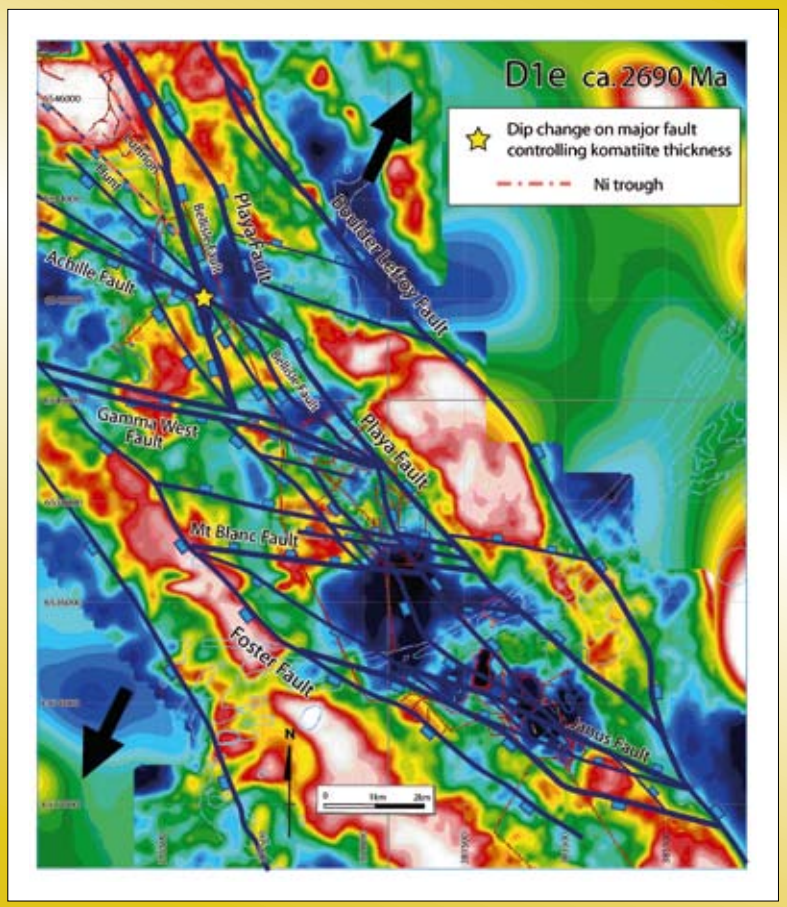


*Figure 3.9.31: Early extensional architecture with high pass filtered gravity.*

the faults acting as feeders for the dolerites versus them acting as a barrier to horizontal flow of magma (producing a sharp dolerite contact) is not known. One interesting aspect is the presence of the key Nickel-associated komatiites flows in the north (and the massive thickness of Lunnon Basalt) compared to the extensive dolerites in the south. This stratigraphic difference may reflect a change in the focus of rifting from north to south from the emplacement of the Lunnon Basalt to the Paringa Basalt (and associated dolerites). This feature is interpreted to reflect a change in the accommodation space that was infilled by the volcanic and intrusive units during the D1 rifting.

### 3.9.4.2 D2 inversion (E-W compression)

Previous workers have inferred an early thrusting event within the Yilgarn Craton (termed D1 by Swager, 1997). Faults that have been related to this event are folded by later D2 folds, and commonly imbricate the Lunnon Basalt. In the study area the Foster Fault is an example of one of these structures (Figures 3.9.3, 3.9.4) that has previously inferred to be a D1 thrust fault. Apart from the repetition of the Lunnon Basalt, and the folded nature of the Foster Fault, there is a complete lack of mesoscale field evidence for N-S thrusting. In contrast, all other deformation events can be documented from the extensive pit and underground exposures. In most orogens small scale structures mimic larger scale deformation and, with the exception of some imbrication internally within the Kapai Slate, earlier D1 thrusts have not been identified (see Blewett et al., 2008a). The Foster Fault is inferred to be a roof thrust with a folded geometry that developed during progressive D2 compression, but it may have been an early D1 normal fault. In this scenario the Foster Fault imbricated the Lunnon Basalt, and was then folded during ongoing NE-SW D2 contraction. This interpretation does not preclude early N-S thrusting in other areas of the Yilgarn.

The D2 event is the first major inversion of the earlier rift architecture with reactivation of older normal faults, and also the formation of new neoformed faults (Figure 3.9.32). A component of the development of the Kambalda Antiform occurred during D2 (the axis of which is marked on Figure 3.9.32), and the variations in fold tightness along strike (Figure 3.9.5) reflects strain being accommodated by variable amounts of faulting versus folding. The variation

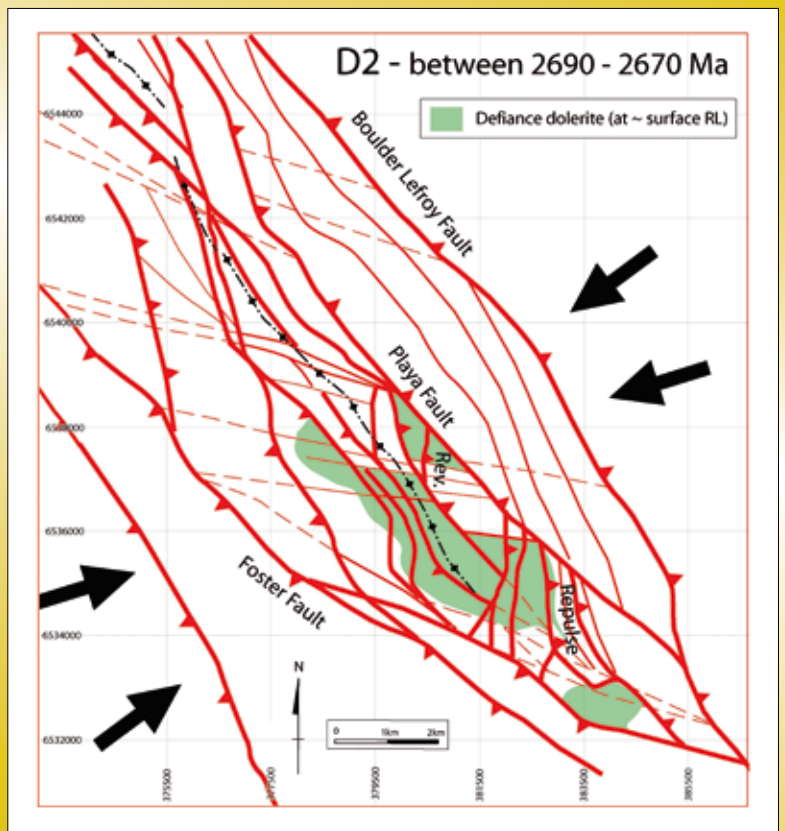


*Figure 3.9.32: D2 inversion of the extensional fault system. Development of the Repulse shear occurred at this time, as did the formation of the main antiform.*

is also inferred to reflect the earlier distribution of volcanic units (Figure 3.9.8), and the Kambalda Dome may have been an initial feature linked to syn-D1 magmatic processes, that was accentuated by D2 compression.

Classic lens-like fault geometries, typical of thrust belts, developed during D2 (Figure 3.9.32). The strike variations associated with these lens-like fault geometries was one control of the development of later compressional and transtensional zones during later reactivation during D4. However, one of the notable features of the structural interpretation for the Greater Revenge Area is that the critical N- and NNE-trending structures associated with the Revenge and West Revenge deposits (Figure 3.9.3) appear to be bounded by WNW-trending faults (the northern one is the Gamma Island Shear the southern one is the Mount Blanc Transfer Fault Zone). This suggests that these WNW-trending faults may control the distribution of these key compressional jogs.

The earlier inherited WNW-trending faults (Figure 3.9.33) introduce architectural complexity, with many of these

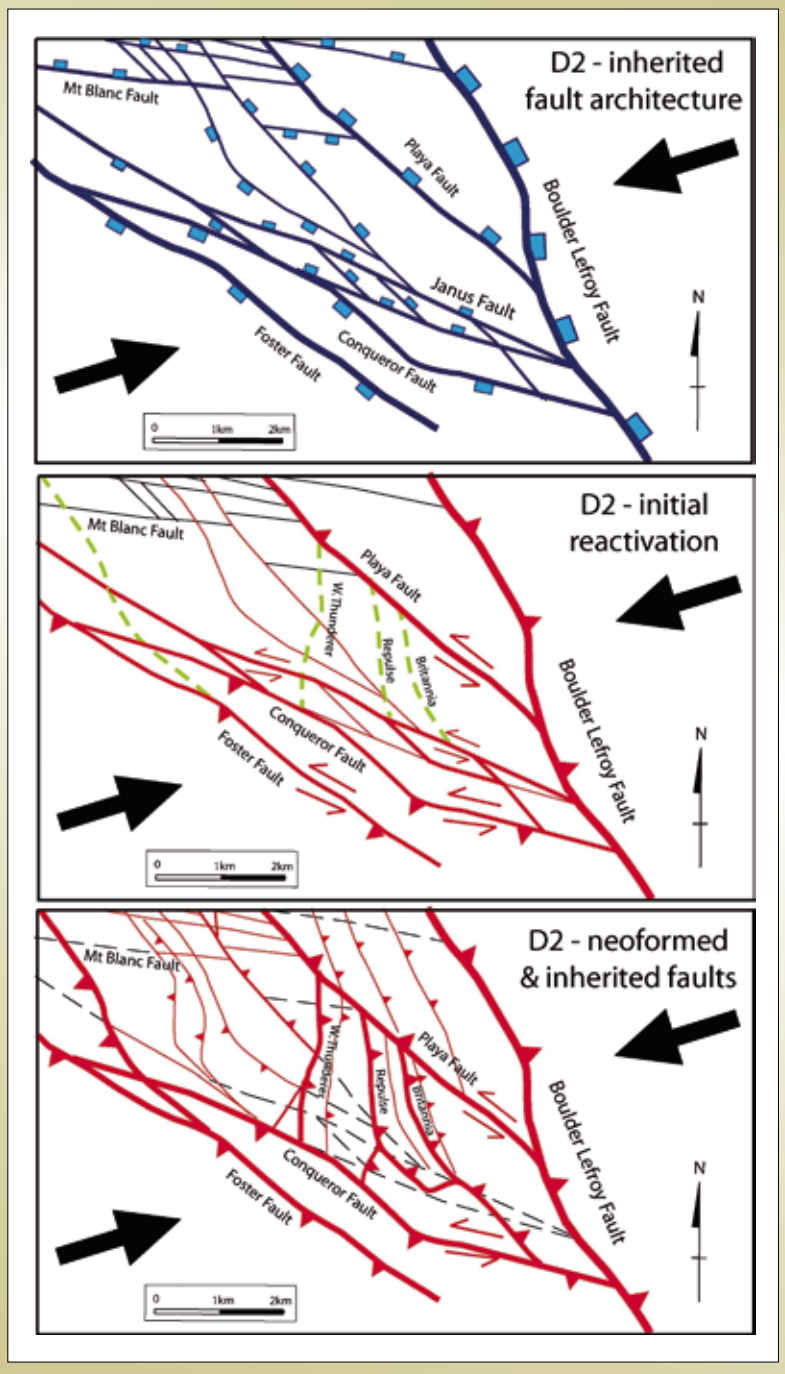


*Figure 3.9.33: Neoformed and inherited faults for D2. The Repulse Shear, which at a later stage becomes a critical contractional jog during main stage gold, and other related shears, developed as linking thrusts between two reactivated D1 extensional faults. The neoformed faults eventually overprint the earlier formed faults in some areas (e.g., the Janus Fault).*

structures not optimally oriented for slip during D2. The evolution during D2 thrusting is inferred to have involved some initial reactivation of the WNW-trending faults (Figure 3.9.33). However, during continued shortening, a series of neoformed N-trending linking faults formed that were optimally orientated for slip. The Repulse Shear, for example, is interpreted to be a linking thrust between two reactivated D1 extensional faults. These linking thrusts at a later stage became critical contractional jogs during main stage D4 gold. In some areas the neoformed faults overprint the earlier formed faults (e.g., the Janus Fault in Figure 3.9.33). However this critical topography links back to the presence of earlier WNW-trending transfer or relay faults. Whilst Figure 3.9.33 is an interpretation for the Greater Victory area, a similar evolution is inferred for the development of the Revenge Fault – this is located between the Gamma West Fault and Mt Blanc Fault in Figure 3.9.30.

The apparent control from WNW-trending faults on the N- and NNE-trending structures associated with the Revenge and West Revenge deposits (Figure 3.9.3) is an additional argument for the existence of the Janus Fault introduced in Figure 3.9.29. Compared to the regions along strike, the Greater Revenge Area has undergone less internal D2 shortening and we have used the camp-scale geometry in this area as a guide to interpreting the Greater Victory Area. The northern boundary of the N-trending Thunderer and Repulse Faults is defined by the Mount Blanc Transfer Zone. We have inferred the southern margin of these two structures was controlled by the early Janus Fault as shown in Figure 3.9.33.

### 3.9.4.3 D3 Extension and late basin development (NE-SW extension)

The D3 extensional event is inferred to be related to NE-SW extension (Figure 3.9.34), and corresponds to the emplacement of the late basin sediments (Nguyen, 1998; Blewett et al., 2008b). The majority of the intermediate porphyry dykes are inferred to have been emplaced during this phase, although some appear to have been syn-D2. The main argument for syn-D3 emplacement of these dykes, and associated larger intrusions, is that the dominant dykes trends are consistent with NE-SW extension (Figure 3.9.34) and there is also an apparent normal fault control on the shape of some of the intrusives

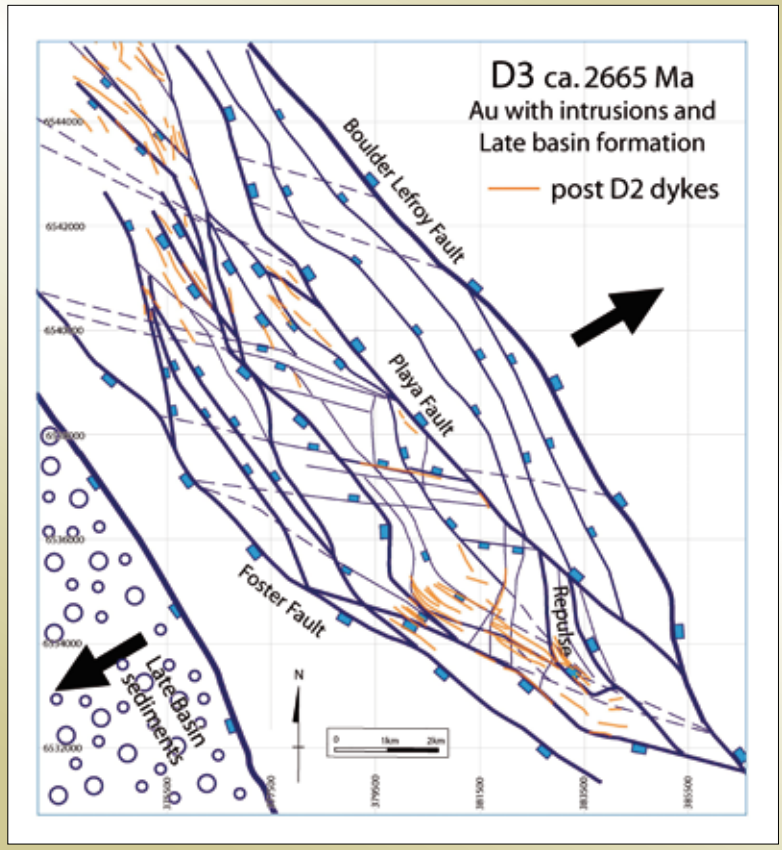


*Figure 3.9.34: D3 extension – deposition of the late basins and emplacement of related intrusions. Note the dykes near the Repulse Shear are interpreted to be utilizing an older fault trend (termed the Janus Fault in Figure 3.9.30). Evidence for D3 extension is preserved on the Repulse Shear (Figure 3.9.13c) and also as steep-dipping normal faults in sections that control intrusive contacts and offset D2 faults (see section lines 1-1' and 2-2' in Figure 3.9.5).*

(Section line 1, Figure 3.9.5). Significantly some of these intrusions (termed high phosphorous intrusions) are associated with drill hole intercepts with substantial interval of low grade gold mineralization. The D3 phase of deformation is inferred to be associated with low grade gold mineralization, however regionally major gold was introduced at Leonora and Laverton (Blewett et al., 2008; Czarnota et al., 2008). Some of the intermediate porphyry dykes also intrude along old WNW-trending transfer dykes (e.g., Figure 3.9.10) with dykes near the Repulse Fault inferred to have utilized the older Janus Fault trend (Figure 3.9.34).

### 3.9.4.4 D4 Main stage gold mineralization (E-W to WNW-ESE compression)

The main stage of mineralization is interpreted to be a reactivation of the pre-existing D1, D2 and D3 architecture. The shortening direction is inferred to have been oriented E-W to WNW-ESE, with compressional and transtensional zones developing within an overall sinistral-slip system that evolved because of the dominant NNW-trend of the faults (Figure 3.9.35). The Playa fault is inferred to have been a major fluid conduit, and it was also a structure that produced deformation induced permeability in its footwall and hangingwall. Fluids are also inferred to have focused along the flanks of the Kambalda antiform and also underlying major dome-shaped intrusive bodies, for example under the Victory Complex (Blewett et al., 2008b).

In some areas WNW-tending faults were reactivated as transfers, particularly where faults with opposing dips were juxtaposed (e.g., Figure 3.9.9), but in other regions these faults remained inactive. However, even in areas where the WNW-trending faults were not active, porphyry dykes intruding along these WNW-trending structures may have acted as fluid aquitards for horizontal flow, and also enhanced upward migration of fluids along the dyke's margins.

The porphyry dykes and intrusions modify the fault architecture creating additional rheology contrasts. As a result, the D4 deformation is not just a simple reactivation of a fracture mesh with an applied stress tensor distinct to previous deformation events. The intrusions stitched the D2 faults in some areas, effectively removing a segment of

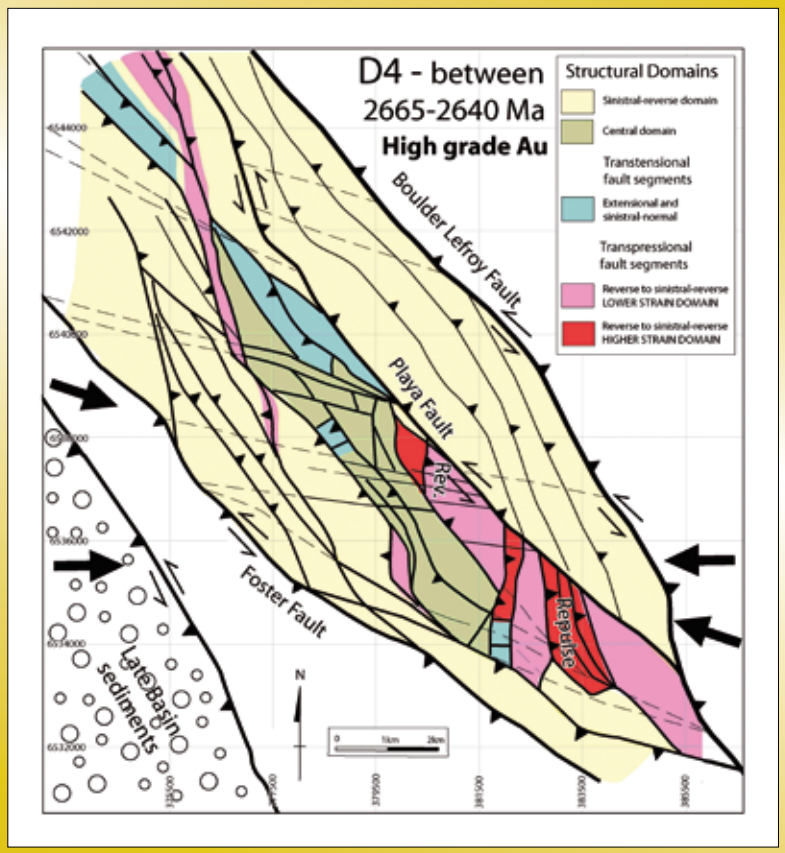


*Figure 3.9.35: Main stage gold event (D4 in the deformation history of Blewett et al., 2008a).*

a cohesionless fault surface from an area, with a subsequent control on how the structures where reactivated. Slip along the margins of the intrusives is also a key control on lode development in many areas (e.g., Mars and Santa Ana) with strike-changes of faults controlled by the intrusive contact. In other areas dykes produce competency contrasts within ductile shear zones predominantly containing ultramafic rocks (e.g., Temaraire, Figure 3.9.21). While slip along porphyry dyke margins occurs in some deposits, these dykes can have variable strikes up and down the belt with some dykes trending WNW and NE in contrast to the dominant NNW trend (Figure 3.9.34).

#### 3.9.4.5 D5 late stage dextral faulting and reactivation (NE-SW shortening)

During D5 new neoformed dextral faults developed, such as the Alpha Island Fault, and the major far field applied stress is inferred to have been NE-SW (Figure 3.9.36). However, the system at this stage is inferred to have been transtensional (NW-SE extension), with resultant development of extensive NE-SW trending vertical vein arrays in most areas that have been associated with low-grade gold in the Victory Deposit (Ruming, 2006). N-S trending fault segments are inferred to have been reactivated during D5 (Figure 3.9.36), with the Thunderer Deposit being an example (Figure 3.9.19). The full extent of gold mineralization associated with the D5 event has not been ascertained, however, the 5 million ounce Mt Charlotte gold deposit to the NNW at Kalgoorlie (Blewett et al. (2008a), is inferred to be related to this event and further deposits of this type may exist within the St Ives gold field.

### 3.9.5 Acknowledgements

This work was part of the Predictive Mineral Discovery Cooperative Research Centre Y4 project. The work utilized the data sets of Gold Fields Pty Ltd, which represents the work of a large number of current and past geologists from both Gold Fields Pty Ltd and also Western Mining Corporation Pty Ltd. The work benefited from discussion with a large number of people, in particular Ned Stolz, Karen Connors, Rick Squire, Phung Nguyen, Stephen Cox, Ed Baltis, Scott Halley, John Walshe, Peter Neumayr, Tony Roache, Jon Hronsky and Greg Hall.

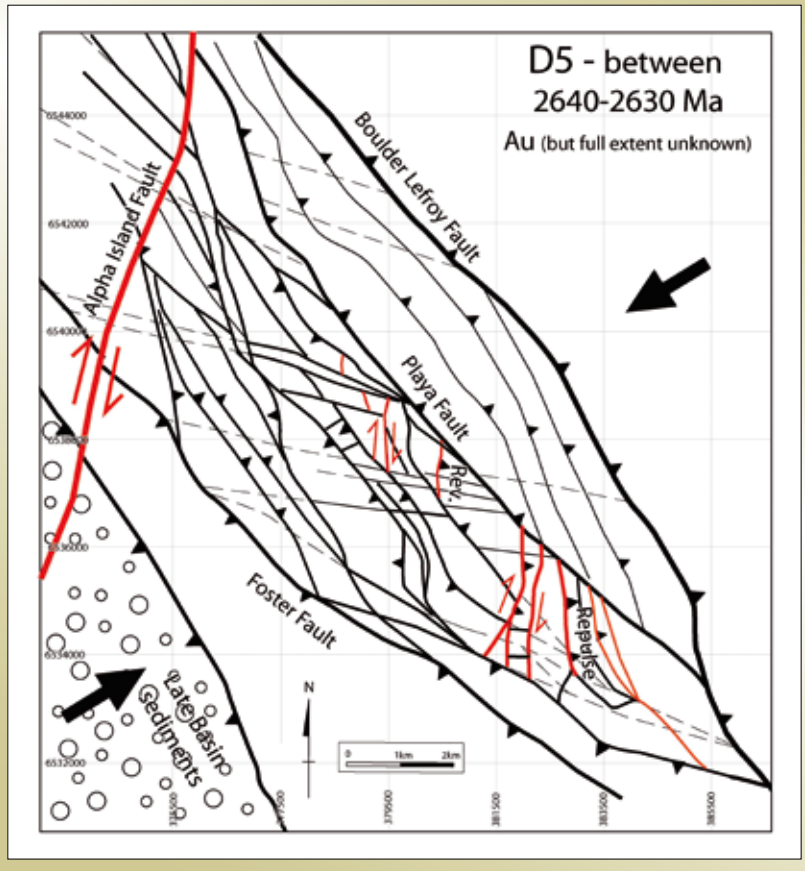


*Figure 3.9.36: Late stage dextral reactivation. This marks the formation of the Alpha Island Fault (Figure 3.9.28) and evidence for reactivation is recorded.*

### 3.9.6 References

Blewett R.S, Czarnota K., 2007, A new integrated tectonic framework of the eastern goldfields superterrane. Kalgoorlie 07 conference "Old Ground. New knowledge". September 2007, Kalgoorlie.

Blewett, R.S., Czarnota, K. Henson, P.A. and Champion D.C., 2008a, A revised tectono-stratigraphic framework for the Eastern Yilgarn Superterrane, this volume

Blewett, R.S., Miller, McL.,J., Squire R., Henson, P.A. and Champion D.C., 2008b, Architecture and geodynamic evolution of the St Ives camp, Kalgoorlie Terrane, Western Australia, this volume

Compston, W, Williams, I S, Campbell, I H and Gresham, J J, 1986. Zircon xenocrysts from the Kambalda volcanics: age constraints and direct evidence for older continental crust below the Kambalda-Norseman greenstones. Earth and Planetary Science Letters, 76:299–311.

Connors, K., Donaldson, J., Morrison, B., Davy, C & Neumayr, P., 2005 The Stratigraphy of the Kambalda-St Ives District:workshop notes Gold Fields Pty Ltd St Ives operation, Technical note No: TN SIG0329, 99 pages.

Cox, S.F., Ruming, K., 2004. The St Ives mesothermal gold system, Western Australia – a case of golden aftershocks? Journal of Structural Geology 26, 1109–1125.

Czarnota, K., Champion, D.C., Cassidy, K.F. Goscombe, B., Blewett, R.S., Henson, P.A. Groenewald, P.B., 2008. Geodynamics of the Eastern Goldfields Superterrane, this volume

Davis, B.K. Blewett, R.S. Squire, R. and Champion, D.C., 2008, Architectural and geodynamic controls during Au mineralisation around the Archaean Scotia-Kanowna Dome, Kalgoorlie Terrane, Western Australia, this volume.

Keep, M., and McClay, K.R. 1997, Analogue modelling of multiphase rift systems, Tectonophysics, 273, 239–270.

Nguyen P. T. 1997. Structural controls on gold mineralisation at the Revenge mine and its tectonic setting in the Lake Lefroy area, Kambalda, Western Australia. Unpublished PhD Thesis, University of Western Australia.

Nguyen, P.T., Cox, S.F., Harris, L.B., and Powell, C.M., 1998, Fault-valve behaviour in optimally oriented shear zones: An example at the Revenge gold mine, Kambalda, Western Australia: Journal of Structural Geology, 20, 1625–1640.

Neumayr, P., Walshe, J.L., Hagemann, S.G., Petersen, K., Roache, R., Frikken, F., Horn, L., and Halley, S., 2008, Oxidised and reduced mineral assemblages in greenstone belt rocks of the St Ives gold camp, Western Australia: vectors to high- grade ore bodies in Archaean gold deposits?: Mineralium Deposita.

Neumayr, P., Walshe, J.L., and Petersen, K., 2008, Alteration architecture of St Ives. this volume.

Ruming, K.J., 2006. Controls on Lode Gold Mineralisation in the Victory Thrust Complex, St Ives Goldfield, Western Australia. Unpublished PhD thesis, The University of Newcastle

Swager C.P., 1997, Tectono-stratigraphy of late Archaean greenstone terranes in the southern Eastern Goldfields, Western Australia, Precambrian Research, 83, 11–42.

Weinberg, R.F., Hodkiewicz, P.H., Groves, D.I., 2004. What controls gold distribution in Archean terranes? Geology 32; 545–548.

Weinberg, R.F., Van der Borgh, P., Bateman, R. J. and D. I. Groves, D.I., 2005, Kinematic History of the Boulder-Lefroy Shear Zone System and Controls on Associated Gold Mineralization, Yilgarn Craton, Western Australia Economic Geology, 100, 1407–1426.

## 3.10 Chemical architecture of the Leviathan Complex, St Ives Gold Camp

**Peter Neumayr, John Walshe and Tony Roache**

### 3.10.1 Introduction

This paper develops a picture of the architectural controls on mineralizing processes at the scale of the Leviathan Complex, St Ives Gold Camp, integrating a revised understanding of the structural and lithological architecture of the complex with new data on zoning of mineralogy and isotopic compositions of sulphides, sulphates and carbonates across the complex. The term Leviathan refers to a group of deposits, namely the Victory-Defiance open pit, Victory underground, East Repulse underground and Conqueror underground. In contrast a reference to a specific mine (e.g., Victory underground) is used to refer to the specific part of Leviathan.

The paper is divided into two sections. Section one (Geological Architecture) presents a revised geological architecture of the Leviathan complex, following a brief introduction to the geological setting of the St Ives Gold Camp. The distribution of lithologies has been reinterpreted using multi-element, whole-rock geochemistry and previously unmapped structures highlighted from 3D modelling of the distribution of gold and porphyries.

Section two (Chemical Architecture) begins with a summary of the mineralogical zoning at the camp scale, proceeds to a brief review of the thermo-chemical controls on mineral and isotopic zoning before discussing the significance of zoning in the Leviathan complex in relation to the structural and lithological architecture.

The discussion encompasses both camp-scale and deposit-scale observations and the exploration implications of the 3D chemical architecture. The paper builds on the concepts of multiple fluid reservoirs and depositional processes developed in (Walshe et al. 2008a; Walshe et al. 2008b).

### 3.10.2 Regional geological setting

The St Ives gold camp, which produced to date 265 t Au (77.7 Mt @ 3.42 g/t Au; Osborne, pers. comm. 2007), is located in the southern part of the Kambalda Domain within the Eastern Goldfields Superterrane of the Yilgarn Craton of Western Australia (Figure 3.10.1). Watchorn (1998) described in detail the geology and a number of the deposits in the St Ives gold camp which are hosted in predominantly late Archaean mafic-ultramafic lavas, minor interflow sedimentary rocks and intrusions that have been metamorphosed to upper greenschist and lower amphibolite facies. The regional stratigraphy in the St Ives camp comprises the 2.71–2.69 Ga Kambalda (mafic-ultramafic) and 2.69–2.66 Ga Kalgoorlie (intermediate to felsic volcaniclastic) sequences, with the 2.66 Ga Merougil Late Stage Basin (siliciclastic) unconformably to disconformably overlying the older sequences. The Kalgoorlie sequence comprises, from oldest to youngest, the Lunnon Basalt, Kambalda Komatiite, Devon Consols Basalt, Kapai Slate, and Paringa Basalt. The sequence is intruded by Defiance, Condenser and Junction dolerites. The Kalgoorlie sequence comprises the volcaniclastic and epiclastic rocks of the Black Flag Group. The camp is bounded by the regional NNW-trending Boulder-Lefroy fault zone to the east and the Merougil fault zone to the west. The structural history is summarised in Table 3.10.1.

Mafic, intermediate and felsic porphyry dykes are particularly abundant and exposed in the Leviathan and Revenge gold deposits and zones of greatest porphyry abundance are centred on distinct lows in detailed gravity data (Figure 3.10.2). Deep diamond drill core intersections and detailed seismic data, coupled with gravity analyses, suggest concealed massive stocks of porphyry intrusions at about 1000 m below the present surface (Edward Stolz, pers. comm., 2002). The Kambalda granodiorite, which is exposed in the Kambalda dome, is considered an equivalent to the concealed felsic porphyry stocks.

### 3.10.3 Geological architecture of the Leviathan Complex

#### 3.10.3.1 Introduction

The Leviathan deposits have been studied and described in detail in the past. A number of studies have focussed on the structural and hydrothermal alteration history, respectively. However, despite considerable effort both the structural and chemical elements, which control the location of gold mineralisation, have only been integrated at the ore shoot scale. As a consequence, typically only

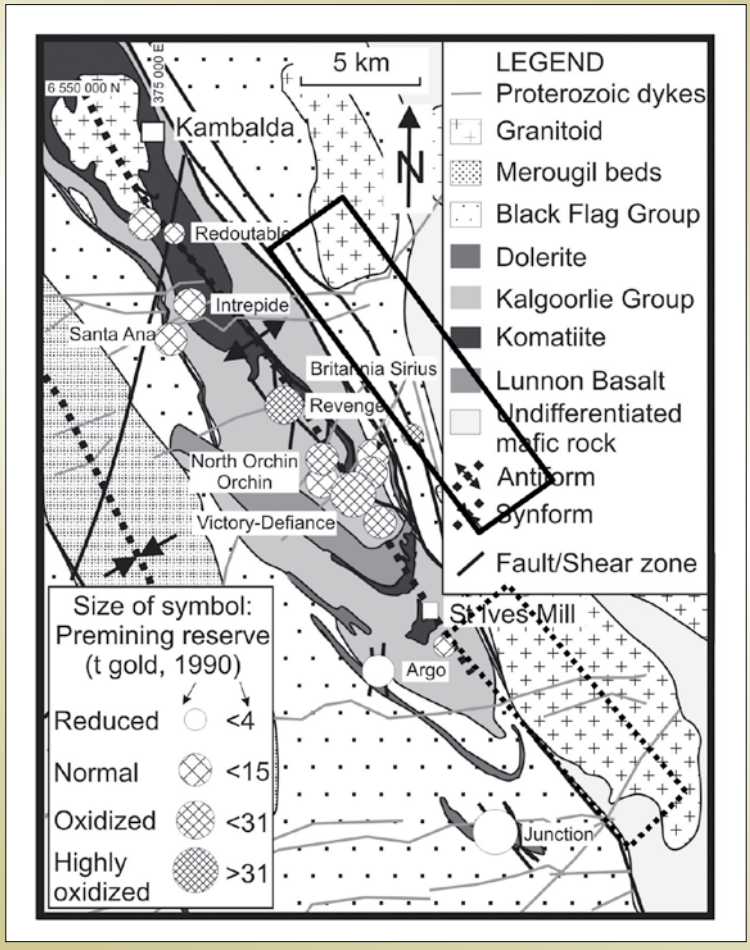


*Figure 3.10.1: Geological map of the St Ives Camp showing main lithologies and structures and domains of gold deposits with dominantly reduced and oxidized hydrothermal alteration, respectively. Solid and dashed line rectangles: domain of deposits with oxidized and reduced alteration assemblages during gold mineralisation, respectively.*

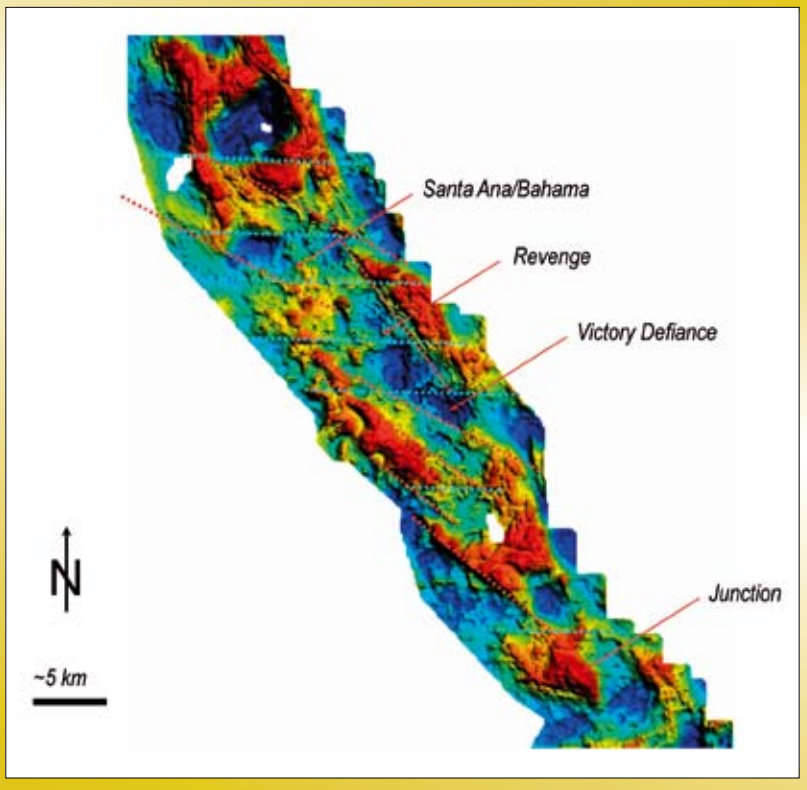


*Figure 3.10.2: Detailed gravity image of the Central Corridor of the St Ives gold camp. Two distinct gravity lows occur in the Victory-Defiance area and SW of the Revenge gold deposits. The gravity lows are interpreted to reflect abundant porphyry intrusions at depths of 1000–2000m below today's surface. In the Victory area, abundant porphyry stocks are confirmed by seismic images and diamond drill core information. Magnetite alteration in interflow sedimentary rocks is focussed at the gravity lows in the Victory area. Interpreted controlling structures for the porphyry intrusions are shown in the red and blue dashed lines.*

Table 3.10.1: Structural history of the St Ives gold camp

| Blewett & Czarnota 2007 | age | Structures and features at St Ives | Mueller 1988 | Swager 1997 | Nguyen 1997 |
|---|---|---|---|---|---|
| D7 | <2400 Ma | Minor ENE contraction - intrusion of Proterozoic dykes | | | |
| D6 | ~2600 Ma? | not recognised at St Ives | | collapse | |
| D5 | 2625–2650 Ma | **Regional Dextral Transpression** (NNE faults): high level textures developed in this long lived event of NE-SW contraction manifest as folding and thrusting as well as dextral strike-slip faulting (e.g., Alpha Island Fault). Minor gold, but regionally very significant (e.g., Mt Charlotte and Sunrsie Dam) - may be what was dated by Clark (1988) and Nguyen (1997) | D3 | D4 | D4 |
| D4b | 2650 Ma | **Regional Sinistral Transpression** (NNW faults): Main gold event in complex architectures with sinistral faults being accomodated across releasing and restraining bends. Releasing bends with extension E-W and ENE-WSW normal fault complexes, restraining bends with top to the NNW and SSE thrusts. Major transfer structures across Tranways and Republicacn Thrusts (they are not 'D1') and transect earlier F2 and F4 folds. Major foliation and vein development. | D2 | D3 | D3 |
| D4a | 2655–2650 Ma | **Regional Contraction** from ENE: inversion of Merougil Basin and upright folding and intense NNW foliation amplification of Kambalda Anticline, extensive thrusting to WSW or ENE. Gold deposition. | D1 | D2 | D2 |
| D3 | 2660–2655 Ma | **Regional Extension** to the NE: deposition of the clastic Merougil Basin, normal faults (e.g., at Santa Anna), NW dykes of porphyry (Flames), enriched porphyries, gentle diping penetrative foliation above expanding granite domes (e.g., Victory). Initial gold mineralisation. | | | DE3 |
| D2 | 2665–2660 Ma | **Regional Contraction** from ENE: Termination of volcanic stratigraphy, intrusion of Kambalda Granodiorite. Amplification of Kambalda Anticline, inversion of earlier growth faults (e.g., Playa, Foster) as thrusts. Some limited foliation development. | | | |
| D1 | >2660 Ma | **Regional Extension** to ENE: formation of Kambalda and Kalgoorlie Sequences. Development of growth faults and initial dome structure (footwall uplift) of the Kambalda Anticline. Pulsed event with internal hiatuses and unconformities | | | DE1-2 |

either the structural controls or the alteration controls are used in isolation to predict further mineralisation. This approach fails to determine and describe an integrated structural and chemical architecture at the deposit to camp scale and hence misses out on providing a much more powerful predictive tool to locate mineralisation. Recognising this shortfall of the previous approaches, we have built a 3D model of both the structural and hydrothermal alteration architecture of the Victory-Defiance gold deposits. During the interpretation of the distribution of the hydrothermal alteration in 3D space it was recognised that some alteration hosting structures were not recognised in previous structural models. More importantly, some ore controlling structures have also not been described in previous structural models. To maximise the output of the 3D models we have developed a new work flow with first constructing the 3D model with existing structural, geological and alteration data. Then the 3D model is interpreted and newly recognised features highlighted. All newly interpreted structures are then characterised in open pits and underground mines and the field data entered into the 3D model. Another advantage of this approach is that drill core, which is likely to answer specific geological questions, can be quickly located in the 3D model and examined in the field.

The Leviathan Complex has been reinterpreted using multi-element, whole-rock geochemistry and the distribution of hydrothermal alteration in 3D. Further, the distribution of felsic and intermediate porphyry intrusions and ultramafic rocks as well as ore shells at different cut-off grades have been modelled in Leapfrog using the internal drill core data base of about 11000 drill holes. Intersections with sedimentary rocks have been reinterpreted in 3D to identify coherent surfaces. The geochemical analyses were used to test the rock type using similar immobile trace-element plots as Prendergast (2007). Although the whole-rock multi-element data set is still limited it allowed some modifications of the geology. The major suggested changes are: 1) better distinction between Devons Consols Basalt (DCB) and Paringa Basalt, 2) some previously interpreted sedimentary layers in individual drill holes are most likely altered shear zones, 3) some of the ultramafic rocks have shapes which are more consistent with an intrusion, and 4) identification of previously not identified structures using alignment of alteration assemblages, porphyry dykes and gold ore shells. The geology and structural architecture is presented in a series of oblique, N-S and E-W sections (Figure 3.10.2 to Figure 3.10.12 inclusive). Location of the sections and the diamond drill holes which have been used to construct the sections are presented in Figure 3.10.3 and Figure. 3.10.4, respectively.

### 3.10.3.2 Geological and structural architecture

The geological model of the Leviathan has been constrained using wireframes from Ruming (2005), the drill core data base and multi-element, whole-rock geochemistry. Ruming (2005) postulates numerous Kapai Slate lithologies in the model. In the process of interpretation and especially using multi-element geochemistry it became clear that a number of these Kapai Slate surfaces were not in their stratigraphic position between DCB and Paringa Basalt. Therefore, only Kapai Slate in its stratigraphic position is termed as such. Other occurrences of Kapai Slate are referred to as "Kapai Slate" regardless whether they represent a different interflow sediment or a highly altered shear zone of similar lithological appearance as a sediment.

The 3D wireframes of Ruming (2005) have been used to show the distribution of Defiance Dolerite. The south-western end of section 1 cuts a major block of Defiance Dolerite which intruded Paringa Basalt (Figure 3.10.8). The Defiance Dolerite intrusion dips relatively gently to the southwest. The footwall of the Paringa Basalt is occupied by a gently SW-dipping Kapai Slate. Beneath the Kapai Slate follows the DCB and ultramafic rocks of the Tripod Hill Komatiite. A second smaller intrusion of Defiance Dolerite, which occurs just to the S of this section, is aligned in a NNW-trending structural corridor that dips steeply to the west. This corridor also includes a zone of subvertical to steeply-dipping, magnetite-bearing "Kapai" slate that has a strike length of at least 1 km and can be traced to the Victory open pit (Figure 3.10.8). It also contains NNW-trending felsic porphyry intrusions which are in contact with the "Kapai" slate. The NNW-trending corridor is intersected by a NW-trending felsic porphyry dyke and E-W trending porphyry dykes (Figure 3.10.8). The northeastern end of section 1 illustrates the irregular distribution of the Tripod Hill Komatiite with respect to the Devons Consols Basalt. The ultramafic rocks are repeated above the inferred position of the Repulse thrust in this section. However, there are also ultramafic rocks in the footwall of the Repulse thrust which possibly indicates additional

structural repetitions along gently SW-dipping shear zones. Based on multi-element geochemistry, there is little evidence for DCB above this ultramafic slice, except for a thin DCB sliver. This contrasts with the interpretation of Ruming (2005) who interpreted significant DCB above the ultramafic slice. However, tighter geochemical sampling is necessary to define the abundance of DCB above the ultramafic slice.

Section 2 also shows the irregular distribution of the DCB (Figure 3.10.9), but on this section the thickness of the Tripod Hill Komatiite is dramatically thinned above the inferred position of the Repulse Fault. Importantly, multi-element whole-rock geochemistry indicates, where available, that DCB does not occur above the ultramafic slice or is reduced to a thin slice locally. The East Repulse ore zone and at least two porphyries occur in the "gap"


*Figure 3.10.3: Geological map of the Victory-Defiance complex showing main lithologies, open pits and the location of the geological sections referred to in the text.*

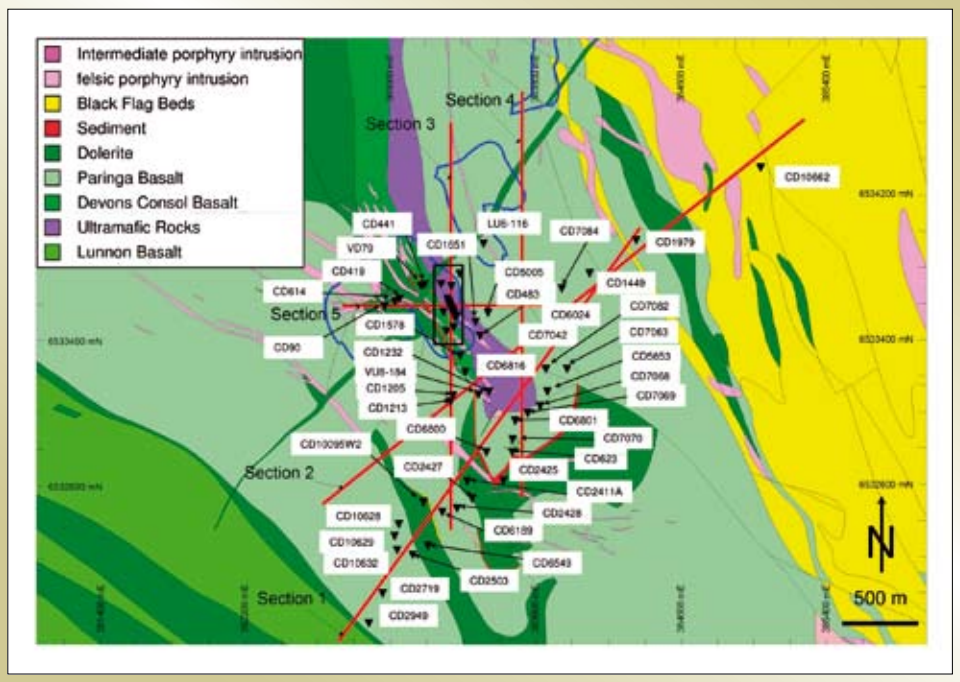


*Figure 3.10.4: Geological map of the Victory-Defiance complex showing the location of diamond drill holes which were used for stable isotope analysis and in the construction of the geological sections. The black solid rectangle shows the location of the section presented in Figure 3.10.5 to illustrate underground holes used for stable isotope analysis.*

between the upper and lower Tripod Hill Komatiite on this section. The along strike thickness variation in Tripod Hill Komatiite is illustrated in sections 3 and 4 (Figure 3.10.10, Figure 3.10.12). Traditionally, the repetition of the Tripod Hill Komatiite above the Repulse Fault has been explained by inversion along the Repulse Fault and thrust-stacking of an ultramafic extrusion (Clark et al. 1989 and references therein). However, it is difficult to explain the significant thickness variations observed in the 3D model of Tripod Hill Komatiite with a thrust-stacking model; or at least a simple thrust-stacking model because a number of thickness variations occur along subvertical contacts. An alternative explanation is that the ultramafic layer represents an intrusion in this position and that the shape reflects the controls of steep NNW-, NW- and WNW-trending structures as well as gently-dipping structures

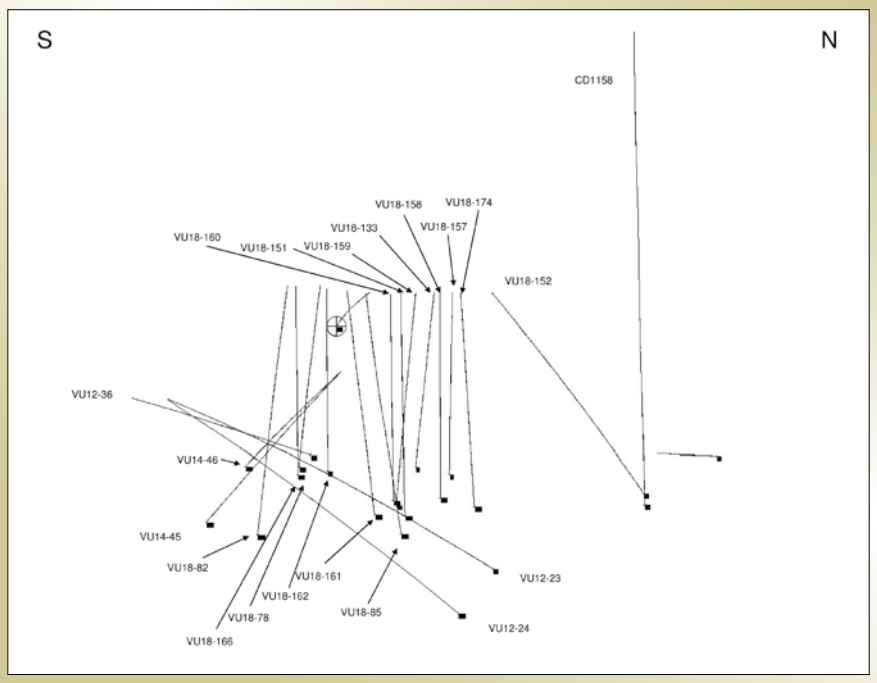


*Figure 3.10.5: North-S section along the section line indicated in Figure 3.10.4. The section shows the distribution of diamond drill holes which were used for isotope analyses.*

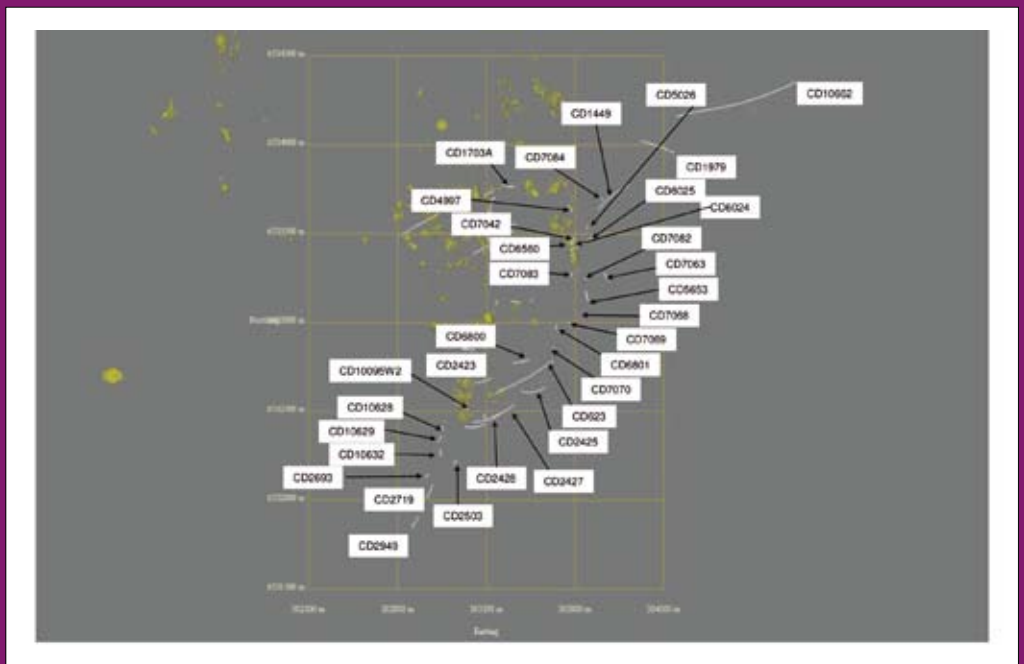


*Figure 3.10.6: Diamond drill hole locations with respect to Au (3 g/t ore shells, yellow; modelled in Leapfrog).*

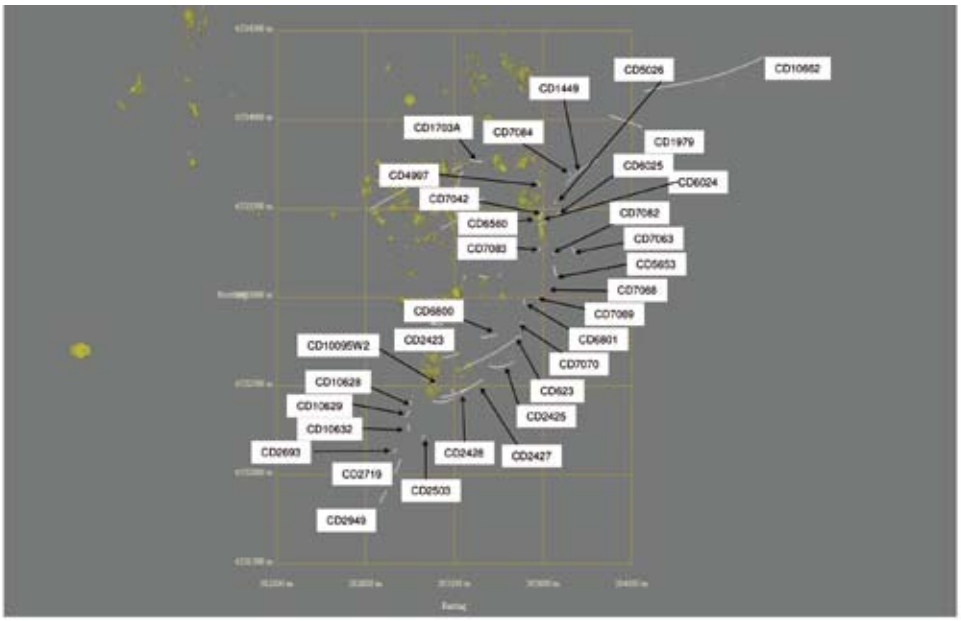


*Figure 3.10.7: Diamond drill hole locations with respect to felsic porphyries (pink; modelled in Leapfrog).*

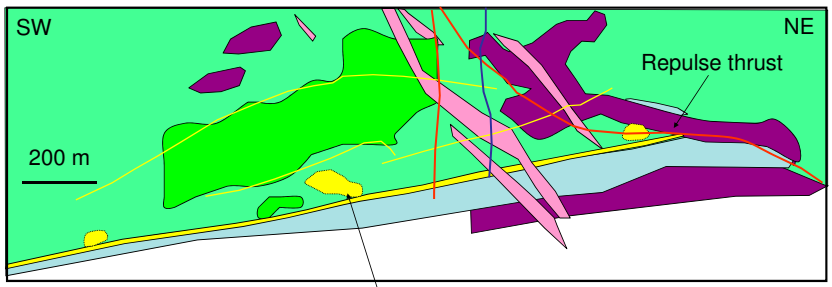


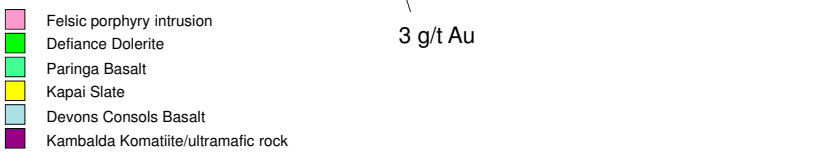


*Figure 3.10.8: Interpreted geology for section 1. The geology was interpreted using SIGMC diamond drill core logging and selected whole-rock, multi-element geochemistry. Yellow lines indicate interpreted sedimentary layers which acted as shear zones. The red line indicates the location of the NNW-trending oxidized structure based on the magnetite distribution. The blue line indicates the location of a WNW-trending structure based on the alignment of porphyry intrusions.*

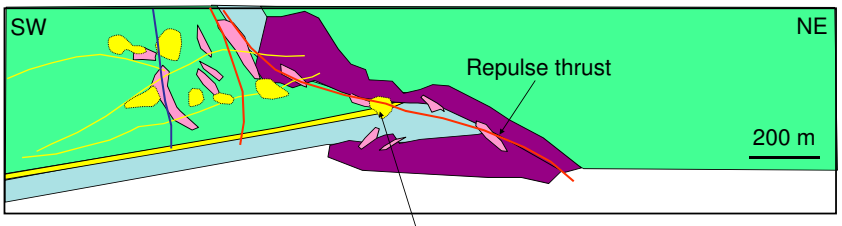





*Figure 3.10.9: Interpreted geology for section 2. The geology was interpreted using SIGMC diamond drill core logging and selected whole-rock, multi-element geochemistry. Yellow lines indicate interpreted sedimentary layers which acted as shear zones. The red line indicates the location of the NNW-trending oxidized structure based on the magnetite distribution. The blue line indicates the location of a WNW-trending structure based on the alignment of porphyry intrusions.*

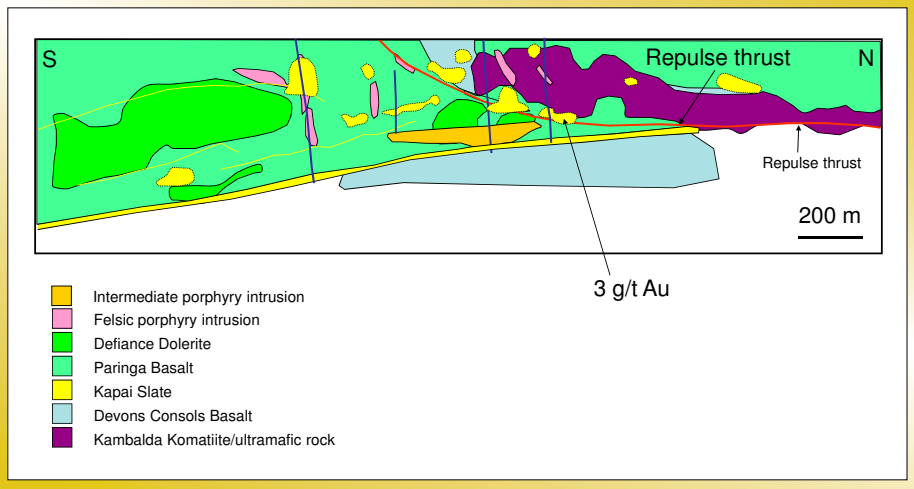


*Figure 3.10.10: Interpreted geology for section 3. The geology was interpreted using SIGMC diamond drill core logging and selected whole-rock, multi-element geochemistry. Blue lines indicate the location of interpreted WNW- and W-trending structures based on porphyry alignment and the alignment of ore shells. Yellow lines indicate the location of sedimentary layers which acted as shear zones and fluid conduits during deformation.*

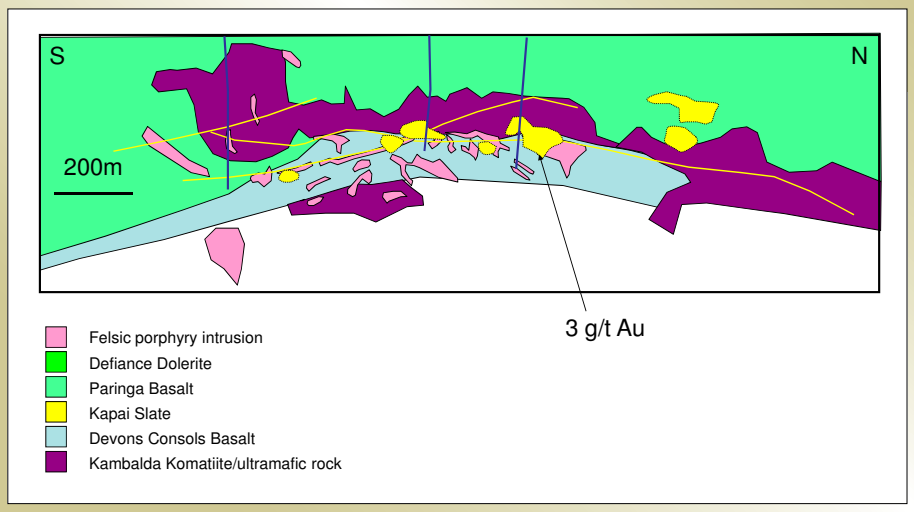


*Figure 3.10.11: Interpreted geology for section 4. The geology was interpreted using SIGMC diamond drill core logging and selected whole-rock, multi-element geochemistry. Yellow lines indicate interpreted sedimentary layers which acted as shear zones. The blue line indicates the location of a WNW-trending structure based on the alignment of porphyry intrusions*

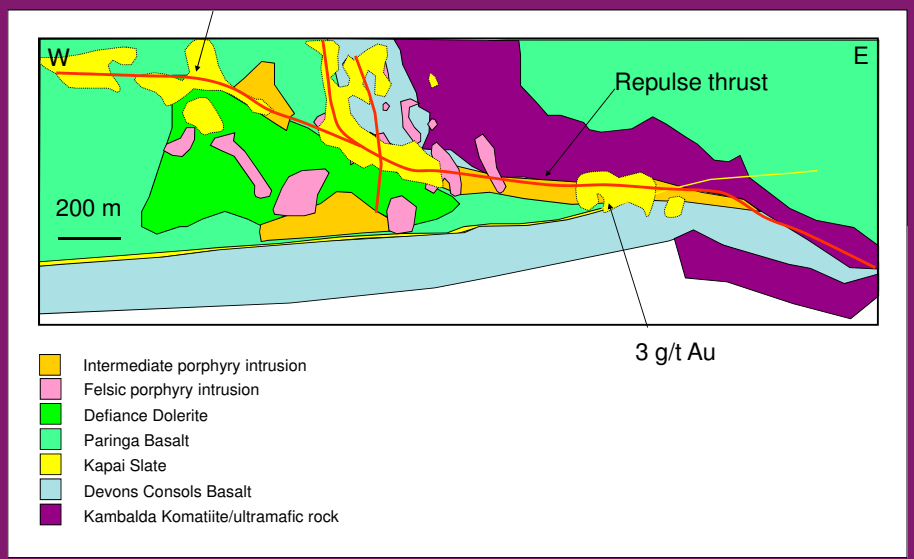


*Figure 3.10.12: Interpreted geology for section 5. The geology was interpreted using SIGMC diamond drill core logging and selected whole-rock, multi-element geochemistry. The red line indicates the location of the NNW-trending structure marked by the alignment of magnetite alteration.*

during the intrusion. Section 4 also shows a complication in the ultramafic slice, DCB and Paringa Basalt relationship (Figure 3.10.11). At the southern end, where the ultramafic slice is thickened, Paringa Basalt occurs in the footwall of the ultramafic slice, but in the middle of the section, DCB forms the footwall of the ultramafic slice. Sedimentary layers occur in positions between the ultramafic slice and DCB as well as between DCB and Paringa which indicates that some of the sedimentary layers were shear zones, or shear zones utilised sedimentary layers and juxtaposed different stratigraphic members.

Although commonly termed a fault, the Repulse structure is most often recognised as a shear zone of up to mylonitic intensity. The last of a series of studies between 1985 and 1995 included a synthesis and reinterpretation of previous data from Leviathan, and also included new data from mapping at Conqueror and East Repulse (Bennett, 1995). In the Victory–Defiance area, ore is localised along an apparently imbricate series of moderately to gently dipping, low displacement thrusts (Cox and Ruming, 2004). The Playa Fault here (known locally as the Repulse Fault in the Victory–Defiance mine area) has a ramp–flat–ramp geometry. A number of low-displacement, ore-hosting thrusts splay from the Playa Fault into its hangingwall where it is more gently dipping. To the west, where the Repulse fault forms a more steeply dipping ramp, low displacement, ore-hosting thrusts occur in the footwall of the Repulse Fault and host the Defiance and Conqueror lodes (Figure 3.10.12). The geometry and kinematics of the Leviathan thrust complex, and its geometric relationship with the Playa Fault indicate that the thrust complex developed within a jog on the Playa Fault, to the NW of where it splays from the Lefroy Fault (e.g., Cox and Ruming, 2004). The overall NW trend and predominantly sinistral shear sense on the Playa Fault, as well as the thrust to oblique thrust-sinistral shear sense on low displacement faults within the imbricate thrust complex, are interpreted to indicate that the gold mineralisation here is localised within a kilometre-scale contractional jog which was active during D4b and the contemporaneous hydrothermal alteration and gold mineralisation (Blewett et al., 2008). Bennett (1995) interpreted the Au-mineralised Repulse Fault within Leviathan as a brittle reactivation of D4a thrusts and accommodated bulk shear during D4b. A revised structural interpretation of the region is provided by Blewett et al. (2008) and Miller et al. (2008).

Hydrothermal alteration mineralogy and Leapfrog® models of ore shells can add additional information to the structural model. In particular, these data can be used to identify previously unidentified structures and these structures are then verified in underground structural mapping. It has to be kept in mind that interpretations are restricted to current drilling information. The architecture of the structures, which had been identified through structural mapping, has been compiled into a 3D model in FracSIS®. In addition, gold grades and felsic and intermediate porphyries have been modelled in Leapfrog® and Leapfrog® meshes added to the FracSIS® model. Further, hydrothermal alteration minerals have been extracted from the St Ives minerals data base and imported into the FracSIS® model as point data. The compilation of all data into a 3D model permits the interpretation of the structural and geochemical (fluid flow and fluid type) architecture. Hydrothermal alteration and felsic porphyry data in 3D also indicate that a number of surfaces (structures?) have previously not been identified. These are (Figure 3.10.13, Figure 3.10.14):

- Subvertical, WNW-trending surfaces which are outlined by the orientation of felsic porphyry intrusions and ore trends along the Repulse thrust,
- Subvertical, NW-trending surfaces which are outlined by the orientation of felsic porphyry intrusions,
- Subvertical, NNW-trending surfaces which are outlined locally by "Kapai Slate" and contain hydrothermal magnetite alteration (this "Kapai Slate" may represent a fluid conduit rather then an interflow sedimentary rock),
- Shallowly dipping sedimentary layers and foliation and shear zones.

The controls of NNW-, NW- and WNW-trending structures on the emplacement of quartz - feldspar porphyries is observed in the 3D model (Figure 3.10.13, Figure 3.10.14). The focus in section 1 of quartz - feldspar porphyries on diamond drill holes CD6801, CD7068, CD7069, CD7070 reflects the controls of steep NW-, NNW- and WNW-trending structures. Controls of WNW-trending structures on porphyry emplacement are particularly obvious in section 3 (Figure 3.10.10), where a steeply-dipping to subvertical porphyry intrusion is located in the hangingwall of the Repulse thrust and another subvertical zone of porphyry intrusions occurs to the N of the Defiance Dolerite in the footwall of the

Repulse thrust. Section 3 also shows two steeply-dipping porphyry dykes in the thickened part of the ultramafic slice. The NNW-trending controls on the porphyry intrusions is documented in section 5 with several steeply E to ENE-dipping intrusions in the hangingwall of the Repulse thrust (Figure 3.10.12). A NW-trending felsic intrusion is depicted in the western part of the section. These dykes dip moderately to the NE. The controls of gently-dipping

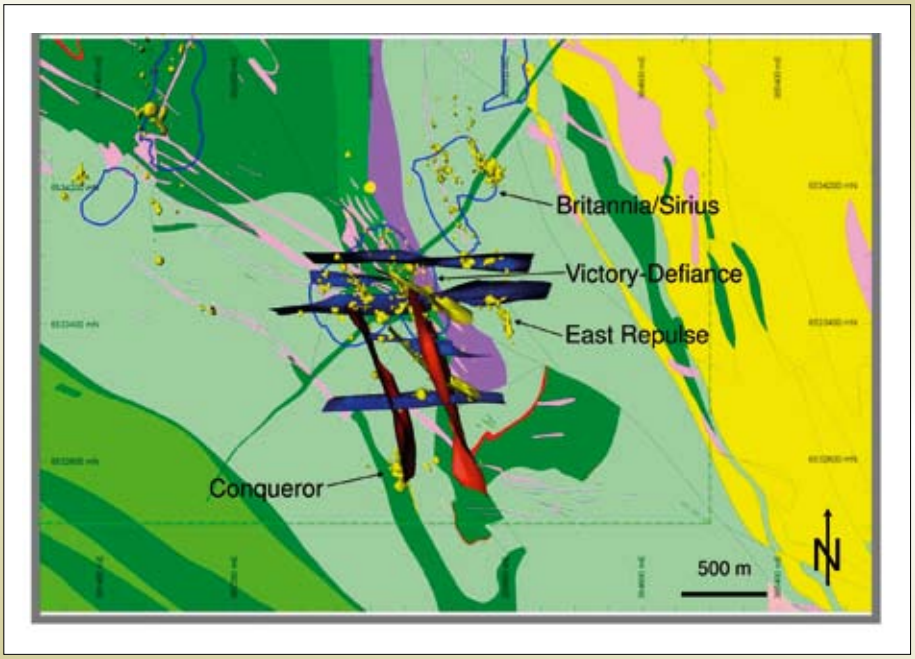


*Figure 3.10.13: Map of the Victory-Defiance complex showing the geology, the distribution of open pits and the location of 3 g/t gold ore shells as modeled in Leapfrog. The location of interpreted E-W to ESE-WNW trending structures is shown in the blue surfaces. These structures have been interpreted in Leapfrog using the alignment of ore shells and porphyry felsic distribution. The location of NNW-trending structures is shown in red surfaces. These structures were modeled in Leapfrog using the distribution of magnetite alteration. Northwest-trending structures are shown in yellow surfaces which have been modeled using the alignment of felsic porphyry intrusions. Note that the map has been lowered to depth to show the relationship of structures modeled in 3D to the map patter at surface. Legend for the map is as for Figure 3.10.4.*

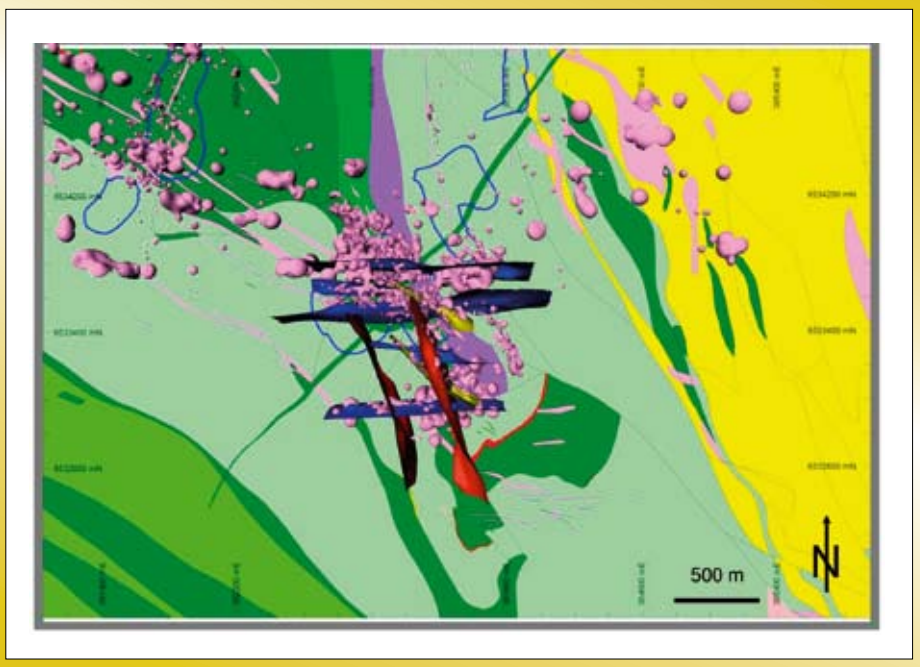


*Figure 3.10.14: Map of the Victory-Defiance complex showing the geology, the distribution of open pits and the location of felsic porphyry intrusions as modeled in Leapfrog. Modeled structures are explained in Figure 3.10.13. Legend for the map is as for Figure 3.10.4.*

structures on the emplacement of porphyry dykes is seen in section 2 in the vicinity of the East Repulse deposit and more clearly in section 4 (Figure 3.10.9, Figure 3.10.11). In particular in the footwall of the ultramafic slice proximal to the E-Repulse mineralisation, several shallowly S- or N-dipping porphyry dykes are indicated. Importantly, the ultramafic slice contains only limited shallowly-dipping porphyry dykes. This can be interpreted that the ultramafic slice, or the Repulse thrust in the footwall of the ultramafic slice, acted as a seal to porphyry intrusions and possibly to hydrothermal fluid flow.

The steeply dipping porphyry dykes mark structures which developed during D3 extension (Blewett et al., 2008). Reactivation of these steep structures during later gold-associated hydrothermal fluid flow would allow steep fluid flow paths. In particular intersections of steeply-dipping, WNW- and NNW-trending structures create focussed fluid flow paths. The shallowly dipping sedimentary layers and shear zones acted as fluid conduits but also compartmentalised fluid flow.

### 3.10.3.3 Fabric development

Detailed structural analysis of diamond drill core and underground exposure also helps to constrain the structural controls on gold mineralisation. The last of a series of studies between 1985 and 1995 included a synthesis and reinterpretation of previous data from Leviathan, and also included new data from mapping at Conqueror and East Repulse (Bennett, 1995). Bennett (1995) interpreted the Au-mineralised Repulse Fault within Leviathan as a brittle reactivation of $D_{4a}$ thrusts and accommodated bulk shear during $D_{4b}$. C32 and C33 reverse shear zones were interpreted as third-order structures within a kilometre-scale contractional jog (Nguyen, 1997), which splayed off the Repulse Fault. Ruming (2006) supported the existing structural interpretation of Leviathan, but work in this study has found that two main generations of structural fabric were integral to the structural controls on $D_{4b}$-age mineralisation at Leviathan. A N-S striking, steeply-dipping foliation, $S_{4a}$, is the first recognizable fabric within the mafic stratigraphy at Leviathan. This fabric is sub-parallel to the long axis of the seismic survey-confirmed antiformal/domal feature that tracks from the Kambalda Dome to the Foster Thrust (Blewett et al., this volume). Predominantly W-dipping foliation zones, $S_{4b}$, vary in orientation from a shallow to moderate SW-dip at Conqueror, to a steeper westerly dip at Victory-Defiance, are over 10 m wide, and bound most of the mineralisation at Victory-Defiance and Conqueror. Multiply-oriented $S_{4b}$ is associated with regional-scale sinistral strike-slip shear zones, but at Leviathan develop a more complex geometry surrounding the Victory Dome. $S_{4b}$ is delineated by gold-stage alteration and will be the focus of attention below; although $S_{4a}$ will be referred to because of the spatial relationship it shares with mineralisation.

A chlorite±biotite foliation, $S_{4a}$, predominantly dips steeply to the east throughout Leviathan, although within the immediate footwall of the Repulse Fault the orientation of $S_{4a}$ may vary to a shallow dip to the west. The point maximum of $S_{4a}$ plunges moderately towards ESE, and is discordant to moderately W-dipping stratigraphic contacts (Figure 3.10.15). Magnetite porphyroblasts overgrew the chlorite-defined $S_{4a}$ foliation that in turn was replaced by biotite and pyrite with proximity to mineralisation.

Due to the affects of extensive hydrothermal alteration post the development of $S_{4a}$, the latter commonly bears the mark of subsequently-developed fabrics, particularly in the vicinity of gold mineralisation. In view of this, the separation of, and therefore documentation of $S_{4a}$ and $S_{4b}$ was only possible where two fabrics were identified in combination with relative timing relationships. There are near orthogonal, yet gradual changes in the orientation of $S_{4a}$ that are associated with the increasing intensity of $S_{4b}$ foliation. Undeformed, steeply-dipping $S_{4a}$ was initially weakly folded, but with increasing differentiation of $S_{4b}$ foliation, $S_{4a}$ was crenulated and transposed by $S_{4b}$ (Figure 3.10.16). $S_{4a}$ is cross-cut by albite+carbonate+quartz-filled veins, but the latter are also sub-parallel to $S_{4a}$ and/or $S_{4b}$ foliations (Figure 3.10.17).

$S_{4a}$ has a major influence in the positioning of the veins associated with mineralisation. The lateral extent of "ladder vein" lodes is defined by the position of $S_{4a}$. Stacked, sub-horizontal 1–2 m-wide vein sets, termed ladder veins, have at least one of the vertical contacts defined by $S_{4a}$. $D_{4b}$-stage quartz+albite-filled veins cross-cut $S_{4a}$, but are also parallel to the latter (Figure 3.10.18). The orientation and continuity of gold lodes is also affected by the distribution of $S_{4a}$. Widely-spaced, narrow zones of $S_{4a}$ spatially coincide with low-angle changes in the dip-direction of the lode. Alternatively, within closely-spaced, wide zones of $S_{4a}$, the lode is non-continuous, relatively narrow, and

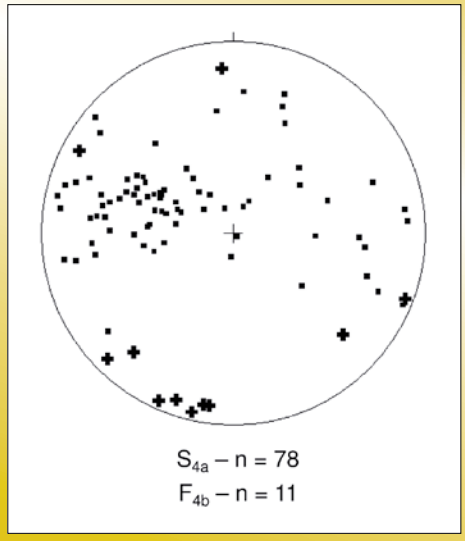


*Figure 3.10.15: Leviathan $S_{4a}$ (squares) and $F_{4b}$ (pluses) stereoplot.*

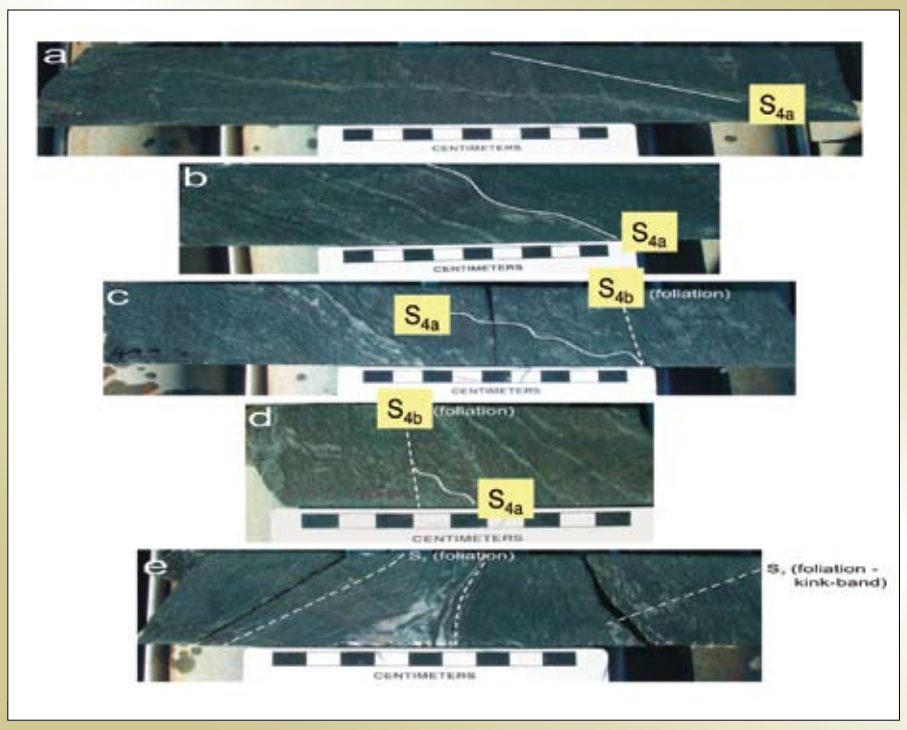


*Figure 3.10.16: Identification of $S_{4a}$ and $S_{4b}$ in diamond drill core.*

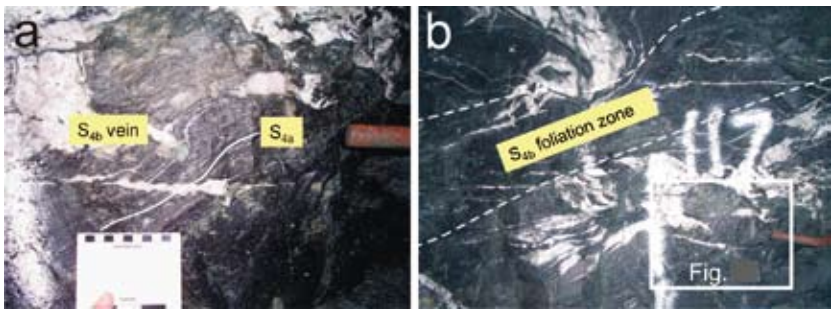


*Figure 3.10.17: $S_{4a}$ and $S_{4b}$ textural relationships at Conqueror.*


*Figure 3.10.18: Structural controls on gold lodes – 1. The second controlling structure – regional metamorphic foliation, $S_2$. Axial planar to regional $D_2$ anticline – now folded by Repulse Fault and $D_3$ foliations and mineralised veins. Locally controls the vertical component of "ladder vein" lodes. $S_2$ foliation was replaced/dilated by $D_3$-stage alteration/veins $S_2$ foliation was replaced/dilated by $D_3$-stage alteration/veins.*

*Figure 3.10.19: Structural controls on gold lodes – 2.*

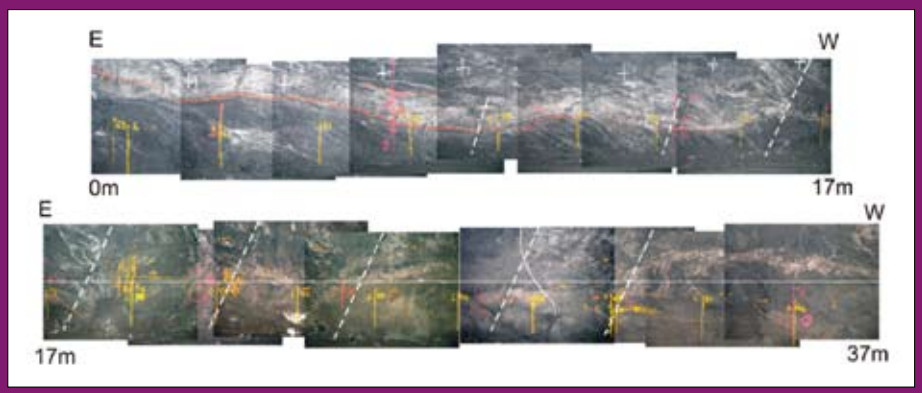


*Figure 3.10.20: Change in S4a dip with proximity to gold lodes.*

is vertically offset (Figure 3.10.19). The orientation of $S_{4a}$ is also significantly affected by cross-cutting $S_{4b}$ veins and foliation. $S_{4a}$ dips steeply within the footwall and hangingwall to shallow-dipping mineralised lodes, but the former was rotated into parallelism with and underwent pervasive albite+pyrite alteration when intersected by mineralisation (Figure 3.10.20).

The relationship of $S_{4b}$ to mineralisation at Leviathan may be summed up in the example of the Conqueror Deposit, which encompasses multiple quartz-hosted lodes hosted within Defiance Dolerite. The six lodes are stacked in an en-echelon fashion, and are bounded by approximately ten metre-wide, westerly-dipping $S_{4b}$ foliation zones in the hangingwall and footwall to the deposit; here termed the Pellew and Conqueror Shear Zones, respectively. Shallowly-dipping, one to five metre-wide $S_{4b}$ foliation zones comprise two dominant orientation sets that dip shallowly to the SE and SW, and link the major set of westerly-dipping $S_{4b}$ (Figure 3.10.21, Figure 3.10.22). Ductile intersection between contrasting orientations of shallowly-dipping $S_{4b}$ within the immediate footwall to each gold lode yielded an overall composite fabric that dips to the SSW. The shallowly-dipping $S_{4b}$ composite fabric is parallel to the plunge of individual gold lodes, whereas the moderately SSW-plunging mineralisation envelope to Conqueror is parallel to the intersection of westerly-dipping $S_{4b}$ and N-S trending $S_{4a}$.

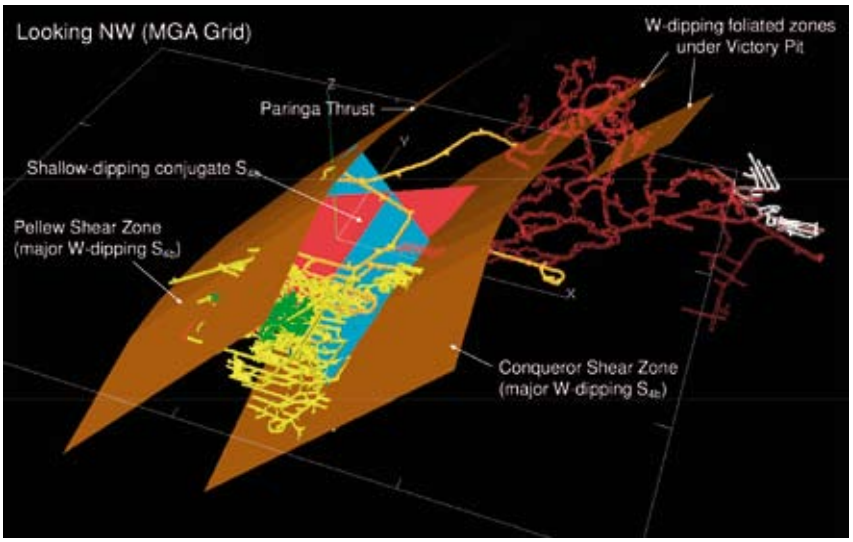


*Figure 3.10.21: $S_{4b}$ at Conqueror.*

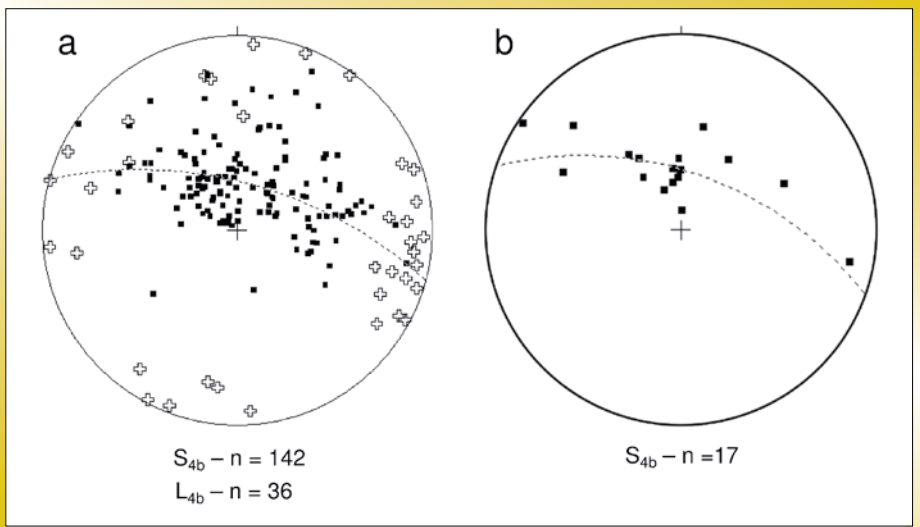


*Figure 3.10.22: Leviathan stereoplots of the $S_{4b}$ (squares) and $L_{4b}$ (pluses) structural elements.*

Lode geometry throughout Leviathan as a whole is complicated by having a number of favourable hosts for mineralisation, compared to predominantly one host rock at Conqueror. Kapai Slate and felsic to intermediate porphyritic intrusions are the main hosts for mineralisation within the East Repulse and Victory deposits. The intersection between west-dipping $S_{4b}$ and steeply-dipping lithological units/contacts at Victory delineate blocks of mineralisation that have a long strike length, but a comparatively limited dip extent. E-W, and N-S trending margins to pipe-shaped, porphyry-hosted mineralisation at Victory coincide with west-dipping $S_{4b}$ and E-W trending $S_{4b}$ vein sets, respectively (Figure 3.10.23).

## 3.10.4 Chemical architecture of the SIGC and the Leviathan Complex

### 3.10.4.1 Camp Scale zoning

The interpretations in this section are based on the entire St Ives Gold Mining Company drill hole data base which comprises over 50000 km of drill core and represents a unique opportunity world-wide to study camp-scale alteration distribution in a data-rich area. The logging by countless company geologists, which is captured in an electronic data base, was used to extract information on hydrothermal alteration. Naturally, there are potential inconsistencies in the logging and data extraction could be erroneous. To avoid or minimise this problem, selected drill core was logged by the research team and results compared to verify the data base. In selected areas, the logging was also cross checked to original hand written logs and then compared to actual drill core.

The distribution of hydrothermal alteration mineral assemblages (Fe-sulphides and oxides, Na-K-Fe-Mg-Ca silicates and Ca-Fe-Mg carbonates) is zoned at the lode to the camp-scale in the St Ives gold camp (SIGC). Using the dominant proximal (to the gold lode) alteration assemblage, the gold deposits in the SIGC can informally be grouped into two types: 1) oxidised, and 2) reduced. Commonly both reduced and oxidised assemblages are found within or proximal to both styles of deposits. The deposits at the northeastern flank of the Kambalda anticline are characterised by relatively oxidised pyrite-magnetite and pyrite-hematite assemblages (Figure 3.10.1, Figure 3.10.24). Deposits in the northwest, proximal to the Kambalda Dome (Figure 3.10.1), typically contain pyrite-only as the main sulphide mineral. Deposits in the southwest of the camp, such as Argo and Junction (Figure 3.10.1), are dominated by reduced arsenopyrite-pyrrhotite and pyrrhotite-pyrite assemblages, respectively. The only other gold deposit with reduced hydrothermal alteration assemblages is Cave Rocks which is hosted in the Zuleika fault. The Cave Rocks deposit is characterised by proximal arsenopyrite-pyrrhotite assemblages.

Given this difference in the oxidation state of the hydrothermal fluids in the proximal mineral assemblages in the gold lodes, a camp-scale domain mapping exercise was carried out using mainly sulphide/oxide mineral assemblages but also silicates (Figure 3.10.24). The domain

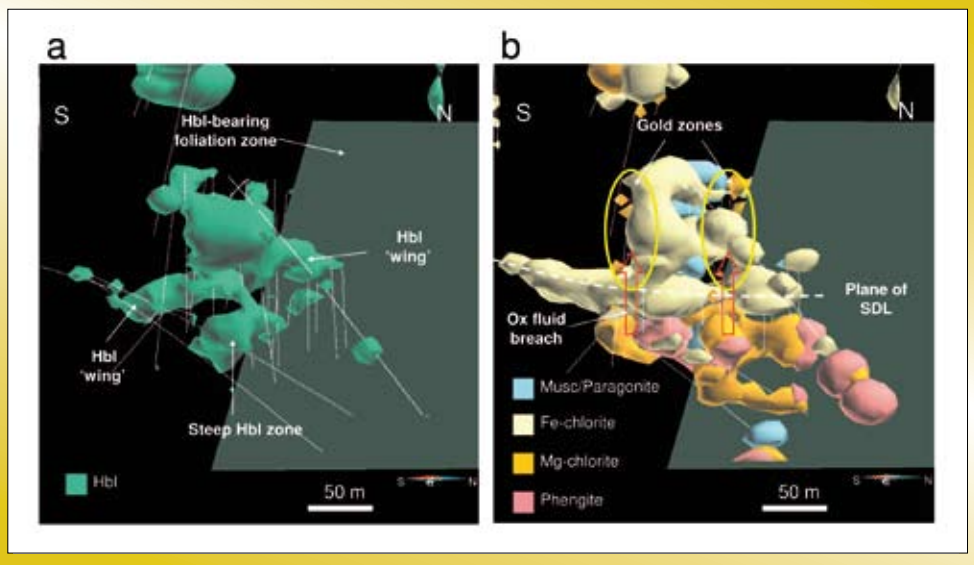


*Figure 3.10.23: Victory Box spectra model. A) Hornblende isosurface showing both steep zones and gently dipping 'wings'. B) Chlorite and white mica isosurfaces showing gold zones.*

mineral mapping, which was done for metasedimentary interflow sedimentary rocks and mafic rocks separately, indicates a distinct distribution pattern. This, in turn, suggests a hydrothermal fluid chemistry zonation within the St Ives gold camp. Also importantly, the emerging distribution pattern is very similar in the interflow sedimentary rocks and the mafic rocks suggesting that the influence of the host rock composition on the alteration mineral assemblage was minimal (i.e. the alteration assemblages were formed in fluid buffered conditions).

Oxidised assemblages, such as magnetite-pyrite and hematite-pyrite assemblages, are focused around some of the Leviathan deposits (Victory-Defiance, East Repulse) and deposits adjacent to Leviathan such as Britannia, Sirius, Orchin and North Orchin. Further oxidised assemblages are recorded to the SE of, and intermittent within, the Greater Revenge area. Oxidised domains with magnetite-pyrite assemblages are aligned along some major structures, such as the NW-trending, NE-dipping Playa fault. The oxidised domain around the Leviathan deposits is focused on a distinct low in the detailed gravity data (Figure 3.10.2) which extends for several kilometres in diameter and is interpreted to represent abundant magmatic intrusions at a depth of about 500–1000 m below present surface. This interpretation is also supported by a seismic cross section (Figure 3.10.25), which shows a total disruption of the reflectors in this domain, and limited deep diamond drill core which intersects very abundant porphyry intrusions at about 900m below present day surface. A genetic link is inferred based on the spatial association of oxidised domains (magnetite and magnetite-pyrite) and the centre of abundant porphyry intrusions that there is (Figure 3.10.2, Figure 3.10.24). The maximum extent and the focus of the oxidised hydrothermal fluid system in the St Ives camp is also highlighted in whole-rock, multi-element analyses. Distribution maps for anomalous Te and Mo show the centre of the oxidised fluid system at Leviathan extends northwards to the Revenge group of deposits (Figure 3.10.26, Figure 3.10.27).

Epidote is focused into the core of the Central Corridor with pyrite ± magnetite ± chalcopyrite (Figure 3.10.28) and is hence also interpreted to represent oxidised fluid conditions. More rarely epidote occurs with pyrrhotite ± chalcopyrite ± magnetite flanking the Central Corridor. The epidote-bearing assemblages show a close spatial association with porphyry intrusions (Figure 3.10.28) and common occurrence in the Devon Consols Basalt. The distribution of epidote indicates a broad correspondence with oxidised domains as indicated by Fe-sulphide-oxide assemblages, suggesting that the distribution of the common rock-alteration silicates (epidote, chlorite, biotite, amphibole, albite, muscovite-phengite) of the SIGC camp were also controlled, at least in part, by the redox state of the hydrothermal fluids.

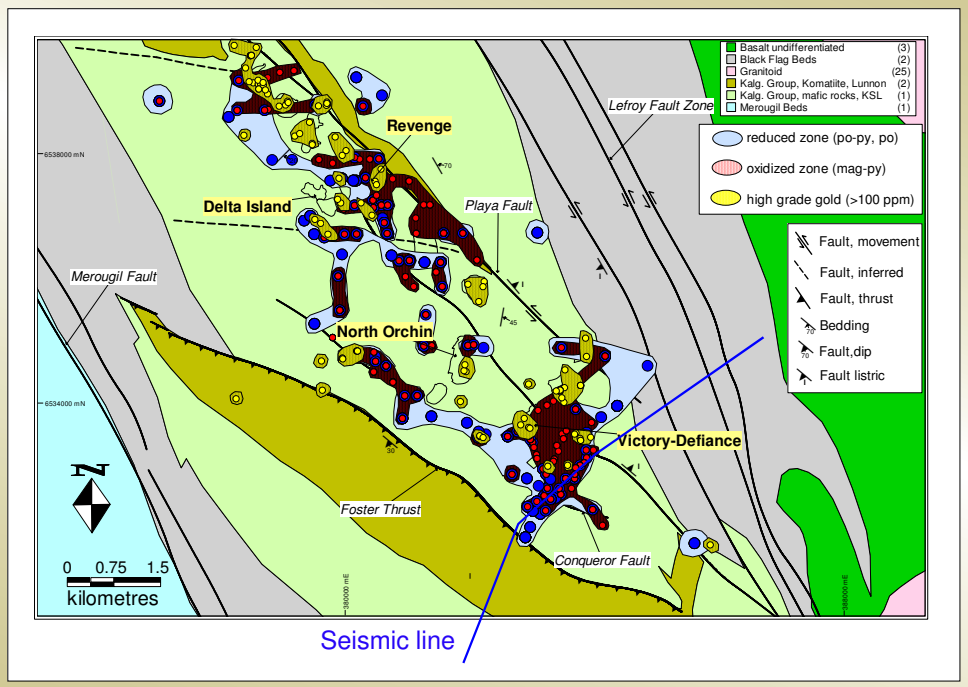


*Figure 3.10.24: Distribution of main sulphide/oxide mineral assemblages in mafic rocks in the Central Corridor of the St Ives gold camp. High-grade (>100 ppm) gold intersections are located in zones where reduced and oxidized mineral assemblages overlap. The location of the seismic traverse in Figure 3.10.25 is shown in a solid blue line.*

Domains with reduced alteration assemblages (pyrrhotite-pyrite) flank those with oxidised assemblages to the NE and SW of the Victory-Defiance, East Repulse and Greater Revenge deposits and also occur intermittently between oxidised domains in the Greater Revenge deposits (Figure 3.10.24). Southwest of Conqueror, reduced assemblages are clearly focused in shallowly SW- to S-dipping faults. Reduced assemblages cluster in particular in a broad band to the S of the Revenge deposits, along trends consistent with interpreted early, E-W trending faults (Connors et al., 2003).

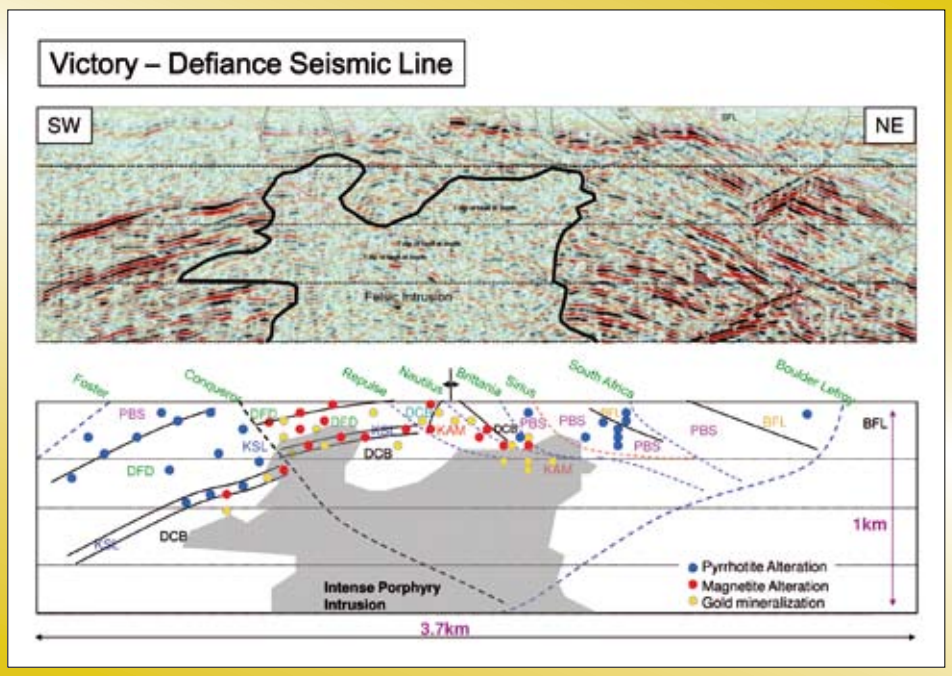


*Figure 3.10.25: Interpreted Victory-Defiance seismic section across the St Ives Camp showing the distribution of the pyrrhotite, magnetite and gold with respect to the interpreted intrusive complex (after Ned Stolz, Karen Connors and Leo Horn, pers. comm., 2002).*

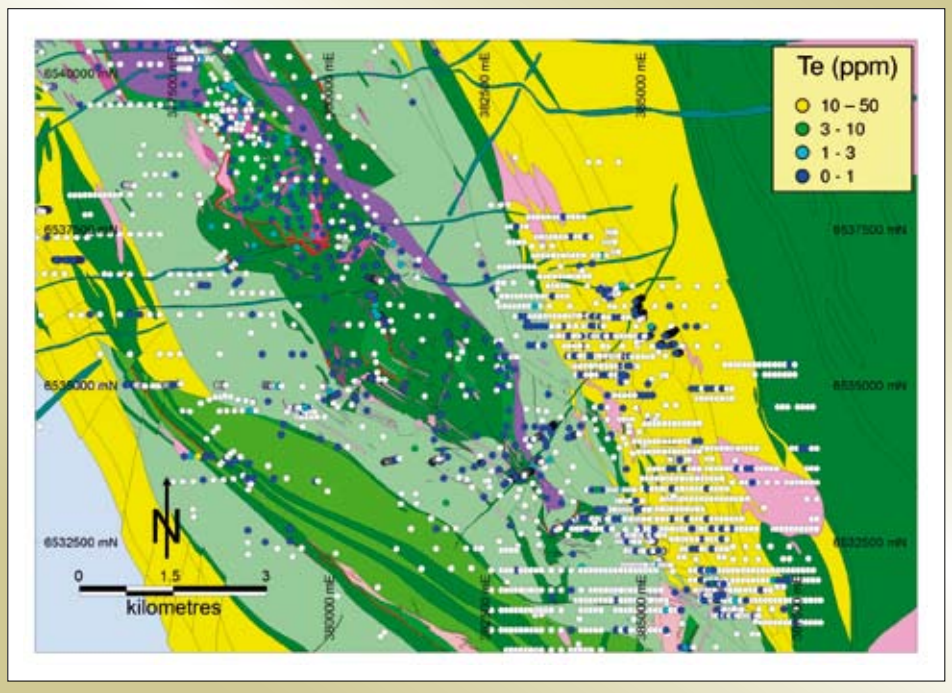


*Figure 3.10.26: Map of the St Ives gold camp showing the distribution of Te whole-rock analyses. Note that the anomalous Te is strongly focused on the Central Corridor indicating the footprint of the oxidized hydrothermal cell. Note also that anomalous Te drops off across the Playa fault indicating that the Playa fault was a seal to the oxidized fluid flow.*

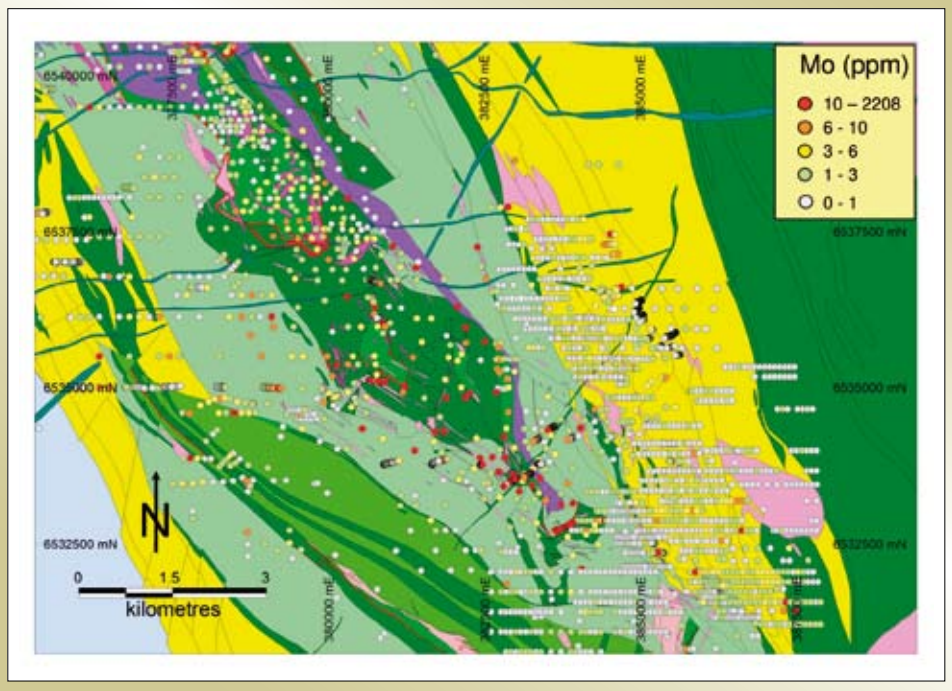


*Figure 3.10.27: Map of the St Ives gold camp showing the distribution of Mo whole-rock analyses. Note that the anomalous Mo is strongly focused on the Central Corridor indicating the footprint of the oxidized hydrothermal cell. Note also that anomalous Mo drops off across the Playa fault indicating that the Playa fault was a seal to the oxidized fluid flow.*

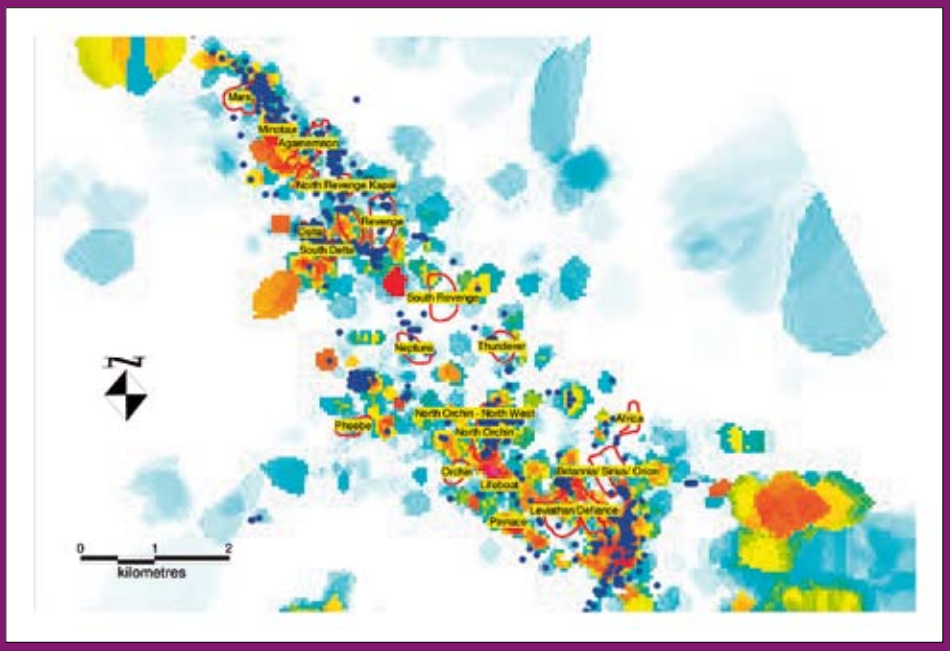


*Figure 3.10.28: Gridded map showing the abundance of felsic porphyry intrusions in the St Ives gold camp and the location of gold mineralisation. The porphyry abundance was determined calculating the total metres of porphyry intersections in drill holes and the projecting to the collar location of the drill hole. The distribution of epidote alteration is shown in blue dots. Note the strong correlation of porphyry abundance and occurrence of epidote.*

### 3.10.4.2 Hydrothermal alteration mapping in chemical space

The observed sulphide/oxide mineral zoning in the St Ives gold camp as discussed above suggests variations in the thermo-chemical conditions of the hydrothermal fluids. It is therefore critical to consider to what extent the common alteration mineral assemblages in the camp may also be controlled by variations in the thermo-chemical conditions of the hydrothermal fluids. The change in alteration mineralogy is not simply a function of host rock, because alteration assemblages change within the same host rock. The silicate and Fe -sulphide - oxide mineral assemblages are stable over a wide range of thermo-chemical conditions (P, T, redox, pH, activity of NaCl, $H_2O$, S and C). The relative stability of the silicate and Fe -sulphide - oxide mineral assemblages as

a function of redox and pH is shown in Figure 3.10.29. Details of the construction of this figure are given in Walshe et al. (2008a).

Sulphur and carbon isotope ratios also vary as a function of redox providing additional constraints on the chemical evolution of the system. Sulphur isotope ratios are a sensitive indicator of the change of oxidation state of the sulphur species in the fluid as fractionation of $^{34}S$ and $^{32}S$ occurs between reduced and oxidised sulphur species (Ohmoto and Goldhaber 1997). Similarly carbon isotope ratios are a sensitive indicator of the change of oxidation state of the carbon species as fractionation of $^{13}C$ and $^{12}C$ also occurs between reduced and oxidised carbon species (Ohmoto and Goldhaber 1997). This means that it is possible to use the patterns of sulphur and carbon isotope fractionation to map redox variations from highly oxidised environments ($SO_4^{2-}$ or $SO_2$ the dominant species in the fluid) through intermediate oxidation states ($H_2S$, $H_2CO_{3(aq)}$ or $CO_2$ the dominant species in the fluid) to highly reduced conditions ($H_2S$ and $CH_4$ the dominant species in the fluid). Details of the interpretation of isotopic data in terms of end-member fluids compositions and fluid interaction processes (fluid-rock reaction, fluid mixing, fluid un-mixing) are provided in Walshe et al. (2008b).

The inferred sulphate/sulphide precipitates of high temperature oxidised magmatic fluids (~ 400 – 500 °C) are:

- Anhydrite with $\delta^{34}S$ of ~ +10 ‰
- Pyrite with $\delta^{34}S$ of ~ - 3.5 to -5 ‰

At lower temperatures (~ 300 °C) values of $\delta^{34}S$ pyrite may be more negative. Positive $\delta^{34}S$ values of pyrite (> 2‰) are taken to represent reduction of oxidised sulphur species via reactions such as:

$$3CH_4 + 4SO_2 = 3CO_2 + 2H_2O + 4H_2S$$
$$3H_2 + SO_2 = 2H_2O + H_2S$$
$$CH_4 + HSO_4^- + H^+ = H_2CO_3 + H_2S + H_2O$$
$$4H_2 + HSO_4^- + H^+ = H_2S + 4H_2O$$

Either $H_2$ or $CH_4$ may be the reducing agent. The oxidation of $CH_4$ to either $H_2CO_{3(aq)}$ or $CO_2$ in the above reactions may be tracked with $\delta^{13}C$ of carbonate. Values of $\delta^{13}C$ < - 8 ‰ are interpreted as domains of significant oxidation $CH_4$ to $CO_2$ by $SO_2$ subjacent to flux zones of

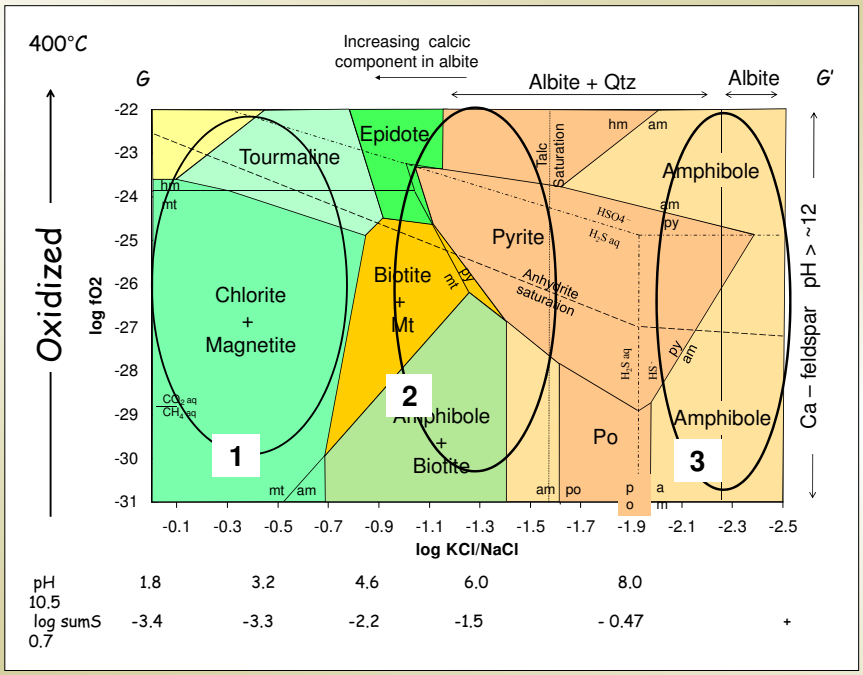


*Figure 3.10.29: Log $f_{O2}$ versus log KCl/NaCl diagram showing the stability range of common alteration mineral assemblages in the St Ives gold camp with the variation of pH and the log sumS indicated at the horizontal axis. Three different conditions for the hydrothermal alteration assemblages are distinguished which are used to classify hydrothermal fluid conditions in the camp. These are: Condition 1: Acidic conditions defined by chlorite ± magnetite ± andalusite or equivalent minerals: chloritoid, pyrophyllite, paragonite, muscovite, tourmaline Condition 2: Mildly acidic to mildly alkaline conditions defined by albite ± phengite ± pyrite ± epidote ± biotite ± actinolite. Epidote may be taken as an indication of more oxidized conditions and biotite/actinolite as an indication of more reduced conditions. Condition 3: Ultra-alkaline conditions defined by albite ± Ca-feldspar ± amphibole ± talc ± carbonate in the absence of sulfides and quartz. Details as in Walshe et al. (2008a).*

$CO_2$ - $SO_2$ – volatiles. Increasing $\delta^{13}C$ carbonate from the inferred $CO_2$ reservoir value of -5 to -6 ‰ tracks the progressive reduction of oxidised carbon species to $CH_4$; a reaction that requires a strong reducing agent in the fluids, most probably $H_2$.

e.g., $CO_2 + 4H_2 = CH_4 + 2H_2O$

Positive correlations between values of $\delta^{13}C$ carbonate greater than -5 ‰ and $\delta^{34}S$ pyrite greater than 0 ‰ imply that $H_2$ rather than $CH_4$ is the dominant reductant species.

The mineralogical zoning coupled with stable isotope constraints as well as fluid inclusion constraints (Petersen et al. 2005) imply significant thermo-chemical gradients in redox, pH as well as activity of $H_2O$, S at the time of gold mineralisation. Temperature gradients appear sub-ordinate and pressure gradients are poorly constrained. From the phase diagram the common silicate alteration mineralogy may be used to define three different conditions with respect to pH: 1) acidic, 2) mildly acidic to mildly alkaline, and 3) alkaline (Figure 3.10.29). Equally sulphide/oxides and silicates can be used to distinguish between reduced and oxidised conditions (Figure 3.10.29). At neutral to alkaline conditions, epidote occurs at oxidised conditions compared with biotite and actinolite (Ca - Fe- Mg - amphibole) that forms at most reduced conditions. For mid – redox conditions (log $fO_2$ ~ pyrite – pyrrhotite – magnetite buffer), chlorite is stable in the acidic domain, biotite at neutral to alkaline conditions and albite at alkaline to highly alkaline conditions.

## 3.10.5 Hydrothermal alteration mapping in the Leviathan complex

This section documents the zoning of key minerals, mineral assemblages and stable isotope ratios ($\delta^{34}S$ pyrite; $\delta^{13}C$ carbonate and $\delta^{18}O$ carbonate) across the Leviathan Complex with respect to the lithological and structural architecture with a view to defining a more comprehensive picture of the variation in redox and pH conditions across the complex and identifying the critical pathways of reduced and oxidised fluid.

From the phase relations documented above (Figure 3.10.29) the minerals/mineral assemblages of most interest are:

- Magnetite-pyrrhotite
- Epidote ± carbonate ± quartz ± feldspar ± biotite ± amphibole ± magnetite ± sulphides
- Feldspar ± carbonate ± biotite ± quartz ± sulphide ± hematite/magnetite
- Amphibole ± biotite ± sulphide ± feldspar ± carbonate ± chlorite.
- Chlorite-rich assemblages
- Anhydrite, quartz, carbonate, ± biotite
- Paragonite-muscovite-chlorite-calcite/dolomite ± tourmaline (timing)
- Talc ± carbonate

### 3.10.5.1 Distribution of magnetite and pyrrhotite

Hydrothermal magnetite occurs in a range of silicate-carbonate mineral assemblages, which are described below in greater detail, in the Leviathan Complex. If the spatial magnetite-pyrite distribution is plotted irrespective of the associated silicate-carbonate mineral assemblage then oxidised magnetite-pyrite assemblages are largely focused around the Victory-Defiance deposit and correlate well spatially with felsic porphyry intrusions in the geological map (Figure 3.10.30, Figure 3.10.31). The bulk of the oxidised magnetite-pyrite and magnetite assemblages are typically located south of the Victory-Defiance ore bodies and north of the Conqueror ore bodies (Figure 3.10.30). Locally magnetite occurs within these ore bodies. At East Repulse magnetite and magnetite-pyrite assemblages occur adjacent to the ore bodies, but are most abundant on the western side of the ore bodies (Figure 3.10.30). Note that oxidised magnetite-pyrite and magnetite assemblages are flanking felsic porphyries on both the eastern and western side at East Repulse. Ore bodies, however, are confined to the eastern side of the felsic porphyries at East Repulse at the boundary between oxidised and the reduced domains, i.e. the greatest chemical gradient in the hydrothermal fluids (Figure 3.10.30, Figure 3.10.31).

Reduced pyrrhotite and pyrrhotite-pyrite assemblages are flanking the main oxidised domain at all sides (Figure 3.10.30, Figure 3.10.31). Most importantly the boundary of oxidised to reduced domains is coincident with significant ore bodies (e.g., Victory-Defiance, East Repulse, Conqueror, Britannia, Sirius). This spatial zoning of oxidised and reduced sulphide/oxide mineral assemblages is similar to that observed at the camp scale.

In detail, different associations of magnetite-bearing assemblages can be distinguished. These are:

- Massive magnetite bands or magnetite veins:
  - magnetite-albite-carbonate-quartz assemblages in Kapai Slate or interflow sedimentary rocks or shear and foliation zones locally,
  - massive magnetite adjacent to porphyry intrusions (Figure 3.10.32)
  - massive to disseminated magnetite with epidote (magnetite-calcite; Figure 3.10.33 Figure 3.10.35)
- disseminated magnetite
  - magnetite around gold lodes (Figure 3.10.33),
  - magnetite-chlorite,
  - magnetite-epidote assemblages.

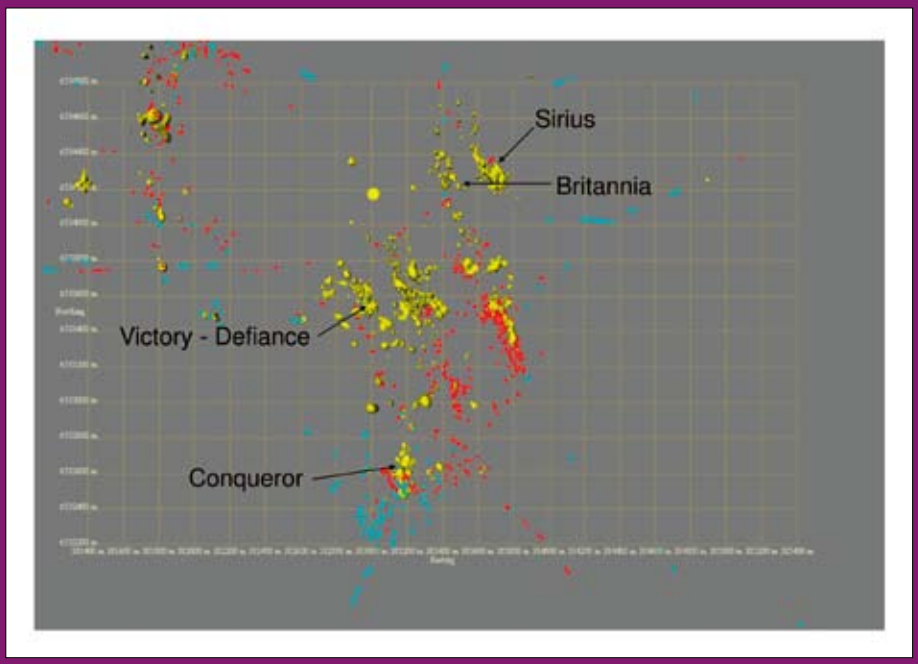


*Figure 3.10.30: Distribution of 3 g/t ore shells as modeled in Leapfrog (yellow surfaces). The distribution of magnetite (red dots) and pyrrhotite (blue dots) is also shown. Note that magnetite is focused in the central part of the Victory complex indicating predominantly oxidized fluid flow. Pyrrhotite is flanking the central part indicating predominantly reduced fluid flow. Note that the main ore bodies are located at the switch from oxidized to reduced fluids.*

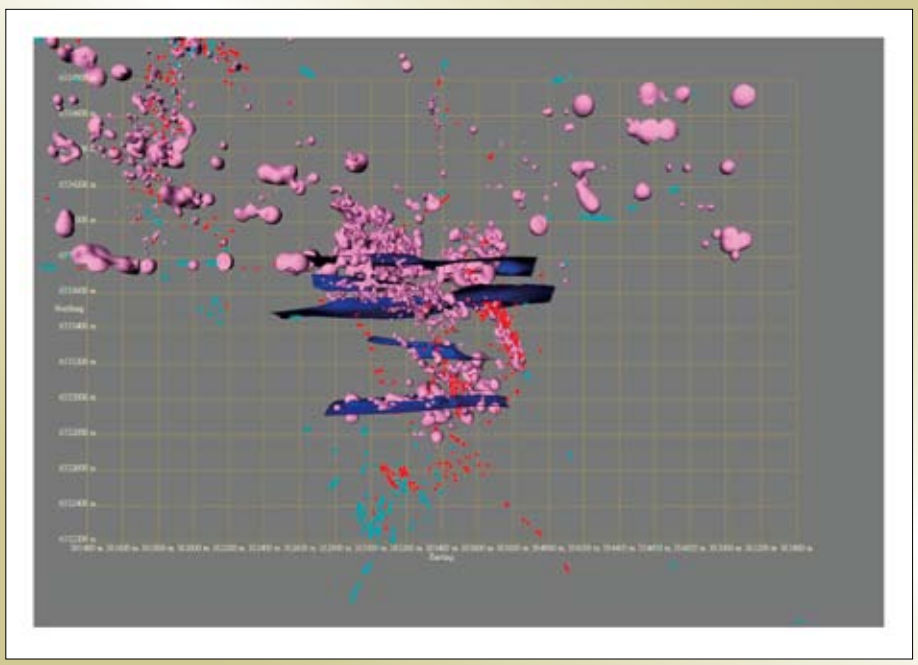

*Figure 3.10.31: Distribution of felsic porphyry intrusions as modeled in Leapfrog (pink surfaces). The distribution of magnetite (red dots) and pyrrhotite (blue dots) is also shown. Interpreted WNW- and W-trending structures are shown in blue surfaces.*

*Figure 3.10.32: Massive magnetite alteration (black area) adjacent to felsic porphyry (pink area) The porphyry body hosts subhorizontal quartz veins associated with boudin necking (and vertical extension).*

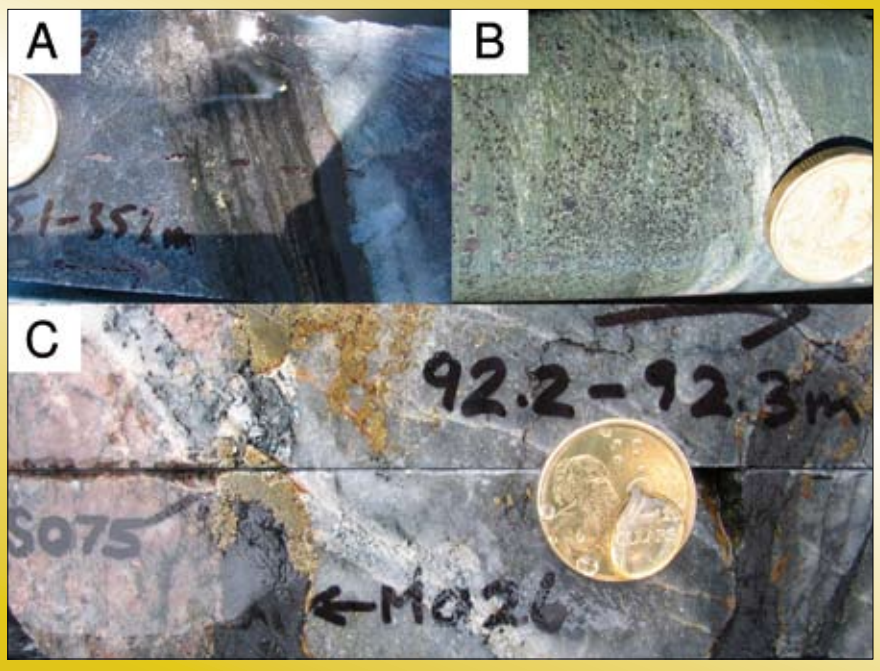


*Figure 3.10.33: Magnetite occurrences Victory-Defiance complex. A) Foliated zone of magnetite-pyrite-biotite-chlorite at porphyry/DCB contact; CD7068/350–351. B) Disseminated magnetite with biotite-chlorite-carbonate; CD5026/136.7. C) Massive magnetite with pyrite in foliated siliceous rock adjacent to pink porphyry and within the NNW structure; CD6816/ 92.2.*

Hydrothermal magnetite alteration was used to constrain magnetite-bearing structures in 3D in the Leviathan Complex by mapping magnetite alteration alignment in successive top sections through the 3D model. These structures have not been documented before by other studies and constraining them in 3D and verifying them in drill core and underground exposure allows refining of the architecture and fluid flow model of Leviathan. The most significant structures of either aligned alteration or porphyries and gold ore shells are:

NNW- and NW-trending steeply-dipping surfaces (magnetite-pyrite, porphyries, Figure 3.10.14),

Broadly E-W-trending surfaces (porphyries, gold ore shells, amphibole, Figure 3.10.14), and

Shallowly-dipping surfaces (magnetite, pyrrhotite, sediments/shear zones, Figure 3.10.34).

A particularly pronounced NNW-trending surface was mapped in 3D from NE of Conqueror to the S of the Victory open pit (Figure 3.10.30, Figure 3.10.31). Traditionally, this surface was mapped locally as subvertical "Kapai Slate" (Ruming, 2005). This trend is also hosting abundant NNW-trending porphyry intrusions and massive hydrothermal magnetite is spatially associated with these felsic porphyry intrusions. It is argued here that this NNW-trending surface and intense $S_{4a}$ foliation zones in this orientation allowed the intrusion of felsic porphyries and the oxidised hydrothermal fluid flow as a direct result of the porphyry intrusions. Importantly, a number of these NNW-trending structures of variable strike length can be constrained in the 3D model. Further it is likely that this zone does not contain stratigraphic Kapai Slate and the "Kapai Slate" type appearance to the rock is due to mylonitization and deformation and intense magnetite alteration. Further, multi-element, whole-rock analyses indicate that Paringa Basalt is exposed both on the western and eastern side of this NNW-trending zone further strengthening the argument of hydrothermally altered rocks rather then stratigraphic Kapai Slate in this position. Disseminated magnetite associated with quartz –carbonate – epidote – chalcopyrite alteration is typically associated with intermediate porphyry intrusions and is described in more detail below.

Sulphur isotopes show a Leviathan Complex scale zonation (Figure 3.10.34). Most of the negative $\delta^{34}S$ values are focussed underneath the Victory-Defiance open pit coincident with magnetite distribution, broadening out with depth. This is taken as indication for focussed oxidised fluid flow underneath the open pit. Positive $\delta^{34}S$ numbers flank the negative focus and indicate zones of partial reduction of $SO_2/SO_4$ to $H_2S$. A number of linear zones with higher positive numbers are either shallowly-dipping around the Conqueror lodes or steeply-dipping, W-trending zones in the centre of the complex. This is interpreted to reflect reduced fluid flow along shear zones in these orientations. Numbers around 0 ‰ are defocused and are interpreted to reflect the background signal.

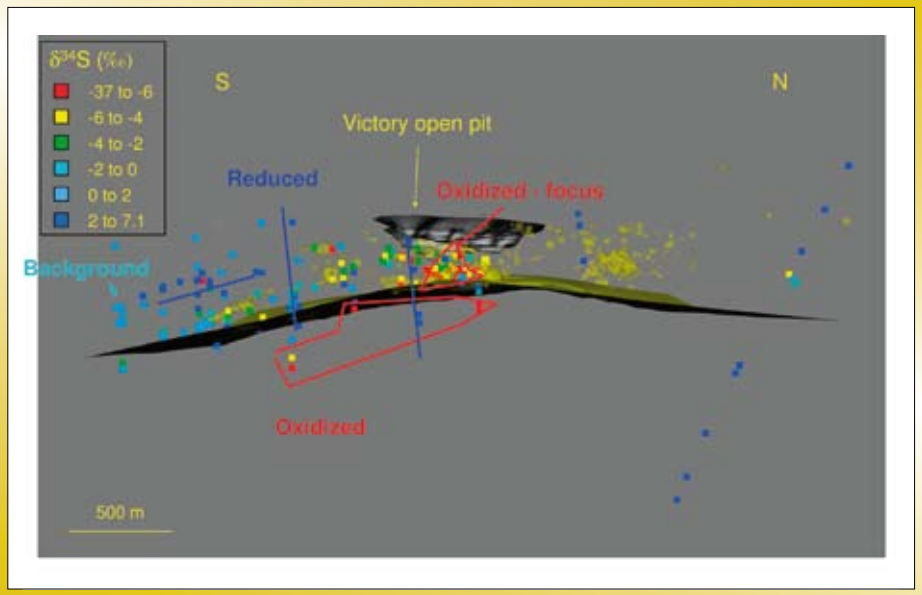


*Figure 3.10.34: View of the Victory deposits to the W showing the distribution of 3 g/t ore shells and $\delta^{34}S$ values. Note that negative S isotope, which indicates oxidised fluid flow, are focussed underneath the Victory open pit. Positive S isotopes, which indicate reduced fluid flow are either aligned along shallowly dipping or along steeply-dipping, WNW-trending structures. The main porphyry intrusion is shown schematically and an idealized alteration zonation with anhydrite and epidote alteration is indicated.*

### 3.10.5.2 Distribution of epidote, biotite, amphibole and anhydrite

The distribution of epidote, biotite and amphibole, coupled with the phase relations and stable isotopic information may be used to map the distribution of oxidised and reduced mineral assemblages. Coupled with the architectural constraints these assemblages allow mapping of the flow paths of oxidised and reduced fluids. Alteration mineral relations and isotope contours are shown from Figure 3.10.35 to Figure 3.10.41.

Epidote in the Leviathan Complex is commonly associated with carbonate ± quartz ± feldspar ± biotite ± magnetite ± pyrite (Figure 3.10.35) but may also occur with pyrrhotite, anhydrite, chalcopyrite or amphibole. Broadly there are two spatially different occurrences of epidote-dominated hydrothermal alteration assemblages:

- A subhorizontal to shallowly-dipping domain(s) that can be traced for 3–4 km across the transect,
- Subvertical domains, aligned along NNW and NW trends of porphyries and structures defined by hydrothermal magnetite alteration described above.

On the western side of the transect, shallowly-dipping, epidote-dominated alteration domains are typically located beneath the Repulse thrust or other shallowly-dipping surfaces (e.g., at Conqueror) and occur predominantly, but not exclusively, in DCB. Epidote alteration can be traced from below the Repulse thrust to the eastern side of the transect (Figure 3.10.36) where it is developed in Paringa Basalt (CD1979) and Black Flag Beds (CD10662,) at similar depths with respect to present day surface.

The common associations of biotite are:

- Biotite - feldspar - carbonate - sulphide assemblages typically in proximal settings to gold lodes (Watchorn, 1998; Clark et al., 1989; Nguyen et al., 1998)
- Disseminated biotite/bands of biotite in epidote-rich assemblages or as distal "haloes" to the subhorizontal to shallowly-dipping domain(s) of epidote alteration, and
- Local zones of intense biotite alteration associated with oxidised alteration assemblages spatially linked to NNW- and NW-trending porphyries.

A zone of anhydrite, broadly coincident with epidote - magnetite - carbonate - biotite assemblages within the DCB, appears to underlie the Leviathan Complex extending from about the position of the Conqueror deposit in the southwest to beyond the position of East Repulse on the north-eastern side of the complex (Figure 3.10.38, Figure 3.10.39). From CD2425 through to CD7068 anhydrite occurs below about 300 metres as pure anhydrite veins (Figure 3.10.35), mixed anhydrite - carbonate ± quartz veins or as anhydrite ± carbonate


*Figure 3.10.35: Oxidized alteration assemblages. A) Intense biotite along contact between ultramafic and porphyry; CD7068/120.8m. B) Epidote-magnetite-pyrite alteration in DCB; CD7068/369m. C) Anhydrite vein CD7069/536.7m.*

*Figure 3.10.36: Hylog of CD7042 illustrating the transition from the epidote-magnetite assemblage (Type 1OR; best developed at ~ 280 to 300m) to Type 2RO assemblage (biotite-magnetite-carbonate at ~270 to 250) and Type 2R assemblage (amphibole-biotite) at ~ 220 -240 m and centred on an intermediate porphyry. All these assemblages are developed within a foliated zone. Several biotite alteration zones occur below ~355m possibly with secondary amphibole although the amphibole in this setting may reflect lithology. Notably white mica highlights the shear zones. Hylogger data from MERIWA project M373. Lithological Code: Mu mafic rocks, un-differentiated; Mb basalt; Md dolerite; Sv volcaniclastic rock; Su sedimentary rock, unclassified; Sc chert; Iz Intermediate intrusion; Iu Intermediate rocks, unclassified; Ua Ultramafic amphibole dominant; Uh Ultramafic chlorite dominant; Uk Komatiite; Ut - Ultramafic talc dominant. Structural Code: My mylonite; Sh shear; Tl – foliation; Vn vein; Fz – fault zone.*

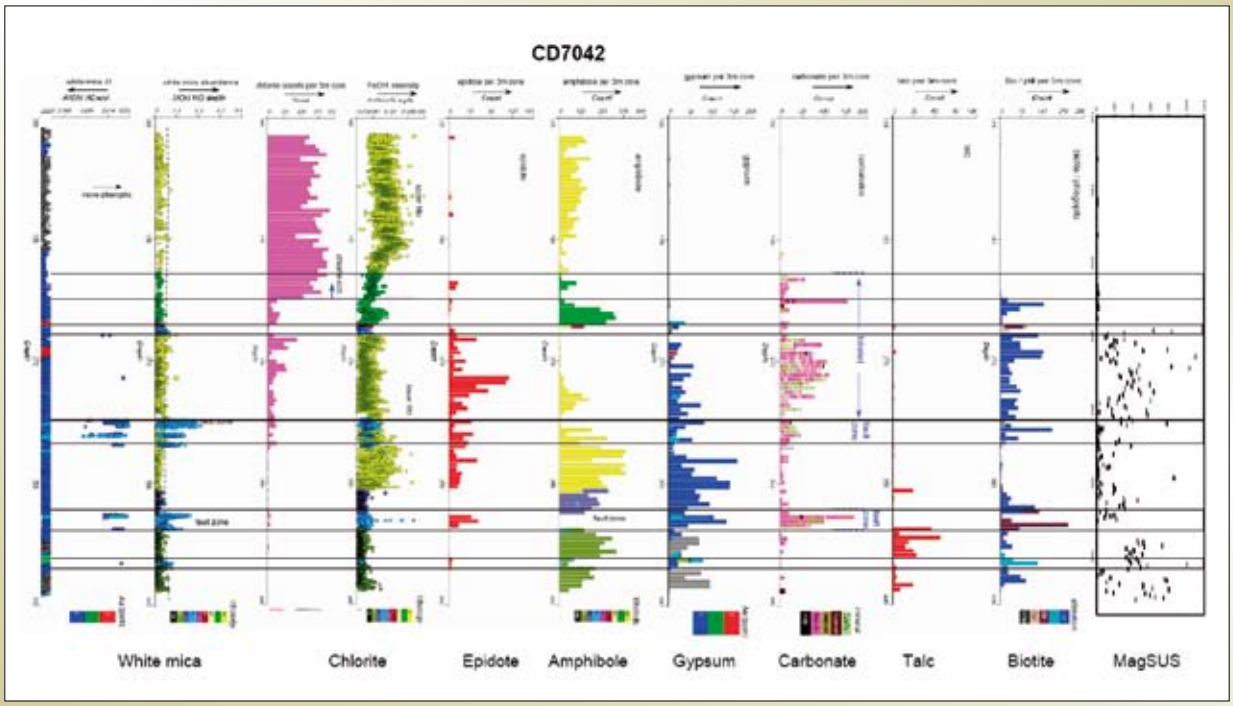


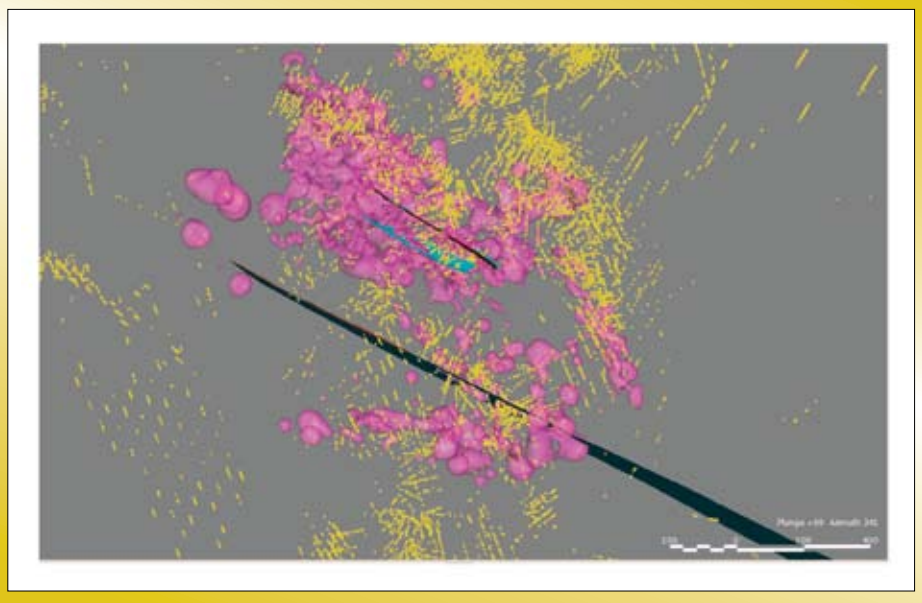

*Figure 3.10.37: 3D model of Victory-Defiance showing the distribution of hydrothermal biotite alteration and felsic porphyries. Note that the bulk of the biotite alteration trends either NW or NNW.*

intergrowths with biotite ± chlorite ± talc ± tremolite fabrics. Tremolite is observed as a reaction rim on anhydrite veins. Above about 300 m the anhydrite is commonly leached. Gypsum may replace anhydrite and the distribution of gypsum is considered a reliable proxy for the original distribution of anhydrite. An extensive domain of negative $\delta^{34}S$ pyrite (Figure 3.10.41), broadly coincident with the zone of epidote alteration between the Conqueror and East Repulse deposits, supports the interpretation that this zone was a major zone of lateral flow of oxidised fluid. Further east in the Maximus area (CD10662), $\delta^{34}S$ pyrite values are positive in the zone of epidote alteration, consistent with more reduced conditions on the flanks of the Leviathan Complex.

A zone of intense secondary biotite (Figure 3.10.35) occurs within both gently-dipping and steep fabrics and along contacts with porphyries is focused on CD6801, CD7068 and CD7069 and co-incident with the thickest section of Tripod Hill Komatiite. The intense biotite alteration is developed in domains up to a metre in width but more commonly several 10s of cm in width and define dominantly gently-dipping fabrics within the ultramafic rocks that link to laterally continuous gently-dipping

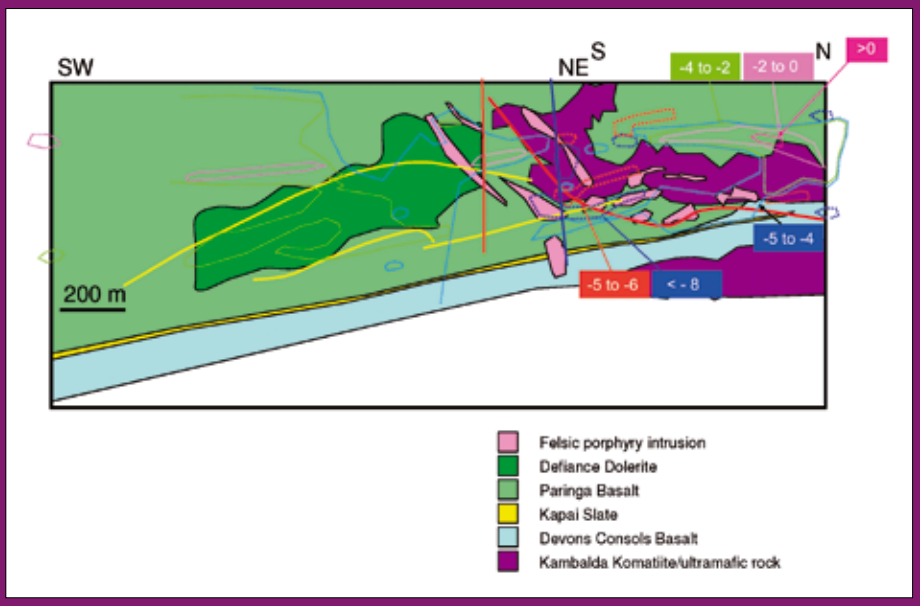


*Figure 3.10.38: Integrated section showing the geology and the $\delta^{13}C$ isotope values on carbonate contoured. Note that values > -4‰ follow shallow dipping structures. These values are interpreted to reflect reduced fluid flow along these structures ($H_2$ and $CH_4$). In contrast, values between -5 and -6 ‰ are interpreted to reflect the $\delta^{13}C$ composition of the incoming fluid. Values < -8 ‰ indicate partial oxidation of $CH_4$ by $SO_2$. Note that these values (< -8 ‰) are focused in the centre of the section.*

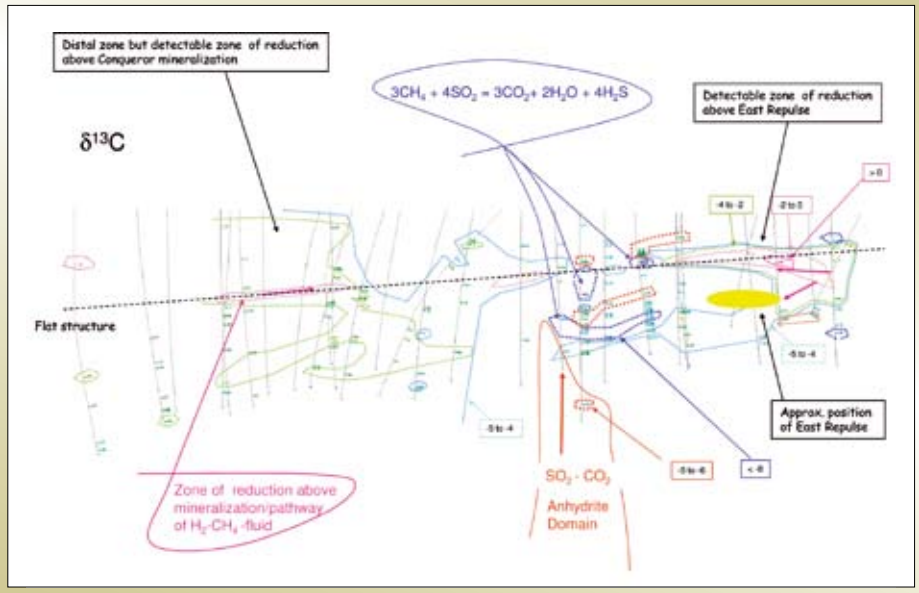


*Figure 3.10.39: Contours for $\delta^{13}C$ in carbonate for the central part of the integrated section with interpreted processes indicated.*

shears across the complex. From the 3D model of the distribution of logged hydrothermal biotite in the Leviathan Complex (Figure 3.10.37), these zones of intense biotite alteration follow trends of felsic porphyries either NW or NNW. Associated carbonate is enriched in $\delta^{18}O$ (>20 ‰; Figure 3.10.40) that is considered to reflect $CO_2$-$SO_2$ -rich parts rather than $H_2O$-$CO_2$-rich parts of the fluid system (Walshe et al., 2008). These data, together with the occurrence of anhydrite veins associated with the porphyries at depth are taken to suggest the zone of intense biotite alteration represent major upflow pathways of $CO_2$-$SO_2$ - volatiles spatially associated with NW- and NNW-trending porphyries.

Amphibole-dominated alteration occurs in at least two different spatial settings: 1) broadly E-W trending, steeply-dipping domains, and 2) shallowly-dipping domains in which abundant pale-green amphibole needles define the foliation, commonly overprinted by chlorite. Locally, randomly-oriented amphibole needles overprint the shear foliation. The E-W trending domains are characterised by cm-wide subvertical amphibole veins which are particularly abundant in E-W trending deformation zones mapped using the alignment of porphyry intrusions and gold ore shells. Shallowly-dipping domains are typically confined to the Repulse thrust above the epidote dominated hydrothermal alteration. In this setting commonly there is a transition from epidote ± magnetite in the DCB at depth to intense biotite ± carbonate ± feldspar ± pyrite with domains of flat fabric to domains of amphibole ± biotite ± chlorite ± pyrite alteration on the contact with alteration. Amphibole alteration extends into the overlying ultramafic rocks, progressively passing in to chlorite-carbonate alteration.

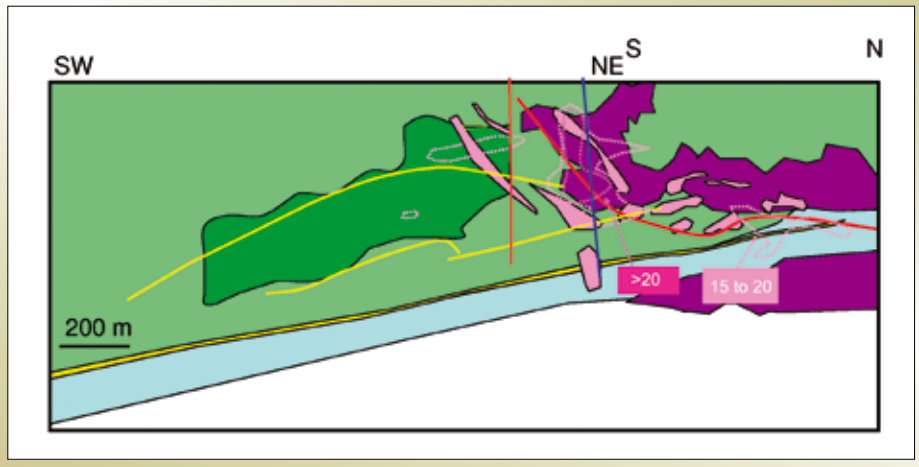


*Figure 3.10.40: Integrated section showing the geology and the $\delta^{18}O$ isotope values on carbonate contoured for the heavy oxygen. Legend for stratigraphy as in Figure 3.10.38.*

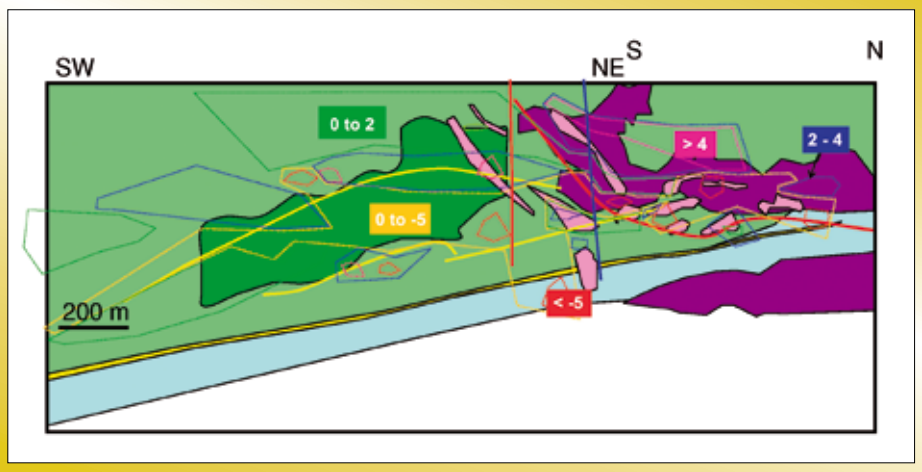


*Figure 3.10.41: Integrated section showing the geology and the $\delta^{34}S$ isotope values contoured. Note that broadly areas with $\delta^{13}C$ > -4 ‰ have $\delta^{34}S$ values > 4 ‰ which is consistent with reduced fluid flow along the shallowly dipping structures. A greater number of zones with $\delta^{34}S$ values < -5 ‰ are focused in the domain with abundant porphyry intrusions to the N of the WNW-trending structure. This zone had indications of oxidation of $CH_4$ by $SO_2$ in the $\delta^{13}C$ values.*

### 3.10.5.3 Tracking redox switches with sulphur and carbon isotopes

The switch from anhydrite ± epidote stable conditions to magnetite and pyrite with increase in amphibole relative to biotite is consistent with a switch from oxidised conditions with sulphate stable in the aqueous fluids or $SO_2$ in $CO_2$-rich volatiles to reduced conditions with $H_2S$ stable in aqueous fluids or reduced anhydrous volatiles. This switch in redox conditions may be tracked by changes in $\delta^{34}S$ pyrite within the sulphide zones from consistently negative zones of $\delta^{34}S$ pyrite to mixed negative/positive to dominantly positive zone, either vertically in a single DDH over 10s of metres or between DDHs over distances of 100s metres. The positive values reflect the reduction of aqueous sulphate implying the influx of a fluid with sufficient reducing capacity to reduce sulphate to $H_2S$ and/or sulphide.

The switch in redox may also be tracked by changes in $\delta^{13}C$ of carbonate that reflect the oxidation of $CH_4$ to $CO_2$ via reactions such as

$$3CH_4 + 4SO_2 = 3CO_2 + 2H_2O + 4H_2S$$

Values of $\delta^{13}C$, which are more negative than ambient magmatic $CO_2$ value of ~ -5 to -6 ‰, are considered to reflect the oxidation of $CH_4$ to carbonate or $CO_2$. Values of $\delta^{13}C$, which are more negative than ~ -8 ‰, are spatially associated with zones identified as zones of upflow of $CO_2$-$SO_2$ – volatiles from the mineralogy and the sulphur and oxygen isotopes (Figures 3.10.38 to 3.10.41).

Increasing $\delta^{13}C$ carbonate from the inferred $CO_2$ reservoir value of -5 to -6 ‰ tracks the progressive reduction of oxidised carbon species to $CH_4$; a reaction that requires a strong reducing agent in the fluids, most probably $H_2$ i.e.,

e.g., $CO_2 + 4H_2 = CH_4 + 2H_2O$

There is a reduced zoned ($\delta^{13}C$> -4 ‰) above the major mineralised centres at East Repulse and Conqueror with a maximum value of +1.99 ‰ above the East Repulse deposit (Figure 3.10.38). The focus of reduction above East Repulse suggests there is a vertical flow path of reduced fluid potentially controlled by the intersection of steeply dipping WNW- and NNW-trending structures. The zones of intense reduction ($\delta^{13}C$> -2‰) highlight a major structure that is gently dipping, which indicates that the reduced fluids dispersed preferentially along at least some of the low angle structures. A carbonaceous zone in CD5653 sits within the high lighted low-angle structure at the cross over from reducing to oxidizing conditions along the structure. Such zones are traditionally interpreted as Kapai Slate, but in this structural setting carbonaceous material is most likely an alteration product from the reaction of $CH_4$ and $SO_2$ i.e.,:

$$3CH_4 + 2SO_2 = 3C + 2H_2S + 4H_2O$$

The pattern of $\delta^{13}C$ enrichment above major mineralised centres implies it will be possible to use the "$H_2$-halo" as a targeting tool. The distal but detectable zone of reduction above Conqueror mineralisation suggests up-flow zones of reduced fluids can be tracked 100s of metres above the zone of mineralisation.

Domains of reduction of $CO_2$ appear to be related to development of chloritic assemblages and texturally to the replacement of carbonate by quartz. Chlorite assemblages are widely distributed in all structures in the Leviathan Complex (EW, NS, shallowly dipping) and chlorite commonly overprints biotite and amphibole although the reverse reactions are observed. It may be that the intensity of chloritic alteration is focused on reduced pathways and that mapping chlorite compositions may provide an effective way of determining the upflow zones of reduced fluid.

### 3.10.5.4 Intersecting fabrics and gold grade

The diamond drill hole CD10628 from the Conqueror area illustrates the control of fabric intersections on gold grades and that oxidised and reduced hydrothermal fluid flow occurred broadly synchronous, at least locally, in the camp (Figure 3.10.42). The hole is close to the camp-scale boundary between the pyrrhotite ± pyrite and magnetite - pyrite domains (Figure 3.10.30, Figure 3.10.31) and magnetite - pyrite formed proximal to gold mineralisation within a steeply-dipping foliation. Pyrrhotite ± arsenopyrite occurs in a shallowly SW-dipping $S_{4b}$ foliation zone (e.g., diamond drill core CD10632), and pyrite is typically absent. Where minor pyrite occurs, gold grades are just above background (less than 1 g/t Au and greater than 0.1 g/t Au). Drill core about 100 m into the magnetite-pyrite zone (e.g., diamond drill core CD10628) shows the development of both alteration styles (reduced pyrrhotite ± arsenopyrite and more oxidised magnetite - pyrite).

The reduced alteration occurs in a shallowly dipping $S_{4b}$ foliation zone, whereas the oxidised assemblage is restricted to a steeply-dipping hydrothermally reactivated $S_{4a}$ foliation zone. Importantly, pyrrhotite inclusions in pyrite and pyrite inclusions in pyrrhotite proximal to the intersection of the two foliation zones indicate that reduced and oxidised fluid flow was broadly synchronous.

High gold grades (>10 Au g/t) occur where both fabrics are developed and form S-C fabrics. It is interpreted that reduced fluids migrated along shallowly dipping deformation zones in the Conqueror area, whereas oxidised fluids used steeply dipping fluid conduits. The intersection of the two structures appears to have resulted in high-grade gold mineralisation.

The chemical composition of hydrothermal fluids associated with the observed hydrothermal alteration zonation has been resolved both spatially as well as temporally. For example, the reduced pyrrhotite-actinolite alteration contains $CH_4$-$N_2$-$CO_2$ fluid inclusions in quartz grains included in the pyrrhotite. These fluid inclusions contain minor $H_2O$ or a distinct $H_2O$ phase cannot be observed implying nearly anhydrous conditions. The overprint of these fluid inclusions by saline aqueous fluid inclusions in secondary trails in the host quartz veins indicates hydrous conditions subsequent to the anhydrous phase.

Fluid inclusions in oxidised alteration assemblages in the Revenge and Conqueror mine are characterised by saline $H_2O$-$CO_2$-NaCl compositions prior to gold deposition. During gold depositions, associated with albite-carbonate alteration, fluid inclusions are dominated by $CO_2$ with a minor $H_2O$ component. Post most of the gold deposition and associated with massive quartz veins, which chemically replace the albite alteration, fluid inclusions are dominated by $H_2O$-$CO_2$-NaCl with increasing salinity with time. In summary the oxidised alteration assemblages formed initially during hydrous conditions followed by nearly anhydrous conditions during gold mineralisation which then was overprinted again by hydrous conditions post gold deposition.

## 3.10.6 Discussion

The structural architecture within the camp controls the distribution of different hydrothermal fluids within the camp at all scales. Importantly, the interplay between faults which formed fluid conduits and others which formed temporary seals allowed fluid flow, intermittent fluid release and isolation of chemically different hydrothermal fluids. The discussion below attempts to fit the structural and geochemical architecture into an integrated framework. Part of this argument was already discussed in Blewett et al. (2008), but needs to be reiterated to assist the integration of the hydrothermal and structural architecture.

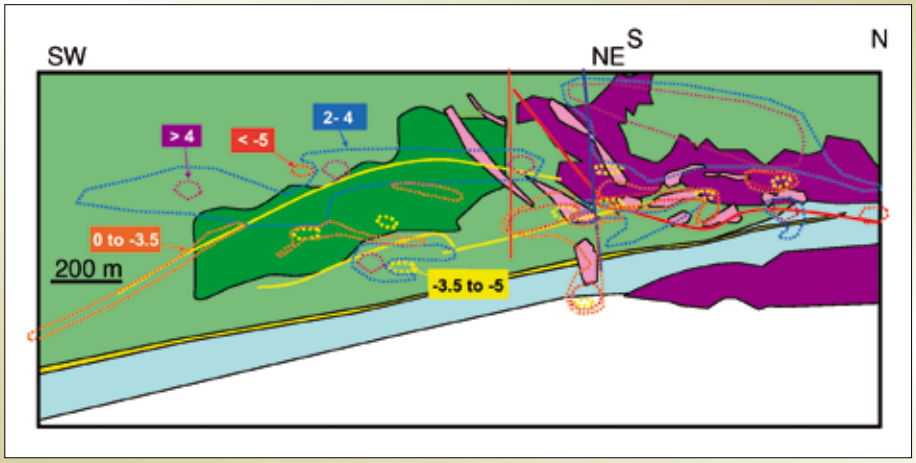


*Figure 3.10.42: Integrated section showing the geology and the $\delta^{34}S$ isotope values contoured. Note that broadly areas with $\delta^{13}C$ > -4 ‰ have $\delta^{34}S$ values > 4 ‰ which is consistent with reduced fluid flow along the shallowly dipping structures. A greater number of zones with $\delta^{34}S$ values < -5 ‰ are focused in the domain with abundant porphyry intrusions to the N of the WNW-trending structure. This zone had indications of oxidation of $CH_4$ by $SO_2$ in the $\delta^{13}C$ values. The range from -3.5 to -5 ‰ has been highlighted (yellow dashed line), because this is believed to reflect the incoming gas composition.*

A multi-fluid model which attempts to explain the distribution of oxidised and reduced fluids needs to address the observations: 1) oxidised alteration assemblages are focused in the Central Corridor and typically centred around felsic and intermediate porphyry intrusions, 2) reduced alteration assemblages flank the oxidised domains and typically reduced deposits are located distal to centres of porphyry intrusions, 3) isotopic and fluid inclusion evidence indicates that even where alteration assemblages are dominantly oxidised, reduced fluids were present during mineralisation, 4) gold deposits are invariably located at sites which show a chemical gradient, i.e., the nature of the alteration assemblages changes rapidly both spatially and temporally in the vicinity of the deposit. This section attempts to summarise the critical parameters in the structural and chemical architecture which appear to facilitate fluid flow of chemically different fluids and gold mineralisation. The distribution of chemically different hydrothermal fluids in the SIGC is controlled by three major factors: 1) location of the fluid reservoirs, 2) shape of the base of the greenstones, 3) large-scale faults, 4) upper-crustal structural architecture.

The critical fluid reservoirs for Archaean gold deposits were discussed in Walshe et al. (2008). In the SIGC the critical fluid reservoirs are 1) oxidised magmatic fluids derived from porphyry intrusions, 2) deeply-derived reduced fluids, 3) ambient metamorphic fluids. It is proposed that the spatial pattern of fluid flow, the chemistry of fluids and nature of hydrothermal alteration assemblages was dictated by:

- the spatial distribution of the major fluid reservoirs,
- fluid pathways that tapped these reservoirs,
- pathways that linked fluids of contrasting chemistry in combination with
- seals which prevented fluid flow.

It is argued that ultimately architectural controls determined the sites of sustained interaction of fluids of contrasting chemistry and deposition of significant amounts of gold.

The shape of the base of the greenstones controls the location of porphyry intrusions (Blewett et al., 2008) which are reflected in distinct lows in detailed gravity data. The base of the greenstones is undulated and forms a distinct dome and basin topography to its surface (Henson et al., 2005). The material beneath the domes is most likely composed of felsic intrusions. One of these domes is located beneath the Leviathan Complex in the SIGC. Seismic reflection data, gravity images and diamond drill core confirm abundant felsic and intermediate intrusions within and above the dome of the base of the greenstones. The interpretation of detailed gravity images of the SIGC reveals four different controls on the location and shape of the gravity lows (Figure 3.10.1, Figure 3.10.2): 1) Kambalda anticline, 2) NW-trending structures, 3) NNW-trending structures, and 4) WNW-trending structures. Most of the gravity lows in the SIGC are aligned along the Kambalda anticline such as the Kambalda dome, the Intrepid area and the Revenge area (Figure 3.10.1, Figure 3.10.2). However, there are also indications of intrusive stocks NW of Santa Ana and Bahama which are distal to the anticlinal axis (Figure 3.10.1, Figure 3.10.2). A second set of controls on the location and shape of the gravity lows is represented by the NW- and NNW-trending structures. Importantly, NW-trending structures control the shape of the gravity low at Leviathan, NNW-trending structures control the shape of the gravity low north of Leviathan to Intrepid and NW-trending structures control the shape of the gravity low at Santa Ana and Bahama. WNW-trending structures appear to limit the N-S extent of the gravity lows.

Large gold deposits (e.g., Wallaby, Kanowna Belle, St Ives) are located close to the apices of broad open domes, imaged as high-amplitude reflections and interpreted as shear zones (Henson et al., 2005). The domal structures are interpreted to have focused magmatic intrusions (see Blewett et al., 2008) and oxidised fluid flow. Therefore, at camp-scale, porphyry-cored gravity lows at the apex of domal structures are taken as indication of oxidised fluid flow. The SIGC contains a number of gravity lows in the Central Corridor and consequently dominant oxidised fluid flow is expected. The extent of the footprint of the oxidised hydrothermal fluids in the SIGC can be appreciated in multi-element, whole-rock analyses. Figure 3.10.26 and Figure 3.10.27 show the distribution of anomalous Mo and Te analyses, which are interpreted to reflect relatively oxidised fluid conditions, centred on the gravity lows. The overall footprint is about 3 km wide and 9 - 10 km long. Individual intrusive centres control the nature and architecture of oxidised and reduced fluid flow within the large-scale oxidised foot print. For example,

Leviathan which is located immediately above the dome in the base of the greenstone surface has well focused porphyry intrusions (Figure 3.10.25). Consequently oxidised magnetite-pyrite alteration assemblages are well focused and only few reduced pyrrhotite-bearing assemblages occur in this domain (Figure 3.10.30). In contrast, porphyry intrusions in the Revenge area, which occur along the flanks of the domes of the base of the greenstones surface, are more dispersed and consequently oxidised magnetite-pyrite assemblages are more dispersed (Figure 3.10.24). Typically, reduced pyrrhotite-bearing assemblages occur intermittently between oxidised magnetite-pyrite assemblages. At Junction, which is located above a basin in the base of the greenstones surface (Figure 3.10.43) and outside the main oxidised footprint of the Central Corridor, very few porphyries intruded the dolerite host rock and oxidised alteration assemblages are rare. Incidentally, major ore bodies occur where more abundant porphyries intruded the Junction deposit and the alteration mineral assemblage appears to indicate more oxidised compositions (pyrite stable over pyrrhotite). This is interpreted that fluid mixing could have been important for ore deposition at Junction, although Junction was not studied in detail in this study.

The second parameter, which controls fluid flow and the chemical nature of the fluids are large-scale structures (Table 3.10.2). Most of the major structures such as the Lefroy and Bardoc represent reduced fluid pathways over most of their active time. This is documented in pyrrhotite alteration along the Bardoc fault and early and late $CH_4$ fluid inclusions in the Lefroy fault at the New Celebration gold deposit (Hodge et al., 2005). However, spatially and temporally focused, segments of these faults contained oxidised fluids, typically proximal to felsic and intermediate porphyry intrusion into or proximal to the faults. For example, at New Celebration 30 km north of the SIGC, the reduced fluid flow along the Lefroy fault was interrupted by an intermittent oxidised fluid flow during gold mineralisation (Hodge et al., 2005). A similar situation occurs in the Lefroy fault at Nelsons Fleet in the SIGC, where locally oxidised fluids infiltrated the fault adjacent to porphyry intrusions (Table 3.10.2).

Within the SIGC, camp-scale structures show evidence of both fluid flow and fluid seal. Importantly, a number of structures prevented fluid exchange across the structure and compartmentalised fluid flow. An example for compartmentalised fluid flow is the Playa fault. A number of geochemical trace element anomalies such as Bi, Cu, S, Ba, Hf, Mo, P, Te occur in the footwall, but terminate at the Playa fault and these anomalies are absent in the hangingwall of the fault. Another example of a structure which seals fluid flow on either side is the N25 at Junction.

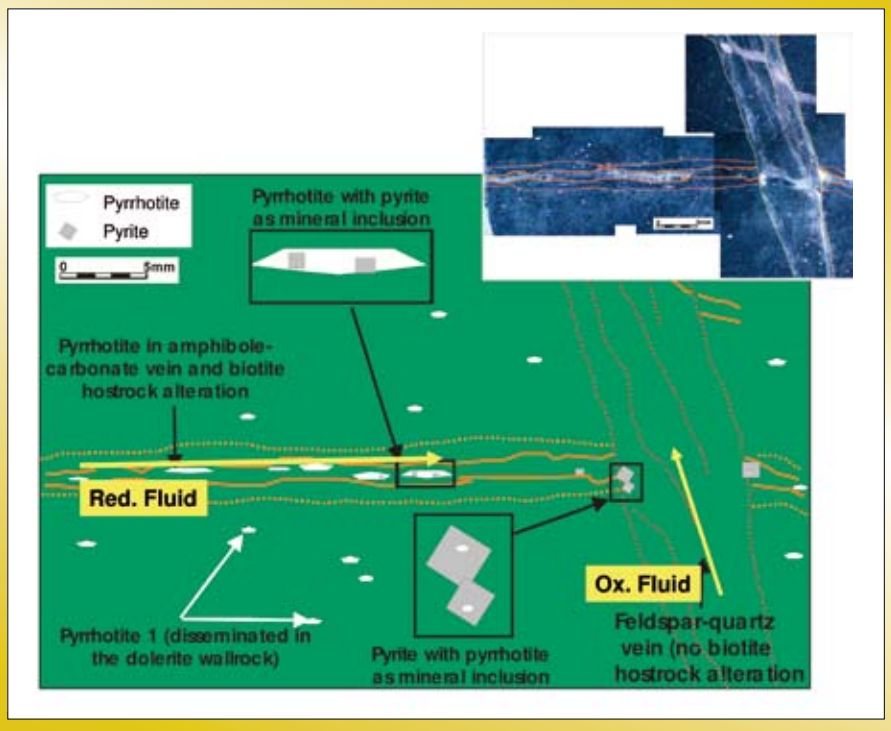


*Figure 3.10.43: Detail of diamond drill core at the Conqueror underground mine. The reduced alteration assemblages are hosted in shallowly SW-dipping shear zones which are intersected by steeply-dipping structures which contain the oxidized alteration assemblages. Pyrrhotite inclusions in pyrite combined with pyrite inclusions in pyrrhotite indicate that reduced and oxidized fluid flow was broadly synchronous. Note that pyrite is located preferentially at the intersection of the reduced and oxidized structures.*

To the W of the structure, epidote is a common alteration phase in the mafic dolerite. However, to the E of the N25, epidote is absent as alteration phase.

At the camp-scale the overall nature of alteration in the Leviathan Complex appears oxidised and spatially related to a gravity low and abundant porphyry intrusions. However, at the lode-scale distinct oxidised and reduced upflow zones and pathways can be identified using a combination of alteration mineral mapping (visual and spectral), stable isotope geochemistry and fluid inclusion chemistry (Figure 3.10.44). Centres of oxidised fluid upflow in the Leviathan deposits are focused on intersections of NNW- and NW-trending porphyry intrusions with WNW-trending subvertical structures, typically intruded by porphyries as well. A detailed stable isotope study has identified a major upflow zone between the Conqueror and Victory Defiance deposits and others are defined on more limited data between the Victory and East Repulse deposits Up-flow zones, characterised by anhydrous $CO_2$-$SO_2$- fluids, are inferred to link laterally to steeply dipping NW trending oxidised flow paths defined by intense biotite alteration, magnetite distribution (Figures 3.10.31 and 3.10.37) and limited stable isotope data. Three major zones have been mapped across the Leviathan complex (Figure 3.10.45) and inferred to connect to the North Orchin mineralisation NW of the Leviathan complex Within the crustal level of the Leviathan deposits, subvertical upflow zones lead into shallowly-plunging zones, preferentially underneath fluid seals such as the Repulse thrust or the ultramafic wedge preventing further subvertical upflow. Incidentally, this shallow-plunging flow zone is also intruded by shallowly-plunging porphyry intrusions adding further weight to the argument of oxidised fluid flow along this shallowly plunging zone.

Table 3.10.2: Compilation of selected structures and interpreted character of hydrothermal fluid chemistry in the SIGC

| Structure | Nature | Evidence |
|---|---|---|
| Lefroy | reduced, small oxidised centres | $CH_4$ fluid inclusions at New Celebration, widespread carbonate alteration |
| Bardoc | reduced | pyrrhotite alteration |
| Speedway | locally oxidised, rest unknown | magnetic corridor at Lut |
| Repulse | complex, temporary seal, reduced, oxidised | vertical zoning from amphibole alteration (reduced) proximal to the hangingwall through biotite-carbonate-magnetite alteration (oxidised) through epidote-magnetite alteration in the footwall (oxidised); mixing domain underneath a seal? |
| Playa | temporary seal, oxidised | multi-element concentrations change across fault; hydrothermal magnetite |
| Foster thrust | temporary seal | multi-element concentrations change across fault; reduced (pyrrhotite) in the hangingwall |
| ESE-WNW trending, subvertical structures | reduced | amphibole-biotite alteration, pyrrhotite alteration |
| SW- and S-dipping (e.g., Conqueror) | reduced and probably acid | $CH_4$-$N_2$±$CO_2$ fluid inclusions at Conqueror, pyrrhotite in the structure, locally oxidised where gold deposition, muscovite in PIMA, stable isotopes |
| Steep NNW-trending structures | oxidised | magnetite in structure, porphyries |
| Steep NW-trending structures | oxidised | magnetite in structure, porphyries |

Reduced fluid conduits in the Leviathan area maybe shallowly SW-dipping structures; such as in the Conqueror area. Here, the structure contains only pyrrhotite-amphibole alteration to the SW of the mine and gold grades within the structure are low (<0.5 g/t). Within the Conqueror mine in the gold ore shoots oxidised pyrite and magnetite ± hematite assemblages are the characteristic sulphide-oxide minerals. The latter mineral assemblage may be associated with another set of structures which intersected the Conqueror fault as documented in small-scale fractures in the area. Other examples of SW-dipping reduced structures occur in the Maximus prospect and along the Bellisle shear zone at the SIGC. There is also evidence for reduced hydrothermal actinolite-biotite alteration locally along the steep WNW-trending structures which probably provided subvertical upflow zones. Again gold-grades are low in these zones (typically <0.2 g/t). Gold deposition occurred in zones where oxidised fluid flow intersected with these reduced upflow zones such as in the pipe area underneath the Victory open pit. An up-flow zone of reduced fluid flow identified from stable isotopes and characterised by fuchsite and pyrrhotite

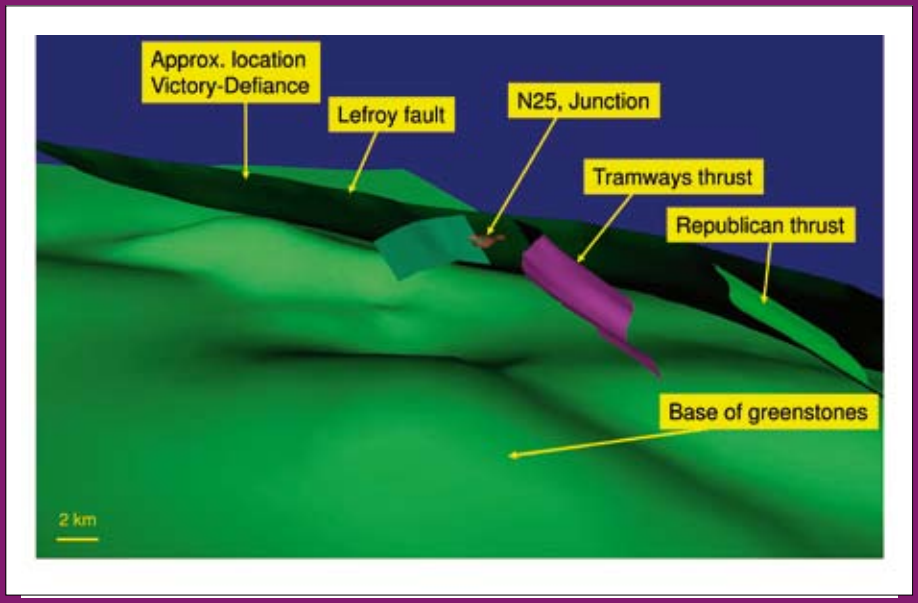


*Figure 3.10.44: Interpreted structures and base of greenstones by SIGMC exploration team and location of selected gold deposits (View to NE). Note that Junction is situated above a trough in the base of greenstones surface, whereas Victory Defiance is located above a high in the base of greenstones surface which is thought to have focused the ascent of porphyritic intrusions and oxidized hydrothermal fluids.*

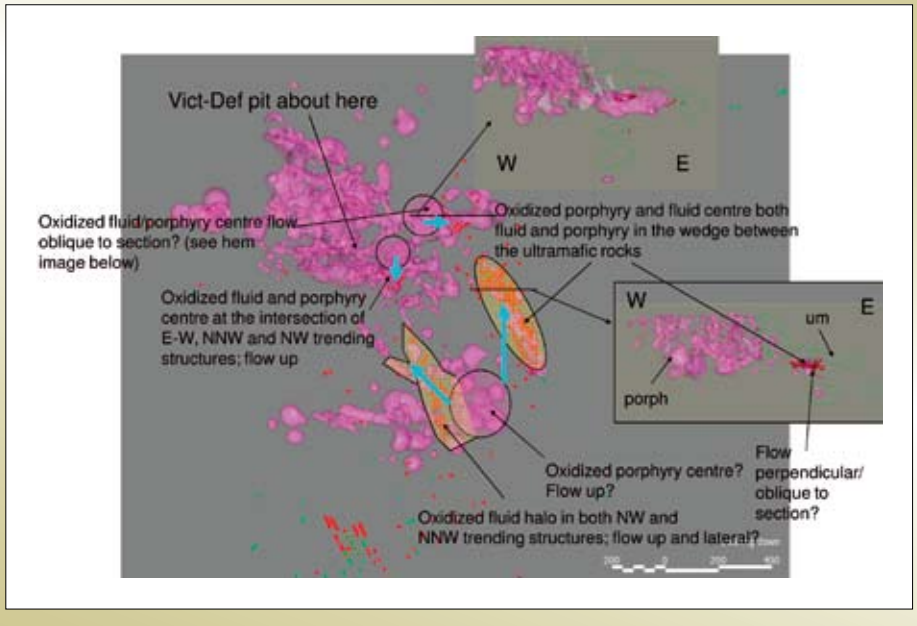


*Figure 3.10.45: 3D model of Victory-Defiance showing the interpreted centres of oxidized fluid flow (pink circles). Insets show cross sections in locations indicated in the main image. Magnetite and pyrrhotite are shown in red and green dots, respectively.*

occurs 200 m east of East Repulse deposit (Figure 3.10.46). The overall pattern of reduction indicated by zoning in the C and S isotopes (Figures 3.10.38 and 3.10.41) in the vicinity of the East Repulse deposits implies focused up-flow of highly reduced fluids at intersections of WNW structure and NNW structures (Figure 3.10.46) and this pattern of reduced fluid flow may be common as illustrated in Figure 3.10.45. Shallowly dipping structures allowed reduced fluids to spread laterally within the complex. Fluid interaction occurred where oxidised and reduced fluids mixed either within shallowly-dipping structures or at the intersection of shallowly and steeply dipping structures. Most of the reduced fluid flow along the major regional structures may well be acidic in nature as indicated by PIMA data on the smaller structures which confirmed muscovite mica compositions.

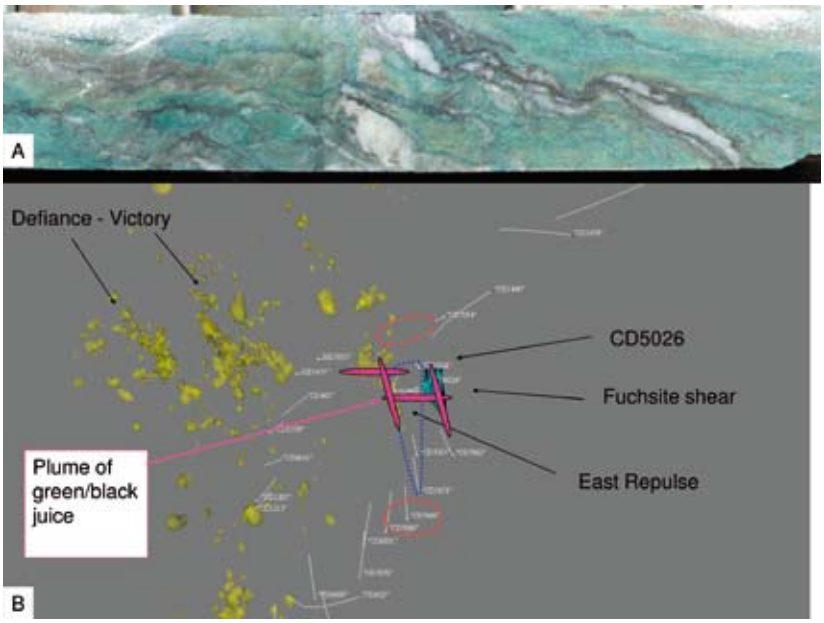


*Figure 3.10.46: Fuchsite in the East Repulse environment. A: Fuchsitic sample from CD6330 1~100. B: Location of the fuchsitic shear, east of East Repulse. Red dotted outline shows approximate positions of up-flow zone of $CO_2$-$SO_2$ – fluids. Blue dotted outline shows approximate location of zone of reduction broadly centred above East Repulse. The Fuchsite shear is also interpreted from C isotopes to be a zone of intense reduction. Pink lozenge shows possible pathway of deep-Earth hydridic fluid in E-W structure/N-S structure.*

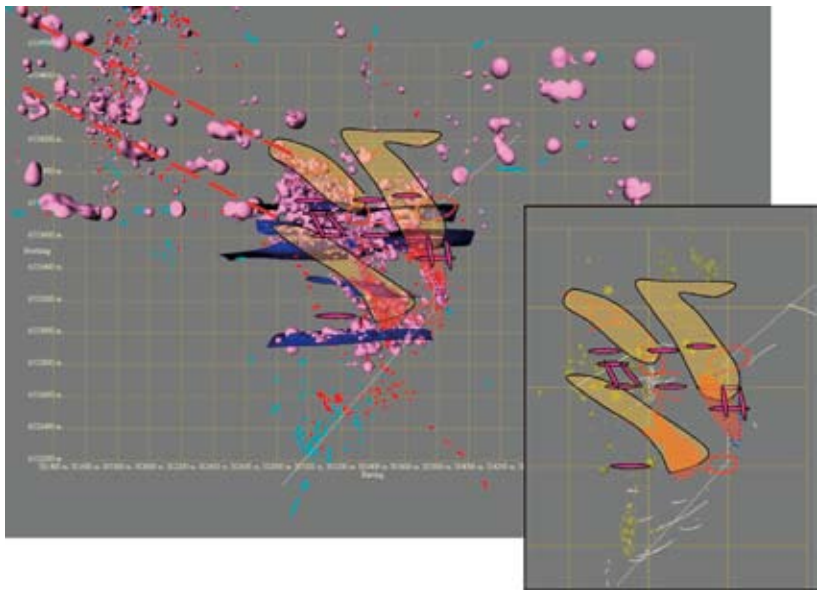

*Figure 3.10.47: Inferred locations of fluid pathways relative to the distribution of felsic porphyry intrusions in the Leviathan complex as modelled in Leapfrog (pink surfaces). Pink lozenges; up-flow zones of deep-Earth hydridic fluids in E-W structure/N-S structures. Oxidized upflow zones (red circles) defined from isotopes. NW trending oxidized flow paths defined by intense biotite alteration and magnetite distribution (Figures 3.10.31 and 3.10.37). Dashed red line is extrapolation of oxidized pathway to NW. Inset: Flow paths shown relative to A. Location of 3 g/t gold ore shells as modeled in Leapfrog. Dashed white line is Integrated Section of the stable isotope study.*

Arguably, the structural patterns that controlled fluid flow in the Leviathan area reflect a basement controlled architecture that controlled camp-scale fluid flow patterns. The salient elements of this architecture are:

- NW-trending basement structures that in part controlled emplacement of intrusions and flow paths of oxidised fluids.
- NNW trending arc-parallel structures and WNW trending cross-arc structures that controlled up-flow zones of highly reduced, deep-Earth fluids
- Domical structures and related flat to shallowly dipping structures that dispersed fluids laterally and connected up-flow zones of high reduced and highly oxidised anhydrous fluids.

## 3.10.7 Conclusions

Hydrothermal alteration in the St Ives gold camp is zoned at all scales from the camp scale to deposit scale to ore shoot scale. The zoning in the alteration has been documented using a range of data sets from mineral mapping (both normal logging and spectral techniques) through multi-element geochemistry and stable isotope geochemistry.

Oxidised deposits are focused around lows in gravity in the Central Corridor, which are interpreted to represent porphyry intrusions at about 1000 m below present surface, whereas reduced deposits are located to the S and SW of the Central Corridor.

The geological and structural architecture in the Leviathan complex has been reinterpreted using hydrothermal alteration and multi-element geochemistry data in a 3D model. In particular, Kapai Slate is only interpreted in its stratigraphic position between Devons Consols Basalt and Paringa Basalt. Most other occurrences of formerly interpreted Kapai Slate represent either other interflow sedimentary rocks or altered shear zones. Mapping alteration in 3D delineated NNW- and NW-trending, steeply-dipping mostly oxidised structures and WNW-trending, subvertical mostly reduced structures in the Leviathan complex.

Mapping oxide-sulphide-silicate mineral assemblages in $fO_2$-pH space allows definition of oxidised and reduced assemblages and acidic, neutral/mildly alkaline and alkaline assemblages. Mapping these assemblages in 3D models allows identification of fluid pathways and the chemical nature of the hydrothermal fluids and gases.

Oxidised magnetite-bearing assemblages in the Leviathan Complex are spatially well correlated with felsic porphyry intrusions and negative sulphur isotopes and are focused south of the Victory-Defiance open pit and north of Conqueror. Reduced pyrrhotite-bearing

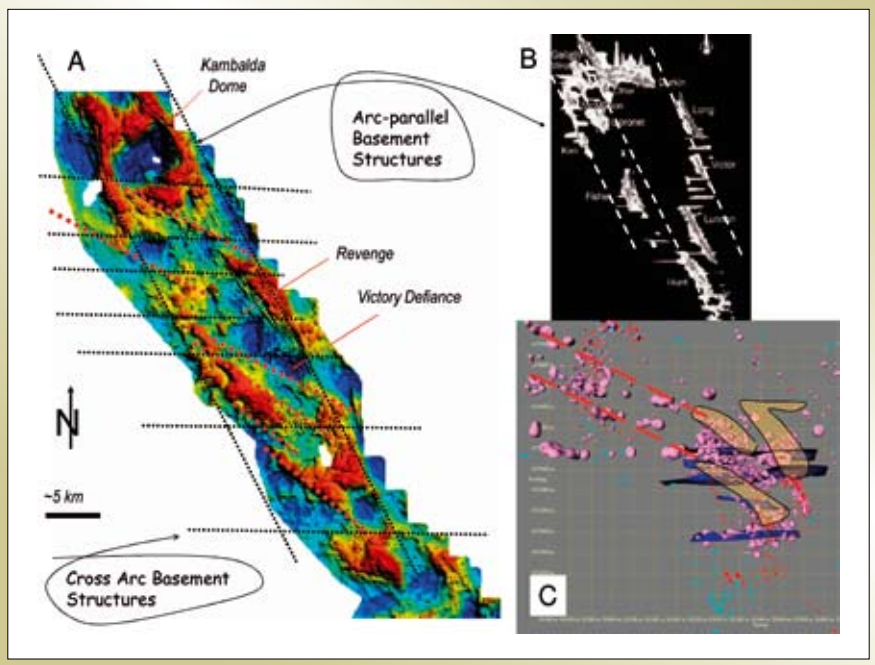


*Figure 3.10.48: Control of basement structures on camp-scale fluid flow patterns. A Detailed gravity image of the Central Corridor of the St Ives gold camp. Highlighted are the NW-trending basement structures that in part controlled emplacement of intrusions and flow paths of oxidized fluids. Up-scaling from the Victory-Defiance complex, up-flow zones of reduced, deep-Earth fluids were controlled by intersections of arc-parallel and cross-arc structures. B Nickel-sulphide shoots of the Kambalda Dome showing orientation of the nickel troughs (after Stone et al., 2005), sub-parallel to arc-basement structures. C Inset of Victory-Defiance highlighting NW-trending oxidized fluid flow pathways defined from mineralogy and stable isotopes.*

assemblages correlate with positive sulphur isotopes and occur in shallowly dipping structures (e.g., Conqueror). Mineralisation occurs where magnetite alteration changes into reduced pyrrhotite-bearing alteration assemblages.

Epidote-bearing alteration assemblages, biotite assemblages, anhydrite, hematite, pyrite-magnetite and pyrrhotite-amphibole assemblages delineate the chemical architecture of the hydrothermal system in the Leviathan complex. Oxidised upflow zones are focused around intersections of WNW-, NNW- and NW-trending structures and porphyries. Gently-dipping shear zones act as both reduced fluid pathways and mixing boxes where oxidised $CO_2$-$SO_2$ gases migrated from steep upflow zones in the gently-dipping shear zones, but locally also formed temporal seals to fluid flow.

Values of $\delta^{13}C$, which are more negative than ambient magmatic $CO_2$ value of ~ -5 to -6 ‰, are considered to reflect the oxidation of $CH_4$ to carbonate or $CO_2$, and values of $\delta^{13}C$, which are more negative than ~ -8 ‰, are spatially associated with zones identified as zones of upflow of $CO_2$-$SO_2$ – volatiles. Increasing $\delta^{13}C$ carbonate from the inferred $CO_2$ reservoir value of -5 to -6 ‰ tracks the progressive reduction of oxidised carbon species to $CH_4$ by a strong reducing agent in the fluids, most probably $H_2$.

Reduced hydrothermal alteration at Conqueror is located in $S_{4b}$ foliation zones is broadly synchronous with oxidised hydrothermal alteration in $S_{4a}$ foliation zones as indicated by mutual mineral overprinting relationships and gold deposition is controlled by fluid interaction/mixing.

The location of oxidised fluid flow and porphyry intrusion in the camp is controlled by domes in the base of the greenstones. In contrast major arc-parallel structures such as the Lefroy and Bardoc represent reduced fluid pathways over most of their active time with up-flow of highly reduced, deep-Earth anhydrous fluids focused on intersections with cross-arc structures, commonly of WNW orientation.

### 3.10.8 References

Bennett MA (1995) The structure and timing of gold mineralisation in the Victory area and its relationship to regional deformation in the eastern Goldfields Western Mining Corporation, Kambalda.

Blewett, R.S. Squire, R., Henson, P.A., Miller, J.M., and Champion, D.C., 2008, Architecture and geodynamic evolution of the St Ives region, south central Kalgoorlie Terrane, Western Australia. Part III, this volume.

Clark ME, Carmichael DM, Hodgson CJ, and Fu M (1989) Wall-rock alteration, Victory Gold Mine, Kambalda, Western Australia: Processes and P-T-X(CO2) conditions of metasomatism In: Keays RR, Ramsay WRH, Groves DI (eds) The geology of gold deposits: The perspective in 1988. Society of Economic Geologists, pp 445–456.

Connors K, Donaldson J, and Morrison RS, C. Ds (2003) Technical Note: The stratigraphy of the Kambalda-St Ives District: Workshop notes St Ives Gold Mining Company, Kambalda, pp 97.

Cox SF, and Ruming K (2004) The St Ives mesothermal gold system, Western Australia - a case of golden aftershocks? Journal of Structural Geology 26: 1109–1125.

Henson PA, Blewett RS, Champion DC, Goleby BR, Cassidy KF, Drummond BJ, Korsch RJ, Brennan T, and Nicoll M (2005) Domes: the characteristic 3D architecture of the world-class lode-Au deposits of the Eastern Yilgarn In: Hancock H, Fisher L, Baker T, Bell T, Blenkinsop T, Chapman L, Cleverley J, Collins B, Duckworth R, Evins P, Ford A, Oliver N, Rubenach M, Williams P (eds) STOMP 2005: Structure, Tectonics and Ore Mineralisation Processes. EGRU, Townsville, pp 60.

Hodge JL, Hagemann SG, and Neumayr P (2005) Characteristics and evolution of hydrothermal fluids from the Archean orogenic New Celebration gold deposits, Western Australia In: Mao J, Bierlein FP (eds) Mineral Deposit Research: Meeting the Global Challenge. Springer, Bejing, pp 529–532.

Miller, J.M., Tunjic, J., Donaldson, J., and Blewett, R.S., 2008, Structural evolution of the Victory to Kambalda region of the St Ives gold camp: the role of early formed structures on the development of a major gold system. Part III, this volume.

Nguyen TP, Cox SF, Harris LB, and Powell CM (1998) Fault-valve behaviour in optimally oriented shear zones: an example at the Revenge gold mine, Kambalda, Western Australia. Journal of Structural Geology 20: 1625–1640.

Ohmoto H, and Goldhaber MB (1997) Sulphur and Carbon isotopes In: Barnes HL (ed) Geochemistry of hydrothermal ore deposits. John Wiley and Sons, Inc., pp 517–611.

Petersen KJ, Neumayr P, Hagemann SG, and Walshe JL (2005) Paleohydrologic evolution of the Kambalda gold camp In: Bierlein FP, Mao J (eds) Mineral Deposit Research: Meeting the Global Challenge. Springer, Berlin, Heidelberg, New York, pp 573–576.

Ruming KJ (2005) Controls on lode gold mineralisation in the Victory Thrust Complex, St Ives Goldfield, Western Australia University of Newcastle, pp 456.

Walshe JL, Mikucki EJ, Neumayr P, Cleverley J, Petersen K, and Andrew A (2008a) Depositional processes in Eastern Yilgarn gold systems. This volume.

Walshe JL, Neumayr P, Cleverley J, Petersen K, Andrew A, Whitford D, Carr GR, Kendrick MA, Young C, and Halley S (2008b) Multiple fluid reservoirs in Eastern Yilgarn gold systems. This volume.

Watchorn RB (1998) Kambalda-St Ives gold deposits In: Berkman DA, Mackenzi DH (eds) Geology of Australian and Papua New Guinean Mineral Deposits. The Australasian Institute of Mining and Metallurgy, Melbourne, pp 243–254.

## 3.11 Architectural and geodynamic controls during gold mineralisation around the Archaean Scotia-Kanowna Dome, Kalgoorlie Terrane, Western Australia

**B.K. Davis[1], R.S. Blewett[2], R. Squire[3], D.C. Champion[2] and P.A. Henson[2]**

[1] Dundee Precious Metals, PO Box 30, Toronto, ON, Canada M5J 2J1

[2] ***pmd*CRC*** c/o Geoscience Australia, GPO Box 378, Canberra, ACT, 2601, Australia

[3] School of Geosciences, Monash University, Clayton, Victoria, 3800, Australia

### Abstract

Archaean domes are associated with many of the larger gold deposits of the Eastern Goldfields Superterrane (e.g., Sunrise Dam, Wallaby, St Ives camp, Kalgoorlie, Lawlers etc), and the Scotia-Kanowna Dome is eroded to sufficiently deep levels to provide insights into the role domes play in controlling gold deposition. At the centre of the Scotia-Kanowna Dome is a granite-cored batholith, which is surrounded by outward-dipping greenstone belts and associated shear zones. A number of small- to medium-sized gold deposits occur on the limbs and the centre of the dome, and the world-class Kanowna Belle gold mine occurs on the nose of the dome. At least three separate gold mineralising events are defined, each of regional significance that can be correlated with other well known gold deposits of the Eastern Goldfields Superterrane.

The history of palaeostress across this region was dominated by both maximum contractional and extensional vectors oriented perpendicular to the north-northwest trending grain. The resultant strain is seen in the architecture of the Scotia-Kanowna Dome, with its margins and associated shear zones controlling the distribution of stratigraphy (which is relatively linear and parallel to the margin).

Throughout most of the tectonic history the marginal shear zones were high-strain domains that recorded multiple stages of contraction, with thrust and mostly sinistral strike-slip shear kinematics. In contrast, the dome hinge/nose region was a relatively low-strain domain as it was somewhat in the strain shadow of the regional contractional events. For example, the early extensional record has been preserved at the nose, with late basins formed in the hangingwall to the extensional faults adding to the stratigraphic complexity of the local region. These late basins may also have contributed to the fluid budget. In contrast along the margins, there is no record of these late basins or the extensional faults that controlled their deposition.

The architecture of the dome played an important role in controlling mineralisation during a significant deviation in the maximum contractional stress vector (to south of east). At this time, basins in the nose region underwent inversion (and their structures) with thrusting to the north and northwest. Shortening was accommodated along the dome margins by sinistral strike-slip shearing that was relatively 'free to move' due to the mostly linear stratigraphy combined with limited anisotropy and perturbations along the margin. The stratigraphic and geometrical complexity around the dome nose however, resulted in localised maximum dilation and gold deposition at this time. The dome nose/hinge area was also a favoured locus for enriched, dominantly Mafic-type magmas that are seen as the extensive porphyry swarms in the region. These felsic-intermediate rocks may have also contributed to the complex fluid budget and these rocks are considered as indicators of particular fertility for gold, and may have been the primary source for much of the metal endowment.

The return of the maximum contraction vector to perpendicular to the strike of the regional structural grain also favoured the deposition of gold in the dome nose region. The complex stratigraphy in the nose region was striking (sub)parallel to the palaeostress vector and resulted in maximum dilation and inflow of gold-bearing fluids. Extensive thrusting on the margins of the dome also resulted in gold deposition away from the nose, especially in the accommodation zones between adjacent thrusts (e.g., at Mulgarrie). This late contraction involved the entire upper crust of this region, with structurally controlled gold deposits also developing at this time in the central granitic core of the dome. What is uncertain is whether these inversion events simply reworked pre-ore endowment (in the Mafic-type felsic magmas that are within or beneath these deposits) or represented a new 'injection' of gold, or both.

The architecture of granite-cored domes has played a critical role in focussing magma as well as mineralising fluids into regions of maximum dilation. They do this by nature of their inherent competence, by influencing the position and geometry of shear zones (fluid pathways) and hence distribution of stratigraphy (depositional sites) across the region. The Scotia-Kanowna Dome is a good example to study this control, and inferences can be made for similar controls by concealed domes, such as beneath Kalgoorlie.

**Key words:** *Archaean, structural geology, gold mineralisation, Eastern Goldfields, Yilgarn Craton, Kanowna Belle*

## 3.11.1 Introduction

The late Archaean Scotia-Kanowna Dome, the centre of which is located about 80 km north of Kalgoorlie in Western Australia, is a doubly plunging antiform that contains the 100-km-long 30-km-wide north-northwest-trending Kanowna Batholith at its core and several major Au deposits near its western, southern and eastern margins (Figure 3.11.1). The close spatial association between the gold deposits and the elongate granitoid batholith in the dome's core has led to suggestions that large granitic bodies in the centre of regional antiforms were a vital ingredient during gold mineralisation (Henson et al., 2005). Similar structural and geometric relationships occur at Wallaby and Sunrise Dam in the Laverton region (Miller, 2007) and Leonora (Blewett and Czarnota, 2007a, b, c; Blewett et al., 2008b), and at Hemlo in the Superior Province of Canada (Beakhouse, 2007).

The precise links between the large granitic batholiths and the gold mineralisation remain unclear (see Groves et al., 1998; Henson et al., 2005). Detailed to regional scaled 3D maps are well-constrained by seismic, gravity and magnetic data, and reveal that granite-cored domes (plutons to batholiths) are present beneath most greenstone belts (Henson et al., 2005; Henson and Blewett, 2006) of the Eastern Goldfields Superterrane (EGST; Cassidy et al., 2006). The Scotia-Kanowna Dome is exposed at a structural level that reveals the core of the dome as well as the flanks and nose. This exposure level presents an opportunity to investigate the potential links between granite batholiths and gold mineralisation.

Questions to answer include; did the batholiths control the distribution of far-field stress at the local site of deposit-scale gold deposition, and thus focus mineralising fluids? Alternatively, or in addition to the architecture, did these large batholiths contribute to the fluid budget? In this paper a case is made for an architectural control by large granite batholiths on the location of gold deposits. That is not say that the batholiths (commonly multiphase – Champion and Sheraton, 1997) did not influence the deposits in terms of fluids, metals and/or heat.

The Scotia-Kanowna Dome contains many well-studied deposits together with abundant geophysical, geochemical and geological data, making it ideally suited to assess the links between mineralisation and the regional architecture and geodynamic evolution. In this paper, these data are integrated with new structural and kinematic results from gold deposits located around and within the dome. Finally, we assess the commonalities of the area's architecture and geodynamic evolution, and assess what implications they have for the structural history of the EGST (e.g., Blewett and Czarnota, 2007a, c).

## 3.11.2 Regional geological setting

The Scotia-Kanowna Dome is located in the northern half of the Boorara Domain (Figure 3.11.1), which forms part of the Kalgoorlie Terrane in the Eastern Goldfields Superterrane (Swager, 1992; Champion, 2006). The Boorara Domain is bound to the west by the Waroonga and Bardoc Fault Systems and the Lefroy Fault, and to the east by the Perseverance and Ockerburry Fault Systems. The doubly plunging Scotia-Kanowna Dome is a multiphase batholith enveloped by outward younging and dipping late Archaean successions. The stratigraphy is divided into lavas, high-level intrusions and volcaniclastic units of the Kambalda Sequence and the coarse volcanic and sedimentary units of the overlying Kalgoorlie Sequence (Table 3.11.1).

At Kanowna Belle the Kalgoorlie Sequence has been subdivided into several units, whereas elsewhere it is broadly divided in to coarse-grained and fine-grained sedimentary units (Tripp et al., 2007). Intruding these successions is a series of deep-level mafic and felsic intrusions, which include the composite Scotia-Kanowna Batholith (Table 3.11.2).

Table 3.11.1: Summary of the characteristics of the Kambalda and Kalgoorlie Sequences comprising the Boorara Domain near the Scotia-Kanowna Dome

| | |
|---|---|
| **Kalgoorlie Sequence (after Tripp et al., 2007)** | |
| **Golden Valley Turbidite** | Feldspar-rich volcanic sandstone, siltstone and lesser mudstone; conformably overlies Golden Valley Conglomerate |
| **Golden Valley Conglomerate** | >400 m thick; poorly sorted, internally massive to weakly graded beds; dominated by porphyritic and equigranular felsic clasts with minor mafic & volcaniclastic clasts; located north of the Fitzroy Fault |
| **Government Dam Turbidite** | >300 m thick; quartz-rich sandstone, siltstone and lesser mudstone; turbidites; beds up to several 10s of cm thick; contact with Grave Dam Grit not exposed |
| **Grave Dam Grit** | Very thick (>1500 m?); strongly to intensely altered unit interpreted to contain abundant quartz & feldspar crystals; interpreted to represent the products of a pyroclastic flow deposit (ignimbrite); (dis)conformably overlies Kanowna Turbidite |
| **Kanowna Turbidite** | Feldspar-rich volcanic sandstone, siltstone and lesser mudstone; conformably overlies Kanowna Conglomerate |
| **Kanowna Conglomerate** | >250 m thick; poorly sorted, internally massive to weakly graded beds; dominated by porphyritic and equigranular felsic clasts with minor mafic, ultramafic and volcaniclastic clasts; conformably overlies Ballarat Turbidite east of Kanowna Belle |
| **Ballarat Turbidite** | Feldspar-rich volcanic sandstone, siltstone and lesser mudstone; conformably overlies Ballarat Conglomerate |
| **Ballarat Conglomerate** | Up to 150 m thick; very poorly sorted & internally massive; dominated by well-rounded feldspar-phyric clasts & angular to subangular ultramafic and high-Mg to basaltic clasts; unconformably overlies units of the Kambalda Sequence |
| **Kambalda Sequence** | |
| **Spargoville Formation** 2698–2687 Ma | Feldspar-rich volcanic sandstone, siltstone and lesser mudstone; conformably overlies units of Upper Basalt in Ora Banda Domain (Tripp et al. 2007); Up to 80 m thick; high Mg basalt; massive lavas & pillow basalt; varioles & amygdales (vesicles) also common; conformably overlies komatiite; detrital zircon & intrusion U/Pb SHRIMP dates constrain the age between 2698 & 2687 Ma (Sircombe et al., 2007) |
| **Upper Basalt** ~2687 Ma | Up to 80 m thick; high-Mg basalt; massive lavas & pillow basalt; varioles & amygdales (vesicles) also common; conformably overlies komatiite |
| **Komatiite** ~2707 Ma | >100 m thick ultramafic lavas & intrusions; texturally zoned (cumulate to spinifex textures); extrusive units are asymmetrically zoned; appears to intrude dacite, thus penecontemporaneous (Trofimovs et al., 2004a) |
| **Dacite** Ma ~2707 | Up to 500 m thick; coherent units of quartz-feldspar-phyric dacite; U/Pb SHRIMP ages of 2708±7 Ma (Nelson, 1996) & 2706±5 Ma (Barley et al., 1998); volcanic debris avalanche associated with emplacement of dacite (Trofimovs et al. 1994b) |
| **Lower Basalt** ~2720 Ma | 30–100 m thick; tholeiitic; massive & pillow basalt with rare interflow sedimentary units; inferred age of 2720–2710 Ma (Swager et al., 1992; Trofimovs et al., 2004a) |
| **Unnamed volcaniclastic unit** | >20 m thick; normally graded beds of feldspar- and quartz-rich volcanic sandstone, siltstone and lesser mudstone; flame structures & load casts are common; has peperitic (high-level intrusive) contact with Lower Basalt (Trofimovs et al., 2004a) |

Table 3.11.2: Summary of the characteristics of the felsic intrusive rocks of the Boorara Domain near the Scotia-Kanowna Dome

**Felsic Intrusive rocks**

The Scotia-Kanowna Monzogranite is a typical High-Ca type granite of TTG affinity (Champion and Sheraton, 1997) that forms the bulk of the core of the Scotia-Kanowna Dome and has an age estimate of around 2660 Ma (2657±5 Ma: Ross, 2002 and 2664±4 Ma: Nelson, 1995). In the centre of the batholith are Mafic-type phases, including the Golden Cities Granodiorite (2656±3 Ma: Cassidy et al., 2002), which hosts the Woodcutters camp and the Scotia-Split Rock Granodiorite (2657±5 Ma: Nelson, 1995).

The majority of the felsic intrusive rocks in the Kanowna area are of the Mafic-type and are lithologically similar. Most of the felsic intrusions are altered and deformed with undulose quartz to granoblastic and myrrmekitic textures indicative of deformation and /or metamorphism. The primary minerals include plagioclase, alkali feldspar, amphibole, biotite, clinopyroxene, quartz, opaques, titanite, zircon, apatite and allanite. The phenocryst assemblages are not distinctive. Background levels of Au are between 2–5 ppb.

| Supersuite | Characteristics |
|---|---|
| Minnie Mabel | Relatively mafic with low Ni and high LREE, Ba, Rb. |
| Gordon-3 | Characterised by higher Th, Ni and Cr, and lower $P_2O_5$, Sr and Y. |
| Government Dam | Felsic with distinctive high FeO*, MgO, $P_2O_5$, Ba, Sr, Nb, LREE, Y, Ni and Cr. |
| Aphyric Hanging Wall | Comprises four units and is distributed in KB and Mulgarrie. Distinctive features are higher MgO, $P_2O_5$, Th, LREE, Ni and Cr. Difference best obvserved in $TiO_2$-$P_2O_5$ and $TiO_2$-La plots. At Mulgarrie this group has higher Zr than other members of this group. |
| White Feather | Characterised by low Ba, Ni, Cr, moderately low Sr, moderate Th and high LREE. |
| White Feather-Consuls | Characterised by low Ba, Sr, Th, moderate LREE, Ni and Cr. |
| Four Mile Hill | Has many similarities with the Kanowna Belle Suite, but differs in higher Ba, Sr, Pb, Th, LREE, Nb, and lower Rb. This supersuite has two units that differ in Sr and Ni levels, and may be related through fractional crystallisation. An age of 2613 Ma for the Four Mile Hill dyke (Nelson, 1995) is interpreted to date a disturbance event rather than the emplacement age of the dyke (Cassidy et al., 2002). |
| Kanowna Belle | Low-LILE silica-rich end-member clan of the Mafic-type granites (Champion and Sheraton, 1997), with a complex supersuite with up to 14 granite units. Has an age of 2656±6 Ma for the Kanowna Belle porphyry (Ross et al., 2004). Distinguished from other supersuites in being relatively low in $P_2O_5$. Has a range in Si, Cr, Ni, Th, LREE. |

### 3.11.2.1 Deposit locations and production histories

The Scotia-Kanowna Dome is encircled by gold deposits: A number of deposits occur on the circumference of the Scotia-Kanowna Dome, which is partially bound on the western margin by the Bardoc Tectonic Zone; Paddington is the largest of the deposits along the western margin in the Bardoc Tectonic Zone; Kanowna Belle, Red Hill and Ballarat-Last Chance are located near the southern hinge; Gordon-Sirdar and Mulgarrie are located on the eastern margin; and Golden Cities and Federal are located in the granitic core of the dome (Figure 3.11.1). The following section outlines a brief history of mining of these deposits.

The Paddington gold mine is located ~35 km north-northwest of Kalgoorlie and is the largest deposit (~40 tonnes) of the Bardoc Tectonic Zone, the major shear system on the western flank of the Scotia-Kanowna Dome (Figure 3.11.1). Between 1985 and 2001, eighteen Mt of ore was mined averaging 2.28 g/t Au, or ~37 tonnes of gold (Sheehan and Halley 2002). A number of other open-pit gold deposits have been mined within the greater Paddington area, including four open pits within the Broad Arrow locality, ~5 km to the north.

Kanowna Belle, located about 20 km north of Kalgoorlie, is the largest of the deposits located along the hinge (southern margin) of the Scotia-Kanowna Dome (with a

*Figure 3.11.1: Solid geological map of the wider Scotia-Kanowna Dome region showing main units, structures and stratigraphy (after Tripp et al., 2007). Total magnetic intensity image and key sites described in this paper, note the splaying of structures about the central nose of the dome.*

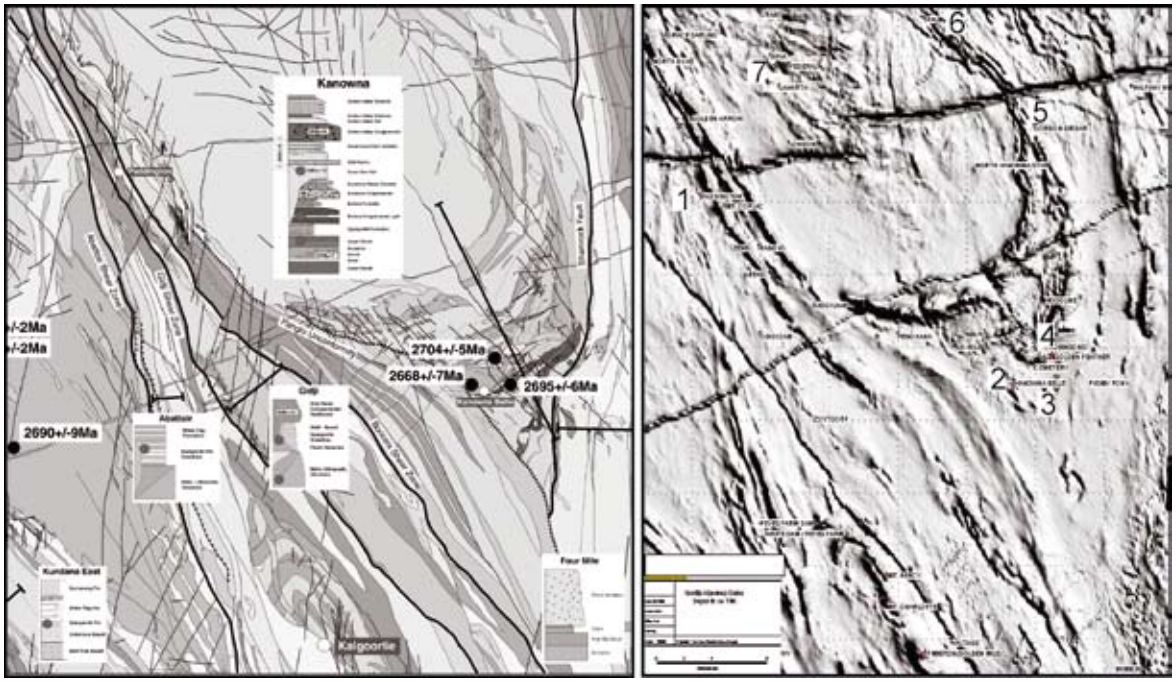


total inferred resource of 48 tonnes and a proved reserve of 29 tonnes (Table 3.11.3). The Kanowna Belle discovery evolved as a conceptual model beginning as an occurrence of steeply-dipping and narrow gold-bearing veins of limited extent. A large area (400 m x 300 m) of anomalous gold-in-soil values, defined in 1989 in the area of the RAB drilling, was viewed as inconsistent with the concept. Follow-up RAB and RC drilling led to the discovery of Kanowna Belle in December 1989. Interpretation of deeper and more widespread (vertical) drilling results throughout 1990 demonstrated an elongation of the deposit to the southwest and suggested a southern dip direction. It was the drilling of deep diamond holes in 1990 that revealed the potential size of Kanowna Belle with intercepts of 50–80 m of 2-5g/t Au.

The Ballarat-Last Chance (BLC) deposit lies within the Kanowna Goldfield southeast of the Kanowna Belle mine, and is the combination of two historical mines named Ballarat and Last Chance. The Last Chance Mine was opened in 1897 and was worked to a depth of 575 feet (167 m) and produced 10245 oz of gold from 27 689 tons (318.7 kg from 28 132 tonnes, i.e. 11.4 g/t) until its closure in 1906. The Ballarat and nearby Sunbeam mines to the west operated between 1898 and 1912, and were worked to depths of 395 feet (120 m) and 302 feet (62 m) respectively,

Table 3.11.3: Resource-Reserve figures for gold at the Kanowna Belle Gold mine (source DOIR)

| | | | |
|---|---|---|---|
| PROVED | Reserves | 4.755Mt | 29,181.435kg |
| PROBABLE | Reserves | 6.939Mt | 30,691.197kg |
| MEASURED | Resources | 2.491Mt | 12,382.761kg |
| INDICATED | Resources | 4.024Mt | 15,866.632kg |
| INFERRED | Resources | 12.118Mt | 48,605.298kg |

producing a total of 7,350 oz of gold from 14174 tons (228.6 kg from 14631 tonnes, i.e. 15.6 g/t). Exploration in the BLC area between 1982 and 1985 led to full-scale mining between 1986 and 1999. Mining was localised in several discrete locations within an open pit, with a number of historical hard-rock stopes and shafts having been intersected by the open-pit development.

Red Hill is a quartz vein-hosted resource located within the Red Hill porphyry approximately 500 m north of the abandoned Kanowna townsite. Underground mining of quartz reefs at Red Hill began in the early 1900's and continued intermittently until the 1980's, with total recorded production 52,000 tonnes at 30g/t for 50,000 ounces of gold. The bulk of production came from gently-dipping quartz reefs that cropped out along the ridge at Red Hill. The potential for the area to host a large volume of low-grade mineralised porphyry was well documented by extensive drilling which was estimated to contain 25 Mt @ 1.0 g/t for 800,000 oz. However, due to the limiting size of the tenement, it was not possible for North Ltd to exploit the resource and no further work was completed. Final resource definition drilling by Delta Gold was completed in 2001, and resource estimation and modelling was completed in early 2002.

The Gordon-Sirdar area is located about 18 km northeast of the Kanowna Belle mine (Figure 3.11.1), and 46 703.3 t of ore for 510.67 kg Au (10.9 g/t Au) was mined between 1899 and 1981. Modern production (post-1988) from the Gordon-Sirdar open pit amounted to 129 535 t of ore for 185.16 kg Au, at an average grade of 1.43 g/t Au (Roberts et al., 2005). The indicated resource of the open pit at the time of writing was 1.39 Mt of ore at 1.65 g/t Au (2307 kg Au).

The Mulgarrie deposit is located on the eastern limb of the Scotia-Kanowna Dome in greenstones that mantle the batholith. During the late 1800's to early 1900's the Mulgarrie Mining Centre produced a total of 5400 oz from 7000 tonnes of ore treated, at an average grade of 22 g/t. Mining activities were at their peak during the period 1913–1923 with the mining of high-grade lodes and rich surface/shallow mineralization by both surface and underground mining methods. The next recorded production from Mulgarrie was during 1986 when BHP Minerals (subsequently Newcrest) commenced trial pit mining of the quartz vein-hosted primary mineralisation. A total of 12000 tonnes of material was removed with some 2850 tonnes being selectively mined. Mining of the present pit shape was completed by Delta Gold in 1999–2000.

The Woodcutters camp includes the Havana-Suva, Jakarta, London and Federal deposits (Figure 3.11.1). These deposits are hosted solely within the 2656±3 Ma Golden Cities Granodiorite (Cassidy et al., 2002), which comprises part of the granitic core of the Scotia-Kanowna Dome. A resource of around 1.4 M oz has been extracted from the camp. Federal comprises part of the Woodcutters Goldfield, with initial discovery of gold in 1996 following drilling of a gold anomaly by AMX Resources NL. Centaur Mining and Exploration Ltd discovered additional gold in 1996–1997. Total reserves and resources on the AMX tenement was approximately 1.05 Moz with a 0.5 g/t cutoff (AMX, 1998) with an additional 0.33 Moz represented in Federal pit (Phillips and Zhou, 1999). Centaur commenced mining of the Federal orebody in July 1998, with ore being trucked to existing treatment facilities at the nearby Mt Pleasant Mine. Mining was completed in late 1999.

### 3.11.3 3D architecture of the Scotia-Kanowna Dome

Goleby et al. (2002) constructed a 3D model (map) of the greater Kalgoorlie region, including the Scotia-Kanowna Dome area. They noted that regional upright domes, such as the Scotia–Kanowna Dome, are very obvious in the seismic images from both the 1991 and 1999 surveys and agreed with earlier interpretations (Drummond et al. 2000) of a duplex structure beneath the dome and above a regional detachment surface. Three deep seismic reflection traverses (91EGF1, 99AGSY2 and 99AGSY5) cross the Scotia–Kanowna Dome. Line 99AGSY5 was orientated northwest-southeast, parallel to the plunge of the dome. Lines 99AGSY2 and 91EGF1 (dynamite line of lower fold and quality) were approximately E-W and crossed the dome to form a 2D grid. The latter two traverses were sub-parallel, crossed similar geology and tested continuity of major structures along strike.

The seismic data and the interpretations of Goleby et al. (2002) were re-examined and input into a revised 3D map for the region (Figure 3.11.2). The batholith is seismically non-reflective, with its base and sides not imaged by the seismic data. Furthermore, there are no truncated

greenstone reflections that could indicate the position of its boundaries (Goleby et al., 2002). Gravity modelling by Bell et al. (2000) showed that the batholith is likely to be around 2.5–3.0 km thick and the greenstones thicker to the east than the west. Immediately beneath the batholith, strong reflections dip towards the centre of the granite.

The greenstone succession surrounding the Scotia–Kanowna Dome is well imaged geophysically. Henson et al.'s (2006) reinterpretation of the 99AGSY2 seismic line defined an open dome (cored by felsic rock) with a breached apex at a depth of 3 km to the west of the axis of the batholith (Figure 3.11.2). The surface projection of this breached fault is in the vicinity of the Panglo Basin to the west of Kanowna Belle. Beneath the entire ~35 km long 99AGSY5 seismic line lies a band of high-amplitude reflectors (the 'detachment') that dips around 10° to the west (4–5 km depth in the east to >9km in the west; Figure 3.11.2). Goleby et al. (2002) interpreted a series of concave lenticular reflective bodies as a broadly folded imbricate thrust stack, although granite doming may have also developed these structures.

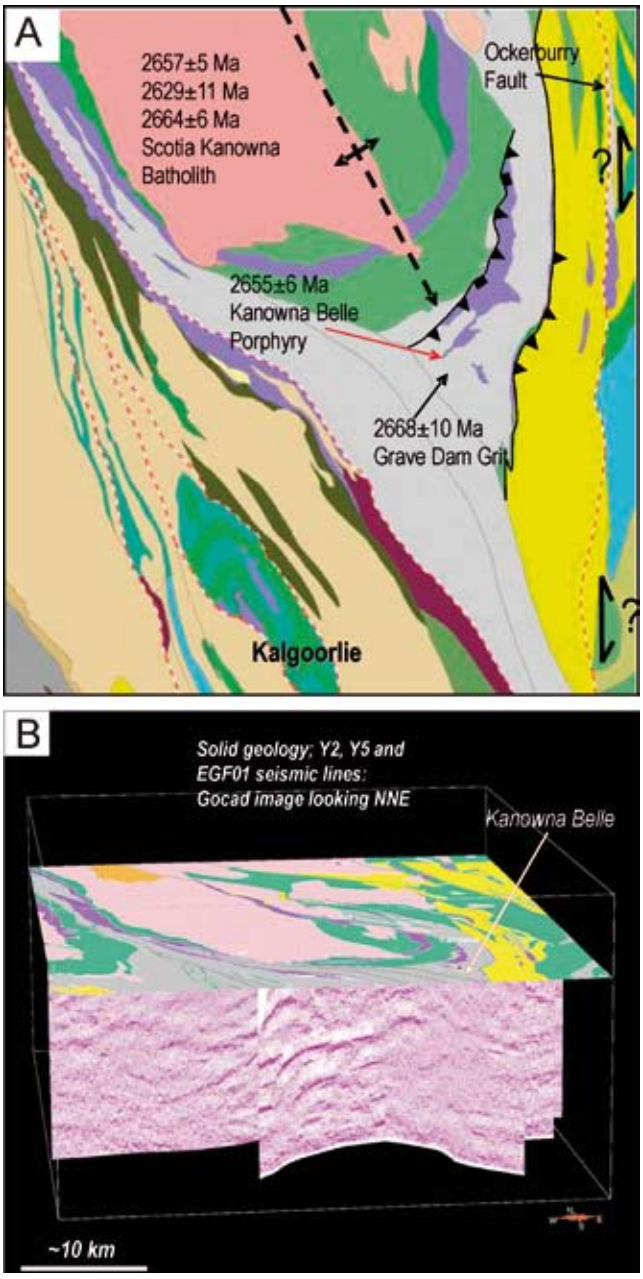


*Figure 3.11.2:*
*a) Simplified solid geology map of the Scotia-Kanowna Dome showing the major faults and stratigraphic units.*
*b) 3D perspective view to the north-northeast of the Scotia-Kanowna Dome with seismic sections. Note the arching (open antiformal structure) defined by the prominent reflectors beneath the dome. Breaching of the prominent domal structure by faults (not displayed) connect to the surface trace of major structures and these are interpreted to be deeper pathways for mineralising fluids.*

A deep magnetotelluric (MT) study was conducted by the ***pmd*CRC*** across the Scotia-Kanowna Dome along the original 91EGF01 deep seismic reflection line. The MT technique measures conductivity of the crust and mantle and is sensitive (in terms of increased conductivity) to the presence of fluids, sulphides, graphite and/or elevated temperature (Cagniard, 1953). The crust beneath the dome has very low resistivity (highly conductive), with values of 15–25 Ohm metres (Blewett et al., 2008a). The source of the elevated conductivity is unknown, but the presence of graphite is a possibility as deep-sourced reduced $CH_4$ fluids dominate much of the alteration (Graham Heinson, pers comm. 2007). Equally important are the likely presence of buried high heat-producing Low-Ca granites at depth beneath the dome. Their presence at depth in the Kalgoorlie Terrane was also hypothesised on the basis of relatively slow crustal velocities in the region (Blewett et al., 2006a; 2008a). This additional crustal heat production may account for the elevated conductivity.

## 3.11.4 Detailed architecture and structural controls on gold mineralisation in key areas

The Scotia-Kanowna Dome has a number of the mines located within its perimeter greenstones and within its granitic core. The bulk of the descriptions and observations that follow are sourced from the extensive unpublished work by Davis (internal confidential company reports). The following section describes the key sites that are located around and within the dome, namely: Paddington (west limb of the dome); Kanowna Belle, Ballarat-Last Chance, and Red Hill (southeast plunging dome hinge); Gordon-Sirdar and Mulgarrie (east limb of the dome), and; Golden Cities-Federal (dome core). Each site is described separately with a local deformation sequence (e.g., PD1 is Paddington first deformation, and MUD2 is Mulgarrie second deformation etc), and then synthesised into the regional deformation framework of Blewett and Czarnota (2007a) and Blewett et al. (2008b). Table 3.11.4 is a summary of the characteristics of each site and its relationship to the regional framework.

### 3.11.4.1 Paddington

The Paddington gold mine is located ~35 km north-northwest of Kalgoorlie and is the largest deposit (~40 tonnes) of the Bardoc Tectonic Zone, the major shear system on the western flank of the Scotia-Kanowna Dome (Figure 3.11.1). The Bardoc Tectonic Zone has been the focus of a recent detailed study by Morey (2007), which showed that its narrow width (10–15 km) between the Scotia-Kanowna Dome and the granitic Mt Pleasant Dome to the west, combined with the parallelism of stratigraphy and structure, had promoted diffuse fluid flow. Consequently, the Bardoc Teconic Zone is considered less prospective than other areas with differing (less restrictive) architecture. The Paddington pit is located at the southern end of this high-strain corridor and is representative of the structure and mineral deposits along the western side of the Scotia-Kanowna Dome.

Paddington comprises an open pit that is oriented north-northwest-south-southeast parallel to the strike of the stratigraphy, foliation and shear zones, and is divided into a northern and southern section by a series of northeast-trending dextral strike-slip faults (Morey, 2007). The stratigraphy faces west and dips steeply (both east and west). From east to west the mine stratigraphy consists of: 1) ultramafic rocks which are dominated by foliated talc-chlorite schist with localised spinifex textures preserved; 2) tholeiitic basalt with thin interflow sedimentary layers; 3) two main dolerite intrusions, the largest up to 100 m thick, and; 4) Black Flag Group volcanoclastic sediments to the west (Sheehan and Halley, 2002). Gold is hosted mostly in the more competent dolerite and basalts in the centre of the pit.

#### Structure and mineralisation

Structures attributable to three phases of penetrative contractional deformation have been recorded at Paddington (Morey, 2007), and they are defined here by the prefix 'P'.

**PD1**

The first phase of deformation at Paddington is recorded as the penetrative PS1 foliation that strikes north-northwest and dips steeply to the southwest (Figure 3.11.3a). This PS1 foliation is associated with a steep down-dip plunging stretching lineation. The PS1 foliation is axial planar to upright isoclinal PF1 folds that plunge moderately to the north-northwest. These PF1 folds are associated with northwest- to north-northwest-trending reverse faults that offset the upright isoclinal folds, and together these structures are interpreted to have developed during

contraction under an east-northeast – west-southwest direction of maximum shortening (Morey et al., 2007).

Two styles of gold-bearing veins have been described (Sheehan and Halley, 2002). The first is a steeply-east dipping laminated shear vein up to 3 m wide that strikes the length of the pit. Morey et al. (2007) described an alteration assemblage comprising carbonate-quartz-muscovite-sulphide-gold, which extended for up to 1 m into the wallrock. The sulphides are dominated by arsenopyrite with lesser pyrite and accompanying base metal sulphides. Stretching lineations associated with the shear zone that hosts the vein plunge steeply and S-C asymmetries indicate E-over-W movements. Progressive deformation has fractured the arsenopyrite and these fractures have been sites of gold deposition (Morey et al., 2007).

The second vein set comprises stacked extension veins that are sub-horizontal to gently northeast- and southwest-dipping conjugate sets (Figure 3.11.3b). These veins are typically only 1–5 cm thick and are associated with a similar alteration assemblage as the main shear vein. The veins are not folded, although a mutual overprinting relationship was locally observed between these veins and the main pS1 foliation (Morey et al., 2007).

### pD2

The second phase of local deformation is recorded in the centre of the pit with a series of folds and reverse faults that developed during north-northwest-south-southeast oriented contraction. The pF2 folds have east-northeast-trending axial surfaces that overprint the main pS1 foliation with a steep plunge to the west-southwest. Morey et al. (2007) noted that these structures were

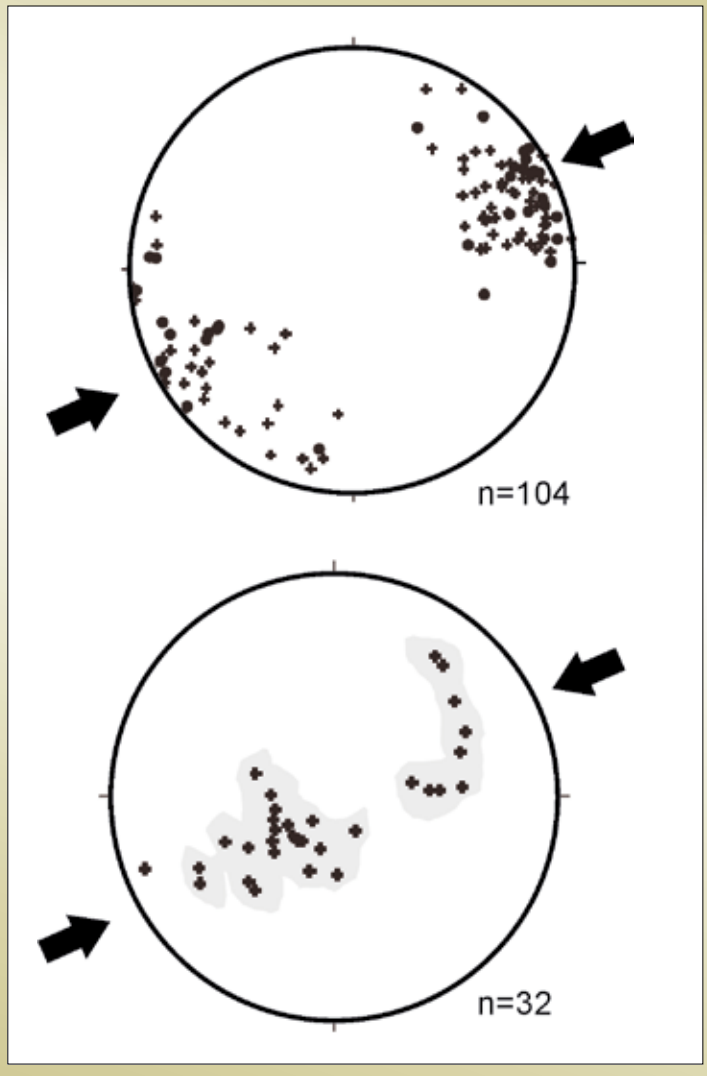


*Figure 3.11.3: Lower hemisphere stereographic projections of a) poles to bedding and S4a foliation, and b) conjugate extension ladder veins (after Morey, 2007). Note the flattening plane defined by the foliation strikes north-northwest and σ1 was oriented east-northeast-west-southwest (arrows). The ladder veins dip gently to moderately to the northeast and southwest, consistent with a conjugate relationship (σ1 east-northeast-west-southwest, σ2 north-northwesr-south-southeast, σ3 vertical).*

barren (quartz-carbonate veins) and suggested that they were developed during a local deviation in the regional stress field.

**pD3**

The third pD3 (and final) deformation event in the Paddington pit produced a series of northeast-trending brittle-ductile dextral faults. These fault arrays have offsets of 10's of metres across strike (Hancock et al., 1990). Slickenlines plunge north on these faults (Morey et al., 2007), suggesting a normal (extensional) component of movement at this stage.

### Regional correlation

The three deformation events (pD1, pD2, and pD3) have the same relative sequence of events seen regionally (D4a, D4b, and D5) and correlate well with the revised regional deformation history (Blewett et al., 2008b). No geochronology is available from the Paddington deposit to confirm this and the correlation is made on common sequence, style and relationship to alteration and mineralisation.

pD1 occurred during intense east-northeast – west-southwest directed contraction that tilted the Kambalda and Kalgoorlie sequence stratigraphy to sub-vertical attitudes. The S-C fabrics and steep pitches of lineations on shear planes suggests that σ3 was vertical and that shear zones accommodated reverse kinematics and tectonic mode. Regionally this event has been described as D4a (or 'D2' in the Swager, 1997 framework), which occurred between 2655 Ma and 2650 Ma and after the post-volcanic late basins. Gold deposition also occurred at this time across the Eastern Goldfields Superterrane (e.g., at St Ives: Nguyen, 1997, and Wallaby and Sunrise Dam: Miller, 2006). The location of the Paddington area in the narrow high-strain Bardoc Tectonic Zone has precluded the elucidation of any earlier structural events in this corridor.

The second deformation (pD2) involved north-northwest-south-southeast oriented contraction. Regionally, this represents an unusual direction for the orientation of σ1 occurred during the D4b event, which occurred at around 2650 Ma (Blewett et al., 2008b). D4b was typified by northwest-directed thrusting and folding, together with sinistral strike-slip shearing along the main north-northwest-trending structural grain. The main north-northwest-trending structural grain does not appear to have been reactivated, and the D4b strain was taken up by minor folding and reverse faulting. Morey et al. (2007) described these structures as barren, however, elsewhere in the region D4b was significant in terms of gold deposition (e.g., Kanowna Belle, St Ives, and Golden Mile).

The third deformation (pD3) involved northeast-southwest contraction and the development of NNE-trending dextral-normal faults. These structures likely correlate with the regional D5 dextral strike-slip event, which occurred around 2640 Ma (Blewett et al., 2008b). Morey et al. (2007) described these structures as barren, however, elsewhere in the region D5 was significant in terms of formation of gold (e.g., Kanowna Belle, St Ives, Mulgarrie, and Mt Charlotte).

## 3.11.4.2 Kanowna Belle

Kanowna Belle is located on the southeast hinge of the regional Scotia-Kanowna Dome (Figure 3.11.1), and is the largest deposit in the camp. Much of the current understanding of the structural architecture of the world-class Kanowna Belle is a product of early work by Archibald (1993), Aaltonen (1997), Davis (1998, 1999) and Davis et al. (2000). Kanowna Belle is hosted by sedimentary volcaniclastic and conglomeratic rocks that are intruded by a Mafic-type porphyry. The youngest host rocks of the Kanowna Belle mine have a U-Pb detrital zircon maximum depositional age of 2656 Ma (Squire, unpublished data), so all penetrative deformation recorded in the open pit is younger than this age.

The main hangingwall and footwall sequences are separated by a major, steeply (60°) south-southeast-dipping zone of structural disruption termed the 'Fitzroy Structure' (Figure 3.11.4), which has accommodated several stages of reverse movement. The steep dip of the structure and associated stratigraphy suggests that most of the reverse movement had occurred prior to being tilted into this present day steep attitude. The 'Fitzroy Structure' has an arcuate geometry and thus appears to be parallel to the geometry of the main Scotia-Kanowna Dome, and to the east and northeast it swings continuously into shear zones that 'mantle' the dome. However, at the western margin of the open pit, these structures are cross cut by the Terminator Fault, and also by an unconformity of the late post-volcanic Panglo Basin (Barrick unpublished

maps). The 'Fitzroy Structure' represents the product of at least three temporally distinct stages of deformation, comprising the Fitzroy Mylonite, the Fitzroy Shear Zone and the Fitzroy Fault (Archibald, 1993; Davis, et al., 2000), which have produced clear structural overprinting relations (Figure 3.11.5). To the north of this structure, the mine sequence stratigraphy dips steeply southwest and northeast at a high angle to the structure. To the south, the stratigraphy dips and youngs south-southeast parallel to the structure.

The 'Fitzroy Structure' has also localised the emplacement of the 2649±4 Ma Kanowna Belle porphyry (Ross et al., 2004), which hosts at least 70% of known mineralisation. Localisation of the highest grade mineralisation and most intense alteration around the composite structure emphasises its importance for acting as the major plumbing system for auriferous fluids (Figure 3.11.4). The porphyry has an enriched chemistry consistent with being classified as Mafic-type and derived from a water-rich metasomatised mantle source (Champion and Sheraton, 1997).

## Structure

The Kanowna Belle area has traditionally been viewed as a classic area demonstrating 'D1' south-over-north thrusting and duplex development (Archibald, 1993; Swager, 1997; Davis, 1999a; Rodgers et al., 2004), with the Fitzroy Mylonite and Fitzroy Shear Zone being the main faults. This phase of deformation was then thought to have been overprinted by 'D2' faults, folds and foliation following a switch in far-field stress axes to the approximately east-northeast – west-southwest. Most mineralisation was emplaced late in this so-called 'D2' event.

A reinterpretation of the deformation history is presented below. Each event is described according to the local (Kanowna Belle) sequence, and is prefixed by the letters KB for clarity.

### KBD1

The stratigraphy of the Kanowna Belle mine and environs includes sequences with maximum depositional ages around 2668±9 Ma (Golden Valley Conglomerate), and 2667±10 Ma (Grave Dam Grit), with the youngest

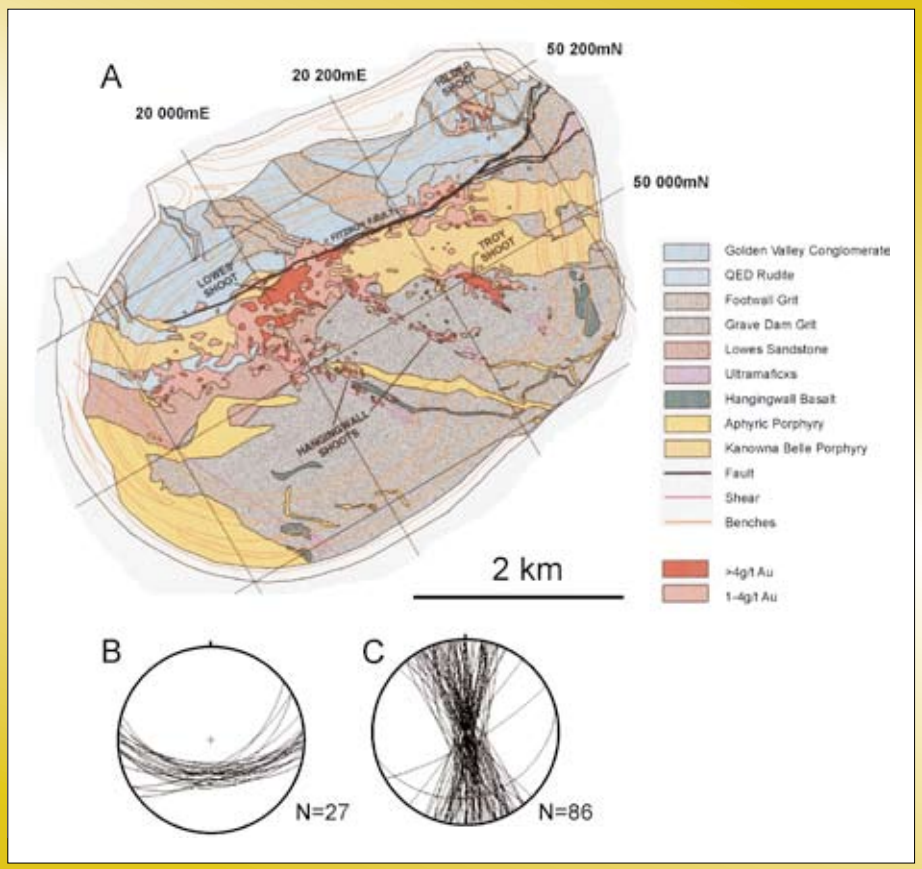


*Figure 3.11.4: a) Geology of the Kanowna Belle pit. Structural architecture is dominated by the Fitzroy Structure, which strikes 070° and has a steep southerly dip. Note that lithology strikes approximately parallel to the Fitzroy Structure on the south of the fault, but has a north-west/south-east orientation subparallel to regional S2a on the northern footwall side. The Fitzroy Structure initiated during D4b (or earlier at D3?) and is the product of several overprinting events. Note that mineralisation is constrained dominantly within the Kanowna Belle Porphyry, which follows the orientation of the Fitzroy Structure. The Troy Shoot is controlled by several suites of D5 faults. b) Stereonet of planes of D4b shears. c) Stereonet of planes of main S5 penetrative foliation.*

*Figure 3.11.5: Flow diagram showing sequential structural evolution of the Fitzroy Structure in the Kanowna Belle deposit.*

*a) Development of the east-west striking, steeply south-dipping Fitzroy Mylonite due to south-over-north thrusting. A mylonitic lineation pitches subvertically in the mylonitic foliation. The mylonite is very fine-grained with the exception of porphyroclasts up to a centimetre in diameter. The figure shows overall block movements at the deposit-scale, the proposed representative width of the Fitzroy Mylonite (shown relative to development), and a schematic representation of the microtextures produced.*

*b) Coplanar overprinting of the Fitzroy Mylonite by the Fitzroy Shear, which effectively destroys much of the original mylonitic texture. Movement is also south-over-north and a similarly-oriented steeply pitching lineation was produced. Although this stage of deformation is coplanar with that of the Fitzroy Mylonite, deformation conditions seem to have been somewhat different. Strain was relatively less (or strain rate was lower), resulting in the formation of coarsely partitioned ductile and locally brittle-ductile S4b foliations. Strain was more widely distributed also, as attested by the much greater width of the Fitzroy Shear relative to the Fitzroy Mylonite. Some strain and volume compensation was accommodated by the formation of subparallel splays, such as the Flynn Fault, which ramp off the main shear zone.*

*c) The Fitzroy Shear has localised emplacement of the tabular Kanowna Belle Porphyry, which occurred in the early stages of regional D5. The orientation of the Fitzroy Shear relative to the D5 principal stress caused sinistral reactivation of this structure, resulting in brecciation of the Kanowna Belle Porphyry. Existing shear fabrics were both re-used and sigmoidally folded to reflect the bulk movement sense due to shear reactivation, which was sinistral based on the development of shallow lineations. Ongoing deformation became progressively more brittle, with formation of discrete subparallel shears and faults that locally cross-cut the brittle-ductile shear fabrics. Extensional stresses were localised at the intersection between the Fitzroy Shear and hangingwall ramps (and footwall structures?) resulting in emplacement of carbonate breccias. Telluride mineralisation overprinted these and was in turn overprinted by the main phase of gold-pyrite stringer mineralisation.*

*d) Emplacement of the Fitzroy Fault (+ pug zone) that cross-cuts all other structures and potentially resulted in a hangingwall block-up movement at the deposit scale.*

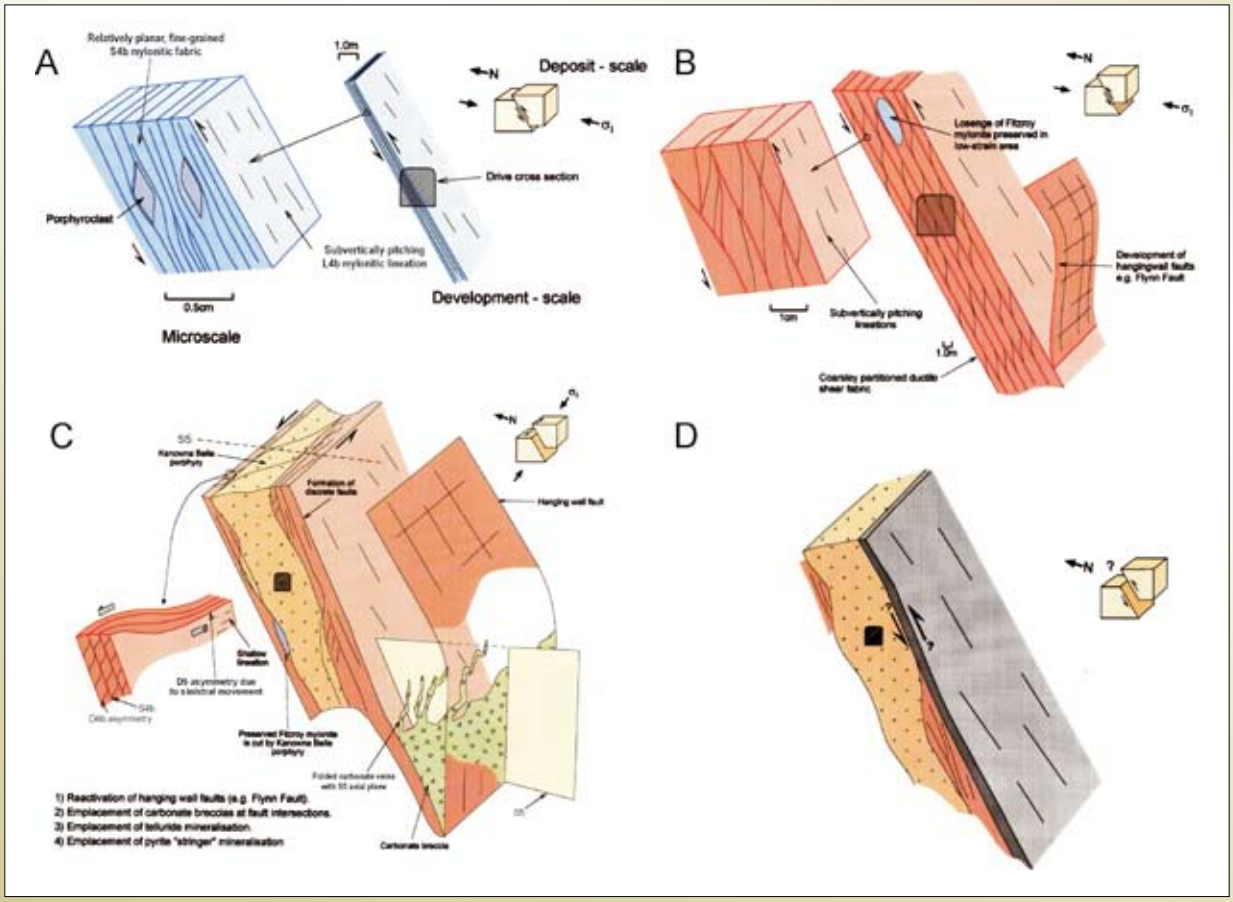

sequence, the Ballarat Turbidite, being deposited after 2656 Ma (Tripp et al., 2007). Accordingly, all penetrative structures in the mine sequence and nearby have to be younger than the youngest depositional age. The map patterns reveal an angular relationship (~90°) of stratigraphy north (footwall) of the east-northeast-trending 'Fitzroy Structure'. This angular discordance indicates that the footwall stratigraphy was tilted (folded) about a north-northwest-south-southeast axis during KBD1, before the main thrusting and development of penetrative foliations and structural disruption (Figure 3.11.5).

### KBD2

The oldest penetrative fabrics in the mine and region is recorded in pods or lozenges of high-strain Fitzroy Mylonite (Davis et al., 2000) preserved in later lower strain thrust fabrics (Figure 3.11.5). These fabrics are preserved in rocks that are younger than 2656 ± 10 Ma (Squire and Cas, 2006), providing a maximum age for this event. Kinematic indicators reveal that this first stage of foliation development involved southeast-over-northwest thrusting. The mylonite comprises a planar fine-grained foliation that dips steeply south and hosts a stretching lineation that plunges down-dip (Figure 3.11.5). Asymmetric porphyroclasts and S-C relationships indicate that movement was reverse, top to the north (Davis et al., 2000).

A second stage of ductile shearing produced the Fitzroy Shear Zone (Archibald, 1993; Davis et al., 2000), which anastomoses around, and is co-planar with, the earlier high-strain Fitzroy Mylonite (Figure 3.11.5). The Fitzroy Shear Zone is a broad zone up to 2 m wide comprising coarsely partitioned ductile S-C fabrics and brittle-ductile shears. The foliations are intimately associated with recumbent folds, thrusts and shears, and are patchily developed away from these structures (Archibald, 1993). A steep down-dip plunging stretching lineation is developed (Figure 3.11.5). Steeper faults represent splays into the hangingwall from the sole thrust (e.g., Flynn Fault). All kinematic indicators suggest continued reverse movements.

The Kanowna Belle porphyry cross-cuts high-strain fabrics associated with the Fitzroy Mylonite and the Fitzroy Shear, providing a minimum age constraint on the reverse movements. However, the porphyry has also been deformed into a series of KBF2 fault propagation folds on the hangingwall of the structure in the upper portion of the mine. Progressive KBD2 deformation therefore occurred before, during, and after the emplacement of the 2649±4 Ma Kanowna Belle porphyry (age from Ross et al., 2004) when σ1 was oriented approximately northwest-southeast.

Minor gold mineralisation is interpreted to have been deposited during the KBD2 event (Archibald, 1993), which produced structures typified by carbonate ± sericite ± tourmaline ± fuchsite alteration. The initiation of the northwest-southeast trending structures that host the Troy shoots may have also initiated at this time. These would likely have developed due to their favourable orientation for dilation in a northeast-southwest direction, perpendicular to KBD2 maximum shortening.

The generalised distribution of gold mineralisation in Kanowna Belle is one of a tabular zone centred about the Fitzroy Fault that dips approximately 60 degrees to the south-southeast (Rodgers et al., 2004). Internally, the dip of the general tabular shape of the ore envelope parallels the plunge of several lineaments that are visible on the long section and is linked to the intersection of various structures with the Fitzroy Shear zone. The ore body is sited east of the flexure point in the Fitzroy shear zone where the strike changes from east to east-northeast on the regional map (east-southeast to east on the mine grid). The flexural hinge line on the Fitzroy shear zone defines the western boundary to the ore body and plunges steeply to the east (Figure 3.11.4). The inference is that the ore body occupies a dilational position on the Fitzroy shear zone, produced during sinistral-reverse fault movement at the time of KBD2.

### KBD3

The mine sequence, together with the Kanowna Belle Porphyry, has been overprinted by a pervasive north-northwest- to northwest-trending flattening foliation (KBS3). The inferred maximum shortening direction rotated anticlockwise to a northeast-southwest orientation with the onset of this third event.

Strain accumulation during KBD3 caused the competent Kanowna Belle porphyry to undergo brittle-ductile sinistral shearing failure about the earlier KBD2 architecture. The result was the emplacement of carbonate breccias

(Figure 3.11.6a), carbonate vein stockworks, siliceous breccias, silica-carbonate-pyrite-sericite veinlets ('stringers') and sheeted vein arrays, all of which host mineralisation. The sinistral strike-slip reactivation of the Fitzroy Shear Zone, the brecciation of the Kanowna Belle porphyry, and the emplacement of mineralisation are all interpreted to have occurred synchronous with formation of KBD3.

A vein paragenetic history comprising eight temporally distinct stages has been resolved (Aaltonen, 1997), with two temporally, mineralogically and spatially distinct styles of mineralisation corresponding to stages 3 and 4 of the vein emplacement history. The first, volumetrically minor, stage of mineralisation is represented by a telluride-associated mineralogy and is restricted to crustiform carbonate (±quartz) veins and breccias in the vicinity of the Fitzroy Shear Zone. Telluride-gold mineralisation occurs as microfracture and microvug infill that overprints these. Free gold occurs in association with altaite, coloradoite and melonite with rare hessite. No gold tellurides have been noted. Veins show structural overprinting relationships consistent with emplacement synchronous with regional northeast-southwest contraction where the E-W Fitzroy Fault moved with a sinistral-reverse sense of movement.

The second stage of gold emplacement comprises the bulk of economic mineralisation and overprints the telluride-associated stage. It represents a telluride-absent mineralisation phase that displays a strong KBD3 control on lode geometry (Figure 3.11.5). Gold occurs within silica-carbonate-pyrite-sericite 'stringers', which comprise stockwork geometries in close proximity to the Fitzroy Shear Zone, but become more regularly aligned with the regional north-northwest trending strike away from the shear zone. Alteration assemblages associated with this stage include albite-sericite-carbonate-chlorite-haematite.

Pyrite varies in inclusion content from inclusion-rich to inclusion-poor. Generally, inclusion-poor pyrite occurs as intensely growth-zoned rims on inclusion-rich cores, with growth zoning tentatively correlated to arsenic content of the fluid from which pyrite was derived. Microtextural relationships indicate emplacement of both inclusion-poor and inclusion-rich pyrite forms to be controlled by, and to have been emplaced during, northeast-southwest contraction. Gold occupies KBD3 extensional sites adjacent to pyrite crystals (Figure 3.11.6b) and occurs as fracture infill of deformed KBD3 pyrite. Consequently, deposit-scale, development-scale and microscale relationships are all consistent with an interpretation of Kanowna Belle as a major gold deposit formed during regional northeast-southwest shortening (KBD3) as a result of reactivation of a major KBD2 structure.

### KBD4

The Fitzroy Fault in the Kanowna Belle deposit is a late brittle fault represented by a 10–20 cm wide zone of cataclastic material (pug zone) that post-dates all other structures. Archibald (1993) described both normal and reverse movement at this stage (Figure 3.11.5).

## Regional correlation

In the region, the first event following, and inverting, the late basin sequences was a contraction oriented east-northeast – west-southwest and called D4a (Blewett et al., 2008b). The KBD1 event may equate to this regional event (Table 3.11.4). The formation of late basin sequences in the region is inferred to have occurred between 2665 and 2655 Ma and associated with D3 extension (Czarnota et al., 2007; Blewett et al., 2008b).

Regionally, the D4b sinistral transpressional event occurred at around 2650 Ma (Blewett et al., 2008b), and was associated with thrusting with both top to the northwest and southeast movements across restraining bends about the noses of domes (see also Miller, 2006 and Henson et al., 2006). The KBD2 thrusting observed at KB is of this age, style, and metamorphic grade, and is therefore likely the local manifestation of this regional event.

The KBD3 veins show structural overprinting relationships consistent with emplacement synchronous with regional northeast-southwest contraction. Telluride mineralisation is commonly associated with the regional D5 deformation event throughout the EGST (Blewett et al., 2008b). At Kanowna Belle the main gold mineralisation was associated with two discrete 'stages' (telluride present and telluride absent) of northeast-southwest contraction. Regionally the D5 event was long lived (2645–2630 Ma) and operated in a number of stages (Blewett et al., 2008b). At Mulgarrie to the northeast of Kanowna Belle (Figure 3.11.1) two stages of gold mineralisation also occur. Both are associated with two stages of northeast-southwest contraction (Davis, et al., 2003).

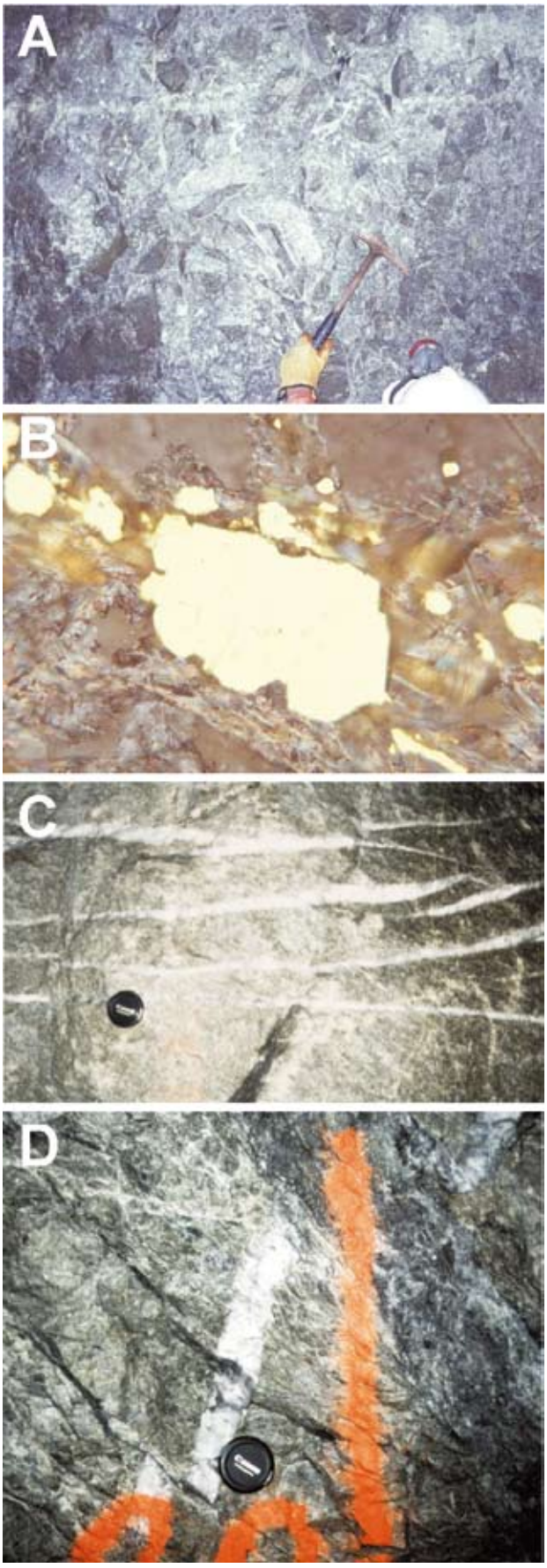


*Figure 3.1 1.6: a) Breccia at Kanowna Belle underground. b) Reflected light photomicrograph of free gold in phyllosilicate-rich matrix adjacent to pyrite grains and as inclusions within pyrite from the Troy Shoot. The large gold grain in the matrix is located within a site of low mean stress and shows a preferred elongation subparallel to the phyllosilicate grains, the long axes of which define the S5 fabric. Sample from the bottom of the Troy open pit. Long edge of photo is 0.4 mm. c) Late-stage subhorizontal quartz veins from Kanowna Belle underground that cut all structures except the 'pug' zone of the Fitzroy Structure.*

*d) Fitzroy Fault (late-stage) showing normal offset on some earlier veins. Shear sense indicators in the cataclasite suggest reverse movements.*

### 3.11.4.3 Ballarat-Last Chance

The Ballarat-Last Chance (BLC) deposit lies within the Kanowna Goldfield on the hinge of the regional Scotia-Kanowna Dome, approximately 3 km northeast of the Kanowna Belle mine. The Last Chance Shear is a major ~east-west trending structural dislocation in the northwestern portion of the pit, and exerted a major influence on the distribution of stratigraphy and mineralisation (Figure 3.11.7). The host lithologies consist of ultramafic, mafic to felsic grits, conglomerate, together with siltstone and sandstone (Truelove et al., 1997). Felsic tuff comprising volcaniclastic sandstone is a minor contributor. These rocks likely represent the upper parts of the Kalgoorlie sequence (Krapež et al., 2000), which are as young as 2665 Ma. As the exhumation and erosion level progressively deepened through time, late basin sequences in general evolved from mafic-ultramafic through to felsic (granite) dominated in the composition of the clasts. Therefore the dominance of mafic and ultramafic components in the conglomerate suggest that if the sequence was part of a late-stage basin (and not the Kalgoorlie Sequence) then it would likely be part of the earliest stage (and >2660 Ma).

A suite of east-west trending felsic intrusive rocks suggests exploitation of similarly oriented structures during emplacement. The observed movement on the Last Chance Shear and sub-parallel structures is interpreted to have been sinistral (Davis, 1999a). Termination of the Last Chance Shear occurs at the eastern end of the deposit on a northwest-southeast trending zone of distributed deformation, the Isabella Trend. The Ballarat Trend is a north-south trending, steeply dipping dextral shear at the western end of the pit (Figure 3.11.7).

#### Structure and mineralisation

Two main stages of deformation are recorded at the BLC deposit, and these structures are likely to be <2660 Ma due to the age of the host rocks. The first deformation (BLCD1) was associated with the formation of the east-west trending Last Chance Shear and the second deformation (BLCD2) was associated with regional northeast-southwest oriented contraction and sinistral strike-slip faulting (on east-west oriented pre-existing structures).

#### BLCD1

The Last Chance Shear existed prior to the BLCD2 overprint and so its formation is ascribed to BLCD1. On regional considerations, Davis (1999a) tentatively suggested that the structure developed during northwest-directed thrusting. Such a deformation would be analogous to the Fitzroy Shear Zone at the nearby Kanowna Belle mine. Davis (1999a) noted that the Last Chance Shear controlled the emplacement of felsic intrusions, the inference being it developed during localised(?) north-south extension. The shear thins in the upper levels of the open pit from several metres to around a few 10's of centimetres.

#### BLCD2

A subvertical northwest-southeast trending penetrative foliation is developed in all lithologies, records northeast-southwest directed contraction, and it provides an event marker across the pit. Most of the mineralisation has been localised in BLCD2 brittle and ductile structures that intersect the Last Chance Shear and which have approximately northwest-southeast strikes. Both the east-west structures and the northwest-southeast structures are steeply dipping. The Last Chance Shear has well developed kinematic indicators that imply sinistral strike-slip deformation during BLCD2 (Figure 3.11.8).

Relatively higher grades of mineralisation are located and predicted to occur where structures with opposing shear senses intersect and localise extension/dilation. Northeast-southwest trending dextral structures are important in this regard, as is the north-south trending Ballarat Trend, which has also accommodated a dextral sense of movement. The highest grade occurred in the northwest portion of the deposit (termed the 'Old Pit') at the intersection of three major structures; the Last Chance Shear, the Ballarat Trend, and a previously unidentified northwest-southeast trending structure. Interaction of these three structures is interpreted to have maximised dilation, fluid flow and mineralisation (Figure 3.11.7).

Late flat-lying quartz veins host significant gold mineralisation and become economically important when they are closely spaced, as in the northeast corner of the deposit (Figures 8a, b). Well developed crack-seal textures are evident in the shallow veins due to incremental extension.

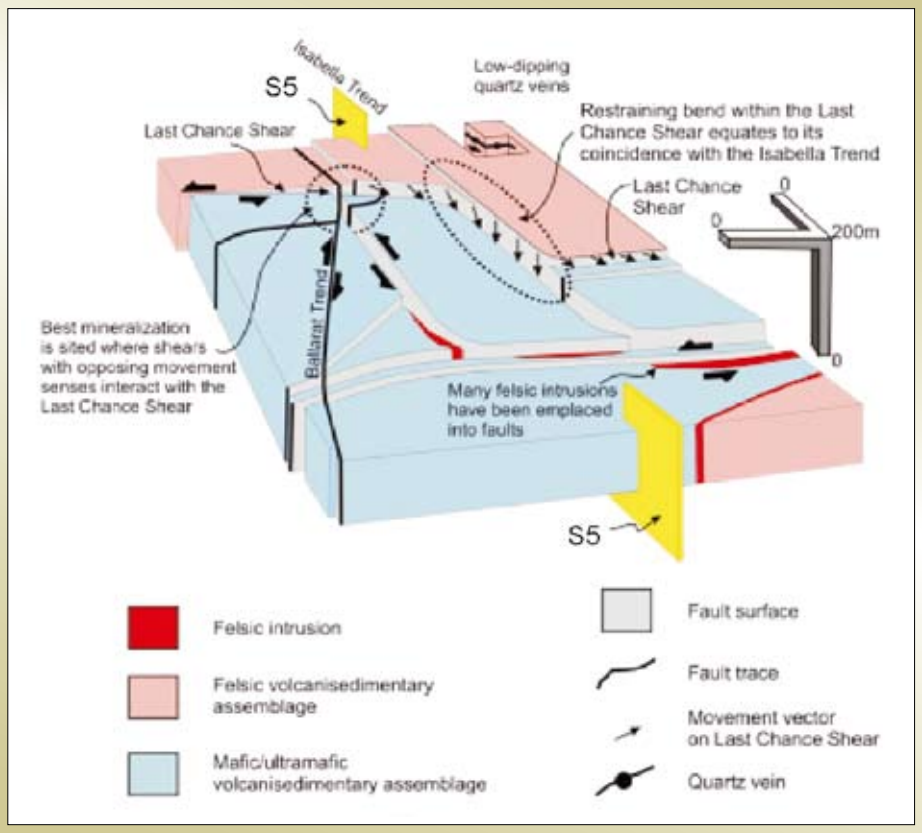


*Figure 3.11.7: Schematic block diagram of the Ballarat-Last Chance gold deposit and controlling effect of the porphyry body on the structures and sites of gold deposition.*

The centre of the deposit is dominated by a mafic-hosted stockwork comprising quartz±carbonate±sulphide (pyrite) veining, which represents a zone of repeated brecciation and fluid inflow. Grades within the stockwork are low, suggesting broad-scale distribution and deposition of the mineralising fluids, and that mineralising fluids occurred as very discrete pulses that may not have been tapped during the main phase(s) of stockwork development. Vein orientations within the stockwork have been controlled by BLCS2 and emplaced synchronously with formation of this fabric. Pre- BLCD2 pyrite (diagentic?) is evident within silicified pyritic shale units that have been brecciated during BLCD2.

A post-D2 stockwork is developed in the western wall of the deposit. Veins comprising the stockwork are typically quartz, with carbonate being a minor contributor. The BLCS2 is well developed in adjacent country rocks but has been destroyed by brecciation and alteration during stockwork formation.

## Summary

The overall architecture of the BLC deposit is that of an E-W trending contractional sinistral strike-slip system. Strike-slip movement has been sponsored by the east-west trending Last Chance Shear and subparallel structures, with major northwest-southeast structures such as the Isabella Trend representing contractional zones that have terminated the strike-slip motion by accommodating displacement into a dip-slip component. The Isabella Trend represents a confining (antidilational) right-hand bend within the system, and is marked by low grade mineralisation in this region. The gently-dipping veins (Figures 8) developed in response to vertical extension during ongoing BLCD2 northeast-southwest contraction.

The majority of structures have accommodated sinistral movements but the Ballarat Trend was in an orientation (north-south) favourable for accommodating dextral shear. The interaction of sinistral shear on the Last Chance Shear, sinistral shear on the major BLCD2-parallel structures, and dextral shear on the Ballarat Trend have maximised gaping in the western end of the Old Pit (Figure 3.11.7).

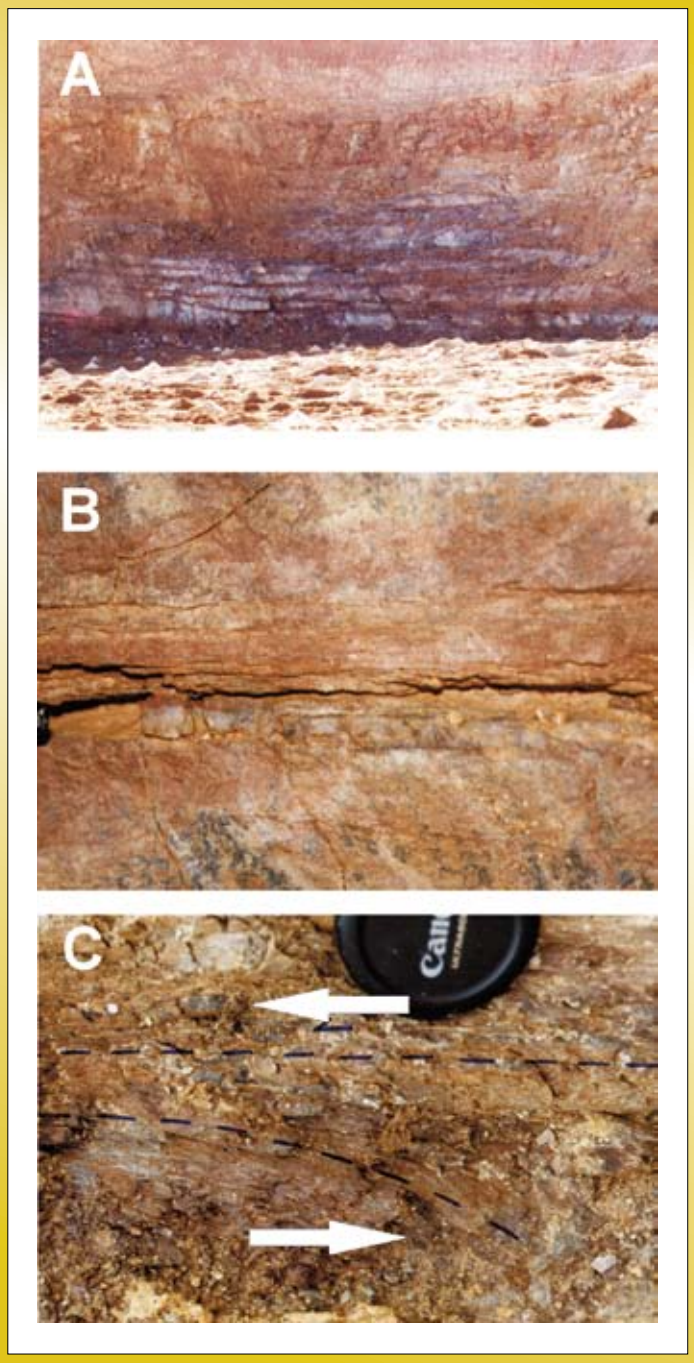


*Figure 3.11.8:*
*a) Subhorizontal quartz veins in the northeast cut-back (looking east) of the BLC pit.*
*b) Shear laminations parallel to the margins of subhorizontal quartz vein from the northeast end of the BLC pit.*
*c) Asymmetric shear fabrics indicative of sinistral reworking of the Last Chance Shear during D5 contraction.*

## Regional correlation

The main gold event was synchronous with the BLCD2 contraction. This northeast-southwest shortening was imposed on a complex architecture that developed during the earlier BLCD1 event. The east-west trending Last Chance Shear is inferred to have developed during northwest-southeast thrusting (Davis, 1999a). Regionally, BLCD1 (like the KBD2 event noted to the west) is linked to ~2650 Ma northwest-directed D4b thrusting that was common across dome noses or hinges (e.g., also at St Ives and Laverton) during sinistral transpression (Blewett et al., 2008b).

The contractional vector of northeast-southwest and the presence of both sinistral (E-W) faults and dextral (north-south) faults suggest that deformation at BLC was the regional D5 (Blewett et al., 2008b). The age of this mineralisation would likely be around 2640 Ma.

### 3.11.4.4 Red Hill

Red Hill was a quartz vein-hosted deposit located within the Red Hill porphyry approximately 500 m north of the abandoned Kanowna townsite, on the hinge of the regional Scotia-Kanowna Dome (Figure 3.11.1). The Red Hill porphyry hosted the mineralisation and is a quartz albite or dacititc boss that is 1500 m long and 250 m wide, with numerous radiating dykes of similar composition (Smith, 1997). Three phases of porphyry have been noted, and all are compositionally similar (Mafic-type) to the nearby Kanowna Belle porphyry (Taylor et al., 1997). Country rocks to the north, south and east are mafic and ultramafic conglomerates of the Kanowna Conglomerate, whereas those to the west comprise the tuffaceous lithic grits and mafic conglomerates (Davis, 2003). The Kanowna Conglomerate has not been dated, but it conformably overlies the Ballarat Turbidite which has a maximum depositional age of 2656 ± 10 Ma (Squire and Cas, 2006). All deformation and porphyry intrusions in this pit are therefore younger than this age.

#### Structure and mineralisation

There is a pronounced rheological control on mineralisation, with the gently dipping veins confined to the coarser phases of the porphyry body (Figure 3.11.9). Vein margins are typically albite-carbonate and pyrite and alteration haloes are up to 1 m wide but commonly overlap due to the proximity of individual veins. Mineralisation occurs as coarse free gold in quartz veins with minor gold associated with a pyritic alteration selvedge.

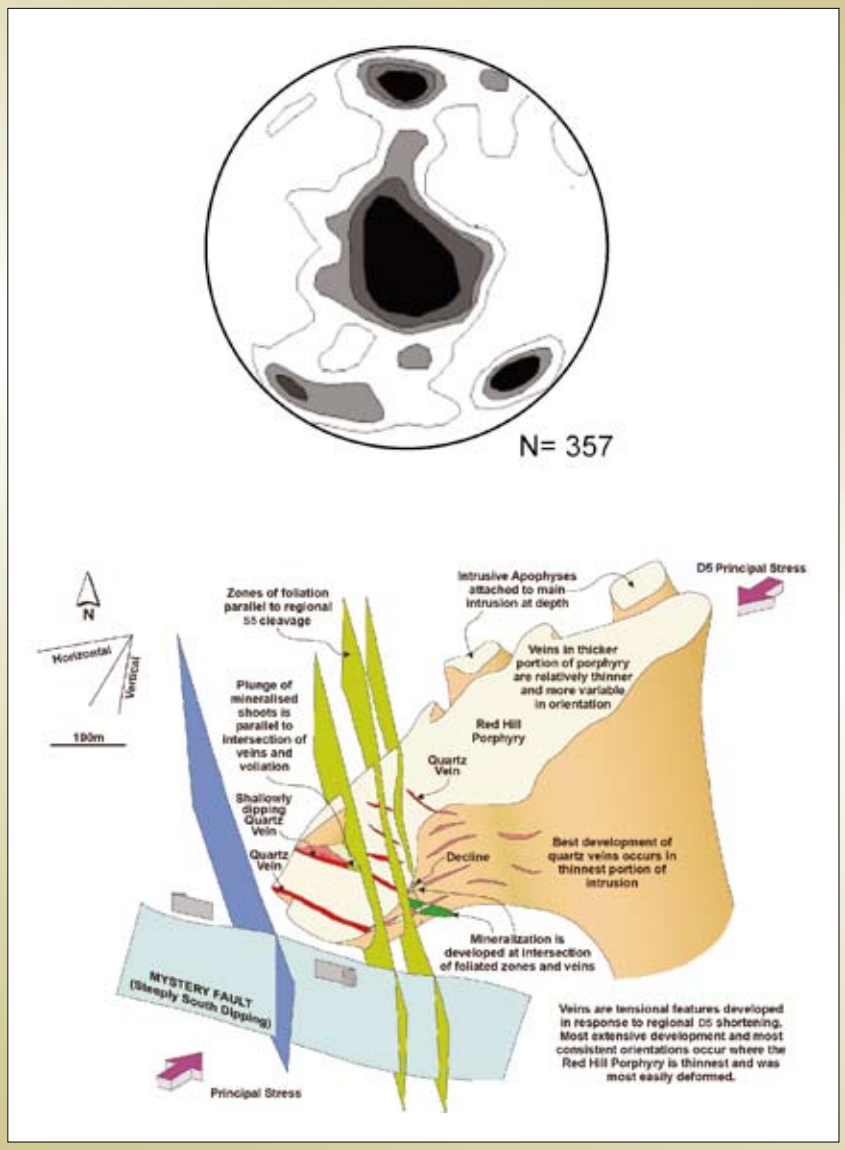


*Figure 3.11.9: Mineralisation at Red Hill is associated with quartz veins that are overwhelmingly flat-lying. Block diagram illustrating the structural relationships controlling gold at Red Hill. Most of the mineralisation occurs at the thin sections of the porphyry and where intense steep (north-northwest) foliation zones transect the boss.*

On a gross scale all mineralisation was hosted within two broad zones, which plunged at a low angle to the northeast. These zones were of the order of 80 m vertical and 150 m wide and show continuity down plunge of >200 m, with average grades of 1.6 to 1.8 g/t. They were separated by about 30 m of material, which ran at background grades of 0.3 to 0.5 g/t. Around 25% of the contained gold graded at 0.3 g/t and was hosted in the altered rock mass. Visible free gold up to 0.2mm in diameter has been observed in carbonate-sericite altered porphyry.

Taylor et al. (1997) and Davis (2003) described two stages of deformation and associated gold mineralisation.

### RHD1

The first stage occurred with early quartz-carbonate-pyrite veins, which are deformed, thin and discontinuous and generally dip moderately to the southeast, and are of variable thickness (5–30 cm, but up to 50 cm). These quartz veins are overwhelmingly gently dipping extension veins, with two subordinate sets having been interpreted (Smith, 1997). The two later sets comprised the Melba Reef and Mystery structures, which were orthogonal, dipping 20° to the northeast and 60° to the southwest respectively, inferring a northeast-southwest oriented σ1 (Figure 3.11.9). Associated with the approximately northeast-southwest contraction is a steep to southwest-dipping penetrative RHS1 cleavage. Three sub-vertical zones of RHS1 foliation that strike north-northwest–south-southeast are associated with the mineralisation, and these likely acted as fluid pathways focusing deep mineralised fluids that controlled both stages of gold.

About 15% of the contained gold is hosted in veins and structures of this RHD1 stage, and include quartz-carbonate and quartz-carbonate-pyrite veins. These veins are in the order of mm to several centimetres wide, and commonly occur in swarms less than 30 m in length, and have highly variable grades. Visible free gold on mm scale is occasionally observed within, or proximal, to them.

### RHD2

The second stage of gold mineralisation involved the emplacement of numerous, thin 1 cm to 20 cm thick, gently dipping quartz veins that occasionally contained coarse, visible gold grains to 1 to 2 cm diameter. The veins occured as low dipping north and northeast striking (up to 60 metres long), parallel quartz vein sets and were associated with a gently (north and south) dipping anastomosing RHS2, associated with top-to-the-north shear (Taylor et al., 1997). The veins were undeformed and crosscut the earlier RHD1 vein sets and the penetrative RHS1 foliation.

The bulk (~60%) of the contained gold at Red Hill Gold was hosted in these late-stage planar, shallowly dipping quartz veins. The quartz veins were highly variable in grade (e.g., between 1–200 g/t), with the better grades proximal to the cross cutting penetrative northwest-southeast trending foliation. These veins occur on a scale of mm to several metres wide, with the wider veins being the focus of historical underground mining. Visible free gold (up to 1 cm in size) was commonly observed and was closely associated with galena and sphalerite (Taylor et al., 1997).

## Regional correlation

The Kanowna Conglomerate (<2656±10 Ma) was deposited during regional D3 extension and was intruded by the Red Hill Porphyry. The Red Hill Porphyry is of the same chemical clan as the Kanowna Belle Porphyry (2649±5 Ma). Clasts of Mafic-type porphyry occur in the sediments, indicating a rapid exhumation of the source region, deposition and burial of the basin, and intrusion by Mafic-type porphyries within temporal error of each other. All penetrative structures and mineralisation at Red Hill is therefore younger than D3.

The Red Hill Porphyry strikes east-northeast (Figure 3.11.9), suggesting that extension and emplacement occurred in a north-northwest-south-southeast direction, perpendicular to maximum shortening of the regional D4a (Blewett et al., 2008b). The penetrative RHS1 and gentle northeast- and southwest-dipping quartz veins are part of this regional event.

The late-stage RHD2 quartz veining (main) occurred together with a gently dipping anastomosing RHS2 foliation was likely developed with top-to-the-north shear associated with regional D4b thrusting. This is main gold event at Red Hill and initiation of gold deposition at Kanowna Belle.

### 3.11.4.5 Gordon-Sirdar area

The Gordon-Sirdar area is located on the eastern margin of the Scotia-Kanowna Dome ~18 km northeast of the Kanowna Belle mine (Figure 3.11.1). The Gordon-Sirdar mine is hosted by sheared felsic and mafic-intermediate conglomerate and fragmental sequence (of the Kalgoorlie sequence) adjacent to a quartz-phenocryst felsic intrusion to the east. The main structure in the region is the northwest-southeast trending steeply dipping Sirdar Shear Zone, which is greater than 500 m wide through the area (Roberts et al., 2005).

Gold mineralisation in the Gordon-Sirdar mine is hosted in an intensely deformed mafic-intermediate fragmental sequence. The main mineralisation and associated alteration assemblage consists of quartz-carbonate-fuchsite that is concentrated into discontinuous elongate pods that are parallel to the main shear foliation in the pit. These pods plunge steeply and coalesce at depth into two main ore zones. The highest grades of mineralisation occur in fuchsite-altered fragmental zones close to the contact with the felsic intrusion. Gold occurs as both free grains and enclosed in pyrite. This deposit has a high silver-gold ratio, but the gold does not occur in direct association with the silver. Roberts et al. (2005) have recently suggested that the mineralisation at Gordon-Sirdar pre-dated contractional deformation and may have been volcanogenic in origin, but this is highly unlikely given its locus in a high-strain zone, which is a similar setting to the other epigenetic deposits around the dome. Similarly, historic workings (typically shafts) define a northerly trend along a zone of high strain to the north of the mine.

#### Structure and mineralisation

Deformation produced an intense GSS1 shear foliation and mylonite (Figure 3.11.10). The strike of the shear zone and the intense foliation that comprise it are parallel to the regional northwest-southeast strike and eastern margin of the Scotia-Kanowna Anticline. Structural analysis has determined that there is essentially only one contractional deformation event (GSD1) in this area, although earlier events may have been transposed due to high strain.

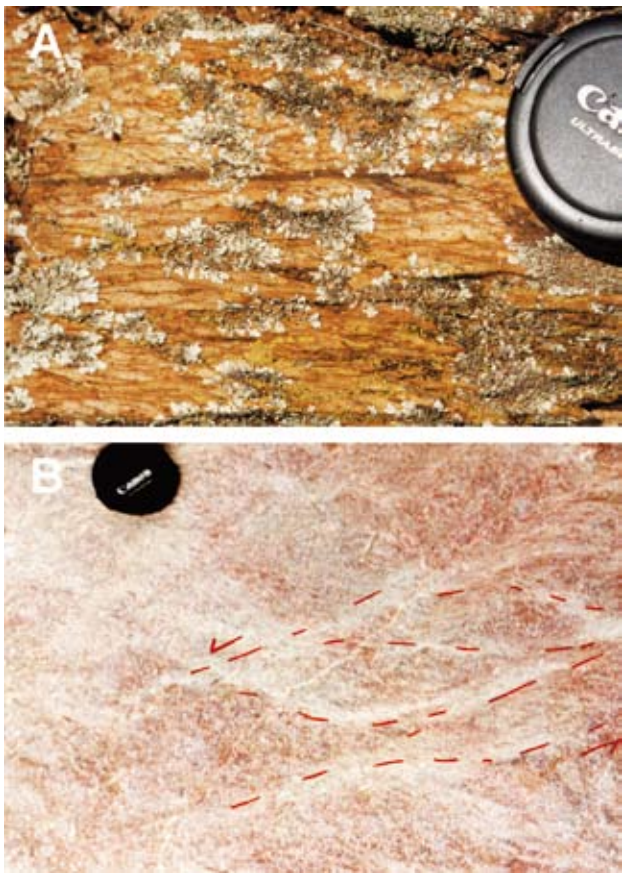


*Figure 3.11.10: a) Sinistral S-C mylonite developed in felsic rocks close to Gordons-Sirdar pit. b) Sinistral S-C relationships developed during D4b deformation in the Gordons-Sirdar pit.*

Kinematic indicators are rare, but where developed show that movement was sinistral oblique slip (east-block up). Locally within the eastern felsic unit, the mylonite has well-developed GSS1 S-C fabrics (Figure 3.11.10), and the lineation plunges to the southeast. The inferred sinistral motion is also supported by deflection of the regional stratigraphy into the Sirdar Shear Zone.

Pyritic veins lie at a slight angle to and cut the main GSS1 mylonitic foliation. These veins are also openly folded with an axial plane parallel to the shear fabric. Fibrous quartz crystals, quartz beards on pyrite and crack-seal veins indicate ongoing deformation during mineralisation and after pyrite deposition.

### Regional correlation

The northwest-southeast strike of the GSD1 Sirdar Shear Zone and GSS1 mylonitic fabrics has been typically correlated with 'D2' of Swager (1997). The sinistral oblique (reverse-flattening) kinematics of the shear zone likely developed during east-southeast-west-northwest oriented contraction. Regionally, contraction of this orientation has been interpreted as the D4b event (Blewett et al., 2008b).

The Sirdar Shear Zone was likely an accommodation structure that operated synchronously with the top-to-the-northwest thrusting on the dome hinge (e.g., Kanowna Belle). The position of Gordon-Sirdar was favourable to a strike-slip tectonic mode with a component of flattening as it was located on the eastern margin of the Scotia-Kanowna Dome.

## 3.11.4.6 Mulgarrie

The Mulgarrie deposit is located on the eastern limb of the Scotia-Kanowna Dome, in the rollover of a large-scale multiphase southwest-vergent thrust structure. The deposit is therefore not strongly influenced by the strike changes on major structures. Several northwest-southeast trending structural corridors comprise the deposit architecture and are, from west to east: 1) a high Mg basalt representing the footwall to the thrust 2) a suite of faults that have accommodated an E-side-up sense of movement and which represent the thrust fault developed at the basalt-ultramafic contact 3) a zone of antiforms and synforms that are developed within the talc-chlorite ultramafic, which have been truncated by splays off the thrust and have segmented the nose of the thrust 4) a zone of west-verging folding representing the eastern long limb of the thrust sheet adjacent to the thrust rollover 5) an extensive zone of consistently E-dipping foliation that defines the bulk of the exposed thrust sheet.

### Structure and mineralisation

The Mulgarrie deposit architecture is the product of two periods of southwest-vergent thrusting, which were separated by a tectonic hiatus during which felsic intrusions were emplaced (Davis, 1999b; Davis et al., 2001).

The first period of thrusting produced the dominant fabric (MUS1) in the deposit, whereas cleavage associated with the second (MUS2) was localised to the hinge of the synchronously developed thrust nose. Thrust 'lock-up' occurred after MUD1, resulting in the accumulation of shortening strain at the thrust tip during MUD2 and the formation of the rollover geometry. On the east limb of the thrust, MUS1 was re-used during MUD2 to produce a composite foliation (Figure 3.11.11). Intense carbonate alteration has been emplaced as massive pods in the hangingwall rocks to the thrust (Figure 3.11.11).

Mineralisation at the Mulgarrie deposit is hosted by veins that comprise two lithologically, temporally and orientationally discrete populations. Quartz-carbonate veins of the first set trend approximately north-south and have been emplaced sub-parallel to the penetrative MUS1 foliation. Veins of the second, volumetrically more important set trend approximately east-west (Figure 3.11.11), and have been localised within carbonate-feldspar alteration that post-dates MUS1.

Carbonate is represented by a range of styles varying from porphyroblasts to veins to pervasive, texturally destructive carbonatisation. Carbonate alteration occurred in response to two separate episodes of fluid ingress; the earliest deposited Mg-rich carbonate species while the later was characterised by Fe-bearing fluids. Well-developed textural relationships between various carbonate morphologies and the MUS1 and MUS2 foliations, indicate that the emplacement of carbonate occurred pre- to early syn-MUD2. This carbonatisation occurred in response to alteration of the ultramafic rocks by mantle-derived fluids that were tapped by regional faults. Carbonate was emplaced subparallel to MUS1, producing pods that are elongate in a northwest-southeast direction and which step

en-echelon northeastward (at right angles) to this trend. Subsequent MUD2 shortening caused extensional fracturing of the massive carbonate pods with infill by steeply dipping east-trending quartz veins (Figure 3.11.11). Ongoing deformation then localised brecciation within both the early and late quartz vein sets, and it is into these sites that most gold was deposited.

Gold mineralisation at Mulgarrie overprints MUD1 and MUD2 structures (including veins) in zones of massive carbonate alteration, suggesting it has a late- to post-MUD2 timing, consistent with the late gold elsewhere in the EGST (Groves et al., 1993).The carbonate alteration at Mulgarrie is not a product of the same event as that responsible for the gold. Rather, the different relative timing of gold mineralisation and carbonate alteration suggests there were two carbonate fluid systems active in the Mulgarrie area, which were overprinted by those that transported gold.

Two fluid systems are interpreted based on the structural timing of the spatially related gold and carbonate. The first protracted episode of fluid flow along the thrust fault was responsible for emplacement of massive magnesite alteration and subsequent dolomitic alteration. Gold-bearing fluids were sourced during a second stage of fluid flow, which was also focussed along the thrust.

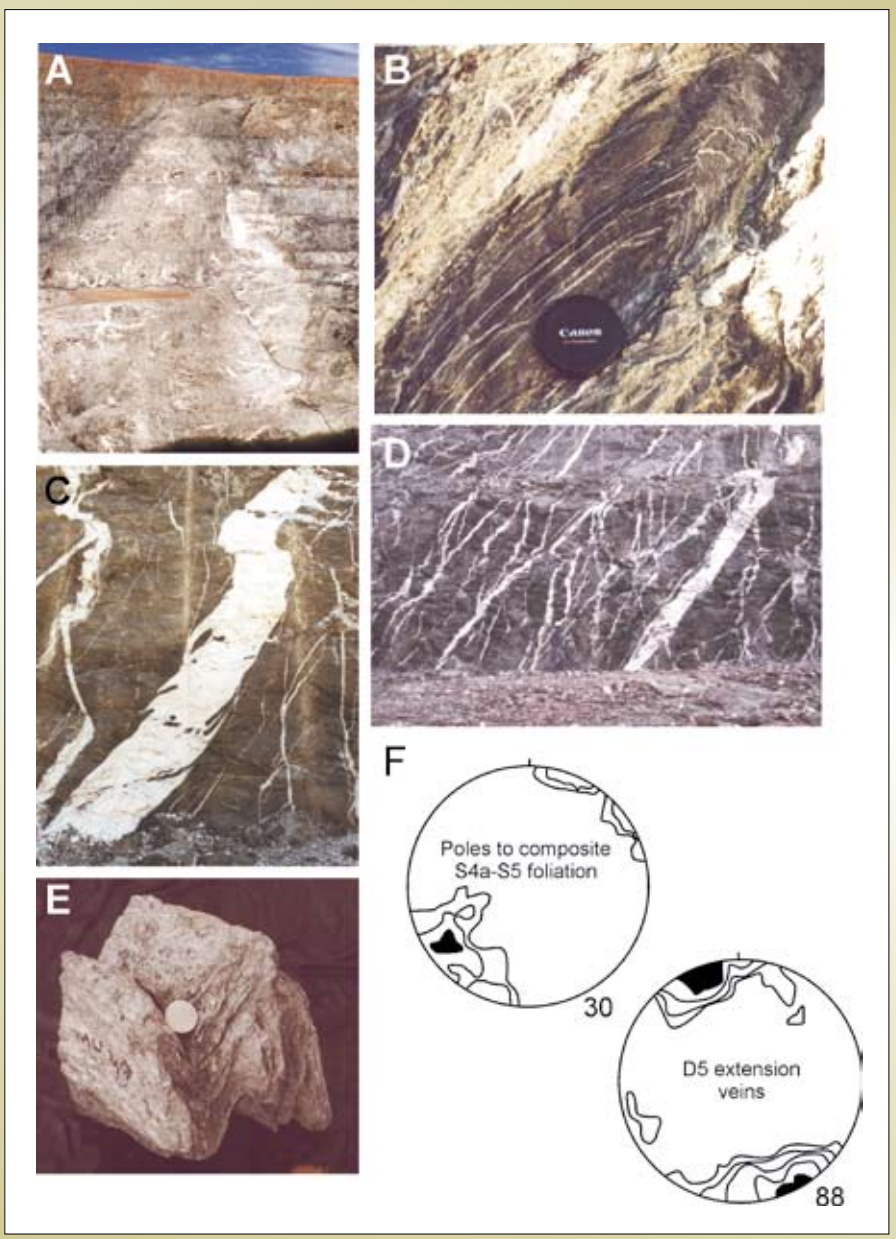


*Figure 3.11.11: Montage of photographs from the Mulgarrie pit on the eastern margin of the Scotia-Kanowna Dome.*
*A) Early carbonate pod with late-stage D5 veining and mineralisation utilising the brittle rheology for fracturing and vein emplacement.*
*B) Early carbonate veins folded and deformed in D5 southwest-directed thrust.*
*C) View northeast on steeply dipping extension and shear veins associated with local extension and dilation in accommodation zones orthogonal to the southwest-directed thrusting.*
*D) View northeast on steeply dipping extension and shear veins associated with local extension and dilation in accommodation zones orthogonal to the southwest-directed thrusting.*
*E) F5 fold of the S4a foliation. S5 is locally a crenulation cleavage.*
*F) Stereonets of the main foliation (essentially co-planar), reflecting shortening and flattening from the northeast-southwest. Extension (and shear) veins as C and D are developed orthogonal to the foliation and parallel to D5 $\sigma 1$.*

### Regional correlation

Contraction was oriented east-northeast – west-southwest to northeast-southwest throughout the recorded history of Mulgarrie (Davis, 1999b; Davis et al., 2001). Like other deposits on the eastern margin of the dome (e.g., Gordons-Sirdar), the strain is high and transposition of earlier deformations is likely. The MUD1 event was probably the result of regional D4a contraction, with the hiatus and emplacement of the porphyries occurring during the northwest-southeast oriented D4b sinistral shearing at around ~2650 Ma (Blewett and Czarnota, 2007c). The MUD2 event probably reflects a return to northeast-southwest contraction and renewed thrusting and refolding of the MUS1 fabric elements during regional D5. This stress switch during regional D5 fostered new fluid ingress into a pre-prepared architecture and, on the basis of regional considerations (Blewett et al., 2008b), was likely to be around 2640 Ma in age.

## 3.11.4.7 Woodcutters

The Woodcutters camp includes the Havana-Suva, Jakarta, London and Federal deposits (Figure 3.11.1), which are hosted solely within the 2656±3 Ma Golden Cities Granodiorite (Cassidy et al., 2002). These deposits are described here because, in contrast to other deposits of the region, they are solely developed in granitic rocks and are located along the inferred hinge-line of the regional Scotia-Kanowna Dome. The nearest greenstone belt is located some 6 km to the west. Phillips and Zhou (1999) suggested that an 'orogenic' fluid and gold were sourced from greenstones at depth beneath the batholith. However gravity data suggest that the basal portion of the dome is entirely granitic and not underlain by greenstone sequences (Henson, 2006), raising interesting questions to the source of gold and fluids.

The Federal deposit occurs along the Burke's Fault Zone, which is part of a regional lineament parallel to the hinge of the Scotia Kanowna Dome and juxtaposes two texturally different granodiorite phases. These phases have been discriminated on grainsize and, to a lesser degree, the presence of mafic xenoliths. Both phases are hornblende-biotite bearing, and were derived from a metasomatised mantle source. The Federal pit is elongate and trends approximately northwest-southeast, subparallel to the inferred hinge-line of the dome (Figure 3.11.12).

A number of thin aplite veins/dykes and relatively more mafic, finer-grained granodiorite dykes have been recorded at the Woodcutters pits. Dykes at Havana-Suva are generally 1 m to 6 m thick, strike E-W and dip steeply to the south.

Regional maps of these deposits (Phillips and Zhou, 1999) show a pronounced northwest-southeast elongate trend (Figure 3.11.12). Crossing this regional trend at a high angle is a series of northeast-trending shears, some of which are mineralised (e.g, Suva and sections of Jakarta).

### Structure and mineralisation

The mineralisation hosting structures at the Woodcutters gold deposits was developed during a single northeast-southwest contractional deformation event (WD1), which was focussed at the Burke's Fault Zone at the Federal deposit. The Havana-Suva pits to the west are located along two intersecting structures; a northwest-striking portion (Havana) and a northeast-striking portion (Suva). A similar geometry occurs at the nearby Jakarta pit further west again (Figure 3.11.12).

The northeast-southwest oriented WD1 contraction developed anastomosing ductile fabrics in the fine-grained phases of the granodiorite at Federal. The same deformation in the coarse-grained phase resulted in brittle structures, in particular closely spaced sub-mm scale fractures. The change in deformation style is potentially a function of differences in both grainsize and feldspar content. The fault zone at Federal has a hangingwall and footwall splay, comprising an 8–10 m wide zone of deformation. Gold mineralisation is located adjacent to the footwall of the footwall splay and comprises lodes sub-parallel to the trend of the structure. Relatively higher grades of mineralisation are evident where zones of silica-pyrite veins (Figure 3.11.12) within the 020° trend intersect the main shear. Disseminated pyrite is ubiquitous within the host rocks, with other sulphides largely absent. Gold occurs in free form and is occluded within pyrite.

Fabric asymmetries and the geometries of fault splays exposed in the southeast end of the Federal pit indicate that the WD1fault was a reverse structure, although a dextral sense component of movement has also been suggested. A penetrative WS1 is evident in the walls of the pit and trends approximately 020°, dipping steeply to the west.

The alteration halo at Federal is dominated by epidote from the breakdown of plagioclase, and can be up to 100 m wide (Phillips and Zhou, 1999). Alteration proximal to the shear involves hornblende and biotite destruction with the stabilisation of muscovite, secondary biotite, and quartz veinlets with gold and pyrite (Figure 3.11.12), and haematite is locally abundant. Carbonate alteration is only weakly developed.

In contrast to Federal, the Havana-Suva deposit has two main trends. The main Havana structure strikes northwest-southeast and dips moderately to steeply northeast and is interpreted to be a southwest-directed reverse fault (Figure 3.11.12). The northeast-southwest splay of Suva is interpreted as an accommodation structure to this reverse fault. The northeast-trending Suva section was oriented parallel to the maximum shortening direction (σ1). Gold mineralisation is hosted by two brittle fracture/vein sets, and these reflect the larger architecture (northwest and northeast trends) of the deposits and the region. The earliest-formed set trends northwest-southeast parallel to the 'main trend', but they contain less than 10% of the gold. This is in contrast to the nearby Federal deposit which hosts all the mineralisation on an equivalent structure. The later main mineralised set comprises veins/fractures that strike at a high angle to the 'main trend' (varying from 010° to 070°), and dip moderately to the northwest. Within both the northeast-southwest (Suva) and northwest-southeast (Havana) trending sections the main mineralised veins developed as extension veins as they are consistently northeast- to east-northeast-trending (parallel to the main contraction). The veins oriented at the extreme range (i.e., 010° and 070°) were likely to have been shear veins.

Mineralisation and alteration at Havana-Suva is controlled by the intensity and density of fractures and veins. The main ore minerals are pyrite, lesser chalcopyrite and coarse gold. Galena, tellurides, native bismuth, bismuthinite and aramayoite ($Ag(Sb,Bi)S_2$) are trace contributors. Gangue alteration minerals include albite, biotite, silica and sericite,

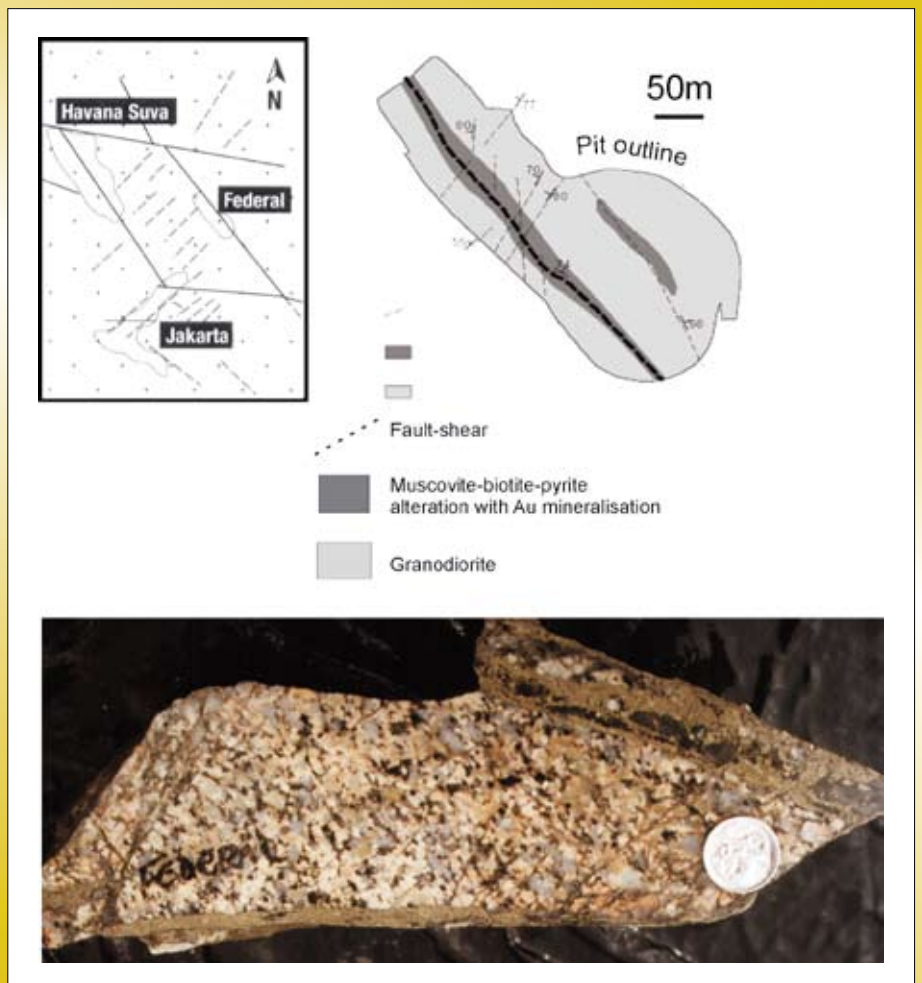


*Figure 3.11.12: Sketch map of the Woodcutters camp of deposits in the centre of the Scotia-Kanowna Dome (after Phillips and Zhou, 1999). Most deposits are northwest to north-northwest trending, parallel to the trace of the dome hinge. Note however the 'L' shaped Jakarta pit with a northeast-trending section of the pit which is parallel to the cross faults and shears. These are likely similar extension structures developed parallel to σ1 during D5 (northeast-southwest), and analogies occur in Mulgarrie. Slabbed sample of Golden Cities Granodiorite showing S5 flattening foliation and fractures hosting muscovite-biotite-quartz alteration associated with mineralisation.*

with minor haematite, chlorite, epidote, carbonate, titanite and apatite. Best gold grades have been encountered in the Havana Primary Lower Lode in association with strong anastomosing fractures and some crackle to mosaic breccias, strong pyrite, chalcopyrite and coarse gold. Minor quartz veining commonly displays coarse gold in close association with chalcopyrite.

Phillips and Zhou (1999) reported fluid inclusions from the gold-bearing veins at the Federal pit as similar to those recorded from many greenstone-hosted gold deposits (e.g., Ho et al., 1990), and being $H_2O$-$CO_2$-dominant, of low salinity, and yielding homogenisation temperatures around 250°-300° C. These fluid properties are considered to be metamorphic in origin, from devolatolisation of greenstones inferred to be at depth.

#### Regional correlation

The age of the granodiorite is 2656±3 Ma (Cassidy et al., 2002) so structures (and mineralisation) that are hosted in it are younger than this. The Mafic-type of granite mostly intruded during the regional D3 extension event, although younger ones were emplaced during regional D4 (Blewett et al., 2008b), for example at Kanowna Belle.

The contractional event responsible for the deformation and mineralisation developed with σ1 oriented northeast-southwest. Regionally across the EGST, the occurrence of base metals and tellurides together with the gold is commonly associated with northeast-southwest contraction and dextral strike-slip faulting during the last main D5 contractional event. This D5 was intense at around 2640 Ma (Blewett et al., 2008b; Czarnota et al., 2008), and was associated with Low-Ca type granites.

The Federal deposit has a relatively simple northwest-southeast trending architecture, with gold being likely focussed and deposited into a relatively high-displacement shear zone that was sufficiently vigorous to develop permeability and focus fluid flow. In contrast, the main mineralised veins at Havana-Suva are at a high-angle to the 'main trend', and they developed in extensional step-over accommodation zones analogous to the main mineralised veins at Mulgarrie (see above). All these deposits represent differing architectures produced within a single regional event. Regional geological maps (Phillips and Zhou, 1999) show many of the northeast-southwest 'shears' and the presence of additional accommodation zones is inferred.

On the above considerations, the deformation and mineralisation at Woodcutters is correlated with the regional D5. Low-Ca granites are typically found in the centres of the regional domes. Although difficult to test, Low-Ca granites would be predicted at depth beneath these deposits, and are a likely driver to the deformation and mineralisation.

### 3.11.5 Regional correlation and implications for predictive mineral discovery

The Scotia-Kanowna Dome, due to the erosion level, provides a good study area to determine the role in large granite-cored domes in their influence on Archaean 'lode' gold systems. Greenstone sequences at all locations surrounding the dome are exposed at, or preserve, approximately the same stratigraphic level, and yet most of the discovered gold endowment is located at the dome hinge in the Kanowna Belle deposit. The margins of the dome, in particular the eastern and western margins, are characterised by high strains, especially those produced during the final main contractional event (D5). Morey (2007) suggested that the narrow elongate architecture of the dome margins (limbs) was too restrictive for an effective permeability system and resultant fluid flow for the western margin (e.g., Paddington). In contrast, the southeast plunging dome hinge was a location of relative lower strain during at least two of the main (east) northeast-(west)southwest contractional events (D4a and D5). Furthermore, the dome hinge favoured creation of new structures at earlier and intermediate times (D3 and D4b) in the deformation history (Table 3.11.4). The dome hinge is not only a 'high point' for deep fluid migration pathways, but its geometry favoured creation of repeated permeability enhancement.

The Kambalda and overlying Kalgoorlie greenstone sequences (Krapež et al., 2000) of the study area were deposited in an evolving intra-arc to back arc environment from 2710 Ma to 2665 Ma (Barley et al., 2003; 2007). Czarnota et al. (2008) ascribed the formation of the regional greenstone 'basin' to a prolonged D1 east-northeast directed extensional event (likely punctuated and episodic). Synchronous with the formation of this basin was the emplacement of voluminous High-Ca granites,

which peaked at around 2665 Ma in the Kalgoorlie Terrane (Cassidy et al., 2002). The geochemistry of these voluminous granites suggest that they were sourced from high-pressure partial melting of mafic rocks (basalt). The depth of melting, together with the need to 'dispose' of a very thick eclogitic residue, suggests that direct slab melting was the source of granite and the method of residue disposal into the mantle (Smithies and Champion, 1999). A retreating subduction zone dipping to the (west) southwest could account for the north-northwest D1 tectonic grain, greenstone volcanism and High-Ca granite magmatism (Czarnota et al., 2008).

The greenstone volcanism ended at around 2665 Ma and was followed by a change to first fluvial and then deep marine clastic sedimentation (Krapež et al., 2000). These post volcanic late basins mark a fundamental change in the geodynamics of the EGST as they record the first emergence of the granite-cored domes when they were exhumed and unroofed into extensional basins. These basins lay with a locally angular unconformity on a pre-folded Kambalda and Kalgoorlie sequence basement (Blewett et al., 2004). The early structures also mark the first major contractional event (D2) to influence the EGST (Blewett and Czarnota, 2007), and mark the termination of the volcanism. The driver for this contraction is uncertain, but the accretion of an exotic body into the retreating trench is one possible mechanism (Collins, 2002; Czarnota et al., 2008). No direct structural evidence (fabrics, folds etc) for the D2 contraction occurs in this study area.

Synchronous with the change in greenstone type (volcanism to sedimentation), was a similar dramatic change in magmatism from High-Ca type to Mafic- and Syenite-types (Champion and Sheraton, 1997; Cassidy et al., 2002; Blewett and Czarnota, 2007c; Blewett et al., 2008b; Czarnota et al., 2007; 2008). A change in source region marks these different granite types, and geochemical data suggest that they were generated from partial melting of the metasomatised mantle wedge (see also Beakhouse, 2005; 2007). This wedge was metasomatised during previous D1 slab melting and the change to D2 contraction and D3 extension permitted access to this wedge.

The record of D3 extension in the study area is preserved as the post-volcanic late basins along the hinge of the dome and in the emplacement of Mafic-type granites. The D3 extension involved granite doming to the northwest as the Scotia-Kanowna Batholith was constructed and subsequently exhumed during D3 extension. A peak in extensional doming occurred with the emplacement of the Golden Cities Granodiorite at 2656 ± 3Ma (Cassidy et al., 2002) in the centre of the dome. These granite types, including lamprophyres and syenites, were derived from melting of a metasomatised mantle wedge and are inherently enriched in incompatible elements (Champion and Sheraton, 1997). Consequently, they may be the primary source for much of the gold (see also Mueller, 2007).

The granitic core (with other Mafic-type granites) of the Scotia-Kanowna Dome was rapidly exhumed and detritus deposited in upper plate basins that developed to the southeast. New extension shear zones are inferred to have developed in the now upper-plate greenstone sequences that mantle the dome, with basins developing in the footwalls of these structures. These shear zones accommodated the upward and outward (top-to-the-northwest) extrusion of the batholith. An analogous relationship has been described from Laverton with the upper-plate Wallaby and Granny Smith basins developed in the hangingwall of extensional shear zones accommodating the extrusion and uplift of the Mt Margaret Anticline (McIntyre and Martin, 2005; Blewett et al., 2008b).

In the Scotia-Kanowna Dome region, structures such as the Fitzroy and Last Chance Shears likely initiated during D3, and controlled the distribution of sediments and enriched magmas at this time. Kinematic proof of this is equivocal. However, the geometry of the Last Chance Shear could be interpreted as an extensional C-prime plane, with only limited D4b inversion being the reason for its preservation (unlike the high-strain Fitzroy Structure).

The EGST returned to east-northeast – west-southwest oriented contraction with the onset of the D4a regional event (Blewett et al., 2008b). This event involved significant flattening with the development of southwest-directed thrusting, upright north-northwest trending F4a folds and steep S4a foliation. This event was previously described as 'D2' by Swager (1997) and others, and 'D2b' by Blewett et al. (2004). This event partitioned strain heterogeneously, with most intense shortening-related deformation developed on the eastern and western margins of the dome. Intense flattening fabrics and greenstone over dome

Table 3.11.4: Correlation table of deformation events at each compared with the regional framework (Blewett and Czarnota, 2007c). Note that gold was deposited during at least three different stages and that the dome hinge areas record the most events, and multiple gold events

| Regional Event | Characteristics (Blewett & Czarnota, 2007c) | Paddington | Kanowna Belle | Ballarat-Last Chance | Red Hill | Gordon Sirdar | Mulgarrie | Woodcutters |
|---|---|---|---|---|---|---|---|---|
| Location on the dome | | West limb | Dome hinge | Dome hinge | Dome hinge | East limb | East limb | Dome core |
| | | Greenstones mantling the dome | | | | | | |
| D6 | Late vertical extension | | | | | | | |
| D5 | **NE-SW contraction** NNW foliation and folds, NNE-dextral, E-W sinistral reactivation **~2650–2625 Ma** | $_{P}$D3: dextral normal | KBD3: sinistral reactivation **Au** | BLCD2: sinistral reactivation Au **Au** | | | $_{MU}$D2: NNW refolds, SE thrusting, steep extension veins **Au** | WD1: SE thrusts, NE extension veins **Au** |
| D4b | **NW-SE contraction** NW-directed thrusting, high-strain (NNW) sinistral transpression **~2650 Ma** | $_{P}$D2: WSW folds | KBD2: NW thrusting, porphyry intrusion **Au** | BLCD1: NW thrusting | RHD2: N-S contraction flat veins and foliation **Au** | GSD1: NNW steep foliation, sinistral reverse shearing, flat extension veins **Au** | Felsic intrusions | |
| D4a | **ENE-WSW contraction** NNW foliation and folds, SE-directed thrusting **2655–2650 Ma** | $_{P}$D1: ENE contraction and flattening **Au** | KBD1: ENE contraction and tilting of footwall | Felsic intrusions? | RHD1: NNW steep foliation and flat extension veins, felsic intrusions? **Au** | | $_{MU}$D1: NNW steep foliation and flat extension veins, felsic intrusions? **Au** | |
| D3 | **SE extension** Granite doming, basin formation **2660–2655 Ma** | Initial tilting of stratigraphy? | Extension and basin formation, granite doming | Extension and basin formation, granite doming | Extension, basin formation, felsic intrusion? | Initial tilting of stratigraphy? | Initial tilting of stratigraphy? | Golden Cities Granodiorite (2656±3 Ma) |

*continued*

Table 3.11.4: Correlation table of deformation events at each compared with the regional framework (Blewett and Czarnota, 2007c). Note that gold was deposited during at least three different stages and that the dome hinge areas record the most events, and multiple gold events *continued*

| Regional Event | Characteristics (Blewett & Czarnota, 2007c) | Paddington | Kanowna Belle | Ballarat-Last Chance | Red Hill | Gordon Sirdar | Mulgarrie | Woodcutters |
|---|---|---|---|---|---|---|---|---|
| D2 | **ENE-WSW contraction** Mostly low strain closes arc, upright NNW folds (weak foliation) **2665–2660 Ma** | ? | ? | | | ? | ? | |
| D1 | **ENE-extension** **>2665 Ma** | Greenstone sequence | Footwall and basement greenstone sequence | | | Greenstone sequence | Greenstone sequence | |

thrusting/reverse faulting-shearing occurred at this time at Paddington (Morey, 2007) and at Mulgarrie (Davis et al., 2001). Lineations plunge steeply to down-dip and the folds are tight to isoclinal with gentle north-northwest or south-southeast plunges. Gold is associated with this event, but its source is uncertain (see above). In contrast to the dome margins, the hinge region of the dome was an area of relative low-strain during D4a time. At Kanowna Belle it was a period of upright folding in the footwall of the Fitzroy Structure and at BLC was associated with porphyry emplacement.

The regional D4b event was associated with a major switch in the palaeostress field, with σ1 oriented south of east west. The complex pre-existing geometry created from a succession of earlier events resulted in extreme local heterogeneities and major deviations in local stress field (Blewett et al., 2008b). The resultant strain was manifest as sinistral transpression on the margins of the domes, especially where they were steepened by the previous D4a contraction, and northwest-directed thrusting on the dome hinge regions. Regionally, these thrusts were ascribed to 'D1' (Swager, 1997 and references therein), but they clearly transect previously folded sequences (D2, D3, D4a), and link kinematically with the sinistral strike-slip faults on the dome edges (Henson et al., 2005). Analogous relationships exist at St Ives (Blewett et al., 2008c) and in Laverton (Henson, et al., 2008).

The Scotia-Kanowna Dome records a linked system of marginal sinistral strike-slip faults and axial (to the dome) thrusts during D4b. In detail, the thrust movements were episodic, especially on the Fitzroy Structure, and also involved intrusion of porphyries such as at Kanowna Belle (Davis et al., 2000). The present steep attitude of the Fitzroy Structure at over 60° suggests that it has been tilted post-D4b thrusting. An interpretation for this geometry is that the northwest-directed thrusting locked up on the nose of the dome and continued D4b shortening was therefore accommodated by folding and steepening against this buttress.

On the southeast and east margin of the dome (Gordons-Sirdar area), D4b was manifest as sinistral transpression with the development north-northwest shear foliation and top to the northwest shearing. Gold was deposited at this time at this location. Further north at Mulgarrie, felsic intrusions were emplaced. The structures at Gordons-Sirdar are analogous to those along the Lefroy Fault at Kambalda (Blewett et al., 2008c).

To the southwest of Kanowna Belle lies the Panglo Basin, which is a somewhat enigmatic panel of rocks that sit with an apparent unconformity (Tripp et al., 2007) across the D4b Fitzroy Structure and mine sequence at Kanowna Belle (Figure 3.11.1). The formation of the Fitzroy Structure occurred across the dome nose due to accommodation of movements from regional sinistral strike-slip faults either side of the dome (e.g., at Gordons-Sirdar), and with the Panglo Basin developing in a strike-slip pull-apart setting (e.g., Krapež et al., 2000; 2007) associated with this D4b shearing. Dating of these sediments is needed to confirm a maximum depositional age, but on regional considerations they would be predicted to be around 2650 Ma or less in age (Blewett et al., 2008b).

### Late-stage contraction

The Scotia-Kanowna area was subject to particularly intense late-stage contraction during the regional D5 (Blewett et al., 2008b). The D5 involved a switch in principal palaeostress back to northeast-southwest and resulted in considerable reworking of older structures (e.g., Davis et al., 2001). The youngest rock sequence, the Panglo Basin, was inverted by intense northeast-directed D5 contraction and thrusting, which folded the sequence, tipped the basal unconformity to its present steep attitude and imparted a penetrative S5 cleavage.

On the dome hinge, the earlier east-northeast-west-southwest structures were favourably oriented to undergo extension and dilation with a sinistral component of shear during D5 contraction (e.g., at Kanowna Belle). Dilation was effective for focusing fluid flow as much of the gold mineralisation was deposited at this time, especially at BLC.

On the eastern margin of the dome renewed flattening and foliation development (S2b of Davis et al., 2001) occurred and was synchronous with gold deposition. Much of the gold at Mulgarrie was deposited in accommodation zones between en echelon thrust tips, and these were oriented northeast-southwest in the extension direction parallel to σ1.

Deformation was intense enough to propagate structures through the centre of the dome, with the Woodcutters camp developing north-northwest trending reverse faults and northeast-southwest extension zones (analogous to Mulgarrie). The nature of the host was important in localising dilation, which was most favourable in the coarser-grained phases of the granite.

Low strain structures at Paddington to the west of the dome, indicate D5 was relatively and was limited to north-northeast trending dextral faults. These are a common style of D5 structure in the southern and western parts of the Kalgoorlie Terrane region in general (e.g., Black Flag Fault west of the Kanowna-Scotia-Dome, the Alpha Island Faults, and the Mt Charlotte lodes at Kalgoorlie).

Regionally, D5 is the late 'orogenic' gold event (Groves et al., 1999) associated with 'D4' in the Swager terminology. It occurred between <2650 and 2625 Ma (~2640 Ma), which is the likely age of mineralisation for Woodcutters, Mulgarrie, BLC and the last stages of Kanowna-Belle. The influence of basinal fluids during D4b and D5 gold is also observed in the occurrence of base metal associations. These reduced fluids were likely driven out of the basins as they were metamorphosed (Goscombe et al., 2007) and may have mixed with magmatic oxidised fluids from deeper Low-Ca granites in a complex architecture during stress switches. The structural position of the Woodcutters camp beneath the greenstone carapace suggests that mineralisation may have already been present (with the emplacement of the Mafic-type granite magmas) and simply reworked and refocussed on intense inversion and during the late heat pulse associated with the regional Low-Ca granites. Alternatively, gold descended from the overlying greenstone carapace.

### 3.11.6 Conclusions

The Scotia-Kanowna area is a classic architecture for many Archaean granite-greenstone gold mineral systems. The erosion level across the system (dome core to limbs to hinge/nose) permits the role of domes and mineralisation to be examined in a structural-stratigraphic context. The main generic conclusions from this study of a large granite-cored dome are:

- the dome control of the distribution of far-field stresses into localised strain and therefore the distribution of rocks in time and space;
- the hinges of domes areas are favourable for complex development of structures and local strain/stress perturbations, as at each stage in the event history an impact is felt – this provides multiple opportunities for new and renewed permeability creation, development of rheological complexity, and reactivation;
- hinges are focus points/pathways as most hot fluid systems, be they magmatic or heated fluids from other sources, are ultimately driven upwards;
- when exploring on the margins of the domes, exploration should look for local complexity that has focused deformation because long straight segments are poor targets, and;
- the centre of domes in granite-cored areas can be favourable, albeit to a lesser degree, especially if the host is a Mafic-type granite and deformation has been sufficient to penetrate and rework such inherent pre-ore endowment.

### 3.11.7 Acknowledgements

We would like to express our gratitude to the sponsors of the ***pmd*CRC***, for their support and encouragement throughout the life of the Y4 project. Published with permission of the CEO of the ***pmd*CRC*** and the CEO of Geoscience Australia (RB, PH, DC).

### 3.11.8 References

Aaltonen, A., 1997, The significance of vein and breccia paragenesis to mineralisation at the Kanowna Belle Gold Mine, Eastern Goldfields Province, Western Australia. Unpublished BSc (Hons) thesis, University of Western Australia, Perth.

Barley, M.E., Brown, S.J.A, Krapež, B., and Cas, R.A.F., 2002, Tectonostratigraphic analysis of the Eastern Yilgarn Craton: an improved geological framework for exploration in Archaean Terranes. AMIRA Project P437a, Final Report.

Beakhouse, G.P., 2007, Gold, granite and late Archaean tectonics: a Superior Province perspective. In: Bierlein,

F.P. and Knox-Robinson, C.M. (editors), Proceedings of Geoconferences (WA) Inc. Kalgoorlie '07 Conference, 25–27 September 2007, Kalgoorlie, Western Australia. Geoscience Australia Record 2007/14, 191–196.

Beakhouse, G.P., and Davis, D.W., 2005, Evolution and tectonic significance of intermediate to felsic plutonism associated with the Hemlo greenstone belt, Superior Province, Canada. Precambrian Research, 137, 61–92.

Bell, B., Goleby, B.R., Fomin, T., Nicoll, M.G., and Owen, A.J., 2000, Gravity and magnetic modelling: Detailed gravity and magnetic modelling to constrain crustal structures within the Eastern Goldfields, Western Australia. In: Crustal structure and fluid flow in the Eastern Goldfields, Western Australia – Results from the Accra's Yilgarn deep seismic reflection survey and fluid flow modelling projects. Australian Geological Survey Organisation, Record 2000/34, 74–84.

Blewett, R.S., Cassidy, K.F., Champion, D.C., Henson, P.A., Goleby, B.R., Jones, L., and Groenewald, P.B., 2004, The Wangkathaa Orogeny: an example of episodic regional 'D2' in the late Archaean Eastern Goldfields Province, Western Australia. Precambrian Research, 130, 139–159.

Blewett, R.S., and Czarnota, K., 2007a, The Y1-P763 project final report November 2005. Module 3 - Terrane Structure: Tectonostratigraphic architecture and uplift history of the Eastern Yilgarn Craton, Geoscience Australia Record 2007/15 112p. [DVD].

Blewett, R.S., and Czarnota, K., 2007b, Diversity of structurally controlled gold through time and space of the central Goldfields Superterrane – a field guide. Geological Survey of Western Australia Record 2007/19, 65p.

Blewett, RS, and Czarnota, K, 2007c, A new integrated tectonic framework of the Eastern Goldfields Superterrane, *in* Kalgoorlie 2007 *edited by* F Bierlien and C Knox-Johnson: Geoscience Australia, Record 2007/14, 27–32.

Blewett, R.S., Cassidy, K.F., Henson, P.A., Roy, I.G., Champion, D.C. and Fomin, T., 2008a, Question 2: Big systems-big signatures – anatomy of the Archaean Yilgarn Craton and implications for world-class gold mineral systems. Part III, this volume.

Blewett, R.S., Czarnota, K., Henson P.A. and Champion, D.C., 2008b, A revised tectono-stratigraphic framework for the Eastern Yilgarn Superterrane. Part III, this volume.

Blewett, R.S. Squire, R., Henson, P.A., Miller, J.M., and Champion, D.C., 2008c, Architecture and geodynamic evolution of the St Ives region, south central Kalgoorlie Terrane, Western Australia. Part III, this volume.

Cagniard, L., 1953, Basic theory of the magneto-telluric method of geophysical prospecting, Geophysics, 18, 605–635.

Cassidy, K.F., Champion, D.C., McNaughton, N.J., Fletcher, I.R., Whitaker, A.J., Bastrakova, I.V., and Budd, A.R., 2002, Characterisation and metallogenic significance of Archaean granitoids of the Yilgarn Craton, Western Australia. Minerals and Energy Research Institute of Western Australia (MERIWA), Report No. 222, 514p.

Cassidy, K.F., Champion, D.C., Krapež, B., Barley, M.E., Brown, S.J.A., Blewett, R.S., Groenewald, P.B., and Tyler, I.M., 2006, A revised geological framework for the Yilgarn craton, Western Australia: Western Australia Geological Survey Record 2006/8, 8 p.

Champion, DC, 2006, Terrane, domain and fault system nomenclature, in 3D Geological Models of the Eastern Yilgarn Craton – Y2 Final Report ***pmd*CRC*** edited by RS Blewett and AP Hitchman: Geoscience Australia, Record 2006/4, p. 19–38 [DVD-ROM].

Collins, W.J., 2002, Hot orogens, tectonic switching, and creation of continental crust. Geology, 30, 535–538.

Czarnota, K., Blewett R.S., Champion D.C., Henson P.A. and Cassidy K.F., 2007, Significance of extensional tectonics in orogenic gold systems: an example from the Eastern Goldfields Superterrane, Yilgarn Craton, Australia. In: Andrew C.L., et al., (eds) Digging Deeper. Proceedings of the Ninth Biennial Meeting of the Society for Geology Applied to Mineral Deposits Dublin, Ireland 20th–23rd August 2007. 1431–1434.

Czarnota, K., Champion, D.C., Cassidy, K.F., Goscombe, B., Blewett, R.S., Henson, P.A. and Groenewald, P.B., 2008, Geodynamics of the Eastern Goldfields Superterrane, *Part III this volume*.

Davis, B.K., 1999a, Structural geology and controls on mineralisation in the Ballarat-Last Chance open pit. Report to the Golden Feather project, June 1999. Report Number WA99.037, unpublished report available on www.doir.wa.gov.au

Davis, B.K., 1999b, Report on structural analysis of the Mulgarrie deposit. Unpublished report to the Golden Feather project, February 1999, Report No. WA99.012. unpublished report available on www.doir.wa.gov.au

Davis, B.K., Archibald, N.J., and Aaltonen, A., 2000, Kanowna Belle Gold Mine – Anatomy and History of a Plumbing System. In: Proceedings of the 15th Australian Geological Convention (Abstract). Sydney, Australia, pp. 23.

Davis, B.K., Hickey, K.A., and Rose, S., 2001, Superposition of Au-mineralization on pre-existing carbonate alteration: structural evidence from the Mulgarrie gold deposit, Yilgarn Craton. Australian Journal of Earth Sciences, 48, 131–150.

Drummond, B.J., and Goleby, B.R., 1998, Yilgarn crustal structure revealed in five seismic profiles. In: Geodynamics and gold exploration in the Yilgarn, workshop abstracts. Perth, 6 August 1998.

Goscombe, B., Blewett, R.S., Czarnota, K., Maas, R., and Groenewald, B., 2007, Broad Thermo-Barometric Evolution of the Eastern Goldfields Superterrane. In: Bierlein, F.P. and Knox-Robinson, C.M. (editors), Proceedings of Geoconferences (WA) Inc. Kalgoorlie '07 Conference, 25–27 September 2007, Kalgoorlie, Western Australia. Geoscience Australia Record 2007/14, 33–38.

Groves, D.I., Barley, M.E. and Ho, S.E., 1989, Nature, genesis, and tectonic setting of mesothermal gold mineralization in the Yilgarn Block, Western Australia. In: Keays, R.R., Ramsay, W.R.H. and Groves, D.I., (eds), The geology of gold deposits: The perspective in 1988. Economic Geology Monograph 6, 71–85.

Henson, P.A., 2006, Chapter 2: An integrated geological and geophysical 3D map for the EYC. Chapter 4: Tomographic studies of the Yilgarn lithosphere. *In:* Blewett, R.S. and Hitchman, A.P. (eds) Final report, 3D geological models of the eastern Yilgarn Craton, Project Y2, September 2001 - December 2004. Geoscience Australia Record 2006/5, 39–52.

Ho, S.E., Groves, D.I., and Phillips, G.N., 1990, Fluid inclusions in quartz veins associated with Archaean gold mineralisation: Clues to ore fluids and ore depositional conditions and significance to exploration. In: Herbert, H.K. and Ho, S.E., eds, Stable isotope and fluid processes in mineralisation. Geology Department and University extension, University of Western Australia, Publication, 23, 35–50.

Krapež, B., Brown, S.J.A., Hand, J., Barley, M.E., and Cas, R.A.F., 2000, Age constraints on recycled crustal material and supracrustal sources of Archaean metasedimentary sequences, Eastern Goldfields Province, Western Australia: evidence from SHRIMP zircon dating. Tectonophysics, 322, 89–133.

Mueller, A., 2007, Copper-gold endoskarns and high-Mg monzodiorite–tonalite intrusions at Mt. Shea, Kalgoorlie, Australia: implications for the origin of gold–pyrite–tennantite mineralization in the Golden Mile. Mineralium Deposita, 42, 737–769.

Nelson, D.R., 1995, Compilation of SHRIMP U-Pb zircon geochronology data, 1994. Western Australia Geological Survey, Record 1995/3, 244p.

Phillips, N., and Zhou, T., 1999, Gold-only deposits and Archaean granite. SEG Newsletter 37, pp 1, 8–13.

Swager, C.P., 1997, Tectono-stratigraphy of late Archaean greenstone terranes in the southern Eastern Goldfields, Western Australia. Precambrian Research 83, 11–42.

Taylor, G.J., Horvath, H.S., and Gatehouse, S.G., 1997, Report No. WA97/25P geological evaluation and sampling reconciliation of the Red Hill gold resource within M27/57 – Red Hill, Kanowna, Western Australia. North Limited unpublished report available on www.doir.wa.gov.au

Tripp, G.I., Cassidy, K.F., Rogers, J., Sircombe K., and Willson M., 2007, Stratigraphy and structural geology of the Kalgoorlie greenstones: Key criteria for gold exploration. In: Bierlein, F.P. and Knox-Robinson, C.M. (editors), Proceedings of Geoconferences (WA) Inc. Kalgoorlie '07 Conference, 25–27 September 2007,

Kalgoorlie, Western Australia. Geoscience Australia Record 2007/14, 203–208.

Truelove, A.J., Wilson, G.M. and Seymour, K.M., 1997, New Resources in an old district – a case study of the discovery of Golden Feather, Kanowna, in New generation gold mines: case histories of discovery: Australian Mineral Foundation, 15.1–15.12.

Roberts, F.I. Witt, W.K. and Westaway, J., 2005, Gold mineralization in the Edjudina–Kanowna Region Eastern Goldfields, Western Australia. Geological Survey of Western Australia, Report 90.

Rodgers, J.R., Joyce, K.A. Masterman, G.J., Halley, S.W. and Walshe, J.L., 2004, Kanowna Belle Gold Mine. Gold and nickel deposits of the Norseman-Wiluna greenstone belt – a field guide. Geological Survey of Western Australia Record 2004/16, 47–51.

Ross, A.A., Barley, M.E., Brown, S.J.A., McNaughton, N.J., Ridley, J.R & Fletcher, I.R. 2004, Young porphyries, old zircons: new constraints on the timing of deformation and gold mineralisation in the Eastern Goldfields from SHRIMP U–Pb zircon dating at the Kanowna Belle Gold Mine, Western Australia. Precambrian Research, 128, 105–142.

Sircombe, K.N., Cassidy, K.F., Champion, D.C. & Tripp, G., 2007, Compilation of SHRIMP U-Pb geochronological data, Yilgarn Craton, western Australia, 2004–2006. Geoscience Australia Record 2007/01.

Squire, R. and Cas, R.A.F., 2006, Project M376 – Stratigraphic and structural architecture of late-basin depositional systems in the Eastern Goldfields Province, Yilgarn Craton, Final meeting and Field Workshop, 7–8 June, 2006.

## 3.12 The 4D architecture of the Laverton camp, Eastern Yilgarn Craton

**P.A. Henson, R.S. Blewett, J. McL. Miller, I. G. Roy, K, Czarnota, Y. Zhang, and P. M. Schaubs**

Predictive Mineral Discovery Cooperative Research Centre (*pmd*CRC*); Geoscience Australia

### Abstract

The Laverton region, located in the Eastern Goldfields Superterrane (EGST), is second only to Kalgoorlie for gold endowment. The combination of high density potential field data, combined with regional and camp scale seismic reflection data; and significant regional and mine scale structural analysis, provided suitable constraints for a 4D architectural study of this region. A variety of software packages were utilised to constrain the 3D geometries of the region; including Gocad™ to visualise and statistically analyse a broad range of 3D data.

At a regional scale, Laverton is dominated by the Mt Margaret Dome in the north-west and the Kirgella Dome in the south-east. These domes are flanked to the east and west by NNW-trending shear zones, while the central zone between the domes is dominated by N- to NNE-trending sigmoidal shear zones. These distinctly different shear zone trends developed early in the architectural history and have resulted a favourable architecture for mineralising processes late in the geodynamic history.

Seismic reflection data have enabled the sub-surface interpretation of shear zones at depth and their connectivity to each other. The Laverton Tectonic Zone (LTZ) is imaged as a major crustal penetrating shear extending to the Moho. It is made up of a basal fault (NNW trending Celia Fault) and a series of steeper faults (e.g., N-NNE trending Childe Harold Fault and Far Eastern Fault) soling into it at depth beneath the Laverton region. Lower angle faults imaged in the seismic reflection data develop parallel to the granite/gneiss domes that postdate the NNW and N-NE trending faults.

The construction of the 3D map combined with structural and lithological analysis has enabled an interpretation of the major structural events and their effects on the architectural evolution of the region. Six district deformation events can be interpreted from current structural kinematics, lithological distributions and geochronological constraints. These constraints have demonstrated that early formed faults are spatially associated with mineralisation within the Laverton region and probably play a large role in mineralisation.

Regional and mine scale structural analysis at the Wallaby and Sunrise Dam deposits indicate that equivalent stress fields operated during the mineralisation phases within both deposits during the (D4b) event. These mine scale similarities raise interesting questions regarding the overarching regional architecture needed to produce a genetic link between both mines. Lithologically, Wallaby and Sunrise Dam are quite different. Wallaby is hosted within a conglomeratic unit, while Sunrise Dam is hosted within intermediate volcanic rocks. Structurally though, both deposits display striking similarities and more interestingly, the gross structures within the Wallaby Mine are the 'mirror image' of those within Sunrise Dam. Although structurally complex, the dominant through going structures are shallow 15–40° thrusts which can be identified in 3D map patterns, dipping to the NW at Sunrise Dam and to the SE at Wallaby Mine. Within both deposits numerous steep structures occur that are variably offset by the thrusts.

Both mines are separated by a large structural corridor (Laverton Tectonic Zone) which records both sinistral and dextral movement during its history. In order to produce co-genetic deposits within an overarching structural framework, critical architectural elements must combine within a specific stress field. The structural model that best fits the current architecture is a restraining stepover within a sinistral strike-slip system during the D4b event.

Two early extensional basement faults are reactivated during northwest-southeast contraction (D4b) producing low-angle thrusts in a pop-up zone. This architecture exists in the region between Wallaby and Sunrise Dam, where both deposits are located on the low-angle thrusts on opposing sides of a sigmoidal structure, produced by sinistral strike-slip movement. This process would provide significant dilation and also drive fluids, through overpressuring to sites of deposition. It is not expected that significant movement occurred on the basement faults during this event. Late dextral movement of the basement faults during NE-SW contraction (D5) reactivated the

low-angle thrusts at Sunrise Dam producing normal movement and further dilation within the overall restraining stepover. This event is not significant at Wallaby Mine. Identification of an architecture resembling a large restraining stepover, controlling the co-genetic nature of both Wallaby and Sunrise Dam deposits, provides an explanation for Au deposition at the two known sites during the (D4b) event and also provides numerous potential sites of Au deposition in the region between them (Blewett et al., 2006).

The development of a 3D architecture within Laverton has enabled numerical modelling to be used to validate Shear and Volumetric strain developed on the constructed 3D geometries during the D4b and D5 events. A diagrammatic 3D model of a restraining stepover was built, and through numerical modelling code, a series of models were run to test the shear and volumetric strain which indicated that localisation occurred at both Wallaby and Sunrise Dam locations.

Miller and Nugus (2006) determined through 3D stress analysis that the most favourable segment of faults to reactivate during the D4b event were orientated at ~30° towards 310°. Mine scale 3D wireframes of the major shear zones in the Sunrise Dam deposit combined with the actual occurrence of gold determined from drilling, provided a suitable test case to compare this stress vector against. Wireframes of the major faults and isosurfaces of the gold occurrences (generated using the software package 'Leapfrog') were imported into the software package Gocad. Individual faults were then assigned orientation parameters within the ranges of 15°-45° dip and 290°-350° dip direction and then these properties were applied to the 3D fault surfaces. This process highlighted areas along the faults that were within the ranges specified by Miller and Nugus (2006). Analysis of this data indicated there is a ~100% relationship between known gold occurrences and fault segments with these orientations at Sunrise Dam mine. It also highlighted down dip extensions distal to the known gold occurrences with suitably orientated segments, which may provide additional targets during future near mine exploration.

**Key Words:** *3-D structure, Laverton, Eastern Goldfields Superterrane, gold mineralisation.*

## 3.12.1 Introduction

The Laverton region ranks second to the Kalgoorlie region for Au endowment and contains the world-class Sunrise Dam (>9 million ounces gold; Newton et al., 1998) and Wallaby (7.1 million ounces gold; Nielsen and Currie, 1999) mines. As part of the research into this region, the ***pmd****CRC* has adopted the use of three dimensional software packages to build 3D geological maps, to provide new insights into the region's architecture and fluid pathways, and to gain a better understanding of the characteristic detectable features of Au deposits.

The software package Gocad™ has been used to visualise a variety of mine and regional scale data to constrain the three dimensional architecture of faults and lithological packages. Significant industry involvement has enabled the compilation of a world class dataset to be integrated into the latest surface and subsurface interpretations of the Laverton region. This has allowed new insights to be made into the architectural elements of Au systems, a greater understanding of the formation of giant deposits, and predictions about additional targets.

Definition of regional architecture is highly dependent on detailed surface solid geology. Reinterpreted solid geology for the Laverton region was constructed using a combination of detailed industry geological data sets, historical regional geological interpretations, and industry potential field data merged with regional geophysical datasets to produce an improved regional coverage. A simplified version of this solid geology was used to aid in the construction process of the 3D map. The area also contains three regional seismic reflection lines and nine short industry lines. These data combined to provide significant constraints used in the interpretation of the three dimensional architecture in the Laverton region.

The structural history of the Laverton region is complex. Examination of map patterns in three dimensions, integrated with pre-existing (Swager, 1989; Hammond and Nisbet, 1992; Henson, et al, 2004; Henson, et al, 2006 and Blewett et al., 2004a; 2004b) and contemporary structural studies (Miller, 2006; Blewett and Czarnota, 2007), have defined regional deformation events that appear to have played dominant roles in developing a suitable architecture for mineralisation (Figure 3.12.1: for details see Blewett et al., 2008 this volume).

The construction of the 3D map combined with other geological techniques has defined architectural geometries that are suitable for statistical analysis using a variety of techniques. Mine scale structural analysis provided the basis for fault orientation analysis at camp to regional scale. These techniques have provided spatial targeting at a range of scales. 3D geometries were also tested, using numerical modelling code, on a generic model depicting a restraining stepover, which provided understanding of shear localization and dilation under a range of different stress vectors.

### 3.12.2 Regional fault orientation and granite/ gneiss domes

The solid geology map of the EGST clearly depicts domes on both the small and large scale. Regionally, the overall architecture displays an elongate NNW-trending dome and basin geometry, although these geometries are clearly complex and in many locations truncated by variably orientated late-stage faults. Many of the domes in the upper crust have been attributed to thrust stacking (Swager, 1997), but they may equally be interpreted as granitic intrusions (laccoliths) coeval with deformation (Henson et al., 2005).

The EYC has two distinctly different structural grains: the first is a series of relatively linear, north/ northwest (NNW) trending shear zones that dominate the tectonic grain. The second is a series of less continuous, broadly N- to NNE-trending, sigmoidal to linear shear zones, which commonly merge with the NNW-trending shear zones. To illustrate the relative importance of these trends regional and camp scale data were analysed to understand the temporal and geometrical relationships to major gold deposits, with the Laverton area being the focus of this paper.

The deformation history of the Kalgoorlie and Laverton regions is inferred to be comparable (Blewett and Czarnota, 2007; Figure 3.12.1), although the way these events interact with the 3D architecture is quite different. This is mainly attributable to differences in the orientation of major shear zones within each region and the location of large coherent granite/gneiss domes. The following discussion will not analyse the fault complexity at a small scale but highlight the gross 3D architectural variations of the highly mineralised regions within the EGST with a focus on the unique architecture within the Laverton region.

The Kalgoorlie region is dominated by long linear ~NNW-trending faults and shear zones that flank a series of granite/gneiss domes, including the Kanowna Scotia Dome and Mt Pleasant Dome to its ~northwest. To the south, the NNW-trending faults continue (or strike?) through a region of dispersed smaller granite domes. These NNW-trending faults have been the focus of numerous structural studies (i.e., Swager, 1997; Blewett, et al, 2004b; Weinberg et al., 2003; Blewett and Czarnota, 2007) and record multiple reactivations that will be not discussed here in detail. An additional feature of this region is the late structural overprint ($D_5$ Blewett and Czarnota, 2007)

| Blewett & Czarnota 2007 | | | Swager 1997 | Blewett *et al.* 2004b | Miller 2006 |
|---|---|---|---|---|---|
| Minor contraction | D7 | -- | | | |
| Minor extension | D6 | | Collapse | Late De | |
| Dextral transtension | D5 | | D4 | (D3 D3) | D4 |
| Sinistral transpression | D4b | | D3 | | D3 |
| | D4a | | D2 | D2b | D2 |
| Extensional doming (Stage 2 Late Basins) | D3b | | DE | D2e | |
| Extensional doming (Stage 1 Late Basins) | D3a | | | | |
| Upright folding and reverse faulting | D2 | | D2 | D2a | D1 |
| Extension with intermittent compression | D1 | | DE | De, D1, D1e | |

*Figure 3.12.1: A simplified structural history for the Laverton region (cf. Blewett and Czarnota, 2007).*

manifested as a series of region-wide, relatively small displacement, north to north-northeast trending dextral faults (i.e., Black Flag Fault) that offset the NNW-trending faults throughout the region.

In contrast to the Kalgoorlie region, the Laverton region is dominated by the large Mt Margaret Dome to the northwest and Kirgella Dome to the southeast. Major NNW-trending faults displaying similar kinematics to the NNW trending faults in the Kalgoorlie region, occur on the eastern and western sides on the domes but the central region (between the domes) is dominated by large linear to sigmoidal N to NNE trending faults. NNW-trending faults in the region display mainly late stage sinistral kinematics, while ~north trending faults (i.e., Childe Harold Fault) display sinistral movement overprinted by significant dextral movement ($D_{4b}$). In effect, the region has architectural affinities with a large restraining step-over during the $D_{4b}$ event (Au deposition at Wallaby and Sunrise Dam) and a releasing step-over during the $D_5$ event (Au event at Sunrise Dam; Figure 3.12.8).

Variations in the gross architecture were established prior to the sinistral ($D_{4b}$) and dextral events ($D_5$) and have resulted in significant variations in the 3D architecture of both regions. The resultant effect is that dilation and potential fluid flow can vary depending on the pre-existing architecture of granite/gneiss domes combined with the orientation of the major fault/shear zones and syn-deformation granite emplacement in each region which will be discussed later.

### 3.12.3 Stratigraphy

The Laverton region is geographically located in the central eastern part of the EGST and has been subdivided into several terranes and domains. These were first defined in detail by Swager et al., (1992) and have subsequently been modified by proceeding researchers following the same nomenclature. The Laverton region is situated across the Kurnalpi and Burtville terranes that are further sub-divided into the Murrin, Laverton, Edjudina, Linden, Duketon and Merolia domains (Cassidy, 2004).

Numerous researchers have described the stratigraphy of the region including: Honman (1917); Hobson and Miles (1950); Hallberg (1985) and Standing (2007). These studies, combined with geochronology data (Blewett and Czarnota, 2007; Cassidy, et al, 2002) have provided a basis for this study. Laverton has comparable age units in the youngest stratigraphy (i.e., 'late basins') to that of the Kalgoorlie terrane but there are significant differences in the older stratigraphic units. Laverton stratigraphy is broadly defined by a ~2800Ma mafic/ultramafic sequence overlain by a ~2715Ma intermediate volcanic sequence, that is overlain by siliciclastic basin sequences (e.g., Granny Smith basin and the Wallaby Conglomerate), and intruded by temporally and chemically distinct suites of felsic to mafic intrusives (Standing, 2007). A significant unconformity occurs between the deposition of the siliciclastic basins and the intermediate volcanic sequence of ~25 Ma indicating there was either a period of non-deposition or significant erosion. Possible evidence for non-deposition lies in the underlying ~2715 Ma intermediate volcanic rocks that preserve a volcanic edifice at Sunrise Dam deposit. If deposition had occurred directly post 2715 Ma volcanism the processes that enabled preservation of the volcanic edifice should have also preserved post 2715 Ma sediments in such an environment, although there are currently no data supporting the occurrence of any units prior to the Granny Smith Basin sequence deposition. This stratigraphic sequence is significantly different to the Kalgoorlie terrain which records significant deposition of felsic volcaniclastic sequences (i.e., Black Flag Group) during this time period.

The youngest units in Laverton defined using detrital zircons, are the 'late' siliciclastic basins. These basins lie unconformable over a variety of lithological units within the stratigraphic sequence. The depositional environments relating to basin formation has been the source of much debate varying from: 1) remnants of a region wide basin (Krapež and Barley, 2007), 2) perched basins developed in a fold and thrust belt (Blewett et. al., 2004b) to rift basins (Hallberg, 1986). There are two distinctly different types of basin sequences. One forming linear geometries (i.e., Mt Lucky Conglomerate) and a second type, the Wallaby Conglomerate, that raps around the southern margin of the Mt Margaret Dome. The Granny Smith Basin sequence covering the central part of the Laverton region is of comparable age to the Wallaby Basin with an age range of 2664±6 Ma to 2673±5 Ma (Standing, 2007). Additionally, outcrop does not allow absolute stratigraphic relationships between the basin sequences to be determined. The previously described linear and arcuate basin geometries are implied to have formed at different

times; however they could have equally developed during a single extensional event, where their geometries are controlled by proximity to domes.

Regional observations indicate linear basins are generally situated in the central parts of the greenstone succession and proximal to regionally extensive anastomosing faults. In contrast the 'late basins' that form proximal to domes generally mirror the dome perimeter and commonly have proximally sourced detritus (granite clasts) (Krapež and Barley, 2007). The extensional processes that gave rise to the formation of different coarse clastic basins may be explained by differences in accommodation space. It is proposed here that accommodation spaces were generated by conventional normal faults in the central parts of the greenstone belts, developing linear basins, while the faults (and accommodation) proximal to the granite/ gneiss domes were driven by inflation during the introduction of additional granites into the central parts of pre-existing granite batholiths and/ or extensional unroofing during the $D_3$ event. This process has been shown to develop low angle faults around batholiths that form topographic highs and the deposition of proximal coarse clastic material in regions formed by the process of core complexing. A composite example of both basin types occurs within the Penny Dam Conglomerate, which displays an overall linear NNW trending geometry that on the northern boundary raps around the nose of the underlying granite in a similar way to the Wallaby Conglomerate.

In summary, even though there is a possibility for two temporally distinct basins (linear and arcuate shaped) there are no geochronological evidence to support this hypothesis in the Laverton region. In contrast, and more probably, the basins are temporally contemporaneous for the reasons previously described.

### 3.12.4 Deep tapping faults (fluid pathways lower crust)

Previous researchers have noted that deep crustal-penetrating faults are spatially associated with giant mineral deposits (Goleby et al., 2003). These researchers implied that the source of mineralising fluids (and, possibly the gold) was deep, migrating via permeability pathways associated with these faults into upper crustal areas, where the gold was deposited in suitable structural and lithological sites. One such east-dipping fault zone is well imaged in the seismic reflection data within the Laverton region. The regionally acquired 01AGS-NY1 seismic reflection line clearly displays a significant shear zone described as the Laverton Tectonic Zone (LTZ), extending down to the Moho. This shear zone is interpreted to have a NNW trend and a strike extent from the northern to the southern craton boundaries. Further evidence of the LTZ can be imaged on both the 01AGS-NY2 (proximal to Wallaby Mine) and 01AGS-NY4 (proximal to Sunrise Dam Mine) seismic reflection lines (Figure 3.12.2). The

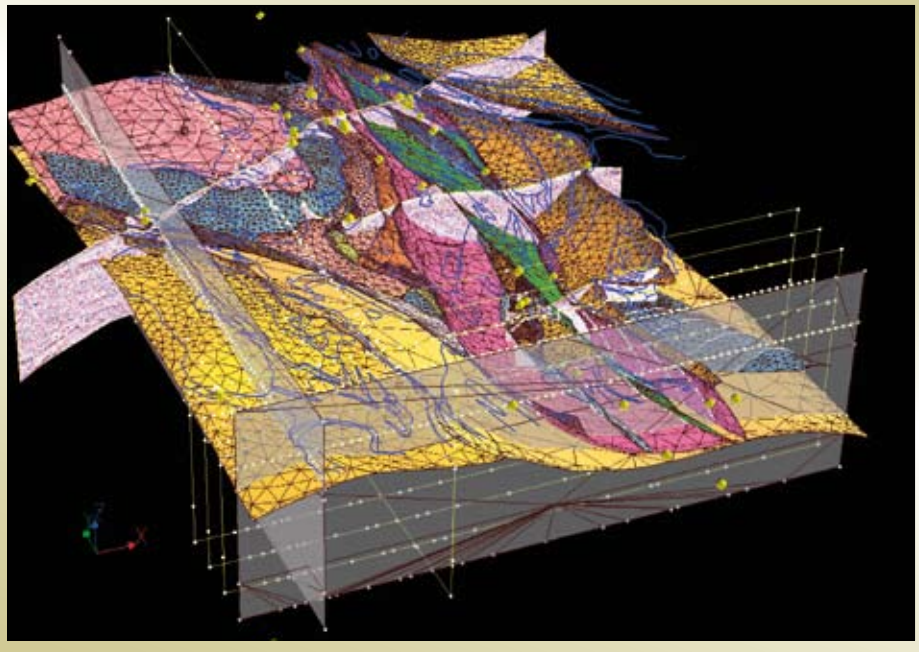

*Figure 3.12.2: 3D Gocad image showing the generation of lines from the intersection of 3D fault surfaces and the location of structural cross-sections.*

LTZ delineates the bulk of mineralisation in the Laverton region, with Sunrise Dam, Wallaby and Granny Smith deposits occurring within the zone. A series of faults delineating the LTZ at surface display a complex array of interconnected often sigmoidal geometries in plan view (Figure 3.12.3). The three dimensional geometry of these faults indicate that they have a variable dip (sigmoidal) and they sole at depth into one large crustal detachment that penetrates (as the LTZ) to the Moho (Figure 3.12.4). It is these deep structural features that provides fluid/melt pathways from the lower crust/mantle that can be further focused into suitable sites within the upper crust. Additionally, the LTZ records multiple reactivations, indicating the propensity of the crustal penetrating shear zones to focus shear stress during tectonic events.

## 3.12.5 Constraining the 3D architecture

Construction of the 3D map of the Laverton region followed a series of processes to constrain the 3D architecture. The initial phase involved both industry and academic involvement to produce a new solid geology map, constrained using both outcrop data and industry drill hole data. When building the 3D map, the solid geology map acted as a foundation for most of the geological interpretations, providing a link between the geology of a region and its geophysical attributes. It was important to construct a solid geology that contains an appropriate level of complexity to comply with the outputs needed within the final 3D map. It is also important to note that this process is constrained by software and hardware

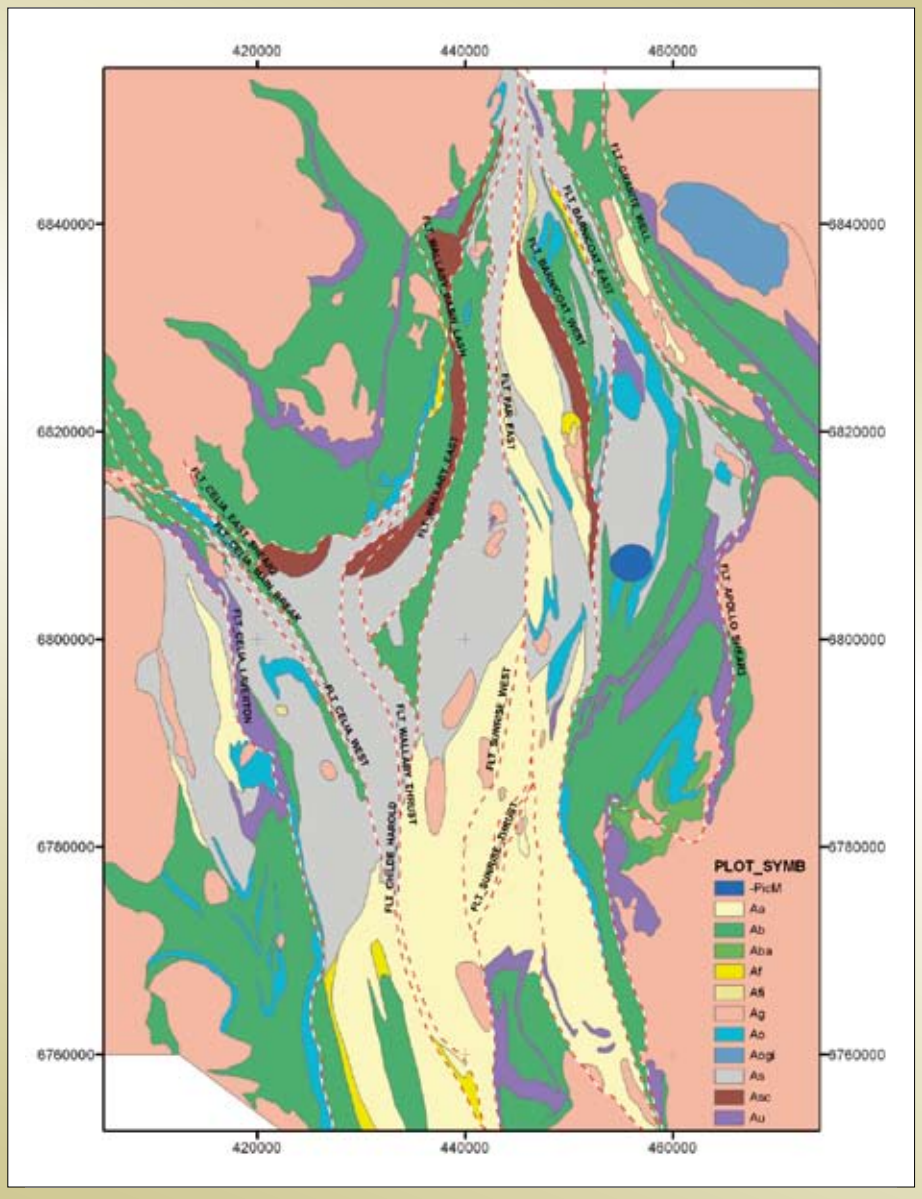


*Figure 3.12.3: Solid geology map used in the construction of the 3D map. MGA, GDA 94.*

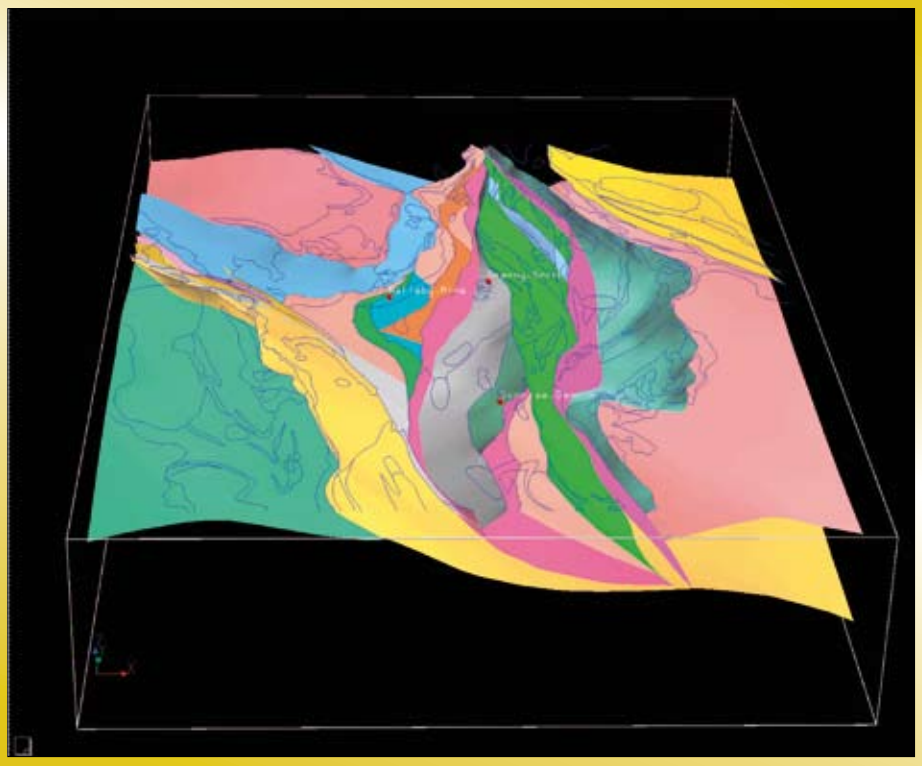

*Figure 3.1 2.4: 3D Image looking north, showing the regional faults and the locations of Wallaby Mine (red dot, left), Granny Smith Mine (red dot, right) and Sunrise Dam (red dot bottom).*

size limitations that will inhibit the construction process if exceeded.

3D maps are becoming common place in academic research and company exploration and resource definition processes. They provide a suitable medium in which multidisiplinary data can be stored, displayed and interpreted. This 3D medium allows all spatially referenced data to be viewed in absolute x, y and z coordinates, and significantly improves our understanding over that obtained using a traditional 2D GIS package.

The Laverton region contains three ~east-west orientated deep seismic reflection lines (01AGS-NY1, 01AGS-NY2 and 01AGS-NY4) and several high resolution seismic reflection lines located around Wallaby and Sunrise Dam mines that are currently restricted by confidentiality agreements and will not be discussed in this paper. The 01AGS-NY1 seismic reflection line was jointly sponsored by Geoscience Australia and the Geological Survey of Western Australia, in conjunction with the Predictive Mineral Discovery Cooperative Research Centre (***pmd*CRC***). Acquisition of the 01AGS-NY2 and 01AGS-NY4 lines occurred under the auspices of Geoscience Australia and the Minerals and Energy Research Institute of Western Australia (MERIWA), involving AngloGold Ashanti, Placer Dome and the University of Western Australia.

Both regional and company depth migrated seismic reflection lines were used to constrain the sub-surface geometries. The software package Gocad™ was used to view and interpret segy seismic data in three dimensional space; initially providing a framework to constrain the faults at depth. The preference of land seismic lines to follow existing roads (for environmental reasons) means that many of the surface traces are not straight. Reflections imaged on a curved seismic line can only be taken in their true context if viewed in their absolute geographic location. Example: A curved reflection, interpreted from a paper copy of the seismic (an unfolded curved seismic line) could be viewed as a fold. This feature may be an artefact of unfolding the line and, in fact, it could be generated by an oblique intersection of a planar structure. For this reason it is highly beneficial to view and interpret seismic lines in their true geographic locations. The 3D medium allows all seismic data, combined with additional data to be viewed and compared spatially, providing better integration of the different data sets in the region.

The three ~E-W orientated regional lines (01AGS-NY1, 01AGS-NY2 and 01AGS-NY4) are ~orthogonal to the

region fault trends enabling good correlation between individual surface fault traces and seismic reflections. Seismic reflection data provides a tool to follow the surface trace of faults into the third dimension. The position of major regional faults was interpreted on the three dimensional seismic reflection surfaces to provide an initial framework for the construction of three dimensional fault surfaces. By using the surface fault trace and the interpreted sub-surface projection of that fault, derived from the seismic reflections lines, a series of three dimensional fault surfaces were constructed by extrapolating between constraints (Figure 3.12.5).

Potential field data were used as an additional tool for interpreting the sub-surface geometries. Initially structural cross sections were constrained using structural readings and lithological contacts to provide a geologically controlled framework. Further depth constraints were provided by applying the potential field modelling software ModelVision™. This technique was applied to validate depth and dip constraints based on gravity data, in conjunction with the constraints derived from seismic reflection data (Figure 3.12.6). The combination of these data provided constraints for building the regional 3D objects and where possible these was analysed in conjunction with mine scale 3D objects to enable linkages with the structures associated with mineralisation.

### 3.12.5.1 Cross-sections

Rock relationships combined with a broad stratigraphic column (described previously) were used to provide a framework for the construction of serial cross-sections. Surface fault traces derived from the solid geology map were combined with fault constraints obtained directly from depth migrated seismic reflection lines in 3D space, to provide constraints for the 3D fault surfaces. These were linked between seismic lines to constrain the geometry of faults at depth and their spatial relationships to linking faults. By initially constructing 3D fault surfaces, a geometrical 'skeleton' framework was established, whereby lithological units were added later within the fault framework.

The 3D faults were used to produce a series of lines at the intersection of the 3D faults and the location of the serial cross-sections (Figure 3.12.2). This process provided the sub-surface geometry of faults along each E-W section ready for the interpretation of lithological units. The fault geometries were exported from Gocad ™ (once rotated through 90°) into ArcGIS as .dxf files and overlain on the solid geology map at the spatial location of each cross-section to enable direct correlation between the sub-surface fault geometry and the distribution of lithological packages within the solid

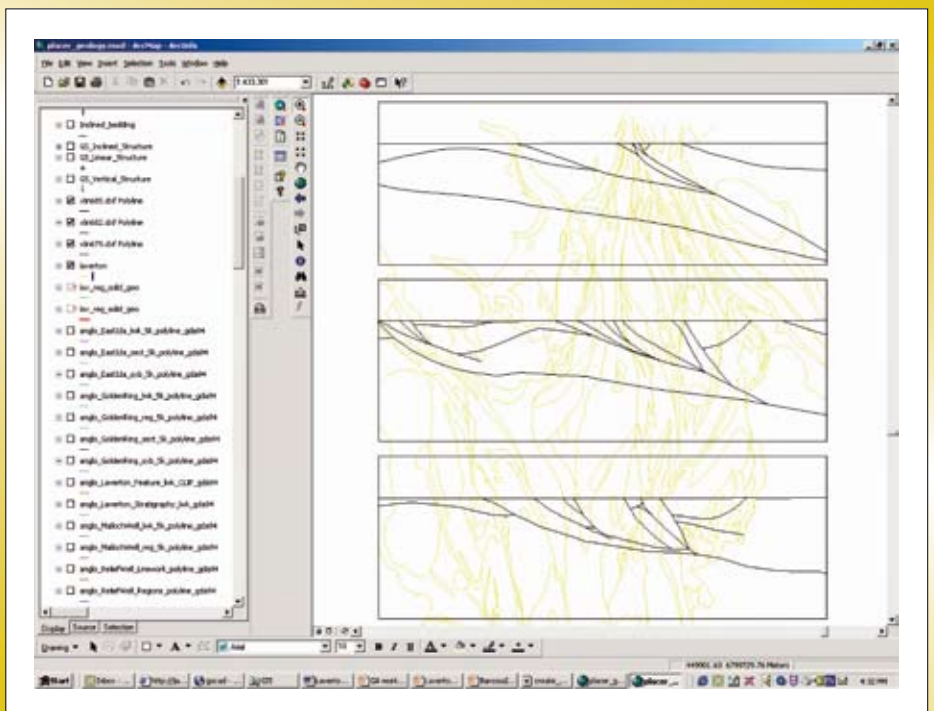

*Figure 3.12.5: Image from ArcGIS showing the imported fault traces spatially located on the solid geology linework.*

geology (Figure 3.12.5). In this study nine E-W orientated structural cross-sections were constructed, based on the spatial distribution of lithologies, the stratigraphy and structural readings along each profile. Structural cross-sections were then imported into ModelVision™ for validations against the potential field responses on each of the nine profiles using the following procedures (Figure 3.12.6).

### 3.12.5.2 Gravity data modelling

In interpreting subsurface geometries or in validating structural settings potential field data modelling plays an important role (Direen et al., 2005; Betts et al., 2003, Ayarza and Martínez Catalán, 2007). With the aid of commercially available software, such as ModelVision™ it is possible to generate interactively 2D or 2.5D model sections via forward modelling the potential field data. Note that the difference between 2D and 2.5D is subtle. A 2D body essentially represents a body with infinite strike length whereas a 2.5D body fits somewhere between 2D and 3D structure, which implies the finiteness of the strike length of the body. In practice, the body with a strike length 5 to 7 times longer than the largest remaining dimension of it is considered 2.5D body; the body with even longer strike length will be considered as a 2D body. In the present context we consider the case of 2.5D forward modelling of residual Bouguer anomaly of gravity data, where the geological units are defined as homogeneous polygonal prisms with appropriate density values and with strike length approximately 5 times larger than the largest of remaining dimensions of the body. Interactive forward modelling may be viewed as an inverse modelling in a crude way where, with a known property value a causative body can be altered till one attains a satisfactory fit between the computed responses and the real data value. Although the measure of fit can be quantified through a root mean squares (RMS) error, in most occasions, eye ball estimation for fitting the data is a standard to an interpreter. The merits of such interpretation technique are:

- Starting with *a priori* geologically conceived architectural settings it is possible to build a model

*Figure 3.12.6: Potential field modelled cross-sections in the Laverton region. Northing location displayed on each section.*

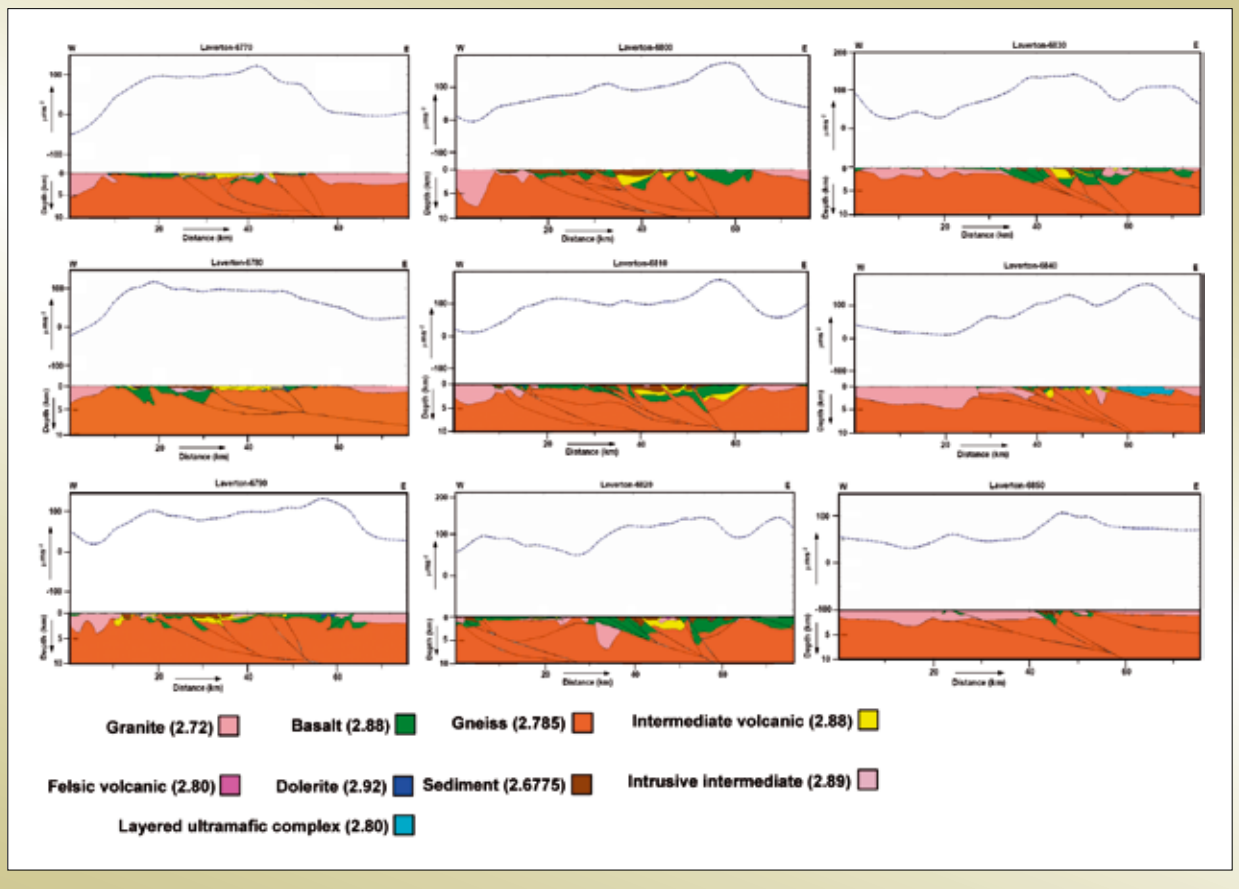

that is at least consistent with the potential field data and that helps to acquire geological insights through visualisation;

- The interactive approach allows interpreter to be cognisant of geological constraints;
- It helps in validating the inversion model that has been generated via automated inversion procedure and,
- A series of such sections obtained in parallel and in sequel would provide a tentative 3D structural setting of the subsurface.

The successful exercise of 2.5D forward modelling of the residual Bouguer anomaly of the gravity data of Laverton region depends strongly on two components, such as (1) the generation of high quality residual Bouguer anomaly map of gravity data and (2) appropriate density values of the rock types in the area.

A high-quality residual Bouguer anomaly map was generated using a model-based anomaly filtering technique (Roy et al., 2006). This technique identifies the domain of interest (DOI) and its physical extents, as well as the density distribution of the residual anomaly. The response generated due to density distribution outside the DOI is the regional anomaly (known as the regional). Once the regional gravity anomaly was computed it was removed from the total gravity anomaly to obtain a residual Bouguer gravity anomaly. Interestingly, we have observed that the model-based anomaly separation technique improves the quality of the residual anomaly substantially compared to other conventional approaches, such as spectral methods, least-squares technique, upward continuation method etc (Roy et al., 2006).

The second major component in 2.5D forward modelling is the density values of the rock types. For rock property values we rely on the published literature (Bourne, 1993) and unpublished reports (Barlow, 2004). We identify major rock types and use statistical methods wherever possible, in selecting density values for the rock types mapped in the area.

The interactive forward modelling approach used templates that are overlayed below the gravity profiles. Such templates, as discussed earlier are made by interpreting reflection seismic data and structural mapping from the outcrop. Therefore, our forward model is well constrained with the existing geological evidence of rock type and structural control of the region. We have modelled nine E-W trending profiles starting from a distance of 6770 km North to 6850 km North with an interval of 10 km (Figure 3.12.6). The gravity anomaly values are expressed in SI unit ($\mu ms^{-2}$). The vertical exaggeration of the sections is kept at 1:1 with the horizontal distance. Note that each of the nine profiles demonstrates excellent agreement between the observed data and the computed response, demonstrating that the proposed architecture honours the independent gravity data.

### 3.12.6 Structural and lithological interpretations

The following interpretations are based on multidisciplinary datasets and prior understandings within the Laverton region. Additionally many of the fault names are based on the 3D map generated within this project and may sometimes differ from faults or fault segments published elsewhere.

#### 3.12.6.1 D1

The earliest geodynamic process operating in the Laverton region was one of broadly E-W extension. It was at this time that the dominant ~NNW and ~N grains were developed via normal faulting. The NNW trend of the major shear zones can also be imaged in the regional Sm-Nd model ages (Figure 3.12.7; Champion and Cassidy, 2007). These data represent the distribution of different crustal ages and therefore indicate that the earliest architecture probably developed with a NNW trend that was subsequently overprinted by the ~N to NNE trending shear zones, which is not strongly represented in the Sm-Nd data although there is a trend similar to this orientation recorded in the Youanmi Terrane. The development of the NNW trend produced the first initiation of crustal penetrating shears. One such shear is visible in the 01AGS-NY1 seismic reflection line as an east dipping shear, into which numerous faults described as the LTZ in the Laverton region sole into. It is interpreted that development of the NNW trend preceded the N to NNE trend, producing a series of fault trends (Figure 3.12.8a), including the Granite Well Fault, Celia Fault, Celia West Fault, Celia Main Break Fault that are surfaces within the 3D map. This extensional event also formed a series of low angle shears including the first order 'lashes' 1 and 2, the

Celia 'lash' and probably the Wallaby lash developed around the Mt Margaret dome and Apollo Shear the forms on the boundary of the Kirgella Dome. These lashes were in some cases reactivated and modified during later events.

The ~N to NNE trend was developed when σ3 rotated clockwise to more ~E-W, superimposing a series of en-echelon faults linking between the NNW trending faults (Figure 3.12.8b) These faults are generally ~N to NNE trending, including the Childe Harold Fault, Far Eastern Fault, Barnicoat East Fault and the ~N-S trending Chatterbox Shear that is inferred to extend under the Wallaby Conglomerate at Wallaby Mine. All of these faults post date the previously mentioned faults and shear zones developed on a more NNW trend. Geometrical relationships can be observed in the

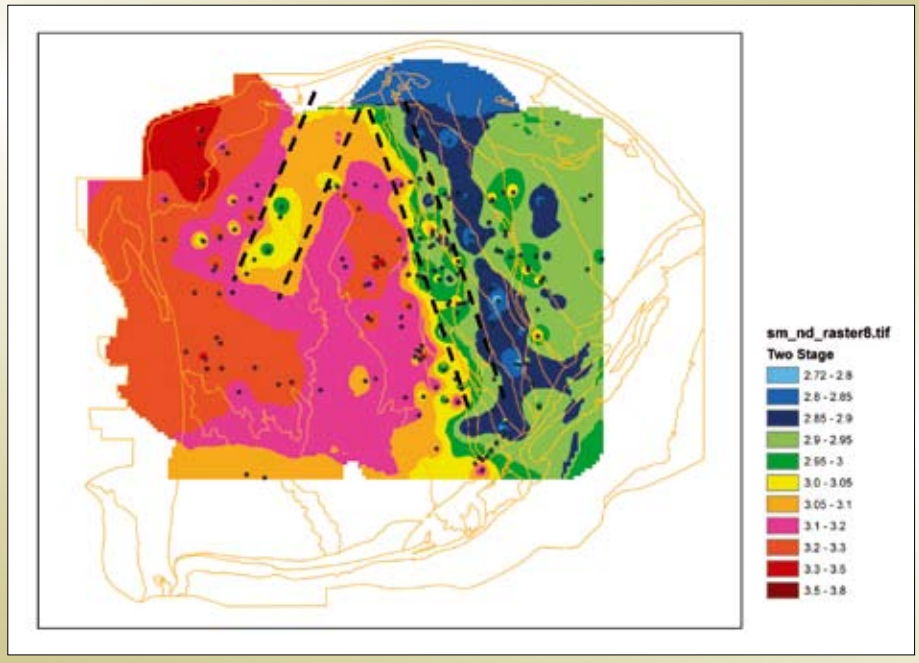


*Figure 3.12.7: Nd depleted-mantle model age map of the Yilgarn Craton. Image produced by griding Nd depleted-mantle model ages calculated from Sm-Nd point data from Champion and Cassidy (2007). Dashed lines delineate two distinct trends in the data; NNW and NNE.*

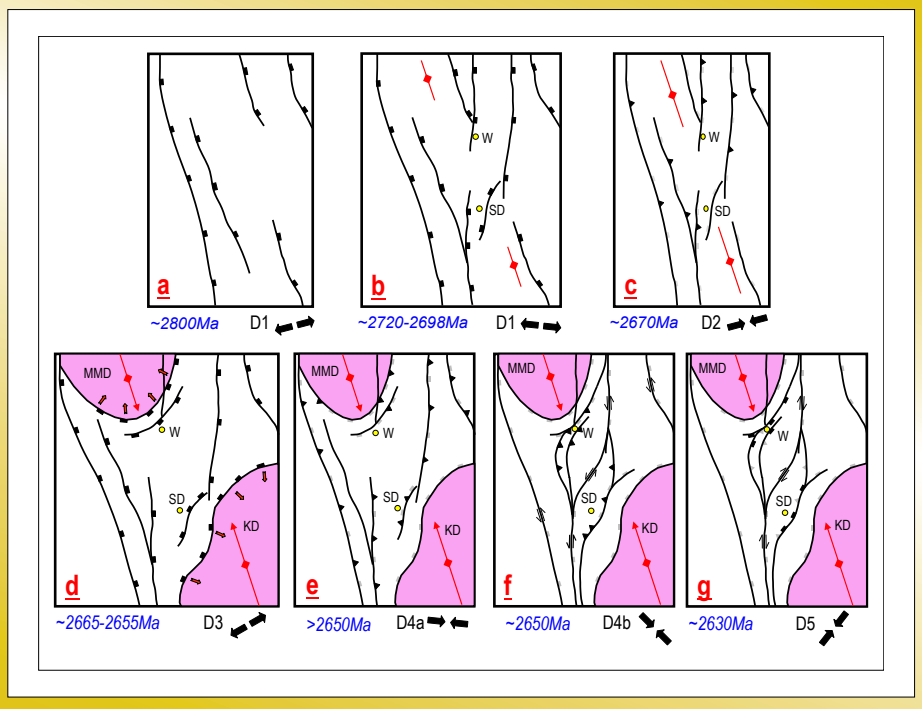


*Figure 3.12.8: Schematic diagrams depicting the gross structural evolution of the Laverton region during the $D_1$ to $D_5$ events. Yellow dots show the approximate locations of the Wallaby (top) and Sunrise Dam (bottom) mines. Approximate movement vectors are located on the faults. The abbreviated locations are as follows: Mt Margaret Dome (MMD); Kirgella Dome (KD); Wallaby Mine (W) and Sunrise Dam Mine (SD).*

interpreted cross-cutting relationships of the 3D fault surfaces. As a consequence of this extensional process intermediate volcanics (~2715 Ma) and High-Ca granites i.e., Mt Margaret Dome 2672±28 Ma (Cassidy et al., 2002) were emplaced into the upper crust producing local heterogeneities (Blewett and Czarnota, 2007) and the first initiation of broad open domes with a N-NNW trend. These heterogeneities controlled the orientation of faults, that at some localities initiating parallel to the igneous margins sympathetic with the regional stress vector. One example of a normal fault initiating at this time is the NNE trending Carey Shear that records syn-depositional movement when the ~2715 Ma intermediate volcanic rocks were emplaced (Mark Doyle pers. comm., 2007), that host the Sunrise Dam deposit. Additionally, a direct link can be drawn between chemically distinct High Ca granite suite of the Mt Margaret Dome with the porphyry's (i.e., Dolly porphyry) located within the Sunrise Dam mine indicating the existence of High Ca granite at depth beneath the deposit (Blenkinsop et al., 2007). Additional evidence for the development ~N to NNE trending faults at this time are within the Kalgoorlie region, where Komatiite thicknesses vary significantly across the ~N trending Alpha Island Fault (Figure 3.12.9) at Kambalda (Conners et. al., 2003). It is also important to note that NNE orientated faults are major controlling structures at both Wallaby mine and Lancefield mine although these structures are also sub-parallel to the margin of the Mt Margaret dome.

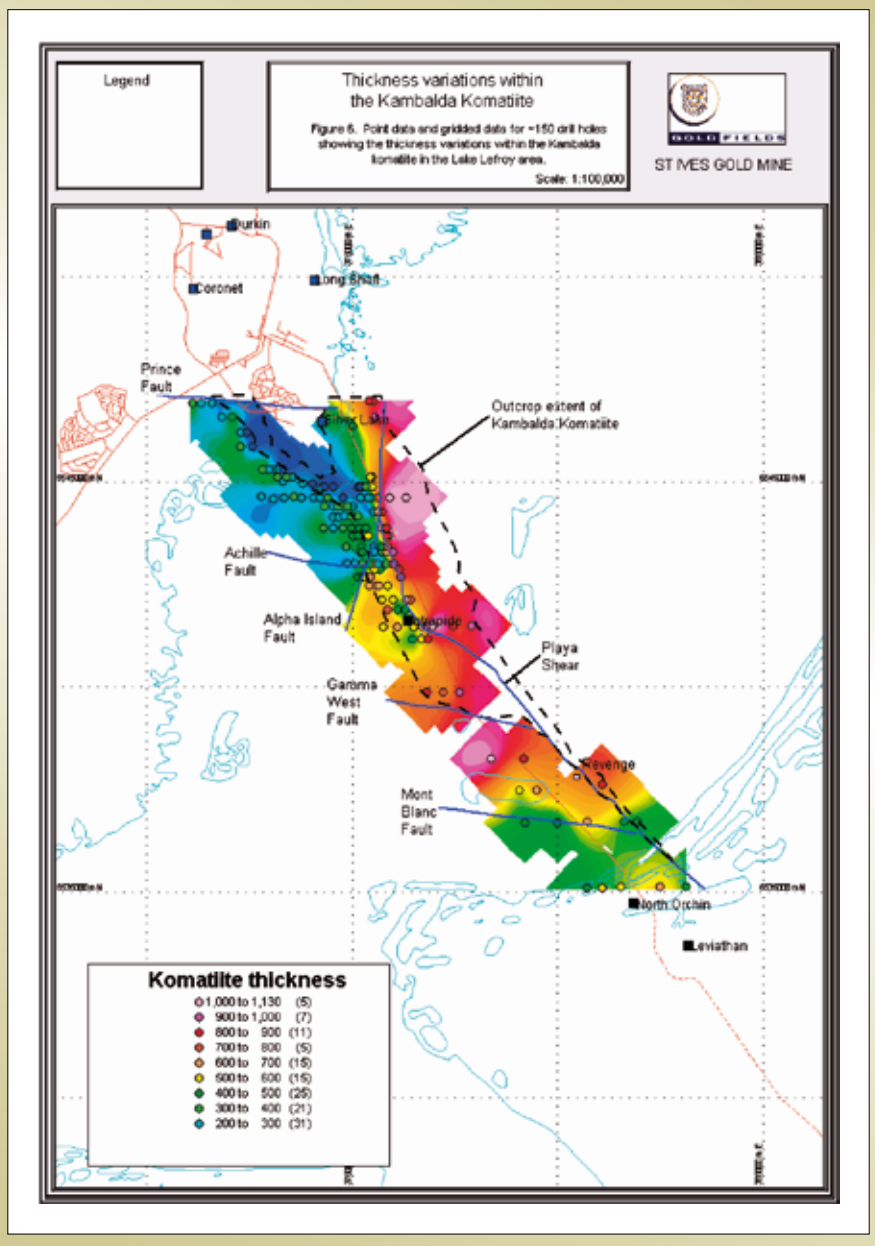


*Figure 3.12.9: Image from Conners et. al., (2003) showing significant komatiite thickness variations across the ~N trending Alpha Island Fault.*

The evidence for two distinctly different trends (1: NNW and 2: ~N to NNE) developing during $D_1$ is difficult to prove conclusively, although if correct would explain some of the regional fault trends that are reused during subsequent tectonic events.

### 3.12.6.2 D2

The ~E-W σ1 stress vector associated with this event is broadly coaxial to σ3 during $D_1$ (Figure 3.12.8c). As a result, minimal strike-slip shear occurred; instead a regional compressive stress vector dominated, producing ~N-S trending folding through sub-horizontal shortening, with thrusts developed on suitably plunging faults (nominally 30°). Pre-existing normal faults at high angle to a sub-horizontal σ1 did not reactivate due to normal stress overcoming shear stress; instead favouring the development of shortcut thrusts, or new thrust surfaces to accommodate crustal shortening.

### 3.12.6.3 D3a/D3b

A switch back to ~ENE-WSW extension reactivated previously developed NNW and N trending faults resulting in the development of significant topography (Figure 3.12.8d). At this time the Mt Margaret and the Kirgella domes developed into area of upstanding topography driven by the extension process, in a similar way to core-complexing. Although unconstrained by geochronology at these localities, the doming process was also probably driven by the injection of additional granites into their cores, as is observed in other composite batholiths in the EYC such as the Scotia-Kanowna Batholith recording ages of 2657±5 Ma, 2629±11 Ma and 2664±6 Ma (Cassidy et al., 2002). Uplift was accommodated around the domes by a series of faults paralleling the batholiths. The central area located between Mt Margaret Dome and Kirgella Dome operated as a depositional centre for the Granny Smith basin sediments, developing a series of ~N-S trending basins within an array of anastomosing shear zones.

The Wallaby Conglomerate is a coarse clastic sequence (Standing, 2007) lithologically resembling a 'late basin' and is preserved as an arcuate shaped basin around the SE margin of the gently south plunging Mt Margaret Dome. Its current geometry, in contrast with a classic 'late basin' (i.e., Kurrawang Basin), indicates that the basin would have preferentially developed during at least a local ~N-S extensional regime which has been described in detail by MacIntyre and Martin (2005), Williams and Whitaker (1993) and Hammond and Nesbit (1992, 1993). The basin is indistinguishable from the Granny Smith basin on geochronological grounds and field relationships do not enable stratigraphic relationships between the respective basins to be tested.

An alternative view is that the basins with linear geometry are temporally different to the arcuate basins (Krapež and Barley, in press; Blewett et al, 2008 and Czarnota et al, 2008) but there is little direct geochronological evidence to support this hypothesis. An alternative hypothesis to explain the different geometries of the two basin types is that they are temporally contemporaneous and their geometries are controlled by differential fault movement influenced by ascending granite/gneiss batholiths. Metamorphic studies indicate the abrupt juxtaposition of high pressure units against lower pressure units across some structures around the perimeter of the Mt Margaret Dome (Goscombe et. al., 2007). These metamorphic breaks are consistent with extension, exhuming high grade footwall material in the regions around the granite domes during this event. The central zone between the Mt Margaret Dome and Kirgella domes in contrast operated as a series of normal faults (~orthogonal to σ3) above an underlying detachment surface (Celia Fault). Relative movement and fault orientation would therefore differ depending on proximity to the large granite/ gneiss batholiths. It is proposed that these gross architectural differences produced significant variation in relative fault movement and that two completely different basin geometries were developed during the same event. These included: 1) arcuate basins around the granite domes as they rose relative to the surrounding terrane, which is reflected in structural observations of radial stretching lineations, produced in part by uplift and; 2) linear basins developing in the central region between the Mt Margaret and Kirgella domes that was instead influenced by the regional stress vector. Preservation of the arcuate basins proximal to domes would, however, be uncommon due to the environment having proportionally less accommodation space than areas distal to the rising domes. The two type-examples of arcuate basins are the Wallaby Conglomerate and the series of coarse clastic units that form on the SE margin of the Kanowna Scotia Dome. Although arcuate in shape

and paralleling the domes interestingly they both form on a broadly ~NNE trend which is the controlling direction of structures at Wallaby, Sunrise Dam and Lancefield deposits in Laverton. This trend is also recorded at Kanowna Belle deposit in the Kalgoorlie terrane (Figure 3.12.10). These observations imply that deposits proximal to large exposed granite domes are controlled by structures parallel to their margins while deposits distal to the domes will be preferentially controlled by structures orthogonal to σ3.

### 3.12.6.4 D4a

This event is characterised as an E-W stress vector producing upright regional folding, further tightening $F_2$ folds and thrusting on suitably orientated faults (Figure 3.12.8e). It also applies the first post-depositional deformation to the Wallaby Conglomerate and the Granny Smith Basin which is temporally linked to the mineralisation using U-Pb dating of monazite at Granny Smith mine (Scott Halley pers comm., 2007). Mineralisation occurs proximal to the contact between the Granny Smith Granodiorite and the Granny Smith basin sediments. This contact acts as a rheological contrast allowing dilation and mineralisation to occur close to the contact.

The Granny Smith deposit occurs in the footwall of the regionally extensive east dipping Far Eastern fault with unknown linking structures. Analysis of the E-W orientated 01AGS-NY2 seismic reflection line located close to the Granny Smith deposit images no significant structures. This may be a consequence of steep structures not being imaged using the seismic reflection technique. The lack of surface outcrop also hinders the identification of linking structures with the Far Eastern Fault directly to the east.

### 3.12.6.5 D4b

This NW-SE contraction event initiated both shear and normal stress on the pre-existing NNW and N to NNE trending structures (Figure 3.12.8f). The pre-developed architecture at this time was not dissimilar to current day architecture with the Mt Margaret and Kirgella domes fully formed and the region between them a series of volcaniclastic (intermediate volcanics ~2715 Ma) and siliciclastic basin sequences, including the Granny Smith Basin (2675±5 and 2663±5Ma; Brown et al, 2007). Low angle NNE trending faults developed during D3a/D3b and/or possibly D1 occur at both Lancefield and Wallaby locations. The NNE trending Carey shear underlying the Sunrise Dam deposit developed during $D_1$ (at 2715 Ma) and reactivated during D3a/D3b, while the Sunrise shear and its sub-parallel shears above the Carey Shear probably developed during D3a/D3b, although their development during D1 can not be ruled out.

The regional architecture during this event played a large part in the development of suitable dilation and sites of mineralisation. During the NW-SE contraction event the Kirgella and Mt Margaret domes operated as coherent units while the central zone between them focussed most

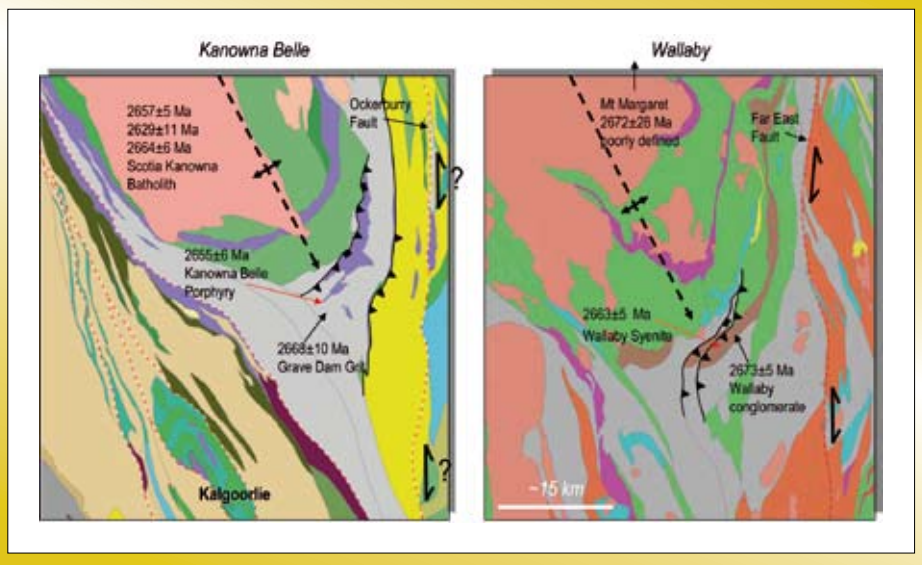


*Figure 3.12.10: Images of Kanowna Belle Mine in the Kalgoorlie region and the Wallaby Mine in the Laverton region. Display similar geometries and timing of sedimentary host rocks and mafic derived intrusives proximal to mineralisation. Ages from Cassidy et al (2002).*

of the shear stress. Shear stress was also focussed around pre-existing structures with a preference to the ~N to NNE trending extensional faults developed during the $D_1$ and $D_3$ events.

The event produced a significant proportion of the Au deposition at both Wallaby and Sunrise Dam mines at 2650±6 Ma (Salier et al., 2004). This event also signalled the emplacement of mantle-derived felsic intrusions (Cassidy et al., 2002; Miller, 2006a) in the region. The contribution of granitoids to the mineralising process is currently equivocal and will be discussed later in this paper.

In the Kalgoorlie region the Kanowna Belle mine displays similar architectural characteristics to Wallaby mine in two dimensional plan view (Figure 3.12.10). In contrast to the shallowly dipping structures (15–40°) at Wallaby mine, the controlling structure at Kanowna Belle is the steeply dipping Fitzroy Fault which was not favourably orientated to reactive during this event (D4b) and consequently does not record significant mineralisation at this time.

### 3.12.6.6 D5

This is a significant gold event with mineralisation occurring at Westralia, Transvaal, Keringal and Sunrise Dam deposits were the ~σ1 vector was NE-SW (Blewett and Czarnota, 2007). The event initiated region wide dextral strike-slip movement on N to NNE trending structures and oblique to thrust movement of NNW to NW trending structures (Figure 3.12.8g). As previously described, it is the belief of the author that the ~N to ~NNE trending structures were developed within the $D_1$ event as a series of extensional structures post dating the NNW trend. This pre-existing architecture provided structural weaknesses along favourably orientated structures where dextral movement was initiated during NE-SW contraction. Interestingly, there are only minor occurrences of conjugate structures (NE-E trending structures) associated with this event, which may also indicates that a heterogeneous distribution of structural trends existed prior to this event. It is not however implied that all ~N to NNE trending faults developed during the $D_1$ event.

The $D_6$ event directly post-dating is a post orogenic response to the $D_5$ event which produces region wide horizontal crenulations and is not attributed to any significant gold deposition (Blewett et al., 2008).

## 3.12.7 Fluid/melt focussing

### 3.12.7.1 Au deposition (Sunrise Dam and Wallaby deposits)

A significant stage of mineralisation associated with the $D_{4b}$ event can be linked temporally between the Wallaby and Sunrise Dam deposits. The $D_{4b}$ high arsenic alteration along the steep-dipping lodes at Sunrise Dam (WSZ, Watu) has been correlated with the sinistral-slip lodes at Wallaby. Xenotime and monazite U-Pb ages from the sinistral-slip lodes at Wallaby (2650±6 Ma; Salier et al., 2004), and the high arsenic Western Shear Zone at Sunrise Dam (2654±8 Ma; Brown et al., 2002) are within 1σ error of each other (Miller and Nugus, 2006). This period was also coincident with emplacement of mantle-derived felsic intrusions (Cassidy et al., 2002; Miller, 2006). These mantle-derived rocks are commonly spatially related with Au deposits (e.g., syenites at Wallaby, Mafic-type granites at Granny Smith) although the timing of such units indicates that they pre-date the mineralisation phases deposited during the $D_4$ and $D_5$ events. In some cases, igneous bodies can be imaged beneath Au deposits using seismic reflection data, although the precise genetic links to mineralisation at Laverton are equivocal using our current datasets. The contribution of granitoids to the main mineralising process is problematic and currently can only be qualitatively linked. The structural trap, however, is clearly delineated at the mine scale as a series of dilational structures and this study demonstrates that regional scale processes can be linked back to these geometries. Seismic reflection data on the 01AGS-NY2 line clearly images a region below the Wallaby deposit that has a seismic character consistent with a granitic source. The upper series of reflections defining this body are downward curving with the Wallaby Mine being located close to its apex. It is interpreted that this body forms the sub-surface extension of the Mt Margaret Dome extending under the Wallaby Mine. Sunrise Dam Mine is located near the western end of the 01AGS-NY4 seismic line and does not image a well defined 'granitic' body although felsic intrusions within the deposit display chemical affinities with the Mt Margaret Dome intrusives (Blenkinsop, et al, 2007) which are interpreted to be located at depth beneath Sunrise Dam mine.

Structural analysis across the region (Blewett et al., 2004a), and at the Wallaby and Sunrise Dam deposits

indicate that equivalent stress fields operated during the mineralisation phases within both deposits (Miller, 2006). These mine scale similarities raise interesting questions regarding the overarching regional architecture needed to produce a genetic link between both mines. Lithologically, Wallaby and Sunrise Dam are quite different. Wallaby is hosted within a conglomeratic unit, while Sunrise Dam is hosted within intermediate volcanic rocks. Structurally though, both deposits display striking similarities and more interestingly, the gross structures within the Wallaby Mine are the 'mirror image' of those within Sunrise Dam. Although structurally complex, the dominant through going structures are shallow 15–40° thrusts which can be identified in 3D map patterns (Figure 3.12.11), dipping to the NW at Sunrise Dam and to the SE at Wallaby Mine. Within both deposits numerous steep structures occur that are variably offset by the thrusts (for details refer to, Miller, 2006).

Both mines are separated by a large structural corridor which records both sinistral and dextral movement during its history (Blewett and Czarnota, 2007). In order to produce co-genetic deposits within an overarching structural framework, critical architectural elements must combine within a specific stress field. In an attempt to categorise a regional structure capable of linking both deposits, the current interpreted 3D geometries were compared with some analogue modelling of strike-slip scenarios, superimposed on early discontinuous 'extensional' faults. This architecture was first described by Chen et. al., (2001) who recognised the architectural relationship between NNW and ~N to NNE trending faults and their interaction with the large granite/gneiss domes. The structural model that best fits the current architecture is a restraining stepover within a sinistral strike-slip system (McClay and Massimo, 2001) (Figure 3.12.12).

In a comparison with this analogue model (Figure 3.12.12), two early extensional basement faults are reactivated during northwest-southeast contraction ($D_{4b}$) producing low-angle thrusts in a 'pop-up zone'. This architecture exists in the region between Wallaby and Sunrise Dam, where both deposits are located on the low-angle thrusts on opposing sides of a sigmoidal structure, produced by sinistral strike-slip movement. The process is further driven by the locations of the Mt Margaret Dome (in the NW) and the Kirgella Dome (in the SE) which represent large buttresses that focus the deformation in the zone between them. This process would provide significant dilation and also drive fluids, through overpressuring to sites of deposition (see Miller, 2006). It is not expected that significant movement occurred on the basement faults during this event. Late dextral movement of the basement faults (LTZ, which is a regional fault zone with late-stage dextral

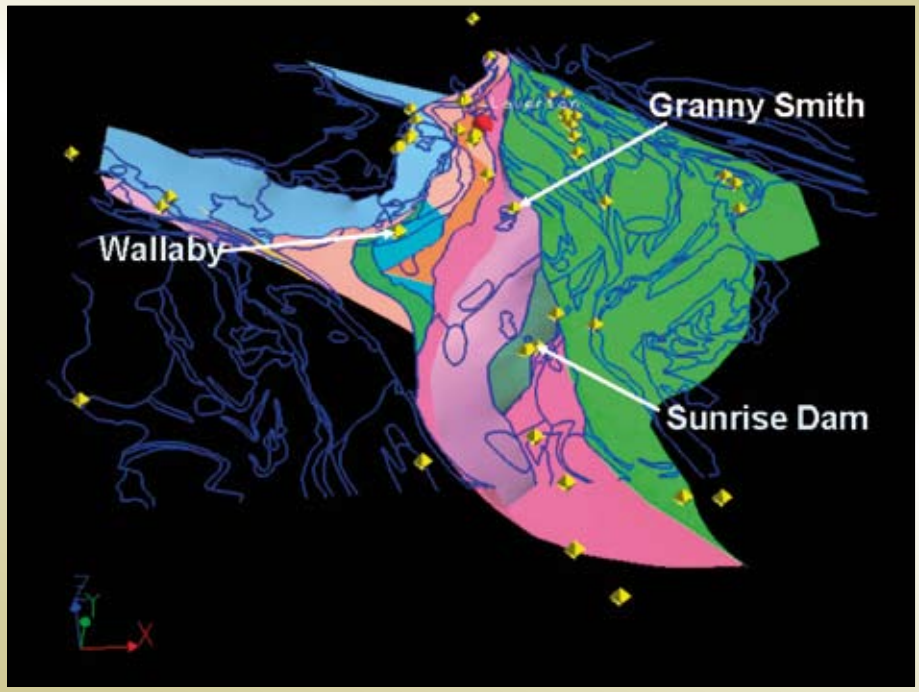


*Figure 3.12.11: Gocad image of the Laverton region looking north, displaying 3D fault surfaces. Opposing low-angle faults (thrusts) at Wallaby and Sunrise Dam sole into a central, steeper strike-slip structural corridor. Blue lines represent fault traces and solid geology outlines.*

movement) during NE-SW contraction ($D_5$) reactivated the low-angle thrusts at Sunrise Dam producing normal movement on shallow dipping structures and dextral movement on steep structures resulting in dilation. The Wallaby gold deposit is farther to the west of the LTZ. The $D_5$ dextral kinematics at Sunrise Dam are not observed at Wallaby (Miller, 2005). This also explains why Wallaby does not have a base metal association, nor does it contain the ultra high grade veins (with coarse visible gold) that occur at Sunrise Dam. This is a major difference between these two world class ore bodies that are located within 30 km of each other.

Identification of a mega structure (large restraining stepover) controlling the co-genetic nature of both Wallaby and Sunrise Dam deposits provides an explanation for Au deposition at the two known sites (Miller, 2006), but also provides numerous potential sites of Au deposition in the region between them (Blewett et al., 2006).

### 3.12.7.2 Porphyries

Mineralisation is often spatially associated with a proportionally high volume of porphyry intrusions when compared to the known un-mineralised areas.

*Figure 3.12.12: Diagram from McClay and Massimo (2001), displaying an analogue model of a restraining stepover within a sinistral strike-slip system. Both plan and section views are displayed. The similarity in geometry between this analogue model and the regional architecture at Laverton are striking.*

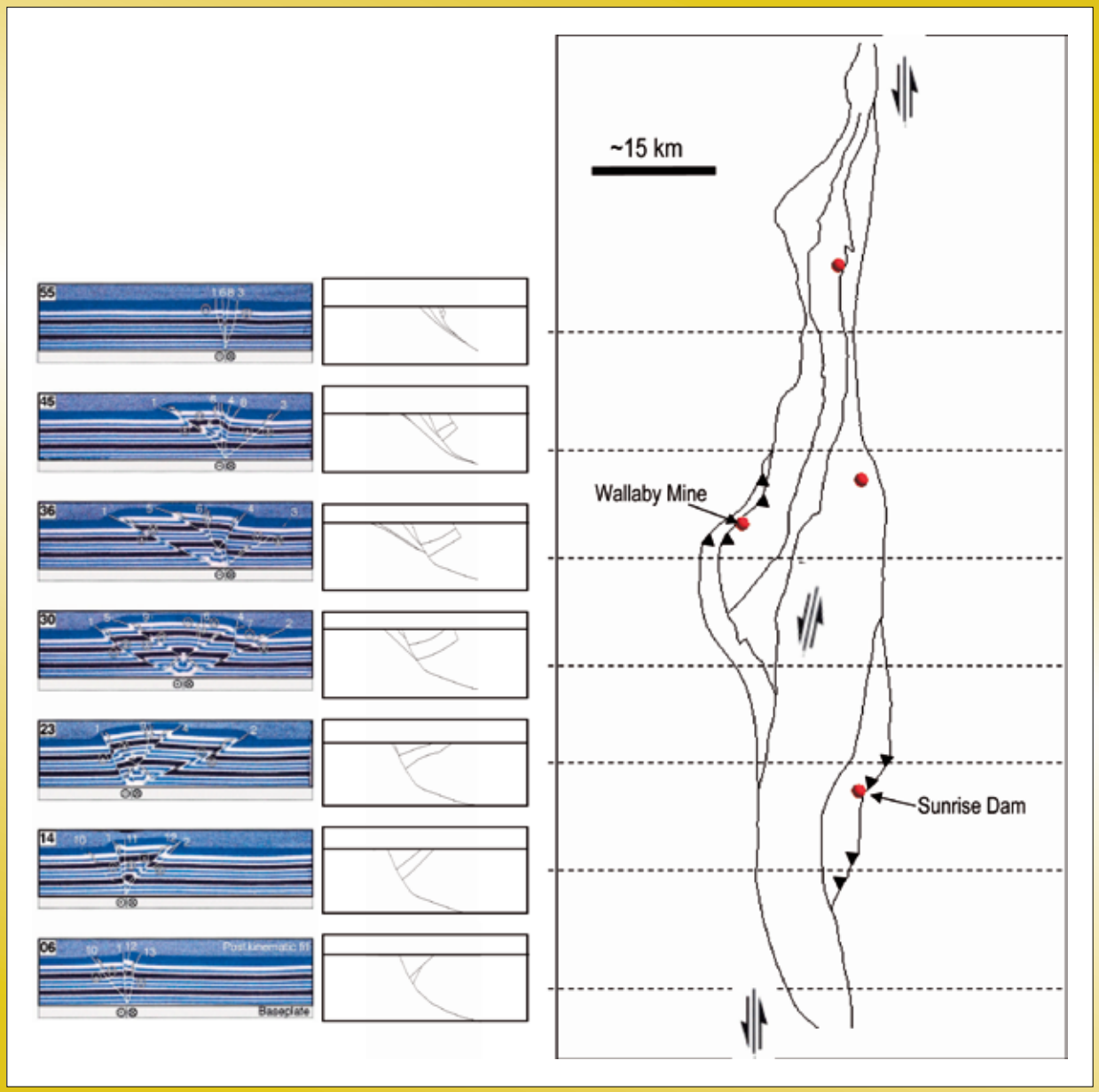

This observation may however, be a function of lack of exposure in those regions. Further work is needed to evaluate the significance of the empirical links between porphyry concentrations and their direct or indirect influence on mineralisation. That aside, several temporally and geochemically distinct generations of porphyries are recorded throughout a range of different deposits in the Laverton region.

The Wallaby deposit occurs in a pipe-like body of magnetite-actinolite alteration linked to the emplacement of a series of intrusions dominated by syenite (e.g., Salier et al., 2004). Debate on the deposit has focused on whether it is genetically a pluton-related deposit linked to the emplacement of the intrusions (e.g., Hall et al., 2001), or an orogenic-style gold system that has localised and overprinted the magnetite-actinolite pipe (Davis, 2000; Salier et al., 2004), with a clear time break between plutonism and gold mineralisation (Salier et al., 2004). All generations of veining within the deposit were determined to be associated with gold by Miller (2005). This includes a series of magmatic calcite veins that have previously been linked to oxidised fluids associated with the intrusions (Wall and Mason, 2001; Drieberg et al., 2004) which implies that at least one phase of gold was intrusion related.

At Sunrise Dam, the spatial coincidence between the main porphyry dykes (e.g., Dolly porphyry) and the D4b/D5 steep-dipping gold lodes (e.g., Cosmo, WSZ, Watu) is because they both exploited the same $D_1$ extensional shear vein trend. U-Pb dating indicates major gold mineralization was not genetically related to dyke emplacement (Brown et al., 2002).

### 3.12.8 Generic numerical models: results for models with a range of far-field stress orientations

A parallel project was established to validate the previously described geometries using numerical modelling code (Zhang et al, 2007). The process involved building a generic geometry similar to that of McClay and Massimo's (2001) stepover geometry, but also including the spatial and lithological parameters of the Laverton region. The model dimensions used in this example are 80 km x 70 km x 30 km thick and consist of three lithological units including a cover sequence, underlying greenstone sequence and granitic basement (Figure 3.12.13).

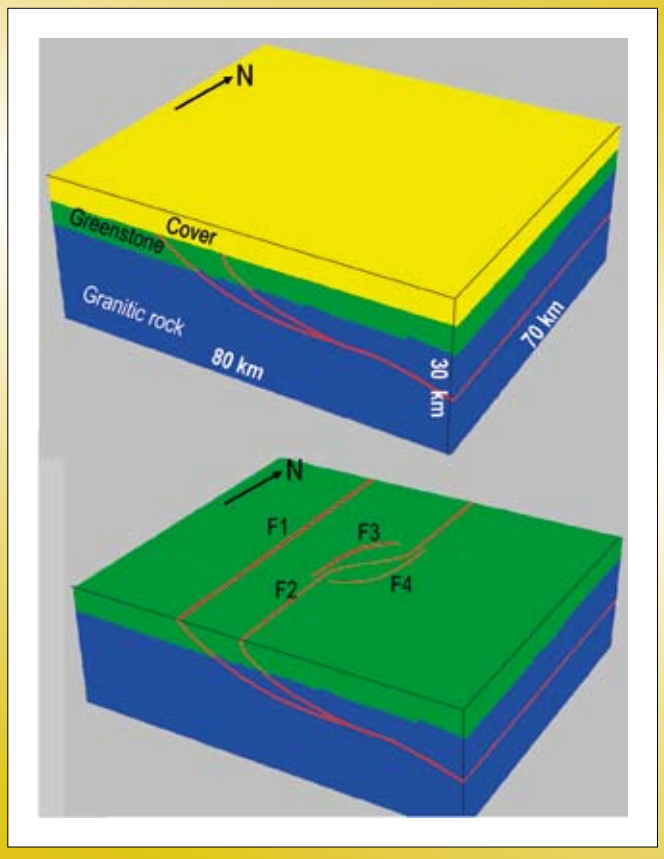


*Figure 3.12.13: Image of the initial model parameters including fault locations and lithological distributions.*

The structure of the numerical model represents a simplified version of the Laverton architecture (Henson et al., 2006) and consisted of a detachment fault intended to represent the Celia Fault (F1). Faults in the hangingwall of this fault included a central curved fault (F2) and two faults (F3 and F4) representing the jog. These faults form a complex stepover to resemble a linkage between the fault surfaces.

Once the mesh was constructed using the software PATRAN™, a series of numerical models were run, using the FLAC 3D code, under a variety of stress vectors to explore the regions of maximum volumetric and shear strain (Figures 3.12.14, 3.12.15, 3.12.16).

A wide range of possible contractional orientations from NW-SE to NNW-SSE ($D_{4b}$) seems to be clearly

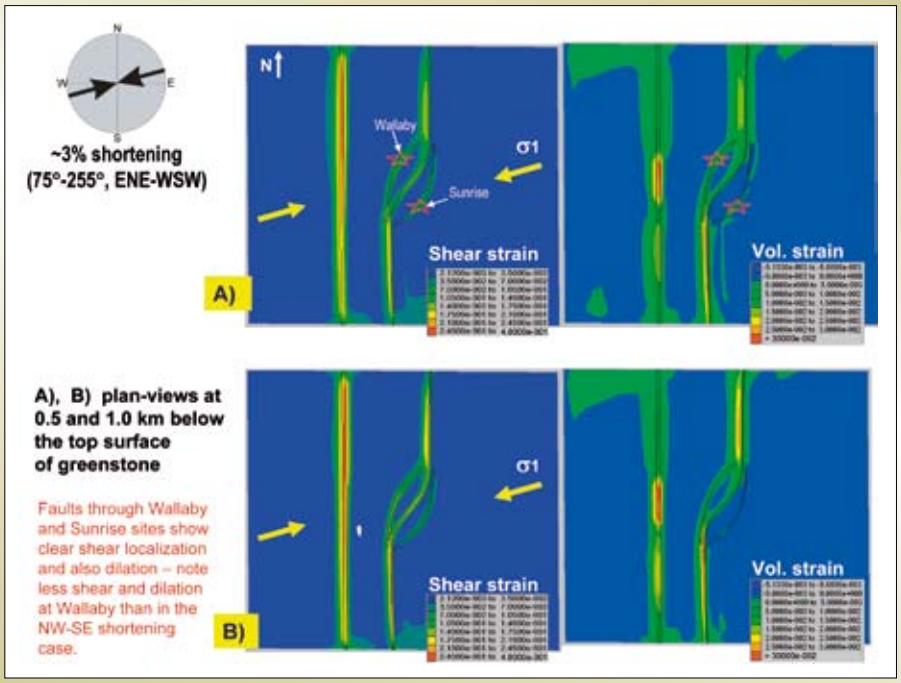


*Figure 3.12.14: Image showing the shear and volumetric strain occurring during a Nw-SE contractional event.*

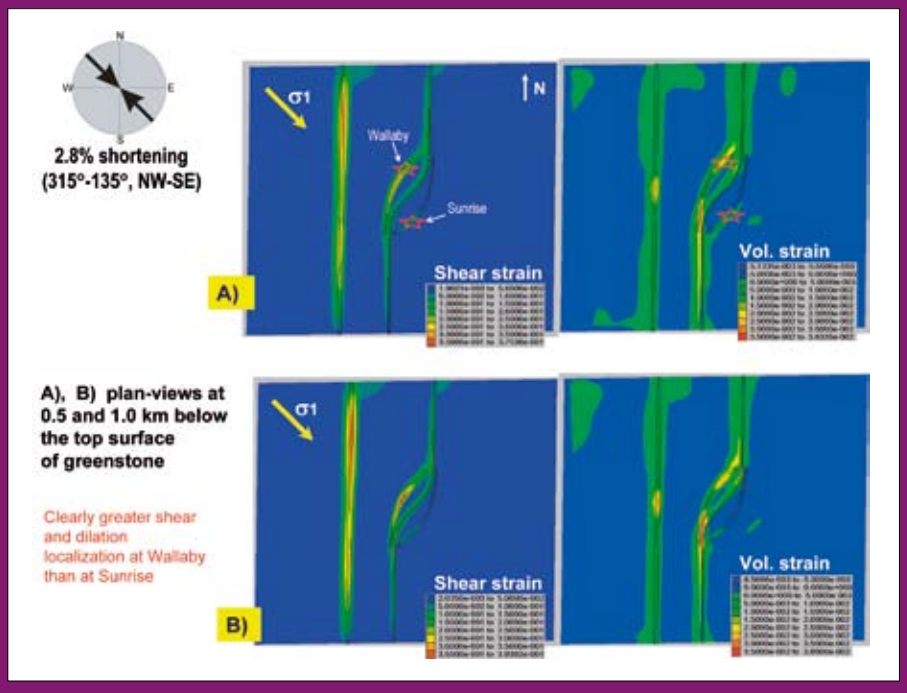


*Figure 3.12.15: Image showing the Shear and Volumetric strain occurring during a ENE-WSW contraction event.*

favourable for structural reactivation (shear and dilation) of the Wallaby system and mineralization. Sunrise Dam also displays some shear localization and dilation under such conditions ($D_{4b}$) but to a much lesser degree (Figure 3.12.14). An ENE-WSW shortening orientation (75 to 255°) led to enhanced shear and dilation at Sunrise Dam, although Wallaby shows weakened activities during this event. Shortening orientations around NE-SW ($D_5$) are unfavourable (Figures 3.12.14, 3.12.15). These models display a consistent spatial distribution between shear and volumetric strain localisation and gold distributions during the $D_{4b}$ and $D_5$ events.

The results from this modelling have demonstrated that a complex geometry can resolve favourable sites of volumetric and shear strain by applying a range of stress vectors (Figure 3.12.16) using 3D geometries. Further work will include the numerical modelling of actual 3D faults geometries extracted from the Laverton 3D map. This work is currently being undertaken and will provide more realistic geometries with real spatial context.

### 3.12.8.1 Painted faults

Detailed structural analysis of both Wallaby and Sunrise Dam mines has provided new insight into gold formation in the Laverton region. Mine scale structural analysis by Miller and Nugus (2006) at Sunrise Dam mine and Miller (2005) at Wallaby mine, provided the basis for the statistical analysis of 3D fault surfaces to ascertain preferential sites of fault reactivation/dilation during a NW-SE contractional event ($D_{4b}$) associated with significant gold deposition at both the Wallaby and Sunrise Dam mines (Figure 3.12.17).

Miller and Nugus (2006) determined through 3D stress analysis that the most favourable segment of faults to reactivate during the $D_{4b}$ event were oriented at ~30° towards 310° (Figure 3.12.17). Mine scale 3D wireframes of the major shear zones in the Sunrise Dam deposit combined with the actual occurrence of gold determined from drilling (Figure 3.12.18), provided a suitable test case to compare this stress vector against. Wireframes of the major faults and isosurfaces of the gold occurrences (generated using the software package 'Leapfrog') were imported into the software package Gocad. Individual faults were then assigned orientation parameters within the ranges of 15°-45° dip and 290°-350° dip direction and then these properties were applied to the 3D fault surfaces (Figure 3.12.18). This process highlighted areas along the faults that were within the ranges specified by Miller and Nugus (2006). Analysis of the data indicated there is a ~100% relationship between known gold occurrences and fault segments with these orientations at Sunrise Dam mine. It also highlighted down dip extensions distal to the known gold occurrences with suitably orientated segments, which may provide additional targets during future near mine exploration.

In an attempt to test the importance of fault orientation regionally, the same principles were applied to the regional scale 3D faults in the Laverton region (Figure 3.12.19). Regional scale faults were constrained using both seismic reflection data and to a lesser extent potential field data. These data provided a suitable framework to apply the

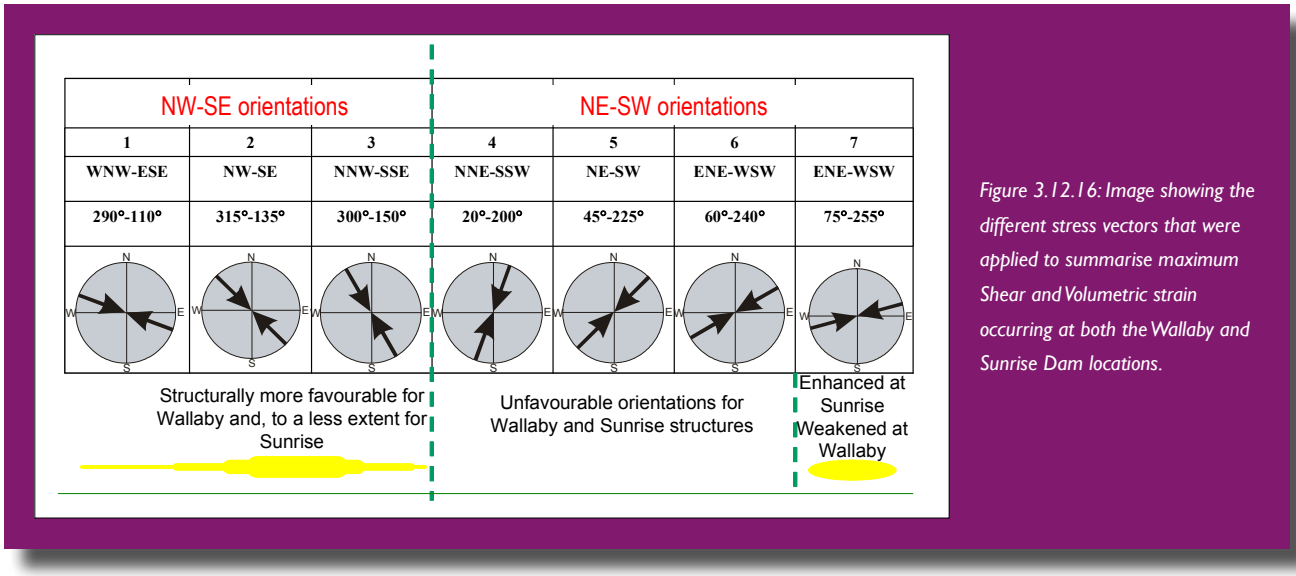


*Figure 3.12.16: Image showing the different stress vectors that were applied to summarise maximum Shear and Volumetric strain occurring at both the Wallaby and Sunrise Dam locations.*

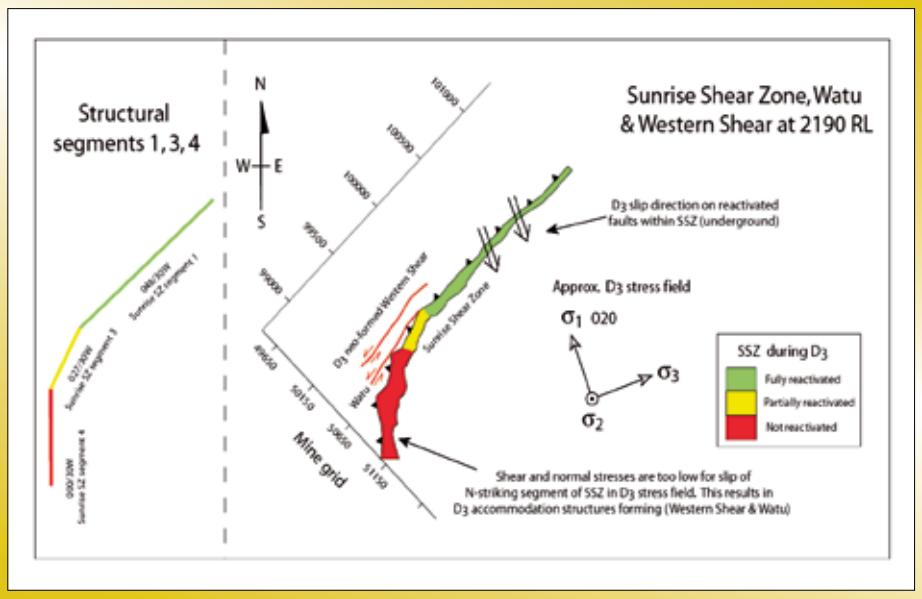


*Figure 3.12.17: Detailed structural analysis of the Sunrise Dam deposit showed that not all segments of the Sunrise Shear were reactivated. Most favourable segments were oriented ~30° to 310 (Miller, 2006).*

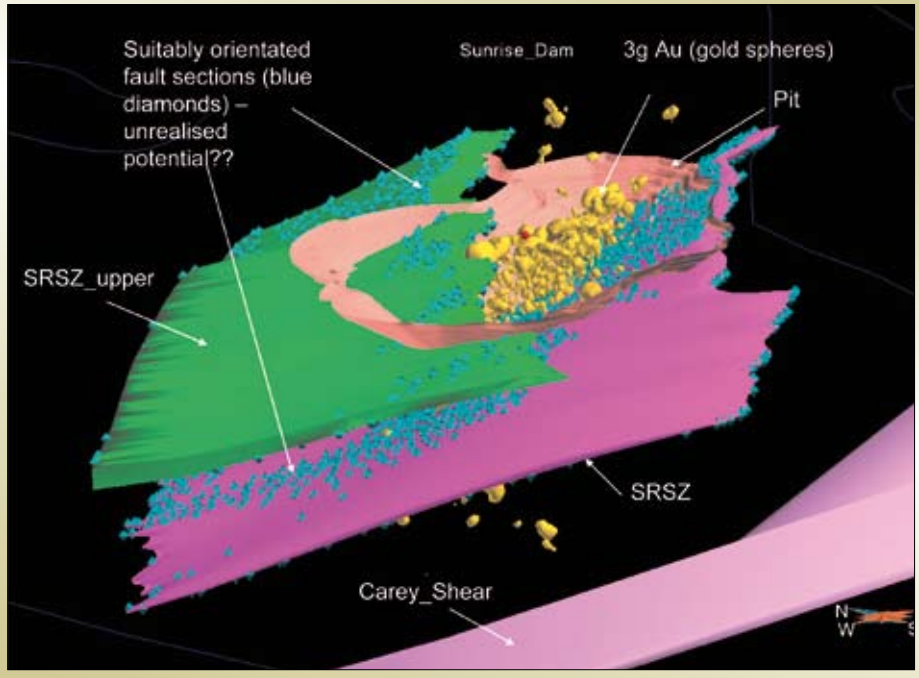


*Figure 3.12.18: 3D image from Gocad looking to the NE of wireframes from Sunrise Dam mine. Blue diamonds show regions of suitably orientated fault segments to reactivate/ dilate during a NW-SE contractional event (D4b).*

same fault parameters that were applied to the mine scale faults to highlight suitably orientated segments on the regional scale. Application of this process highlights areas around Sunrise Dam, Wallaby and Lancefield mines as suitably orientated fault segments (Figure 3.12.19). These empirical relationships indicate that the orientation of faults is fundamental to the mineralisation process at least during NW-SE contraction ($D_{4b}$) event in the Laverton region. Miller and Nugus's (2006) work indicated that the dip of a fault is as important to the reactivation process as the dip direction and hence it would not be possible to apply this type of analysis to 2D faults as traditionally applied in GIS-based proprietary analysis. A well constrained 3D map in contrast is the only potential way of analysing the preferential orientation of faults that will reactive during a specific stress vector. This process demonstrates that on both a mine and regional scale, highlighting areas of the faults with suitably orientated 3D segments provides a technique to critically evaluate additional areas for exploration targeting.

Caution must however be applied when using this technique, due to the potential generation of false positives/ negatives on 3D fault surfaces where orientations are not well constrained. Additionally, this technique only highlights one specific fault orientation dominant at Sunrise Dam and Wallaby mines and there is potential to create reactivation/ dilation within a variety of different fault orientations during the $D_{4b}$ event.

## 3.12.9 Conclusions

The geometries constructed within the Laverton 3D map provide insights into the formation of world class gold deposits. The early extensional architecture provides a critical framework that controls all subsequent deformation. A large crustal penetrating shear zone developed early in the structural history of the Laverton region and provided a suitable conduit for tapping mineralising fluids at depth. This structural zone and its subsidiary extensional structures facilitated the early intrusion of significant felsic igneous bodies into the upper crust. The extensional process unloaded the crust developing core complexes and doming of the units surrounding the syn-intrusive granites (McIntyre and Martyn, 2005). This domal architecture provided a focussing mechanism for rising mineralising fluids concentrating their flow in the mid-upper crust. Late-stage mantle-derived intrusive bodies are spatially related to many Au deposits and, and although some mineralisation can be linked temporally to the intrusion at Wallaby (Wall and Mason, 2001; Drieberg et al., 2004), the bulk of mineralisation post dates it. Seismic reflection data delineate bodies with a seismic reflection character similar to that of granites below some major deposits. A genetic link can be drawn between Wallaby and Sunrise Dam deposits placing them within a large scale restraining stepover, developed during sinistral strike-slip movement of pre-existing basement faults, that was reactivated during late dextral strike-slip movement. This is evident in the architecture, geochronology and structural histories of both deposits.

Key targeting criteria in the Laverton region are as follows:

1. ~N to NNE trending extensional faults developed during $D_1$ at ~2720–2698Ma are temporally unrelated to the NNW trending $D_1$ structures formed at ~2800Ma. It is argued here that all major deposits are located in close proximity to these structures: e.g. Wallaby Mine is located above the ~N-S trending Chatterbox Fault, Sunrise Dam in the hangingwall to the ~NNE trending Carey Shear and Granny Smith Mine proximal to the Far Eastern Fault. Identification of structures that were active via normal faulting at ~2720–2698Ma with a ~N to NNE trend is a critical targeting criteria.

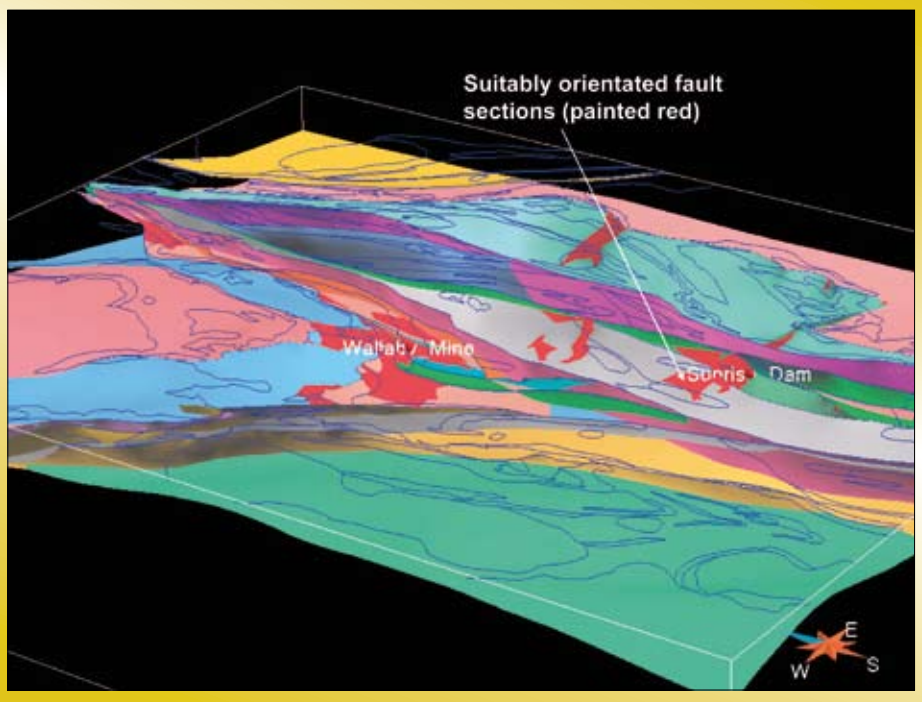


*Figure 3.12.19: 3D image from Gocad looking to the NE of the regional faults in the Laverton region. Blue diamonds show regions of suitably orientated fault segments to reactivate/ dilate during a NW-SE contractional event ($D_{4b}$).*

2. Structural analysis of mine scale structures have determined the stress vector operating during different gold events (Miller, 2005; Miller and Nugus, 2006), these are coincident with regional scale studies (Blewett and Czarnota, 2007). The identification of suitably orientated fault segments to dilate during these events, have been used to statistically analyse a variety of 3D fault surfaces from mine to regional scale. These have provided direct spatial targeting criteria.

3. Numerical modelling was used to model maximum volumetric and shear strain on a generic model of the Laverton region. These techniques allow the range of model conditions to be varied and also a range of stress vectors. The models constructed were able to test and validate the validity of vectors determined from conventional structural analysis and further work on the realistic geometries of the region (currently underway) will also produce regional targeting criteria.

4. Identification of local rheological contrasts generated from: lithological contacts; intrusive contacts and fault contacts can generate suitable dilation sites during the mineralisation process.

5. Seismic reflection data delineates connectivity between crustal penetrating shear zones and surface faults linked to zones of mineralisation. It also delineates domes and anticlines that focus fluid eg. 01AGS-NY2 line delineates an anticline beneath Wallaby deposit. For mineralisation to occur though, these low angle structures must be breached by steeper faults.

6. Gold is concentrated in structures suitably orientated to dilate during the $D_{4b}$ (NW-SE contraction) and $D_5$ (NE-SW contraction) events, which is dominantly the ~N to NNE trending structures. The proximity to granite/ gneiss domes will also influence this due to the propensity of faults to develop parallel to the dome margins.

## 3.12.10 References

Ayrza, P. and Martínez Catalán, J. R., 2007. Potential field constraints on the deep structure of Lugo gneiss dome (NW Spain): Tectonophysics, 439, 67–87.

Barlow, M., 2004. Density and susceptibility characterization of the Minerie 100,000 geology sheet: implications for detailed gravity inversions: unpublished report of Y2 project of ***pmd*CRC***, Geoscience Australia

Betts, P.G., Valenta, R. K. and Finlay, J., 2003. Evolution of Mount Woods Inlier, Northern Gawler Craton, Southern Australia: an integrated structural and aeromagnetic anomalies: Tectonophysics, 366, 83–111.

Blewett, R.S., Cassidy, K.F., Champion, D.C. and Whitaker, A.J. 2004a. The characterisation of granite deformation events in time across the Eastern Goldfields Province, Western Australia. Geoscience Australia Record 2004/10 [CD-ROM].

Blewett, R.S., Cassidy, K.F., Champion, D.C., Henson, P.A., Goleby, B.R., Jones, L. and Groenewald, P.B. 2004b. The Wangkathaa Orogeny: an example of episodic regional 'D2' in the late Archaean Eastern Goldfields Province, Western Australia: Precambrian Research, 130, 139–159.

Blewett, R.S. and Czarnota, K., 2007. The Y1-P763 project final report November 2005. Module 3 - Terrane Structure: Tectonostratigraphic architecture and uplift history of the Eastern Yilgarn Craton, Geoscience Australia Record 2007/15.

Blewett, R.S., Czarnota, K., Henson P.A. and Champion, D.C., 2008. A revised tectono-stratigraphic framework for the Eastern Yilgarn Superterrane. Part III, this volume.

Bourne, B.T., Trench, A., Dentith,M.C. and Ridley, J., 1993. Physical Property Variations within Archaean Granite-Greenstone Terrane of the Yilgarn Craton, Western Australia: The Influence of Metamorphic Grade Exploration Geophysics, 24, 367–374.

Cassidy, K.F., Champion, D.C., Fletcher, I.R., Dunphy, J.M., Black, L.P. and Claoue-Long, J.C. 2002. Geochronological constraints on the Leonore-Laverton transect area, north eastern Yilgarn Craton. In Cassidy, K.F. (ed.), Geology, geochronology and geophysics of the north eastern Yilgarn Craton, with an emphasis on the Leonora - Laverton transect area. Geoscience Australia Record 2002/18, pp. 37–58. (online)

Cassidy, K.F., 2004. Chapter 1: Geological evolution of the eastern Yilgarn Craton (EYC). In: Blewett R.S. and Hitchman A.P. (eds) 3D Geological models of the eastern Yilgarn Craton. ***pmd*CRC*** Y2 Final Report, 1–38.

Champion, D.C. and Cassidy, K.F. 2007. An overview of the Yilgarn Craton and its crustal evolution. In: in Bierlein, F.P., and Knox-Robinson, C.M., (eds), 2007. Proceedings of Geoconferences (WA) Inc. Kalgoorlie '07 Conference. Geoscience Australia Record 2007/14, p13–35.

Chen, S.F., Witt, W.K. and Liu, S., 2001. Transpression and restraining jogs in the northeastern Yilgarn craton, Western Australia. Precambrian Research, 106, 309–328.

Connors, K., Donaldson, J., Morrison, B., Davy, C., and Neumayr, P., 2003. The Stratigraphy of the Kambalda-St Ives District: workshop notes Goldfields Pty Ltd St Ives operation, unpublished Technical note No: TN SIG0329, 99 p.

Davis, B.K., 2000. Structural analysis of the Wallaby deposit: Report to the Placer-Granny Smith Joint Venture, April 2000.

Direen, N. G., Brock, D. and hand, M., 2005. geophysical testing of balanced cross-sections of fold-thrust belts with potential field data: an example from the Fleurieu Arc of Delamerian Orogen, South Australia: J. Structural Geology, 27, 964–984.

Blenkinsop, T., Baker, T., McLellan, J., Cleverley, J. and Nugus, M., 2007. Final Report Sunrise Dam Gold Mine Geological Study Project, Project G15. Predictive Mineral Discovery Cooperative Research Centre, report, March 2006 - March 2007.

Brown, S.M., Fletcher, I.R., Stein, H.J., Snee, L.W., Groves, D.I., 2002. Geochronological constraints on Pre-, Syn-, and Postmineralization Events at the World-Class Cleo Gold Deposit, Eastern Goldfields Province, Western Australia, Economic Geology, 97, 541–559.

Goleby, B.R., Blewett, R.S., Groenewald, P.B., Cassidy, K.F., Champion, D.C., Jones, L.E.A., Korsch, R.J., Shevchenko, S. and Apak, S.N. 2003. The 2001 Northeastern Yilgarn Deep Seismic Reflection Survey: GA Record 2003/28, Geoscience Australia.

Goscombe, B., Blewett, R., Czarnota, K.,. Maas, R and Groenewald. B., 2007. Broad thermo-barometric evolution of the Eastern Goldfields Superterrane. In: in Bierlein, F.P., and Knox-Robinson, C.M., (eds), 2007. Proceedings of Geoconferences (WA) Inc. Kalgoorlie '07 Conference. Geoscience Australia Record 2007/14, p33–38.

Drieberg, S., Walshe, J.L, Halley, S., Hall, G., 2004. Embedded Insights into the Wallaby gold deposit, Western Australia. In Barnicaot, A.C and Korsch, R.J. editors, 2004. Predictive Mineral Discovery Cooperative Research Centre - Extended Abstracts from the June 2004 Conference: Geoscience Australia, Record 2004/09. p. 31–32.

Hall, G.A., Wall, V.J., Massey, S., 2001. Archaean pluton-related (thermal aureole) gold: the Kalgoorlie exploration model. 2001 – A Hydrothermal Odyssey, extended abstracts volume: James Cook University EGRU, Townsville, Australia, pp 66–67.

Hallberg, J.A., 1985. Geology and mineral deposits of the Leonora–Laverton area, northeastern Yilgarn Block, Western Australia. Hesperian Press, Perth, Western Australia, 140p.

Hallberg, J.A. and Giles, C.W., 1986. Archaean felsic volcanism in the northwestern Yilgarn Block, Western Australia. Australian Journal of Earth Sciences, 33, 413–427.

Halley, S. 2007. Personal communication.

Henson, P.A., Blewett, R.S., Champion, D.C., Goleby, B.R., and Cassidy, K.F., 2004. A dynamic view of orogenesis and the development of the Eastern Yilgarn. In: Barnicoat, A.J., and Korsch, R.J., (Eds) Predictive Mineral Discovery Cooperative Research Centre Extended Abstracts from April 2004 conference, Geoscience Australia Record 2004/9, 91–94.

Henson P.A., Blewett R.S., Champion D.C., Goleby B.R. and Czarnota K., 2006. Towards a unified architecture of the Laverton region, WA. In: A.C. Barnicoat and R.J. Korsch (eds.), Predictive Mineral Discovery CRC-Extended Abstracts for the April 2006 Conference. Geoscience Australia Record 2006/7, 47–51.

Hobson R.A. and Miles K.R., 1950. Geology of portion of the Mt Margaret Goldfield. Geol. Surv. West. Aust. Bull., 103, 1–107 pp.

Hammond, R.L., and Nisbet, B.W., 1992. Towards a structural and tectonic framework for the Norseman-Wiluna Greenstone Belt, Western Australia. In Glover, J.E., and Ho, S.E., (Eds), The Archaean – Terrains, Processes and Metallogeny. Geology Department and

University Extension, The University of Western Australia, Publication 22, 39–50.

Hammond, R.L., Nisbet, B.W., 1993. Archaean crustal processes as outlined by structural geology, Eastern Goldfields Province of Western Australia. In: Williams, P.R., Haldane, J.A. (Compilers), Kalgoorlie 93 – An international conference on crustal evolution, metallogeny, and exploration of the Eastern Goldfields. Aust. Geol. Surv. Org., Rec 1993/54, 39–46.

Honman C.S., 1917. The geology of the North Coolgardie Goldfield. Part 1. The Yerilla district. Geol. Surv. West. Aust. Bull., 73, 98 pp.

Krapež B. and Barley, M.E., 2007. Late Archaean synorogenic basins of the Eastern Goldfields Superterrane, Yilgarn Craton, Western Australia. Part III: Signatures of tectonic escape in an arc-continent collision zone. Precambrian Research (2007), doi:10.1016/j. precamres.2007.06.020

McClay, K.R. and Massimo, B. 2001. Analog models of restraining stepovers in strike-slip systems. AAPG Bulletin, 85, pp. 233–260.

McIntyre, J.R., and Martyn, J.E., 2005. Early extension in the Late Archaean northeastern Eastern Goldfields Province, Yilgarn Craton, Western Australia, Australian Journal of Earth Sciences, 52, 975–992.

Miller J. McL. 2005. The structural evolution of the Wallaby Gold Deposit, Laverton, W.A., Y4 ***pmd*CRC*** project report, July 2005.

Miller, J. McL., 2006. Linking structure and mineralisation in Laverton, with specific reference to Sunrise Dam and Wallaby. predictive mineral discovery: Extended abstract, the Predictive Mineral Discovery CRC conference, 19–20 April 2006, Perth, Western Australia, pp. 62–67.

Miller, J. McL. and Nugus, M., 2006. The structural evolution of the Sunrise Shear Zone and the overlying Watu and Western shear zones, Sunrise Dam gold depost, Laverton, W.A. Project Y4, Predictive Mineral Discovery-CRC report

Roy, I. G., Lane, R. and Blewett, R., 2006. Regional-residual separation: an essential first step for building and validating 3D maps using gravity data, Abstract, Proceedings of Predictive Mineral Discovery-CRC Conference at Perth, April 19–20.

Salier, B.P., Groves, D.I., McNaughton, N.J. and Fletcher, I.R. 2004. The world-class Wallaby gold deposit, Laverton, Western Australia: An orogenic-style overprint on a magmatic-hydrothermal magnetite-calcite alteration pipe?. Mineralium Deposita, 39, 473–494.

Standing, J.G., 2007. Terrane amalgamation in the Eastern Goldfields Superterrane, Yilgarncraton: evidence from tectonostratigraphic studies of the Laverton Greenstone Belt, Precambrian Research, (2007).

Swager, C.P., Witt, W.K., Griffin, T.J., Ahmat, A.L., Hunter, W.M., McGoldrick, P.J., and Wyche, S., 1992. Late Archaean granite-greenstones of the Kalgoorlie Terrane, Yilgarn Craton, Western Australia, In Glover, J.E., and Ho, S.E., (Eds), The Archaean – Terrains, Processes and Metallogeny. Geology Department and Extension Service, University of Western Australia Publication 22, 107–122.

Swager C.P., 1997. Tectono-stratigraphy of late Archaean greenstone terranes in the southern Eastern Goldfields, Western Australia, Precambrian Research, 83, 11–42.

Wall, V., Mason, D., 2001. Wallaby Petrology: Part of a geological review of the Wallaby lode-gold project, Laverton region, Western Australia: Report to the Placer-Granny Smith Joint Venture, October 2001.

Weinberg, R.F., Moresi, L., and van der Borgh, P., 2003. Timing of deformation in the Norseman-Wiluna Belt, Yilgarn Craton, Western Australia. Precambrian Research, 120, 219–239.

Williams, P.R., and Whitaker, A.J., 1993. Gneiss domes and extensional deformation in the highly mineralised Archaean Eastern Goldfields Province, Western Australia, Ore Geology Reviews, 8, 141–162.

Zhang, Y., Schaubs, P.M., Henson, P.A., Czarnota, K., Ord, A., Sheldon, H.A. and Blewett, R.S., 2007. Laverton regional numerical model: understanding strain localisation In: Bierlein, F.P., and Knox-Robinson, C.M., (eds), Proceedings of Geoconferences (WA) Inc. Kalgoorlie '07 Conference. Geoscience Australia Record 2007/14, 249.

## 3.13 Fluid-chemical evolution of the Sunrise Dam mineral system

**James Cleverley[1] and Mike Nugus[2]**

[1] CSIRO Exploration and Mining, Australian Resources Research Centre (ARRC), 26 Dick Perry Ave, Kensington WA 6151, Australia

[2] AngloGold Ashanti, PO Box Z5046, Perth, WA, 6831, Australia

### 3.13.1 Introduction

The Sunrise Dam Gold Mine (AngloGold Ashanti Ltd) is situated 50 km south of Laverton on the edge of Lake Carey. The deposit is dominated by narrow vein- and breccia-hosted gold, within a thick sequence of andesitic lava flows and domes, volcanogenic sedimentary rocks and chemical BIFS. The stratigraphy is folded and cut by a series of stacked, shallow dipping (30–40°) shear zones dominated by the Upper, Sunrise and Carey shear zones with depth. There are a multitude of ore bodies, and mineralisation styles in the Sunrise Dam deposit, and the previous work has helped to describe the chemical and structural affinity of these ore bodies. The mine is a combination of open pit and underground operations with current exploration drilling to targets below the Carey shear zone (>1500 m).

This work attempts to summarise the Sunrise Dam deposit in the context of the fluid, geochemical evolution and chemical architecture, as well as linking these observations to the structural architecture. This report builds on the work throughout the ***pmd****CRC*, previous mine-based work and other research projects conducted within the system. While all attempt has been made to recognise the large number of workers that have contributed to the understanding we apologise to anyone that we may have overlooked. As always "if I have seen further it is on the shoulders of giants" (Sir Isaac Newton).

### 3.13.2 Geological Setting

The Sunrise Dam Gold Mine is located 29°05'S, 122°25'E, approximately 850km ENE of Perth and 45km SSE of the township of Laverton. The deposit is currently owned by AngloGold Ashanti Australia and, as at 31 March, 2007, has produced in excess of 5.40Moz of ore, with Resources of 36.7Mt@3.08g/t Au (3.68Moz Au) with 16.7Mt@3.51g/t Au (1.90Moz Au) reserves (Erickson et al., 2006). Sunrise Dam is the single largest gold deposit in the Laverton Tectonic Zone of the Eastern Goldfields Superterrane, Western Australia. The Sunrise Dam Operation consists of a well-established open cut operation and an underground operation, which has been operating since 2003 as part of a Life-of-mine and underground feasibility study.

#### 3.13.2.1 Lithology

The stratigraphy that hosts gold mineralisation at Sunrise Dam forms part of the lower greenstone sequence (2715 Ma) of the Laverton Tectonic domain and predates the "late basin" stratigraphy (~2665 Ma), which hosts the nearby Wallaby deposit (Standing, 2008). The Laverton greenstone belt is a typical Archaean greenstone belt insofar as it consists of a differentiated suite of volcanic rocks and mafic and granitic intrusions of numerous generations. The majority of the Laverton and EGST area have undergone lower-mid greenschist facies metamorphism, with higher-metamorphic grades around granite plutons (Chen and Wyche, 2001; Goscombe et al., 2007).

The Sunrise Dam stratigraphy consists of a complexly deformed and altered package of shallowly NW-dipping units dominated by coherent and incoherent rocks of intermediate affinity. These have been overlain by a turbidite sequence containing generally well-sorted siltstones, sandstones and magnetite-haematite-rich shales (BIF *sensu lato*), which consistently fine upwards. The composition of these silts and sands mirrors that of the underlying andesitic volcanic package. These sediments have been intruded by dolerite sills, which inflate the sequence by up to 100% and are most evident in the northern end of the deposit. Minor units include quartz diorite sills, ultramafic (dykes?) and felsic porphyry dykes.

### 3.13.3 Methods for Determining Geochemical Architecture and 4D Evolution

In attempting to map the chemical architecture in a number of ore systems as part of the ***pmd****CRC*, a workflow has been developed using a number of key software packages, to help understand the geochemical spatial data

sets. The packages and workflow used at SRD are briefly described here; they are not exhaustive but are indicative of the types of approaches that need to be used. A more comprehensive description and workflow can be found in the enabling technologies report (M9/F6).

#### 3.13.3.1 Workflow used at SRD

3D datasets, visualised and modelled in the Leapfrog package (Zaparo), included the assay data (Au, As), spectral data (previous PIMA and the HyChipper survey) and all mine wireframes. Later models using Leapfrog v2. beta made use of the ability to visualise the geological and structural logging data also. Site visits and examination of core was conducted where possible with the Leapfrog model so that the spatial relationships of the chemical architecture could be maintained.

Spectral data from the HyChipper survey was also include and analysed in a Leapfrog model. It was found that the best results were when the TSG (Spectral Geologist) software was used to analyse the data and then exported with hole id, from, to and scalar data down sampled to 1m resolution. Weighting was placed on the mineral 1 scalar error (i.e. the better the fit the more weighting).

Mass transfer models for alteration and vein systems were completed using a modification of the isochon method (see Grant, 1995 and Oliver et al., 2004).

### 3.13.4 3D Geochemistry

Only limited whole rock data were collected as part of this study and as such the 3D geochemistry is defined on the basis of assay results within the mine databases (Au and to a lesser extent As). The following section uses Leapfrog isosurface techniques to develop a framework for understanding the geochemical architecture of the system.

#### 3.13.4.1 Assay Isosurfaces

Leapfrog isosurfacing was used to map out the distribution of Au and As at the deposit scale. In the first instance a simple isotropic fit was used with range 80 and a 0.6 nugget value to fit the shells to the Au, and a nugget free value was used for the As (typically broader halo than the Au, see Figure 3.13.1). Where necessary the isosurface intercepts with the wireframes was also calculated to determine lineation controls on grade. The Leapfrog isosurfaces are a mathematical indication of the location of Au or As and should not be treated as grade shells, as there is no rigorous geostatistical treatment of the data in this work.

*Figure 3.13.1: Example of broader As halo vs Au in TSG profiles for CD720 (bottom two lines), relative to lithology (top line).*

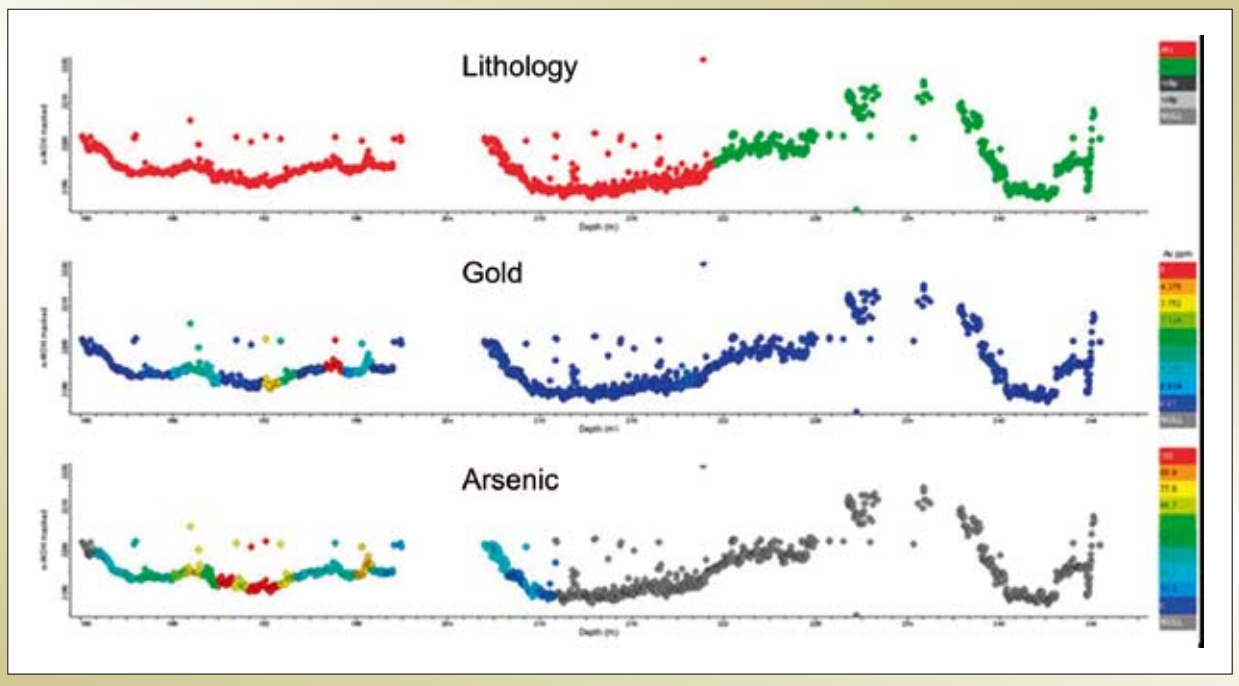

### Trends in Au and As

The key features that emerged from the initial Leapfrog model were the "pipe-like" structures in the As/Au shells that appear beneath the Sunrise Shear zone that are not evident above. Structures above the SSZ include the Western and Watu shear zones which apparently focus the flow from the pipes. Figures 3.13.2 and 3.13.3A and B are examples from the pre-2007 Leapfrog model (see details in G15 report, Blenkinsop et al., 2007).

## 3.13.5 3D Stable Isotopes

Brown et al. (2003) collected a range of stable and radiogenic isotope samples with the Sunrise Dam hydrothermal system. The stable isotopes ($\delta^{34}S$, $\delta^{18}O$ and $\delta^{13}C$) have been imported from the data presented in Brown et al. (2003) into the October 2007 Leapfrog model to reference the data spatially. The data (although not entirely as isotope pairs) are collected from close to a E-W (mine NE-SW) section through the Sunrise Shear Zone (SSZ), Dolly Porphyry, Cosmo and Western Shear Zone (WSZ) intersection point (Figure 3.13.4). Figures 3.13.5 and 3.13.6A,B show the distribution of the isotope sample values relative to the Dolly porphyry, Cosmo, Sunrise Shear Zone and Western Shear Zone wireframes (in a N looking view). This discussion uses the results of measurements at St Ives (*cf.* Walshe et al., 2008) to constrain the ranges within the goldfields.

### 3.13.5.1 Carbon

The interpretation made on $\delta^{13}C$ carbonate data within gold deposits of the EGST is that -5‰ represents close to mantle values, while excursions away from this are functions of partial oxidation of $CH_4$ (+) or partial reduction of $CO_2$ (-). The St Ives data ranges from a mean of --5‰ to -15 and + 8‰.

Figure 3.13.5 is a rough sketch of the $\delta^{13}C$ >3.5‰ and <3.5‰ (including -6). Using this simple interpretation it can be seen that broadly the lighter numbers are associated with flat shear structures (SSZ and Midway shear zone). The heavier numbers are associated with steeper structures (Cosmo, WSZ, Dolly Porphyry).

### 3.13.5.2 Oxygen

$\delta^{18}O$ is observed at St Ives ranging from ~8–10‰ up to heavy values >20‰, where the heavy values are interpreted to be related to the dry, volatile-rich magmatic fluid. Values to lower values <8‰ are likely related to low temperature retrogression (i.e., cooling curve on isotope plots in Walshe et al., 2008).

### 3.13.5.3 Sulphur

$\delta^{34}S$ in sulphides ranges from negative to positive values in many of the gold systems in the EGST (Walshe et al., 2008a,b), and it is suggested that this

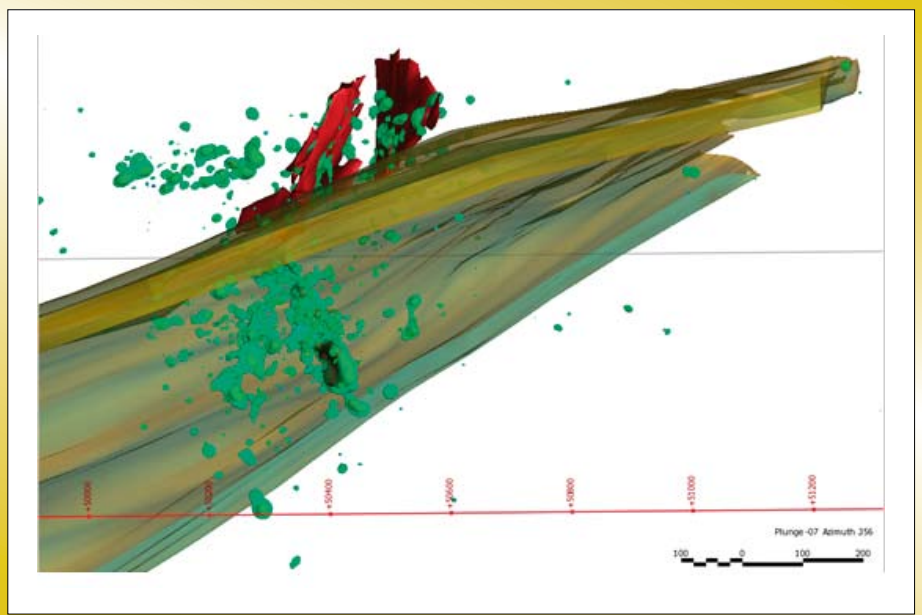

*Figure 3.13.2: As isosurfaces (250 ppm) for the pre-2007 dataset showing pipe like structures beneath the Sunrise Shear Zone (view NE). Red wireframes are the Western and Watu shear zones.*

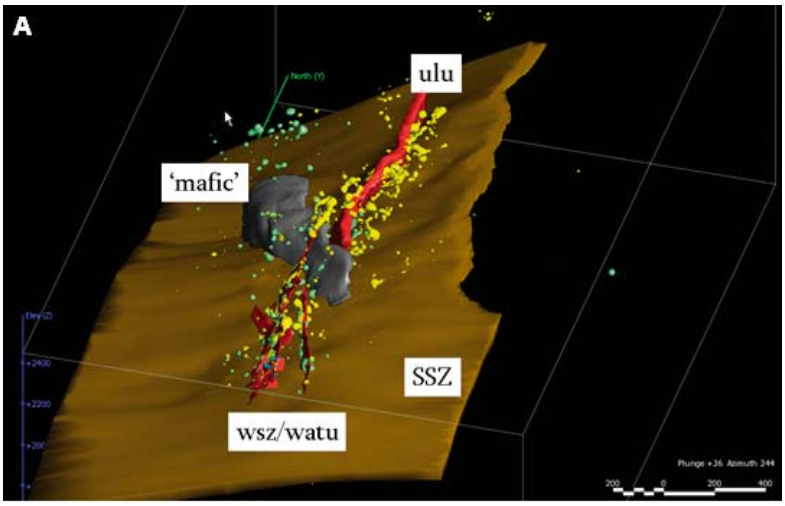


*Figure 3.1 3.3: Gold (yellow blobs) and As (green blobs) shells looking down onto the Sunrise Shear Zone and B) up at the SSZ with the Midway shear zone (grey).*

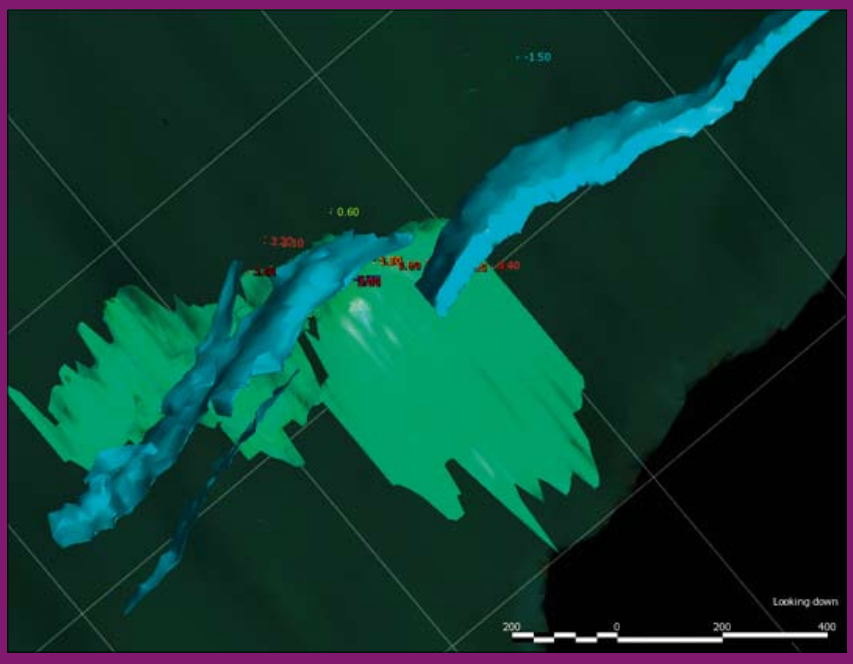


*Figure 3.1 3.4: $\delta^{34}S$ isotope locations from Brown (2003) relative to key structures and ore bodies in the Sunrise Dam hydrothermal system. Top down view orientated approximately magnetic north up.*

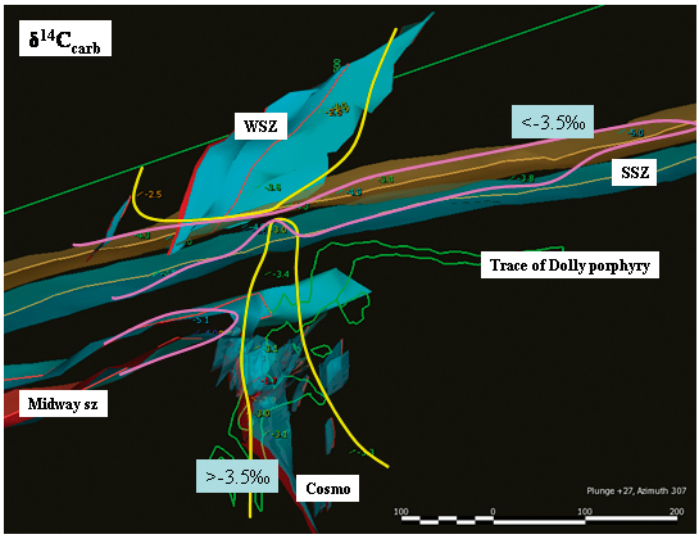


*Figure 3.13.5: Carbon isotope patterns for the Brown (2003) data relative to the key wireframes along the E-W section (looking N). Areas of > -3.5 (yellow) and <- 3.5 (purple) appear to delineate flat vs. steep pathways.*

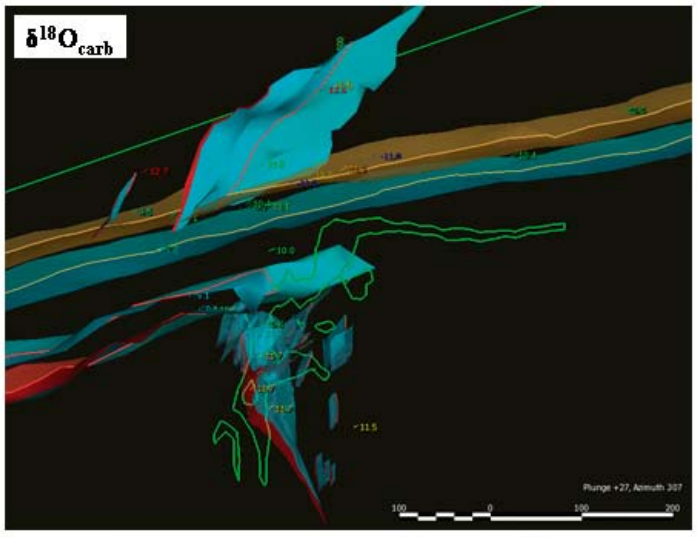


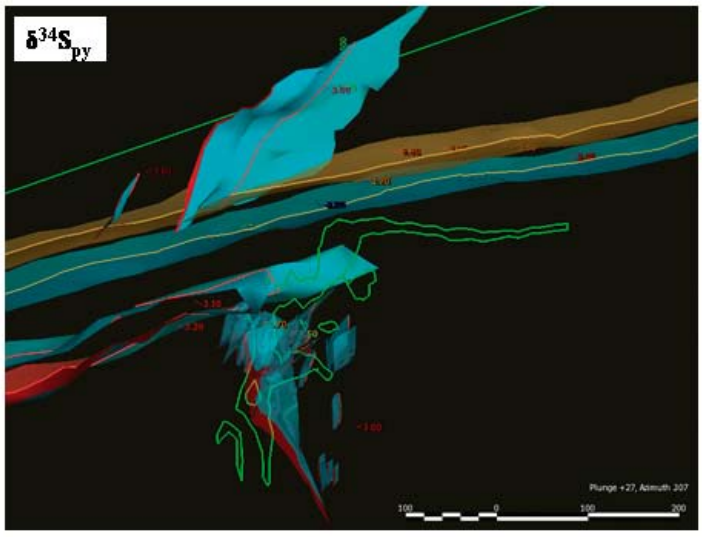


*Figure 3.13.6: A) Oxygen, and B) S isotope distribution on the same section as Figure 3.13.5.*

represents the variable redox condition of sulphide precipitation in the deposits (i.e. + $\delta^{34}S$ is total reduction of $SO_4$, while - $\delta^{34}S$ is partial oxidation of $H_2S$). Sulphates (not analysed at SRD) range from ~+8 to +30‰ and likely represent different $SO_4$ sources between magmatic $SO_2$ (+8–11‰) and seawater or equivalent > +20‰.

The most negative of the SRD $\delta^{34}S$ (-7.7‰) is sampled within logged banded Fe formation (ACI) with subordinate siltstone (AST), but this occurs on the edge of Dolly porphyry dykes and the main body of the intrusion (Figure 3.13.7). This needs to be re-examined during further studies as there are many examples, over and above the normal BIF units in the mine sequence, of Fe-stone development next to porphyry. Are they hydrothermal or sedimentary iron stones? The most positive values (+3 to +4) are also hosted in banded iron formation and volcanogenic sandstone.

Could the Fe-stone be metasomatic? Initial investigation of samples from BIF hosted mineralisation indicate the presence of phases such as $SrCO_3$, $BaSO_4$, $WO_4$ etc which in turn indicate relatively oxidised conditions (possibly rock buffering see above). In this case the S isotopes (of the sulphides) might reflect the partial reduction of oxidised S sources based on the wall rock buffering, however they may still represent a consequence of the fluid environment.

## 3.13.6 3D Logging Data

### 3.13.6.1 Banded Iron Formation (ACI)

There is some suggestion from the logging data that some occurrences of banded iron formation (logged as ACI in either MAJ or MIN fields) maybe related to the presence of adjacent porphyries. Leapfrog was used to generate images of the logging intersections containing ACI in either the major or minor field (Figure 3.13.8A and B). The distribution of ACI below the SSZ can be seen to define antiformal structures (plunging shallowly towards the SE). The trend of the ACI unit is to turn vertical at the location of the Cosmo ore body. Above the SSZ the ACI occurs as two distinct areas, a) north section as a halo around the mine mafic wireframe and b) south section as a cluster at the central section of the WSZ and Watu structures.

If the entire ACI unit, especially that logged as ACI/AST is primary lithology some of the relationships are harder to explain (i.e. as a halo around the mine mafic, on the margins of the porphyry units. It is recommended that some of the key ACI relationships from the mine be reinterpreted based on the available core to determine if there is a distinction between alteration and lithology.

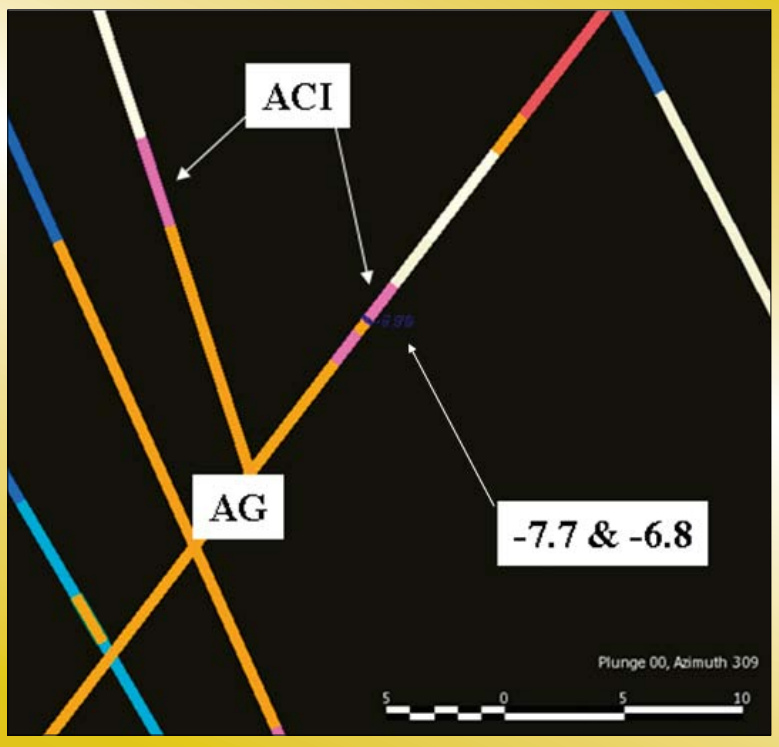


*Figure 3.13.7: View of lithological logging with the location of two of the most negative S isotope values from Brown (2003). According to the drill logging these values occur in ACI ("BIF") that is limited to the margin of the porphyry granite (AG).*

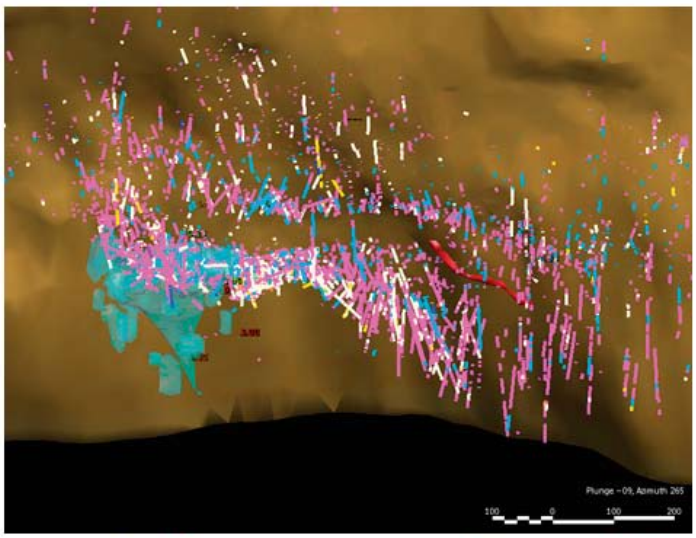

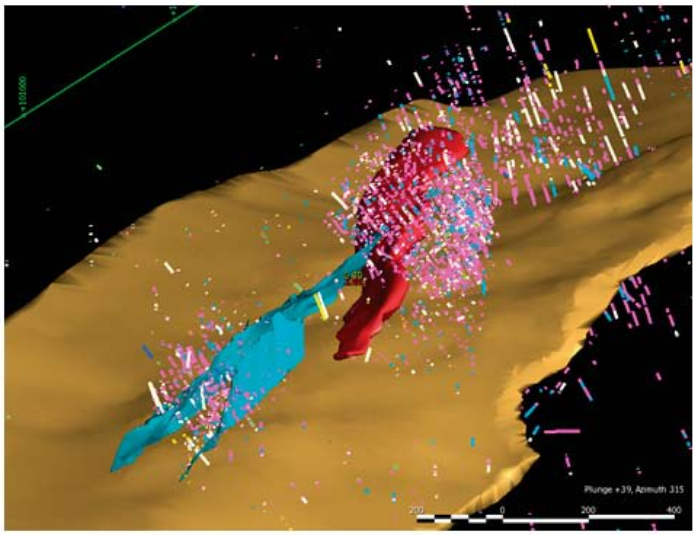

*Figure 3.13.8: Distribution of logged ACI ("BIF") as pink intervals, A) under and B) on top of the SSZ.*

### 3.13.6.2 Fuchsite Alteration

Logged fuchsite (FUCH in major alteration code) was plotted for the SRD model to look at the spatial relationship to the structures and mineralisation. Figure 3.13.9 shows two views of the model with fuchsite intervals in red. The majority of the logged fuchsite occurs within the SSZ, but in heterogeneous distribution. There appears to be a relationship between the steeper gold bearing systems below the SSZ and "patches" of fuchsite within the shear zone. There are also two linear areas of fuchsite with the SSZ aligned with, but slightly offset from the WSZ and Watu ore zones.

The fuchsite in the lower NW of the SSZ occurrences (area 1 on Figure 3.13.9B) has not been thoroughly drilled beneath the SSZ and this maybe an area of interest for further examination as an extension of the ore system beneath the SSZ.

## 3.13.7 Previous Geochronology

Previous geochronology has been completed by Brown et al. (2002) and Mueller (unpublished company report, 2002), the latter is a comprehensive review and reassessment of some of the previous age dating. The framework from Mueller (2002) has been used here to make some assessment of the interplay of different architectural and deformation events with mineralisation and geochemistry. Figure 3.13.10 is a compilation of age dates presented in Brown et al. (2002) and Mueller (2002). The data have been categorised into 1) felsic porphyry zircons (High Ca group, see below), 2) xenotimes from

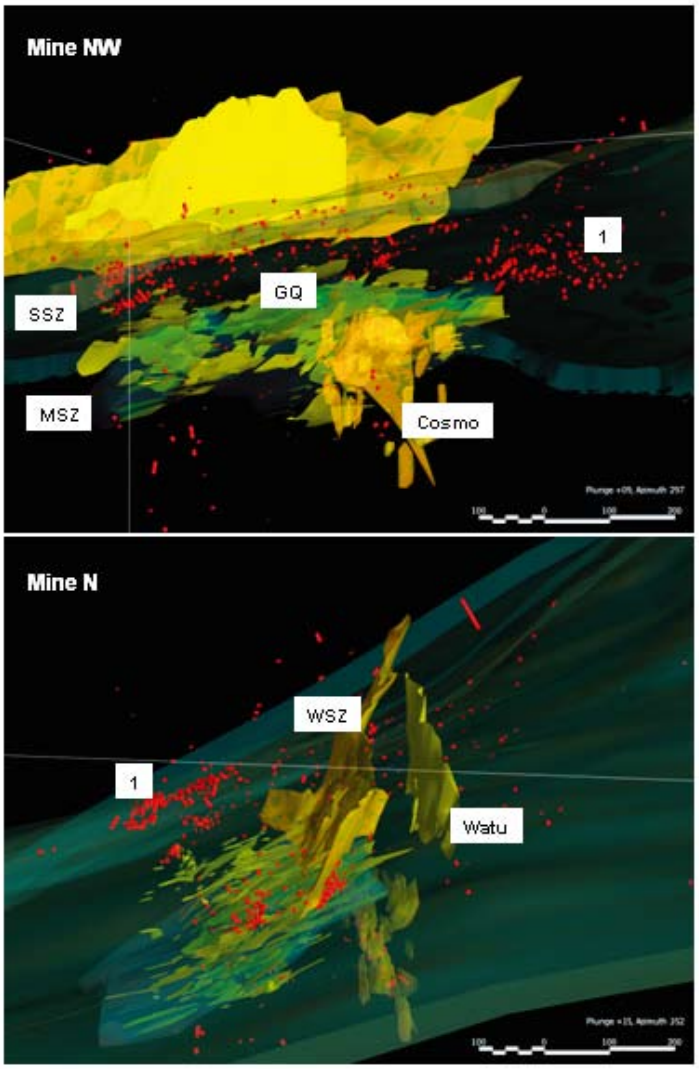


*Figure 3.13.9: Intersections of logged fuchsite as a major alteration product (red) relative to the Sunrise and Midway Shear zones (transparent blue) and gold ore bodies. Azimuth is relative to mine grid. A) Under and B) on top of the SSZ.*

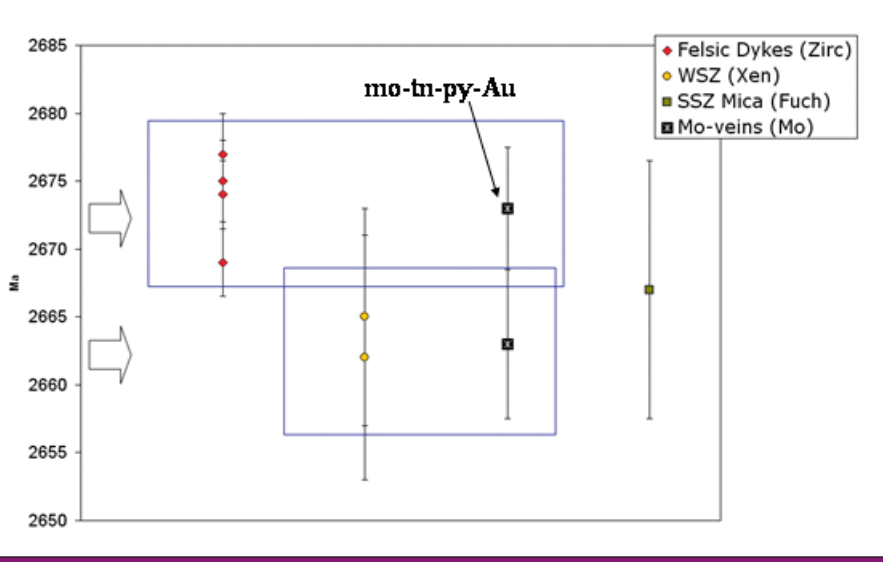


*Figure 3.13.10: Compilation of geochronology for SRD (after Mueller, 2002; and Brown, 2003). Felsic dykes are porphyries in the deposit (upper levels) based on zircons, WSZ – western shear zone (xenotime), SSZ – Sunrise Shear Zone (fuchsite, isochon age – total fusion age 2635 Ma) and Mo-veins – Molybdenite bearing veins (one with Au) (Re-Os Molybdenite).*

WSZ mineralisation, 3) molybdenite that appears to be from two distinct events and, 4) a single fuchsite Ar-Ar data from the Sunrise Shear Zone.

### 3.13.7.1 Molybdenite

The molybdenite ages summarised in Mueller (2002) give two distinct dates, 2673±9 Ma and 2663±13 Ma. The 2673 Ma age is from molybdenite textural associated with pyrite and tennantite (Mueller, 2002), and reported to be from a "high-grade ore zone" in the "Sunrise Upper Shear, HW10". The association with tennantite-pyrite-gold is similar to early laminated veins from elsewhere in the system (i.e., folded veins in the SSZ). This drill hole was not present in the AngloGold Ashanti database. The younger age is from molybdenite in a relatively gold-poor zone (0.05 g/t Au, 35 ppm As), although there is a small 2.4 g/t Au intercept 10 m above this location. Because of the lack of description and distance from Au mineralisation the relationship of this age data to mineralisation is uncertain.

Based on the compiled age dates it can be seen that despite the errors there are two broadly separate events (2674 Ma and 2660 Ma), and the earlier event is in agreement with observations within Blenkinsop et al. (2007) showed that some Au-bearing mineralisation was associated with the high-Ca granite hosted, syn-intrusive vein stockworks.

## 3.13.8 Geochemistry and Petrography

An initial appraisal of the geochemistry of porphyries and ore lodes has been presented within Blenkinsop et al, 2007 (G15 report, SRD 1-on-1). This is a summary of some of that work, but the reader is referred to the G15 report for more details.

A total of 33 whole rock analyses were collected at SRD in the G15 (22) and Y4/F6 (11) projects. The G15 samples have been analysed at Analabs using a comprehensive 57 element suite (including majors, traces, some REE's and volatiles). These data have been used to look at the whole rock classification, immobile element suites and alteration within the SDGM. Individual samples have been analysed using the isochon method (Grant, 1986) to characterise specific alteration and mass balances and this is presented in the following section.

Plotting the $Al_2O_3$ vs. $TiO_2$ for the sample dataset shows that in the most part all samples of ore and associated alteration have a consistent Al/Ti which indicates a consistent bulk composition (Figure 3.13.11A). This is probably related to the fact the host rock sequence in most of the SDGM are related to the 2715 Ma intermediate volcanic dome complex (intrusives, lavas, conglomerates, pyroclastics and sediments) and the overall bulk compositions are the same. The porphyries however do have different Al/Ti showing that they have a different geochemical providence. Another common immobile element, Zr, is plotted against $Al_2O_3$ in Figure 3.13.11B, and while this shows broadly the same consistent ratio there is more scatter.

The immobile elements can be used to ration other elements in order to distinguish actual changes as opposed to relative changes related to dilution in the sample. The shift in Al/Ti towards 0/0 (Figure 3.13.11A) will represent progressive dilution by a component (i.e., mass/volume change).

### 3.13.8.1 Key Alteration Indices

The constant Al/Ti but spread of data along the trend line towards zero indicates a process that causes dilution of the immobile components. Typically the diluting components include the volatile phases such as $SO_4$ (sulphide/sulphate), $CO_2$ (carbonate) and bulk LOI (indicated hydration that can be caused by phases such as sericite). Carbonate is a commonly observed alteration product in the mine and so Figure 3.13.12A is a plot of $Al_2O_3$ vs. $CO_2$ to look for dilution by carbonate in the samples. It can be seen that there is a strong trend to increased $CO_2$ with diluted $Al_2O_3$ and this indicates that most samples are affected to vary degrees by carbonate alteration. If this was calcite alone there would be a trend to the pure calcite composition at $CO_2$ = 43 wt% (Al = 0), however the actual trend is shifted down from this. Other diluting components might be interacting in the samples to cause the shift from the pure calcite trend, or else the carbonate alteration is dominated by other carbonate phases (e.g. dolomite). Figure 3.13.12B is a plot of $Al_2O_3$ vs. LOI (including the extra dataset). Comparison between Figures 3.13.12A and 3.13.12B shows that the bulk of the LOI is accounted for with $CO_2$, and other volatile species are minimal. The carbonate alteration can account for some of the low-Si porphyry data and is explained further in a later section.

The important aspect of these data is the strong mine-wide carbonate alteration which is observed and known about in other deposits in the EGST (i.e., MERIWA/Y4 work).

### 3.13.8.2 Thick Laminated Veins

Using two whole rock geochemical samples from the ***pmd*CRC*** Y4/F6 project dataset (analysis at JCU, 2005) an analysis was completed for "fresh" wallrock (pre-D3 altered) and D3 breccia vein associated with laminated veins in the SSZ ore body. The isochon (Figure 3.13.13) plotted through Al, Ti and Zr shows significant mass gain in the breccia body with $F_m$ = 1.18 and a distinctive lack of elements plotting in the losses domain. This indicates that the alteration associated with these veins/breccias is purely mass additive with little wall rock exchange taking place. The main components added into the breccia vein include: extreme Au, Ag, Pb, Te, found in the sulphide assemblages; moderate Sr, CaO, Rb, Sb, Cd associated with the presence of carbonate; and minor Ba, LOI, $Na_2O$, La, Yb, and Ni.

### 3.13.8.3 Target 9 porphyry Gold

The "Target 9 porphyry" (SLD061, 330–341m) is a felsic porphyry of the High-Ca (2674 Ma) suite that exhibits strong, pink to green alteration around a vein-rich, grey coloured core (Figure 3.13.14). The core zone contains quartz vein-hosted gold (6.3 m@35.4 g/t). Isochon comparison between the grey, core zone and the pink edge zone is presented in Figure 3.13.15 with the isochon plotted through Al, Ti, Zr and Y. This is an isochon plotted for two alteration zones (refer to introduction and examples) and hence the element patterns presented here are relative between the alteration. The Au-rich, grey, core zone in the porphyry is enriched in As, Au, Te, $SO_4$, Pb, Rb and W, K. The pink coloured edge of the porphyry is enriched in Na, $CO_2$, Ca, Mn, Sr and Fe, Mo. These elements are all (except Mo) distinctive in their association with carbonate minerals and are also similar in part to the wallrock alteration described in the Summercloud system.

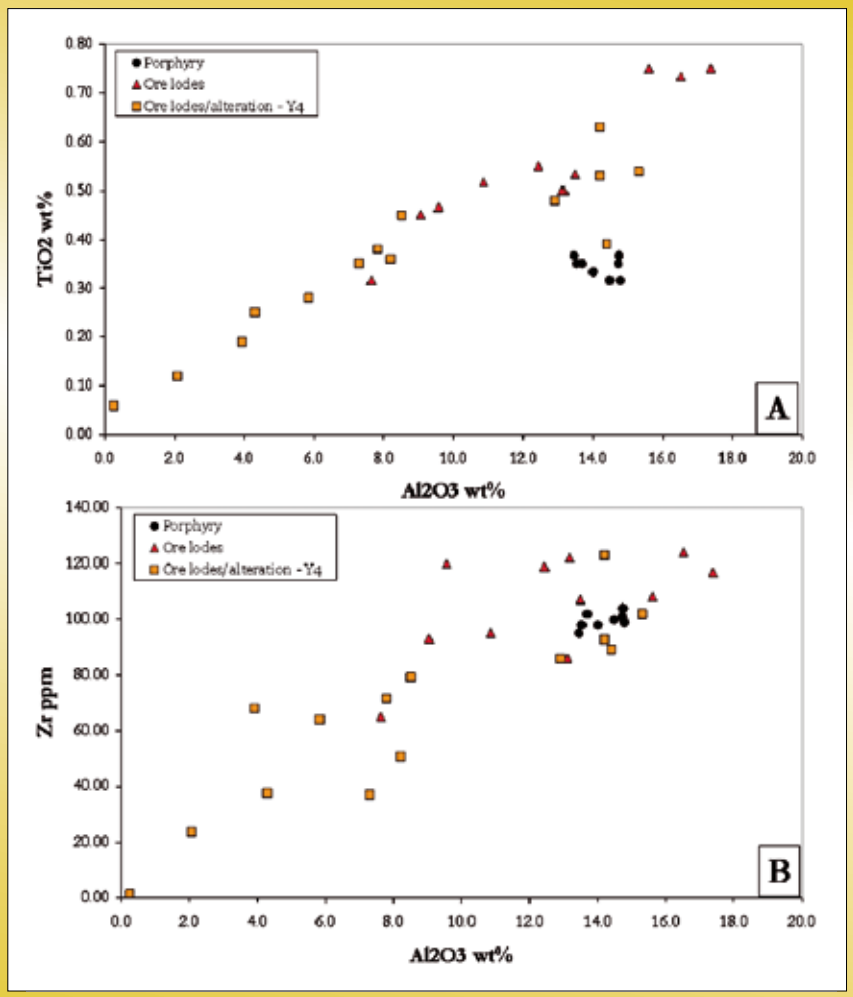


*Figure 3.13.11: A) Al2O3 vs. TiO2 and B) Al2O3 vs. Zr for SGDM porphyry, lodes and wallrock samples in the G15 project (circles, triangles) and Y4 project (squares).*

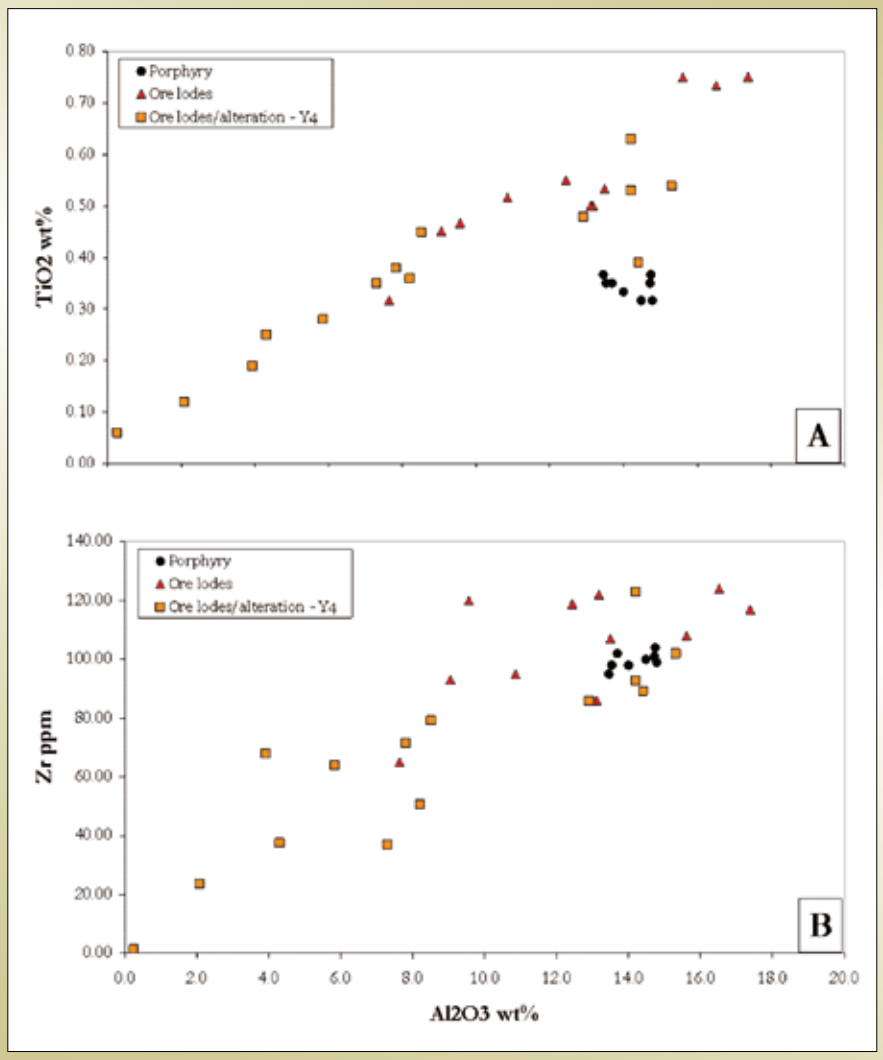


*Figure 3.13.12: Plots of Al2O3 (as an immobile component) and A) $CO_2$ (G15 data only) and B) LOI (loss on ignition, G15 & Y4).*

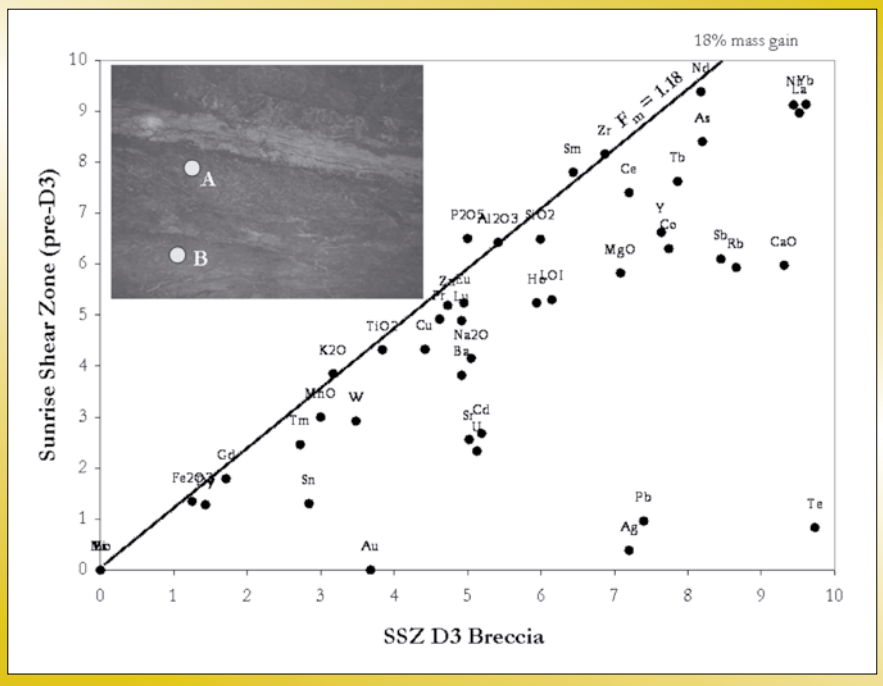


*Figure 3.13.13: Isochon plot for the SSZ D3 breccia veins associated with the laminated quartz veins (see photo).*

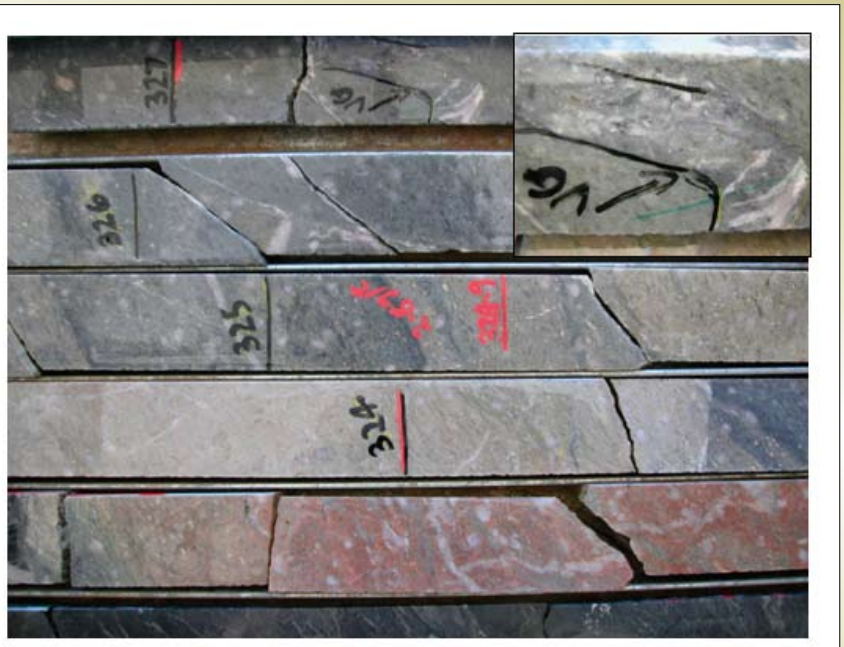

*Figure 3.13.14: Photo of the Target 9 porphyry core showing the pink edge zone and transition into the grey core zone with quartz veins and visible gold (see inset).*

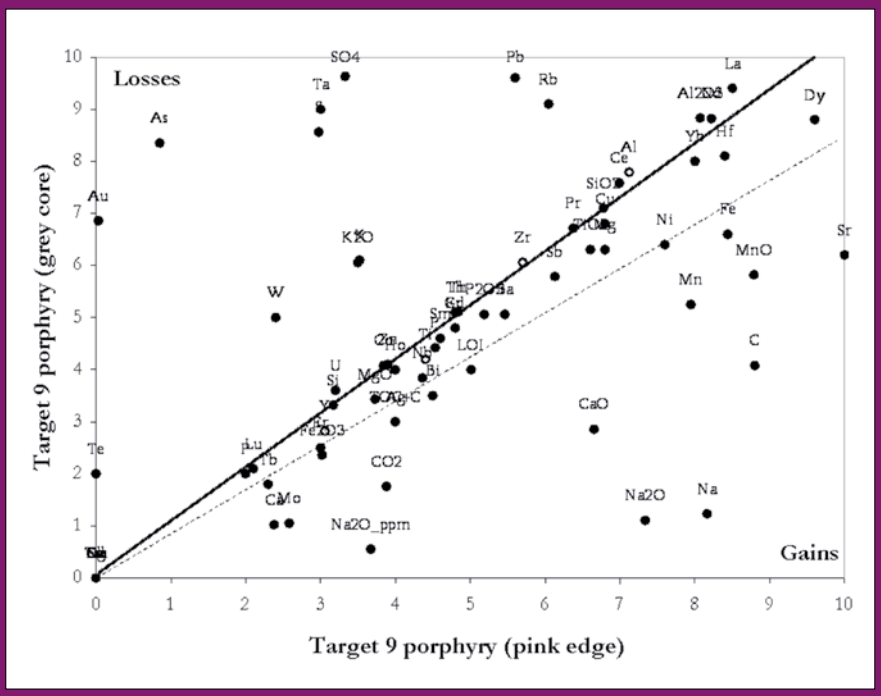


*Figure 3.13.15: Isochon plot for the pink edge versus gold-rich, grey core zone of the Target 9 porphyry. This is a good example of Na-$CO_2$ wallrock alteration and Au-Te-As-Pb-SO4 gold zone alterations. The PIMA spectra show a transition from higher to lower AlOH wavelengths across this zone.*

### 3.13.8.4 Mafic Unit

The "Mine Mafic" cuts across the deposit in a N-S orientation terminating and displacing the WSZ and Watu shears, and separating these systems form the ULU in the northern section (Figure 3.13.16). The role or genesis of this unit is uncertain and it is suggested that this is a mafic intrusive (see work by Mark Doyle, AngloGold Ashanti). Geochemical analysis as part of the initial Y4 batch contain samples within the Sunrise Shear zone from the region close or within the mine mafic, and these indicate that the dark rocks have a chemistry similar to other volcanic rock sequences in the mine but with mass addition of Cr and Ni (Figure 3.13.17).

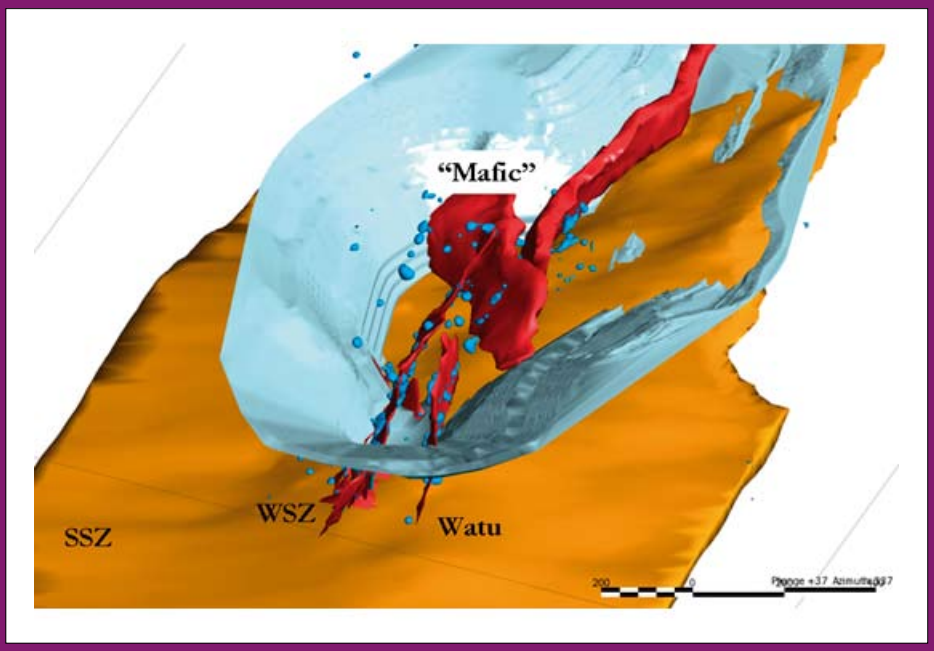


*Figure 3.13.16: Wireframes for the Western and Watu shear zones, the mine mafic and the ULU (relative to the pit) showing the offset of structures across the mine mafic domain.*

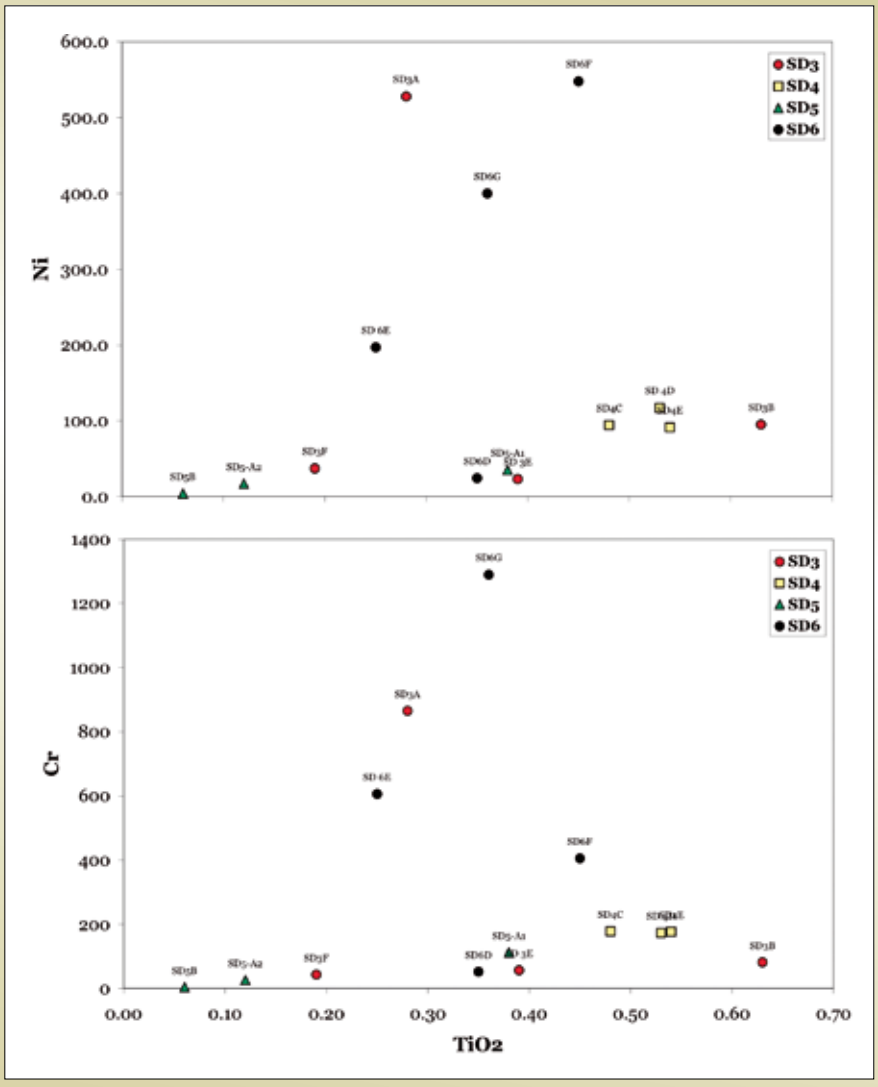


*Figure 3.13.17: Whole rock geochemical plots for Y4 samples from SRD. SD6 samples are from dark altered rocks in the mine mafic domain, and the samples (black dots) show mass addition of Cr and Ni (upward trend) relative to other samples.*

### 3.13.8.5 Porphyry Geochemistry

A total of 8 porphyry samples from intrusive rocks within the mine sequence have been sampled and analysed as part of the G15 project. In order to help evaluate the linkages between the porphyries and the mineralization it is important to evaluate how these rocks fit with the regional Laverton and Eastern Goldfields Superterrane data. Using the classification criteria of Champion and Cassidy (2001) the SRDG porphyry data is plotted on a $K_2O$ vs. Ce plot (green dots, Figure 3.13.18). It is found that the SDGM data fit very well in the High-Ca, low-LILE group, in particular the data have a strong affinity to the Beasley Well Supersuite (grey dots in white squares, Figure 3.13.18), apart from some apparent K enrichment within the Target 9 porphyry data.

These rocks have been dated in the Laverton district at 2672±2 Ma (L. Black, AGSO, see Champion and Cassidy, 2001), and this is consistent with the dates by Brown et al. (2002) of 2674±3 for a porphyry within the SDGM.

There is petrographic evidence for an association of the **High-Ca** porphyries with intrusion related chalcopyrite-molybdenite–Bi-Te±Au (Baker, G15 report, 2007; Brown et al., 2002), and this maybe related to the molybdenite age of 2673 Ma reported in Mueller (2002). Texturally this mineralisation is found in small stockwork fracture systems internally to the porphyries. It is difficult to ascertain how much Au is associated with this stage of mineralisation.

Where this mineralisation is observed in spectral logs there is small magnitude, but fluctuations of the mice AlOH wavelength with depth (Figure 3.13.1 lines).

**Lamprophyres** have been logged in sections of Sunrise Dam but there is no petrographic, geochemical or structural data on the timing and relationships to Au.

**Mafic** or **syenite** series intrusives have not been sampled or positively identified within the upper portions of the SRD system (i.e., as part of the G15 project). However recent observations within the deeper drilling (i.e., around and below the Carey Shear Zone) have discovered at least some porphyry with phenocrystic mafic mineral phases. Further work will be needed to ascertain whether the deeper parts of the SRD system contain more of the mafic series granites, as predicted in the 3D geometry of this or the St Ives system (Henson et al, 2008; Neumayr et al, 2008).

## 3.13.9 Assemblages and Fluids at SRD

### 3.13.9.1 Nominally Reduced assemblages

Work within the St Ives project has identified various assemblages and datasets that can be used to track the reduced fluid pathways. Early observations included the presence of pyrrhotite > magnetite, the presence of heavy S and C isotopes as indicators of oxidised parts of the system. More recently shear zones rich in Cr-mica (fuchsite) have been proposed as possible reduced pathways

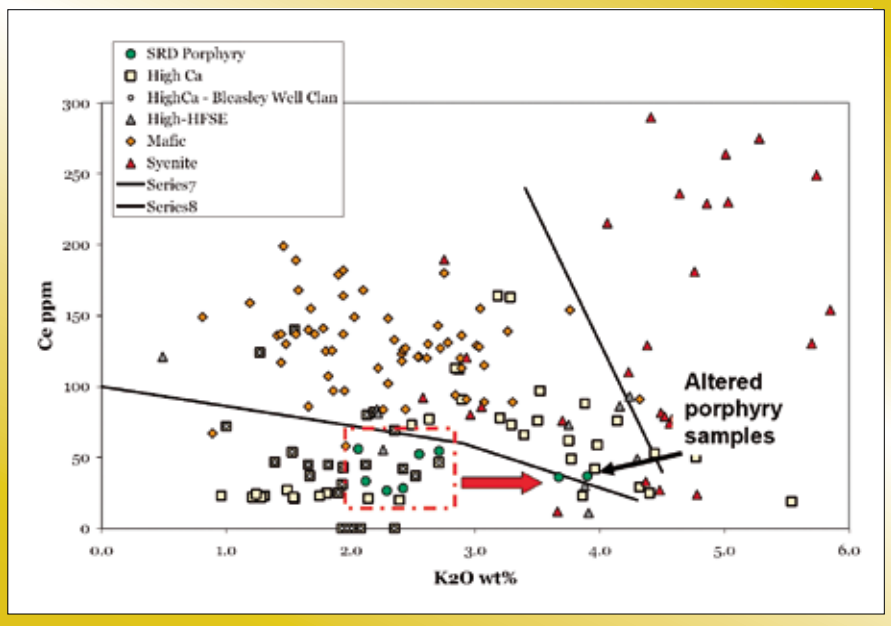


*Figure 3.13.18: Regional and SDGM porphyry (green) data on a granite classification diagram as defined by Champion & Cassidy (2002). SDGM porphyries plot in the High-Ca, Low-LILE box and are the most similar to Beasley Well clan porphyries. This matches with the 2674 Ma age dates for these rocks.*

based on the association of negative C isotopes (see Walshe et al. 2008a,b and Neumayr, 2008). Reduced pathways have also been suggested from the presence of As-rich domains, however these might be more complicated as As can be found in a range of minerals over a range of oxidation states (see ***pmd*CRC*** I7 report for As apatite at Ernest Henry).

### 3.13.9.2 Nominally Oxidised assemblages

#### Logged alteration

Using the Leapfrog model a plot of the occurrence of haematite alteration was made, as this is locally observed relative to the margins of many of the porphyries in and above the Sunrise Shear Zone (Figure 3.13.19). The haematite is locally quite extensive and in 3D appears to form discreet zones, although no obvious pattern was seen.

#### Zones beneath the Carey

Hyperspectral logging (May 2007, HyChipper survey by AGA) of some of the deep drilling (CD112W2, CD678W2) showed the presence of anhydrite/gypsum in some samples. Although follow up work has not been completed to substantiate the presence of anhydrite in these samples, if this is correct the deep drilling of zones beneath the Carey Shear Zone may start to approach the alteration described in the deeper parts of the St Ives system, where high temperature anhydrite-bioite-celestine veins appear to form from magmatic $CO_2$-$SO_2$ fluids (S and Sr isotope evidence).

#### Local host-rock controls

While the SDGM lithologies are relatively uniform in their overall redox state (pyrite stable), alteration and mineralisation in the BIF units does appear to involve local oxidation and fluid-rock interaction dominant processes. Good examples of infiltration fronts, similar to those described from the larger BIF-hosted Au deposits (Cuiaba, Oliver et al., 2005), are observed underground at SRD (Figure 3.13.20). Alteration fronts in this environment propagate away from small reverse structures and show magnetite-BIF altered progressively to (distal) haematite – carbonate – sulphide (distal). HCh modelling of the reaction between greenstone derived fluid and BIF has been used to demonstrate that reduced fluids can generate oxidised assemblages along a rock infiltration pathway (Figure 3.13.21), and this may explain the assemblages observed in the SRD BIF mineralisation. However, in general these assemblages are limited in extent (unless the system is large such as the Cuiaba BIF-hosted Au).

## 3.13.10 Mineral Assemblages and Textures

### 3.13.10.1 Thick Laminated Veins (SSZ)

A detailed examination of mineral chemistry and petrography has been conducted on the "thick laminated veins" that are found within the Sunrise Shear Zone and provide a moderate contribution to the total SSZ resource (Figure 3.13.22). The veins are composite in nature with a) quartz brecciation, b) dark laminations and c) cross-cutting steeper structures.

*Figure 3.13.19: Red coloured porphyry with xenoliths of sericite altered volcanic rock. The red colouration and veining is associated with Chalcopyrite-molybdenite-Bi-Te-Au mineralisation typical of intrusive related systems. Photo courtesy of Tom Blenkinsop (G15 project report).*

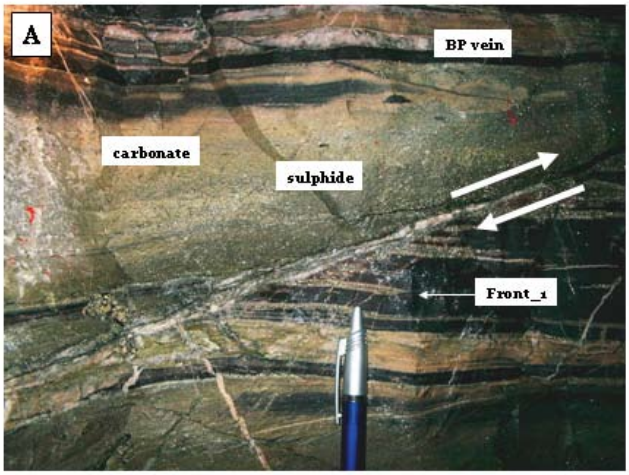


*Figure 3.13.20: Infiltration fronts in BIFs in the SRD system. A) Underground (2077 RL) view of sulphidation and carbonate fronts propagating away from reverse faults. Infiltration progress is likely a function of the grain size of the individual layers in the BIF. B) Hand specimen view of the same phenomena with the thin section locations (SD5A4-1 and SD5A4-2).*

*Figure 3.13.21: HCh model results for infiltration of fluid (from left to right) with NaCl molality 0.2, KCl 0.5, $CaCl_2$ 0.4, $FeCl_2$ 0.03, $H_4SiO_4$ 0.035 (and other varying redox and sulphur parameters as below) into metabasalt with mineralogy shown on the right of the diagrams (buffering log $aO_2$ –31). The models were run under isothermal, isobaric conditions at 380°C and 250 MPa. The x-axis is the nominal distance the front has travelled for a fixed time, fluid velocity and permeability. Alternately it can be regarded as the time taken for a reaction front to reach a certain distance for a given fluid flow rate. The last step shown on the log $aO_2$ diagrams represents the limit of infiltration of the exotic fluid. a) Reduced fluid with molality of [BE1]$CO_2$ 2.0, $CH_4$ 0.1, $H_2S$ 0.1 and $SO_2$ 10-10, pH of 3.5 and[BE2] log $aO_2$ –32.0 showing sulphidation assemblages characteristic of proximal zones of many ore deposits; b) Moderately reduced fluid with $CO_2$ molality 4.0, $CH_4$ 0.01, $H_2S$ 0.1 and $SO_2$ 10-7, pH of 3.25 and log $aO_2$ –31.1, in which exhaustion of the fluid's sulphidation capacity leads to formation of oxidized assemblages ahead of the front, including the anhydrite- and hematite-bearing assemblages found in several large depsits in the Yilgarn.*

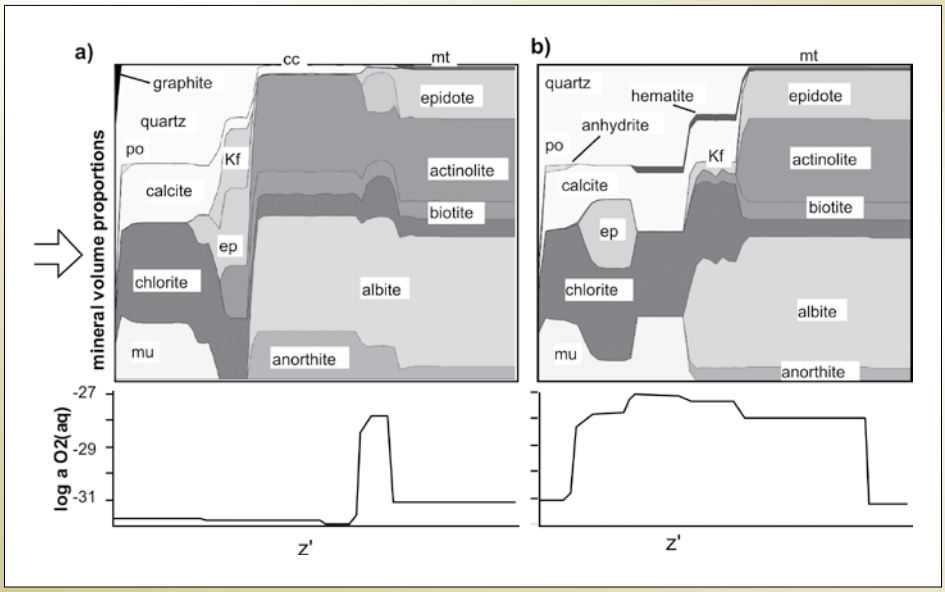

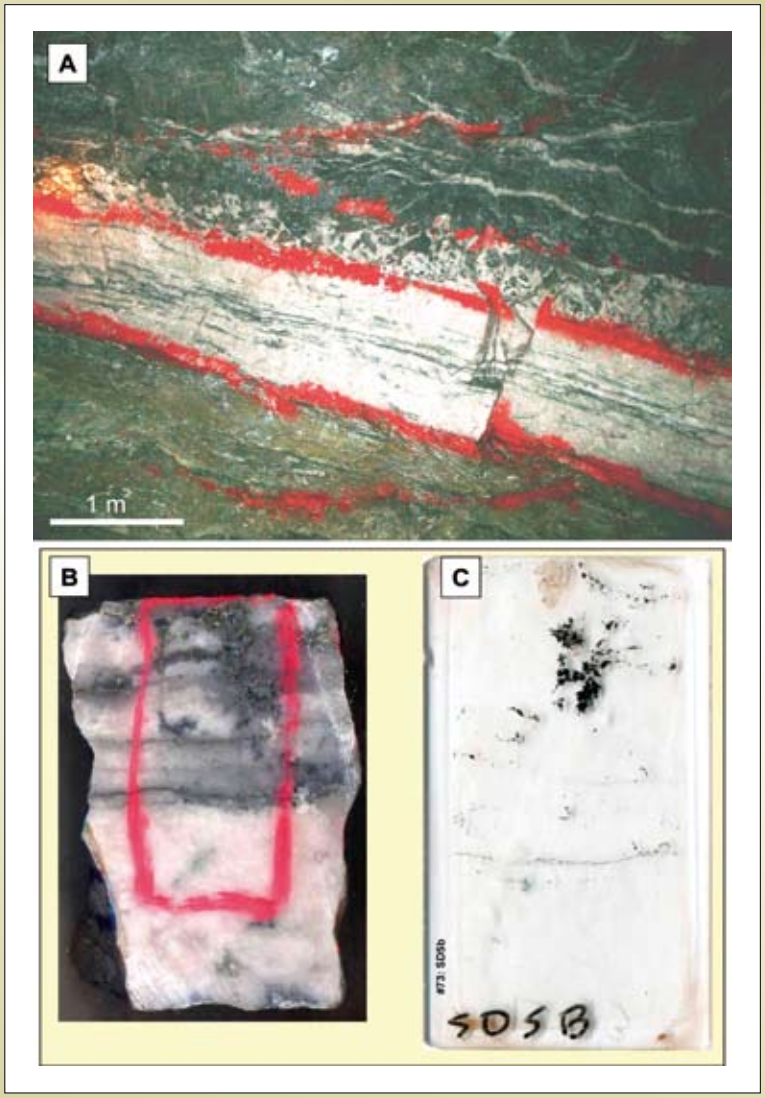


*Figure 3.13.22: "Thick laminated vein" from the 2077 ore drive within the Sunrise Shear Zone. This vein and ore style is in contrast to the thinner laminated (Te-bearing) veins (Fsz). A) Exposure of typical vein with thick quartz and included dark laminations, often containing a breccia at the margins. B) Thin section sample showing the horizontal laminations and steeper cross-cutting structures. C) Thin section of sample SD5B showing the clumps of sulphide in the steeper cross-cutting structures.*

## Dark Laminations (low angle)

Figure 3.13.23 is a typical example of a dark lamination from the laminated veins set in sample SD5b (D5-equivelent, Nugus et al., 2007; or D3-equivelent this is unresolved fully). It is dominated by discrete mineral precipitation events superimposed on each other including 1) tourmaline – minor muscovite – rutile, 2) tourmaline – pyrite, 3) coarse pyrite-apatite, and 4) quartz – zoned Fe-Mg dolomite. The quartz – dolomite layers appear to have formed during extensional 'pop-open' events with fragmented quartz and open space growth dolomite (note zoning in Figure 3.13.23 dolomite). The nature of the timing relationships between the different 'lamination' events is very cryptic however in Figure 3.13.24A and B illustrates something of these relationships. In Figure 3.13.24A the coarse pyrite (with native gold inclusions) appears to be closely associated with the dolomite brecciation and open space event as does the apatite although commonly brecciated during this event as well. The tourmaline-muscovite-(rutile) laminations overprint this breccia event. This is confirmed in Figure 3.13.24B where the infilling dolomite is zoned to Fe-rich compositions (bright) near the pyrite grain boundary indicating simultaneous growth. Although the apatite is brecciated itself, there is evidence for quartz breccia fragments inside the apatite as well as simultaneous dolomite-apatite growth (dashed box on Figure 3.13.24B). The tourmaline-dominant stylolitic lamination cuts and invades the dolomite breccia assemblages. Although the relationships in Figure 3.13.24A and B are typical there is evidence for multiple dolomite and tourmaline events (Figure 3.13.23), and the system was probably fluctuating between the two types.

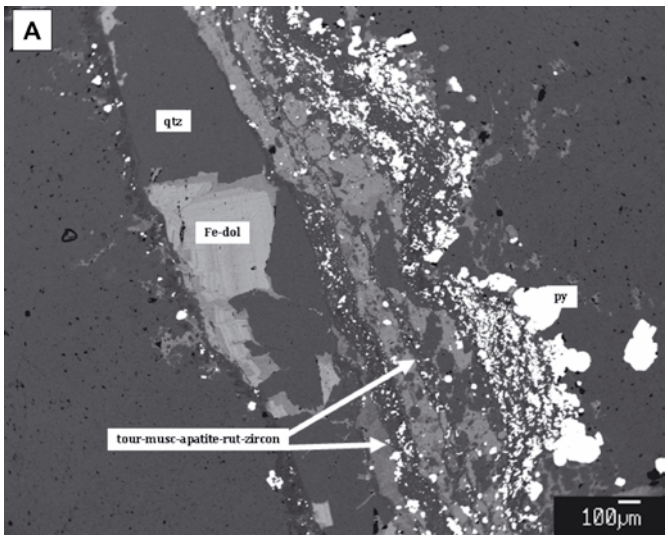


*Figure 3.13.23: Backscatter electron images of laminations in sample SD5B. A) Composite lamination showing multiple episodes of infill and brecciation of the surrounding quartz vein (tourmaline-muscovite-pyrite and dolomite) and C) detailed view of tourmaline-muscovite-dolomite lamination with course pyrite and apatite. The lamination contains fragments of the surrounding quartz without obvious precipitation or dissolution of $SiO_2$.*

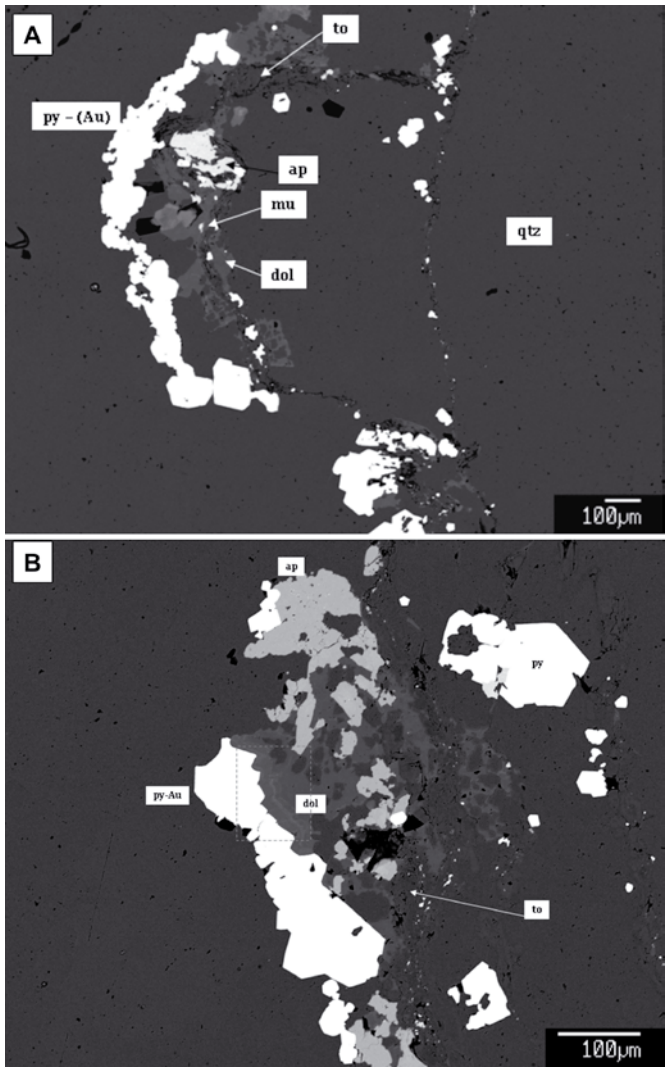


*Figure 3.13.24: Two backscattered electron images of gold bearing dark laminations within thick quartz veins. A) Details of a stylolitic lamination showing the coexisting phases common in these features (to – tourmaline, mu – muscovite, dol – dolomite, ap – apatite and py – pyrite with intergrown gold). Overprinting structures can be seen with dolomite-apatite-pyrite overprinted by tourmaline-muscovite. B) Detailed view of a small micro-breccia zone in a dark lamination showing the brecciated fragments of quartz from the host vein with infill precipitation of dolomite-apatite and coarse pyrite with Au. The co-existence of pyrite with dolomite-apatite (including magnetite inclusions) indicates that redox gradients existed even at the micro-scale in these systems. In most cases the tourmaline-muscovite appears to post-date the gold.*

Gold is observed inside the coarse pyrites (Figure 3.13.24A and B) and this is shown for the area from Figure 3.13.24B pyrite in Figure 3.13.25. The Au is slightly enriched in Ag with Au/Ag around 90/10 mass% (EDS quantification). The Au in pyrite from the laminations is typically large with sizes between 50–100 µm.

The wallrocks immediately next to the laminated veins contain extensive tourmaline-muscovite alteration with the tourmaline decreasing from the contact and muscovite dominating. The muscovite-dolomite tends to form the bulk of the alteration in rocks within the ore drives, while tourmaline is only observed in very vein proximal positions (<1 cm).

Although the laminations are very similar between samples there are subtle differences in the amount of tourmaline (SD5b is the most) compared to mica. Also the laminations in sample SD6d_1 (mica only) contain molybdenite and the mica contains approximately 1–2 wt% $Cr_2O_3$.

## Carbonate-sulphide (steep)

The quartz – carbonate outside the laminations (see breccia in CL, Figure 3.13.26) also contain sulphide assemblages but these are very different from those in the laminations. Here the sulphides tend to infill within the subtle breccia textures seen in SEM-CL or associated with open-space infilling zoned dolomite. The sulphides form as aggregates of sphalerite with chalcopyrite rims coring zoned tetrahedite-tennantite all cross-cut or containing inclusions of galena (Figure 3.13.27A, sample SD5b). This assemblage is rarely closely associated with pyrite growth (in fact pyrite appears to be clast-derived) and is most strongly associated

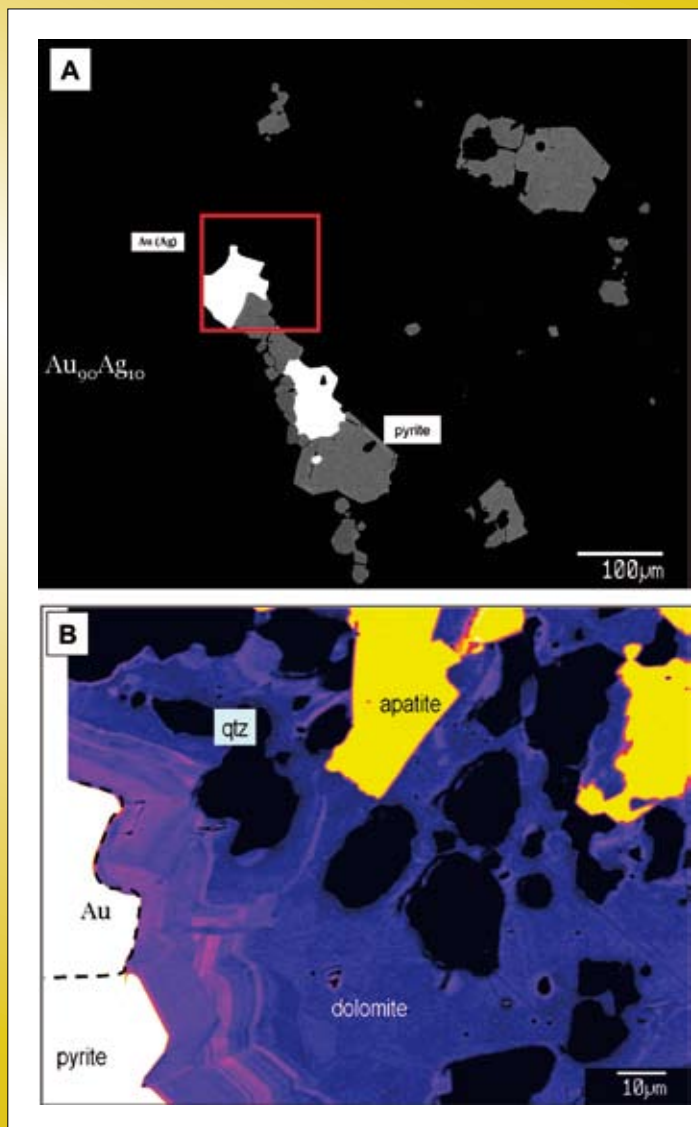


*Figure 3.13.25: A) BSE image of coarse pyrite from lamination showing the intergrown gold (Au90Ag10) and B) false coloured BSEI showing the inset region from A and the chemical zonation (Fe – bright) in the dolomite. The chemical zonation follows the crystal edge of the pyrite but appears to continue around the gold.*

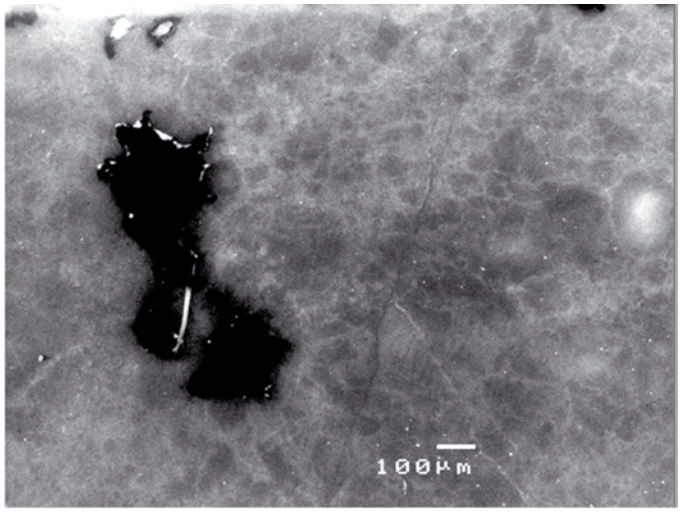


*Figure 3.13.26: Cathodoluminescence image of quartz rich area in laminated veins showing the complex brecciated textures and cross-cutting (dark) quartz stringers. Note the sulphide (black) appears to be within the quartz breccia and not associated with a cross-cutting structure.*

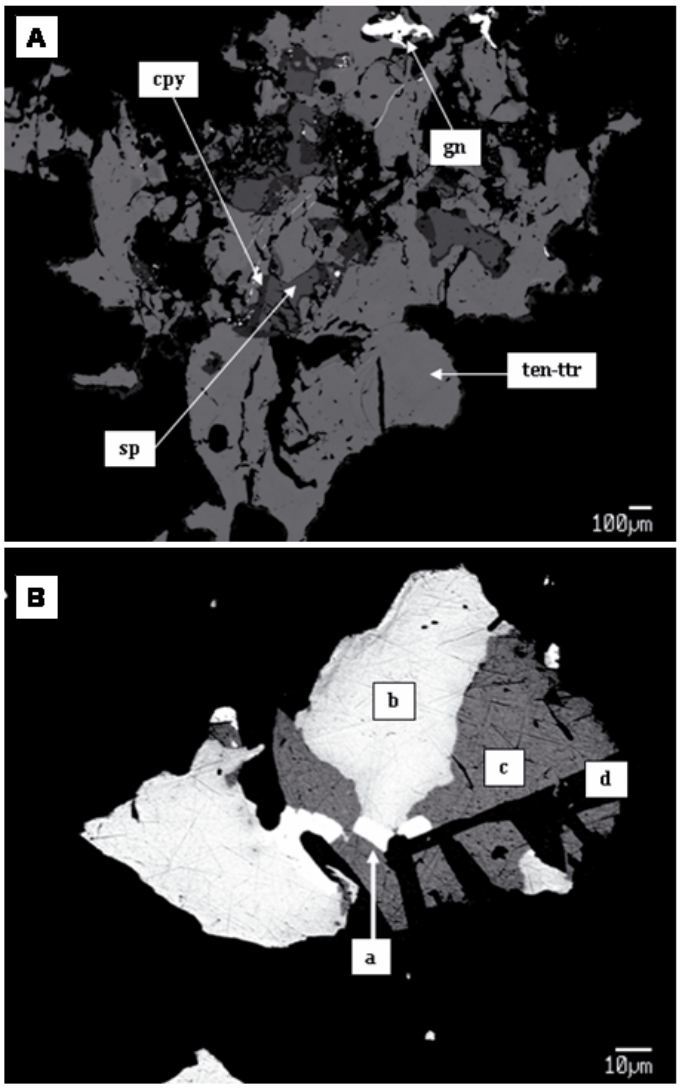


*Figure 3.13.27: A) Aggregate of sphalerite-chalcopyrite – tetrahedrite-tennantite and galena in sample SD5b quartz. The tennantite-tetrahedrite is slightly zoned in Sb-As. B) Detailed view of telluride minerals with contrast set to show differences. Minerals identified by EDS as (a) altaite, (b) calaverite, (c) petzite and, (d) tellurantimony (see text).*

with open space in fills of dolomite (zoned from Mg- to Fe-rich).

Sample SD3a also contained rich concentrations of telluride minerals. These were found as independent aggregates from the sulphide-assemblage (discussed above) but are likely spatially related, and often observed in fracture fills close to dolomite within the quartz vein. Tellurides have not been observed in the laminations. The spatial distribution of a complex telluride aggregate is illustrated in detail in Figure 3.13.27B. The zones consist of (bright-dark), a) PbTe (altaite), b) $AuTe_2$ (calaverite), c) $AuAg_3Te_2$ (petzite) and, d) $Sb_2Te_3$ (tellurantimony). All these minerals have previously been reported in the Yilgarn gold districts. One rare occurrence of $PbTeCl_2$ (as a solid phase, kolarite) was observed in contact with pyrite within the quartz fracture domains. Telluride minerals have not been observed in any of the other sections or samples from this work.

Figure 3.13.28A and B shows examples of the association between the sphalerite - galena - tennanite-tertrahedite assemblage and Fe-enriched dolomite in open space veins (Figure 3.13.28A, sample SD6d_1), along with second generation quartz. Also as zoned dolomite infilling open space from a larger laminated vein (Figure 3.13.28B, sample SD3a).

The Te-bearing assemblages in the steeper structures are only found in some of the samples. These assemblages are similar to those described by T. Baker (G15 report) as directly related to the High-Ca porphyries

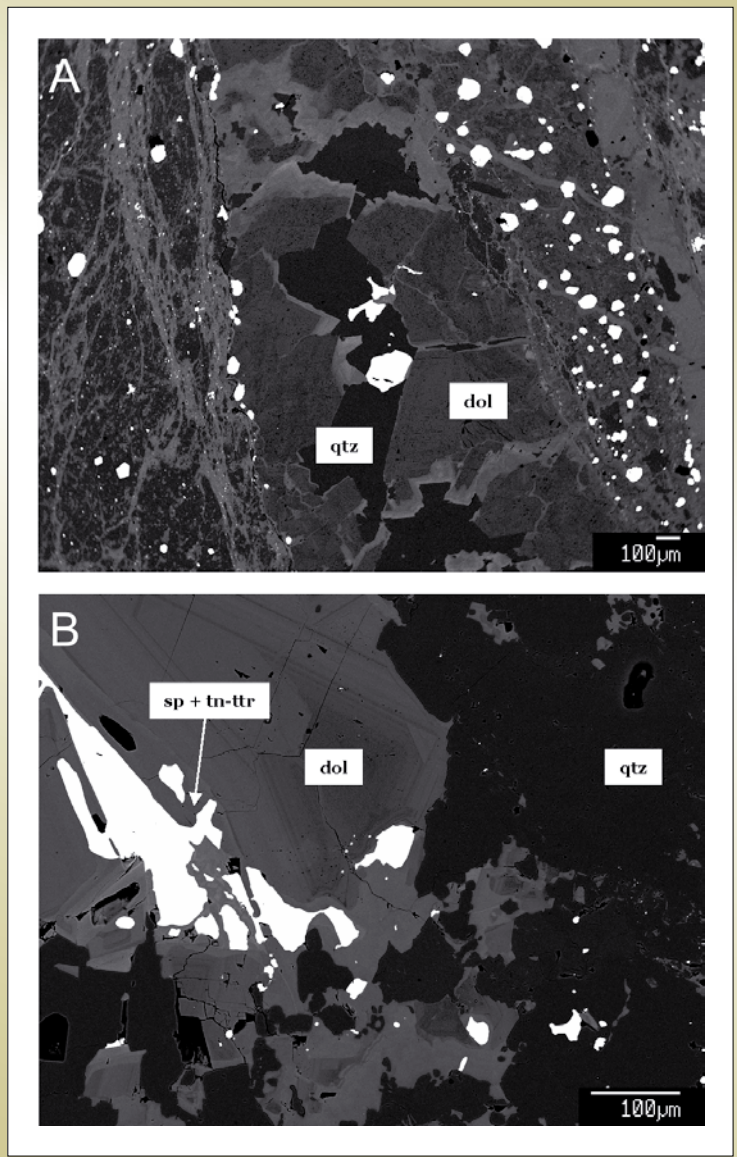


*Figure 3.1 3.28: Association of sulphides to brecciation and infill within dark laminations in quartz veins. A) Open space infill within the centre of the dark laminations and sulphide grains forming in the quartz. B) Zoned dolomite with complex intergrown sphalerite and tenantite-tetrahedrite mineral all part of brecciation infill within quartz vein.*

(Tn-Mo-Cpy-Gn). Are these assemblages and the brecciated quartz associated with the intrusion of the High-Ca porphyries at 2670 Ma?

## Micro-CT Scanning Textures

Because of the complex nature of the textures in the thick laminated quartz veins a sample was analysed using the CSIRO Minerals desktop CT-scanner. This technique, which is similar to medical CAT scanning, reveals the hidden 3D textural relationships based in the response of X-rays in a series of slices through the sample. By using this technique the question of whether these are simple crack-seal veins or something more complicated is explored.

Figure 3.13.29 shows the model of carbonate and sulphide for two different views of the sample. Figure 3.13.29A shows the planes of the dark laminations as recorded in the model while Figure 3.13.29B is an illustration of the two key orientations in a view onto the side of the laminations. Some of the laminations appear to form en-echelon arrays. Figure 3.13.30 is a 3D transparent view of the model showing a discrete carbonate filled fracture cutting obliquely through the sample, as well as some steeper structures. The red shells in Figure 3.13.30 are modelled gold and show that the oblique fracture is post-gold and does not contain any gold grains.

Although this technique is cutting edge and has rarely been applied to this type of analysis before, these models at least illustrate the problem of hidden structure within

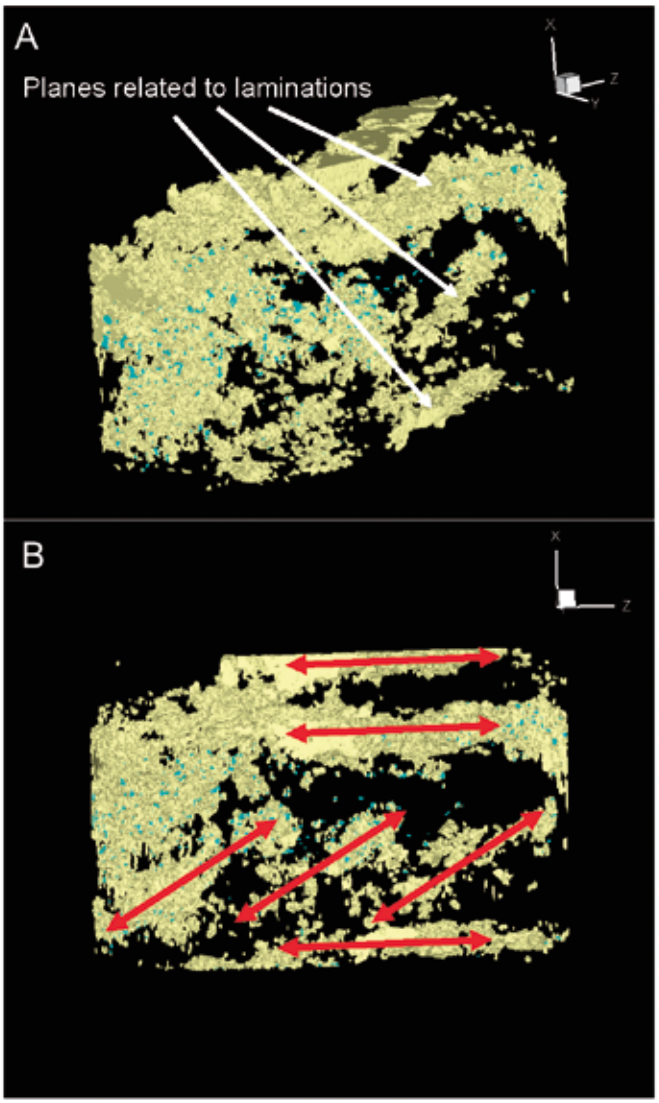


*Figure 3.13.29: CT-Scan model for carbonate (pale yellow) and sulphide (blue) showing A) planes orientated Y-Z related to the dark laminations, and B) view onto the X-Z plane showing two distinct orientations recorded in the carbonate model.*

these samples. The dark laminated veins contain a variety of over printing structures and the laminations themselves appear to be structures overprinting the original quartz breccia vein. Structural measurements of these veins should be treated with due care relative to the complexity illustrated here. In the future this technique should be applied to samples that are orientated relative to structural measurements in order to expose the hidden structure.

Further work is also needed to conclusively say whether the steeper structures with Te-minerals are a true cross cutting feature (post-Au lamination) or steeply orientated breccia infill as part of the quartz event.

### 3.13.11 Apatite Chemistry and Deep Fluids

The dark laminations in the thick laminated veins are often dominated by apatite as an infill phase (see Figure 3.13.25B). Figure 3.13.31 shows a typical apatite in BSEI with the relationships to other phases from the lamination (Figure 3.13.31A), mainly Na-tourmaline and muscovite (and coarse pyrite with gold), and details of the BSE zonation in the apatite itself (Figure 3.13.31B). Chemically the apatites are all F-apatite with no measurable Cl and no calculated $H_2O$. In many cases the F is > 2 atomic formula units indicating the presence of $CO_2$ in the structure (*cf.* ***pmd*CRC*** I7 Q3 report). The core of the apatite is dominated by magnetite and REE mineral inclusions, and this is the only place outside of the BIFs with magnetite. The rim of the apatite is intergrown with the tourmaline and coarse pyrite related to Au. The main chemical difference between the core and rim of the apatite is the Sr concentration. The Sr vs. F is plotted in Figure 3.13.32. The range of Sr values in carbonatite apatite (from the literature) are shown as a black arrow. For the most part the core of the SRD apatites fall within this range and they are extremely Sr-rich. Also in all samples the F is > 2 afu (the standards are also shown at exactly 2 afu).

A key question that emerged from these data was whether the apatites represented input of carbonatite-related fluids into the Au-bearing laminated veins. Because of the concentrated nature of the Sr an initial program of Sr isotope work was carried out to ascertain the signal of the Sr input (crustal vs. mantle sources). LA-ICP-MS isotopic analysis of the apatite was conducted at Melbourne University (Roland Maas). Results are still preliminary but correct at this stage. Results for the apatite (at 2665 Ma) give a $^{87}Sr/^{86}Sr$ value of 0.7016 for all the analysed apatites. This is plotted vs. age on Figure 3.13.33 along with data from Brown et al. (2003) for two SRD samples and Clout (1989) for anhydrite at the Golden Mile. The Brown et al. (2003) data have been reinvestigated relative to the drilling database from SRD and the samples are both outside of the ore zones but the trend from high to low is in the direction of the ore zone. The apatite data are akin to the data from Clout (1989) and fall very close to the

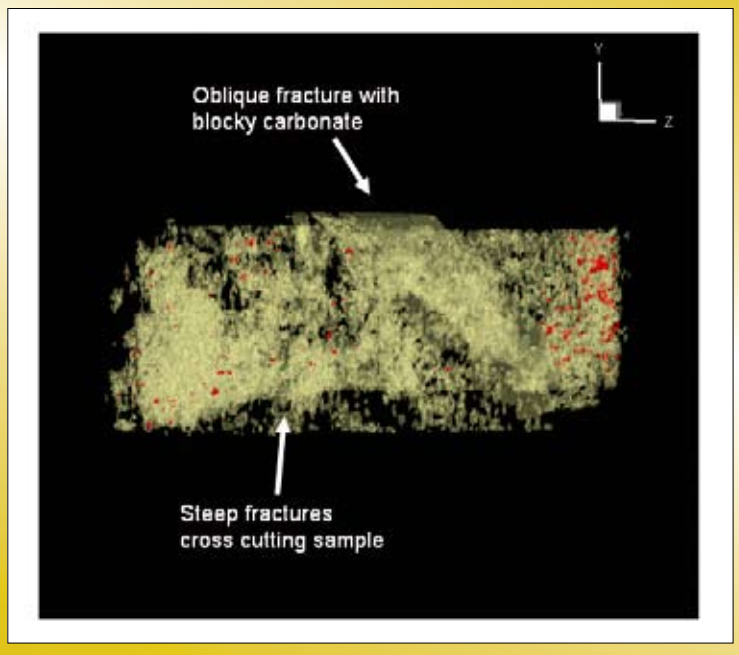


*Figure 3.13.30: CT-Scan of laminated quartz vein sample showing modelled carbonate (pale yellow) and gold (red) looking on the Y-Z plane (cf. Figure 3.13.29). Note the oblique fracture with blocky carbonate cutting steeply through the sample.*

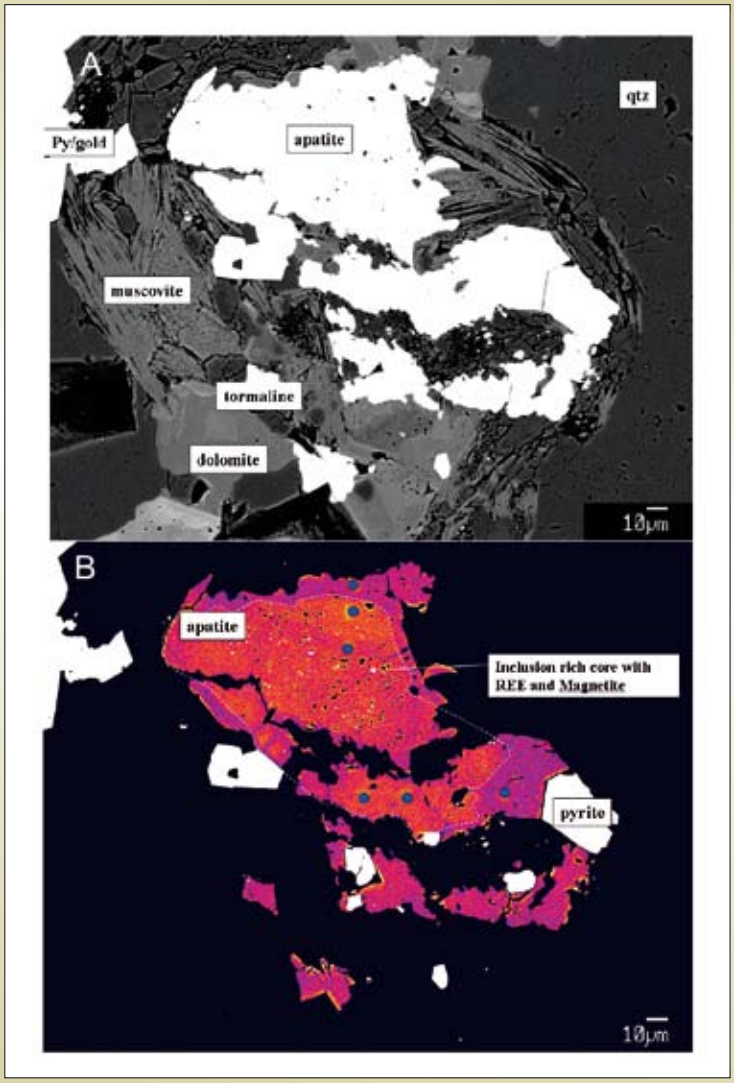


*Figure 3.13.31: A) BSEI of course apatite from gold bearing lamination intergrown at the edge with pyrite-tourmaline-muscovite. B) Same apatite crystal as A false coloured BSEI showing the zonation and details of the magnetite-REE inclusions.*

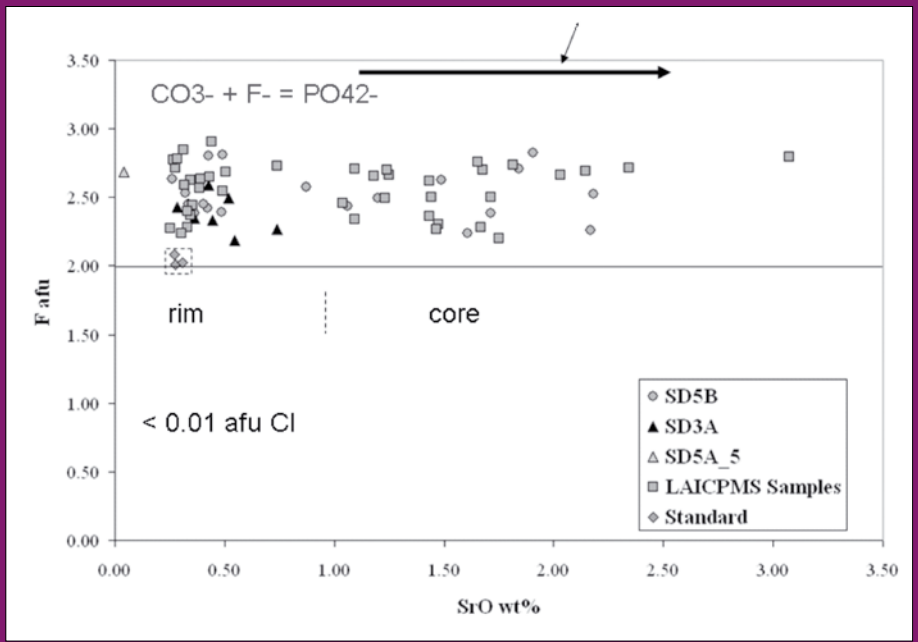


*Figure 3.13.32: F-Sr Apatite chemistry (afu – atomic formula units) from laminations as measured by electron microprobe. Chemical zonation illustrated in Figure 3.13.5B is a consequence of Sr variations. Black arrow is the range of literature values for Sr apatites from carbonatites. Values of F > 2 afu are probably a consequence of the coupled substitution of $CO_2$+F for $PO_4$ (see equation on graph).*

primitive mantle line at that time. The range of values that are calculated for TTG (basement crust) at 2.65 Ga is shown in the blue box and overlap with the numbers from Brown et al. (2003).

The Sunrise Dam apatite appears to form from fluids with a deep, mantle source, and this is in agreement with the observations about Sr concentrations in carbonatites. These values are also similar to those recorded by Clout (1989) in anhydrite and this has been repeated for deep anhydrite veins at St Ives. The presence of magnetite in the apatite also indicates (like the anhydrite) that these fluids were relatively oxidised, however the lack of S in the apatite (as $SO_4$) may suggest that the SO in the fluids has been precipitated further down the flow path.

## 3.13.12 Summary of the chemical evolution of SRD

The Sunrise Dam mineral system represents a long lived gold system where structures have been reactivated and hydrothermal systems are consecutively overprinted. There is evidence for Te-Mo-Bi-Au mineralisation, all be it minor, associated with intrusion of High Ca porphyries and then subsequent Au-rich mineralisation with associated with progressively base-metal rich assemblages in the later structures (i.e. epithermal type D4b breccia zones).

Broadly the geochemical patterns at the deposit are consistent with interactions between steep and flat (moderately dipping shears) pathways, and these are reflected in the subtle shifts in carbon isotopes between < and > -3.5‰ (Figure 3.13.5).

Deeper parts of the SRD system, beneath the Carey Shear Zone, appear to change character slightly and there is some evidence from HyChipper data for the presence of anhydrite in the deeper drill core (CSIRO report to AngloGold, 2006). This is similar to the broad-scale zonation observed at St Ives (Walshe et al., 2008 and Neumayr et al. 2008) in which oxidised magmatic volatiles, derived from mantle melts within the domes, drive anhydrite and carbonate precipitation.

The post-D2 gold sited in muscovite-dolomite-tourmaline laminated veins has been shown to contain apatite which is oxidised and records a deep mantle input into part of the system. The pyrite-gold also in these laminations is good evidence for at least local fluid mixing between a deeply derived, probably magmatically transported fluid and some other more reduced fluid (either ambient or a "Black Juice").

The Sunrise Dam Gold System is long lived and epithermal (boiling) textured quartz-carbonate from the high grade, structurally late, Western Shear Zone indicates that the 2–3kb of confining pressure in the early system is now gone and there has been a period of "unroofing" or uplift (*cf.* Canadian systems in Beakhouse, 2007).

The temporal and vertical zonation in the SRD mineral system is of great importance and might explain the overall

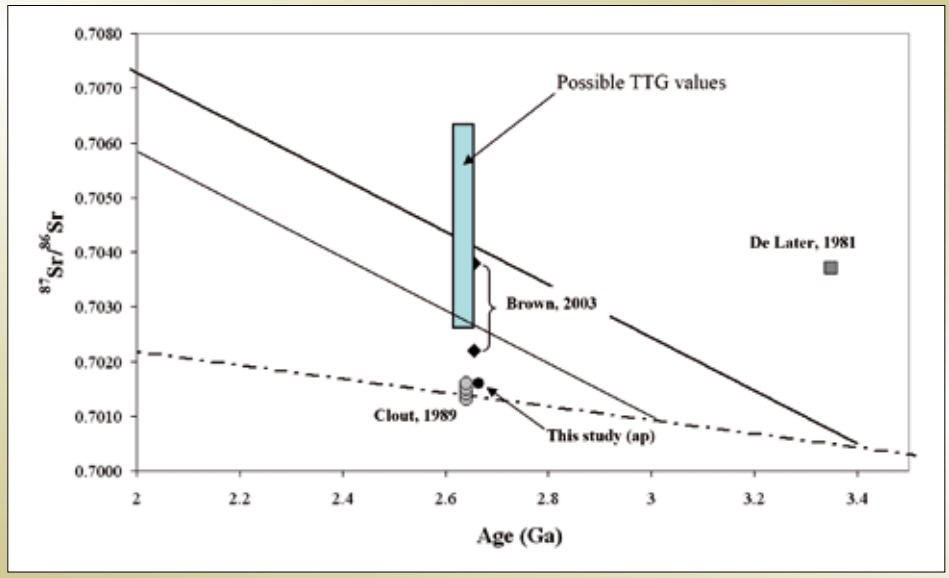


*Figure 3.13.33: Sr isotope data for the SRD deposit.*

size of the system. Unlike the studies at St Ives, the SRD system has not been fully geochemically mapped and it is likely that sampling (drilling and mining) never steps out of the immediate hydrothermal footprint (see Henson et al. 2008). One of the critical factors about SRD is the distance from the inferred granite domes, and potentially the source of deeper fluids. The bulk of the Au is found within the late (D5) breccias and appears to have tapped base metal rich fluids (something not observed in all systems).

One possible candidate for mapping the passage or product of a deeper fluid in the systems appears to be related to the fuchsite distribution. The details are unclear but intersections of a deeper, steeper pathway and the flatter shears delineates fuchsite and related Au-bearing breccia systems (Figure 3.13.9).

## 3.13.13 References


Beakhouse, G., 2007, Links between mantle-derived magmatism and gold systems: the Superior story, Kalgoorlie07 conference, Sept. 2007.

Blenkinsop, T., Baker, T., McLellan, J., Cleverley, J. and Nugus, M., 2007, Sunrise Dam Gold Mine Geology Study Project; Project G15 Final Report; Internal Report for AngloGold Ashanti and Predictive Mineral Discovery Cooperative Research Centre.

Brown, S. M., Fletcher, I. R., Stein, H. J., Snee, L. W., and Groves, D. I., 2002, Geochronological constraints on pre-, syn-, and post mineralization events at the world-class Cleo gold deposit, Eastern Goldfields Province, Western Australia. Economic Geology and the Bulletin of the Society of Economic Geologists 97, 541–559.

Brown, S.M., Johnson, C.A., Wattling, R.J., and Premo, W.R. (2003) Constraints on the composition of ore fluids and implications for mineralising events at the Cleo gold deposit, Eastern Goldfields Province, Western Australia. Australian Journal of Earth Sciences 50: 19–38.

Champion, D.C. and Cassidy, K.F., 2001, Granites of the northern Eastern Goldfields: their distribution, age, geochemistry, petrogenesis, relationship with mineralisation, and implications for tectonic environment, M281-P482 report.

Chen, S.F., Libby, J.W., Greenfield, J.E., Wyche, S., and Riganti, A., 2001, Geometry and kinematics of large arcuate structures formed by impingement of rigid granitoids into greenstone belts during progressive shortening. Geology 29, 283–286.

Clout, J.M.F., 1989, Structural and isotopic studies of the Golden Mile gold-telluride deposit, Kalgoorlie, Western Australia. Ph.D. thesis, Monash University (unpublished).

Cuiaba, Oliver et al., 2005, Unpublished report to AngloGold Ashanti (Brazil), G14 Project ***pmd*CRC***.

Erickson, M., Kent, M., Biggam, J. and Nugus, M.J., 2006, Sunrise Dam Gold Mine Mineral Resource Statement At 31 December 2006. AngloGold Ashanti Australia Limited; Report No. SDGM 13264

Goscombe, B., Blewett, R.S, Czarnota, K., Maas, R., and Groenewald, B.A., 2007, Broad thermo-barometric evolution of the Eastern Goldfields Superterrane, this volume.

Grant, J.A., 1986. The Isochon Diagram – a simple solution to Gresen's equation for metasomatic alteration. Economic Geology 81, 1976–1982.

Henson, P.A., Miller J.M., Zhang Y., Blewett R.S. and Czarnota K., 2008. The 4D architecture of the Laverton camp, Eastern Yilgarn Craton. This volume.

Neumayr, P., Walshe, J. L., Roache, A. and Petersen, K., 2008, Alteration architecture of St Ives. Part III, this report.

Nugus et al., 2007, Geology of Sunrise Dam Gold Mine. Internal and Unpublished Technical Report for AngloGold Ashanti Australia; Sunrise Dam.

Oliver, N. H. S., Cleverley, J.S., Mark, G., Pollard, P.J., Fu, B., Marshall, L.J., Rubenach, M.J., Williams, P. J., and Baker, T., 2004, Modelling the role of sodic alteration in the genesis of iron oxide-copper-gold deposits, Eastern Mount Isa Block, Australia. Economic Geology 99, 1145–1176.

Standing, J.G., 2008, Terrane amalgamation in the Eastern Goldfields Superterrane, Yilgarn Craton: Evidence from tectonostratigraphic studies of the Laverton Greenstone Belt. Precambrian Research 161, 114–134.

Walshe J.L., Neumayr P., Cleverley J., Petersen K., Andrew A., Whitford D., Carr G.R., Kendrick M.A., Young C. and Halley S., 2008, Multiple fluid reservoirs in Eastern Yilgarn gold systems. This volume.

# PART IV: PROJECT DELIVERABLES

A total of fifteen deliverables were completed as the main outputs of the Y4 project. What are printed here are the high-level summaries of the major findings or metadata lists for each deliverable. For the complete deliverable please view the accompanying DVD. Some deliverables contain very significant (several hundred pages long) reports (e.g., Deliverables 3, 7, 8, 11 and 14).

***Deliverable #1.*** ***New time-space event history database, charts, and maps***

***Deliverable #2.*** ***Reports on an updated structural history/ stratigraphy (unravelling the D's)***

***Deliverable #3.*** ***Maps and reports of regional metamorphism and PTt history integrated with structural and alteration history***

***Deliverable #4.*** ***Report on likely geodynamic models of the Yilgarn, with appropriate tests and possible analogues, and a workshop***

***Deliverable #5.*** ***3D maps/GIS of specific districts to be build on Y2 regional 3D map (Laverton, Kalgoorlie-Kambalda, Agnew)***

***Deliverable #6.*** ***Map and report on the early extensional architecture and history***

***Deliverable #7.*** ***Reports on the character of key faults, especially the deep-tapping 'cracks'. Acquire new data (MT and tomography).***

***Deliverable #8.*** ***Report on an improved geologically intelligent geophysical inversions, supported by a rock property database***

***Deliverable #9.*** ***Reports and chemical models on the end-member fluids (magmatic, basinal, meteoric, metamorphic, mantle?)***

***Deliverable #10.*** ***Reports, maps and databases on integrated mineral paragenesis and architecture and chemical modelling for selected camps and deposits***

***Deliverable #11.*** ***Reports on integrated numerical models of fluid flow for generic and site specific scenarios***

***Deliverable #12.*** ***Regional footprint maps of alteration and fluid flow based on geochemistry, ASTER, HYMAP etc***

***Deliverable #13.*** ***Map the chemical and PT gradients for selected sites (e.g., Wallaby, Sunrise, St Ives, KB), and regionally***

***Deliverable #14.*** ***Reports on the integrated structural controls of ore shoots with the regional framework, linked to alteration and mineralogy (e.g., Wallaby, Sunrise, St Ives, KB)***

***Deliverable #15.*** ***Report on reactive transport models tested against specific sites where paragenesis and structure understood***

## Summary of Deliverable #1 New time-space event history database, charts, and maps

**Richard Blewett (Geoscience Australia)**

The new-time-space event history Deliverable 1 was synthesised into the Geodynamic History Deliverable 4. A poster of the geodynamic history is given in this deliverable. A database as such was not completed although Geoscience Australia's Provinces-Events database was populated with geological constraints. At the time of writing a 'self drawn' output of the relationships (the Geodynamics handout chart) is still the best way to display and analyse these temporal event data.

Deliverable 1 has a number of reports on geochronology, namely:

1. Sircombe et al 2007 (GA Record 2007/1) provides thirteen new U-Pb SHRIMP dates of mostly Black Flag Group rocks in the Kalgoorlie region. These data confirm the presence of a hiatus between 2690 Ma and 2680 Ma in the region.

2. Concordia plots of two rocks analysed in 2005 from Puzzle mine near Kookynie and Tarmoola.

3. A short report from Rick Squire on the detrital zircon work (including seven new ages) dating Black Flag Group and Late Basin sequences using a laser and comparing these results with SHRIMP dates.

Three Excel spreadsheets with compiled published age data for rock units and gold mineralisation are provided, along with a bibliography of age data.

David Champion compiled a photographic atlas of the different porphyry types from the St Ives camp and these are catalogued in a pdf document. The report shows the diversity of porphyry types and their differing alteration.

A total of seven talks (PowerPoint files) relevant to Deliverable 1 are provided. They include mostly reports at PDT meetings on age constraints. A talk from Louis Gautier on timing at the Golden Mile is also included.

## Summary of Deliverable #2 Reports on an updated structural history/stratigraphy (unravelling the D's)

**Karol Czarnota (Geoscience Australia)**

Gold deposits of the Eastern Goldfields Superterrane (EGST) are structurally controlled and hence the study of structure has been one of the key points of focus during the Y4 project. The unravelling of the significance, timing, duration and relationship of structures to gold mineralisation has been the focus of this deliverable.

**D2 Reports and Abstracts folder**:

- **Structure northern EGST folder** – Contains all of the results of a couple of weeks of field work by Lloyd White and Karol Czarnota around Wiluna in the northern part of the EGST. The results verified the conclusions that arose from Y1 and provided added confidence the sequence of structural events observed in the central EGST is craton wide.
- **Revised Y1 summary folder** – Contains a summary of structural crosscutting relationships from 50 deposits and 30 granite sites across the central and northern Yilgarn. A ~3 m long banner (see below) provides a correlation of the deformation events with individual A0 posters illustrating the spatial distribution of the events.
- **A new integrated tectonic framework of the EGST** – provides a high level summary of the revised structural event framework.
- **EGST structural field guide** – presents the revised deformation framework for the EGST while also highlighting structural relationships at key localities.
- **Caution using foliations to … and don't hang it on a foliation** – highlights the potential pit fall of using a pervasive fabric in the EGST as a time marker for the purpose of regional structural correlation.
- **Significance of extensional tectonics in the EGST** – provides a review of the extensional events in the Yilgarn highlighting the dominance of an extensional tectonic model for the EGST and the significance of extension in initiating significant gold mineralisation in the EGST.
- **A modified P-T dihedra method…** – outlines a new method for regional structural correlation.

**D2 talks and posters folder** - Contains talks and posters related to the above outputs while also including:

- **St Ives structural observations underground** – A review of the structures observed at St Ives and how they related to the regional deformation framework.
- **St Ives structure** – An overview of the structures at St Ives.
- **Strain mapping** – A short presentation highlighting the intense strain localisation in the EGST using a semi-quantitative method.
- **Regional structure of the Laverton belt** – A summary of the kinematic evidence for various deformation events in the Laverton region.

## Summary of Deliverable #3 Maps and reports of regional metamorphism and PTt history integrated with structural and alteration history

**Ben Goscombe (ITAC)**

### [A] Text, Outcomes, Interpretations and Figures

The main body of text outlining the essential details of the background of the project, methodologies used, description of metamorphic samples, PT calculations,

summary of results and interpretations are contained in the file **EYCMP_Text(NOTES_TOTAL)v11.pdf**. This draft text is a work in progress that contains ideas, details and findings of the project up to 10th December 2007. The text is not finalised and has not as yet been fully referenced to the existing literature, but does cover the full range and evolution of interpretations considered during the course of the project. The text contains reference to supporting appendices listed below that make up the body of research behind Deliverable #3 (EYCMP). The most important supporting appendices that need to be read in conjunction with the main text file are listed below:

- Appendix 33 contains the methodology and outcome figures for the **integration** of metamorphic conditions (peak PT estimates), metamorphic evolutions (PT loops) and structural data (from Blewett and Czarnota, 2007). The three different final outcome datasets have been integrated using metamorphic field gradients and the map outlining distinct metamorphic domains as a basis.
- Appendix 34 contains the methodology for recognising domains of different metamorphic conditions, metamorphic evolutions (PT paths) and interpreted age of metamorphism (metamorphic event). This **metamorphic domain analysis** is presented as a map outlining the recognised domains, as well as PT plots collating the PT conditions and evolutions in each of the recognised domains.
- Appendix 35 is a folder containing 470 individual **Key Site Descriptions**; bringing together the petrography, whole rock analyses, mineral analyses, PT calculations, interpreted PT paths, field photos and microphotographs at each Key Site described by the project.
- Appendix 37 contains the methodology for constraining the **PT path** in each Key Site that has been well described by petrology, sequence of mineral growth and PT calculations. This appendix contains a library of interpreted P-T evolutions at each Key Site, constrained by what is interpreted to be the most appropriate published PT pseudosections.
- Appendix 40 contains a library of all **map figures** generated in the course of the project.
- Appendix 41 contains a library of all figures involving **PT plots** of data at different stages in the project.
- Appendix 42 contains a library of all figures describing different models and interpretations.
- Appendix 50 contains the methodology and outcome figures for the PT arrays that can be fitted to calculated PT results in every domain and terrane in the EYC.
- Appendix 51 contains the methodology and outcome figures for metamorphic field gradients along 6 profiles and 2 composite profiles across the EYC.

### [B] Methodologies

The methodologies used to extract data from the three different sources; geological survey datasets, published literature and new data generated in the course of this project are outlines in Appendices 3, 4 and 5 respectively. A series of appendices outline the background arguments behind different aspects of the project. Concepts behind metamorphic mapping are contained in Appendices 6 and 7. Background behind bulk strain mapping and rock flow regime are contained in Appendices 8 and 9 respectively. The methodologies used to calculate absolute PT estimates are contained in Appendices 39 and 43. The background behind the definition, utility and interpretation of metamorphic field gradients and average thermal gradient is outlined in Appendix 13.

### [C] Datasets

The database used to collate all the metamorphic and structural data used in this project is described in Appendix 1 and the parameters and attributes used are listed in Appendices 14 and 2 respectively. Appendix 44 is the final data table of all point data used as the basis of the GIS database. Details of all samples collected and analysed for this project are contained in Appendix 38.

The models used for mineral activity calculations are contained in Appendix 17 and resultant mineral activities are contained in Appendix 18. Output files from THERMOCALC experiments are contained in Appendix 19 and all THERMOCALC variables and results are tabulated in Appendix 21. All conventional geothermobarometer calculations are contained in Appendix 26. A complete set of all metamorphic calculations undertaken, by all methods, are organised by sample (Appendix 47) and by domain (Appendix 46).

Specific raw datasets are contained in the following Appendices. Raw and recalculated whole rock analyses are contained in Appendices 11 and 12, and comparison with bulk compositions of published pseudosections is contained in Appendix 27. The total dataset of all raw and recalculated mineral analyses are presented in Appendices 15, 16, 20 and 48. Libraries of garnet compositional maps, microphotographs and field photographs are contained in Appendices 28, 29 and 30 respectively. All petrographic descriptions and XRD determinations of difficult to interpret fine-grained samples are contained in Appendices 31 and 32 respectively.

Appendices 22, 23 and 24 are incomplete in December 2007 and will ultimately contain all description, methodology an outcomes from U-Pb, Sm-Nd and Lu-Hf geochonology studies when finalized. All available geochronology from the EYC is tabulated in Appendix 25.

### [D] Delivered talks and abstracts

Also delivered are Power Point files of talks delivered to stakeholders in 2006, 2007 and Kalgoorlie07 conference and the Kalgoorlie07 extended abstract.

### [E] Further supporting documents

Appendix 10 contains a library of published PT pseudosections in a wide range of bulk compositions. The published pseudosections with bulk compositions represented by rocks in the EYC have been drafted and listed in a library of pseudosections (Appendix 36) that were used to constrain the PT paths of EYC samples (Appendix 37). Appendix 49 is a library of figures drawn from literature that has been drawn upon throughout the project.

## Summary of Deliverable #4
## Report on likely geodynamic models of the Yilgarn, with appropriate tests and possible analogues, and a workshop

**Karol Czarnota (Geoscience Australia)**

The gold deposits of the Eastern Goldfields Superterrane (EGST) are the products of a large scale vigorous tectonic cycle. The unravelling of this tectonic cycle is the focus of this deliverable. A key achievement has been the integration of the stratigraphy, magmatism, structure, metamorphism and timing of gold mineralisation summarised in the **geodynamic handout**. This plot shows that variations in one of these elements is marked by a change in all other elements thereby indicating the EGST developed through a series of discrete yet related events.

**D4 Reports and Abstracts folder**:

- **GA cadet tectonic comparison project folder** – contains a summary of the Barimian and Massif Central Gold mineral system for comparison with the EGST. Also contains a flow diagram for classifying granites.
- **Geodynamic timing diagram** – a time, space synthesis of the: stratigraphy; magmatism; structure; metamorphism; and timing of gold mineralisation in the EGST in pdf and Corel Draw format.
- **A deeper view of the EGST** – A summarises the big scale data sets and insights into the geodynamics of the EGST.
- **An integrated tectonic framework of the EGST** – A high level summary of the geodynamics of the EGST
- **An orogenic surge model for the EGST implications for gold mineralising systems** – An overview of a contractional model for the EGST since outdated by the view that extension is the dominant tectonic mode of the EGST
- **An overview of the Yilgarn craton** – A summary of the granite types and tectonic implications
- **Big system-big picture integrating geology, geophysics, seismology, geochemistry and geochronology to determine why the Yilgarn is there**
- **Domes the characteristic 3D architecture of the EGST** – High level overview for the presence and significance of domes at a number of scales in the EGST.
- **Geodynamic and metallogenic evolution of the Yilgarn Craton** – Outline of key data sets and features of the EGST gold mineral system at a range of scales.
- **Implications for crustal evolution and mineralization area selection** – An outline of the development and implication of domal structures at a number of scales.
- **Key finding from the 2007 Penrose conference** – An outline of key findings from the 2007 Penrose conference on extension.

- **Metamorphic evolution of the Eastern Goldfields Superterrane** – A high level overview of the main metamorphic events in the EGST

**D4 talks folder** - Contains talks and posters related to the above outputs also including:

- **Geodynamics workshop folder** – Contains presentations on: drivers and mantle involvement; stress switches; granites; lithosphere; and greenstones, from the geodynamics workshop.
- **A Systems Approach to Mineralization** – Views by Bruce Hobbs as to the geodynamic evolution of the EGST.
- **Concepts to targets in the Laverton region to Mt Isa project** – An overview of process based geodynamic thinking applied to exploration in the Laverton Region.
- **Flavours of mantle lithosphere** – R. Patton views on the geodynamics of the EGST.
- **Notes on Geodynamics** – A review of end member geodynamic models.
- **Superior Province granites & gold geology review**
- **Thoughts on geodynamics** – A cyclic view of geodynamics in the Kalgoorlie Terrane highlighting the significance of prolonged magmatism in the Kalgoorlie Terrane.

**D4 maps folder**

- **Nd Yilgarn depleted mantle model age maps** – the old and new maps of the Yilgarn Craton.
- **Terranes and Domains map of the Yilgarn Craton**

## Summary of Deliverable #5 3D maps/GIS of specific districts to be built on Y2 regional 3D map (Laverton, Kalgoorlie-Kambalda, Agnew)

**Paul Henson (Geoscience Australia)**

The integration of 3D maps into the ***pmd*CRC*** Y4 project has provided different ways to visualise, interrogate and deliver the data. This medium allows multidisciplinary data generated by a range of researchers from different disciplines to be compared spatially in the context of the mineral system. The data collected within the project covers a range of scales, from mine scale through to studies of the lithosphere. By using 3D software these data can be viewed in the same space providing a better understanding and linkages between the datasets.

Data collected within the ***pmd*CRC*** Y4 project have both complimented data generated within the ***pmd*CRC*** Y2 project and significantly added to them. The data have been generated from a variety of localities and formats throughout the Yilgarn Craton, W.A. The 3D data are available in Part V of this report (on the accompanying 1Tb usb hard drive). Highlights of the new 3D data and documentation generated within this project are as follows:

**Appendix_1**

- PowerPoint presentations describing 3D maps and concepts

**Appendix_2**

- Reports:
  - Sunrise Dam – deep targets (document)
  - Painted faults – targeting (document)
  - Yilgarn undercover – targeting (document)

**Appendix_3**

- 3D workshop document
  - Workshop Notes How to make a 3D map: a ***pmd*CRC*** workshop (document)

## Summary of Deliverable #6 Map and report on the early extensional architecture and history

**Richard Blewett (Geoscience Australia)**

The recognition of the extension has been noted and is included in many of the other deliverables (e.g. Deliverable 4 – Geodynamics and Deliverable 5 – 3D maps, as well as the papers in Part III).

Extension has been mapped at a range of scales, including:

- Rick Squire made a revised map of the St Ives camp using constraints provided by different clasts of the Black Flag Groups.
- Miller in his paper on St Ives describes the D1 extensional control on the distribution of komatiites and intrusive dolerites.

- The new Sm-Nd map is a map of the largest scale of extension that operated at 2800 Ma and this 'event' established up the major architecture of the entire Eastern Goldfields Superterrane.
- The seismic architecture is also inferred to be a function of largely extensional tectonics, and a poster and extended abstract (from Karol Czarnota) describes this.

A number of talks made at various PDT meetings by Gerard Tripp, Rick Squire and Karol Czarnota are concerned specifically with the early extension.

The recognition of the importance of extension is illustrated in the Targeting section (Part II) and the significant architectural pathways (and gold deposits) that were developed by extensional processes.

## Summary of Deliverable #7
## Reports on the character of key faults, especially the deep-tapping 'cracks'. Acquire new data (MT and tomography).

**Richard Blewett (Geoscience Australia)**

Deliverable 7 has the PhD thesis of Anthony Morey which was asking the question about what are the key criteria regarding endowed (Boulder-Lefroy) as opposed to poorly mineralised (Bardoc Tectonic Zone) faults (his thesis abstract is reproduced here). The Y4 project also acquired a new magnetotelluric survey across the Kalgoorlie Terrane, coincident with the EGF01 seismic line of 1991. A number of PowerPoint presentations are found in the deliverable and the images are located in the regional gocad in Part IV. A copy of the paper from Goleby et al. (2006) on integrated seismic studies for understanding the architecture and geodynamics of the Yilgarn is also provided.

A 130 km long magnetotelluric (MT) transect was carried out across the Eastern Yilgarn along the deep seismic line EGF01 on May 2006. In that 25 stations with an interval of 5 km were selected for MT measurements. All measurements were calibrated with a GPS clock, for use in latter stage processing as remote referenced (RR) MT data. The objective of the entire exercise was to understand deep crustal to mantle electrical conductivity structure from a 2D conductivity image obtained from multi-component MT data along the line and its relation to the subsurface architecture delineated by the seismic data of EGF01.

The MT method deals with a natural source electromagnetic (EM) field which contains a ultralow- to very high-frequency range of the EM signal. In multi-component MT measurements, we measure three magnetic field components, such as Hx (East-West), Hy (North-South) and Hz (vertical) and two electric field components Ex (East-West) and Ey (North-South). The data measured are time series, and the record is collected over several days by the instrument stationed at a site. Such time series data after appropriate processing yield impedance tensor ($Z_{xx}$, $Z_{xy}$, $Z_{yx}$, $Z_{yy}$) and other accessory parameters such as tipper, skewness, ellipticity etc. While impedance tensor are used to determine apparent resistivity tensor ($\rho_{xx}$, $\rho_{xy}$, $\rho_{yx}$, $\rho_{yy}$) and phase tensor ($\phi_{xx}$, $\phi_{xy}$, $\phi_{yx}$, $\phi_{yy}$) which in turn helps in determining conductivity structure through inverse modelling. On the other hand the accessory parameters help in determining structural dimension of the anomaly and its attitude.

We have made both 1D and 2D inversion of MT data to determine the electrical conductivity structure of the subsurface. The electrical conductivity image clearly demonstrates prominent (anomalous) region of high conductivity (low resistivity) in the upper crust below the Kalgoorlie Terrane. Other geological features such as deep crust penetrating faults are also been revealed in the conductivity image.

### Abstract from Morey 2007 PhD thesis

The Bardoc Tectonic Zone (BTZ) is a major shear system within the late-Archaean Eastern Goldfields Province (EGP) Western Australia, which is connected along strike to the Boulder-Lefroy Shear Zone (BLSZ). The BTZ has only produced ~100 t Au from approximately 80 orogenic deposits whereas the BLSZ is associated with one giant (>500 t Au) and at least two world-class (>100 t Au) deposits or camps. The aim of this thesis is to understand why these linked shear systems have a difference in gold endowment of one order of magnitude.

Structural mapping of three well-spaced open pit deposits (Paddington, New Boddington, Yunndaga) within the broad (5–12 km) and uniformly oriented BTZ has revealed that the structural evolution of this shear system was

dominated by the intense development of NNW-trending reverse to transpressional shear zones and upright folds related to the second regional deformation event (D2). These D2 structures controlled gold deposition. Within the BTZ, strike-slip ductile shearing (D3) did not significantly develop and low offset (<100 m displacement) brittle-ductile faults (D4) are common, but consistently post-date gold mineralisation. This is in contrast with many other major gold deposits in the region, which are controlled by these late deformation phases.

Multi-scale gravity gradients indicate the strike-parallel granite domes, which closely bound the BTZ, continue to a depth of 20 km as steep NNW-trending structures, suggesting that the narrow corridor of greenstones that define the BTZ does not significantly broaden at depth. As substantiated by surface mapping, the competent granite domes likely localised bulk strain during regional ENE–WSW shortening to within the less competent 5- to 12-km wide greenstone corridor, causing intense deformation. During this deformation the supracrustal units rapidly rotated towards the flattening vertical plane. Consequently, this architecture created a broad network of shear zones that were uniformly oriented orthogonal to the regional shortening direction, which restricted D3 strike-slip deformation within this shear system. These shear zones dispersed the majority of upwelling auriferous fluids during orogenesis. Moreover, competent mafic rocks favourable for hosting vein-gold structures were strongly attenuated, so that the dispersed fluids had limited sites for gold mineralisation. In contrast, systems such as the narrow (<2 km), variably-striking BLSZ, which intersects large competent host units, acted as high permeability conduits that focused auriferous fluids to localised depositional sites.

Despite the gold-bearing veins from a number of BTZ deposits (Paddington, Talbot South, New Boddington, Yunndaga and Nerrin Nerrin) being either brittle, brittle-ductile or ductile in nature, and the metamorphic grade of the host mafic units varying between greenschist or lower-amphibolite facies, optical and backscatter electron (BSE) microscopy shows that the sulphur-bearing minerals from across the BTZ underwent a uniform three-stage alteration history. Stage 1 is characterised by the formation of pyrrhotite, which was overprinted by Stage 2 arsenopyrite + invisible gold, which in turn was overprinted by Stage 3 pyrite + visible gold + base metal sulfides ± rutile ± ilmenite. Stable sulfur isotope ratios (δ34 S) of Stage 2 arsenopyrite range between +1 and +9 ‰ and Stage 3 pyrite between 0 and +7 ‰. These isotopic data, alongside the presence of pyrrhotite and ilmenite, and the alteration history, suggests that alteration within the BTZ was characterised by uniformly reduced hydrothermal conditions, which is consistent with a regionally homogenous fluid system throughout the BTZ. Although these data are typical of many other Archaean orogenic gold systems, a number of world-class and giant gold deposits associated with the BLSZ and elsewhere within the EGP have larger δ34 S ranges (-10 to +10 ‰) and also contain haematite and sulfate as alteration minerals (e.g., Golden Mile). In agreement with previous studies, results herein suggest a greater variation in δ34 S values and alteration mineralogy to be a potential identifying characteristic of richly-endowed shear systems, as opposed to the uniform, reduced hydrothermal conditions characterised by the far less well endowed BTZ.

Backscattered electron images of arsenopyrite from the BTZ, and pyrite from the Boorara shear zone (located east of the BLSZ), reveal that the fracture margins and grain boundaries of arsenopyrite are characterised by <250 μm-wide hydrothermal alteration rims. Unaltered portions of the same grains contain invisible gold (up to ~30 ppm), whereas alteration rims control the distribution of visible gold particles. Electron microprobe (EMP) and BSE data reveal that the alteration rims in arsenopyrite grains from the BTZ are characterised by an average As enrichment of ~1.5 At %. Phase relationships and EMP data on arsenopyrite from the BTZ indicate that the alteration of Stage 2 arsenopyrite + invisible gold to Stage 3 altered arsenopyrite + visible gold is associated with a temperature increase (maximum change of the fluid from 310° to 415° C) and an increase in sulfur fugacity (up to 6 orders of magnitude). As the gold distribution of arsenopyrite from the BTZ is typical of many other gold deposits, understanding the evolution of their associated alteration rims potentially reveals the hydrothermal processes associated with ore genesis.

## Summary of Deliverable #8
## Report on an improved geologically intelligent geophysical inversions, supported by a rock property database

**Nick Williams (University of British Columbia, Geoscience Australia)**

Extracting geologically realistic physical property models from gravity and magnetic inversions requires high quality geophysical data, an understanding of the geological environment, and a solid understanding of the physical properties of the rocks in the area. Recent advances in 3D geological modelling capabilities, such as those available in the GeoModeller software package, facilitate the rapid creation of 3D subsurface models that look geologically feasible. The process of integrating a variety of datasets and building such geometry-based models is a powerful way to enhance our understanding of subsurface geology. However many of these models are unsuitable for use in constraining potential field inversions because they may be based on limited physical property data, don't apply the available property data directly to the model, or ambitiously apply constraints in areas of the model where no reliable geological information is available. As physical property information becomes more accessible through increased measurement and the availability of public databases, such as Canada's rock property database (http://www.mirageoscience.com/rpds), it is important to ensure that the data are included effectively into constraining geophysical inversions to enhance the value of the inversion results.

To develop an understanding of the relative contribution of different types of constraints to an inversion result, a simple synthetic density model of Yilgarn-like geology had a gravity response calculated. The gravity data were then inverted using the UBC–GIF GRAV3D inversion package in a series of geologically-constrained inversions with progressively more detailed geological data to simulate the contribution of knowledge at different stages of an exploration program. The results showed that the most effective constraints are those based on 1) surface maps, 2) reliable 3D models defined in small areas of abundant geological information, and 3) deep drill holes. All require reliable physical property information to guide the inversion towards a geological realistic result. Importantly the results showed that a full 3D physical property model for the entire inversion volume was not required to recover predictive results.

Since geological observations will generally be limited to surface exposures and relatively shallow drill holes in all but the most advanced projects, the reliability of a 3D subsurface model built for the entire inversion volume will be questionable. Yet any full 3D model that is built will primarily be based on those near surface geological observations. This suggests a simpler method for developing constraints for geophysical inversions. Ideally, this method would automatically build a physical property model from the raw geological observations in only those regions where sufficient information is available to warrant constraints. This new method of generating constraining models for UBC–GIF inversions moves away from hypothesis testing and towards tight integration of geological data with the geophysics. A demonstration version of this model building code is being developed by N. Williams as part of his ongoing Ph.D. research and the preliminary method is documented (in this deliverable). The approach limits the amount of interpretation required for building the model, and ensures that all available geological datasets are used, including (in order of priority and reliability):

1. Physical property measurements on surface samples
2. Physical property measurements on drill core or down drill holes
3. Geology logs from drilling
4. Outcrop geology maps
5. Basement geology map interpretations
6. 3D geological models (if available)

In this approach, available physical property measurements (items 1 and 2) are applied directly to a constraining model. They are also used to develop a physical property database for all geological units for which property measurements are available. The database is used to automatically apply physical property estimates to geological observations present in maps, drilling logs, and 3D geological models (items 3–6). An option exists to extrapolate the observed physical properties outwards a short distance from the observed locations but most cells which contain no observations retain default property values that are

not-enforced as constraints in UBC–GIF inversions. Initial results suggest that geological structure and geometry can be resolved based on these sparse physical property and geological observations without specifying the geometry directly.

Any geophysical inversion result, whether geologically-constrained or not, must be interpreted in terms of geology. In early targeting stages it may be sufficient to loosely correlate regions of density or susceptibility highs with rocks known to have higher physical property values. More advanced exploration may require more quantitative interpretations to extract geological information from the inversions' physical property models. Williams and Dipple (2007) describe a method for calculating the possible range of mineral abundances present in a sample, either a rock or an inversion model cell, based on the density and susceptibility of the sample, the expected mineralogy, and known petrological relationships between each of the minerals present.

Certain minerals are known to influence the physical properties of rocks more than others – densities and magnetic susceptibilities are strongly controlled by magnetite and other oxides, sulphides, and low density alteration phases such as sericite and serpentine. Ore deposit models will provide some additional knowledge regarding the associations between those minerals: Fe-oxide Cu-Au deposits like Olympic Dam usually contain more oxides than sulphides; heavily serpentinised ultramafic rocks are likely to contain more magnetite than less-altered equivalents; volcanic-hosted massive sulphide deposits will typically have more pyrite than other sulphides. The method proposed by Williams and Dipple (2007) allows this information to be supplied as mathematical constraints on a linear programming optimisation problem that calculates the range of abundances for each of the components. Used to calculate the percentages of haematite, magnetite, and sulphides present in regional-scale gravity and magnetic inversion models of Olympic Dam, the technique clearly identified the largest known mineral occurrences in the region, including Olympic Dam, but also identified several smaller target regions where the available geological knowledge may be insufficient to explain the observed geophysical responses. The technique provides a quantitative way to evaluate targets based on their likely mineralogy rather than some more tenuous proxy.

Indrajit Roy has written a comprehensive report documenting the use of inversions at a range of scales (entire Yilgarn Craton to specific areas such as Laverton). A new methodology of regional-residual separations is described for improving the inversion process. A number of forward models have been generated in establishing architectures for 3D maps, and these are also described and illustrated in this report. Although part of Deliverable 7, the methodologies and processing steps applied to the magnetotelluric data are described here. Horizontal derivative images (worms) were generated at a range of scales and used in various other Deliverables. Their generation is also described in this report.

## Summary of Deliverable #9 Reports and chemical models on the end-member fluids (magmatic, basinal, meteoric, metamorphic, mantle?)

**John Walshe (CSIRO)**

Deliverable 9 contains a range of abstracts, data, images, poster, publications and talks. It is emphasized here that the deliverables 10 and 12 also contain files which are equally pertinent to deliverable 9, but have been filed in the respective folders.

In a range of Reports, Petersen outlines the paragenetic and fluid evidence collected in the St Ives gold camp. Especially the abstracts for Beijing, Dublin and ECROFI conferences contain key new information. The ECROFI abstract also discusses laser ICPMS analyses which give indications of the metal composition of the hydrothermal fluids.

The abstracts are accompanied by a range of posters and presentations. These files show more evidence in detail and demonstrate the two fluid types ($CH_4$-$N_2$-$CO_2$, $CO_2$-$H_2O$) in the St Ives gold camp and their spatial distribution. Laser ICPMS data show that in fact the reduced fluids contained abundant metals, a result which is unexpected given the results of previous studies, which focused mainly on the $H_2O$ rich part of the hydrothermal systems. Importantly, some talks contain detailed evidence which support the hypothesis that hydrothermal fluids mixed in the St Ives gold camp and that fluid mixing directly contributed to the precipitation of gold.

The St Ives fluid inclusion presentations are supported by a data file which contains all the measurements collected. A series of images are also delivered which are designed to support a manuscript in preparation.

In the publications folder, a manuscript is presented about the fluid evolution in the New Celebration gold deposit. Interestingly at New Celebration, the fluid evolves from a $CH_4$ dominated fluid through a possibly magmatically derived $CO_2$-$H_2O$ fluid back through to $CH_4$ dominated fluids. This indicates again that at least two different fluids are present in these gold systems.

## Summary of new findings

The end member fluids are modelled as:

1. Fluid 1 is modelled as a background or ambient aqueous fluid with low concentrations of salt and $CO_2$.
2. Fluid 2 is modelled as an anhydrous carbonic fluid of magmatic affinity with significant levels of $SO_2$ and $CO_2$ sourced from the mantle.
3. Fluid 3 is modelled as a hydridic deep-Earth fluid that transported volatile species such as $CH_4$, $N_2$ as well as $H_2$, $H_2S$, HCl ± HF, precious metals and hydrides of alkali and alkali-earth elements e.g., Na and Mg.

These end member fluids are defined from alteration mineralogy, fluid inclusions stable isotopes and radiogenic isotopes as discussed in Part III.

### Fluid 1

Modelled as background aqueous fluids with low concentrations of salt and $CO_2$. This $H_2O$ - $CO_2$ ± NaCl fluid is the most commonly observed fluid type in fluid inclusion studies of Archaean Au deposits and is inferred to have been moderately oxidizing with $CO_2$ and $H_2S$ the dominant C and S species. It equates to fluids of potentially diverse origins, basinal brines, metamorphic fluids or even magmatic fluids that equilibrated with the greenstones. In comparison with the fluids of the Au stage, its single diagnostic characteristic is that it is a hydrous fluid. Late in the evolution of the system, this hydrous fluid is commonly much more saline. It is likely that the major reservoirs of water during gold mineralization, late in the metamorphic history were in the late basins, although this remains largely conjectural.

### Fluid 2

The oxidized end-member fluid of magmatic affinity is modelled as anhydrous, dominated by $CO_2$ and $SO_2$ with the following isotopic properties

- $\delta^{34}S$ of $SO_{2(g)}$ is ~ 0 ‰
- At ~ 400 – 500 °C, $\delta^{34}S$ of coexisting $H_2S_{(g)}$ was ~ - 3.5 to -5 ‰
- Magmatic $CO_2$ was mantle derived with a $\delta^{13}C$ value of ~ -5 to -6 ‰
- Radiogenic Pb isotope signature ($^{207}Pb/^{204}Pb$ > ~ 15.5)

The radiogenic lead signal that corresponds with $^{34}Spy$ ~ -3 to -5 ‰ is interpreted as the isotopic Pb signal condensation of volatiles of magmatic affinity (data from the Leviathan Complex, St Ives)

### Fluid 3

The deep-Earth fluid is modelled as a hydridic fluid with volatile species such as $CH_4$, $N_2$ as well as $H_2S$, HCl ±HF, precious metals and hydrides of alkali and alkali-earth elements e.g., Na and Mg. The reduced fluid is assumed to contain sufficient $H_2$ to permit reduction of $CO_2$ to $CH_4$ and the acid species (HCl ±HF) are added to the reduced fluid to account for the inverse correlation of oxidized alteration assemblages with acidic alteration assemblages.

Au-related fluid inclusion samples show a relationship between Ar compositions and Fluids 1, 2 and 3 (Kendrick et al. 2008).

- $H_2O$-NaCl-dominated fluid inclusions with minor $CO_2$ have the lowest $^{40}Ar/^{36}Ar$ values of ~700–2300 and are interpreted to represent 'ambient' fluids of the mid-crust.
- $CO_2$-$H_2O$-NaCl fluid inclusions in oxidised veins spatially associated with intrusions imaged by seismic, or felsic porphyries exposed in the mine area have $^{40}Ar/^{36}Ar$ values of ≥17,000.
- $CH_4$ fluid inclusions in reduced veins have the highest $^{40}Ar/^{36}Ar$ values of up to ~ 48,000 and are inferred to contain parts-per-trillion $^{36}Ar$. The high $^{40}Ar/^{36}Ar$ values are similar to the modern day convecting mantle.

## Summary of Deliverable #10
## Reports, maps and databases on integrated mineral paragenesis and architecture and chemical modelling for selected camps and deposits

**Peter Neumayr (CET-UWA)**

Deliverable 10 contains a range of abstracts, reports, presentations and three 3D models. It is emphasized here that the Deliverables 9 and 12 also contain files which are equally pertinent to Deliverable 10, but have been filed in the respective folders.

The delivery focuses mostly on St Ives, Kanowna Belle, and the Laverton camp. Henson presents a detailed analysis of the Laverton district and emphasizes the importance of deep tapping faults, buried domes and the district-scale structural architecture to determine further target areas in the district.

The Kanowna Belle deposit and surrounds is analysed in a number of presentations and a memo by Young. The presentations show the importance of using a well-constrained 3D model in data rich areas to carefully analyse the detailed structural controls on gold mineralization, but also on the different alteration types. In a second step the hydrothermal alteration and the pathways of the different fluids are analysed in 3D. The analysis of the architecture in the 3D model is followed by practical hand sample descriptions and backed up by spectral and isotopic data.

The architecture and alteration mineral paragenesis of the St Ives gold camp and it's deposits is presented in 3D models and presentations. Neumayr presents three 3D models of the Leviathan complex, Junction and Revenge gold deposits. The models contain alteration point data, Leapfrog modelled ore shells and rock shells as well as interpreted structures using hydrothermal alteration data, shape of felsic porphyry intrusions and ore shell shapes. Importantly, the models led to the prediction of a number of structures the significance of which has not been recognized before. The significance of these structures is shown in presentations by Neumayr. The model also contains a number of surfaces presented by Ruming in his Ph.D. thesis which are useful architectural elements for comparison to the analysis carried out by the ***pmd*CRC***.

Roache presents a novel approach to tackle both small scale and gold deposit to camp scale analysis of the structural controls on gold mineralisation. In a conventional structural mapping approach, the problem of extrapolation of local results typically occurs. Roache resolved this problem by first a detailed structural mapping and core logging exercise which is backed up by spectral data along diamond core. Importantly, distinct alteration assemblages can be tagged to particular structural elements. This allows the prediction of similar structures elsewhere in the camp using spectral data on diamond drill core.

Petersen presents a talk which details the evidence for fluid mixing in the St Ives gold camp in Deliverable 10 as well as in Deliverable 9. The evidence includes textural criteria of structures and alteration, mutual overprinting relationships and fluid inclusion evidence.

Chopping presents insightful thoughts on the use of seismic to constrain alteration pathways and how to identify zones in the seismic which contain abundant hydrothermal alteration.

## Summary of Deliverable #11
## Reports on integrated numerical models of fluid flow for generic and site specific scenarios

**Heather Sheldon (CSIRO)**

Deliverable 11 describes a suite of numerical models exploring various aspects of the processes involved in Archaean gold mineralisation in the Yilgarn. The models include varying degrees of coupling between deformation, fluid flow, magmatic/metamorphic fluid production and heat transport. Various generic and site-specific geometries were used in the models, including a 1D column of basalt and granite; a simple box model representing three intrusions and a vertical fault; a generic 2D representation of a late basin overlying domed granite-greenstone basement; a simplified representation of the major fault structure in the Laverton region; and a realistic model of major faults in the Kalgoorlie region.

Deliverable 11 describes 6 sets of models:

**(i) Granite intrusions I: Preliminary models with implications for fluid flow, heat transport and deformation**

- Relationship between convective fluid flow and metamorphic patterns;
- Stress regimes around intrusions

**(ii) Patterns of deformation and fluid flow associated with late basins under extensional and compressional settings**

- Downflow in extension, upflow during inversion
- Shear zones on margin of granite domes
- Fluid focusing in fault and conglomerate units
- Basin acting as a seal

**(iii) Metamorphic fluids in the Yilgarn: Source, timing and migration pathways**

- Metamorphic fluids removed from the crust within ~1 Myr
- Extensional deformation traps fluids
- Focused fluid sufficient for mineralisation

**(iv) Granite intrusions II: Coupled models of deformation, heat transport and magmatic/ metamorphic fluid production**

- Stress regimes around intrusions
- Relative significance of magmatic and metamorphic fluid
- Magmatic fluid overrides convection
- Creation of permeable pathways by thermal-fluid flow feedback

**(v) Kalgoorlie regional model: deformation and fluid flow patterns**

- Bardoc fault more active under E-W extension, Ida more active under E-W shortening
- Hydrofracturing driven by fluid production in a dome

**(vi) Laverton regional model: deformation and fluid flow patterns**

- Confirmation of field-based interpretation of stress regimes at time of mineralisation at Wallaby and Sunrise Dam

An overview of the key outcomes structured around the 5 questions is provided in Part III of the Final Report.

## Summary of Deliverable #12 Regional footprint maps of alteration and fluid flow based on geochemistry, ASTER, HYMAP

**Peter Neumayr (CET-UWA)**

Deliverable 12 contains a range of abstracts, data, reports and publications, and talks. It is emphasized here that the deliverables 10 and 13 also contain files which are equally pertinent to Deliverable 12, but have been filed in the respective folders.

In a range of Reports, the concept of alteration footprints is explained and the nature of the different alteration footprints characterized. A number of abstracts deal also with the translation of the alteration footprints into exploration using the concept that gold deposits commonly occur in places where the chemistry of the hydrothermal alteration changes both spatially and temporally.

The abstracts are supported by presentations which contain numerous images demonstrating the alteration footprints but also exploring the concepts to explain the different alteration footprints. In combination with Deliverable 10, which presents evidence for both the chemical and structural architecture in selected deposits, the presentations here explain the pathways, their chemical nature and the impact on regional footprints. As in the Reports, the presentations also aim to translate the alteration footprints into exploration targets. The presentations and abstracts are supported by spectral data in the data folder.

The publication and reports folder contains firstly three files with images and figure captions for the footprints in the Kanowna Belle, Wallaby and St Ives gold camps. Secondly, there is an in press paper for Mineralium Deposita which outlines the alteration footprints in the St Ives gold camp. Thirdly, there is a very detailed account of the geological setting and the alteration footprint in the St Ives gold camp which was published as a GSWA record for a field guide to the 2004 SEG excursion into the area.

Importantly, this Deliverable also contains a zip archive in the root directory authored by Goscombe. He took the alteration mineral mapping, as outlined in the posters

to the 5 answers, and mapped in his database the spatial distribution of the different mineral assemblages. This is a terrane scale attempt to map the different hydrothermal systems. See Deliverable 3 for more details.

A detailed report from Simon van der Wielen on an assessment of the utility of ASTER data to map hydrothermal footprints and a comparison with PIMA data is also provided in the Reports section of Deliverable 12. This Report focuses on the data rich area around Kanowna Belle. Targets have also been generated from these results – see Part II of this Final Report. Although, spatially and spectrally coarse ASTER mineral index maps highlight the same features as bottom of hole PIMA spectra and can provide regional framework. The most useful mineral index maps are Quartz (identifies silification), Phengite (identifies sericite alteration) and epidote-chlorite amphibole (identifies ultramafic lithologies).

Seismic reflection data can also map alteration and a short paper from Richard Chopping is provided in the Reports section of Deliverable 12. In the Laverton region, regional and mine-scale seismic data have been used to map out potential palaeo-fluid flow systems and provide details on the distribution of mineralisation in the Laverton region.

## Summary of Deliverable #13 Regional footprint maps of alteration and fluid flow based on geochemistry, ASTER, HYMAP

**John Walshe (CSIRO)**

Chemical gradients are modelled as interactions between 3 - end member fluids and fluid-rock reactions. The end-members fluids and gradients are defined from alteration mineralogy, fluid inclusions, stable isotopes and radiogenic isotopes as discussed in Part III of this Final Report. Relationships between alteration minerals and end-member fluids are illustrated in Figure 1.1

The study has significantly enhanced understanding of gradients in redox, pH, sulphur activity, water activity and salinity and the nature of the chemical species that sustained the chemical gradients.

- Redox gradients were sustained by reacting oxidised fluid species (sulphate and $SO_2$) with reduced fluid species ($CH_4$, $H_2$)
- The pH variation was possibly upwards of 5 to 6 units from ~ 3 – 4 (pyrophyllite/chloritoid/paragonite) to ~ 8 – 9 (albite/pyrrhotite). Gold is preferentially deposited in near neutral to alkaline environments.
- Release of excess HCl from deep-Earth fluids into aqueous ambient fluids generated acidic conditions
- Release of excess NaH from deep-Earth fluids into aqueous ambient fluids created ultra-alkaline conditions.
- Potential sulphur activity varied 3–4 orders of magnitude from ~ $10^{-3}$ to $10^{-4}$ m$\Sigma$S in distal settings in ambient fluids to ~ 1 m$\Sigma$S in proximal settings with albite/pyrrhotite stable.

In the Leviathan Complex, St Ives Gold Camp combined mapping of alteration mineralogy and isotopic variation has identified:

- upflow zones of anhydrous oxidized fluids ($CO_2$-$SO_2$) focused on porphyries
- lateral flow of oxidised aqueous fluid resulting from dispersion of $CO_2$-$SO_2$ - rich into the ambient aqueous fluids
- upflow and lateral flow zones of reduced fluid
- lithological partitioning of fluid flow

Domains of mixing of a "deep-earth" fluid ($H_2$ - NaH - HCl - $CH_4$ - $N_2$) with magmatic volatiles are considered to be most favourable for the formation of high grade gold deposits.

Domains of mixing of a "deep-Earth" fluid ($H_2$ - NaH - HCl - $CH_4$ - $N_2$) with aqueous crustal fluids led to acid alteration (paragonite-muscovite) and gold dispersion. A domain of acid alteration has been mapped in the hangingwall of the Kanowna Belle deposit.

District-scale domains of acidic alteration (paragonite, muscovite, chloritoid) identified in the Laverton district lead to the developed of a district-scale model of fluid interaction between "deep-Earth" fluid ($H_2$ - NaH - HCl - $CH_4$ - $N_2$) and ambient fluids to drive acid production. The key to exploration in the district is to identify the domains of mixing of magmatic volatiles with deep-Earth fluids with limited in-mixing of ambient fluids.

## Summary of Deliverable #14
## Reports on the integrated structural controls of ore shoots with the regional framework, linked to alteration and mineralogy (e.g., Wallaby, Sunrise, St Ives, KB)

**John Miller (CET-UWA)**

Three detailed reports (~100 pages each) are provided in Deliverable 14 from extensive new field work in the pits and underground at Wallaby, Sunrise Dam and the St Ives camp. Deliverable 14 also includes PowerPoint presentations (mostly by John Miller) made at site and at PDT meetings relevant to this deliverable.

New work at Wallaby showed established a new structural model for the Wallaby gold deposit. This is based on a structural mapping program done in conjunction with Leapfrog modelling of gold, rock types and alteration. FracSIS was used to compile the Leapfrog isosurfaces with existing mine data (development, grade shells, wire frames of ductile shears, faults, dykes etc) to produce a 3-D digital model that was used to target the mapping program. The report and three A0 sized plates cover key overprinting criteria, orientation data, as well as the structural controls on ore-shoot formation, the alteration assemblages associated with each phase of deformation and the results of limited gold assays from niche sampling of specific veins or alteration types.

The new Sunrise Dam report includes:

- A review of previous structural models
- A summary of key macro- to meso-scale structural features, overprinting criteria and kinematics, in conjunction with targeted microstructural work.
- An integrated series of structural observations with a 3-D Fracsis model.
- Use of Leapfrog arsenic isosurfaces to identify and link kinematics between the variably oriented high arsenic gold-bearing structures within the deposit.
- Use of data from the above points to undertake stress inversion, 3-D Mohr circle analysis and calculations of theoretical resolved shear stresses for different stress fields and stress shape ratios.
- Regional structural correlations with the Wallaby gold deposit, this has been used as in put to developing predictive targeting capabilities regionally.
- A revised structural evolution for the Sunrise Dam gold deposit.

The new St Ives work involved camp-scale structural field work and interpretation to provide a revised structural framework to integrate with camp-scale alteration footprint mapping (See Deliverables 10, 13) being done in Y4 (and previously in Y3).

The project involved:

- Creating a set of new 1:25000 and 1:15000 scale structural interpretation maps from Greater Victory to the Kambalda dome.
- Using FracSIS to compile gravity, magnetics, previous 2-D and 3-D structural interpretations and geology maps.
- Obtaining new kinematic data and integrating existing data (publications, pit maps and thesis work).
- Integrating the new kinematics at the 1:25000 and 1:15000 scale.
- A summary poster of the new findings at St Ives is also included.

Importantly a series of targeting recommendations were made and these may be found in Part II of this Final Report.

## Summary of Deliverable #15
## Report on reactive transport models tested against specific sites where paragenesis and structure understood

**James Cleverley (CSIRO)**

Deliverable 15 was completed under different ***pmd****CRC* projects. See the F6 and A3 Final Reports for more information on reactive transport.

The report by Chopping and Cleverley from F6 is included in this Final Report as it directly pertains to the 'generic' late basin and granite model (see Deliverable 11). The ***pmd****RT reactive transport (RT) modelling code, through its simulations of heat and fluid flow, and chemical

reactions, produces models of mineralogy that vary both spatially and temporally. These models of mineralogy can be used to produce physical property models and hence predict the geophysical response of the alteration system which has been simulated by the chosen reactive transport model.

The prediction of geophysical responses for geochemical simulations provides a new tool to explore, especially in undercover regions. The calculations are likely to be fast enough to be implemented directly in the RT modelling code, although currently they are utilised by calculating on completed RT model time steps. By using these methods on a simple reactive transport model, there is the potential to generate geophysical targets directly from geochemical simulations. These targets compare favourably with known mineralisation at the Victory-Defiance region of the St Ives Gold Mine.